

25  
2/17/89 JS (2)

DR# 0660-2

Bk 2

DOCUMENT NO. 87SDS4213  
DECEMBER 15, 1988



*GE Astro Space*

# FINAL SAFETY ANALYSIS REPORT FOR THE GALILEO MISSION

## VOLUME II (BOOK 2) ACCIDENT MODEL DOCUMENT - APPENDICES

GENERAL PURPOSE HEAT SOURCE  
RADIOISOTOPE THERMOELECTRIC GENERATOR  
PROGRAM  
CONTRACT DE-AC01-79ET32043

PREPARED FOR  
U.S. DEPARTMENT OF ENERGY

DO NOT MICROWAVE  
THIS PAGE

## **DISCLAIMER**

**This report was prepared as an account of work sponsored by an agency of the United States Government. Neither the United States Government nor any agency Thereof, nor any of their employees, makes any warranty, express or implied, or assumes any legal liability or responsibility for the accuracy, completeness, or usefulness of any information, apparatus, product, or process disclosed, or represents that its use would not infringe privately owned rights. Reference herein to any specific commercial product, process, or service by trade name, trademark, manufacturer, or otherwise does not necessarily constitute or imply its endorsement, recommendation, or favoring by the United States Government or any agency thereof. The views and opinions of authors expressed herein do not necessarily state or reflect those of the United States Government or any agency thereof.**

## **DISCLAIMER**

**Portions of this document may be illegible in electronic image products. Images are produced from the best available original document.**

# FINAL SAFETY ANALYSIS REPORT FOR THE GALILEO MISSION

## VOLUME II (BOOK 2) ACCIDENT MODEL DOCUMENT - APPENDICES

GENERAL PURPOSE HEAT SOURCE  
RADIOISOTOPE THERMOELECTRIC GENERATOR  
PROGRAM  
CONTRACT DE-AC01-79ET32043

PREPARED FOR  
U.S. DEPARTMENT OF ENERGY

ASTRO-SPACE DIVISION  
SPACECRAFT OPERATIONS  
Valley Forge Space Center  
P.O. Box 8555 Philadelphia, PA 19101



**MASTER**

JB

### DISCLAIMER

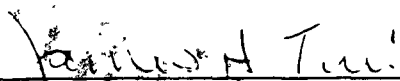
This report was prepared as an account of work sponsored by an agency of the United States Government. Neither the United States Government nor any agency thereof, nor any of their employees, makes any warranty, express or implied, or assumes any legal liability or responsibility for the accuracy, completeness, or usefulness of any information, apparatus, product, or process disclosed, or represents that its use would not infringe privately owned rights. Reference herein to any specific commercial product, process, or service by trade name, trademark, manufacturer, or otherwise does not necessarily constitute or imply its endorsement, recommendation, or favoring by the United States Government or any agency thereof. The views and opinions of authors expressed herein do not necessarily state or reflect those of the United States Government or any agency thereof.

This Final Safety Analysis Report was prepared by the General Electric Company under Contract De-AC01-79ET-32043 with the U.S. Department of Energy.

When Government drawings, specifications, or other data are used for any purpose other than in connection with a definitely Government-related procurement, the United States Government incurs no responsibility or any obligation whatsoever. The fact that the Government may have formulated or in any way supplied the said drawings, specifications, or other data, is not to be regarded by implication, or otherwise in any manner construed, as licensing the holder, or any other person or corporation; or as conveying any rights or permission to manufacture, use, or sell any patented invention that may in any way be related thereto.

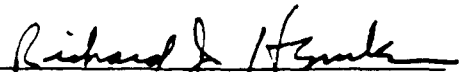
This report has been authored by a contractor of the United States Government. Accordingly, the United States Government retains a nonexclusive, royalty-free license to publish or reproduce the material contained herein, or allow others to do so, for the United States Government purposes.

This technical report has been approved for publication.



---

James A. Turi  
Director, Office of Special Applications  
U. S. Department of Energy



---

Richard J. Hemler  
Manager, RTG Programs  
General Electric Company

FINAL SAFETY ANALYSIS REPORT  
FOR THE  
GALILEO MISSION  
ACCIDENT MODEL DOCUMENT  
VOLUME II, BOOK 2

PREFACE

This section of the Accident Model Document (AMD) presents the appendices which describe the various analyses that have been conducted for use in the Galileo Final Safety Analysis Report II, Volume II. Included in these appendices are the approaches, techniques, conditions and assumptions used in the development of the analytical models plus the detailed results of the analyses. Also included in these appendices are summaries of the accidents and their associated probabilities and environment models taken from the Shuttle Data Book (NSTS-08116), plus summaries of the several segments of the recent GPHS safety test program. The information presented in these appendices is used in Section 3.0 of the AMD to develop the Failure/Abort Sequence Trees (FASTs) and to determine the fuel releases (source terms) resulting from the potential Space Shuttle/IUS accidents throughout the missions.

The Appendices contained in this Book are as follows:

- A. ACCIDENT DEFINITION AND PROBABILITIES
- B. ACCIDENT ENVIRONMENTS
- C. HYDROCODE ANALYSIS OF RTG RESPONSE TO ACCIDENT ENVIRONMENTS
- D. LAUNCH ACCIDENT SCENARIO EVALUATION PROGRAM (LASEP)
- E. JPL REENTRY BREAKUP ANALYSIS
- F. GPHS REENTRY RESPONSE - VEEGA CONDITIONS
- G. SAFETY TEST PROGRAM SUMMARY AND RESULT
- H. VAPORIZATION OF  $\text{PuO}_2$  IN A SPACE SHUTTLE FIREBALL
- I. RTG/GPHS REENTRY RESPONSE

BLANK

APPENDIX A  
ACCIDENT DEFINITION AND PROBABILITIES

The purpose of this appendix is to document the accident scenarios and failure probabilities defined by NASA for the Space Transportation System (the Shuttle Data Book NSTS-08116 and supporting documentation) and used in the Galileo Mission Final Safety Analysis Report, Version II (FSAR II). The version of NSTS-08116 used as reference is based on the recommendations, corrections, and changes provided by JPL to the 1 October 1987 release (Reference A-1) and the corrections and replacements to Reference A-1 provided also by JPL (Reference A-2) plus the recommended changes to the upper stage sections by Boeing (Reference A-3). Reference A-4 is the source of the failure probabilities used in this FSAR.

NASA utilized a systematic approach to identify the credible accident scenarios that might pose a threat to the RTGs. First, the Shuttle system was divided into the following seven elements:

- 1) Launch Support Equipment (LSE)
- 2) Payload
- 3) Orbiter
- 4) External Tank (ET)
- 5) Solid Rocket Boosters (SRB)
- 6) Space Shuttle Main Engines (SSME)
- 7) Range Safety System (RSS)

Each element was further divided into its major components, and these components were then subdivided until all known failure modes were identified. The approach used to develop the different accident scenarios was to divide the mission into phases and subphases as necessary. The phases were keyed to specific events that resulted in significant changes in vehicle configuration and/or in the potential consequences to the RTG. See Section 1.0 for a definition of the mission phases. After the phases were defined,



the accident scenarios for each phase were analyzed by developing detailed fault trees for each of the seven major systems as applicable. An examination of the accident scenarios thus developed revealed that, subsequent to some point in the sequence of the accident, irrespective of the initiating failure, many of the scenarios looked similar. This observation led to the concept of representative accident scenarios, which are presented in the following paragraphs. These descriptions are taken essentially verbatim from Reference A-2.

## A.1 ACCIDENT SCENARIOS

### A.1.1 ON PAD ACCIDENT SCENARIOS

Two accidents were chosen as representative of on-pad events during Phase 0: Pad Fire and Pad Explosion. Although the initiation of these two scenarios may be from the same source at any point in time, the potential sources vary and the potential threat increases with time as the propellant volume increases (the ET is full at T-4 hours, with only topping off continuing). For example, prior to SSME ignition at T-6 seconds, the LSE system is a source of initiation, with a component failure or auto-ignition from fretting or contamination causing a LOX/LH<sub>2</sub> leak. With SSME ignition at T-6 seconds, an aft compartment explosion becomes an alternative source.

#### A.1.1.1 Pad Fire Scenario, -8 Hours To 0 Seconds MET.

For the Pad Fire Scenario, an uncontrolled pad fire develops as a result of the initial leak of LOX/LH<sub>2</sub>, where the fire control system is unable to attenuate the fire. The pad fire, fed by the remaining LH<sub>2</sub> made available by the failure of the LH<sub>2</sub> ET tank due to thermal effects, develops into a fireball. Tanks containing onboard propellants burst as the propellants vaporize and/or decompose from the heat input. LOX and LH<sub>2</sub> from at least one set of burst PRSDS tanks pool on the aft bulkhead of the Orbiter and explode. The RTGs, in proximity to these tanks, are subjected to the blast and fragment environment from these tanks.

#### A.1.1.2 Pad Explosion, -8 Hours To 0 Seconds MET.

For this scenario, blast effects and fragments from initiating sources in the Orbiter or LSE would be sufficiently severe to rupture the 17-inch diameter (ID) LOX and LH<sub>2</sub> lines.

It is also hypothesized that these fragments may puncture the ET LH<sub>2</sub> tank. However, the blast effects and fragments from an aft compartment explosion are not expected to effect the RTG environment due to the separating bulkhead between the aft compartment and payload bay and the shielding afforded by the IUS.

Upon rupture of the LOX and LH<sub>2</sub> feed lines, significant propellant flow rates are expected due to the combination of the line size and head of liquid propellant. The liquids ignite as they flow toward the ground. However, a significant portion is expected to remain unburned due to the poor mixing taking place. These unburned propellants will pool in the trench and horizontal surfaces of the MLP. Impact with these surfaces will produce turbulence and mixing and thus promote the formation of an explosive mixture. At some point, an explosive reaction will take place. The blast wave, propagating from the origin of the explosion, travels up along the Orbiter. Due to the blast's intensity (pressure and impulse), the Orbiter's structural capability will be exceeded, particularly elements such as the payload bay doors. Structure torn loose by the blast may fly clear and impact the ground. Additional smaller explosions and fire fed by the remaining propellants continue.

#### A.1.2 NEAR-PAD ACCIDENT SCENARIOS

Near-pad accident scenarios which occur at, or shortly after, SRB ignition and concurrent tiedown release are more diverse compared to the previously discussed on-pad scenarios and include Tower Impact, Aft Compartment Explosion, SRB Case Rupture, and Inadvertent Range Destruct as discussed in the following subsections.

A.1.2.1 Tower Impact Scenario, After Failure During 0 to 2 S MET.

High fidelity Shuttle trajectory simulations with an animated display of the Orbiter stack with respect to its launch pad and launch area were utilized to study the consequences of SRB failures. In the event of an SRB Thrust Vector Control (TVC) actuator failure, adequate control is maintained by the remaining actuators to avoid a tower collision or ground impact for approximately 30 seconds, with adequate time for RSO destruct before impact.

For right SRB nozzle burnthroughs, the simulations indicate that these failures will result in vehicle breakup during early ascent (see Section A.1.2.2). However, for a left SRB loss of thrust or nozzle burnthrough prior to an MET of 2 seconds, the Orbiter stack will subsequently impact the launch tower within a MET of 7 seconds.

Upon failure of the left SRB prior to 2 seconds, tower impact, expected before 7 seconds, would cause the ET to rupture. After the impact, the system may be configured with the Orbiter and ET connected and the right SRB breaking free. It is more probable that all structural connections between the elements of the stack will fail. The elements will continue to tend to move in their preimpact direction due to their original momentum, eventually falling back to the ground.

The rupture of the ET allows propellant to flow toward the ground. As with the on-pad explosion scenario, although the propellants ignite, a significant portion is expected to remain unburned due to poor mixing. Pooling of the unburned propellants after impacting horizontal surfaces promotes the formation of an explosive mixture. Unlike the on-pad event, the Orbiter's location with respect to the explosion source is not well defined since the Orbiter's response after the impact is not well known.

Structures torn loose by the blast wave may fly clear and impact the ground. Additional smaller explosions and fire, fed by the remaining propellants, continue.

A.1.2.2 Aft Compartment Explosion Scenario, 0 To 10 S MET.

As described in Section A.1, rupture of 17-inch ID LOX and LH<sub>2</sub> lines, plus a possible puncture of the ET, can be anticipated as a result of an SSME propulsion system failure and ensuing aft compartment explosion. The details of this scenario continue to parallel those of the on-pad event, except that:

- a) The Orbiter stack continues its ascent due to SRB thrust until the blast wave from the explosion originating in the pool formed on the ground breaks up the Orbiter.
- b) Both SRBs continue ascent until RSS destruct if the flight duration after the initiating event is long enough (estimated at 10 s).

Flight dynamics analyses by MSFC has indicated that total loss of flight control due to SRB thrust disruption during the early mission phases will result in Orbiter breakup due to aerodynamic and/or dynamic forces. It is expected that this breakup will cause failure of the Orbiter/ET MPS interface, thereby releasing LOX and LH<sub>2</sub> through the 17-inch feed lines. The rate of propellant released should be comparable to the aft compartment explosion. Therefore, the aft compartment explosion environment is also used for vehicle breakup for 0 to 10 seconds MET.

A.1.2.3 SRB Case Rupture Scenario, 0 To 10 S MET.

In addition to TVC actuator failure and nozzle burnthrough, an SRB case rupture is a credible event as evidenced by documented failures. When the case ruptures, fragments of the rocket motor impact the adjacent ET and Shuttle structure, causing their complete failure. Further, these impacts induce motions perpendicular to the nominal flight motion, thus resulting in a lateral dispersal of Orbiter elements along the line of flight.

A massive dump of LOX and LH<sub>2</sub> occurs, with the unburned cryogenics pooling in the trench and on other horizontal surfaces. The turbulence which results from impacting these surfaces promotes mixing, finally leading to an explosive reaction. As the blast wave propagates from the origin of the explosion, intact structure is subjected to the blast's intensity. Secondary explosions, fire fed by the remaining propellants, and chunks of solid rocket propellant characterize the area in which Orbiter elements (including the payload) may impact.

Fragments from the rupturing SRB are not expected to severely damage the opposite SRB due to the shielding of the ET and its propellants. Therefore, the remaining SRB will continue to fly until extinction or range destruct action is taken.

#### A.1.2.4 Inadvertent Range Destruct Scenario, 0 To 10 S MET.

This scenario assumes that the linear shaped charges (LSC) on both SRBs and the ET inadvertently detonate. Unlike the SRB case rupture scenario, this causes fragmentation of the upper segments of both SRBs as well as the ET. The aft segments (that have no LSC) of both SRBs will fall back to the ground.

A massive dump of LOX and LH<sub>2</sub> occurs, with the unburned cryogenics pooling in the trench and on other horizontal surfaces. The turbulence which results from impacting these surfaces promotes mixing, finally leading to an explosive reaction. Structure which had survived after the fragmentation of the upper segments of both SRBs is now subjected to the blast's intensity. Secondary explosions, fire fed by the remaining propellants, and chunks of solid rocket propellant characterize the area in which Orbiter elements (including the payload) may impact.

### A.1.3 IN-FLIGHT REPRESENTATIVE SCENARIOS.

Many of the failures which initiate near-pad accident scenarios are also sources for in-flight events. However, even though this may be the case, the sequence and primary energy releasing phenomena associated with the in-flight case may differ significantly from its near-pad counterpart.

#### A.1.3.1 SRB Case Rupture Scenario, 10 To 128 S MET.

If a SRB case ruptures, fragments of the rocket motor impact the adjacent ET and Shuttle structure, causing their complete failure. Fragments from the rupturing SRB are not expected to severely damage the opposite SRB due to the shielding by the ETs intervening structure and propellants. Therefore, the remaining SRB will continue to fly until extinction or range destruct action is taken. The impact of the SRB fragments induces motions perpendicular to the nominal flight motion and consequently a lateral dispersal of Orbiter elements along the flight path. Likewise, this also promotes dispersal of the LOX and LH<sub>2</sub> and thus minimizes any vapor cloud explosion. Because the propellants tend to be so spread out, a trailing fire is more probable.

Simulations suggest that, when this accident scenario occurs during MET less than or equal to 17 seconds, debris would impact within the bounds of the land mass in the vicinity of Cape Canaveral. For MET greater than 17 seconds, impact is over water.

#### A.1.3.2 Range Destruct Scenario, 10 To 128 S MET.

Several potential failures, most notably an aft compartment explosion, preclude an intact or contingency abort. For this situation, it will be incumbent on the Range Safety Officer to take action. Range destruct would fire the linear shaped charges on both SRBs and the ET. This results in complete failure of the Orbiter by fragments from the upper SRB segments and the ET. The aft SRB segments (no LSC) remain intact, impacting within the

land mass bounds for a MET less than 17 seconds, and on water for an MET greater than 17 seconds, with an impact velocity in the order of 300 to 500 ft/sec. As with the SRB case rupture, the fragment impacts induce lateral dispersal of Orbiter elements as well as LOX and LH<sub>2</sub>. This minimizes the potential for a vapor cloud explosion. Since the propellants have been so dispersed, a trailing fire is more probable. This scenario is also applicable to an inadvertent range destruct.

A.1.3.3 In-Flight Breakup Scenario, 10 To 30 S MET.

Although an initial structural failure of the ET may be relatively small, catastrophic structural failure of the ET may quickly ensue due to small local explosions and aerodynamic loads. The massive dump of LOX and LH<sub>2</sub> during this portion of the flight regime will most probably result in a hydrogen/air vapor cloud explosion since the reactants can adequately mix to form a continuum which can propagate an explosive reaction, as contrasted with the dispersed situation in the SRB case rupture scenario. As the blast wave propagates from the origin of the explosion, the Orbiter's structure is subjected to the blast's intensity, causing breakup and subsequent ground impact.

A.1.3.4 In-Flight Breakup Scenario, 30 To 128 S MET.

Although this scenario initiates in the same manner as the 10 to 30 second scenario, the massive dump of LOX and LH<sub>2</sub> results in a trailing fire with small, local explosions as in the 51-L accident. Structural breakup of the Orbiter does occur as a result of both hydrodynamic interaction with the LOX and LH<sub>2</sub> and aerodynamic effects during this flight regime. The impact point is in water.

A.1.3.5 In-Flight Breakup Scenario, 128 S To MECO MET.

Although initiated in the same manner as the 10 to 30 second scenario, and characterized by a trailing fire with small local explosions as a consequence of the propellant dump as with the 30 to 128 second scenario, the Orbiter's structural response may take three forms:

- a) Immediate breakup followed by reentry with aerodynamic heating of structural elements.
- b) Out of control reentry, at conditions which vary depending on time of event.
- c) Minimal failure which allows controlled reentry, but which could result in an Orbiter ditch or crash landing.

Several important parameters differ for this in-flight case compared to earlier ones:

- a) Shock wave intensities are negligible at these altitudes.
- b) Aerodynamic loads are small in this flight regime, although an out-of-control Orbiter would be subjected to severe aerodynamic loading upon reentry into the atmosphere.

A.1.4 ON-ORBIT REPRESENTATIVE SCENARIOS.

Uncontrolled Orbiter reentry is the representative scenario chosen for the on-orbit phase.

A.1.5 PAYLOAD DEPLOY REPRESENTATIVE SCENARIOS.

Upper-stage and/or spacecraft reentry is representative of the scenarios which may occur during the IUS free-flight phase of the mission.



#### A.1.6 RETURN WITH PAYLOAD REPRESENTATIVE SCENARIOS

The abort crash scenario is representative of events which may occur during return with payload during the launch and second stage phases of the mission.

#### A.2 ACCIDENT PROBABILITIES

NASA has developed a set of failure probabilities for the accident scenarios defined in the Shuttle Data Book, NSTS-08116, as described in Section A.1 of this appendix. The probability values provided are deemed by NASA to be conservative engineering estimates provided to the Department of Energy for the purpose of the analysis for this FSAR. NASA states that "we believe that, as a result of the extensive redesign and changes made to the Space Shuttle since STS 51-L and the accompanying management, process, checkout, procedural, and oversight improvements, the reliability of the Space Shuttle is significantly higher than is indicated by the midpoint of the range of failure probability estimates" which were provided to DOE. The NASA provided probabilities are based on previous studies and historical data for systems representative of those used on the Shuttle. The previous and current studies that have been used in developing the probabilities include those by the J.H. Wiggins Co. and Acta, Inc. pertaining to STS failure probabilities, range safety hazards analysis and STS/IUS/GLL spacecraft failure probabilities all of which relied extensively on the results of the Rasmussen reactor safety study (WASH-1400). Others include the STS/Centaur draft Safety Evaluation Report (SER) prepared by the Interagency Nuclear Safety Review Panel (INSRP) in preparation for the flight safety approval for the Galileo and Ulysses missions around the time of the Challenger accident and the NASA-JSC/Boeing fault tree study in support of JSCs Safety Division and the GPHS-RTG (Galileo and Ulysses missions) safety analysis requirements. This ongoing study is currently based on FMEA/CILs, hazards reports, engineering studies, OMRSD/OMI, limited life lists, and PRACA/failure reports. Other data sources include the SRM industry group report on the history and potential of SRMs for use as reliable space boosters, the Lockheed PRA on the Shuttle main propulsion pressurization system, and the Eastern Space and Missile Command's (ESMC) data base on solid and liquid booster failures.

The probability values presented in the following paragraphs are currently under review by NASA Headquarters. Based on the background and approach used in developing the probability numbers and based also on historical launch vehicle data, the values presented appear to be as reasonable as can be expected for the FSAR application.

○ SRB Failures (Case Rupture and Loss of Thrust)

50%	0-10 Sec*
25%	10 - 30 Sec*
25%	30 Sec - End of Burn * @

\* Failure rate is assumed constant within the time interval.

@ Between 120 and 128 sec., chamber pressure is rapidly decreasing. Therefore probability is assumed to be zero.

○ Other Failures

Constant rate throughout the phase

○ Range safety applies from T-6 sec to T+ 260 sec

○ Dual engine shutdown to abort landing applies from liftoff to 425 sec (1 engine TAL)

Table A-1 presents the failure probabilities for each of the accident scenarios by mission phase. Tables A-2 and A-6 give the system failure to accident scenario relations for Phases OB and 1 combined and for Phase 2, respectively.

A.2.1 SPACE SHUTTLE ACCIDENT PROBABILITIES

The following probability summary is given for the mission through deployment of the IUS/spacecraft per Reference A-4.

<u>PHASE (Time Period)</u>	Probability x 10 <sup>4</sup>	
	<u>Minimum</u>	<u>Maximum</u>
Prélaunch (T-8 hrs to T-6 sec)	0.5	5.0
Powered Flight (T-6 sec to T+532 sec)		
Orbiter	1.0	10
External Tank	.08	0.8
Space Shuttle Main Engines	5.2	52
Solid Rocket Boosters	12	120
Payload	0.1	1.0
Range Safety	.01	0.1
MECO to Payload Deploy (T+532 sec to payload deploy)	0.5	5.0
Abort Crash/Ditch (SSME multiple shutdown)	0.8	8.0

The groundrules for phase/subphase probabilities are as follows:

Tables A-3 through A-5 give the subphase failure probability distributions for Range Destruct, SRB Case Rupture, and Vehicle Breakup, respectively.

A.2.2 IUS ACCIDENT PROBABILITIES

The failure probabilities for the IUS on the Galileo Mission are presented in detail in Section 14.0 of the Shuttle Data Book. Failures that can occur prior to deployment of the IUS from the Orbiter have been included in the Payload failures through Phase 3 in the previous section (A.2.1) for the Space Shuttle. The failure probabilities presented in this section are applicable only to those failures that can occur after the IUS with spacecraft is free-flying in Earth orbit. The probability summary for these failures is as follows:

<u>FAILURE</u>	Probability x 10 <sup>4</sup>	
	<u>TOTAL</u>	<u>PRIOR TO EARTH ESCAPE</u>
1) Motor or avionics failure resulting in no ignition, loss of thrust, or guidance error	96.29	82.88
2) Motor case burst	1.64	1.30*
3) Motor burn through	<u>1.64</u>	<u>1.30*</u>
TOTALS	99.57	85.48

\*Failure Proportion

SRM - 1	59.4%
SRM - 2	40.6%

Those failures in Category 1) above that result in no ignition, loss of thrust, or guidance errors have been analyzed to determine their effect on the subsequent trajectories of the IUS and/or spacecraft as given in Section 11.0 of the Shuttle Data Book. The majority of these result in reentry into the Earth's atmosphere. Table A-7 presents the results of that analysis which gives the types of reentries that can occur. In addition, some of these failures that can occur result in the IUS and spacecraft escaping the Earth's gravitational influence and then going into a solar orbit. The total probability of escape resulting from these failures is  $1341 \times 10^{-6}$ .

A.3 REFERENCES

- A-1 Letter from M. Joseph Cork (JPL) to Robert H. Brown (JSC) dated March 14, 1988, Subject: Corrections to NSTS 08116, 1 October 1987 Release, and Replacements to Section 5.2 and Section 6, 230-MJC-88-023.
- A-2 Letter from M. Joseph Cork (JPL) to Robert H. Brown (JSC) dated January 8, 1988, Subject: Recommendations, Corrections and changes to NSTS 08116, 1 October 1987, Release, 2130-MJC-88-005.
- A-3 Letter from T. E. Jolley, Boeing, to R. H. Brown (JSC), Subject: Recommended changes to the Upper Stage Sections of NSTS 08116, 1 October 1987 Release, 2-3948-3088-013.
- A-4 Letter from L. A. Fisk, Associate Administrator for Space Science and Applications, NASA, to Dr. Delbert Bunch, Principal Deputy Assistant Secretary for Nuclear Energy, DOE, with enclosure, dated 13 July 1988.

Table A-1. Mission Phase/Scenario Probability Summary

Probability x 10<sup>4</sup>

Mission Phase Accident Scenario	0A T-8 Hr. To T-6S	0B/1 T-6S To T+128S	2 T+128S To T+532S	3 STS On Orbit	4 IUS Deploy To Escape	5 Abort**
Pad Fire/* Explosion	0.5/5	.067/ .67				
Tower Impact		.65/ 6.5				
SRB Case Rupture		3.24/ 32.4				
Range Destruct		.005/ .05				
Vehicle Breakup		9.642/ 96.42	4.786/ 47.86			
Uncontrolled Orbiter Entry				0.5/5		
Crash Landing		.012/ .12	.028/ .28			
Ocean Ditch		.228/ 2.28	.532/ 5.32			
IUS Failure and Entry					82.9	
IUS Case Burnthrough					1.3	
IUS Case Burst					1.3	

\* Apportion Equally between fire and explosion scenarios.

\*\* Entries for abort/phase are sum of entries for phases 0B/1 and 2, where initial failures may occur. These are not separate failures.

Table A-2. Phase OB and 1 System Failure to Accident Scenario Mapping  
Probability x 10<sup>4</sup>

	Orbiter	External Tank	SSME		SRB Left Loss Of Thrust			SRB Right Loss Of Thrust			Payload	Range Safety
			Explosion	Multiple Shutdown	No Ignition	Case Rupture	No Ignition	Case Rupture				
Pad Fire/Explosion	.01/ .1		.057/ .57									
Tower Impact					.24/ 2.4	.41/ 4.1						
SRB Case Rupture							1.62/ 16.2		1.62/ 16.2			
Range Destruct											.005/ .05	
Vehicle Breakup	.24/ 2.4	.02/ .2	1.248/ 12.48			3.73/ 37.3		.24/ 2.4	4.15/ 41.5	.024/ .24		
Uncontrolled Orbiter Entry												
Crash Landing				.012/ 0.12								
Ocean Ditch				.228/ 2.28								

REPRODUCED FROM  
BEST AVAILABLE COPY



Table A-3. Range Destruct Subphase Distribution for Phases OB and 1  
Probability x 10<sup>4</sup>

System Range Destruct (Phase OB and 1)	Launch Support Equip	Orbiter	External Tank	SSME		SRB Left			SRB Right			Payload	Range Safety
				Explosion	Multiple Shutdown	No Ignition	Loss Of Thrust	Case Rupture	No Ignition	Loss Of Thrust	Case Rupture		
Inadv. Range Destruct -6 - OS													.00002
Inadv. Range 0 - 10													.00037
Range Destruct 10 - 1285													.0044

NOTE: Upper end of Probability Range is obtained by multiplying the lower end values provided in this table by 10.

Table A-4. SRB Case Rupture Subphase Distribution for Phase 1  
Probability x 10<sup>4</sup>

System SRB Case Rupture (Phase 0B and 1)	Launch Support Equip	Orbiter	External Tank	SSME		No Ignition	SRB Left Loss Of Thrust		No Ignition	SRB Right Loss Of Thrust		Payload	Range Safety
				Explosion	Multiple Shutdown		Case Rupture	Case Rupture					
SRB Case Rupture 0 - 10S								.81			.81		
SRB Case Rupture 10 - 20S								.2025			.2025		
SRB Case Rupture 20 - 70S								.3825			.3825		
SRB Case Rupture 70 - 105S								.1575			.1575		
SRB Case Rupture 105 - 120S								.0675			.0675		
SRB Case Rupture 120 - 128S								0			0		

NOTE: Upper end of Probability Range is obtained by multiplying the lower end values provided in this table by 10.

Table A-5. Vehicle Breakup Subphase Distribution for Phase 1  
Probability x 10<sup>4</sup>

System Vehicle Breakup (Phase 0B and 1)	Launch Support Equip	Orbiter	External Tank	SSME		SRB Left			SRB Right			Payload	Range Safety
				Explosion	Multiple Shutdown	No Ignition	Loss Of Thrust	Case Rupture	No Ignition	Loss Of Thrust	Case Rupture		
Aft Comp. Ev. & Breakup 0 - 10S		.019	.002	.096			1.65		.24	2.07		.002	
Inflight Breakup 10 - 30S		.037	.003	.195			1.04			1.04		.004	
Inflight Breakup 30 - 128S		.184	.015	.957			1.04			1.04		.018	

NOTE: Upper end of Probability Range is obtained by multiplying the lower end values provided in this table by 10.

Table A-6. Phase 2 System Failure to Accident Scenario Mapping  
Probability x 10<sup>4</sup>

Field System Accident Scenario	Launch Support Equip	Orbiter	External Tank	SSME		SRB Left Loss Of Thrust			SRB Right Loss Of Thrust			Payload	Range Safety
				Explosion	Multiple Shutdown	No Ignition	Case Rupture	No Ignition	Case Rupture				
Pad Fire/Explosion													
Tower Impact													
SRB Case Rupture													
Range Destruct													
Vehicle Breakup		0.75/ 7.5	.06/ 0.6	3.895/ 38.95								.076/ 0.76	.005/ .05
Uncontrolled Orbiter Entry													
Crash Landing					0.28/ 2.8								
Ocean Ditch					0.532/ 5.32								

Table A-7. Errant Upper Stage Summary, Galileo Mission

<u>Failure Mode</u> Resulting Orbit	Configuration	Total <sup>(2)</sup> Probability x 10 <sup>6</sup>
<u>No Ignition</u>		
Orbit Decay, Circular	S/C + Stages 1 & 2	10
Orbit Decay, Elliptical <sup>(1)</sup>	S/C	600
<u>Incomplete/Low Impulse</u>		
Orbit Decay	S/C	883
<u>Tumbling</u>		
Orbit Decay	S/C	2063
<u>Erratic Burns</u>		
Orbit Decay	S/C	1575
Delayed	S/C	707
Prompt	S/C + Stage 2**	66
Powered		
Burn 1	S/C + Stages 1 & 2	0
Coast 1	S/C + Stages 1 & 2*	528
Burn 2	S/C + Stage 2	53
<u>Stable Misaligned Burns</u>		
Orbit Decay	S/C	501
Delayed	S/C	562
Prompt	S/C + Stage 2	238
Powered		
Burn 1	S/C + Stages 1 & 2	0
Coast 1	S/C + Stages 1 & 2*	449
Burn 2	S/C + Stage 2	53

(1) Continued staging assumed via IUS mission sequence software with nominal subsequent burns and spacecraft separation.

(2) Additional failures can occur in each of the modes that result in escape from Earth (i.e., no reentry) with a combined probability of  $1341 \times 10^{-6}$ .

\*Stage 1 Empty  
\*\*Stage 2 Empty

APPENDIX B  
ACCIDENT ENVIRONMENTS

This appendix presents a summary of the accident environments defined in the October 1, 1987, release of the Shuttle Data Book, NSTS-08116 including subsequent proposed changes thereto (see References A-1 through A-3 in Appendix A). The accidents and associated environments included are listing in Table B-1.

B.1 SHOCK WAVE ENVIRONMENTS FOR SHUTTLE FAILURES

In order for the response of structures and objects in the path of a blast wave to be analyzed, the wave must be characterized by specifying not only its peak static overpressure and static overpressure impulse but also its peak reflected pressure, dynamic pressure, and dynamic pressure impulse. In addition, the shape of the blast pulse is important for performing loading estimates in the near field where the blast intensity is very high. The Liquid Propellant Blast Hazards Program (Project PYRO, Reference B-1) represents the only large body of experimental data from LOX/LH<sub>2</sub> spill explosions using quantities greater than laboratory amounts. However, the blast measurements made were not intended to provide the complete free-field characteristics that are necessary for predicting near-field blast loading. A current experimental effort being undertaken by NASA (Reference B-2) eventually is intended to provide appropriate blast loading data. Until such experimental data are available, analysis, matched to the most pertinent existing data (PYRO and other), is the approach that has been used by NASA. Thus, analytical approaches (Reference B-3) were used to estimate free-field blast characteristics for above-ground pools of spilled propellants and for in-flight vapor clouds. The blast loading parameters are discussed below for reference.

Static Overpressure is defined as the transient incident pressure, exceeding the ambient pressure, which occurs in the blast pulse from an explosion. The variation of the overpressure with time at a fixed close-in spatial position depends on the nature of the energy release of the explosion, the distance from the explosion, and the medium through which the blast wave has traveled. The peak overpressure at a point in space is the maximum value sensed at that location and is generally experienced at the instant the blast front just passes the location.

Static Overpressure Impulse is defined as the integral of the static overpressure with respect to time, where the integration extends over the interval between the time of arrival of the blast front to the time at which the overpressure returns to zero at the fixed spatial location. The time profile of the static overpressure pulse is very important because it determines the profile for loading via the parameters discussed below.

Peak Reflected Pressure is defined as the amplitude of the reflected blast wave front that would result after impingement of the front with a rigid surface placed normal to the direction of blast front travel. The impingement of the blast front with a body of finite dimensions will produce a transitory reflection pressure with the peak value occurring at the leading stagnation point. The reflection pressure that the body feels diminishes as the front passes over the body. The peak amplitude and the time history of the reflection pressure determine the diffracted-flow phase of blast loading. Since the peak reflected pressure can be quite high, the diffraction phase controls deformation and initial acceleration of the body if it is free to move.

Dynamic Pressure is defined as half the product of the density and the square of the velocity of the convective flow behind the blast front. For locations close to the explosion source, the convective flow may contain combustion products as well as air and unburned reactants. Peak dynamic pressure occurs just behind the front and decays with distance behind the front.

Dynamic Pressure Impulse is defined as the integral of the dynamic pressure with respect to time over the period from front arrival to the complete passage of the blast pulse past a fixed spatial location. Peak dynamic pressure and dynamic pressure impulse control the drag phase of blast loading and largely determine the final velocity of a body if it is free to move.

### B.1.1 ET PROPELLANT NEAR-PAD EXPLOSIONS

This section characterizes the blast wave which would emanate from a chemical explosion of the ET LOX/LH<sub>2</sub> propellants which are spilled, collected, and mixed for near-pad accidents as described in Appendix A, Sections A.1.1 and A.1.2. These environments are specified in tabular format for four percentile levels of increasing severity, 50%, 10%, 1% and 0.1% for each of several specified distances above the surface of the MLP or trench as appropriate in the respective sections below.

#### B.1.1.1 SRB-Failure-Initiated Breakup or Tower Impact. MET: 0 < T < 10

This class of accident supposes that the ET is grossly ruptured in early times such that LO<sub>2</sub>/LH<sub>2</sub> spills massively toward the pad in bulk free-fall, mixing and collecting temporarily on the MLP or in the flame trench with equal probability. Operating booster engines (either SSME or SRM) assure abundant ignition sources. The blast environments for on-pad and in-trench explosions are specified in Tables B-2 and B-3 respectively. Note that the trench is about 90 feet below the MLP. The MLP provides a substantial intervening structure between the Orbiter stack and the trench for which no allowance is made in the specified blast environments.

#### B.1.1.2 Aft-Compartment-Initiated Explosions. MET: -6 < T < 10

This class of accident is postulated to occur due to an explosion in the Orbiter aft compartment causing LO<sub>2</sub> and LH<sub>2</sub> MPS feed lines to rupture, resulting in significant propellant flow to the MLP (trench collection is assumed to be



nil). This event is treated as a variation of the on-pad explosion. In this case the pool depth is generally less than for the massive ET rupture because of the reduced bulk of propellant available from the ruptured feed lines. The explosion environment is specified in Table B-4.

## B.1.2 ET PROPELLANT IN-FLIGHT EXPLOSIONS

### B.1.2.1 Structural Breakup. MET: 10 < T < 30

This class of accident is postulated to occur after a rapid breakup of the ET due to a massive structural failure (similar to STS 51-L) as described in Appendix A, Section A.1.3.3. It is further supposed that the lower air-stream dynamic pressure and higher ambient pressure (relative to 51-L) would cause less rapid dispersion of the hydrogen. The higher ambient pressure also assures a greater concentration of atmospheric oxygen. Thus, a flammable vapor cloud of gaseous hydrogen and air is presumed possible as described in Reference B-3. The explosion environment as a function of distance from the center of explosion is specified in Table B-5. Thermochemical calculations indicate that the severity of the blast does not increase by more than about 28% even with only ET LO<sub>2</sub> participating in the reaction stoichiometrically.

### B.1.2.2 Structural Breakup. MET: 30 < T < MECO

During this period, the flight dynamic pressure (q) through 73 seconds is similar to 51-L, while beyond 73 seconds, the q rapidly decreases, but so does the atmospheric oxygen. Thus, the explosion threat is considered to be nil.

## B.1.3 AUXILIARY PROPELLANT EXPLOSION AND FRAGMENTS.

### B.1.3.1 Caused by Fire

For this case of auxiliary propellant explosion hazards, the propellant tank failure is assumed caused by a fire from some source external to the tank.

STS auxiliary propellants are required for the Orbital Maneuvering Subsystem (OMS), the Aft Reaction Control Subsystem (ARCS), the Power Reactants Storage and Distribution Subsystem (PRSDS), and the Auxiliary Power Units (APU). The forward RCS is remote from the RTGs and is shielded from them by the Orbiter forward section; therefore, it is not considered to be a threat.

Propellant tanks are also carried aboard Galileo for retropropulsion and the IUS upper-stage booster. In addition, gaseous helium is used in two storage tanks at 2853 psi as pressurant gas for the RPM propellant tanks. Data on all tanks are listed in Table B-6. The location of the STS tanks is shown in Figure 1.10, the Galileo tanks in Figures 13.1 and 13.9, and the IUS tank in Figure 8.8 (Tank No. 2) of the Shuttle Data Book.

Hydrazine/Monomethylhydrazine Explosions. Significant explosions from bipropellant MMH or  $N_2H_4$ -NTO mixing as a result of fires are not considered to be credible; however, thermal explosions from rapid decomposition of heated MMH and  $N_2H_4$  are possible. NASA has assumed that external heating causes formation of propellant vapor and decomposition of the vapor in the propellant tank. The pressure rise due to the vapor formation and its decomposition has been assumed to cause tank failure at the rated burst pressure. Also the relief valves have been assumed to fail to function and the tanks rupture at their burst pressure. From the source pressure and volume driving the tank rupture, the airblast amplitude is estimated at the RTG location as shown in Table B-7.

PRSDS Explosions. Explosion overpressures from the PRSDS tank are estimated based on spilling the  $O_2$  and  $H_2$  reactants from one pair of failed tanks onto the cargo-bay walls and structure. The cryogen blast environment estimates are developed using the pool explosion data from Reference B-3, assuming a precursor fire is present. The airblast environments at the RTG location are shown in Table B-7.

The simultaneous failure of the PRSDS O<sub>2</sub> and H<sub>2</sub> tanks caused by fire is an unlikely event. The O<sub>2</sub> and H<sub>2</sub> tanks are separated from one another by the frames of the cargo bay. In some cases, the tanks are on opposite sides of the bay.

Fragment Specifications. Fragment velocities are estimated for the burst-pressure failure of the MMH and N<sub>2</sub>H<sub>4</sub> tanks. The PRSDS tanks are not considered to be fragment sources since they are double walled. Table B-7 shows the MMH and N<sub>2</sub>H<sub>4</sub> tank fragment velocities.

For these estimates, the tank failure occurs at the rated tank burst pressure. Because a propellant tank may be damaged during a fire, tank failure at a pressure below the burst pressure may occur, in which case the fragment velocity will also be reduced.

He Tank Burst. Thermal analysis by NASA indicates that under high enough thermal input the helium tanks will burst at about 3500 psi at a time when bulk temperatures of the tank wall and helium gas have reached about 370 degrees F. Blast and fragment characteristics for individual tank failures of this type are shown in Table B-6. The burst pressure of 3500 psi is reduced from the design value of 4716 due to the elevated tank wall temperature.

It should be noted, depending upon the actual rate of thermal input to the tanks, that many minutes may be required to reach the burst pressure. During this time, depletion of the thermal source or failure of lines from the tanks may preclude reaching the burst pressure.

#### B.1.3.2 Caused By Crash

Crash Environments. Certain propellant tanks may pose a threat to an RTG in a crash situation. The impact environment experienced by each tank of interest has been estimated by NASA (similarly as given in Section 6 of the Shuttle Data Book) and is listed in Table B-8.

Tank Rupture. Calculations based on elastic versus plastic tank material failure were also performed by NASA to determine which conditions of crash environment and tank usage are likely to cause rupture. The results are shown in Figure B-1.

Explosion. The only auxiliary propellant explosion caused by crash that is a credible hazard to the RTGs is from the potential rupture of PRSDS tankage. Considering the probable dispersion of the  $LH_2/LO_2$  from tank ruptures during a crash, the most likely explosion is a vapor  $H_2/O_2$ /air detonation. Since the RTG would be located within the reacting mixture, a blast environment equivalent to that inside the reaction volume for the in-flight vapor cloud (Table B-5) would apply.

## B.2 SRB AND ORBITER FRAGMENT ENVIRONMENTS

This section represents the fragment environments to which the Galileo RTGs may be subjected as a result of potential explosions of the STS SRBs or ET propellants or of aerodynamic breakup. These environments describe impact either of the fragments upon the RTGs or of the RTGs or pieces of the RTGs upon the fragments.

Fragments are expected to interact with the RTGs in two ways. First, flat flyer plates could impact an RTG and impart momentum directly to it but are unlikely to act as penetrators. Flyer plates are assumed to be thin flat objects, such as portions of the Orbiter skin.

The second class of fragments are the objects which may be termed shrapnel and have the necessary attributes of density, shape, and structural strength to act as penetrators. These objects (bolts, struts, and transformers inside electronic boxes) may, however, act as flyer plates depending upon their orientation upon impact with an RTG. As a general rule, an explosion or breakup of high-pressure vessels is required to produce shrapnel, since the

necessary acceleration requires the large static or dynamic pressure associated with a blast wave.

Fragment environments may be generated by rupture of an SRB (either accidentally or by RSO command destruct), aerodynamic breakup of the Orbiter (as in the STS 51-L accident), or as a result of an LOX/LH<sub>2</sub> or other propellant explosion. A separate model for each of these fragment environments is presented in this section. The size, velocity, and directional distributions of fragments resulting from an SRB rupture discussed here are based upon analysis of films of the command destruct of SRBs resulting from the Challenger (STS 51-L) and the Titan 34D-9 accidents supplemented by hydrocode calculations and analytical modeling. The SRB environment is presented in a Monte Carlo methodology format because of the complexity of the SRB breakup process and the large number of variables involved.

#### B.2.1 SRB FRAGMENT MODEL

The position of the RTGs for Galileo are such that SRB case wall fragments, joint fragments, and clevis pins could present a hazard to RTGs. The fragment environments presented here are either an RSO destruct or a random failure.

Specification of fragment size and trajectory distributions is given below for each of these possibilities in Sections B.2.1.1 and B.2.1.2 for both large and small fragments. Small fragments consists of pieces of joints and clevis pins; large fragments are pieces of case wall which may or may not have joints attached. The effect of intervening Orbiter structure on fragment velocities is specified in Section B.2.1.3.

A simplified SRB cylinder nomenclature has been adopted and is presented in Figure B-2; Figure B-3 specifies SRB and Shuttle coordinate systems. Both of these specifications are used throughout Section B.2.1.

### B.2.1.1 RSS Destruct Model

#### B.2.1.1.1 Fragment Size, Location, and Mass

Large Fragment Reference. The statistical distribution of SRB fragment size and location data are assumed to be identical to those observed for the Titan 34D-9 RSS destruct case. Large fragments from RSS destruct are treated as emerging laterally from the SRB (i.e., with zero elevation angle). Figure B-4 shows the fragment map for SRM1 along with a summary of the corresponding raw fragment size data. Specifically, data from cylinders 1 through 5 were used to derive the fragment size and location distributions which follow. The heavy vertical line in the center of the fragment map is the cutline created when the destruct charge was detonated.

RSS Destruct Large Fragment Procedure. A procedure has been developed to permit the selection of a set of fragments to be used in the determination of the probability of hit of an RTG under RSS destruct conditions. This procedure is used to define a circumferential band of fragments about an SRB opposite an RTG. In general, each fragment of the set is larger than the size of an RTG. The band of fragments which threatens an RTG is a circumferential strip 360 degrees around the SRB and is as wide axially as the target RTG is long.

The first step of the procedure to build a band of threatening fragments is to define the fragments adjacent to the cutline (called cutline fragments) and then to progress to fragments further and further away from the cutline (called noncutline fragments). Figure B-5 presents an outline of this procedure, which uses standard Monte Carlo techniques to define the fragment characteristics. In general, the database required for cutline fragments is different from that for noncutline fragments. The in-band length of each fragment affects the probability of a hit. The center of gravity (C.G.), length, and mass of each whole fragment determines its flyout characteristics (direction, speed, and spin rate). The band is filled starting at the cutline.

Figure B-6 shows a typical whole noncutline fragment and its in-band portion. For a cutline fragment, the left-hand perimeter of the in-band portion (only) must coincide with the cutline. The irregular nature of the fragment shape in the band is accounted for by a compression factor defined in the figure. For the RSS destruct case, the average value of this factor was found to be 1.38, based on Titan 34D-9 data. Because the compression factor is of secondary importance compared with other fragment parameters, this value will be used for all fragments.

The cutline fragment is defined first. Figure B-7 shows the cumulative distribution of the in-band circumferential length (CL) for cutline fragments. Fragment length data from Titan 34D-9 are given in degrees (rather than feet) to allow direct application to Shuttle SRBs. To use this figure, enter a random number drawn from a uniform distribution in the range from zero to unity (0 to 1) into the ordinate. The intersection of this value with the curve (based on Titan 34D-9 data) provides the in-band circumferential length from the abscissa. The in-band C.G. can then be approximated by considering both the compression factor and the circumferential length. Next, the characteristics of the whole cutline fragment are similarly determined from Figures B-8, B-9 and B-10, using a different random number for each. Figure B-8 provides the whole fragment C.G. relative to the in-band C.G. Figure B-9 provides the whole fragment average circumferential length. Figure B-10 provides the fraction of the full cylinder area for the whole cutline fragment. The mass of the whole fragment can then be calculated from this area. Figure B-11 provides an alternate method of determining the whole fragment C.G., avoiding some computer program difficulties that might arise from the use of Figure B-8.

In Figures B-8 through B-11, more than one curve appears. Care must be taken to use the correct curve, based on the value of the CL obtained from Figure B-7 or the  $CL_{AVE}$  obtained from Figure B-9. Once the cutline fragment has

been determined, then successive (noncutline) fragments are defined, as shown in Figure B-5.

Proceeding to the noncutline fragment, Figure B-12 shows the cumulative distribution of the in-band circumferential length. To use this figure, a random number between zero and one is entered into the estimate. The intersection of this value with the appropriate curve provides the desired in-band length. The correct curve is dependent on the end point of the previous (in this case, a cutline) fragment.

Note that Figure B-12 shows no curve if the end point of the previous fragment is greater than 180 degrees. This is because any fragment beyond this point would not be a threat to hit an RTG for the RSS destruct case. Next, the characteristics of the whole (noncutline) fragments are determined from Figures B-10, B-13 and B-14 using the same procedure as outlined above for cutline fragments. Figure B-15 is an alternative to Figure B-13. The steps outlined in the previous two paragraphs are repeated as many times as required to fill the band, as indicated in Figure B-3. Each repetition, however, requires a new set of random numbers to be entered into the ordinates of Figures B-10 and B-12 through B-15. After the band is filled, and it has been determined whether or not an RTG is hit, the process is repeated until a statistically significant estimate of the probability of hit can be computed.

Fragment Mass. Observational evidence from STS 51-L and Titan 34D-9 shows that, at early MET, case wall fragments are dissociated from the propellant early in the SRB breakup process; whereas, at late MET, the propellant remains attached to case wall fragments. On the basis of analysis, MET = 105 seconds is chosen as the value before which SRB fragments are devoid of propellant and after which propellant remains attached to fragments. Values for fragment areal masses and mass per linear foot of SRB are as follows:



MET	lb <sub>m</sub> /ft	lb <sub>m</sub> ft
0 to 20 seconds	23.9	900
20 to 70 seconds	23.9	900
70 to 105 seconds	23.9	900
105 to 120 seconds:		
Cylinder 4	28.8	1100
Cylinder 5	47.7	1820
Cylinder 6	28.8	1100
Cylinder 7	47.7	1820

Fragment masses after MET = 105 seconds vary with SRB cylinder because of the variation in initial propellant loading. Although fragment mass steadily decreases to the pre-105-second value after MET = 105 seconds due to burning, fragment masses given here are the values at MET = 110 seconds. This is done for the sake of modeling simplicity.

Small Fragments - Mass and Geometry. Joint pieces are cylinders of the outer leg of female joints having a cross-section of 0.5x4.0 inches and lengths of 1 to 5 feet. The joint pieces have a mass of 7.0 lb/ft of joint length. Clevis pins are steel pins 0.75 inch long and 0.5 inch in diameter, weighing 0.042 lb. Each joint has 180 pins (including 3 alignment pins). The center-to-center spacing of these pins around the joint circumference is 2.55 inches.

#### B.2.1.1.2 Fragment Velocities, Azimuth Angles, and Spin Rates.

The RSS destruct model is divided into two MET regimes. For MET < 105 seconds, the case and propellant debond, permitting a cavity region to form between the two, as shown in Figure B-16, and the escaping chamber gas fills the cavity and acts to deform and accelerate the case. After MET = 105 seconds, the case and propellant remain attached, and the chamber pressure acts directly on the propellant. The sequence for both regimes is the same. After the destruct cut is made, the internal pressure causes the case to clam

open about a line parallel to and 180 degrees away from the cutline. At some point due to its deformation, the case breaks up. For MET < 105 seconds, it is assumed that the fragments fly out laterally, i.e. their velocity vectors remain in a plane perpendicular to the SRB centerline. For MET > 105 seconds, it is assumed that the fragments can have flight paths up to  $\pm 20$  degrees from this plane. This is necessary because of the very large propellant mass differences of the cylinders adjacent to the RTG locations as depicted in Figure B-17. The model distinguishes between heavy cylinders 5 and 7 and light cylinders 4 and 6.

Because of the complexity of analyzing the interaction of escaping chamber gas with the deformation of the propellant and case, a hydrocode program was used to calculate fragment velocities, azimuth angles, and spin rates. Through a process of comparing the program output with a reconstruction of the Titan 34-D range data, the bracketing ranges of the two key parameters, breaktime and cavity pressure scaling factor ( $k_p$ ) were determined. Breaktime is defined as the time between failure initiation and complete breakoff of a fragment. The cavity pressure scaling factor is a multiplying factor used to raise or lower the nominal hydrocode calculation cavity pressure time history so that the calculations agree with the range data. Table B-4 presents these parameter changes as a function of MET. Analysis and observational data indicate that cutline fragment velocity distributions are asymmetrical. For example, in Figure B-16, fragment velocities on the left side might tend to be high while corresponding fragments on the right side might be low. A linear probability of occurrence is assumed within the ranges. Two  $K_p$  ranges are given in Table B-9, a high and a low. In the application of the model, it is assumed that either side of the break could be the high side with equal probability.

Figure B-18 contains the hydrocode axes system and nomenclature. The program was written to keep track of the X and Y coordinates and velocities of every 1.978-degree increment of SRB case for the full 360 degrees as a function of time after RSS destruct, dividing the case into 182 equal circumferential units. In making the calculations, it is assumed that the case deforms but

stays intact. To obtain the X and Y components of a fragment at a particular breaktime, first the X and Y components of momentum at that time for the included 1.978-degree units are added up and divided by the included mass. Next, the fragment is analytically broken off, and the additional velocity due to the remaining chamber or cavity pressure pulse (which would act on it if it were still attached) is added. The azimuth angle, as shown in Figure B-16, is obtained from the arctangent of the velocity components. The spin rate is obtained by determining the rate of change of the slope of a line between the coordinates of the extremity units making up the fragment at two times.

Six-degree-of-freedom Titan T34D velocity/azimuth reconstruction analyses indicate that fragments rotating clockwise will swerve counterclockwise, and consequently their breakoff azimuth angles will be larger than their no swerve recovered angles. To account for swerve, a correction equivalent to half the swerve of an idealized flat plate (considered an upper bound) has been added to the no swerve azimuth. The corrected azimuth is:

$$AZ = AZ \text{ (no swerve)} + (2.1533 R - 0.1015 R^2 + .002 R^3)$$

where:

R is the fragment spin rate in revs/sec obtained from the hydrocode database as discussed above. The azimuth correction has the same sign as the no swerve azimuth.

The complete hydrocode output is available from the Radiation Shielding Information Center as a function of breaktime for the different METs and  $K_p$ . There are 120 hydrocode output elements in the complete database. Each element is uniquely identified by a five digit code word in Table B-10. As an example, the hydrocode output element for  $0 < \text{MET} < 20$  seconds, a breaktime of

20 ms, and a  $K_p$  of 1.0 is presented in Table B-11. The element contains only the first 180 degrees of circumference; the remaining 180 degrees are the mirror images of the first and are deduced from the first set.

Table B-12 contains a sample FORTRAN program for processing the hydrocode output, and Table B-13 contains some typical results from the program for the data element in Table B-11. Table B-14 contains the additional  $\Delta V$ s which must be added to account for the remaining pressure pulse. For MET < 105 seconds, the values in Table B-14 must be multiplied by  $K_p$ .

For reference, Table B-15 contains a summary of the minimum and maximum cutline octant and quadrant velocities, azimuth angles, and spin rates for the different MET ranges. For METs < 105 seconds, the results are for the  $K_p$  range of 0.8 to 1.0.

#### B.2.1.1.3 Joint Fragment Velocity Distributions

Joint fragments were defined in Section B.2.1.1.1 as clevis pins and 1 to 5 foot lengths of outer joint legs. The RSS destruct model described in Section B.2.1.1.2 is to be used for joint fragment velocities, except that a  $\pm 5$  degree elevation angle range with uniform distribution should be assumed for MET 105 seconds. A  $\pm 20$  degree elevation angle applies for MET < 105 seconds.

Clevis pins are to be treated as 2 degree increments specified in the model database. Joint leg fragments range from 10 to 50 degrees in circumferential extent. Breaktime and  $K_p$  should be varied in the same manner as described in Section B.2.1.1.2.

### B.2.1.2 Random Failure Model

#### B.2.1.2.1 Large Fragment Size, Location, And Mass.

The fragment size and location data are summarized in this section for the Titan 34D-9 random failure case. Figure B-19 shows the fragment map for the failed cylinder of SRM2 along with a summary of the raw fragment size data. Figure B-20 shows the same information for the non-failed cylinders of SRM2. These data from cylinders 1 through 4 were used to derive the fragment size and location distributions which follow.

Figure B-21 presents an outline of the steps used to define a set of fragments for evaluation of the probability of hit of an RTG. The steps outlined here apply to both the failed cylinder and the non-failed cylinders for random failure scenarios. Two basic sets of data are required for both cases. First, fragment circumferential length and location must be identified as they appear in a band which threatens an RTG. These in-band lengths affect the probability of hit. Second, C.G., length, and mass of each whole fragment (which appears in the band of interest) must be defined. These data determine the flyout characteristics (direction, speed, and spin rate) of the fragments. In the case of a random failure, fragments are assumed to act independently of one another, and therefore there is no concern about correlation from fragment to fragment as there was in the RSS destruct case.

Figure B-22 shows cumulative distribution of fragment in-band circumferential length (CL) for the failed cylinder. Figure B-23 presents the same for the non-failed cylinders. Titan 34D-9 fragment length data are given in degrees (rather than feet) to allow direct application to Space Shuttle SRBs. The length data include the fact that fragments are irregularly shaped. The irregular nature of these shapes is accounted for by a compression factor (Figure B-24). For the failed cylinder, this factor is 1.64. For the non-failed cylinders, the factor is 1.25.

The description of the whole fragment which is the parent of the in-band portion can be developed from Figures B-25, B-27 and B-28 for the failed cylinder. Figure B-25 is used to derive the whole fragment C.G. ( $CG_F$ ), which is a function of the difference between the in-band fragment C.G. and the full fragment C.G. (Figure B-26 provides an alternate form of the data in Figure B-25 - this form will avoid some computer programming difficulties that might otherwise arise.) Figure B-27 is used to define the average circumferential length ( $CL_{AVE}$ ) of the full fragment. (The combination of  $CG_F$  and  $CL_{AVE}$  for the full fragment is used to determine fragment flyout characteristics.) Figure B-27 allows determination of the fragment area (and, therefore, its mass) for use in probability-of-breach calculations.

Figures B-22, B-25, B-27 and B-28 are to be used to define the failed cylinder fragments as described above. Figures B-23, B-29, B-31, B-37 and B-32 are to be used in an equivalent manner to define all non-failed cylinder fragments. (Figure B-30 is an alternate to Figure B-29 just as Figure B-26 is to Figure B-25) These latter figures are in the same format as the former.

#### B.2.1.2.2 Large Fragment Velocity, Azimuth, and Spin Rate

The random fragment size, velocity, azimuth, and spin-rate models are keyed to the RSS destruct model predictions, but parameters are varied consistent with observed results from the Titan 34D-9 failure. The steps in applying the model input are as follows:

##### Step 1. Failed Cylinder and Reference Azimuth

Failure in any of the nine SRB cylinders is considered equally probable. Randomly select one. Also, randomly select a reference azimuth.

Step 2 Fragment Size Distribution at Cylinder "N"

Randomly select a cylinder (or band) from the 34D-9 SRM2 accident data base (Section B.2.1.2.1). Use cylinder 1 data for the failed cylinder. Orient the nominal cutline to coincide with the reference Azimuth. In assessing cylinders of concern to the RTG, assume a  $\pm 20$  degree fragment elevation range with uniform distribution.

Step 3 Velocities, Azimuths, and Spin Rate for Cylinder "N"

- a. Velocity. The velocities of the fragments in the "N" cylinder are randomly selected from the range presented in the table below. Assume linear probability with the stipulation that range end points be included in the distribution for each cylinder. The velocity ranges given below were calculated with the destruct model and correlated to fragment velocity estimates from the Titan 34D-9 accident.

VELOCITY RANGES

<u>MET (sec)</u>		<u>Velocity Range (fps)</u>
0-20		125-345
20-70		125-320
70-105		170-340
105-120	Heavy (Cyl. 5 and 7)	250-450
	Light (Cyl. 4 and 6)	380-715

Each velocity selected must be multiplied by a factor based on position with respect to the failed cylinder as follows. This factor was derived by hydrocode depressurization analyses based upon a crack propagation rate of 1050 ft/sec for Titan 34D-9. The resulting peak velocity amplification/attenuation factors agree closely with observed fragment range data.

Failed Cylinder	FRAGMENT VELOCITY FACTOR, $K_V$				
	Cylinders Away From Failed Cylinder				
	+1	+2	+3	+4	+5
1.07	0.93	0.80	0.70	0.60	0.50

- b. Azimuth. The azimuth angle (AZ), referenced to an outward radial through the center of the fragment, is randomly selected in the following ranges: failed cylinder =  $0 \pm 110$  degrees and other cylinders =  $0 \pm 130$  degrees. The distribution to be used for azimuth is specified in Figure B-33, based on Titan 34D-9 data. For fragment trajectory calculations, assume that the initial fragment center of mass is on the SRB outer surface.
- c. Spin Rate. Spin rate is related to fragment velocity, size, and azimuth.

$$\text{Spin Rate} = k_v \left| \text{Az}/\text{Az}_{\text{max}} \right| S_{\text{ref}}$$

where  $k_v$  is the velocity amplification/attenuation factor and  $(\text{Az}/\text{Az}_{\text{max}})$  is the ratio of randomly selected azimuth to the maximum value possible.  $S_{\text{ref}}$  is the maximum spin rate in revs/sec of a fragment as a function of its circumferential length derived from the RSS destruct model.  $S_{\text{ref}} = a - b/l$  where  $l$  is the average circumferential length of the fragment being considered (in degrees), and  $a$  and  $b$  are given in the table below.



MET (sec)	$S_{ref}$		
	<u>d</u>	<u>b.</u>	
0 - 20	13.0	0.0556	
20 - 70	11.5	0.0444	
70 - 105	14.5	0.0639	
105 - 120	Heavy (Cyl. 5 and 7)	13.0	0.0500
	Light (Cyl. 4 and 6)	22.0	0.0833

Small Fragment Velocity Distributions. Clevis pins and joint leg fragments have the same mass characteristics as specified in the RSS destruct model. Velocities are specified to have an elevation angle uniformly distributed within a range defined by

$$k_v (V_{min} \text{ to } 1.35 V_{max})$$

where  $k_v$ ,  $V_{min}$ , and  $V_{max}$  are the parameters defined in Section B.2.1.2.2.  $k_v$  varies as a function of cylinder location with respect to the failed cylinder, while  $V_{min}$  and  $V_{max}$  vary as a function of MET. the 1.35 factor on  $V_{max}$  is based on review of joint fragment range data from Titan 34D-9 and hydrocode calculations for small fragments. Azimuth and spin rate for the joint fragments are handled in the same way as specified for the large fragments in Section B.2.1.2.2.

### B.2.1.3 Intervening Structures

SRB fragments may be slowed in transit to an RTG by intervening Orbiter structures and by the upper stage and/or spacecraft. This subsection presents velocity reduction factors to be used in treating the effect of intervening structures. The velocity reduction factor (VRF) is defined as the ratio of the SRB fragment velocity after interaction with all intervening structure to the original fragment velocity prior to striking the intervening structure.

A number of assumptions and approximations has been made in this analysis:

- a) Each Galileo RTG is effectively shielded from the SRB farthest from it by the spacecraft and upper stage. The Ulysses RTG is exposed to fragments from both SRBs.
- b) SRB destruct or case failure is considered to be the initial event of the applicable scenario. Therefore, all Orbiter structures are considered to be in their original design locations.
- c) The large scale structural strength of the Orbiter is ignored. Very small fragments, such as clevis pins, perforate the structures and VRFs are taken for appropriate experimental data and analytical results. Larger fragments are treated using a cookie cutter or momentum sharing approach. The effect of fragment rotation is included in this calculation.
- d) For the purpose of determining which Orbiter structures a given fragment interacts with, fragments are treated as having no spatial extent. The path is tested to see if it intersects or misses the Orbiter wing. A minimum or maximum value of the VRF is assigned accordingly.

#### B.2.1.3.1 Wall and Joint Fragments

Since, for random destruct, elevation angles for SRB fragment trajectories of  $\pm 20$  degrees are allowed, RTGs may be struck by fragments originating in any of several SRB cylinders. For the purposes of this discussion, the nomenclature illustrated in Figure B-34 will be used.

For wall and joint fragments, the VRF may vary depending upon whether or not the fragment strikes the Orbiter wing and whether or not propellant is attached to the fragment. VRFs for Galileo and Ulysses will differ slightly

due to the slightly different RTG locations for these missions. To determine whether or not a particular fragment (given that it strikes an RTG) passes through the wing, a path angle  $\beta$  is computed and compared to a critical path angle  $\beta_{cr}$ . Tables B-16 and B-17 present wing intersection angles as a function of fragment cylinder of origin and minimum and maximum values of VRF corresponding to whether or not fragment  $\beta$  exceeds  $\beta_{cr}$  (i.e., strikes or misses the wing, respectively). Cylinder 5 is broken down into three subcylinders because of the rapid variation of the wing profile in the region where fragments from cylinder 5 intersect the butt plane of the Orbiter. The 5/6 joint is specifically included since fragments from this joint may strike an RTG.

#### B.2.1.3.2 Clevis Pins

Clevis pins for the 5/6 joint may impact RTGs for the Galileo mission. The VRF of clevis pins does not vary with the MET but does depend upon whether or not pins impact stringers during passage through the major structural elements of the Orbiter. Table B-18 presents maximum and minimum VRFs for clevis pins, depending upon whether the pin flight path intersects the Orbiter wing. The wing intersection angle for the 5/6 joint is given in Tables B-16 and B-17. Relative probabilities for maximum and minimum values in each case were computed for the finite size of the pins.

#### B.2.2 ET PROPELLANT EXPLOSIONS

In Appendix A, section A.1.1 and A.1.2, various scenarios leading to massive rupture of the ET are described. The corresponding blast conditions for each scenario are estimated in Sections B.1.1 and B.1.2. In this section, a description is presented of the models used to estimate the velocities that would be attained by fragments if subjected to these blast loading conditions.

### B.2.2.1 Fragment Velocity Models

This section describes the models used for the various accident scenarios to predict the velocities of the fragments as they collide with the RTGs. Each scenario considered leads to a rupture of the ET. For accidents during the very early parts of the launch, the LH<sub>2</sub> and LOX are assumed to mix and collect in pools of various depths on the launch pad and/or ground. The mixture is then assumed to be ignited by an unspecified source such that detonation occurs. This blast wave is assumed to travel vertically from the pool and to decay as described in Section B.1.1. For failures during later parts of the launch, when the STS is well clear of the launch area, a vaporous cloud forms and ignites at some distance from the Shuttle, as specified in Section B.1.2. The blast wave acts initially on the exterior surface of the STS, causing breakup and accelerating the resultant fragments. For purposes of specifying the fragment environment for the RTGs, only payload bay structure in the vicinity of the RTGs is considered.

For accidents occurring during the early portions of the launch, it is likely that the Shuttle will be essentially vertical. For this case, the loading on the structure around the RTGs is due almost entirely to the static pressure in the blast wave. It is conceivable that situations could occur in which the Shuttle is tilted over at some angle (designated  $\phi$ ). For those situations, the component of flow perpendicular to the surface is stagnated on the surface, resulting in higher static pressures. Therefore, the results are presented for a number of intermediate angles,  $\phi$ .

The fragments resulting from a strong blast wave can be separated broadly into two categories: flyer plates and shrapnel. Separate models have been developed for each category and will be described in the following sections.

## B.2.2.1.1 Flyer-Plate Piston Model

A model is described here which predicts the velocities of flyer-plate-type fragments at impact with the RTGs. The model treats the Orbiter payload bay doors/mid-fuselage region as a cylinder tilted at an angle ( $\phi$ ) to the vertical and exposed to a decaying air shock with free-stream characteristics specified in Sections B.1.1 and B.1.2. The Orbiter surface is modeled as a flyer-plate which is accelerated by the high pressure in the airblast. Due to the motion of the flyer-plate, there is an increase of pressure ahead of the flyer-plate and a reduction behind, which oppose the motion. These are estimated by assuming the flyer-plate acts as a piston in a shock tube (Figure B-35) and applying classical 1-D shock tube equations.

The approach is to integrate Newton's equation of motion,  $F = ma$ , numerically. An assumption is made that the only force of importance acting on the flyer-plate is due to the pressure difference across the two faces of the plate. The calculation is terminated when either (a) the pressure difference across the plate reaches zero or (b) the fragment has traveled 46 inches, corresponding to impact with the RTG. As a simplification, the pressure acting on all parts of the door is assumed to be the same and specified by the free-stream conditions at the height of the RTG above the pool. The small time delays for shock arrival at different locations are ignored. The time histories of the free-stream conditions behind the blast wave indicate that the overpressure and dynamic pressure are well approximated by exponential decays. The decay time constants are calculated by dividing the impulse by the maximum value. For  $\phi = 0$ , the driving pressure is given by the free-stream static pressure following the airblast. When the Orbiter is tilted at some other angle,  $\phi$ , the driving pressure is modified to include the components of the reflected pressure and the dynamic pressure.

The final velocity depends only on the flyer-plate's areal density,  $\beta$  ( $\text{psi}$ ), and not on its overall dimensions. Since the RTGs are very close to the payload bay doors and sidewall, these are treated as the only sources of

flyer plates. A representative value of beta of 0.024 psi was used, corresponding to the total mass of the payload bay doors and radiators (mounted internally on the doors) divided by the total area of the doors. Values for the sidewall range from 0.01 to 0.04 psi, spanning the value for the doors.

#### B.2.2.1.2 Shrapnel Model

The shrapnel pieces are assumed to be attached to a parent flyer plate initially. For the initial acceleration phase, the shrapnel is treated as a flyer plate. The acceleration is determined by the pressure difference acting across the shrapnel/flyer-plate combination. The velocity is assumed to be normal to the original orientation of the flyer plate. Being denser, the shrapnel accelerates more slowly than the flyer plate. The displacements of the shrapnel and the flyer plate are tracked until the separation distance between the two reaches the arbitrary value of 0.5 inch. At this point, the two objects separate and the static pressure about the shrapnel equalizes. From this point onwards, the continued acceleration of the shrapnel is due to the dynamic pressure in the free-stream. The direction of the acceleration is now in the direction of travel of the air following the blast wave. The trajectory of the shrapnel is tracked until it has (a) reached the RTG location or (b) attained a maximum velocity and has started to decelerate. The tabulated velocity corresponds to the condition which occurs first.

The sources of shrapnel are small dense objects in the vicinity of the RTG. Table B-19 contains an inventory of high density items located between stations  $X_{0807}$  and  $X_{01090}$ , and between water lines  $Z_{0370}$  and  $Z_{0430}$  near the payload bay door hinge lines and mid-fuselage sills.

#### B.2.2.2 Fragment Velocity Model Results

The final velocities of the flyer plates are presented in Tables B-20 through B-23 for a number of RTG distances above the pool. For each case, four

possible blast wave strengths are considered corresponding to percentiles of 50%, 10%, 1% and 0.1%. For each set of driving conditions, the final velocities of the flyer plate are calculated for four orientations to the incident blast:  $\phi = 0, 30, 60,$  and  $90$  degrees.

The predicted velocities shown in Tables B-20 through B-23 are considered to be somewhat conservative since the calculated external driving pressure calculation is one-dimensional and, thus, overpredicts the actual driving pressure.

The shrapnel velocities are presented in Tables B-24 through B-31. The results are given for the same four scenarios as for the flyer-plate model. The first four tables are for  $\phi = 0$  degrees; the second four are for  $\phi = 90$  degrees. Several values of the ballistic coefficient ( $\beta$ ) are used for each case.

### 5.2.3 FRAGMENTS DUE TO AERODYNAMIC BREAKUP

This section considers structural breakup during the period 30 sec T 128 sec into the flight. Observation from the Challenger accident (Mission 51-L) is used as the basis for the values presented.

The ultimate load capability of the wing-to-fuselage area, although constant in absolute load capability (neglecting changes due to thermal effects, etc.), varies when normalized by the system weight. For the extreme case in which the Orbiter is still attached to the ET (as assumed for the 51-L accident), the normalized ultimate load capability drops below 1 g. For the Orbiter unattached to the ET, the wing-to-fuselage ultimate load capability varies from 2.8 g to 3.5 g for gross vehicle weight of 256,000 lb and 211,000 lb, respectively. Thus, although the effective system mass instantly before breakup is not known, the intact Challenger Orbiter would not have experienced an acceleration greater than 3.5 g (more probably less than 1 g) before it started to breakup. The breakup mode for the IUS from the Orbiter (for

Galileo) is expected to occur around 3.7 g, it being similar to the load capability of the TDRSS/IUS on Challenger with its mass and mass distribution being similar.

The ultimate load capability of the Galileo spacecraft with respect to the IUS has been estimated at 8 g. Components within the spacecraft, such as the attachment of the RTG, can be estimated using the mass acceleration curve, Figure B-36. The mass acceleration curve (MAC) represents the design limit load for which a component was designed. In this Figure, the effective mass would be the actual mass for the single degree-of-freedom system. Therefore, a 70-kg RTG would have a design limit load of about 14 g with the ultimate limit load of approximately 19 g (1.4 x design limit load). Therefore, it is expected that the RTG would remain attached to the spacecraft until the aerodynamic loads on the exposed spacecraft or RTG exceed this value.

For the IUS-to-Orbiter failure scenario, the relative velocity at impact is the result of the IUS/spacecraft free-flight motion within the cargo bay and the motion of the fuselage structure which continues to be subjected to the aerodynamic loads which initiated the failure. Neglecting the transient oscillation which occurs instantly before the failure, the initial velocity of the IUS/spacecraft after breaking free is assumed equal to that of the fuselage. The fuselage, accelerating at 3.7 g (neglecting any changes in the rigid body motion of the fuselage due to changes in aerodynamic loading) is increasing in velocity until the relative distance is decreased to zero and impact occurs. The impact velocity for this sequence is given by

$$\text{Impact Velocity} = (2S_0 a_0)^{0.5}$$

where  $a_0$  is the acceleration of the fuselage and  $S_0$  is the initial distance between the IUS/spacecraft RTG and the fuselage.



For the Galileo configuration, the initial distance between the IUS/spacecraft RTG and the fuselage is taken as 30 inches, with the impact velocity estimated at 25 ft/s. The fuselage, acting as the flyer plate, is characterized by the following areal densities: Shuttle bay floor is 0.028 psi and the Shuttle bay door is 0.024 psi.

### B.3 ORBITER ACCIDENT ENVIRONMENTS

#### B.3.1 UNCONTROLLED ORBITER REENTRY

This section considers reentry of the Orbiter following a failure during the ascent at times between 128 and 510 seconds; i.e., after the SRBs have separated and before orbital conditions are attained. The resulting reentry would be a ballistic return of the Orbiter (assuming that the ET has separated). The study was conducted by JPL, and the details are presented in Section 6.0 of the Shuttle Data Book. The objective was to determine if the RTG could reach the surface intact either alone or attached to the spacecraft/IUS/Orbiter.

The results are shown on Figures B-37 and B-38. Figure B-37 shows the height at which several events occur as a function of the initial speed and time in the nominal ascent at which the failure occurs. Also, lines for levels of 400, 800, and 1200 BTU/ft<sup>2</sup> of the time integrated reference heating are shown. These values are for melting of the RTG case and were taken from a previous study by JPL of the IUS powered reentry. Figure B-38 shows the longitude from launch for the events of the uncontrolled reentry as a function of the initial time and speed of the failure in the nominal ascent. The predictions for the various breakup events for Galileo are as follows:

- The Orbiter and the IUS will always break up during reentry and will not reach the surface intact.

- For t between 128 and 155 seconds ( $v = 4.4$  to  $4.9$  kft/sec.), the RTGs may reach the surface without melting.
- For t between 155 and 210 seconds ( $v = 4.9$  to  $6.3$  kft/sec), the RTGs may reach the surface without melting or the GPHS modules may be released prior to reaching the surface.
- For t above 210 seconds ( $v = 6.3$  kft/sec), the GPHS modules are released prior to surface impact.
- For t less than about 495 seconds, the RTGs or GPHS modules reach the surface over the Atlantic Ocean.

### B.3.2 ABORT CRASH LANDING ENVIRONMENTS

An Orbiter crash can be caused by control error, insufficient altitude for stall recovery, nonrecoverable spin, or mechanical failure. Based on credible failure modes and on examination of the Orbiter flight profile and characteristics, four crash scenarios have been selected: two landing crash scenarios and two ocean ditch scenarios. Figure B-39 presents the vehicle configuration and impact conditions for these scenarios.

#### B.3.2.1 Landing Accidents

A landing accident includes any impact accident resulting from long or short landings, hard landings, unlocked or unlowered gear, gear failure, or crash landings. A landing accident may be due to pilot error, if the Orbiter is under manual control, or mechanical failure during approach, flare, and rollout. Mechanical failures include those of the guidance, landing gear, and flight control systems.

During final approach, the airspeed of the Orbiter will drop from about 520 ft/s prior to flare at 2000 feet altitude to 340 ft/s at main gear touchdown.

The flight path angle of the Orbiter will drop from 17 degrees to nearly zero during approach. These figures are for a heavy Orbiter. If a landing accident occurs prior to completion of the flare, impact conditions will be more severe than a post-flare crash. Two landing crash scenarios are defined to allow separate analysis of pre-, mid-, or post-flare impacts.

#### B.3.2.2 Ocean Ditch

Ocean ditch is a crash of sorts and is the only abort option during certain portions of the launch profile. Ditch flight procedures will be developed to maximize crew survival chances. As planned, the autopilot will maintain constant Orbiter speed after crew bailout until impact.

Expected impact conditions are a speed of 300 ft/s, a flight path angle of 15 degrees, and a sink rate of 100 ft/s. If a flare is possible and were to be executed prior to ditch, the velocity on impact will be about 300 ft/s with flight path angle and sink rate near zero. As for landing accidents, two separate scenarios are considered to allow for analysis of the ditch with flare case.

#### B.3.2.3 RTG Impact Environment

Two independent methods were used to determine RTG impact environment resulting from Orbiter crash. One method uses structural similarity of the Orbiter to conventional aircraft combined with available data on conventional aircraft crashes to develop an energy attenuation factor. This factor is then used to determine the severity of the RTG impact. The other method is based on Orbiter decelerations and relative RTG/Orbiter motions generated during a crash. Simplifying assumptions are made and relative Orbiter structure/RTG impact velocities are calculated. These methods produce results which represent lower and upper limits to the expected RTG impact environment.

The RTG impacting environment during Orbiter crash on abort for the Galileo and Ulysses missions is presented in Table B-32. A uniform distribution within the given ranges is assumed.

#### B.4 UPPER STAGE (IUS) ENVIRONMENTS.

Since the IUS is dormant during the launch and ascent to orbit, there are no failures which can occur that would present accident environments to the RTGs directly from the IUS itself. Failures of the payload (including the IUS and the Galileo spacecraft) that could result in vehicle breakup have been included in the accident scenarios discussed in Appendix A. However, accident environments resulting from the ten representative Space Shuttle accident scenarios given in Section 3.4 of the Shuttle Data Book plus crash landing and ocean ditch were considered as potential initiating sources for upper stage responses which could produce a secondary threat to the RTGs.

##### B.4.1 IUS RESPONSE TO SPACE SHUTTLE ACCIDENT ENVIRONMENTS

Of the two sources of secondary threat, i.e., IUS solid rocket motors (SRMs) or RCS propellant tank, the RCS tank response was quantified in Section B.1.3. Briefly, the significant response of the RCS tank is the explosion hazard associated with a fire from an external source which might cause an internal pressure rise resulting in rupture at its burst pressure if the relief valves fail to operate. The threat due to blast environment from such a failure is nil. Fragments of 0.060 inch thick titanium alloy from the ruptured tank would have to penetrate the spacecraft adapter structure before reaching a RTG, and the initial fragment velocity of 226 feet per second would be reduced by approximately 34 percent to 149 feet per second at the RTG. Since these lightweight fragments at this relatively low velocity are not expected to present a significant threat to the RTGs, only the accident environment components of primary concern, which are the SRMs, are addressed herein.

The details of the studies and background test information that were used to evaluate the response of the IUS SRMs to the accident environments from the Space Shuttle failures are presented in Section 10.3 of the Shuttle Data Book. Only the conclusions from that evaluation are given in this discussion.

#### Response to Blast Environment

Shock levels to the SRM's are well below the threshold for detonation of the IUS propellant. While some damage to the propellant in the form of cracking might occur at the higher blast overpressures, ignition of the propellant is not expected.

#### Response to Fire

Detonation of the SRM propellant is not expected to occur as a result of any fire environment. The high heating rates from liquid propellant and solid propellant fires will result in a loss of all structural integrity of both the IUS motor cases before the propellant can reach the auto ignition temperature. Therefore, the only response will be possible ignition and burning of unconfined propellant with no secondary threat to the RTGs.

#### Response to Fragment Impact

Impact of the IUS SRMs by large SRB fragments will damage the motor case to the extent that containment is lost and pressure rupture producing high velocity fragments is not possible. No spalling of the propellant grain interior surface occurs. Therefore, ignition of the interior surface and pressurization of the entire motor case will not occur. Also, fragment impact results in local surface damage causing possible ignition of the damaged propellant and venting of combustion products through the damaged case with no threat to the RTGs.

SRB shrapnel posing a potential threat to the IUS include the clevis pins and segments of the joint flanges. Even if the SRM is penetrated by a clevis pin, however, no response of the SRM is expected. Impact by a joint segment with the IUS SRMs will prompt a flat plate response when the fragment orientation is greater than 10 degrees. The response to a flat plate impact is benign, despite possible propellant ignition, since the motor case cannot pressurize due to the extensive local damage from the impact and subsequent burning. With a fragment orientation less than 10 degrees, impact and penetration of the SRM case will imitate a response similar to a bullet penetration. For long rod penetrators like the joint fragments with residual energies greater than 1600 ft/lb, the response is ignition of the propellant, pressurization of the motor case, and destruction of the case through failure at the nominal internal burn pressure associated with early burn parameters for the IUS SRMs. For the Galileo configuration, SRM-2 shields the RTGs from SRM-1 fragments. Therefore, only the environment specified in Table B-36, Level 1 column, is a threat. The conditional probability of a SRM-2 level 1 response, assuming a SRB failure ranges from  $0.7 \times 10^{-3}$  to  $1.1 \times 10^{-3}$  based on the SRB joint fragment characteristics in a random SRM failure, on the temporal distribution of SRB random failures, and on the geometric parameters pertaining to defining the target area.

#### Response To Surface Impact

Surface impact may be either ground or water, depending on MET. Detonation as a result of ground impact at the terminal velocity of the IUS (determined to be 450 feet per second or less) will not occur because the resulting induced shock levels are below the detonation threshold level. Neither will explosive reactions (including fading reactions) occur at these velocities for the SRM propellant.

#### B.4.2 IN-FLIGHT IUS FAILURES

Upper stage in-flight failures take place in the vacuum of space where the blast effects are minimal. Therefore, fragment environments constitute the only threat to the RTG. Fragment environments are produced when a solid rocket motor fails while operating, resulting in a pressure burst of the motor case. Two failure scenarios resulting in two different levels of response are considered. First, a case defect scenario assumes failure at normal burn pressures and propellant masses for the motor during flight. Such a failure would probably be due to a defect in the liner which would result in a local burn through of the case, initiating failure in the dome area near the boundary of the propellant grain burning surface. Second, a propellant defect scenario assumes that cracks or porosity in the propellant cause an increased burning rate with corresponding increase in chamber pressure prompting failure at the burst strength of the case. This type of failure would also likely initiate in the dome area where the case is the thinnest.

##### B.4.2.1 Fragment Environment Model

Fragment Characteristics - Fragmentation characteristics of Kevlar motor cases are not well understood. Case burst tests are normally performed under hydrostatic pressurization, and the resulting case failures generally do not show fracture into distinct pieces but rather a general disintegration into a tangle of broken fibers. On the other hand, an accidental failure during a test firing of an early IUS SRM-1 resulted in fragmentation of the aft dome into a dozen or more distinct pieces of varying sizes. The failure occurred under conditions closely approximating a case defect failure scenario at mid burn time. The pieces of the motor case showed very ragged edges and appeared to resemble fibrous mats rather loosely held together by considerably damaged resin matrix. These pieces, of low initial areal density, must pass through intervening IUS interstage or spacecraft adapter structure before reaching an RTG. This intervening structure would considerably reduce their velocity and

cause further disintegration of the fragments into little more than clumps of fibers of indeterminate but unsubstantial areal density and mechanical properties which would not constitute a threat to the RTGs. Fragments constituting a potential hazard environment to the the RTGs will consist of chunks of propellant. These propellant chunks can be assumed essentially cubic in geometry and will vary in size from small to large, with the maximum size depending on the amount of unburned propellant remaining in the forward dome area of the motor at the time of failure.

Fragment Size Distribution - A simple density distribution of fragments vs size is assumed. For convenience, this distribution has been discretized into ten fragment sizes representing average weights for each of ten equal increments from zero to maximum fragment weight, as illustrated in Figure B-40. Thus, for a total of 100 fragments, the numbers in each size category are as indicated in the figure, and their total weight is 33.5 times the maximum fragment weight. Knowing this and the weight of propellant in the forward dome, the total numbers and sizes of fragments produced from the forward dome area can be determined at any time during the burn.

Fragment Size and Velocity Variation with Burn Time - Burn times for the motors have been divided into three zones: early, mid, and late. The functions of maximum fragment size and fragment velocity are continuous functions of burn time, but to provide a useable model, the three zones have been adopted. Fragment maximum weight and fragment velocity vs size, as determined for the mid burn time within each zone, will be assumed constant over the zone.

Maximum fragment sizes vs. burn time are shown in Figure B-41. These data were determined from estimates of maximum fragment size based on thickness of propellant in the forward dome at  $t = 0$  and assumed linear variation with time to zero at the end of the burn.



Propellant Fragment Mechanical Properties - Propellant mechanical properties representative of the high strain rates associated with impact at the range of fragment velocities determined for the IUS motors are given below. These values were estimated for impact at 500 feet per second at 70°F from extrapolation of test data.

Modulus	$E = 14,000 \text{ psi}$
Failure Stress	$\sigma = 1300 \text{ psi}$
Maximum Strain	$\epsilon = 0.50 \text{ in/in}$
Density	$\rho = .0635 \text{ lb/in}^2$

### Fragment Environment Specifications

Fragment environment specifications for the SRM-1 and the SRM-2 and for failures during early, mid, and late burn times are given in Tables B-33 through B-38. Each table shows, for each of the ten fragment size ranges, fragment average weight, average size, average areal density, velocity ranges for both failure scenarios, and the numbers of fragments per square foot of exposure area at the RTG locations. The velocity numbers include the reduction for intervening structure calculated for the Galileo configuration.

### B.5 IUS ERRANT REENTRY

This section addresses the results of potential anomalies originating within the upper stage flight system subsequent to deployment from the Orbiter. The result of most upper stage anomalies is to place the spacecraft in some anomalous orbit or trajectory. Major interest is in those trajectories or orbits that cause the spacecraft to reenter the Earth's atmosphere since spacecraft breakup and RTG reentry survival are the safety issues of concern.

The consequences of all significant upper stage anomalies, with the exception of an SRM case rupture, will be one of the following five failure modes:

- a) Failure to ignite.
- b) Low or incomplete impulse.
- c) Tumbling.
- d) Erratic (attitude) burn(s).
- e) Stable misaligned burn(s) (SMB).

Three other failure modes not included on the list - premature stage separation, failure of stage to separate, and recontact of stages after separation - have been incorporated into the tumbling mode category. The expected result from those events is damage to the next stage, most significantly the SRM nozzle bell and/or actuators. The consequence of such damage typically is to cause the vehicle to tumble.

#### B.5.1 REENTRY CONFIGURATIONS

The resulting reentry configuration for a majority of the failure modes is a separated spacecraft. The only credible failure modes which cause the spacecraft and some part of the upper stage to reenter intact are those which totally preclude IUS ignition or result in either a prompt elliptic or powered reentry. Separated spacecraft is the predominate reentry configuration due to the design implementation of the IUS Operation Flight Software (OFS) and the Mission Data Load (MDL) software. The sequencing of the IUS mission events is controlled by the OFS using the parameters set by the MDL for each specific mission. The OFS is designed to sequence through the mission events in a success oriented manner. For example, even if SRM-1 ignition does not occur as commanded (due to an ignitor failure, for instance), the OFS will continue to sequence through the mission event table resulting in staging and SRM-2 ignition, and so on. Uplink commands from the ground station can also serve as a backup for spacecraft separation in the event of an upper stage failure.

## B.5.2 V-GAMMA MAPS

Figures B-42 and B-43 contain V-gamma entry data for the Galileo mission. The V-gamma data are for an initial parking orbit of 160 nautical miles and 200-second coast-times between burns. Only the SMB data are presented since the re-entry conditions of all other cases fall within or are a subset of these data. The data encompass the extremes in entry conditions (velocity, flight path angle, propellant remaining, configuration, and angle-of-attack). The vertical bars in Figure B-43 for the powered entry correspond to regions of constant angle-of-attack. It is noteworthy that the angles-of-attack are generally very large. From an inspection, it appears that the mean is about 90 degrees. For an angle-of-attack of 90 degrees, the thrust vector is perpendicular to the flight path. The conditional probabilities for the various reentry modes are given in Table A-7 of Appendix A.

B.6 REFERENCES

- B-1. Willoughy, A.B., Wilton, C. and Mansfield, J. , Liquid Propellant Explosive Hazards, Final Report, AFRPL TR-68-92, URS Research Company, 1968.
- B-2. LO<sub>2</sub>/LH<sub>2</sub> Explosion Hazards Program Plan, JPL D-5113, Jet Propulsion Laboratory, Pasadena, CA January 29, 1988.
- B-3. Srinivasa, D.S., Kuhl, A.L., Crawford, R., Asano, W., and Mo, C., LOX/LH<sub>2</sub> Explosion Environment Estimates for the STS-Galileo and Ulysses Projects, RDA-TR-203500-003, R & D Associates, Marina del Rey, CA, March 1, 1988.

Table B-1. Environments Defined With Corresponding accidents

Shock Wave for On-Pad Explosions Due to SRB-Failure - Initiated Breakup or Tower Impact

Shock Wave for In-Trench Explosions Due to SRB-Failure - Initiated Breakup or Tower Impact

Shock Wave for Aft-Compartment Initiated Explosions.

Shock Wave for In-Flight Vapor-Cloud Explosions.

Auxiliary Tank Fragments and Shock Wave Caused by Fire.

SRB Fragments Due to SRB Failures

SRB Fragments Due to Range Destruct

Orbiter Payload Bay Door and Wall Fragments for On-Pad Explosions Due to SRB-Failure-Initiated Breakup or Tower Impact

Orbiter Payload Bay Door and Wall Fragments for In Trench Explosions Due to SRB-Failure-Initiated Breakup or Tower Impact

Orbiter Payload Bay Door and Wall Fragments for Aft-Compartment-Initiated Explosions.

Orbiter Payload Bay Door and Wall Fragments for In-Flight Vapor-Cloud-Initiated Explosions.

Orbiter Payload Bay Shrapnel for On-Pad Explosions Due to SRB-Failure-Initiated Breakup or Tower Impact

Orbiter Payload Bay Shrapnel for In-Trench Explosions Due to SRB-Failure-Initiated Breakup or Tower Impact

Orbiter Payload Bay Shrapnel for Aft-Compartment-Initiated Explosions.

Orbiter Payload Bay Shrapnel for In-Flight Vapor-Cloud-Initiated Explosions.

RTG Breakup Conditions Arising from Inadvertent Suborbital Ballistic Reentry of Untrrolled Orbiter

RTG Impact Conditions Arising From Orbiter Crash Landing Following Abort.

Fragments from IUS SRMs Due to Case Defect or Propellant Defect Failures.

Upper Stage Reentry Conditions Due to Motor or Avionics Failures Resulting in No Ignition, Loss of Thrust, or Guidance Errors.

Table B-2. Probabilistic Blast Environments for On-Pad Explosions Due to SRB-Failure-Initiated Breakup or Tower Impact

HEIGHT X ft	PERCENTILE %	BLAST PARAMETER				
		$\Delta P$ STAT psi	P DYN psi	P REFL psi	I STAT psi-s	I DYN psi-s
3*	N/A	2075	810	5300	0.58	0.058
3**	N/A	659	1720	5169	2.01	0.33
20	50	41	36	167	0.25	0.076
	10	106	123	552	0.71	0.19
	1	206	294	1271	1.34	0.36
	0.1	349	524	2407	1.83	0.60
30	50	27	22	103	0.22	0.078
	10	77	83	366	0.69	0.21
	1	143	194	808		0.38
	0.1	322	505	2189	1.86	0.82
40	50	18	15	67	0.19	0.071
	10	59	59	261	0.61	0.22
	1	114	146	605	1.23	0.38
	0.1	203	318	1249	1.93	0.69
55	50	9	10	37	0.16	0.069
	10	42	39	172	0.53	0.21
	1	86	100	423	1.11	0.42
	0.1	154	217	887	1.55	0.73
70	50	7	7	31	0.14	0.066
	10	33	30	129	0.49	0.21
	1	72	81	336	1.07	0.44
	0.1	129	200	709	1.72	0.76
100	50	1	4	17	0.11	0.057
	10	21	18	78	0.41	0.20
	1	47	47	197	0.90	0.42
	0.1	92	117	461	1.54	0.79
150	50	Nil	Nil	Nil	Nil	Nil
	10	11	11	43	0.32	0.19
	1	36	34	142	0.83	0.48
	0.1	49	51	207	1.78	0.64
200	50	Nil	Nil	Nil	Nil	Nil
	10	6	7	29	0.28	0.18
	1	25	24	94	0.72	0.46
	0.1	48	55	202	1.24	0.82

$Q_0 = 1050 \text{ Cal/g}; 0.00032 < \rho_0 < 0.30 \text{ g/cm}^3; 0.1 < X_0 < 3 \text{ ft.}$

- \* Inside pool surface @  $X_0 = 3 \text{ feet}; \rho_0 = 0.0056 \text{ g/cm}^3;$   
 $Q_0 = 1050 \text{ cal/g}$
- \*\* Outside pool surface @ same pool conditions

Table B-3. Probabilistic Blast Environments for In-Trench Explosions Due to SRB-Failure-Initiated Breakup or Tower Impact

HEIGHT X ft	PERCENTILE %	BLAST PARAMETER				
		$\Delta P$ STAT psi	P DYN psi	P REFL psi	I STAT psi-s	I DYN psi-s
6*	N/A	2075	810	5300	1.20	0.12
6**	N/A	659	1720	5169	4.02	0.66
110	50	22	18	82	0.66	0.24
	10	64	66	289	1.91	0.64
	1	122	157	660	3.36	1.17
	0.1	163	236	953	4.19	1.55
130	50	18	15	67	0.63	0.24
	10	55	55	239	1.82	0.65
	1	108	136	566	3.27	1.22
	0.1	150	230	850	5.42	3.00
150	50	14	12	53	0.57	0.23
	10	47	44	197	1.68	0.64
	1	91	110	454	3.03	1.20
	0.1	136	230	744	5.10	2.65
200	50	8	8	34	0.47	0.21
	10	34	31	133	1.50	0.63
	1	72	83	336	2.82	1.24
	0.1	124	187	675	4.60	2.10
290	50	3	5	7	0.40	0.20
	10	22	19	82	1.26	0.62
	1	49	50	207	2.46	1.26
	0.1	87	110	429	3.94	2.17

$$Q_0 = 1050 \text{ cal/g}; 0.00032 < \rho_0 < 0.30 \text{ g/cm}^3; 0.1 < X_0 < 6 \text{ ft}$$

- \* Inside pool surface @  $X_0 = 6 \text{ ft}$ ;  $\rho_0 = 0.0056 \text{ g/cm}^3$ ;  
 $Q_0 = 1050 \text{ cal/g}$
- \*\* Outside pool surface @ same pool conditions

Table B-4. Probabilistic Blast Environments for Aft-Compartment-Initiated Explosions

HEIGHT X ft	PERCENTILE %	BLAST PARAMETER				
		$\Delta P$ STAT psi	P DYN psi	P REFL psi	I STAT psi-s	I DYN psi-s
1*	N/A	2075	810	5300	0.19	0.019
1**	N/A	659	1720	5169	0.67	0.11
20	50	18	15	67	0.093	0.037
	10	49	47	207	0.24	0.088
	1	95	115	480	0.43	0.16
	0.1	175	297	1040	0.67	0.29
30	50	9	8	37	0.072	0.033
	10	32	29	124	0.20	0.090
	1	72	83	336	0.41	0.19
	0.1	117	172	627	0.61	0.30
40	50	4	6	24	0.061	0.031
	10	23	20	86	0.17	0.088
	1	50	52	212	0.35	0.18
	0.1	88	121	435	0.59	0.31
55	50	Nil	Nil	Nil	Nil	Nil
	10	14	13	53	0.14	0.082
	1	36	34	142	0.30	0.17
	0.1	84	111	409	0.54	0.39
70	50	Nil	Nil	Nil	Nil	Nil
	10	9	9	37	0.13	0.077
	1	27	25	102	0.26	0.17
	0.1	78	104	373	0.57	0.46
100	50	Nil	Nil	Nil	Nil	Nil
	10	4	6	24	0.11	0.074
	1	16	15	60	0.21	0.16
	0.1	32	32	124	0.34	0.27
150	50	Nil	Nil	Nil	Nil	Nil
	10	Nil	Nil	Nil	Nil	Nil
	1	8	9	34	0.17	0.15
	0.1	17	17	63	0.26	0.25
200	50	Nil	Nil	Nil	Nil	Nil
	10	Nil	Nil	Nil	Nil	Nil
	1	4	6	24	0.15	0.13
	0.1	14	15	53	0.25	0.26

$$Q_0 = 1050 \text{ cal/g}; 0.1 < x_0 < 1.0 \text{ ft}; 0.00032 < \rho_0 < 0.30 \text{ g/cm}^3$$

\* Inside pool surface @  $X_0 = 1 \text{ ft}$ ;  $\rho_0 = 0.0056 \text{ g/cm}^3$ ;

$Q_0 = 1050 \text{ cal/g}$

\*\* Outside pool surface @ same pool conditions



Table B-5. Blast Environments for In-Flight Vapor-Cloud Explosions

DISTANCE FROM COE ft	$\Delta P$ STAT psi	P DYN psi	P REFL psi	I STAT psi-s	I DYN psi-s
263*	298	122	1991	3.23	1.60
265**	263	142	1714	3.22	1.69
291	136	181	759	2.49	1.67
396	63	61	284	1.48	1.43
528	33	21	129	0.93	1.08
792	14	5	53	1.13	0.48
924	10	3	40	1.28	0.31
1056	8	2	34	1.19	0.22

\*Just inside reaction volume  
\*\*Just outside reaction volume

Table B-6. Auxiliary Propellant Tank Design Data

	ORBITER							IUS	GLL		
	APU	ARCS		OMS		PRDS		RCS	RPM		
CONTENTS WEIGHT LB*	N <sub>2</sub> H <sub>4</sub> 350	MMH 956	NTD 1530	MMH 2740	NTD 4300	LOX 701	LH <sub>2</sub> 92	N <sub>2</sub> H <sub>4</sub> 123	MMH 397	NTD 635	He
CONSTRUCTION	28" DIA SPHERE Ti	30.5" DIA SPHERE Ti	30.5" DIA SPHERE Ti	49" D x 96" L CYL Ti	49" D x 96" L CYL Ti	33.5" DIA DBL SPH AL - AL	41.5" DIA DBL SPH INCONEL AL	21" DIA SPHERE Ti	29.5" DIA SPHERE Ti	29.5" DIA SPHERE Ti	17.5" DIA SPHERE Ti
WORKING PRESSURE PSIG	355 MAX	243 NOM 350 MAX	243 NOM 350 MAX	250 TO 313	250 TO 313	1050 MAX	335 MAX	415 RATED	300 (50 AT LAUNCH)	300 (50 AT LAUNCH)	2053
ACCEPTANCE TEST PRESSURE PSIG	970	455	455	345	345	-	-	630	-	-	-
BURST SPEC PRESSURE PSIG	1070 1321 ACTUAL	525	525	470	470	1575	502	1750	ULT SFTY FCTR = 1.5	ULT SFTY FCTR = 1.5	4710
NUMBER	3	2	2	2	2	3	3	1	2	2	2
LOCATION	AFT EQ COMP	1 EACH OMS POD	1 EACH OMS POD	1 EACH OMS POD	1 EACH OMS POD	LOWER PIL BAY	LOWER PIL BAY	AFT PIL BAY	MID PIL BAY	MID PIL BAY	MID PIL BAY

\*TYPICAL PROPELLANT LOAD GIVEN FOR ARCS AND PRDS. UNDERSTOOD OMS PROPELLANT LOAD FOR GLL/ULS MISSIONS

Table B-7. Tank Fragment and Airblast Environments at RTG Design Locations; Caused by Fire

SYSTEM	P <sub>BURST</sub> psi	V <sub>FRAG</sub> fus	GALILEO					
			D <sub>RTG</sub> ft	ΔP <sub>ST</sub> psi	P <sub>DYN</sub> psi	P <sub>REFL</sub> psi	L <sub>ST</sub> psi ms	L <sub>DYN</sub> psi ms
<b>MMH</b>								
OMS	485	367	28.8	3.8	8.21	21.2	6.4	0.30
ARCS	548	174	22.1	NIL	NIL	NIL	NIL	NIL
GLL (RPM)	588	187	5.2	4.5	8.47	24.1	1.9	0.14
<b>N<sub>2</sub>H<sub>4</sub></b>								
APU	1885	287	27.4	NIL	NIL	NIL	NIL	NIL
ULS (RCE)	1828	233	-	-	-	-	-	-
WUS (RCS)	1758	226	8.8	5.3	8.85	28.8	3.8	0.29
<b>He</b>								
GLL (RPM)	3588**	1858	6.1	14.2	4.3	54.7	8.5	1.3
<b>LO<sub>2</sub>/LN<sub>2</sub></b>								
PRSDS	-	-	23.3	138.8	312.8	776.8	368.8	988.8

\*ASSUMED MIXED POOL/AIRBLAST CONDITIONS X<sub>0</sub> = 4.63 ft (ONE TANK SET); ρ<sub>0</sub> = 0.0056 g/cm<sup>3</sup>.  
 PRECURSORY ABOVE POOL TEMPERATURE = 2500K

\*\*AT 378°F TANK WALL TEMPERATURE

Table B-8. Estimated Impact Velocities for Auxiliary Propellant Tanks  
Caused by Abort Crashes

	ORBITER				IUS	GLL	
	APU N <sub>2</sub> H <sub>4</sub>	ARCS MMH AND NTO	OMS MMH AND NTO	PRSDS LO <sub>2</sub> AND LH <sub>2</sub>	RCS N <sub>2</sub> H <sub>4</sub>	RPM MMH & NTO	RPM He
OCEAN DITCH NO FLARE	70-120	70-120	70-120	90-130	70-120	70-120	70-120
OCEAN DITCH WITH FLARE	50-100	50-100	50-100	70-110	50-100	50-100	50-100
LANDING CRASH PRE-FLARE	40-100	40-100	40-100	70-120	50-110	50-110	50-110
LANDING CRASH POST-FLARE	30-50	30-50	30-50	60-70	40-50	40-50	40-50

Table B-9. Hydrocode Parameters

MET (sec)	Breaktime (ms)	$K_p$	
		High	Low
0-20	10-20	0.8-1.0	0.2-0.4
20-70	10-20	0.8-1.0	0.2-0.4
70-105	8-16	0.8-1.0	0.2-0.4
105-120	6-12	NA	NA

Table B-10. Hydrocode Database File Identification Code,  
File Name = O(A)O(BCC)

A, B or CC	←A MET Regime (sec)	←B K <sub>p</sub> Range	←CC Breaktime (ms)
0		0.0 <sup>(3)</sup>	
1	0-20	1.0	2
2	20-70	0.8	4
3	70-105	0.4	6
4	(105-120)L <sup>(1)</sup>	0.2	8
5	(105-110)H <sup>(2)</sup>		10
6			12
7			14
8			16
9			18
10			20

- (1) Light, cylinders 4 and 6
- (2) Heavy, cylinders 5 and 7
- (3) B = 0 for METs > 105 seconds

Table B-11. Typical Hydrocode Output Element (MET = 0 to 20 Seconds,  
Kp = 1.0, Breaktime = 20 ms)

IE	X (CM)	Y (CM)	XV (M/S)	YV (M/S)
1	242.26	250.12	169.54	-34.69
2	241.99	243.64	152.76	-29.71
3	241.77	237.17	140.97	-27.00
4	241.55	230.69	135.22	-26.28
5	241.22	224.22	131.34	-25.70
6	240.71	217.76	128.28	-27.32
7	240.03	211.31	125.78	-29.78
8	239.25	204.88	122.47	-30.24
9	238.45	198.45	119.71	-28.43
10	237.67	192.02	117.83	-25.37
11	236.95	185.58	111.81	-21.59
12	236.28	179.13	102.86	-18.84
13	235.67	172.68	96.09	-20.89
14	235.05	166.23	88.81	-22.19
15	234.38	159.78	81.52	-20.72
16	233.69	153.33	78.67	-20.61
17	232.98	146.89	77.75	-20.24
18	232.27	140.27	74.58	-17.57
19	231.60	134.01	70.37	-13.87
20	231.06	127.55	66.38	-13.22
21	230.70	121.07	60.75	-14.49
22	230.40	114.59	54.15	-13.36
23	230.07	108.11	49.83	-12.83
24	229.73	101.64	48.97	-12.31
25	229.41	95.17	50.53	-11.98
26	229.13	88.69	48.42	-13.95
27	228.85	82.22	39.32	-12.81
28	228.56	75.74	29.05	-10.17
29	228.27	69.26	23.84	-8.83
30	227.91	62.78	22.15	-7.53
31	227.40	56.32	23.07	-5.61
32	226.77	49.86	24.71	-5.16
33	226.08	43.41	23.70	-7.03
34	225.41	36.96	22.51	-10.43
35	224.76	30.51	23.71	-11.54
36	224.06	24.07	23.51	-9.68
37	223.16	17.66	19.39	-8.21
38	222.03	11.28	15.25	-6.93
39	220.78	4.92	9.25	-5.01
40	219.43	-1.42	1.56	-3.63
41	217.92	-7.72	1.19	-3.26
42	216.30	-14.00	6.06	-2.87
43	214.56	-20.24	9.60	-4.10
44	212.70	-26.45	12.83	-6.90
45	210.65	-32.59	13.30	-10.70
46	208.86	-38.78	11.28	-2.30
47	206.82	-44.78	7.01	-0.69
48	204.68	-50.76	6.11	-2.75
49	202.47	-56.70	4.25	-4.16
50	200.21	-62.63	1.41	-4.64

Table B-11. Typical Hydrocode Output Element (MET = 0 to 20 Seconds,  
Kp = 1.0, Breaktime = 20 ms) (Cont'd)

51	197.84	-68.51	3.76	-6.07
52	195.33	-74.33	8.92	-7.36
53	192.62	-80.06	5.37	-6.45
54	189.69	-85.68	-3.06	-7.59
55	186.65	-91.23	-0.96	-4.19
56	183.52	-96.76	5.84	-5.26
57	180.29	-102.22	7.27	-4.11
58	176.93	-107.60	7.78	-6.33
59	173.48	-112.92	5.82	-8.12
60	169.88	-118.14	0.96	-7.98
61	166.08	-123.22	-3.21	-7.81
62	162.08	-128.13	-5.07	-6.92
63	157.92	-133.90	-3.87	-10.47
64	153.63	-137.56	-6.00	-12.78
65	149.24	-142.12	-9.00	-10.07
66	144.74	-146.57	-7.12	-12.15
67	140.06	-150.84	-4.21	-13.93
68	135.25	-154.96	-2.60	-10.56
69	130.39	-159.02	-3.51	-9.32
70	125.49	-163.02	-3.35	-9.12
71	120.46	-166.89	-1.01	-6.65
72	115.34	-170.63	-0.09	-4.10
73	110.15	-174.28	-0.52	-3.38
74	104.89	-177.82	-0.48	2.56
75	99.56	-181.27	0.79	-1.13
76	94.14	-184.57	0.48	-1.67
77	88.60	-187.68	0.23	-3.49
78	82.92	-190.52	1.87	-6.25
79	77.10	-193.02	3.10	-7.98
80	71.15	-195.24	2.56	-7.89
81	65.12	-197.21	0.50	-6.98
82	59.04	-199.01	-1.29	-0.72
83	52.94	-200.76	-3.23	5.88
84	46.81	-202.40	-2.71	2.19
85	40.64	-203.85	-0.87	-5.77
86	34.43	-205.16	-0.59	-8.93
87	28.21	-206.39	0.09	-9.32
88	21.95	-207.46	-0.84	-8.51
89	15.66	-208.21	-1.92	-5.64
90	9.33	-208.62	-0.12	-2.74
91	2.99	-208.71	0.57	-2.38



Table B-12. FORTRAN Hydrocode Output Processor Program

```

C -----
C HYDRO - F.JAFFE 12/18/87
C HYDROCODE OUTPUT PROCESSOR PROGRAM
C THIS PROGRAM DOES NOT ADD REMAINING PRESSURE IMPULSE VELOCITY
C TWO INPUT FILES FOR TWO SEQUENTIAL BREAK-TIME ELEMENTS REQUIRED
C - FL1 CONTAINS THE ELEMENT DATA FOR THE BREAK-TIME OF INTEREST
C - FL2 CONTAINS THE ELEMENT DATA FOR THE PAST 2 MS BREAK-TIME
C -----
C
C
C     PARAMETER (MX=182)
C     CHARACTER FL1*10,FL2*10,ANS*1
C     DIMENSION IP(MX),X(MX),Y(MX),XV(MX),YV(MX)
C     DIMENSION X2(MX),Y2(MX)
C
C
C     DEL1=180./91.
C     RD=57.29578
C
C NOMENCLATURE:
C     IP IS PIECE NUMBER MEASURED CLOCKWISE; #1 IS AT CUTLINE
C     EACH PIECE IS 180/91 DEGREES IN CIRCUMFERENCE
C     X & Y ARE CARTESIAN COORDINATES OF CENTER OF PIECE IN CM
C     MEASURED FROM CENTER OF SRB; +X IS TO THE RIGHT, +Y
C     IS UP. X=0 COINCIDES WITH CUTLINE.
C     XV & YV ARE VELOCITY COMPONENTS OF PIECE IN METERS/SEC
C -----
C
C OPEN ELEMENT DATA FILES
C
C     PRINT *, ' ENTER INPUT FILE NAMES FOR FL1,FL2 > '
C     READ *,FL1,FL2
C     OPEN (7, ERR=200, FILE=FL1, STATUS='OLD')
C     OPEN (8, ERR=200, FILE=FL2, STATUS='OLD')
C
C READ IN FL1 & FL2
C
C     DO 2 I=1,91
C     READ (7,100) IP(I),X(I),Y(I),XV(I),YV(I)
C     2 READ (8,100) IP2,X2(I),Y2(I),XV2,YV2
C     100 FORMAT (I9,4F17.2)
C
C GENERATE HYDRO DATA BASE FOR 3RD & 4TH QUADRANTS
C
C     DO 5 IDUM=1,91
C     I=183-IDUM
C     X(I)=-X(IDUM)
C     Y(I)= Y(IDUM)
C     XV(I)=-XV(IDUM)
C     YV(I)= YV(IDUM)
C     X2(I)=-X2(IDUM)
C     5 Y2(I)= Y2(IDUM)
C
C ENTER THE BEGINNING & LENGTH OF PIECE
C BOTH ARE IN DEGREES CIRCUMFERENTIAL
C

```

Table B-12. FORTRAN Hydrocode Output Processor Program (Cont'd)

```

10 PRINT *, ENTER: PIECE START, PIECE LENGTH (DEG)
   READ *, FSTART,PLEN
   ISTART=NINT(FSTART/DELI)+1
   INUM =NINT(PLEN/DELI)
   ISTOP =ISTART+INUM-1
   IF (ISTOP.GT.182) GO TO 10
   UNITS =INUM
C
C "UNITS" REFERS TO MASS UNITS
C
   XVS=0.0
   YVS=0.0
C
C CALCULATE VELOCITY COMPONENTS OF PIECE & TOTAL VELOCITY
C UNITS ARE METERS/SEC
C
   DO 20 I=ISTART,ISTOP
   XVS=XVS+XV(I)
20 YVS=YVS+YV(I)
C
   XVT=XVS/UNITS
   YVT=YVS/UNITS
   VT =SQRT(XVT*XVT+YVT*YVT)
C
C CALCULATE AZIMUTH ANGLE, AZ, OF PIECE IN DEGREES
C AZ POSITIVE CLOCKWISE FROM +Y AXES
C
   AZ=ATAN2(XVT,YVT)*RD
C
C CALCULATE SPIN RATE IN CPS
C
   DELX1=X(ISTOP)-X(ISTART)
   DELY1=Y(ISTOP)-Y(ISTART)
   DELX2=X2(ISTOP)-X2(ISTART)
   DELY2=Y2(ISTOP)-Y2(ISTART)
   THETA1=ATAN2(DELY1,DELX1)*RD
   IF(THETA1.LT.0.0) THETA1=360.+THETA1
   THETA2=ATAN2(DELY2,DELX2)*RD
   IF(THETA2.LT.0.0) THETA2=360.+THETA2
   DLTHET=ABS(THETA1-THETA2)
   SPIN=DLTHET/(.002*360.)
C
C DETERMINE X & Y COORDINATES OF MID-POINT OF PIECE
C COORDINATES ARE IN CM FROM ORIGINAL CENTERLINE OF SRB
C
   UHALF=UNITS/2.
   UHALFX=AINT(UHALF)
   IF (UHALF.GT.UHALFX) GO TO 30
C
C EVEN NUMBER OF UNITS
C
   IMID1=INUM/2
   IMID2=IMID1+1
   XMID=0.5*(X(IMID1)+X(IMID2))
   YMID=0.5*(Y(IMID1)+Y(IMID2))

```

Table B-12. FORTRAN Hydrocode Output Processor Program (Cont'd)

```

      GO TO 40
C
C ODD NUMBER OF UNITS
C
      30 IMID=INT(UHALF)+1
        XMID=X(IMID)
        YMID=Y(IMID)
      40 CONTINUE
C
C OUTPUT RESULTS
C
      WRITE (6,140) PLEN,PSTART
140  FORMAT (' OUTPUT FOR PIECE ',F6.1,' DEG LONG, STARTING AT ',
        & F6.1,' DEG')
      WRITE (6,150) VT,AZ,SPIN
150  FORMAT (' VELOCITY= ',F6.0,' M/S      AZIMUTH= ',F6.0,' DEG',
        & ' SPIN= ',F5.1,' CPS')
      WRITE (6,160) XMID,YMID
160  FORMAT (' X & Y MID-POINT COORDINATES ARE ',F8.0,
        & ' AND ',F8.0,' CM')
C
      PRINT *, '
      PRINT *, ' ANOTHER PIECE? (Y/N) > '
      READ *,ANS
      IF (ANS. EQ. 'Y' .OR. ANS. EQ. 'y') GO TO 10
      GO TO 300
200  PRINT *, ' *** INPUT FILE ERROR *** '
300  CLOSE (7)
      CLOSE (8)
      STOP
      END

```

Table B-13. Typical Results for Table B-11 Output Element

PIECE LENGTH (DEG)	STARTING POINT (DEG)	VELOCITY (FT/SEC)	AZIMUTH (DEG)	SPIN (REV/SEC)
15.0	0.	465.	102.	13.1
	10.	388.	102.	10.5
	20.	300.	103.	11.8
	30.	224.	103.	9.4
	40.	162.	105.	7.8
	50.	100.	107.	5.6
	60.	77.	110.	3.5
	70.	59.	117.	3.6
	80.	31.	116.	1.2
	90.	24.	126.	2.1
30.0	0.	408.	102.	11.6
	10.	328.	103.	11.1
	20.	250.	103.	9.9
	30.	179.	104.	8.2
	40.	124.	106.	6.2
	50.	81.	110.	4.5
	60.	55.	114.	3.0
	70.	35.	118.	2.3
	80.	24.	129.	1.1
	90.	23.	136.	1.4
45.0	0.	344.	102.	11.0
	10.	270.	103.	9.8
	20.	198.	104.	8.5
	30.	144.	105.	6.6
	40.	94.	108.	5.2
	50.	64.	111.	3.5
	60.	44.	116.	2.5
	70.	30.	124.	1.7
	80.	23.	141.	0.6
	90.	23.	169.	0.8
90.0	0.	214.	104.	7.7
	10.	162.	105.	6.5
	20.	118.	106.	5.3
	30.	85.	109.	4.1
	40.	57.	116.	2.9
	50.	39.	129.	2.1
	60.	28.	139.	1.4
	70.	23.	153.	0.9
	80.	19.	165.	0.7
	90.	19.	176.	0.3
180.0	0.	109.	108.	4.1
	10.	83.	111.	3.4
	20.	61.	115.	2.7
	30.	44.	121.	2.0
	40.	32.	129.	1.4
	50.	25.	141.	0.9
	60.	22.	151.	0.6
	70.	20.	163.	0.3
	80.	19.	172.	0.1
	90.	19.	179.	0.0

Table 5-14. Remaining Pressure Pulse Velocity (ft/Sec)

Breaktime (ms)	0-20	20-70	MET 70-105	105-120(H)	105-120(L)
0.00	290.07	237.35	203.44	166.00	605.40
0.50	272.81	223.23	191.34	148.83	577.00
1.00	259.69	196.12	168.10	131.82	548.86
1.50	209.62	171.52	147.02	114.96	520.98
2.00	182.88	149.64	128.26	298.26	493.75
2.50	159.22	130.28	111.67	281.71	465.98
3.00	138.38	113.23	97.05	265.43	439.05
3.50	120.03	98.22	84.18	249.51	412.72
4.00	103.84	84.97	72.83	233.96	387.00
4.50	89.78	73.46	62.97	218.78	361.88
5.00	77.82	63.68	54.58	203.96	337.38
5.50	67.42	55.16	47.28	189.63	313.66
6.00	58.02	47.47	40.69	175.88	290.92
6.50	49.62	40.60	34.80	162.72	269.16
7.00	42.24	34.56	29.62	150.15	248.37
7.50	35.85	29.34	25.15	138.17	228.56
8.00	30.27	24.77	21.23	126.77	209.69
8.50	25.28	20.68	17.73	115.92	191.74
9.00	20.87	17.08	14.64	105.63	174.72
9.50	17.06	13.96	11.96	95.89	158.62
10.00	13.83	11.32	9.70	86.71	143.43
10.50	11.06	9.05	7.76	78.10	129.19
11.00	8.62	7.05	6.05	70.07	115.90
11.50	6.50	5.32	4.56	62.61	103.57
12.00	4.71	3.85	3.30	55.73	92.19
12.50	3.24	2.65	2.27	49.44	81.77
13.00	2.06	1.69	1.44	43.65	72.20
13.50	1.14	0.94	0.80	38.31	63.37
14.00	0.49	0.40	0.34	33.41	55.27
14.50	0.10	0.08	0.07	28.96	47.91
15.00				24.96	41.28
15.50				21.33	35.28
16.00				18.01	29.80
16.50				15.01	24.83
17.00				12.32	20.37
17.50				9.94	16.43
18.00				7.80	12.91
18.50				5.86	9.70
19.00				4.11	6.80
19.50				2.55	4.21
20.00				1.17	1.94

Table B-15. Summary of Cutline Octants and Quadrants

MET Range (sec)	Fragment Size	Vel. Range (ft/sec)	AZ Range (deg)	Spin-Rate Range (rev/s)
0-20*	Octant	273-344	84-102	9.6-12.5
	Quadrant	181-227	96-104	6.6-8.5
20-70*	Octant	233-319	82-104	8.0-11.5
	Quadrant	158-206	93-113	5.7-7.7
70-105*	Octant	240-339	92-106	7.7-11.2
	Quadrant	193-261	106-117	5.4-7.8
105-120(H)	Octant	413-450	69-82	8.6-11.0
	Quadrant	326-339	83-92	5.8-8.4
105-120(L)	Octant	650-717	72-89	10.9-19.8
	Quadrant	514-537	83-95	7.9-14.1

\*K<sub>p</sub> 0.8 to 1.0

Table B-16. Velocity Reduction Factors for SRB Wall and Joint Fragments Impacting Intervening Orbiter Structure for Ulysses Mission

Cylinder	Fragment Station of Origin	Values for Hit Wing/Miss Wing		Wing Intersection Angle (deg)
		MET < 105 sec	MET ≥ 105 sec	
4	1213	0.81/0.90	0.88/0.94	29.9
5a	1093	0.81/0.90	0.84/0.92	36.8
5b	1053	0.81/0.90	0.92/0.96	38.2
5c	1013	0.81/0.90	0.84/0.92	39.1
5/6 joint	973	0.81/0.90	0.82/0.91	40.5
6	893	0.81/0.90	0.88/0.94	42.1
7	733	0.81/0.90	0.84/0.92	44.1

Table B-17. Velocity Reduction Factors for SRB Wall and Joint Fragments Impacting Intervening Orbiter Structure for Galileo Mission

Cylinder	Fragment Station of Origin	Values for Hit Wing/Miss Wing		Wing Intersection Angle (deg)
		MET < 105 sec	MET ≥ 105 sec	
4	1213	0.80/0.91	0.88/0.94	28.1
5a	1093	0.80/0.91	0.82/0.90	38.3
5b	1053	0.80/0.91	0.82/0.90	41.0
5c	1013	0.80/0.91	0.82/0.90	43.9
5/6 joint	973	0.80/0.91	0.80/0.91	47.8
6	893	0.80/0.91	0.88/0.94	46.0
7	733	0.80/0.91	0.82/0.90	52.1

Table B-18. Velocity Reduction Factors for Clevis Pins Impacting Intervening Orbiter Structure for Both Galileo and Ulysses Missions

	Hit Wing Reduction		Miss Wing Reduction	
	Max	Min	Max	Min
Relative Probability	0.23	0.77	0.22	0.78
Velocity Reduction Factor	0.70	0.77	0.85	0.92

Table B-19. Potential RTG Shrapnel Sources From Nearby Orbiter Structural Components and Equipment Due to ET Propellant Near-Pad and In-Flight Explosions

Fragment	No.	Location			Weight (lb)	Size (in)	Area (in <sup>2</sup> )	Beta (psi)
		X <sub>o</sub>	Y <sub>o</sub>	Z <sub>o</sub>				
GALILEO								
PLBD Hinges	8	851	±106	420	10.6	1.0Dx3.1	2.83	3.7
		918, 966			11.9	0.6Dx1.8	0.99	12.0
		1033			9.9	0.8Dx1.8	1.38	7.2
PLBD Hinge Covers	4	851, 918	±108	420	1.0	0.6Dx1.8	0.99	1.0
PLBD Hinge Actuators	4	904, 966	±98	404	6.0	4x4x4	24	0.25
Radiator Hinges	10	857, 927	±100	423	1.1	3x4x1	9.5	0.12
		966, 1011		429				
		1056						
LH <sub>2</sub> Fill and Drain	3	815	-100	371	1.0	0.8Dx2	1.51	0.66
		819, 824				0.6Dx2	1.08	0.93
N <sub>2</sub> Bottle Fill	1	851	-100	371	1.0	0.5Dx2	0.88	1.1
LOX Vent	1	855	-100	371	0.9	0.5Dx1	0.49	1.8
PLB Floodlights	2	968	±92	376	7.5	10x5x7	77.5	0.097
PLB Vent Filters	4	915	±105	381	2.3	15.5x5.8x0.6	51.3	0.045
		1006				17.5x5.8x0.6	57.7	0.040
PLB Vent Door Actuators	4	925	±99	383	10.9	6x6x6	54	0.20
		995		393	9.0	6x6x6	54	0.17
ULYSSES								
PLBD Latch Housings	6	828, 873 918, 966 1011, 1056	1	496	8.9	4x4x3	20	0.44
PLBD Latch Actuators	2	856 1028	8	497	15	8x12x4	88	0.17



Table B-20. Probabilistic Flyer-Plate Velocity at RTG for On-Pad Explosions Due to SRB-Failure-Initiated Breakup or Tower Impact

Height X (ft)	Percent- tile (%)	Pdelta stat (psi)	P dyn (psi)	P refl (psi)	I stat (psi-s)	I dyn (psi-s)	--FLYER PLATE VELOCITY (fps) --			
							<--AREA DENSITY = 0.0240 psi-->			
							Phi=0	Phi=30	Phi=60	Phi=90
3	N/A	2075	810	5300	0.580	0.058	678*	1363*	1973*	2186*
3	N/A	659	1720	5169	2.010	0.330	1078	1640	2431	2661*
20	50.0	41	38	187	0.250	0.078	188*	201*	447*	544*
20	10.0	106	123	332	0.710	0.190	429*	518*	833*	1096
20	1.0	206	294	1271	1.340	0.380	687	888	1424	1589
20	0.1	349	324	2407	1.830	0.600	888	1187	1848	2034
30	50.0	27	22	103	0.220	0.078	151*	185*	307*	381*
30	10.0	77	83	386	0.690	0.210	384*	412*	772*	897*
30	1.0	143	194	808	1.270	0.380	601	678	1271	1328
30	0.1	322	305	2189	1.860	0.620	872	1139	1789	1993
40	50.0	18	15	67	0.190	0.071	121*	133*	203*	278*
40	10.0	58	58	261	0.610	0.220	331*	361*	635*	734*
40	1.0	114	148	805	1.230	0.380	550	581	1028	1172
40	0.1	203	318	1248	1.830	0.690	758	872	1434	1612
55	50.0	8	10	37	0.160	0.068	83*	94*	116*	157*
55	10.0	42	39	172	0.530	0.210	275*	303*	488*	585*
55	1.0	88	100	423	1.110	0.420	481	524	884	1000
55	0.1	154	217	887	1.550	0.730	652	734	1242	1407
70	50.0	7	7	31	0.140	0.066	69*	78*	99*	127*
70	10.0	33	30	128	0.490	0.210	241*	268*	400*	488*
70	1.0	72	81	336	1.070	0.440	444	489	768	888
70	0.1	129	200	708	1.720	0.760	627	683	1128	1286
100	50.0	1	4	17	0.110	0.057	18*	26*	42*	55*
100	10.0	21	18	78	0.410	0.200	184*	208*	277*	356*
100	1.0	47	47	197	0.900	0.420	354	385	570	684
100	0.1	82	117	461	1.340	0.790	536	600	830	1072
150	50.0	0	0	0	0.000	0.000	nil	nil	nil	nil
150	10.0	11	11	43	0.320	0.190	122*	143*	183*	224*
150	1.0	38	34	142	0.830	0.480	308	349	478	575
150	0.1	49	51	207	1.780	0.640	417	460	618	732
200	50.0	0	0	0	0.000	0.000	nil	nil	nil	nil
200	10.0	8	7	28	0.280	0.180	82*	100*	133*	153*
200	1.0	25	24	94	0.720	0.460	247*	286	372	450
200	0.1	48	55	202	1.240	0.820	388	444	612	727

\* = numerical solution terminated at approximately V-max.  
 - = just below pool surface @ X<sub>0</sub> = 3 ft; rho<sub>0</sub> = 0.0036 g/cm<sup>3</sup>; Q<sub>0</sub> = 1830 cal/s.  
 + = just above pool surface @ same conditions.

Table B-21. Probabilistic Flyer-Plate Velocity at RTG for In-Trench Explosions Due to SRB-Failure-Initiated Breakup or Tower Impact

Height X (ft)	Percent tile (%)	Pdelta		P		I		--FLYER PLATE VELOCITY (fps) --			
		stat (psi)	dyn (psi)	refl (psi)	stat (psi-s)	dyn (psi-s)	<--AREA DENSITY = 0.0240 psi-->				
								Phi=0	Phi=30	Phi=60	Phi=90
6 <sup>-</sup>	N/A	2075	810	5300	1.200	0.120	1025*	1386*	2000*	2220*	
6 <sup>+</sup>	N/A	659	1720	5189	4.020	0.660	1297	1654	2451	2691	
110	50.0	22	18	82	0.660	0.240	228*	248*	315	388*	
110	10.0	64	66	289	1.910	0.640	476	522	737	862	
110	1.0	122	157	660	3.360	1.170	677	747	1123	1278	
110	0.1	163	236	953	4.190	1.550	781	868	1326	1497	
130	50.0	18	15	67	0.830	0.240	200*	224*	277	338*	
130	10.0	55	55	239	1.820	0.650	441	485	667	786	
130	1.0	108	136	566	3.270	1.220	641	710	1051	1200	
130	0.1	150	230	650	5.420	3.000	770	879	1281	1459	
150	50.0	14	12	53	0.570	0.230	188*	191*	234*	283*	
150	10.0	47	44	197	1.660	0.640	405	447	599	711	
150	1.0	91	110	454	3.030	1.200	590	656	950	1080	
150	0.1	136	230	744	5.100	2.630	735	845	1222	1385	
200	50.0	8	8	34	0.470	0.210	115*	133*	168*	194*	
200	10.0	34	31	133	1.500	0.630	340	378	482	575	
200	1.0	72	83	336	2.820	1.240	527	589	823	953	
200	0.1	124	187	675	4.600	2.100	701	794	1161	1318	
290	50.0	3	5	7	0.400	0.200	57*	71*	100*	114*	
290	10.0	22	19	82	1.250	0.620	284	296	384	430	
290	1.0	48	50	207	2.480	1.280	433	488	641	754	
290	0.1	67	110	429	3.840	2.170	591	670	946	1084	

\* = numerical solution terminated at approximately V-max.  
 - = just below pool surface @ X<sub>0</sub> = 6 ft; rho<sub>0</sub> = 0.0056 g/cm<sup>3</sup>; Q<sub>0</sub> = 1050 cal/g.  
 + = just above pool surface @ same conditions.

Table B-22. Probabilistic Flyer-Plate Velocity at RTG for Aft-Compartment-Initiated Explosions

Height (ft)	Percent tile	Pdelta stat (psi)	P dyn (psi)	P refl (psi)	I stat (psi-s)	I dyn (psi-s)	--FLYER PLATE VELOCITY (fps) --			
							Phi=0	Phi=30	Phi=60	Phi=90
[---AREA DENSITY = 0.0240 psi---]										
1	N/A	2075	810	5300	0.190	0.019	407*	1360*	1973*	2185*
1	N/A	659	1720	5169	0.670	0.110	616*	1630*	2394*	2631*
20	50.0	18	15	67	0.093	0.037	82*	90*	190*	261*
20	10.0	49	47	207	0.240	0.088	192*	226*	318*	621*
20	1.0	95	115	480	0.430	0.160	322*	462*	674*	1005*
20	0.1	175	297	1040	0.670	0.290	477*	765*	1286*	1449*
30	50.0	9	8	37	0.072	0.033	56*	62*	82*	140*
30	10.0	32	29	124	0.200	0.090	152*	168*	353*	443*
30	1.0	72	83	336	0.410	0.190	290*	355*	716*	837*
30	0.1	117	172	627	0.610	0.300	409*	560*	1012*	1161*
40	50.0	4	6	24	0.061	0.031	36*	43*	55*	73*
40	10.0	23	20	86	0.170	0.068	125*	141*	257*	337*
40	1.0	50	52	212	0.350	0.180	238*	268*	538*	647*
40	0.1	88	121	435	0.590	0.310	372*	441*	844*	976*
55	50.0	0	0	0	0.000	0.000	nil	nil	nil	nil
55	10.0	14	13	53	0.140	0.062	84*	108*	152*	224*
55	1.0	36	34	142	0.300	0.170	187*	224*	408*	506*
55	0.1	84	111	408	0.540	0.380	350*	424*	821*	952*
70	50.0	0	0	0	0.000	0.000	nil	nil	nil	nil
70	10.0	9	9	37	0.130	0.077	75*	88*	112*	156*
70	1.0	27	25	102	0.260	0.170	166*	192*	315*	406*
70	0.1	78	104	373	0.570	0.460	352*	416*	789*	924*
100	50.0	0	0	0	0.000	0.000	nil	nil	nil	nil
100	10.0	4	6	24	0.110	0.074	47*	57*	78*	90*
100	1.0	16	15	60	0.210	0.160	121*	144*	198*	271*
100	0.1	32	32	124	0.340	0.270	202*	238*	363*	464*
150	50.0	0	0	0	0.000	0.000	nil	nil	nil	nil
150	10.0	0	0	0	0.000	0.000	nil	nil	nil	nil
150	1.0	8	8	34	0.170	0.150	80*	98*	133*	163*
150	0.1	17	17	63	0.260	0.250	137*	167*	228*	300*
200	50.0	0	0	0	0.000	0.000	nil	nil	nil	nil
200	10.0	0	0	0	0.000	0.000	nil	nil	nil	nil
200	1.0	4	6	24	0.150	0.130	53*	67*	95*	108*
200	0.1	14	15	53	0.250	0.260	124*	153*	207*	266*

\* = numerical solution terminated at approximately V-max.  
 - = just below pool surface @ X<sub>0</sub> = 1 ft; rho<sub>0</sub> = 0.0058 g/cm<sup>3</sup>; Q<sub>0</sub> = 1650 cal/g.  
 + = just above pool surface @ same conditions.

Table B-23. Flyer-Plate Velocity at RTG for In-Flight Vapor  
Cloud Initiated Explosions

Height X (ft)	Percent tile (Z)	Pdelta		P		I		--FLYER PLATE VELOCITY (fps) --			
		stat (psi)	dyn (psi)	refl (psi)	stat (psi-s)	dyn (psi-s)	<--AREA DENSITY = 0.0240 psi-->				
								Phi=0	Phi=30	Phi=60	Phi=90
283 <sup>-</sup>	N/A	298	122	1991	3.230	1.600	858	1114	1751	1949	
285 <sup>+</sup>	N/A	283	142	1714	3.220	1.690	815	1047	1658	1848	
291	N/A	136	181	759	2.490	1.670	683	775	1201	1362	
398	N/A	63	61	284	1.480	1.430	454	518	745	889	
528	N/A	33	21	129	0.930	1.080	305	344	458	549	
782	N/A	14	5	53	1.130	0.480	290	214	264	285	
824	N/A	10	3	40	1.280	0.310	185	174	193	219	
1056	N/A	8	2	34	1.190	0.220	141	147	161	180	

- \* = numerical solution terminated at approximately V-max.,
- = just inside reaction zone.
- + = just outside reaction zone.

Table B-24. Probabilistic Shrapnel Velocity at RTG for On-Pad Explosions Due to SRB-Failure-Initiated Breakup or Tower Impact (Phi = 0 degrees)

Height X (ft)	Percent tile (%)	Pdelta stat (psi)	P dyn (psi)	P refl (psi)	I stat (psi-s)	I dyn (psi-s)	Phi angle (deg)	SHRAPNEL VELOCITY (fps)					
								FLYER P=0.024 psi/ Beta psi (below)					
								0.1200	0.2500	0.5000	1.0000	3.0000	8.0000
3	N/A	2075	810	5300	0.580	0.058	0	86°	40°	20°	10°	3°	1°
3	N/A	659	1720	5189	2.010	0.330	0	87°	42°	21°	11°	4°	1°
20	50.0	41	38	187	0.250	0.078	0	24°	11°	5°	3°	nil	nil
20	10.0	108	123	552	0.710	0.190	0	52°	24°	12°	6°	2°	nil
20	1.0	208	294	1271	1.340	0.380	0	83°	44°	22°	11°	4°	1°
20	0.1	348	524	2407	1.830	0.600	0	148°	71°	35°	18°	6°	2°
30	50.0	27	22	103	0.220	0.078	0	22°	10°	5°	3°	nil	nil
30	10.0	77	83	388	0.880	0.210	0	54°	25°	13°	6°	2°	nil
30	1.0	143	194	808	1.220	0.380	0	84°	45°	22°	11°	4°	1°
30	0.1	322	505	2189	1.860	0.620	0	187°	84°	47°	24°	8°	3°
40	50.0	18	15	87	0.180	0.071	0	18°	8°	5°	2°	nil	nil
40	10.0	38	38	281	0.810	0.220	0	55°	28°	13°	6°	2°	nil
40	1.0	114	148	605	1.230	0.380	0	83°	44°	22°	11°	4°	1°
40	0.1	203	318	1248	1.830	0.680	0	185°	78°	40°	20°	7°	2°
55	50.0	8	10	37	0.180	0.088	0	18°	8°	4°	2°	nil	nil
55	10.0	42	38	172	0.530	0.210	0	52°	25°	12°	6°	2°	nil
55	1.0	86	100	423	1.110	0.420	0	101°	48°	24°	12°	4°	1°
55	0.1	154	217	887	1.550	0.730	0	175°	84°	42°	21°	7°	2°
70	50.0	7	7	31	0.140	0.088	0	17°	8°	4°	2°	nil	nil
70	10.0	33	30	128	0.480	0.210	0	51°	25°	12°	6°	2°	nil
70	1.0	72	81	338	1.070	0.448	0	107°	51°	28°	13°	4°	1°
70	0.1	128	200	708	1.720	0.780	0	182°	88°	44°	22°	7°	2°
100	50.0	1	4	17	0.118	0.057	0	14°	7°	3°	2°	nil	nil
100	10.0	21	18	78	0.418	0.200	0	48°	24°	12°	6°	2°	nil
100	1.0	47	47	187	0.800	0.420	0	103°	48°	25°	12°	4°	1°
100	0.1	82	117	481	1.548	0.780	0	183°	83°	47°	23°	8°	3°
150	50.0	0	0	0	0.000	0.000	0	nil	nil	nil	nil	nil	nil
150	10.0	11	11	43	0.320	0.180	0	46°	22°	11°	6°	2°	nil
150	1.0	38	34	142	0.830	0.480	0	118°	57°	28°	14°	5°	2°
150	0.1	48	51	287	1.780	0.840	0	158°	77°	38°	18°	6°	2°
200	50.0	0	0	0	0.000	0.000	0	nil	nil	nil	nil	nil	nil
200	10.0	6	7	28	0.280	0.180	0	44°	21°	11°	5°	2°	nil
200	1.0	25	24	84	0.720	0.480	0	115°	55°	28°	14°	5°	2°
200	0.1	48	55	282	1.348	0.820	0	205°	88°	50°	25°	8°	3°

\* = numerical solution terminated at approximately V-max.  
 - = just below pool surface @ X<sub>0</sub> = 3 ft; rho<sub>0</sub> = 0.0058 g/cm<sup>3</sup>; Q<sub>0</sub> = 1050 cal/g.  
 + = just above pool surface @ same conditions.

Table B-25. Probabilistic Shrapnel Velocity at RTG for In-Trench Explosions Due to SRB-Failure-Initiated Breakup or Tower Impact (Phi = 0 degrees)

Height X (ft)	Percent- tile (%)	Pdelta stat (psi)	P dyn (psi)	P refl (psi)	I stat (psi-s)	I dyn (psi-s)	Phi angle (deg)	----- SHRAPNEL VELOCITY (fps) -----					
								----- FLYERP=0.024 psi/ Beta psi (below) -----					
								0.1200	0.2500	0.5000	1.0000	3.0000	9.0000
6 <sup>-</sup>	N/A	2075	810	3300	1.200	0.120	0	101°	47°	23°	11°	4°	1°
6 <sup>+</sup>	N/A	659	1720	3189	4.020	0.660	0	176°	84°	42°	21°	7°	2°
110	50.0	22	18	82	0.660	0.240	0	59°	28°	14°	7°	2°	nil
110	10.0	64	66	289	1.910	0.640	0	158°	76°	38°	19°	6°	2°
110	1.0	122	157	660	3.360	1.170	0	289°	139°	70°	35°	12°	4°
110	0.1	183	236	953	4.180	1.550	0	383°	185°	93°	46°	15°	5°
130	50.0	18	15	67	0.630	0.240	0	59°	28°	14°	7°	2°	nil
130	10.0	55	55	239	1.820	0.650	0	162°	78°	39°	20°	7°	2°
130	1.0	108	138	568	3.270	1.220	0	304°	146°	73°	37°	12°	4°
130	0.1	150	230	850	5.420	3.000	0	764	389	185°	92°	31°	10°
150	50.0	14	12	53	0.570	0.230	0	57°	27°	14°	7°	2°	nil
150	10.0	47	44	197	1.680	0.640	0	160°	77°	39°	19°	6°	2°
150	1.0	91	110	454	3.030	1.200	0	301°	145°	72°	36°	12°	4°
150	0.1	136	230	744	5.180	2.850	0	671	323°	162°	81°	27°	8°
200	50.0	8	8	34	0.470	0.210	0	52°	25°	12°	6°	2°	nil
200	10.0	34	31	133	1.500	0.630	0	159°	77°	38°	19°	6°	2°
200	1.0	72	83	336	2.820	1.240	0	314°	151°	76°	38°	13°	4°
200	0.1	124	187	675	4.600	2.100	0	530	255°	128°	64°	21°	7°
290	50.0	3	3	7	0.400	0.200	0	49°	24°	12°	6°	2°	nil
290	10.0	22	19	82	1.280	0.620	0	158°	76°	38°	18°	6°	2°
290	1.0	48	50	207	2.460	1.280	0	323	156°	78°	39°	13°	4°
290	0.1	87	110	429	3.940	2.170	0	553	268	134°	67°	22°	7°

\* = numerical solution terminated at approximately V-max.  
 - = just below pool surface @ X<sub>0</sub> = 6 ft; rho<sub>0</sub> = 0.0036 g/cm<sup>3</sup>; Q<sub>0</sub> = 1050 cal/g.  
 + = just above pool surface @ same conditions.

Table B-26. Probabilistic Shrapnel Velocity at RTG for  
Aft-Compartment-Initiated Explosions (Phi = 0 degrees)

Height X (ft)	Percent- tile (Z)	Pdelta stat (psi)	P dyn (psi)	P refl (psi)	I stat (psi-s)	I dyn (psi-s)	Phi angle (deg)	SHRAPNEL VELOCITY (fps)					
								0.1200	0.2500	0.5000	1.0000	3.0000	8.0000
1 <sup>-</sup>	N/A	2075	810	5300	0.190	0.019	0	58°	28°	14°	7°	2°	nil
1 <sup>+</sup>	N/A	659	1720	5169	0.670	0.110	0	55°	25°	12°	6°	2°	nil
20	50.0	18	15	67	0.093	0.037	0	13°	6°	3°	1°	nil	nil
20	10.0	49	47	207	0.240	0.088	0	27°	13°	6°	3°	1°	nil
20	1.0	95	115	480	0.430	0.160	0	45°	21°	11°	5°	2°	nil
20	0.1	175	297	1040	0.670	0.290	0	76°	37°	18°	9°	3°	1°
30	50.0	8	8	37	0.072	0.033	0	10°	5°	2°	1°	nil	nil
30	10.0	32	28	124	0.200	0.090	0	25°	12°	6°	3°	nil	nil
30	1.0	72	83	336	0.410	0.190	0	49°	23°	12°	6°	2°	nil
30	0.1	117	172	627	0.610	0.300	0	76°	36°	18°	9°	3°	nil
40	50.0	4	6	24	0.061	0.031	0	8°	4°	2°	1°	nil	nil
40	10.0	23	20	86	0.170	0.086	0	23°	11°	6°	3°	nil	nil
40	1.0	50	52	212	0.350	0.160	0	45°	22°	11°	5°	2°	nil
40	0.1	88	121	435	0.590	0.310	0	76°	36°	18°	9°	3°	1°
55	50.0	0	0	0	0.000	0.000	0	nil	nil	nil	nil	nil	nil
55	10.0	14	13	53	0.140	0.082	0	21°	10°	5°	2°	nil	nil
55	1.0	38	34	142	0.300	0.170	0	42°	20°	10°	5°	2°	nil
55	0.1	84	111	409	0.540	0.300	0	84°	45°	22°	11°	4°	1°
70	50.0	0	0	0	0.000	0.000	0	nil	nil	nil	nil	nil	nil
70	10.0	9	9	37	0.130	0.077	0	19°	9°	5°	2°	nil	nil
70	1.0	27	25	102	0.280	0.170	0	42°	20°	10°	5°	2°	nil
70	0.1	78	104	373	0.570	0.400	0	110°	53°	27°	13°	4°	1°
100	50.0	0	0	0	0.000	0.000	0	nil	nil	nil	nil	nil	nil
100	10.0	4	6	24	0.110	0.074	0	18°	9°	4°	2°	nil	nil
100	1.0	16	15	60	0.210	0.100	0	39°	19°	9°	5°	2°	nil
100	0.1	32	32	124	0.340	0.270	0	66°	32°	16°	8°	3°	nil
150	50.0	0	0	0	0.000	0.000	0	nil	nil	nil	nil	nil	nil
150	10.0	0	0	0	0.000	0.000	0	nil	nil	nil	nil	nil	nil
150	1.0	6	9	34	0.170	0.130	0	36°	17°	8°	4°	1°	nil
150	0.1	17	17	63	0.280	0.250	0	61°	29°	15°	7°	2°	nil
200	50.0	0	0	0	0.000	0.000	0	nil	nil	nil	nil	nil	nil
200	10.0	0	0	0	0.000	0.000	0	nil	nil	nil	nil	nil	nil
200	1.0	4	6	24	0.150	0.130	0	31°	15°	7°	4°	1°	nil
200	0.1	14	15	53	0.250	0.260	0	64°	31°	15°	8°	3°	nil

\* = numerical solution terminated at approximately V-max.,  
 - = just below pool surface @ X<sub>0</sub> = 1 ft; rho<sub>0</sub> = 0.0036 g/cm<sup>3</sup>; Q<sub>0</sub> = 1030 cal/g.  
 + = just above pool surface @ same conditions.

Table B-27. Shrapnel Velocity at RTG for In-Flight Vapor Cloud Initiated Explosions (Phi = 0 degrees)

Height X (ft)	Percent tile (%)	Pdelta		P		I		Phi angle (deg)	SHRAPNEL VELOCITY (fps)					
		stat	dyn	refl	stat	dyn	FLYER=0.024 psi/Beta psi (below)							
		(psi)	(psi)	(psi)	(psi-s)	(psi-s)	0.1200		0.2500	0.5000	1.0000	3.0000	9.0000	
283 <sup>*</sup>	N/A	288	122	1991	3.230	1.800	0	415	200 <sup>*</sup>	100 <sup>*</sup>	50 <sup>*</sup>	17 <sup>*</sup>	8 <sup>*</sup>	
285 <sup>*</sup>	N/A	283	142	1714	3.220	1.880	0	436	210 <sup>*</sup>	103 <sup>*</sup>	53 <sup>*</sup>	18 <sup>*</sup>	8 <sup>*</sup>	
291	N/A	136	181	759	2.490	1.670	0	418 <sup>*</sup>	202 <sup>*</sup>	101 <sup>*</sup>	51 <sup>*</sup>	17 <sup>*</sup>	8 <sup>*</sup>	
396	N/A	63	61	284	1.490	1.430	0	367	177 <sup>*</sup>	88 <sup>*</sup>	44 <sup>*</sup>	15 <sup>*</sup>	5 <sup>*</sup>	
528	N/A	33	21	128	0.830	1.060	0	278	135	68 <sup>*</sup>	34 <sup>*</sup>	11 <sup>*</sup>	4 <sup>*</sup>	
782	N/A	14	5	53	1.130	0.480	0	125	61 <sup>*</sup>	30 <sup>*</sup>	15 <sup>*</sup>	5 <sup>*</sup>	2 <sup>*</sup>	
824	N/A	10	3	40	1.260	0.310	0	81	38 <sup>*</sup>	20 <sup>*</sup>	10 <sup>*</sup>	3 <sup>*</sup>	1 <sup>*</sup>	
1036	N/A	8	2	34	1.180	0.220	0	58	28 <sup>*</sup>	14 <sup>*</sup>	7 <sup>*</sup>	2 <sup>*</sup>	nil	

\* = numerical solution terminated at approximately V-max.,

- = just inside reaction zone.

+ = just outside reaction zone.



Table B-28. Probabilistic Shrapnel Velocity at RTG for On-Pad Explosions Due to SRB-Failure-Initiated Breakup or Tower Impact (Phi = 90 degrees)

Height (ft)	Percent tile (%)	Pdelta stat (psi)	P dyn (psi)	P refl (psi)	I stat (psi-s)	I dyn (psi-s)	Phi angle (deg)	SHRAPNEL VELOCITY (fps)					
								0.1200	0.2500	0.5000	1.0000	3.0000	9.0000
6 <sup>-</sup>	N/A	2075	810	9300	1.200	0.120	90	125°	38°	29°	14°	5°	2°
6 <sup>+</sup>	N/A	659	1720	5189	4.020	0.660	90	226°	107°	53°	27°	9°	3°
110	50.0	22	18	82	0.660	0.240	90	68	33°	18°	8°	3°	nil
110	10.0	64	66	289	1.910	0.640	90	171	84	42°	21°	7°	2°
110	1.0	122	157	660	3.360	1.170	90	296	148	75	38°	13°	4°
110	0.1	163	236	953	4.190	1.550	90	367	193	98	49°	16°	5°
130	50.0	18	15	67	0.630	0.240	90	68	33°	16°	6°	3°	nil
130	10.0	55	55	238	1.820	0.650	90	171	85	43	21°	7°	2°
130	1.0	108	136	586	3.270	1.220	90	301	153	78	38°	13°	4°
130	0.1	150	230	850	5.420	3.000	90	548	307	177	84	32°	11°
150	50.0	14	12	53	0.570	0.230	90	64	31	15°	6°	3°	nil
150	10.0	47	44	197	1.680	0.640	90	165	83	42	21°	7°	2°
150	1.0	91	110	454	3.030	1.200	90	288	148	77	38°	13°	4°
150	0.1	136	230	744	5.100	2.650	90	525	287	166	83	28°	8°
200	50.0	8	8	34	0.470	0.210	90	57	28	14°	7°	2°	nil
200	10.0	34	31	133	1.500	0.630	90	148	80	41	21°	7°	2°
200	1.0	72	83	338	2.820	1.240	90	281	150	78	40	13°	4°
200	0.1	124	187	675	4.600	2.100	90	432	243	130	67	22°	7°
290	50.0	3	3	7	0.400	0.200	90	51	25	13°	6°	2°	nil
290	10.0	22	19	82	1.280	0.620	90	133	75	40	20	7°	2°
290	1.0	49	50	207	2.460	1.280	90	250	140	77	40	14°	5°
290	0.1	87	110	428	3.940	2.170	90	371	225	128	68	23°	8°

\* = numerical solution terminated at approximately V-max.  
 - = just below pool surface @ X<sub>0</sub> = 8 ft; rho<sub>0</sub> = 0.0036 g/cm<sup>3</sup>; Q<sub>0</sub> = 1050 cal/g.  
 + = just above pool surface @ same conditions.

Table B-29. Probabilistic Shrapnel Velocity at RTG for In-Trench Explosions Due to SRB-Failure-Initiated Breakup or Tower Impact ( $\Phi = 90$  degrees)

Height (ft)	Percent (%)	Pdelta stat (psi)	P dyn (psi)	P refl (psi)	I stat (psi-s)	I dyn (psi-s)	Phi angle (deg)	----- SHRAPNEL VELOCITY (fps) -----					
								----- FLYER=0.024 psi/ Beta psi (below) -----					
								0.1200	0.2500	0.5000	1.0000	3.0000	9.0000
3*	N/A	2075	410	5300	0.580	0.058	90	82*	43*	21*	11*	4*	1*
3*	N/A	659	1720	5169	2.010	0.330	90	122*	59*	30*	15*	5*	2*
20	50.0	41	36	187	0.250	0.078	90	33*	15*	8*	4*	1*	nil
20	10.0	106	123	332	0.710	0.190	90	70*	33*	16*	8*	3*	nil
20	1.0	206	294	1271	1.340	0.380	90	120*	56*	28*	14*	5*	2*
20	0.1	348	324	2407	1.830	0.600	90	188*	88*	44*	22*	7*	2*
30	50.0	27	22	103	0.220	0.078	90	30*	14*	7*	3*	1*	nil
30	10.0	77	83	366	0.690	0.210	90	70*	33*	16*	8*	3*	nil
30	1.0	143	194	808	1.220	0.380	90	117*	56*	28*	14*	5*	2*
30	0.1	322	505	2189	1.860	0.820	90	234	111*	55*	28*	9*	3*
40	50.0	18	15	87	0.190	0.071	90	28*	12*	6*	3*	1*	nil
40	10.0	59	59	281	0.810	0.220	90	69*	33*	16*	8*	3*	nil
40	1.0	114	148	605	1.230	0.380	90	114*	54*	27*	13*	4*	1*
40	0.1	203	318	1248	1.930	0.690	90	195	93*	46*	23*	8*	3*
55	50.0	9	10	37	0.160	0.069	90	23*	11*	5*	3*	nil	nil
55	10.0	42	39	172	0.530	0.210	90	64*	31*	15*	8*	3*	nil
55	1.0	86	100	423	1.110	0.420	90	121	58*	29*	14*	5*	2*
55	0.1	154	217	667	1.530	0.730	90	202	96*	48*	24*	8*	3*
70	50.0	7	7	31	0.140	0.066	90	22*	10*	5*	3*	nil	nil
70	10.0	33	30	128	0.490	0.210	90	63*	30*	15*	7*	2*	nil
70	1.0	72	81	336	1.070	0.440	90	124	59*	30*	15*	5*	2*
70	0.1	129	200	708	1.720	0.780	90	206	99*	49*	25*	8*	3*
100	50.0	1	4	17	0.110	0.057	90	18*	8*	4*	2*	nil	nil
100	10.0	21	18	78	0.410	0.200	90	56	28*	14*	7*	2*	nil
100	1.0	47	47	197	0.900	0.420	90	117	56	28*	14*	5*	2*
100	0.1	82	117	461	1.540	0.790	90	208	102	51*	26*	8*	3*
150	50.0	0	0	0	0.000	0.000	90	nil	nil	nil	nil	nil	nil
150	10.0	11	11	43	0.320	0.190	90	53	28*	13*	6*	2*	nil
150	1.0	36	34	142	0.830	0.400	90	128	63	32*	16*	5*	2*
150	0.1	48	51	207	1.780	0.840	90	168	83	42	21*	7*	2*
200	50.0	0	0	0	0.000	0.000	90	nil	nil	nil	nil	nil	nil
200	10.0	6	7	29	0.280	0.180	90	49	24	12*	6*	2*	nil
200	1.0	25	24	94	0.720	0.460	90	118	60	30	15*	5*	2*
200	0.1	48	55	202	1.240	0.820	90	186	104	53	26*	8*	3*

\* = numerical solution terminated at approximately V-max.  
 - = just below pool surface @  $X_0 = 3$  ft;  $\rho_{00} = 0.0056$  g/cm<sup>3</sup>;  $Q_0 = 1050$  cal/g.  
 + = just above pool surface @ same conditions.

Table B-30. Probabilistic Shrapnel Velocity at RTG for Aft-Compartment-Initiated Explosions (Phi = 90 degrees)

Height X (ft)	Percentile (%)	Pdelta stat (psi)	P dyn (psi)	P refl (psi)	I stat (psi-s)	I dyn (psi-s)	Phi angle (deg)	SHRAPNEL VELOCITY (fps)					
								----- FLYER=0.024 psi/ Beta psi (below) -----					
								0.1200	0.2500	0.5000	1.0000	3.0000	9.0000
1 <sup>-</sup>	N/A	2075	810	5300	0.190	0.019	90	58°	29°	14°	7°	2°	nil
1 <sup>+</sup>	N/A	659	1720	3169	0.670	0.110	90	36°	26°	13°	6°	2°	nil
20	50.0	18	15	67	0.093	0.037	90	18°	8°	4°	2°	nil	nil
20	10.0	48	47	207	0.240	0.088	90	37°	17°	9°	4°	1°	nil
20	1.0	95	115	480	0.430	0.180	90	61°	29°	14°	7°	2°	nil
20	0.1	175	287	1040	0.670	0.290	90	102°	48°	24°	12°	4°	1°
30	50.0	9	8	37	0.072	0.033	90	15°	7°	3°	2°	nil	nil
30	10.0	32	29	124	0.200	0.090	90	34°	18°	8°	4°	1°	nil
30	1.0	72	83	338	0.410	0.190	90	64°	30°	15°	7°	2°	nil
30	0.1	117	172	627	0.610	0.300	90	96°	45°	23°	11°	4°	1°
40	50.0	4	6	24	0.061	0.031	90	12°	6°	3°	1°	nil	nil
40	10.0	23	20	86	0.170	0.088	90	31°	15°	7°	4°	1°	nil
40	1.0	50	52	212	0.350	0.160	90	58°	28°	14°	7°	2°	nil
40	0.1	88	121	435	0.580	0.310	90	94°	45°	22°	11°	4°	1°
55	50.0	0	0	0	0.000	0.000	90	nil	nil	nil	nil	nil	nil
55	10.0	14	13	53	0.140	0.082	90	28°	13°	6°	3°	1°	nil
55	1.0	36	34	142	0.300	0.170	90	53°	25°	13°	6°	2°	nil
55	0.1	84	111	408	0.540	0.390	90	112	53°	27°	13°	4°	1°
70	50.0	0	0	0	0.000	0.000	90	nil	nil	nil	nil	nil	nil
70	10.0	9	8	37	0.130	0.077	90	25°	12°	6°	3°	nil	nil
70	1.0	27	25	102	0.260	0.170	90	52°	25°	12°	6°	2°	nil
70	0.1	78	104	373	0.570	0.460	90	128	61°	31°	15°	5°	2°
100	50.0	0	0	0	0.000	0.000	90	nil	nil	nil	nil	nil	nil
100	10.0	4	6	24	0.118	0.074	90	22°	10°	5°	3°	nil	nil
100	1.0	16	15	60	0.210	0.160	90	47	22°	11°	6°	2°	nil
100	0.1	32	32	124	0.340	0.270	90	77	37°	18°	9°	3°	1°
150	50.0	0	0	0	0.000	0.000	90	nil	nil	nil	nil	nil	nil
150	10.0	0	0	0	0.000	0.000	90	nil	nil	nil	nil	nil	nil
150	1.0	0	0	34	0.170	0.150	90	42	20°	10°	5°	2°	nil
150	0.1	17	17	63	0.260	0.250	90	69	33°	17°	8°	3°	nil
200	50.0	0	0	0	0.000	0.000	90	nil	nil	nil	nil	nil	nil
200	10.0	0	0	0	0.000	0.000	90	nil	nil	nil	nil	nil	nil
200	1.0	4	6	24	0.150	0.130	90	35	17°	8°	4°	1°	nil
200	0.1	14	13	53	0.250	0.280	90	71	34	17°	8°	3°	nil

\* = numerical solution terminated at approximately V-max.  
 - = just below pool surface @ X<sub>0</sub> = 1 ft; rho<sub>0</sub> = 0.0056 g/cm<sup>3</sup>; Q<sub>0</sub> = 1050 cal/g.  
 + = just above pool surface @ same conditions.

Table B-31. Shrapnel Velocity at RTG for In-Flight Vapor Cloud Initiated Explosions (Phi = 90 degrees)

Height X (ft)	Percent tile (%)	Pdelta stat (psi)	P dyn (psi)	P refl (psi)	I stat (psi-s)	I dyn (psi-s)	Phi angle (deg)	----- SHRAPNEL VELOCITY (fps) -----					
								----- FLYER=0.024 psi/ Beta psi (below) -----					
								0.1200	0.2500	0.5000	1.0000	3.0000	9.0000
263*	N/A	298	122	1981	3.230	1.600	90	354	197	106	54	18°	6°
265*	N/A	263	142	1714	3.220	1.600	90	368	208	111	56	19°	6°
291	N/A	136	181	759	2.490	1.670	90	385	205	106	53	18°	6°
396	N/A	63	61	284	1.480	1.430	90	277	157	88	46	15°	5°
528	N/A	33	21	129	0.930	1.080	90	184	104	61	34	12°	4°
792	N/A	14	5	53	1.130	0.480	90	83	50	28	16	5°	2°
924	N/A	10	3	40	1.280	0.310	90	62	35	20	10	3°	1°
1056	N/A	8	2	34	1.190	0.220	90	46	27	15	8°	3°	nil

- \* = numerical solution terminated at approximately V-max.,
- = just inside reaction zone,
- ^ = just outside reaction zone.

Table B-32. RTG Impact Environment - Orbiter Crash on Abort

CRASH SCENARIO	GALILEO MISSION (FT/S)
DITCH NO FLARE	65 - 125
DITCH WITH FLARE	50 - 110
LANDING PRE-FLARE	60 - 120
LANDING POST FLARE	50 - 65

Table B-33. Fragment Environment at RTG: SRM-1 Early t = 0 - 49 Sec

Fragment Size Range (W/Wmax)	Fragment Average Wt. (lb)	Fragment Average Area (in <sup>2</sup> )	Average Areal Density (lb/in <sup>2</sup> )	Velocity at RTG (GLL) (ft/sec)		Density at RTG (No. of Frags./ft. <sup>2</sup> )	
				*Level 1 Range	*Level 2 Range	GLL	ULS
0 - .1	4.17	16.3	.256	139 - 278	225 - 450	.043	.022
.1 - .2	12.50	33.8	.369	136 - 272	221 - 441	.038	.019
.2 - .3	20.83	47.5	.438	132 - 263	214 - 427	.034	.017
.3 - .4	29.17	59.6	.490	127 - 254	206 - 412	.029	.015
.4 - .5	37.50	70.4	.533	123 - 245	199 - 397	.025	.012
.5 - .6	45.83	80.4	.570	118 - 236	191 - 381	.020	.010
.6 - .7	54.17	90.0	.602	113 - 225	183 - 366	.016	.008
.7 - .8	62.50	98.9	.632	108 - 216	175 - 350	.011	.006
.8 - .9	70.83	107.5	.658	103 - 206	167 - 334	.007	.003
.9 - 1.0	79.17	115.9	.684	98 - 196	159 - 318	.002	.001

\*Level 1: Case Defect Scenario - failure at normal burn pressure

\*Level 2: Propellant Defect Scenario - failure at case burst strength

Table B-34. Fragment Environment at RTG: SRM-1 Mid t = 49 - 98 Sec

Fragment Size Range (W/Wmax)	Fragment Average Wt. (lb)	Fragment Average Area (in <sup>2</sup> )	Average Areal Density (lb/in <sup>2</sup> )	Velocity at RTG (GLL) (ft/sec)		Density at RTG (No. of Frags./ft. <sup>2</sup> )	
				*Level 1 Range	*Level 2 Range	GLL	ULS
0 - .1	2.50	11.6	.216	229 - 458	297 - 594	.044	.022
.1 - .2	7.50	24.1	.312	225 - 450	292 - 584	.039	.020
.2 - .3	12.50	33.8	.369	218 - 437	283 - 566	.037	.018
.3 - .4	17.50	42.3	.413	211 - 422	274 - 547	.030	.015
.4 - .5	22.50	50.1	.449	203 - 406	264 - 527	.025	.013
.5 - .6	27.50	57.2	.480	195 - 390	253 - 506	.021	.010
.6 - .7	32.50	64.0	.508	187 - 374	243 - 486	.016	.008
.7 - .8	37.50	70.4	.533	179 - 358	232 - 465	.012	.006
.8 - .9	42.50	76.5	.556	171 - 342	222 - 445	.007	.004
.9 - 1.0	47.50	82.4	.576	164 - 327	212 - 423	.002	.001

\*Level 1: Case Defect Scenario - failure at normal burn pressure

\*Level 2: Propellant Defect Scenario - failure at case burst strength

Table B-35. Fragment Environment at RTG: SRM-1 Late 1 t = 98 - 147 Sec

Fragment Size Range (W/Wmax)	Fragment Average Wt. (lb)	Fragment Average Area (in <sup>2</sup> )	Average Areal Density (lb/in <sup>2</sup> )	Velocity at RTG (GLL) (ft/sec)		Density at RTG (No. of Frags./ft. <sup>2</sup> )	
				*Level 1 Range	*Level 2 Range	GLL	ULS
0 - .1	0.83	5.5	.150	249 - 498	384 - 767	.029	.015
.1 - .2	2.50	11.6	.216	246 - 492	380 - 759	.026	.013
.2 - .3	4.17	16.3	.256	240 - 479	369 - 738	.023	.012
.3 - .4	5.83	20.4	.286	232 - 463	358 - 715	.020	.010
.4 - .5	7.50	24.1	.312	223 - 446	344 - 689	.017	.008
.5 - .6	9.17	27.5	.333	215 - 430	332 - 663	.014	.007
.6 - .7	10.83	30.8	.352	206 - 413	318 - 636	.011	.005
.7 - .8	12.50	33.8	.369	198 - 395	305 - 610	.008	.004
.8 - .9	14.17	36.8	.385	188 - 377	291 - 582	.005	.002
.9 - 1.0	15.83	39.6	.400	180 - 360	278 - 555	.002	.001

\*Level 1: Case Defect Scenario - failure at normal burn pressure

\*Level 2: Propellant Defect Scenario - failure at case burst strength



Table B-36. Fragment Environment at RTG: SRM-2 Early t = 0 - 34 Sec.

Fragment Size Range (W/Wmax)	Fragment Average Wt. (lb)	Fragment Average Area (in <sup>2</sup> )	Average Areal Density (lb/in <sup>2</sup> )	Velocity at RTG (GLL) (ft/sec)		Density at RTG (No. of Frags./ft. <sup>2</sup> )	
				*Level 1 Range	*Level 2 Range	GLL	ULS
0 - .1	2.08	10.2	.203	132 - 265	214 - 428	.079	.030
.1 - .2	6.25	21.3	.293	129 - 258	208 - 417	.070	.027
.2 - .3	10.42	30.0	.348	124 - 249	202 - 403	.062	.024
.3 - .4	14.58	37.5	.389	120 - 241	194 - 389	.054	.021
.4 - .5	18.75	44.3	.423	116 - 231	187 - 374	.046	.018
.5 - .6	22.92	50.7	.452	112 - 223	180 - 359	.037	.014
.6 - .7	27.08	56.7	.478	106 - 213	172 - 344	.029	.011
.7 - .8	31.25	62.3	.501	102 - 204	164 - 329	.021	.008
.8 - .9	35.42	67.8	.523	97 - 194	157 - 314	.012	.005
.9 - 1.0	39.58	73.0	.542	92 - 185	150 - 299	.004	.002

\*Level 1: Case Defect Scenario - failure at normal burn pressure

\*Level 2: Propellant Defect Scenario - failure at case burst strength

Table B-37. Fragment Environment at RTG: SRM-2 Mid t = 34 - 68 Sec

Fragment Size Range (W/Wmax)	Fragment Average Wt. (lb)	Fragment Average Area (in <sup>2</sup> )	Average Areal Density (lb/in <sup>2</sup> )	Velocity at RTG (GLL) (ft/sec)		Density at RTG (No. of Frags./ft. <sup>2</sup> )	
				*Level 1 Range	*Level 2 Range	GLL	ULS
0 - .1	1.25	7.3	.171	216 - 432	279 - 558	.078	.030
.1 - .2	3.75	15.2	.247	210 - 421	272 - 543	.069	.027
.2 - .3	6.25	21.3	.293	204 - 407	262 - 525	.061	.024
.3 - .4	8.75	26.7	.328	196 - 393	253 - 506	.053	.021
.4 - .5	11.25	31.5	.357	189 - 378	244 - 487	.045	.017
.5 - .6	13.75	36.1	.381	182 - 363	234 - 468	.037	.014
.6 - .7	16.25	40.3	.403	174 - 349	224 - 449	.028	.011
.7 - .8	18.75	44.3	.423	166 - 333	215 - 430	.020	.008
.8 - .9	21.25	48.2	.441	159 - 318	205 - 410	.012	.005
.9 - 1.0	23.75	51.9	.458	152 - 303	196 - 391	.004	.002

\*Level 1: Case Defect Scenario - failure at normal burn pressure

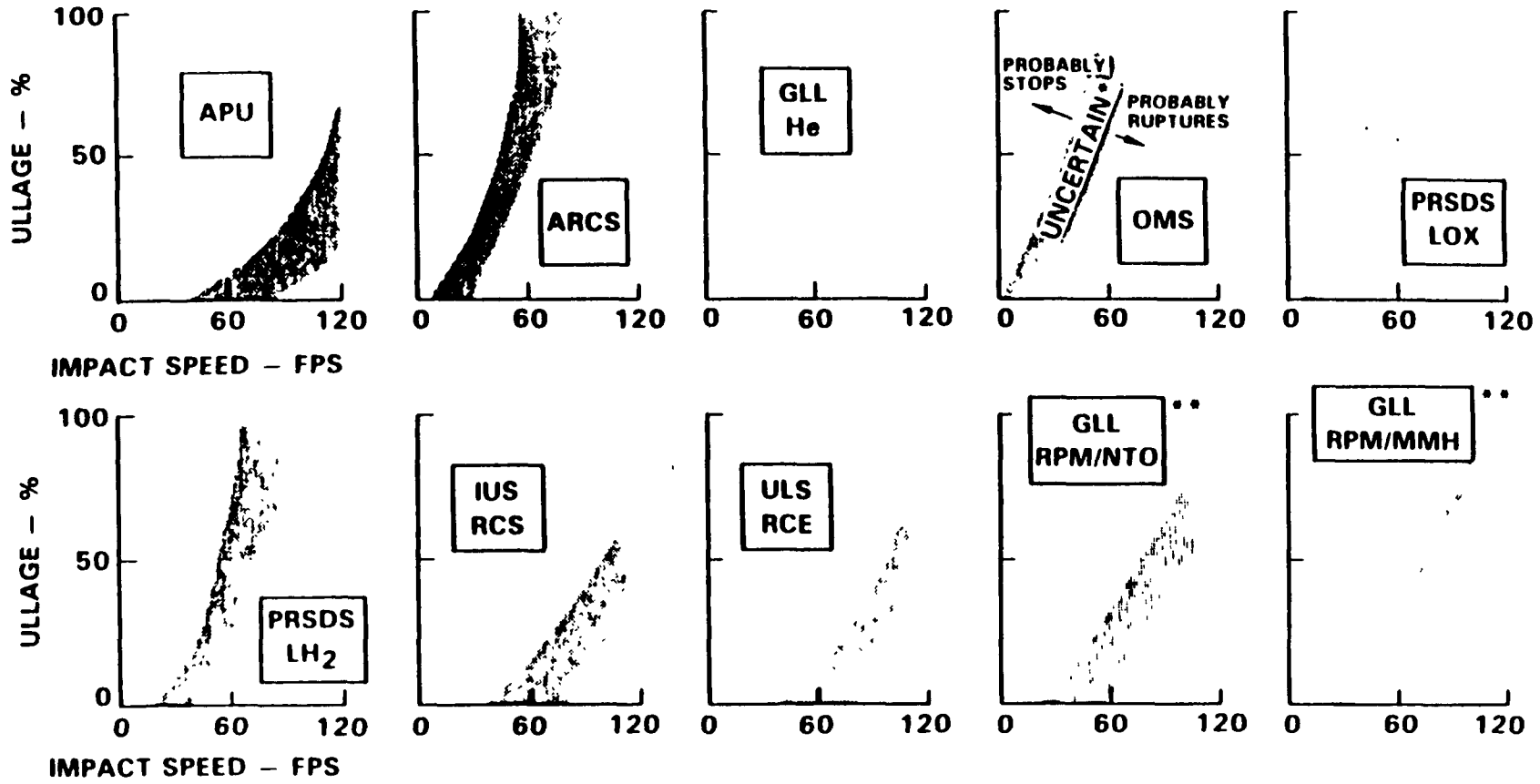
\*Level 2: Propellant Defect Scenario - failure at case burst strength

Table B-38. Fragment Environment at RTG: SRM-2 Late t = 68 - 102 Sec

Fragment Size Range (W/Wmax)	Fragment Average Wt. (lb)	Fragment Average Area (in <sup>2</sup> )	Average Areal Density (lb/in <sup>2</sup> )	Velocity at RTG (GLL) (ft/sec)		Density at RTG (No. of Frags./ft. <sup>3</sup> )	
				*Level 1 Range	*Level 2 Range	GLL	ULS
0 - .1	0.42	3.5	.119	228 - 457	364 - 728	.046	.018
.1 - .2	1.25	7.3	.171	223 - 446	356 - 712	.041	.016
.2 - .3	2.08	10.2	.203	216 - 432	345 - 690	.036	.014
.3 - .4	2.92	12.8	.227	208 - 417	332 - 665	.031	.012
.4 - .5	3.75	15.2	.247	200 - 401	320 - 641	.026	.010
.5 - .6	4.58	17.3	.264	193 - 386	308 - 615	.022	.008
.6 - .7	5.42	19.4	.280	184 - 369	295 - 590	.017	.007
.7 - .8	6.25	21.3	.293	177 - 354	282 - 564	.012	.005
.8 - .9	7.08	23.2	.306	168 - 337	270 - 539	.007	.003
.9 - 1.0	7.92	25.0	.317	161 - 322	256 - 513	.002	.001

\*Level 1: Case Defect Scenario - failure at normal burn pressure

\*Level 2: Propellant Defect Scenario - failure at case burst strength



\* UNCERTAINTY BAND DUE TO ELASTIC vs PLASTIC BEHAVIOR

\*\* RUPTURE CALCULATIONS ASSUME RPM BOTTLES PRESSURIZED TO 50 PSIG. IF AT WORKING PRESSURE (300 PSIG) BOTTLES WOULD BE NOTICEABLY BUT NOT IMPORTANTLY MORE VULNERABLE

Figure B-1. Influence of Impact Speed and Ullage on Tank Rupture

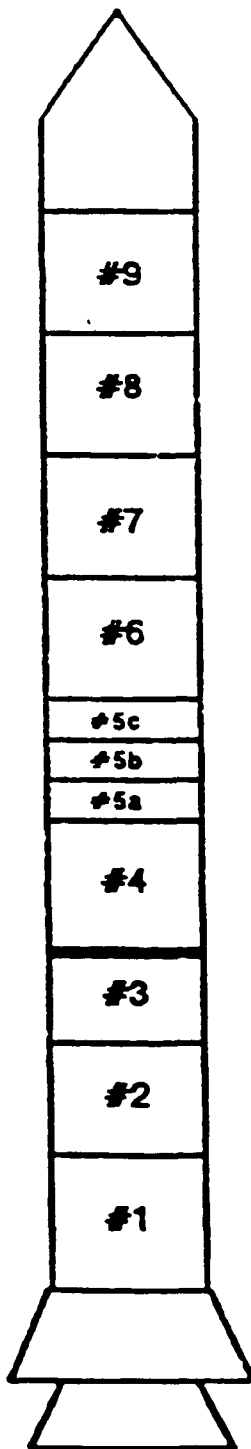
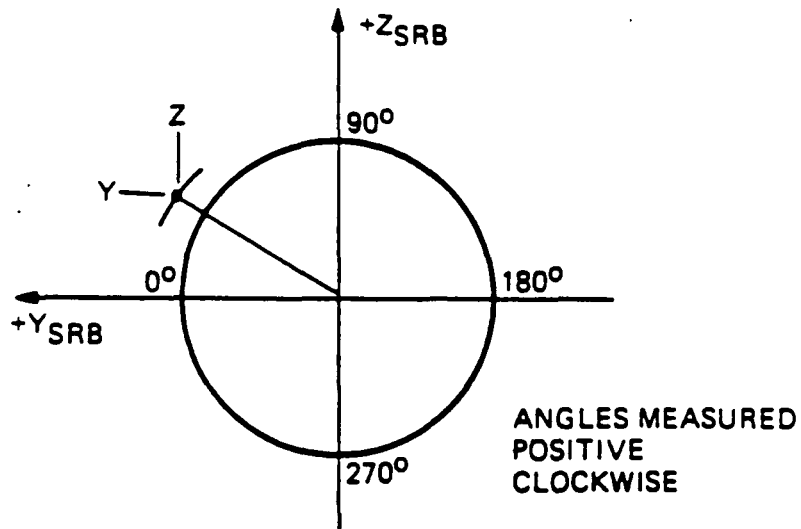


Figure B-2. SRB Cylinder Nomenclature

SRB COORDINATE SYSTEM (IN LASEP)



SRB AND SHUTTLE COORDINATE SYSTEMS

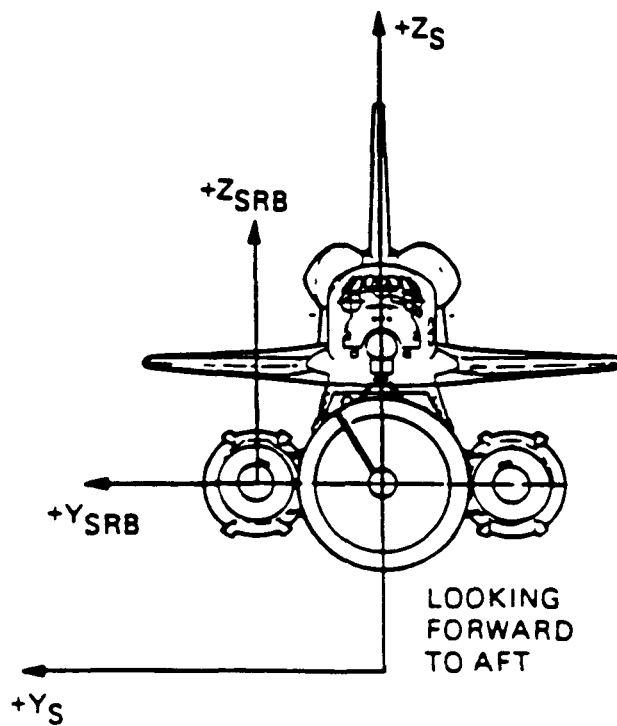
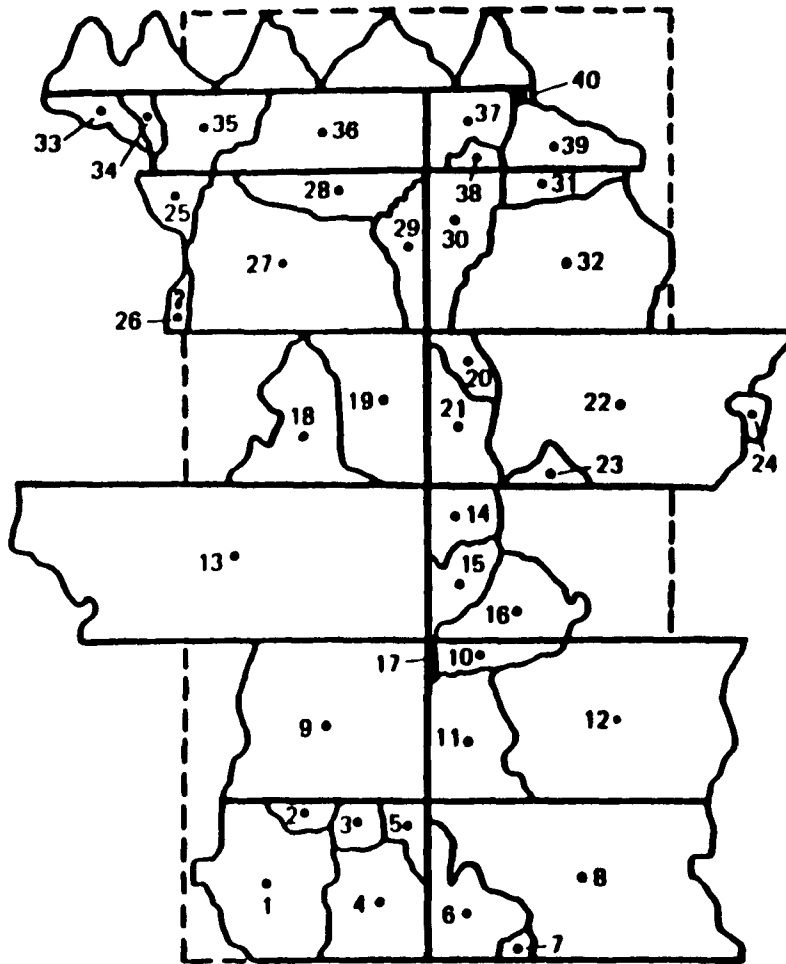


Figure B-3. SRB and Shuttle Coordinate Systems



SEGMENT NO.

6

5

4

3

2

1

SEGMENT NO.	FRAGMENT NO.	FRAGMENT AREA (FRACTION OF FULL CYLINDER AREA)	FRAGMENT AVERAGE LENGTH (deg)	
1	1	0 207	69	
	2	0 029	34	
	3	0 019	29	
	4	0 137	57	
	5	0 029	23	
	6	0 137	46	
	7	0 010	17	
	8	0 433	160	
2	9	0 369	126	
	10	0 051	74	
	11	0 131	57	
	12	0 446	149	
	17	0 003	6	
3	13	0 758	264	
	14	0 061	46	
	15	0 061	46	
	16	0 120	57	
4	18	0 146	46	
	19	0 185	57	
	20	0 029	29	
	21	0 102	34	
	22	0 500	172	
	23	0 019	34	
	24	0 019	17	
	5	25	0 051	34
26		0 019	17	
27		0 315	126	
28		0 076	92	
29		0 067	23	
30		0 115	34	
31		0 041	69	
32		0 315	115	
6		33	0 041	29
		34	0 019	17
	35	0 092	57	
	36	0 182	126	
	37	0 061	46	
	38	0 019	29	
	39	0 083	69	
	40	0 003	11	

Figure B-4. Titan 34D-9 SRM1 Fragment Description - RSO Destruct Case

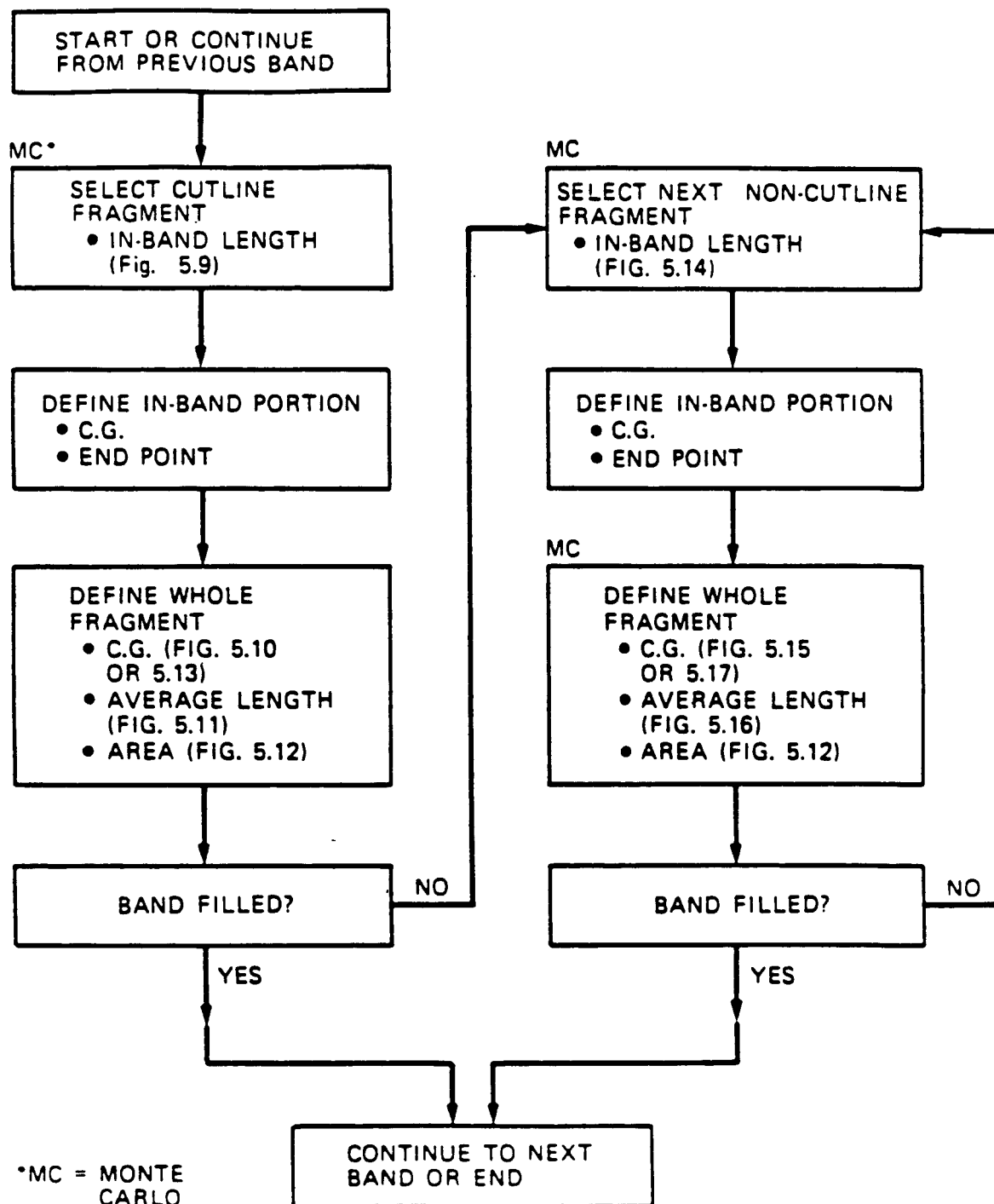


Figure B-5. Steps for Building Bands - RSO Destruct Case



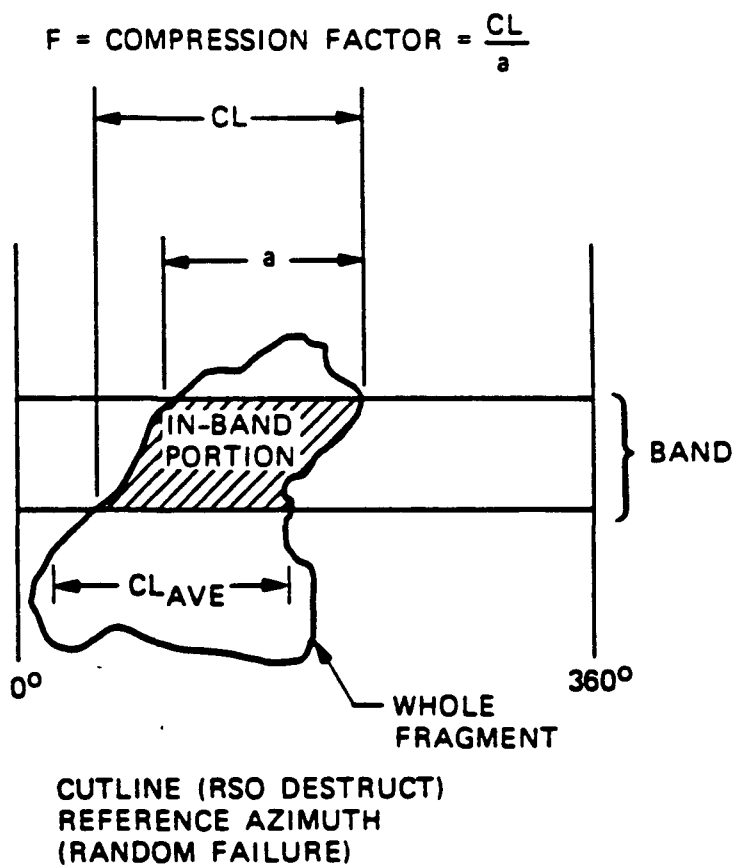


Figure B-6. Typical Whole Noncutline Fragment and Its In-Band Portion - RSO Destruct Case and Random Failure Case. (For a cutline fragment, the left-hand perimeter of the in-band portion, only, coincides with the cutline.)

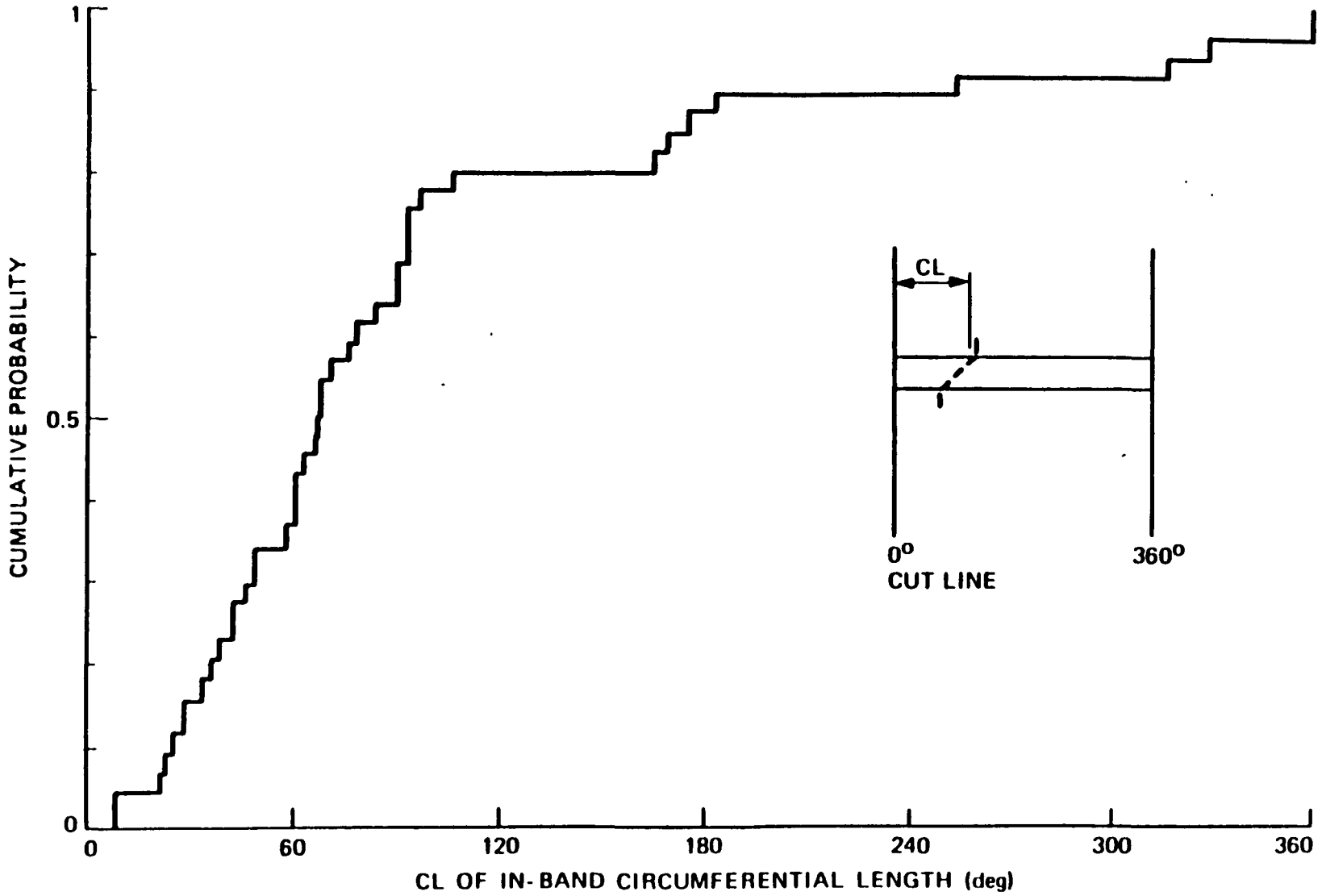


Figure B-7. In-Band Circumferential Length Distribution for Cutline Fragments - RSO Destruct Case

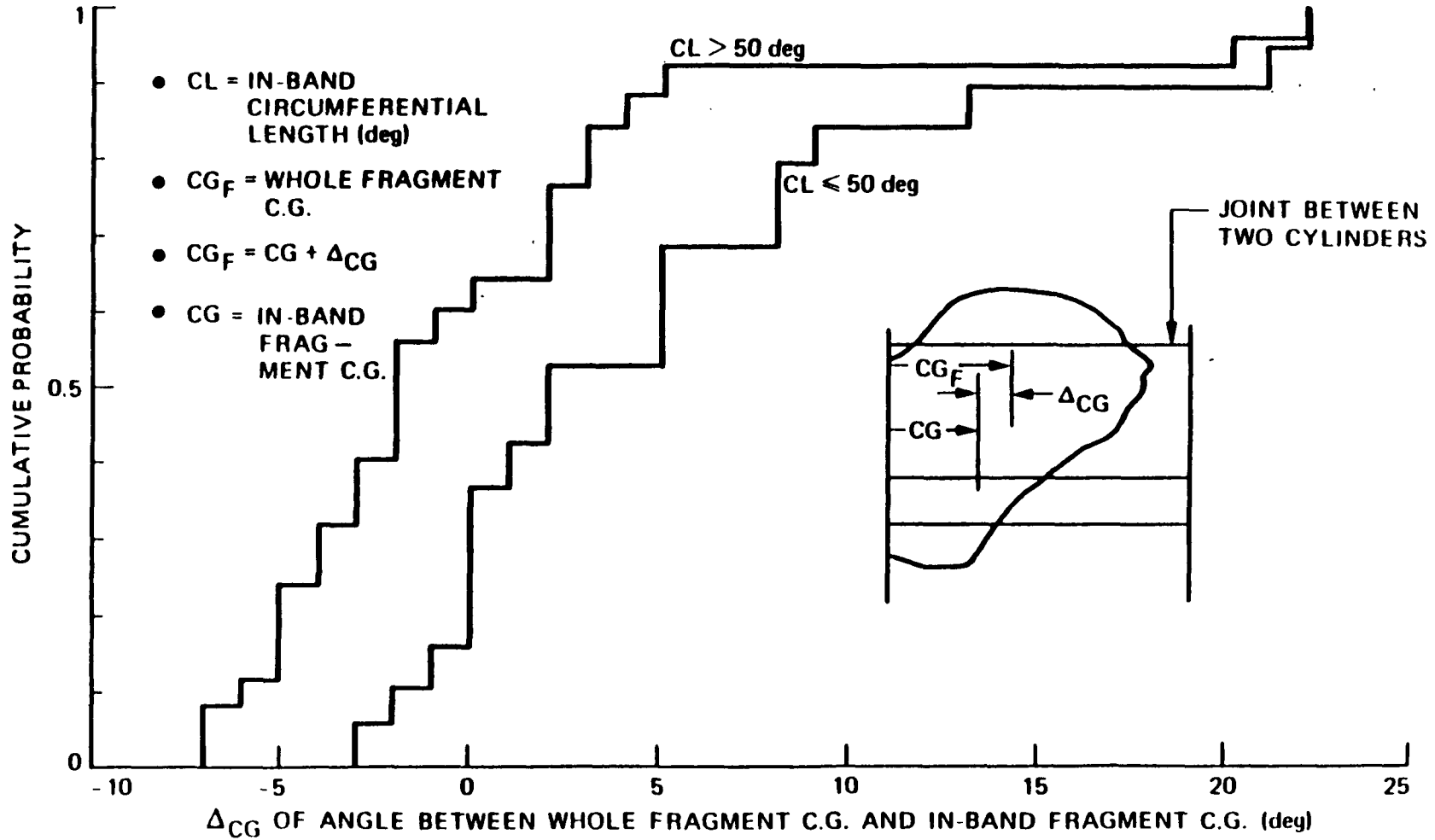


Figure B-8.  $\Delta CG$  Distribution for Cutline Fragments - RSO Destruct Case

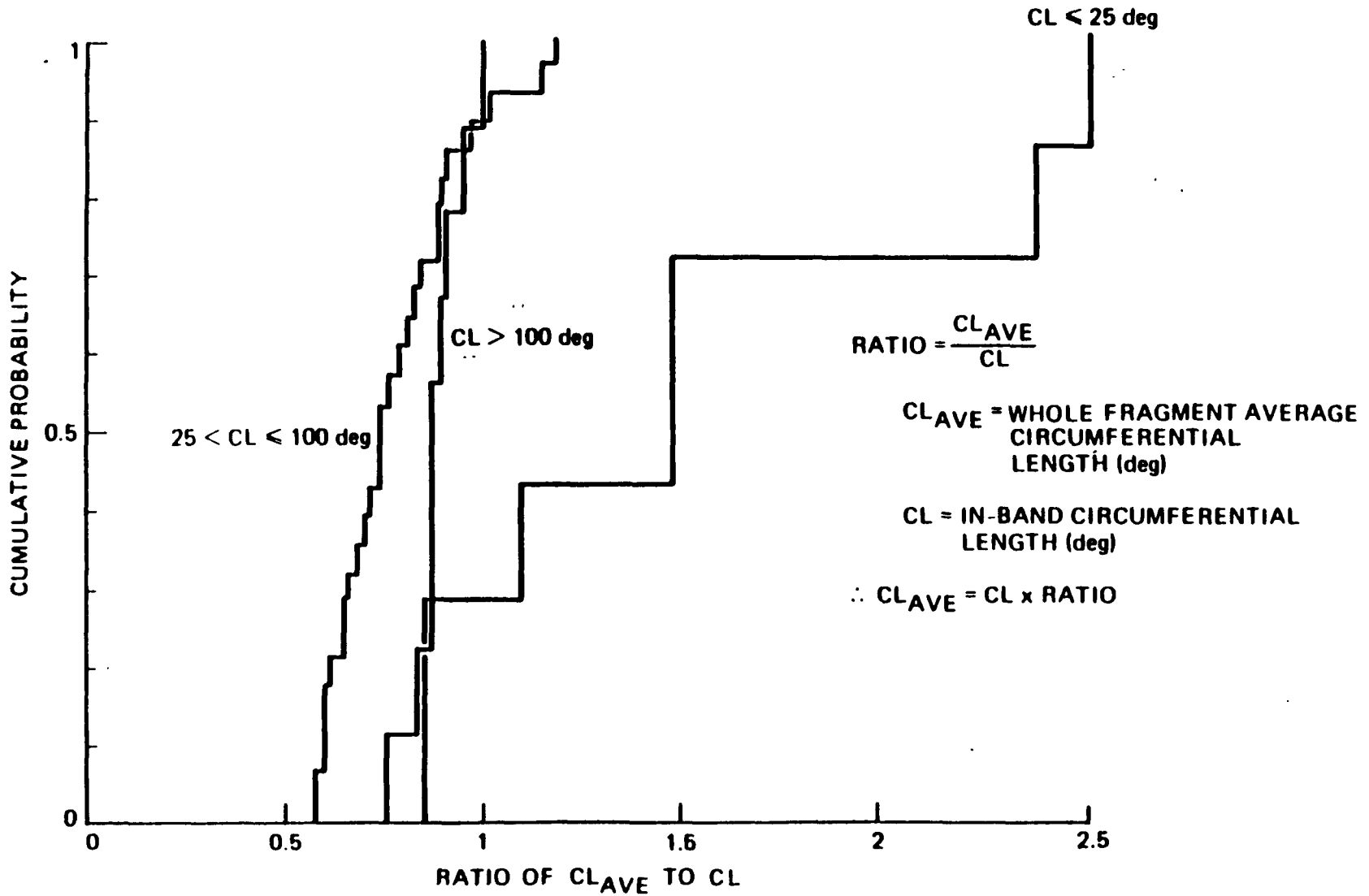


Figure B-9. Whole Fragment Average Length for Cutline Fragments - RSO Destruct Case

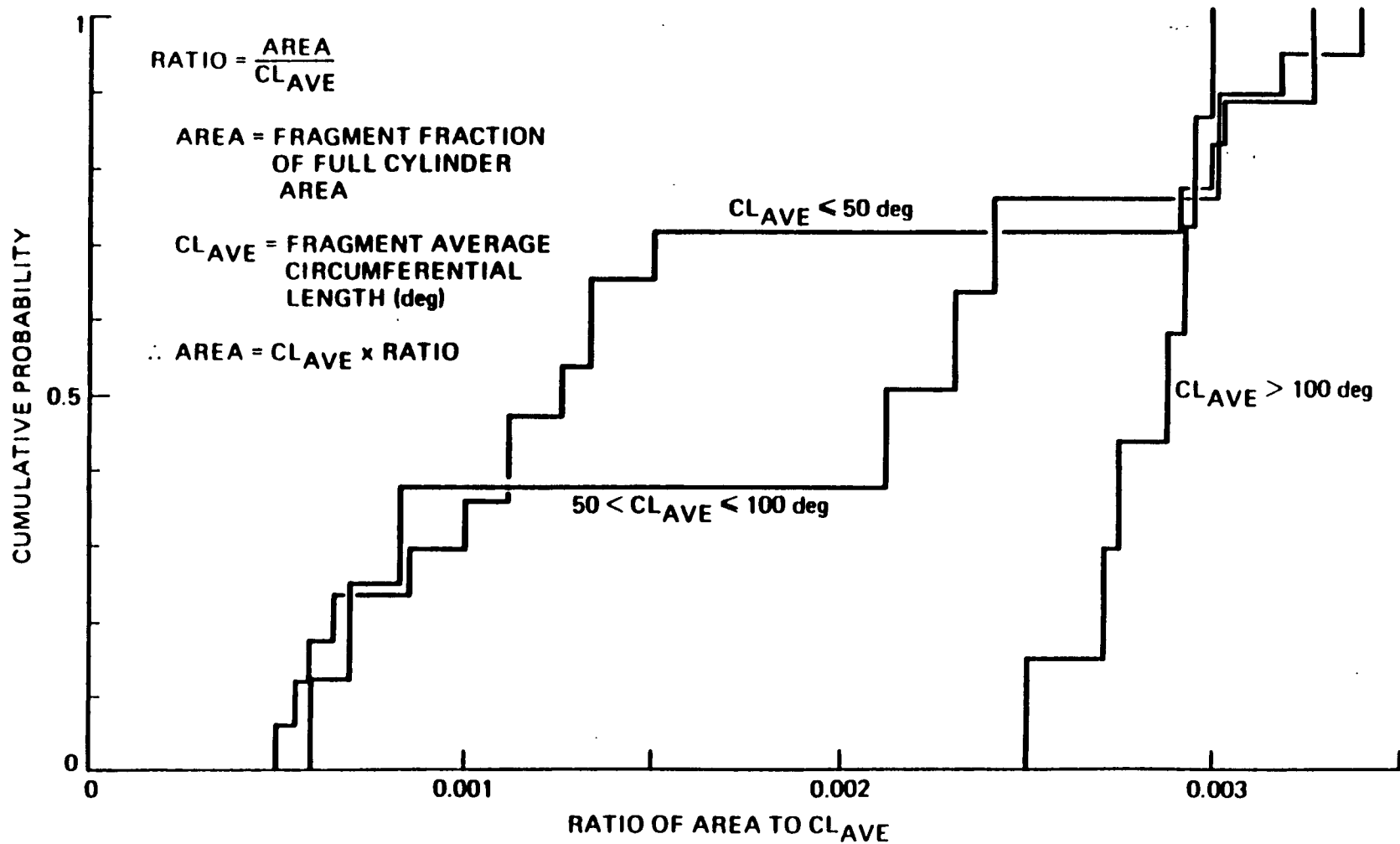


Figure B-10. Whole Fragment Area - RSO Destruct Case

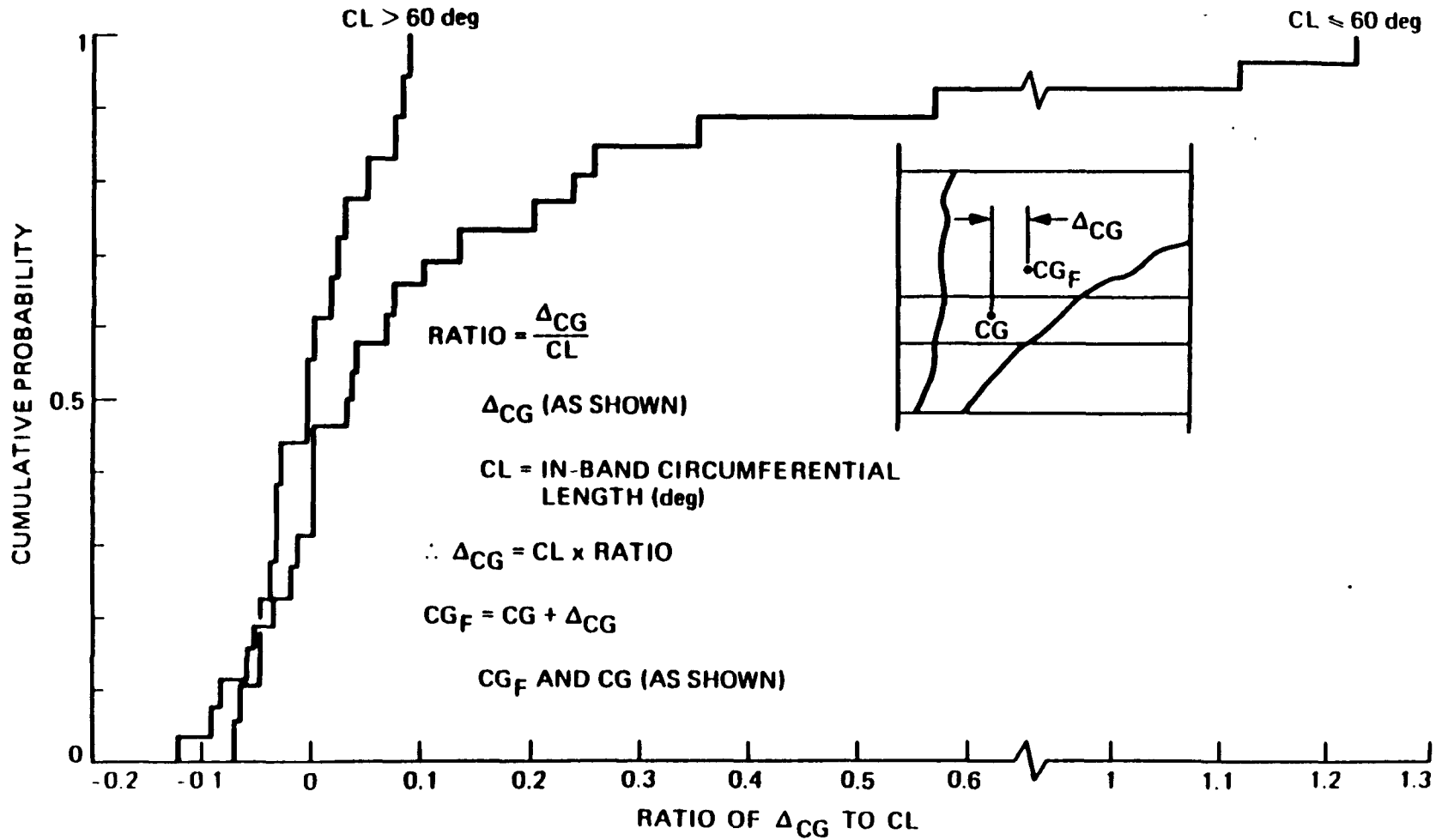


Figure B-11. Alternative Delta C.G. Distribution for Cutline Fragments - RSO Destruct Case

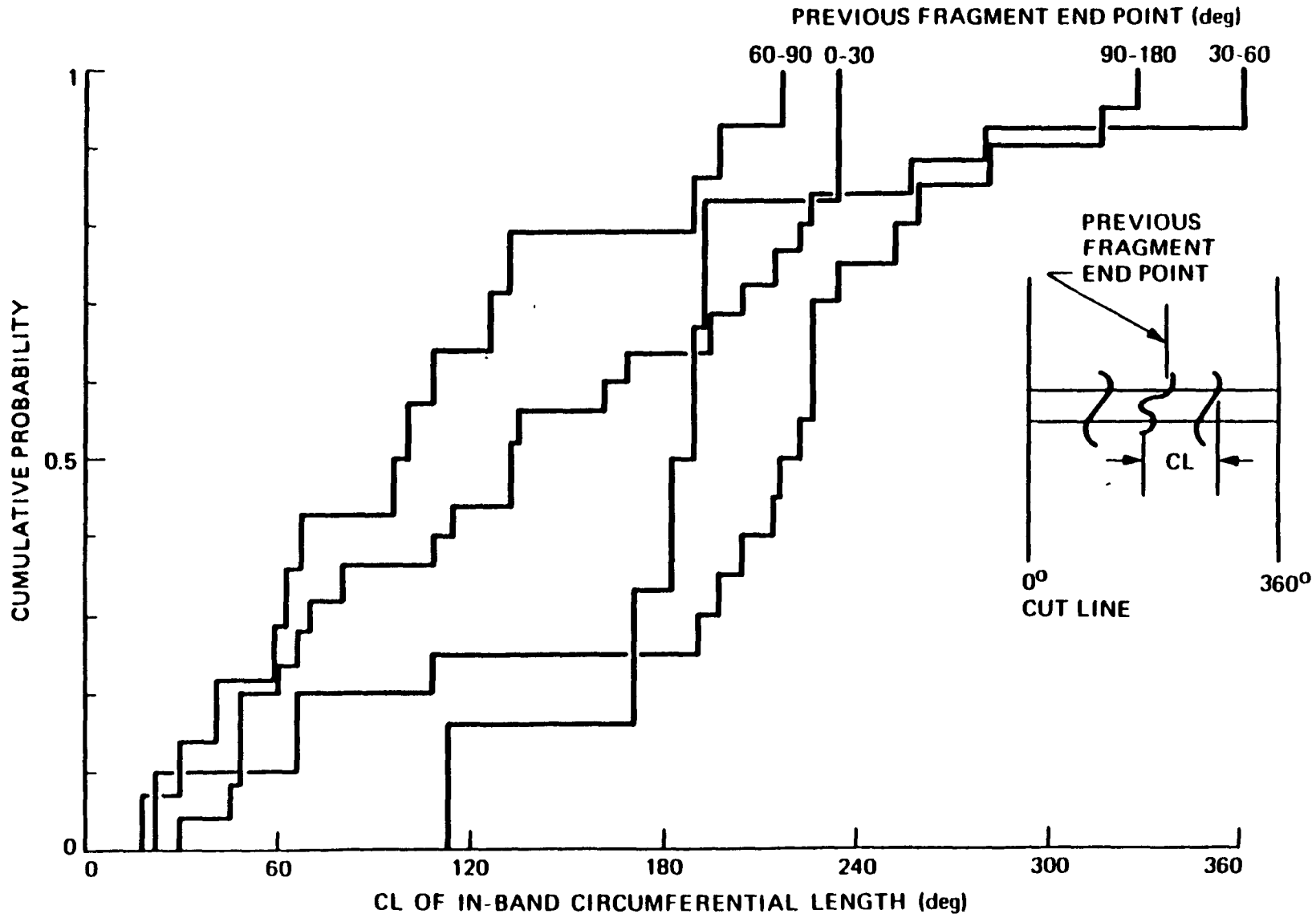


Figure B-12. In-Band Circumferential Length Distribution for Noncutline Fragments - RSO Destruct Case

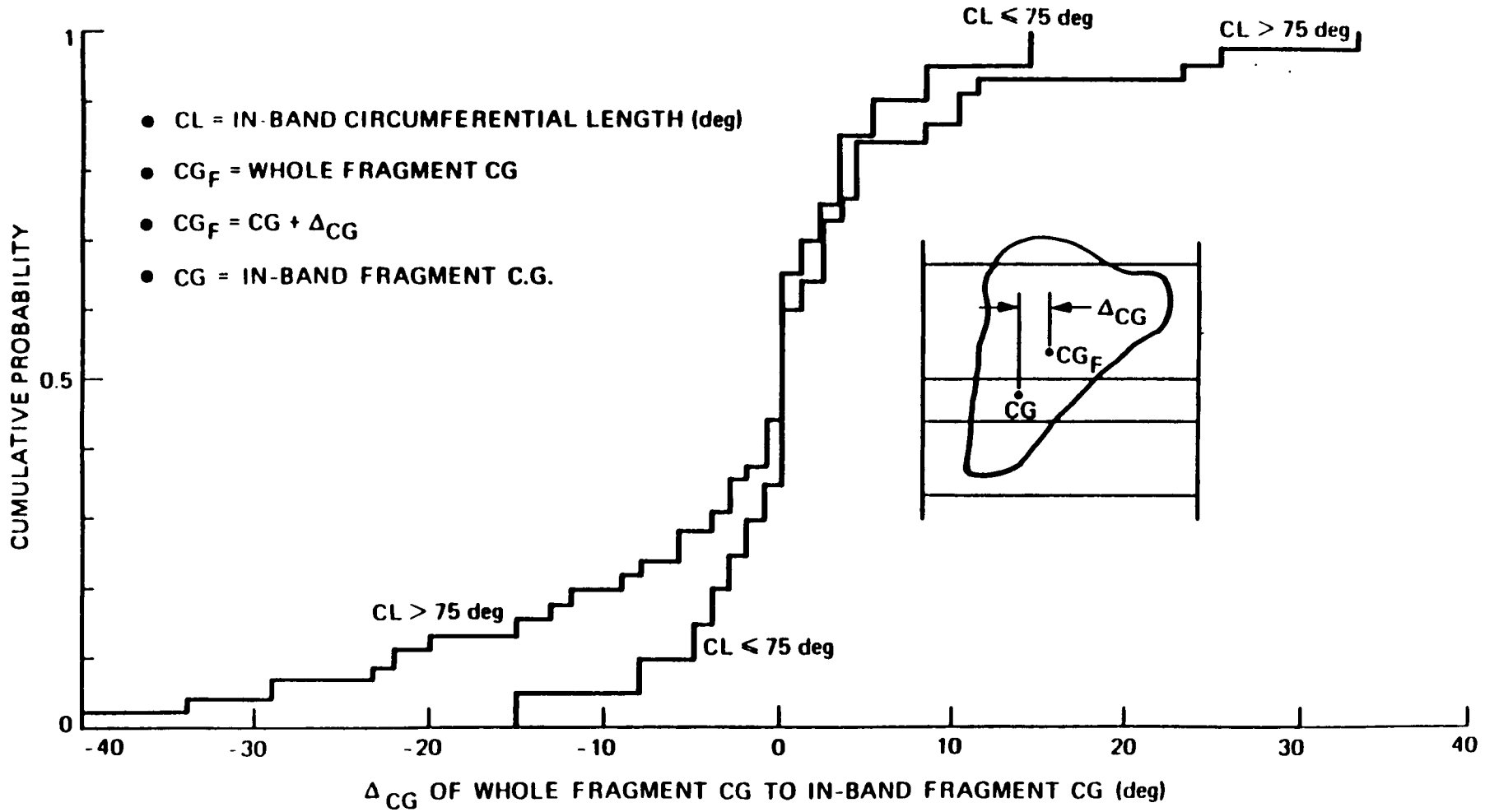


Figure B-13. Delta<sub>CG</sub> Distribution for Noncutline Fragments - RSO Destruct Case



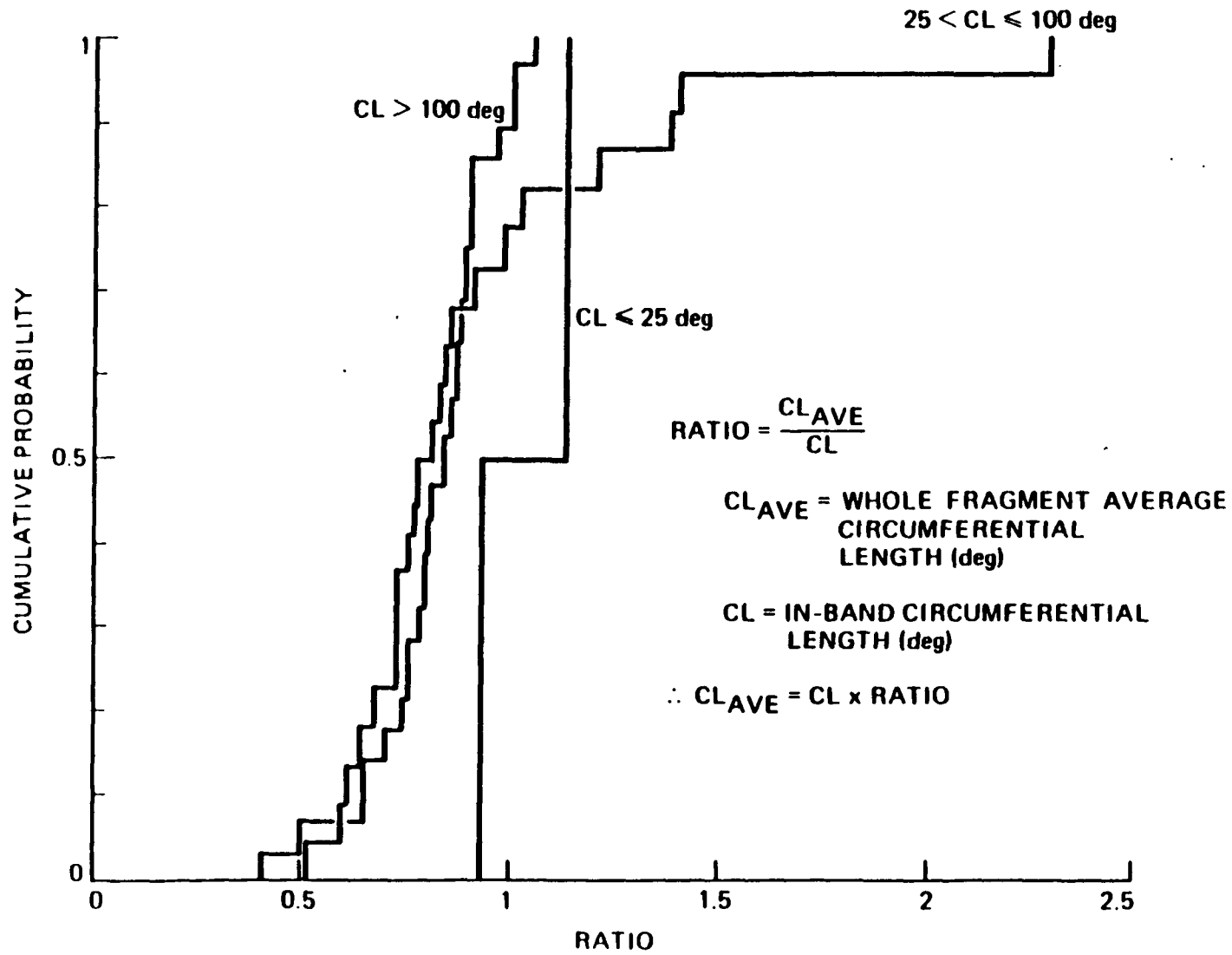


Figure B-14. Whole Fragment Average Length for Noncutline Fragments - RSO Destruct Case

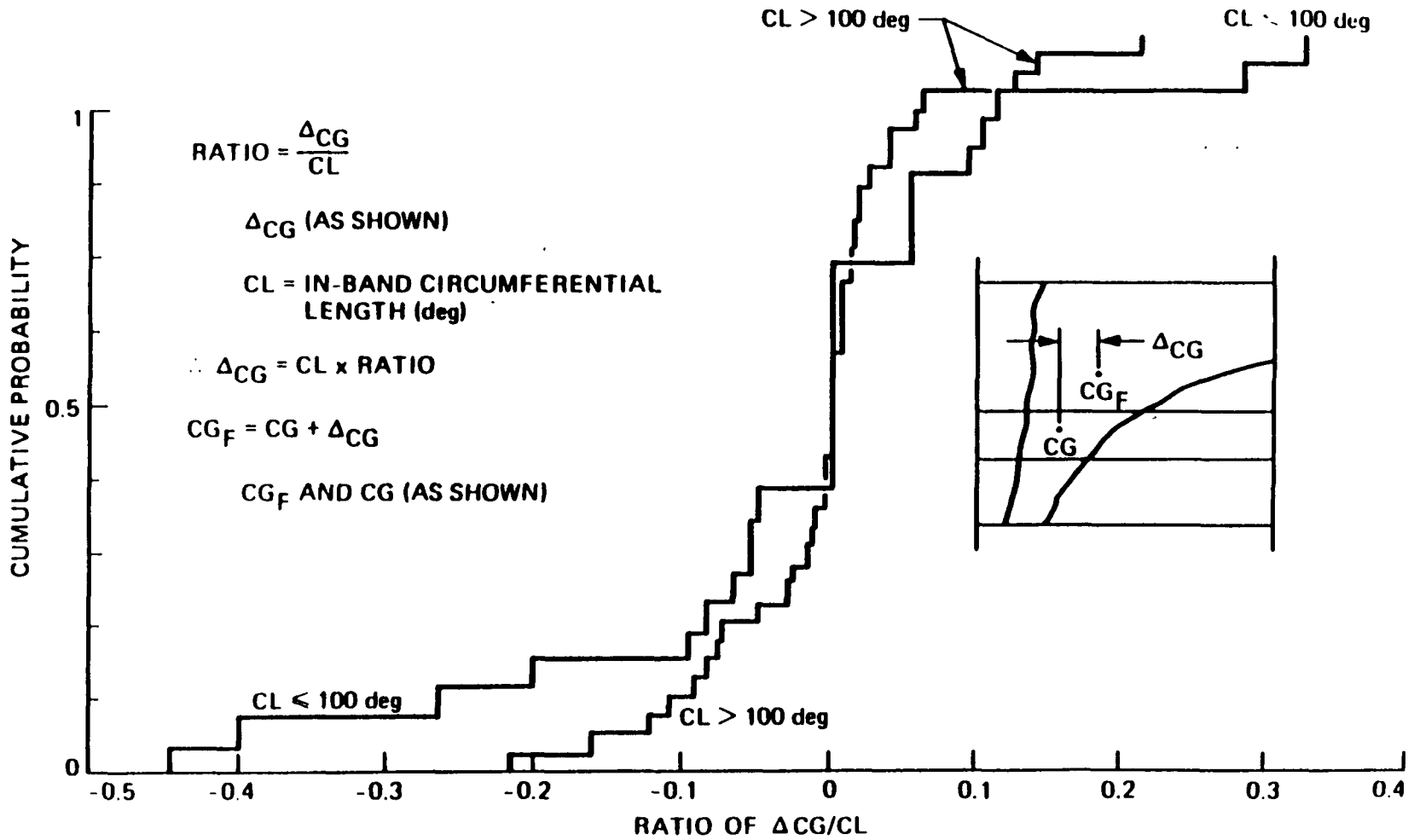


Figure B-15. Alternative Delta C.G. Distribution for Noncutline Fragments - RSO Destruct Case

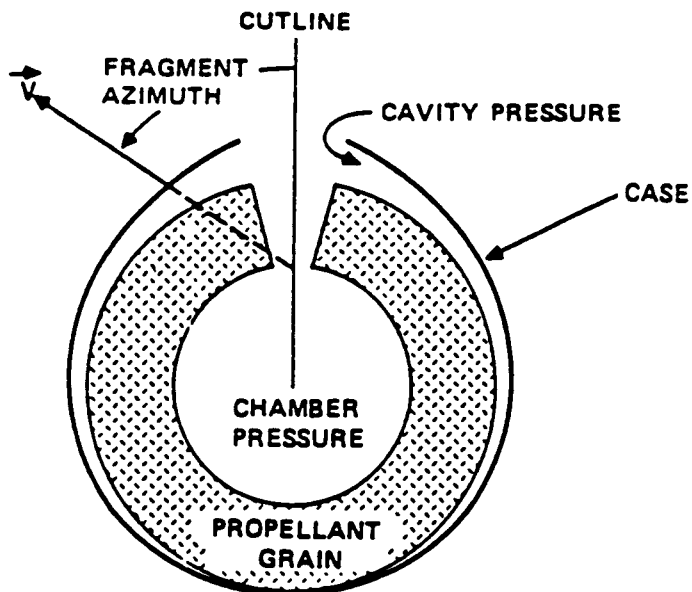


Figure B-16. Pressure Definitions - RSO Destruct Case

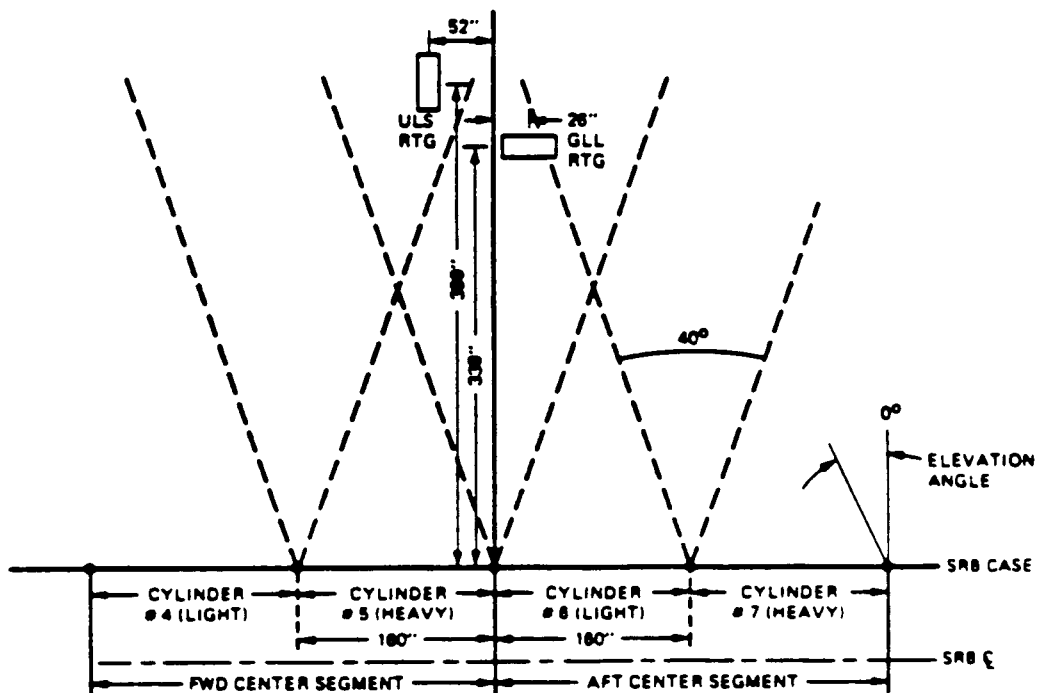
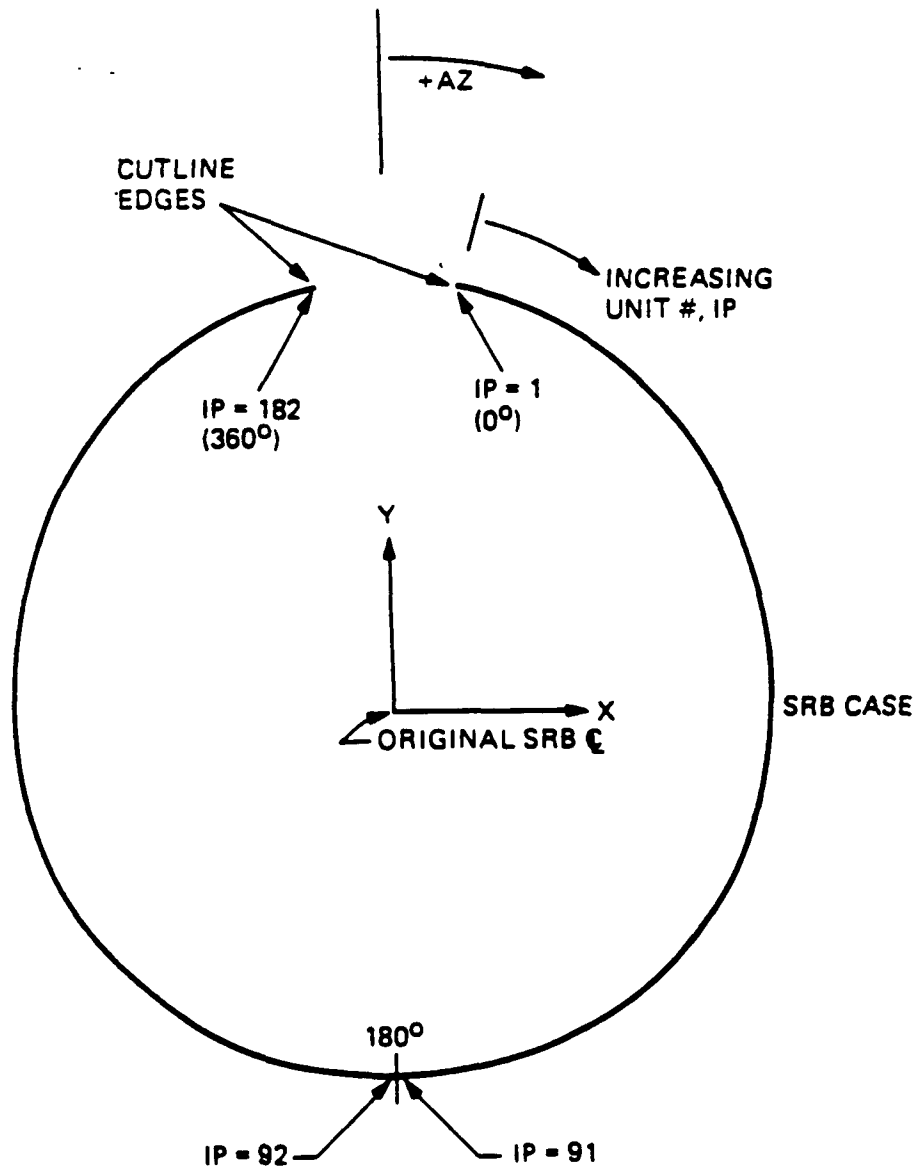


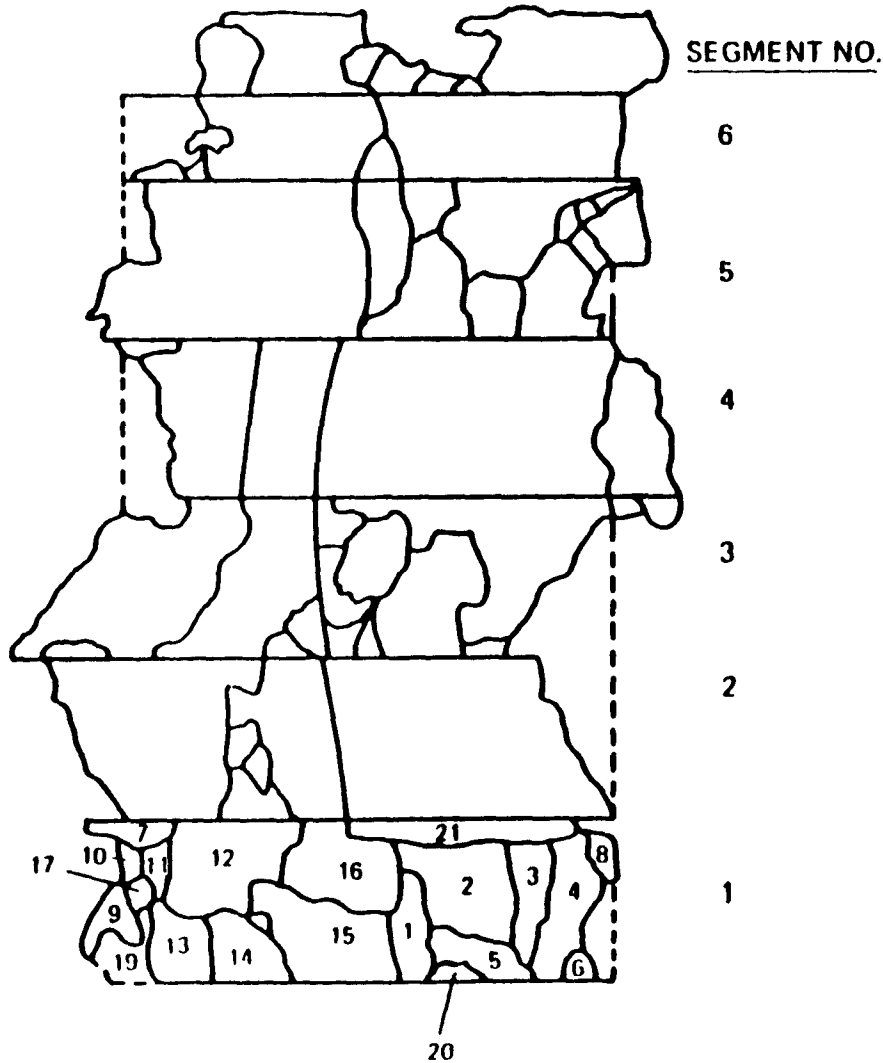
Figure B-17. SRB/RTG Geometry and Cylinder Weights at MET = 110 Seconds



NOTE: THE X-AXIS OF THE HYDROCODE PROGRAM  
CORRESPONDS TO THE Z-AXIS OF THE SRB  
(SEE FIGURE 5.5)

Figure B-18. Hydrocode Program Axes System and Nomenclature

SEGMENT 1



FRAGMENT NO.	FRAGMENT AREA (FRACTION OF FULL CYLINDER AREA)	FRAGMENT AVERAGE LENGTH (deg)
1	0.045	17
2	0.099	63
3	0.051	23
4	0.089	34
5	0.045	63
6	0.013	23
7	0.022	57
8	0.010	17
9	0.035	34
10	0.006	17
11	0.013	17
12	0.137	80
13	0.051	40
14	0.054	46
15	0.108	80
16	0.099	69
17	0.003	6
18	0.010	6
19	0.025	34
20	0.010	34
21	0.076	160

Figure B-19. Titan 340-9 SRM2 Fragment Description - Random Failure Case (Failed Segment)

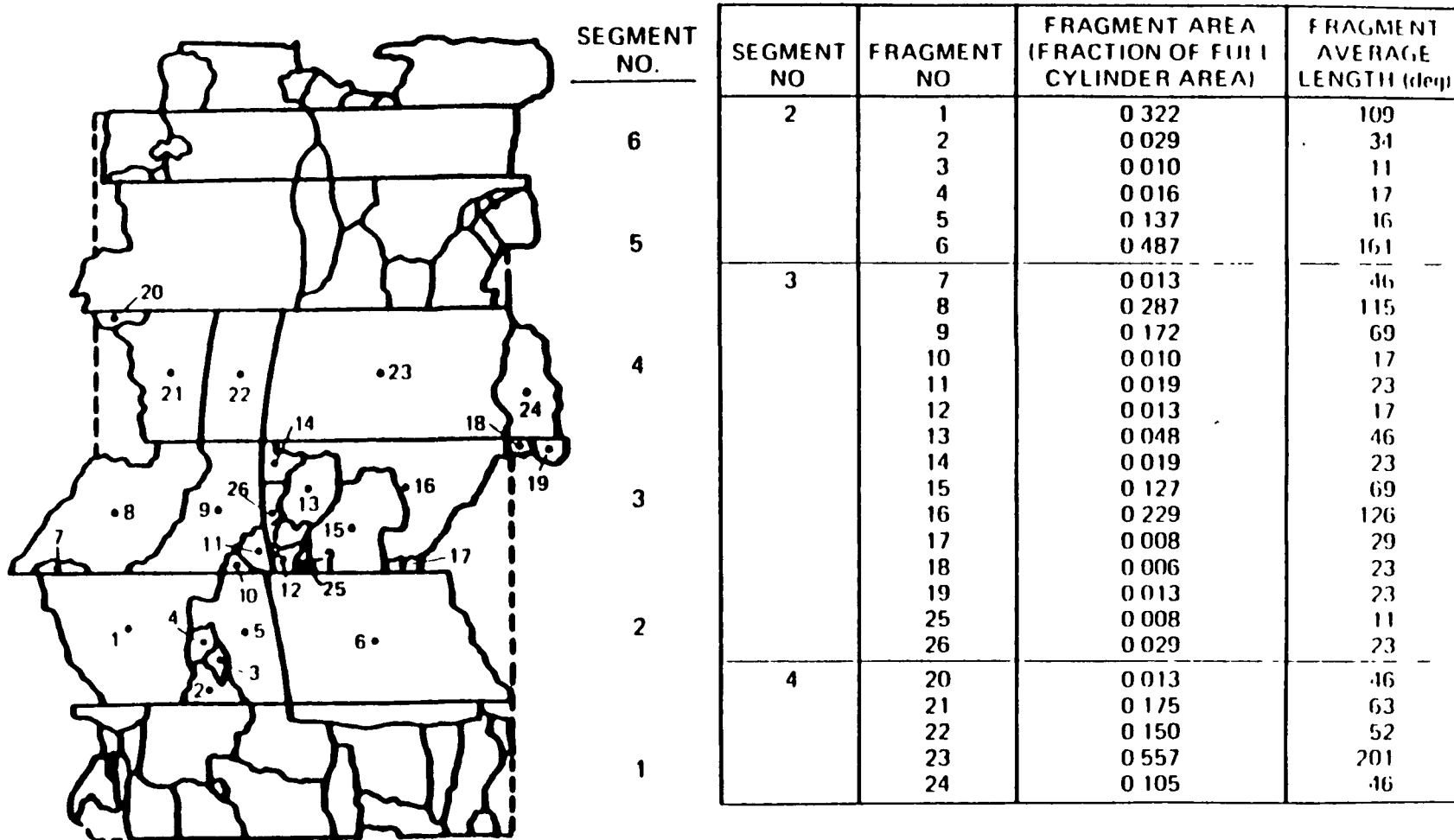


Figure B-20. Titan 34D-9 SRM2 Fragment Description - Random Failure Case (Non-Failed Segments)

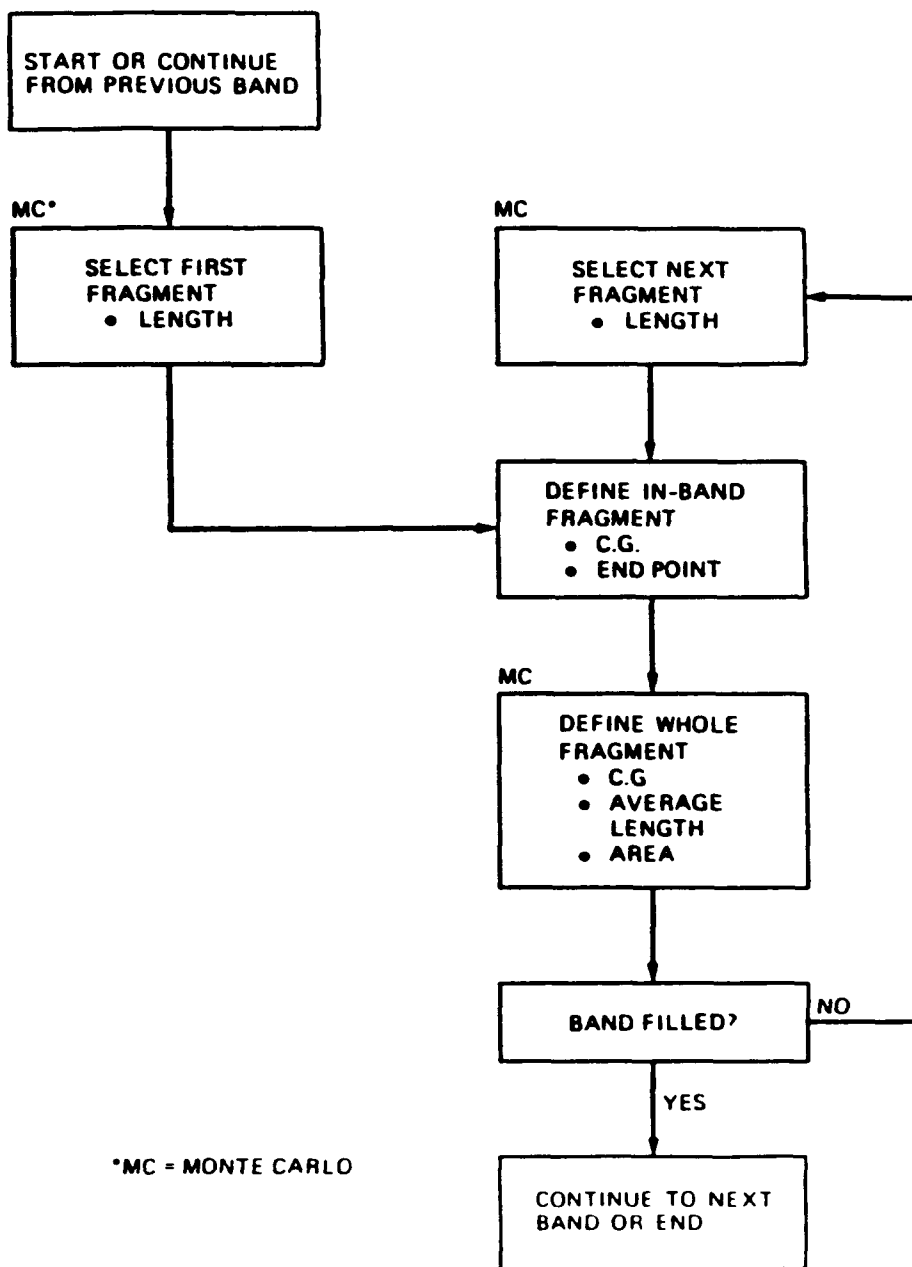


Figure B-21. Steps for Filling Bands with Fragments - Random Failure Case (Failed Cylinder)

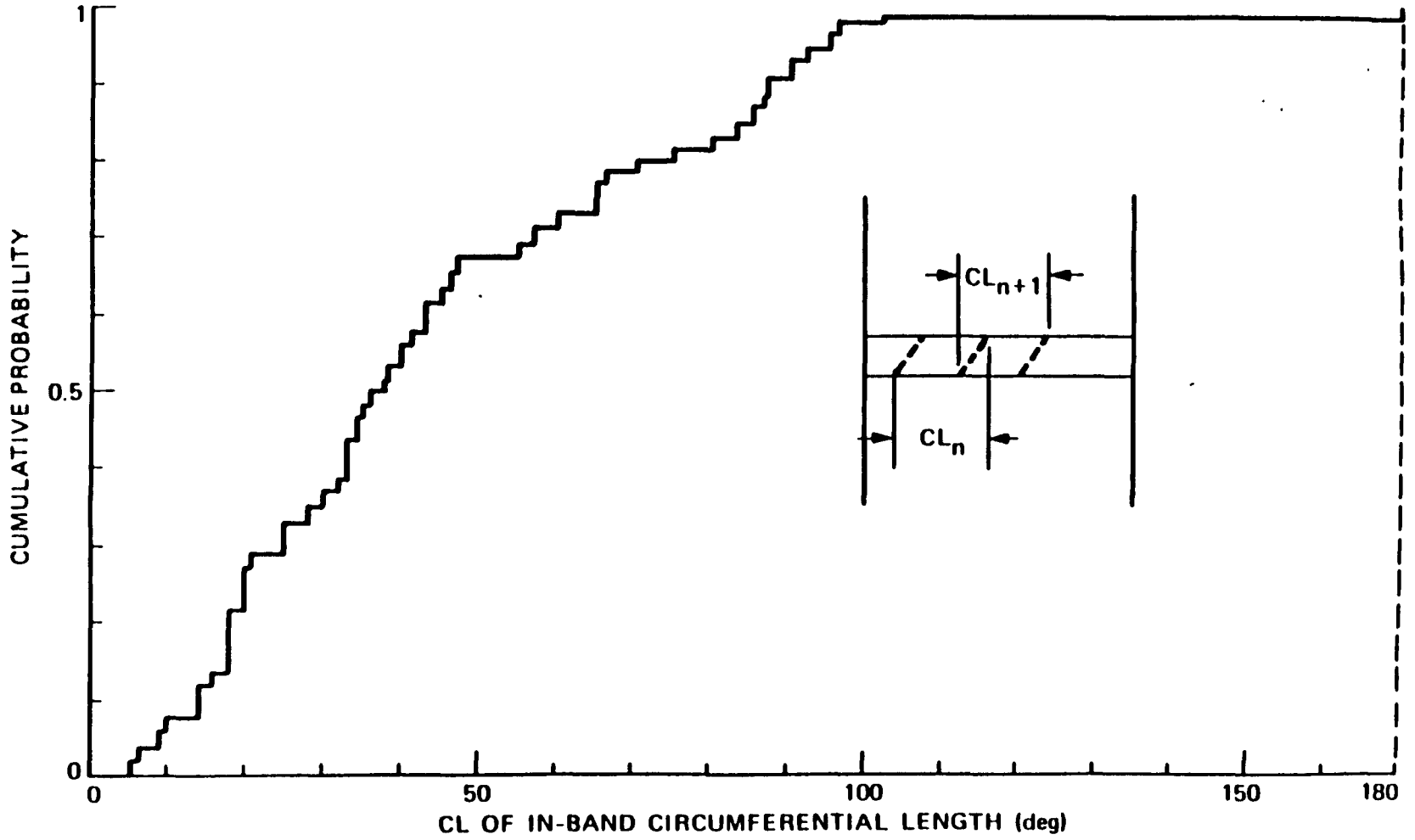


Figure B-22. In-Band Circumferential Length Distribution - Random Failure Case (Failed Cylinder)



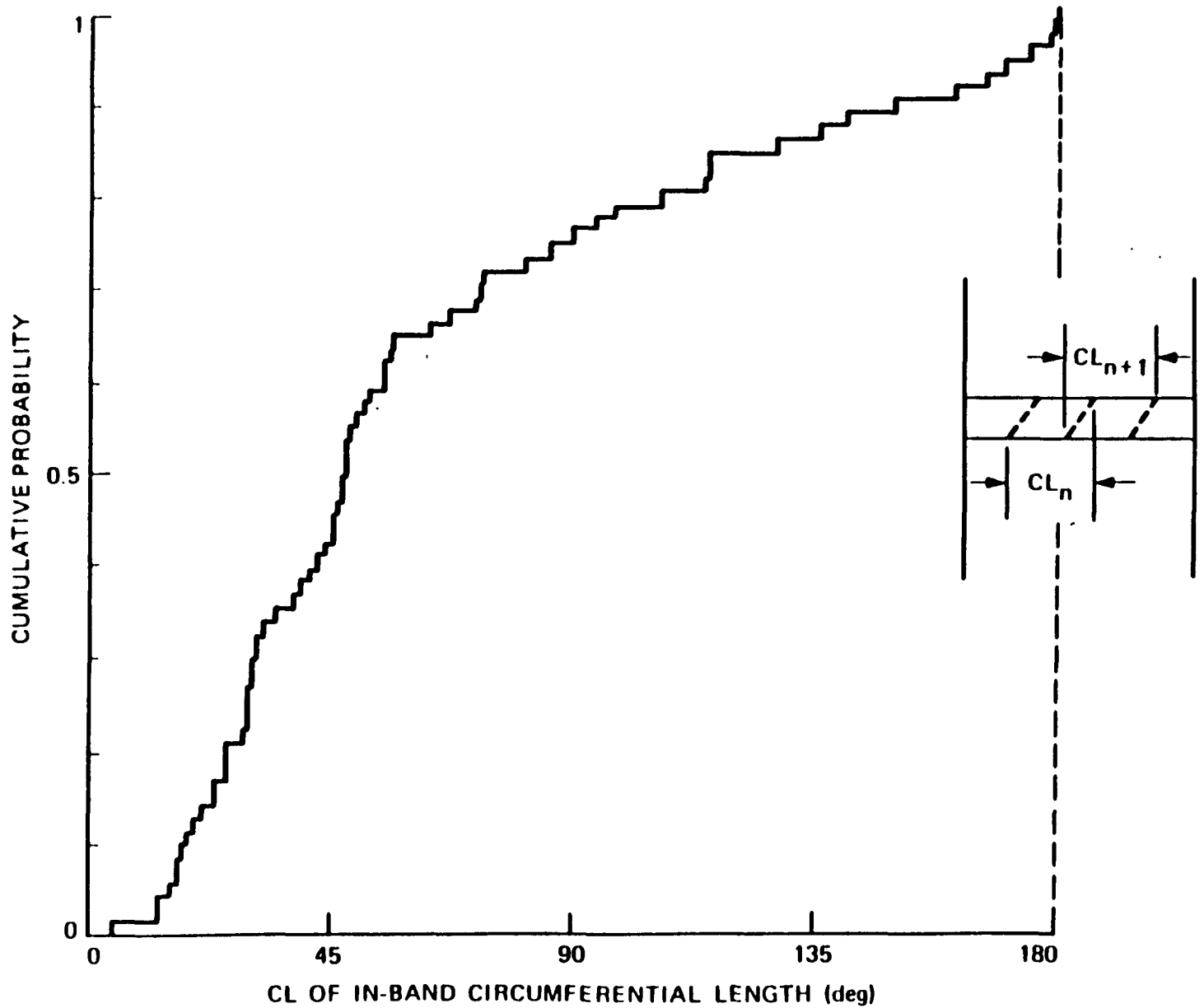
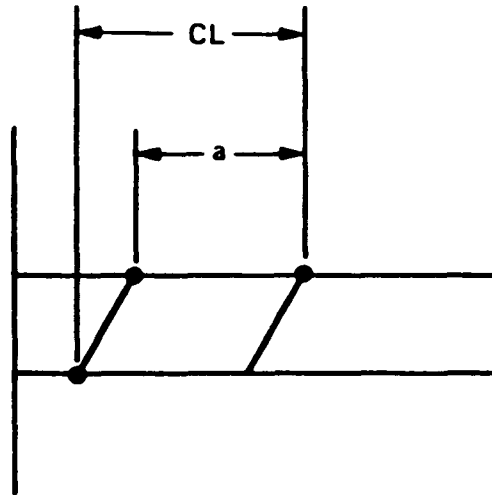


Figure B-23. In-Band Circumferential Length Distribution - Random Failure Case (Non-Failed Cylinders)



$F = \text{COMPRESSION FACTOR} = \frac{CL}{a}$

	FAILED SEGMENT	NON-FAILED SEGMENTS
F	1.64	1.25

Figure B-24. Compression Factor - Random Failure Case (See Figure 5.8)

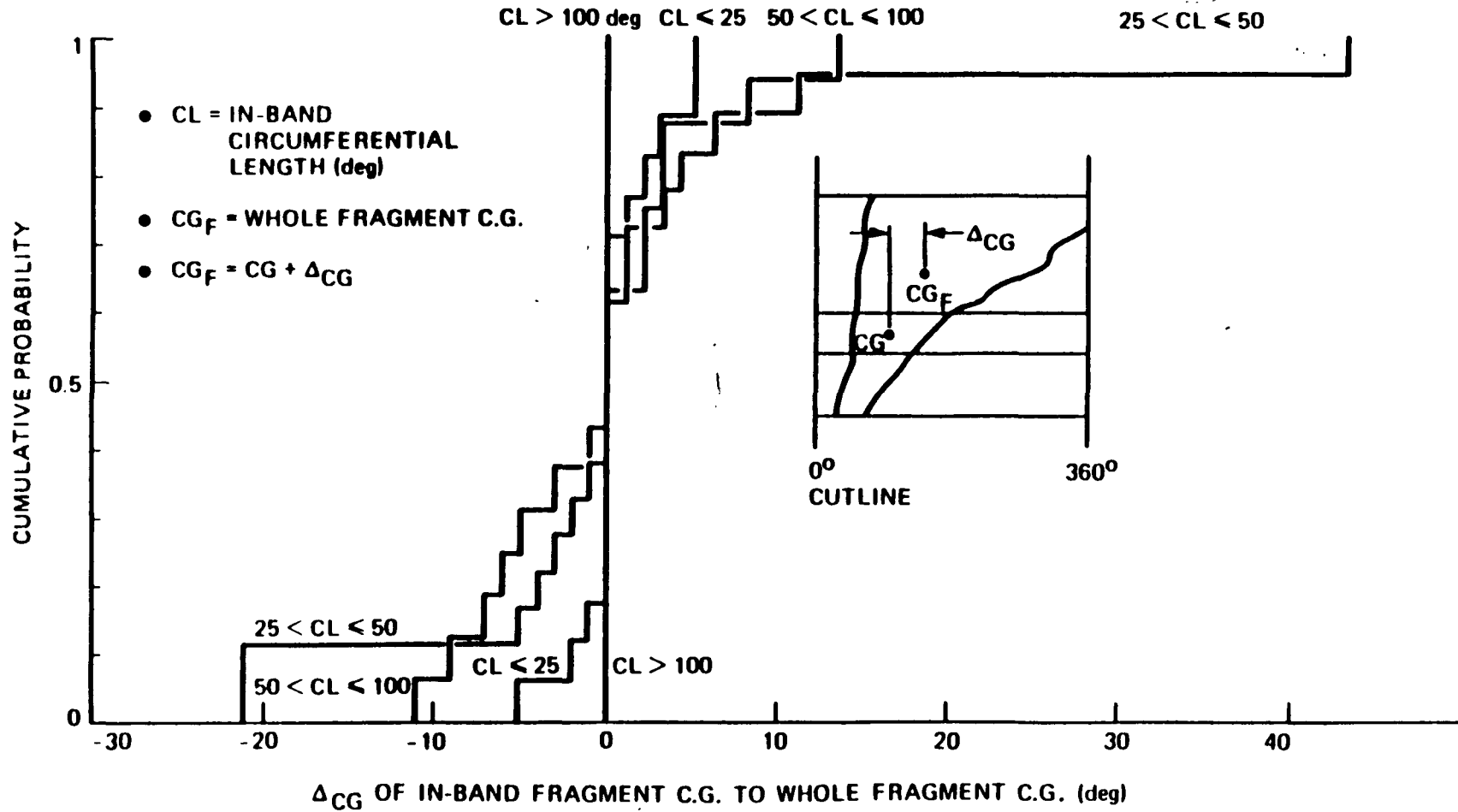


Figure B-25.  $\Delta_{CG}$  Distribution - Random Failure Case (Failed Cylinder)

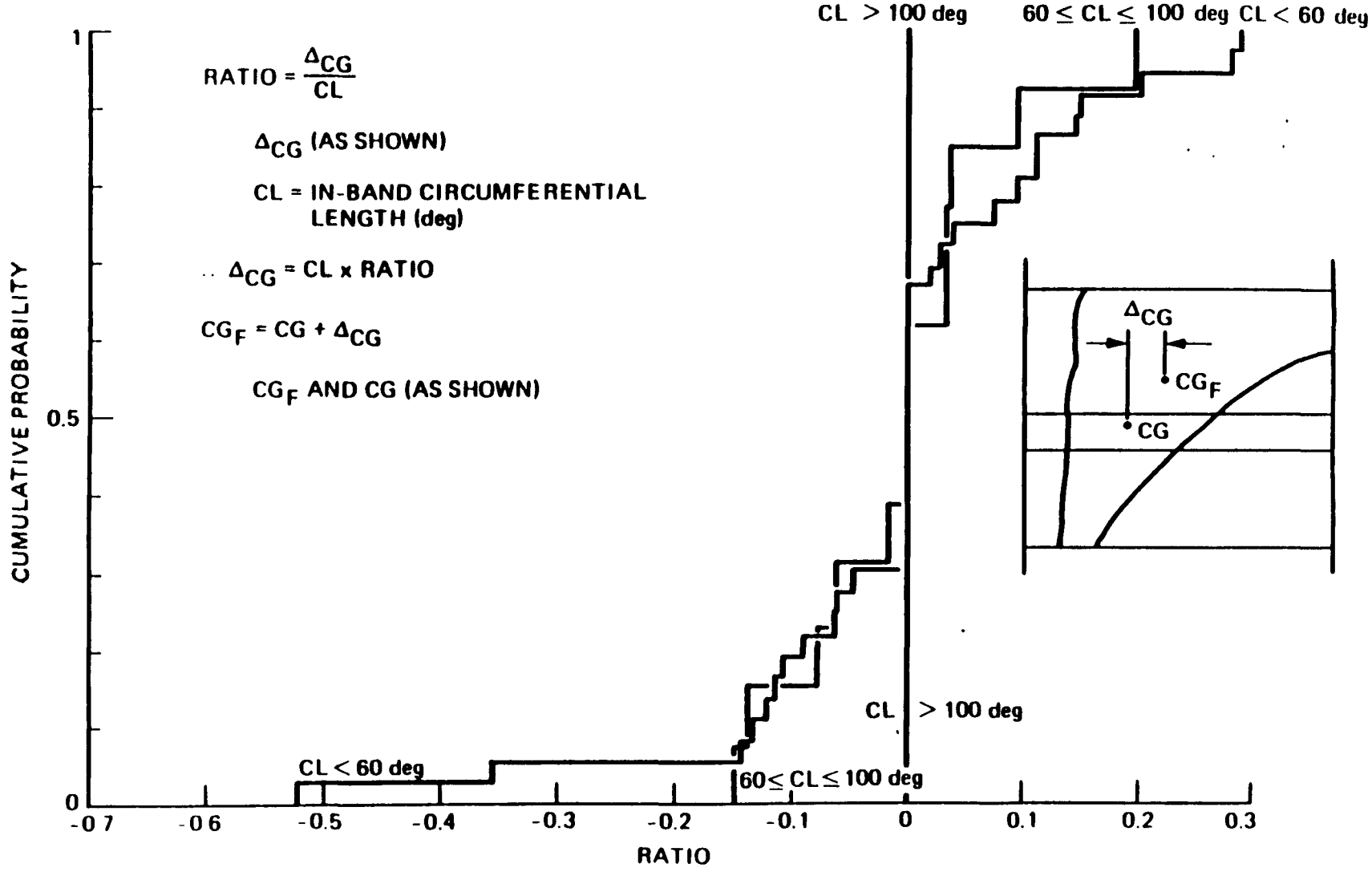


Figure B-26. Determine Whole Fragment C.G. WRT In-Band C.G. - Random Failure Case (Failed Cylinder)

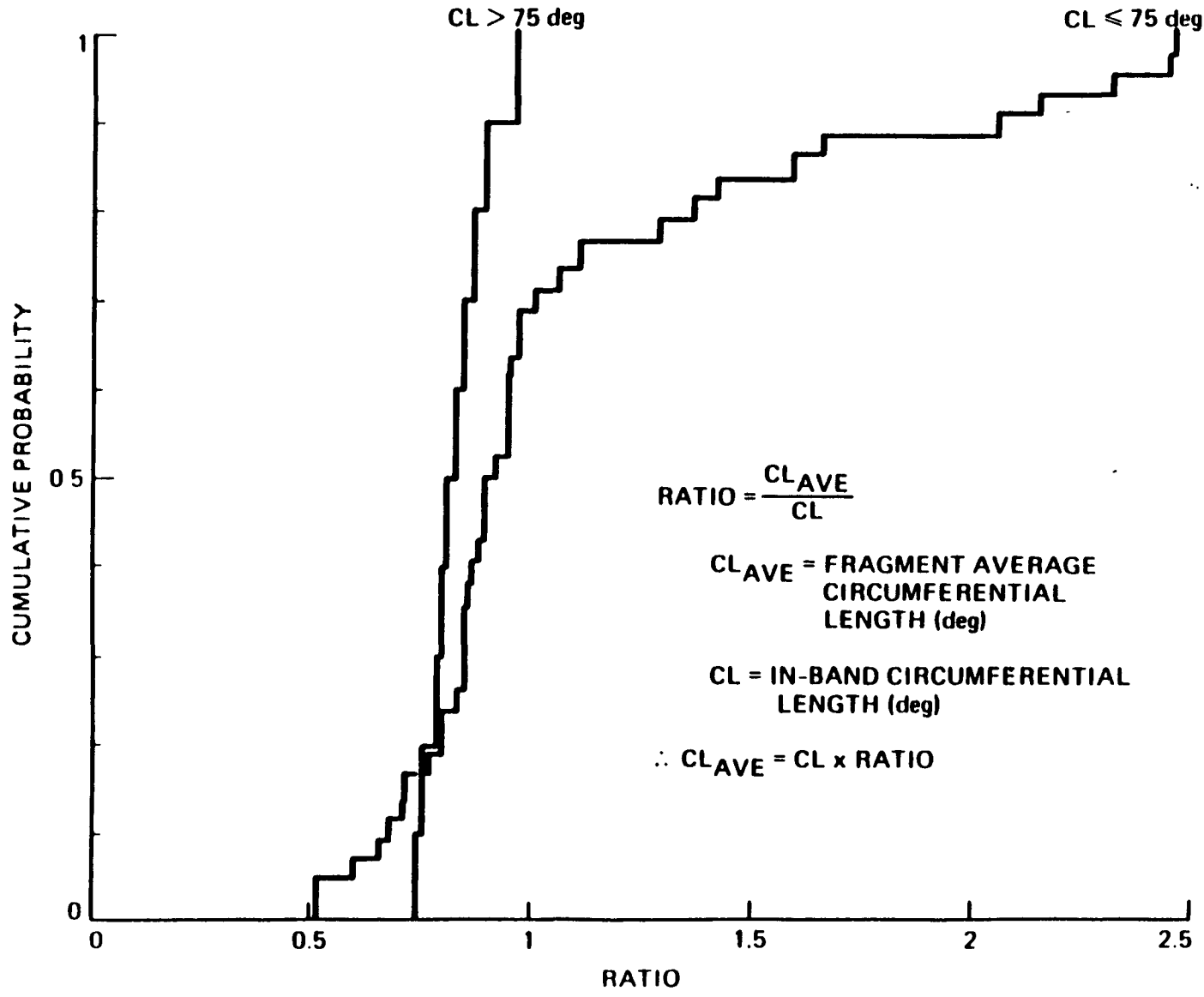


Figure B-27. Whole Fragment Average Length - Random Failure Case (Failed Cylinder)

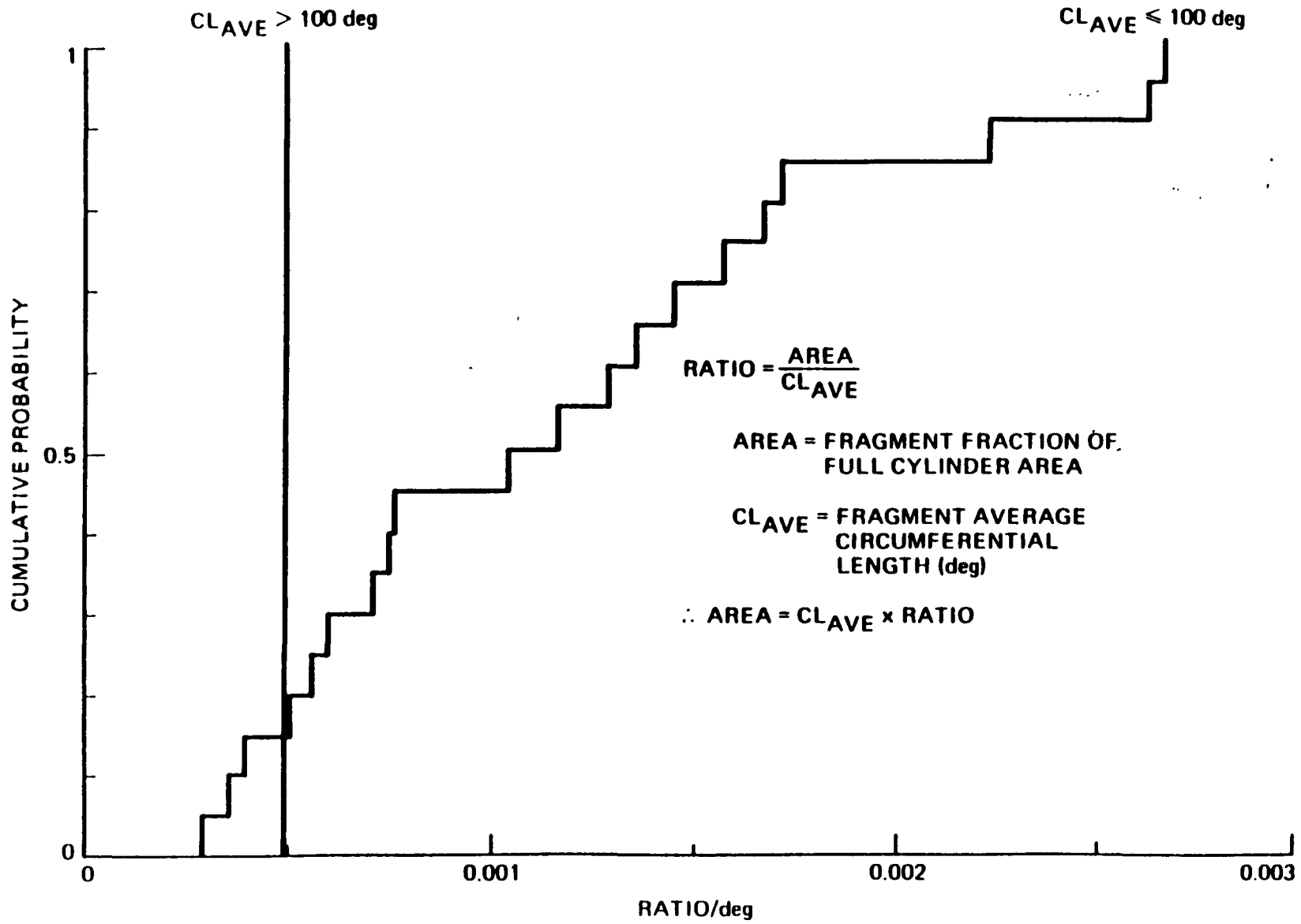


Figure B-28. Whole Fragment Area - Random Failure Case (Failed Cylinder)

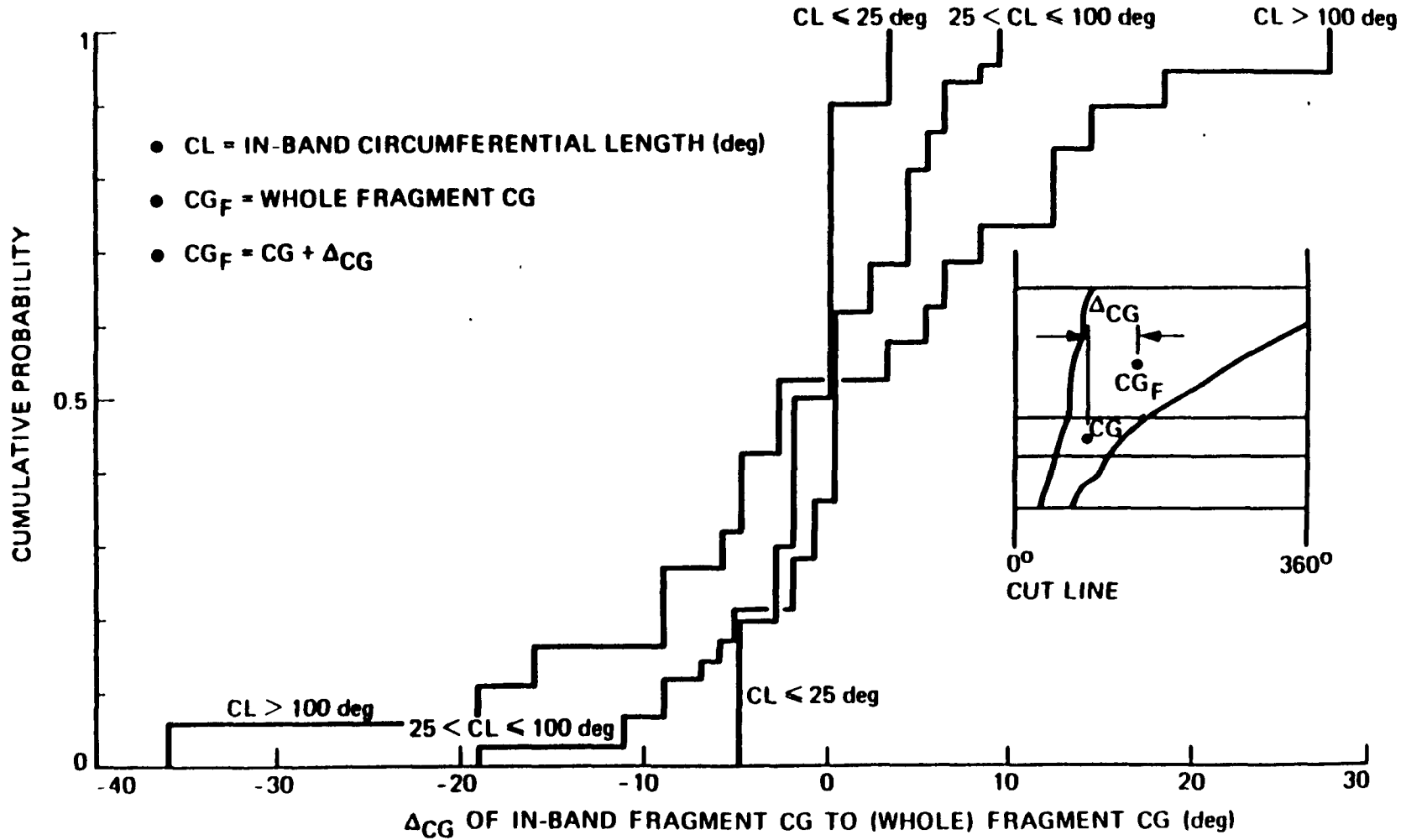


Figure B-29.  $\Delta CG$  Distribution - Random Failure Case (Non-Failed Cylinders)

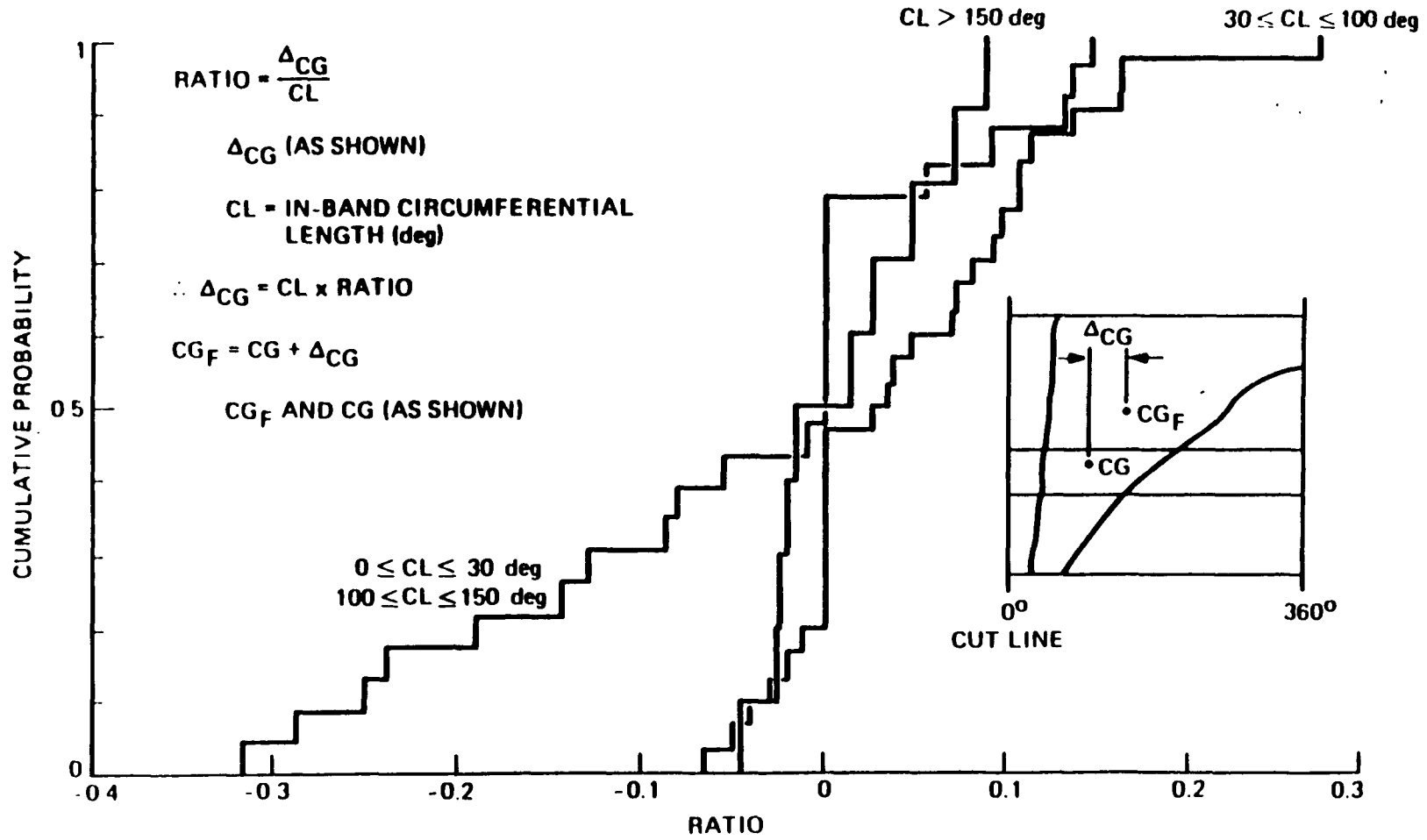


Figure B-30. Determine Whole Fragment C.G. WRT In-Band C.G. - Random Failure Case (Non-Failed Cylinders)



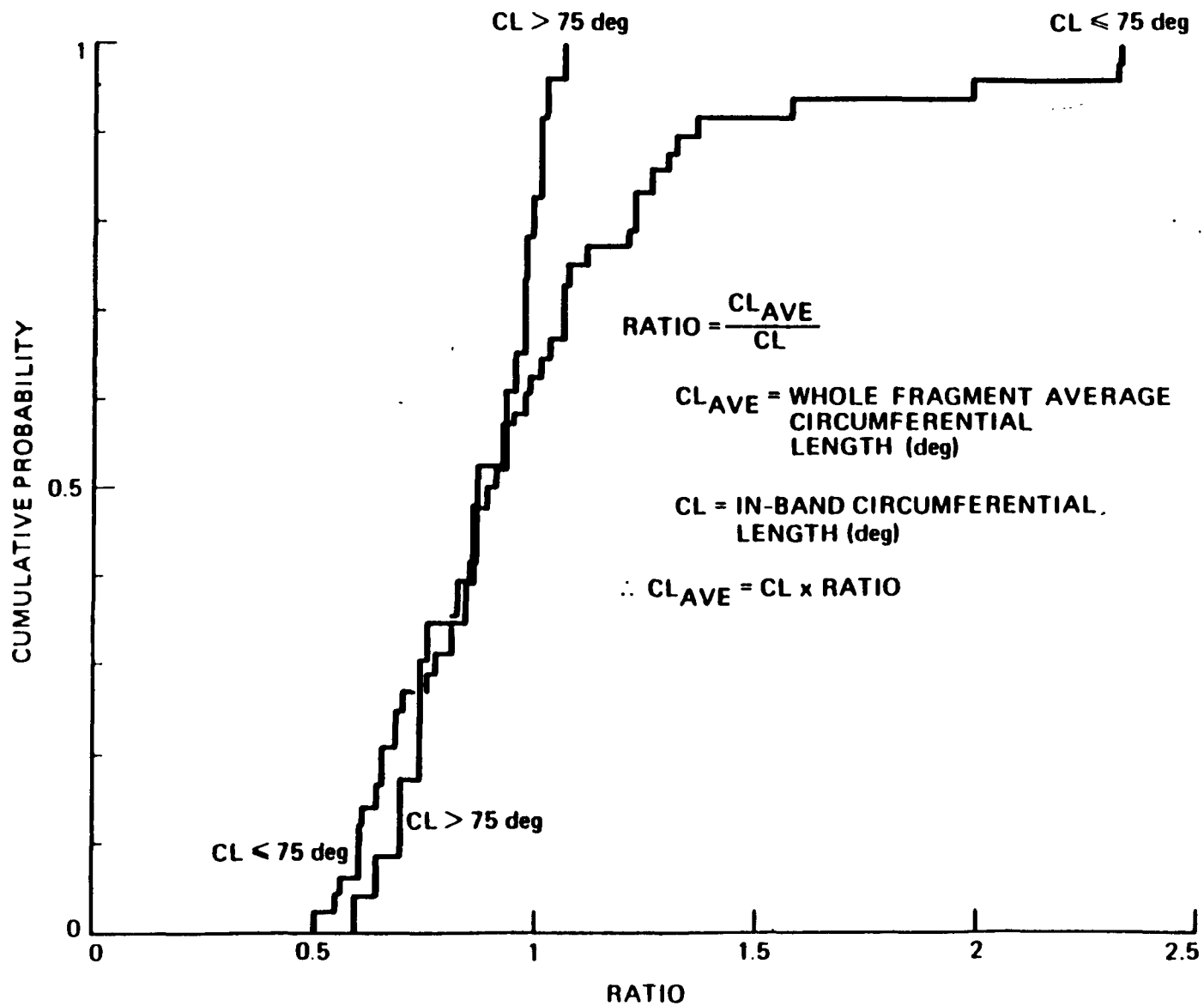


Figure B-31. Whole Fragment Average Length - Random Failure Case (Non-Failed Cylinders)

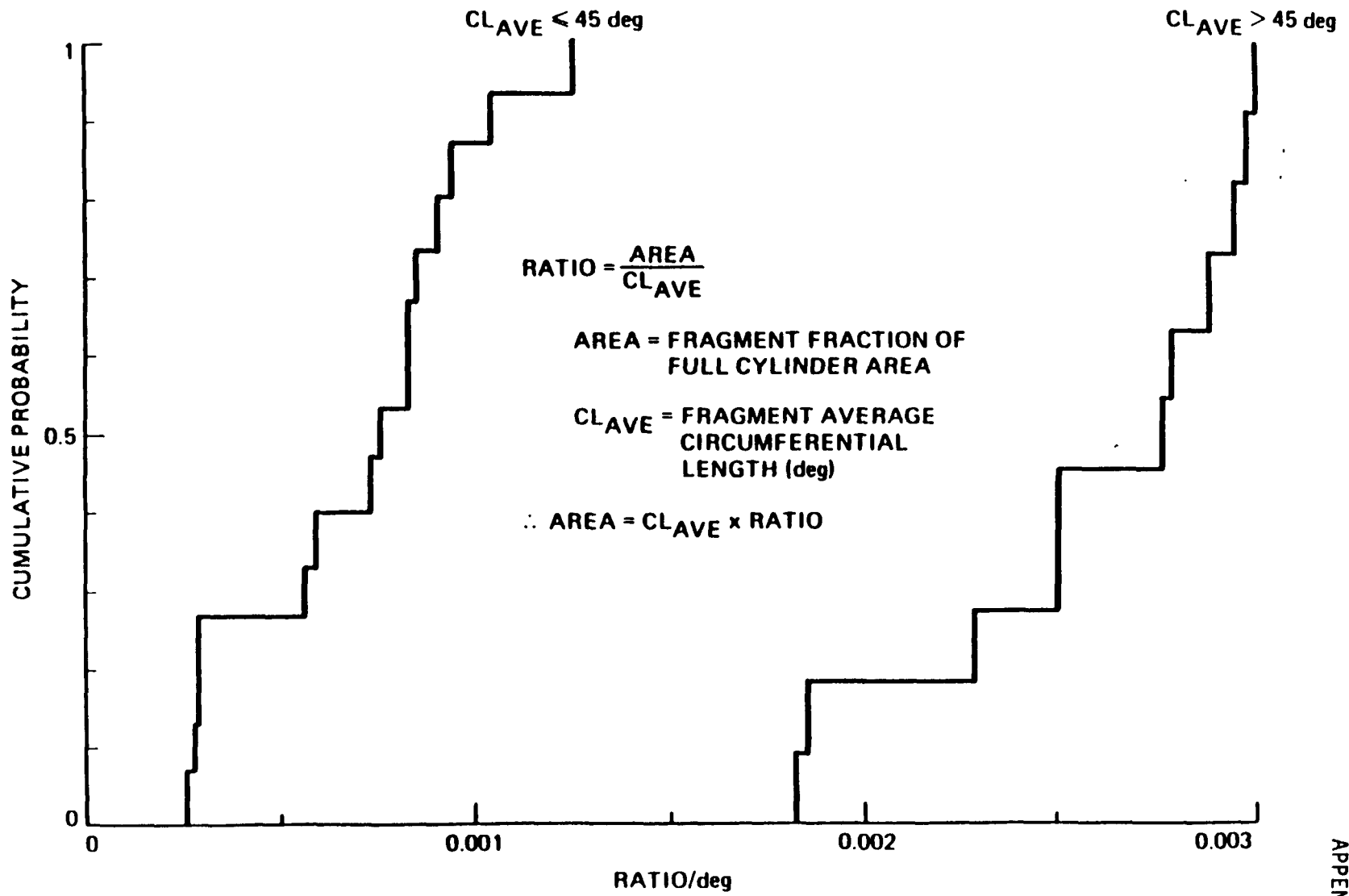


Figure B-32. Whole Fragment Area - Random Failure Case (Non-Failed Cylinders)

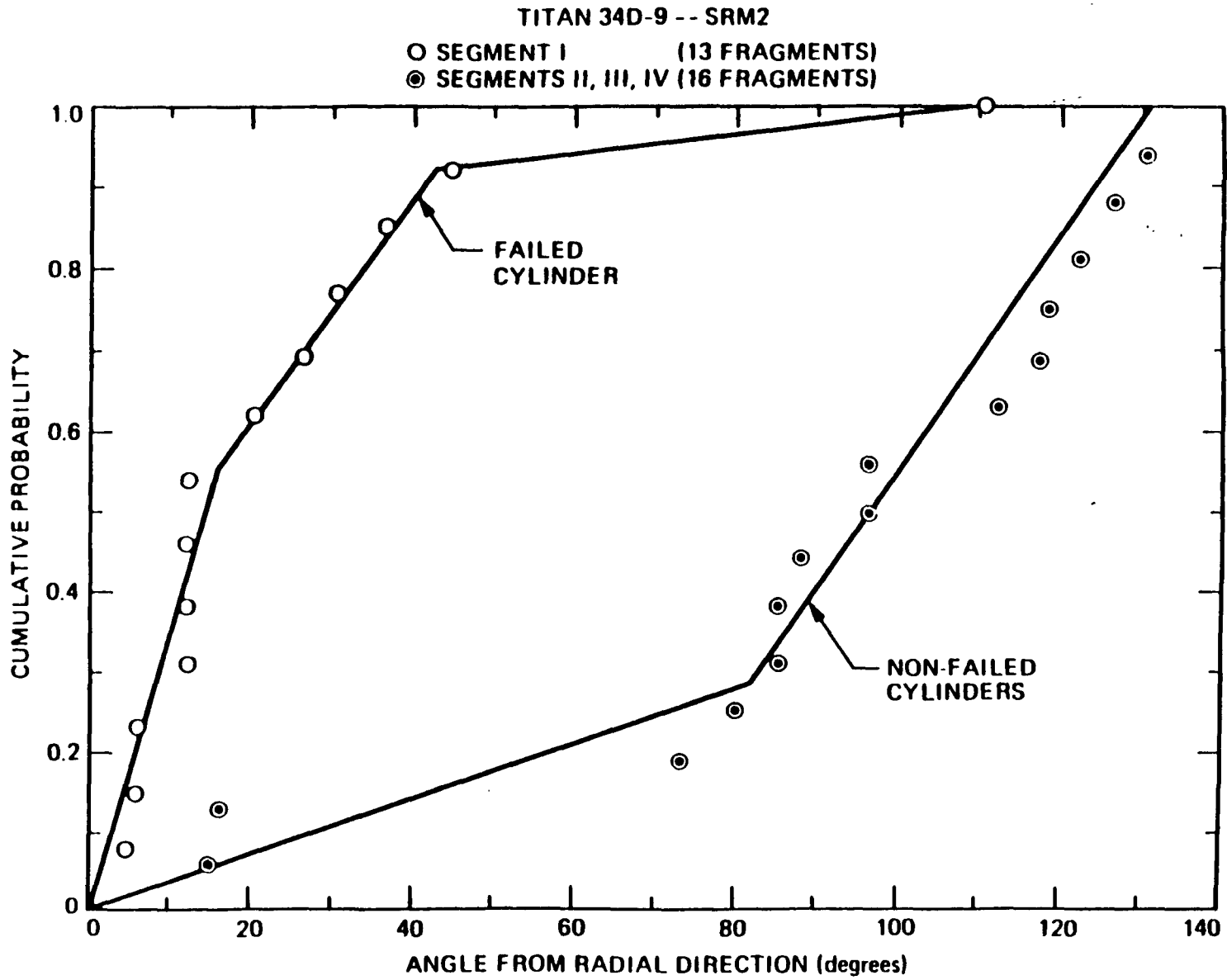


Figure B-33. Azimuth Distributions for Random Failure

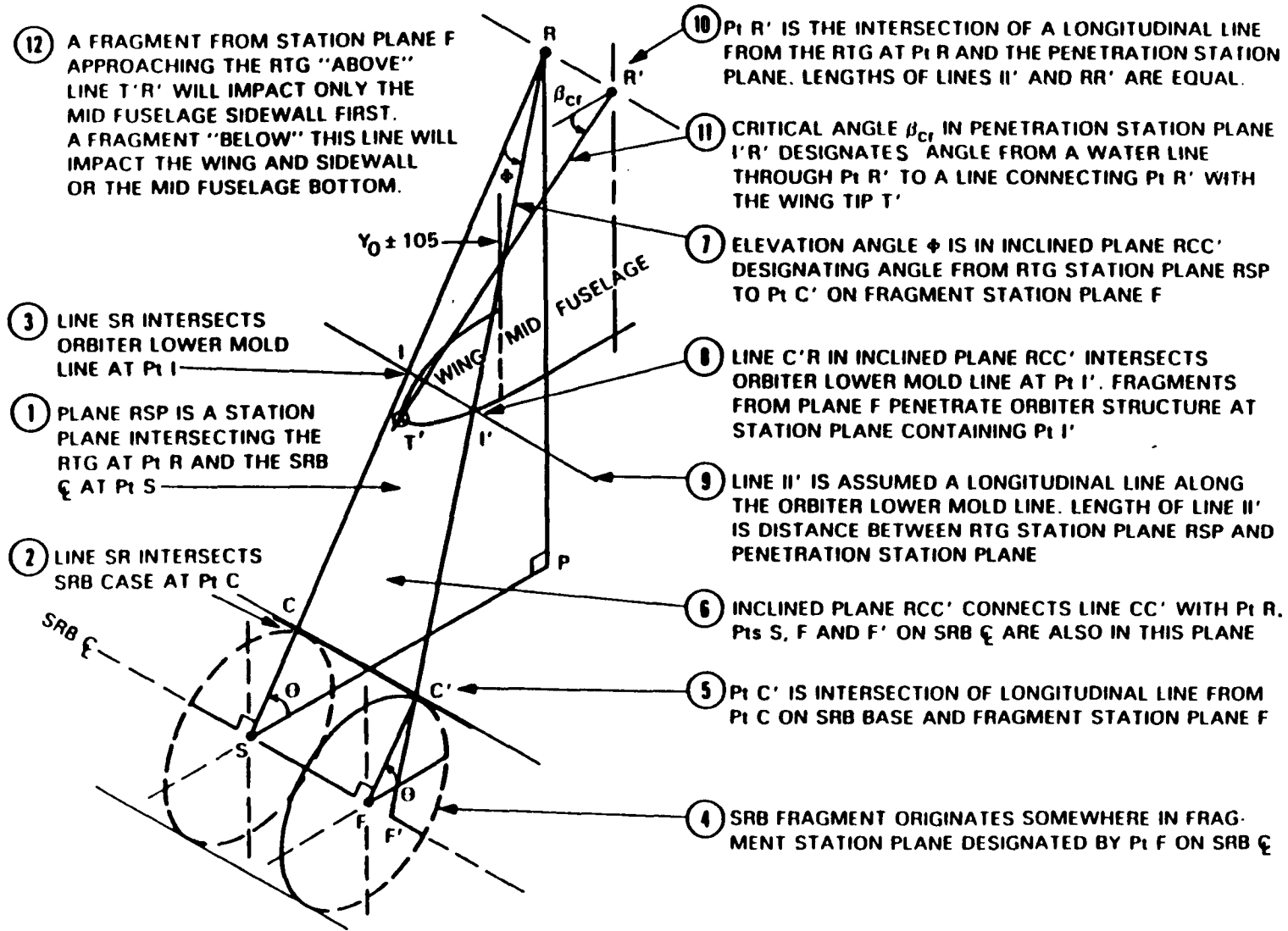


Figure B-34. Determination of the Critical Angle for an SRB Fragment Which Impacts an RTG (For Use of This Diagram, Follow Circled Numbers in Order)

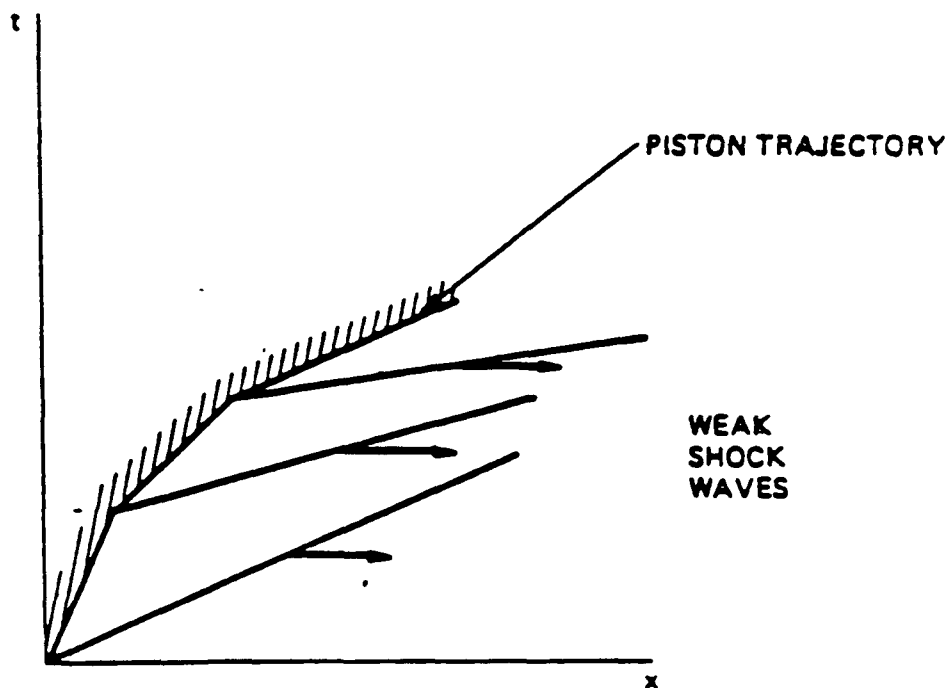
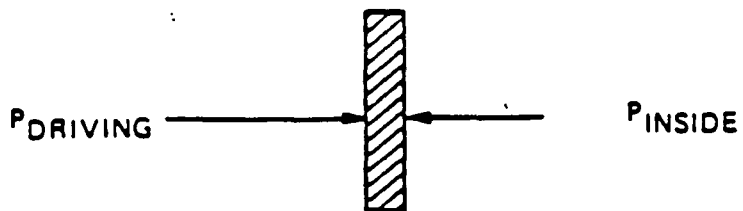


Figure B-35. Piston Model

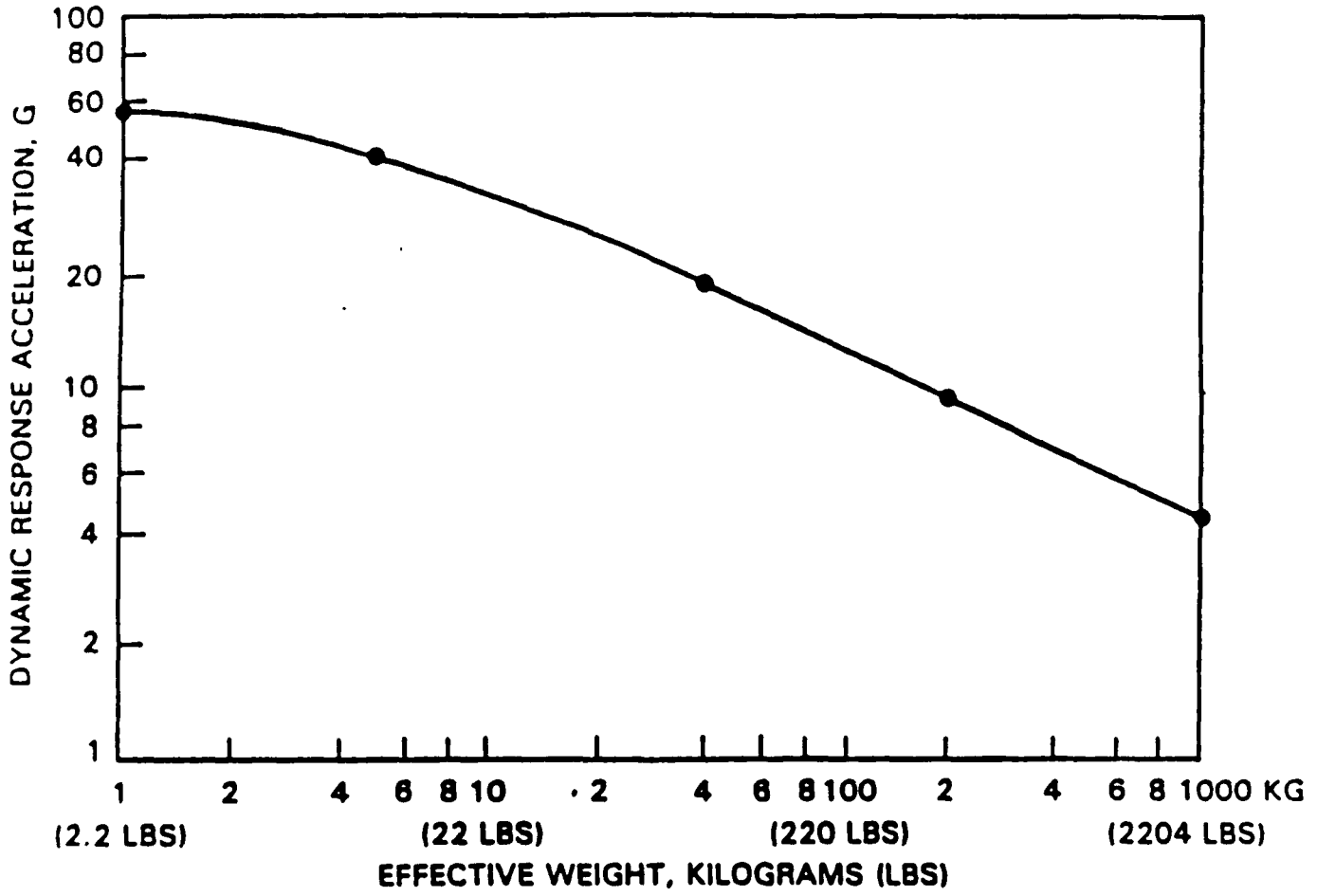


Figure B-36. Mass Acceleration Curve (MAC)

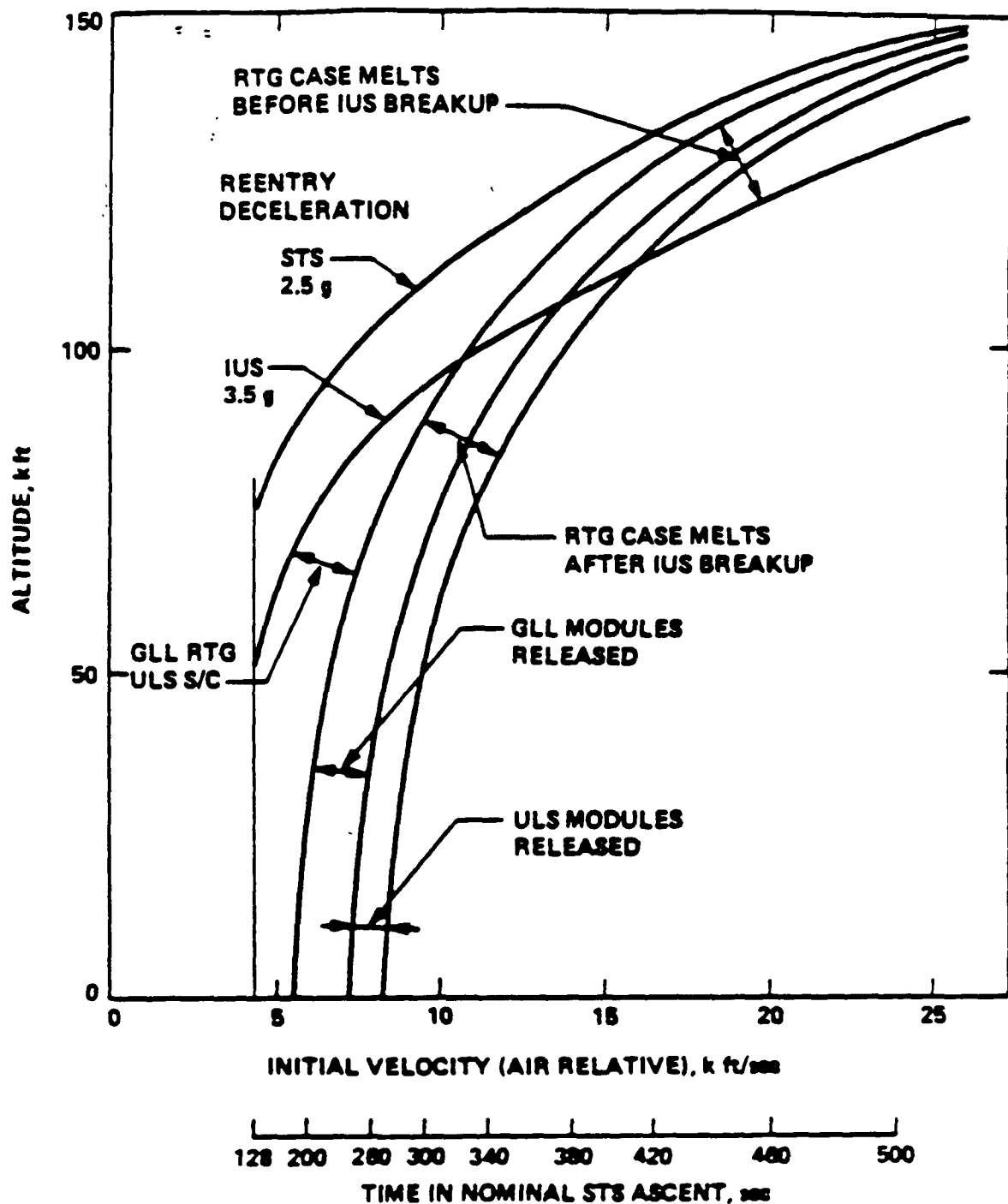


Figure B-37. Altitude for Various Orbiter Breakup Events as a Function of the Initial Speed and Time in the Ascent at Which the Fault Occurs

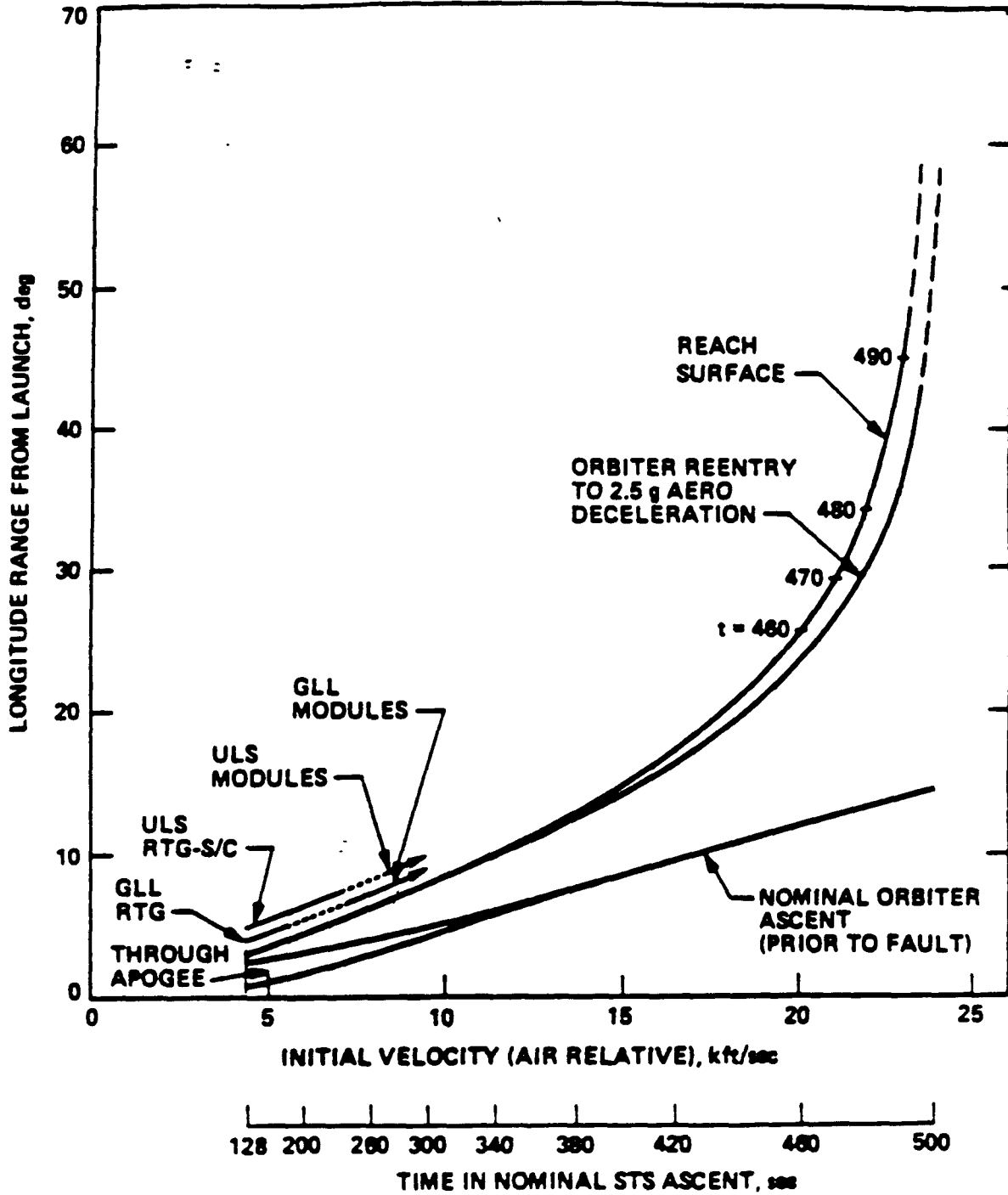
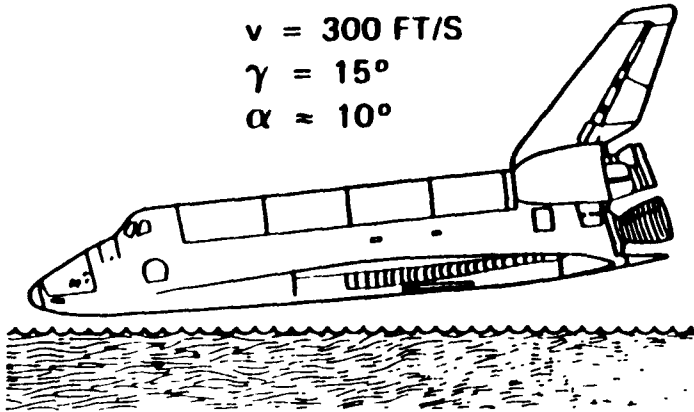


Figure B-38. Longitude Range From Launch for Orbiter Breakup and Surface Impact, as a Function of the Speed and Time in the Ascent at Which the Fault Occurs



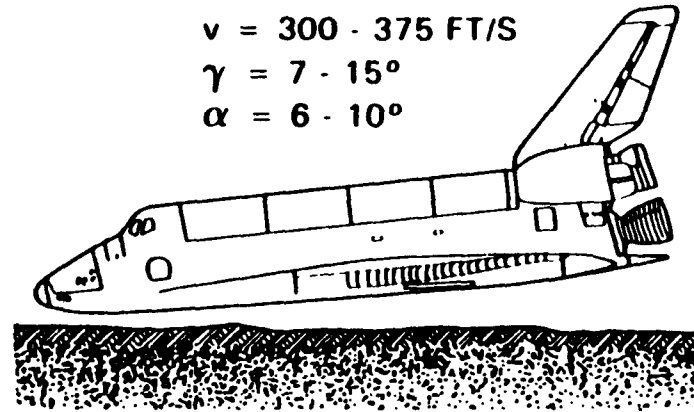
**OCEAN DITCH  
CONSTANT GLIDE SLOPE**

$v = 300 \text{ FT/S}$   
 $\gamma = 15^\circ$   
 $\alpha \approx 10^\circ$



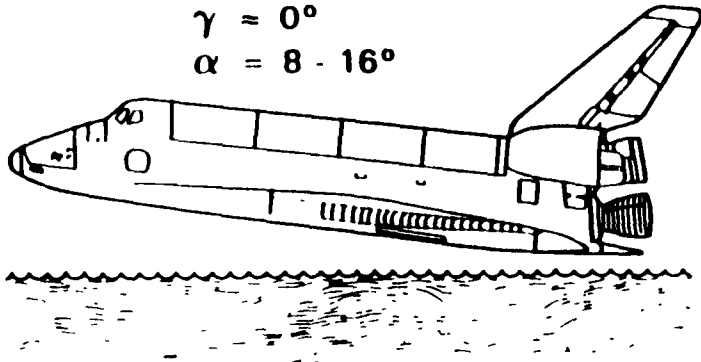
**LANDING CRASH  
PRE-FLARE**

$v = 300 - 375 \text{ FT/S}$   
 $\gamma = 7 - 15^\circ$   
 $\alpha = 6 - 10^\circ$



**OCEAN DITCH  
WITH FLARE**

$v = 250 - 325 \text{ FT/S}$   
 $\gamma \approx 0^\circ$   
 $\alpha = 8 - 16^\circ$



**LANDING CRASH  
POST FLARE**

$v = 300 - 375 \text{ FT/S}$   
 $\gamma = 0^\circ$   
 $\alpha = 7 - 11^\circ$

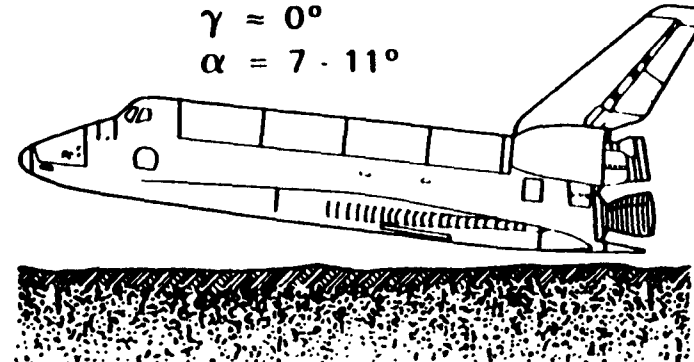
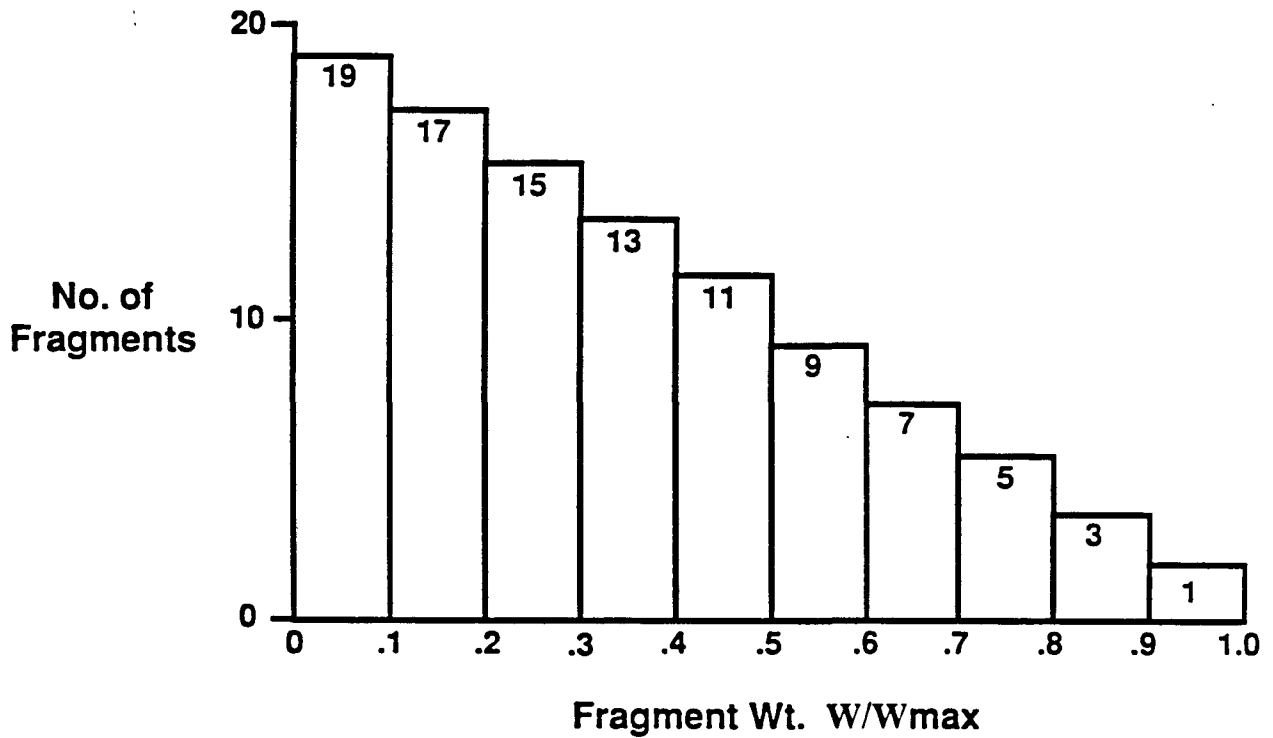


Figure B-39. Crash Scenarios and Conditions



**Total No. of Fragment = 100**  
**Total Wt. of Fragments = 33.5 Wmax**

Figure B-40. Fragment Size Distribution

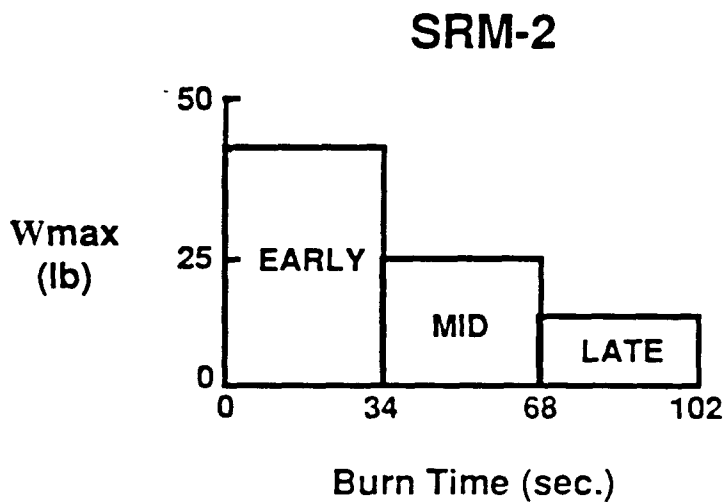
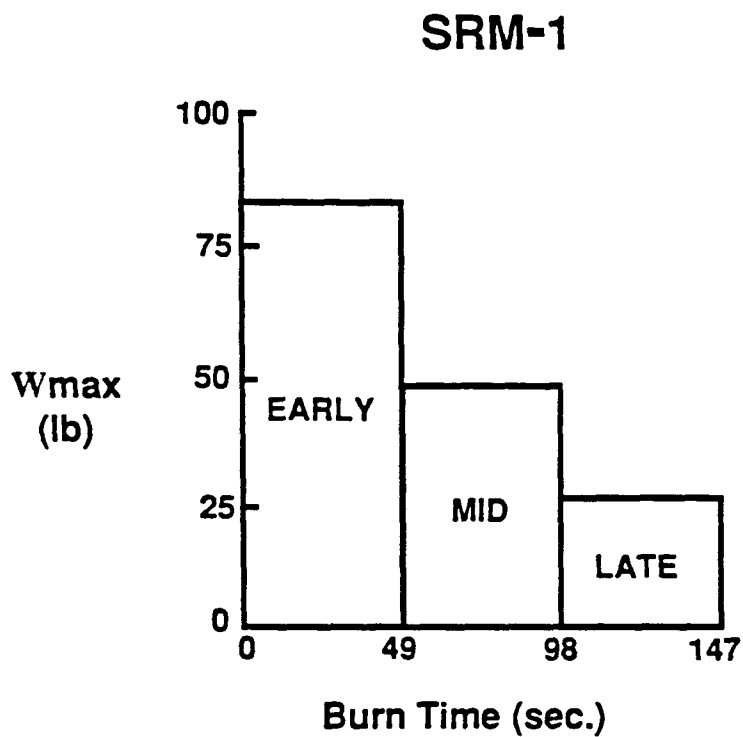


Figure B-41. Maximum Fragment Size vs Burn Time

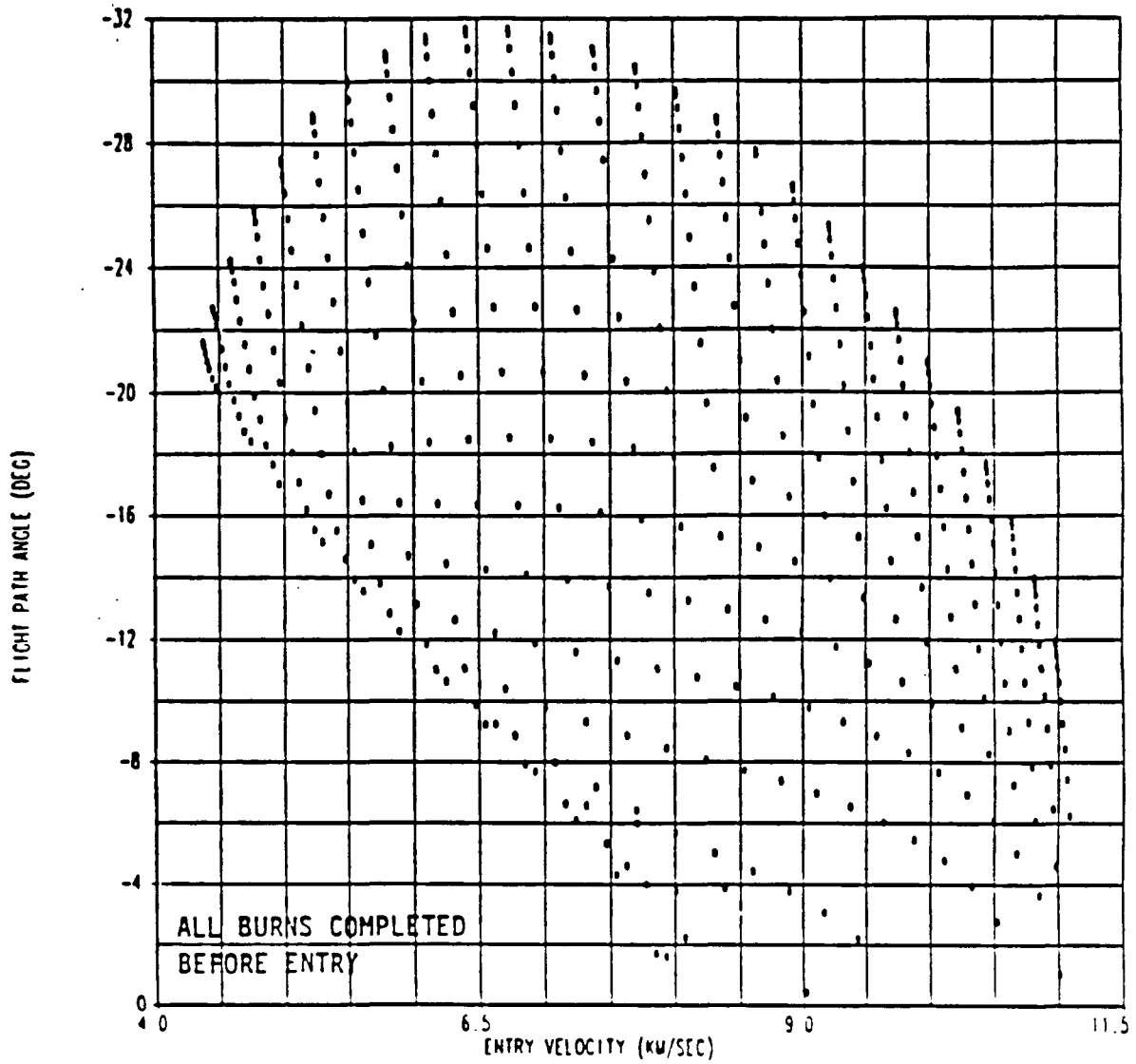


Figure B-42. Entry Conditions for Complete Consecutive Burns (Galileo)

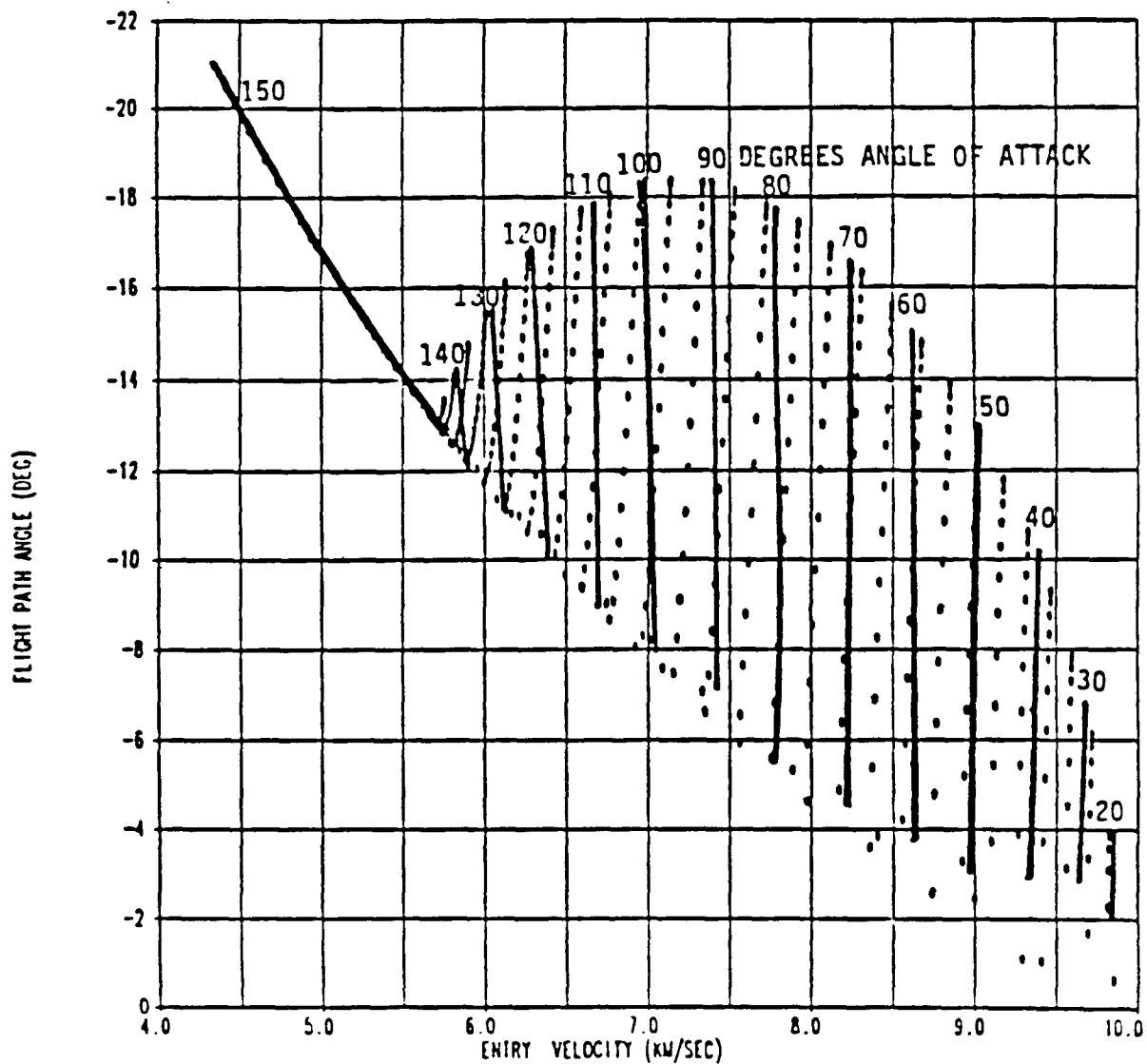


Figure B-43. "Powered" Entry Conditions, Coast 1, Burn 2 (Galileo)

APPENDIX C  
HYDROCODE ANALYSIS OF RTG RESPONSE TO ACCIDENT ENVIRONMENTS

The material presented in this Appendix constitutes the data base upon which the LASEP Program was exercised. This data base was generated using the normalized hydrocode models described in FSC-ESD-217/88/427. The LASEP Program is used to determine release probabilities for the GPHS fueled capsules when they are subjected to a number of adverse events. Among these are:

- A. Side-On Impact by Solid Rocket Motor (SRM) Fragments.
- B. Edge-On Impact by SRM Fragments.
- C. Impact of an Intact RTG Against the STS-Bay Door
- D. Impact of a Bare Module Against the STS-Bay Door.
- E. Impact of a Bare Capsule Against the STS-Bay Door.
- F. Side-On Impact of a Bare GIS Against Concrete.
- G. End-On Impact of an Intact RTG on Concrete, Steel and Wet Sand.

The results of calculations performed to describe the above events are presented in this Appendix. As has been suggested previously, there is no way to test the plutonia fueled capsule in a full scale environment. As a result, it was necessary to predict the distortion of the uranium simulant used in the LFTs prior to predicting the potential plutonia results, and to establish material response uncertainty bounds based on the results of the BCI and FGT plutonia fueled events. The results of the LFT series are presented in Table 1 for reference. A fueled capsule impact sensitivity study was conducted after calibration of the analytical models. This study resulted in the data base referenced above.

A. Side-On SRM Fragment Impact

The material properties used for the models discussed in this Appendix are presented in Table 2. The analyses used a very detailed zoning of two GPHS modules with dummy mass concentrations on either side of these two fine zoned modules. The early time geometry of a typical RTG stack model is

shown in Figure 1. These snapshots are taken just as the fragment-housing-insulation sandwich impacts the module stack. Also shown in Figure 1 is the device used for approximating the effects of modules at various longitudinal positions within the generator. Note that in the first panel of Figure 1, the two modules with fine zoning are shown in the second and third position from the bottom of the stack and the mass simulants are located in the 1 and 4 positions. In the third panel of Figure 1, note that the active modules are in the 4 and 5 positions while the mass simulants are in the 3 and 6 positions. The remainder of the stack is simulated with distributed mass blocks having the mechanical properties of poco graphite. The thicker than actual plate used to investigate three-dimensional fragment bending stiffness effects is also shown in the third panel of Figure 1.

More than one hundred cases were calculated to provide a data base for the LASEP input. These calculations varied impact point on a fragment, fragment rotation rate and translational velocity, as well as plate thickness and the module location within the stack. It was noted early in the generation of this data base that the distortion predicted for any given stack location was the function of the point velocity of the fragment, i.e., the vector summation of its rotational velocity and its translational velocity at any point from the center of the fragment to 87 percent of the distance from the center to the tip of the fragment. Observed nonlinearities occurred when the module of interest was impacted by the last twelve percent of the fragment's length. It appeared that the stiffness in both the 1/2 and 3/4 inch plate configurations was a factor only in the last 12 percent of the distance from the rotational center of the fragment to the tip of the fragment. This observation greatly simplified the generation of the data base because it became necessary to look only at point velocities on the fragment and any combination of distance and rotational speed could be modeled as a simple translational impact having that velocity. The special case which occurred for impacts on the final 12 percent of the fragment was handled as a separate set of calculations. The model used for these calculations was shown in the second panel of Figure 1.

Best results for correlation with the Large Scale Fragment Tests (LFT) were obtained using the model which was calibrated against the BCI tests and the FGT tests using weak urania (U6H11H) and 1/2 inch plate properties. During calibration, the bounds of these properties were shifted only in terms of the strength of the urania and the fragment thickness. The fragment thickness changes which were made to calibrate the model in the LFT-1 did not seem appropriate in the LFT-2. Therefore, it appears that the 1/2 inch plate case using the weak plutonia (PU2H6H) model may be a better approximation of an upper bound than of the nominal event. Possible mechanisms for these differences are presented in FSC-ESD-217/88/427 and are beyond the scope of this Appendix. This work was completed prior to running the LFT-2. As a result the 1/2 inch thick plate, weak plutonia model was defined as the nominal rather than the worst case for the purposes of this effort.

A complete compilation of the side-on fragment impact data base developed using the PISCES code is presented in Table 3. This data base was treated statistically by A. Mowery of DOE and R. Vaughn of NUS, to determine the means and distributions of distortion as a function of the fragment rotation rate, translational velocity, and stack position and fragment impact location. Much of the following description was taken from A. Mowery's memo on the treatment of that data base. It should be noted that this data base was generated on quadrant sized fragments and that the calculation set contained equivalent fragment translational velocity variations ranging from 100 to 350 m/s. Rotation rates of 0, 7, 12, and 17 Hz were investigated prior to determining that capsule distortion resulting from impacts over the majority of the fragment was a function only of point velocity. Six impact points on the fragment were considered. These were 0, 25, 50, 75, 87.5 and 100 percent of the fragment radius. Fragment impacts at 100 percent of fragment radius were called tip impacts. In this case, the tip of the fragment was aligned with the centerline of the module in the number two stack position. The other variable used in the calculational set was the module position. Results were calculated for the 2, 3, 4 and 5 module positions. The position 1 module was not calculated directly and was always used as a concentrated mass simulant because of difficulty in



modeling the heat source support system. It was assumed that module position 2 will produce the equivalent distortion of position 1. Figure 2 shows the plot of the data base for the 1 and 2 positions in the stack. These results are typical of the cases studied. The equation shown below was used to fit the results shown in Table 3, and is shown graphically as the nominal curve in Figure 2.

$$D(p,v,f/a) = D_m \left[ 1 - \exp\left(-\frac{a(v-v_0)n}{100}\right) \right] \quad (1)$$

Where D is the clad distortion as a function of module position, p, point fragment velocity, v, and forward or aft clad, f/a.

D<sub>m</sub> is the maximum clad distortion over the velocity range.

v is the point fragment velocity.

v<sub>0</sub> is the velocity offset below which there is clad damage.

a and n are fit constants.

Fit parameters were generated for each module position assuming that position 1 was equivalent to position 2. Fore and aft clads were also treated. Separate fits were developed for non-tip and tip fragment impacts. Impact at the fragment tip was assumed to be any impact between 0.875 and 1.00 of the fragment length. Each quadrant sized fragment has a radius of 4.7 ft, the fragment tip is therefore, about 6 inches wide. A least squares fit of the hydrocode was prepared by R. Vaughn of NUS. These fits are shown in Table 4 for non-tip impact cases and in Table 5 for tip impact cases. The sigma shown in the tables is a measure of the accuracy of the fit to the hydrocode results. It is not an indication of the overall uncertainty of one sigma. Note that grouping of the hydrocode results was required because functional relations were not generated for every module position. Groupings were therefore required to provide missing velocity dependent

functions. The following is a description of the manner in which the hydrocode results were fit to functional relations.

Non-Tip/Fwd Clads - Functional form was selected from the 2nd position results and the  $D_m$  taken as the average of the values above 200 m/s. Reason: A functional relation was not available for position 4 and 5 and 2 provided an adequate fit for 3.

Non-Tip/Aft Clads - Functional form selected from 3rd position results and treated as above for similar reasons.

Tip-Forward Clads - Second position distortions were unique so the least squares fit was used directly. Position 4 was the best available curve fit so that functional form was used for 3 and 5 with best estimates of  $D_m$ .

Tip-Aft Clads - Adequate results were available for a reasonable least squares fit so the NUS fit parameters are listed.

It was noted that further simplification of the clad distortion relations for non-tip impacts could be realized without significant loss of accuracy. If forward clads in positions 3, 4, and 5 were combined, the range of results would be covered by the 10 percent one sigma uncertainty in the calculations. The aft clad deformations could be adequately described by a single equation with an average  $D_m$  and the functional parameters listed in Table 5. A similar treatment could be applied to the forward clad fragment tip impact by combining positions 3, 4 and 5 with an average  $D_m$  using the functional parameters in Table 5. For aft clads, a single set of average parameters would adequately describe the hydrocode results.

The LFT-2 seems to indicate that the plateaus observed in the predicted distortions at higher velocities (Figure 2) are real. It is speculated that this plateau is caused by the movement of the forward part of the aeroshell

into the space previously occupied by the CBCF insulation. The effect of this is to fill the volume into which the fuel clads can expand. This limits the maximum diametrial growth of the fuel capsules. This hypothesis was tested against the experimental results. In the LFT-2 tests it was noted that at the higher velocities (212 m/s) the diameter of the fuel capsules did not increase proportionally. In some cases this diameter was not greatly different from the original diameter (in one case it was less than the original diameter) while the fuel capsule height and length were observed to change significantly. A summary of the LFT results (this test used urania fueled capsules) was presented in Table 1 for reference. It is seen that the capsule height and length changes are significantly different in the 100 and 200 m/s cases; however, the diameters are nearly equal. Further it is observed that the post impact shape of these capsules is different from that noted in the SVT and FGT tests. The exact cause of this difference is unknown; however, it should be noted that the hydrocode predicted diameter behavior correlated very well with the observed behavior. Comparison of the post-impact geometries shown in Figure 3 with the observations presented previously in Table 1 is instructive in this regard.

#### B. Edge-On Impacts by SRM Fragments

It was shown in the hydrocode calibration report (FSC-ESD-217/88/427) that peak distortion occurred at a 10 degree angle of attack for edge-on impacts. A number of urania and plutonia edge-on impact calculations were performed to calibrate the model against the edge-on test results. These tests are planned, but as of 27 July 88 they had not been run. The analytical model which is being used is really only valid for Ulysses geometry impacts. The Galileo impact geometry (the geometry which will be tested) requires that the centerline of the SRM and the centerline of the RTG be parallel. This will produce an edge-on impact such that the edge of the fragment is coincident with all 18 forward capsules on one side of the RTG. In the configuration modeled, the edge of the SRM fragment hits only two capsules in the leading GIS. This produces a significantly different impact orientation than would occur in the test. Several attempts were made to make the available model more applicable to the Galileo geometry. The

most appropriate was to set to zero the Y-velocity of the upper and lower surfaces of the module being impacted. Calculations performed in this manner still do not account for the transverse displacement of the face of the aeroshell as would occur in the Galileo geometry impact. As a result, it is expected that the predicted distortions will be significantly greater than those observed in the planned tests. Models which had the proper geometry for the Galileo could be configured but were not undertaken at this time because of the uncertainty of the fragment orientation which will actually occur given the results of the wing and the fuselage transit tests which are continuing. The results of the edge-on tests are summarized in Table 6. Typical post-impact overall model geometry is shown in Figure 4.

It should be noted that significant releases are predicted from edge-on impacts; however, the probability that impacts will occur in this exact orientation is extremely low. In addition, the calculations show that, based on distortion/release criteria developed by others, most release will be confined to the forward capsules and that the aft capsules will be contiguous for the purposes of defining a source term. If fragments impact the module in the calculated orientation at velocities of more than 200 m/s, some release from the aft capsules may occur based on the predicted distortions. However, fragment velocities of this magnitude occur only at late MET and the consequences of these releases may not be great. Detailed post-impact geometries for plutonia fueled capsules are shown in Figure 5 for initial velocities of 100 and 200 m/s respectively.

#### C. RTG - Bay Door Impacts

Calculations were performed to predict the results of intact RTG impacts on the STS-Bay Doors at 365 m/s. The results of these calculations are presented in Table 7. Typical post impact geometry is shown in Figure 6.

#### D. Bare Module - Bay Door Impacts

Calculations were performed to predict the results of various velocity impacts of individual modules on the STS-Bay Doors. These impacts would

occur in those cases in which the modules were ejected from the RTG within the Bay (explosive disassembly of the RTG). This action was modeled as an acceleration of the modules and subsequent impact on simulated STS-Bay Doors having two assumed areal densities. The results of these calculations are presented in Table 8. Typical post-impact geometry is presented in Figure 7.

#### E. Bare Capsule - Bay Door Impacts

Calculations were performed to predict the results of various velocity impacts of bare fueled capsules on STS-Bay Doors having two areal densities. This event results from the case in which the graphite was stripped from the capsules by an explosion which did not disassemble the STS-Bay. The results of these calculations are presented in Table 9. Typical post-impact geometries are presented in Figure 8.

#### F. Bare GIS Impacts on Concrete

Calculations were performed to predict the distortion of plutonia fueled capsules which impact concrete while still in the Ground Impact Shell (GIS). This event could occur in early aborts in which the aeroshell was stripped either by collisions with shrapnel or the STS structure. It could also occur in reentry cases in which the aeroshell failed and released the GIS. The results of these calculations are presented in Table 10. Typical post impact geometries are presented in Figure 9 for two impact velocities.

#### G. End-On Impacts of an Intact RTG

Large fueled capsule deformation will occur if the RTG impacts at its terminal velocity in an end-on configuration on hard surfaces such as concrete or steel. Lesser amounts of deformation will occur if the RTG impacts a softer surface such as wet sand. The end-on impact analyses were limited in the number of modules which could be modeled at one time. This came about because of the code limitation which allows only 20 impact polygons to be used. As a result, the strategy which was used in modeling the side-on fragment impacts had to be applied. This strategy modeled two

modules in fine detail and simulated the rest of the stack with mass mock-ups. The end-on impacts were modeled with point mass mock-ups so that inertial hard points adjacent to the fine zoned modules would provide the proper stress concentrations. The remainder of the stack was modeled by a distributed mass having the mechanical properties of poco graphite. As in the case of the side-on model, the finely zoned modules were moved from the second and third locations to the fourth and fifth locations. In all cases it was assumed that the number one module would be distorted by locally high stress concentrations brought about by the sharp edges of the RTG stack spider. A summary of fuel capsule distortion as a function of the nature of the impact surface, impact velocity, and the module position in the stack is shown in Table 11. Somewhat more distortion occurs when impacting steel than concrete; however, this difference should wash out by the fifth stack position. Impacts on sand show that large amounts of distortion are limited to the first two stack locations. These observations were all made for terminal velocity impacts. Additional calculations were performed at reduced impact velocity to simulate the case in which the STS does not achieve the height necessary for the RTG to reach terminal velocity before impacting the reference surface. Post-impact geometries for two impact velocities and two target materials are shown in Figure 10.

Table 1  
SUMMARY OF THE LARGE FRAGMENT TEST (LFT) RESULTS

FORWARD CAPSULE RESPONSE TO LFT EVENTS								
Stack Position 2								
IMPACT VELOCITY		115				212		
LOCATION	STRAIN				STRAIN			
	DIAMETER	HEIGHT	LENGTH	PARAMETER	DIAMETER	HEIGHT	LENGTH	PARAMETER
	%	%	%	%	%	%	%	%
OPEN VENT CUP	0.9	-2.9	1.0	3.9	1.3	-10.8	10.3	13.5
OPEN SOLID CUP	0.9	-2.1		3.1	1.3	-11.2		14.0
BLIND VENT CUP	0.2	-2.6	0.6	2.9	.6	- 9.1	8.1	6.0
BLIND SOLID CUP	0.9	-2.3		3.2	-	-	-	-
Stack Position 5								
OPEN VENT CUP	2.9	-2.8	2.0	5.9	.3	-8.5	4.8	9.7
OPEN SOLID CUP	3.1	-2.8		6.1	.9	-3.4		4.4
BLIND VENT CUP	2.8	-4.9	1.8	8.2	2.4	-4.3	8.4	7.0
BLIND SOLID CUP	2.2	-2.1		4.4	.3	-4.3		4.8
AFT CAPSULE RESPONSE TO LFT ENVIRONMENT								
Stack Position 2								
OPEN VENT CUP	2.9	-1.5	2.1	4.4	0.1	- 1.8	-1.1	1.9
OPEN SOLID CUP	2.6	-5.7		8.8	-0.1	- 2.4		2.4
BLIND VENT CUP	0.3	-0.6	-1.3	0.9	0.9	- 2.6	0.2	3.7
BLIND SOLID CUP	0.2	-1.3		1.5	0.6	- 3.2		4.0
Stack Position 5								
OPEN VENT CUP	0.6	-1.0	0.9	1.6	0.7	-2.6	0.0	3.4
OPEN SOLID CUP	0.8	-2.6		3.6	1.0	-3.1		4.2
BLIND VENT CUP	0.4	-0.6	-0.7	1.0	0.5	-2.3	-0.9	2.9
BLIND SOLID CUP	0.3	-0.9		1.1	0.9	-3.3		4.3

C-10

Table 2

**SUMMARY OF MATERIAL PROPERTIES USED IN THE SRM FRAGMENT IMPACT ANALYSES**

MATERIAL	EQUATION OF STATE						YIELD MODEL			SPALL STRENGTH KBAR	DATA SOURCE
	TYPE	$\alpha^{(1)}$	BULK MODULUS KBAR	Y1 KBAR	Y2 KBAR	REF DENSITY ( $\rho_0$ ) gm/cc	TYPE	SHEAR MODULUS KBAR	YIELD STRENGTH KBAR		
WEAK PLUTONIA (PU2H6H)	P- $\alpha$	0.84	730	0.677	1.33	11.5	VON MISES	270	0.677	0.200	LOS ALAMOS DATA SHEETS MAY 1986
STRONG PLUTONIA (PU4H13H)	P- $\alpha$	0.84	730	1.30	1.33	11.5	VON MISES	270	1.30	0.400	
WEAK URANIA (URH11H)	P- $\alpha$	0.87	1370	1.10	1.22	11.0	VON MISES		1.10	0.600	LOS ALAMOS DATA SHEETS MAY 1986
STRONG URANIA (URH12H)	P- $\alpha$	0.87	1370	1.20	1.22	11.0	VON MISES	598	1.20	0.800	
POCO GRAPHITE	POLY-NOMIAL	-	301			3.19	VON MISES	20	0.50	1.0	W W TARBELL (1979) AFWL-TR-79-38
3-D GRAPHITE	SHOCK	-	25.9			1.95	VON MISES	20	1.00	1.0	
IRIDIUM	POLY-NOMIAL	-	3510			22.5	VON MISES	1618	2.00	1000	ORNL-5611 APRIL 1980 (3) FSAR GESP 7200 AUGUST 1985
INSULATION T/E	P- $\alpha$	0.59	8.9			0.90	VON MISES	6.7	1.00	0.1	GE MEMO (2) C J EARDLEY 1/7/88
ALUMINIUM	POLY-NOMIAL	-	785			2.77	VON MISES	294.0	6.50	1000	BAKKEN & ANDERSON, SANDIA
D6A STEEL	POLY-NOMIAL	-	1670			7.86	VON MISES	816.0	12.9	1000	LADISH DATA SHEET FSCM # 07703 (1987)

(1)  $\alpha = \frac{\text{DENSITY OF UNCOMPACTED MATERIAL}}{\text{DENSITY OF COMPACTED MATERIAL}}$

(2) DERIVED FROM EXPERIMENTS CONDUCTED AT GE AND MODIFIED BY FSC PERSONNEL TO ACCOUNT FOR THERMOELECTRIC ELEMENT INITIAL COMPRESSIVE STRENGTH

(3) YIELD CORRECTED FOR THE BIAxIAL TENSION CREATED BY THE ALMOST SPHERICAL NATURE OF THE IRIIDIUM SHELL

REPRODUCED FROM  
BEST AVAILABLE COPY



Table 3

## DATA BASE FOR SIDE-ON FRAGMENT IMPACT EVENTS

For Impacts from 0 to 87.5% of the Distance from Fragment Center to Fragment Tip (Non-Tip Cases)							
DATA SET NAME	STACK LOCATION/ FWD-AFT LOCATION	DISTANCE FROM FRAGMENT CENTER	FRAGMENT THICKNESS	IMPACT VELOCITY	FUEL TYPE	ROTATION RATE	DISTORTION
		%	INS	M/S		HZ	%
4R07_PU2H6H_100	2F	87.5	0.5	100	WEAK	7	26.0
4R07_PU2H6H_100	2A	87.5	0.5	100	WEAK	7	10.7
4R07_PU2H6H_100	3F	87.5	0.5	100	WEAK	7	18.7
4R07_PU2H6H_100	3A	87.5	0.5	100	WEAK	7	7.7
4R12_PU2H6H_100	2F	87.5	0.5	100	WEAK	12	42.0
4R12_PU2H6H_100	2A	87.5	0.5	100	WEAK	12	14.3
4R12_PU2H6H_100	3F	87.5	0.5	100	WEAK	12	29.3
4R12_PU2H6H_100	3A	87.5	0.5	100	WEAK	12	6.2
4R17_PU2H6H_100	2F	87.5	0.5	100	WEAK	17	42.4
4R17_PU2H6H_100	2A	87.5	0.5	100	WEAK	17	14.7
4R17_PU2H6H_100	3F	87.5	0.5	100	WEAK	17	14.9
4R17_PU2H6H_100	3A	87.5	0.5	100	WEAK	17	27.7
2R07_PU2H6_100	2F	75.0	0.5	100	WEAK	7	25.1
2R07_PU2H6_100	2A	75.0	0.5	100	WEAK	7	10.8
2R07_PU2H6_100	3F	75.0	0.5	100	WEAK	7	16.1
2R07_PU2H6_100	3A	75.0	0.5	100	WEAK	7	8.0
2R12_PU2H6_100	2F	75.0	0.5	100	WEAK	12	38.1
2R12_PU2H6_100	2A	75.0	0.5	100	WEAK	12	12.5
2R12_PU2H6_100	3F	75.0	0.5	100	WEAK	12	25.8
2R12_PU2H6_100	3A	75.0	0.5	100	WEAK	12	9.7
2R17_PU2H6_100	2F	75.0	0.5	100	WEAK	17	40.4
2R17_PU2H6_100	2A	75.0	0.5	100	WEAK	17	18.1
2R17_PU2H6_100	3F	75.0	0.5	100	WEAK	17	27.5
2R17_PU2H6_100	3A	75.0	0.5	100	WEAK	17	7.9

Table 3 (cont.)

3R07_PU2H6_100	2F	50.0	0.5	100	WEAK	7	22.0
3R07_PU2H6_100	2A	50.0	0.5	100	WEAK	7	11.2
3R07_PU2H6_100	3F	50.0	0.5	100	WEAK	7	12.6
3R07_PU2H6_100	3A	50.0	0.5	100	WEAK	7	7.8
3R12_PU2H6_100	2F	50.0	0.5	100	WEAK	12	30.6
3R12_PU2H6_100	2A	50.0	0.5	100	WEAK	12	15.6
3R12_PU2H6_100	3F	50.0	0.5	100	WEAK	12	19.8
3R12_PU2H6_100	3A	50.0	0.5	100	WEAK	12	10.2
3R17_PU2H6_100	2F	50.0	0.5	100	WEAK	17	40.8
3R17_PU2H6_100	2A	50.0	0.5	100	WEAK	17	15.7
3R17_PU2H6_100	3F	50.0	0.5	100	WEAK	17	29.5
3R17_PU2H6_100	3A	50.0	0.5	100	WEAK	17	11.4
5R07_PU2H6H_100	2F	25.0	0.5	100	WEAK	7	15.1
5R07_PU2H6H_100	2A	25.0	0.5	100	WEAK	7	9.6
5R07_PU2H6H_100	3F	25.0	0.5	100	WEAK	7	12.1
5R07_PU2H6H_100	3A	25.0	0.5	100	WEAK	7	4.2
5R012_PU2H6H_100	2F	25.0	0.5	100	WEAK	12	20.9
5R012_PU2H6H_100	2A	25.0	0.5	100	WEAK	12	7.9
5R012_PU2H6H_100	3F	25.0	0.5	100	WEAK	12	10.5
5R012_PU2H6H_100	3A	25.0	0.5	100	WEAK	12	5.6
5R017_PU2H6H_100	2F	25.0	0.5	100	WEAK	17	23.4
5R017_PU2H6H_100	2A	25.0	0.5	100	WEAK	17	12.9
5R017_PU2H6H_100	3F	25.0	0.5	100	WEAK	17	14.3
5R017_PU2H6H_100	3A	25.0	0.5	100	WEAK	17	6.5
OR07_PU2H6H_100	2F	0.00	0.5	100	WEAK	7	7.6
OR07_PU2H6H_100	2A	0.00	0.5	100	WEAK	7	0.0
OR07_PU2H6H_100	3F	0.00	0.5	100	WEAK	7	7.6
OR07_PU2H6H_100	3A	0.00	0.5	100	WEAK	7	0.0

Table 3 (cont.)

4R07_PU2H6H_200	2F	87.5	0.5	200	WEAK	7	40.8
4R07_PU2H6H_200	2A	87.5	0.5	200	WEAK	7	12.7
4R07_PU2H6H_200	3F	87.5	0.5	200	WEAK	7	24.4
4R07_PU2H6H_200	3A	87.5	0.5	200	WEAK	7	15.4
4R012_PU2H6H_200	2F	87.5	0.5	200	WEAK	12	40.2
4R012_PU2H6H_200	2A	87.5	0.5	200	WEAK	12	21.3
4R012_PU2H6H_200	3F	87.5	0.5	200	WEAK	12	23.1
4R012_PU2H6H_200	3A	87.5	0.5	200	WEAK	12	16.1
4R017_PU2H6H_200	2F	87.5	0.5	200	WEAK	17	47.3
4R017_PU2H6H_200	2A	87.5	0.5	200	WEAK	17	21.8
4R017_PU2H6H_200	3F	87.5	0.5	200	WEAK	17	29.0
4R017_PU2H6H_200	3A	87.5	0.5	200	WEAK	17	20.5
2R07_PU2H6H_200	2F	75.0	0.5	200	WEAK	7	42.4
2R07_PU2H6H_200	2A	75.0	0.5	200	WEAK	7	20.7
2R07_PU2H6H_200	3F	75.0	0.5	200	WEAK	7	24.9
2R07_PU2H6H_200	3A	75.0	0.5	200	WEAK	7	15.8
2R12_PU2H6H_200	2F	75.0	0.5	200	WEAK	12	44.7
2R12_PU2H6H_200	2A	75.0	0.5	200	WEAK	12	31.0
2R12_PU2H6H_200	3F	75.0	0.5	200	WEAK	12	24.3
2R12_PU2H6H_200	3A	75.0	0.5	200	WEAK	12	21.3
2R17_PU2H6H_200	2F	75.0	0.5	200	WEAK	17	47.0
2R17_PU2H6H_200	2A	75.0	0.5	200	WEAK	17	37.1
2R17_PU2H6H_200	3F	75.0	0.5	200	WEAK	17	27.4
2R17_PU2H6H_200	3A	75.0	0.5	200	WEAK	17	23.5
3R07_PU2H6H_200	2F	50.0	0.5	200	WEAK	7	43.1
3R07_PU2H6H_200	2A	50.0	0.5	200	WEAK	7	20.6
3R07_PU2H6H_200	3F	50.0	0.5	200	WEAK	7	29.4
3R07_PU2H6H_200	3A	50.0	0.5	200	WEAK	7	23.2
3R12_PU2H6H_200	2F	50.0	0.5	200	WEAK	12	42.4
3R12_PU2H6H_200	2A	50.0	0.5	200	WEAK	12	23.9
3R12_PU2H6H_200	3F	50.0	0.5	200	WEAK	12	27.8
3R12_PU2H6H_200	3A	50.0	0.5	200	WEAK	12	18.3
3R17_PU2H6H_200	2F	50.0	0.5	200	WEAK	17	43.1
3R17_PU2H6H_200	2A	50.0	0.5	200	WEAK	17	29.7
3R17_PU2H6H_200	3F	50.0	0.5	200	WEAK	17	24.5
3R17_PU2H6H_200	3A	50.0	0.5	200	WEAK	17	22.3

Table 3 (cont.)

5R07_PU2H6H_200	2F	25.0	0.5	200	WEAK	7	41.7
5R07_PU2H6H_200	2A	25.0	0.5	200	WEAK	7	12.2
5R07_PU2H6H_200	3F	25.0	0.5	200	WEAK	7	26.4
5R07_PU2H6H_200	3A	25.0	0.5	200	WEAK	7	22.9
5R12_PU2H6H_200	2F	25.0	0.5	200	WEAK	12	42.4
5R12_PU2H6H_200	2A	25.0	0.5	200	WEAK	12	15.0
5R12_PU2H6H_200	3F	25.0	0.5	200	WEAK	12	27.6
5R12_PU2H6H_200	3A	25.0	0.5	200	WEAK	12	22.8
5R17_PU2H6H_200	2F	25.0	0.5	200	WEAK	17	43.1
5R17_PU2H6H_200	2A	25.0	0.5	200	WEAK	17	19.2
5R17_PU2H6H_200	3F	25.0	0.5	200	WEAK	17	27.4
5R17_PU2H6H_200	3A	25.0	0.5	200	WEAK	17	17.0
OR07_PU2H6H_200	2F	0.00	0.5	200	WEAK	7	42.6
OR07_PU2H6H_200	2A	0.00	0.5	200	WEAK	7	18.0
OR07_PU2H6H_200	3F	0.00	0.5	200	WEAK	7	28.6
OR07_PU2H6H_200	3A	0.00	0.5	200	WEAK	7	16.1
23_WP_3RO_255	2F	50.0	0.5	255	WEAK	0	42.0
23_WP_3RO_255	2A	50.0	0.5	255	WEAK	0	9.0
23_WP_3RO_255	3F	50.0	0.5	255	WEAK	0	28.0
23_WP_3RO_255	3A	50.0	0.5	255	WEAK	0	15.0
45_WP_3RO_330	4F	50.0	0.5	330	WEAK	0	36.0
45_WP_3RO_330	4A	50.0	0.5	330	WEAK	0	29.0
45_WP_3RO_330	5F	50.0	0.5	330	WEAK	0	32.0
45_WP_3RO_330	5A	50.0	0.5	330	WEAK	0	25.0
45_WP_3RO_255	4F	50.0	0.5	255	WEAK	0	32.0
45_WP_3RO_255	4A	50.0	0.5	255	WEAK	0	24.0
45_WP_3RO_255	5F	50.0	0.5	255	WEAK	0	20.0
45_WP_3RO_255	5A	50.0	0.5	255	WEAK	0	10.0
45_WP_3RO_200	4F	50.0	0.5	200	WEAK	0	36.0
45_WP_3RO_200	4A	50.0	0.5	200	WEAK	0	13.0
45_WP_3RO_200	5F	50.0	0.5	200	WEAK	0	29.0
45_WP_3RO_200	5A	50.0	0.5	200	WEAK	0	13.0

Table 3 (cont.)

45_WP_3R0_255	4F	50.0	0.5	255	WEAK	0	32.0
45_WP_3R0_255	4A	50.0	0.5	255	WEAK	0	12.0
45_WP_3R0_255	5F	50.0	0.5	255	WEAK	0	24.0
45_WP_3R0_255	5A	50.0	0.5	255	WEAK	0	10.0
23_SP_4R17_100	2F	87.5	0.5	100	STRONG	17	17.0
23_SP_4R17_100	2A	87.5	0.5	100	STRONG	17	1.0
23_SP_4R17_100	3F	87.5	0.5	100	STRONG	17	14.0
23_SP_4R17_100	3A	87.5	0.5	100	STRONG	17	1.0
23_SP_2R17_100	2F	75.5	0.5	100	STRONG	17	15.0
23_SP_2R17_100	2A	75.5	0.5	100	STRONG	17	1.0
23_SP_2R17_100	3F	75.5	0.5	100	STRONG	17	11.0
23_SP_2R17_100	3A	75.5	0.5	100	STRONG	17	1.0
T23_SP_4R12_200	2F	87.5	0.75	200	STRONG	12	33.0
T23_SP_4R12_200	2A	87.5	0.75	200	STRONG	12	20.0
T23_SP_4R12_200	3F	87.5	0.75	200	STRONG	12	19.0
T23_SP_4R12_200	3A	87.5	0.75	200	STRONG	12	12.0
T23_SP_2R17_200	2F	75.5	0.75	200	STRONG	17	31.0
T23_SP_2R17_200	2A	75.5	0.75	200	STRONG	17	11.0
T23_SP_2R17_200	3F	75.5	0.75	200	STRONG	17	25.0
T23_SP_2R17_200	3A	75.5	0.75	200	STRONG	17	2.0
T23_SP_2R12_200	2F	75.0	0.75	200	STRONG	12	33.0
T23_SP_2R12_200	2F	75.0	0.75	200	STRONG	12	16.0
T23_SP_2R12_200	2F	75.0	0.75	200	STRONG	12	17.0
T23_SP_2R12_200	2F	75.0	0.75	200	STRONG	12	11.0
T45_SP_2R17_200	4F	75.0	0.75	200	STRONG	17	25.0
T45_SP_2R17_200	4A	75.0	0.75	200	STRONG	17	13.0
T45_SP_2R17_200	5F	75.0	0.75	200	STRONG	17	26.0
T45_SP_2R17_200	5A	75.0	0.75	200	STRONG	17	13.0

Table 3 (cont.)

T23_SP_3R17_200	2F	50.0	0.75	200	STRONG	17	25.0
T23_SP_3R17_200	2A	50.0	0.75	200	STRONG	17	16.0
T23_SP_3R17_200	3F	50.0	0.75	200	STRONG	17	17.0
T23_SP_3R17_200	3A	50.0	0.75	200	STRONG	17	11.0
T23_WP_3RO_200	2F	50.0	0.75	200	WEAK	0	53.0
T23_WP_3RO_200	2A	50.0	0.75	200	WEAK	0	27.0
T23_WP_3RO_200	3F	50.0	0.75	200	WEAK	0	31.0
T23_WP_3RO_200	3A	50.0	0.75	200	WEAK	0	23.0
T45_WP_3RO_200	4F	50.0	0.75	200	WEAK	0	35.0
T45_WP_3RO_200	4A	50.0	0.75	200	WEAK	0	17.0
T45_WP_3RO_200	5F	50.0	0.75	200	WEAK	0	27.0
T45_WP_3RO_200	5A	50.0	0.75	200	WEAK	0	19.0
T23_WP_3RO_255	2F	50.0	0.75	255	WEAK	0	50.0
T23_WP_3RO_255	2A	50.0	0.75	255	WEAK	0	45.0
T23_WP_3RO_255	3F	50.0	0.75	255	WEAK	0	27.0
T23_WP_3RO_255	3A	50.0	0.75	255	WEAK	0	28.0
T45_WP_3RO_255	4F	50.0	0.75	255	WEAK	0	33.0
T45_WP_3RO_255	4A	50.0	0.75	255	WEAK	0	33.0
T45_WP_3RO_255	5F	50.0	0.75	255	WEAK	0	27.0
T45_WP_3RO_255	5A	50.0	0.75	255	WEAK	0	25.0
T23_WP_3RO_330	2F	50.0	0.75	330	WEAK	0	56.0
T23_WP_3RO_330	2A	50.0	0.75	330	WEAK	0	28.0
T23_WP_3RO_330	3F	50.0	0.75	330	WEAK	0	25.0
T23_WP_3RO_330	3A	50.0	0.75	330	WEAK	0	4.0
T45_WP_3RO_330	4F	50.0	0.75	330	WEAK	0	35.0
T45_WP_3RO_330	4A	50.0	0.75	330	WEAK	0	11.0
T45_WP_3RO_330	5F	50.0	0.75	330	WEAK	0	26.0
T45_WP_3RO_330	5A	50.0	0.75	330	WEAK	0	13.0
T23_WP_4R12_200	2F	87.5	0.75	200	WEAK	12	51.0
T23_WP_4R12_200	2A	87.5	0.75	200	WEAK	12	35.0
T23_WP_4R12_200	3F	87.5	0.75	200	WEAK	12	22.0
T23_WP_4R12_200	3A	87.5	0.75	200	WEAK	12	13.0

Table 3 (cont.)

T23_WP_4R17_200	2F	87.5	0.75	200	WEAK	17	51.0
T23_WP_4R17_200	2A	87.5	0.75	200	WEAK	17	15.0
T23_WP_4R17_200	3F	87.5	0.75	200	WEAK	17	27.0
T23_WP_4R17_200	3A	87.5	0.75	200	WEAK	17	00.0
T45_WP_4R17_200	4F	87.5	0.75	200	WEAK	17	37.0
T45_WP_4R17_200	4A	87.5	0.75	200	WEAK	17	13.0
T45_WP_4R17_200	5F	87.5	0.75	200	WEAK	17	38.0
T45_WP_4R17_200	5A	87.5	0.75	200	WEAK	17	11.0
T45_WP_2R17_200	4F	75.0	0.75	200	WEAK	17	36.0
T45_WP_2R17_200	4A	75.0	0.75	200	WEAK	17	13.0
T45_WP_2R17_200	5F	75.0	0.75	200	WEAK	17	33.0
T45_WP_2R17_200	5A	75.0	0.75	200	WEAK	17	20.0
T23_WP_R17_200	2F	0.00	0.75	200	WEAK	17	51.0
T23_WP_R17_200	2A	0.00	0.75	200	WEAK	17	27.0
T23_WP_R17_200	3F	0.00	0.75	200	WEAK	17	27.0
T23_WP_R17_200	3A	0.00	0.75	200	WEAK	17	21.0
T23_WP_R17_100	2F	0.00	0.75	100	WEAK	17	9.0
T23_WP_R17_100	2A	0.00	0.75	100	WEAK	17	3.0
T23_WP_R17_100	3F	0.00	0.75	100	WEAK	17	8.0
T23_WP_R17_100	3A	0.00	0.75	100	WEAK	17	2.0

Table 3 (cont.)

For Impacts from 87.5% - 100% of the Distance from Fragment Center to Fragment Tip (Tip Cases)							
DATA SET NAME	STACK LOCATION/ FWD-AFT LOCATION	DISTANCE FROM FRAGMENT CENTER	FRAGMENT THICKNESS	IMPACT VELOCITY	FUEL TYPE	ROTATION RATE	DISTORTION
		%	INS	M/S		HZ	%
R07_PU2H6H_100	2F	100.0	0.5	100	WEAK	7	16.3
R07_PU2H6H_100	2A	100.0	0.5	100	WEAK	7	9.4
R07_PU2H6H_100	3F	100.0	0.5	100	WEAK	7	20.0
R07_PU2H6H_100	3A	100.0	0.5	100	WEAK	7	6.3
R12_PU2H6H_100	2F	100.0	0.5	100	WEAK	12	22.0
R12_PU2H6H_100	2A	100.0	0.5	100	WEAK	12	12.7
R12_PU2H6H_100	3F	100.0	0.5	100	WEAK	12	37.8
R12_PU2H6H_100	3A	100.0	0.5	100	WEAK	12	16.0
R17_PU2H6H_100	2F	100.0	0.5	100	WEAK	17	42.6
R17_PU2H6H_100	2A	100.0	0.5	100	WEAK	17	13.9
R17_PU2H6H_100	3F	100.0	0.5	100	WEAK	17	41.1
R17_PU2H6H_100	3A	100.0	0.5	100	WEAK	17	23.3
R07_PU2H6_200	2F	100.0	0.5	200	WEAK	7	43.5
R07_PU2H6_200	2A	100.0	0.5	200	WEAK	7	12.9
R07_PU2H6_200	3F	100.0	0.5	200	WEAK	7	40.6
R07_PU2H6_200	3A	100.0	0.5	200	WEAK	7	20.6
R12_PU2H6_200	2F	100.0	0.5	200	WEAK	12	52.5
R12_PU2H6_200	2A	100.0	0.5	200	WEAK	12	12.5
R12_PU2H6_200	3F	100.0	0.5	200	WEAK	12	38.4
R12_PU2H6_200	3A	100.0	0.5	200	WEAK	12	20.1
R17_PU2H6_200	2F	100.0	0.5	200	WEAK	17	56.0
R17_PU2H6_200	2A	100.0	0.5	200	WEAK	17	10.6
R17_PU2H6_200	3F	100.0	0.5	200	WEAK	17	38.8
R17_PU2H6_200	3A	100.0	0.5	200	WEAK	17	21.8



Table 3 (cont.)

45 WP R17 200	4F	100.0	0.5	200	WEAK	17	50.0
45 WP R17 200	4A	100.0	0.5	200	WEAK	17	33.0
45 WP R17 200	5F	100.0	0.5	200	WEAK	17	32.0
45 WP R17 200	5A	100.0	0.5	200	WEAK	17	18.0
45 WP R 150	4F	100.0	0.5	150	WEAK	0	16.1
45 WP R 150	4A	100.0	0.5	150	WEAK	0	6.2
45 WP R 150	5F	100.0	0.5	150	WEAK	0	12.9
45 WP R 150	5A	100.0	0.5	150	WEAK	0	7.7
45 WP R 250	4F	100.0	0.5	250	WEAK	0	44.2
45 WP R 250	4A	100.0	0.5	250	WEAK	0	20.0
45 WP R 250	5F	100.0	0.5	250	WEAK	0	27.3
45 WP R 250	5A	100.0	0.5	250	WEAK	0	16.1
45 WP R 300	4F	100.0	0.5	300	WEAK	0	44.2
45 WP R 300	4A	100.0	0.5	300	WEAK	0	30.4
45 WP R 300	5F	100.0	0.5	300	WEAK	0	21.8
45 WP R 300	5A	100.0	0.5	300	WEAK	0	21.7
45 WP R 350	4F	100.0	0.5	350	WEAK	0	44.2
45 WP R 350	4A	100.0	0.5	350	WEAK	0	31.6
45 WP R 350	5F	100.0	0.5	350	WEAK	0	34.6
45 WP R 350	5A	100.0	0.5	350	WEAK	0	18.3
T23 WP R17 200	2F	100.0	0.75	200	WEAK	17	87.0
T23 WP R17 200	2A	100.0	0.75	200	WEAK	17	17.0
T23 WP R17 200	3F	100.0	0.75	200	WEAK	17	46.0
T23 WP R17 200	3A	100.0	0.75	200	WEAK	17	00.0
T45 WP R17 200	4F	100.0	0.75	200	WEAK	17	47.0
T45 WP R17 200	4A	100.0	0.75	200	WEAK	17	11.0
T45 WP R17 200	5F	100.0	0.75	200	WEAK	17	38.0
T45 WP R17 200	5A	100.0	0.75	200	WEAK	17	00.0

Table 3 (cont.)

T23_WP_R17_100	2F	100.0	0.75	100	WEAK	17	57.0
T23_WP_R17_100	2A	100.0	0.75	100	WEAK	17	15.0
T23_WP_R17_100	3F	100.0	0.75	100	WEAK	17	29.0
T23_WP_R17_100	3A	100.0	0.75	100	WEAK	17	18.0
T23_WP_R_100	2F	100.0	0.75	100	WEAK	0	7.7
T23_WP_R_100	2A	100.0	0.75	100	WEAK	0	2.2
T23_WP_R_100	3F	100.0	0.75	100	WEAK	0	7.7
T23_WP_R_100	3A	100.0	0.75	100	WEAK	0	2.2
T23_WP_R_150	2F	100.0	0.75	150	WEAK	0	21.7
T23_WP_R_150	2A	100.0	0.75	150	WEAK	0	7.7
T23_WP_R_150	3F	100.0	0.75	150	WEAK	0	22.7
T23_WP_R_150	3A	100.0	0.75	150	WEAK	0	9.4
T23_SP_R07_200	2F	100.0	0.05	200	STRONG	7	15.0
T23_SP_R07_200	2A	100.0	0.05	200	STRONG	7	3.0
T23_SP_R07_200	3F	100.0	0.05	200	STRONG	7	21.0
T23_SP_R07_200	3A	100.0	0.05	200	STRONG	7	8.0
T23_SP_R17_200	2F	100.0	0.75	200	STRONG	17	92.0
T23_SP_R17_200	2A	100.0	0.75	200	STRONG	17	3.0
T23_SP_R17_200	3F	100.0	0.75	200	STRONG	17	27.0
T23_SP_R17_200	3A	100.0	0.75	200	STRONG	17	00.0
T45_SP_R17_200	4F	100.0	0.75	200	STRONG	17	30.0
T45_SP_R17_200	4A	100.0	0.75	200	STRONG	17	9.0
T45_SP_R17_200	5F	100.0	0.75	200	STRONG	17	27.0
T45_SP_R17_200	5A	100.0	0.75	200	STRONG	17	2.0

Table 4

SUMMARY OF PARAMETERS USED IN EQUATION (1) FOR NON-TIP CASES  
Impact with Fragment Inner Surface (0 to 87.5% of Radius)

Stacked Position	Forward Clad				Aft Clad			
	Dm	a	n	Sigma	Dm	a	n	Sigma
p1 = p2	43.5	1.08	2.40	2.0	27.5	0.46	2.04	
p3	27.1	1.08	2.40		21.3	0.46	2.04	
p4	34.0	1.08	2.40		29.0	0.46	2.04	
p5	26.2	1.08	2.44		25.0	0.46	2.04	

Table 5

SUMMARY OF PARAMETERS USED IN EQUATION (1) FOR TIP CASES  
Impact with Fragment Tip (87.5 to 100% of radius)

Stacked Position	Forward Clad				Aft Clad			
	Dm	a	n	Sigma	Dm	a	n	Sigma
p1 = p2	58.3	0.43	2.76		12.5	0.90	3.76	1.1
p3	39.4	0.43	2.76		21.4	0.21	4.29	1.2
p4	47.0	0.43	2.76	2.3	34.7	0.17	2.53	1.4
p5	32.0	0.43	2.76		19.1	0.50	2.23	1.7

Table 6

EFFECT OF BOUNDARY CONSTRAINTS, FUEL TYPE, AND VELOCITY ON  
THE FUELED CAPSULE DISTORTION RESULTING FROM SRB  
EDGE-ON IMPACTS ON THE ULYSSES RTG

Fuel Type	Boundary Constraint	Fragment Velocity	Fwd Capsule Distortion	Aft Capsule Distortion
		m/s	%	%
PU2H6H	NONE	100	121	14
PU2H6H	YVEL(Zero)	100	100	21
U6H11H(1)	YVEL(Zero)	100	64	5
PU2H6H	YVEL(Zero)	200	305	64

(1) Urania simulant case planned for test. Predictions for this case included for reference.

Table 7

FUELED CAPSULE DISTORTION RESULTING FROM THE IMPACT OF AN  
 INTACT GALILEO RTG ON THE STS-BAY DOORS<sup>(1)</sup> AT 365 M/S

Stacked Position	Distortion	
	Forward Capsule %	Aft Capsule %
2	9.3	0.0
3	6.1	0.0
4		
5		

(1) Areal Density = 3.96 lb/ft<sup>2</sup>

Table 8

FUELED CAPSULE DISTORTION RESULTING FROM BARE MODULE -  
STS-BAY DOOR(1) IMPACTS

Impact Velocity	Fwd Capsule Distortion	Aft Capsule Distortion
m/s	%	%
335	37.5	10
365	65.0	10

(1) Areal Density = 3.46 lb/ft<sup>2</sup>

Table 9

FUELED CAPSULE DISTORTION RESULTING FROM A BARE CLAD IMPACT  
ON THE STS-BAY DOOR(1) OF TWO VELOCITIES

Impact Velocity	Capsule Distortion
m/s	%
335	43
365	55

(1) Areal Density = 3.46 lb/ft<sup>2</sup>

Table 10

FUELED CAPSULE DISTORTION RESULTING FROM BARE GIS IMPACT  
ON CONCRETE AT TWO VELOCITIES

Impact Velocity	Capsule Distortion
m/s	%
63	51
70	58



Table 11

RTG END-ON IMPACTS ON CONCRETE AND WET SAND AT VARIOUS VELOCITIES

Target	Impact Velocity	Stack Position 2 Distortion	Stack Position 3 Distortion
	m/s	%	%
Concrete	55	36	39
Concrete	70	52	52
Concrete	85	74	67
Concrete	100	101	77
Concrete	120	123	102
Steel	120	130	109
Wet Sand	120	26	13

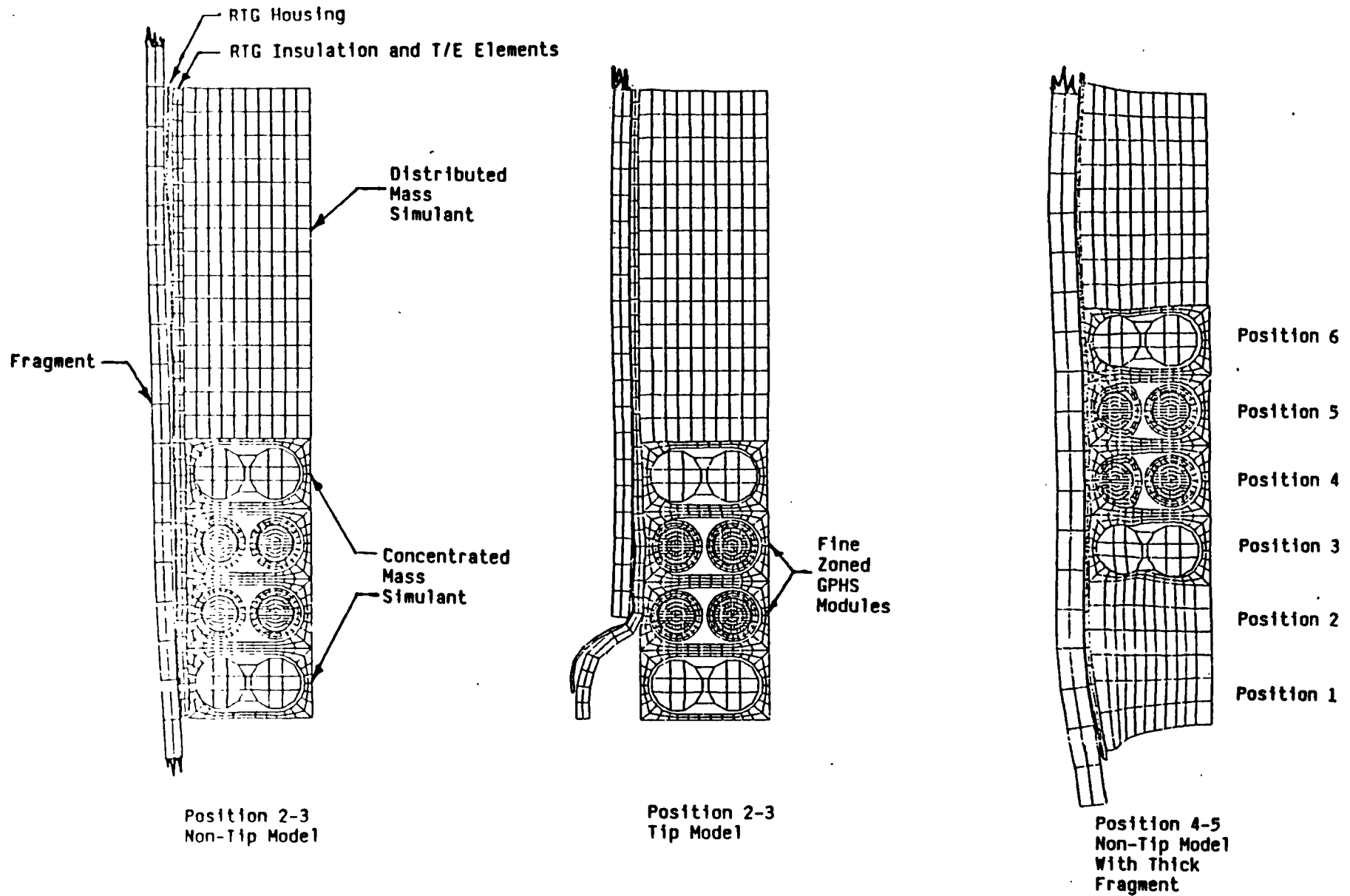


Figure 1: MODELS USED IN DEVELOPING THE SRM FRAGMENT DATA BASE

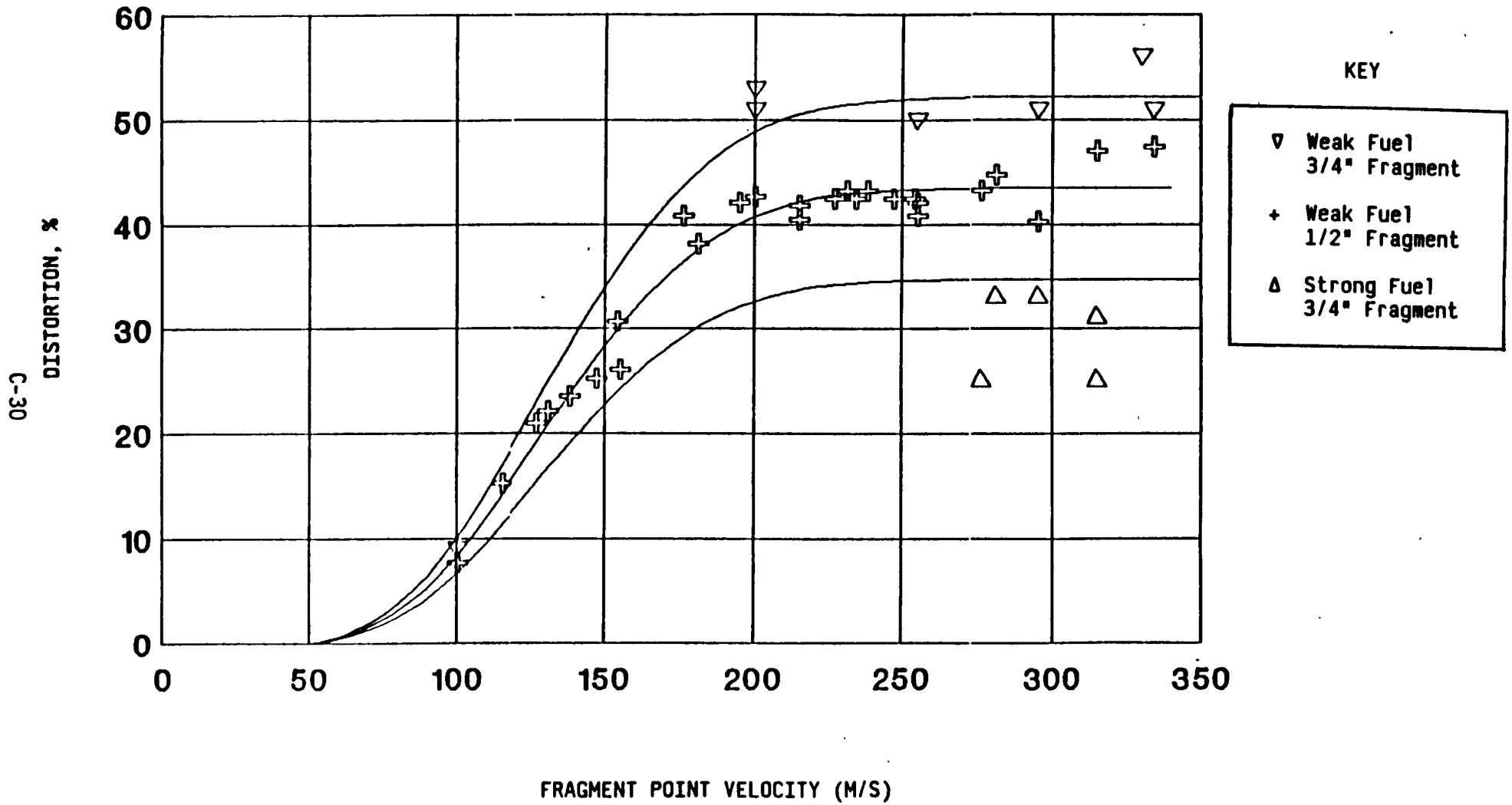
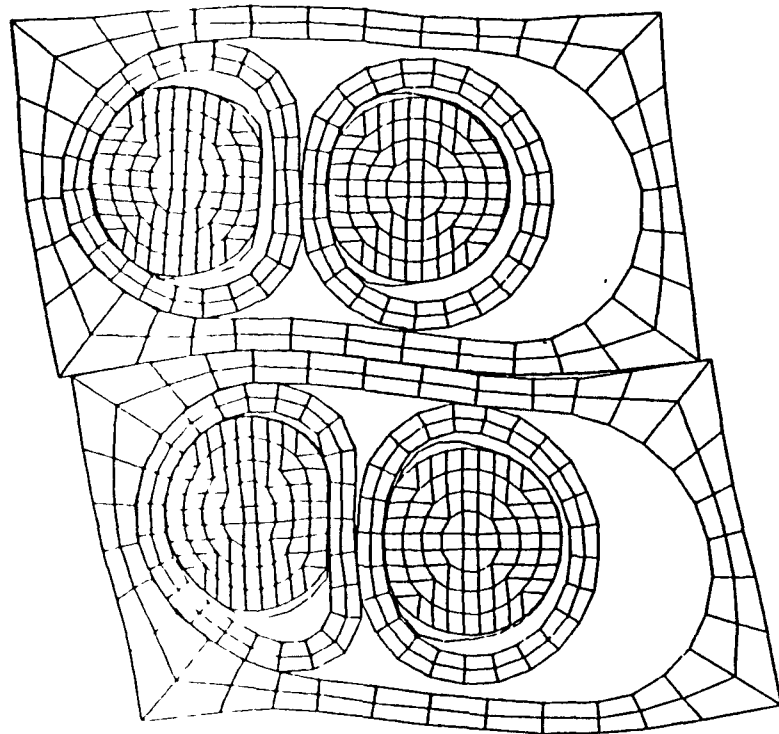
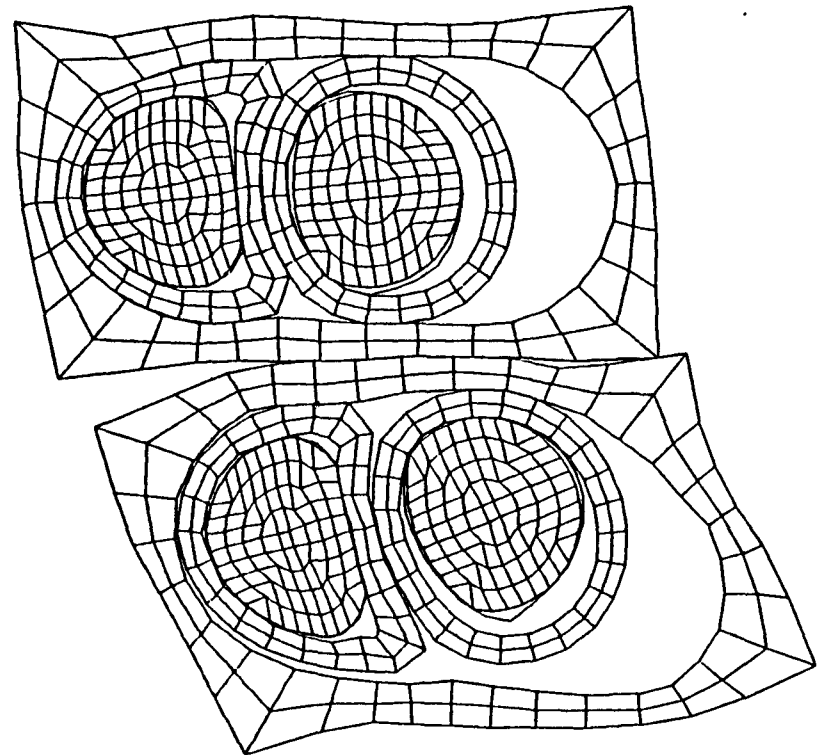


Figure 2. POSITION 2 AND 3 FUELED CLAD DISTORTION AS A FUNCTION OF FRAGMENT THICKNESS, VELOCITY AND PLUTONIA MECHANICAL PROPERTIES



Impact Velocity = 100 m/s



Impact Velocity = 200 m/s

NOTE: The diametrial growth of the capsules is limited by the aeroshell response and that little difference results from impacts at 100 and 200 m/s. These results appear consistent with the LFT results presented in Table 2.

Figure 3. GEOMETRY OF GPHS MODULES IN THE SECOND AND THIRD STACK POSITION AFTER THE IMPACT AT 100 AND 200 M/S OF A QUADRANT SIZED SRM FRAGMENT ON THE GALILEO RTG

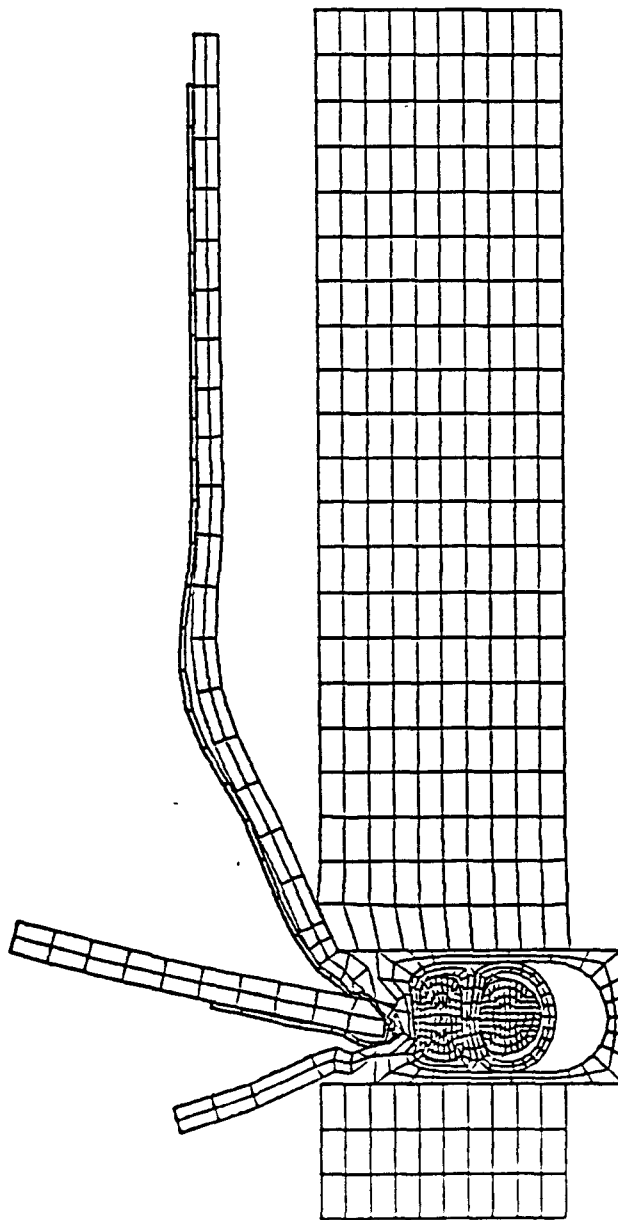
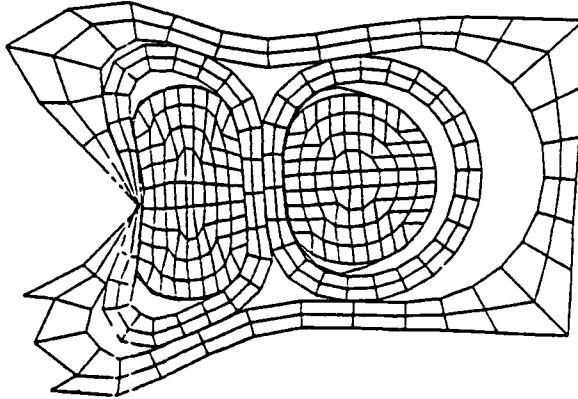
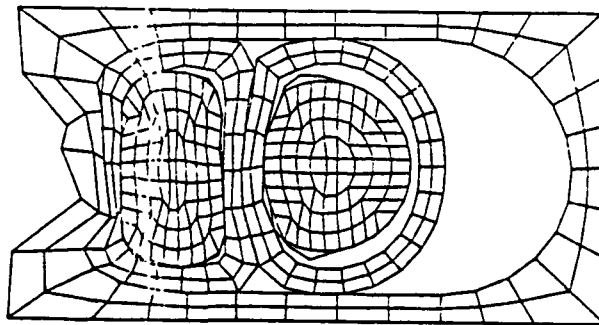


Figure 4. GEOMETRY RESULTING FROM A QUADRANT SIZED SRM FRAGMENT IMPACT ON A GPHS RTG IN A ULYSSES CONFIGURATION

No Y-Velocity Constraint  
Impact Velocity = 100 m/s



Y-Velocity = 0  
Impact Velocity = 100 m/s



Y-Velocity = 0  
Impact Velocity = 200 m/s

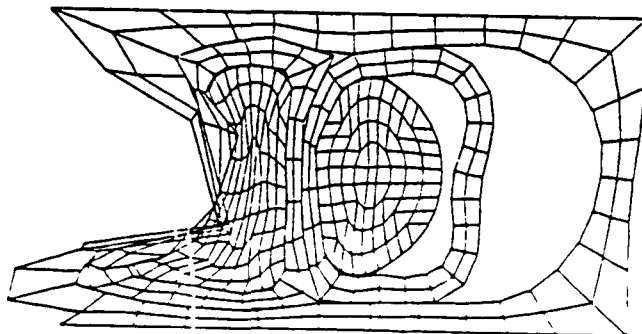


Figure 5. EFFECTS OF BOUNDARY CONSTRAINT AND VELOCITY ON THE FUELED CAPSULE POST-IMPACT GEOMETRY RESULTING FROM THE EDGE-ON IMPACT OF AN SRM FRAGMENT ON A ULYSSES RTG

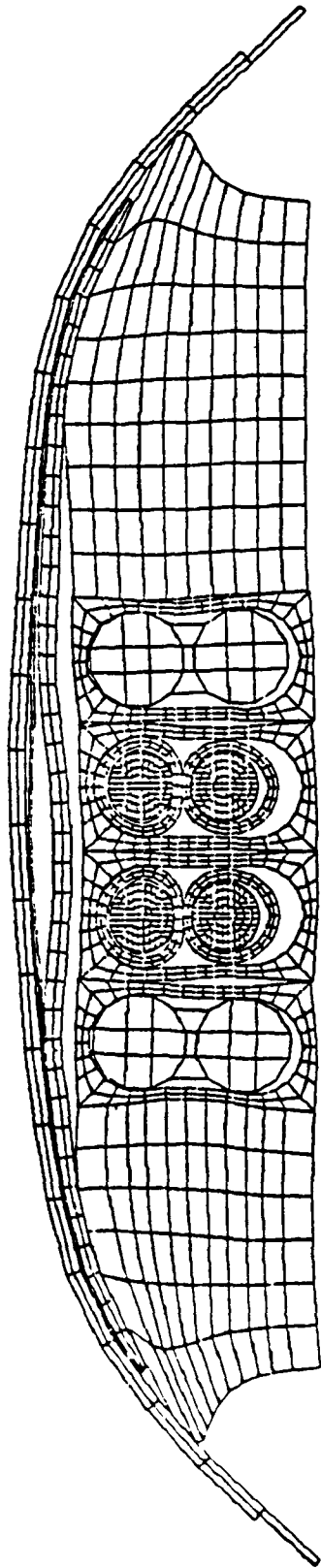


Figure 6. POST-IMPACT GEOMETRY OF THE GALILEO RTG AFTER IMPACT ON THE STS-BAY DOORS AT 365 M/S

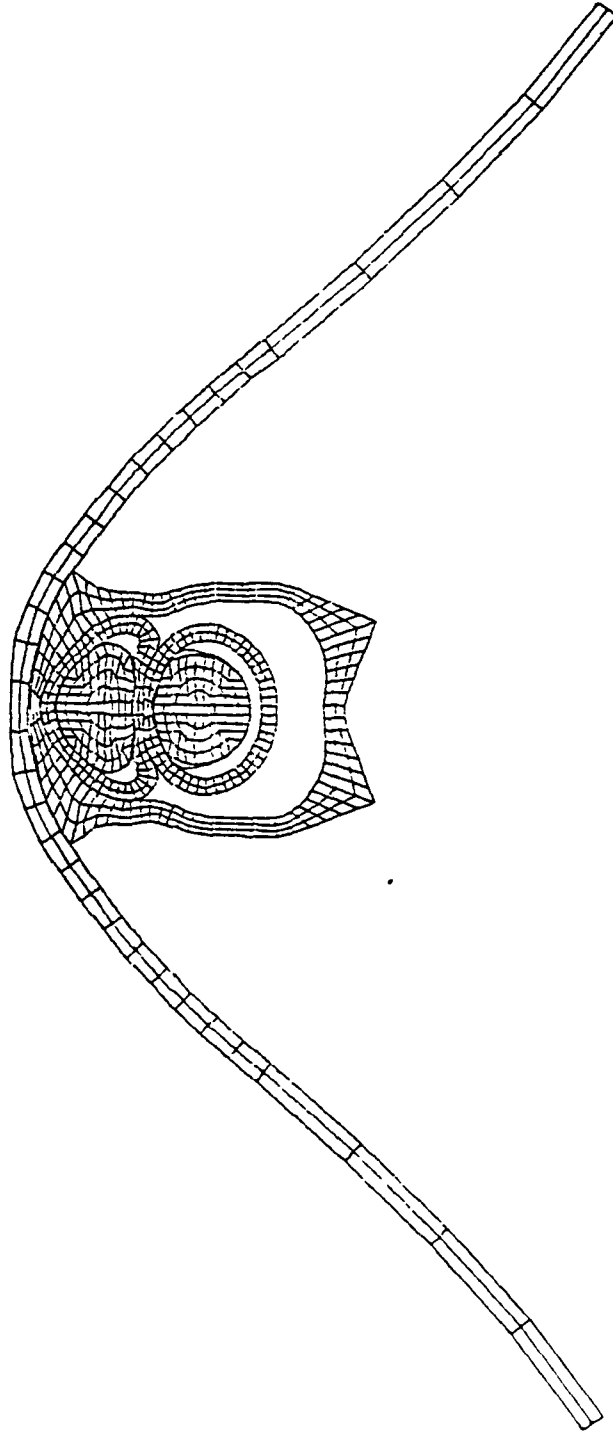
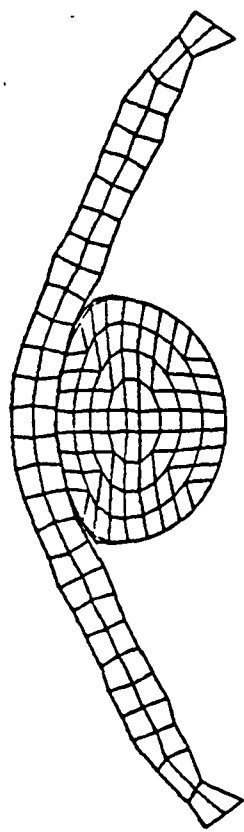
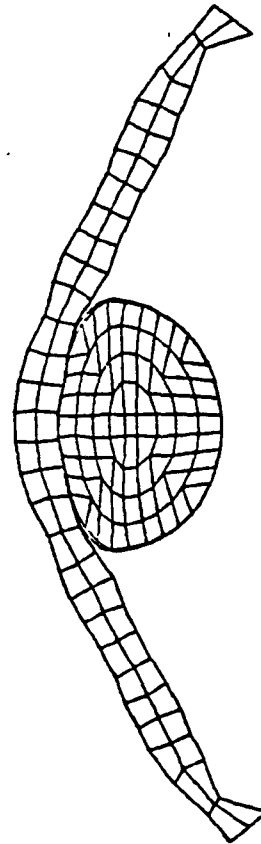


Figure 7. POST-IMPACT GEOMETRY OF A GPHS MODULE AFTER IMPACT ON THE STS-PAY DOORS AT 335 M/S





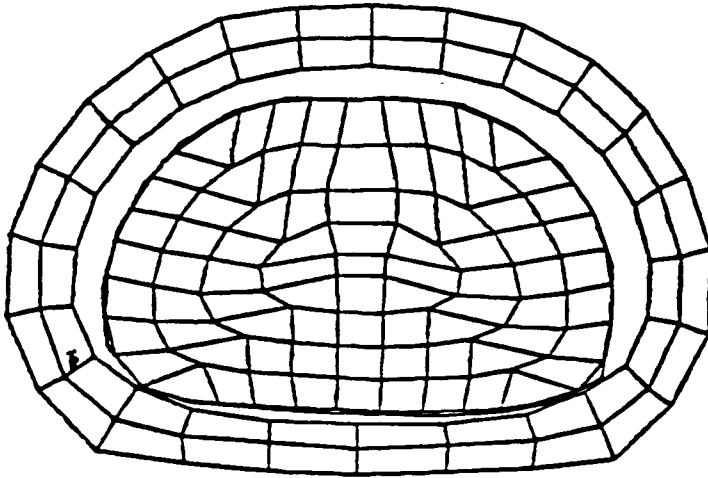
335 m/s



365 m/s

Figure 8. POST-IMPACT GEOMETRY OF A BARE GPHS FUELED CLAD AFTER IMPACT ON THE STS-BAY DOORS AT 335 and 365 M/S

Prediction for 70 m/s and PU2H6H Fuel



Prediction for 63 m/s and PU2H6H Simulant

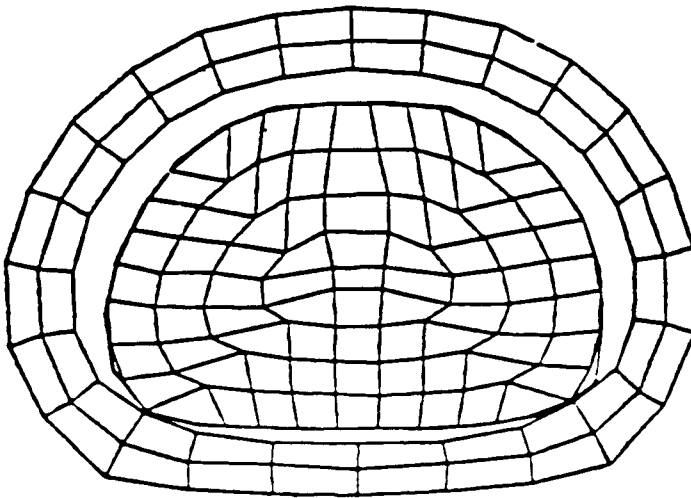


Figure 9. POST-IMPACT GEOMETRY OF A BARE GIS AFTER IMPACT ON A CONCRETE at 63 and 70 M/S

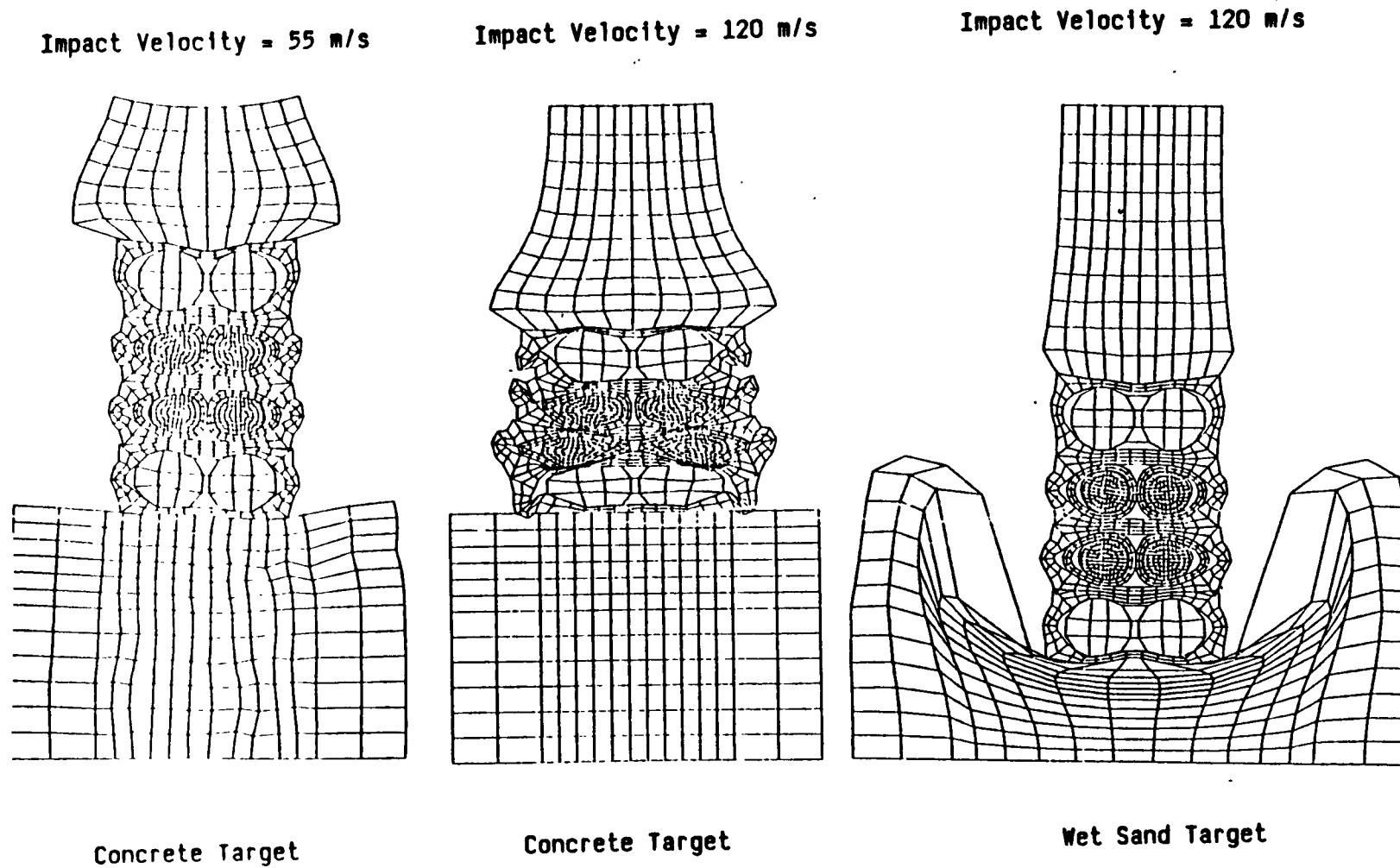


Figure 10. EFFECT OF IMPACT VELOCITY AND TARGET MATERIAL ON THE POST IMPACT GEOMETRY OF A GALILEO RTG UNDERGOING AN INTACT, END-ON IMPACT

APPENDIX D  
LAUNCH ACCIDENT SCENARIO EVALUATION PROGRAM (LASEP)

D.1 INTRODUCTION AND OVERVIEW

A major requirement of the Galileo Mission Final Safety Analysis Report (FSAR) is the evaluation of the response of the two Galileo RTGs (Radioisotope Thermoelectric Generators) to accident environments defined for specific launch phases of the mission. To accomplish this task, a comprehensive FORTRAN computer program termed LASEP2 was developed. The program title is an acronym representing Launch Accident Scenario Evaluation Program - Version 2. Specifically, the LASEP2 program analyzes the following five launch accident cases:

- Case 1. Tipover on Launch Pad - Tower Impact
- Case 2. ET (External Tank) Propellant Near Pad Explosions. This accident case encompasses the MLP (Mobile Launch Platform), in-trench, and aft compartment initiated pool explosion events.
- Case 3. ET Propellant In-Flight (Vapor Cloud) Explosion
- Case 4. SRB (Solid Rocket Booster) Random Failure
- Case 5. Range Destruct.

Each of these accidents is evaluated separately by the LASEP2 program. Table D-1 shows the time ranges for which the evaluations of these cases are applicable. For accident cases 4 and 5, which deal with the failure or destruct of a SRB, an ET propellant pool explosion accompanies the SRB accident in the early time range of 0 to 10 seconds. The scenarios for the accident cases and the corresponding environments are completely described in Reference [1], the Shuttle Data Book. The data bases provided by this document constitute a large portion of the inputs to the LASEP2 program.

In the LASEP2 program, a separate model of each accident case is developed which simulates the accident scenario. Figure D-1 provides a general overview of the analysis performed for the various accident cases. The analysis conducted for each accident case is comprehensive since it evaluates the response of the RTG from the initiation of the accident event, to the final

Table D-1. Launch Accident Cases Evaluated by the LASEP2 Program

Case	Accident	Time Range (sec. MET) (1)
1	Tipover on launch pad - Power Impact	0-2
2	ET Propellant Near Pad Explosions	0-10
3	ET Propellant In-Flight Explosion	10-30
4	SRB Random Failure (2)	0-120
5	Range Destruct (3) (4)	0-120

NOTES: (1) MET = Mission Elapsed Time

(2) For 0-10 sec. accident has combined SRB failure with ET propellant pool explosions.

(3) For 0-10 sec. accident is classified as inadvertent range destruct.

(4) For 0-10 sec. inadvertent range destruct is combined with ET propellant pool explosions.

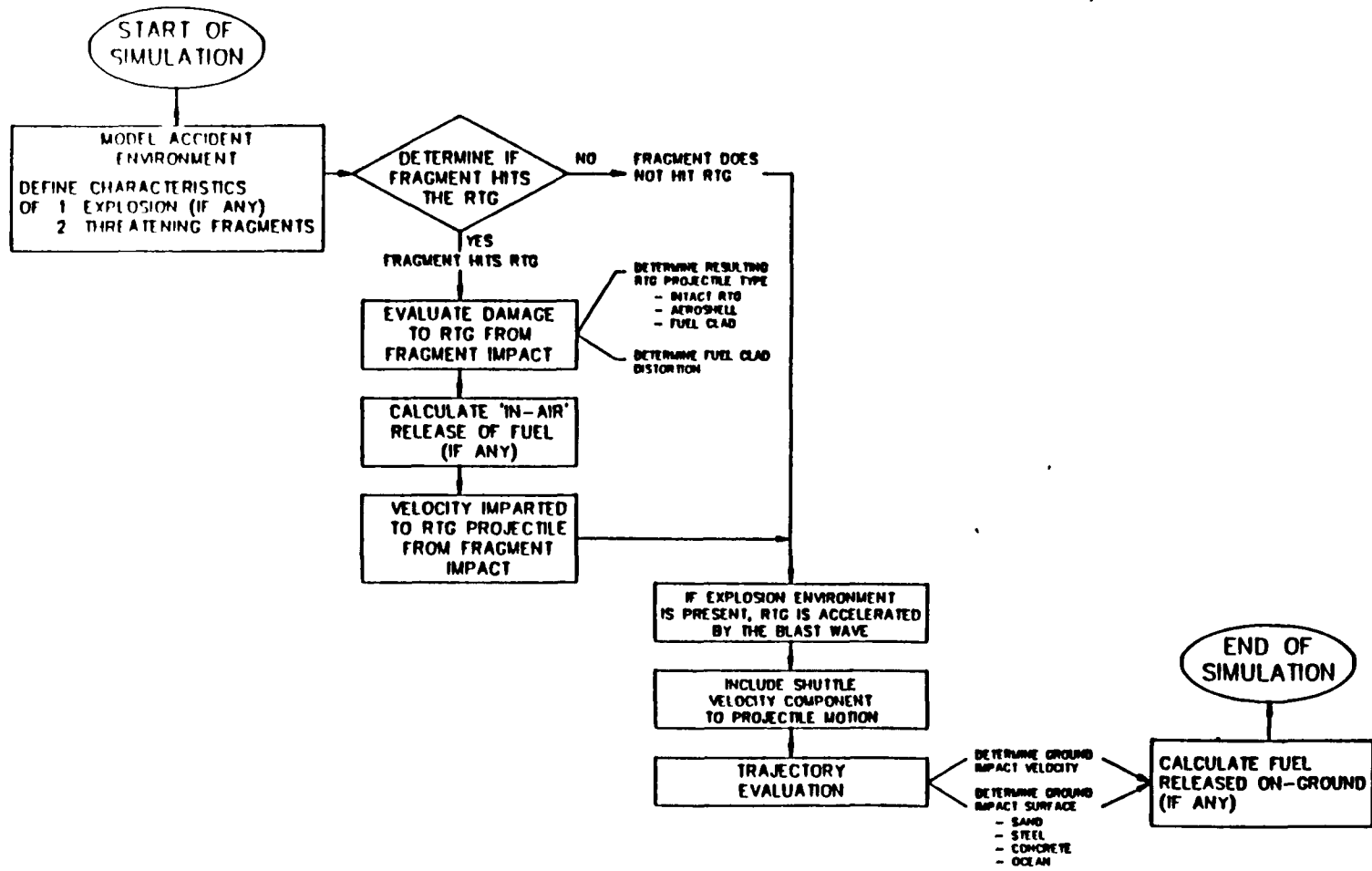


Figure D-1 Overview of the Analysis Performed For the Accident Scenarios

impact of the RTG or RTG components on the Earth's surface. As shown in Figure D-1 each accident simulation involves the following elements:

1. Modeling of the accident environment
2. Determination if the RTG is hit by a fragment
3. Damage evaluation of the RTG if it is hit by a fragment
4. Calculation of in-air fuel release, if any
5. Trajectory Analysis of RTG or RTG components
6. Calculation of the fuel released on-ground, if any.

When an RTG is impacted by a fragment, it is possible, depending on the severity of the impact, for the RTG to be separated into its individual components. Also, as a result of this impact, the fueled clads within the RTG may become distorted and maybe breached, allowing the release of fuel. The terminology used to describe the post fragment impact status of the RTG is RTG projectile. In the LASEP2 program three categories of RTG projectile are evaluated:

1. Intact RTG - The RTG case is not failed by fragment impact, all 18 modules remain inside the RTG shell.
2. Aeroshell - The RTG shell is failed, aeroshells are released. Each aeroshells contains 4 fueled clads.
3. Fuel clads - The RTG and aeroshells are failed, individual fueled clads are released by the impact.

As part of the damage evaluation process, both the RTG projectile status and fueled clad distortion are determined. The specification of RTG projectile type is required to properly assign the ballistic characteristics to the projectile for the trajectory analysis. The determination of fueled clad distortion is required, since this parameter is used to determine if any fuel is released and the amount of fuel released.

As indicated on Figure D-1, the LASEP2 program calculates fuel releases in two separate classifications:

1. In-air release
2. On-ground release.

The in-air release is caused by fragment impact, and refers to the fact that the RTG is above zero ground elevation at the time of impact. The on-ground release is caused by impact of an RTG projectile on the ground or ground structure such as the tower or rotating service structure. As part of the process to calculate the fuel released on-ground, the velocity of impact and the type of surface impacted are determined. Four categories of ground impact surface are assigned to the launch pad area:

1. Sand
2. Steel
3. Concrete
4. Ocean.

REPRODUCED FROM  
BEST AVAILABLE COPY

A Monte Carlo sampling technique is used by the LASEP2 program to numerically determine the outcome of each accident case. Output results from the LASEP2 program are provided on a statistical basis. In the reference frame of a Monte Carlo analysis, each simulation of an accident case is regarded as a single trial. Within each simulation there is a set of random selections which are related to the sequence of events that occur during the accident scenario. Generally, the majority of the random selections are associated with choosing values from distributions or ranges of input data. These selections are used to describe the severity and characteristics of the accident environment. A random number, generated within the LASEP2 program, is used as the device to select the outcome of each random process. The end result of a single trial or simulation is directly related to the random values selected throughout the evaluation process. The final outcome of an accident case is determined by performing a large number of individual trials and statistically combining the results from these trials.

In applying the Monte Carlo method to determine the outcome of an accident case, a sufficiently large number of trials must be run in order to provide statistically meaningful results. In addition to this criteria, care must be taken in each random process to ensure that:



1. The proper dependency of the randomly selected parameters describing the accident environment is maintained (i.e., The selection of dependent variable values from input data is based on the same random number, whereas independent parameters are determined using separate random numbers).
2. The distribution type from which the random sampling variable is produced must correspond to the distribution type of input data to which it is applied (i.e., If input data is provided on the basis of a uniform distribution, then the random sampling variable used to extract a value from this input data must also be from a uniform distribution).

The principal input data to the LASEP2 program falls into two categories:

1. Inputs provided by the Shuttle Data Book describing the environments for the various accident cases. Basically, these inputs describe explosion characteristics such as overpressure and impulse and fragment environment details such as velocity and direction.
2. A database of hydrocode impact analysis results which are used to determine the distortion of a fueled clad resulting from a fragment impact. These impact analyses are based on results from the safety test program.

The second category of input data represents the compilation of an extensive set of hydrocode impact studies which have been performed by FSC (Fairchild Space Company). The results of these studies are used to determine fuel clad distortion over a wide range of fragment insults. The distortion data provided in the database have been calibrated to test results from the various safety tests performed by Los Alamos such as the Large Fragment Tests (LFT-1, 2) (see Appendix G, Section G.5).

The primary outputs of the LASEP2 program for each accident case which results in fuel releases are:

1. The average mass of fuel released in-air and the corresponding mass released and average particle size distributions.
2. The average mass of fuel released on-ground and the corresponding mass released and average particle size distributions.

In addition to these outputs the LASEP2 program also provides a probabilistic breakdown of ground impact velocity and surface for each RTG projectile type. The complete set of LASEP2 output predicts the quantity and characteristics of any fuel released for a particular accident case and the probability of getting these releases. These fuel released statistics are used to perform subsequent source term and risk analyses. The statistical results which are generated directly by the LASEP2 program represent only the conditional probabilities of an accident outcome. To calculate the actual probability of an accident outcome, the results of the LASEP2 program must be combined with the accident event probability.

The majority of the analysis contained within the LASEP2 code, which has been developed for the Galileo mission, can be adapted to evaluate the Ulysses mission. However, modifications will be required primarily due to the spacecraft and RTG mounting configuration differences.

A complete description of the analysis performed by the LASEP2 program is provided in Section 2. The description includes details in the following areas:

1. Analysis assumptions
2. Random sampling processes
3. Application of input data
4. Generation of output results

A brief discussion on the verification of the program is provided in Section 3.

## D.2 DESCRIPTION OF LASEP2 PROGRAM ANALYSIS

The five accident cases evaluated by the LASEP2 program can be separated into two distinct accident environments:

1. ET Propellant Explosion Environment
2. SRB Fragment Environments.

The ET propellant environment includes the accident cases of:

1. Tipover on Launch Pad - Tower Impact
2. ET Propellant Near Pad Explosions (MLP, In-Trench, Aft Compartment Initiated Pool Explosions)
3. ET Propellant In-Flight (Vapor Cloud) Explosion.

The SRB Fragment Environment includes the accident cases of:

1. SRB Random Failure
2. Range Destruct.

Within each of these accident environments, the analysis performed on the individual accident cases is very similar. A description of the LASEP2 program analysis is therefore provided by reviewing the evaluation process of each accident environment. Figure D-2 shows an outline of the evaluation process for both accident environments. For each accident environment, the evaluation process displayed represents a single simulation or trial. The primary inputs to the LASEP2 program and the area of application are also provided on this figure. Each of the principal steps in the evaluation process is supplied with a sequence number. These sequence numbers are used to identify the subsection which describes the analysis performed in each step. As shown in Figure D-2 both accident environment evaluations share common trajectory and ground impact analysis functions. A complete description of each environment evaluation is provided in the following subsections.

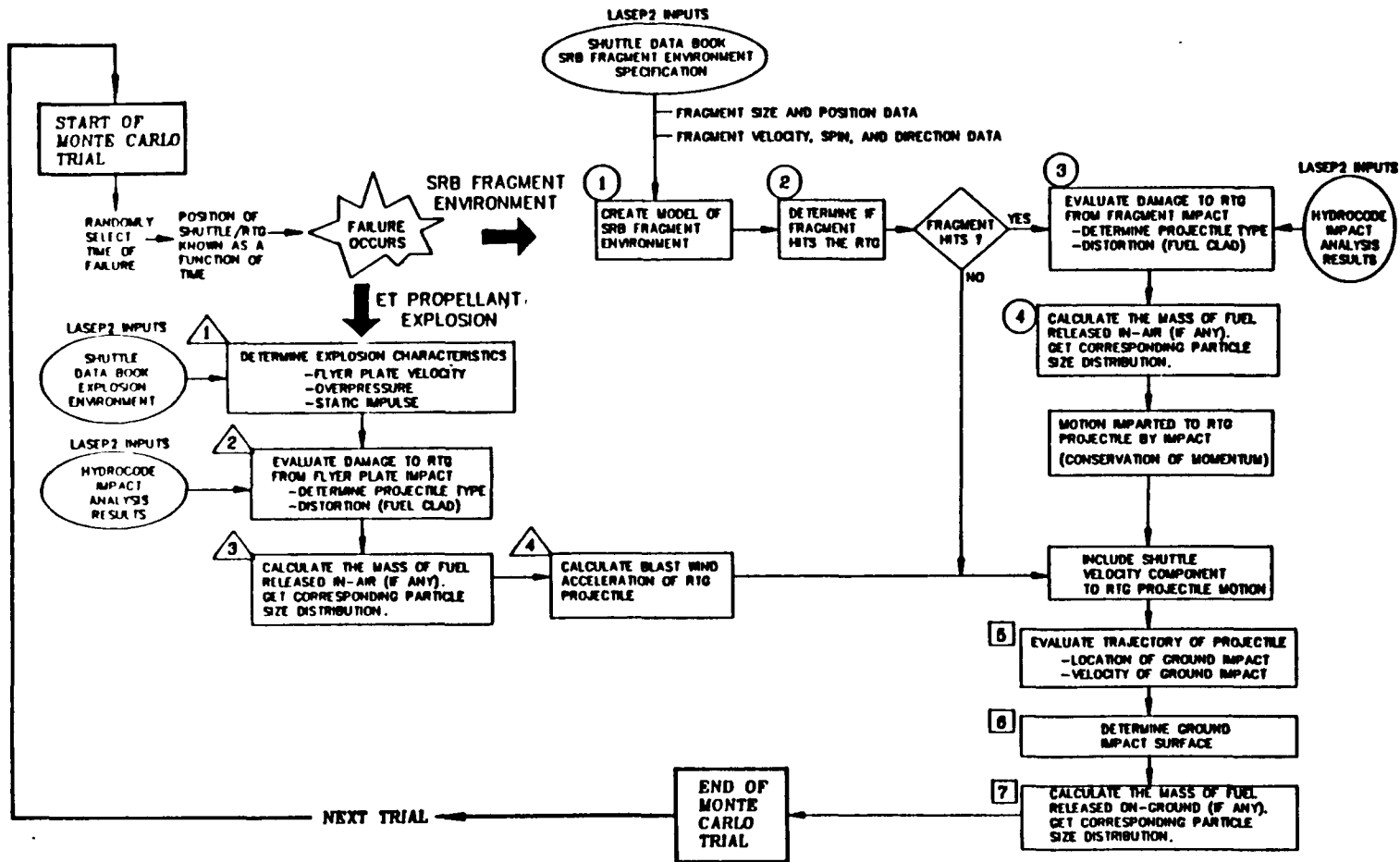


Figure D-2. Outline of Evaluation Process for Explosion and Fragment Accident Environments

### D.2.1 SRB FRAGMENT ENVIRONMENT EVALUATION

When a SRB random failure or a range destruct occurs, fragments, which are pieces of the SRB case, are propelled outward in all directions from the longitudinal centerline of the SRB. The mechanism, which breaks the SRB case and propels fragments from the SRB, is distinctly different for the random failure and range destruct cases. Consequently, the Shuttle Data Book provides two unique data bases for the fragment environments of each accident case. Since each of the Galileo RTGs is in close proximity to a SRB, the potential exists for a RTG to be hit by a SRB fragment.

As specified in the Shuttle Data Book, the stowed configuration of the RTGs on the Galileo spacecraft causes each RTG to be threatened only by the single SRB nearest to it. Figure D-3 shows several views of the Shuttle with the positions of the Galileo RTGs indicated. Because of the intervening spacecraft structure between the RTGs, only fragments from the right SRB can damage the right RTG, and similarly, only fragments from the left SRB can damage the left RTG. As a result, a SRB random failure threatens only a single RTG. In the LASEP2 program, the failure side (left/right) is randomly selected with even probability for each trial performed. In the range destruct case, both SRBs are fragmented, causing both RTGs to be threatened.

While there are basic differences between the random failure and range destruct cases, the overall process developed to evaluate the response of the RTGs to these accidents is identical. Thus, studying the evaluation of the general SRB fragment environment encompasses the analyses of both individual cases. In evaluating the fragment environment of both cases, the LASEP2 program only considers the fragments categorized as large case wall fragments. Fragments classified as shrapnel, such as pins, clevises, and joint sections, are treated separately outside the LASEP2 program.

At the initiation of the fragment environment evaluation, the time at which the failure or destruct occurs is randomly selected on a uniform distribution from an input range. The input time range typically corresponds to the time zones for which mission failure probabilities are provided. Once the time of failure is known, the position, orientation and velocity of the Shuttle are

determined. Prior to the time of failure, the Shuttle is assumed to be traveling along its nominal trajectory. The position of the RTG with respect to the launch pad is determined from the Shuttle position. This calculated RTG/Shuttle position and velocity data is used later in the LASEP2 program in the trajectory and ground impact analyses.

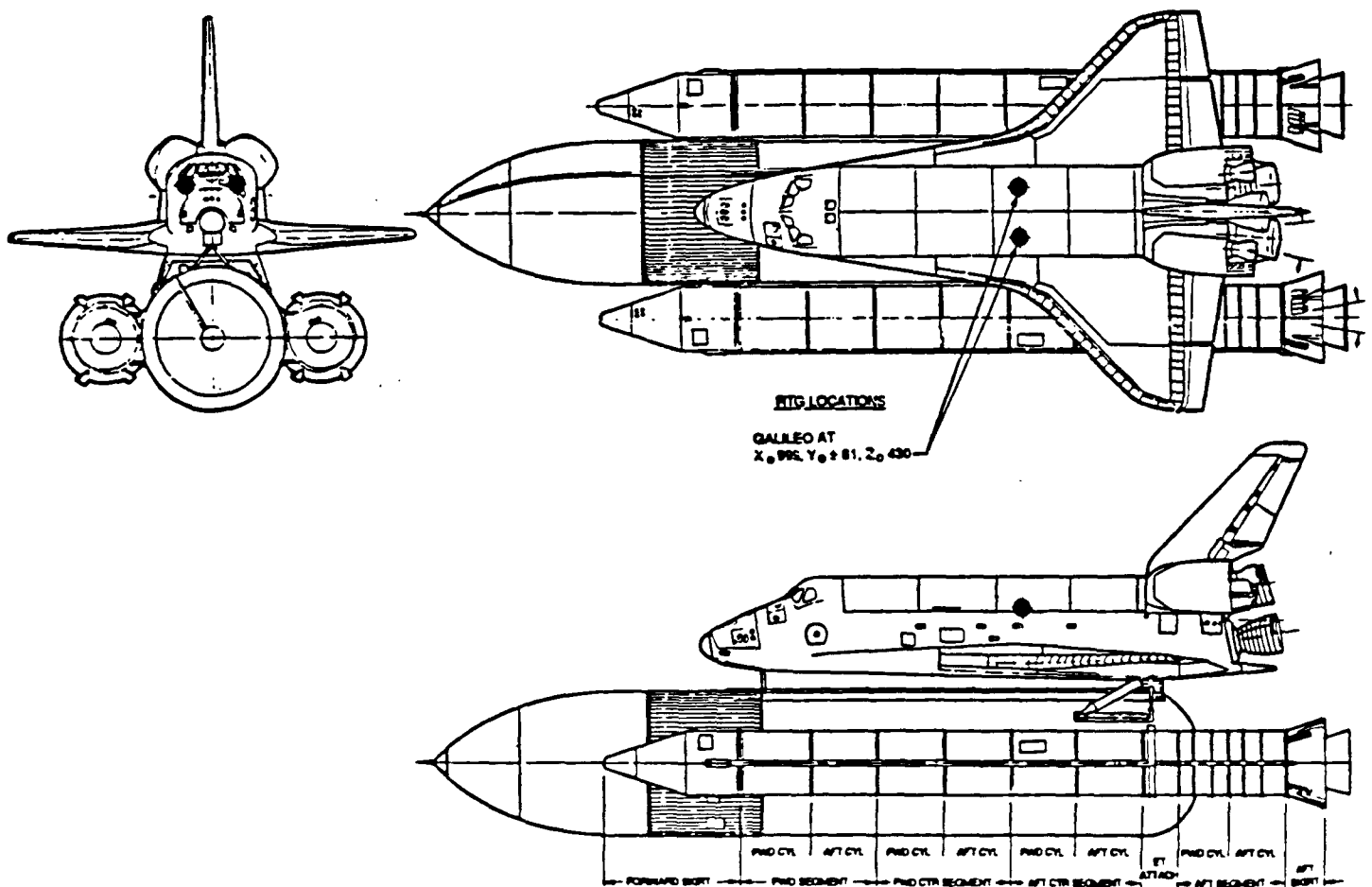


Figure D-3. Illustration of Galileo RTGs Position in the Shuttle

D.2.1.1 Model of SRB Fragment Environment

The first and most significant step in evaluating the fragment environment is to randomly create a model of the SRB fragment field which threatens the RTG. The simulation of the fragment field is based on the concept of the fragment band model. An illustration of the band model is shown in Figure D-4. Essentially, a band of fragments 360° in circumference, equal in height to the RTG, is randomly reconstructed from input data contained in the Shuttle Data Book.

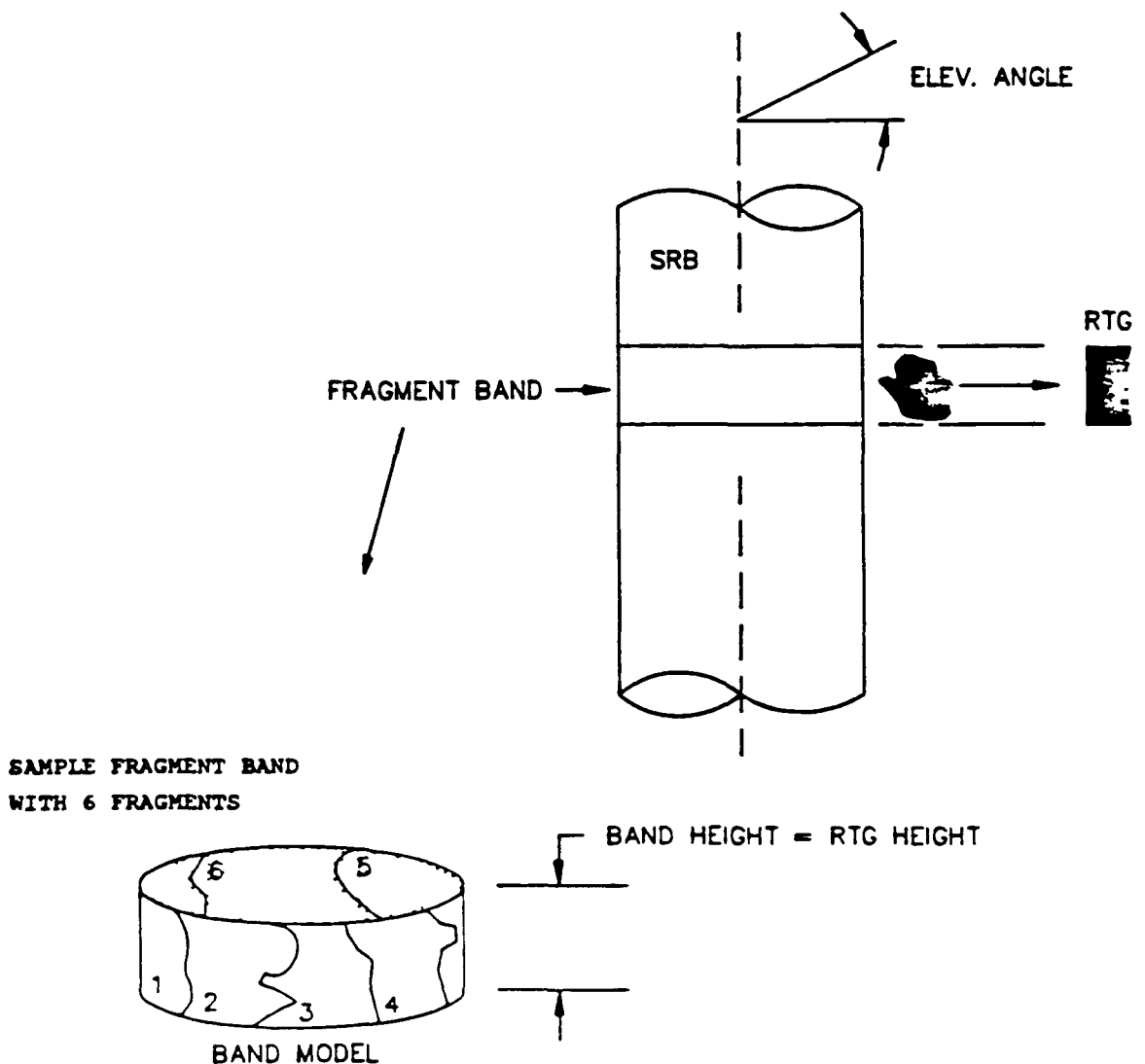


Figure D-4. Fragment Band Model

The band is positioned directly across from the RTG along the SRB longitudinal centerline. The fragments in the band represent those fragments which threaten the RTG during an accident. Each fragment in the band is assigned the following characteristics:

1. Flight Path (or direction)
2. Velocity
3. Spin Rate
4. Size (circumferential length and area)
5. Mass
6. Position of fragment on SRB (prior to failure or destruct)
7. Break-off position (distance offset from SRB center where the fragment is released)

Creation of the fragment band model is a two step process. The first step geometrically constructs the band. The location, size, area and C.G. position of the fragments in the band are determined. For each fragment, these geometry details are independently selected by a random process from input distributions. The second step in the process assigns velocity, direction, spin and break-off position to each fragment in the band. In the random failure case, the velocity, direction, and break-off position are randomly selected independent of each other. The spin rate for the random failure case is randomly determined as a function of the fragment length. In the range destruct case, all of the characteristics defining fragment motion are dependent upon two parameters, cavity pressure and break off time. For a detailed explanation of these parameters, refer to Appendix B of this FSAR, Section B2.1.1.2. Within LASEP2, the cavity pressure and break time are both selected randomly. They are then used as indices into the data base for determination of the values of spin, velocity, direction, and break off position.

In assigning the size and motion characteristics of the fragments, separate input data bases are used for the random failure and range destruct cases. A complete description of these databases along with a fundamental description of the band concept is supplied in the Shuttle Data Book. The application of



these databases in the LASEP2 program, to create fragment bands, is consistent with the details provided in the Shuttle Data Book.

Before a SRB fragment can impact the RTG, it must first travel through the intervening structure of the Orbiter. The velocities and spin rates of the fragments are adjusted (reduced) to account for the interaction between the fragment and the Orbiter structure. Two sets of velocity and spin reduction factors are supplied to the LASEP2 program. One set of factors is provided for the fragment traveling through the wing and fuselage prior to impact with the RTG. A separate set is provided if the fragment passes only through the Orbiter fuselage. A geometrical analysis based on the fragment initial position and flight path is performed to determine the orbiter structure intersected by the fragment. Table D-2 lists the velocity and spin rate reduction factors used in the LASEP2 program. The values in this table are based on the conservative interpretation of the data provided by the fragment/fuselage tests (refer to Appendix G, Section G.5). The results of the fragment/fuselage tests represent an update to the velocity reduction factor data contained in the Shuttle Data Book.

Table D-2. Velocity and Spin Rate Reduction Factors for a Fragment Traveling Through the Orbiter Structure

	Velocity	Spin Rate
Fuselage Only	0.15	.5
Wing and Fuselage	0.35	.5

Using the characteristics of size and motion, each fragment in the band is evaluated to determine if it can impact the RTG. In performing this evaluation the fragments in the band are investigated in descending order of velocity. The fastest fragment in the band is evaluated first, the slowest fragment is evaluated last. Each fragment in the band is evaluated until an impact with the RTG occurs or all of the fragments miss. When a fragment impacts the RTG, an assessment of the RTG damage is made, and a subsequent

trajectory analysis performed. Secondary hits of SRB fragments into the RTG are rare, since the RTG is accelerated by the fragment impact away from the threatening fragment field. If none of the fragments in the band impact the RTG, then the trial results in a non SRB fragment impact condition.

From its original conception, the band model was devised to represent only fragments with pure azimuthal or planar motion. In the initial band model, fragments did not have an elevation angle velocity component. Definition of elevation and azimuth angle is shown in Figure D-5. As a consequence of the original band concept, the analysis technique developed within the LASEP2 program, to determine fragment impacts into the RTG, is based only on the planar motion of the fragment. As the specification of the SRB fragment environment evolved, the addition of fragment elevation angle motion was included in the model description. Definition of the elevation angle range for each accident case is found in Table D-3. For each fragment modeled in an accident, an elevation angle is randomly selected along a uniform distribution from the range provided in Table D-3. The selection of elevation angle for each fragment is independent of all other fragment characteristics.

The inclusion of non-zero elevation angles into the fragment specification permits fragments from SRB cylinders, other than the cylinder opposite the RTG, to impact the RTG. To organize the ensuing discussion, a numbered identity system is defined for the cylinders of the SRB as shown in Figure D-6. In the initial zero elevation angle fragment environment specification, only fragments from cylinder #5 could impact the RTG. With a  $\pm 20^\circ$  elevation angle, fragments from cylinders #4 through #7 are able to impact the RTG. The hit determination analysis for the zero elevation angle case is a two dimensional problem requiring only the evaluation of the planar fragment motion. To determine an impact by a fragment having non-zero elevation angle, a three dimensional analysis is required. Both the azimuth and elevation components of the fragment motion are considered in a three dimensional analysis.

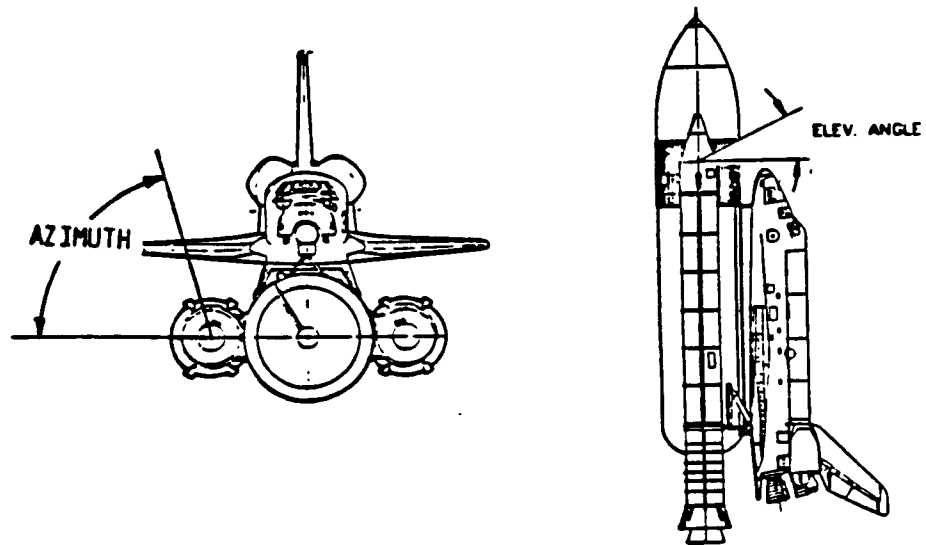


Figure D-5. Definition of Azimuth and Elevation Angles

CASE	TIME (MET-SEC)	ELEVATION ANGLE RANGE (DEGREES)
RANDOM FAILURE	0-105	+/- 20
	105-120	+/- 20
RANGE DESTRUCT	0-105	0
	105-120	+/- 20

Table D-3. Elevation Angle Ranges

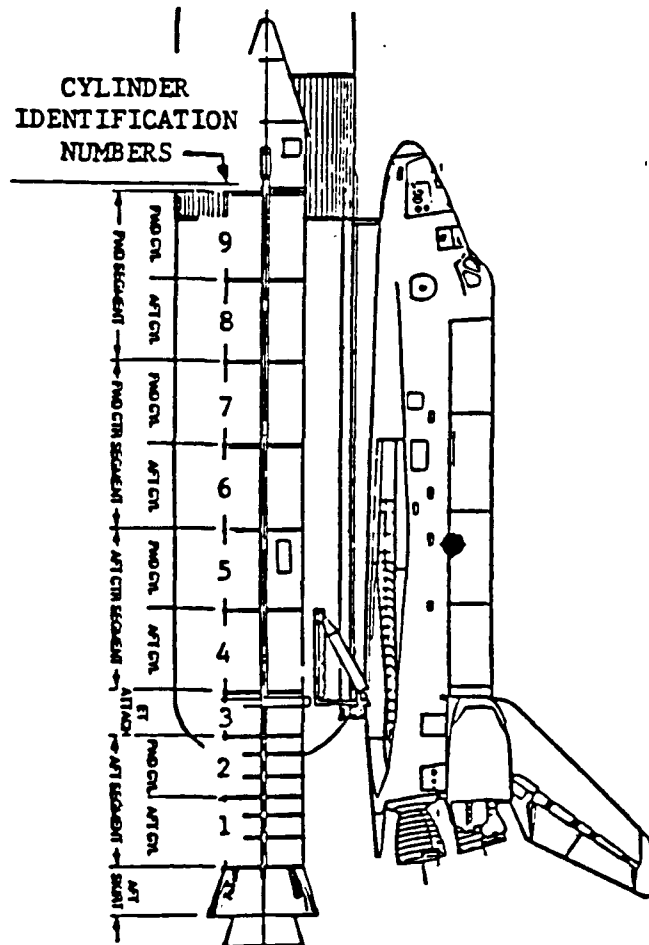


Figure D-6. SRB Cylinder Identification Numbers

An extensive study was performed to address the significance of elevation angle effects upon the original band model concept and the hit determination analysis. This study included the development of a separate analysis program, termed CYLMOD (Cylinder Model), which employed the Monte Carlo technique to investigate the probability of fragment impact on the RTG as a function of elevation angle. The CYLMOD program models the SRB fragment environment in three dimensions. Full height, full circumference fragment representations of SRB cylinders #4 through #7 are randomly constructed from the database used by LASEP2. The motion of each fragment in these cylinders, both azimuth and elevation components, is evaluated to determine the probability of impact with the RTG. Results from the CYLMOD program demonstrate that the elevation angle

velocity component does not significantly affect the probability of fragment impact with the RTG. A sample result of the CYLMOD code, which plots the probability of impact as a function of elevation angle for the random failure case, (time range 0-105 sec.) is shown in Figure D-7. The probability of fragment impact into the RTG is increased by only 2.5 percentage points at the  $\pm 20^\circ$  elevation angle from the zero elevation angle case. The accuracy or repeatability of these results, which are based on the Monte Carlo method, to within  $\pm 2$  of the total percentage, must be considered in the interpretation of this output. In addition to providing results regarding impact probability, a coordinated series of experimental analysis runs performed with the CYLMOD program strengthened and improved the understanding of the interaction between the fragment environment and the RTG. A further description of the CYLMOD program is contained in Reference [2].

While the effects of elevation angle upon impact are small, they are not considered negligible. To account for these effects in the LASEP2 program, an adjustment in the implementation of the band model is made for non-zero elevation angle cases. For zero elevation angle accident cases, no modification is required, since these cases are consistent with the original band model concept. For the evaluation of non-zero elevation angle cases, the number of bands built in a single trial is adjusted to account for the variation of fragment density at the RTG caused by the elevation angle velocity component. For the zero elevation angle case, exactly one band is constructed per trial and the fragments of the band have the motion and geometry characteristics of cylinder #5. In the case of non-zero elevation angles, the number of bands built per trial is varied from 0 to 3, with the fragments in these bands having characteristics belonging to cylinders #4 through #7. The process of selecting the number of bands per trial is based on CYLMOD program results. A typical distribution of the number of bands created per trial for a complete LASEP2 analysis run of a non-zero ( $\pm 20^\circ$ ) elevation angle case is:

Percentage of trials in which 0 band(s) are created = 10%  
 Percentage of trials in which 1 band(s) are created = 70%  
 Percentage of trials in which 2 band(s) are created = 18%  
 Percentage of trials in which 3 band(s) are created = 2%.

CYLMOD Parametric Study  
Effects of Elevation Angle on the Probability of Hit  
RANDOM FAILURE CASE (0-105 sec)

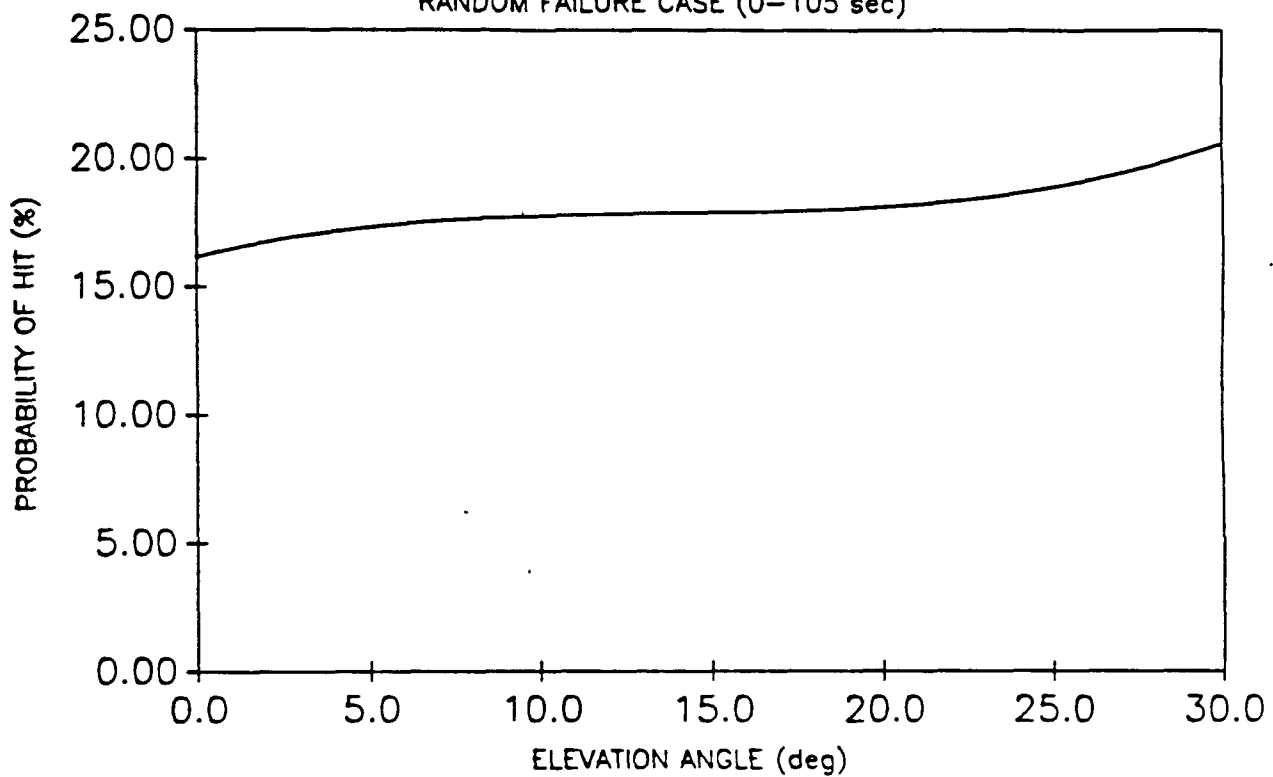


Figure D-7. CYLMOD Program Results Probability of Fragment Impact vs. Elevation Angle Random Failure Case: 0-105 sec.

For this distribution, the average number of bands per trial is 1.12. These percentages, listed for the number of bands per trial, represent output from a particular LASEP2 analysis run. Since the compilation of these values is part of the Monte Carlo process, the distribution provided is only representative, and the individual percentages can vary by  $\pm 2$  for different analysis runs. The technique of using a variable number of bands (0 to 3) to represent the fragment environment for non-zero elevation angle cases permits the use of the original hit determination analyses and properly accounts for the fragment impact probability into the RTG. From this perspective, output results of the CYLMOD program convert the three dimensional fragment environment into an equivalent two dimensional problem.

In summary, the fragment environment of both the random failure and range destruct cases can be represented using the band model and its corresponding input data. A series of investigative analyses using the CYLMOD and LASEP2 programs have demonstrated the capability to model zero and non-zero elevation cases with the fragment band concept. In addition, Reference [3] documents an organized set of sensitivity studies which substantiate the validity of the SRB fragment input data provided by the Shuttle Data Book.

#### D.2.1.2 Fragment Hit Determination

The next step in the fragment environment evaluation process is to determine if the fragments in the band model impact the RTG. Complete motion and size specification of each fragment has been defined in the construction of the band. Beginning with the highest velocity fragment in the band and proceeding in descending order of velocity, an individual analysis of each fragment is performed to determine if an impact occurs. A two dimensional hit/no-hit analysis, in a plane normal to the SRB longitudinal axis, is performed based on the break-off position, velocity, spin, and fragment circumferential length. An illustration of the analysis is shown in Figure D-8.

With a finite difference technique being used, the motion of the fragment is modeled in successive time steps. Both the translational and rotational components of fragment motion are included in the evaluation. A hit is determined to have occurred when the fragment and RTG geometries intersect. A

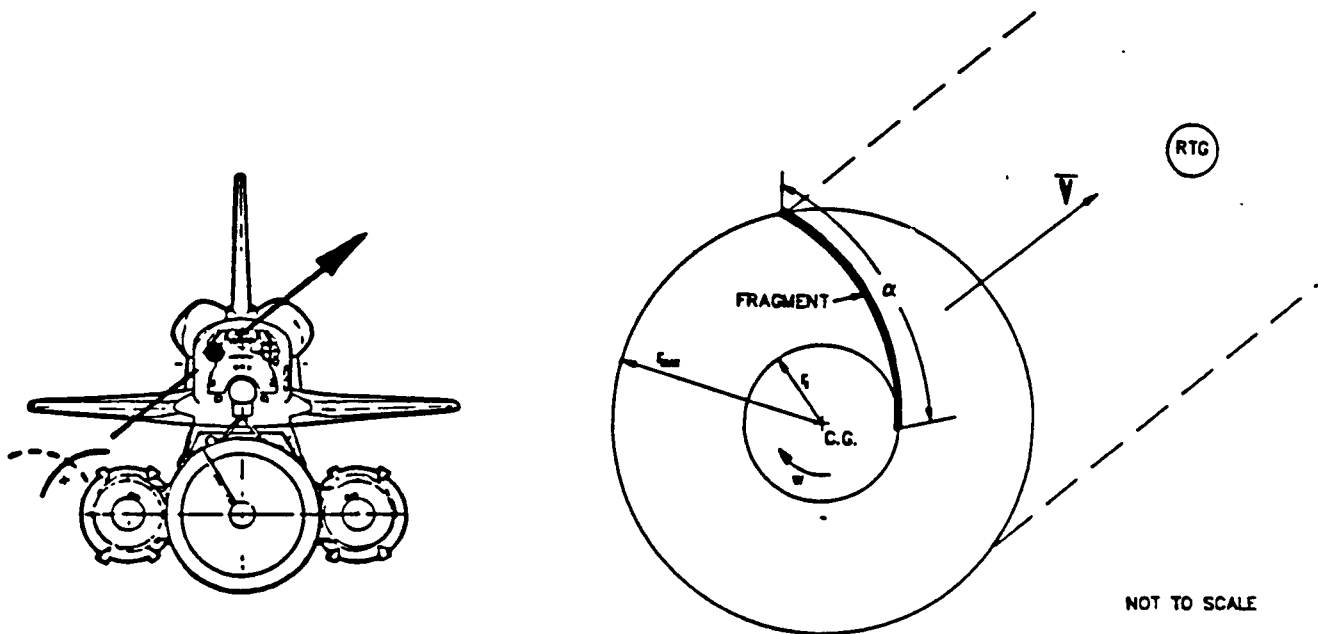


Figure D-8. Two Dimensional Fragment Hit Determination Analysis

sufficiently small time step, based on the velocity and spin rate of the fragment, is used in this analysis to compute the motion of the fragment accurately. The orientation and position of the fragment are calculated at the instant of impact. Based on this orientation, the hit is classified as either edge-on or face-on. A graphic description of edge-on/face-on impacts is shown in Figure D-9. Identification of edge-on/face-on impacts is required, since the damage and corresponding evaluation of these impacts are different. An impact is considered edge-on if the tangent to the fragment edge is within  $\pm 20^\circ$  of a line normal to the RTG impact surface. A series of hydrocode impact analyses, documented in Reference [4], established this tolerance angle specification. The position of the fragment with respect to the RTG at the time of impact is used to compute the total impact velocity of the fragment and the unit vector normal to the fragment surface at the point of impact. The total impact velocity of the fragment is defined as the vector sum of the fragment C.G. velocity and the translated velocity component based on the fragment rotation rate and the impact point on the fragment.





Figure D-9. Description of Edge-on/Face-on Impact

In the hit determination analysis the following assumptions are made:

1. The azimuthal flight path direction of the fragment C.G. is unaltered by impact with the intervening wing and fuselage structure
2. The fragment axis of rotation remains parallel to the SRB longitudinal axis.

The initial rotational orientation of the fragment is randomly selected on a uniform basis from the range  $0^{\circ}$  to  $360^{\circ}$ . Graphic examples of the hit determination analysis, generated from a customized software package, are shown in Figure D-10. The fragment motion relative to the RTG at specified time intervals is displayed. Note that the time interval used to graphically display the fragment motion is not the same as the time step used in the analysis. The time step used in the analysis is typically much smaller than the graphic time interval. The probability of impact with the RTG is dependent upon the fragment characteristics of direction, velocity, spin and

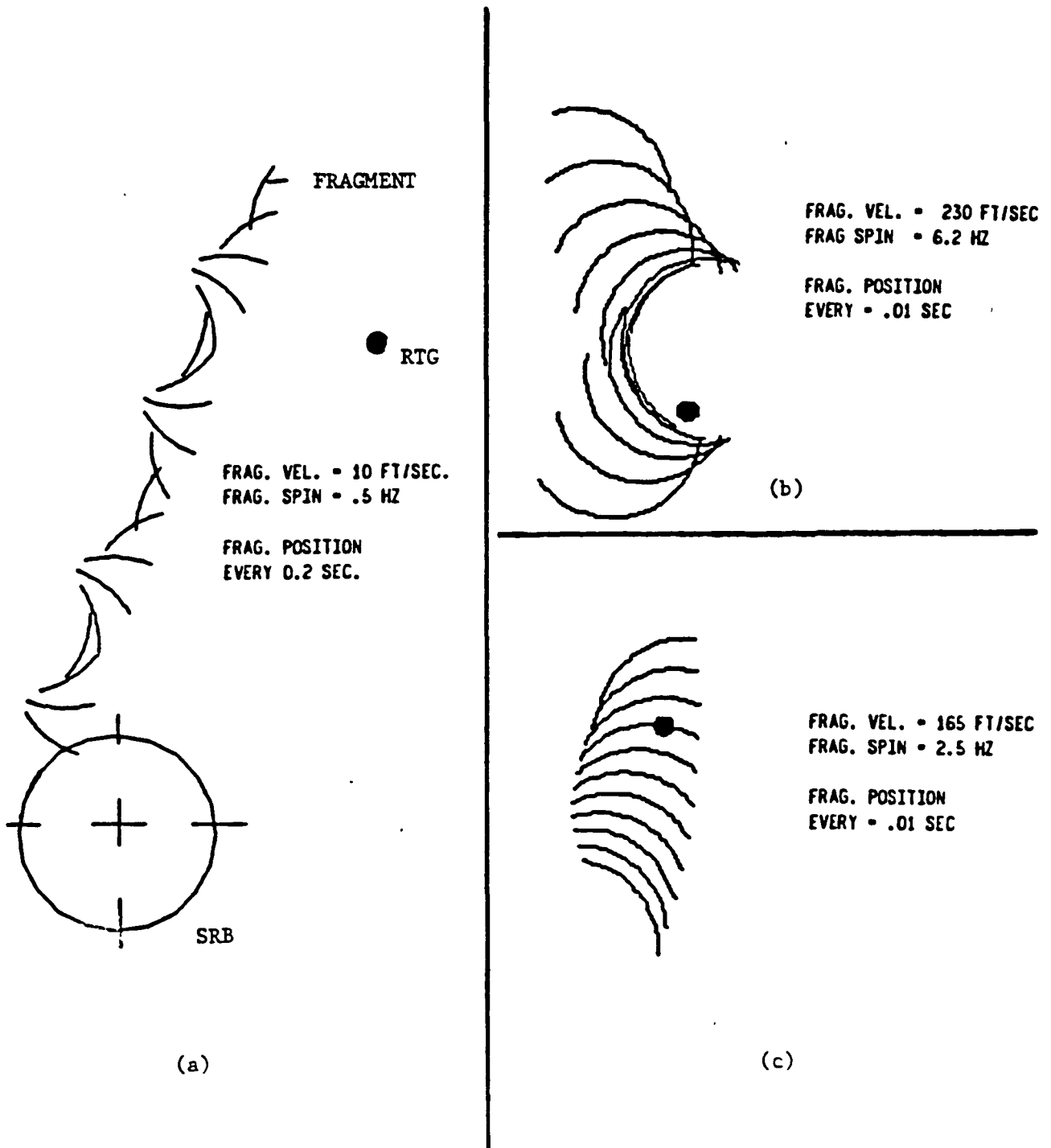


Figure D-10. Examples of the Hit Determination Analysis

size. The importance of modeling all of these parameters is evidenced in Figure D-10b. The complex motion of the fragment, such as the spinning-away shown in this figure, demonstrates the need to consider all of the fragment characteristics in a hit determination analysis.

The statistics of impact on the RTG by the SRB fragments are presented in Table D-4. These results are obtained from the CYLMOD program. Figures D-11 and D-12 present the cumulative distributions of impact as related to fragment effective velocity for the random failure and range destruct scenarios, respectively. The effective velocity is the vector sum of the translational velocity of the fragment center-of-gravity and the rotational component of velocity at the point on the fragment that contacts the RTG (i.e., the radius of spin from the fragment c.g. to the point of contact with the RTG).

Table D-4. Overall Impact Results for Random Failure and Range Destruct Cases

Case	Time MET (sec)	Elevation Angle (Degrees)	Probability Of Impact With The RTG (%)	Fragment Orientation At Impact	
				(%) Face-On	(%) Edge-On
Random Failure	0-105	<u>+20</u>	23	97.3	2.7
	105-120	<u>+20</u>	20	97.5	2.5
Range Destruct	0-105	0	26	98.8	1.2
	105-120	<u>+20</u>	33	98.6	1.4

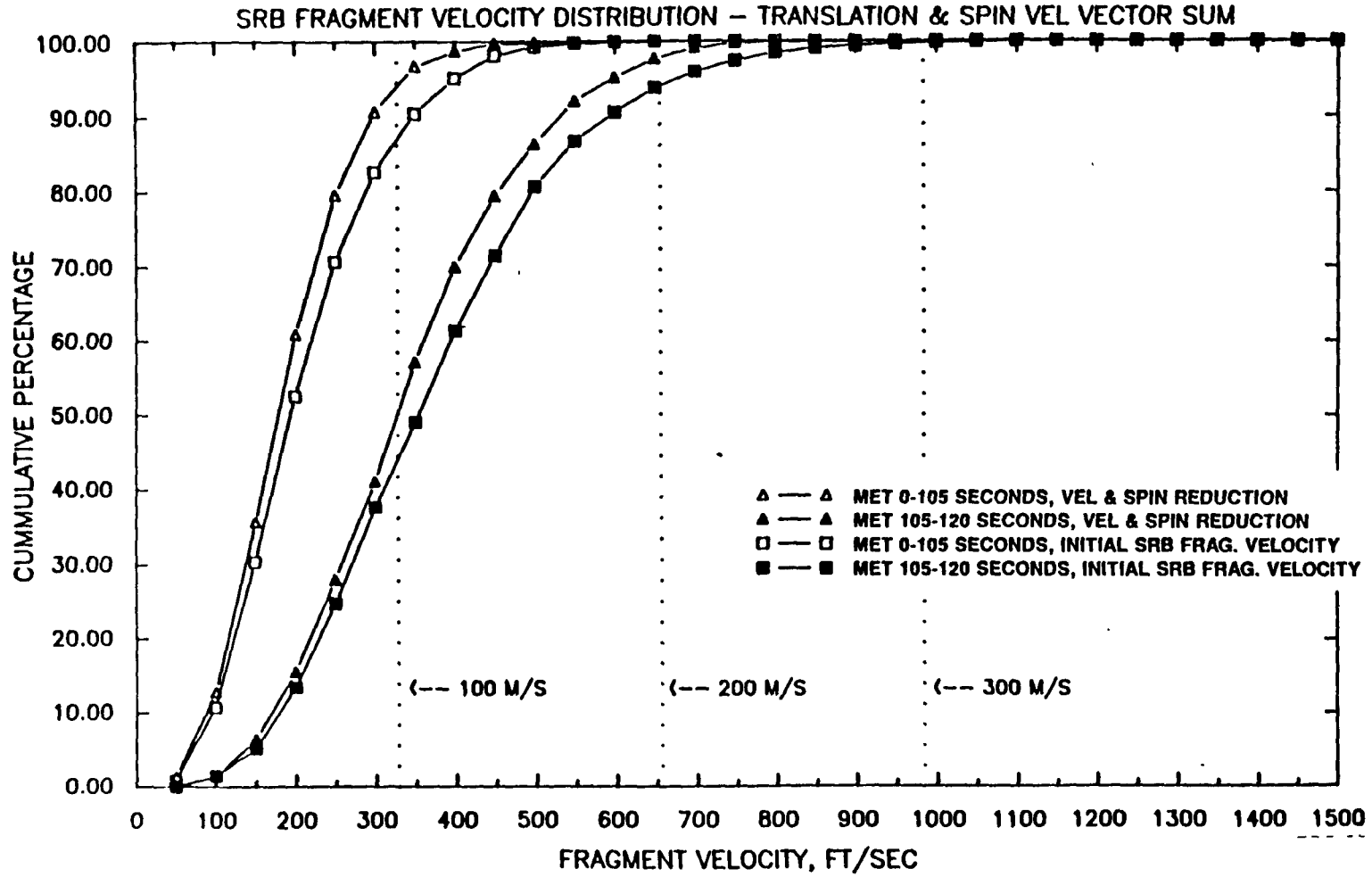


Figure D-11. Random Failure

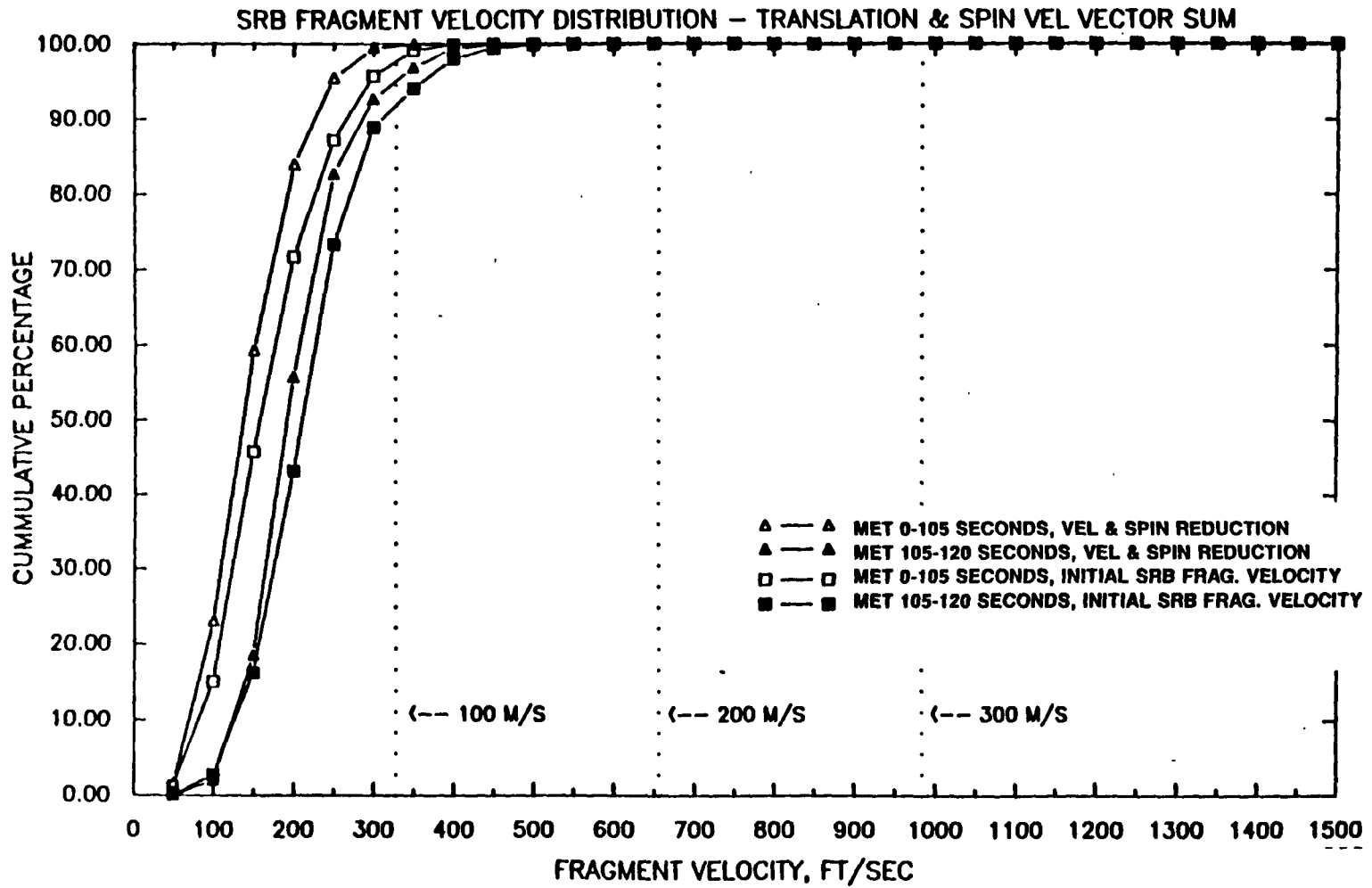


Figure D-12. Range Destruct

When an RTG is hit by a fragment, it is assumed that the RTG is accelerated away from the threatening SRB fragment environment. Multiple SRB fragment impacts are considered to be implausible. The number of modules impacted by a fragment, in the event of a hit, is randomly determined on a uniform basis using output data generated by the CYLMOD program. Figure D-13 shows a distribution providing the probability of the number of modules impacted for the random failure and range destruct cases. The capability of the CYLMOD code to evaluate the fragment environment in three dimensions enabled the development of these statistics. Following an impact by a fragment, a damage analysis is performed on the RTG. In performing the damage analysis the LASEP2 program accounts for the impacted/not-impacted module groups. Evaluations of the fragment environments that have no impacts into the RTG do not require a damage analysis. Referring to Figure D-2, the trajectory analysis of the RTG projectile follows the determination of no fragment impacts.

#### D.2.1.3 RTG Damage Evaluation

The total damage to the RTG caused by a SRB fragment hit is actually the result of two individual impacts. The first impact is the SRB fragment into the RTG. Following this impact, the RTG projectile(s) resulting from the SRB fragment hit are driven into the payload bay wall. The combined consequences of these two impacts are used in determining the RTG damage. For each of these impacts, the damage evaluation is a two part process. Part one of the evaluation is the determination of the post impact RTG projectile status. In this portion of the evaluation process, the status of the RTG projectile is assigned as one of the following types:

1. Intact RTG
2. Aeroshell
3. Fueled clad.

The second part of the evaluation process is the calculation of the fueled clad distortion caused by the impact. Determination of the fuel clad distortion is significant since it is later used in the LASEP2 program to determine the amount of fuel released. The database of hydrocode impact

PROBABILITY OF THE NUMBER OF MODULES HIT  
IN THE EVENT OF A SRB FRAGMENT IMPACT  
(DISCRETE PROBABILITY DISTRIBUTION)

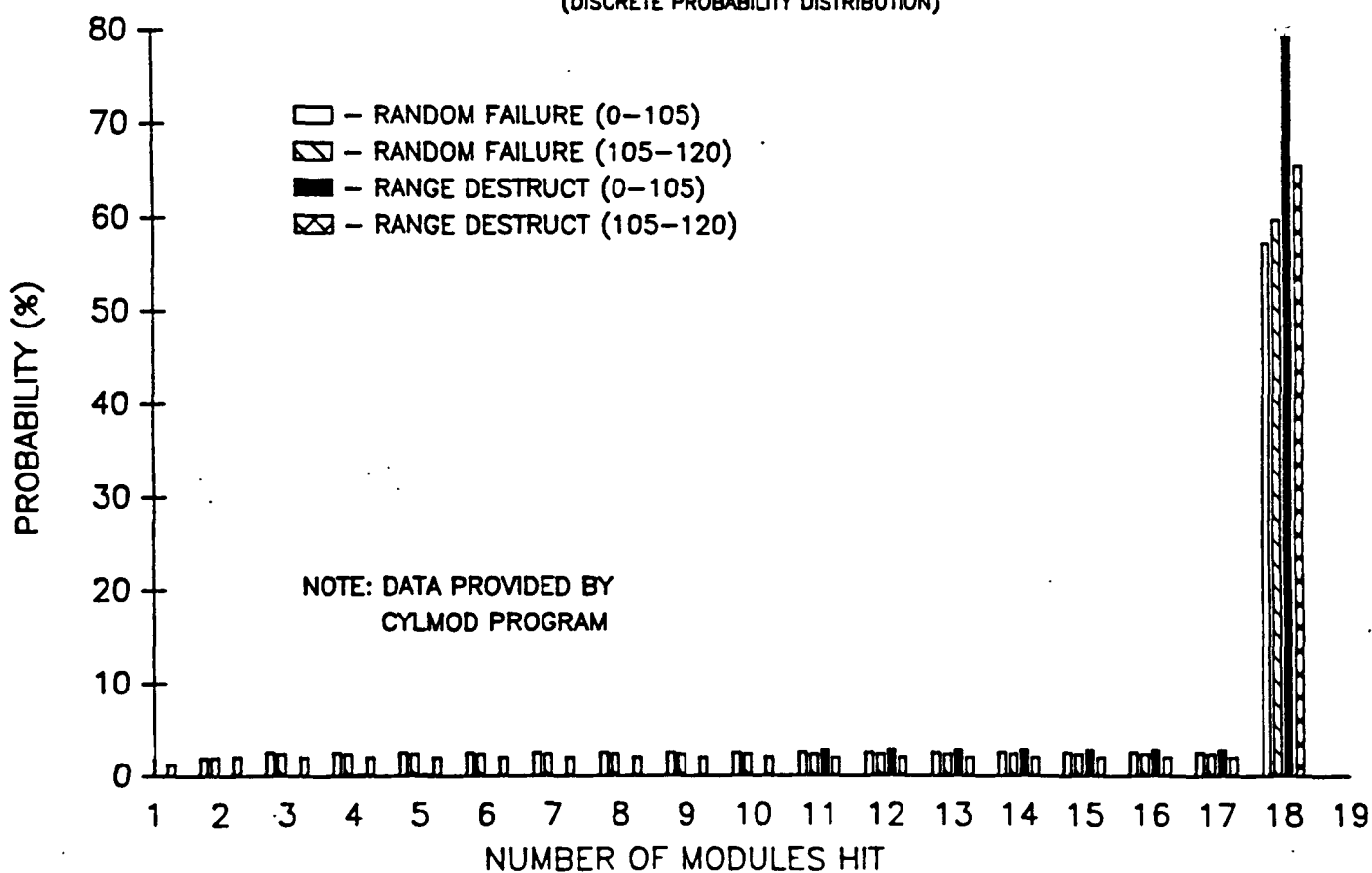


Figure D-13. Distribution for the Number of Modules Hit in the Event of a Fragment Impact

analysis results and specific details of the impact are used to compute the distortion.

The impact of a SRB fragment into the RTG produces one of three possible projectile types. Each of these RTG projectile types has a subsequent impact into the payload bay wall which causes additional damage and the possible further breakup of the RTG projectile. Figure D-14 shows the possible impacts and resultant projectiles which are initiated by a SRB fragment hit. There are five possible impact cases which can occur in the evaluation of the SRB fragment environment:

1. Initial SRB fragment edge-on into the RTG
2. Initial SRB fragment face-on into the RTG
3. Intact RTG into the payload bay wall
4. Aeroshell into the payload bay wall
5. Fueled clad into the payload bay wall.

Each of these impacts cases has a unique data base to analyze the RTG or RTG projectile damage.

The approach used to determine the RTG post impact projectile status is the same for each of the five impact cases. Inputs are supplied to the LASEP2 program which are used to specify the threshold energy levels of the impacting fragment that cause the RTG case and aeroshell to breakup or fail. For each applicable impact case, energy ranges are specified for the RTG case and aeroshell failure. Table D-5 list the minimum and maximum energy levels used in the LASEP2 analysis for each impact case. The energy values provided in this table are based on flyer plate impact test results. The derivation of these values is provided in Addendum I to this appendix.

For a particular impact evaluation, the threshold energy levels of RTG case and aeroshell failure are determined by randomly selecting between the minimum and maximum values for the appropriate impact case. The random selection is based on a uniform distribution. To determine the post impact projectile status, the energy contained by the impacting fragment, based on the total impact velocity, is compared to the selected failure threshold energy values.



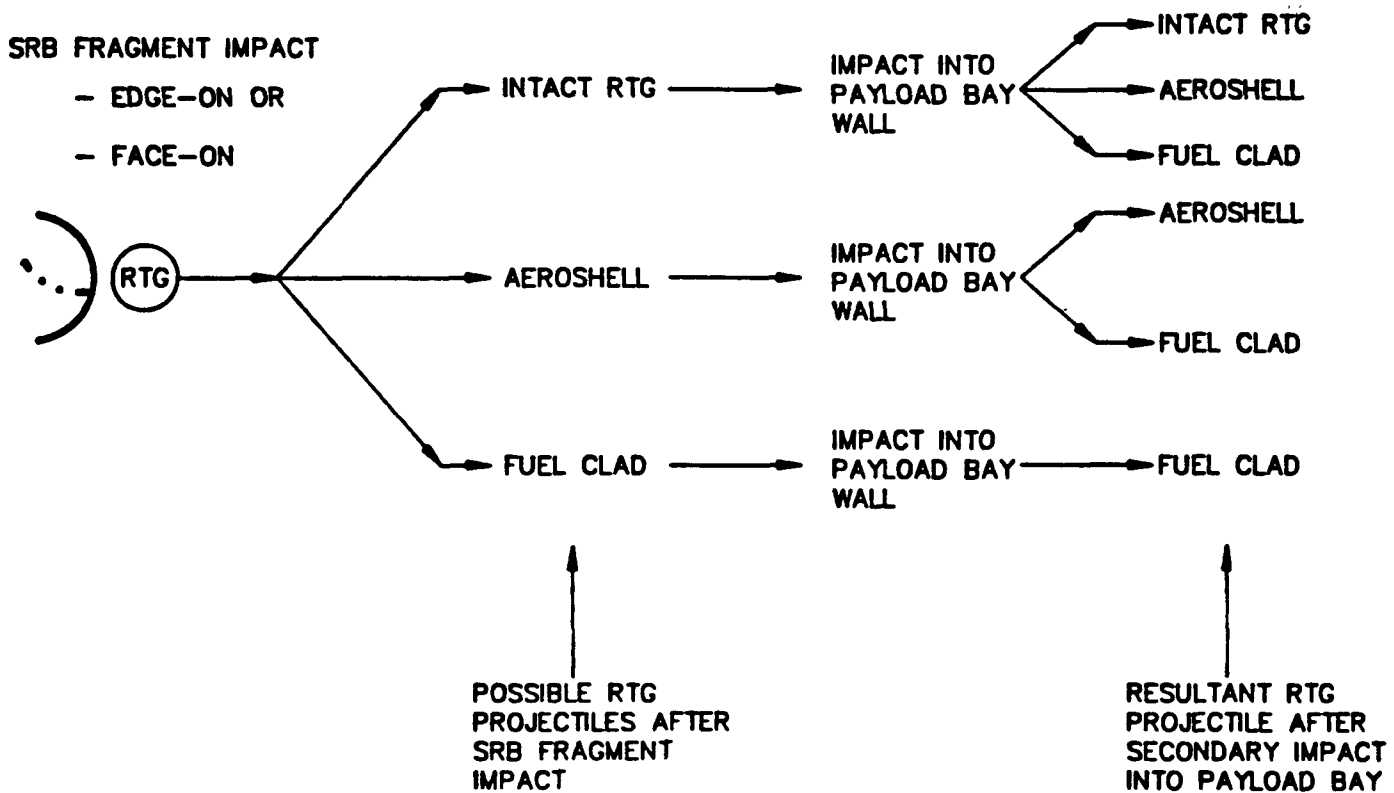


Figure D-14. Possible Outcomes Initiated by SRB Fragment Impact

Table D-5. Energy Values Ranges for RTG Case and Aeroshell Failure Caused by Impact

IMPACT CASE	RTG CASE FAILURE ENERGY LEVELS			AEROSHELL FAILURE ENERGY LEVELS			
	ft-lb			ft-lb			
	MIN	MAX	MEAN	MIN	MAX	MEAN	
-1- EDGE-ON SRB FRAGMENT INTO THE RTG	1727	2111	1919	*	44216	54041	49129
-2- FACE-ON SRB FRAGMENT INTO THE RTG	9114	11139	10126	209993	256658	233325	
-3- INTACT RTG INTO THE PAYLOAD BAY	9114	11139	10126	209993	256658	233325	
-4- AEROSHELL INTO THE PAYLOAD BAY	NA	NA	NA	209993	256658	233325	
-5- FUEL CLAD INTO THE PAYLOAD BAY	NA	NA	NA	NA	NA	NA	

NA = NOT APPLICABLE

\* This value should have been the mean; it was put into LASEP as the minimum, in error.

If the fragment energy quantity exceeds the RTG case failure threshold, then the projectile is not an intact RTG. Since the RTG case is failed, an additional check is required to determine if the projectile is an aeroshell or a fueled clad. If the fragment energy is above the selected aeroshell failure threshold, the resulting projectile type is fueled clad. Figure D-15 summarizes the RTG projectile status determination method. The RTG projectile type is determined for both the initial SRB fragment impact and the secondary payload bay wall impact. In the case of the secondary impact, the payload bay fragment velocity is considered to be equivalent to the relative velocity between the RTG and the payload bay wall.

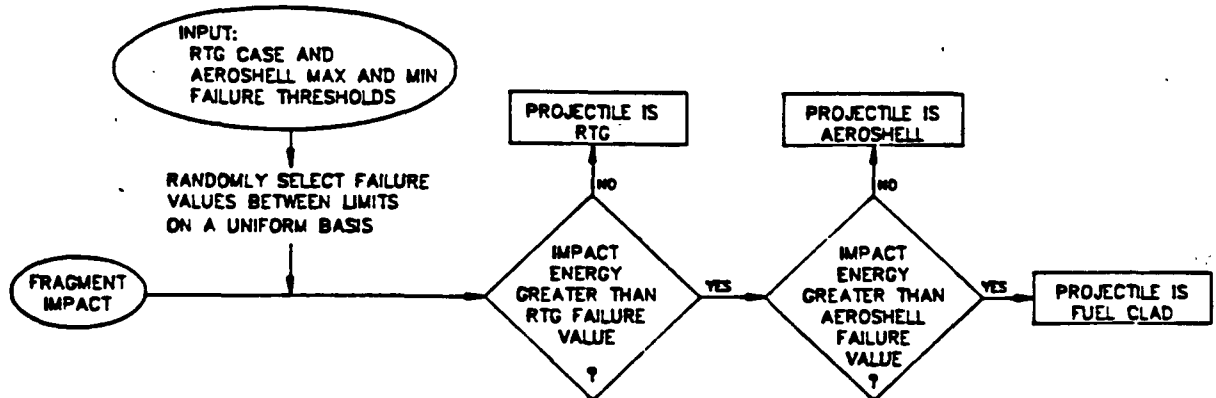


Figure D-15. RTG Projectile Status Determination Process

The second part of the damage evaluation process is the determination of the fueled clad distortion resulting from an impact. An overview of the analysis procedure used to perform this task is given in Figure D-16. An extensive set of hydrocode impact analyses, conducted by Fairchild, has established a data base which provides the distortion of fueled clad as a function of impact velocity for the complete range of impact cases. For each of the five impact cases, a unique hydrocode data base is supplied. Since the response of the fueled clad differs for each fragment impact type, a further breakdown of each hydrocode data base is necessary to account for the positional dependencies of:

1. Leading on trailing fuel clad position in the impact
2. Interior or exterior module position in the RTG stack.

For each of these categories a unique function of the fueled clad distortion is provided. In every trial of the LASEP2 program, the distinction between leading and trailing fueled clads is made in the damage evaluation process. The variation of fueled clad distortion due to stack position (interior or

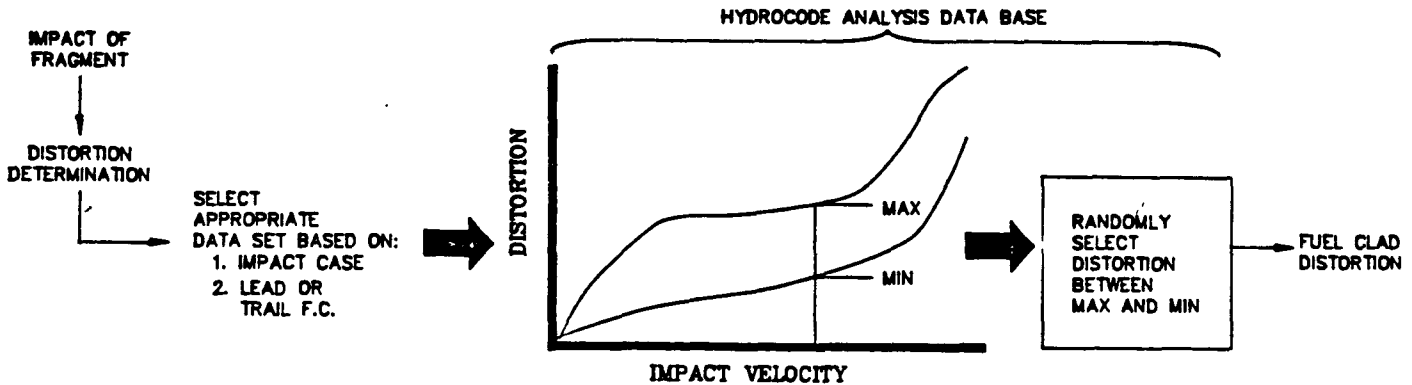


Figure D-16. Fuel Clad Distortion Determination Process

exterior) is accounted for by performing multiple runs of the LASEP2 program for each SRB fragment accident case. In one particular run, the distortion data relating to exterior modules is used throughout the entire analysis. In a separate run, the distortion data pertaining to interior modules is used. The results of these runs are combined to achieve the final outcome of an accident case.

Each data set in the hydrocode fragment impact data base, which describes the fueled clad distortion for a specific impact condition, gives the maximum and minimum possible distortions of the fueled clad as a function of the total impact velocity. A graphic representation of a data set is shown in Figure D-16. The range of distortion values between minimum and maximum produced by the hydrocode analysis represents the variation of distortion data found in actual test results. In the LASEP2 program, the first step in determining the fueled clad distortion is the selection of the appropriate data set from the hydrocode analysis inputs. Based on the impact velocity, a minimum and maximum distortion value can be determined from the input

hydrocode data set. For face-on fragment impacts, the mean value of the distortion limits is used as a function of impact velocity. For edge-on impacts, the fueled clad distortion is randomly selected on a uniform basis between the maximum and minimum values. (The latter should produce conservative results compared with a normal or log-normal distribution.) Distortion of the fueled clad is determined for both the initial SRB fragment impact and secondary impact of the RTG projectile into the payload bay wall. The total distortion of a fuel clad as a result of these impacts is taken as the square root of the sum of squares of each distortion value from both damage evaluations.

#### D.2.1.4 Calculation of the Mass of Fuel Released In-Air

In an SRB fragment environment evaluation, the total distortion of the fueled clads is used to determine the amount of in-air fuel released, if any. The term in-air refers to the position of the RTG above ground level at the time of impact. In each trial of the LASEP2 analysis, the mass of fuel released is computed. For each occurrence of a release, the particle size distribution of the fuel released is determined. Combining the results of each individual trial, the following output is produced for each accident case:

1. The average mass of fuel released in-air
2. Probability distribution of the mass of fuel released in-air
3. Distribution of average particle size for the mass of fuel released in air.

An outline of the algorithm used in each trial to calculate the mass of fuel released and the related particle size distribution is shown in Figure D-17. As presented in Reference [5], the basis of this algorithm is established by results from numerous tests investigating the response of fueled clads to various impact environments. Figure D-18 shows the BCI and SVT test data. The solid line shows the curve fit to these data points, given by:

$$R = 1.0 - \text{EXP}[-0.4 ((D-15)/33)^5]$$

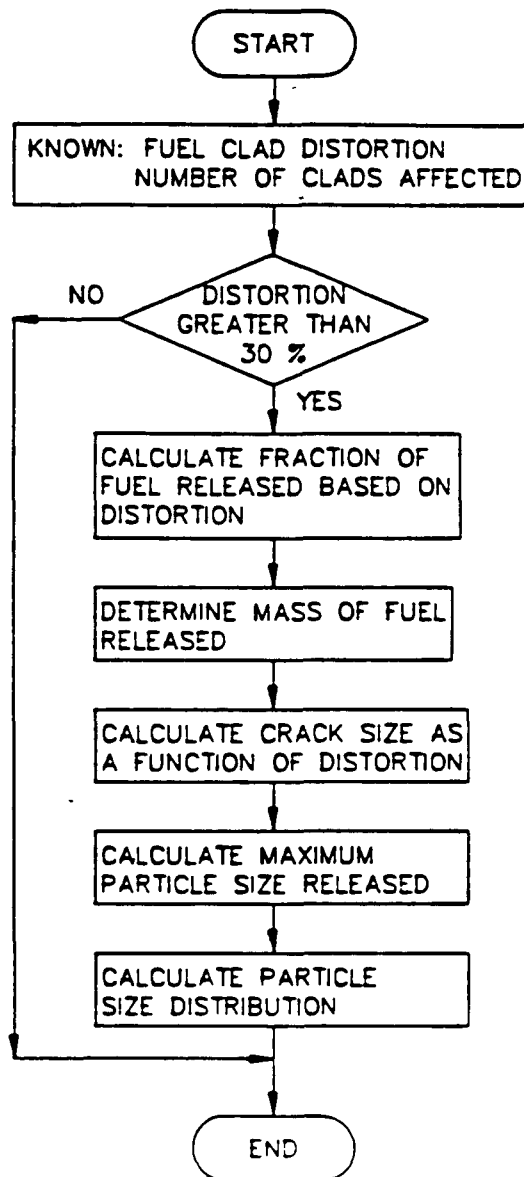


Figure D-17. Calculation of In-air Mass of Fuel Released and Corresponding Particle Size Distribution

We see that  $R=0$  when  $D=15$ . Since this curve is being used for in-air release, the RTG case is still present. In the FGT (Fragment Gun Tests) done at Los Alamos, a module with a simulated RTG case in front of it was thrown at a steel fragment. The distortion of the leading fuel clads ranged from 27% to 33%, and there was no clad failure or release. A value of 30% distortion was then selected as the threshold below which there was no release. As a result, the dashed curve in Figure D-18 was shifted to zero at 30%. The equation of this shifted curve, shown by the solid line, is:

$$R = 1.0 - \text{EXP}[-0.4 ((D-30)/33)^5]$$

This equation is used to compute the fraction of fuel released when the fuel clad distortion is above 30%.

The size distribution of the fuel released is based on the maximum particle size of the fuel which escapes through the crack in the clad. The maximum particle size (diameter),  $D_{P\_MAX}$ , is considered to be half of the maximum crack size,  $W_{MAX}$ .

$$D_{P\_MAX} = \frac{W_{MAX}}{2}$$

The maximum crack size for a clad is based on the clad distortion. A curve was fit to the data points shown in Figures 19a and 19b. This curve, shown as a dashed line, is given by the equation:

$$W_{MAX} = .17 (D-20)$$

Since, as discussed previously, there is assumed to be no release below 30% distortion, the curve is shifted so that the zero point occurs at 30% distortion. This curve, shown as a solid line, is then given by the equation:

$$W_{MAX} = .17 (D-30)$$

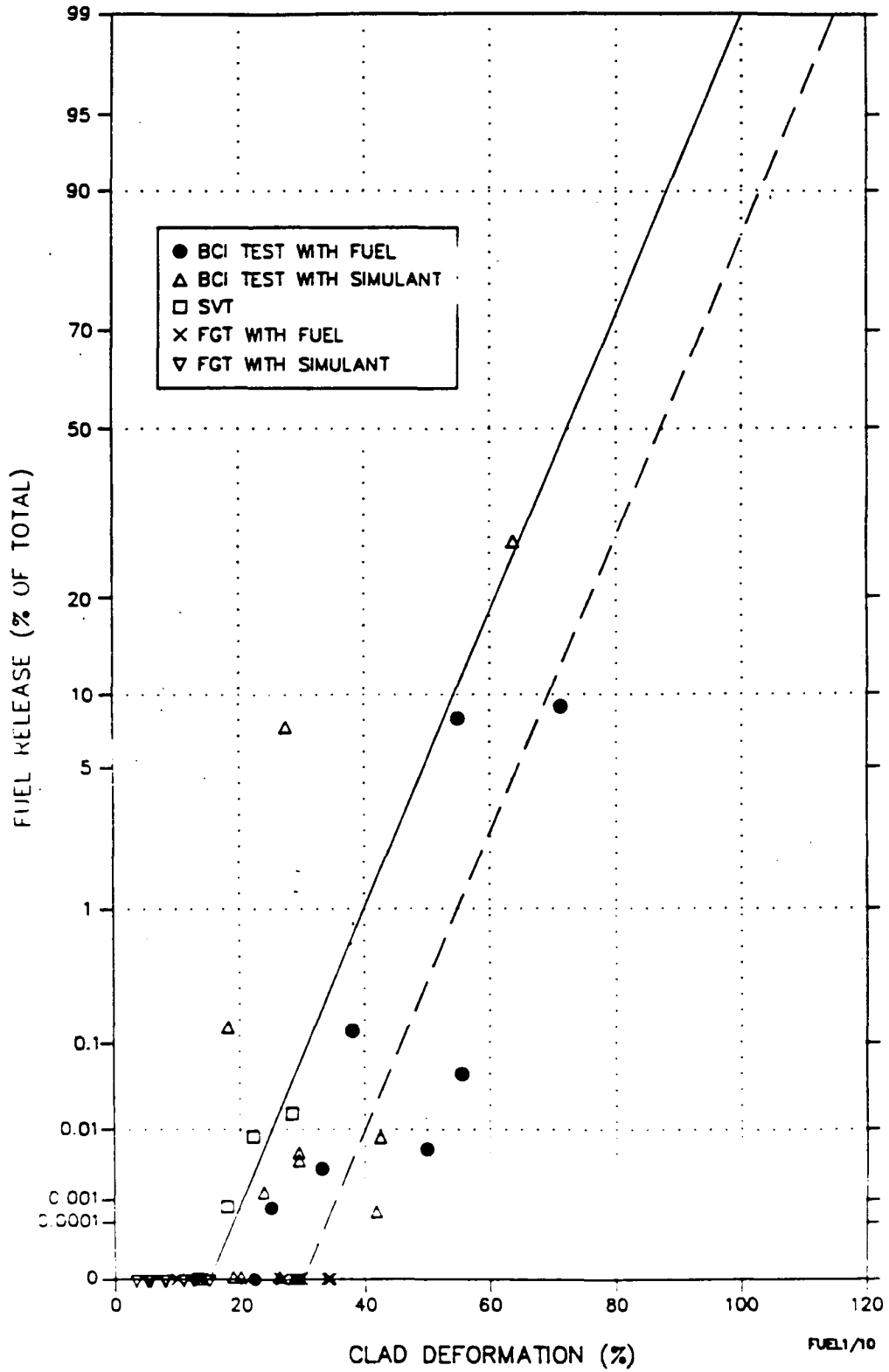
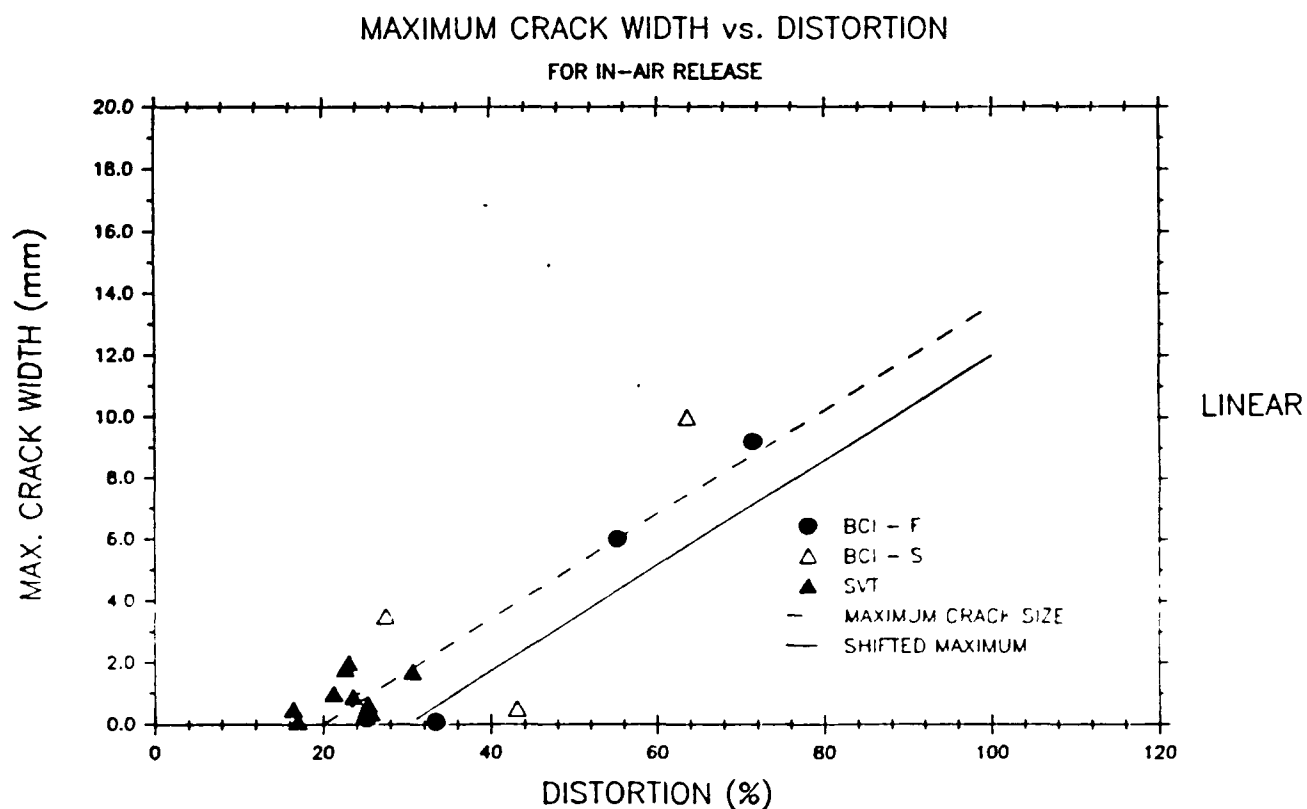
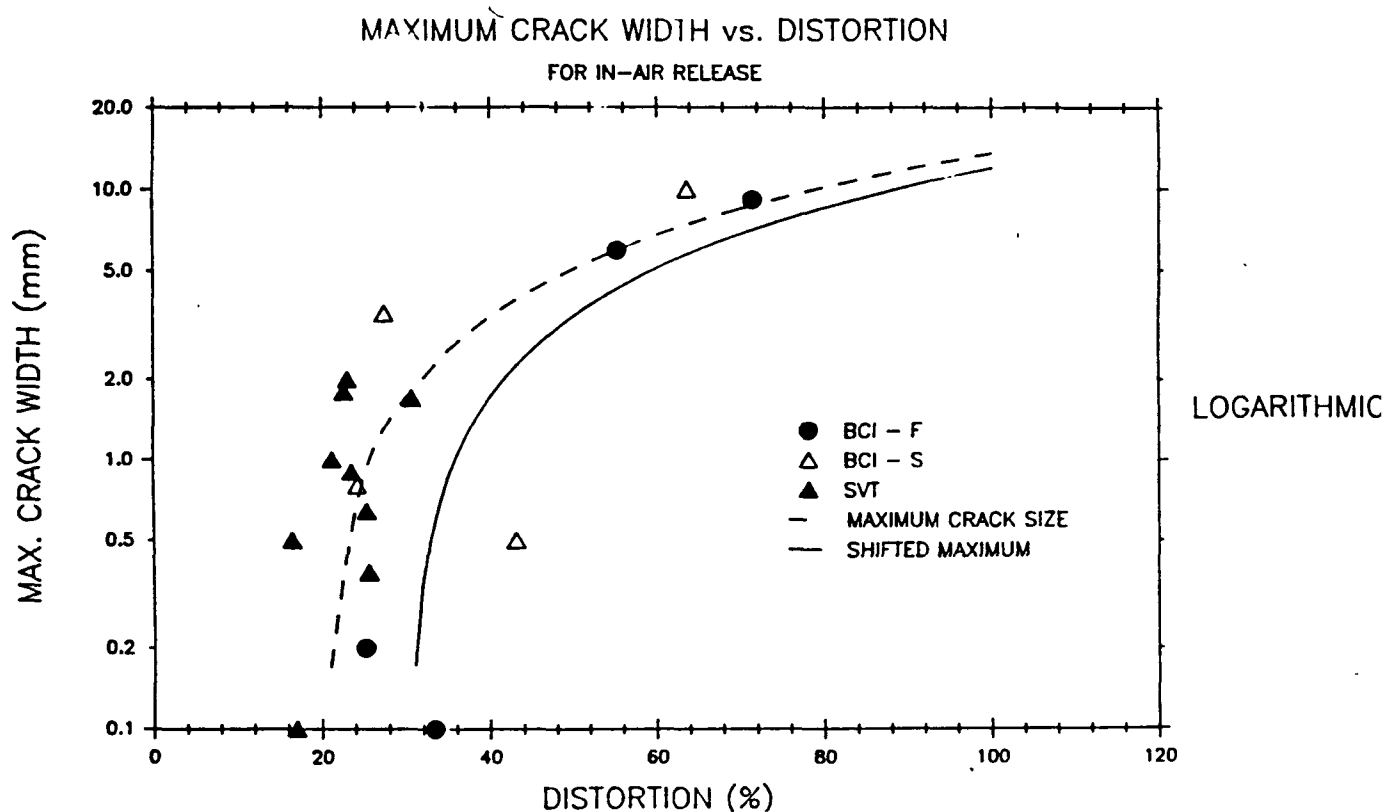


Figure D-18. Fraction of Fuel Release as a Function of Distortion for SRB Fragment Impacts





Figures 19a,b. Maximum Fuel Clad Crack Width as a Function of Distortion

Particle size distributions have been established for the fuel retained (not released) in the clad after an impact. Two separate distributions have been developed; one for impact against steel, and the second for impact against concrete. Each size distribution is split into two particle size regimes:

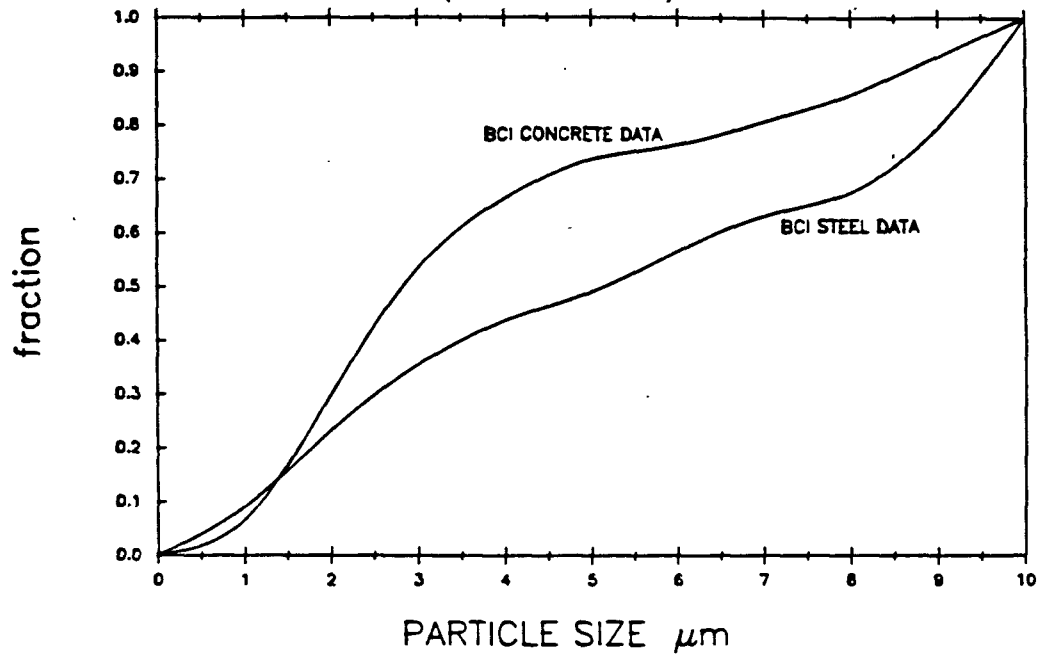
1. Particle sizes ranging from 0-10 microns
2. Particle sizes greater than 10 microns.

Definition of the retained particle size distributions, based on BCI (Bare Clad Impact) test results, are provided by Reference [6]. Plots of the distributions on a cumulative basis for each size regime are shown on Figures D-20a,b. A Weibull distribution is used for particle sizes greater than 10 microns. The appropriate scale and shape parameters are noted on Figure D-20b. In the determination of the particle size distributions for fuel released due to SRB or payload bay wall impacts, the particle size data related to steel impacts is employed. The retained particle size distributions for concrete impacts are used later in the evaluation of ground impacts. In the calculation of the particle size distribution for the fuel released, it is assumed that the released distribution follows the retained particle size distribution. The particle size distributions for a specific mass release is then computed by normalizing the retained size distribution on the basis of the maximum released particle size,  $D_{p-max}$ .

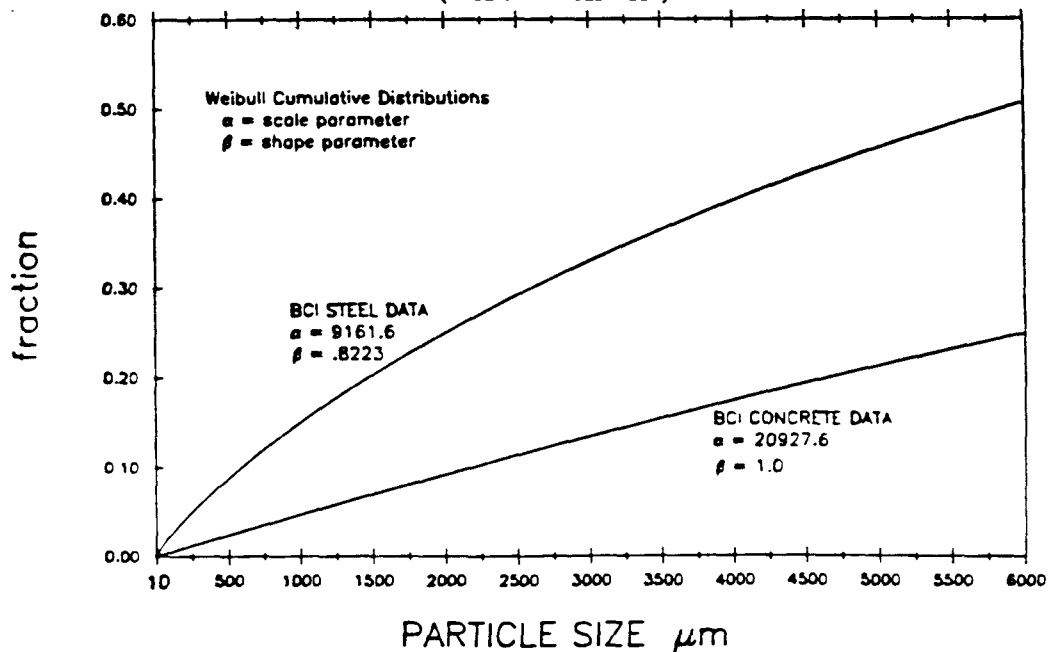
#### D.2.1.5 Trajectory Analysis of RTG Projectile

A trajectory analysis of the RTG projectile is performed to determine the location and velocity of ground impact. Inputs to the trajectory analysis are the initial in-air position, velocity, and direction of the RTG projectile at the time of the accident. The position of the projectile is determined at the accident time from the nominal Shuttle flight path. If the RTG is hit by an SRB fragment, the velocity and direction of the projectile are the result of both the Shuttle motion and the motion imparted to the RTG by impact. The principle of momentum conservation for inelastic impacts is applied to determine the velocity and direction component of the projectile motion due to a SRB fragment hit. A reduction factor to decrease this imparted velocity is used to account for the secondary impact of the RTG projectile into the

PARTICLE SIZE DISTRIBUTION 0. to 10. microns  
CUMULATIVE RETAINED PARTICLE SIZE DISTRIBUTIONS  
(IN CLAD PARTICLE SIZES)



PARTICLE SIZE DISTRIBUTION GREATER THAN 10. microns  
CUMULATIVE RETAINED PARTICLE SIZE DISTRIBUTIONS  
(IN CLAD PARTICLE SIZES)



Figures 20a,b. Fuel Clad Retained Particle Size Distributions

payload bay wall. If the RTG is not hit by a fragment, the projectile is assumed to separate from the Galileo spacecraft with an initial velocity vector equal to the Shuttle motion.

The trajectory of the RTG projectile is determined by formulating and solving the differential equations of motion of a point mass under gravitational and drag forces. The trajectory analysis is a three degree of freedom evaluation, and models only the translational motion of the projectile C.G. A fifth order Runge-Kutta finite difference technique is employed to solve the equations of motion. To enhance the trajectory solution, the following capabilities are included in the analysis:

1. The drag coefficient of the projectile is evaluated as a function of velocity
2. Air density is evaluated as a function of altitude.

Unique sets of ballistic data which describe each RTG projectile type are supplied as inputs to the LASEP2 program. Appropriate selections of these data sets are made based on the projectile type resulting from the fragment environment. The accuracy of the trajectory analysis was confirmed using closed form analytical solutions for zero and constant drag, shallow angle, projectile motion cases. Each analytical check verified the Runge-Kutta solution technique used in the LASEP2 program.

In each trajectory evaluation, the position and velocity of the projectile are continually monitored to determine if the projectile strikes a steel structure such as the tower or rotating service structure. A database which represents the launch complex steel structures as solid rectangular objects is provided as an input to the trajectory analysis. If the flight path of a projectile intersects any rectangular steel solid, the trajectory analysis is stopped and the location and velocity of the impact are recorded. Collisions into steel structures are categorized as steel surface ground impacts in the output of LASEP2. If a projectile does not impact a steel structure, the trajectory analysis continues until ground impact. The location of the ground impact and the corresponding velocity are determined in the process.

#### D2.1.6 Determination of Ground Impact Surface

A digitized surface map of the launch pad (39A) and surrounding area has been developed to determine the surface type of projectile ground impacts. Four material categories have been established to describe the launch pad surface types:

1. Sand
2. Steel
3. Concrete
4. Ocean.

A rectangular mesh placed over the entire launch pad area is used to identify surface elements on the map. The size of an individual element is 25ft x 25ft. Each square element has a material or surface type assigned to it. Figure D-21 graphically shows the digitized launch pad map with the surface categories displayed. For each trajectory analysis performed, the location of ground impact is used to define an element position and the corresponding impact surface.

In addition to performing the required function of impact surface determination, the launch pad surface map assists in the verification of the LASEP2 program. The positions of projectile ground impacts from numerous trials can be illustrated directly on the launch pad map. A review of these impact locations provides confirmation on the proper operation of specific program functions. Examples of projectile impacts displayed on the launch pad map are shown in Figures D-22 and D-23, for the random failure and near pad ET explosion accident cases, respectively. A ghost image of the launch pad is shown to highlight the impact positions. The data presented on these figures represents the output produced for 20 sample trial LASEP2 program runs.

#### D.2.1.7 Calculation of the Mass of Fuel Released On-Ground

The final step in the evaluation process of the SRB fragment environment is the calculation of the mass of fuel released on-ground. An outline of the procedure to determine the on-ground fuel release is shown in Figure D-24.

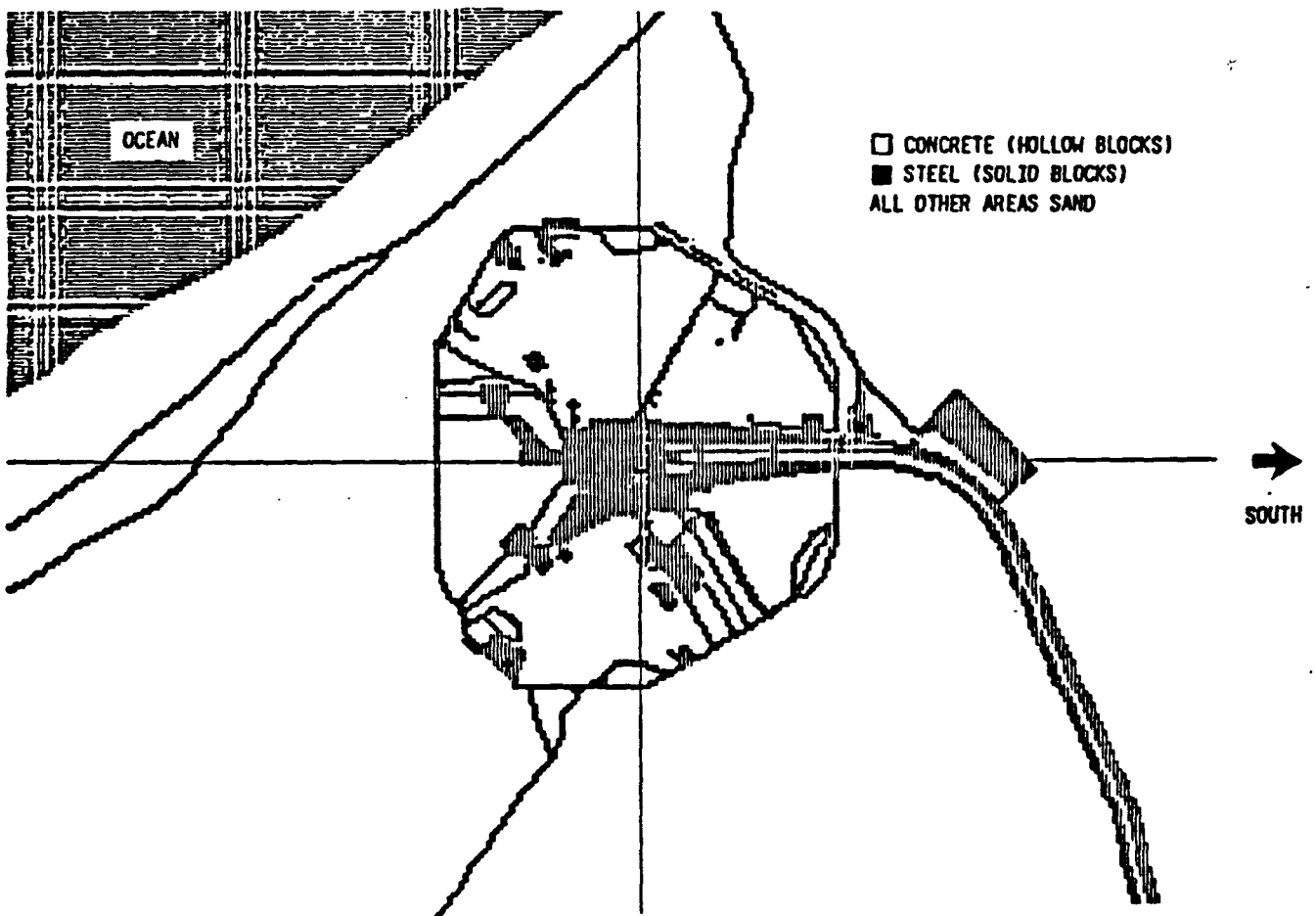


Figure D-21. Launch Pad (39A) Surface Map

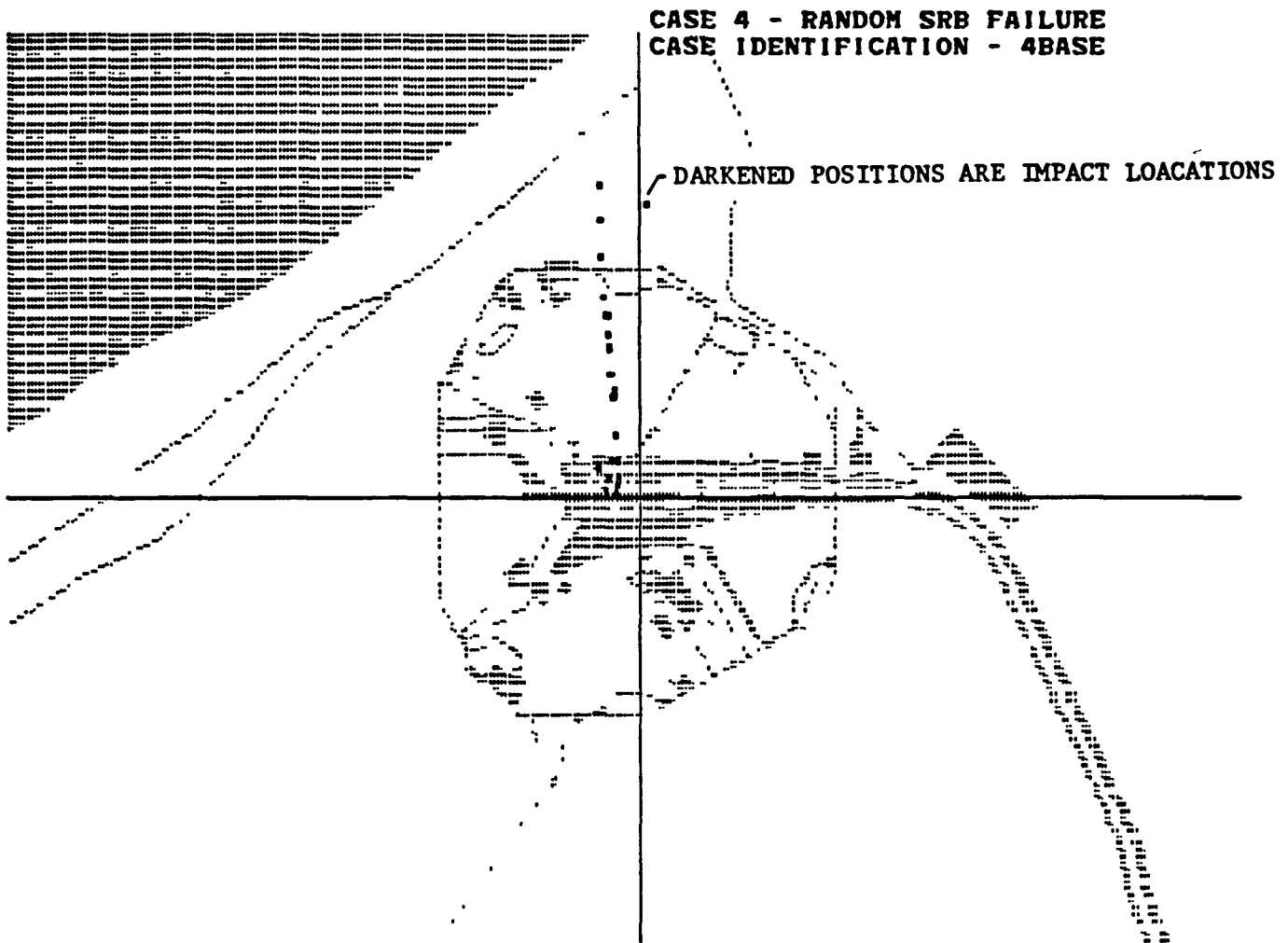


Figure D-22. Launch Pad Map Displaying Ground Impacts  
SRB Random Failure Case

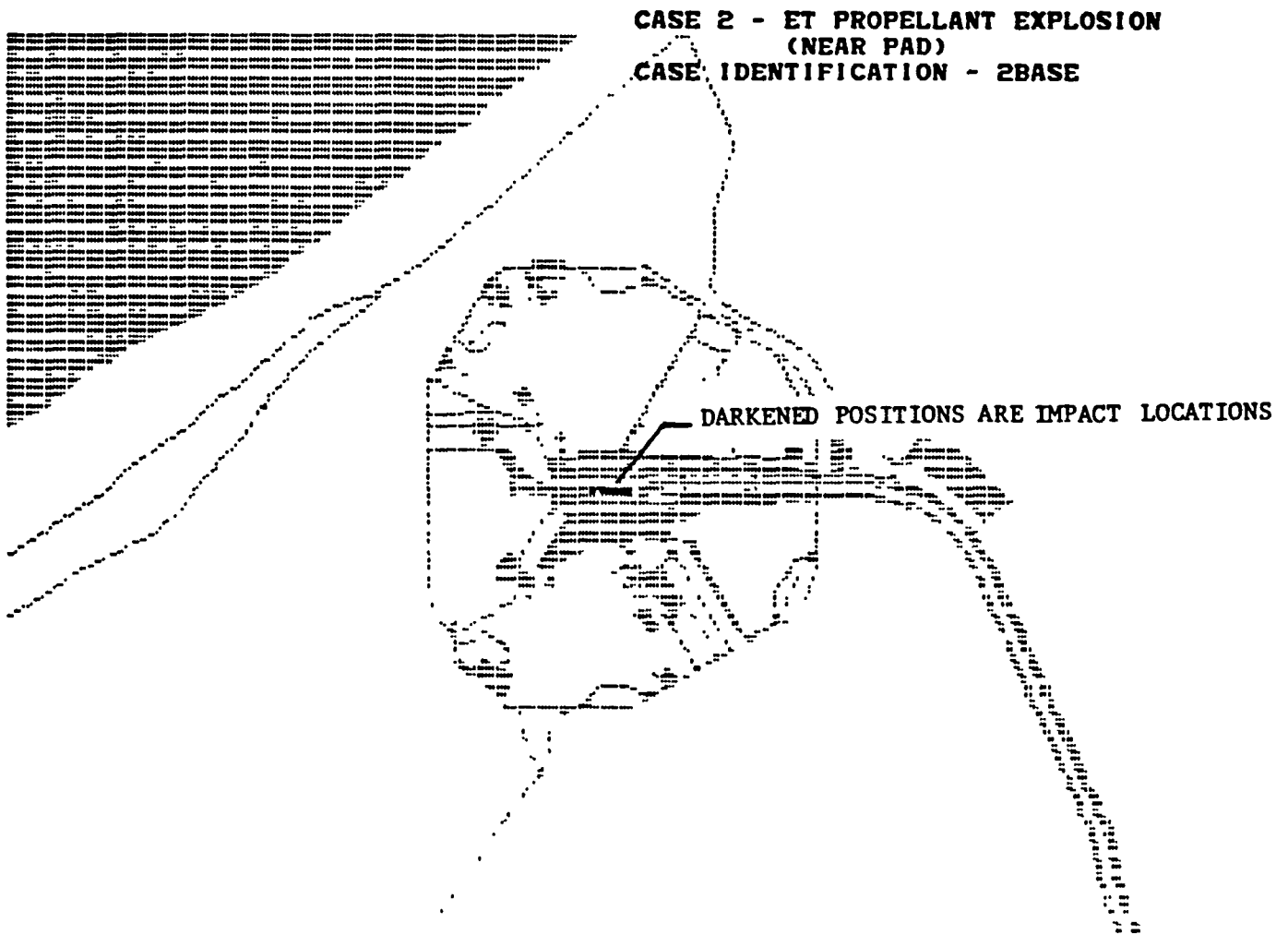


Figure D-23. Launch Pad Map Displaying Ground Impacts  
ET Propellant Near Pad Explosion Case



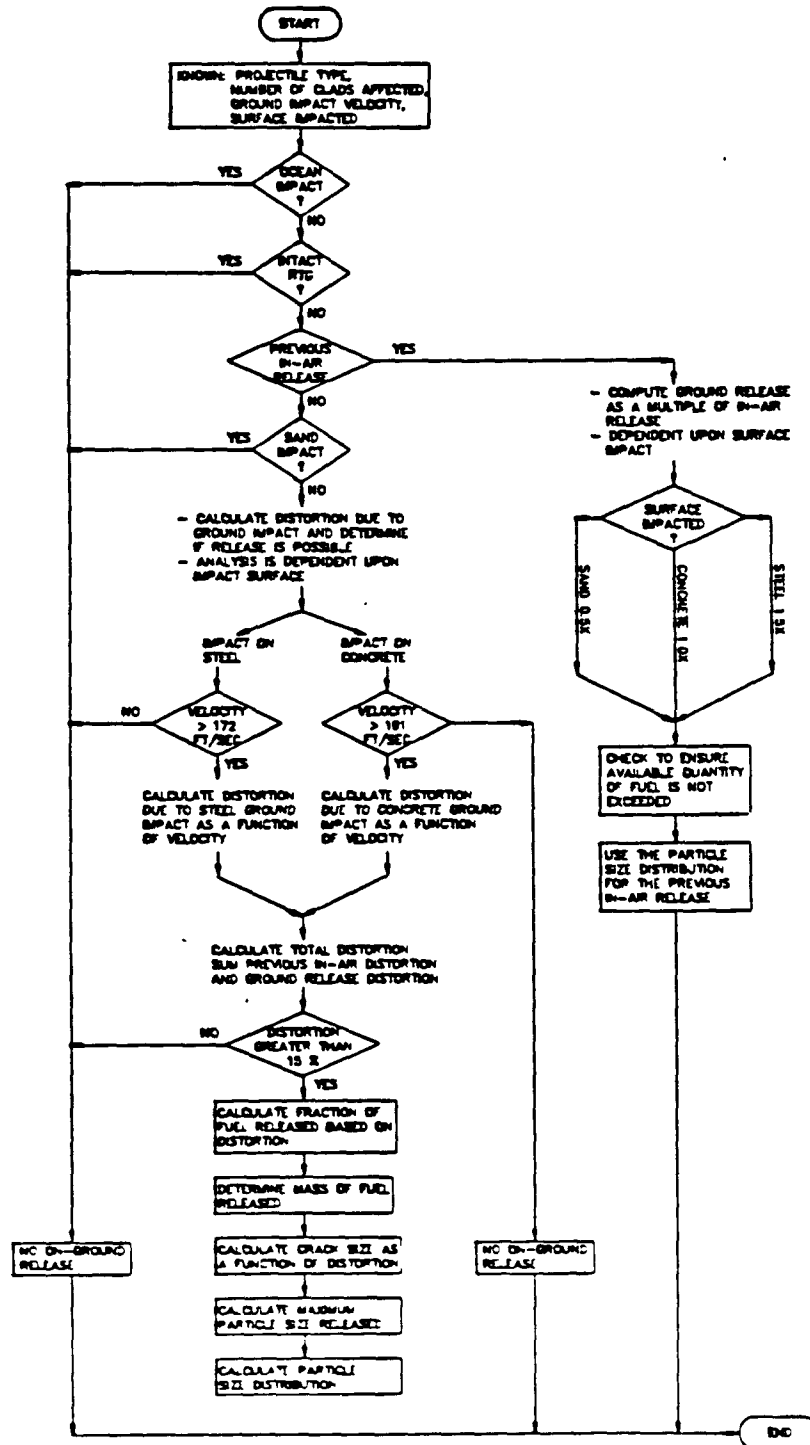


Figure D-24. Calculation of On-ground Mass of Fuel Released and Corresponding Particle Size Distribution

Several aspects of this algorithm are similar to the in-air fuel release analysis (Subsection D.2.1.4). The on-ground release determination is, however, more complex than the in-air evaluation, since the on-ground analysis must consider 1) the instances where an in-air release has occurred prior to ground impact, and 2) the additional distortion of the fuel clad caused by impact with the ground. For each trial in the accident evaluation, the mass of fuel released on-ground, if any, is determined. If a release occurs, the corresponding particle size distribution of the released fuel is calculated. The combined results of each individual trial are used to produce the following final output for each accident case:

1. The average mass of fuel released on-ground
2. Probability distribution of the mass of fuel released on-ground
3. Distribution of average particle size for the mass of fuel released on-ground.

The impact velocity and surface, which have been determined prior to this evaluation, are the primary inputs to the calculation of on-ground release. Referring to Figure D-24, if the RTG projectile lands in the ocean, no release is computed by the LASEP2 program. In addition, if the projectile resulting from the fragment environment is an intact RTG, a release determination is not performed. Impact of an intact RTG is treated outside of LASEP as described in Section 3.4.2.2.3 of Book 1, Volume II of this FSAR. A statistical breakdown of the impact surfaces and velocities for each projectile type is provided in the program output along with the on-ground fuel release results. A review of this surface impact data must be included to define completely the outcome of an accident case.

The impact of the RTG is treated separately outside of the LASEP program as mentioned above. The extent of damage (i.e., deformation) to the fueled clads in a RTG impact is based on the analysis presented in Appendix C. However, the trajectory characteristics of the vehicle and their relation to the surface media around the launch pad must be taken into account. The instantaneous impact point (IIP) of the vehicle is no longer over the MLP

(steel surface) after 5.5 seconds MET; that for concrete corresponds to a MET of 8.5 seconds. For these times, the effective impact velocity of the RTG cannot exceed 147 fps (44.8 m/s) and 245 fps (74.7 m/s), respectively, if vacuum free fall conditions are assumed. This latter condition does not exist in reality, and thus, the impact velocities will be even lower than the values quoted. For concrete impacts toward the upper end of the impact velocity range (i.e., 74.7 m/s), Appendix C indicates that moderate deformations could result for an end-on impact of the RTG. However, the judgment is made that, at these moderate velocities, the RTG will stay intact (i.e. although badly damaged, it will still contain the GPHS modules within the insulation package) and provide effective containment. Impacts of the RTG on sand can occur at higher velocities, but Appendix C indicates that, even at the terminal velocity of the RTG in the stable end-on attitude, the resulting deformation of the clads is not large enough to cause a breach.

In the determination of an on-ground release, a distinction is made for those events which have an in-air release and those events which have no in-air fuel release. Figure D-24 shows the separate analysis paths for these two conditions. For the evaluation of the no in-air release case, only projectile impacts upon steel and concrete are considered for possible on-ground fuel releases. If the RTG projectile (aeroshell or fueled clad) impacts sand, no fuel release is evaluated. The distortions caused by ground impacts are calculated from relationships derived from BCI test results. A separate linear relationship of fuel clad distortion as a function of impact velocity is provided for steel and concrete ground impacts. These analytical expressions are applied to both fueled clad and aeroshell projectile type impacts. In addition to the results supplied on distortion, BCI test data also provides impact velocity threshold values below which there is no release. If the impact of a projectile on concrete does not exceed 191ft/sec (58.3m/sec) or the velocity of projectile impact on steel is not above 172ft/sec (52.6m/sec), then no on-ground fuel release is calculated. If these velocities are exceeded, the distortions resulting from concrete and steel impacts are computed as follows based on a least squares linear fit to the data:

For concrete:  $D' = -32.19 + .2905V$

For steel:  $D' = -38.44 + .3444V$

where  $V$  is velocity in ft/sec and  $D'$  is percent distortion. The distortion,  $D'$ , obtained from the ground impact, is combined with distortion from the in-air fragment impacts. The square root of the sum of the squares of these two values is the total ground distortion used to calculate the mass of fuel released on ground. (See note in Section D.2.1.3 on addition of distortions for source terms in this AMD.)

Using this total distortion value, the calculation of the on-ground fuel release is similar to the in-air determination. If the total ground distortion is less than 15%, then there is zero release of fuel on-ground.

For distortions above 15%, the fraction of available mass released is computed as

$$R = 1.0 - \text{EXP} \left[ -.04 \left[ \frac{D - 15}{33} \right]^5 \right]$$

where  $D$  is the total on-ground distortion. The particle size distributions of ground releases are computed in the same manner defined for the in-air releases (Subsection D.2.1.4). The maximum crack width for on-ground releases is computed from

$$W_{\text{MAX}} = .17 (D-15)$$

The maximum corresponding particle size is

$$D_{\text{P\_MAX}} = \frac{W_{\text{MAX}}}{2}$$

Referring back to Figure D-20, the retained particle size BCI data for steel and concrete is used for on-ground released particle size distributions for steel and concrete ground impacts respectively.

The calculation of the on-ground fuel release for events which had a previous in-air release is a straightforward process as shown in Figure D-24. The on-ground mass of fuel released is computed as a multiplying factor of the in-air fuel mass released. These factors, which depend upon the ground impact surface are:

1. Sand impact: On-ground release = .5 x in-air release
2. Concrete impact: On-ground release = 1.0 x in-air release
3. Steel impact: On-ground release = 1.5 x in-air release

The value of these multiplying factors and the approach to calculate secondary on-ground releases is consistent with the analysis provided in the 1985 safety analysis report, Reference [7]. In the application of this method, a check is performed in the LASEP2 code to ensure that the available amount of fuel is not exceeded in an on-ground release. In each of these events, the particle size distribution for the secondary ground release is assigned to follow the same release distribution determined for the initial in-air release.

Determination of the on-ground release completes the simulation of an accident environment. The response of an RTG from the instant of accident initiation to the final impact on ground has been determined. The data accumulated during a trial is recorded and stored for the purposes of statistically reporting the outcome of an accident. As illustrated in Figure D-2, the next trial of the accident case is initiated after the completion of the on-ground release analysis.

#### D.2.2 ET PROPELLANT EXPLOSION ENVIRONMENTS

A number of component or system failures can lead to the massive dump of ET tank propellants (LOX/LH<sub>2</sub>). For the tower impact and near pad explosion cases, the propellants pool on the horizontal surfaces of the MLP (mobile launch platform) or collect in the flame trench. Ample mixing of the ET propellants occurs during the formation of these pools, and a subsequent ignition causes an explosion. Three types of pool explosions have been defined in the Shuttle Data Book:

1. MLP pool explosion
2. In-trench (flame trench) pool explosion
3. Aft compartment initiated pool explosion.

For the tower impact and near pad accidents, an input to the LASEP2 code specifies which pool explosion types are used in the accident evaluation. In the in-flight accident case, the released propellants may form an explosive vapor cloud. A complete description of the accident scenarios and environments is provided in the Shuttle Data Book. The explosion characteristics and the location of the Shuttle differ in each explosion case, but the same basic methodology is applied to analyze these accidents. Thus, a general description of the ET propellant explosion evaluation describes the analysis performed in the LASEP2 program for each individual accident case.

The evaluation of the ET propellant explosion environment has similar or common analysis elements with the SRB fragment environment. An overview of the evaluation process for the ET propellant explosion environments is shown in Figure D-2. The start of each simulation or trial begins with the random selection of the accident failure time from an input range. For specific cases of evaluating an explosion environment prior to launch, the input range can be set to zero, causing all simulations to occur with the Shuttle on-pad (prelaunch position). The accident time is used to determine the Shuttle position and motion from its nominal trajectory. For the tower impact (tipover) case, the location of the Shuttle is treated as a special case. A tilt angle of 0° to 25° from vertical is randomly selected for the Shuttle orientation. The random selections of the accident time and the tilt angle are performed on a uniform basis.

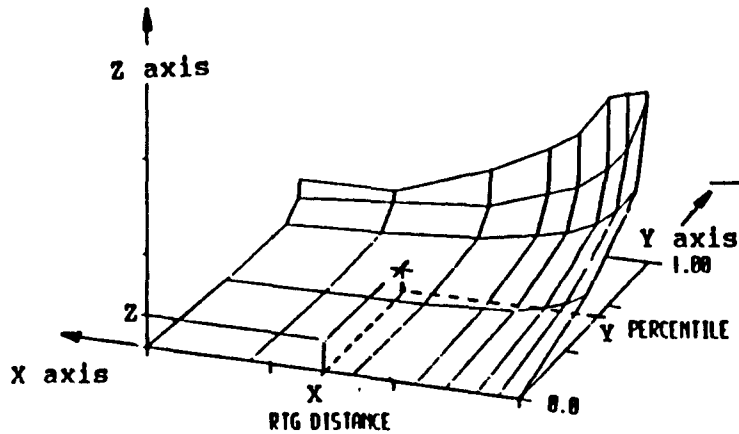
#### D.2.2.1 Determination of ET Explosion Characteristics

The explosion of the ET propellants results in a blast wave which implodes the payload bay wall and doors into the RTGs. Sections of the payload bay, which are driven into the RTG, are regarded as payload bay fragments or flyer plates. Since each Galileo RTG is positioned very near to the payload bay walls, the flyer plates are assumed to always impact the RTG. In each impact, all 18 modules are hit. In modeling the implosion of the Orbiter structure,

it is assumed that no motion is imparted to the RTG projectile as a consequence of a flyer plate impact. The basis for this assumption is the symmetric or near symmetric blast wave pressure loading on the external payload bay walls and doors. The impact of the flyer plate into the RTG is assumed to separate the RTG from the Galileo spacecraft and move it towards the center of the payload bay. Since the implosion conditions are relatively equal about the circumference of the Orbiter fuselage, no resultant flyer plate forces exist to propel the RTG away from the center of the payload bay. Thus, the net motion of the post impact RTG projectile due to impact is zero. Following the flyer plate impact, the RTG projectile resulting from the hit is subjected to the explosion blast wind which accelerates the projectile. To evaluate the specific response of the RTG to these events, the following characteristics of the explosion must be determined:

1. Flyer plate velocity
2. Peak static overpressure
3. Static impulse.

For the tower impact and near pad explosion accident cases, these three characteristics are determined as a function of RTG distance from the explosion and a randomly selected number. An example of the determination process is shown in Figure D-23. The Shuttle Data Book provides tabulations of the explosion characteristics based on the RTG distance from explosion and the percentile level of explosion severity. A unique data base is provided for each pool explosion type and additional tabulations are provided at various Shuttle tilt angles. The example of Figure D-25 is provided for an MLP pool explosion at a zero tilt angle. The data bases provided by the Shuttle Data Book can be graphically represented as the three dimensional surfaces shown on this figure. The RTG distance from the explosion is determined from the Shuttle location at the accident failure time. Using this distance and randomly selecting a number between 0 and 1 from a uniform distribution, the function value or required characteristics are determined. The selection of the three explosion characteristics is performed using the same random number. Only a single random number is required since the explosion characteristics are interdependent.

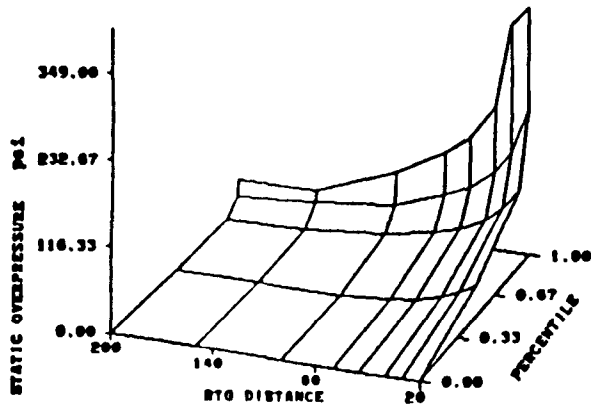


**GENERAL EXPLOSION CHARACTERISTIC  
DETERMINATION PROCESS**

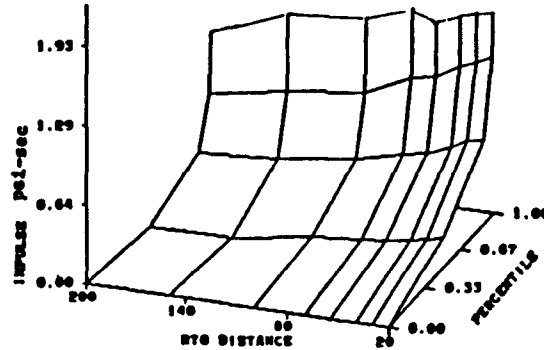
1. KNOW X - CALCULATED VALUE OF RTG DISTANCE FROM EXPLOSION
2. KNOW Y - RANDOMLY SELECTED VALUE BETWEEN 0 AND 1
3. GET Z - DETERMINE FUNCTION VALUE DEPENDENT UPON X AND Y

D-53

**PEAK STATIC OVERPRESSURE  
AS A FUNCTION OF EXPLOSION SEVERITY  
AND RTG DISTANCE FROM EXPLOSION**



**STATIC IMPULSE  
AS A FUNCTION OF EXPLOSION SEVERITY  
AND RTG DISTANCE FROM EXPLOSION**



**FLYER PLATE VELOCITY  
(SHUTTLE TILT = 0)  
AS A FUNCTION OF EXPLOSION SEVERITY  
AND RTG DISTANCE FROM EXPLOSION**

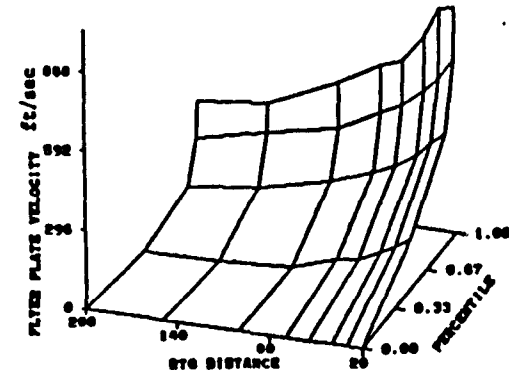


Figure D-25. Determination of ET Propellant Explosion Characteristics for Tower Impact and Near Pad Explosion Cases

WP2690/1886-728/JD



The method of determining the explosion characteristics for the vapor cloud explosion is substantially different than the procedure used for pool explosions. The characteristics of the vapor cloud explosion are provided as a function of the RTG distance from the center of explosion. The distance to the RTG from the explosion center is determined by using the Shuttle vehicle velocity at the instant of the accident times a one (1) second interval as suggested in the Shuttle Data Book.

#### D.2.2.2 Damage Evaluation of RTG from Flyer Plate Impact

The damage evaluation process of a flyer plate impact into the RTG is similar to the analysis procedure for a SRB fragment impact into the RTG. As described in Section D.2.1.3, the evaluation is a two part process:

1. Determination of RTG projectile status after flyer plate impact
2. Calculation of the fueled clad distortion resulting from the impact.

The RTG post impact projectile status is defined by evaluating the threshold energy levels of the impacting flyer plate. The possible projectile types caused by a flyer plate impact are shown in Figure D-26. Table D-6 provides the range of energy levels for RTG case and aeroshell failure. The method of determining the projectile status, from these energy level inputs, is outlined in Figure D-15.

Similar to the process described for SRB fragment insults, the fueled clad distortion caused by a flyer plate impact into the RTG is calculated from a database of hydrocode impact analyses. The analytical procedure used to determine the fuel clad distortion is given in Figure D-16. As before, the distortion response between the leading and aft clads is differentiated.

In the evaluation of ET propellant explosion environments, only flyer plate impacts are considered in determining the in-air damage to the RTG. The relatively low overpressures produced by the explosions do not represent a damaging threat to the RTGs. In addition, significant secondary in-air impacts of the RTG projectile are regarded to be implausible. Thus, for ET

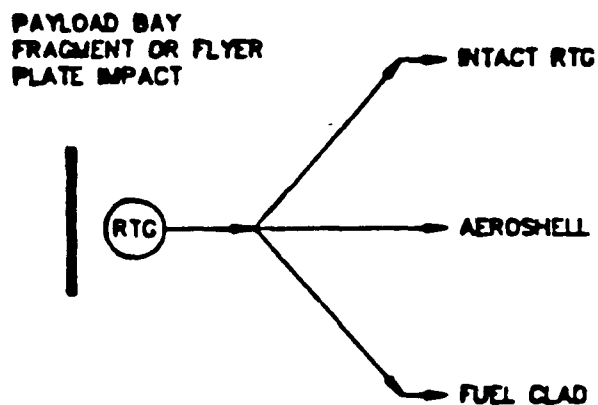


Figure D-26. Possible RTG Projectile Types Resulting from Flyer Plate Impacts

Table D-6. Threshold Energy Levels of RTG Case and Aeroshell Failure for Flyer Plate Impacts

IMPACT CASE	RTG CASE FAILURE ENERGY LEVELS			AEROSHELL FAILURE ENERGY LEVELS		
	ft-lb			ft-lb		
	MIN	MAX	MEAN	MIN	MAX	MEAN
PAYLOAD BAY FRAGMENT OR FLYER PLATE INTO THE RTG	9114	11139	10126	209993	256658	233325

propellant explosion environments, the amount of fuel released in-air is based solely on the damage caused by flyer plate impacts.

#### D.2.2.3 Calculation of the Mass of Fuel Released In-air

The distortion of the fueled clads resulting from flyer plate impacts is used to calculate the amount of fuel released in-air and the corresponding particle size distribution. The method used to determine these quantities has been previously described in Subsection D.2.1.4. The procedure used to calculate the in-air release and particle size distribution for ET propellant explosion environments is exactly the same as the process employed for SRB fragment environment evaluations.

#### D.2.2.4 Acceleration of the RTG Projectile by the Explosion Blast Wind

In each accident case, the blast wind generated by the propellant explosion accelerates the RTG projectile. For the pool explosion accidents, the direction of acceleration is assumed to be vertically upward from the pad or flame trench surfaces. In the vapor cloud explosion case, the direction is taken along the nominal flight path of the shuttle (aft to forward). Within the LASEP2 program, the acceleration of the projectile is based on the dynamic component of the air following the blast shock wave in the drag phase of loading. The effect of static pressure and reflected pressure during the diffraction phase of loading is not evaluated, but this contribution would be expected to be negligible. In calculating the projectile acceleration, the force of gravity is neglected, since the duration of the blast wave dynamic component is typically on the order of hundredths of a second. On this basis, the projectile equation of motion is

$$m \left[ \frac{d}{dt} V \right] = \frac{1}{2} \cdot C_D \cdot A \cdot \rho_g \left[ V_g - V \right]^2$$

where:

m = projectile mass  
V = projectile velocity  
V<sub>g</sub> = velocity of the gas  
C<sub>D</sub> = projectile coefficient of drag  
A = projectile frontal area  
ρ<sub>g</sub> = density of the surrounding gas (air) behind the blast front  
t = time.

The ballistic coefficient is defined as

$$\beta = \frac{m \cdot g}{C_D \cdot A} \quad 1)$$

where g is gravitational acceleration. In computing the projectile acceleration, a separate ballistic coefficient is assigned to each projectile type. The following ballistic coefficients were used in the LASEP2 program for the ET propellant explosion evaluations:

RTG (side on): = 14.02 lb/ft<sup>2</sup>  
Aeroshell: = 32.44 lb/ft<sup>2</sup>  
Fueled Clad: = 69.00 lb/ft<sup>2</sup>.

The values of these coefficients are not varied as a function of projectile velocity. Rearranging Equation 1) and integrating gives the projectile change in velocity caused by the blast wind

$$\Delta V = \frac{1}{2} \cdot \frac{C_D \cdot A}{m} \cdot \int_0^T \rho_g \cdot [V_g - V]^2 dt \quad 2)$$

The upper bound of integration, T, is the total duration of the overpressure pulse. The quantities of gas flow velocity (V<sub>g</sub>) and density (ρ<sub>g</sub>) are functions of time and vary throughout the time span of the overpressure pulse. The duration of the overpressure pulse can be determined for the values of static impulse (I<sub>s</sub>) and peak static overpressure (P<sub>s\_peak</sub>).

Determination of these two explosion characteristics is described in Subsection D.2.2.1. The static impulse is defined as

$$I_S = \int_0^T P_S dt$$

Assuming the pulse to be triangular as shown in Figure D-27, the pulse duration is computed as

$$T = \frac{2 \cdot I_S}{P_{S\_PEAK}}$$

and the static overpressure at any time after the shock wave is calculated as

$$P_S = \left[ \frac{T-t}{T} \right] \cdot P_{S\_PEAK} \quad 3)$$

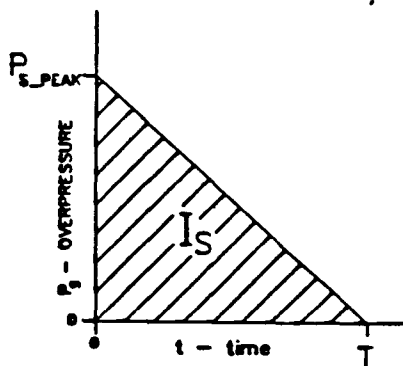


Figure D-27. Triangular Overpressure Pulse

The density and velocity of the air behind the shock wave can be computed using the Rankine-Hugoniot relationships for a normal shock wave. The density is given by

$$\rho_g = \frac{2 \cdot \Gamma \cdot P_o + (\Gamma + 1) \cdot P_S}{2 \cdot \Gamma \cdot P_o + (\Gamma - 1) \cdot P_S} \cdot \rho_o \quad 4)$$

and the velocity is calculated from

$$V_g = a_o \cdot \sqrt{\frac{2 \cdot P_S^2}{\Gamma \cdot P_o \cdot (\Gamma + 1) \cdot P_S + 2 \cdot \Gamma \cdot P_o}} \quad 5)$$

where:

- $P_o$  = ambient atmospheric pressure
- $\Gamma$  = ratio of specific heats for air
- $\rho_o$  = ambient atmospheric density
- $a_o$  = local speed of sound in air.

Substituting Equations 3) through 5) back into Equation 2) gives the complete expression for the acceleration of the projectile by the blast wave. Since the Rankine-Hugoniot relation applies only to the relatively thin layer of shocked gas behind the shock front, the manner in which it is used should produce conservative results. However, regardless of the conservatism, the contribution to the velocity of the propelled object should be minor because of the relatively low overpressures. In the LASEP2 program, Equation 2) is integrated numerically using a fifth order Runge-Kutta technique. The solutions provided by the Runge-Kutta method were independently verified by an analysis based on the Euler integration technique.

#### D.2.2.5 Trajectory, Ground Impact and Ground Release

The velocity and direction of the projectile due to the blast wind are combined with the Shuttle motion to provide the input velocity vector for the trajectory analysis. From this point onward, as shown in Figure D-2, the remainder of the ET propellant explosion evaluation is the same as the SRB fragment evaluation. The trajectory analysis determines the ground impact location and velocity. The impact location identifies the impact surface. The impact velocity, impact surface, and projectile type are then used to compute the on-ground fuel release, if any, and the particle size

distribution. A description of the trajectory analysis, impact surface determination, and on-ground release calculation are contained in Subsections D.2.1.5, D.2.1.6, and D.2.1.7, respectively. Following the computation of on-ground release, the evaluation process is restarted for the next trial.

### D.3. LASEP VERIFICATION

The LASEP2 program was developed in a modular fashion using standard FORTRAN 77. Each analysis function and utility function was represented as a subroutine or a FORTRAN function. There were three phases to the code verification process:

1. Module Verification
2. Program Verification
3. Program Validation

#### Module Verification

Checks were performed on each module, subroutine, or group of subroutines separate from the rest of the program. Test driver programs were written to exercise and verify each module. These test driver programs were run with various sets of input, and the corresponding outputs were checked for correctness. Extensive write statements were used, and the modules were verified to have the correct values at each point.

#### Program Verification

Several compiler options were utilized to assist in finding and correcting programming errors.

- Bounds check: This option checks all the arrays in the program and verified that the declared array bounds are not exceeded.

- **List File:** The compiler list file was created with the cross reference mapping option on. This produced a list of all the variables, arrays and characters, and the line number where they are assigned, used, declared, etc.
- **Debug:** This option allows additional printout to be obtained by compiling lines that contain a "D" in column 1 as executables. If this option is not selected, these lines are compiled as comments. (NOTE: This is a VAX FORTRAN compiler option.)
- **Implicit None:** This option forces all variables to be explicitly declared. (NOTE: This is a VAX FORTRAN compiler option.)

Using these aids, the parameters passed in all subroutine and function calls were checked. The printout at each step in the program again verified correctness. It also verified that the subroutines and functions were behaving the same way within the main program as they did in the test programs. Use of the implicit none command helped catch spelling mistakes. All the controlled database user options were exercised so that each possible path was verified in the same manner.

### Program Validation

The LASEP2 program output was validated, that is checked for reasonableness, in several ways. In general, subroutine/program outputs were checked or duplicated with one or more of the following: a third party software program, another independent piece of in-house software, graphically, by hand calculations, or against test results.

Some of the specific validation techniques are described below.

The hit determination subroutine was checked with different graphics tools: 1) Adams, a dynamics analysis package, and 2) a separate VAX program developed in-house. Both of these programs showed excellent agreement for type of hit (edge-on or face-on) and hit or miss determination for given fragment azimuth, initial orientation and spin rate.



The projectile trajectory calculation is performed using a fifth order Runge-Kutta solution. The output from this subroutine was checked using closed form analytical solution for zero and constant drag, shallow angle projectile motion cases. LASEP2 also provided graphical output of ground impact locations. This showed that the ground impact locations did follow the shuttle flight path.

The momentum exchange subroutines for determining projectile resultant velocity were checked with hand calculations for the whole range of coefficients of restitution.

The distortion calculation subroutines used a hydrocode database supplied by Fairchild. The distortion output compared well with test results.

With the LASEP2 analysis, there were two aspects that determined the release of fuel: 1) the probability of an SRB fragment hit (specifically an edge-on hit), and 2) the velocity of the fragment at the point of impact (translational and spin). Because of their importance in driving fuel releases, these two areas received some additional attention.

The probability of getting an edge-on hit, according to LASEP2, was very low, .3 to .7%. In order to validate this low value, an analysis was made independently of LASEP of the edge-on hit probability. This analysis was based on the RTG hitting anywhere along the perimeter of the fragment with equal probability. The resulting, probability .5-.9%, compared well with the numbers coming out of LASEP2. Also, since these type of hits are so rare, a method of retaining the initial seeds of the random process for edge-on impacts was devised. This allowed these hits to be closely scrutinized with the debug output.

Probability of impact for both face-on and edge-on fragments received independent validation from Research and Development Association (RDA). They developed a model, completely separate from LASEP2, that determined whether or not an SRB fragment could hit the RTG. In the random SRB failed case, RDA's numbers on probability of hit, 17-19%, compare well with the ones produced by LASEP2, 18-20%. Both of these models compare well with an impact probability

determined strictly from a fragment flux density approach, 17.7%. The Range Destruct case has a higher probability of hit out of LASEP2, 23-33% for each RTG, because of the azimuthal swerve that was included by JPL.

The fragment velocity distributions and spin rate values were verified to match the input distributions. Reasonable impact velocities resulted from the vector sum of the spin and translational velocities. These velocities correspond to the measured velocity of fragments in a previous Titan 34-D accident.

#### D.4 LASEP OUTPUT FOR ACCIDENT SCENARIOS

Table D-7 presents a matrix of the LASEP cases run and their relation to the representative accident scenarios, accident environments, and subphase time periods. The alphanumeric designations in each block (e.g., 1S2, 1E, 1V, etc.), refer to the FAST branches to which they apply. The numeric values in the lower right hand corner of some of the blocks refer to the conditional probability of the accident occurring in the given time period; they add to a value of unit (1.0) for any given accident (e.g., SRB Random Failure). One can see that a total of 13 individual accident scenarios/environments/time period combinations were analyzed with the LASEP. The total number of runs made was 21, which included the eight (8) additional runs needed for the end-module deformation relation as contrasted with the mid-module relation. These additional runs were associated with the SRB Random Failure scenario (5 runs) and the Range Destruct scenario (3 runs).

Typical output from the LASEP is shown in Tables D-8, D-9 and D-10 for the SRB Case Rupture scenario and environment during the 0-10 second period of Phase 1. Near the top of Table D-8 are shown the "in-air impact breakdown of projectile types". The large numbers shown under each object (i.e., RTG, Aeroshell, Fuel Clad) are the total number of clads included since LASEP records all events by number of clads. The total of the numbers for the three (3) objects is 1,440,000 which is simply the total number of fueled clads in two (2) RTGs times 10,000 trials. Table D-9 shows the average in-air and on-ground releases, the maximum or largest release in-air and on-ground out of the 10,000 trials made, and the particle size distributions for each.

Table D-7. LASEP Accident/Subphase Matrix

	MET	LEFT SRB FAILS TOWER IMPACT	ET FAILURE ON/NEAR PAD	ET FAILURE IN FLIGHT	SRB RANDOM FAIL	RANGE DESTRUCT
PHASE 0	T-0		PAD/TRENCH EXPL. 0'			
	2 SEC	PAD/TRENCH EXPL. 1S2	AFT COMP. EXPL. 1E		SRB FRAG. W/P&T EXPL.*	SRB FRAG. W/P&T EXPL.*
	10 SEC		PAD/TRENCH EXPL. 1V		1S1 0.500	1R .0776
	20 SEC			VAPOR CLOUD EXPLOSION 1S3 1S4 1E 1V	SRB FRAG. 1S1 0.125	SRB FRAG. 1R
PHASE 1	30 SEC				SRB FRAG. 1S1	
	70 SEC				0.2361	
	105 SEC				SRB FRAG. 1S1 0.0972	0.7426
	120 SEC				SRB FRAG. 1S1 0.0417	SRB FRAG. 1R 0.1172
	128 SEC					0.0625

\*INDICATES INCLUSION OF THE ENVIRONMENT FOR THE PAD AND TRENCH EXPLOSIONS.

Table D-8. Excerpts from Typical LASEP Output

RANDOM SOLID ROCKET BOOSTER (CASE RUPTURE) FAILURE

MISSION ELAPSED TIME RANGE : 0- 10  
NUMBER OF MONTE CARLO TRIALS : 10000

TOTAL NUMBER OF FRAGMENTS EVALUATED : 83124  
NUMBER OF EVENTS THAT RESULTED IN A HIT : 1933 ( 18.33%)  
TOTAL NUMBER OF FACE-ON HITS : 1889 ( 18.89%)  
TOTAL NUMBER OF EDGE-ON HITS : 44 ( 0.44%)  
TOTAL NUMBER OF PROPELLANT SIDE HITS : 746 ( 7.46%)

IN-AIR IMPACT BREAKDOWN OF PROJECTILE TYPES

RTG	AEROSHELL	FUEL CLAD
808064	456180	75756
63.06%	31.68%	5.26%

BREAKDOWN OF GROUND IMPACT VELOCITIES AND SURFACES BASED ON IN-AIR DISTORTIONS

RTG PROJECTILE : 63.06%

OVERALL SURFACE BREAKDOWN:

SAND : 0.03%  
STEEL : 60.82%  
CONCRETE : 39.15%  
OCEAN : 0.00%

AEROSHELL PROJECTILE : 31.68%

OVERALL SURFACE BREAKDOWN:

SAND : 4.07%  
STEEL : 72.89%  
CONCRETE : 23.04%  
OCEAN : 0.00%

FUEL CLAD PROJECTILE : 5.26%

OVERALL SURFACE BREAKDOWN:

SAND : 42.85%  
STEEL : 26.00%  
CONCRETE : 31.15%  
OCEAN : 0.00%

IN-FIRE BREAKDOWN OF GROUND IMPACT VELOCITIES AND SURFACES BASED ON IN-AIR DISTORTIONS IN FIRE RADIUS LIMIT = 500.0

RTG PROJECTILE :

OVERALL SURFACE BREAKDOWN:

SAND : 50.00%  
STEEL : 100.00%  
CONCRETE : 100.00%  
OCEAN : 0.00%

AEROSHELL PROJECTILE :

OVERALL SURFACE BREAKDOWN:

SAND : 58.30%  
STEEL : 100.00%  
CONCRETE : 97.98%  
OCEAN : 0.00%

FUEL CLAD PROJECTILE :

OVERALL SURFACE BREAKDOWN:

SAND : 18.81%  
STEEL : 99.43%  
CONCRETE : 62.82%  
OCEAN : 0.00%

Table D-9. Typical LASEP Output for Source Term Data

AVERAGE MASS OF FUEL RELEASED STATISTICS (GRAMS)

IN-AIR : 0.009318652  
 DN-GROUND : 0.051703032

MAXIMUM MASS FUEL RELEASES (GRAMS)

IN-AIR : 47.172245026 AT 10 SECONDS  
 DN-GROUND : 75.554672241 AT 10 SECONDS

AVERAGE PARTICLE SIZE DISTRIBUTION

PARTICLE SIZE (MICRO-M)	IN - AIR	DN - GROUND
0. - 1. ]	0.1142	0.0943
1. - 2. ]	0.1780	0.2286
2. - 3. ]	0.1563	0.2250
3. - 4. ]	0.1055	0.1310
4. - 5. ]	0.0684	0.0892
5. - 6. ]	0.0955	0.0490
6. - 7. ]	0.0826	0.0651
7. - 8. ]	0.0545	0.0570
8. - 9. ]	0.1538	0.1161
9. - 10. ]	0.2621	0.1658
10. - 20. ]	0.9731	1.0858
20. - 30. ]	0.8839	1.0460
30. - 40. ]	0.8298	1.0704
40. - 50. ]	0.7916	1.0017
50. - 60. ]	0.7638	0.9905
60. - 70. ]	0.7360	0.9766
70. - 80. ]	0.6978	0.9593
80. - 90. ]	0.7221	0.9703
90. - 100. ]	0.6874	0.9546
100. - 200. ]	6.2805	9.2553
200. - 300. ]	5.6208	8.9279
300. - 400. ]	5.2039	8.7086
400. - 500. ]	4.8902	8.5413
500. - 600. ]	4.6173	8.3818
600. - 700. ]	4.4565	8.2790
700. - 800. ]	4.2492	8.0612
800. - 900. ]	4.0752	7.0392
900. - 1000. ]	3.8750	5.7394
1000. - 2000. ]	32.1485	13.8680
2000. - 3000. ]	16.2262	2.9769
3000. - 4000. ]	0.0000	0.0000
4000. - 5000. ]	0.0000	0.0000
5000. - 6000. ]	0.0000	0.0000
> 6000. ]	0.0000	0.0000

CORRESPONDING PARTICLE SIZE DISTRIBUTION

PARTICLE SIZE (MICRO-M)	IN - AIR	DN - GROUND
0. - 1. ]	0.1089	0.0799
1. - 2. ]	0.1698	0.1473
2. - 3. ]	0.1490	0.1361
3. - 4. ]	0.1006	0.0861
4. - 5. ]	0.0652	0.0570
5. - 6. ]	0.0910	0.0585
6. - 7. ]	0.0788	0.0569
7. - 8. ]	0.0520	0.0415
8. - 9. ]	0.1467	0.1045
9. - 10. ]	0.2500	0.1692
10. - 20. ]	0.9280	0.7595
20. - 30. ]	0.8429	0.7066
30. - 40. ]	0.7912	0.6740
40. - 50. ]	0.7548	0.6509
50. - 60. ]	0.7283	0.6348
60. - 70. ]	0.7018	0.6178
70. - 80. ]	0.6654	0.5951
80. - 90. ]	0.6886	0.6096
90. - 100. ]	0.6555	0.5889
100. - 200. ]	5.9889	5.5296
200. - 300. ]	5.3599	5.1274
300. - 400. ]	4.9626	4.8722
400. - 500. ]	4.6680	4.6807
500. - 600. ]	4.4230	4.5164
600. - 700. ]	4.2707	4.4176
700. - 800. ]	4.0720	4.2822
800. - 900. ]	3.9396	4.1882
900. - 1000. ]	3.8072	4.1018
1000. - 2000. ]	32.9074	35.6406
2000. - 3000. ]	17.6322	15.8690
3000. - 4000. ]	0.0000	0.0000
4000. - 5000. ]	0.0000	0.0000
5000. - 6000. ]	0.0000	0.0000
> 6000. ]	0.0000	0.0000

D-66

MP2690/1886-728/JD

Table D-10. Typical LASEP Output

MASS RELEASE DISTRIBUTION

NUMBER OF IN-AIR RELEASES : 7  
NUMBER OF ON-GROUND RELEASES : 178

MASS RANGE	IN-AIR	ON-GROUND
0. - 1.]	42.86% (3)	35.96% (64)
1. - 2.]	14.29%	17.88%
2. - 3.]	0.00%	22.47%
3. - 4.]	0.00%	6.18%
4. - 5.]	0.00%	6.18%
5. - 6.]	0.00%	2.81%
6. - 7.]	14.29%	0.56%
7. - 8.]	0.00%	2.25%
8. - 9.]	0.00%	1.12%
9. - 10.]	0.00%	1.12%
10. - 20.]	0.00%	2.25%
20. - 30.]	0.00%	0.56%
30. - 40.]	14.29%	0.00%
40. - 50.]	14.29% (1)	0.00%
50. - 60.]	0.00%	0.00%
60. - 70.]	0.00%	0.00%
70. - 80.]	0.00%	0.56% (1)
80. - 90.]	0.00%	0.00%
90. - 100.]	0.00%	0.00%
100. - 200.]	0.00%	0.00%
200. - 300.]	0.00%	0.00%
300. - 400.]	0.00%	0.00%
400. - 500.]	0.00%	0.00%
500. - 600.]	0.00%	0.00%
600. - 700.]	0.00%	0.00%
700. - 800.]	0.00%	0.00%
800. - 900.]	0.00%	0.00%
900. - 1000.]	0.00%	0.00%
1000. - 2000.]	0.00%	0.00%
2000. - 3000.]	0.00%	0.00%
3000. - 4000.]	0.00%	0.00%
4000. - 5000.]	0.00%	0.00%
5000. - 6000.]	0.00%	0.00%
6000. - 7000.]	0.00%	0.00%
7000. - 8000.]	0.00%	0.00%
8000. - 9000.]	0.00%	0.00%
9000. - 10000.]	0.00%	0.00%
10000. - 11000.]	0.00%	0.00%
11000. - 12000.]	0.00%	0.00%
12000. - 13000.]	0.00%	0.00%
13000. - 14000.]	0.00%	0.00%
14000. - 15000.]	0.00%	0.00%
15000. - 16000.]	0.00%	0.00%
16000. - 17000.]	0.00%	0.00%
17000. - 18000.]	0.00%	0.00%
18000. - 19000.]	0.00%	0.00%
19000. - 20000.]	0.00%	0.00%
20000. - 21000.]	0.00%	0.00%
21000. - 22000.]	0.00%	0.00%
22000. - 23000.]	0.00%	0.00%
> 23000.]	0.00%	0.00%

The particle size distributions are for the plutonia fuel that is released from the fueled clads as a result of the accident environment.

The average releases shown are relative to the total number of trials made, or the average releases per trial. These values are subsequently modified (outside LASEP, currently) to arrive at the average release per release event as follows:

From Table D-9

av. air release	0.009318652	7 trials
av. ground release	0.051703032	178 trials

Modified Releases

$$\text{air } \frac{0.009318652 \times 10,000}{7} = 13.3 \text{ gm/release event}$$

$$\text{ground } \frac{0.051703032 \times 10,000}{178} = 2.90 \text{ gm/release event}$$

These are the values shown in Table D-11 which presents a summary of the results from all of the LASEP cases analyzed for this FSAR. Table D-11 includes the values that are used in the determination of the source terms developed in Section 3.4 of the AMD in this FSAR and summarized in Table 3-8. Table D-12 presents a summary of the additional details provided in the LASEP output.

Table D-11. LASEP Accident Results

ENVIRONMENT	SUB PHASE	TIME SEC	MODULE POSITION	AIR RELEASE-gm				GROUND RELEASE-gm			
				AV.	N <sub>av.</sub>	MAX	N <sub>max</sub>	AV.	N <sub>av.</sub>	MAX	N <sub>max</sub>
Pad/Trench Expl.	0 <sup>(1)</sup>	0	All	0	0	0	0	3.52	28	11.2	1
SRB Frag.	1S1 <sup>(2)</sup>	0-10	Mid	13.3	7	47.2	1	2.90	178	75.6	1
M/P&T Expl.			End	0.127	1	0.127	1	2.31	162	11.7	1
SRB Frag.	1S1 <sup>(2)</sup>	10-20	Mid	0.491	3	1.15	1	16.7	175	185	1
			End	.0123	2	.0234	1	11.0	209	71.8	1
SRB Frag.	1S1 <sup>(2)</sup>	20-70	Mid	1.06	2	1.50	1	12.6	1	12.6	1
			End	0.192	1	0.192	1	.0959	1	.0959	1
SRB Frag.	1S1 <sup>(2)</sup>	70-105	Mid	5.96	2	9.55	1	-	-	-	
			End	12.6	2	27.2	1	-	-	-	
SRB Frag.	1S1 <sup>(2)</sup>	105-120	Mid	405	19	3163	1	-	-	-	-
			End	121	21	1371	1	-	-	-	-
Pad/Trench Expl.	1S2	0-2	All	0	0	0	0	4.6	25	18.1	3
Vapor Cloud Expl.	1S3	10-30	All	0	0	0	0	73.1	1325	148	557
Vapor Cloud Expl.	1S4	10-30	All	0	0	0	0	73.1	1325	148	557
SRB Frag.	1R <sup>(3)</sup>	0-10	Mid	.0348	2	.0624	1	4.19	463	29.5	7
M/P&T Expl.			End	0	0	0	0	4.51	453	207	1
SRB Frag.	1R <sup>(3)</sup>	10-105	Mid	136	1	136	1	22.7	62	83.0	1
			End	0.503	3	0.820	1	27.0	53	244	1
SRB Frag.	1R <sup>(3)</sup>	105-120	Mid	8.87	2	16.8	1	-	-	-	
			End	8.87	2	16.8	1	-	-	-	
Aft Comp. Expl.	1E	0-10	All	0	0	0	0	0	0	0	0
Vapor Cloud Expl.	1E	10-30	All	0	0	0	0	73.1	1325	148	557
Pad/Trench Expl.	1V	0-10	All	0	0	0	0	2.10	105	16.7	2
Vapor Cloud Expl.	1V	10-30	All	0	0	0	0	73.1	1325	148	557

ALL VALUES BASED ON 10,000 TRIALS  
 (1) INCLUDES INADVERTENT RANGE DESTRUCT  
 (2) SRB RANDOM FAILURE (CASE BURST)  
 (3) RANGE DESTRUCT

D13#2



Table D-12. Additional Details Provided in LASEP Output

**Distortion Distribution for RTG/GPHS/FC**

- Percentage of hits in 10% bands

**Distribution of Ground Impact Velocities**

- For each object (i.e., RTG/GPHS/FC)
- By surface type in velocity ranges:

< 54 m/s	Sand
54-65	Steel
65-76	Concrete
76-100	
100-120	
120-146	
146-200	
> 200	

- For each 10% distortion range (i.e., for prior distortion by SRB/payload bay fragments)

**Percentage of Impacts Within Fireball Radius**

- For each object (i.e., RTG/GPHS/FC)
- By surface type in velocity ranges
- For each 10% distortion range

**Distribution of SRB C. G. Impact Velocity**

- In 50 fps velocity ranges
- For both face-on and edge-on impacts

**Distribution of SRB Vector Sum Impact Velocity**

(i.e., for vector sum of C. G. velocity plus tip velocity due to rotation)

- In 50 fps velocity ranges
- For both face-on and edge-on impacts

D.5 REFERENCES

1. Space Shuttle Data for Planetary Mission Radiosotope Thermoelectric Generator Safety Analysis, REV. A, NSTS 08116, JSC, Houston, Texas, March 1988.
2. Braun, J.F., "CYLMOD - SRB Fragment Environment Evaluation:, PIR NO: 1R12-FSAR-6766, General Electric Co., Philadelphia, PA, February 1988.
3. Grant, J. and DelReal, J., "Project Galileo and Ulysses Case Wall Fragment Size Distribution Data for Input to the Shuttle Data Book," RDA-TR-0113000011-008, R & D Associates, Marina Del Rey, CA., March 1988.
4. Eck, M.B., "SRM Fragment Impact Hydrocode Analysis: Review and Predictions," Fairchild Space Co., Germantons, Maryland, Safety Analysis Mtg., March 30-31, 1988.
5. Bradshaw, C.T., "Safety Briefing on Galileo and Ulysses Missions", General Electric Co., Philadelphia, PA, Safety Analysis Mtg., March 30-31, 1988.
6. Vaughan, F.R., "Particle Size Distribution Function Review," Ref No: FRV-88-014, NUS Corporation, Gaithersburg, Maryland, July 1988.
7. Final Safety Analysis Report for the Galileo Mission and the Ulysses Mission, General Electric Co., Prepared for the Department of Energy, Contract DE-AC01-79ET32043, October 1985.

ADDENDUM I TO APPENDIX D  
DAMAGE CRITERIA FOR FRAGMENT IMPACT

To determine the probability of fragment damage to the RTG, GPHS aeroshell and fuel capsules, a criteria for estimating impact damage is required. Based on analysis and data from tests simulating fragment impacts of the GPHS RTG, five expressions were derived to describe the threshold of damage described herein.

1. RTG impacted by face-on fragment resulting in aeroshell (GPHS module) in free flight.
2. RTG impacted by edge-on fragment resulting in aeroshell (GPHS module) in free flight.
3. RTG impacted by face-on-fragment resulting in fueled clads in free flight.
4. RTG impacted by edge-on-fragment resulting in fueled clads in free flight.
5. Bare aeroshell impacted by face on fragment resulting in fueled clads in free flight.

I.1 ASSUMPTIONS

1. The shear strength of the RTG aluminum outer shell is 24000 psi.
2. The RTG weight of approximately 122 pounds is divided into 57 pounds for the heat source and 65 pounds for the converter.
3. Impacts on the RTG by large fragments accelerate the converter which impacts the heat source and, if the energy level is sufficient, causes release of the aeroshells.

4. Fragments have the same area as the projected area of the RTG (42 in. by 8.4 in.)
5. The change in fragment velocity due to impacting the outer shell is negligible.

## I.2 ANALYSIS

As the large fragment impacts the outer shell of the RTG, the outer shell and the fragment impact the heat source stack. The total force is equal to the heat source shearing out an area of the outer shell. The magnitude of this force (F) is shown below:

$$F = (l + w) \times t_s \times F_{su}$$

where

- l = heat source length (38.37 in)
- w = heat source width (3.826 in)
- t<sub>s</sub> = thickness of outer shell (.060 in)
- F<sub>su</sub> = shear strength (24000 psi)
- F = 121, 524 lbs.

In calculating this force, the effect of the insulation, the thermoelectrics and outer shell rings and stiffeners are neglected. It is recognized that the force will not be constant from the time of impact with the outer shell to the time of impact with the GPHS modules. It is assumed that the calculated force is an average of the forces acting and that it can be further assumed that the average or calculated force is applied for a time (t), and that this is the time for the fragment and RTG outer shell to travel 2.4 inches (the maximum distance front the RTG shell to the GPHS modules. Based on the assumption that the fragment velocity is unchanged by impact with the outer shell, this time is 2.4/v. The product of this time and the average force is equal to the momentum of the outer shell and fragment. This expression is shown below:

$$F\left(\frac{2.4}{V}\right) = \frac{65 + w}{g} \cdot v$$

where

v = velocity (in/sec)

w = fragment weight (lbs)

g = gravitational constant (386.4 in/sec<sup>2</sup>)

This expression rewritten and solved for the velocity is shown below as Equation 1.

$$V = \sqrt{\frac{121,524}{.070 + .0011w}} \quad \text{Equation 1}$$

It should be noted that the form of Equation 1 is equivalent to the kinetic energy equation solved for the velocity, v:

$$E = \frac{wv^2}{2g}$$

$$V = \sqrt{\frac{E}{w/2g}}$$

The manner in which Equation 1 is used in LASEP is the equivalent kinetic energy relation. The numerator under the square root sign is used as the effective energy level with units of in-pounds. The denominator is equal to the quotient of weight divided by twice the gravitational constant. Thus, the effective energy level of the SRB fragment coupled with the RTG converter to separate the GPHS module from the converter while leaving the module intact is 121,524 in-lb or 10127 ft-lb, the latter value being shown in Table D-4. The velocity obtained from Equation 1 is the equivalent velocity of the SRB fragment. With this value of velocity being used, the minimum kinetic energy of the SRB fragment to produce this effect can be calculated, with the weight of the fragment being 57.8 pounds (26.3 kg). The SRB kinetic energy is found to be 68,100 in-lb (7694J).

With the use of Equation 1, the SRB fragment velocity (in the face-on orientation) necessary to remove the RTG converter is found to be 79.8 fps (24.3 m/s) for the 57.8 pound fragment. In the first large fragment test (LFT-1, see Appendix G, Section G.3.3) at a fragment velocity of 377 fps (114.9 m/s) and a weight of 520 pounds (236 kg), the RTG converter was severely cracked and crushed but essentially remained in place around the GPHS modules. At a fragment weight of 520 pounds, the velocity for removal of the RTG converter is found to be 36.3 fps (11.1 m/s) from Equation 1. Thus, it can be seen that Equation 1 is very conservative; that is, the predicted values of fragment energy and velocity to remove the converter are predicted to be much lower by the equation than actually occur by test. To state it differently, the converter would provide much greater protection for the GPHS modules than would be predicted by Equation 1.

Figure I-1 shows the relation of SRB fragment velocity to produce a given configuration as a function of fragment weight as determined by Equation 1. It also includes the relations for the edge-on fragment as well as removal of the GPHS aeroshell in addition to the RTG converter (Equations 2, 3, and 4). The notation shown on the figure is related to these equations as follows:

RTG case : FCO	Equation 1 (face-on)
RTG case : EDO	Equation 2 (edge-on)
Aeroshell: FCO	Equation 3 (face-on)
Aeroshell: EDO	Equation 4 (edge-on)

The effective energy level to remove the aeroshell when a bare module strikes the payload bay walls was used as being equal to that in Equation 3. It was assumed that the energy necessary to be imparted to the GPHS module in order to remove the aeroshell would be the same regardless of the manner in which it was applied.

For an edge-on fragment impact, it is assumed that the fragment and outer shell impact two modules and shear out a segment of the outer shell equal to the projected area of two modules. The force necessary to shear out this segment of the outer shell is

$$F = (3.826 + 4.18) \times 2 \times 24000 \times .060$$

$$F = 23,057 \text{ lbs.}$$

Equation (2) shows the threshold velocity for a fragment of weight (w) impacting the RTG edge on, necessary to cause the aeroshells to separate from the RTG converter while still retaining the fueled clads in the aeroshell.

$$V = \sqrt{\frac{23057}{.070 + .0011w}} \quad \text{Equation (2)}$$

The SRB fragment kinetic energy associated with this edge-on impact is found to be 12,900 in-lbs (1458J).

The impact velocity necessary to cause the unbreached fueled clads to be separated from the aeroshell subsequent to the release of the aeroshell from the RTG converter was derived from impact tests on a simulated RTG. In a series of tests conducted with a 1/2 thick steel plate (SRB fragment) impacting a simulated RTG, it was found that the aeroshells contained the fuel capsules at impact velocities up to 114.9 m/sec (4523 in/sec). The data from these tests are included in Appendix G to this AMD. At a velocity of 120 m/sec (4724 in/sec) the fuel capsules, unbreached, were released from the aeroshell. Based on this test, equation (1) is modified for the increased velocity necessary to cause the release of the unbreached fueled clads from the aeroshell. This equation is shown as equation (3).

$$V = 4.8 \sqrt{\frac{121,524}{.070 + .0011w}} \quad \text{Equation (3)}$$

In this equation, the effective kinetic energy is taken as the product of  $4.8^2 \times 121,524$ ; units are inch-pounds. The SRB fragment kinetic energy associated with this threshold velocity is 1,569,000 in-lbs.

The velocity necessary for a fragment of weight (w) impacting the RTG edge-on and causing the release of unbreached fueled clads from the aeroshell is shown below as equation (4). Equation (4) is equation (2) modified for the increases in velocity necessary to cause release of the fueled clads from the aeroshell.

$$V = 4.8 \sqrt{\frac{23,057}{.070 + .0011w}}$$

Equation (4)



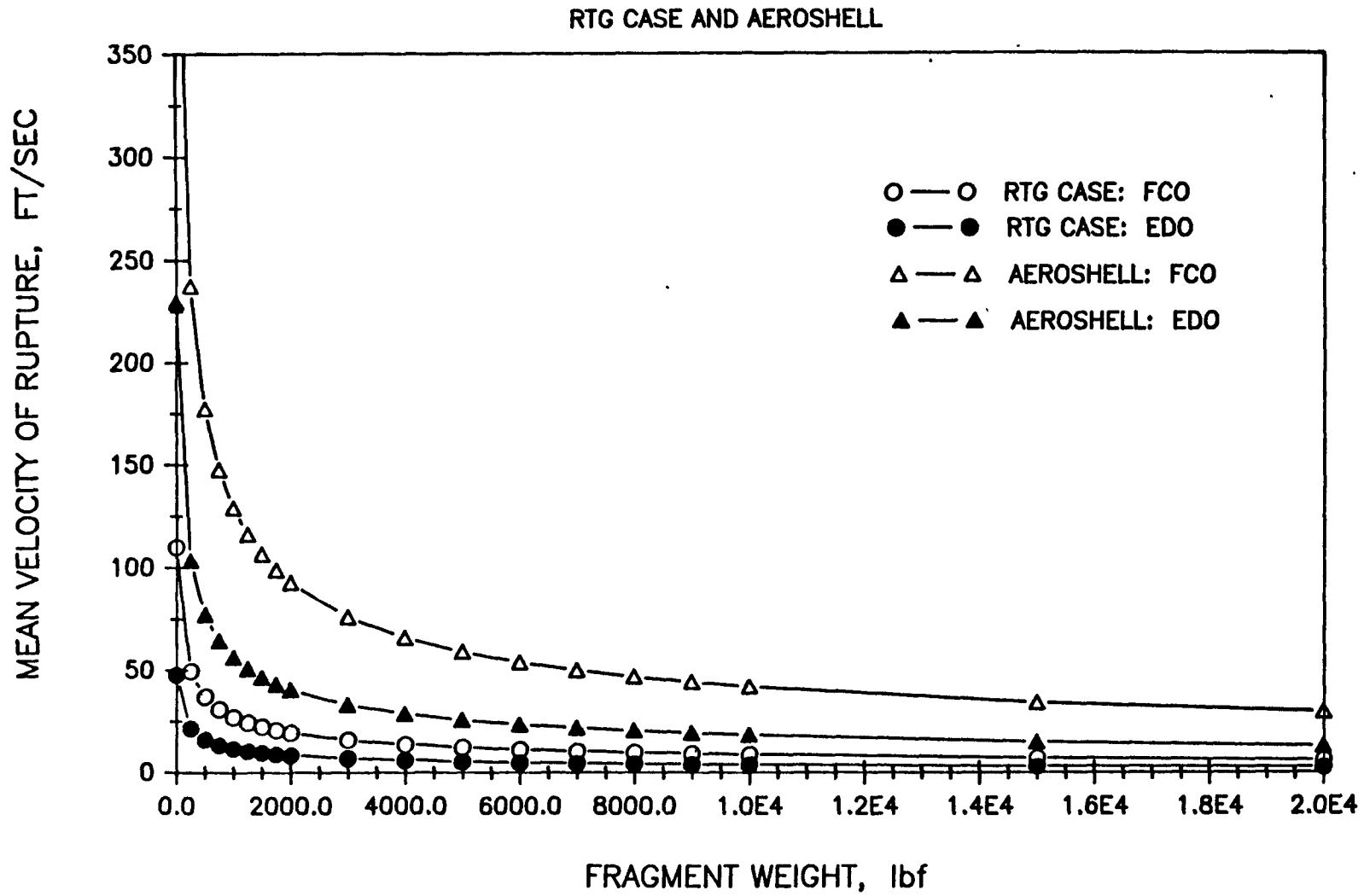


Figure I-1. Velocity of Rupture for a Given Fragment Weight

APPENDIX E  
 JPL REENTRY BREAKUP ANALYSIS

This appendix presents the studies conducted by JPL to determine the environments imposed on the GPHS-RTGs arising from: 1) the powered reentry of the upper stage(s) with spacecraft used in the Galileo Mission (IUS), and 2) the reentry of the Galileo spacecraft under potential conditions arising from malfunctions occurring during the VEEGA maneuvers. Results from the latter study are used in Appendix F in which the subsequent reentry of the GPHS-RTG is analyzed. The results from the powered reentry of the upper stage(s) give conditions for RTG release that fall in between those for the orbital decay and the powered reentry of the Centaur stage presented in the previous FSAR (GESP 7200, Volume II (Book 2), Accident Model Document - Appendices, Appendix I, 8 October 1987). For those cases, the resulting aeroshell ablation was from 5.9 to 41 mils or 3.2 to 22.2 percent of the total minimum thickness (this includes effects of stable vs. tumbling of the GPHS module); thermal stress was not a problem. Therefore, the powered reentry case with breakup and subsequent RTG reentry has not been analyzed from the viewpoint of the RTG for this FSAR II. The results of the JPL powered reentry breakup study, however, are included herein for reference.

The complete report of the JPL study for the powered reentry breakup is given in: "Galileo & Ulysses Breakup Analysis: Powered Entry of Upper Stage Plus Spacecraft," P. Bahrami et al, July 1987 (Preliminary version only - no document number), Jet Propulsion Laboratory. The VEEGA breakup analysis report is: Report No. 1625-331, "Galileo VEEGA Earth Reentry Breakup Analysis," A. McRonal, July 1987, Jet Propulsion Laboratory. Refer to these reports for more details of both studies. This appendix is an excerpt of those two reports.

E.1 UPPER STAGE POWERED REENTRY ANALYSIS

Because of the adverse potential this case offers, the analysis of the powered entry case was designed as much to investigate what can't happen as what does. Three issues critical to RTG nuclear safety were addressed: 1) is there a possibility that one of the upper stage motors will burst and send

damaging fragments to the RTG; 2) are there other identifiable events, such as the bursting of a pressure vessel, which could put the RTG in jeopardy; and 3) is there a powered entry scenario which could result in the whole RTG surviving reentry and thus impacting the ground intact? The analysis indicates that for the predominant baseline case of 2nd stage reentry, and with the exception of an explosion of one of the motors itself (not considered in the analysis), the answer to all three questions is no. In all cases the RTG heat source modules break free of the RTG before any catastrophic event could occur. The altitude where they are set free ranges from 293 kft to 116 kft depending upon a variety of factors, from entry speed and angle to relative RTG position and assumed heating factors.

#### E.1.1 REENTRY PARAMETERS

For the purpose of analysis, powered entry is taken to mean those reentry cases which occur before all upper stage burns and coasts have been completed. (Reentry is assumed to have commenced when the vehicle descends to an altitude of 400 kft.) In the case of Galileo this means IUS Burn 1, Coast 1 and Burn 2. Two types of errant burns have been identified as leading to powered entry: 1) stable misaligned burns (SMB) and 2) erratic (attitude) burns (refer to Appendix A, Section A.2.2., Appendix B, Section B.5, of this FSAR II and also Section II of the Shuttle Data Book).

Two key factors can be deduced from the results: 1) there are no Burn 1 reentries (the burn time is too short for reentry to occur) and 2) the preponderance of reentries occur during Coast 1. In the selection of cases for analysis it was decided to take the baseline as entry during Coast 1 but with the pre Burn 2 configuration. To maximize (analytically) the possibility of bursting the SRM-2 motor it was further decided to start the baseline reentry 20 seconds before Burn 2 ignition in order to match the peak (under thrust) chamber pressure better, which occurs at 50 seconds into the motor burn, with the anticipated point at which the strength of the Kevlar case material would be significantly degraded due to aerodynamic heating. Also, to maximize the heating on the motor case while recognizing that Kevlar is a poor conductor, a shallow entry angle of 6 degrees was selected. The velocity point chosen was at about the mid point of the V-Gamma maps, 24.6 kft/s, and

the corresponding angle-of-attack of 90 degrees. To summarize, the baseline trajectory is:

Entry Velocity                    24.6 kft/sec  
 Entry Angle                        6.0 degrees  
 Configuration                    Pre-Burn-2 ignition  
 Angle-of-attack                  90 degrees  
 Entry Time                        20 seconds before SRM-2 ignition

Other possible adverse occurrences, such as intact reentry, and non-adverse events, specifically release or breakup of the RTG are also of interest. Toward this end several other entry trajectories were considered; Table E-1 summarizes the trajectories. The configuration was the same in all cases: pre Burn 2 upper stage plus spacecraft.

Table E-1. Trajectories Considered

#	V (kft/s)	Gamma (Deg)	Burn-Time* (Sec)	Angle of Attack (Deg)	Comment
1	24.60	6	20	90	Baseline
2	24.60	6	20	0	Alpha Invest.
3	24.60	18	20	90	Steep
4	24.60	18	100	90	No Burn
5	14.76	20	-10	150	Min energy

\*Time of SRM-2 ignition; (-) means ignition before entry.

These trajectory points have been spotted on the V-Gamma map of Figure E-1. As can be seen they correspond to extremities on the map. It is expected that results using these five trajectories should encompass almost all of the events and ranges that can possibly occur during a powered reentry.

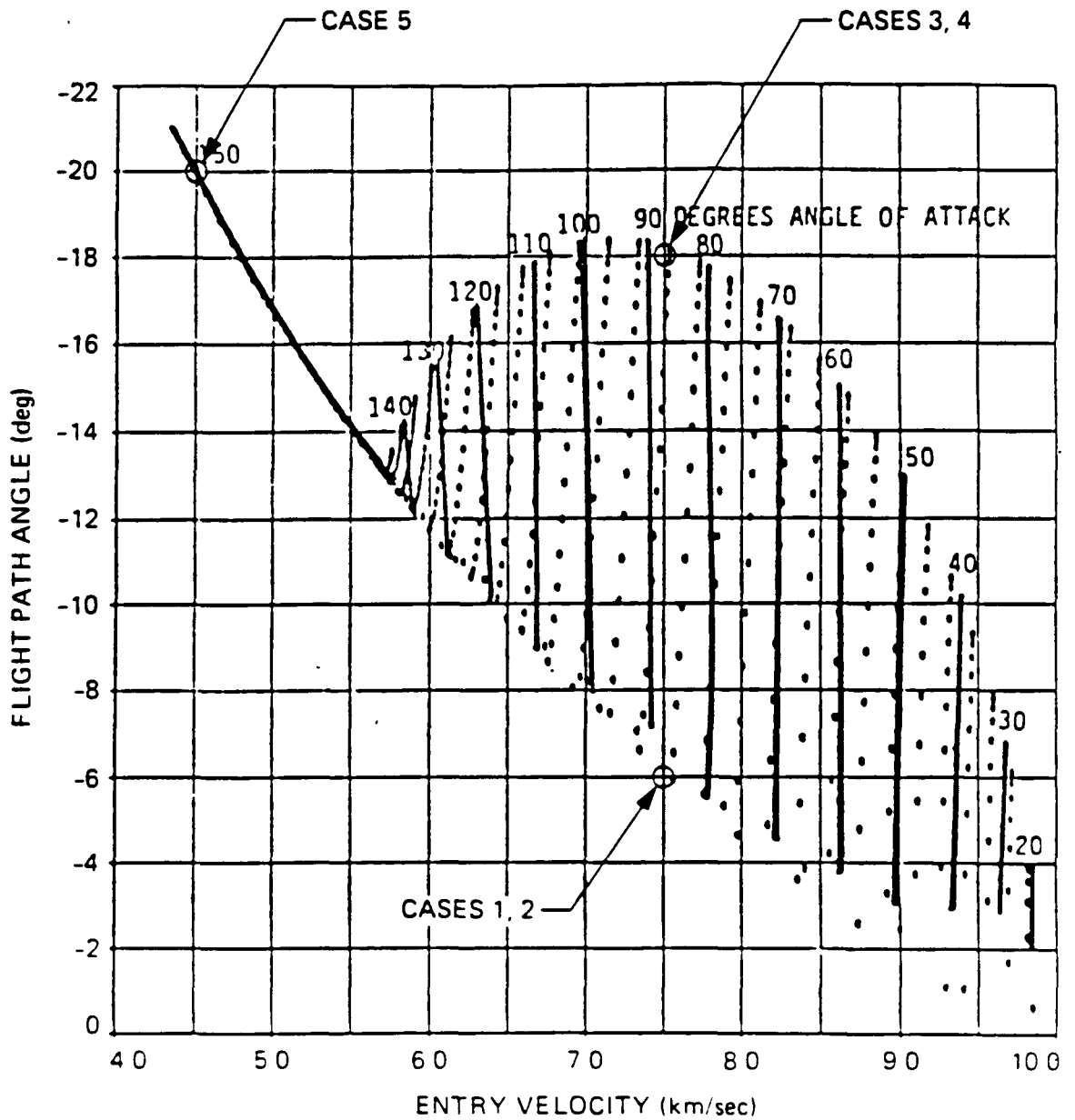


Figure E-1. Entry During Coast 1, Burn 2 (Galileo)

### E.1.2 TRAJECTORY ANALYSIS

Figures E-2 through E-7 contain several of the more important entry parameters for Trajectories 1, 3 and 5 as a function of altitude. As shown in Figure E-3, the vehicle tends to trim somewhat with the nozzle toward the flow. The angle-of-attack presented here is the total angle-of-attack comprised of components in pitch and yaw. Both components are present in the data, i.e., the oscillatory motion is not planar. Figure E-3 also shows that the vehicle typically descends below 300 kft before it departs much from its initial orientation. This is because the dynamic pressure (Figure E-7) is very small early in the entry. Figures E-4 and E-5 contain the reference heat flux and the time-integrated heat flux. The integrated heating for Trajectory 1, the baseline trajectory, is very high and that, coupled with the long entry time (Figure E-2), will (analytically) maximize the thermal degradation of the exposed portion of the vehicle.

### E.1.3 SRM-2 MOTOR RESPONSE

The event that makes the powered entry case of particular concern is the possibility that the thrusting motor will burst and send high speed fragments toward the RTG. To determine what happens, it is necessary to find out which of the competing events will occur first: 1) motor burst due to the action of the internal pressure against the thermally degraded Kevlar case; 2) failure of the aluminum interface structure supporting the motor and separation of the motor from the rest of the vehicle; or 3) RTG breakup or separation from the spacecraft.

#### E.1.3.1 SRM-2 Motor Case And Support Structure Response

The SRM-2 Kevlar motor case and aluminum support structure were modeled by the 19 element nodal model shown on Figure E-8. Preliminary analysis indicated that the key to establishing if and when the case would burst was in determining the depth of penetration of the applied heat flux as a function of time. If most of the case remains relatively cool, its resistance to bursting stays high. Subsequently, the node 12 region of the model was subdivided through the thickness since previous work indicated it would heat up most, and

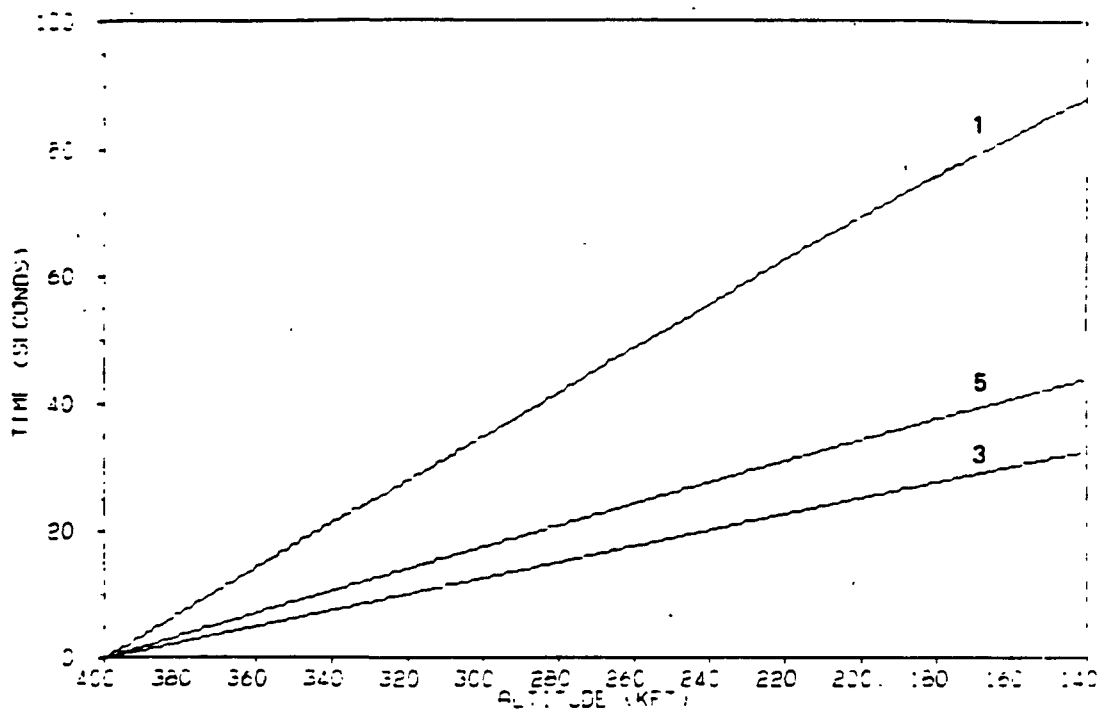


Figure E-2. Time vs. Altitude

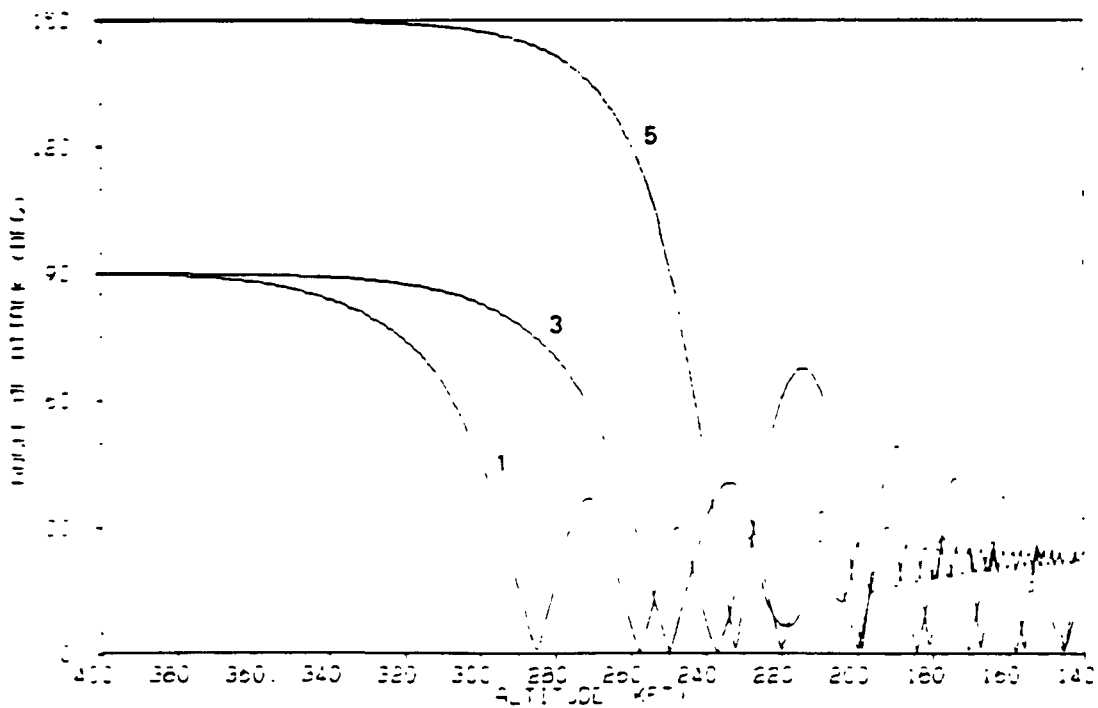


Figure E-3. Total Angle-of-Attack vs. Altitude

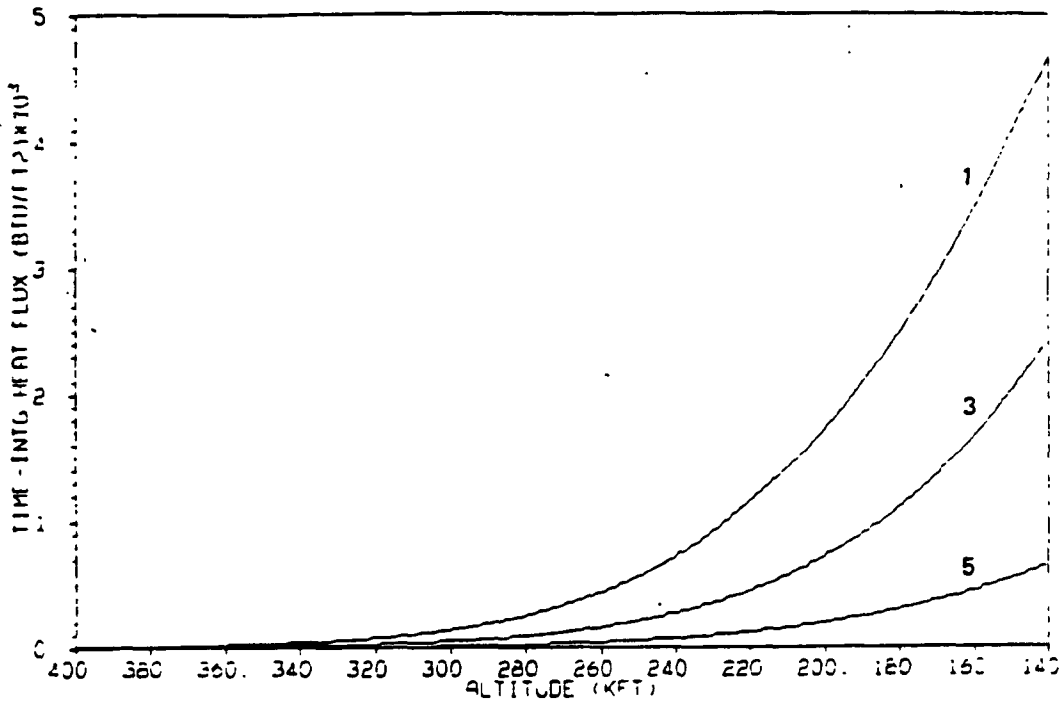


Figure E-4. Integrated Heating on 1-ft Radius Cyl vs. Altitude

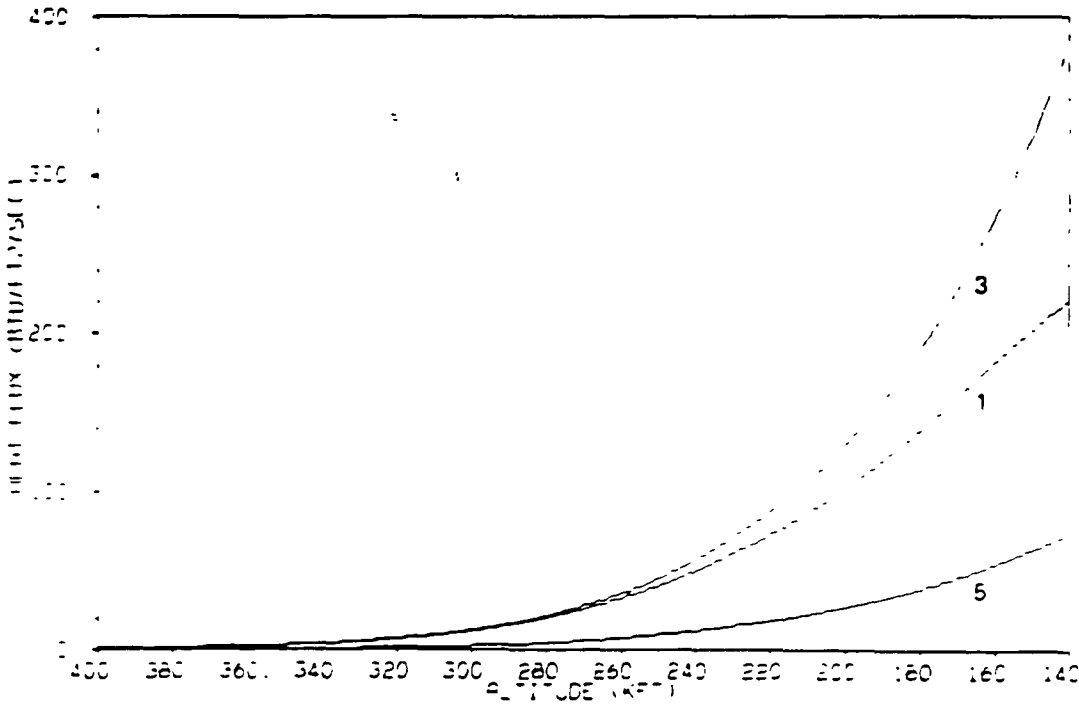


Figure E-5. Heat Flux vs. Altitude



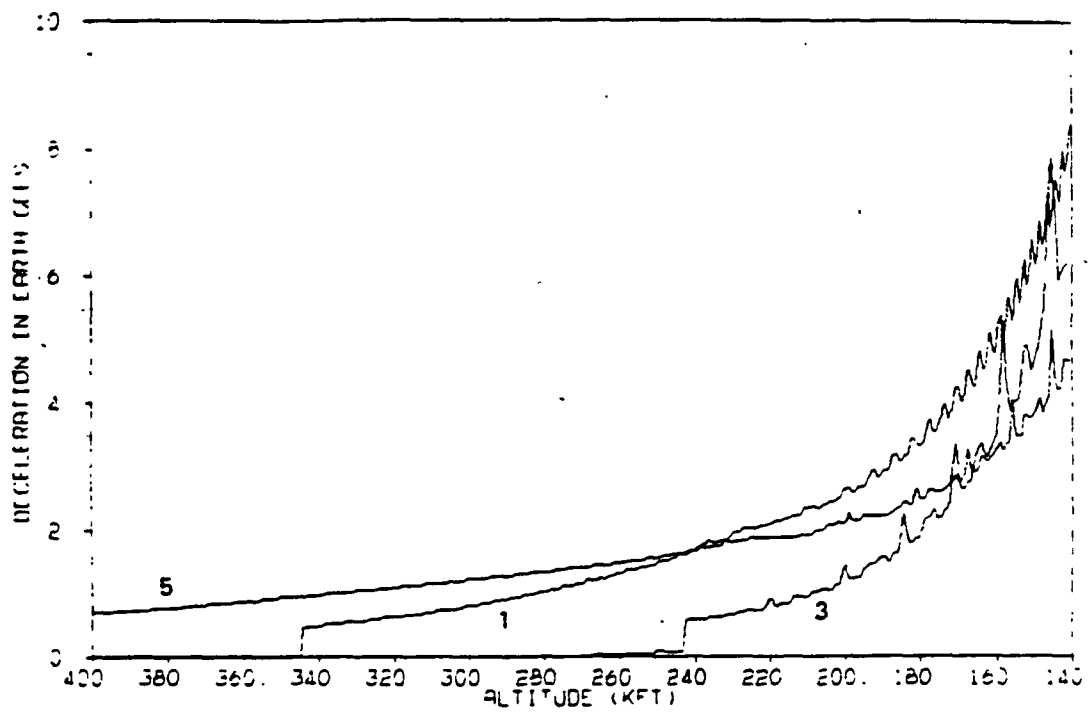


Figure E-6. Axial Deceleration vs. Altitude

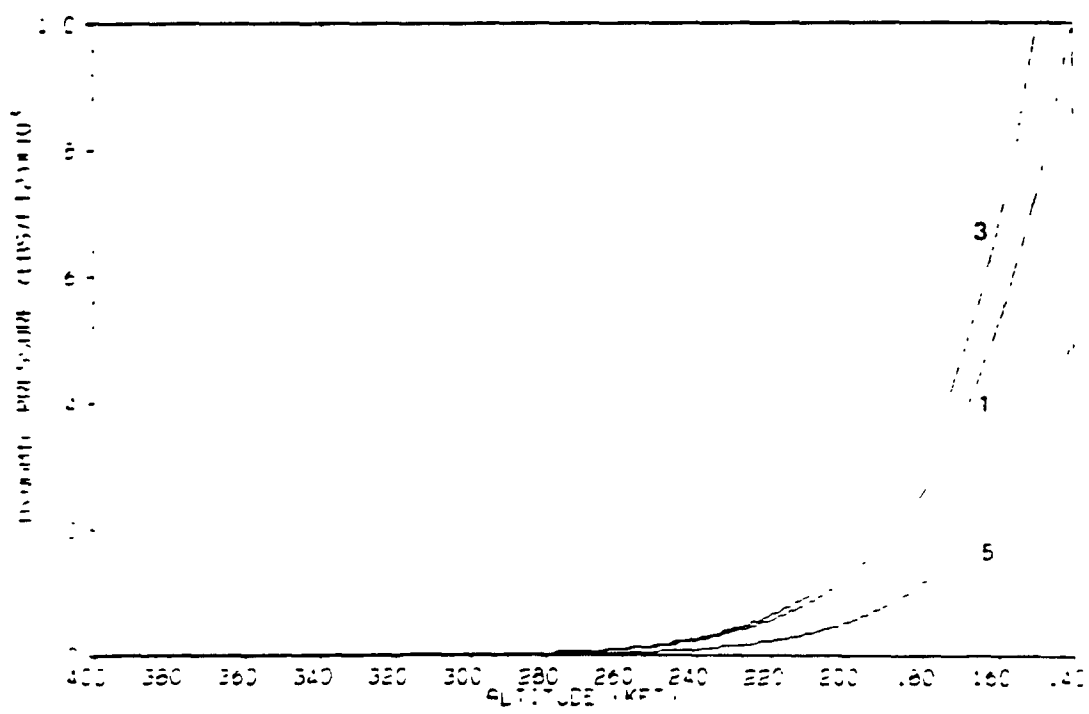


Figure E-7. Dynamic Pressure vs. Altitude

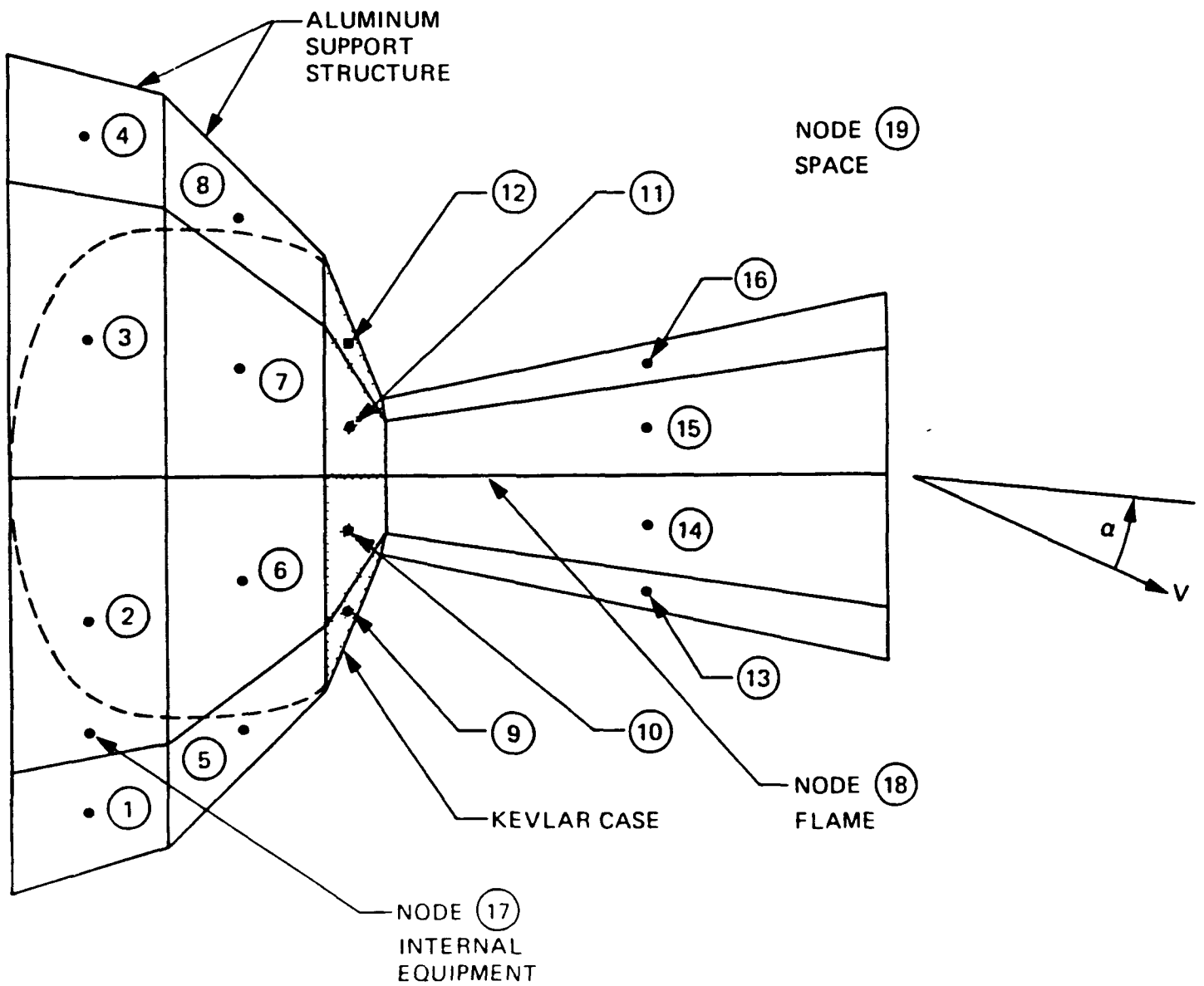


Figure E-8. Nodal Breakdown of SRM-2 Motor and Support Structure

it was the thinnest region of the case, 0.2 inches. Also the more detailed characteristics of the Kevlar material were modeled to account for phase transition and decomposition as the material heats up along with an increase in heat capacity resulting from the endothermic process occurring plus ablation and surface charring. A thermal/structural analysis was then performed, and the results are shown on Figure E-9. The intersection of the pressure allowable curve with the motor chamber pressure loading indicates a predicted motor case failure at about 61 sec for the nominal +20 sec ignition time. The earliest possible case failure time (for an earlier assumed ignition time) is about 59 sec.

Figure E-9 also shows the allowable loading for the support structure in the critical areas, node 9. The intersection of the support structure allowable and load curves indicates a predicted crippling of the support structure at about 67 sec. When this occurs, the motor will pivot and cause the vehicle to tumble rapidly, causing extreme inertial forces to act on the spacecraft and RTGs.

#### E.1.4 RTG THERMAL RESPONSE

While the Kevlar case and aluminum support structure are experiencing reentry heating, the RTG is similarly being heated. The RTG aluminum housing was modeled as a cylinder whose diameter was the mean of the fins and the inner shell and whose areal density was the mass of the housing divided by the area of the cylinder and end-caps. The cylinder diameter and areal density used were 12.6 inches and 1.54 lb/ft<sup>2</sup>, respectively. Figure E-10 depicts the nodal breakdown. The cylindrical surface was broken up into eight equal nodes, 45 degrees apart, and the end-caps were each made a node. For Galileo, two additional nodes were used, one corresponding to the titanium RTG support strut and one for a representative graphite epoxy boom member. For external heating, the RTG was modeled as a cylinder of diameter 8.6 inch (fins melted away).

The heating of the RTG is dependent upon its relative position with respect to the flow. In order to bracket the breakup time, two positions were selected: Position 1 had the axis of the RTG in the same plane as the vehicle axis and

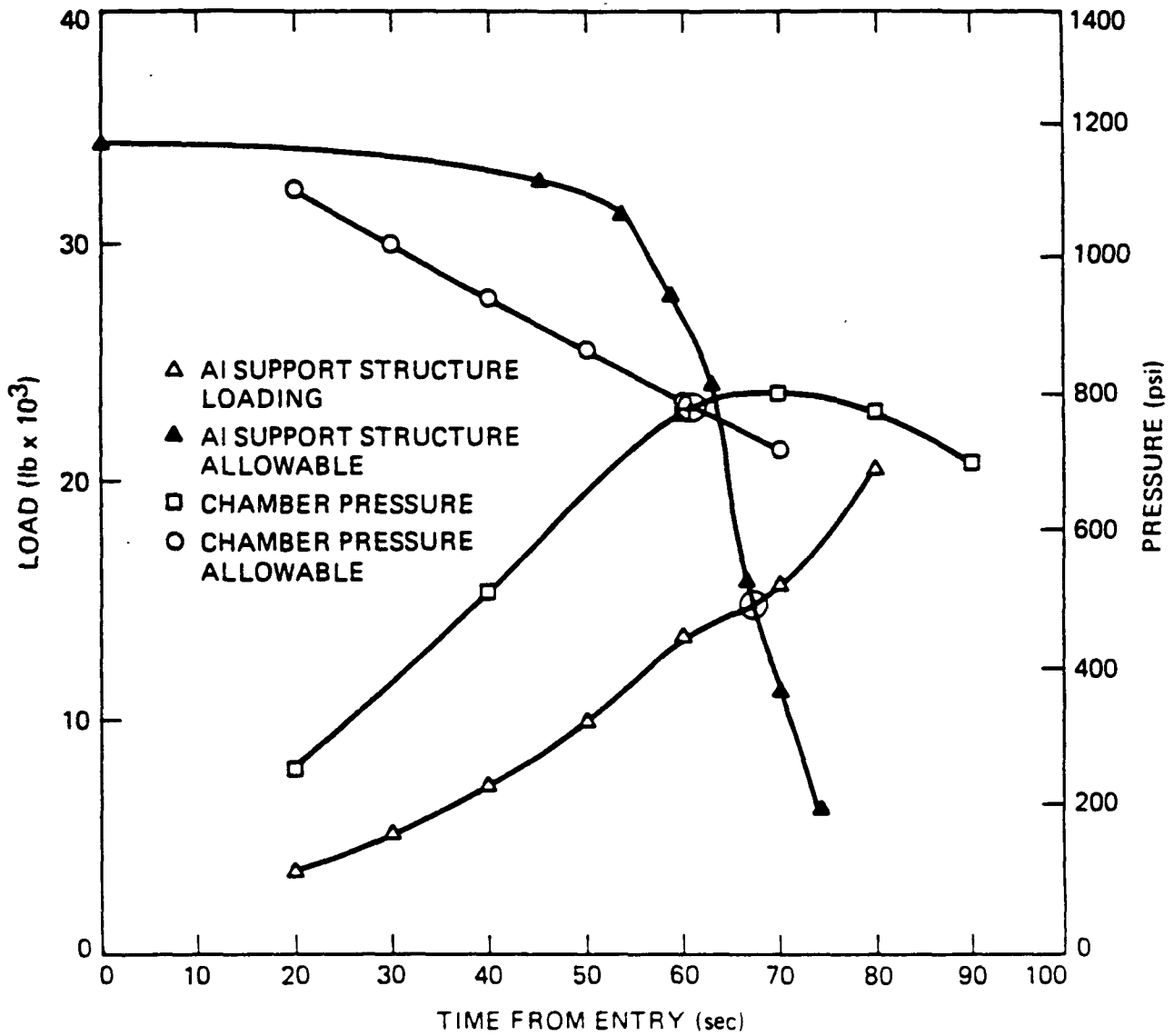


Figure E-9. Allowable Chamber Pressure and Aluminum Support Structure Load vs. Time

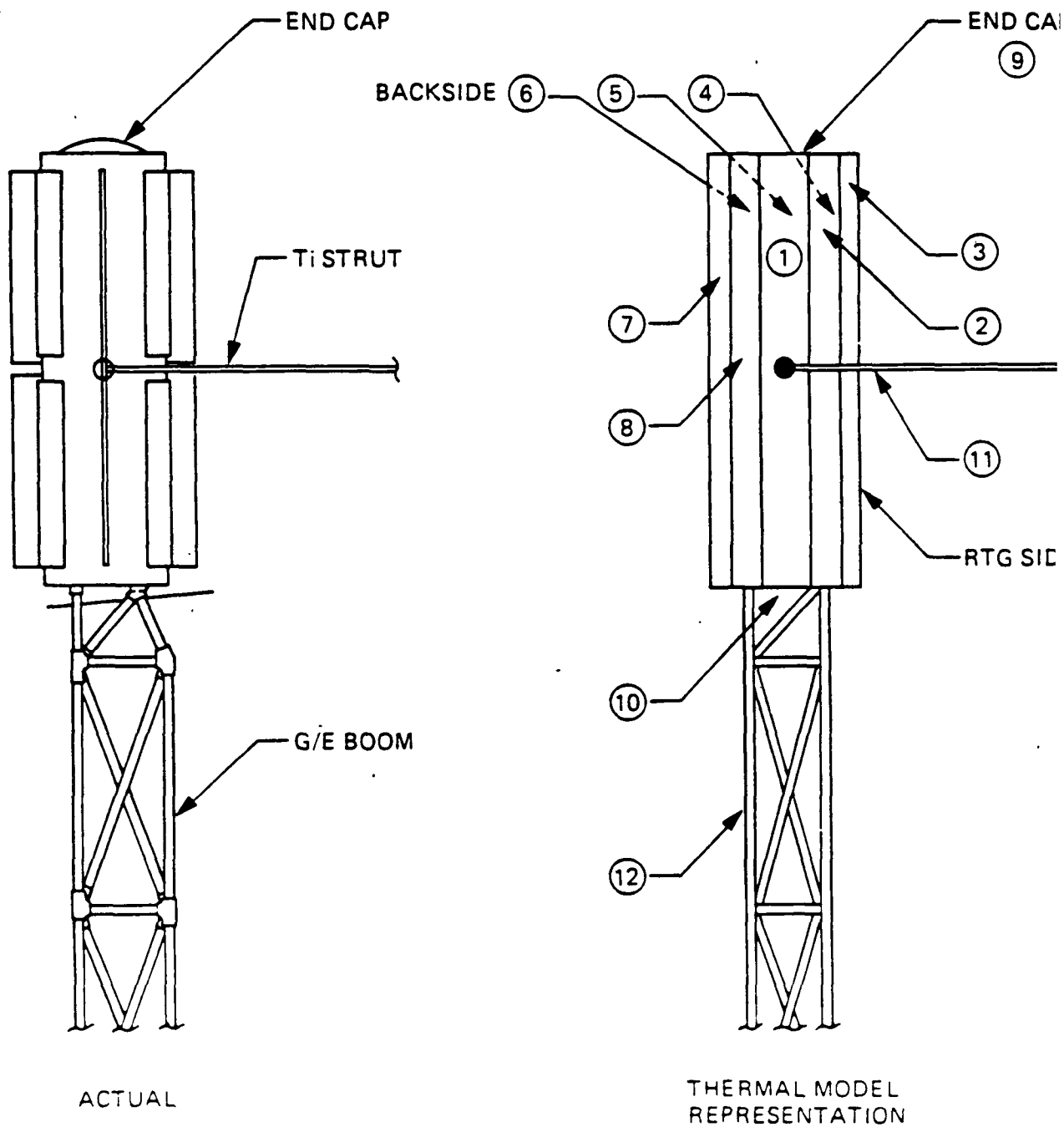


Figure E-10. Actual Layout and Nodal Model of RTG and Supports

velocity vector, and side-on to the flow when the vehicle was at an angle-of-attach of 90 degrees (an angle-of-attack of 90 degrees places the velocity vector perpendicular to the vehicle axis); Position 2 results if the vehicle and spacecraft are then rolled 180 degrees so that the RTG is in the wake of the flow for an angle-of-attack of 90 degrees. For Position 2, heat flux shadowing factors were included for angles-of-attack greater than 30 degrees. This means that for trajectories Nos. 1, 3, and 5 in Table E-1, no RTG heating would occur until the vehicle descended below 300 kft. as shown on Figure E-3.

Figures E-11 and E-12 show the node temperature histories for Trajectory 1, Galileo Positions 1 and 2. For Position 2 the minimum heating position, the heat flux was reduced an additional 25% as a factor of safety in the analysis. The temperature profiles as presented go beyond the melt point, simply an artifice to indicate that more heating is occurring. The temperature of the end-cap (Node 9), the most windward RTG node, reached the melt point (~1200 F) at about 42 and 47 seconds, respectively, for the nominal and reduced heat flux. The corresponding temperature of a three node section of side wall (a 135 degree section) reaches approximately 900 degrees for Position 1, but only 600°F for Position 2. Referring to Figures E-2 and E-6, the axial acceleration at that time is about 1.2 g's. This acceleration is acting to push the heat source modules out through the end-dome. So, even allowing an additional 5 seconds of heating, stress and internal RTG breakup, the modules would surely come out before failure of the SRM at 47 to 52 seconds. This, of course, is many seconds before the SRM-2 support structure fails.

Table E-2 contains a chronological breakdown of the significant events for the baseline case. The breakup scenario is as follows: at about 40 sec the IUS, initially at 90 deg angle-of-attack, has reached zero angle in its first pitch ascillation, and will thereafter be confined to an angle-of-attack envelope of about 30 deg maximum, first oscillating and later coning. The earliest burst time of the SRM-2 is 61 sec for the earliest baseline case, and if the ignition time of the SRM-2 is varied (it was 20 sec from entry in this baseline case) the earliest burst time could be 59 sec, if it is assumed that the thermal degradation of the case coincides with the maximum chamber

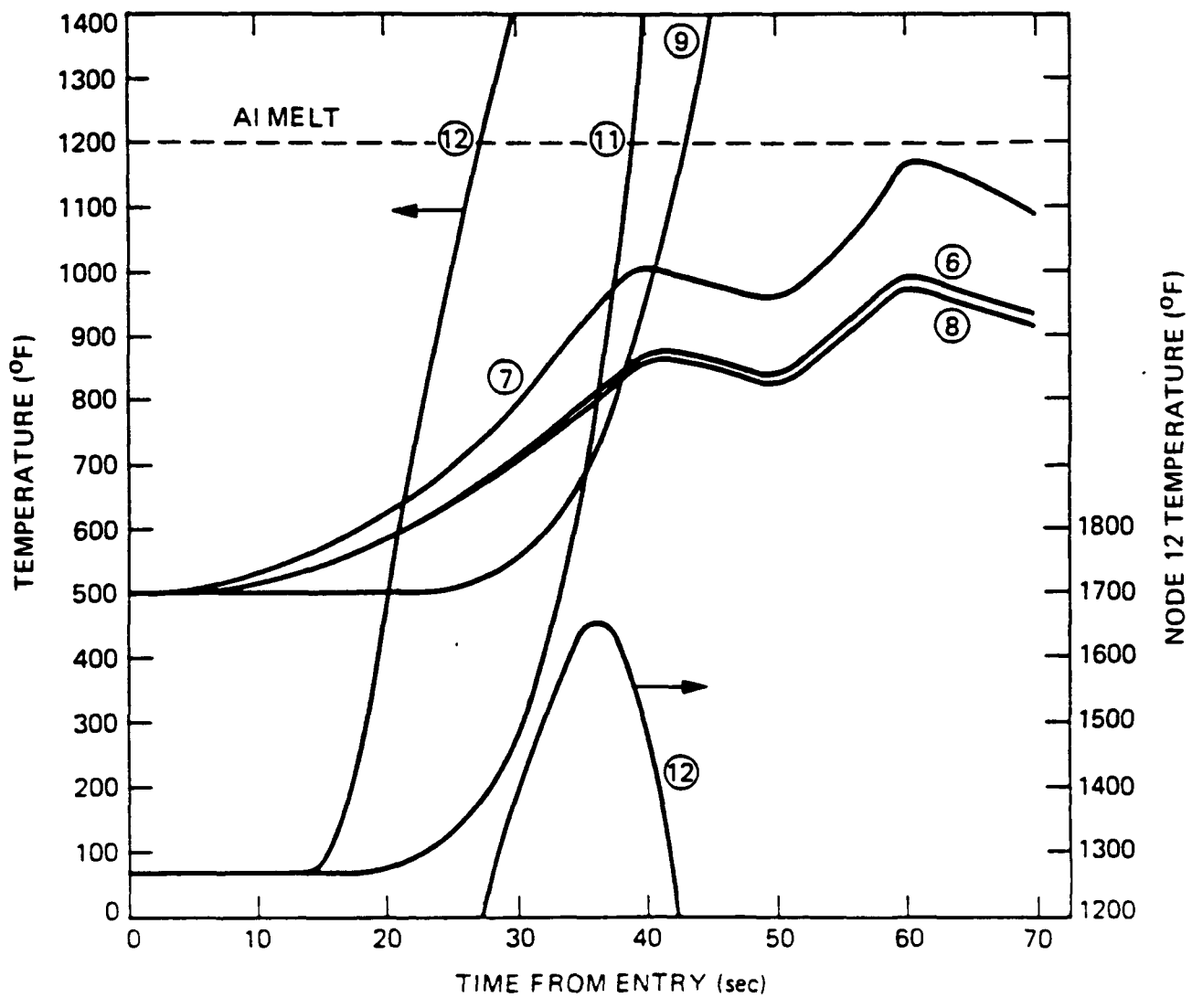


Figure E-11. Temperature History of Galileo RTG and Support Structure Nodes. RTG Position 1

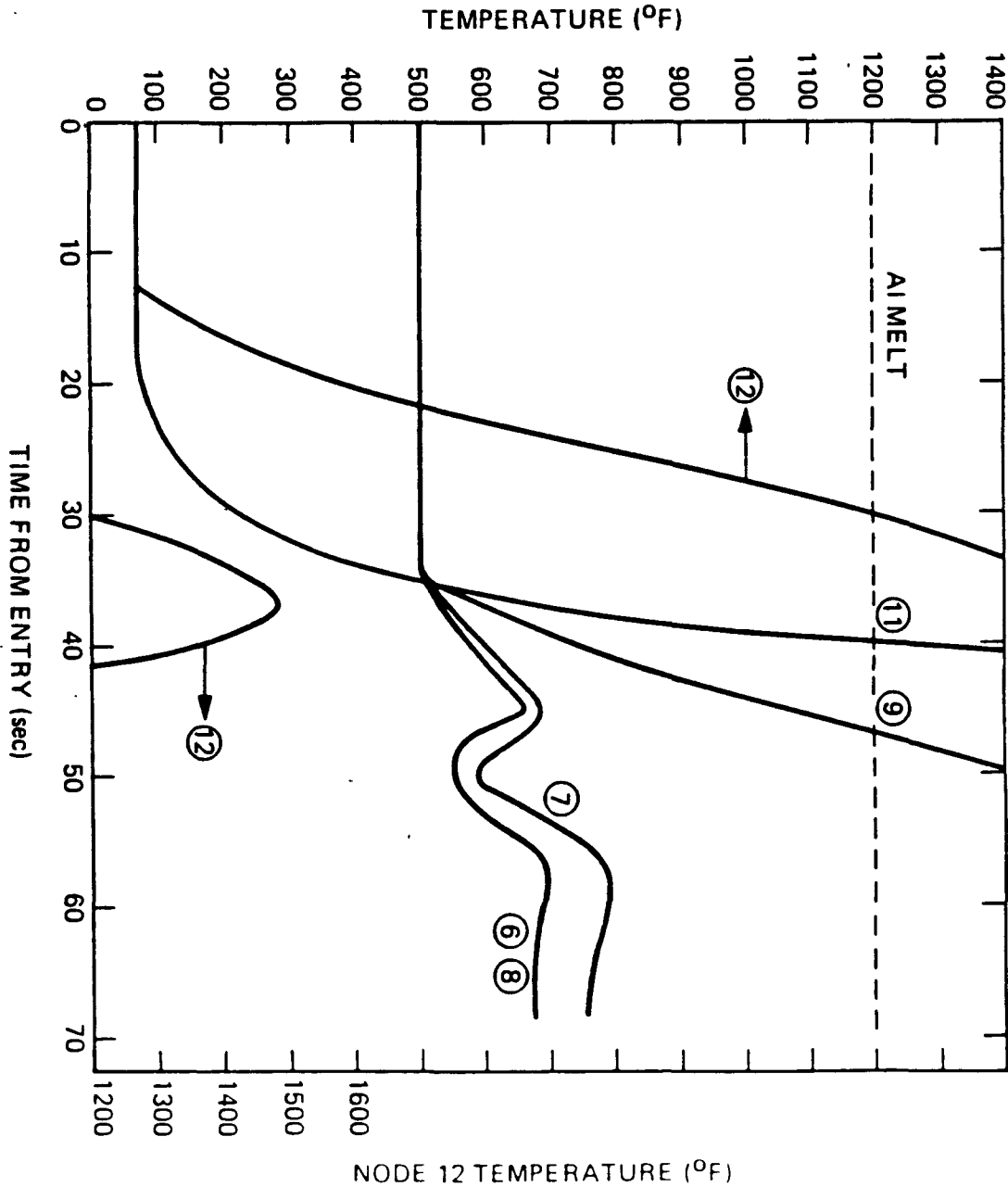


Figure E-12. Temperature History of Galileo RTG and Support Structure Nodes. RTG Position 1, 25% Reduced Heating



Table E-2. Chronology of Significant Events, Baseline Entry

Time (sec)	Altitude (kft)	Event	Comment
0	400	entry begins;	IUS in pre Burn-2 configuration, angle of attack 90 deg;
15-43	353-264	sunshade on RTG boom fails	Boom exposed to flow; time range for RTG initially in flow or in wake;
20	337	SRM-2 ignites thrust begins	assumed
26-40	318-273	boom longerons fail, RTG moves back, held by Ti strut	not much change in RTG position and heating
43-47	263-251	RTG outboard end-cap melts, <u>modules free (earliest)</u>	reaches 1200 F; acceleration (-1.2 g's) causes heat source modules to slip out along axis, released into free flight;
48-52	248-235	<u>modules free (latest)</u>	5 sec allowed for motion of IUS to dislodge modules
51-55	239-226	titanium strut fails	Residue of RTG (molybdenum interior structure) held by RTG cable
59	213	earliest burst of SRM-2 casing	reduced strength equals peak chamber pressure
60-70	210-178	support structure fails, SRM-2 skewed	IUS begins to pitch at increasing rate
63-73	201-169	SRM-2 breaks away	

pressure. The aluminum support structure fails at 67 sec; thereafter, the SRM-2 moves to a skewed position relative to the IUS to spin up and release the SRM-2, at an earliest time of about 70 sec.

The RTG boom fails between 26 and 40 seconds, depending on whether the RTG is initially facing the flow or in the wake; after the boom fails, the RTG is free to move a small distance until restrained by the titanium latching truss and pressed against the IUS by the acceleration from the SRM-2 thrust. At about 43 to 47 sec the RTG end cap facing the flow melts, and the column of heat source modules is rapidly released into free flight under the action of the acceleration from the SRM-2. The conclusion from Table E-2 is that in the baseline case, the RTG modules are released a considerable time before the SRM-2 could burst.

#### E.1.5 HEAT SOURCE MODULE RELEASE TIMES

To determine the release times and altitudes for the GPHS modules, the breakup point of the RTG was determined for each of the trajectories in Table E-1 as described in Section E.1.4. To insure catching the late time, a 25 percent reduction in heating was applied to Galileo Position 2. For Trajectory 5, the low energy entry case, the factor was increased to 50 percent. The criteria used to define release were as follows: the end-cap temperature had to be greater than 1200 F, and there had to be at least 0.5 g acceleration in the end-cap direction.

Table E-3 summarizes the results. In the column headed case, the first number corresponds to the trajectory and the second to the vehicle (spacecraft) position; a following "x" means a 25 percent reduction in heating was applied. For Galileo the highest release altitude is 293 kft (Case 2-1) and the lowest is 139 kft (Case 5-2X). Of particular significance is the fact that, for the low energy trajectory, there still is enough reentry energy to guarantee RTG breakup.

Table E-3. Thermal Response of RTG for Various Trajectories

CASE END CAP REACHES 1200 F

Case	Time (sec)	Alt (kft)	G's axial
1-1	46	269	1.20
1-2X	47	266	1.24
1-3			
1-3X			
2-1	37	293	0.89
2-2			
3-2X	23	219	0.84
3-3X			
4-2X	23	219	0.29
4-3X			
5-2X	44	139	4.84

#### E.1.6 OTHER EVENTS

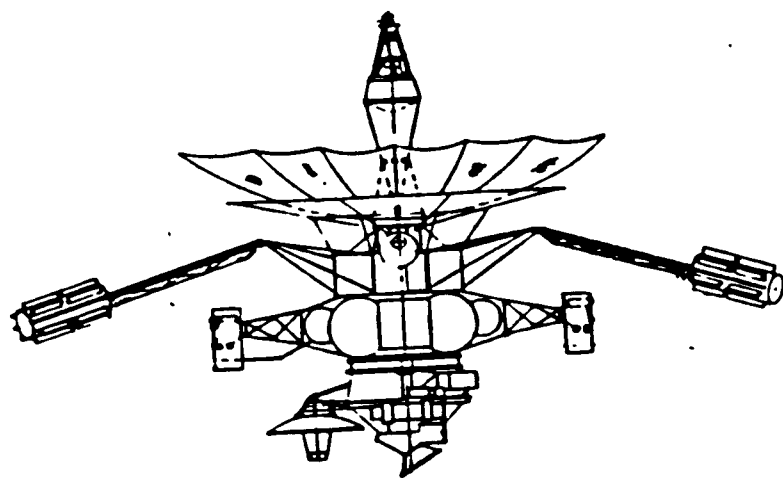
This section discusses the other events which could have a major impact on the breakup sequence but which were found not likely to occur during the time frame of interest. Among those considered are the possibilities of 1) a monomethyl hydrazine/nitrogen tetroxide (MMH/NTO) reaction, 2) burst of a high-pressure GHe tank, 3) auto-ignition of pyrotechnic devices designed to separate the spacecraft from the IUS, and 4) bursting of liquid or gas tanks on the IUS. The MMH/NTO and GHe tanks are in the RPM (retro-propulsion module), the Superzip disconnect ring is where the spacecraft meets the IUS, and a series of 13 explosive bolts is located on the trusses latching the three booms.

E.1.6.1 MMH Tank

The RPM contains 800 lb of MMH and 1300 lb of NTO, which would react if combined, and is located about 10 ft from the RTGs. Each of the two MMH tanks is 29.6 inch in diameter, and pressurized with GHe to 45 psia. The MMH tank can fail in two ways: a) by a rise in bulk temperature, reducing the ullage, increasing the internal pressure, weakening the tank; and b) by local heating of the tank leading to local burnout failure at about 1000°F. A bulk rise of 160°F would be required for a type (a) failure, and a local heating rate of more than 54 btu/ft<sup>2</sup>/sec would be required for a type (b) failure. With the RPM treated as a sphere of diameter 6 ft and heat losses being neglected, the equivalent reference values are  $Q$  (ref) = 3900 btu/ft<sup>2</sup> and  $q$  (ref) = 66 btu/ft<sup>2</sup>/sec. From Figures E-4 and E-5, the earliest altitudes and times at which failure could occur are seen to be 150 kft, 85 sec for (a) and 230 kft, 60 sec for (b), respectively, provided that the RPM is exposed to the flow, i.e., that the IUS has been removed or separated. The earlier of these possibilities clearly comes after the RTG modules have been released.

E.1.6.2 GHe Tank

The two GHe tanks located in the RPM module of the Galileo spacecraft (Figure E-13) are of interest because of concern that the blast or shrapnel from a burst tank could damage the RTG heat source modules prior to their release. Each of the 17.6 inch diameter spherical tanks is nominally pressurized to 2500 psia and has no provision for pressure relief. The tank is constructed of T1-6Al-4V and has 0.167 inch wall thickness. Burst is rated at 5000 psi at room temperature. The empty tank weighs about 26 lb (excluding the mounting hardware) and is filled with about 2.6 lb of He. The tanks are located about 10 ft from the RTGs. The timing of the GHe tank fracture was bounded by considering the extremes of high and low wall conduction relative to the surface convection. In the good conduction case, the tank would fail at 3900 psi, requiring a  $Q$  (ref) of 800 btu/ft<sup>2</sup>; in the poor conduction case, the tank would fail when the wall is heated to 1000°F, requiring a  $Q$  (ref) of 610 btu/ft<sup>2</sup>, both presuming exposure of the RPM to the flow. The equivalent altitudes and times are 230 kft, 60 sec and 240 kft, 56 sec, and the earliest of these occurs after the RTG modules are released.



(CRUISE CONFIGURATION)

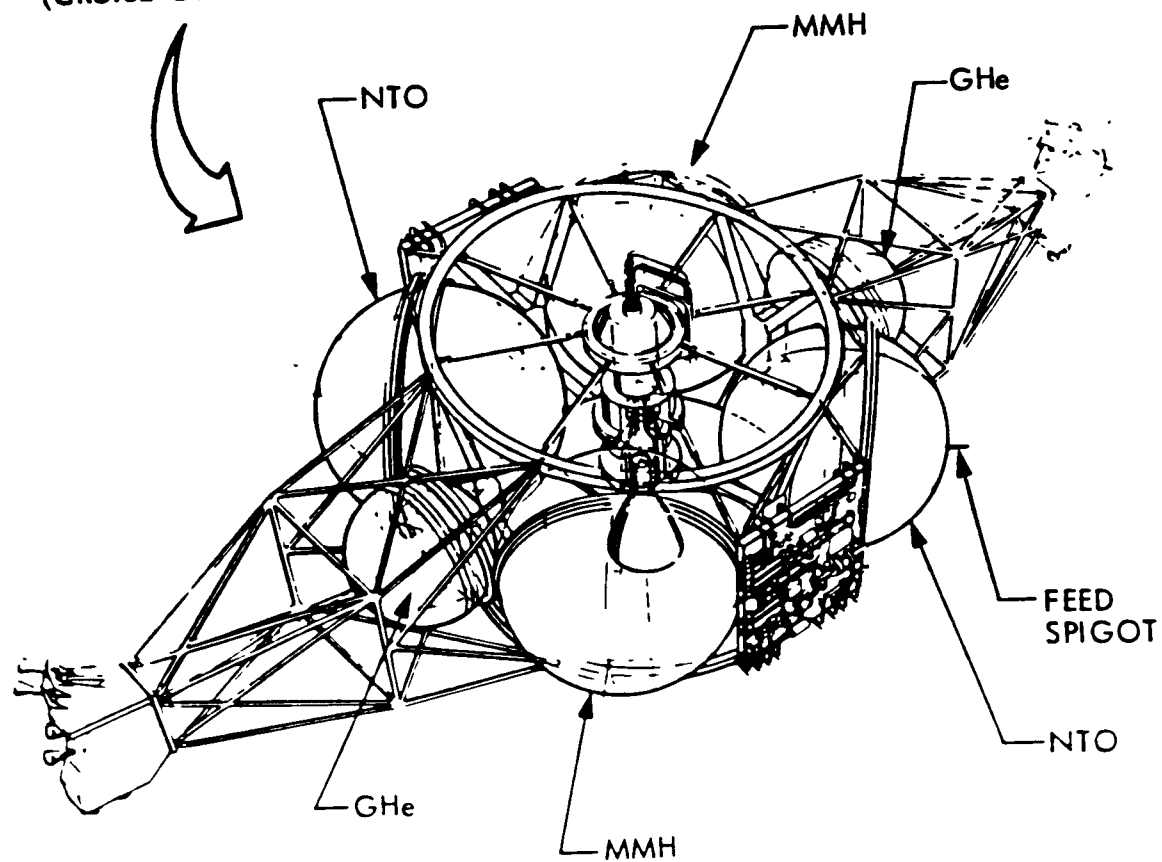


Figure E-13. Galileo Retro-Propulsion Module (RPM)

### E.1.6.3 Auto-Ignition Of The Pyrotechnics

This is of interest because the resulting major change of the vehicle configuration would greatly affect the entry trajectory and heating, e.g., separation of the spacecraft from the IUS. To separate the Galileo spacecraft, two items must both be actuated: a) a Superzip ring near the spacecraft end of the adapter, and b) a total of 13 individual explosive bolts arranged in groups on the four sides of the adapter. These bolts are intended to free or unlatch the two RTGs, the Science boom, the scan platform, and the despun electronics. Figure E-14, shows the location of the bolts. Although the Superzip could be activated by thermal ignition of the igniter due to heating of the igniter block, it is concluded that (a) explosive rupture of the ring joint may not be complete; (b) it is improbable that all 13 of the explosive bolts on the adapter latching the truss struts could be actuated thermally; and (c) the IUS SRM-2 thrust (acceleration of 1g) would prevent separation of the spacecraft even if the pyrotechnics had been actuated. For these reasons, it is unlikely that the pyrotechnic devices of the spacecraft can materially affect the breakup scenario described.

### E.1.6.4 IUS Tanks

The IUS has a number of propellant and gas pressurant tanks used for attitude control and similar in general to the MMH and GHe tanks of the RPM. They are located inside the adapter, on the spacecraft side of the SRM-2 motor, and as such are shielded from the flow until the SRM-2 is separated or breaks up. Because they then require substantial heating when exposed directly to the flow before they can burst, they appear unlikely to affect the release of the RTG modules.

## E.2 VEEGA REENTRY ANALYSIS

The purpose of this study was to estimate breakup conditions for the Galileo spacecraft if the spacecraft accidentally reentered the atmosphere at the time of either Earth flyby, by comparing the entry conditions with those of the analysis in the report, "Galileo RTG Reentry Breakup Analysis," A.D. McDonald, JPLD-1876, September, 1984, Jet Propulsion Laboratory. Two cases were

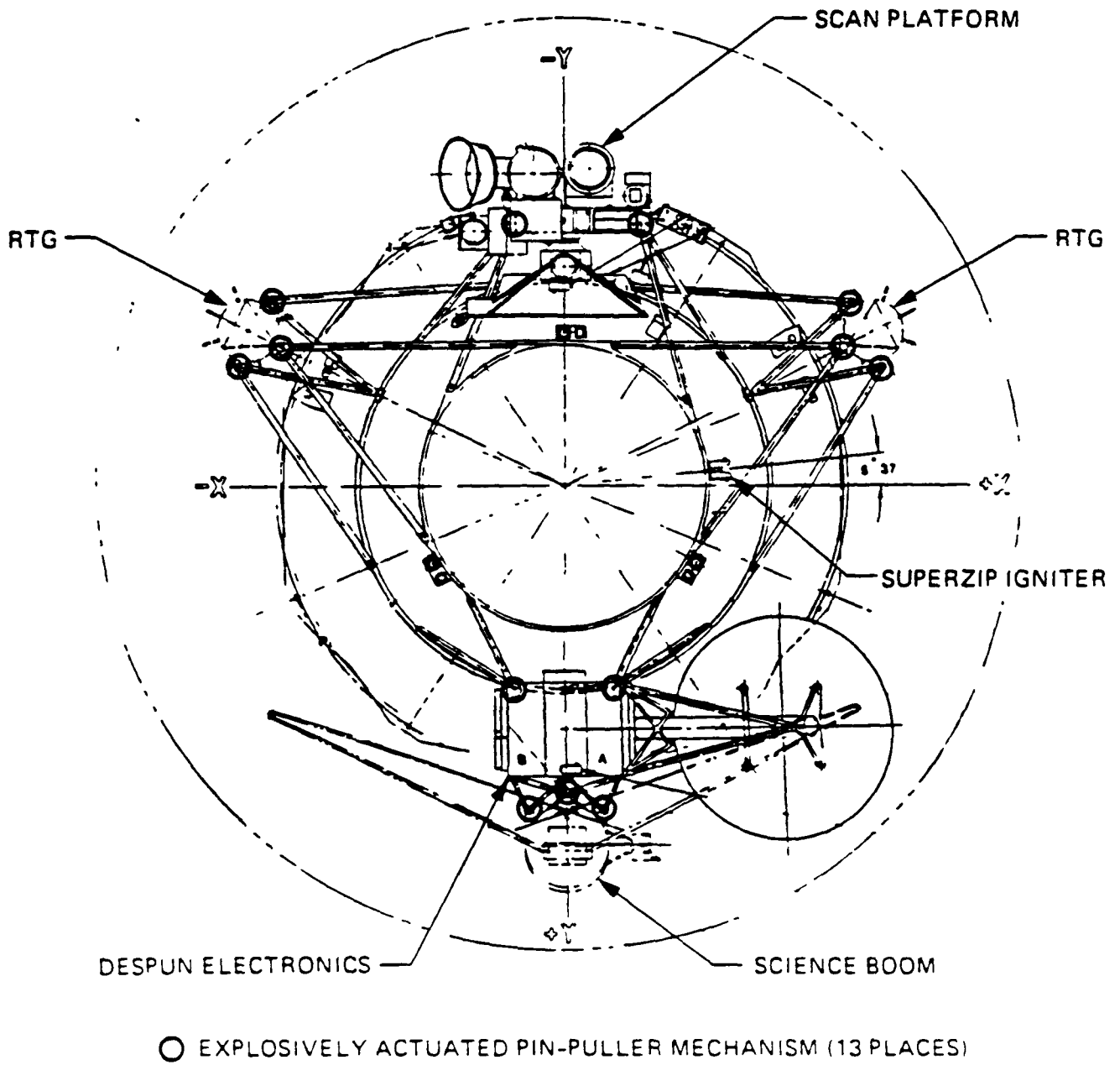


Figure E-14. Location of Pyrotechnic Devices, Stowed Spacecraft

studied: 1) a steep entry case, represented by a 90 deg entry angle, and 2) a minimum gamma case, where the spacecraft skips along in the atmosphere before descending. These represent two extremes of breakup mechanisms, and are thought to bracket all the real cases. The steep entry results in the greatest heating rate and the greatest deceleration, aero force and thermal stress. The skip-along entry results in relatively low heating rate and forces, but for the longest time, and produces the greatest ablation and time-integrated heating.

The main difference between the prior breakup cases (direct launch) and the new VEEGA cases is the entry speed, which is in the range of 45.6 to 49.2 kft/sec instead of 36 kft/sec. Since the aero force varies as the square of the velocity, and the heating rate varies as the cube of velocity, one would expect the spacecraft to meet the breakup levels of force and heating at a lower value of atmospheric density, i.e., at a higher altitude, and this is found. Also, the higher speed makes a dramatic change, later in the entry, in the radiative heating to the GPHS modules from the hot plasma in the shock layer.

### E.2.1 INITIAL CONDITIONS

As in the prior analysis (JPLD-1876), the entry spacecraft geometry is the deployed Galileo spacecraft, as illustrated in Figure E-15. The previous analysis considered two spacecraft attitudes: a non-spinning spacecraft at the aero trim attitude, with the magnetometer boom trailing astern, and a spinning spacecraft with the spin axis at 90 deg to the velocity vector. Summary tables of the breakup analysis for the steep and minimum gamma reentry cases from JPLD-1876 are reproduced here as Tables E-4 and E-5, respectively.

The VEEGA trajectory entails two Earth flybys, called EGA 1 and EGA 2, in December 1990 and 1992, respectively. The Earth approach velocity, calculated at 100 km altitude, depends strongly on the launch date (for a chosen arrival date), as shown in Table E-6, which gives a minimum, a maximum and a most probable velocity. For the purpose of this study, low and high limits of 13.9 and 15.0 km/sec (45.6 and 49.2 kft/sec) were adopted for evaluation, with corresponding entry angle limits of 90 deg and 7 deg. In the 7 deg case, the



NOTE: VEEGA configuration changes not shown

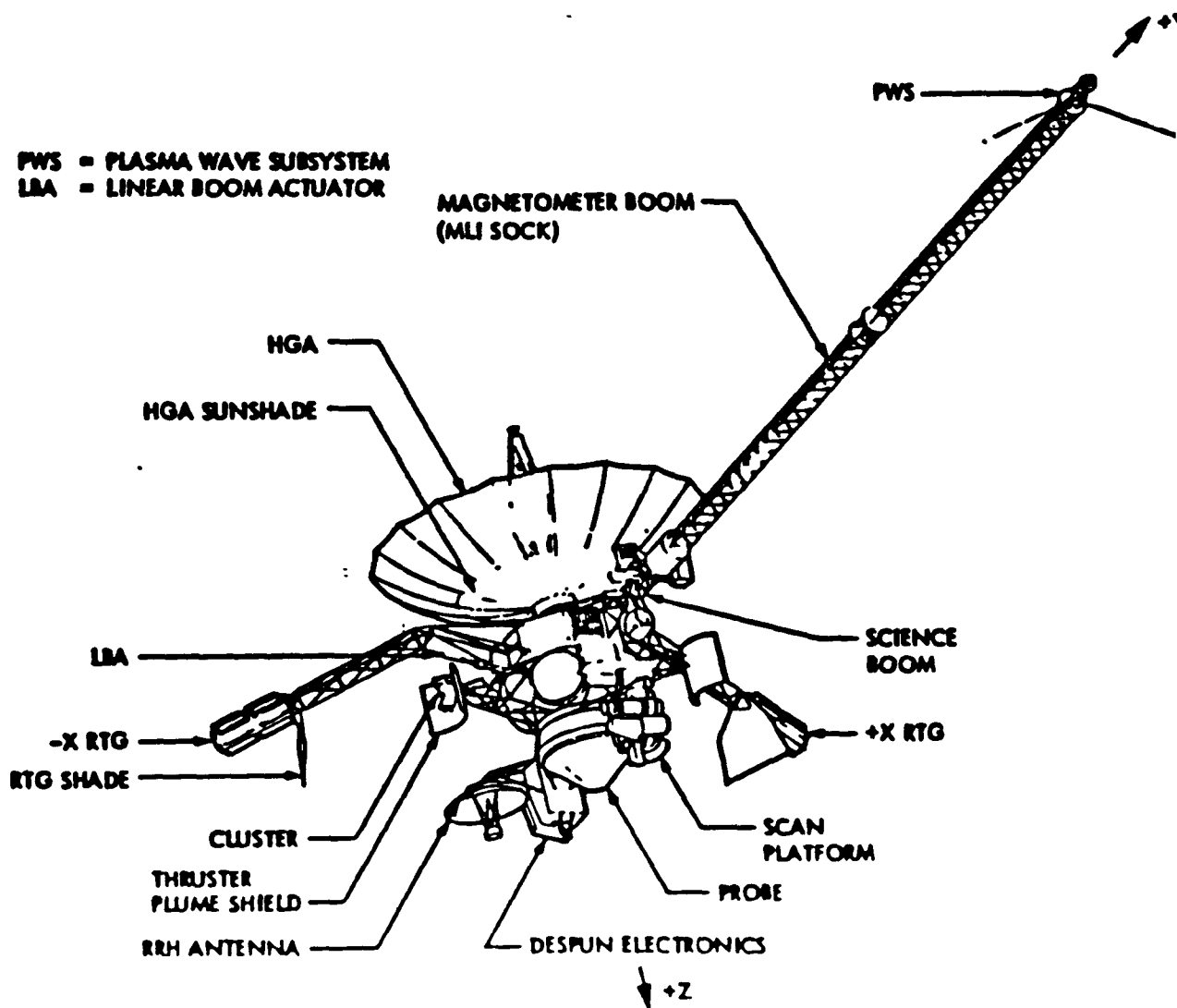


Figure E-15. Deployed Galileo Spacecraft (Cruise Mode)

Table E-4. Breakup Events, Case 1

CONDITIONS: Entry at 400 kft, speed 36 kft/sec (inertial), angle 39 degree non-spinning spacecraft, deployed booms, RTGs leading at 60 degree to flow, magnetometer boom astern.

Time (sec)	Altitude (kft)	Events
0	400	Entry begins
2.7	339	Meteorite shield (kapton) along RTG boom fails thermally; power cables now exposed
3.6	318	RTG boom diagonal tubes (graphite-epoxy) begin to fail
3.8	314	RTG boom longeron tubes fail (eroded to $\pm 60$ deg from windward line)
4.0	309	RTG boom fails near hinge, begins to swing back on power cable
4.3	302	Exposed side of meteorite shield on mag boom fails
5.3	280	Remainder of mag boom shield fails; vehicle tends to move to new aero trim governed by Science boom and RTGs swinging on cables
5.6	273	Melting of (original) outboard end of RTG allows outboard half-stack (9) of fuel modules to be released (centrifugal force due to swing) into free flight and separate from stack (earliest): RTG axis about 130 deg to flow.
5.8	269	Tension in RTG cable reaches 180 lb, angle 152 deg to flow; electrical connectors pull out of plug insulators.
6.0	264	Tension in RTG cable reaches 230 lb., angle 176 deg to flow; braided shield separates from attachment point; RTG released into free flight.
6.4	253	Melting of leading end of RTG releases inboard latch pins, differential drag pulls back case, allowing inboard half-stack of modules to slip out and separate in free flight as individuals (latest).

Table E-5. Breakup Events, Case 2

CONDITIONS: Entry at 400 kft, speed 36 kft/sec (inertial), angle 5 deg (minimum gamma): (a) non-spinning at aero trim (mag boom trailing); (b) spinning spacecraft (3.1 RPM) with axis at 90 deg to flow.

Time (sec)	Altitude (kft)	Events	
		Non-Spinning Spacecraft	Spinning Spacecraft
0	400	Entry begins	Entry begins
14.5	357	MLI blankets begin to fail (outer layer reaches 1500 F) on small items on windward side	
17	350	RTG boom longeron tubes (graphite-epoxy) fail (erode to $\pm 60$ deg from stagnation line): RTG begins to swing back on cable from original 60 deg.	
17-20	350-342		RTG boom fails, range depends on initial orientation; RTG continues to rotate on cable
22.5	336	Axis at 90 deg. outboard end begins to melt:	
24	332	latch pin released, outboard half-stack of fuel modules slips out under centrifugal force, released into individual free flight (earliest)	
24-29	332-319		RTG rotation on cable reverses, outboard end of case melts
26.5	326	RTG passes through wake of spacecraft, cable wraps around neck of bus near high-gain antenna	
25-33	330-311		Cable end of RTG melts, plugs pull out of case; heat source is exposed
28	323	At angle 220 deg, inboard end begins to melt, exposes heat source modules	

Table E-5. Breakup Events, Case 2 (Cont'd)

Time (sec)	Altitude (kft)	Events	
		Non-Spinning Spacecraft	Spinning Spacecraft
29	320	At angle 240 deg, motion reverses, RTG begins to swing back in opposite direction	
28-36	323-307		Interconnect straps melt, remnant of case + modules is released into free flight; aligns with flow, differential drag pulls case and insulation back, allowing inboard modules to slip out (latest)
32	314	Copper internal straps begin to melt, RTG is released into free flight, trims inboard end leading	
36	306	Differential drag pulls case back from half-stack of modules; modules slip out and separate in free flight (Latest)	

Table E-6. Possible Entry Conditions

	Velocity, km/sec			Entry Angle Range
	Most Probable	Minimum	Maximum	
EGA 1	14.24	13.88	14.97	7° to 90°
EGA 2	14.24	14.21	14.97	7° to 90°

spacecraft can enter either downwind (i.e., with the Earth rotation) or upwind (i.e., against Earth rotation, see Figure E-16), the air relative velocity then being less than or greater than the inertial velocity by about 1500 ft/sec. As the approach velocity vector is generally within a few degrees of being in the Earth ecliptic plane, it must make an angle of about 0-23 deg to the Earth rotation vector at entry, depending on the entry direction; accordingly a value of 1400 ft/sec was taken as the Earth rotation velocity in-plane component at entry. Table E-7 shows the cases analyzed.

The geometry for EGA entry can be seen from Figure E-17, which relates to the two flybys of Earth during the VEEGA sequence. It can be seen that the Spacecraft in EGA 1 approaches Earth at about 90 deg to the terminator, on the dark side, while in EGA 2 it approaches Earth at about 45 deg to the terminator, on the sunlit side. The nominal Flyby entails a rotation of the relative velocity vector by about 45 deg. During the Earth flyby parts of the VEEGA flight, the spacecraft is likely to be spinning and pointing along the velocity vector, or at 45 deg to it, depending on the malfunction predicated to lead to the entry instead of the flyby. However, because, of the deployed graphite-epoxy booms and the analysis done previously, it is clear that the uncertainty in the EGA entry conditions is likely to result in a range of RTG release altitudes comparable to that found in JPLD-1876.

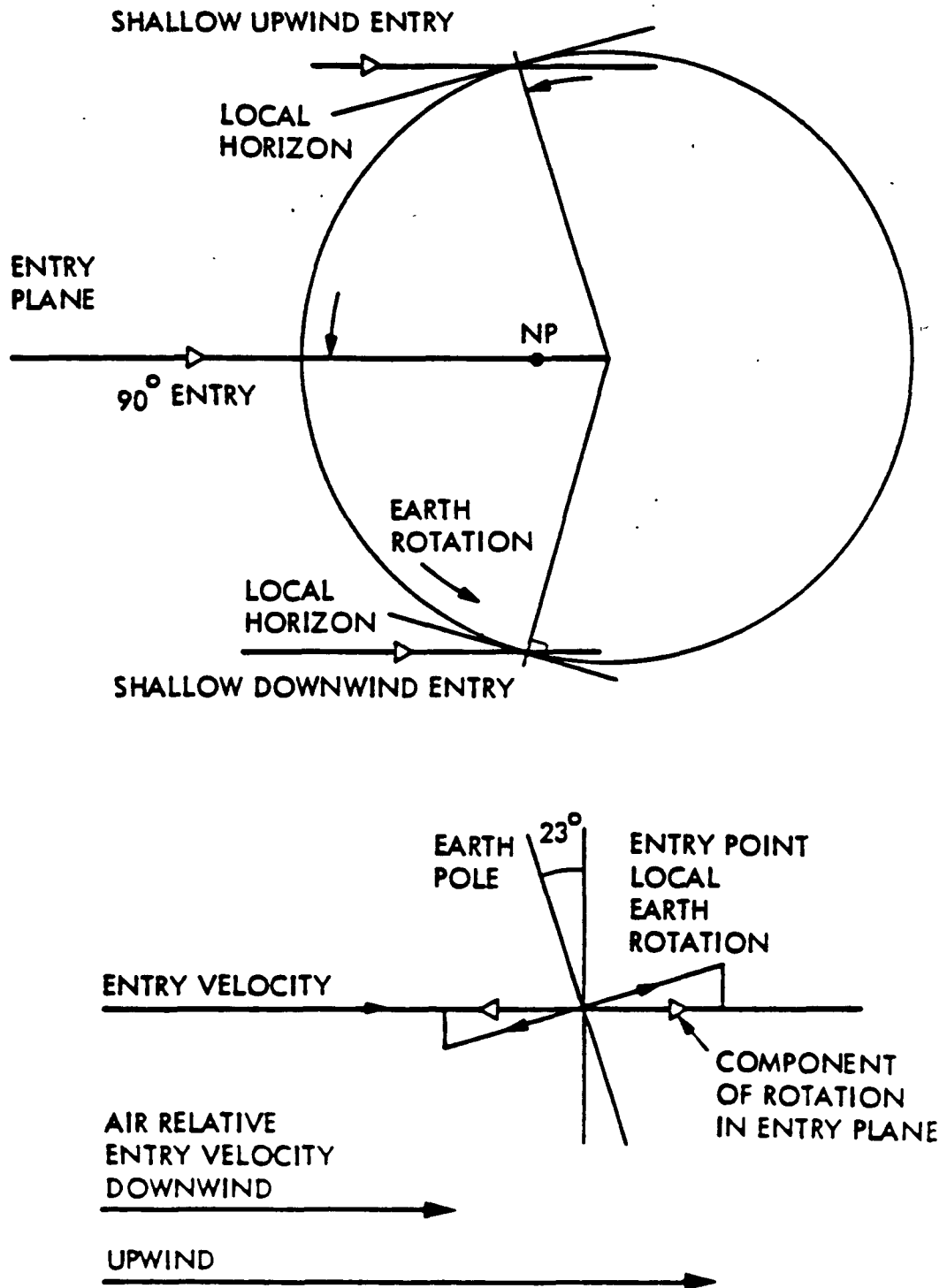
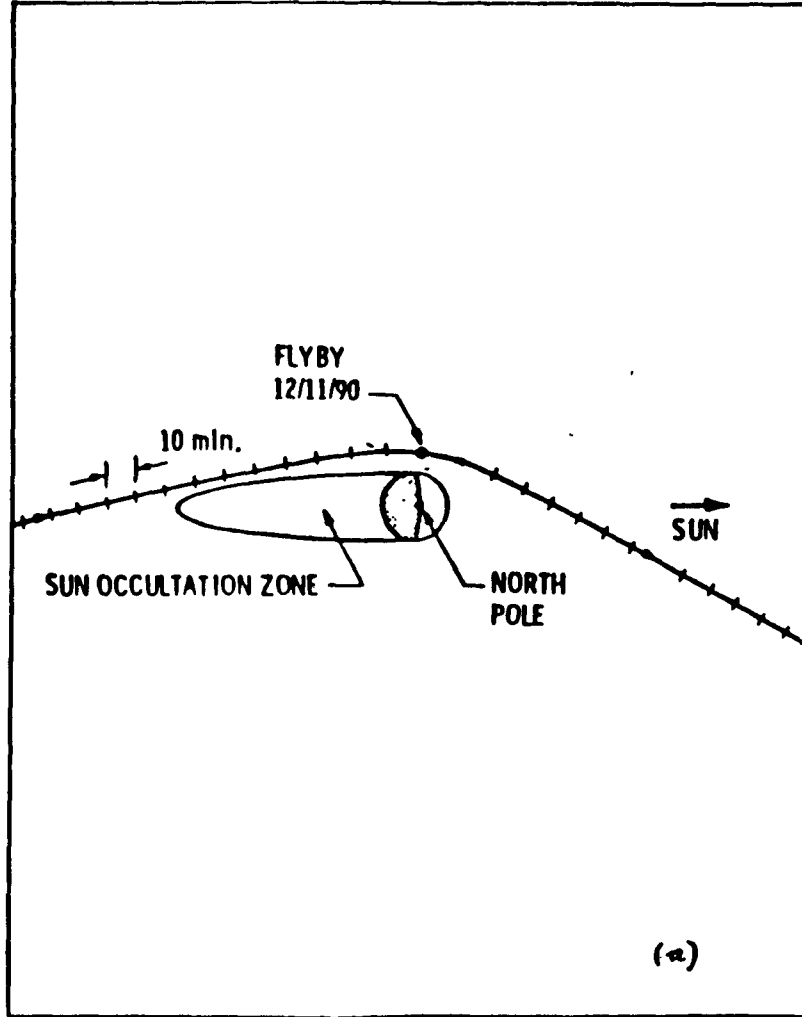


Figure E-16. Upwind and Downwind Entry at Shallow Angle

Table E-7. Cases Analyzed

Case	Entry Angle (deg)	Entry Velocity (kft/sec)	Comment
1a	-90	49.21	maximum speed over launch period
1b	-90	45.6	minimum speed
2a	-7	49.21	upwind
2b	-7	45.6	upwind
2c	-7	45.6	downwind

1989 VEEGA : EARTH FLYBY (1)



1989 VEEGA : EARTH FLYBY (2)

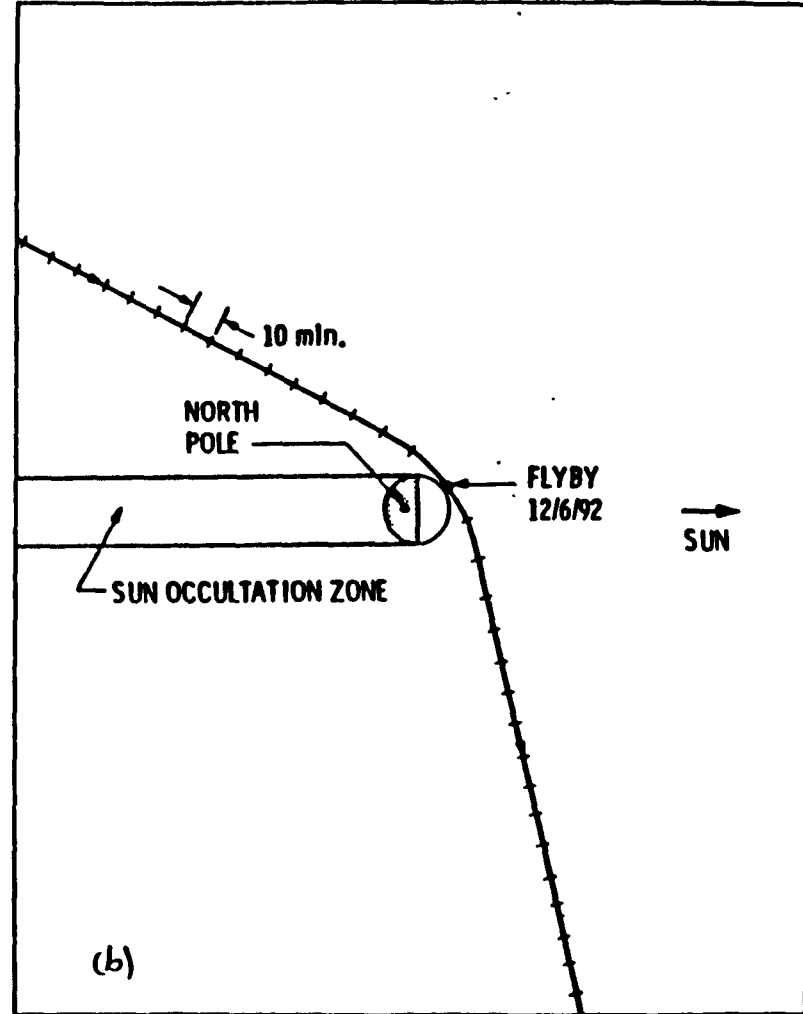


Figure E-17. Earth Flyby Geometry: (a) EGA 1 (b) EGA 2



### E.2.2 COMPARISON OF TRAJECTORY PARAMETERS

The reference parameters for the previous analysis and the new EGA trajectories are compared, as a function of altitude, in Figure E-18 for the steep entry cases (speeds 49.2 and 45.6 kft/sec, called Cases 1a and 1b), and in Figure E-19 for three shallow entry cases (speeds 49.2 upwind, 45.6 upwind and 45.6 downwind, called Cases 2a, 2b and 2c, respectively). The reference parameters are the convective heating rate  $q$ , shown only for the early part of the entry (near the transition from free-molecular to continuum flow), the time-integrated reference heating  $Q$ , and the stagnation pressure  $p$  (approximately equal to the product of the density and the velocity squared). Although the radiative heating is relatively large later in the trajectory, it does not play a major part in the release of the RTGs and the modules. For comparison of the JPLD-1876 and the new EGA trajectories, the release points predicted for free flight of GPHS modules are as shown in Table E-8.

From the analysis conducted, the following conclusions can be drawn:

- 1) The initial conditions for Earth reentry of the Galileo spacecraft are sufficiently similar for the comparison of RTG release to be made from comparing the aerodynamic heating rates and forces for the VEEGA and the direct launch cases.
- 2) Such a comparison indicates that the RTGs will release at an altitude from 4 to 17 km above the values found for the direct launch case, for both the steep and the minimum gamma entries.

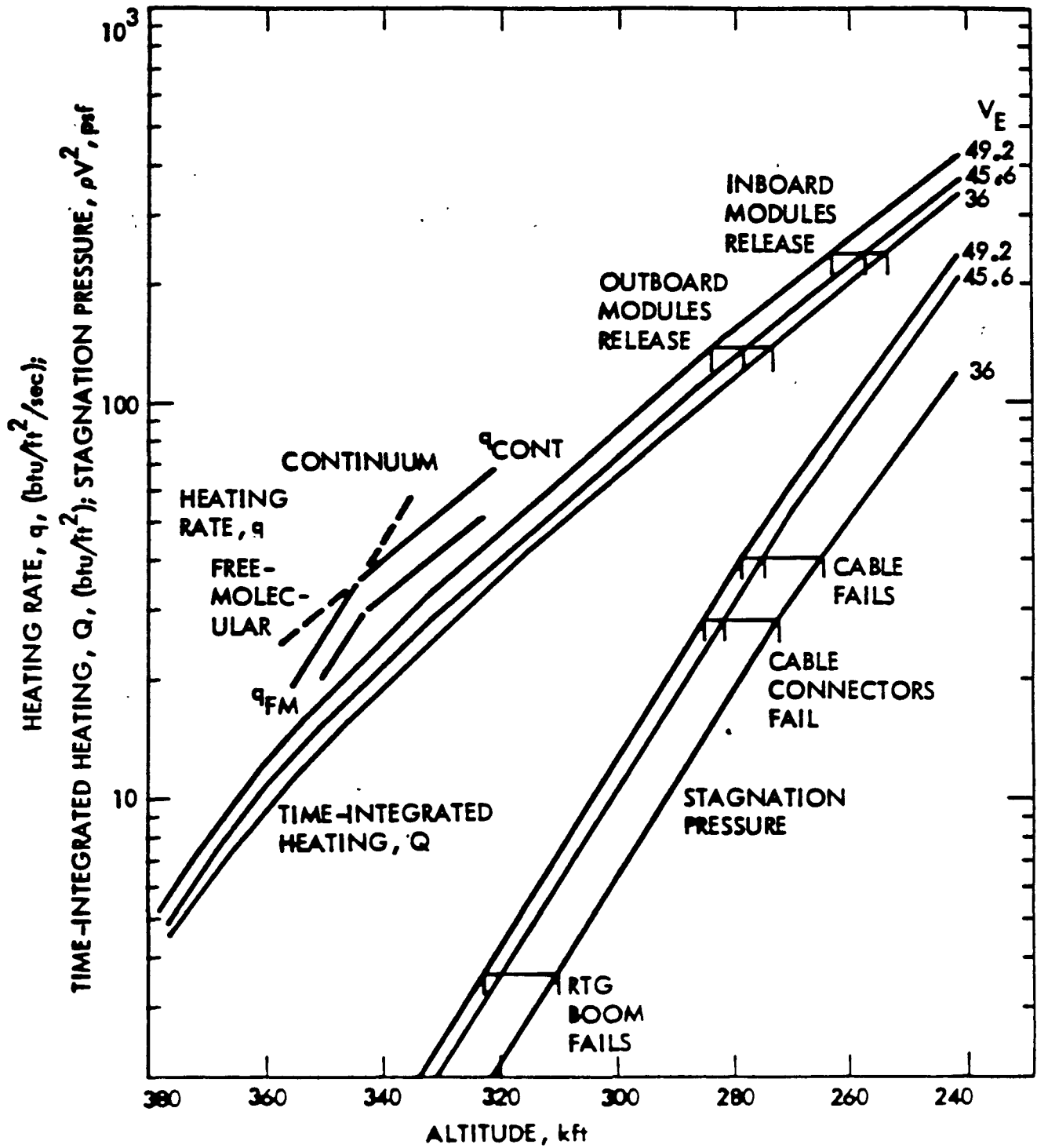


Figure E-18. Reference Stagnation Heating Rate, Stagnation Pressure, and Time-Integrated Heating Vs. Altitude for Steep Entry: 39 Deg. for JPLD-1876; 90 Deg. for VEEGA

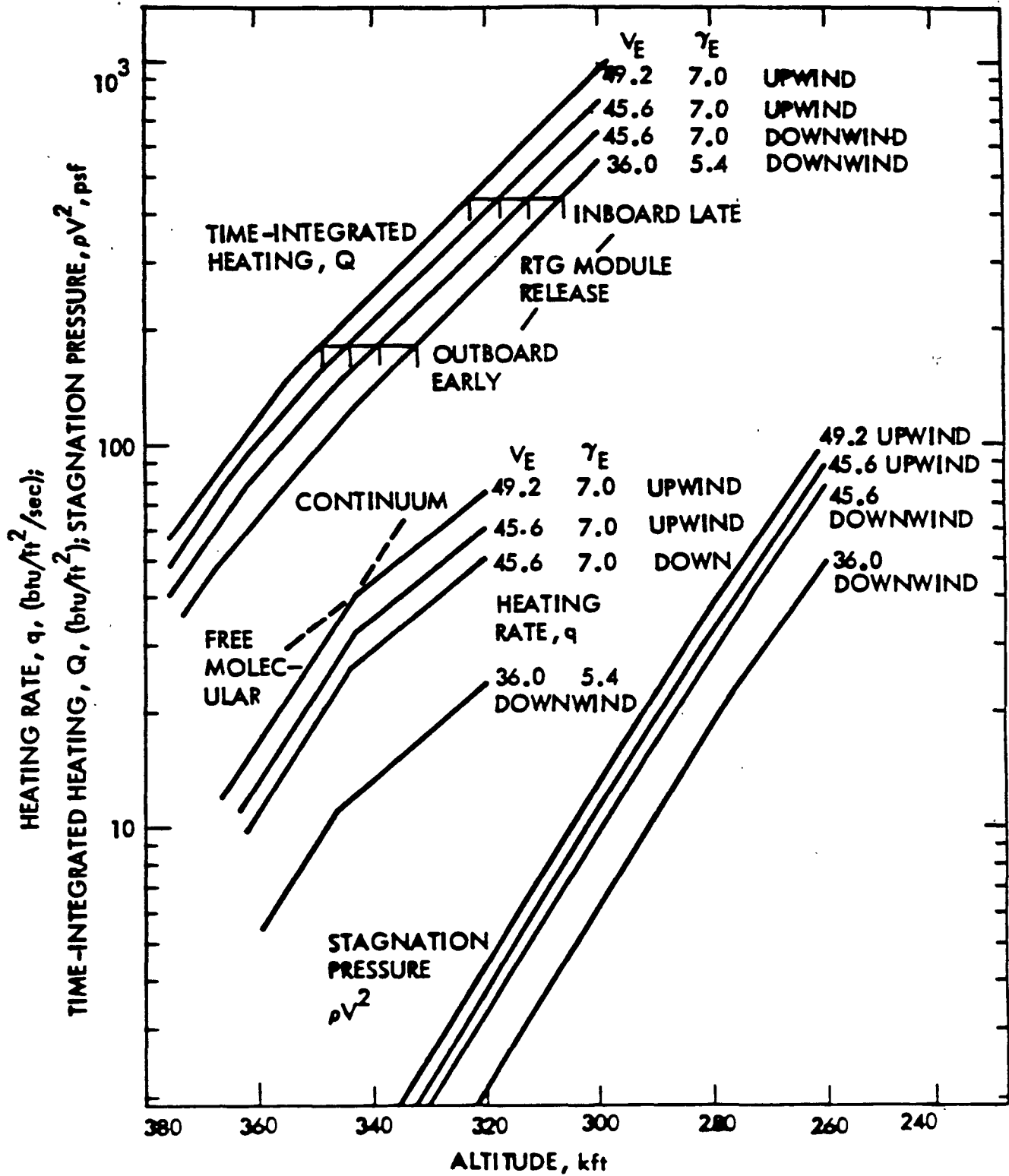


Figure E-19. Reference Stagnation Heating Rate, Stagnation Pressure, and Time-Integrated Heating Vs. Altitude for Shallow Entry: 5.4 Deg. for Ref. 2; 7 Deg. for VEEGA

Table E-8. GPHS Module Release Points

Case	Time From Entry, Sec	Altitude kft	Inertial Speed kft/sec	Inertial Path angle, deg	Comment
Ref. 2	5.6	273	36.10	-38.79	steep entry at 39 deg, speed 36 kft/sec
	6.0	253	36.11	-38.76	
Ref. 2	24	333	36.06	- 3.85	minimum gamma, 5.6 deg, speed 36 kft/sec
	36	306	36.07	- 3.28	
EGA	2.3	284	49.28	-90	steep entry at 90 deg, speed 49.2 kft/sec
	2.8	263	49.29	-90	
EGA	2.7	278	45.68	-90	steep entry at 90 deg, speed 45.6 kft/sec
	3.1	257	45/69	-90	
EGA	8.8	349	49.24	- 6.15	minimum gamma, 7.0 deg, speed 49.2 kft/sec upwind
	14.4	323	49.26	- 5.61	
EGA	12.0	339	45.64	- 6.00	minimum gamma, 7.0 deg, speed 45.6 kft/sec, downwind
	17.6	312	45.66	- 5.53	

We can see that the higher speed and different angles of the EGA entries have reduced the time from entry to breakup by approximately a factor of two.

APPENDIX F  
GPHS REENTRY RESPONSE - VEEGA CONDITIONS

This appendix presents the analyses that have been conducted to determine the GPHS response to thermal environments as a result of Earth reentry at the time of VEEGA flyby. The initial GPHS flight path conditions were taken from References F-1 and F-2. Section F.1 discusses the initial conditions on which the analysis is based. An overview of the analyses and results is presented in Section F.2 along with the influence of the variation in several factors and assumptions employed. The techniques and models used in the analysis are included in Section F.3. Detailed results are presented in Section F.4 along with other supporting studies.

F.1 INITIAL CONDITIONS

In Reference F-1, initial conditions were given for four steep and six shallow trajectories. (In the current context, steep and shallow refer to initial flight path angles of  $-90$  degrees and between  $-5$  and  $-7$  degrees, respectively. In the steep case, there are essentially two initial speeds and, for each speed, two initial altitudes. In the shallow case, there are also two initial speeds with two initial altitudes corresponding to the higher speed and four initial altitudes corresponding to the lower speed. The actual initial trajectory conditions analyzed are shown in Table F-1.

In Reference F-2, initial conditions were given for one initial speed (the higher speed) in the form of a range of initial altitudes as a function of initial flight path angle. The upper and lower bounds for the altitude range were adjusted in order to be consistent with the high speed, steep and shallow cases of Reference F-1. The resulting initial flight path conditions for the intermediate flight path angles are also shown in Table F-1 as cases I1 thru I16. A plot of the initial module flight conditions is shown in Figure F-1.

## F.2 OVERVIEW

Several of these trajectories were utilized in a reentry thermal analysis assuming a face-on-stable module orientation and using the 3-D (three dimensional) THTD (Transient Heat Transfer - Version D) computer program. (A limited 6 degree-of-freedom trajectory analysis will be discussed later as a basis for assuming the face-on-stable altitude.) This program was incapable of reaching satisfactorily converged solutions due to the extreme reentry environments as a result of the VEEGA earth flyby flight conditions.

Successful solutions were realized with a 1-D (one-dimensional) reentry program. These solutions showed aeroshell front face temperatures in the vicinity of 3870°C (7000°F) throughout the thickness of the aeroshell within the first few seconds of flight.

It was assumed that, at these temperatures, the aeroshell would fail resulting in a GIS release. The GIS release conditions are given in Table F-2 and are based upon the assumption of aeroshell failure when its inner surface temperature reached 3760°C (6800°F) which is approximately the middle of the range for melting of the graphite.

Subsequent GIS reentry thermal analyses were performed with the 3-D THTD program assuming a side-on orientation (i.e., the GIS axis of symmetry normal to the velocity) and a spinning motion about the axis of symmetry. The lower speeds and the spinning motion resulted in a less severe heating environment, permitting successful solutions with the 3-D program for a wide range of initial flight path angles.

Results in the form of iridium clad conditions at impact have been calculated for initial flight path angles between -30 and -70 degrees, the higher of the two initial speeds, and the lower of the initial altitudes. The GIS reentry analyses showed iridium clad melt thru at -30, -40, -50 and -70 degrees because the iridium temperature exceeded the graphite/iridium eutectic. At an initial flight path angle of 60°, the peak iridium clad temperature was

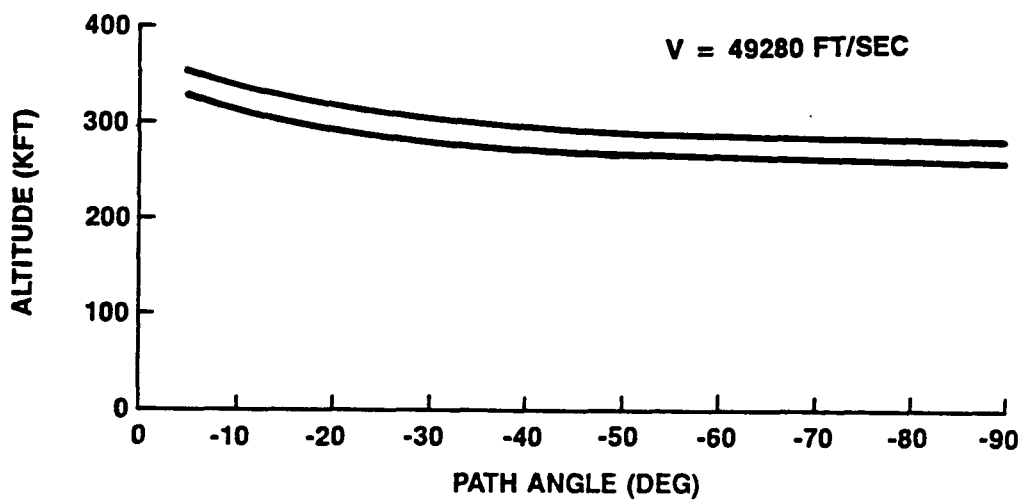


Figure F-1 GPHS Module Initial Flight Path Conditions

Table F-1. GPHS Initial Trajectory Conditions

INERTIAL VALUES

CASE No.	ALTITUDE (FT)	SPEED (FT./SEC.)	FLIGHT PATH ANGLE (DEG.)
1A	284000	49280	-90
1A2	263000	49290	-90
1B	278000	45680	-90
1B2	257000	45690	-90
2A	349000	49240	-6.15
2A2	323000	49260	-5.61
2B	344000	45640	-6.13
2B2	317000	45650	-5.59
2C	339000	45640	-6.00
2C2	312000	45660	-5.53
I1	311000	49280	-10
I2	340000	49280	-10
I3	295000	49280	-20
I4	322000	49280	-20
I5	282000	49280	-30
I6	307000	49280	-30
I7	274000	49280	-40
I8	297000	49280	-40
I9	269000	49280	-50
I10	289000	49280	-50
I11	266000	49280	-60
I12	286000	49280	-60
I13	264000	49280	-70
I14	285000	49280	-70
I15	263000	49280	-80
I16	284000	49280	-80



2303°C (4177°F), and at impact, the clad temperature ranged between 769°C (1417°F) and 842°C (1547°F). The iridium was assumed to melt due to eutectic formation with the FWPF GIS material at 2316°C (4200 °F), and its heat of fusion was taken to be 34.2 cal/gm (61.6 BTU/LB). Based on the trend in variation of the GIS and iridium clad temperatures over this range, the judgement was made that the clad would melt over the entire flight path angle range from -5.53 to -90 degrees.

As mentioned above, the GIS release times, for any given initial module flight path angle, were based upon the higher initial speed and the lower initial altitude. The 1-D reentry program was used to determine the effect of initial module altitude on the initial GIS flight path conditions. Calculations were performed at initial module path angles of -30, -50, and -80 degrees. The results showed that for each flight path angle, the GIS release conditions were rather insensitive to module initial altitude. The results are shown in Table F-2. At -30 degrees the GIS initial flight conditions varied by about 2.5% as the module initial altitude varied between its lower and upper limits. The variance in GIS conditions was less than 1% at -50 and -80 degrees.

As a check of the GIS release times as computed with the 1-D program, the shock layer radiative heating was arbitrarily reduced to the point where 3-D module calculations were possible. The results showed that, at a path angle of -30 degrees, the 1-D release time was 0.3 seconds earlier than that of the 3-D calculation, and at -50 degrees, the difference was 0.1 seconds. It was assumed that the difference became negligible at -90 degrees. This data was used to adjust the GIS release times based upon the 1-D calculations; the adjusted values appear in Table F-2.

Prior to the establishment of the GIS release times of Table F-2, a preliminary set of release conditions had been estimated and used as the basis of several 3-D GIS reentry thermal analyses. A comparison of the data of Table F-2 and the data used for the 3-D GIS reentry calculations are given in

Table F-2. GIS Release Conditions

MODULE INITIAL CONDITIONS		GIS RELEASE TIME (SEC)	GIS INITIAL FLIGHT CONDITIONS		
PATH ANGLE (DEG)	ALTITUDE (KFT)		ANGLE (DEG)	ALTITUDE (KFT)	SPEED (FT/SEC)
-20	295	9.12	-19.231	150526	38935
-20	322	---	---	---	---
-30	282	5.88	-29.555	143648	40056
-30	307	7.06	-29.461	140742	39082
-40	274	4.71	-39.678	132034	38294
-40	297	---	---	---	---
-50	269	3.94	-49.774	127291	38152
-50	289	4.46	-49.741	127655	38288
-60	266	3.47	-59.845	124668	38298
-60	286	---	---	---	---
-70	264	3.18	-69.902	123211	38548
-70	285	---	---	---	---
-80	263	3.03	-79.953	122321	38632
-80	284	3.44	-79.946	123281	38959
-90	263	---	---	---	---
-90	284	3.38	-89.537	123389	39269

Table F-3. As discussed above, the 3-D GIS reentry analyses resulted in iridium clad melt thru at initial path angles of -30, -40, -50, and -70 degrees, and a peak clad temperature of 2316°C (4177°F) at -60 degrees. At impact, the -60 degree case showed clad temperatures ranging between 769°C (1417°F) and 842°C (1547°F).

In Table F-3, it can be seen that all of the preliminary release times which were used for the GIS 3-D reentry analyses were somewhat later than the final set of release times. The differences in release times for the -30 and -70 degree path angle cases are insignificant, and the prediction of clad melt thru for these cases should be unaffected.

In the remainder of the cases, the time difference between the early and late release times are all approximately 0.3 seconds, and, as is apparent from Table F-3, this is not necessarily an insignificant difference.

As an indication of the consequence of such a difference in release time, calculations were performed for the -40 and -50 degree path angle cases assuming a 0.7 second time difference in the -40 degree case and a 0.5 second time difference in the -50 degree case between early and late GIS release times. The GIS release conditions are given in Table F-4. The results of this sensitivity study are shown in Figures F-2 and F-3 in terms of the net energy absorbed by the GIS. The absorbed energy is defined as the algebraic sum of the convective heating, the radiant heating from the hot gases of the shock layer, and the reradiation from the surface to surrounding space. The absorbed energy is significantly greater in each case for the early release time. In addition, the calculations also showed greater energy transfer to the iridium clad for the early release time. The data presented on Figures F-2 and F-3 represent the results of 1-D calculations. The same behavior was seen when the 3-D program was applied to the same cases. Based upon these results, it is expected that iridium clad melt thru will result for the case of the final GIS release times given in Table F-3 for the -40, and -50 degree

Table F-3 Preliminary and Final GIS Release Conditions

MODULE INITIAL CONDITIONS*		PRELIMINARY			FINAL		
		GIS RELEASE			GIS RELEASE		
PATH ANGLE (DEG)	ALTITUDE (KFT)	TIME (SEC)	ALTITUDE (FT)	SPEED (FT/SEC)	TIME (SEC)	ALTITUDE (FT)	SPEED (FT/SEC)
-30	282	5.9	143245	39936	5.88	143648	40056
-40	274	5.0	125180	35336	4.71	132034	38294
-50	269	4.2	119992	34904	3.94	127291	38152
-60	266	3.8	114346	33488	3.47	124668	38298
-70	264	3.2	122466	38283	3.18	123211	38548

\*MODULE INITIAL SPEED = 49280 FT/SEC

path angles, since for later release times (the preliminary release times of Table F-3) at these angles, the GIS reentry calculations resulted in clad melt thru.

In the case of the -60 degree path angle, the peak clad temperature was 13°C less than the melt temperature. Assuming the same behavior as for the -40 and -50 degree path angle cases, earlier release would result in increased clad temperatures during the heating portion of the reentry. Consequently, the clad would either experience some degree of melting or would increase in temperature by something less than 13°C. However, since the -60 degree path angle case resulted in the temperature of the clad being very close to the eutectic melt temperature, the assumption was made that, for purposes of this FSAR II, the clad would melt also at this angle.

If melt thru occurs, then clad failure is assured. If partial or no melting occurs, the inference is that the heating environment at the earlier release time was not much greater than at the later time. This would suggest that the impact temperatures would also see little change.

For flight path angles outside the range of Table F-3, i.e., -30 to -70 degrees, one can see from Table F-2 that the GIS release conditions between -70 and -90 degrees vary by no more than 2% in speed and 1% in altitude. Since there is clad melt thru at -70 degrees, it seems likely that the same will be true between -70 and -90 degrees.

Table F-4 Sensitivity Study/GIS Release Conditions

MODULE INITIAL* CONDITIONS*		EARLY RELEASE**			LATE RELEASE		
		GIS RELEASE TIME (SEC)	ALTITUDE (FT)	SPEED (FT/SEC)	GIS RELEASE TIME (SEC)	ALTITUDE (FT)	SPEED (FT/SEC)
PATH ANGLE (DEG)	ALTITUDE (KFT)						
-40	274	5.0	125180	35336	5.7	111439	27120
-50	269	4.2	119992	34904	4.7	108072	27762

\* MODULE INITIAL SPEED = 49280 FT/SEC

\*\* THESE ARE THE PRELIMINARY CONDITIONS OF TABLE F-3

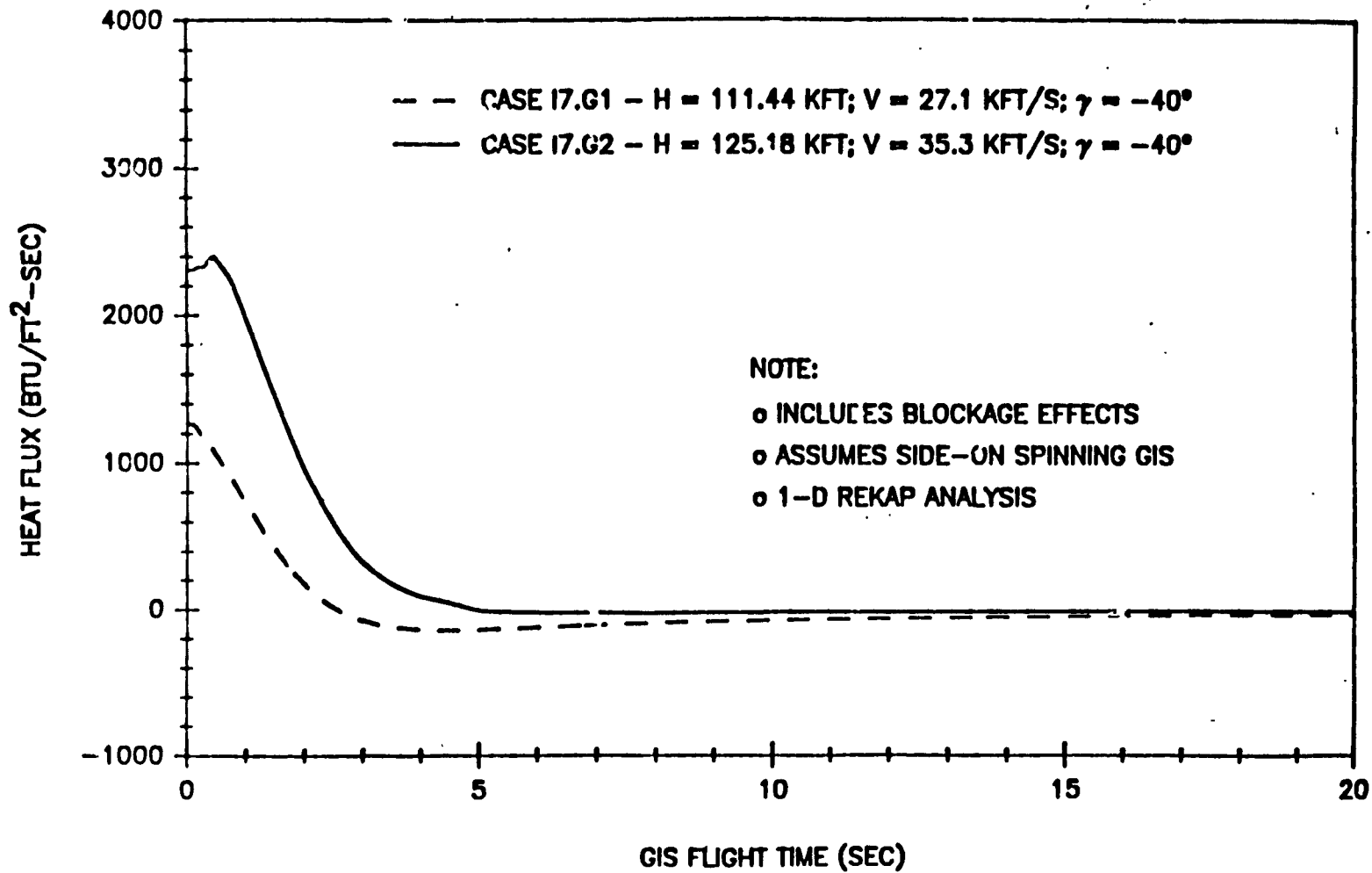


Figure F-2 Net Energy Transfer Into The Surface

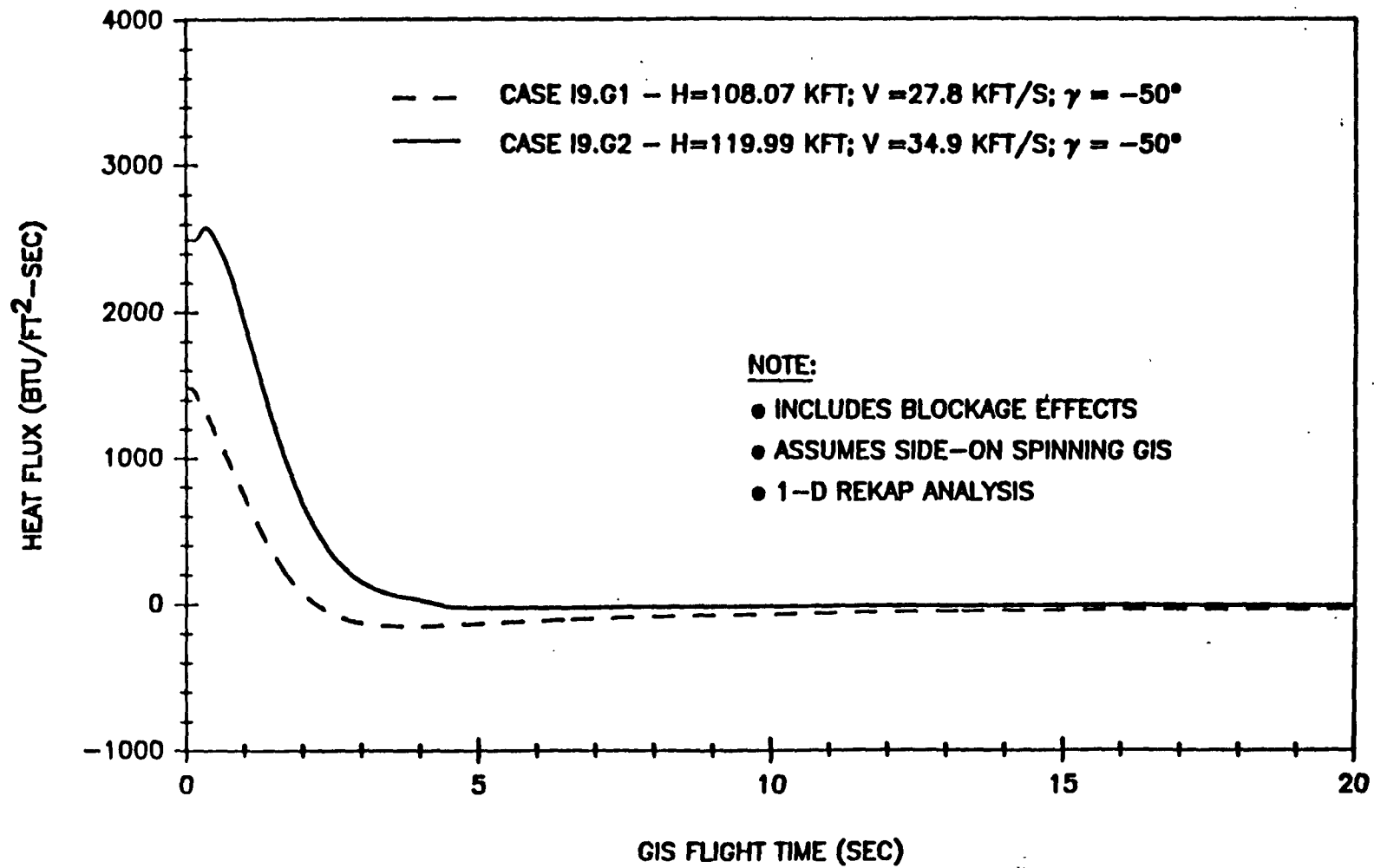


FIGURE E-2 Net Energy Transfer Into The Surface



### F.3 ANALYTICAL MODELS AND TECHNIQUES

#### F.3.1. GPHS THERMAL MODEL

The nodal model used for the GPHS reentry thermal analysis uses essentially the same construction as used in the previous FSAR (GESP-7200). The main difference arises in the use of more nodes through the thickness of the aeroshell. The current model uses eight (8) nodes through the aeroshell wall as opposed to two (2) in the previous model; a total of 1534 nodes makes up the model. Figures F-4 and F-5 show the details of the model.

#### F.3.2 GIS GEOMETRICAL MODEL

The term GIS in this analysis refers to the graphite impact shell and its contents. The contents consist of two fuel pellets with iridium clads and one floating membrane.

Given the chosen orientation of the GIS during reentry, i.e., side-on orientation, and given the assumed spinning motion about its axis of symmetry, the problem becomes a two dimensional (R,Z) calculation. The choice of node definition for the thermal analysis is shown in Figure F-6. The GIS is represented by 86 nodes. The graphite impact shell itself is represented by 56 of those nodes. The impact shell has five bulk nodes thru its thickness plus one zero thickness node on each of its inner and outer surfaces. The iridium clad is one node in thickness and the fuel, three nodes in the radial direction and five nodes in the axial direction.

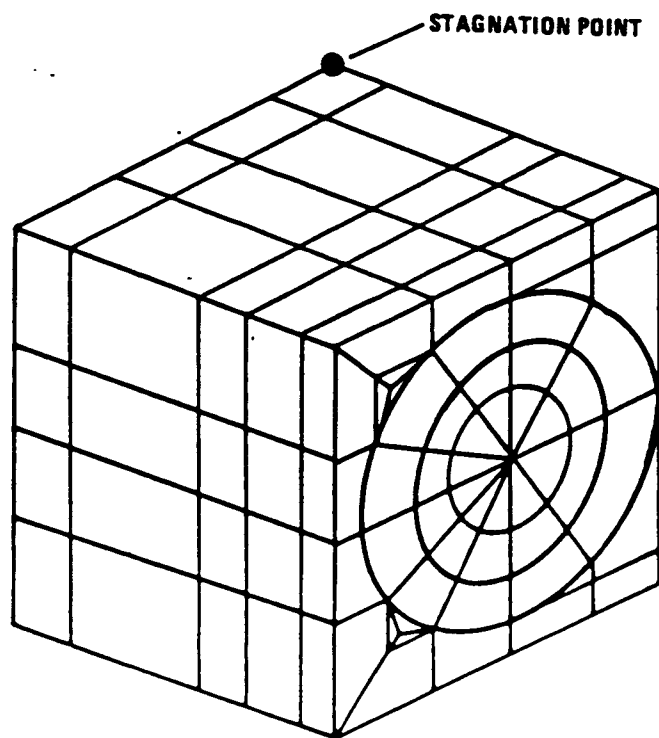


Figure F-4 GE Reentry Thermal Model. 1/4 GPHS Model.

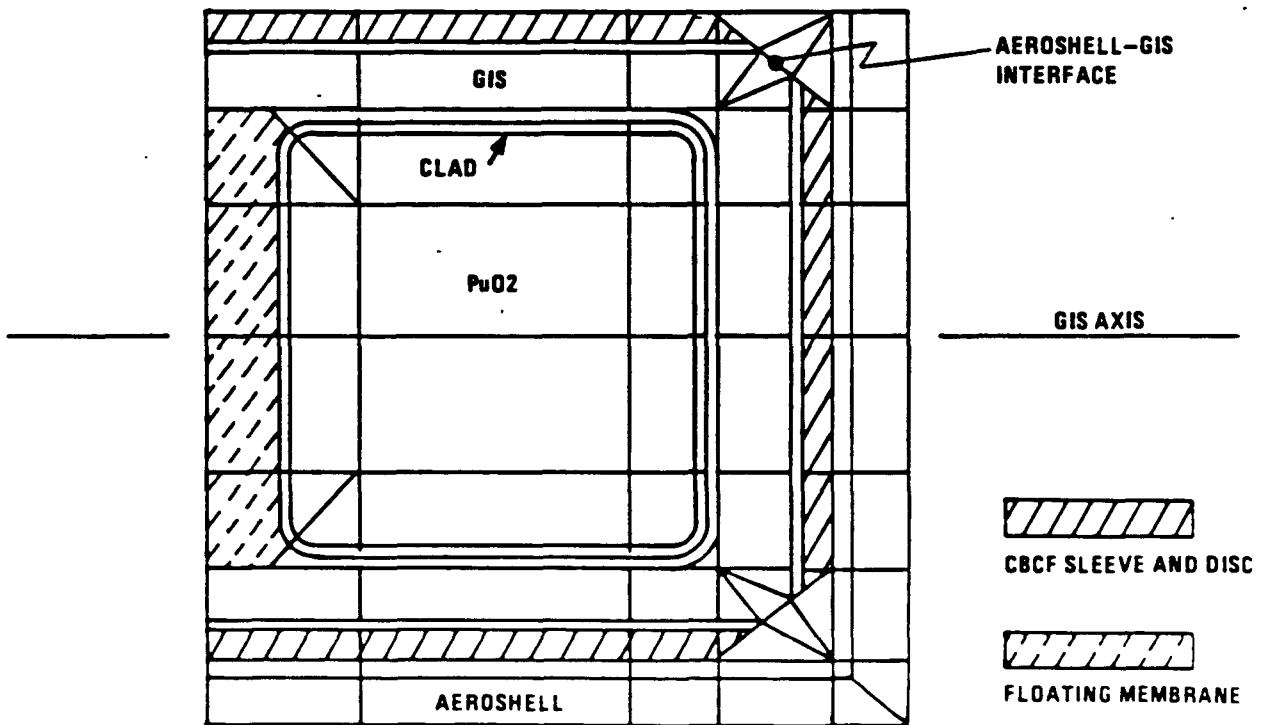


Figure F-5 GE Reentry Thermal Model. Section Thru GIS Axis Parallel To Broad Face

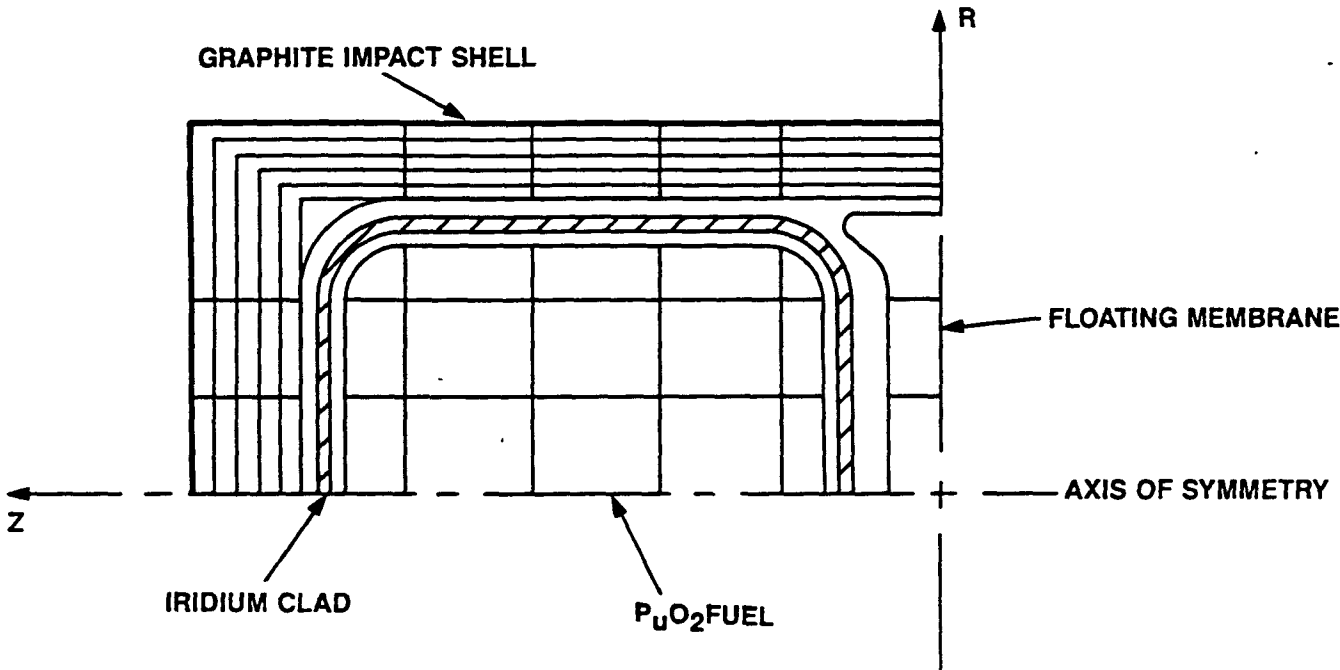


Figure F-6 GIS Geometrical Model

### F.3.3 MODULE ATTITUDE DURING REENTRY

Two six degree-of-freedom (6DOF) trajectories were calculated for the GPHS module during reentry under VEEGA conditions. The module properties were taken from Reference F-3.

The initial flight conditions for the two cases were as follows:

<u>Case</u>	<u>Altitude</u> <u>(ft)</u>	<u>Inertial</u> <u>Speed (ft/sec)</u>	<u>Path</u> <u>Angle (deg)</u>
steep	263,000	49,290	-90
shallow	312,000	45,660	-5.53

In each case, the initial total angle of attack and all rotation rates about the GPHS axes were set to zero. The results of the calculations in terms of attitude and rotation or oscillation rates are shown on Figures F-7 through F-18.

The total angle of attack for the two cases is shown on Figures F-7 and F-13. In the steep angle case, the module remains in the face-on-stable attitude (zero total angle of attack) for about four (4) seconds. In the shallow angle case, the corresponding time is around 35 seconds. Referring to Figures F-25 and F-33 of Section F.4.1, one can see that, for the steep reentry (i.e., at  $-90^\circ$  path angle), the peak heating pulse occurs around 3 seconds. Thus, if the module starts out in a stable, face-on attitude, it will maintain that attitude through the peak heating pulse as evidenced in the extremes of the reentry path angle. The use of the face-on stable attitude for the reentry thermal calculations is thus considered to be reasonable while, at the same time, conservative. The conservatism arises from the fact that the module would most probably reenter with a tumbling motion arising from the way it would be released from the RTG converter.

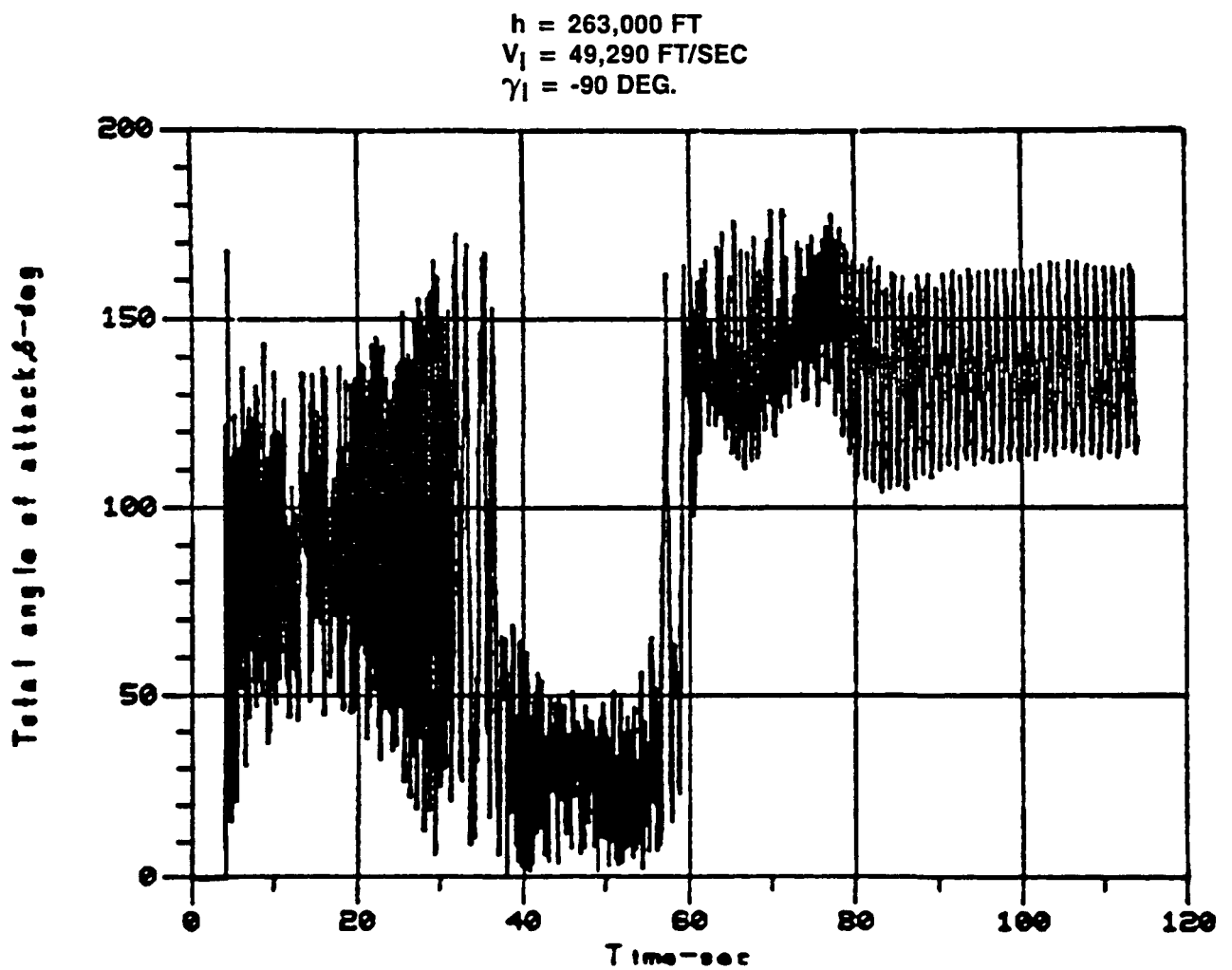


Figure F-7 Steep Reentry - Total Angle of Attack vs. Time

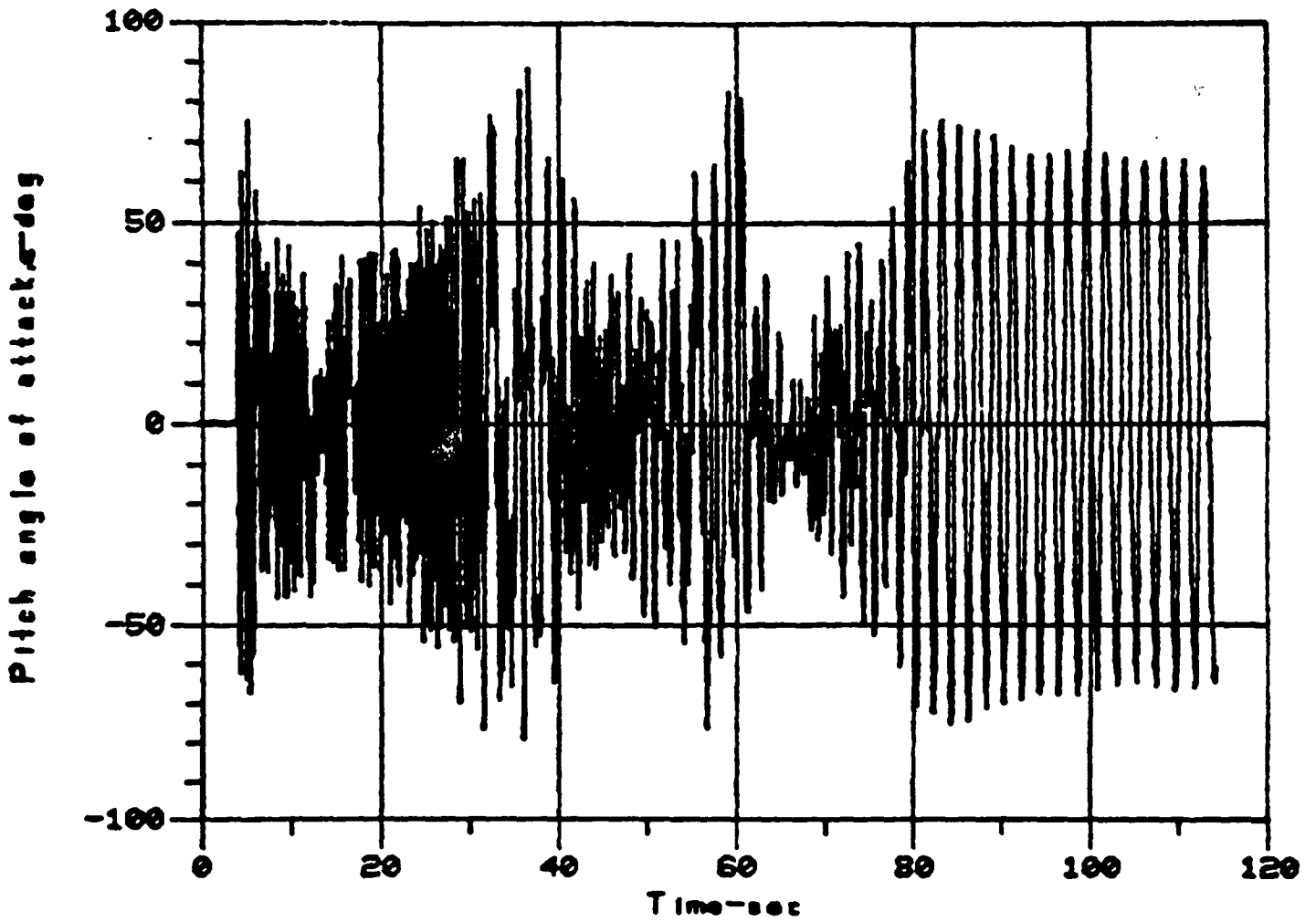


Figure F-8 Steep Reentry - Pitch Angle vs. Time.

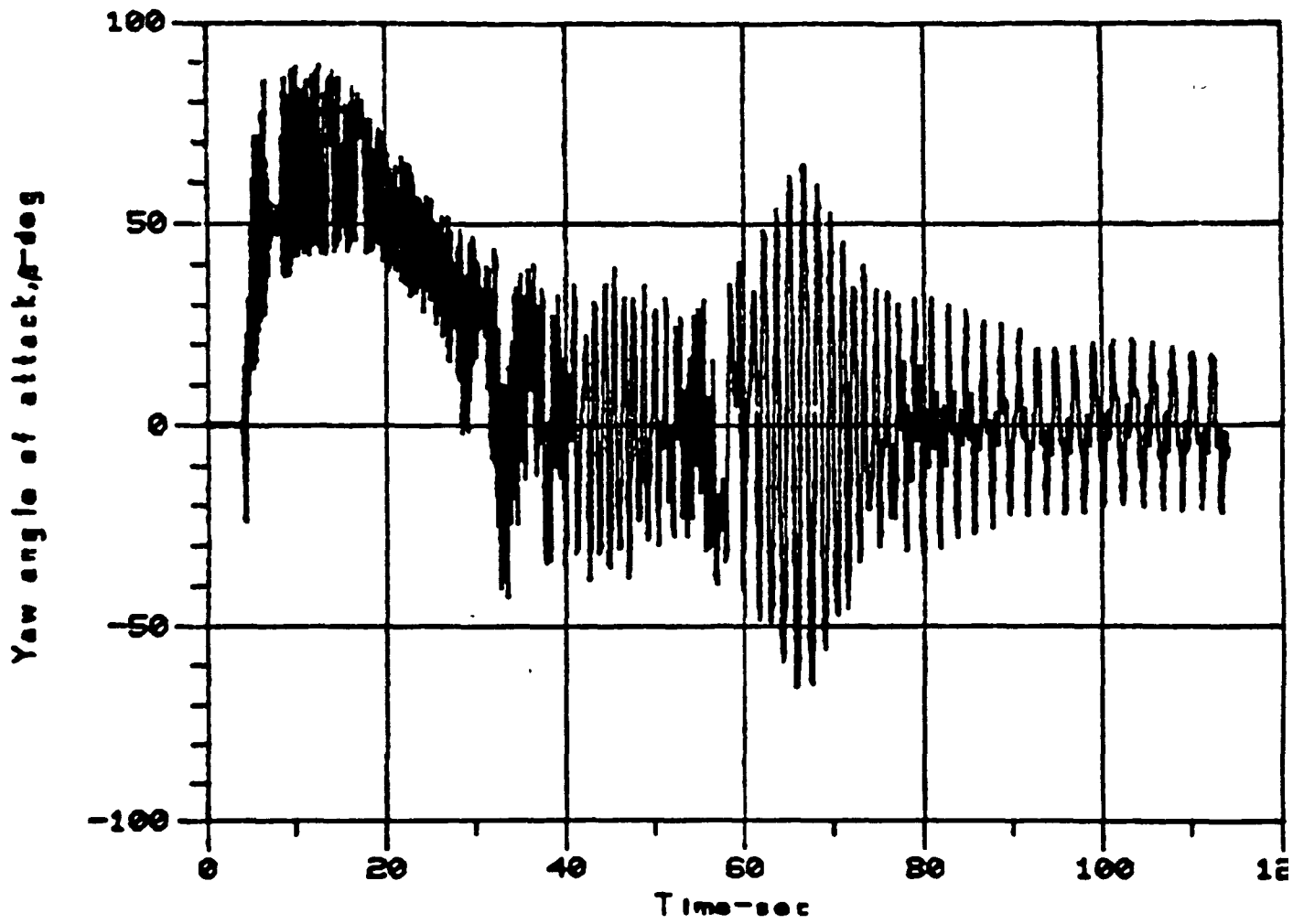


Figure F-9 Steep Reentry - Yaw Angle vs. Time



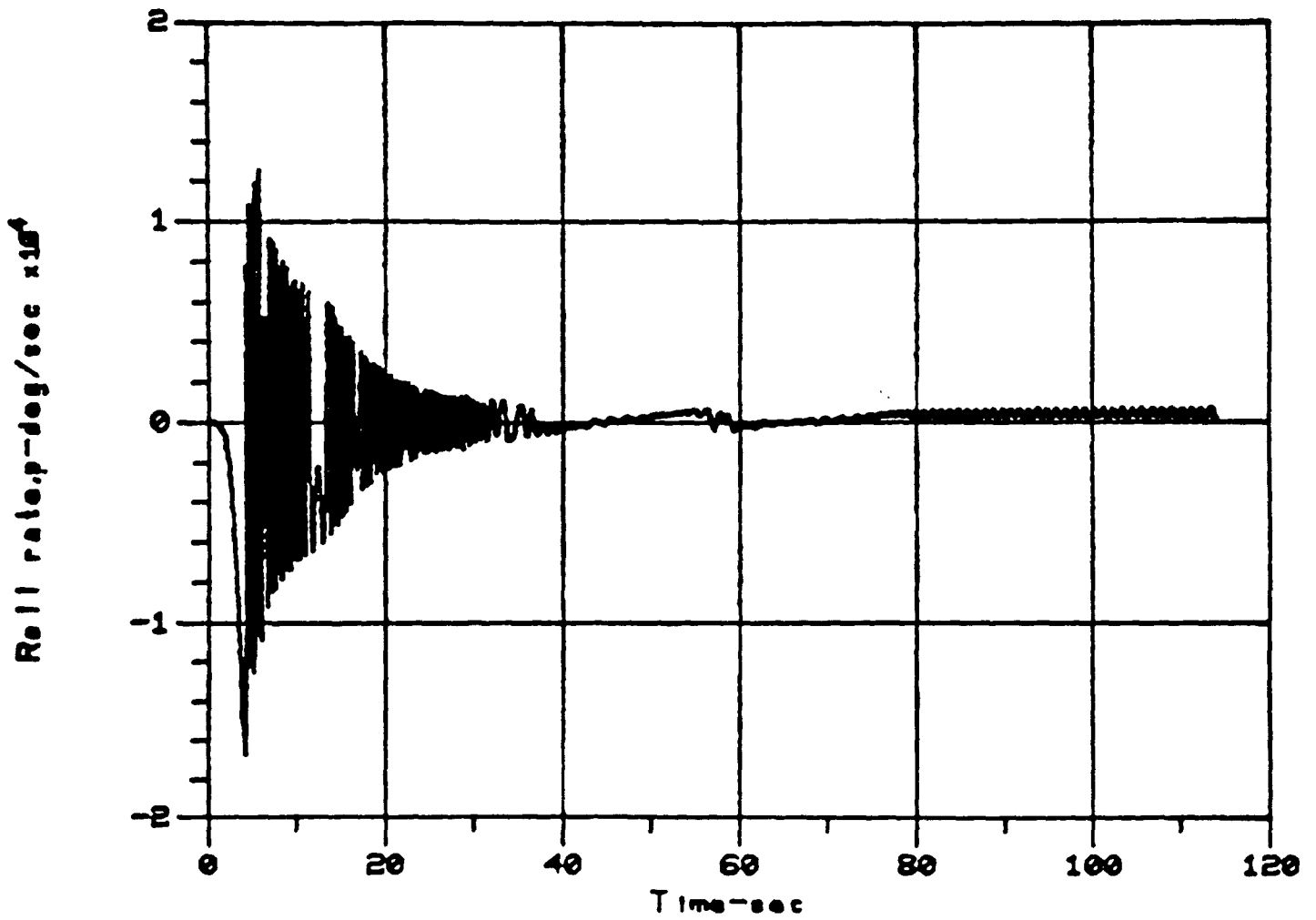


Figure F-10 Steep Reentry - Roll Rate vs. Time

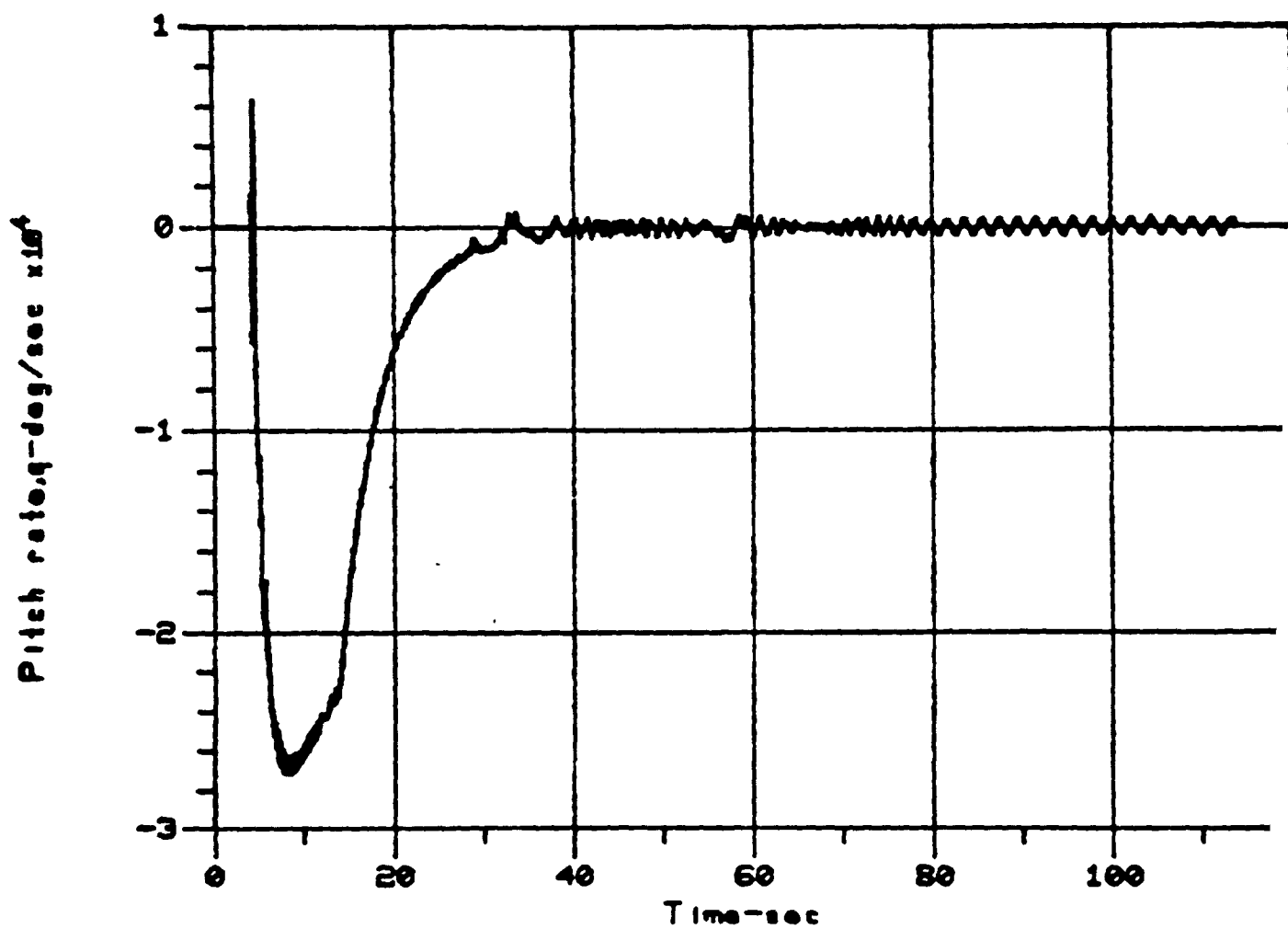


Figure F-11 Step Reentry - Pitch Rate vs. Time

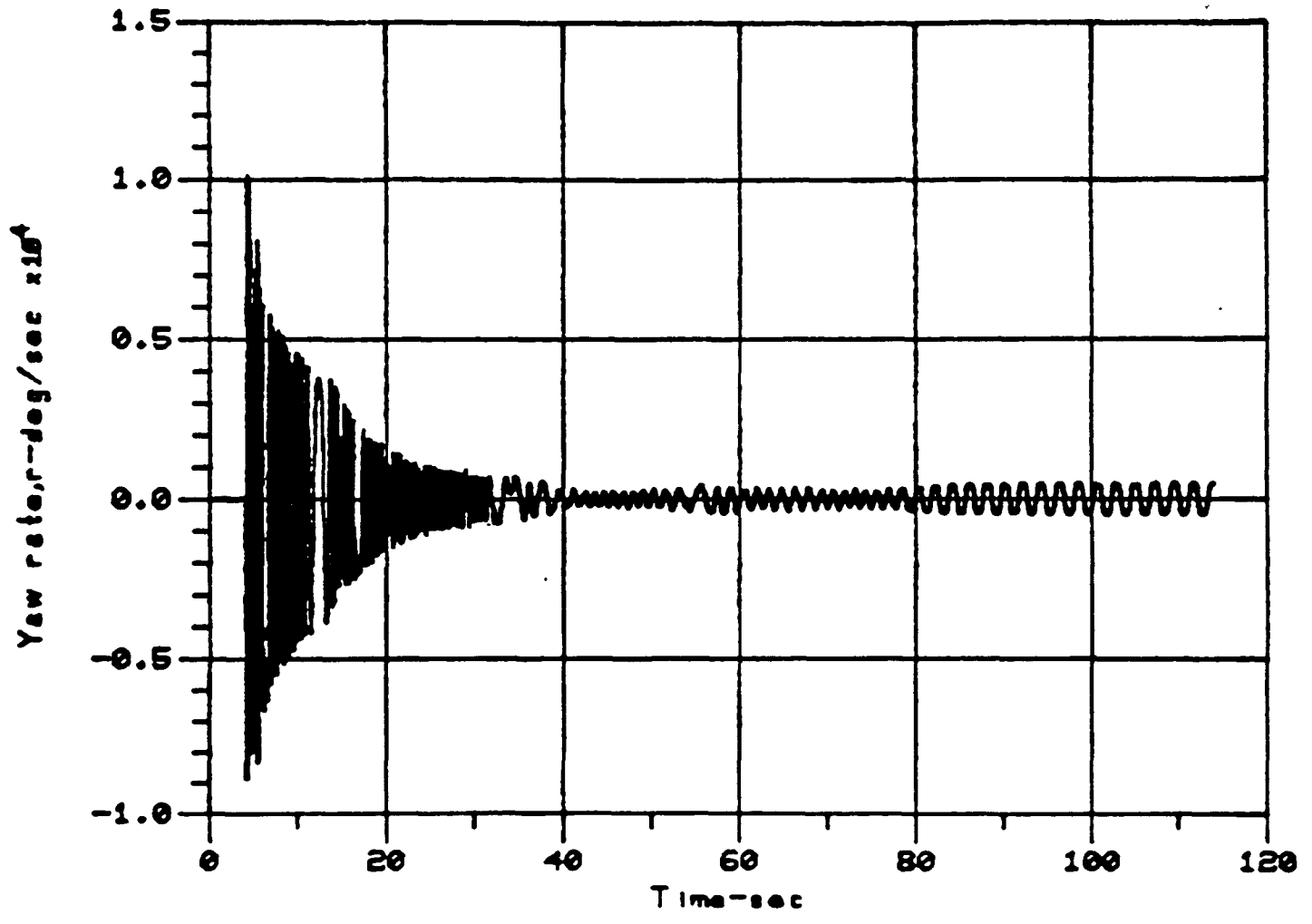


Figure F-12 Steep Reentry - Yaw Rate vs. Time

$h = 312,000$  FT  
 $V_1 = 45,660$  FT/SEC  
 $\gamma_1 = -5.53$  DEG.

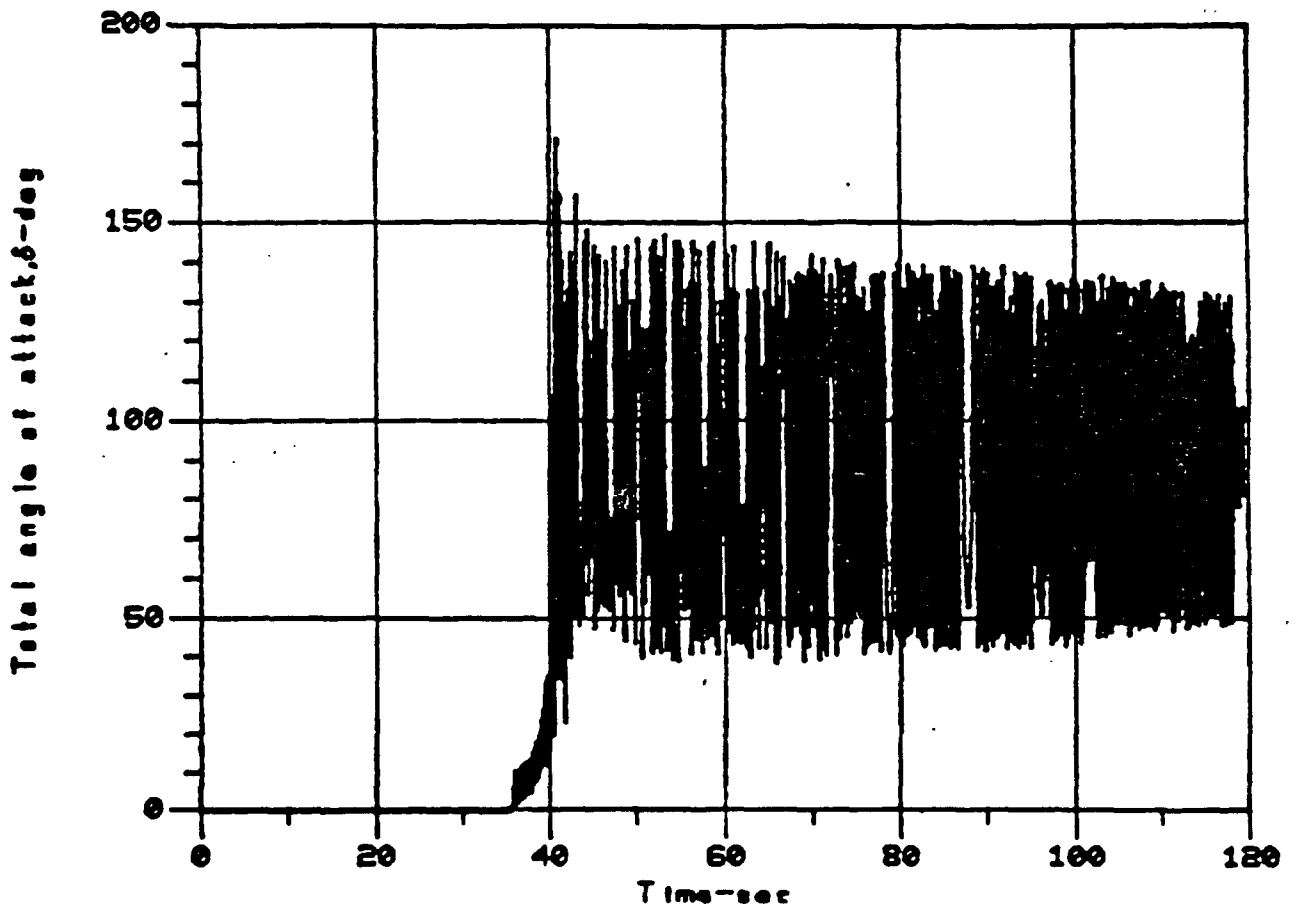


Figure F-13 Shallow Reentry - Total Angle of Attack vs. Time

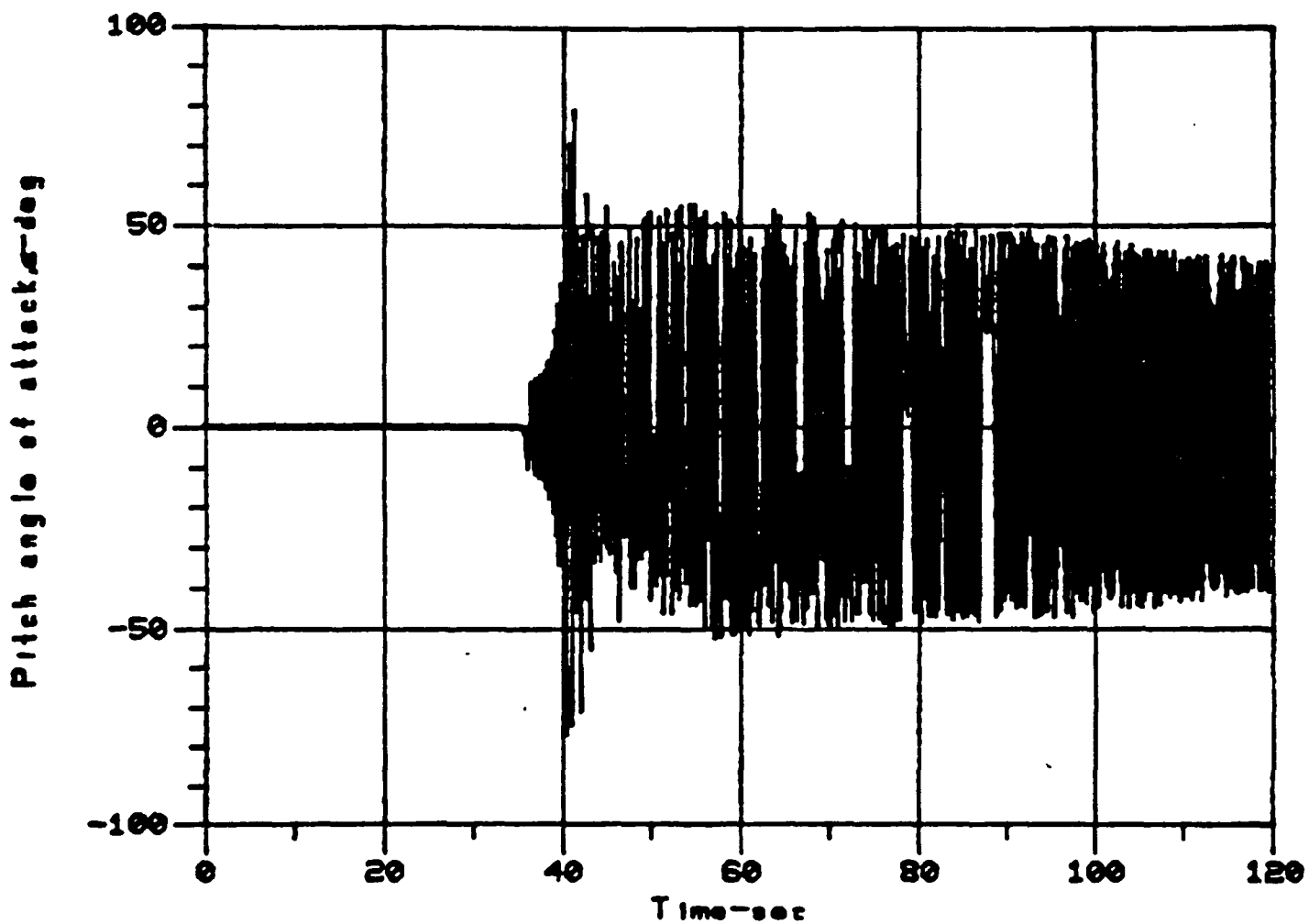


Figure F-14 Shallow Reentry - Pitch Angle vs. Time

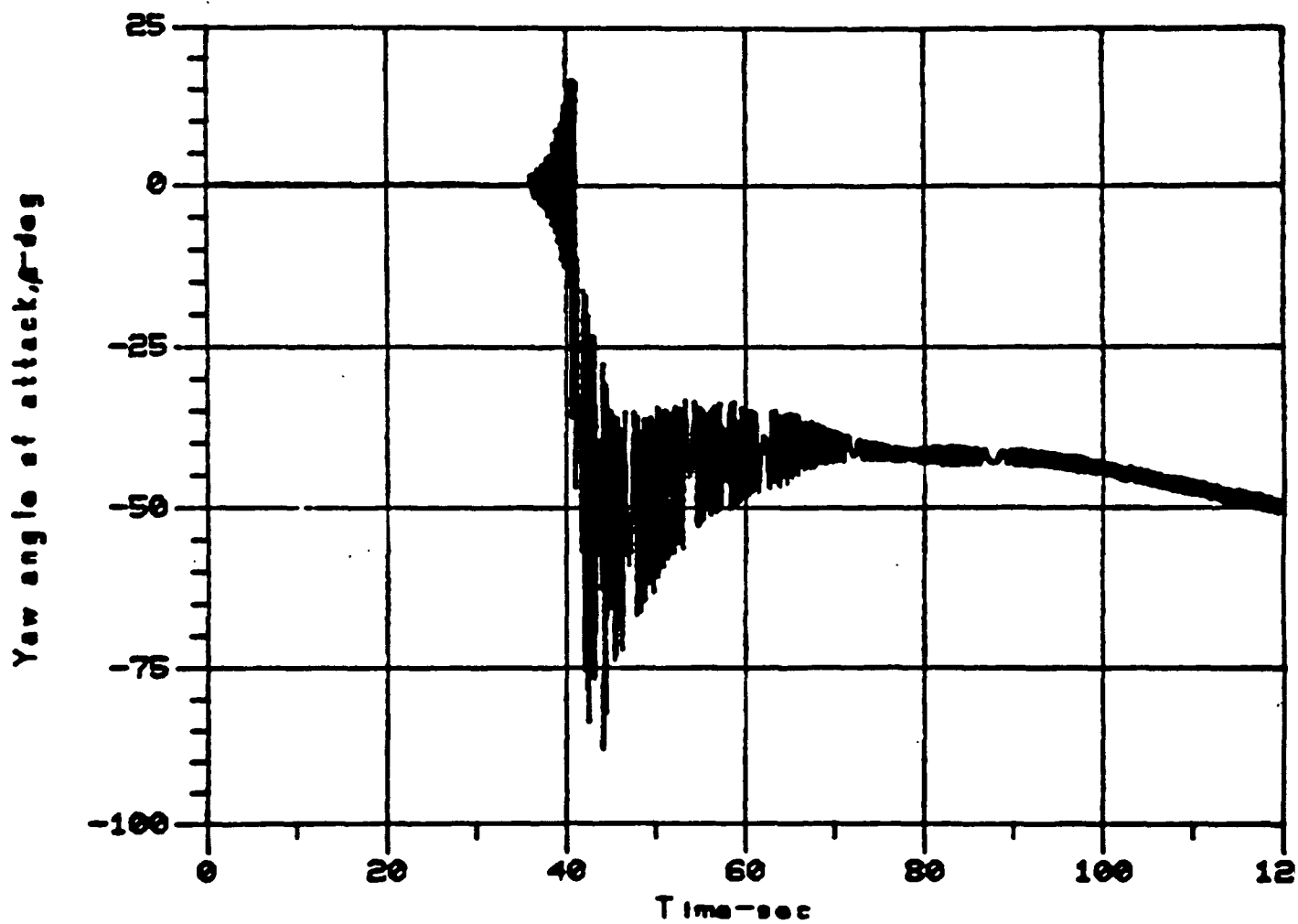


Figure F-15 Shallow Reentry - Yaw Angle vs. Time

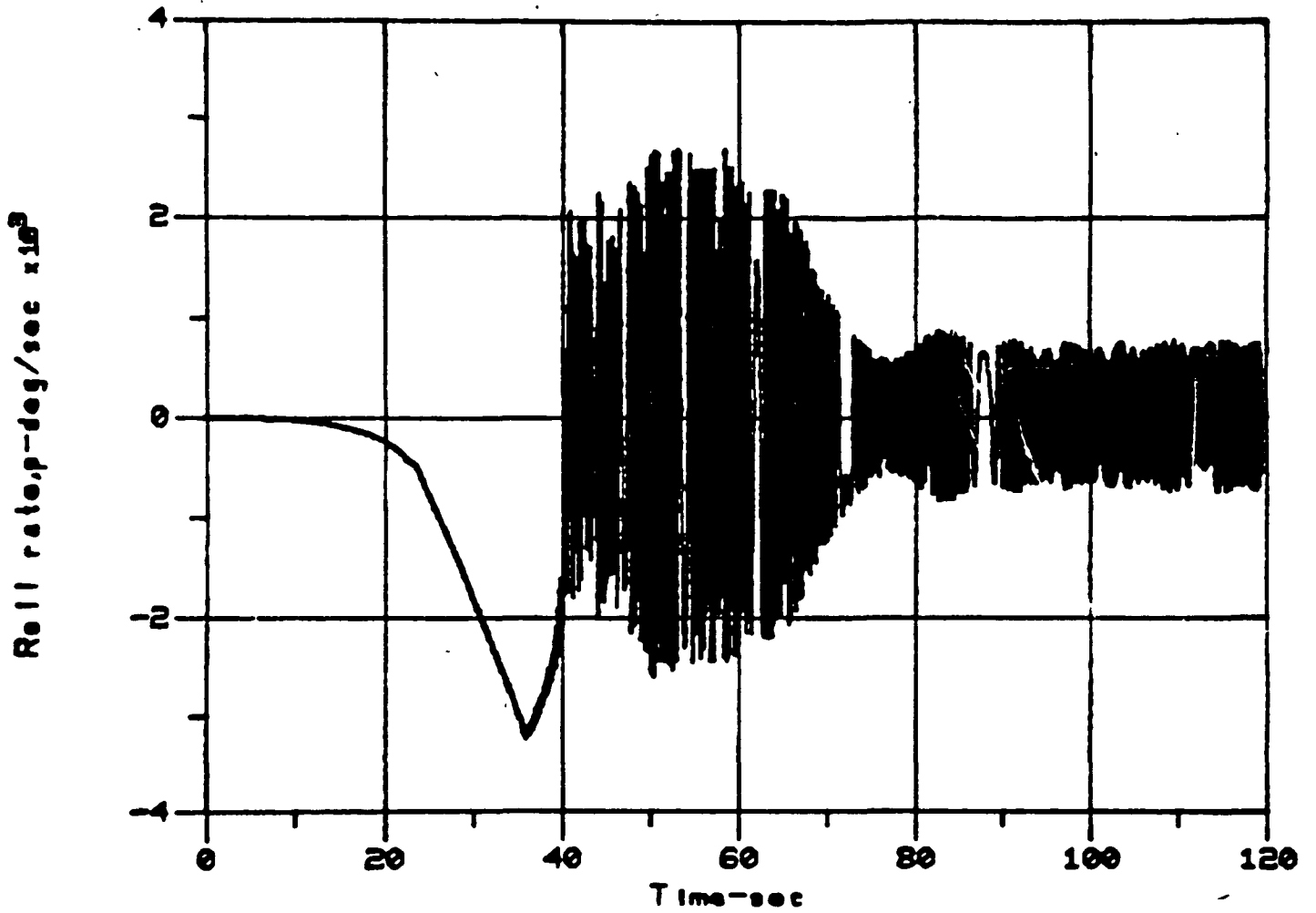


Figure F-16 Shallow Reentry - Roll Rate vs. Time

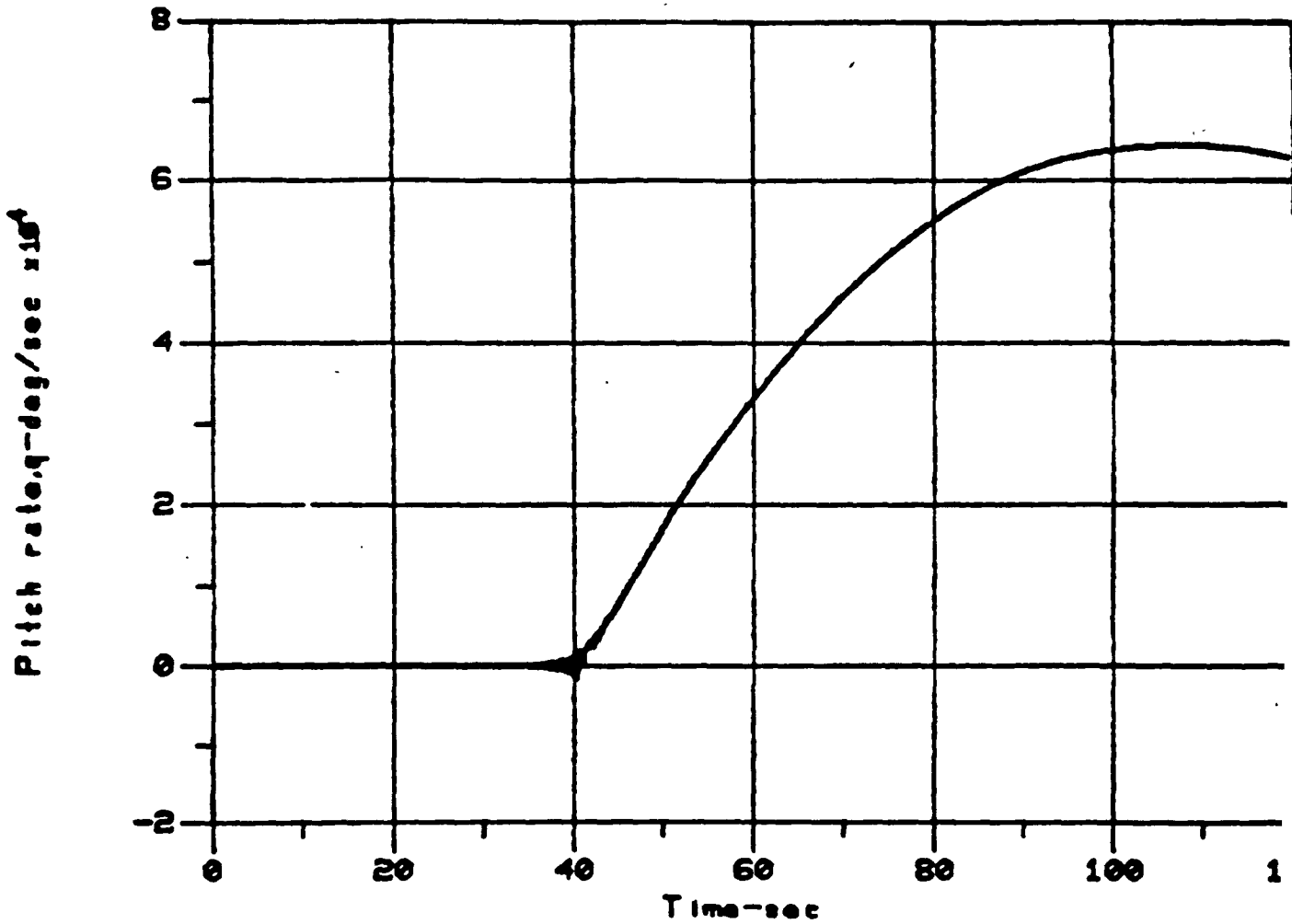


Figure F-17 Shallow Reentry - Pitch Rate vs. Time



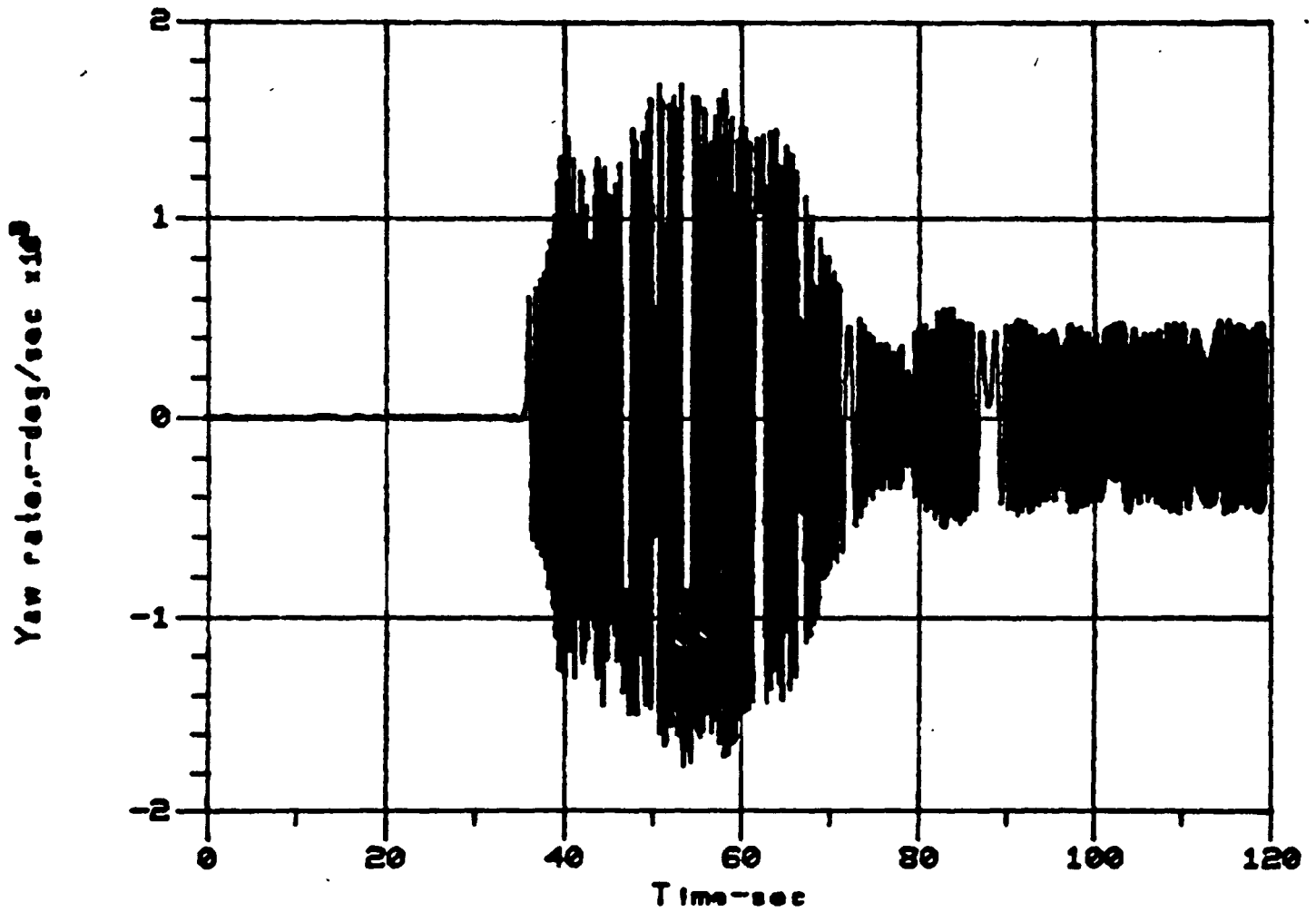


Figure F-18 Shallow Entry - Yaw Rate vs. Time

#### F.3.4 USE OF PREVIOUS ANALYTICAL MODELS

In addition to the geometric similarity of the GPHS nodal model used in the VEEGA reentry analysis, most of the heat transfer mechanisms and details used in the previous FSAR (GESP-7200, Volume II, Book 2, Appendix I) have also been used for the current analysis. These include the following:

- CBCF Thermal Conductivity in Vacuum and in Air
- FWPf and CFCF Thermal Conductivity Anisotropy
- CBCF Disc/Aeroshell Contact Coefficient
- Air Thermal Conduction in the GPHS Inter-Component Gaps
- Contact Conductance at the aeroshell-GIS interface.
- CBCF Graphitization Model
- Aerodynamic Heating Model

Refer to Appendix I of this FSAR for a complete description of the reentry analyses conducted for the previously planned Shuttle/Centaur launches of Galileo and Ulysses. The details of the topics listed above are given in that appendix. Other heating and ablation models used in the VEEGA reentry analysis of the GPHS modules and GISs are discussed in the following sections.

#### F.3.5 SHOCK LAYER RADIATION MODEL

The shock layer radiation model was based on the work of References F-3 and F-4. For altitudes below 224,000 feet, the equations of Reference F-3 were used. Above this altitude, the equations of Reference F-4 were used. Both models give estimates of equilibrium radiation only. The significance of this will be discussed later.

The lower altitude model is complete in the sense that it includes radiation cooling, both the continuum and atomic lines contributions, and nongray self-absorption. On the other hand, the upper altitude model does not include the atomic lines contribution to the radiation field. Neither model includes the effect of radiation absorption by ablation products. The correction used for this effect is described later.

The equations for the low altitude model provide shock layer radiative heating for spheres. In order to apply the model to the GPHS module or GIS, it was assumed that the stagnation point radiative heating for a given altitude and speed would be the same for any of these shapes if they all had the same shock layer thickness. Hence, for a given module or GIS shock layer thickness, a sphere radius was calculated which would result in a sphere shock layer thickness equal to that of the module or GIS.

The shock layer thicknesses for each of these bodies were calculated with the following formulae:

$$\begin{aligned} \delta \quad \text{Sphere} &= 0.667 R / (K-1) \\ \delta \quad \text{Module} &= 2.18 / (K-1)^{1/2} \text{ (inches)} \\ \delta \quad \text{GIS} &= 0.041R \text{ EXP} \left[ \frac{5.37}{.623 + \ln K} \right] \end{aligned}$$

R = radius of body

K =  $\varphi_2 / \varphi^\infty$

$\varphi_2$  = density behind the shock wave

$\varphi^\infty$  = free stream density

The equation for the module shock layer thickness will result in a dimension of inches.

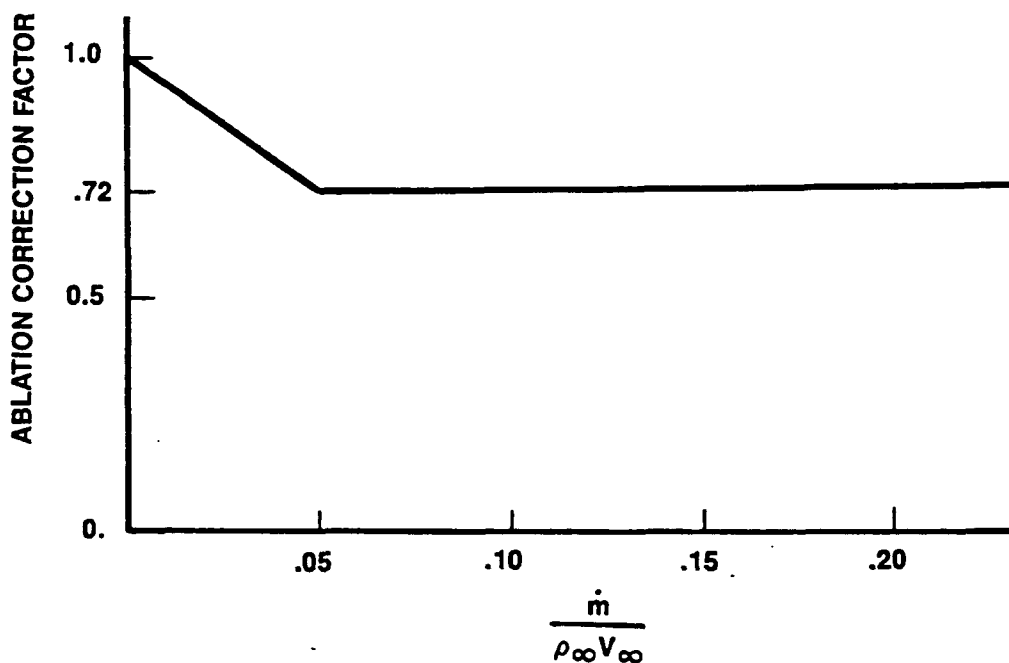
In the high altitude regime, the radiative heating is given by equation 13 of Reference F-5. Except for the short and long wavelength absorption coefficients and the shock layer thickness used in that equation, all of its terms are evaluated from data given in Reference F-5. In the case of the absorption coefficients, the presentation of Reference F-8, pages 9 thru 11, was used. The shock layer thickness was evaluated by the equations given above.

As mentioned above, the high altitude model does not include atomic line contributions to the radiation field. Their contribution can be approximately one third of the total radiation heating at the reentry body surface (see Reference F-9). Given the approximate nature of the high altitude model, it was decided that, rather than apply an atomic line correction factor, a velocity dependent correction factor would be applied to force agreement between the two models at an altitude of 224,000 feet. The correction factor so determined varied between about 1.5 and 3.

The effect of absorption by ablation products was based upon the work of Reference F-9. A multiplicative correction factor was devised as a function of the ratio of the ablation rate to the mass flux of the free stream. It is given in Figure F-19.

In the case of GPHS module reentry, a face-on-stable orientation was assumed, and the shock layer radiative heating was assumed constant over the front face and equal to the stagnation point heating determined by the models described above. No radiative heating was applied to any of the other module faces.

In the case of the GIS, a side-on spinning attitude was assumed. No radiative heating distribution could be found for side-on cylinders, but a partial distribution was found in Figure 9 of Reference F-7 for a hemisphere. The distribution was given for angular positions between 0 and 40 degrees,



CORRECTION FACTOR = 0.72 FOR  $\frac{\dot{m}}{\rho_{\infty} V_{\infty}} \geq 0.05$

Figure F-19 Ablation Correction Factor For Shock Layer  
Radiation Heating

0 degrees being the stagnation point. This curve was extrapolated to a body angle of  $90^{\circ}$  where the heating was assumed to go to zero. The distribution, in the form of the ratio of the radiative heating at a given angle to that at the stagnation point, was then averaged between 0 and 180 degrees. This average, 0.18, was then applied to the stagnation point heating to give a radiative heating value assumed to be constant over the curved surface, or sides, of the GIS. No heating was applied to the ends of the GIS. Finally, it was assumed that both the module and the GIS surface absorptivities was 0.8.

As mentioned earlier, the shock layer radiative heating models used here assumed equilibrium conditions within the shock layer. A brief study of the effect of this assumption suggested that:

- 1) The models are probably appropriate for the GIS flight conditions assumed in this study.
- 2) The models are probably inappropriate for the very early portions of the module trajectories.
- 3) The GIS release times are probably not seriously effected by non-equilibrium conditions.

F.3.6 AERODYNAMIC HEATING AND GRAPHITE ABLATION MODEL:

The convective component of the aerodynamic heating is determined by Equation 1,

$$Q_c = C_h \left[ H_T - H_w + \frac{\dot{m}_w}{C_h} (h_c - H_w) \right] \quad (1)$$

where:

- $C_h$  = heat transfer coefficient with ablation
- $H_T$  = Total free stream enthalpy
- $\dot{m}_w$  = mass loss rate (ablation rate) at the surface
- $h_c$  = static enthalpy of solid carbon

The ratio  $\dot{m}_w/C_h$  is referred to as the mass transfer parameter and represented here as  $B'$ , i.e.,

$$B' = \dot{m}_w/C_h \quad (2)$$

(For a fuller discussion of Equations 1 and 2 above the reader is referred to Appendix I, Book 2, Volume II, of this FSAR.)

The total enthalpy is trajectory dependent only and can be determined independent of the thermal analysis (neglecting the effect of ablation on the trajectory). The remaining terms on the right hand side of Equation 1 will depend upon the thermal response of the reentry body. The static enthalpy of solid carbon is a known function of temperature and is evaluated at the surface temperature of the body. The evaluation of the remaining terms,  $C_h$ ,  $H_w$ , and  $\dot{m}_w$ , is effected with the application of either one of two models, chosen on the basis of the ablation mechanism.

At low enough temperatures, mass loss by way of sublimation is negligible, and an oxidation model is used to complete the convective heating and ablation calculations. A second model is employed to include graphite sublimation effects when they become significant.

F.3.6.1 Low Temperature Mass Loss Model:

At the very lowest temperatures, the mass loss is reaction rate controlled, i.e., is due to chemical reactions at the wall/gas interface. As the temperature increases, the oxidation rate increases exponentially until the effects of diffusion rates become controlling, the so-called diffusion limited regime. A detailed discussion of the predictive technique utilized in the 3-D model to determine the carbon oxidation rate under these conditions can be found in Reference F-10 where the mass loss rate is expressed as:

$$\dot{m}_w = C_{hO} \left[ \frac{1}{1 + \frac{C_{hO}}{\varphi_w}} \right] \ln \left[ 1 + \frac{2M_c}{M_{O_2}} \left( C_{O_2} \right)_e \right] \quad (3)$$

where:

C = heat transfer coefficient with no ablation

$\varphi_w$  = gas density at the wall

k = reaction rate coefficient

M = molecular weight

$\left( C_{O_2} \right)_e$  = Mass fraction of Oxygen at the edge of the boundary layer.



The reaction rate coefficient,  $k$ , is temperature dependent and is calculated as

$$k = Ae^{-E/T}$$

The constants  $A$  and  $E$  represent the pre-exponential factor and the activation temperature, respectively. A different set of constants ( $A$  and  $E$ ) is used to compute the reaction rate coefficient for each of the two basic modes of burning, i.e., flaming and glowing combustion. Glowing combustion occurs at the higher altitudes where the air is either dry or humid but moderately low in temperature. The presence of  $H_2O$  vapor is required for flaming combustion and therefore assumed to occur at altitudes below 40 kft. A direct measurement of the activation temperature for each of the two modes of combustion yielded the following values (Reference F-10):

$$E, \text{ glowing combustion} = 26,500^\circ\text{K}$$

$$E, \text{ flaming combustion} = 40,000^\circ\text{K}$$

The pre-exponential factors given in Reference F-10 are:

$$A, \text{ glowing combustion} = 2.0 \times 10^{10} \text{ cm/sec}$$

$$A, \text{ flaming combustion} = 3.2 \times 10^{14} \text{ cm/sec}$$

The value of  $A$  for glowing combustion was modified for the current study. A discussion of the modification will be found below.

The predictive technique used to compute low temperature ablation rates for the simple 1-D model assumes that, when the oxidation rate is diffusion-limited, i.e., limited by the amount of oxygen able to diffuse through the boundary layer to the surface, the mass transfer parameter ( $B'$ ) is equal to 0.175. However, since  $B'$  is not defined for the reaction rate regime, this expression is modified by multiplying the diffusion mass loss rate by a

ramping factor. The ramping factor varies from 0 to 1 between 1790 and 1800°R and simulates the change between the reaction rate and diffusion controlled regimes.

In order to evaluate the ablating heat transfer coefficient,  $C_h$ , Equation 14 of Reference F-11 was used, which gives  $C_h$  as a function of  $C_{h_0}$  and  $\dot{m}$  for the case of graphite ablation. That equation is reproduced here.

$$C_h/C_{h_0} = 1 - 0.6563B_0 + 0.0179B_0^2 + 0.06365B_0^3 - 0.01125B_0^4 \quad (4)$$

The quantity  $B_0$  is defined as:

$$B_0 = \dot{m}/C_{h_0} \quad (5)$$

#### F.3.6.2 Sublimation Mass Loss Regime:

Graphite sublimation occurs when the surface temperature exceeds 4000°R. In both the 1-D and 3-D analyses, equilibrium surface thermochemistry tables supplied by APL (Reference F-12) were utilized in predicting the sublimation rate of graphite. The previously defined parameters,  $B'$  and  $H_w$ , are provided in the tables as a function of surface temperature,  $T_w$  and wall pressure,  $P_w$ . In order to use the equilibrium data to compute the mass loss rates, curve fits were developed to approximate the data over a wide range of temperatures and pressures.

Given a value of  $B'$ , a value of  $C_h$  was determined from:

$$C_h = \frac{C_{h_0}}{2B'} \ln(1 + 2B') \quad (6)$$

Equation 6 is taken from Equation 11 of Reference F-11 using the following assumptions:

$$C_h = C_m \quad (7)$$

$$\lambda_m = 1.0 \quad (8)$$

The ablation rate is then evaluated from the definition of B' (see Equation 2):

$$\dot{m} = C_h * B' \quad (9)$$

#### F.3.6.3 FWPF Oxidation Rate At Very Low Speeds:

The oxidation rate of AVCO FWPF was measured at Teledyne Energy Systems at very low air speeds. The test included temperatures between 480°C (900°F) and 926°C (1700°F) and pressures of 0.1 and 1.0 atm (see Reference F-13). The results of the test were used to determine the constants in the equation:

$$\dot{m} = (P_{O_2})^n A_1 * \exp [-\Delta E_1 / (RT)] \quad (10)$$

where  $\dot{m}$  = oxidation rate

$P_{O_2}$  = partial pressure of  $O_2$  at the oxidizing surface.

R = gas constant

T = temperature of the oxidizing surface

n, A,  $\Delta E$  = constants determined from fit to test data

The constants were evaluated as

$$n = 0.7$$

$$A = 2.99 \times 10^6 \text{ lb/ft}^2 \cdot \text{sec} \cdot \text{atm}^m$$

$$E = 48.4 \text{ Kcal/mole}$$

The oxidation model used in the 3-D thermal analysis program uses the equation (see Reference F-10)

$$\dot{m} = C_{h_0} \left[ \frac{0.159}{1 + \frac{C_{h_0}}{k\varphi_w}} \right] \quad (11)$$

where  $C_{h_0}$  = non-ablating heat transfer coefficient

$\varphi_w$  = gas mixture density at the oxidizing surface

$$k = A_2 e^{-E_2/RT}$$

The constants  $A_2$  and  $E_2$  were evaluated on the basis of test data presented in Reference F-14.

The air flow speeds used in the Teledyne tests varied between 0.0012 and 0.06 ft/sec, whereas those of Reference F-14 varied between 2 and 186 ft/sec. Since Equation 10 does not include a dependence upon the air flow speed, it was decided to evaluate the oxidation rate as given by Equation 11 for a speed of 0.06 ft/sec in order to compare the results of the two expressions. At such a low speed, the only speed dependent term is the non-ablative heat transfer coefficient,  $C_{h_0}$ .

Reference F-9 used the following equation for the non-ablating heat transfer coefficient,

$$C_{h_o} = 0.225 * \left( - \frac{dV}{dZ} \right) \quad (12)$$

where V is the component of the speed normal to the oxidizing surface, and Z is position along the normal to the same surface. In order to evaluate the velocity gradient used in Equation 12, the following approach was used. Equation 1 of Reference F-14 gives the following expressions for the radial and axial velocity gradients for frictional axisymmetric flow near the stagnation point.

$$U = ar \quad (13)$$

$$V = -2az \quad (14)$$

where U is the velocity parallel to the surface, r is the distance from the stagnation point measured along the surface, and V and z are as defined above. The gradient  $dU/dr$  from Equation 13 was identified with the velocity gradient employed in the Sibulkin-Lees equation for stagnation point heat transfer. Hence, one can write for the very low speed in the present case,

$$\frac{dU}{dr} = \frac{1.273 V_{\infty}}{D} \quad (15)$$

where  $V_{\infty}$  = free stream speed

D = equivalent body diameter.

Given the test set-up described in Reference F-14, there is no obvious body diameter. However, if one uses the nozzle diameter of this test set-up in Equation 15, the reported velocity gradients are reproduced within 2%.

From Equations 13 and 14,

$$\frac{-dV}{dz} = 2 \frac{du}{dr} \quad (16)$$

The evaluation of the oxidation rate from Equations 10 and 11 was performed for the following set of conditions:

total pressure = 1 atm  
 wall temperature = 1144°K (1600°F)  
 free stream speed = 0.06 ft/sec  
 $P_{O_2}$  = 0.21 atm

Employing Equation 10 resulted in an oxidation rate of  $5.68 \times 10^{-4}$  lb/ft<sup>2</sup> - sec while Equation 11 gave  $3.2 \times 10^{-5}$  lb/ft<sup>2</sup>-sec. For the given conditions, these oxidation rates differ by a factor of approximately 18. At lower temperatures and speeds, the difference is more like a factor of 5, Equation 10 again giving the higher oxidation rate.

On the face of it, it would appear that, for the same conditions, the oxidation rate of the AVCO FWP is significantly greater than that of the carbon test specimen used in the tests reported in Reference F-14. However, the assumptions used to make the above comparison, such as Equation 15, have not been justified. In addition, the available test data reflects speeds of 186 ft/sec or less, whereas the reentry calculations treat speeds between about 500 and 45000 ft/sec when the ablation rate is somewhere between the reaction rate and diffusion rate controlled regimes.

In view of the uncertainties, it was simply decided to increase the factor  $A_2$  by a factor of 20 when evaluating the reaction rate as in Equation 11. A single sensitivity to the factor  $A_2$  was conducted for a GIS reentry trajectory with a value of -30 degrees for the initial flight path angle. Two values of  $A_2$  were used, i.e.  $4 \times 10^{11}$  cm/sec and  $4 \times 10^{12}$  cm/sec. These values were 20 and 200 times the value given in Reference F-10.

The results of the sensitivity calculations are shown in Figures F-20 and F-21. In Figure F-20 temperatures are shown for nodes representing the inner and outer surfaces of the graphite impact shell and a clad node. The node locations are also shown in the figure. The temperatures are given for the lower oxidation rate, i.e., for  $A_2$  set at  $4.0 \times 10^{11}$  cm/sec.

In Figure F-21, a plot of the temperature difference at each node location induced by increasing  $A_2$  by a factor of 10 is shown as a function of time. There is no significant graphite oxidation beyond about 40 seconds, and, as can be seen in Figure F-21, the difference in clad temperature for the two cases has dropped to about  $12^\circ\text{C}$  at 70 seconds. Keeping in mind that the trajectory is the same in both cases, it becomes obvious that the temperature at impact at 153 seconds will be nearly the same for both cases.

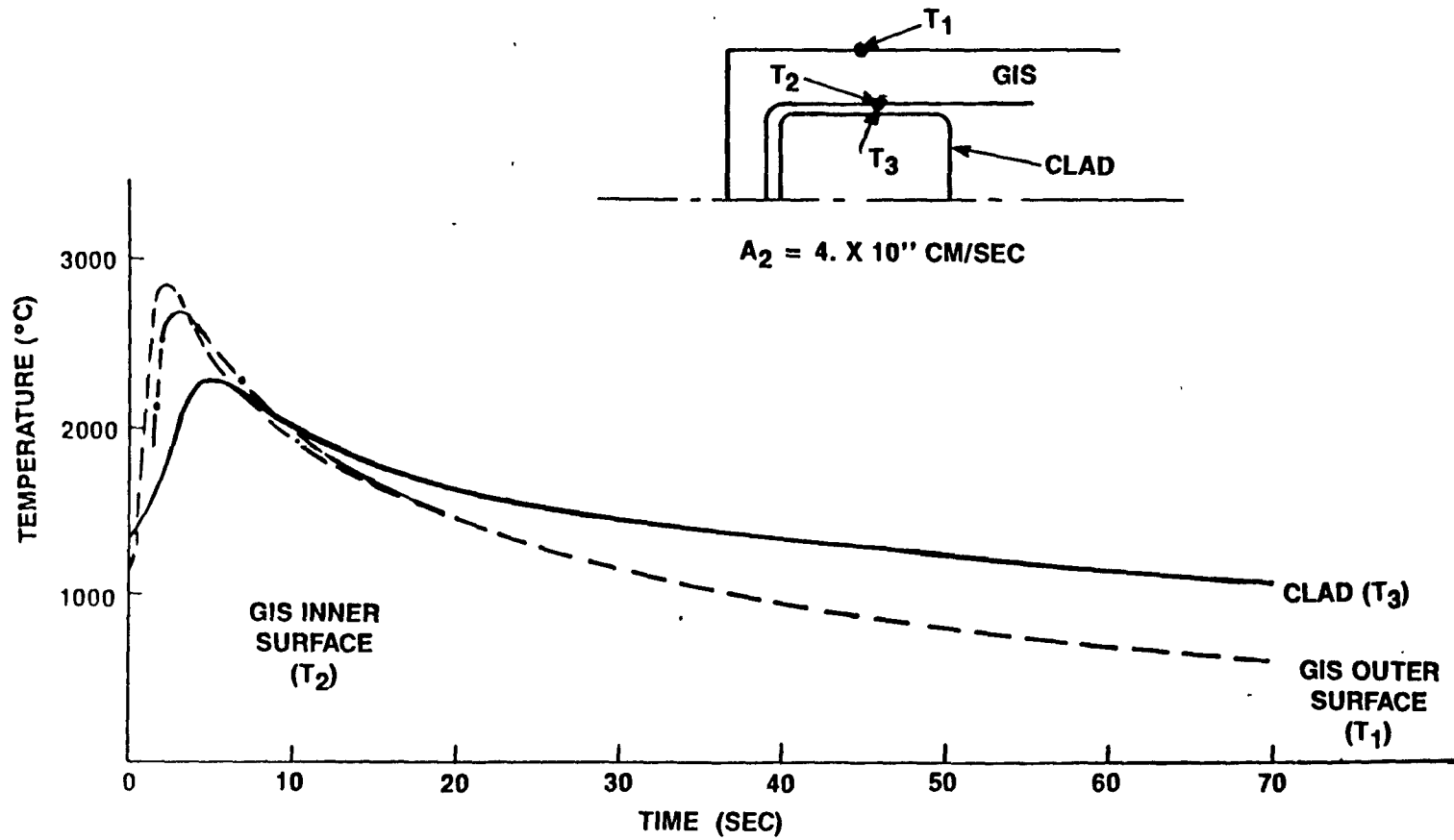


Figure F-20 Temperature vs. Time With  $A_2 = 4 \times 10^{11} \text{ cm/sec}$



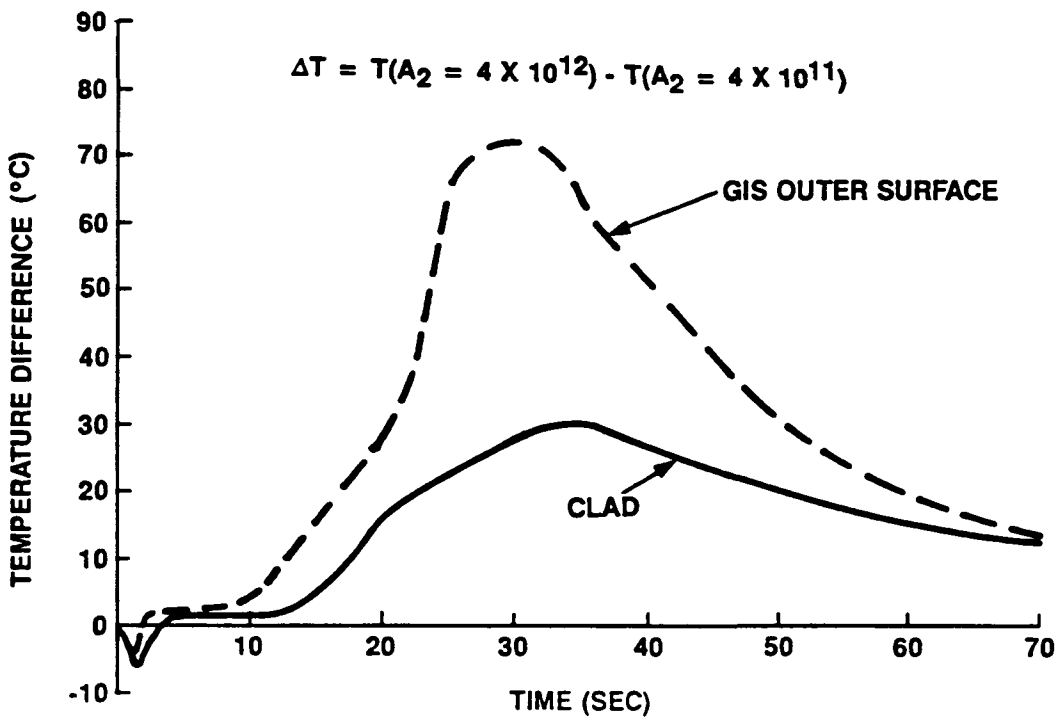


Figure F-21 Effect of Increasing The Oxidation Rate By A Factor Of 10 - Temperature vs. Time

## F.4 RESULTS

### F.4.1 GPHS MODULE REENTRY

The results of the thermal analysis of the GPHS module reentry are presented in a series of figures. Table F-5 is a listing of those figures and their content. These figures give the results for the limits of the flight path angle range as an indication of the extremes of the conditions seen by the modules. Table F-6 gives a summation of the results for the entire range of reentry path angle as determined by the 1-D analysis.

As mentioned previously, the 3-D THT-D computer program could not complete the thermal analysis for the entire reentry from the point at which the modules are released from the RTG until impact on the Earth's surface because of instability problems in attempting to arrive at a converged solution. This is believed to arise because of the extreme heating environments resulting from the potential VEEGA reentry conditions. Because of this problem, an attempt was made to analyze the reentries with a simpler 1-D model and program. Successful solutions were attained with this approach, and the subsequent analyses were based on the 1-D results with comparisons being available from the 3-D runs as far as they could be completed as a function of reentry time before the instability arose in the solution. From Table F-6, one can see that the maximum recession of the aeroshell, 116 mils, at a path angle of -5.53 degrees is well below the aeroshell minimum thickness of 186 mils. Figure F-42, shows the ablation profile across the leading face in the -5.53 degree reentry at a time of 62.4 seconds after which the 3-D solution was no longer attainable. However, from Table F-6, the aeroshell temperatures can also be seen to be in the 6170-7378<sup>o</sup>F (3410-4081<sup>o</sup>C) range. At these temperatures, the FWPF material is postulated to have very little strength, possibly being in the range of the estimated strength of bulk graphite at 5000 psi or less. (Tensile strength data on FWPF has only been measured to 3000<sup>o</sup>F - 1649<sup>o</sup>C, where it is of the order of 26,000 psi.) Also sources in the literature indicate that graphite will melt in the range of 6300-7300<sup>o</sup>F

Table F-5 List of Figures Showing Results of GPHS Reentry

Figure No	Content
F-22	-90° Non-Ablatival Heat Transfer Coefficient vs Time
F-23	-90° Total Enthology vs. Time
F-24	-90° Edge Pressure vs. Time
F-25	-90° Stagnation Heating Rates
F-26	-90° Net Energy Transfer into Surface
F-27	-90° Surface Temperature History (1-D)
F-28	-50° to -90° Clad Temperature Response (1-D)
F-29	-5.53° to -40° Clad Temperature Response (1-D)
F-30	-5.53° Non-Ablative Heat Transfer Coefficient vs Time
F-31	-5.53° Total Enthlpy vs Time
F-32	-5.53° Edge Pressure vs. Time
F-33	-5.53° Stagnation Heating Rates .
F-34	-5.53° Net Energy Transfer into Surface
F-35	-5.53° Temperature Response (1-D)
F-36	-5.53° Temperature Response (3-D)
F-37	-5.53° Surface Temperature History (1-D vs 3-D)
F-38	-5.53° Clad Temperature Response (1-D vs 3-D)
F-39	-90° Recession History (1-D)
F-40	-5.53° Recession History (1-D)
F-41	-5.53° Recession History (3-D; nodes near stagnation point & center line)
F-42	-5.53° Ablation Response (across leading face of aeroshell; 3-D)

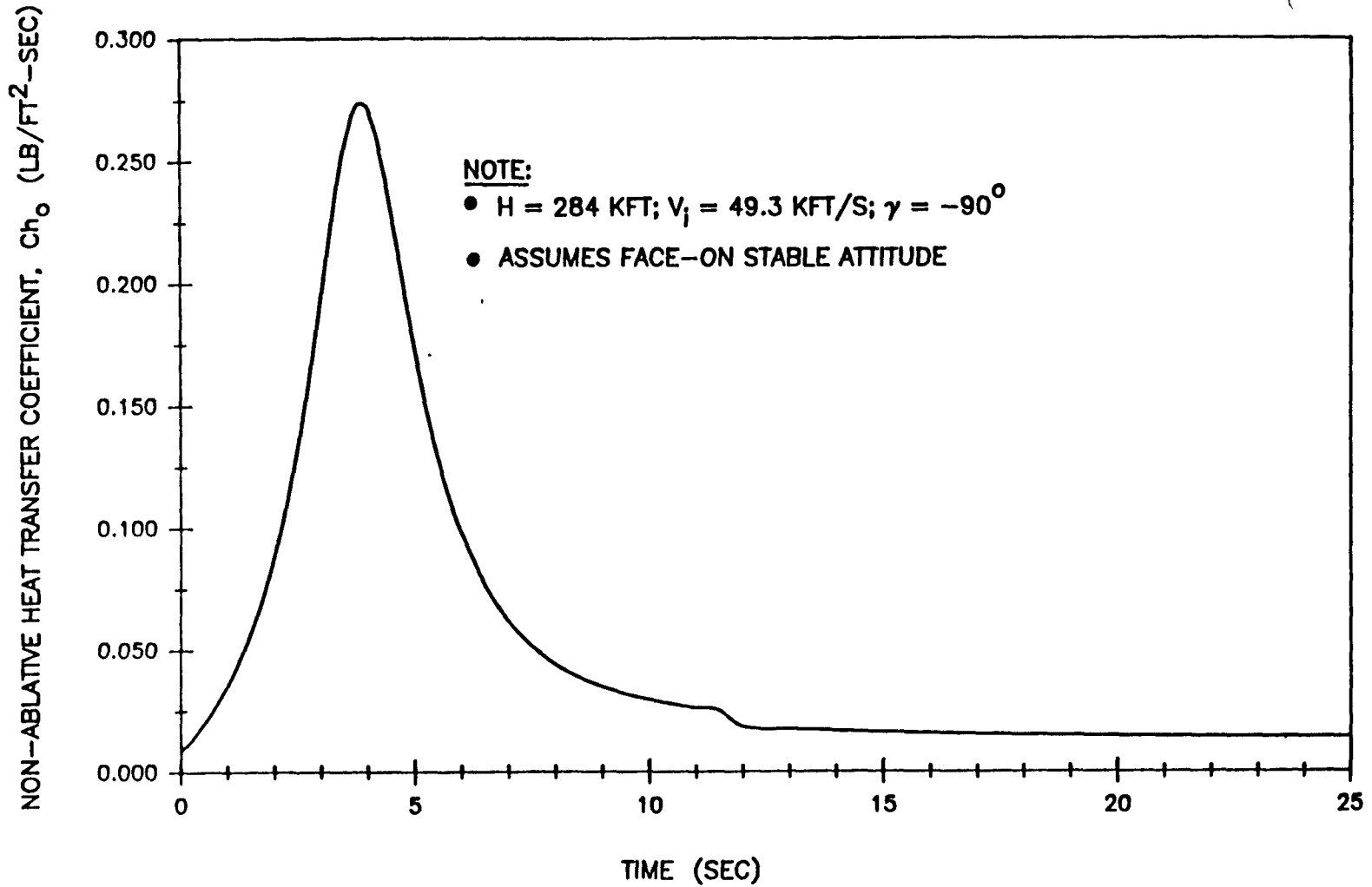


Figure F-22 GPHS Module Transfer coefficient vs. time Heat

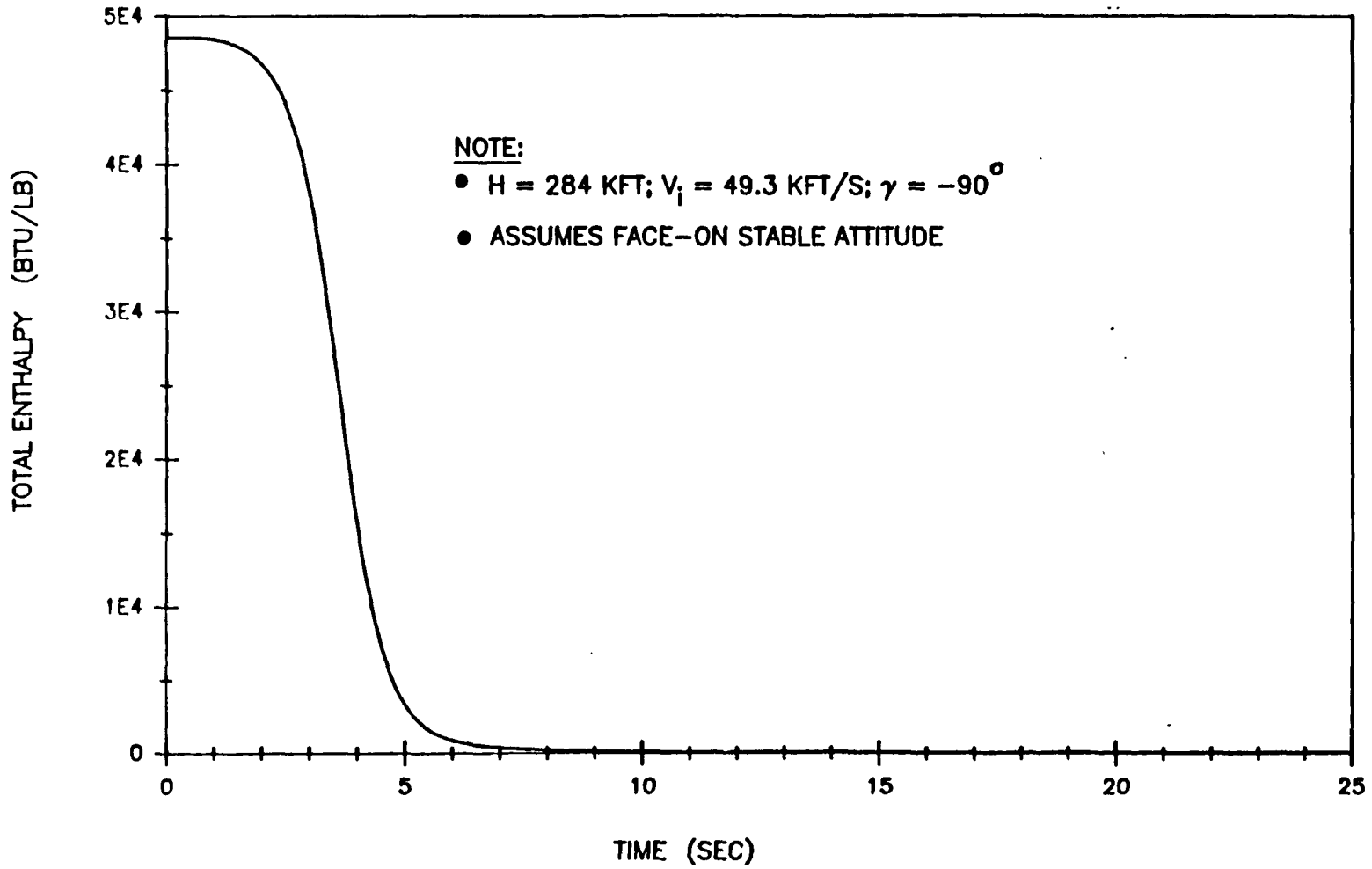


Figure F-23 GPHS Module - Steep Reentry (Case 1A.1) Total Enthalpy vs. Flight Time

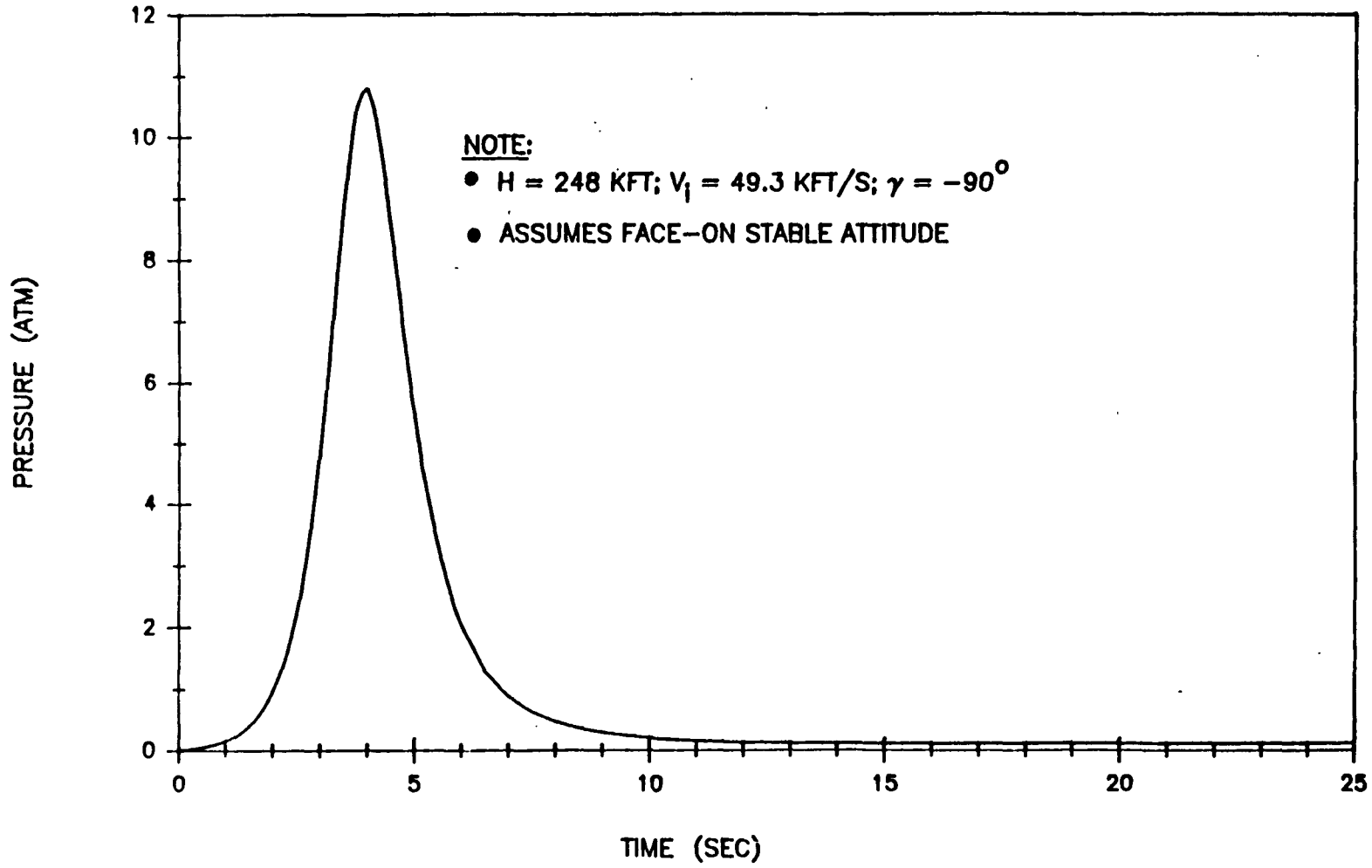


Figure F-24 GPHS Module - Steep Reentry (Case 1A.1) Edge Pressure vs. Flight Time

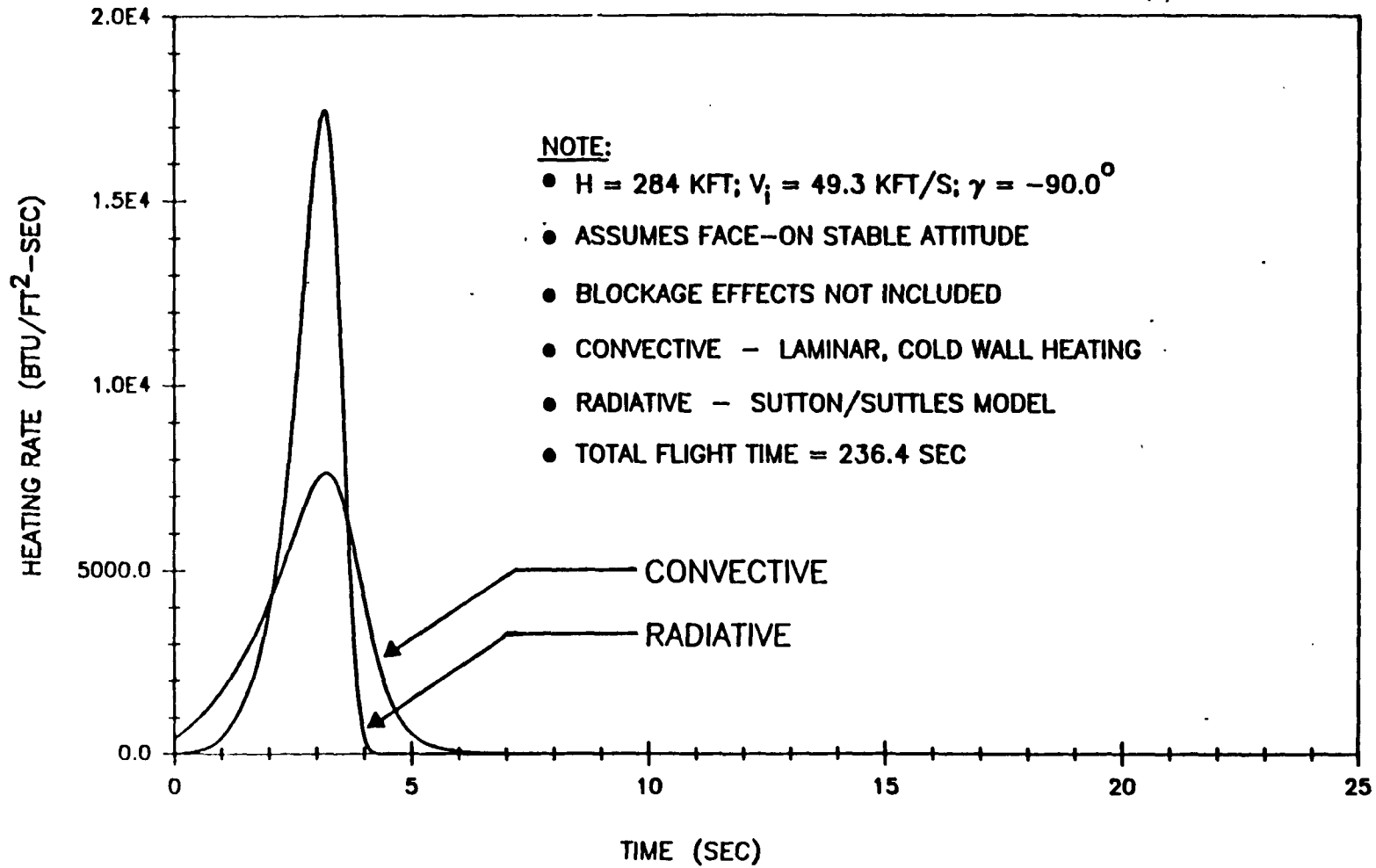


Figure F-25 GPHS Module - Steep Reentry (Case 1A.1) Stagnation Heating Rates

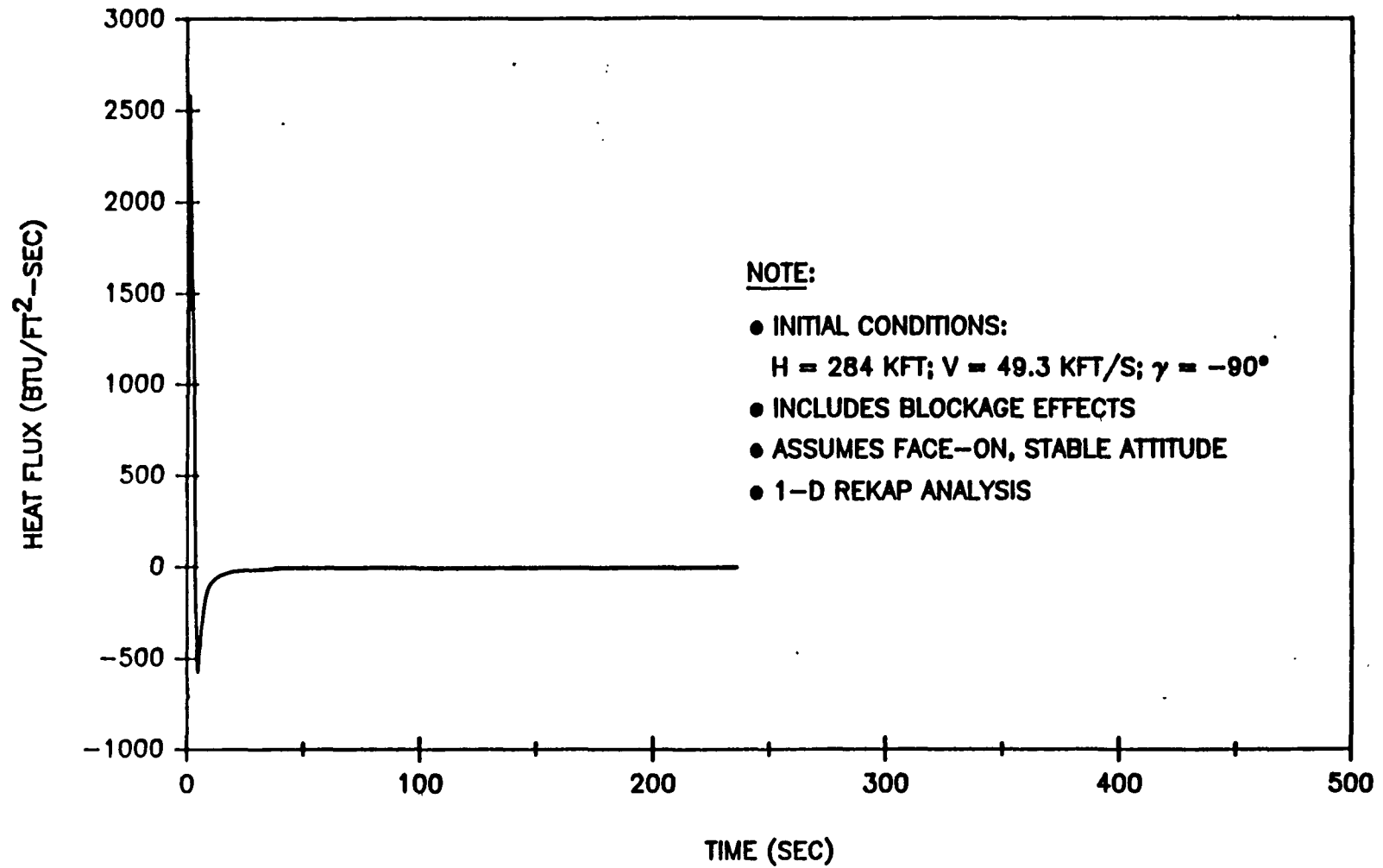
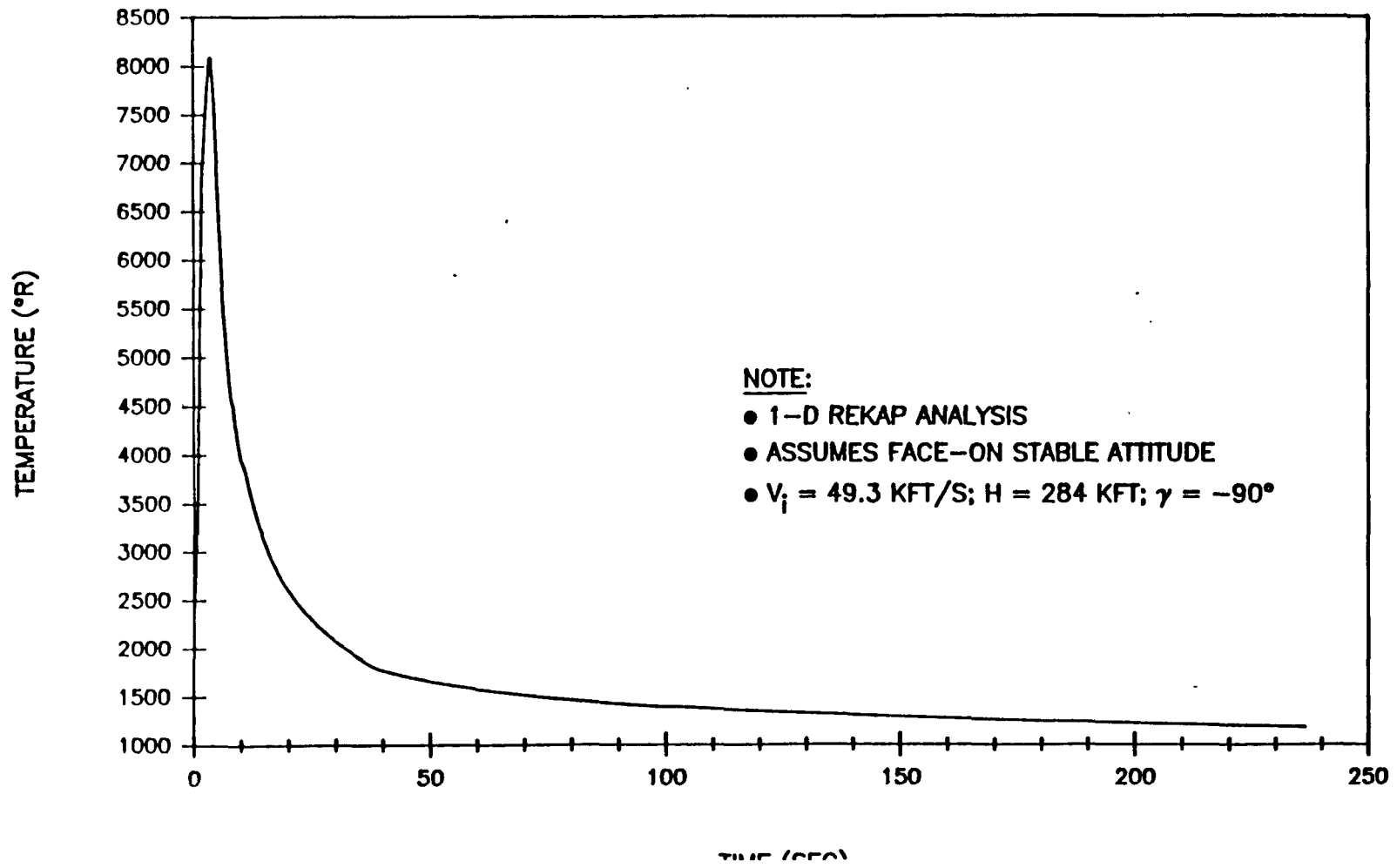


Figure F-26 GPHS Module - VEEGA Re-Entry Net Energy Transfer Into The Surface





Fig

e History

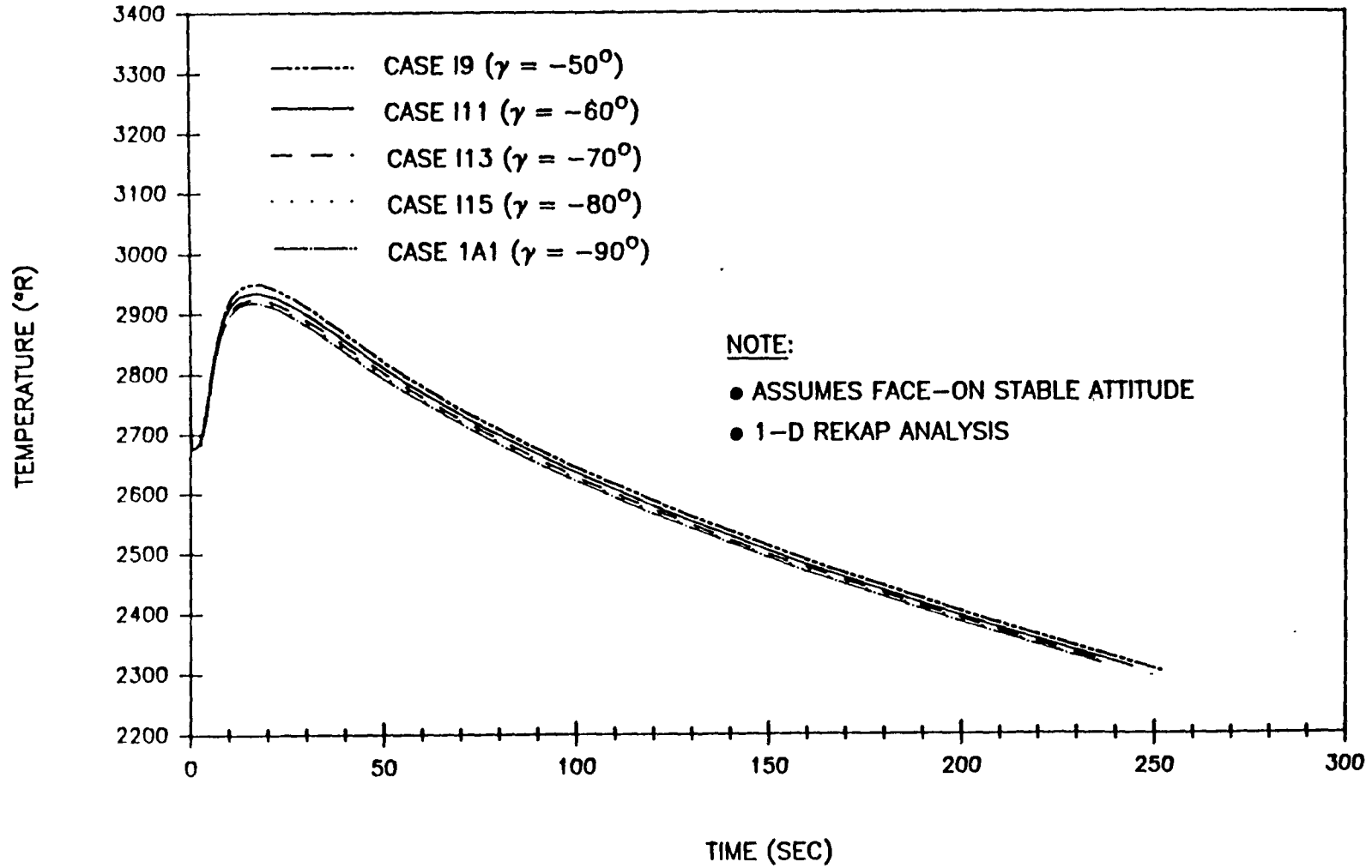


Figure F-28 GPHS Module - VEEGA Re-Entry Clad Temperature Response

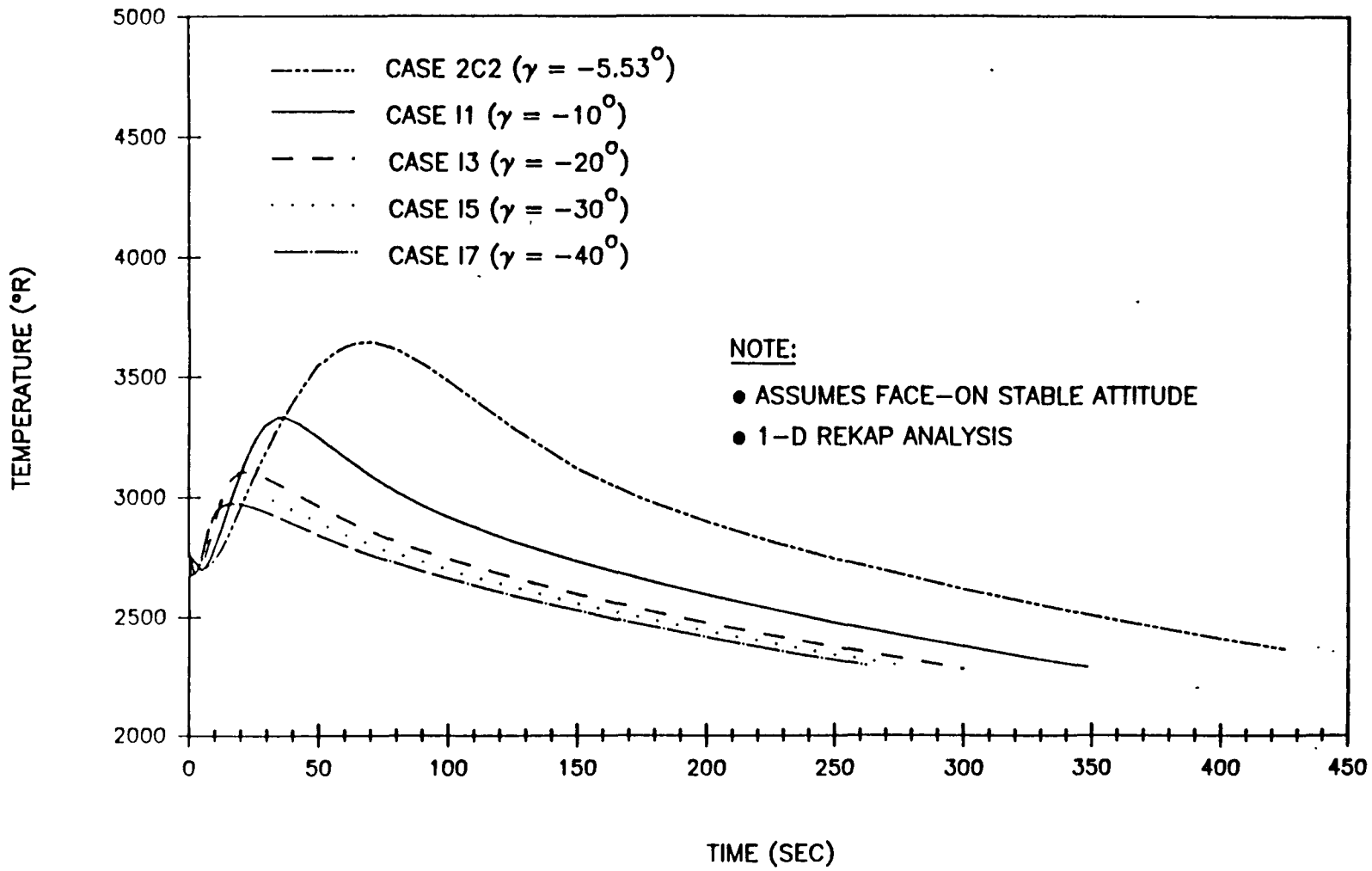


Figure F-29 GPHS Module - VEEGA Re-Entry Clad Temperature Response

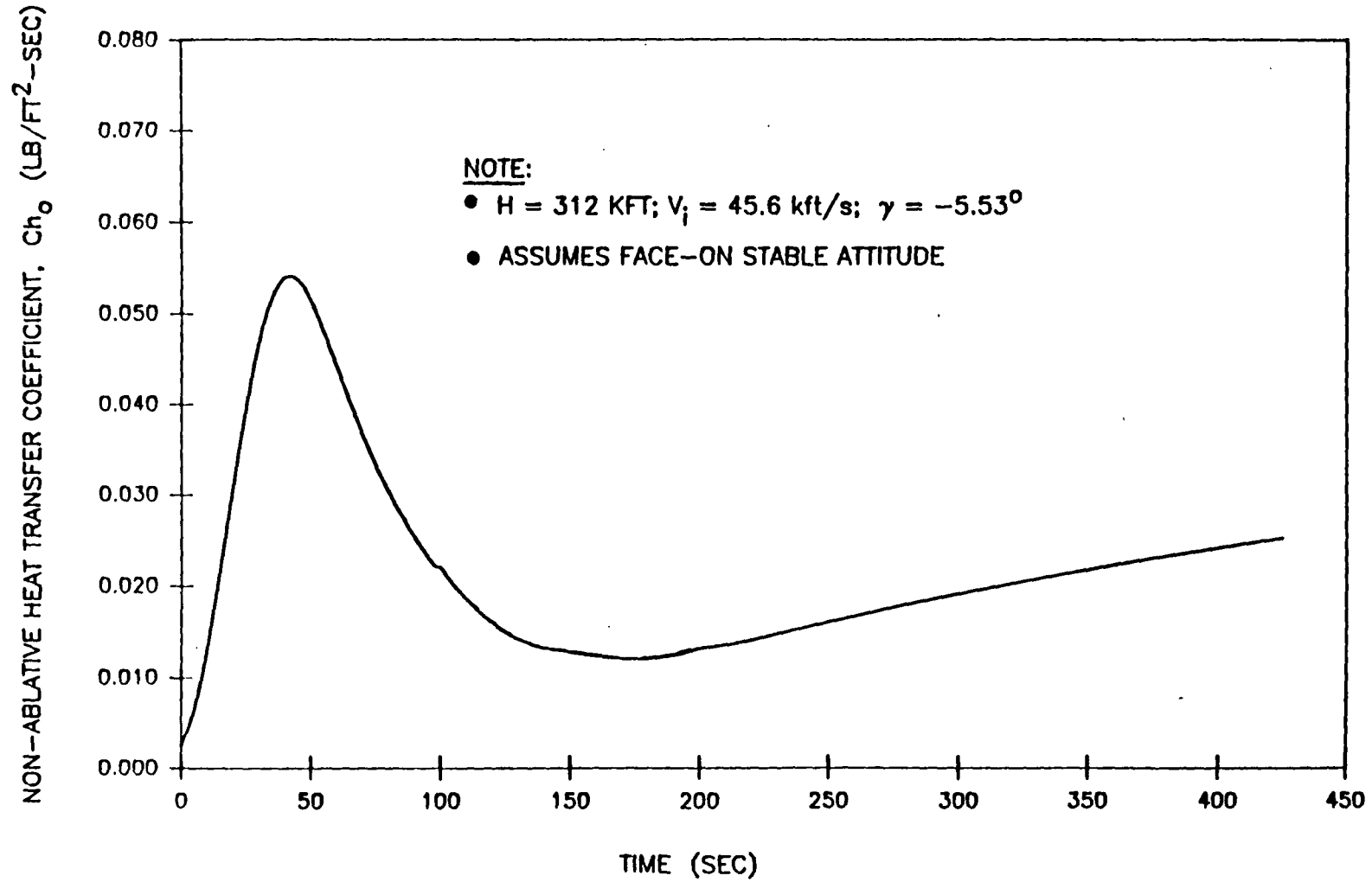


Figure F-30 GPHS Module - Shallow Reentry (Case 2C.2) Non-Ablative Heat

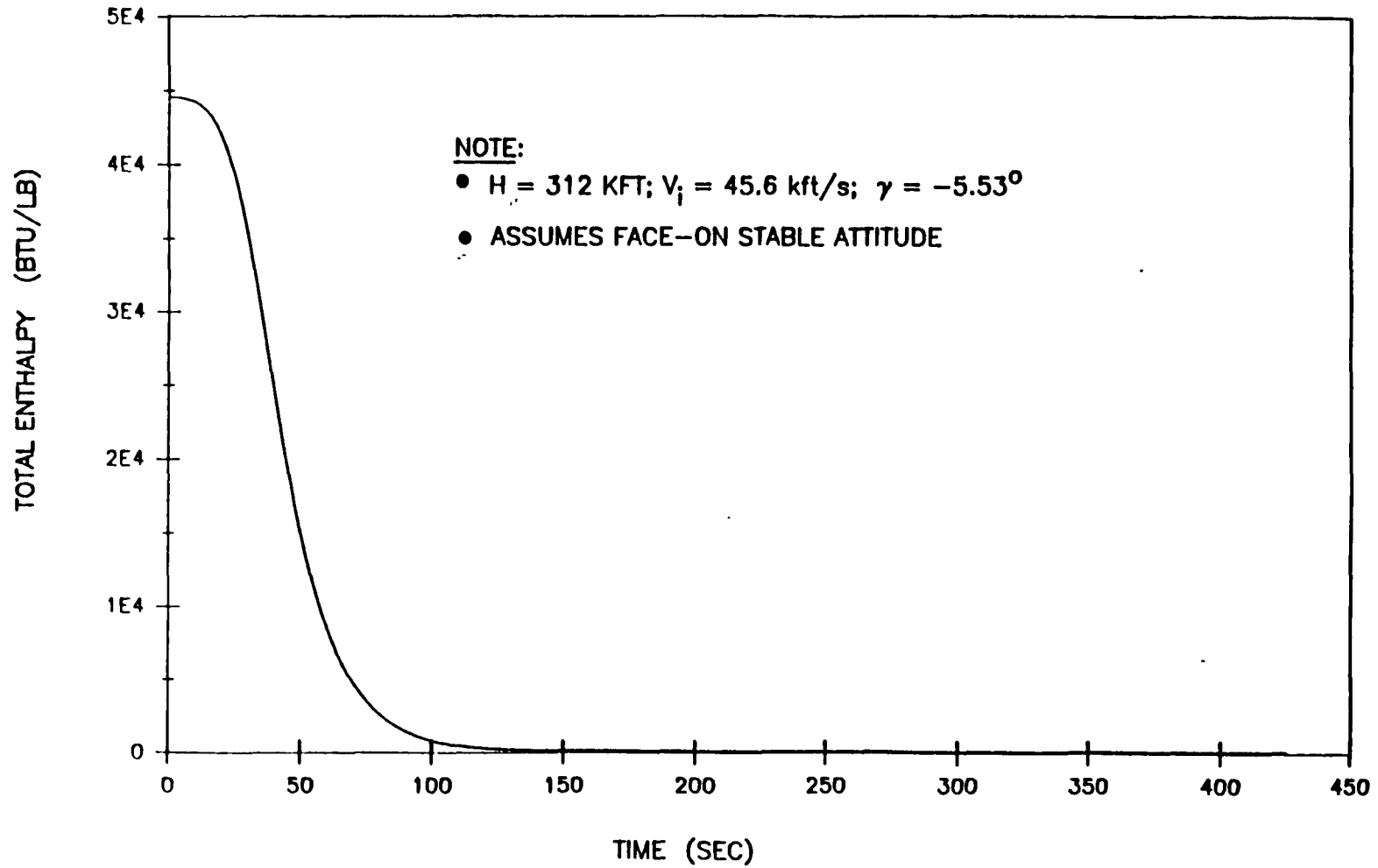


Figure F-31 GPHS Module - Shallow Reentry (Case 2C.2) Total Enthalpy vs. Flight Time

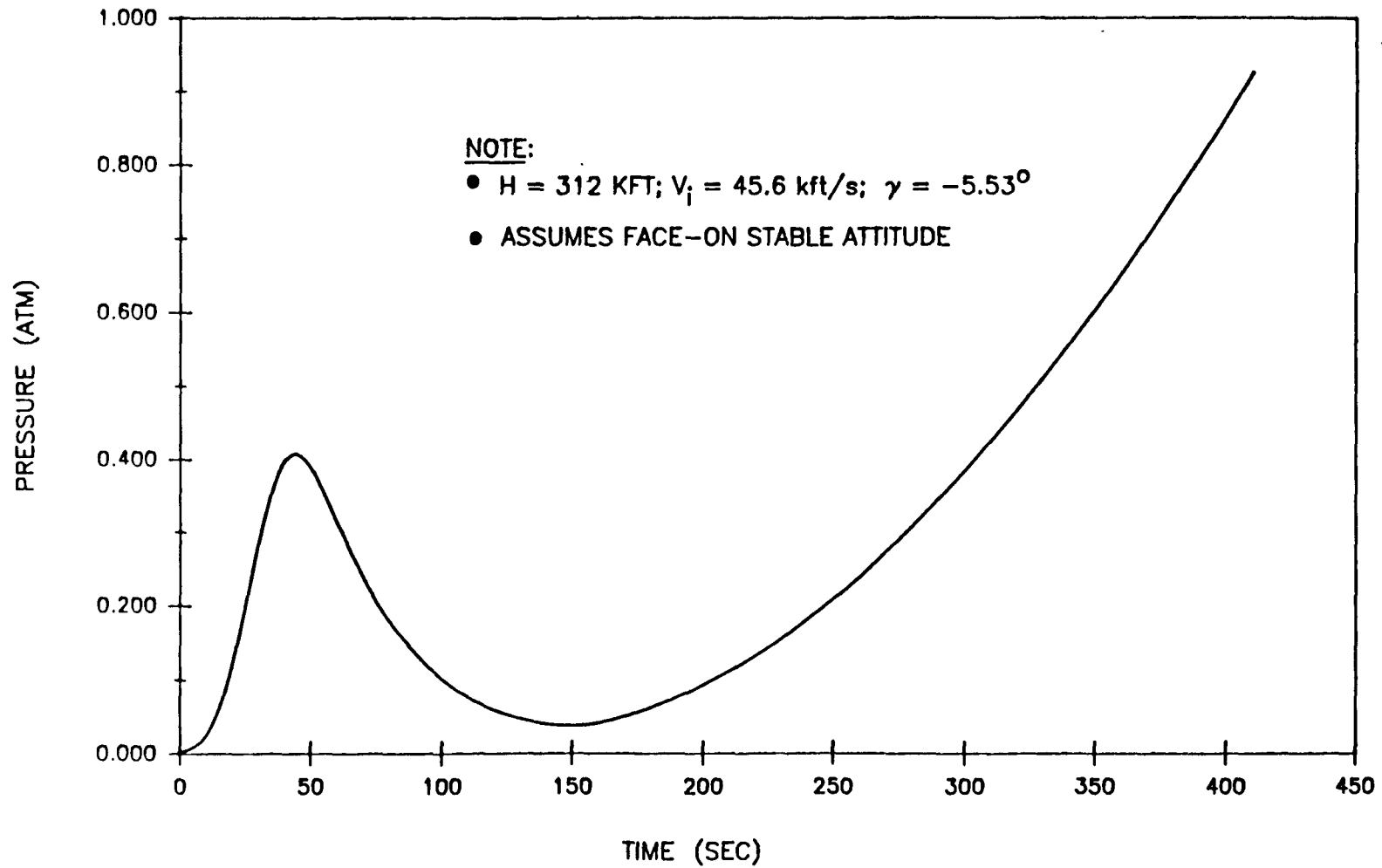


Figure F-32 GPHS Module - Shallow Reentry (Case 2C.2) Edge Pressure vs. Flight Time

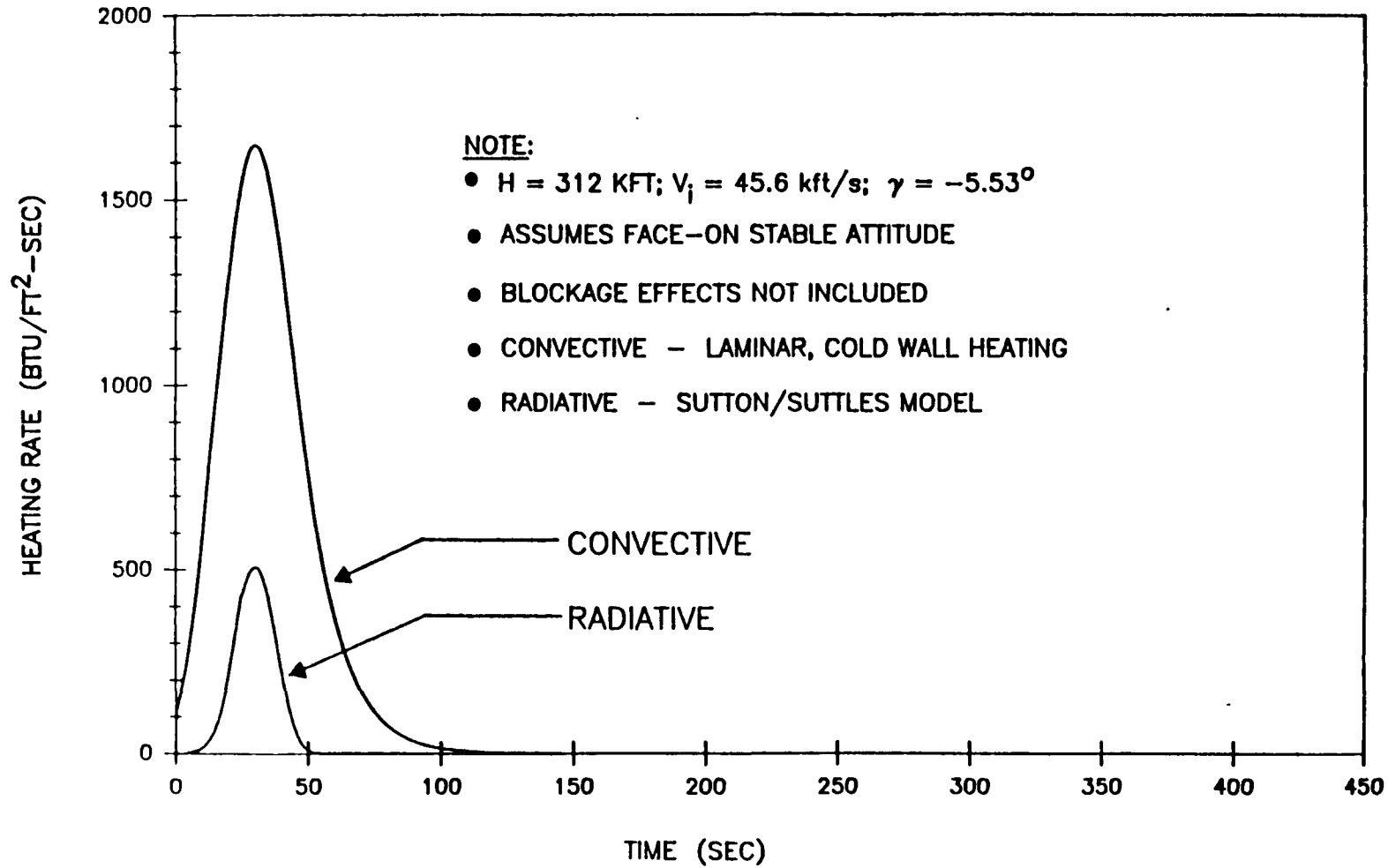


Figure F-33 GPHS Module - Shallow Reentry (Case 2C.2) Stagnation Heating Rates

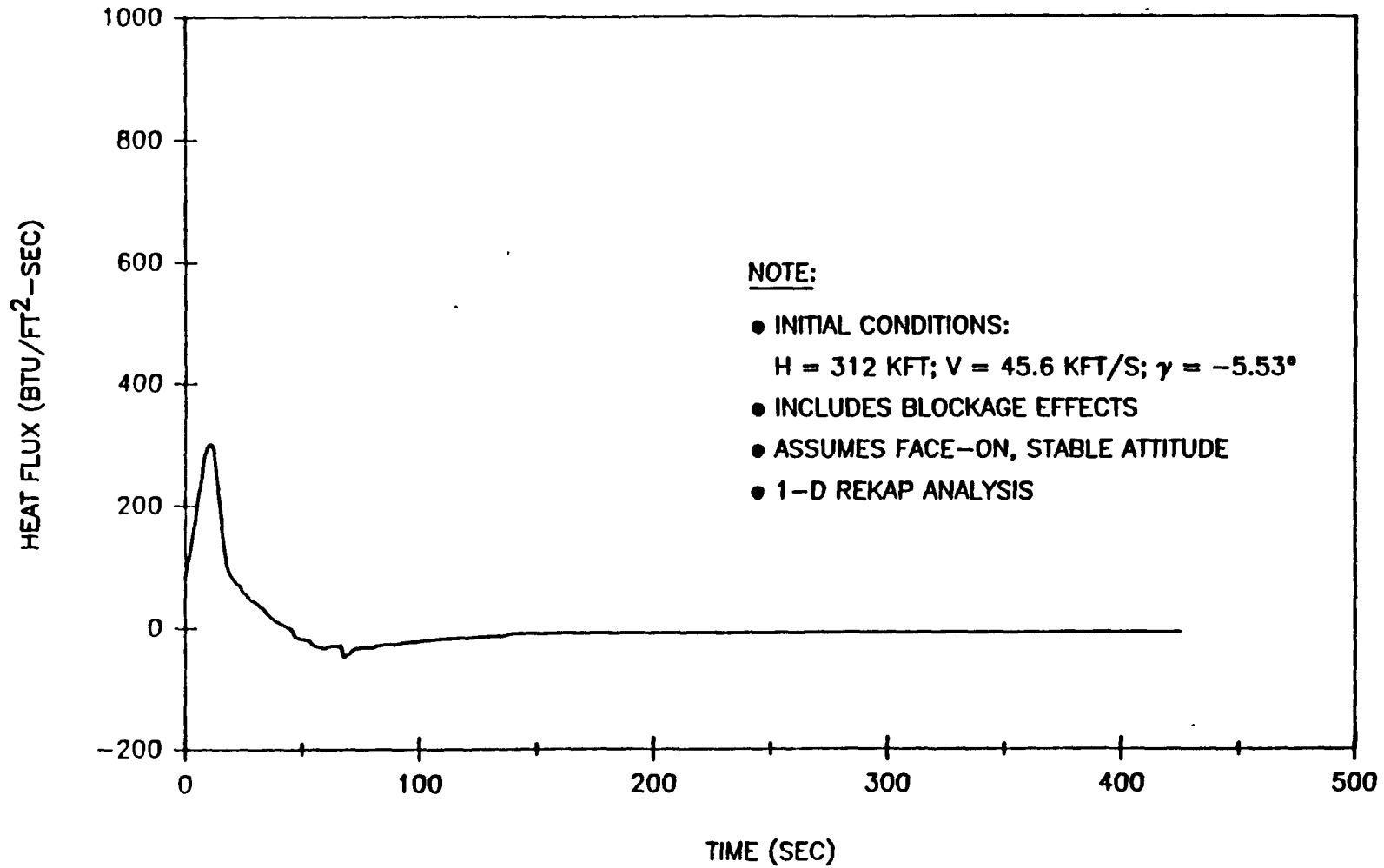


Figure F-34 GPHS Module - VEEGA Re-Entry Net Energy Transfer into the Surface



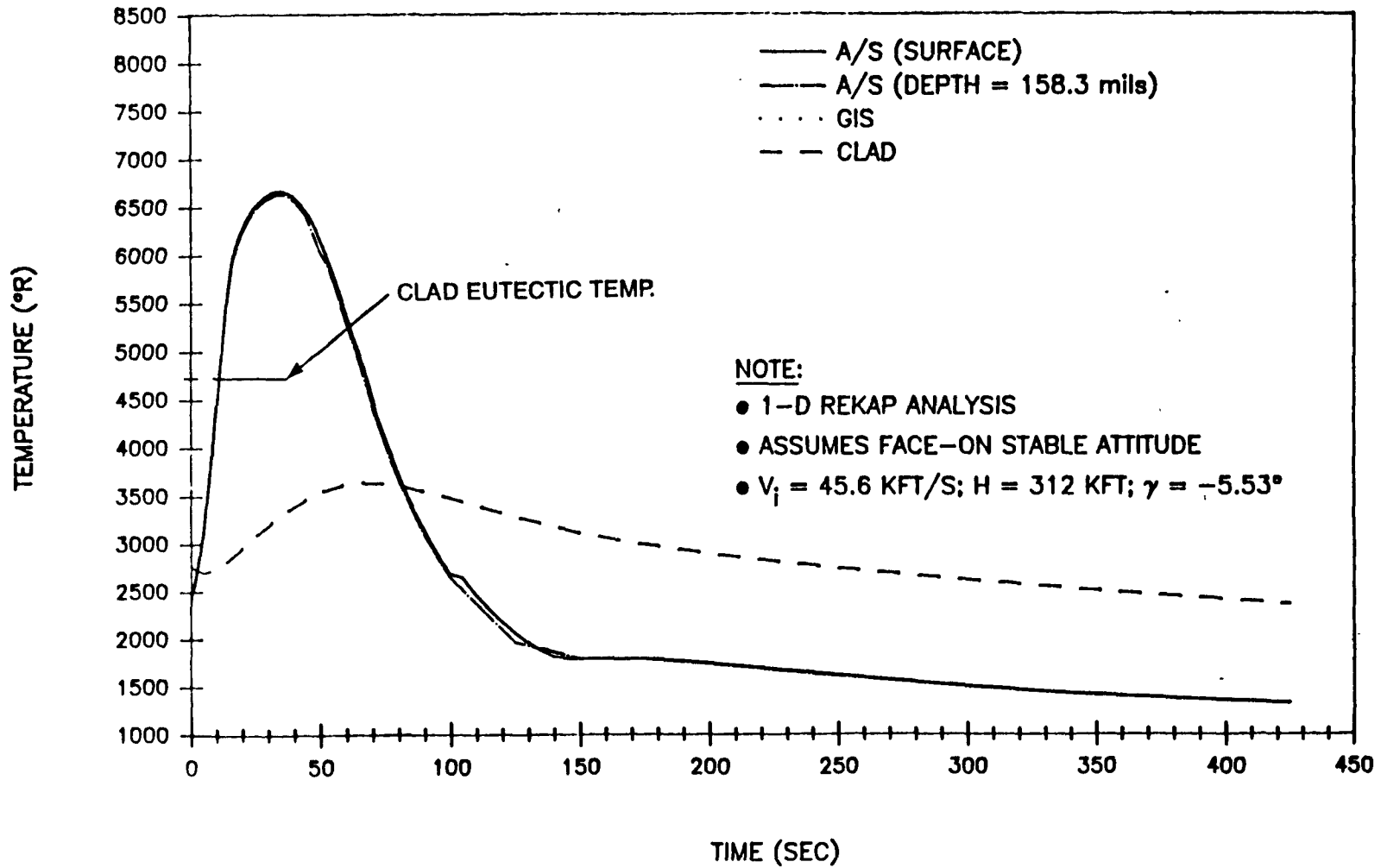


Figure F-35 GPHS Module - Shallow Re-Entry Temperature Response

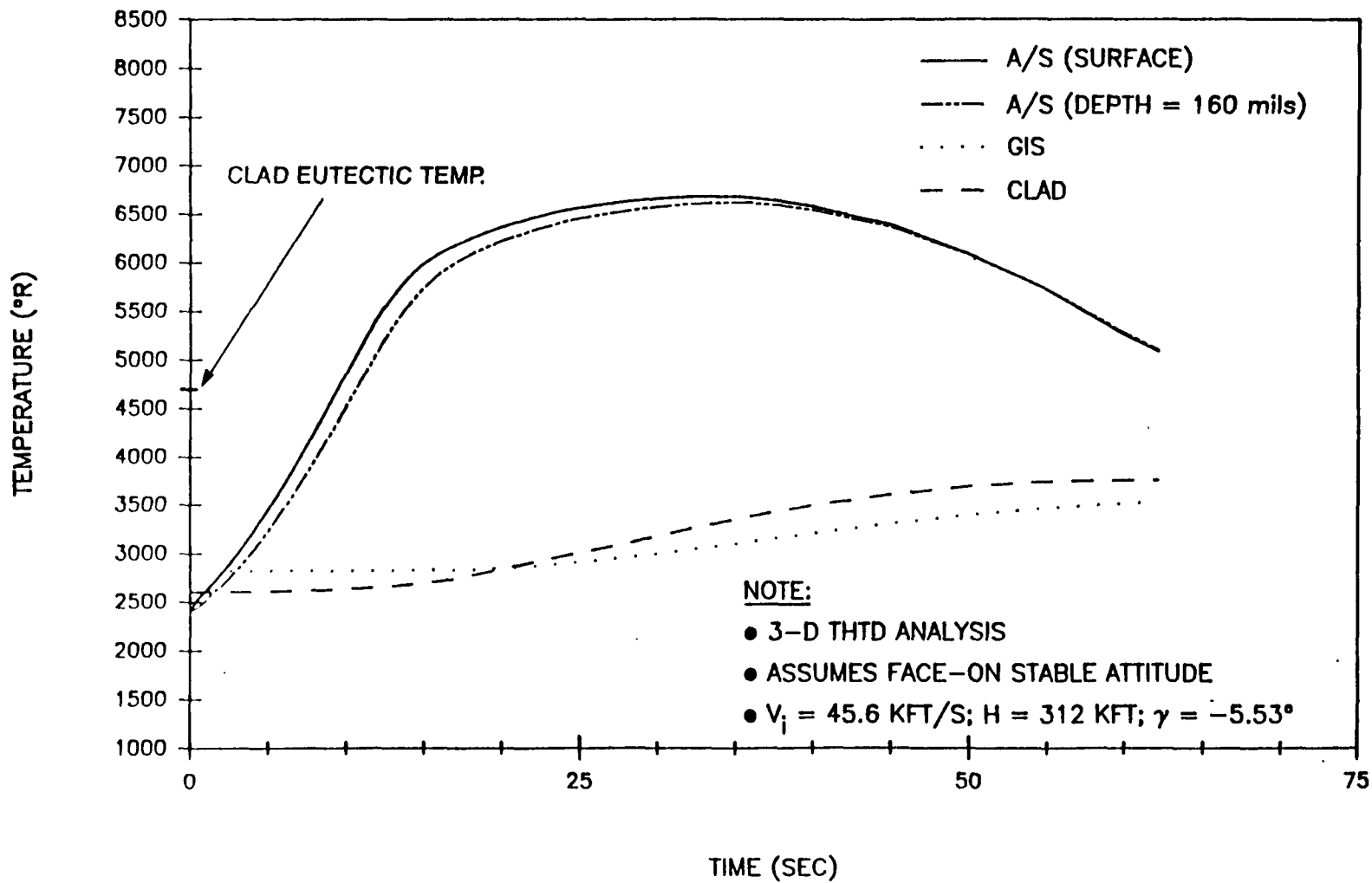


Figure F-36 GPHS Module - Shallow Re-Entry Temperature Response

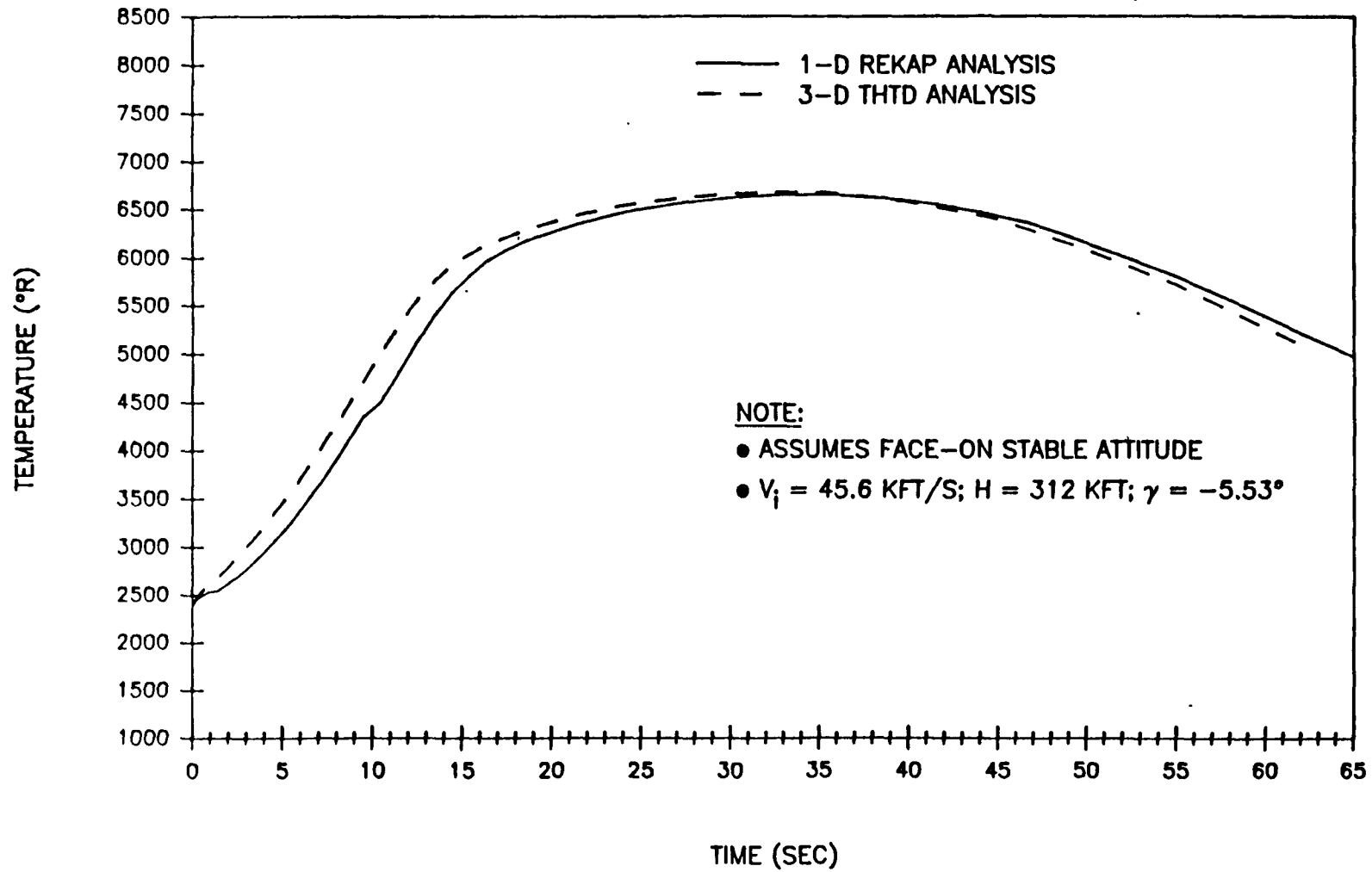


Figure F-37 GPHS Module - Shallow Re-Entry Surface Temperature History

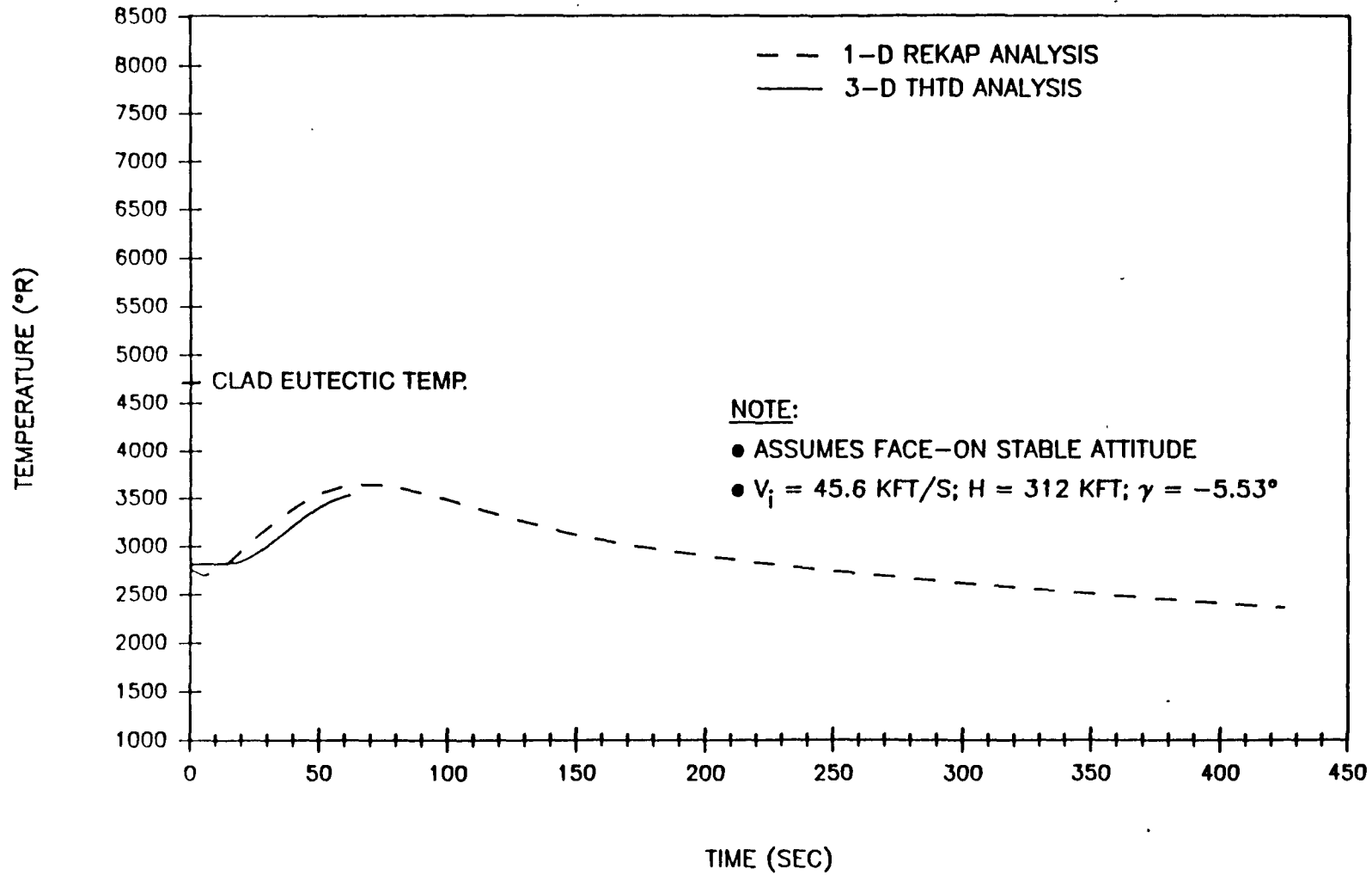


Figure F-38 GPHS Module - Shallow Re-Entry Clad Temperature Response

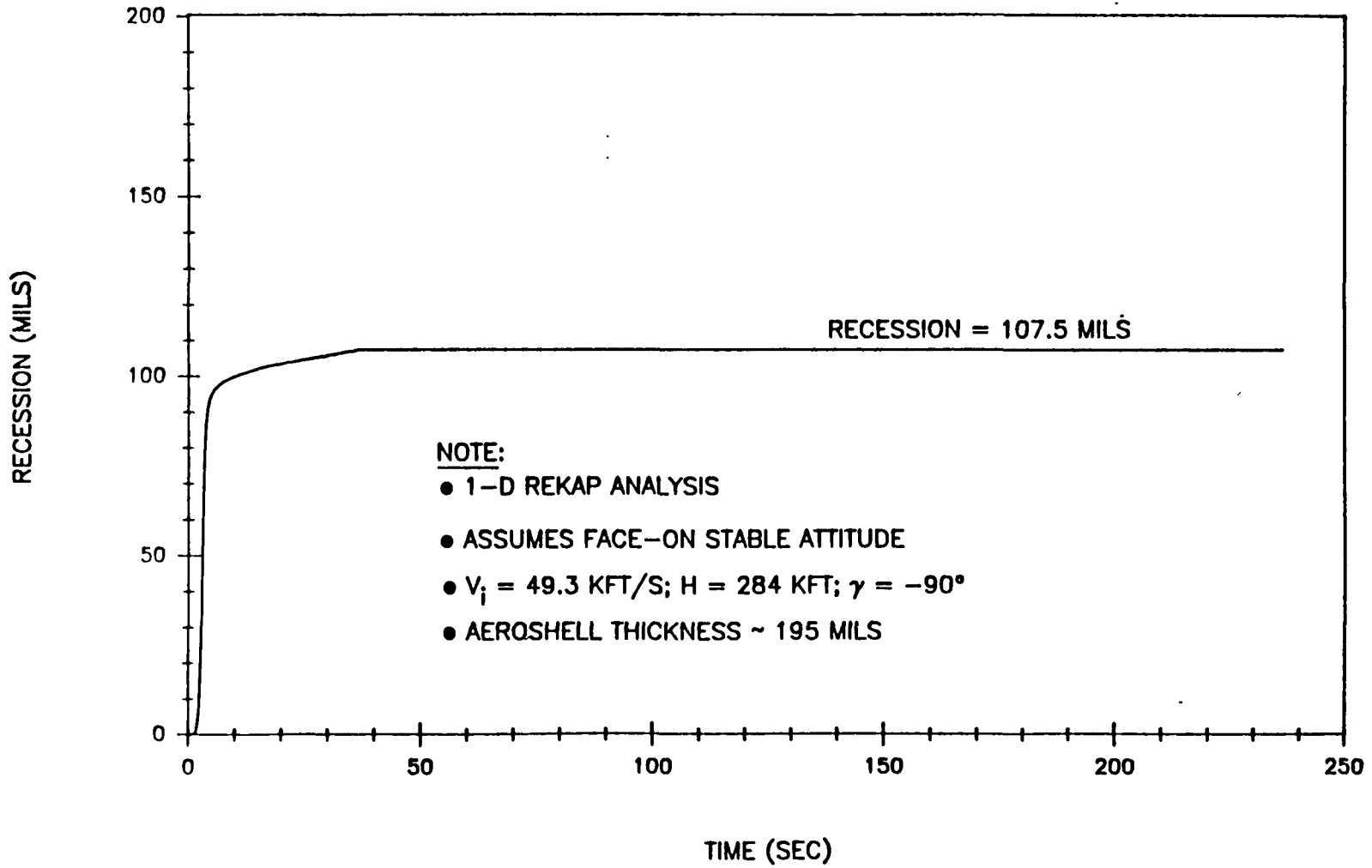


Figure F-39 GPHS Module - VEEGA Re-Entry Recession History

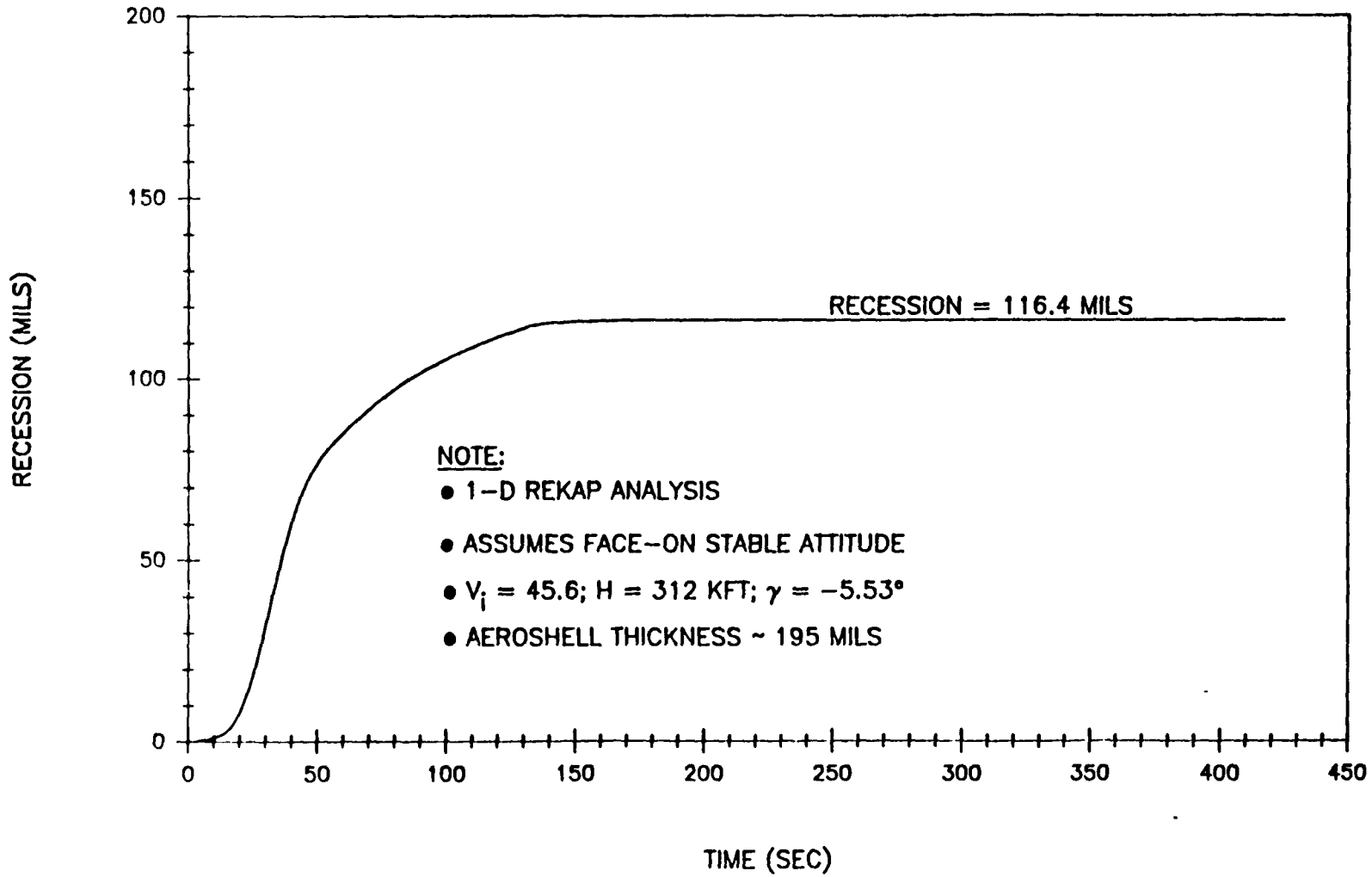
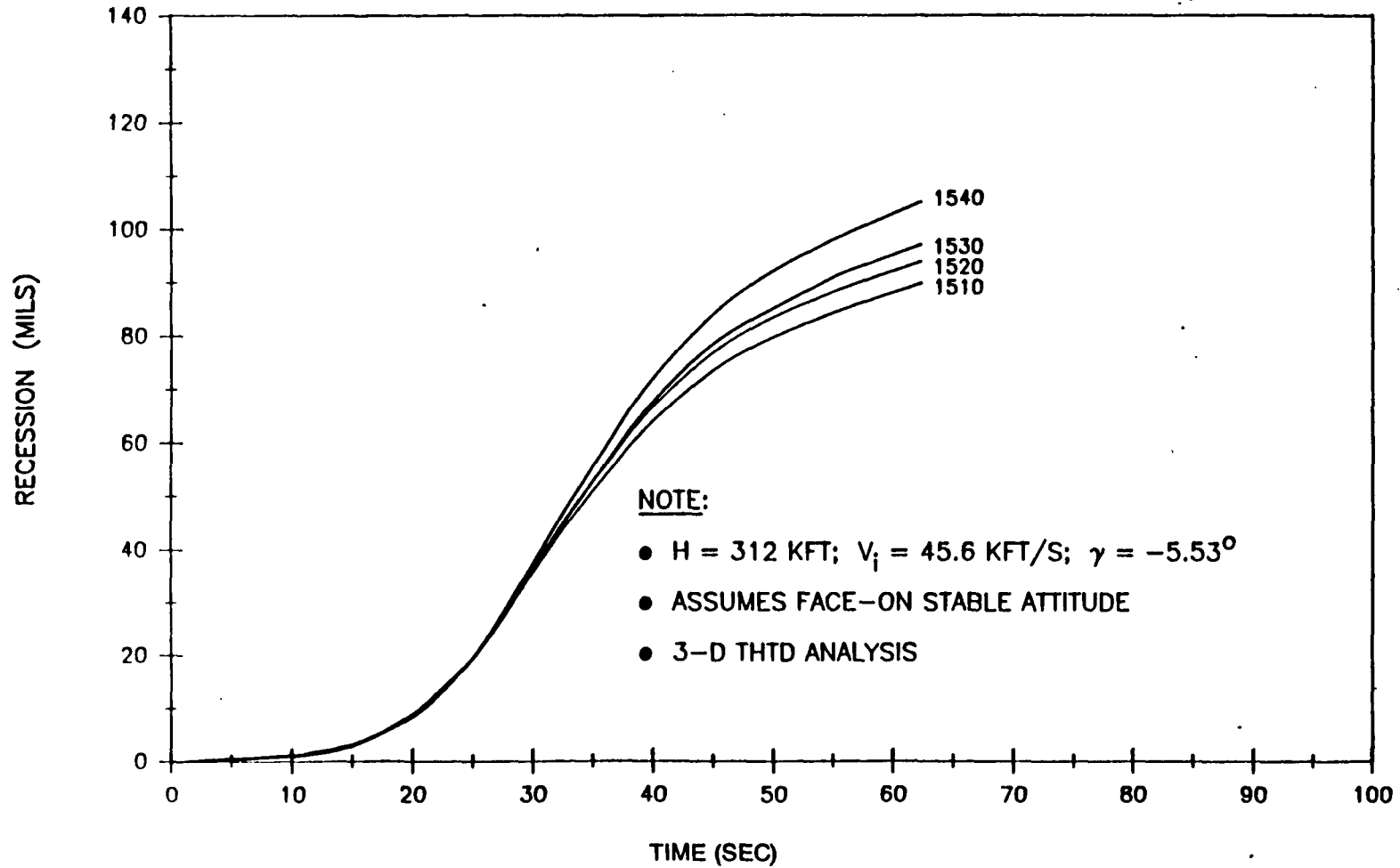


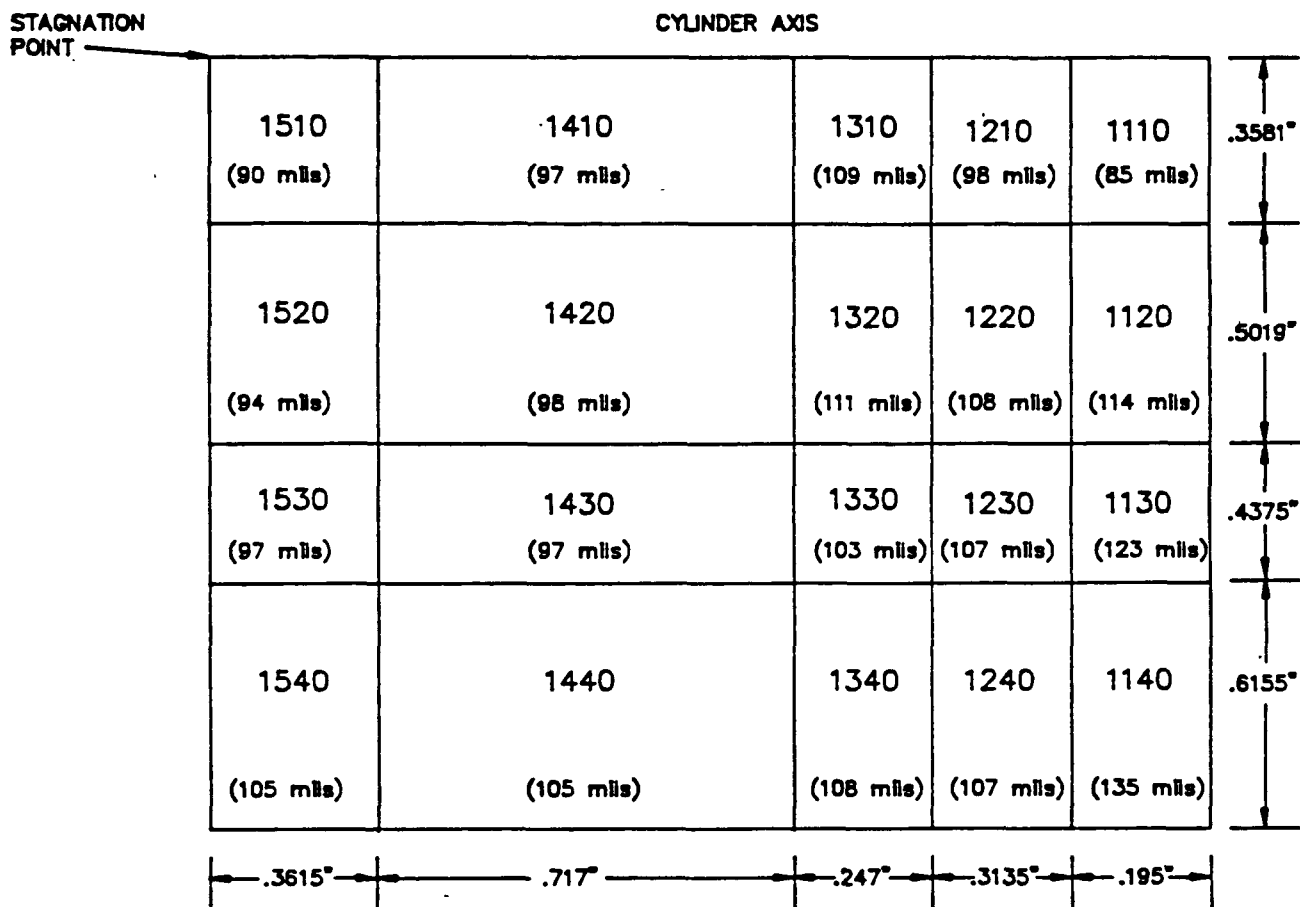
Figure F-40 GPHS Module - Shallow Re-Entry Recession History



Flow

History

CASE 2C2 FLIGHT TIME = 62.4 SECONDS



**NOTE:**

- 3-D THTD ANALYSIS
- ASSUMES FACE-ON STABLE ATTITUDE
- $V_1 = 45.6$  KFT/S;  $H = 312$  KFT;  $\gamma = -5.53^\circ$
- IMPACT TIME = 425 SEC
- ABLATION NOT COMPLETED AT 62.4 SEC

Figure F-42 GPHS Module - VEEGA RE-Entry Ablation Response



Table F-6 Results of GPHS Re-Entry Analysis

NOTE:

- ASSUMES FACE-ON, STABLE ATTITUDE
- 1-D REKAP ANALYSIS

Module Case	Path Angle (Deg)	Total Flight Time (Sec)	Aeroshell Stag Recession (Mils)	Max. Surface Temp. (F)	Max. Clad Temp. (F)
1A.1	-90	236.4	107.5	7378	2458
I15	-80	236.6	102.5	7361	2459
I13	-70	239.5	102.3	7355	2464
I11	-60	244.6	102.0	7343	2475
I9	-50	252.0	104.1	7305	2489
I7	-40	262.5	103.1	7247	2515
I5	-30	277.3	105.9	7158	2570
I3	-20	300.2	102.8	6957	2646
I1	-10	348.5	113.9	6625	2878
2C.2	-5.53	425.0	116.4	6170	3185

(3480-4040°C), depending on pressure. Because of these high temperatures and lack of mechanical properties at these temperatures, a stress analysis could not be performed. This coupled with the potential for melting of the FWPF led to the decision to assume that the aeroshell failed if the temperatures through the thickness at the stagnation point exceeded a value of 6800°F (L3760°C), this being the mid-point of the potential melt range. If this occurred, then the graphite impact shells (GISs) with the fueled clads inside would be released from the aeroshells.

The subsequent reentry of the free GISs was then analyzed. As observed from Table F-6, the temperature of the iridium clads does not approach the melting point of iridium, 2454°C (4449°F), nor does it approach the eutectic point with FWPF, 2322°C (4212°F), recently measured by Los Alamos (currently unpublished). Therefore, the clads will be intact for any reentry of the module at the time the GISs are released.

#### F.4.2 AUXILIARY STUDIES

##### F.4.2.1 Radiative Heating Sensitivity Study

The model used to determine the radiative heating to the GPHS module has a number of uncertainties. One of the significant uncertainties is the effect of the non-equilibrium of the hot gases in the shock layer, which is neglected in the model. This effect occurs early in the reentry when the radiative heating is high.

Because of this uncertainty, a sensitivity study was performed on the effect of the varying the radiative heating to the module. Three 1-D 90 degree reentry runs were performed on the module with different factors placed on the calculated stagnation point radiative heating,  $Q_{RAD}$ . These three cases included:

- A) 50% of calculated  $Q_{RAD}$  to module
- B) 100% of calculated  $Q_{RAD}$  to module.
- C) 150% of calculated  $Q_{RAD}$  to module.

The calculated radiative heating at the stagnation point of the aeroshell assumed thermodynamic equilibrium for the hot gases in the shock layer. The minimum value (50% of the calculated value) is not meant to be the expected lower limit. In fact, for the first 0.5 seconds of the re-entry, the radiative heating might be significantly lower, but this uncertainty would have to be evaluated.

Figures F-43, F-44, and F-45 show the interior and exterior surface temperatures of the aeroshell resulting from this study. The maximum temperatures experienced by each surface and the maximum gradients (not necessarily corresponding to either maximum temperature) are as follows:

<u>Input</u>	Max. Temperature - °F		Max. Temperature Gradient - °F
	<u>Interior Surface</u>	<u>Exterior Surface</u>	
50% Quad.	5975	7319	2292
100% Quad	7209	7661	2440
150% Quad.	7743	8640	2523

The front face recession for each of these cases was 10.1, 95.1, and 133.1 mils, respectively. The peak dynamic pressure and acceleration were 81.6 psi and 605.5 g's, respectively.

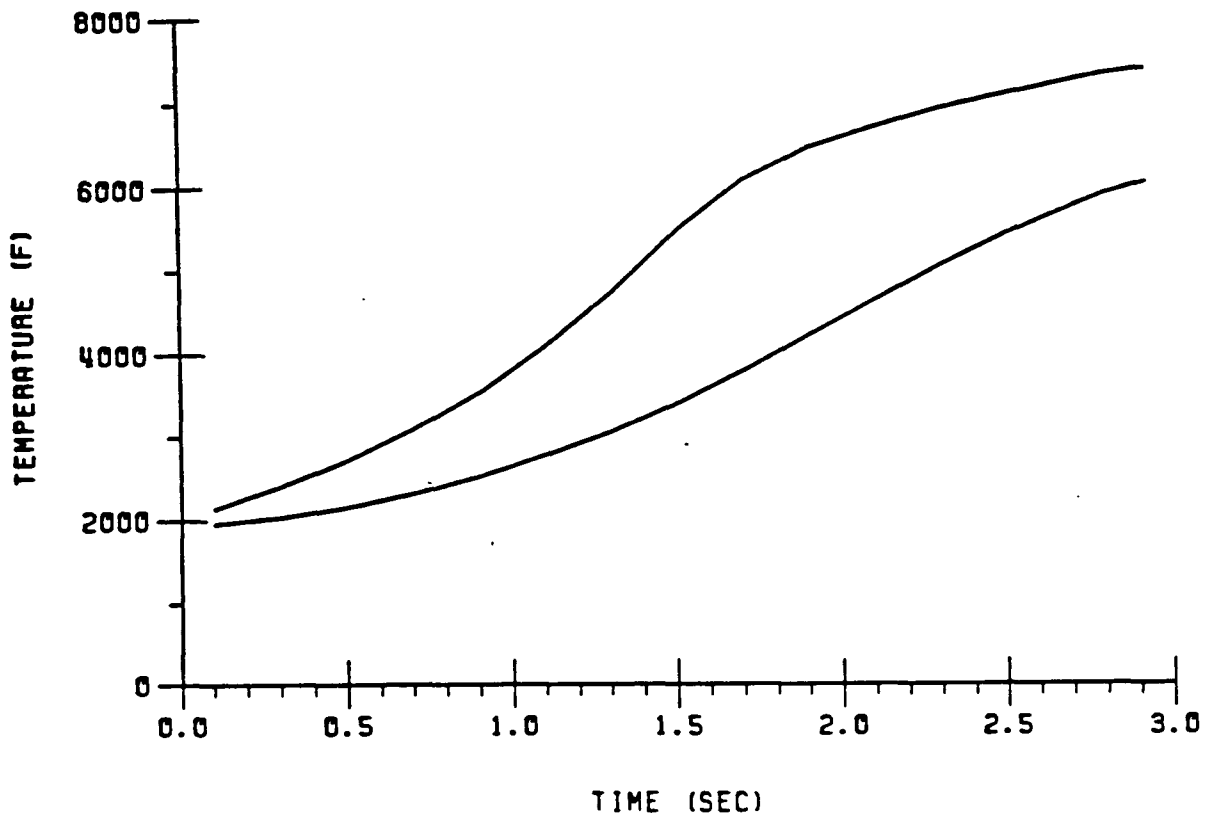


Figure F-43 Interior and Exterior Surface Temp ( $^{\circ}$ F) vs. Time  
Case A (50%  $Q_{RAD}$  Applied)

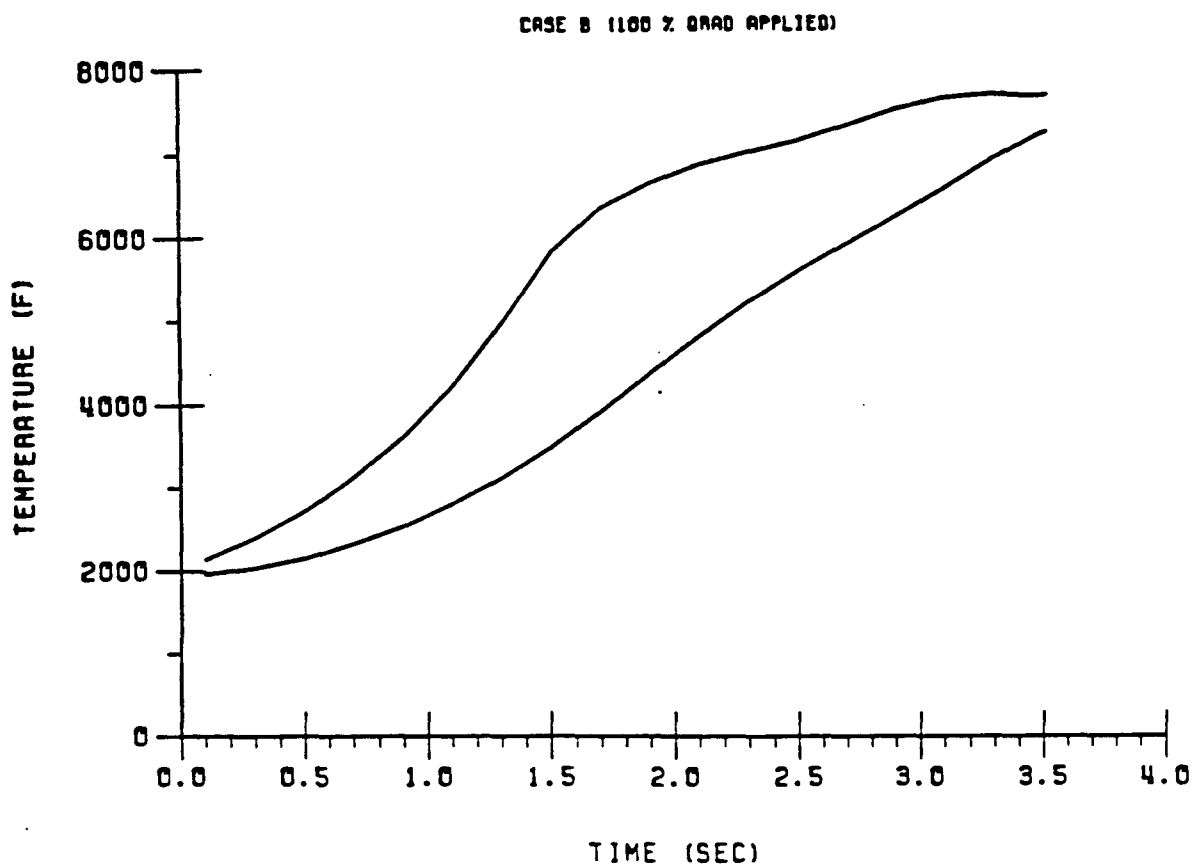


Figure F-44 Interior and Exterior Surface Temp (<sup>o</sup>F) vs. Time  
Case B (100% Q<sub>RAD</sub> Applied)

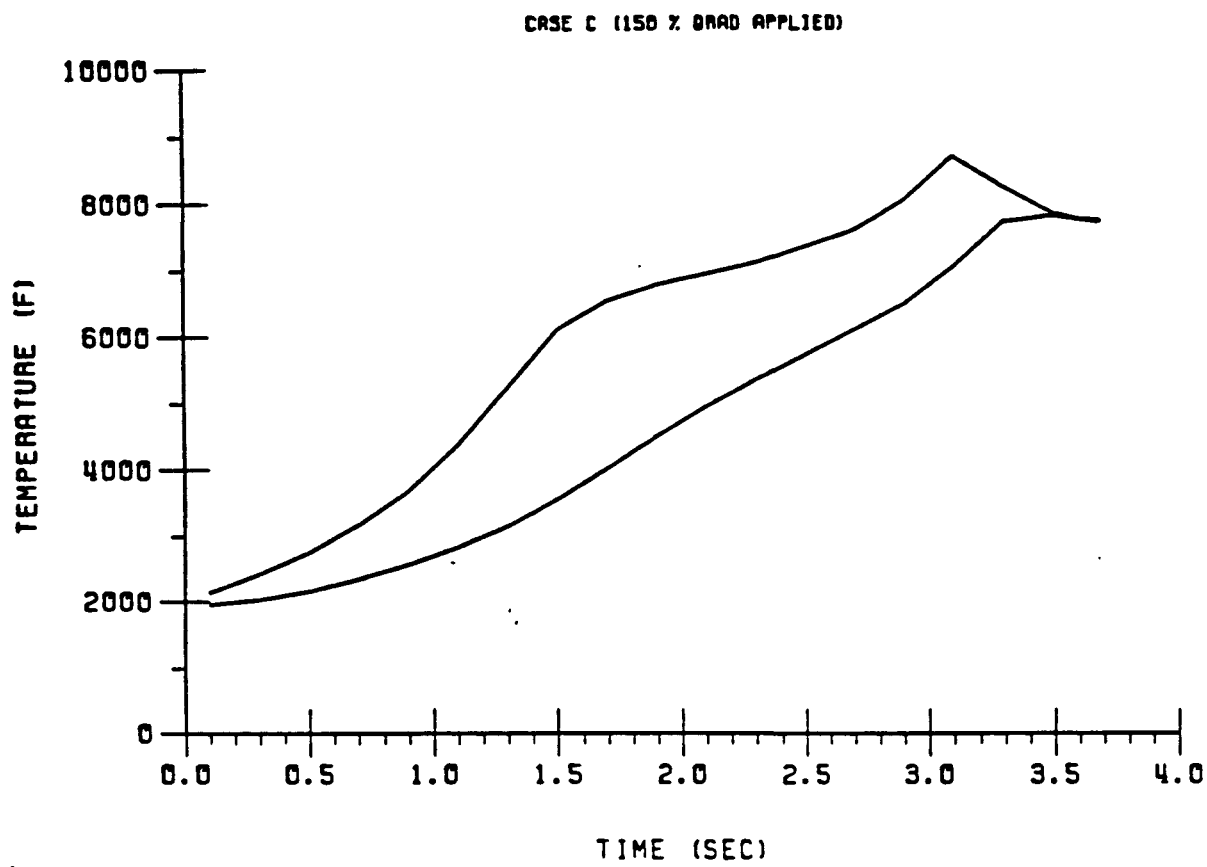


Figure F-45 Interior and Exterior Surface Temp. (<sup>o</sup>F) vs. Time  
Case C (150% Q<sub>RAD</sub> Applied)

F.4.2.2 Time-To-Failure of Aeroshell

In order to provide a preliminary indication of the time of GIS release, a simplified stress analysis of the GPHS module aeroshell was performed for the steep angle reentry of the module. The analysis treated the face of the aeroshell as a simply supported beam. The temperatures, accelerations, and dynamic pressures were obtained from the results of the radiative heating sensitivity study reported in Section F.4.2.1 above. The aeroshell bending stress resulted from the dynamic pressure impinging on the aeroshell lessened by the acceleration force. The net result was a tension on the inner surface and a compression on the outer surface. The thermal stress, which would also produce tension on the inner surface and compression on the outer surface, was neglected.

A one inch strip from the face of the aeroshell was assumed to be uniformly loaded by the dynamic pressure and the inertia forces due to acceleration. Based on a graphite density of .0686 lbs/cu. in., the aeroshell bending stress (f) was expressed as:

$$f = \frac{6.38q - .438tg}{t^2}$$

where

- q = dynamic pressure (psi)
- t = aeroshell thickness (in)
- g = acceleration

For each of the three radiative heating rates, the stress in the aeroshell and the margin of safety were computed. Figure F-46, taken from Appendix I of GESP - 7200 shows the strength of the FWPF as a function of the temperature. Tensile strength data for FWPF below 3000°F were taken from Reference F-15. Between 3000°F and 4500°F, tensile strength was obtained from normalized

data from Reference F-16. Beyond 4500°F no strength data exists.

---

NOTE: DOE has initiated plans to obtain additional test data on the higher temperature strength properties of the FWPF material. The intent is, at a minimum, to obtain tensile and compressive strength data to at least 6000°F; the test program might be extended to obtain other mechanical properties as well in the higher temperature range.

---

Reference F-17 gives a melting point for graphite in the range between 6380°F and 7289°F. Figure F-47 shows graphically the expected time to failure of the aeroshell for each of the three heating rates. Failure of the aeroshell can be seen to occur at 2.65, 2.6, and 2.4 seconds, respectively, for radiative heating rates equal to 50%, 100%, and 150% of the calculated values.

If thermal stresses were added to the stresses calculated here it would appear that the aeroshell should fail much sooner than predicted. However, thermal stresses may be completely relieved by very small distortions, and as the temperature increases, the elongation required to cause failure increases. These factors tend to reduce the magnitude of the thermal stress. On the other hand, the dynamic pressure impinging on the aeroshell causes stresses which are not relieved by distortions. For these reasons, it is believed that thermal stresses can be neglected in predicting aeroshell failure.



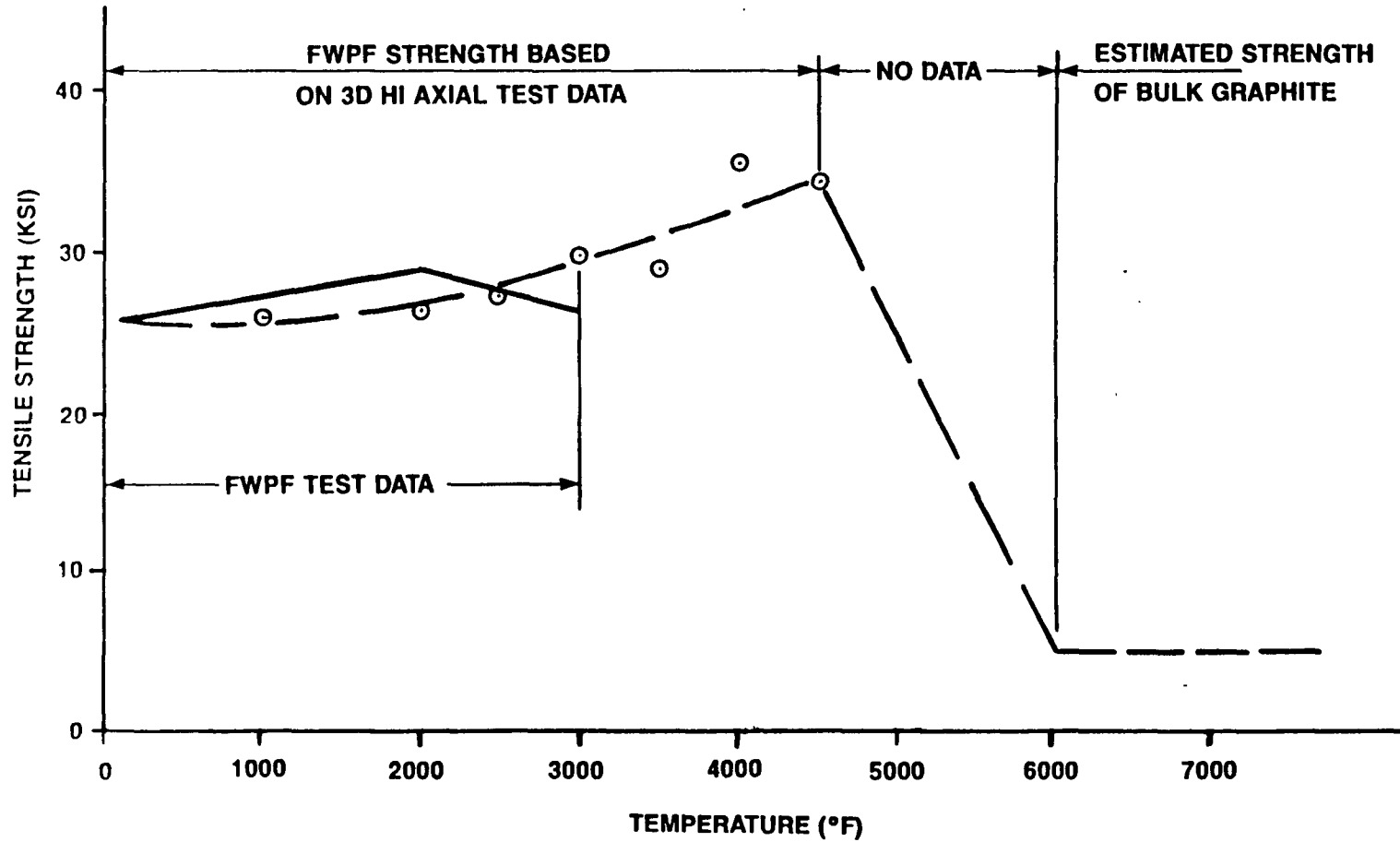


Figure F-46 FWPF Allowable Tensile Strength in X, Y, Dir

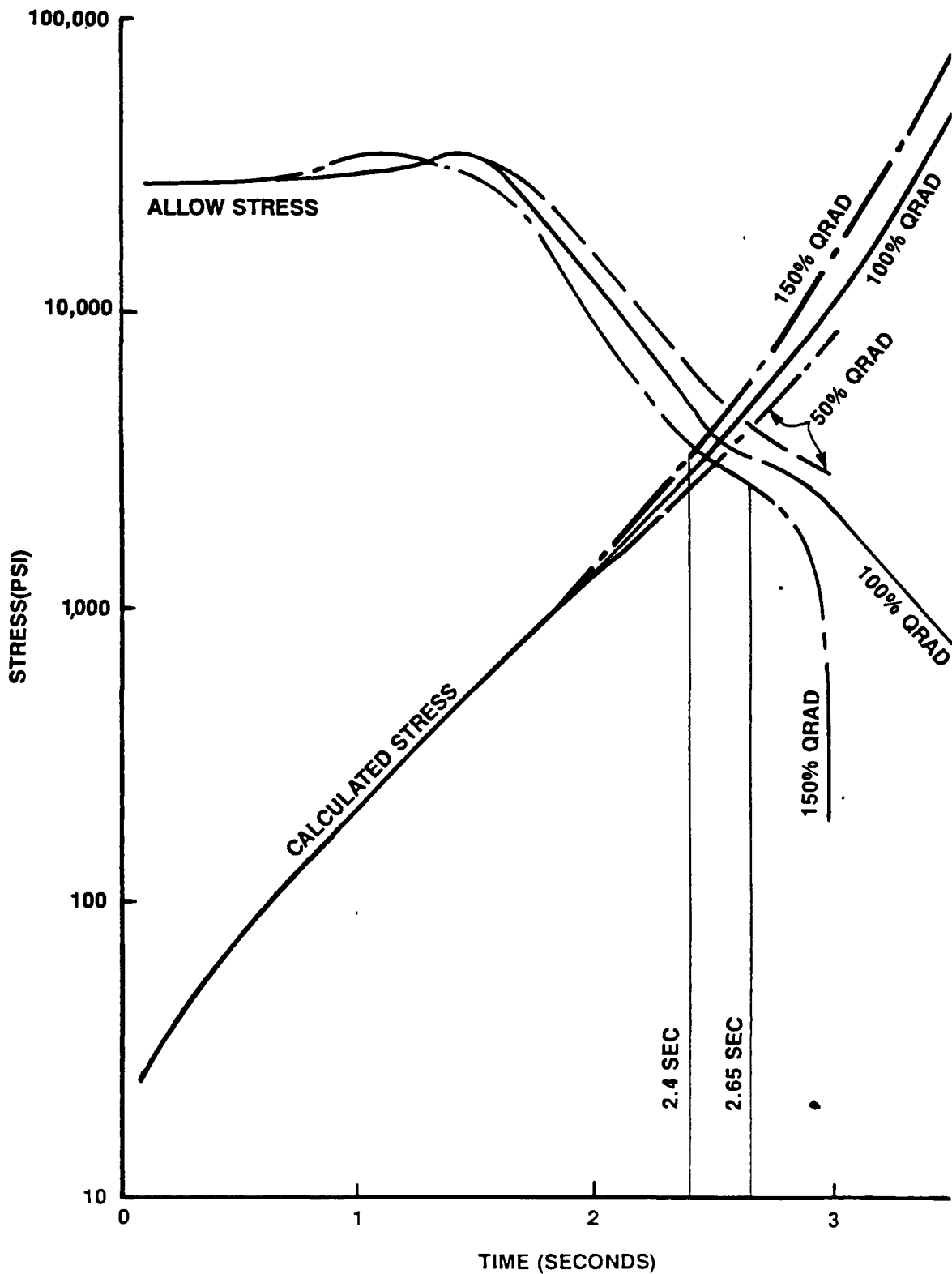


Figure F-47 Steep Angle Reentry

## F.4.3 GIS REENTRY

The results of the ensuing GIS reentry after its release from the aeroshell of the GPHS module have been previously covered in the Overview, Section F.2. For these analyses, the 3-D THT-D computer program was employed, and satisfactorily converged solutions were obtained. Whenever the  $2322^{\circ}\text{C}$  ( $4212^{\circ}\text{F}$ ) eutectic temperature (i.e., between iridium and FWPF) was attained, the computation was terminated. This occurred for all GIS reentries at angles of  $-30$ ,  $-40$ ,  $-50$ , and  $-70$  degrees. Since the  $-60$  degree GIS reentry resulted in the clad temperature being very close to the eutectic temperature, failure of the clad was taken to occur. Because of the trend of the GIS and iridium clad temperatures over this range of reentry path angles, the judgement was made that the iridium-graphite (FWPF) eutectic temperature would also be exceeded for the total range of path angles from  $-5.53$  to  $-90$  degrees.

F.5 REFERENCES:

- F-1 McDonald, A. "VEEGA Earth Reentry Breakup Analysis", Doc. No. 1625-331, NASA Jet Propulsion Laboratory, March 1987.
- F-2 Letter from A. McDonald, NASA Jet Propulsion Laboratory to J.C. Hagan, Applied Physics Laboratory, Johns Hopkins University, Subject: VEEGA Flyby Intermediate Flight Path Angle Reentries, August 17, 1987.
- F-3 Oberholtzer, N. "Reentry Trajectory Characteristics of the GPHS Configuration C" Document No. PIR-32-007, General Electric Co., June 16, 1986.
- F-4 Shuttles, J.T., Sullivan, E.M., Margolis, S.B., "Curve Fits of Predicted Inviscid Stagnation - Point Radiative Heating Rates, Cooling Factors, and Shock Standoff Distances for Hyperbolic Earth Entry" Langley Research Center.
- F-5 Anderson Jr., J.D., "An Equation for Rapid Calculation of Stagnation Point Radiative Heat Transfer (Including Shock Layer Radiative Cooling and Nongray Self-Absorption)", Doc. No. NOLTR 68-56, United States Naval Ordnance Laboratory, White Oak, Maryland, 1968.
- F-6 Callis, L.B., "Solutions of Blunt-Body Stagnation-Region Flows with Nongray Emission and Absorption of Radiation by A Time-Asymptotic Technique", Doc. No. NASA TR R-299, Langley Research Center, Langley Station, Hampton, VA , 1968.
- F-7 Hoshizaki, H., Wilson, K.H., "Convective and Radiative Heat Transfer During Superorbital Entry", AIAA Paper No. 66-106, AIAA 3rd Aerospace Sciences Meeting, New York, Jan. 24-26, 1966.
- F-8 Anderson Jr., J.D., "Stagnation Point Heat Transfer From A Viscous Nongray Radiating Shock Layer", Doc. No. NOLTR 67-189, United States Naval Ordnance Laboratory, White Oak, Maryland, 6 Nov. 1967.

- F-9 Wilson, K.H., Hoshizaki, H., "Effect of Ablation Product Absorption and Line Transitions on Shock Layer Radiative Transport", Doc. No. NASA CR-1264, Lockheed Missiles and Space Co., Palo Alto, Calif., Feb. 1969.
- F-10 Hunter, L.W., Perini, L. L., Conn, D.W., Brenza, P.T., "Calculation of Carbon Ablation on a Reentry Body During Supersonic/Subsonic Flight", Journal of Spacecraft and Rockets, Vol. 23, No. 5, Sept. - Oct. 1986, Pg. 487.
- F-11 Putz, K.E., Bartlett, E.P., "Heat Transfer and Ablation-Rate Correlations for Reentry Heatshield and Nosedip Applications, Acurex Corporation, Mountain View, CA., AIAA Paper No. 72-91, AIAA 10th Aerospace Science Meeting, San Diego, Calif., Jan. 17-19, 1972.
- F-12 Letter of July 30, 1987 from C.C. Chan of the Johns Hopkins University Applied Physics Laboratory, Laurel, Maryland, to J.A. Loffreda of Astro Space Division, General Electric Co., King of Prussia, PA (Doc. No. ATS-P-CCC-87-54, JCH-87-030).
- F-13 "Improved MHW Heat Source Aeroshell Project, Galileo Program, Task 12" Teledyne Energy Systems, Doc. No. TES-33009-43, May 1979.
- F-14 Matsui, K., Koyama, A., Vehara, K., "Fluid-Mechanical Effects on The Combustion Rate of Solid Carbon", Combustion and Flame, Vol. 25, 1975, Pg. 57.
- F-15 Summary of Mechanical and Thermal Property Information for AVCO's Fine Weave Pierced Fabric, John Hopkins University, Applied Physics Laboratory, K. R. Waeber, 7/16/80.

- F-16 PIR U-74-97-PW-A243, Characterization of 3D High Axial Carbon-Carbon Composites: Preliminary Data, A. Levine, J. Roetline, P. Quinn, 10/7/74.
- F-17 SAMSO-TR-79-6, Non Equilibrium Ablation of Carbon, P.G. Crowell, 11/15/78.

APPENDIX G  
SAFETY TEST PROGRAM SUMMARY AND RESULTS

G.1 INTRODUCTION

Prior to the Challenger accident in January 1986, the GPHS had been subjected to an extensive test program based on the environments and other conditions attendant to accidents involving the Space Shuttle/Centaur launch vehicle that were considered to be predominant at that time. The test program was initially structured to complement the development of the GPHS and to contribute to the safety evaluation for the Galileo (and Ulysses) mission. The original test program was subsequently expanded and modified as more data and information emerged concerning the definition of the accident environments and their effect on the GPHS-RTG.

Although the prior test program was extensive in scope, many of the tests were specific to the launch vehicle and to the mission configuration. The Challenger accident along with the attendant investigative findings and detailed accident analyses, the deletion of the Centaur as the upper stage, and the reconfiguration of the mission profile necessitated additional mission/vehicle-specific safety tests. In these tests, primary emphasis has been placed on accidents in which the propagated air shock from explosive events has become diminishingly small at the RTG location, and heavy walled SRB motor case fragments have become the major threat. Additional testing has also been performed to obtain basic response data on the heat source components and against which to calibrate the analytical models developed for determining the response of the GPHS under accident environment conditions that are outside the limited test ranges.

To provide an overall perspective of the safety test effort completed for the GPHS program, this appendix includes summaries of both segments of the test program: 1) the segment completed for the original missions for Galileo and Ulysses scheduled for launch in 1986, and 2) the subsequent segment, still in progress, that has been performed since the Challenger accident and that addresses the Galileo and Ulysses launches using the Shuttle/IUS vehicle.

Descriptions and results from each of these segments are presented in the following sections.

## G.2 PRE-1986 SAFETY TEST PROGRAM

The test series that were included in the GPHS safety test program for accident environments related to the Shuttle/Centaur launch vehicle prior to 1986 included the following:

- Shock Tube Tests
- Fragment/Projectile Tests
- Solid Propellant Fire Test
- Bare Clad Impact Tests
- Module Impact Tests

In addition to these tests, the results of the previously run Design Iteration Test series are included. These were conducted during the development program using flight quality hardware. A synopsis of each of the test series follows. Subsequent sections of this appendix present the detailed results of each of the tests.

### CST - Converter Segment Tests

In several of these tests, a GPHS module was sandwiched between two dummy modules and placed behind a flat plate simulation of the converter housing and thermopile. The tests covered shock overpressures between 429 and 2212 psi (2.96 and 15.3 MPa). In other tests, a cylindrical simulation of the converter longitudinal section was employed.

### Fragment/Projectile Tests

Aluminum bullets were fired into GPHS half-module targets with simulant (depleted  $\text{UO}_2$ ) fueled clads at velocities in the range from 319 to 555 m/s (1046 to 1820 fps). Titanium bullets were fired into bare fueled clads with simulant at velocities in the range from 423 to 684 m/s (1387 to 2244 fps). Other bullet tests were run on FWPf flat plate specimens (representative of



the aeroshell and GIS) to determine velocity attenuation. Another test was run in which an aluminum plate (representative of a Shuttle or Centaur tank section) was propelled edge-on into a GPHS module with simulant at a velocity of 915 m/s (3000 fps).

#### Solid Propellant Fire Test

A Fueled Clad (FC) and an impact assembly (GIS w/2 FCs) with  $UO_2$  simulant were exposed to a 10.5 minute fire from a cube of UTP-3001 solid propellant. Those GPHS members were initially in contact with the burning propellant.

#### BCI - Bare Clad Impact Tests

Fueled clads were fired against concrete, steel, and sand targets, impacting at velocities between 51.8 and 250 meters/second (170 and 820 feet/second)  $PuO_2$  fuel was used in the first five tests, designated BCI-1 and BCI-5. Subsequent tests were run to determine effects of test conditions on impact response.

#### SVT - Safety Verification Tests

GPHS modules were fired against concrete and steel targets impacting at velocities between 53.5 and 75.5 m/sec, at an approach angle from 0 to 90 degrees. This angle was measured between the flat target surface and the largest surface of the module, with the module rotated about an axis parallel to the GIS axis. For approach angles greater than 0 degrees, the GIS in the leading position is designated the "A" GIS, and the one in the trailing position, the "C" GIS. Targets of steel, concrete, and granite were used.

#### DIT - Design Iteration Tests

GPHS modules, in whole or one-half configurations, were tested to similar conditions as in the SVT tests. Impact velocities were from 50 to 60.5 m/sec, at approach angles from 0 to 30 degrees.

## G.2.1 SHOCK TUBE TEST SERIES

The Shock Tube Test series included Bare Module Tests (BMTs) and Converter Segment Tests (CSTs) with GPHS modules. This test series evaluated the effects of a shock wave hitting the RTGs resulting from an on-pad explosion of the Shuttle. In the bare module tests, the modules were oriented with the side surface normal to the direction of the shock wave propagation. A three module stack was arranged by placing dummy graphite blocks on opposite sides of the test module to simulate the stack of modules that would be present in the GPHS-RTG. The dummy blocks were equal in exterior configuration and size to the GPHS aeroshell and lightly clamped to it. The test modules were preheated to the temperature of the iridium clad at launch, 1090°C.

The GPHS modules were exposed to progressively higher static overpressures starting at 200 psi in an attempt to determine the failure thresholds for the various components--aeroshell, Graphite Impact Shell (GIS) and the iridium clad. The tests are reported in References G-1 through G-3. At the 200 psi overpressure with a 1.22 psi-sec static impulse, the module remained intact with the only damage being a chipped corner. This same module was then exposed to a second test at a static overpressure of 735 psi and an impulse (static) of 3.2 psi-sec. In this test, the aeroshell was broken on a broad face that had been oriented parallel to the blast direction. One impact shell (GIS) was broken, but the other was undamaged. The four fueled clads exhibited light overall deformation. Capsule IRG-118, which was in the broken GIS, had the greatest local deformation, but the inner and outer clad surfaces were found to be crack-free.

The third explosion test was conducted on a new GPHS module at a static overpressure of 1035 psi and an impulse of 3.75 psi-sec. All graphite components were stripped from the fueled clads. Fragments of the PWWF components (aeroshell and impact shells) were recovered throughout the vermiculite filling in the box. Three of the fueled clads were recovered near the rear wall of the catch box at the 10 foot locations. The fourth fueled clad penetrated the 0.75 inch plywood rear wall of the catch box and buried about four (4) inches into the dirt banked behind the catch box. This clad

had the greatest diametral strain, but no cracks were present in the iridium clad.

Subsequent to these Bare Module Tests (BMTs), the full scale simulated GPHS-RTG explosion test with a flight quality GPHS module plus graphite blocks to simulate the remainder of the heat source stack was conducted on the DIRECT COURSE event (see Reference G-4 for a complete description of the test and results). The test resulted in complete destruction of the RTG and the GPHS test module at a static overpressure in the range of 1300-1800 psi with an impulse of 4.4 to 4.8 psi-sec. An investigation of the significance and pertinence of this test to a launch abort situation was conducted by a special explosion working group convened by the Department of Energy. Analysis by the group revealed that close proximity of the simulated GPHS-RTG to the center of explosion of the ANFO (38 foot from the surface of the 36.5-foot-diameter sphere of explosive) produced significant influence of explosive combustion products on the effects of the blast on the GPHS. The force on a test article increases with both velocity and density of the explosion products passing the test article. Peak response stresses in the GPHS from DIRECT COURSE were predicted to have been up to 100 kilobars, more than enough to have produced the destructive consequences on the GPHS. Since the explosive combustion products of DIRECT COURSE are not applicable to liquid propellant explosions at separation distances appropriate to launch abort scenarios, the explosion working group predicted lower peak responses in launch abort scenarios than for DIRECT COURSE. The group also concluded that detonation of solid rocket propellant was not expected to occur. Considering those reasons together with the uncertainty associated with the DIRECT COURSE blast environment at the GPHS-RTG location, the explosion working group concluded that DIRECT COURSE consequences cannot be applied to launch abort scenarios (Reference G-5). A similar conclusion was reached by the NASA Management Review Panel on the safety of the Shuttle RTG missions (Reference G-6). Therefore, the results of this test have not been used in the FSAR safety evaluation.

However, the DIRECT COURSE test and the investigation which followed did provide valuable information in pointing out the need to consider the role of intervening structure, particularly the RTG converter shell, in increasing rather than decreasing the damage to be expected to the GPHS modules in an

explosion environment. As a result of the intervening structure or flyer plate issue, follow-on testing was deemed necessary to determine more precisely the effect of the converter shell on the structural response of the GPHS modules. A converter simulation test program was established in which simulated sections of the GPHS-RTG converter with GPHS heat source modules were tested. The details of these tests are presented in the following paragraphs.

The first tests in the Converter Segment Test (CST) series were conducted using a flat plate representation of a quarter section (circumferential direction) of the converter housing with thermopile. This is shown in the sketch on Figure G-1. The width of this quarter section (i.e., in the RTG longitudinal direction) spanned three module thicknesses. A dummy graphite module was placed on either side (i.e., against both large faces of the flight type GPHS module) of the test module to simulate the adjacent modules in the flight type converter. The arrangement of this configuration in the shock tube is shown by sketch on Figure G-2.

Because of the concern raised that this configuration might not be representative of the GPHS-RTG configuration, Fairchild Industries was tasked by DOE to conduct a detailed hydrocode analysis of the test configuration to determine whether or not it was appropriate. An additional concern was that the location of the test configuration in the upper part of the shock tube might also give different conditions than those desired. The results of this analysis were presented to the INSRP at a meeting in Valley Forge, Pennsylvania (General Electric Company Space Systems Division) on January 24, 1985 (Reference G-7). A capsule summary of those results is shown on Figure G-3. The dashed line indicated the predicted overpressure. This figure shows that the flat plate configuration with the angled wings (refer to Figure G-1), or mechanical corner stops referred to on the figure, and located at the top of the shock tube does adequately duplicate the impact velocity of the converter shell hitting the module (as seen in the cylindrical shell point shown for the 1070 psi test). Nevertheless, tests were subsequently planned and conducted in which full cylindrical sections of the converter shell with sections of a thermopile were tested.

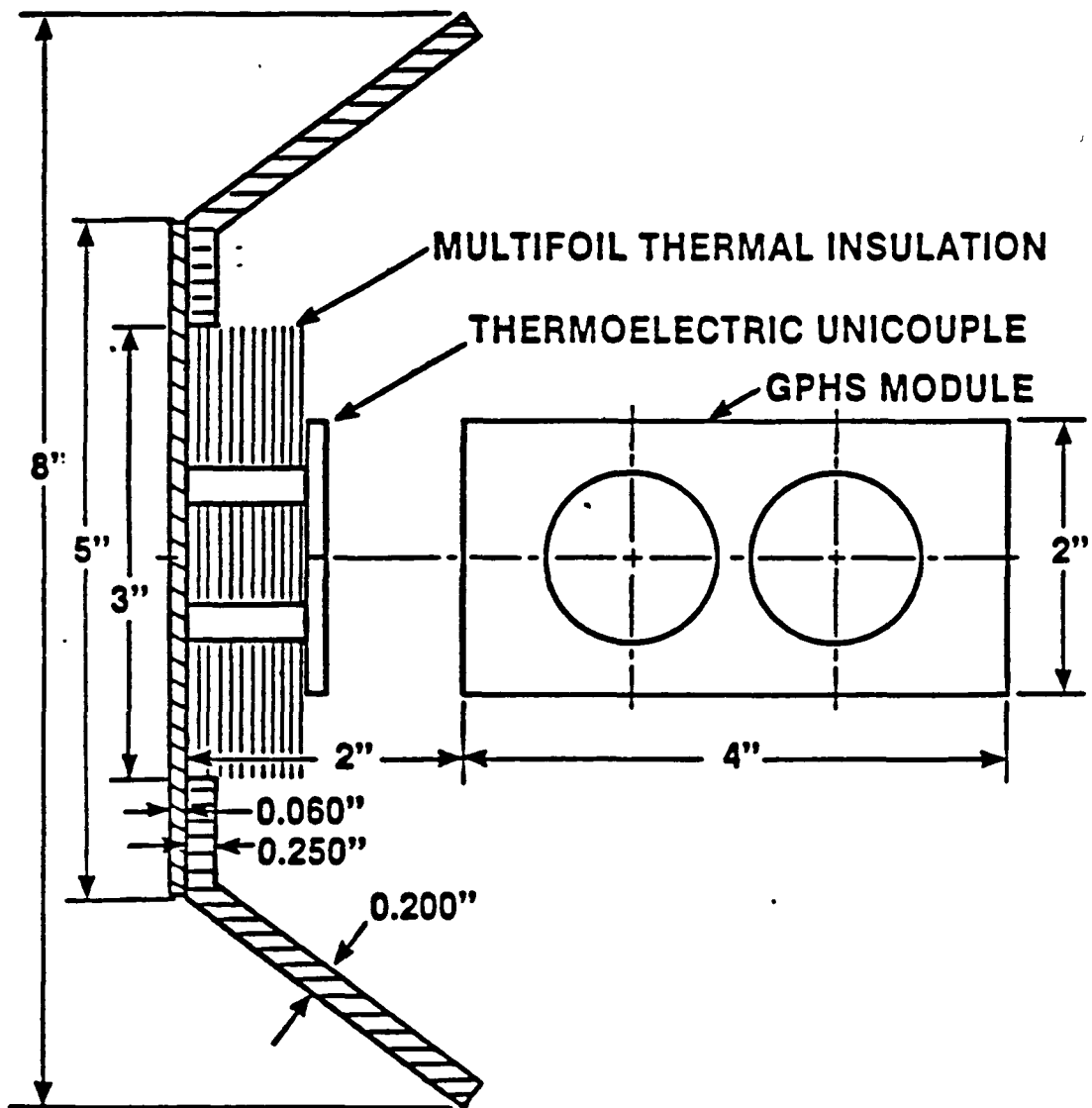


Figure G-1. Channel Test Configuration (Dimensions Approximate)

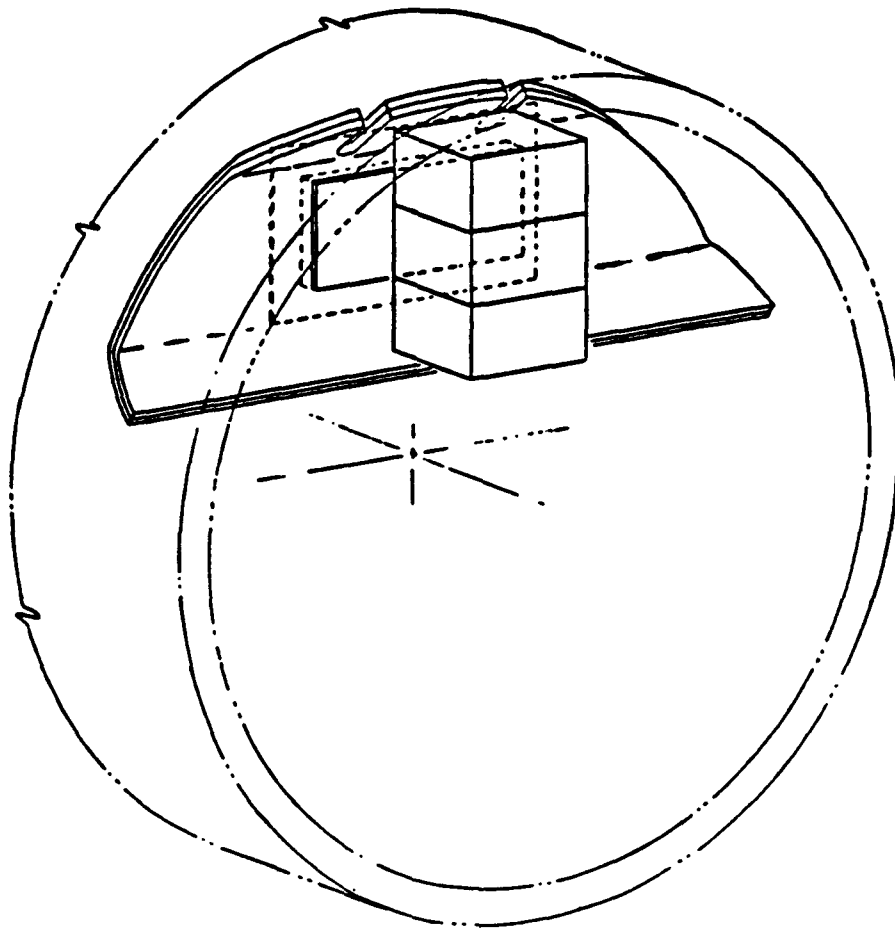


Figure G-2. Channel, Test Assembly, and Heat Source Stack Mounted in Shock Tube

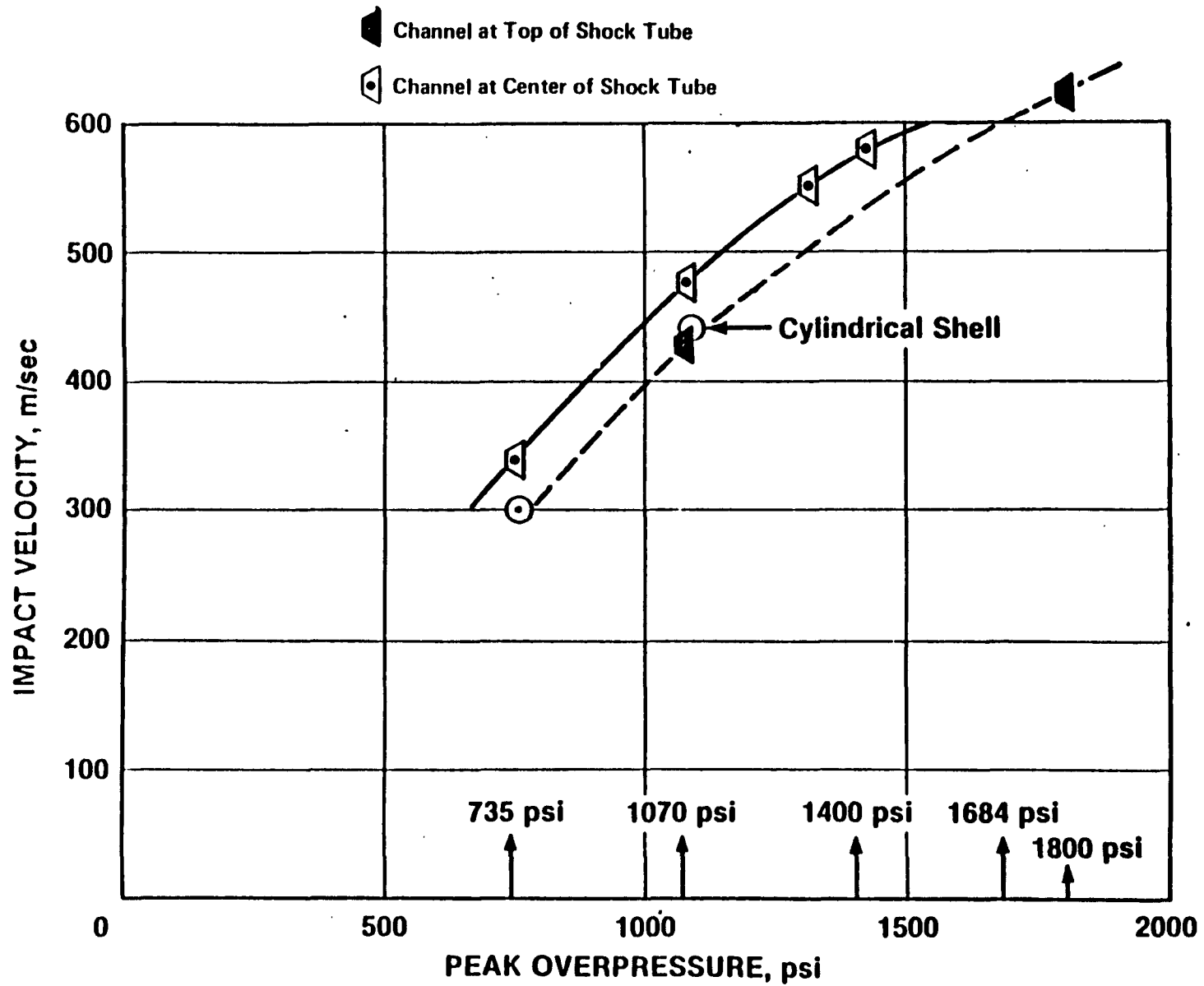


Figure G-3. Predicted Impact Velocity of Converter Shell vs. Test Overpressure

The simulated converter cylindrical section used in the first CST test is shown on Figure G-4. This section has a length of 14 inches representative of the middle section in one-half of the converter (i.e., between the end support and the mid-span support for the half stack of the GPHS modules). This configuration also used one flight type GPHS module and two dummy graphite modules. Unicouples and foil insulation were placed only in the upstream and downstream faces of the converter section. The remainder of the section was weighted to simulate the mission unicouples and insulation. Figure G-5 shows the converter test section located in the end of the shock tube.

In this test series, the GPHS module was preheated to a temperature which would result in an iridium clad temperature of 1090°C at the time of detonation. The arrangement for the heating furnace and test article in the shock tube is shown by the sketches shown on Figures G-6, G-7, and G-8. Figure G-6 shows the GPHS module stack lowered into the converter cylinder section. On Figure G-7, the module stack is shown raised upward into the heat-up furnace, and the final test position is shown on Figure G-8 which shows the door closed over the opening to the furnace and the lowering mechanism for the GPHS modules completely retracted. Testing was conducted over the range of 736 psi to 1815 psi in the CST series. Table G-1 shows the test conditions used for both the Bare Module Tests (BMTs) and the Converter Segment Tests (CSTs). The particle size distribution for the depleted UO<sub>2</sub> simulant used in the tests as determined from selected unbreached clads in tests CST-1 to CST-4 is shown in Tables G-2 and G-3. Table G-3 shows the distribution in the 10 micron and under range.

Flash X-ray equipment was used to try to catch the image of the fueled clads and module debris after exiting from the shock tube. The geometry of the X-ray set-up for test CST-5 is shown on Figure G-9. This is the first test in which the images were obtained successfully. Figure G-10 shows the coordinates of the clads and other pieces as determined from the X-ray film images. Based on this data, the average velocity of the clads was determined to be 463 m/sec for the maximum distances traveled as deduced from the film for this 1815 psi test.



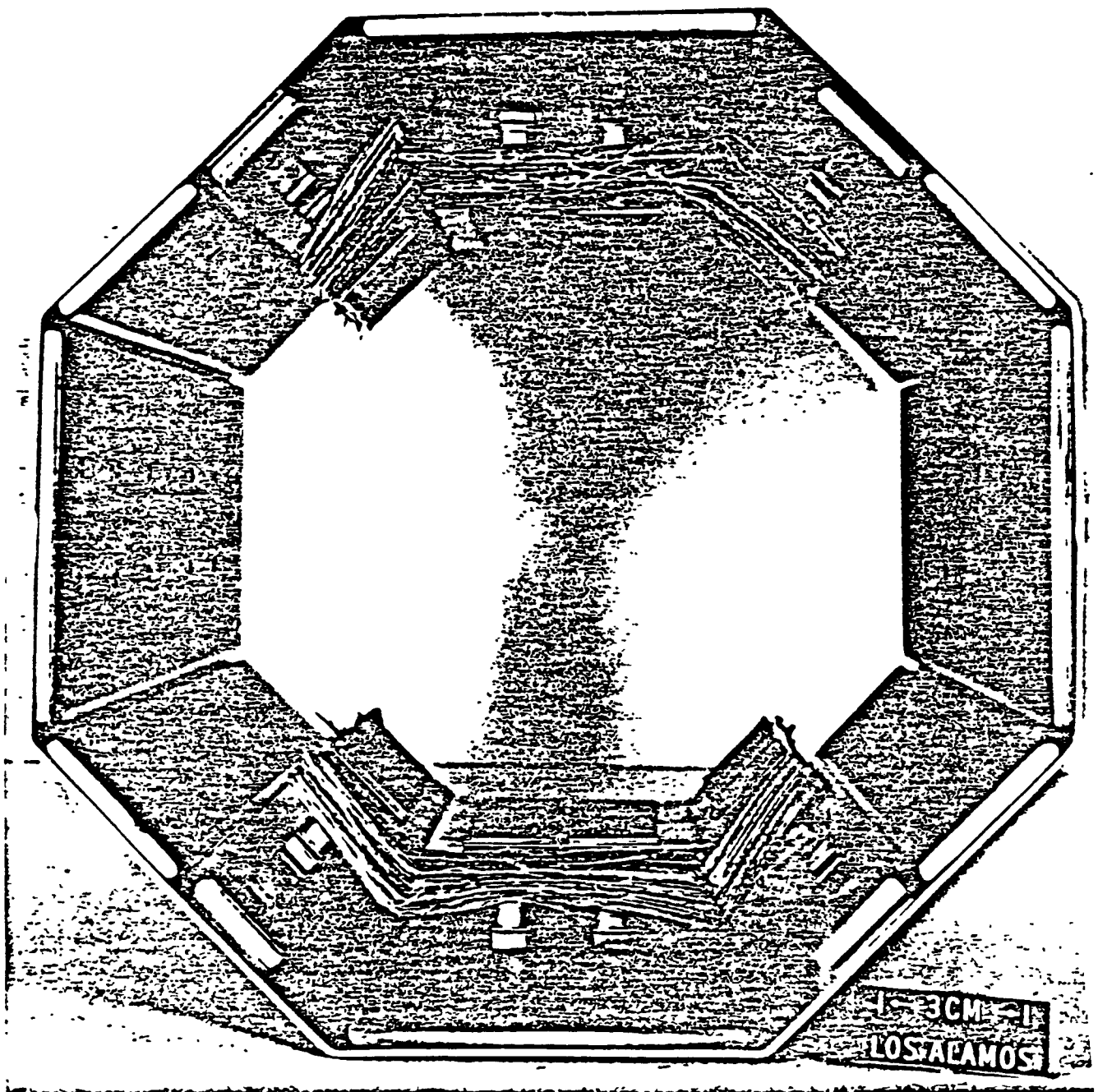


Figure G-4. Simulated Converter Ring Section for Shock Tube Test  
(Looking Downward - Long Axis)

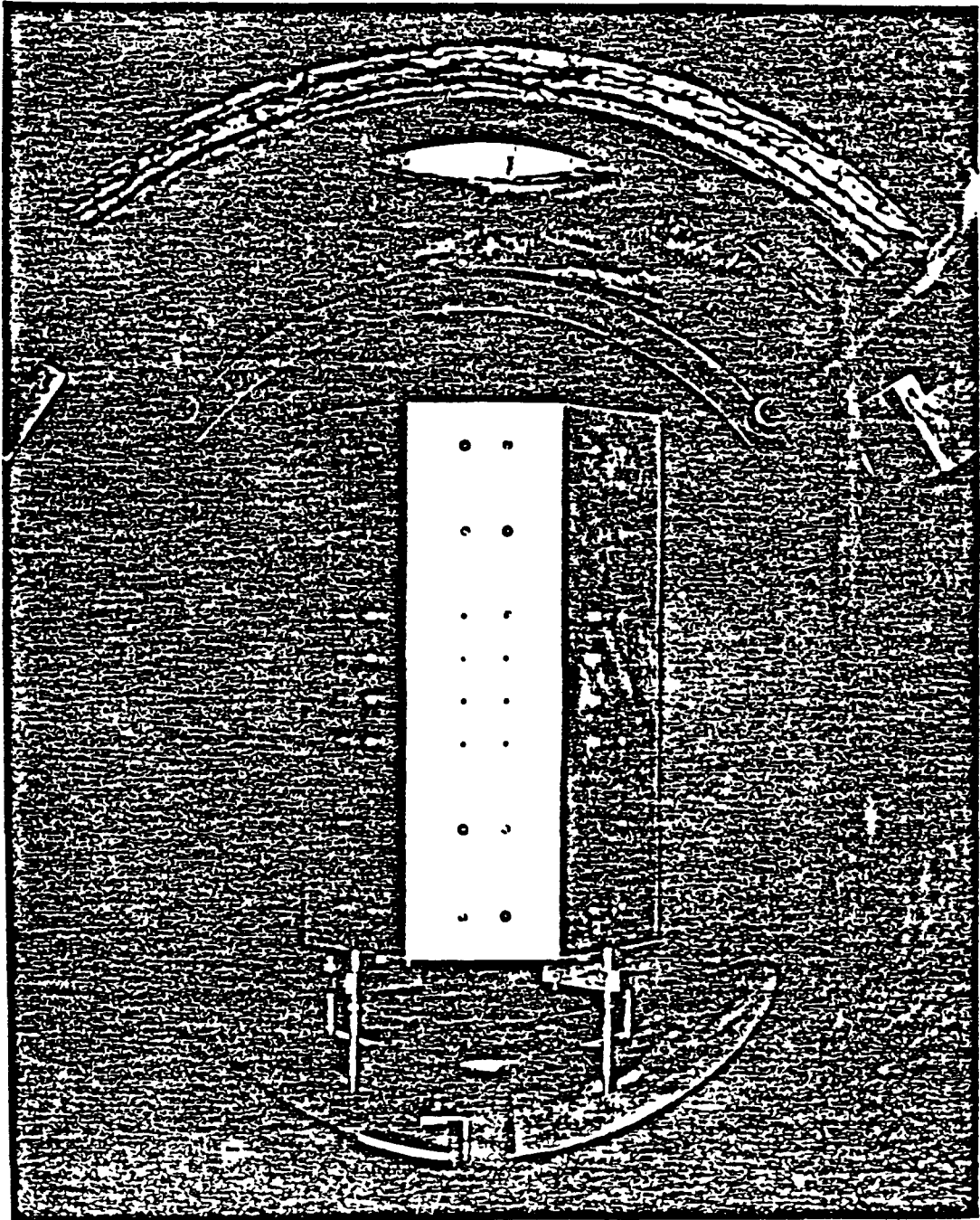


Figure G-5. Converter Ring Section Positioned in Shock Tube

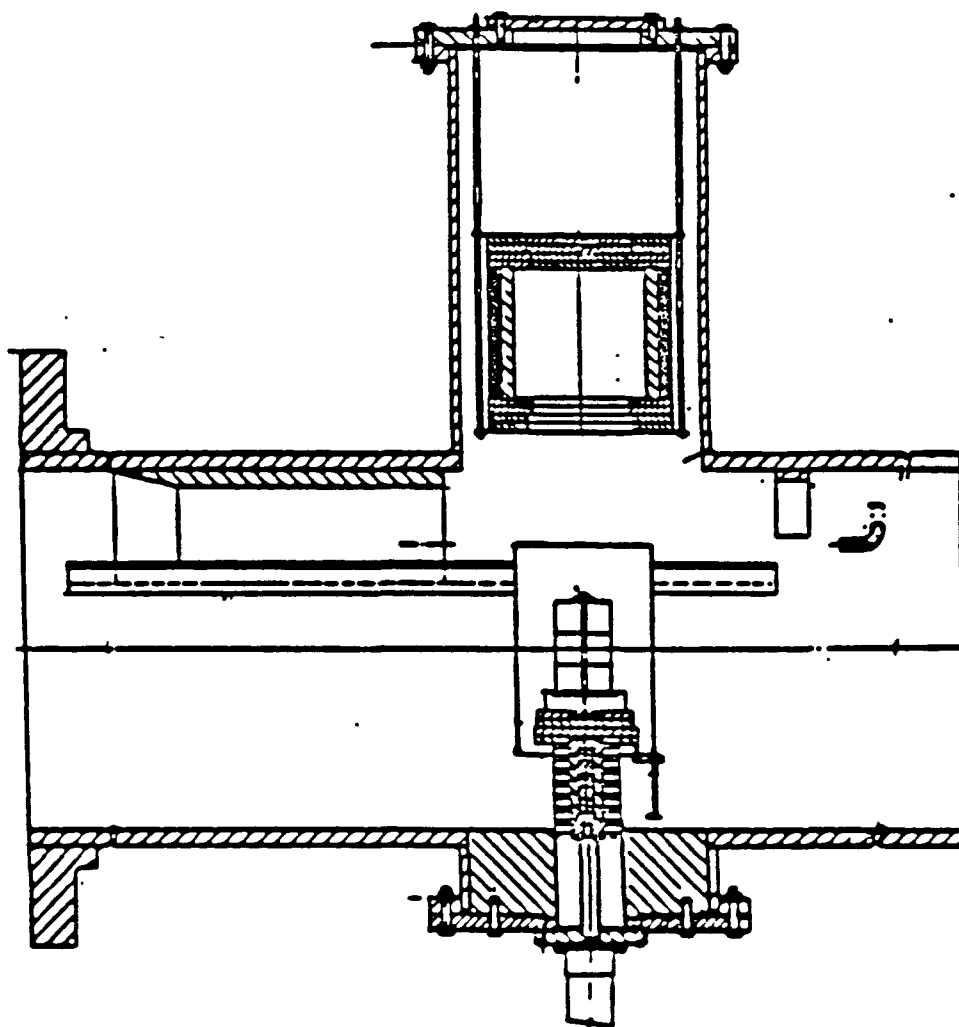


Figure G-6. RTG Overpressure Test Module Stack Lowered Into  
GE Converter Cylinder Section

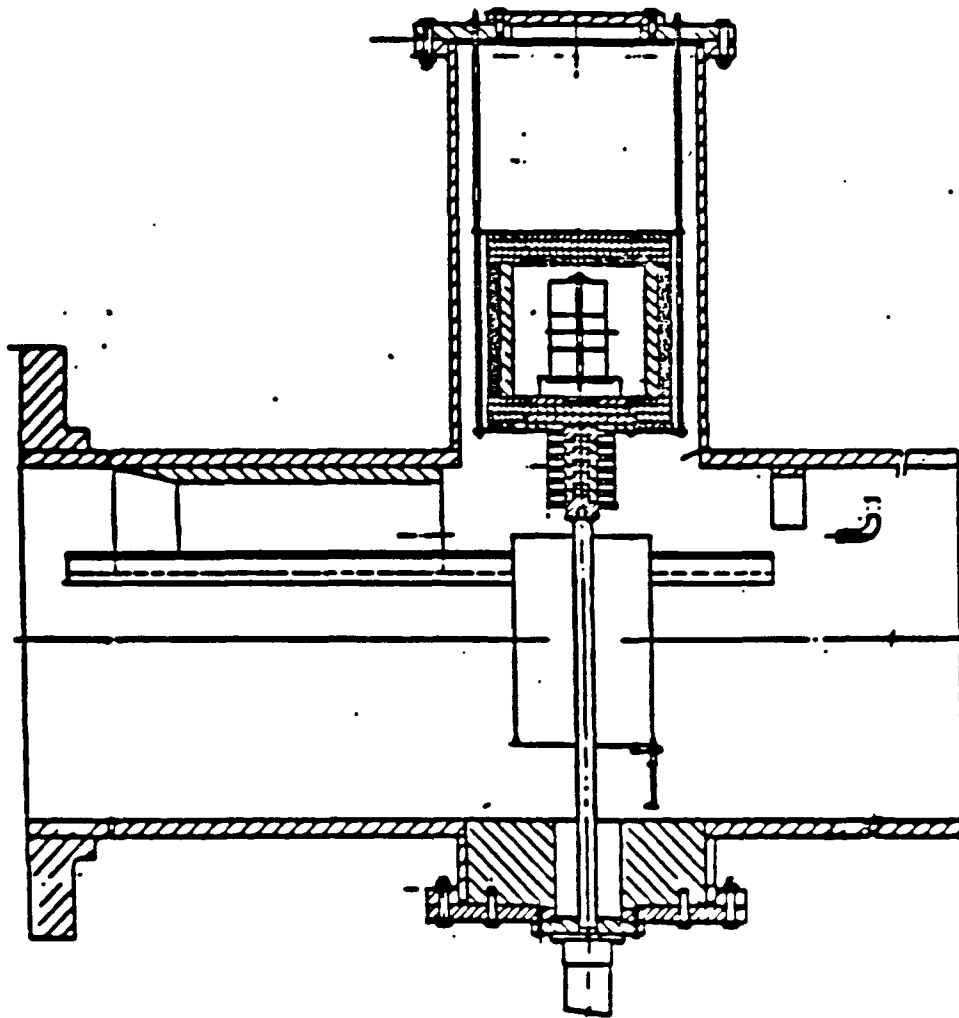


Figure G-7. RTG Overpressure Test Module Stack in Furnace  
Heat-Up Location Pretest Position

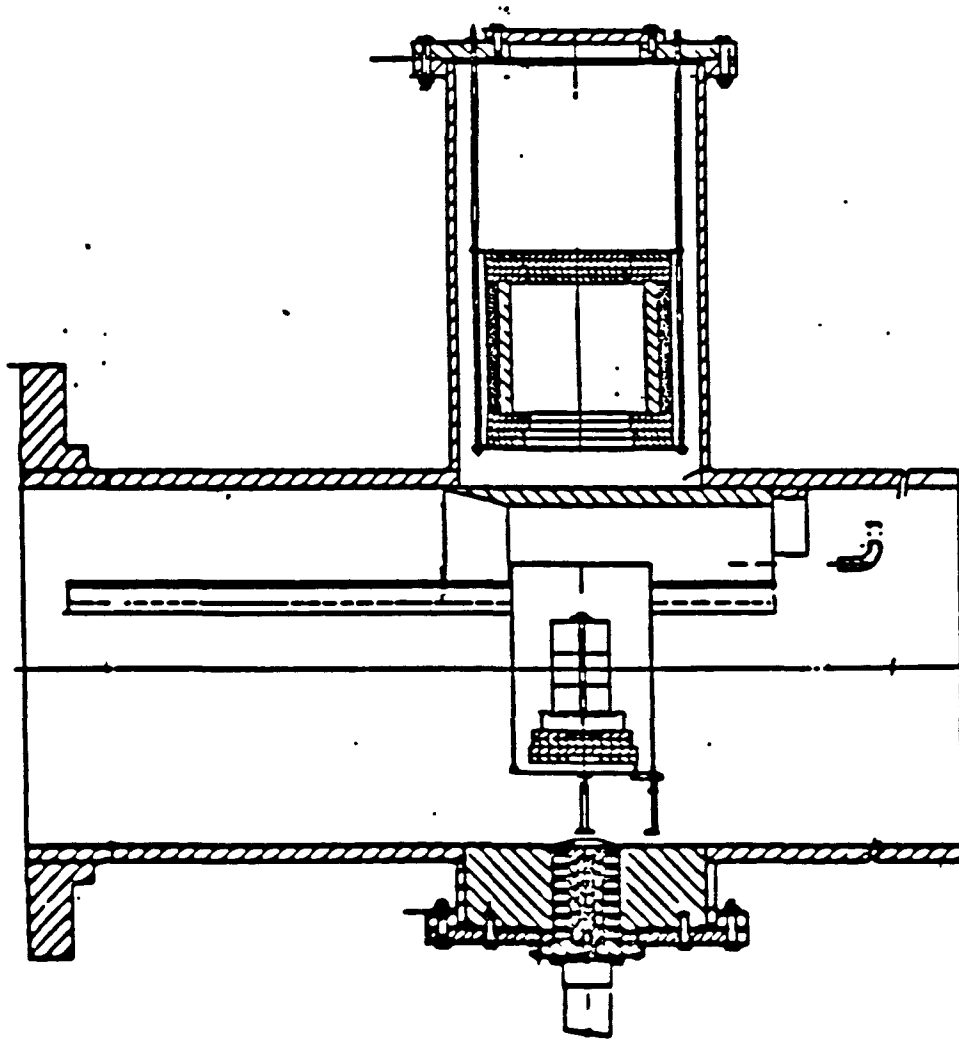


Figure G-8. RTG Overpressure Test Final Test Position at Shock Tube HE Charge Detonation

Table G-1. Explosion Overpressure Tests Shock Tube Conditions at the Test Position and the Tube Configuration at Test

TEST DESIGNATION	OVERPRESSURE PSI	IMPULSE PSI-S	TUBE LENGTH FEET	HE CHARGE LBS C-4
BARE MODULE TEST-1	200 ± 10	1.22 ± .2	66	13
BMT-2	735 ± 30	3.2 ± .4	66	60
BMT-3	1070 ± 50	3.75 ± .5	66	110
CST-1	736 ± 70	3.2 ± .4	58	60
(CONVERTER SEGMENT TEST)				
CST-2	1028 ± 100	3.75 ± .5	61	106
CST-3	1684 ± 300	4.2 ± .8	68	178.5
CST-4	1750 ± 175	4.0 ± .8	62	256.5
(RTG CYLINDER TEST)				
CST-5/RTG-1	1815 ± 180	4.0 ± .8	62	256.5
CST-6/RTG-2	1962 ± 190	3.36 ± .7	49	300
CST-7/RTG-3	1873 ± 360	3.4 ± .4	48	277
CST-8/RTG-4	429 ± 40	2.1 ± .4	64	27.5
CST-9/RTG-5	2212 ± 220	2.4 ± .5	48	205
				(COMP B)

Table G-2. Overpressure Tests Urania Particle Size Coarse Distributions

TEST DESIGNATION PARTICLE SIZE, MICRONS	CST-1 (CLAD 1)	CST-2 (IRG-12B)	CST-3 (L-12)	CST-4 (L-10)	CST-5 (L-24)	CST-7 (M-35)	CST-8 (IRG-133)	CST-9 (M-46)	CST-9 (M-40)
	WEIGHT FRACTION								
+ 6000	.6774	.9263	.3567	.8104	.8407	.8765	.9009	.1276	.3726
-6000 + 2000	.1836	.0437	.1905	.0580	.0701	.0818	.0556	.3027	.2450
-2000 + 841	.0850	.0179	.2794	.0572	.0481	.0242	.0274	.2912	.2076
- 841 + 420	.0308	.0058	.1094	.0394	.0212	.0075	.0067	.1374	.0968
- 420 + 177	.0141	.0033	.0379	.0228	.0121	.0045	.0044	.0825	.0500
- 177 + 125	.0024	.0007	.0140	.0037	.0023	.0011	.0011	.0177	.0081
- 125 + 74	.0024	.0009	.0054	.0037	.0023	.0011	.0013	.0179	.0069
- 74 + 44	.0012	.0004	.0022	.0018	.0009	.0007	.0008	.0080	.0033
- 44 + 30	.0009	.0003	.0015	.0010	.0008	.0005	.0006	.0052	.0029
- 30 + 20	.0004	.0001	.0007	.0005	.0002	.0004	.0003	.0019	.0013
- 20 + 10	.0005	.0002	.0007	.0006	.0003	.0006	.0003	.0026	.0017
- 10	.0013	.0004	.0017	.0010	.0008	.0010	.0006	.0053	.0039
* DEFORMATION RATIO (M/m)	1.069	1.059	1.080	1.094					

NOTE: DISTRIBUTIONS ARE CORRECTED FOR CHEMISTRY

\* M/m MAJOR TO MINOR DIAMETER RATIO POSTTEST

Table G-3. Overpressure Tests Urania Particle Size Fines Distributions

TEST DESIGNATION MAXIMUM SIZE IN THE RANGE MICRONS	CST-1 (CLAD 1)	CST-1 (IRG-128)	CST-3 (L-12)	CST-4 (L-10)	CST-5 (L-24)	CST-7 (M-35)	CST-8 (IRG-133)	CST-9 (M-46)	CST-9 (M-40)
	WEIGHT FRACTION								
1.00	0.000169	0.000023	0.000218	0.000141	0.000108	0.000076	0.000030	0.000140	0.000235
2.00	0.000152	0.000038	0.000327	0.000318	0.000126	0.000056	0.000091	0.000273	0.000578
3.00	0.000199	0.000052	0.000293	0.000149	0.000133	0.000084	0.000117	0.000896	0.000737
4.00	0.000263	0.000046	0.000066	0.000173	0.000085	0.000134	0.000101	0.001021	0.000536
5.00	0.000128	0.000059	0.000100	0.000095	0.000066	0.000146	0.000054	0.001056	0.000390
6.00	0.000101	0.000035	0.000123	0.000018	0.000069	0.000078	0.000044	0.000668	0.000248
7.00	0.000032	0.000035	0.000039	0.000000	0.000055	0.000069	0.000026	0.000327	0.000113
8.00	0.000096	0.000030	0.000234	0.000043	0.000027	0.000021	0.000052	0.000487	0.000337
9.00	0.000068	0.000011	0.000083	0.000000	0.000077	0.000088	0.000019	0.000174	0.000359
10.00	0.000093	0.000030	0.000228	0.000085	0.000053	0.000282	0.000076	0.000238	0.000329

NOTE: FINAL VALUES CORRECTED FOR CHEMISTRY



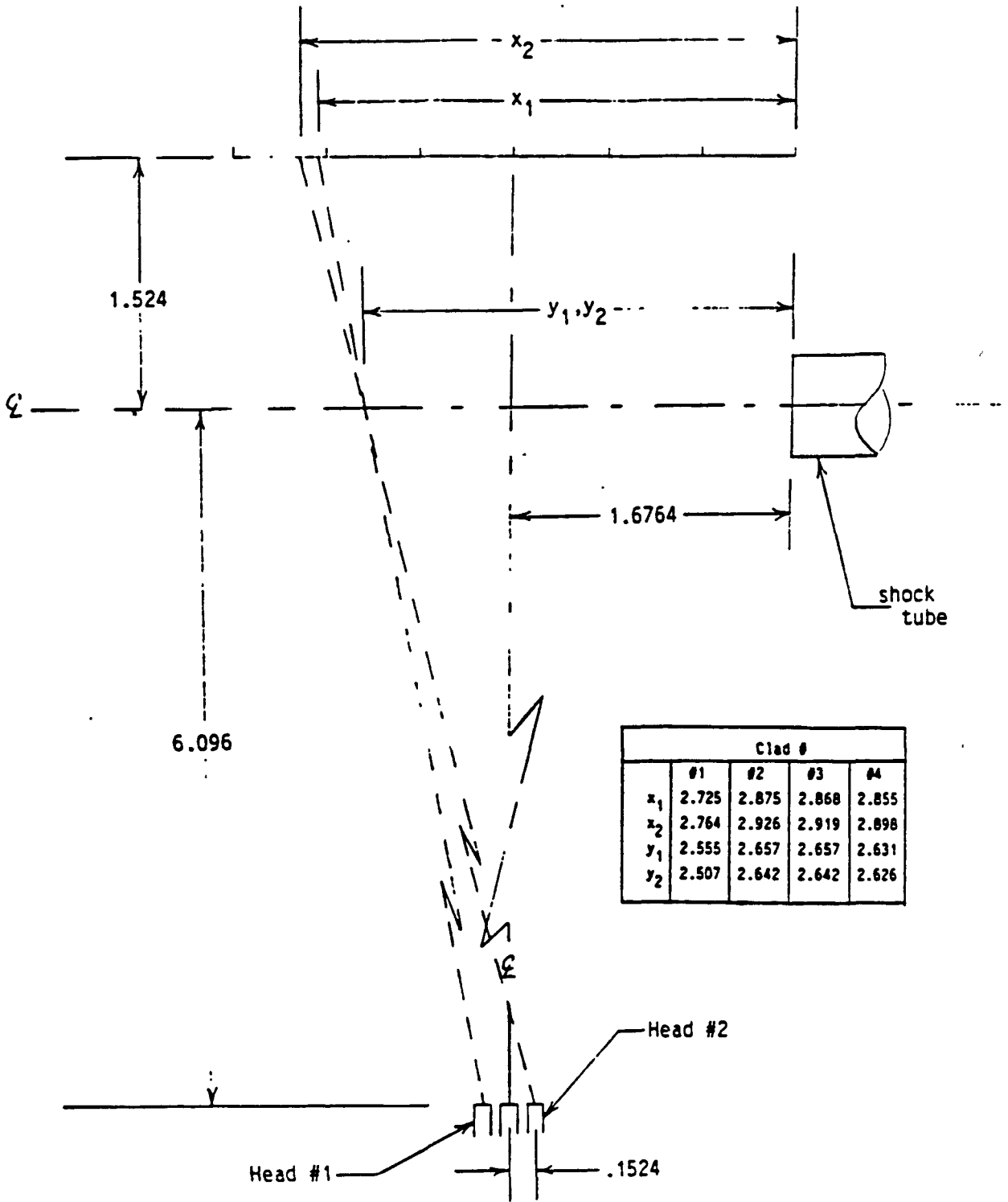


Figure G-9. X-ray Geometry

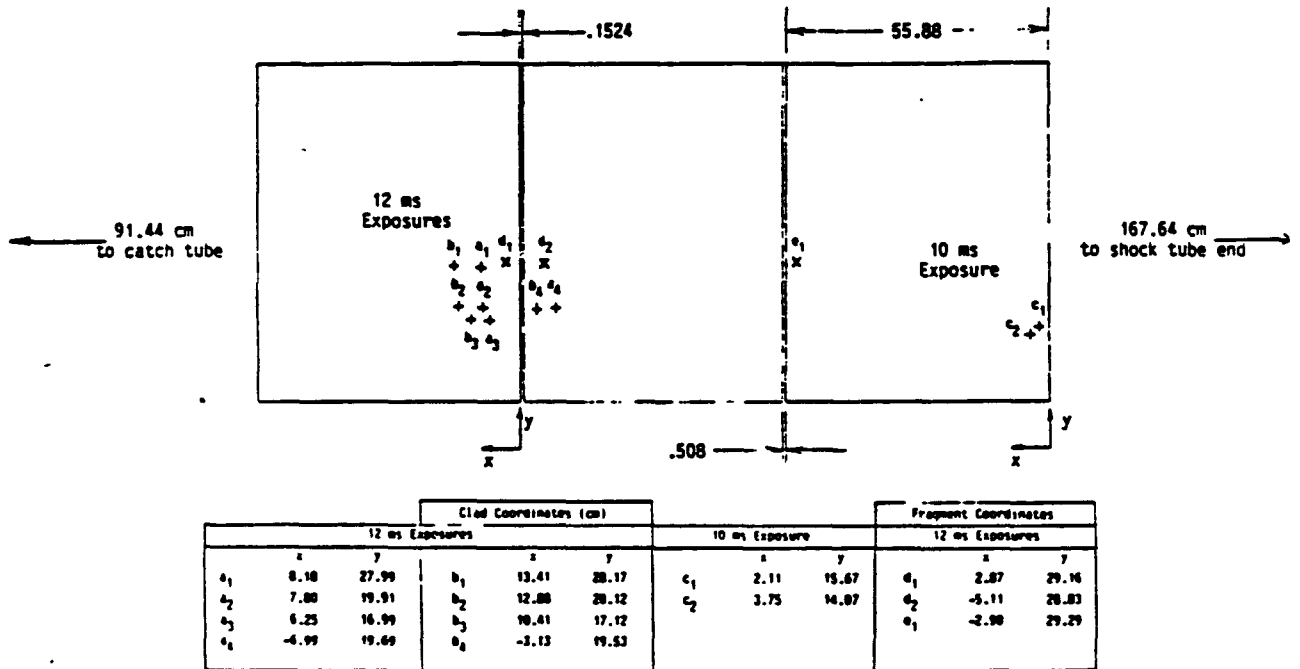


Figure G-10. CST-5 Clad Locations on X-ray Films

Test CST-6 was planned, first of all, to conduct a test at the 2000 psi level (which is the upper range of the explosion overpressure for any of the vehicle failure modes given in the Shuttle Data Book). In addition, the decision was made to use three (3) full modules (i.e., 12 fueled clads) in order to provide clads for subsequent sequential tests (e.g., explosion shock followed by fragment penetration or impact on surface media representative of the materials in the vicinity of the launch complex). In test CST-6, the retracting and lowering mechanism for translating the test module from heat-up furnace to the simulated converter cylindrical section evidently functioned properly, but the module stack became hung up within the furnace. Also, the sliding door that is supposed to cover the opening to the furnace section failed to close more than half-way. Consequently, the test module stack was ejected through the furnace section of the shock tube.

Following this test failure, the fueled clads were recovered and inspected to determine whether or not they could be used in other tests. Table G-4 summarizes the extent of clad damage. The first four clads were originally in the uppermost module in the furnace. Only clad M-15 was not recovered within a GIS. The last three clads were from the middle module; M-9 was the only clad recovered still in a GS. The remaining clads from CST-6 were either breached (3 clads) or not recovered (2 clads). As a result of the inspection, two clads (M-10 and M-9) were selected for flyer plate tests and two other clads (M-15 and M-12) were selected for bullet tests to be conducted. Except for M-11 and M-23 clads which experienced significant secondary impact environments, the diametral ratios for the CST-6 clads are smaller than those from the first three CST tests which were 1.069 for CST-1 (736 psi), 1.059 for CST-2 (1028 psi) and 1.08 for CST-3 (1684 psi).

A summary of the results from the BMT series and the first five tests in the CST series is given in Table G-5. None of the clads in these tests were breached as a result of the initial shock wave interaction, even in the CST configuration which included the effect of the converter housing and thermopile impacting the GPHS modules. The breach of the one clad in the CST-5/RTG-1 test is concluded to have been caused, subsequent to the clad existing the shock tube, by the impact of one of the rigid steel plates used in the converter section to simulate the missing weight of the thermopile

Table G-4. Fueled Clad Damage from CST-6

Clad ID	Diametral Ratio	X-Ray	Comment
M-11 (A-O)*	1.106	General fuel cracking	Extensive deformation two impact flats on cylindrical surface.
M-10 (A-B)	1.033	General fuel cracking	Similar to M-11 but much less deformation.
M-15 (C-O)	1.026	Fuel relatively intact	Little distortion of clad. Graphite impact print.
M-12 (C-B)	1.011	Fuel relatively intact	Clad nearly round. Graphite impact print.
M-9 (A-B)	1.048	Fuel separated by midplane crack gaps: FC and Fuel	Moderate deformation. Circumferential indentation at weld.
M-23 (C-B)	1.100	General cracking of fuel	Chemical stain. Severe deformation. Impact scrape.
M-26 (C-O)	1.015	General cracking of fuel	Chemical stain. Moderate deformation. Multiple impact.

\*Parentheses enclose GIS ident. (A or C) and location within GIS: Blind (B) or Open (O).

Table G-5. Overview Shock Tube Test Results

<u>TEST NO.</u>	<u>OVERPRESSURE,</u> <u>PSI</u>	<u>RESPONSE</u>	<u>R A N G E ,</u> <u>M/m<sup>(1)</sup></u>
<b>BARE MODULES</b>			
BMT-1	200	NO GRAPHITE DAMAGE	1.001-1.003
BMT-2	735	MINOR GRAPHITE DAMAGE	1.002-1.029
BMT-3	1035	STRIPPED GRAPHITE FREE FLIGHT FUEL CLADS	1.003-1.020
<b>CONVERTER SEGMENT</b>			
CST-1	736	FREE FLIGHT FUEL CLADS	1.022-1.069
CST-2	1028	FREE FLIGHT FUEL CLADS	1.018-1.059
CST-3	1684	FREE FLIGHT FUEL CLADS	1.052-1.113
CST-4 (RTG CYLINDER TEST )	1750	FREE FLIGHT FUEL CLADS	1.009-1.094
CST-5/RTG-1	1815	FREE FLIGHT FUEL CLADS	1.082-1.104 <sup>(2)</sup>
CST-6/RTG-2	1962	SEE TABLE C-4	
CST-7/RTG-3	1873	FREE FLIGHT FUEL CLADS	1.038 <sup>(3)</sup>
CST-8/RTG-4	429	RETAINED IN GRAPHITE	1.004-1.055
CST-9/RTG-5	2212	FREE FLIGHT FUEL CLADS	1.066 <sup>(4)</sup>

- (1) RATIO OF MAJOR DIAMETER, (M), TO MINOR DIAMETER, (m), POST TEST
- (2) 1 CLAD BREACHED, POST TEST (NOT MEASURED FOR OVALITY)
- (3) THREE CLADS RECOVERED INTEGRAL
- (4) ONE CLAD RECOVERED INTEGRAL

sections. This is based on the evidence that: 1) the clads appeared to be in their normal configuration in the X-ray film images, and 2) the appearance of the large steel plate fragment in those X-rays, plus 3) the determination that the velocity of that fragment exceeded that of the fueled clads by more than 100 meter per second. Also, the shape of the deformation in the vicinity of the breach is indicative of an object impacting into the clad.

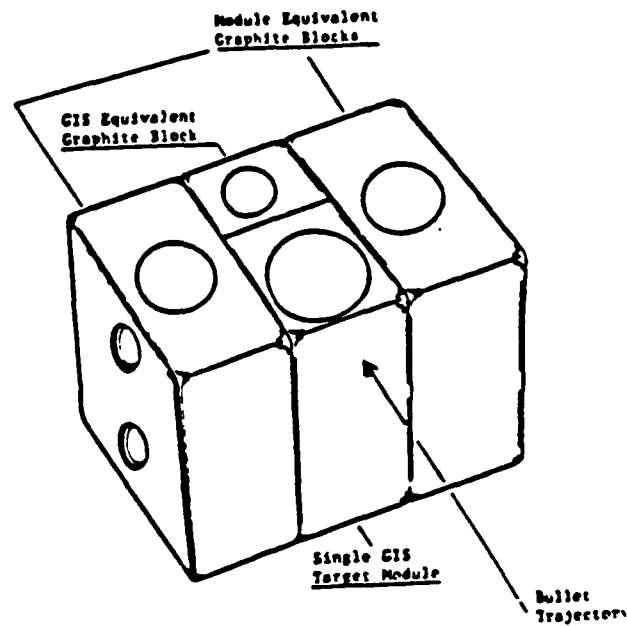
As can be seen from Table G-5, the module and GIS graphite was stripped from the clads for overpressure above 736 psi for tests with the converter segment, and at 1035 psi for bare modules. Minor graphite damage was sustained at 735 psi for the bare modules, and no damage occurred at 200 psi.

For completeness of data, the tables of results from the shock tube overpressure tests originally presented in the previous FSAR for Galileo and Ulysses, from which this section is taken, have been updated to include all tests conducted. However, the more detailed descriptions and pictures of the results are not included in this FSAR. These details can be obtained in Reference C-13.

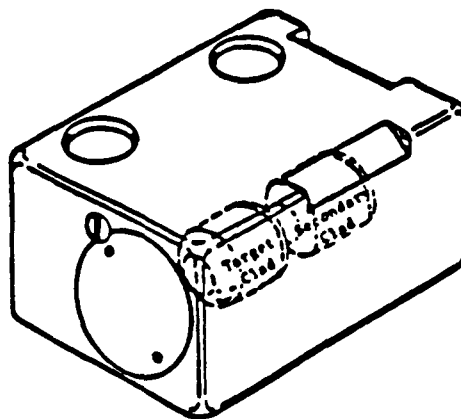
#### G.2.2 FRAGMENT/PROJECTILE TESTS

These tests were conducted to determine the interaction phenomena when fragments and projectiles resulting from a launch explosion impinge on the GPHS. Initial evaluations focused on behavior of the FWPf graphite used in the GPHS, followed by GPHS configuration tests.

Los Alamos National Laboratory conducted a series of tests in which 18 gram, 50-caliber, blunt nose aluminum alloy bullets were fired into GPHS half-module targets with simulant (depleted  $UO_2$ ) filled fueled clads. The iridium clads were preheated to their launch temperature of 1090°C. Figure G-11 shows the test module array for the test along with the target clad location, and the bullet configuration is shown on Figure G-12. The tests were conducted using a 50 caliber powder driven gun in which the powder loading can be adjusted to produce the desired velocity of the bullet. The detailed description of the tests and their results are given in Reference G-8. The results and conditions

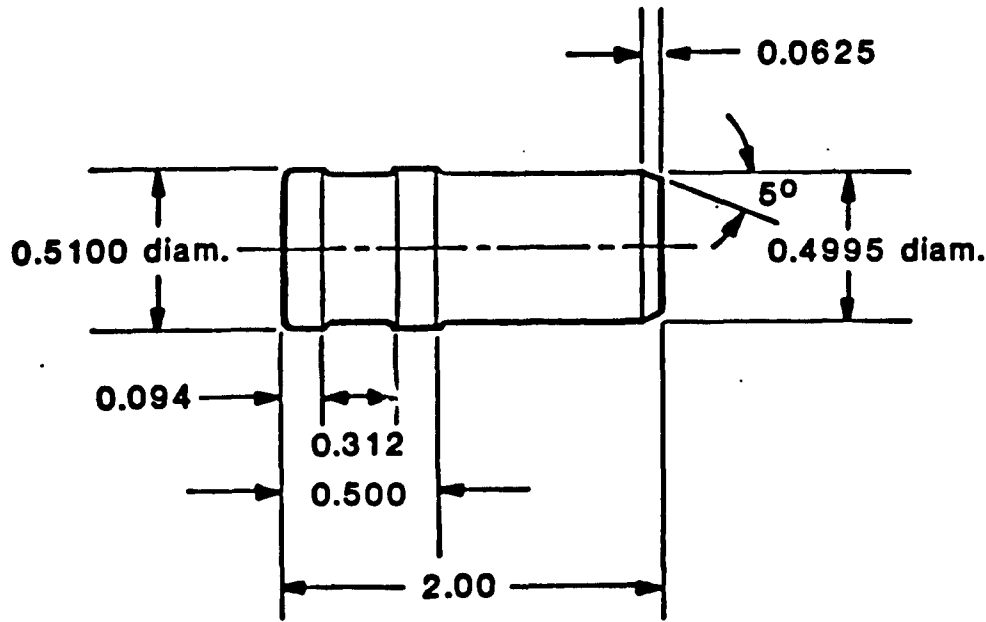


## SVT Bullet / Fragment Test Module Array

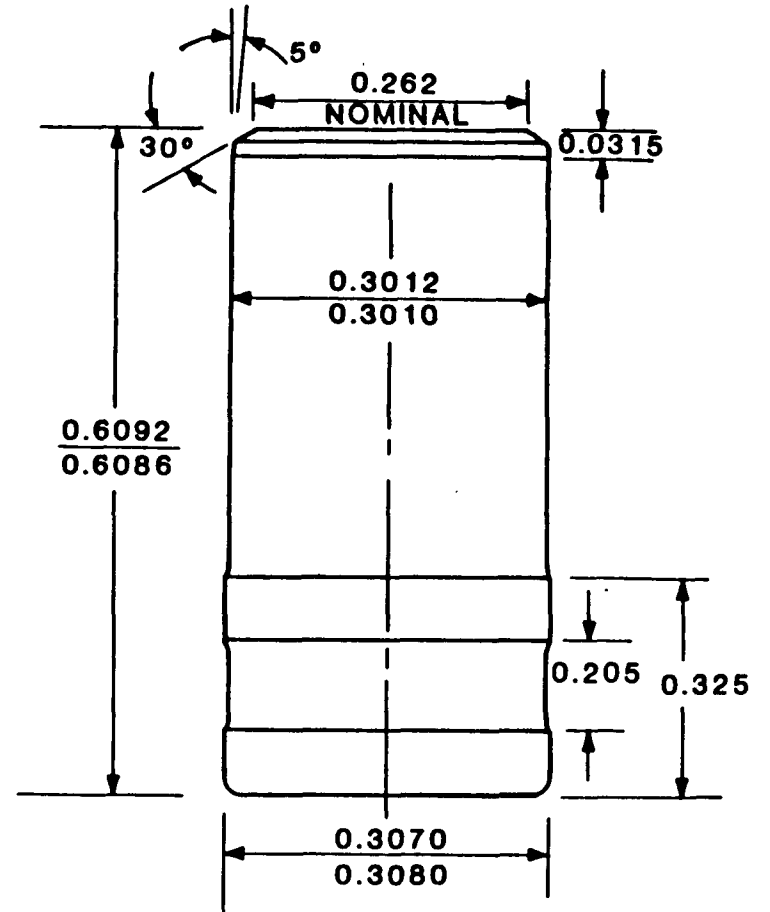


## Target Clad Location

Figure G-11. Bullet Test Configuration



MATERIAL: 2219 - T87 ALUMINUM



MATERIAL: TI-6AL-4VA

Figure G-12. Bullet Configurations



for each bullet test are summarized in Table G-6. These tests covered a velocity range from 319 m/s to 555 m/s. Table G-7 lists the post-test strains of the target clads.

Before the simulant fueled modules were tested, a series of bullet tests was conducted to determine the attenuating effects of the FWPF graphite. In these tests, 18 gram, 50 caliber aluminum alloy bullets were fired into FWPF graphite plates at velocities of 320, 633 and 900 m/s (1050, 2076 and 2952 fps, respectively). The thickness of each plate (0.191 inch) corresponds to the thinnest section of the GPHS module aeroshell in the small face. The test arrangement is shown on Figure G-13. The initial bullet velocity is determined by the  $V_1$  screens, and the residual velocity after passing through the graphite target, by the  $V_2$  screens. Table G-8 contains the results of these tests.

A second series of plate tests was conducted in which the target consisted of two FWPF graphite plates of thickness 0.191 inch and 0.166 inch simulating the GPHS aeroshell and the GIS wall thickness. The results of those tests are given in Table G-9.

Another series of tests was conducted by Los Alamos National Laboratory in which 3.25 gm (.007 lb), 30-caliber, blunt nose titanium alloy bullets were fired into bare fueled clads containing full simulant (depleted  $UO_2$ ). The clads were also preheated to the nominal launch temperature of 1090°C. The detailed description of these tests and their results are given in Reference G-9. The bullet configuration is shown on Figure G-12. Table G-6 presents the conditions and a summary of the results for each test. This series of tests covered a velocity range of 423 m/s to 684 m/s (1397 fps to 2244 fps).

Another test was conducted by LANL in the Sandia rocket sled test facility in which an aluminum plate fragment was propelled at a velocity of 3000 fps in an edge-on orientation into a GPHS module. The GPHS module was preheated to 1107°C and was oriented with the broad face parallel to the plane of the fragment. The fragment was 8 x 8 x 0.125 inches and was oriented so that the edge would impact on the centerline of the fueled clads. This fragment was defined as being representative of the upper range of velocity with

Table G-6. Summary of Bullet Impact Tests

FSAR  
APPENDIX G

## ALUMINUM BULLET TESTS - MODULES

Test No.	Temperature (°C)	Velocity (m/s)	Clad	Bullet Contact Area (mm <sup>2</sup> )	Remarks
1	1091	319	IRG-113	93	Bullet struck the clad $\approx 3.5$ mm above the weld centerline and did not fully penetrate the impact shell; no breach.
2	1030	415	IRG-119	288	Bullet struck the clad tangentially along the weld centerline; weld unzipped over 330°. Breaching crack measured 2.5 mm at widest point. Three small areas of Ir/Al reaction observed on clad surface.
3	1080	458	IRG-130	342	Bullet impacted $\approx 4.0$ mm above the weld centerline, remained in place, and melted. Brittle intermetallic formed at Ir/Al interface. Large hole (10 mm $\times$ 3.5 mm) observed on vent-cup impact face.
4	1060	460	IRG-111	266	Bullet struck the clad $\approx 6.0$ mm above the weld centerline; no breach. Two small areas of Ir/Al reaction observed on clad surface.
5	1120	555	IRG-112	169	Bullet impacted approximately 9.0 mm above the weld centerline; hairline crack on blind-cup radius ( $\approx 6.0$ mm in length) and along weld centerline ( $\approx 4.0$ mm in length). No evidence of Ir/Al reaction.

## TITANIUM BULLET TESTS - FUELED CLADS

Test	Target	Temp. (°C)	Bullet Velocity (m/s)	Results
TiB-Eng	Virgin EUO <sup>a</sup> Clad	1095	446	Bullet struck the clad approximately 6.0 mm above the weld centerline (vented cup). The impact produced several small, breaching cracks (total crack area = 25.25 mm <sup>2</sup> ).
TiB-1	CST-6 Clad <sup>b</sup>	1085	423	Bullet struck the clad approximately 6.0 mm below weld centerline (blind cup). The impact produced several small cracks within the bullet contact area, two of which breached the clad (total crack area = 1.3 mm <sup>2</sup> ). After impact the bullet was deflected away from the clad.
TiB-2	CST-6 Clad <sup>b</sup>	1110	684	Bullet struck the clad approximately 7.0 mm above the weld centerline (vent cup) and was deflected. The clad breached, with the vent cup radius of the impact face opened (total crack area = 215 mm <sup>2</sup> ); 86.5% of the uranium fuel simulant remained within the clad.

<sup>a</sup>The EUO clad used in TiB-Eng was fabricated from two blind cups and was vented at Los Alamos by drilling a 1/16-in. hole through one cup.

<sup>b</sup>Both clads were recovered bare, after the CST-6 test.

Table G-7. Post-Impact Capsule Strains

Capsule No.	Bullet Test	Impact Velocity (m/s)	Vent Cup		Weld		Blind Cup		Max. Axial Strain (%)
			min	max	min	max	min	max	
IRG-113	1	319	0	0	-1.0	0	-3.4	0	0
IRG-119	2	415	-1.0	0	-3.0	+1.7	0	0	+10.7*
IRG-130	3	458	-3.0	+2.0	-13.1	+6.0	-12.8	+4.4	+4.0
IRG-111	4	460	0	0	+2.0	+2.3	-11.1	+3.4	+4.0
IRG-112	5	555	0	0	-1.0	+2.3	-20.2	+2.3	+2.7

\*The IRG-119 closure weld unzipped over 330° of the clad circumference.

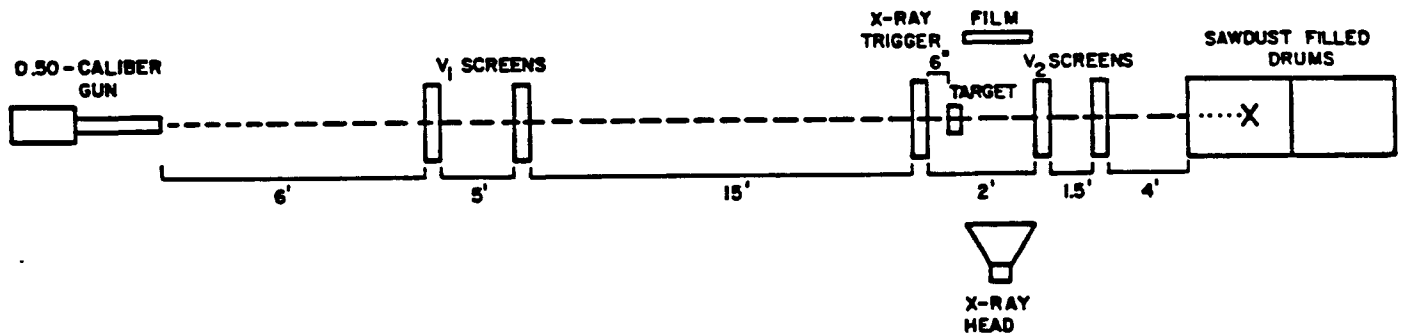


Figure G-13. SVT Graphite Stopping Power Test Setup

Table G-8. Attenuation of Bullet Velocity in FWPF Graphite

Bullet Velocity (m/s)		Velocity Decrement		Bullet Deformation		
Initial	Exit	(m/s)	(%)	Orig. Diam.	Max. Final Diam.	% Change
320	288	32	10.0	0.500	0.518	3.6
633	580	53	8.4	0.500	0.590	18.0
900	832	68	7.5	0.500	0.638	27.6

\*As determined from the trajectories of 18-g .50-caliber aluminum-alloy bullets fired through a 4.86-mm FWPF graphite plate.

Table G-9. Summaries of the SVT FWPf Graphite Stopping Power Tests

<u>SUMMARIES OF THE SVT FWPf GRAPHITE STOPPING POWER TESTS</u>				
<u>SUMMARIES OF THE SVT FWPf GRAPHITE STOPPING POWER TESTS*</u>				
(All velocities are given in m/s)				
<u>Bullet Velocity</u>		<u><math>\Delta V</math></u>	<u><math>\Delta V_e</math></u>	<u>Velocity Drop Due to Graphite</u> ( <u><math>\Delta V - V_e</math></u> )
<u>Initial</u>	<u>Final</u>			
960	832	128	35	93
600	501	99	23	76
357	258	99	3	96

$\Delta V = V_{\text{initial}} - V_{\text{final}}$

$\Delta V_e =$  Velocity drop (without target in place) of a projectile traveling the 17' between velocity screens

\*The graphite target used for these tests consisted of two FWPf graphite plates (4.86 and 4.23 mm thick) which simulated the GPHS aeroshell and GIS wall thicknesses.

<u>BULLET DEFORMATION IN THE SVT FWPf GRAPHITE STOPPING POWER TESTS</u>			
<u>Bullet Velocity</u> (m/s)	<u>Bullet Deformation*</u>		
	<u>Orig. Diam.</u>	<u>Max. Final Diam.</u>	<u>% Change</u>
960	0.500	0.680	36.0
600	0.500	0.560	12.0
357	0.500	0.510	2.0

\*Bullet dimensions are given in inches.

corresponding size that could be generated in an upper range explosion of the Space Shuttle in a launch abort accident, such as caused by a LOX tank overpressurization failure. This test resulted in the fragment completely slicing through all four (4) fueled clads. (Note: In the test, the plate fragment did not release as planned from the rocket sled, so the module may have been hit by the fragment while it was still attached to the sled fixture.) The aluminum plate was held to the sled by a fixture designed to release it prior to impact to provide a free flying fragment with an edge-on orientation. The test was designed to hold the aluminum plate to the rocket sled until the last possible moment before impact in order to maintain the edge-on orientation. If the plate was released too early, tests showed that it would rotate so that it was no longer in the edge-on position.

### G.2.3 SOLID PROPELLANT FIRE TEST

A test was conducted at Los Alamos in which GPHS components were exposed to a 10.5 minute fire from a 3 foot cube of TUP-3001 solid propellant (Reference G-9) which is essentially the same as the Shuttle SRB propellant. A bare GPHS fueled clad with  $UO_2$  fueled simulant was preheated to  $1091^{\circ}C$ , representing the launch temperature, and dropped next to one vertical face of the propellant cube immediately before it was ignited. Also, an impact assembly consisting of two fueled clads with  $UO_2$  simulant in a GIS was preheated to  $1091^{\circ}C$  and exposed in the same manner to the propellant cube as was the bare fueled clad.

A glassy deposit that formed on the exterior of the iridium clad of the bare fueled clad resulted in erosion of approximately 15% of the shell thickness, but the shell was not breached nor otherwise affected, and there was no damage to the interior. The test of the impact assembly resulted also in roughly a 20% reduction in the thickness of the graphite shell wall nearest the burning solid propellant, but there was no apparent damage to either iridium clad. Thus, exposure of either intact fueled clads or GIS with fueled clads to a long duration, single proximity, solid-propellant fire would not be expected to result in a breach of the clad and release of the plutonia to the environment. While there was no self-heating produced as in the plutonia

fueled flight capsules, this would not be expected to raise the resulting temperature by an appreciable extent over the duration of the fire.

#### G.2.4 BARE CLAD IMPACT TESTS

The Bare Clad Impact (BCI) tests were conducted by Los Alamos to determine the response of the GPHS bare Fueled Clads (FC) as the result of their striking different surface media. These tests have been conducted to reflect conditions that can potentially occur as the result of a launch pad or early ascent explosion involving the Shuttle/Centaur vehicle. If the graphite members of the GPHS module are stripped off by an explosion, the bare clads will then impact on the surfaces in the vicinity of the launch pad over a wide range of velocities.

The first four tests (BCI-1 through BCI-4) were conducted to determine the response of the FCs against concrete as a function of velocity. This surface is the highest probability hard surface around the launch pad (sand is the most probable of all surfaces). The maximum velocity tested in these four tests was 90 m/sec which is the upper limit for the LANL contained impact facility in which live  $\text{PuO}_2$  fuel can be tested. The fifth test (BCI-5) was conducted on steel as a comparison with the concrete tests. Also BCI-5 provided a comparison with the SVT full module impacts, the majority of which have been conducted at the module terminal velocity against steel (refer to Section G.2.5).

The results of the first five bare clad tests are summarized in Table G-10. Figures G-14 through G-18 show photographs of the clads post-test. Based on these results, the threshold for incipient failure of the bare FC on concrete is around 65 m/sec. That for steel is seen to be around 54 m/sec. These values are used in the accident evaluation in Section 3.0 of this AMD. Notice from Table G-10 that the first test, BCI-1, performed at 76 m/sec, deviates significantly from the trend of failure magnitude and fuel release quantity from the other three tests. In the post-test examination of the BCI-1 clad, LANL discovered that a reaction had occurred apparently between the iridium clad and the tantalum thin walled can used to encapsulate the FC for the test. This reaction probably occurred during the preheat operation used to

Table G-10. Bare Fueled Clad Impact Tests (Pre-1986 Test Program)

Pre-test Aging : 200 hours @ 1287°C in vacuum.  
 Configuration : Bare FC in welded Ta can w/2 psia. Helium (amb. T).  
 Orientation : FC axis parallel to target face.  
 Impact Temp. : 1091°C (clad).

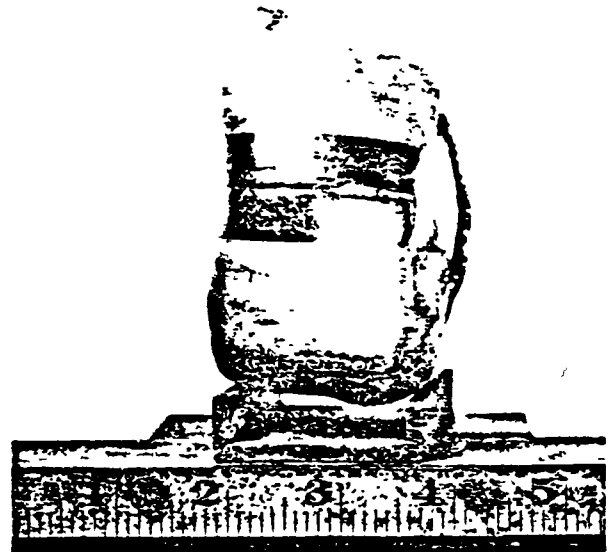
FC No.	NDE Value	Vel. m/s	Gross Deformation			Failures	Pu Release-gms.	
			Diam.-%	Height-%	Length-%		Total	<10 μm.
BCI-2 : KSC Concrete Target								
164	1.4	53.7	+ 9.6	-10.2	+11.2	None	0	0
BCI-3 : KSC Concrete Target								
351	2.1	64.77	+12.3	-10.3	+15.2	(a) 2 Trans:** on impact face	0.0008	0.0001
BCI-1 : KSC Concrete Target								
209	2.0	76.24	+31.7	-23.2	+27.0	(a) Severe on back side (b) 2 Trans. on impact face (c) weld	14.2076	0.2215
BCI-4 : KSC Concrete Target								
353	2.6	90.45	+24.4	-19.9	+23.6	(a) Severe on back side (b) 2 Trans. on impact face	12.9*	0.1553
BCI-5 : Steel Target								
346	7.5	53.19	+14.5	-14.2	+14.2	(a) 2 Trans. on impact face	0.0064	0.0023

\* Includes an estimated less than 1.0 grams of tungsten foil particles.

\*\* Transverse cracks.



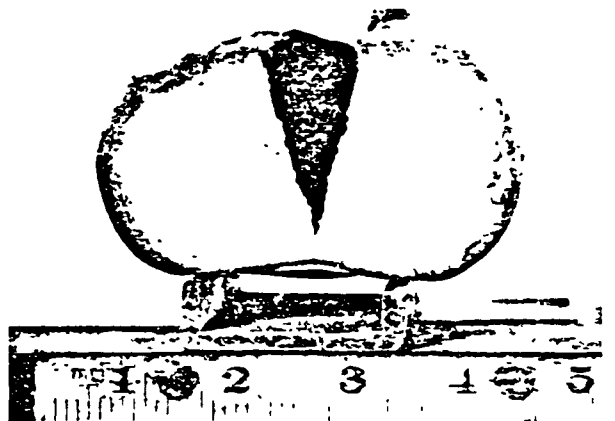
(a)



(b)



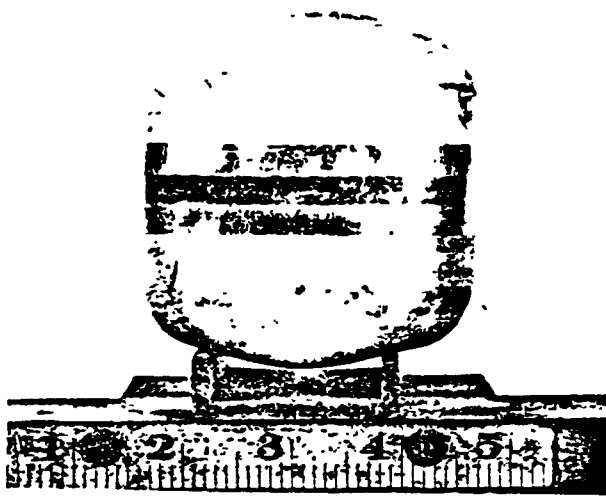
(c)



(d)

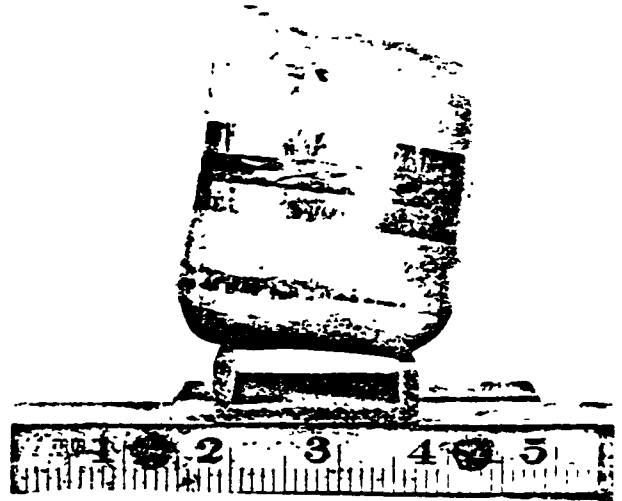
Figure G-14. Photographs of the Impacted Fueled-Clad, FC-209, BCI-1  
(a) Impact Face, (b) Side Profile, (c) Back Side  
(d) Blind End Profile. All Approximately 1.5X





BCI-2

(a)



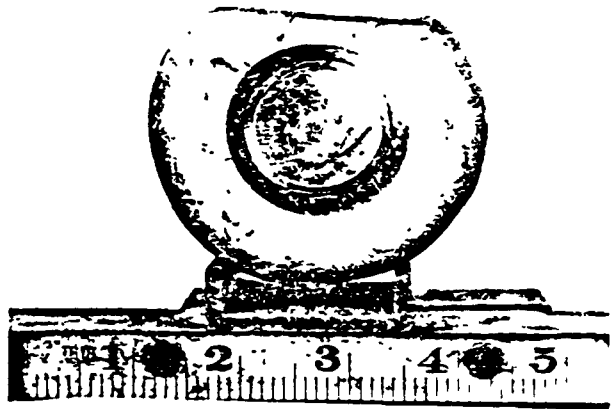
BCI-2

(b)



BCI-2

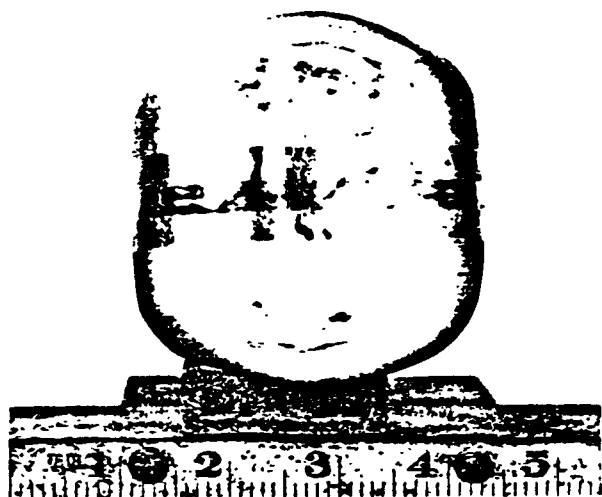
(c)



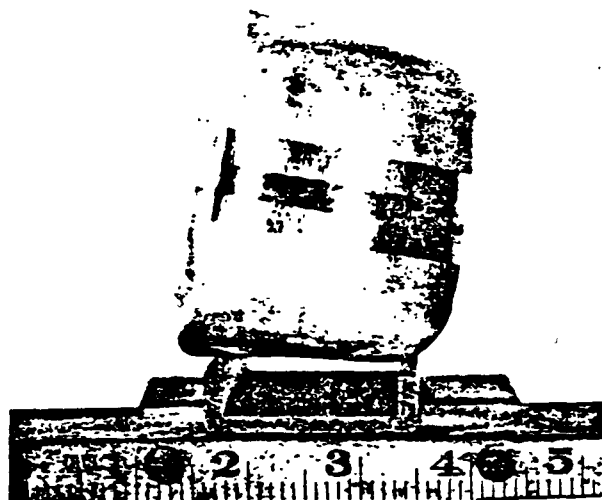
BCI-2

(d)

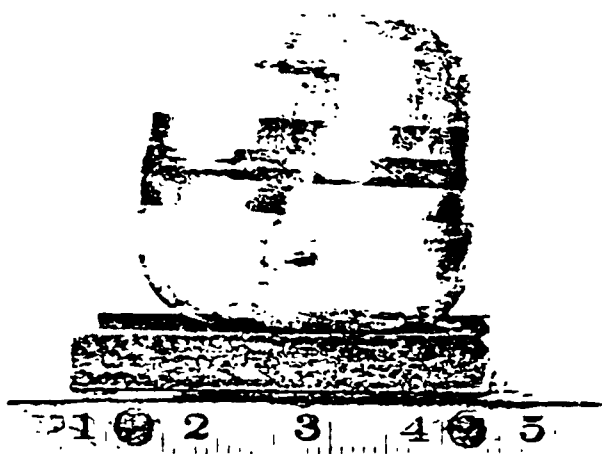
Figure G-15. Photographs of the Impacted Fueled-Clad, FC-164, BCI-2  
(a) Impact Face, (b) Side Profile, (c) Back Side, (d) Vent End View



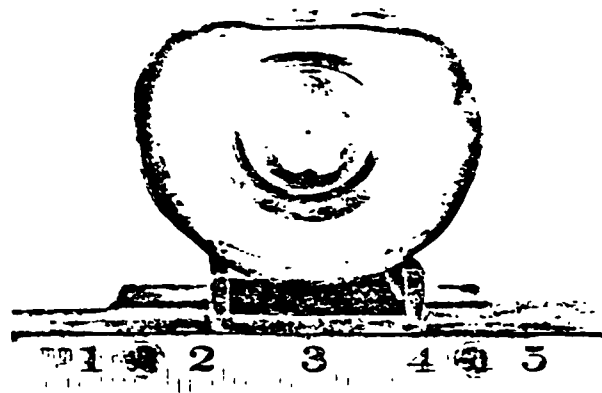
(a)



(b)



(c)



(d)

Figure G-16. Photographs of the Impacted Fueled-Clad, FC-351, BCI-3

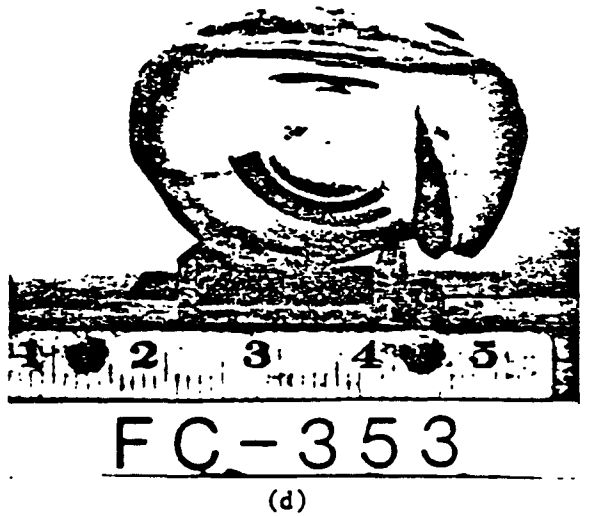
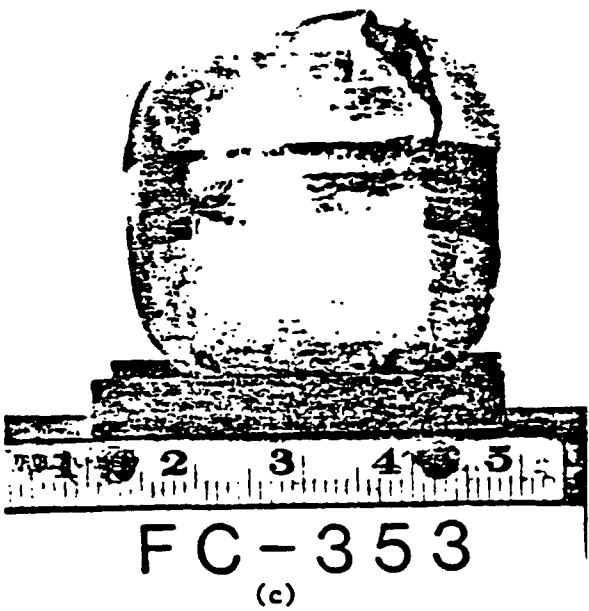
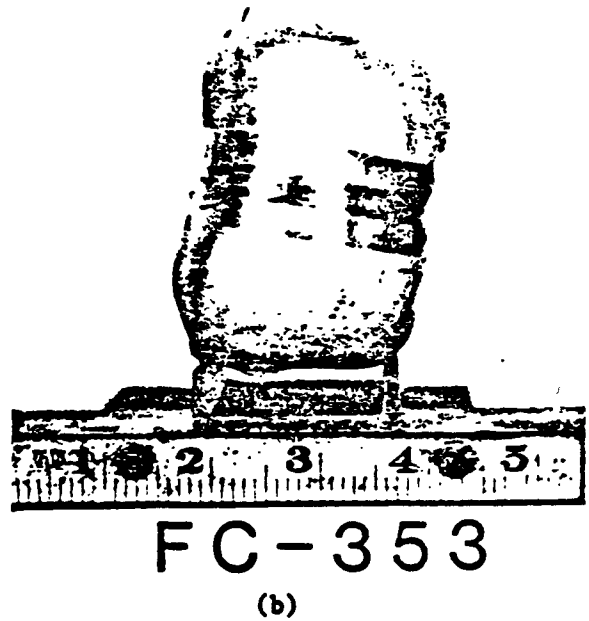
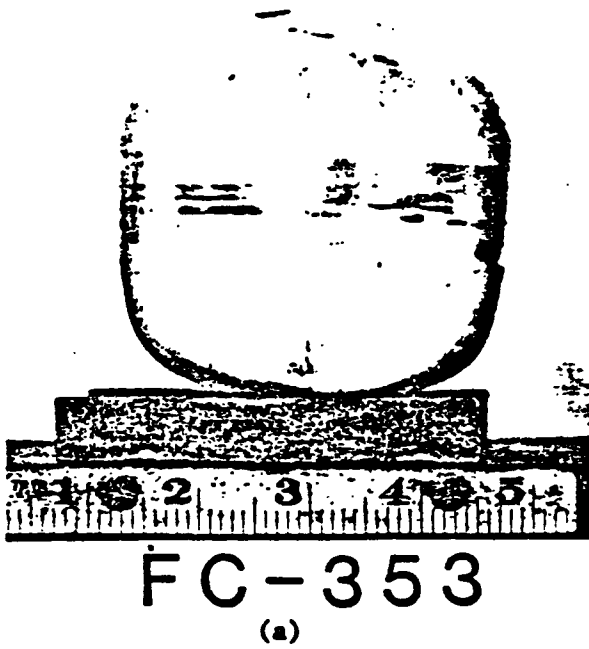


Figure G-17. Photographs of the Impacted Fueled-Clad, FC-353, BCI-4  
(a) Impact Face, (b) Side Profile, (c) Back Side,  
(d) Vent End View. All Approximately 1.5X

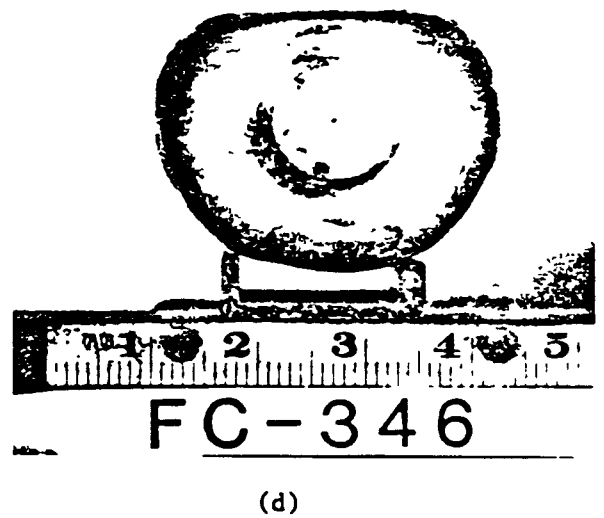
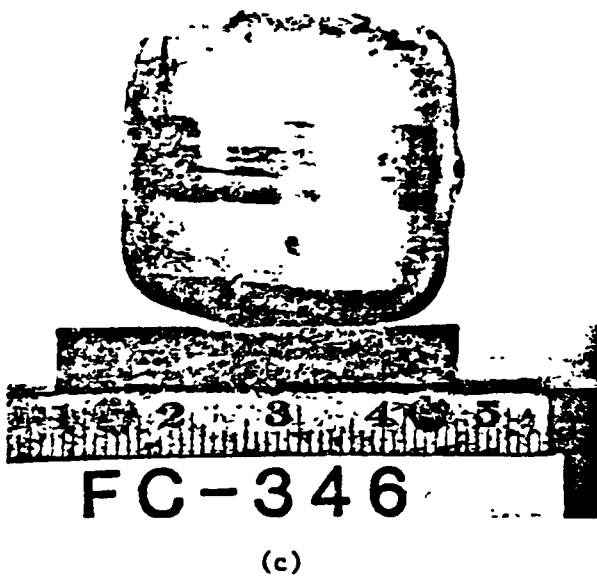
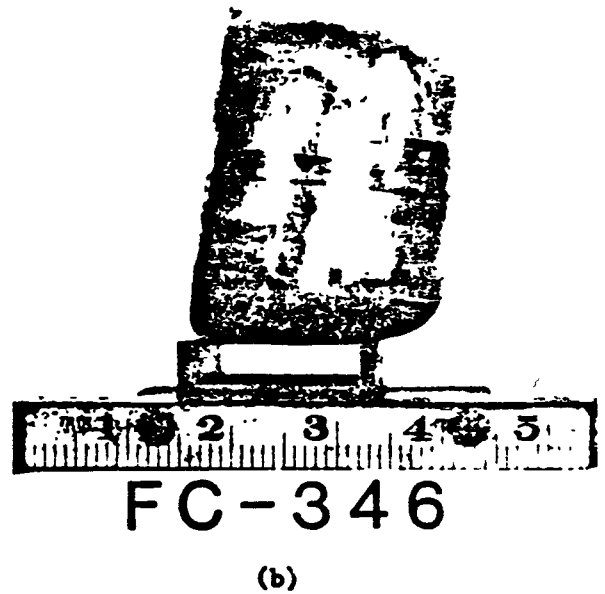
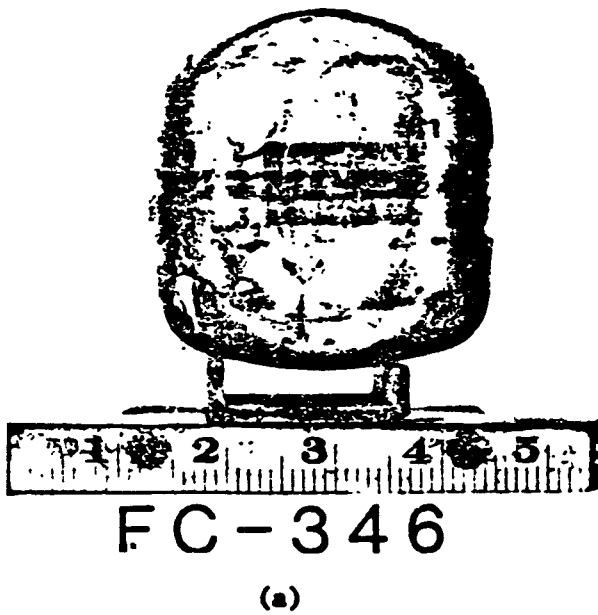


Figure G-18. Photographs of the Impacted Fueled-Clad, FC-346, BCI-5  
(a) Impact Face, (b) Side Profile, (c) Back Side,  
(d) Vent End View. All Approximately 1.5X

raise the temperature of the clad to that representative of the launch temperature. The material reaction could have possibly affected the iridium grain boundary chemistry so that its mechanical strength would be altered. In subsequent tests, a standoff was used to isolate the FC from the tantalum can, and the tantalum hardware was outgassed at about 1200°C for one hour.

During the course of the impact testing on the bare clads and also concurrent with the converter segment testing, the recommendation was made that sequential testing be conducted for impact of FCs having first been subjected to an explosion. This occurred around the time of the CST-4 test at the 1750 psi overpressure level. However, the CST-4 test, LANL discovered (in the post-test examination of the clads) that a surface reaction had occurred between the thermally hot iridium (it have been heated to 1090°C for the shock tube test) and (probably) the vermiculite used as the cushioning material in the catch box to prevent uncontrolled secondary impacts of the clads.

Subsequently, a clad from CST-4 was grit blasted to remove the adhering vermiculite and tested against concrete at a velocity of 54 m/sec (BCI-6). Because of the concern with the potential iridium interaction with vermiculite in the CST-4 test and its potential effect on sequential tests, the validity of the BCI-6 test was questioned. Subsequently, two as-fabricated PCs (with UO<sub>2</sub> simulant) were impacted against steel (BCI-7 and BCI-8) for comparison with BCI-6 and for comparison of the fuel simulant with the PuO<sub>2</sub> fuel used previously in BCI-5. These two tests did demonstrate that the microcracks observed in non-impact areas on BCI-6 were most likely caused by clad degradation resulting from exposure to the vermiculite thermal decomposition products. Two additional bare clad impact tests were performed in which one clad was first heated to 1120°C, dropped into sawdust, subsequently grit blasted, and then impacted on steel (BCI-9). This sequence was performed to duplicate the treatment given to BCI-6 and at the same time to assess the capability of a different catch medium as far as precluding a material interaction with the iridium. The other of these tests (BCI-10) duplicated BCI-9 except that the iridium clad was not grit blasted. Based on the results, the grit blasting may have had a small effect, but this apparently was negligible compared with the initial effect of iridium clad degradation from material interaction.

Table G-11 shows the pre-treatment given to the clads used in impact tests BCI-6 through BCI-10. The results of those tests are shown in Table G-12. Table G-13 presents particle size distributions from the results available from the BCI tests with simulant as well as those from BCI-1 and BCI-2 with  $\text{PuO}_2$ . These results are plotted on Figure G-19. One can see that tests BCI-8, BCI-10 and even BCI-6 with the  $\text{UO}_2$  simulant yield particle sizes that are comparable with that from BCI-2 with  $\text{PuO}_2$ . The  $\text{UO}_2$  simulant appears to produce a larger fraction in the 10 micron and smaller range by roughly a factor of two based on the average of the BCI-6, -8, -9 and -10 results compared with that of BCI-2. The particle size distribution from BCI-1 is about an order-of-magnitude larger in all sizes less than 74 microns than that of BCI-2.

#### G.2.5 GPHS MODULE IMPACT TESTS

The GPHS Module Impact Tests supporting Safety Verification consisted of two series of tests. The first of these included the impact tests conducted in the design verification program after the flight design of the GPHS had been finalized. Flight type fueled clads that were prepared by DOE's Savannah River Plant were used. These are the tests in the Design Iteration Test (DIT) series which begin with DIT-2. All previous testing had been conducted on hardware that was produced during the development phase. The results of these tests are presented in Table G-14. Also included in that table is the Early Compatibility Test (ECT-1) in which the fueled clads were subjected to six months aging at operating temperature to determine the long term compatibility effects on the impact capability of the module.

The second test series, the Safety Verification Test (SVT), included the impact of GPHS modules simulating conditions that would occur as the result of an unplanned reentry followed by impact on the Earth surface media. The original plan for this series was to address the types of reentries that would span the temperature range expected at impact. An orbital decay type of reentry was chosen to represent the most probable with corresponding impact temperatures in the upper range. For lower range of impact temperatures, the minimum-gamma ( $\gamma_{\min}$ , reentry angle) superorbital reentry was chosen, a low probability of occurrence. The lower range of impact temperature is of

Table G-11. Pre-Impact Test History of Impacted Simulant Bare Fueled Clads

Test No.	Pellet No.	History
BCI-6(S)	L-9	(a) Recovered from overpressure test CST-4, 1750 psi. (b) Grit blast surface to remove adhering vermiculite.
BCI-7(S)	L-6	As fabricated.
BCI-8(S)	L-5	As fabricated.
BCI-9(S)	M-3	(a) Heat to 1120°C and dropped into sawdust. (b) Grit blast surface.
BCI-10(s)	M-4	(a) Heat to 1120°C and dropped into sawdust.

Table G-12. Simulant Bare Clad Impact Tests (Pre-1986 Test Program)

Target : Steel							
Orientation : Axis parallel to target							
Temperature : 1091°C							
Pellet No.	Vel. m/s	Gross Deformation			Failures	Uranium Release-gm.	
		Diam.-%	Height-%	Length-%		Total	-10 μm
L-9	54.34	+9.1	-14.4	+19.4	<u>BCI-6(S)</u> (a) Severe on vent end face normal to target about 2/3 of height. (b) Transverse on impact face at the vent end. (Exterior surface micro-cracks on the vent end)	11.233	0.246
L-6	53.64	+6.7	-9.6	+14.0	<u>BCI-7(S)</u> (a) Transverse on impact face at the vent end.	0.204*	n.d.
L-5	54.50	+8.4 (+11.4)**	-9.6	+12.7	<u>BCI-8(S)</u> None	0	0
M-3	54.48	+10.2	-14.9	+14.8	<u>BCI-9(S)</u> (a) Transverse on impact face at the vent end (Non-penetrating micro-cracks on the end of shield cup)	0.0090	0.0078
M-4	54.19	+10.3	-13.4	+11.3	<u>BCI-10(S)</u> None (Minor micro-cracking on the end of the shield cup)	0	0

\* Recovered amount (tube weld failure on impact can)  
 \*\* Maximum at the edge of a pellet fragment push-through.



Table G-13. Particle Size Analyses Bare Clad Impact Tests

WEIGHT FRACTIONS OF TOTAL PELLETS							
TEST	BCI-6	BCI-8 #	BCI-9	BCI-10 #		BCI-2 #	BCI-1 <sup>Δ</sup>
PARTICLE SIZE	URANIA SIMULANTS					PLUTONIA FUEL	
-MICRONS	L-9*	L-5*	M-3	M-4*	AVG.**	FC-164	FC-209
+6000	0.6094	0.5500	0.8228	0.5068	0.6223	0.7749	n.d.
-6000+2000	0.1487	0.2259	0.0482	0.2197	0.1606	0.1260	n.d.
-2000+841	0.1168	0.1334	0.0640	0.1621	0.1191	0.0319	0.4898
-841+420	0.0589	0.0422	0.0342	0.0623	0.0494	0.0114	0.0987
-420+177	0.0338	0.0255	0.0199	0.0295	0.0272	0.0178	0.0754
-177+125	0.0083	0.0051	0.0027	0.0058	0.0055	0.0097	0.0263
-125+74	0.0078	0.0056	0.0034	0.0043	0.0053	0.0106	0.0360
-74+44	0.0042	0.0032	0.0015	0.0024	0.0028	0.0077	0.0670
-44+30	0.0032	0.0023	0.0009	0.0017	0.0020	0.0045	0.0822
-30+20	0.0013	0.0010	0.0005	0.0008	0.0009	0.0038	0.0811
-20+10	0.0026	0.0018	0.0006	0.0011	0.0015	0.0000	0.0278
-10	0.0052	0.0040	0.0014	0.0033	0.0035	0.0017	0.0156

\* NOT CORRECTED FOR IMPURITIES.

\*\* AVERAGE OF BCI-6, -8, -9, -10.

# UNBREACHED CLADS - SIZE ANALYSIS IS FOR MATERIAL CONTAINED.

Δ RELEASED MATERIAL ONLY - NOT FOR TOTAL PELLET.

G-44

WP2693/1889-736/JD

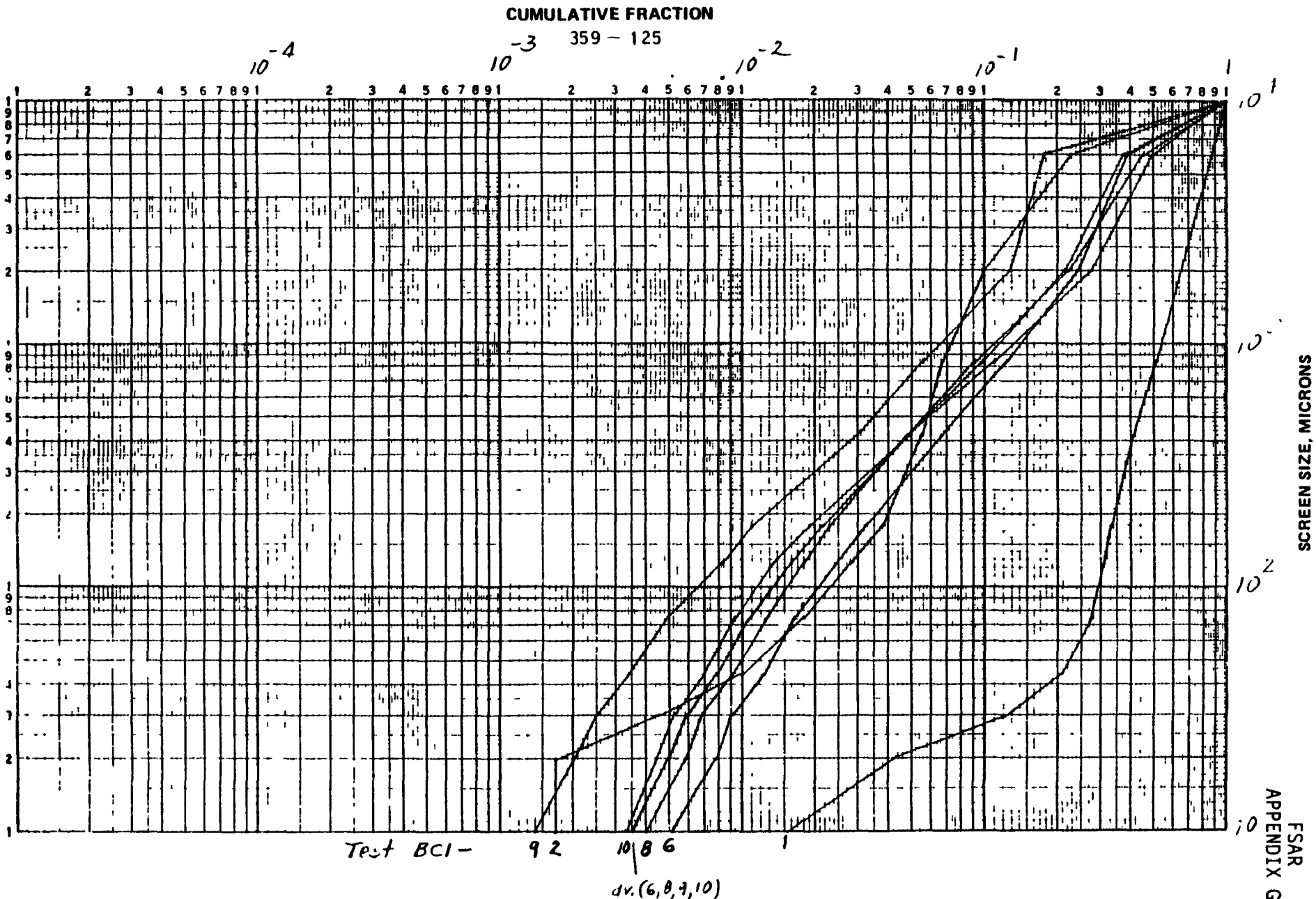


Figure G-19. Cumulative Fraction of UO<sub>2</sub> or PuO<sub>2</sub> Less than Screen Size Shown for Bare Clad Impact Tests

FSAR APPENDIX G  
SCREEN SIZE, MICRONS

Table G-14. Design Verification Impact Test Program Results

Capsule No.	Test 1) ID	Aging		Impact				% Strain						Fuel Ref.	Crack Size mm	Comments	
		Time Hr.	Temp. °C	Date	Vel m/sec	Temp. °C	Angle 2) Deg.	Max. Diam.	Diag.	Max. Weld.	Local	Length	Height				
IRG-105	DIT 2	100	1305	1 Oct. 81	58	925	0	5.7	-3.0	5.1	-	-	3.5	yes	-	small	first production (flight) welded clads by SRP
IRG-106	DIT 2	100	1305	1 Oct. 81	58	925	0	6.3	-4.2	6.3	-	-	3.4	no	no	-	
IRG-107	DIT 2	100	1305	1 Oct. 81	58	925	0	7.4	-5.1	7.4	-	-	5.4	yes	yes	4 x .02	
IRG-110	DIT 2	100	1305	1 Oct. 81	58	925	0	8.0	-3.5	8.0	-	-	6.7	yes	yes	5 x .04	
SRP-127	DIT-3	720	1312	22 Jul. 82	58	930	30°	-3.15	-1.45	-1.53	-	3.2	-	no	no	-	NDT = 9.0
SRP-140	DIT-3	720	1312	22 Jul. 82	58	930	30°	-4.56	-4.43	3.05	-	4.29	-	no	no	-	= 11.5
SRP-251	DIT 3	720	1312	22 Jul. 82	58	930	30°	4.48	-2.35	1.78	-	4.45	-	no	no	-	= 8.0
SRP-317	DIT 3	720	1312	22 Jul. 82	58	930	30°	-6.22	-0.70	6.70	-	1.22	-	no	no	-	= 10.4
SRP-394	DIT 4	720	1310		58	930	0	10.3	-6.2	12.4	-	5.0	-	no	no	-	half module
SRP-398	DIT 4	720	1310		58	930	0	-11.6	-3.5	12.4	-	4.0	-	no	no	-	
HF-2	ECT-1	(6 mo.) 4320	1310	2 Sep. 82	59.3	930	0	10.9	-	-	-	4.9	-12.9	yes	yes	38 x 1.5 max. multiple	half module, no re-entry
HF-5	ECT-1	(6 mo.) 4320	1310	2 Sep. 82	59.3	930	0	8.8	-	-	-	5.1	-7.9	yes	yes	2 x 0.1 7 x 0.5	
SRP-423	DIT 5	(30 days) 720	1310	10 Nov. 82	60.5	930	0	9.4	-	10.3	-	6.3	-	yes	yes	10 x 0.1	(2 poles)
SRP-444	DIT 5	(30 days) 720	1310	10 Nov. 82	60.5	930	0	10.9	-	12.3	-	5.6	-	yes	yes	10 x 0.2 89 x 2	(4 poles)
HF-430	DIT 6/ NIT-1	(30 days) 912	1287	7 Sep. 83	53.9	975	0	8.7	-	-	-	4.3	-9.0	no	no	-	
HF-450	DIT 6/ NIT 1	(30 days) 912	1287	7 Sep. 83	53.9	975	0	8.9	-	-	-	4.6	-7.5	no	no	-	

NOTES: 1) Acronyms used are: DIT - Design Iteration Test, ECT - Early Compatibility Test, NIT - Nominal Impact Test  
 2) The angle is measured between the horizontal and the large flat face of the GPHS module rotating about an axis parallel with the GIS axis in the module.

interest because of the iridium material approaching the potential ductile-to-brittle transition range. Because of the low probability event represented by the  $\gamma_{\min}$  type of reentry, only two of the module tests in the SVT series have addressed these conditions. These are the SVT-1 and SVT-2 module tests that had the following treatment prior to impact:

Pre-Test Aging

200 Hours at 1287°C

Reentry thermal pulse equivalent to  $\gamma_{\min}$  reentry

Impact

919°C

Tests SVT-3 through SVT-13 were originally planned to be tested under orbital decay reentry conditions as follows:

Pre-Test Aging

90 days at 1287°C

Reentry thermal pulse equivalent to orbital decay reentry

Impact

975°

These orbital decay related tests were to investigate the effects of impact orientation or angle on the impact response of the module. Because of the increased attention placed on the effects of the launch pad and early ascent accidents on the survival capability of the GPHS module, the original test series was altered after the first ten (10) tests (i.e., two with  $\gamma_{\min}$  conditions and eight with orbital decay conditions on SVT-1 through SVT-10).

At that point, the conclusion was reached that there was sufficient test data available to identify the failure threshold as related to impact orientation, at least with respect to the broad face of the module. Therefore, the remaining test articles could be used to investigate launch pad area type impacts. Earlier in the GPHS development program, the impact testing had demonstrated that the broad face forward type of impact with the FC axis parallel to the impact resulted in the most severe strain in the weld area of the clads. This is related to the alpha ( $\alpha$ ) angle orientation shown on

Figure G-20. The angle testing in the SVT test series corresponds to this angle. Development testing conducted at the other angular relations shown on Figure G-20 resulted in higher localized strains in the area of the clad around the side wall juncture with end area, but these occurred in the virgin areas of the clad unaffected by the weld heating and thus were not as sensitive to failure.

Test SVT-11 was subsequently conducted on a sample of the concrete obtained from Pad B, Launch Complex 39, at the Kennedy Space Center. This test was conducted under the same pre-treatment and impact conditions as those for the orbital decay reentry and thermal pulse. The judgment was made that these factors would not be expected to alter the impact capability significantly. Although the impact velocity duplicated also the terminal impact velocity associated with reentry, this velocity was in the range predicted to be possible as a result of the GPHS module being propelled by the explosion shock wave either for low overpressure explosions or when the module was propelled upward and thus approached terminal velocity prior to impact. Moreover, this test provided a means of comparison of the module impact capability on steel as tested under reentry conditions in SVT-1 through SVT-10 with that on concrete at the same velocity.

Another test on the launch pad concrete material was conducted in the SVT-12 test at a higher velocity around 86 m/sec which provided another comparison of the module capability with that of the bare clads as well as the trend on concrete versus velocity. The final test in the SVT impact series, SVT-13, was conducted on granite at the terminal velocity of the GPHS module. This was intended to correspond to a reentry situation on a surface material representative of the rock media of the Earth's surface rather than the steel used in the previous ten tests since the latter were believed to result in a greater insult than rock or concrete. It was judged that if the test on granite at the zero (0°) angle was successful, there would be a basis for predicting that all impacts following reentry could be treated as producing no failures. However, SVT-13 did result in a failure in one of the fueled clads. This failure was essentially like those that had occurred in SVT-2, -3 and -4 at the 0° angle on the steel target; thus, there was no basis provided for eliminating all failures due to impact following reentry.

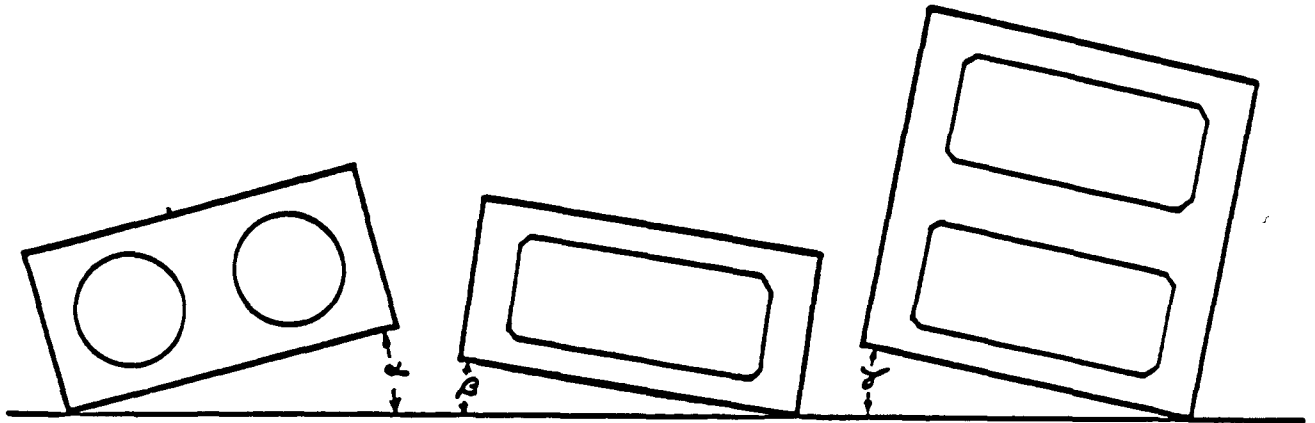


Figure G-20. Three Angles Describe the Orientation Sensitivity of the GPHS Module to Impact

The results of the SVT test series are presented in Table G-15. More detailed results can be obtained from the monthly progress reports in the Space Nuclear Safety Program and in the SVT quick look reports, both issued by Los Alamos, which are too numerous to include in the list of references. These tests, along with the DIT tests, have been conducted over a period from September 1981 until June 1985.

Table G-16 is a summary of the fuel released from the first ten SVT tests showing the distribution between the 10 micron and smaller range and greater than 10 micron range. Table G-17 is a complete hoisting of the particle size distribution from unbreached fueled clads in tests SVT-1, -3, -4, -5, -6, -8, -9 and 2 clads from SVT-10. For more detailed results from SVT-1 through SVT-13, refer to References G-10 through G-12.

Table G-15. Safety Verification Test (SVT) Program Impact Test Results

CAPSULE NO.	SVT NO.	AGING <sup>1)</sup>		IMPACT				% STRAIN			FAIL	FUEL REL.	CRACK SIZE MM	NDE: VALUE	COMMENTS
		TIME HR.	TEMP °C	DATE	VEL. M/SEC	TEMP °C	ANGLE <sup>2)</sup> DEG	MAX. DIAM.	HEIGHT	AXIAL					
FC-232	1	200	1287	7 OCT 83	54.4	919	0 (FLAT)	13.5	-11.1	5.8	NO	NO	--	3.0	0.11 GM PuO <sub>2</sub> RELEASE 11.6% < 10 μM
FC-238								9.6	- 7.3	3.8	NO	NO	--	5.0	
FC-261		(90 d)	1287	7 OCT 83	54.4	919	0	11.7	-11.1	5.6	YES	YES	0.3 x 20	8.7	25.4 mm <sup>2</sup>
FC-410								9.8	- 9.6	1.4	YES	YES	0.2 x 13 0.9 x 37	12.6	
FC-343	3	2160	1287	1 NOV 83	54.4	975	0	12.3	- 9.0	5.7	NO	NO	--	2.9	0.01 77 GM 8.8% ≤ 10 μM CRACK ACROSS WELD AFFECTED ZONE 0.4MM <sup>2</sup>
FC-350								10.0	- 8.5	2.6	NO	NO	--	1.1	
FC-454								9.5	- 6.4	2.9	YES	?	0.1 x 5.5	12.8	
FC-457	2	200	1287	29 NOV 83	55.0	917	0	10.8	- 7.2	5.6	NO	NO	--	9.8	3.4 mm <sup>2</sup> 14.2% ≤ 10 μM 0.0289 GM
FC-355								10.0	-10.4	4.1	NO	NO	--	6.8	
FC-369								9.1	- 9.3	4.1	NO	NO	--	6.0	
FC-449								12.5	-10.5	4.4	YES	?	0.5 x 20 0.4 x 15 0.3 x 10	13.7	
FC-273		(90 d)	1287	5 DEC 83	54	975	0	10.3	-10.3	5.6	NO	NO	--	10.3	1.8 mm <sup>2</sup> 29.6% > 10 μM 0.0257 GM
FC-318								11.5	-11.3	6.4	YES	?	0.38 x 11	1.0	
FC-354		2160	1287	5 DEC 83	54	975	0	8.5	- 8.2	4.0	NO	NO	--	3.2	1.8 mm <sup>2</sup> 29.6% > 10 μM 0.0257 GM
FC-139								11.0	- 8.5	5.1	NO	NO	--	13.7	
FC-162	5	2160	1287	17 JAN 84	54.0	975	90°	10.8	- 9.3	3.4	NO	NO	--	10.7	
FC-267								10.4	- 9.1	5.5	NO	NO	--	3.0	
FC-260								10.9	-13.7	4.1	NO	NO	--	4.0	
FC-415								5.5	- 4.5	1.2	NO	NO	--	9.4	
FC-426								5.0	- 6.9	0	NO	NO	--	9.6	

NOTES:

- 1) MODULES SVT NO. 1 AND SVT NO. 2 WERE ALSO GIVEN A HEAT PULSE IMMEDIATELY PRIOR TO IMPACT EQUIVALENT TO THAT OCCURRING IN A  $\gamma$  MIN. SUPERORBITAL TYPE OF RE-ENTRY  
MODULES SVT NO. 3 THROUGH SVT NO. 5 WERE GIVEN A HEAT PULSE EQUIVALENT TO THAT OCCURRING IN AN ORBITAL DECAY RE-ENTRY
- 2) THE ANGLE IS MEASURED BETWEEN THE HORIZONTAL AND THE LARGE FLAT FACE OF THE GPS ROTATING ABOUT AN AXIS PARALLEL WITH THE GIS AXIS IN THE MODULE

Table G-15. Safety Verification Test (SVT) Program Impact Test Results  
(Cont'd)

CAPSULE NO.	SVT NO.	AGING		IMPACT			% STRAIN			FAIL	FUEL REL.	CRACK SIZE MM	NDE: VALUE	COMMENTS	
		TIME HR	TEMP °C	DATE	VEL. M/SEC	TEMP °C	ANGLE DEG	MAX DIAM.	HEIGHT						AXIAL
FC-361	6	2160	1287	10 APR 84	54.6	975	90	12.3	- 17.6	8.8	NO	NO	--	4.4	24.1 MM <sup>2</sup> CRACK AREA 61.5% ≤ 10 μM
FC-373	↓	↓	↓	↓	↓	↓	↓	11.2	- 14.9	6.2	YES		0.3 x 7.7	4.1	
FC-225	↓	↓	↓	↓	↓	↓	↓	7.8	- 8.8	3.7	NO	NO	--	13.2	
FC-189	↓	↓	↓	↓	↓	↓	↓	6.4	- 7.2	2.9	NO	NO	--	13.3	
FC-364	7	2160	1287	15 MAY 84	53.5	975	15	9.9	- 13.5	5.3	YES		2 x 4.5	2.0	
FC-368	↓	↓	↓	↓	↓	↓	↓	9.5	- 9.9	5.4	YES		0.2 x 1	1.6	
FC-165	↓	↓	↓	↓	↓	↓	↓	10.7	- 10.0	5.7	YES		0.5 x 1	13.0	
FC-112	↓	↓	↓	↓	↓	↓	↓	8.0	- 9.5	4.0	YES		1 x 3.5	11.0	
FC-437	8	2160	1287	18 JUN 84	54.3	975	15	8.8	- 7.9	5.4	NO	NO	--	1.0	
FC-436	↓	↓	↓	↓	↓	↓	↓	6.2	- 5.2	3.6	NO	NO	--	1.0	
FC-391	↓	↓	↓	↓	↓	↓	↓	10.4	- 10.0	6.5	YES		1.8 x 30	9.8	
FC-441	↓	↓	↓	↓	↓	↓	↓	8.9	- 8.1	5.3	NO	NO	--	9.6	
FC-591	9	2088	1287	6 AUG 84	54.6	975	30	7.1	- 8.9	3.7	NO	NO	--	1.6	
FC-592	↓	↓	↓	↓	↓	↓	↓	6.0	- 6.1	2.4	NO	NO	--	3.0	
FC-473	↓	↓	↓	↓	↓	↓	↓	6.0	- 5.1	2.0	NO	NO	--	10.3	
FC-501	↓	↓	↓	↓	↓	↓	↓	6.7	- 5.7	4.3	NO	NO	--	11.4	
FC-589	10	2196	1287	6 SEPT 84	54.3	975	30	4.2	- 3.5	2.5	NO	NO	--	1.7	
FC-590	↓	↓	↓	↓	↓	↓	↓	5.4	- 6.6	5.0	NO	NO	--	3.7	
FC-152	↓	↓	↓	↓	↓	↓	↓	6.9	- 7.3	3.6	NO	NO	--	11.0	
FC-185	↓	↓	↓	↓	↓	↓	↓	6.5	- 6.8	3.7	NO	NO	--	1.5	
FC-372	11	2160	1287	23 OCT 84	54.4	975	0	6.8	- 7.1	2.9	NO	NO	--	8.2	
FC-345	↓	↓	↓	↓	↓	↓	↓	8.2	- 7.9	3.2	NO	NO	--	7.6	
FC-365	↓	↓	↓	↓	↓	↓	↓	7.0	- 8.9	1.7	NO	NO	--	9.3	
FC-341	↓	↓	↓	↓	↓	↓	↓	9.1	- 8.2	2.7	NO	NO	--	8.9	
FC-628	12	2160	2187	26 DEC 84	75.5	975	0	8.9	- 5.1	4.5	YES		0.1 x 3.3	1.3	
	↓	↓	↓	↓	↓	↓	↓						0.1 x 14	1.3	
FC-629	↓	↓	↓	↓	↓	↓	↓	8.8	- 9.1	6.±	NO	NO	--	1.3	
FC-226	↓	↓	↓	↓	↓	↓	↓	13.0	- 11.5	6.2	YES		1 x 15.3	14	
FC-277	↓	↓	↓	↓	↓	↓	↓	10.4	- 9.8	5.6	NO	NO	--	12.9	
FC-605	13	2160	1287	26 APR 84	53.4	975	0				NO		0.5 x 16	1.0	
FC-604	↓	↓	↓	↓	↓	↓	↓				YES			2.3	
FC-546	↓	↓	↓	↓	↓	↓	↓							10.8	
FC-526	↓	↓	↓	↓	↓	↓	↓							12.0	

G-50

WP2693/1889-736/JD

FSAR  
APPENDIX G



Table G-16. GPHS SVT Impact Fuel Test Release

PU CONTENT (G) *						
MODULE	REENTRY MODE	< 10 $\mu$ M	> 10 $\mu$ M	TOTAL	AREA MM <sup>2</sup>	RELEASE DENSITY $\mu$ G/MM <sup>2</sup>
SVT-1	MIN- $\gamma$	0.0128	0.0972	0.1100	25.4	0.0043
SVT-2	MIN- $\gamma$	0.0041	0.0248	0.0289	8.4	0.0034
SVT-3	O-DECAY	0.0051	0.0126	0.0177	0.4	0.0443
SVT-4	O-DECAY	0.0076	0.0181	0.0257	1.8	0.0143
SVT-5 $\neq$	O-DECAY	0.0020	0	0.0020	0	--
SVT-6	O-DECAY	0.0091	0.0056	0.0147	24.1	0.0006
SVT-7	O-DECAY	0.1390	0.0837	0.2227	53.4	0.0042
SVT-8	O-DECAY	0.0687	0.0173	0.0860	54.0	0.0016
SVT-9 $\neq$	O-DECAY	0.0024	0	0.0024	0	--
SVT-10 $\neq$	O-DECAY	0.0026	0	0.0026	0	--
SVT-11 $\neq$	O-DECAY	0.0027	0	0.0027	0	--
SVT-12	O-DECAY	0.0377	0.0081	0.0458	17.0	0.00269
SVT-13	O-DECAY	0.0144	0.0069	0.0183	8.0	0.00229

\* SVT-1 TO -5. COMBUST GRAPHITICS AT 850, 900°C SIEVE ASH AND ANALYZE.  
SVT-6. ULTRASONIC WASH OF A/S AND SIC, PLASAMA-ASSISTED COMBUSTION

$\neq$  NO CLAD FAILURES OCCURRED IN SVT-5, SVT-9, SVT-10 and SVT-11; ALL FUEL RELEASE RESULTED FROM TRANSPORT THROUGH THE CAPSULE VENTS

Table G-17. SVT Impact Fuel Size Distribution for Unbreached Clads

SVT FC	<u>1</u> 232	<u>3</u> 343	<u>6</u> 361	<u>8</u> 437	<u>4</u> 139	<u>5</u> 260	<u>9</u> 473	<u>10</u> 590	<u>10</u> 152	<u>11</u> 345	<u>12</u> 629	<u>13</u> 605
SIZE, $\mu\text{m}$	WEIGHT FRACTION											
+ 6000	0.1209	0.1027	0.0464	0.1585	0.1631	0.1949	0.5025	0.2509	0.1447	0.1607	0.2483	0.2112
+ 2000 TO 6000	0.2263	0.2228	0.1901	0.4663	0.3637	0.2072	0.3370	0.5288	0.5869	0.3774	0.2357	0.3058
+ 841 TO 2000	0.3309	0.3532	0.3146	0.2224	0.2620	0.3020	0.1096	0.1433	0.1805	0.2477	0.2413	0.2907
+ 420 TO 841	0.1568	0.1546	0.2193	0.0807	0.0957	0.1472	0.0278	0.0423	0.0482	0.1140	0.1259	0.0978
+ 177 TO 420	0.0957	0.0917	0.1296	0.0408	0.0573	0.0795	0.0122	0.0199	0.0228	0.0600	0.0741	0.0529
+ 125 TO 177	0.0149	0.0142	0.0212	0.0065	0.0102	0.0127	0.0018	0.0030	0.0037	0.0093	0.0142	0.0093
+ 74 TO 125	0.0171	0.0176	0.0242	0.0064	0.0119	0.0150	0.0019	0.0030	0.0035	0.0092	0.0170	0.0093
+ 44 TO 74	0.0084	0.0115	0.0174	0.0047	0.0098	0.0110	0.0016	0.0023	0.0028	0.0063	0.0136	0.0064
+ 30 TO 44	0.0078	0.0085	0.0104	0.0034	0.0077	0.0087	0.0013	0.0016	0.0019	0.0040	0.0095	0.0043
+ 20 TO 30	0.0062	0.0074	0.0122	0.0047	0.0063	0.0079	0.0019	0.0022	0.0025	0.0050	0.0102	0.0052
+ 10 TO 20	0.0070	0.0089	0.0048	0.0027	0.0070	0.0092	0.0070	0.0008	0.0010	0.0031	0.0058	0.0036
- 10	0.00808	0.00691	0.00978	0.00277	0.00551	0.00475	0.00107	0.00183	0.0019	0.0033	0.0044	0.0035
10	0.001531	0.002523	0.003001	0.00096	0.001995	0.001834	0.00015	0.00053	0.00047	0.0008	0.0008	0.0017
9	0.001116	0.001430	0.001094	0.00018	0.000534	0.000594	0.00006	0.00027	0.00019	0.0002	0.0003	0.0005
8	0.000784	0.000861	0.000769	0.00019	0.000375	0.000417	0.00012	0.00015	0.00027	0.0005	0.0008	0.0003
7	0.000263	0.000192	0.000172	0.00025	0.000419	0.000140	0.00016	0.00013	0.00018	0.0004	0.0004	0.0002
6	0.000992	0.000242	0.000972	0.00023	0.000422	0.000308	0.00008	0.00023	0.00010	0.0001	0.0004	0.0002
5	0.000383	0.000315	0.001000	0.00014	0.000428	0.000299	0.00010	0.00009	0.00007	0.0003	0.0004	0.0001
4	0.000441	0.000341	0.000800	0.00025	0.000344	0.000313	0.00007	0.00012	0.00006	0.0002	0.0004	0.0001
3	0.000579	0.000235	0.000635	0.00016	0.000336	0.000253	0.00008	0.00007	0.00008	0.0002	0.0003	0.0001
2	0.000398	0.000260	0.000492	0.00014	0.000387	0.000243	0.00009	0.00008	0.00007	0.0003	0.0003	0.0001
1	0.001593	0.000511	0.000846	0.00027	0.000309	0.000417	0.00016	0.00016	0.00010	0.0003	0.0003	0.0002

G-52

WP2693/1889-736/JD

APPENDIX G  
FSAR

### G.3 SAFETY TEST PROGRAM FOR GALILEO FSAR

The tests included in the current test program are as follows:

- Bare Fueled Clad Impact Tests (BCI)
- SRB Fragment Test in Gas Gun (FGT)
- Large SRB Fragment Impact Tests (LFT)
- SRB Fragment/Orbiter Fuselage Tests (FFT)
- GIS Impact Tests (GIT)

A synopsis of each of these test series is given in the following paragraphs. Subsequent sections of this appendix present the detailed results of each test series.

#### BCI - Bare Clad Impact Tests

The purpose of the BCI series was to augment the previous BCI data and to fill in areas in which data was lacking. The present series has concentrated mainly on a velocity range centered on the terminal velocity of the fueled clads which is in the 73-74 m/s range. The major purpose of this test series was to get additional data on the particle size distribution as a function of the quantity of fuel released. An additional purpose of the current series has been to improve the data base on the comparison between fuel and simulant and on the differences in fueled clad response on various media.

#### FGT - SRB Fragment Tests in Gas Gun

The gas gun referred to here is the Isotope Fuels Impact Tester (IFIT) facility at the Los Alamos National Laboratory (LANL), a 178 mm-diameter gun using a pneumatically propelled, upward firing sabot with provision for containment of the impacted test article in a totally enclosed catch tube. Both simulant and live fuel tests can be conducted in this facility. In these tests a simulated RTG housing section, similar to the configuration used previously in the early Converter Segment Test (CST) series, containing flight configuration thermoelements and layered insulation and a GPHS module sandwiched between dummy weighted modules was propelled into a 1.27 cm

(0.5 inch) SRB case fragment (i.e., a turn-around test). Tests were run with simulant and with fuel in the velocity range of 100-120 m/s. The purpose of the tests was to determine the GPHS fueled clad response to SRB fragment impacts in a simulated RTG configuration and to make a comparison between clads containing fuel and those containing simulant. A comparative evaluation between the fuel and simulant response was provided by direct replication impact tests. The plutonia basic response data and urania response relationship were necessary for calibration of the analytical models and to evaluate the large SRB fragment field tests (i.e., on a rocket sled track) in which only urania fueled clads can be tested (see the LFT series discussion).

#### LFT - Large SRB Fragment Impact Tests

A SRB plate fragment 142 cm (56 inch) square and 1.27 cm (0.5 inch) thick was propelled by rocket sled into a flight configuration RTG housing of one-half axial length containing two simulant fueled test modules and six mass simulant modules. Two tests were run in which the SRB fragment was oriented face-on to the RTG housing at velocities of 115 m/s and 212 m/s. A third test is planned in which the same size SRB fragment is to be oriented in an edge-on configuration to a simulated half-length converter section with two simulant fueled GPHS modules and impacted at a velocity around 100 m/s. When this report was prepared, this latter test had not yet been performed. The purpose of these tests was to determine the response of the GPHS modules in the full RTG configuration to impact by a SRB fragment. Differences in response between modules near the end and central modules in the RTG and between leading and trailing clads also were to be determined.

#### FFT - Fragment/Fuselage Tests

SRB fragments 58.4 cm (23 inches) square were explosively propelled through sections of the Orbiter wing and/or payload bay wall structure at velocities of approximately 180 m/s and with rotation rates of 7-15 revolutions/sec. The purpose of these tests was to determine the velocity attenuation and alteration of rotational motion of the SRB fragment due to its interaction with the Orbiter structure prior to arrival of the fragment at the RTG location. Fragment interaction with the RTG was not a part of these tests.

GIT-GIS Impact Test

Tests are planned in which free Graphite Impact Shells (GIS) will be impacted at their terminal velocity, estimated to be around 63 m/s (208 fps), onto a hard surface. The necessity for these tests was a result of the potential reentry conditions associated with the VEEGA trajectory. Under some of these conditions, the potential exists that the GPHS aeroshell might be completely ablated at some locations or otherwise fail due to aerodynamic loading coupled with low strength at the extremely high temperatures involved, thus leaving the intact GIS to complete the reentry and impact on the Earth's surface.

The tests presented in this appendix are those for which results were available in June 1988, at which time this FSAR was prepared for review. Results which became available after this date have not been factored into the FSAR analysis.

G.3.1 BARE CLAD IMPACT TESTS (BCI)

Table G-18 presents the results of all the bare clad impact tests that have been conducted. In Section G.2.4 for the pre-1986 Safety Test Program, tests BCI-1 through BCI-10 were summarized. They are included in Table G-18 for completeness. It should be remembered that the early series of tests was conducted to address the consequences to the GPHS as a result of the potential environments associated mainly with the Centaur dominant failures. The tests were designed to investigate the impact response of the bare fueled clads on media in the immediate vicinity of the launch pad after the RTG converter and the GPHS graphitics had been stripped off by the initial explosion. That series of tests was continued after the previous FSAR was published and prior to the Challenger accident.

Tests BCI-11 and BCI-14 were run on concrete to determine if the velocity threshold for complete failure (i.e., total release of fuel) estimated and extrapolated from the prior tests could be substantiated. The estimated threshold was 146 m/s. Test BCI-11 at 160 m/s did result in essentially total release of the fuel (simulant), whereas, BCI-14 at 117 m/s resulted in a low

Table G-18. Bare Clad Impact Tests - Results

BCT NO.	FUELED CLAD ID	FUEL OR SIM	TGT(1)	VEL m/s	DEFORMA %	BREACH AREA mm <sup>2</sup>	TOTAL RELEASE (2)		RELEASE ≤ 10µm			% STRAIN			CRACK SIZES mm	REMARKS
							gm	%	gm	DIA	HGT	LGT	DIA	HGT		
1*	209	F	C	76.24	71.5	288	14.208	10.53	0.222	+31.7	-23.2	+27.0	35x9, 18x1, 12x1, 8x0.2	TA CAN CONTAMINATION		
2*	184	F	C	53.7	22.0	0	0	0	0	+9.6	-10.2	+11.2	—			
3*	351	F	C	64.77	25.2	0.94	0.0006	0.0005	0.0001	+12.3	-10.3	+15.2	14.3x0.2, 7.1x0.2			
4*	353	F	C	90.45	55.3	67	11.9	8.82	0.155	+24.4	-19.9	+23.6	40x6.0, 18x0.4, 12x0.2			
5*	348	F	S	53.19	33.4	0.33	0.0084	0.0047	0.0023	+14.5	-14.2	+14.2	8.0x1.0, 3.0x0.1			
6*	L-9	S	S	53.34	27.5	42	11.23	8.33	0.246	+9.1	-14.4	+19.4	3.5 MAX WIDTH	FROM CST-4 (1750 psi)		
7*	L-8	S	S	53.64	18.0	1.1	0.204	0.151	NA	+6.7	-9.6	+14.0	—	AS FABRICATED		
8*	L-5	S	S	54.50	19.9	0	0	0	0	+8.4	-9.6	+12.7	—	AS FABRICATED		
9*	M-3	S	S	54.48	29.5	0.63	0.009	0.0067	0.0078	+10.2	-14.9	+14.8	—	SAWDUST TEST		
10*	M-4	S	S	54.19	27.4	0	0	0	0	+10.3	-13.4	+11.3	—	SAWDUST TEST		
11	M-5	S	C	160	NA	NA	135	100	NA	NA	NA	NA	—	AS FABRICATED		
12	M-11	S	D	206	11.0	0	0	0	0	+5.9	-4.6	-2.4	—	FROM CST-6 (ABORTED TEST)		
13	"D"-CLAD	S	D	250	7.0	0	0	0	0	+3.3	-3.5	+0.3	—	FROM CST-2 (1070 psi)		
14	M-48	S	C	116.6	10.2	0.6	0.0145	0.0107	0.0075	+6.3	-3.0	+9.6	—	FROM CST-8 (435 psi)		
15	214	F	S	53.34	50.2	4.35	0.0114	0.0085	0.0072	+14.3	-23.9	+19.1	—			
16	L-11	S	S	51.84	19.1/18.8	1.1	0.0020	0.0015	0.0002	+7.5	-9.5	+10.0	—			
										+10.8	-7.0	+14.2	—			
17	M-25	S	C	75.1	12.1/12.1	NA	NA	NA	NA	+4.7	-6.6	+6.6	NA	HOT ISOSTATIC PRESS		
										+7.1	-4.5	+11.0	—	HOT ISOSTATIC PRESS		
18	M-6	S	S	58.89	14.0/14.0	3.36	0.0116	0.0086	0.0030	+4.9	-8.0	+7.7	10x0.3	HOT ISOSTATIC PRESS W/SVT VIB		
										+7.5	-5.7	+10.8	—			
19	M-16	S	S	55.04	23.9/19.0	0.27	0.0025	0.0018	0.0012	+8.2	-12.7	+14.8	—	WITH SVT VIBRATION		
										-9.1			—			
20	M-45	S	S	66.28	24.3	16.4	0.0056	0.0041	0.0008	+11.1	-10.6	+16.4	27x0.8, 18x0.1, 7x0.1, 7x0.5, 6x0.1			
21	M-49	S	S	75.89	43.1	15.5	0.0129	0.0096	0.0017	+16.2	-18.8	+21.0	20x0.1, 13x0.5, 12x0.5, 4x0.1, 2x0.1			
22	M-43	S	S	85.59	63.7/56.6	278	43.74	32.4	0.688	+27.5			—			
										+22.0	-22.1	+25.3	50x0.8, 45x10, 32x0.2, 16x0.3			
23	Q-4	S	S	55.48	18.7	0	0	0	0	+8.1	-8.9	+10.9	—			
24	Q-5	S	S	65.08	41.9/36.6	NA	0.0004	0.0003	NA	+10.4			—			
										+6.3	-22.2	+3.2	5x0.5, 5x0.1	58° IMPACT ANGLE (UNPLANNED)		
25	536	F	S	65.66	56.2		<0.1			+18.4	-24.2	+23.8	—			
26	212	F	S	74.86	38.5		<0.2			+19.4	-13.8	+27.7	—			
27	297	F	S	85.74	54.7					+20.8	-21.9	+27.4	—			

\* PREVIOUSLY REPORTED

(1) C - CONCRETE (2) REPORTED AS Pu FOR FUELED TESTS (NOT PuO<sub>2</sub>)  
 S - STEEL REPORTED AS U FOR SIMULANT TESTS (NOT UO<sub>2</sub>)  
 D - SAND

G-56

WP2693/1889-736/JD

FSAR  
 APPENDIX G

distortion and minor breach with a very small release of fuel simulant (.015 gm or .01% of the total).

Tests BCI-12 and BCI-13 were conducted on sand at the upper end of the velocity range that resulted from the secondary impact analysis associated with the near pad accidents in the previous FSAR. Neither of the tests resulted in a breach of the clads at these high velocities. These two tests were actually sequential tests since the clads used in the impact tests had previously been subjected to shock waves representative of the environment in an explosion of the Centaur in the CST series (Converter Segment Test).

Test BCI-15 was performed on steel with live fuel in order to obtain a comparison of the particle size distribution with the  $UO_2$  simulant for the same target and velocity. As a result of this test, the clad received a large deformation (50.2%) but with a small breach and a small release of fuel (.011 gm, 0.14 Ci or .008% of the total). See Table G-19 for the resulting particle size distribution.

Based on experimental evidence resulting from some of the earlier tests, in particular, the converter segment shock tube series-CST, the observation was made by LANL that the fueled clads were swaged to the fuel by the isostatic pressure in the shock wave. This isostatic conformation of the clads was believed to provide more resistance to breaching in a subsequent insult such as an impact following an explosion. In addition, when a clad breach was observed to occur, the released fuel quantity was believed to be limited by the mechanical constraint of the clad on the retained fuel. In order to investigate this effect, BCI-16 through BCI-19 were conducted. The test articles for BCI-16, -17, and -18 were subjected to a hot isostatic pressing (HIP) at high temperature and pressure prior to being impacted.

If BCI-16 is compared to similar tests such as BCI-7 and BCI-8, the deformations are seen to be essentially the same. The breach area for BCI-16 is identical to that for BCI-7 ( $1.1 \text{ mm}^2$ ), but the release for BCI-7 is two orders of magnitude larger. There is no breach or release for BCI-8. However, BCI-6, impacted at a similar velocity shows a larger deformation, a much larger breach area, and a much larger release. It had previously been

Table G-19. Particle Size Distributions - Bare Clad Impact Tests

PARTICLE SIZE MICRONS	PLUTONIA FUELED CLADS					WEIGHT FRACTION OF OXIDE URANIA (SIMULANT) FUELED CLADS														
	BCI 1	BCI 2	BCI 4	BCI 5	BCI 15	BCI 6	BCI 8	BCI 9	BCI 10	BCI 12	BCI 13	BCI 14	BCI 16	BCI 18	BCI 19	BCI 20	BCI 21	BCI 22	BCI 23	
	+ 8000		0.7748			0.3837	0.5643	0.5501	0.8228	0.5068	0.4715	0.8312	0.7759	0.3646	0.7000	0.5465	0.2958	0.4713	0.0441	0.5981
-8000	+ 2000	0.1280			0.3677	0.1490	0.2259	0.0482	0.2197	0.2497	0.0979	0.0924	0.2700	0.1755	0.2037	0.2838	0.1927	0.2759	0.1908	
-2000	+ 841	0.4898	0.0319		0.1199	0.1171	0.1335	0.0840	0.1621	0.1747	0.0408	0.0738	0.2413	0.0786	0.1404	0.2321	0.1745	0.3325	0.1208	
- 841	+ 420	0.0987	0.0114		0.0412	0.0755	0.0422	0.0342	0.0823	0.0808	0.0135	0.0303	0.0758	0.0224	0.0453	0.0908	0.0702	0.1578	0.0464	
- 420	+ 177	0.0754	0.0178		0.0254	0.0484	0.0258	0.0199	0.0295	0.0289	0.0087	0.0189	0.0333	0.0119	0.0279	0.0530	0.0489	0.1073	0.0283	
- 177	+ 125	0.0283	0.0087		0.0085	0.0129	0.0061	0.0027	0.0058	0.0048	0.0018	0.0032	0.0050	0.0027	0.0055	0.0109	0.0095	0.0184	0.0036	
- 125	+ 74	0.0380	0.0108		0.0092	0.0111	0.0058	0.0034	0.0043	0.0044	0.0022	0.0033	0.0047	0.0031	0.0089	0.0109	0.0114	0.0229	0.0047	
- 74	+ 44	0.0870	0.0077		0.0120	0.0081	0.0032	0.0015	0.0024	0.0021	0.0014	0.0020	0.0018	0.0018	0.0042	0.0055	0.0057	0.0094	0.0019	
- 44	+ 30	0.0822	0.0045		0.0135	0.0048	0.0023	0.0009	0.0017	0.0014	0.0008	0.0011	0.0013	0.0012	0.0041	0.0039	0.0045	0.0075	0.0015	
- 30	+ 20	0.0811	0.0038	0.9560	0.0113	0.0018	0.0010	0.0005	0.0008	0.0008	0.0005	0.0008	0.0005	0.0007	0.0019	0.0020	0.0024	0.0035	0.0007	
- 20	+ 10	0.0278	0.0000	0.0320	0.0438	0.0034	0.0017	0.0008	0.0011	0.0008	0.0005	0.0001	0.0008	0.0009	0.0037	0.0027	0.0033	0.0051	0.0010	
-10		0.0158	0.0017	0.0120	0.3582	0.0051	0.0038	0.0014	0.0033	0.0019	0.0009	0.0008	0.0013	0.0015	0.0098	0.0090	0.0077	0.0157	0.0023	
1 00		0.002333	0.000207	0.001247	0.053381	0.000482	0.000384	0.000188	0.000508	0.000185	0.000045	0.000019	0.000080	0.000288	0.000290	0.000214	0.000400	0.001509	0.000178	
2 00		0.001085	0.000158	0.000988	0.048228	0.001024	0.000388	0.000305	0.001043	0.000500	0.000198	0.000061	0.000313	0.000183	0.000588	0.000671	0.001309	0.001852	0.000308	
3 00		0.001137	0.000123	0.000489	0.044380	0.001138	0.000400	0.000254	0.000429	0.000381	0.000250	0.000129	0.000142	0.000157	0.001488	0.001455	0.001933	0.002106	0.000419	
4 00		0.001311	0.000082	0.000453	0.022152	0.000725	0.000205	0.000188	0.000230	0.000128	0.000158	0.000123	0.000075	0.000113	0.001219	0.001844	0.001407	0.002883	0.000341	
5 00		0.000711	0.000058	0.000322	0.028844	0.000214	0.000275	0.000082	0.000112	0.000088	0.000083	0.000076	0.000028	0.000143	0.001101	0.001259	0.000828	0.003249	0.000289	
6 00		0.001898	0.000101	0.000895	0.031151	0.000222	0.000582	0.000080	0.000130	0.000051	0.000025	0.000012	0.000072	0.000087	0.000720	0.001143	0.000339	0.002174	0.000130	
7 00		0.000781	0.000080	0.000441	0.019787	0.000235	0.000480	0.000085	0.000183	0.000040	0.000054	0.000049	0.000057	0.000071	0.000327	0.000805	0.000431	0.000288	0.000242	
8 00		0.002331	0.000080	0.001318	0.029538	0.000178	0.000205	0.000047	0.000154	0.000120	0.000040	0.000029	0.000057	0.000053	0.000810	0.000774	0.000482	0.000429	0.000052	
9 00		0.001659	0.000258	0.000938	0.021027	0.000500	0.000583	0.000087	0.000000	0.000171	0.000057	0.000042	0.000081	0.000227	0.000174	0.000184	0.000458	0.000811	0.000220	
10 00		0.002379	0.000584	0.005148	0.057887	0.000343	0.000400	0.000185	0.000800	0.000235	0.000038	0.000029	0.000388	0.000208	0.003334	0.001008	0.000314	0.000839	0.000101	
CONTAINED OR RELEASED	R	C	R	R	C	R	C	R	C	C	C	C	C	C	C	C	C	C	R	C

G-58

WP2693/1889-736/JD

FSAR  
APPENDIX G



subjected to a blast overpressure in CST-4 at 1750 psi; thus, it had the isostatic pressing prior to the impact.

Prior to the HIP treatment, BCI-18 was also given a vibration equivalent to that of the SVT modules. As a direct comparison to this test, BCI-19 was given the same vibration pre-treatment, but without the HIP, and then impacted at the same velocity. The resulting deformation of 19-23.9% for BCI-19 is seen to be higher than the 14% for BCI-18. However, the breach area for BCI-18 ( $3.36 \text{ mm}^2$ ) is an order of magnitude larger than that of BCI-19 ( $0.27 \text{ mm}^2$ ), and the release is larger by a factor of 4.6. Comparing BCI-18 with a later test BCI-23 at the same velocity, the BCI-18 deformation is lower than that of BCI-23 (18.7%), but BCI-23 did not breach as did BCI-18.

Thus, it is believed that there is minimal benefit, if any, from the HIP treatment of the fueled clads. On the other hand, there are several intuitive arguments that support the possibility that the HIP treatment could be detrimental to the overall impact capability of the GPHS, especially from the viewpoint of reentry and impact. First of all, swaging the clads to the fuel takes up all available space for the expansion of the fuel when it is distorted by the impact, which process definitely occurs in the more severe impacts. Also, swaging of the clads results in their being pre-stressed before any other insult. During reentry heating with the considerably higher temperatures of the GPHS internal components, the fuel will expand faster than the iridium clad which will stress the clad even further. Thus, its resistance to breaching on impact could be greatly diminished.

The remaining tests in the bare clad impact series, BCI-20 through BCI-27, were performed to obtain more complete data on the response of the clads as a function of velocity in the range where failure occurs but not extending into the region beyond where complete release occurs. The intent, also, was to obtain a better comparison of the simulant and fuel in terms of quantity released and particle size distribution. These tests were performed on steel to preclude any appreciable response by the surface impacted, such as occurs in concrete where the surface is cracked and chipped away in the more severe impacts. In addition, these tests were desired to be performed with bare clads to preclude any alteration of the resulting particle size distribution

of the released material such as may occur in the presence of the graphite components in the SVT series previously reported. As seen in Table G-18, some of the results from the post test analyses of the last tests were not available in time for this FSAR. Tables G-19 and G-20 present the particle size distributions determined in the post-test analyses for the bare clad impact tests.

### G.3.2 SRB FRAGMENT TESTS IN GAS GUN (FGT)

The conditions and results for the four fragment gas gun tests are given in Table G-21. There were no clad failures in any of the tests even at the relatively large distortions seen in the fueled tests, FGT-2 and FGT-4, on the leading clads. Also, from these tests, the simulant clads can be seen to distort much less than the fuel clads. On an average, the deformation of the leading clads in the tests with fuel are approximately three times (3x) that of the tests with simulant; the trailing clad deformations are higher by a factor slightly larger than two (2x+).

### G.3.3 LARGE SRB FRAGMENT IMPACT TESTS (LFT)

In the first large fragment test (LFT-1), the GPHS test modules were located in the second and fifth positions from the bottom of the stack of eight (8) modules used in the test. The remaining six (6) modules were made of polycrystalline graphite with solid molybdenum simulants representing the fueled clads. The velocity of the 56-inch (1.42 m) square SRB casing fragment at impact was 377 fps (114.9 m/s). The converter half-section was damaged such that approximately a quarter section of the housing or shell to the right of center of the impact face was completely broken out over the length of the shell. The remainder of the converter was severely flattened; the majority of the insulation foil assembly remained inside the remains of the shell. Figure G-21 shows converter shell after the test.

The RTG test assembly was propelled into a 4.5 m-long corrugated steel catch tube filled to 4.0 m with vermiculite. The catch tube slid on the sled track rails for about 180 m, leaving the test articles behind and located between and along the rails. The converter section dropped out of the catch tube and

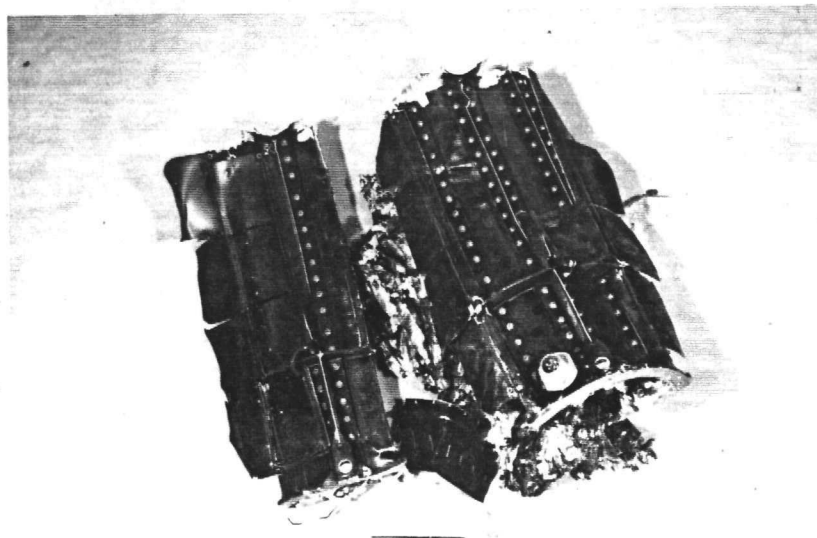
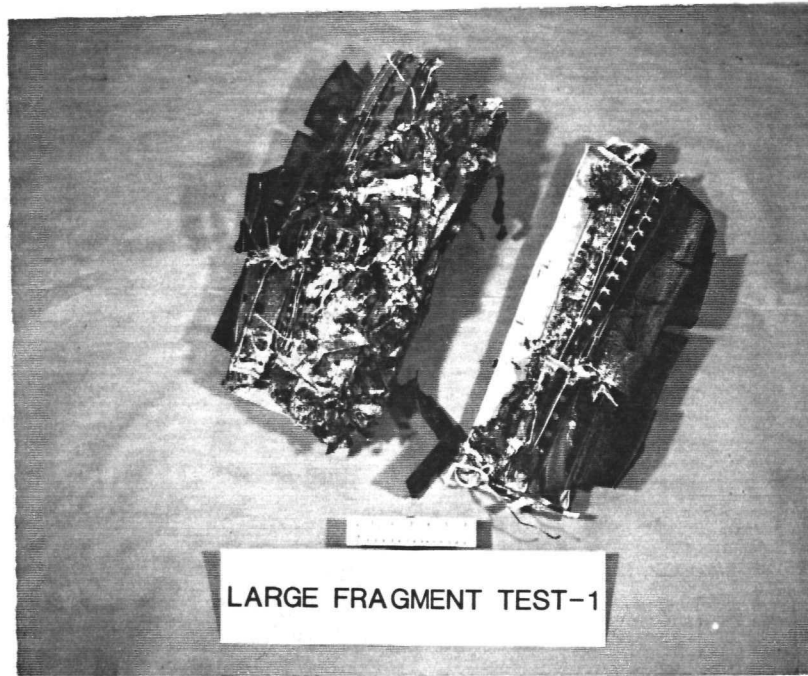
Table G-20. BCI-22 Particle Size Distributions

PARTICAL SIZE MICRONS	WT. FRAC. OF REL. UO <sub>2</sub>	WT. FRAC. OF RET. UO <sub>2</sub>	WT. FRAC. OF PELLET REL.	WT. FRAC. OF PELLET RET.	WT. FRAC. OF TOTAL PELLET
+6000	0.0441	0.4203	0.0145	0.2823	0.2968
-6000 +2000	0.2759	0.2098	0.0906	0.1409	0.2315
-2000 +841	0.3325	0.1869	0.1092	0.1255	0.2347
-841 +420	0.1576	0.0743	0.0518	0.0499	0.1017
-420 +177	0.1073	0.0530	0.0353	0.0356	0.0709
-177 +125	0.0184	0.0082	0.0061	0.0055	0.0116
-125 +74	0.0229	0.0134	0.0075	0.0090	0.0165
-74 +44	0.0094	0.0062	0.0031	0.0042	0.0072
-44 +30	0.0075	0.0054	0.0025	0.0036	0.0061
-30 +20	0.0035	0.0028	0.0012	0.0018	0.0030
-20 +10	0.0051	0.0047	0.0017	0.0031	0.0048
-10	0.0157	0.0149	0.0052	0.0100	0.0152
1.00	0.001509	0.000587	0.000496	0.000394	0.000890
2.00	0.001852	0.001201	0.000608	0.000806	0.001414
3.00	0.002106	0.002662	0.000692	0.001788	0.002480
4.00	0.002683	0.002774	0.000881	0.001863	0.002744
5.00	0.003249	0.001558	0.001067	0.001046	0.002113
6.00	0.002174	0.001287	0.000714	0.000864	0.001578
7.00	0.000288	0.001673	0.000094	0.001123	0.001218
8.00	0.000429	0.002219	0.000141	0.001490	0.001631
9.00	0.000611	0.000395	0.000201	0.000265	0.000466
10.00	0.000839	0.000542	0.000275	0.000364	0.000639

Table G-21. SRB Fragment - Gas Gun Test Results

TEST ID.	FUELED CLAD ID	FUEL OR SIM.	LOCATION		POSITION		VEL. M/S	% DEFORMATION	
			LEAD	TRAIL	CLOSED END	OPEN END		SHIELD CUP	VENT CUP
FGT-1	Q-13	S	✓			✓	100	8.1	6.7
	Q-12	S	✓		✓		100	7.7	12.4
	M-38	S		✓		✓	100	7.1	7.9
	Q-14	S		✓	✓		100	3.0	3.4
FGT-2	489	F	✓			✓	100	27.3	33.9
	490	F	✓		✓		100	17.9	29.1
	349	F		✓		✓	100	13.2	12.4
	326	F		✓	✓		100	9.2	11.7
FGT-3	Q-9	S	✓			✓	120	6.3	15.0
	Q-8	S	✓		✓		120	10.8	7.4
	Q-11	S		✓		✓	120	5.2	4.8
	Q-10	S		✓	✓		120	5.7	4.4
FGT-4	767	F	✓			✓	120	22.9	29.5
	769	F	✓		✓		120	26.4	26.3
	761	F		✓		✓	120	13.7	13.2
	758	F		✓	✓		120	8.5	9.9

NOTE: THE FUELED CLADS DID NOT BREACH IN EITHER OF THESE TESTS.



LARGE FRAGMENT TEST-1

Figure G-21. RTG Case After LFT-2

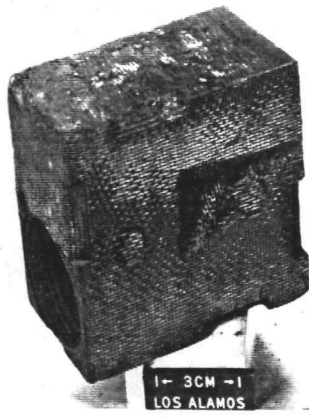
came to rest about 30 m down the track from the impact point. Both test modules were released from the converter section as were the dummy modules. The test module in the fifth position was essentially intact and was found beside the converter housing. Both GISs from the module in the second position were released from the aeroshell, but the fueled clads remained in the GISs. The aeroshell from this module had a penetrating corner deformation, shown in Figure G-22, resulting from what was deduced to be an impact on one of the tie down brackets for the rocket sled rails. This caused the GISs to be released.

The SRB fragment was found about 60 m down the track from the impact point. The fragment was found to have a central area nearly flattened in a permanent deformation with an inverse protrusion in the deformed area approximately the size of the RTG test article. This protrusion was roughly 2-3 mils from the surrounding surface.

The results of the test are shown in Table G-22. There were no breaches in any of the clads. The deformations from this test are seen to be relatively small, especially when distortions of 1.7-4.3% are possible just by closing up the clearance between the clad and fuel in one direction based on the manufacturing tolerances.

In the second large fragment test (LFT-2), the GPHS test module arrangement in the half-RTG stack was the same as in the first test: second and fifth position from the bottom of the stack of eight (8) modules. The velocity of the 56-inch (1.42 m) square SRB casing fragment at impact was 695 fps (212 m/s); the temperature of the fueled clads was 1091°C (1996°F). The RTG section was severely damaged and fragmented as shown on Figure G-23.

The catch tube for this test was a 14 ft (4.3 m)-long corrugated steel culvert tube filled to 4 ft. (1.2 m) with sawdust followed by 6 ft. (1.8 m) of vermiculite at the open or catch end of the track. In addition, the catch tube was front loaded with about 500 lb. (227 kg) of lead to assist in decelerating the SRB fragment. The catch tube was severely damaged and separated into two pieces when it was propelled by the fragment onto the concrete pad to one side (east) of the track. The smaller portion of the



MODULE 076 - STACK LOCATION #2  
LARGE FRAGMENT TEST #1 - 114.9 m/s

Figure G-22. Aeroshell from Module 076 Recovered After LFT-1

Table G-22. Post-Test Dimensions of LFT-1 Urania Fueled Clads

FUELED CLAD ID	LOCATION		POSITION		FUELED CLAD HALF	% STRAINS			% DEFORMATION
	LEAD	TRAIL	CLOSED END	OPEN END		DIA.	HGT.	LGT.	
<b>2ND POSITION MODULE (076)</b>									
Q-17	✓			✓	VENT CUP SHIELD CUP	+0.9 +0.9	-2.9 -2.1	+1.0	3.9 3.1
Q-15	✓		✓		VENT CUP SHIELD CUP	+0.2 +0.9	-2.6 -2.3	+0.6	2.9 3.3
Q-18		✓		✓	VENT CUP SHIELD CUP	+2.9 +2.6	-1.5 -5.7	+2.1	4.5 8.8
Q-16		✓	✓		VENT CUP SHIELD CUP	+0.3 +0.2	-0.6 -1.3	-1.3	0.9 1.5
<b>5TH POSITION MODULE (077)</b>									
Q-23	✓			✓	VENT CUP SHIELD CUP	+2.9 +3.1	-2.8 -2.8	+2.0	5.9 6.1
Q-19	✓		✓		VENT CUP SHIELD CUP	+2.8 +2.2	-4.9 -2.1	+1.8	8.1 4.4
Q-22		✓		✓	VENT CUP SHIELD CUP	+0.6 +0.8	-1.0 -2.6	+0.9	1.6 3.5
Q-20		✓	✓		VENT CUP SHIELD CUP	+0.4 +0.3	-0.6 -0.9	-0.7	1.0 1.2



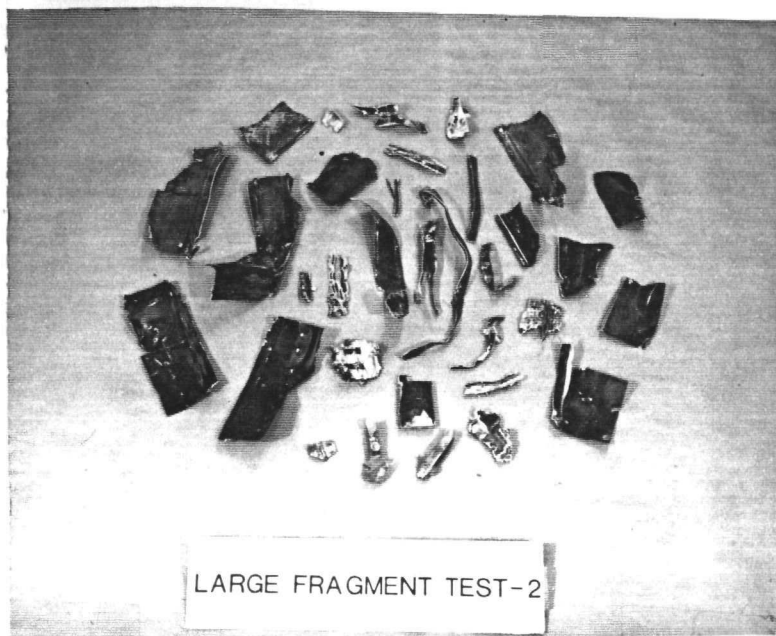
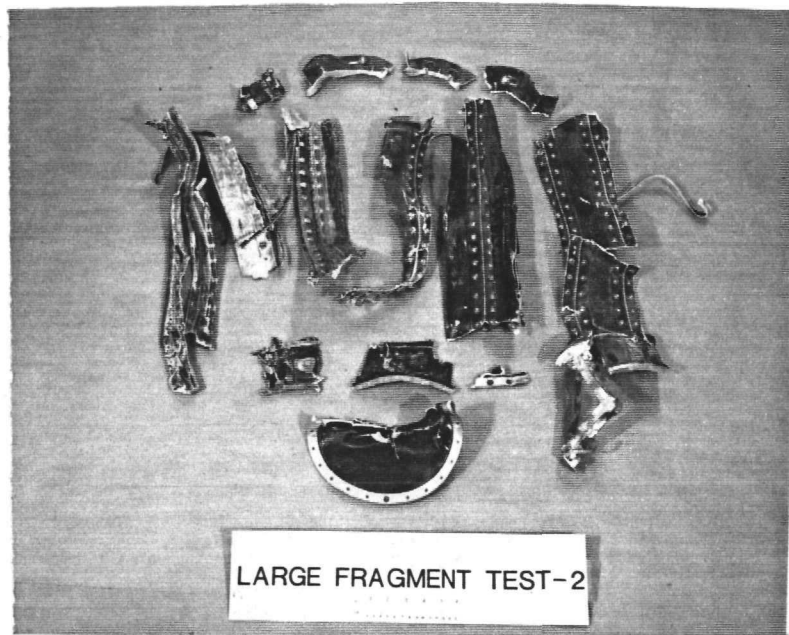


Figure G-23. RTG Case After LFT-2

catch tube was found about 130 ft. (40 m) from its original position; the larger portion traveled 130 ft. (40 m) farther down the track, also on the east side.

The SRB fragment was shattered into four (4) pieces. Two of the smaller pieces were found in the heavily damaged catch tube. These may have caused the clad breaches that were found.

Except for clad Q-27, the graphite was completely stripped from the fueled clads in both modules. Q-27, from the C or trailing GIS, blind end location of the GPHS module in the fifth stack position, was recovered in a GIS remnant. Figure G-24 shows the graphite pieces of the modules recovered. The fueled clads (except for Q-27) were recovered in or near the major section of the catch tube. One clad, Q-25, from the module in the second stack position was breached, and about .023 gm of fuel was released. Another clad, Q-33, from the module in the fifth stack position was also breached, and about 1.73 gm of fuel was released. Both of these clads had sharp discontinuities which were believed to be caused by secondary impacts with pieces of the SRB fragment that had been arrested in the catch tube. In addition, clad Q-34 from this same module had a large indentation, apparently from a secondary impact.

The post-test dimensions of the simulant fueled clads are shown in Table G-23. The deformations shown are well below any deformation that would be expected to result in breaching, especially in the full-up RTG configuration as used in the test. Thus, these results support the supposition that the breaches that occurred were a result of secondary impacts and not by the initial fragment impact.

The third and final large fragment test (LFT-3) was conducted in which a 56-inch (142 cm) square SRB fragment was propelled edge-on into a simulated half-RTG containing eight (8) graphite modules. The simulated half-RTG was similar to that used in the earlier CST series (see Section G.2.1) but longer in length. Two of the modules (in positions 2 and 5 from the bottom end of the stack) were FWPf graphite and contained simulant fueled iridium capsules. The other six (6) modules were made of bulk graphite containing molybdenum

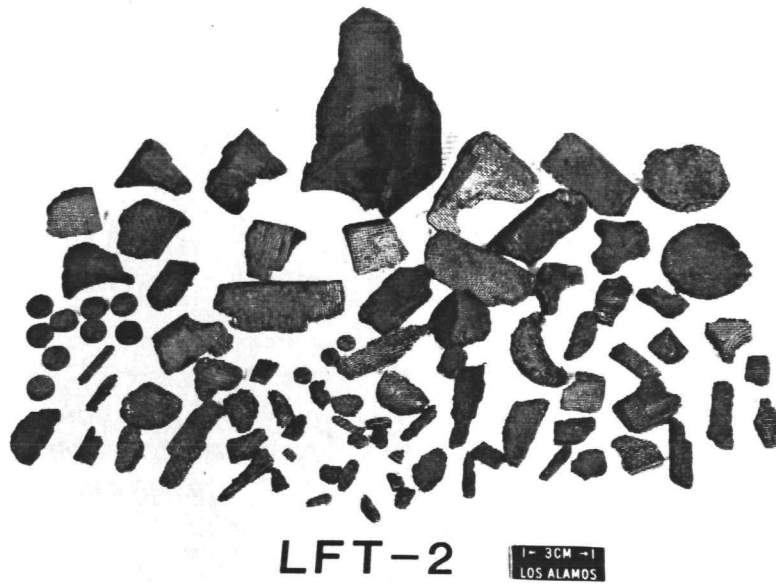


Figure G-24. Graphite Pieces Recovered from LFT-2

Table G-23. Post-Test Dimensions of LFT-2 Urania Fueled Clads

FUELED CLAD ID	LOCATION		POSITION		FUELED CLAD HALF	% STRAINS			% DEFORMATION
	LEAD	TRAIL	CLOSED END	OPEN END		DIA.	HGT.	LGT.	
<b>2ND POSITION MODULE (PAL - 0078)</b>									
Q-34	✓			✓	VENT CUP	1.3	-10.8	10.3	13.6
					SHIELD CUP	1.3	-11.2		14.0
Q-33	✓		✓		VENT CUP	0.6	-5.1	8.1	6.0
					SHIELD CUP	NOT MEASURED - SECONDARY IMPACT MODIFIED AS-IMPACTED DIMENSIONS			
Q-32		✓		✓	VENT CUP	0.1	-1.8	-1.1	1.9
					SHIELD CUP	-0.1	-2.4		2.4
Q-31		✓	✓		VENT CUP	0.9	-2.6	0.2	3.6
					SHIELD CUP	0.6	-3.2		3.9
<b>5TH POSITION MODULE (PAL - 0080)</b>									
Q-26	✓			✓	VENT CUP	0.3	-8.5	4.8	9.6
					SHIELD CUP	0.9	-3.4		4.4
Q-25	✓		✓		VENT CUP	2.4	-4.3	8.4	7.0
					SHIELD CUP	0.3	-4.3		4.8
Q-28		✓		✓	VENT CUP	0.7	-2.6	0.0	3.4
					SHIELD CUP	1.0	-3.1		4.2
Q-27		✓	✓		VENT CUP	0.5	-2.3	-0.9	2.9
					SHIELD CUP	0.9	-3.3		4.3

mass simulants in place of the fueled clads. The velocity of the fragment at impact was 313 fps (95.4 m/s), and the right edge of the fragment cut through the simulated RTG about 1.13 inch (2.86 cm) to the right of the RTG centerline. The fragment edge at impact was oriented so that the entire module stack would be struck along the transverse centerline of one of the leading fueled clads.

There was no catch tube used for this test. Instead, two very large mounds of dirt were piled up on either side of the sled track to act as a catch medium. Based on engineering tests conducted with the use of dummy modules and clads for the purpose of checking out the test arrangement, the dummy clads were observed to be ejected obliquely toward the opposite side of the track with respect to the side of the RTG (off center target point of the fragment) that would be hit. This path of the clads was indeed seen to occur in the actual test, and the clads were all found in the left dirt mound. The dirt mounds had been covered with plastic sheets to enhance the recovery of the clads by indicating their entry points into the mound.

All eight (8) of the iridium capsules were recovered from the left dirt mound. Two (2) of the capsules were breached, one (1) was recovered bare, two (2) were recovered intact GIS, and three (3) were recovered in partial GISs. Sixteen (16) of the 24 molybdenum slugs were also recovered. Three (3) of those showed evidence of being hit by the SRB fragment. The fuel releases resulting from the breaches in the iridium capsules were around 49 grams from Q-46 in module #2 and 7.5 grams from Q-50 in module #5.

The post-test dimensions of the simulant fueled clads are shown in Table G-24. Except for the clads that were impacted directly by the SRB fragment, the deformations are seen to be very small, as might be expected. Even in the half clad from capsule Q-50, the deformation of 6.6% is seen to be relatively small.

Table G-24. Post-Test Dimensions of LFT-3 Urania Fueled Clads

FUELED CLAD ID	LOCATION		POSITION		FUELED CLAD HALF	% STRAINS			% DEFORMATION
	LEAD	TRAIL	CLOSED END	OPEN END		DIA.	HGT.	LGT.	
<b>2ND POSITION MODULE</b>									
Q-46	✓			✓	VENT CUP SHIELD CUP	INDETERMINATE <sup>(1)</sup> 0.0 -1.0			
Q-49	✓		✓		VENT CUP SHIELD CUP	-0.6 -0.8 0.0 -1.0	}	-0.4	+0.2 +1.0
Q-30		✓		✓	VENT CUP SHIELD CUP	-0.8 -0.7 -0.9 -0.8			}
Q-29		✓	✓		VENT CUP SHIELD CUP	+0.8 -2.2 +1.1 -2.0	}	+0.9	
<b>5TH POSITION MODULE</b>									
Q-50	✓			✓	VENT CUP SHIELD CUP	+2.9 -3.5 +9.4 -17.0	}	+25.9/ +11.7 <sup>(2)</sup>	+6.6 +31.8
Q-51	✓		✓		VENT CUP SHIELD CUP	-0.5 -0.8 -0.6 -0.8			}
Q-41		✓		✓	VENT CUP SHIELD CUP	+0.3 -0.3 0.0 -0.7	}	-0.6	
Q-43		✓	✓		VENT CUP SHIELD CUP	+0.3 -2.8 +1.2 -2.0			}

(1) FUELED CLAD SEPARATED IN HALF AT WELD JOINT. SECONDARY IMPACT DEFORMATIONS PRECLUDED ACCURATE MEASUREMENTS.

(2) INCLUDES BREACH WIDTH/EXCLUDES BREACH WIDTH.

#### G.3.4 FRAGMENT/FUSELAGE TESTS (FFT)

The plan view for the first SRB fragment/Orbiter fuselage interaction test (FFT-1) is shown on Figure G-25. This figure shows the overall layout of the test including the relation of the fragment to the Orbiter wing section and the camera locations. Figure G-26 is a photograph of the setup. The wing section is the large rectangular structure in the middle of the picture and is actually positioned on its end. If the Orbiter fuselage could be seen, it would be located nose down to the right of the wing section with the payload bay doors facing out of the picture (i.e., toward the viewer). In other words, the wing section shown is from the starboard or right wing. The outline of the white structure to the left of the wing section is the blast shield with the rectangular window through which the fragment is propelled toward the wing section. The blast shield attenuates the air shock and explosion products fireball to minimize damage to the wing structure other than by the SRB fragment. In this test, the direction of travel of the fragment was normal to the wing surface. The plain vertical panel of plywood seen to the right of the wing section was used as a witness board to aid in determining the path of travel and orientation of the fragment.

The parameters and results of FFT-1 are given in Table G-25 as are those of FFT-2 through FFT-5. For FFT-1, the velocity and rotation rate reductions were thus 25% and 81%, respectively. The flight path of the fragment was determined to be deflected 8° upward at the point of exit from the wing surface.

In FFT-2, a 8 x 12 ft. plywood witness panel was positioned to simulate the Orbiter payload bay sidewall, and the fragment initial flight path was aligned at a 55° angle to the plane of the wing section. Figure G-27 is a layout of the test setup. A closeup of the wing section and simulated sidewall is shown on Figure G-28. The hole in the wing section occurred in FFT-1. Figure G-29 is another view of the setup showing the fragment held in the blast shield ready for firing. The blast shield is the white structure to the left of the wing section, now positioned on its long side which would be at the Orbiter fuselage.

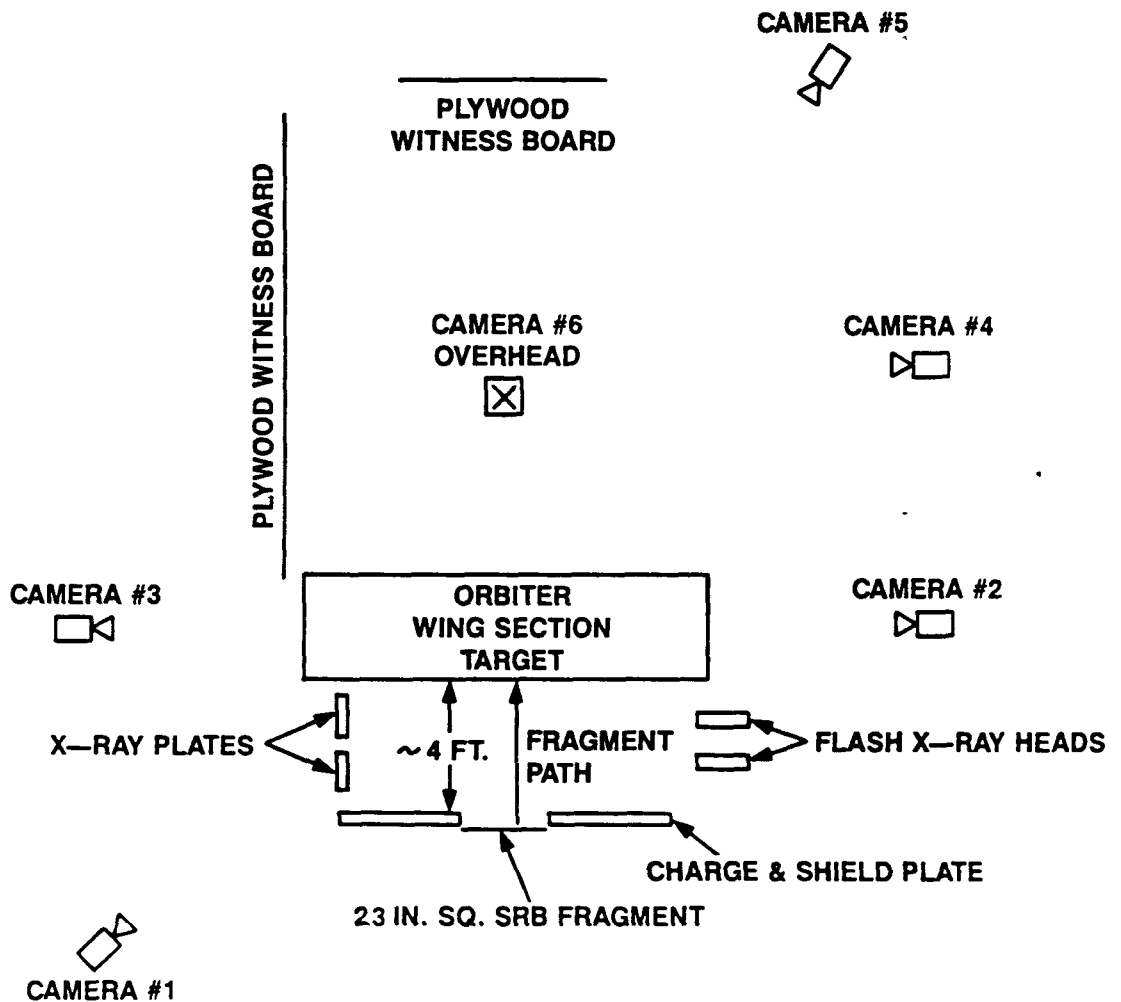


Figure G-25. FFT-1 Layout - Plan View



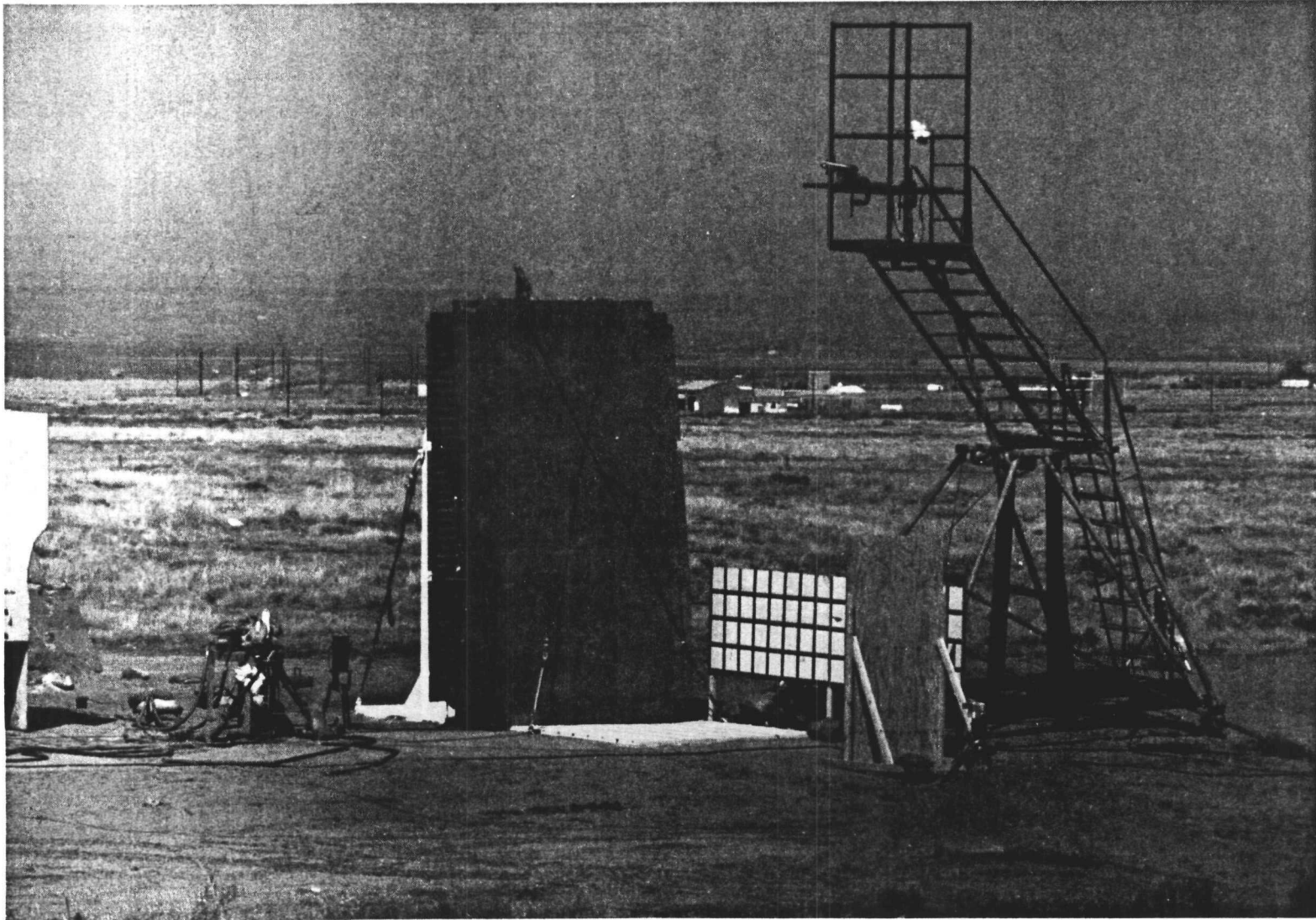


Figure G-26. Photograph of Test Arrangement for FFT-1

Table G-25. Test Parameters and Results of FFTs

<u>TEST NO.</u>	<u>FFT-1</u>	<u>FFT-2</u>	<u>FFT-3</u>	<u>FFT-4</u>	<u>FFT-5</u>
<b>ORBITER STRUCTURE TESTED</b>	<b>WING SECTION LI-30</b>	<b>WING SECTION LI-30</b>	<b>WING SECTION &amp; P/L BAY WALL SECTION</b>	<b>SIDEWALL SECTION MFA-08</b>	<b>WING SECTION LI-30</b>
<b>STRUCTURE ORIENTATION</b>	<b>NORMAL TO FLIGHT PATH</b>	<b>FLIGHT PATH 55° TO WING PLANE</b>	<b>FLIGHT PATH 55° TO WING PLANE<sup>(6)</sup></b>	<b>FLIGHT PATH 42° TO SIDEWALL PLANE</b>	<b>NORMAL TO FLIGHT PATH</b>
<b>WITNESS BOARD</b>	<b>4' X 8' PLYWOOD 1/2" THICK</b>	<b>8' X 12' PLYWOOD 1/2" THICK</b>	<b>NONE</b>	<b>?</b>	<b>?</b>
<b>WITNESS BOARD ORIENTATION</b>	<b>PARALLEL TO WING PLANE</b>	<b>90° TO WING PLANE</b>	<b>N/A</b>		
<b>INITIAL VELOCITY</b>	<b>180 m/s</b>	<b>181 m/s</b>	<b>183 m/s</b>	<b>186 m/s</b>	<b>187 m/s</b>
<b>INITIAL ROTATION</b>	<b>10.7 REV/SEC</b>	<b>6.6 REV/SEC</b>	<b>8.3 REV/SEC</b>	<b>8 REV/SEC</b>	<b>8.9 REV/SEC</b>
<b>IMPACT ANGLE TO WING SECTION OR SIDE WALL</b>	<b>24° (WING)</b>	<b>18.4° (WING)</b>	<b>21.6° (WING)</b>	<b>10° (SIDEWALL)</b>	<b>108° (WING)</b>
<b>DEFLECTION ANGLE OF FLIGHT PATH</b>	<b>8°</b>	<b>7°</b>	<b>NET YET AVAILABLE</b>	<b>0<sup>(7)</sup></b>	<b>9.8° TOWARD WING INTERIOR</b>
<b>POST IMPACT VELOCITY</b>	<b>135 m/s</b>	<b>98 m/s</b>	<b>137 m/s<sup>(2)</sup> 110 m/s<sup>(3)</sup></b>	<b>158 m/s<sup>(8)</sup></b>	<b>165 m/s</b>
<b>POST IMPACT ROTATION<sup>(5)</sup></b>	<b>2 REV/SEC</b>	<b>~0</b>	<b>3 REV/SEC<sup>(4)</sup></b>	<b>TBD</b>	<b>TBD</b>

- 1) AFTER WING SECTION AND WITNESS BOARD
- 2) AFTER WING ONLY
- 3) AFTER WING AND SIDEWALL COMBINED
- 4) RELATIVE TO INITIAL ROTATION AXIS - SPUN UP TO 4 REV/SEC ON ORTHOGONAL AXIS
- 5) PRELIMINARY
- 6) PAYLOAD BAY WALL SECTION ORIENTED 90° TO THE WING ROOT SECTION.
- 7) NO NOTICEABLE DEFLECTION PRIOR TO SECONDARY IMPACT WITH SIDEWALL SUPPORT
- 8) DETERMINED BEFORE SECONDARY IMPACT WITH SIDEWALL SUPPORT

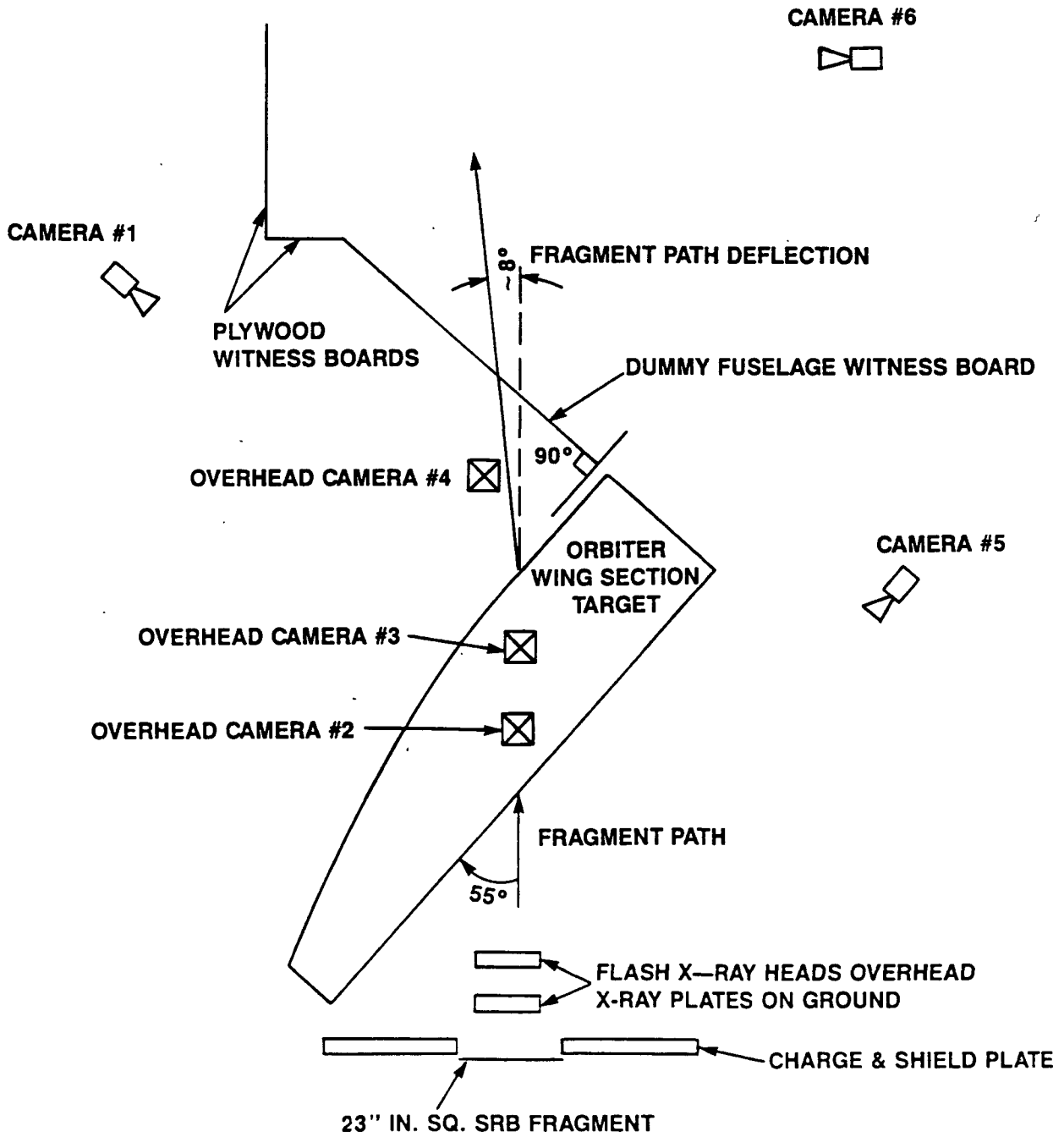


Figure G-27. FFT-2 Layout - Plan View

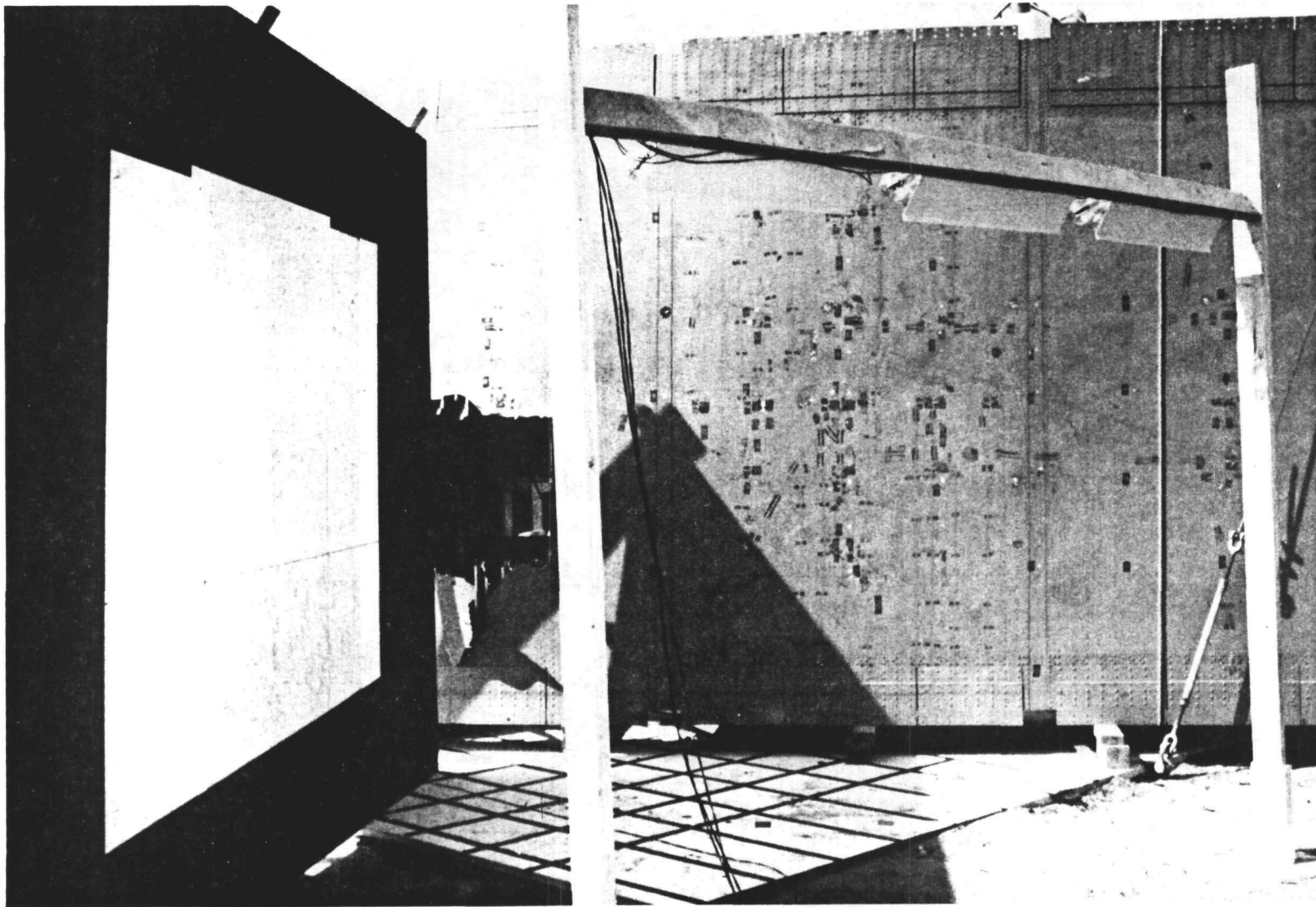


Figure G-28. Photograph Showing Wing Section and Sidewall Witness Board For FFT-2

G-79

MP2693/1889-736/JD

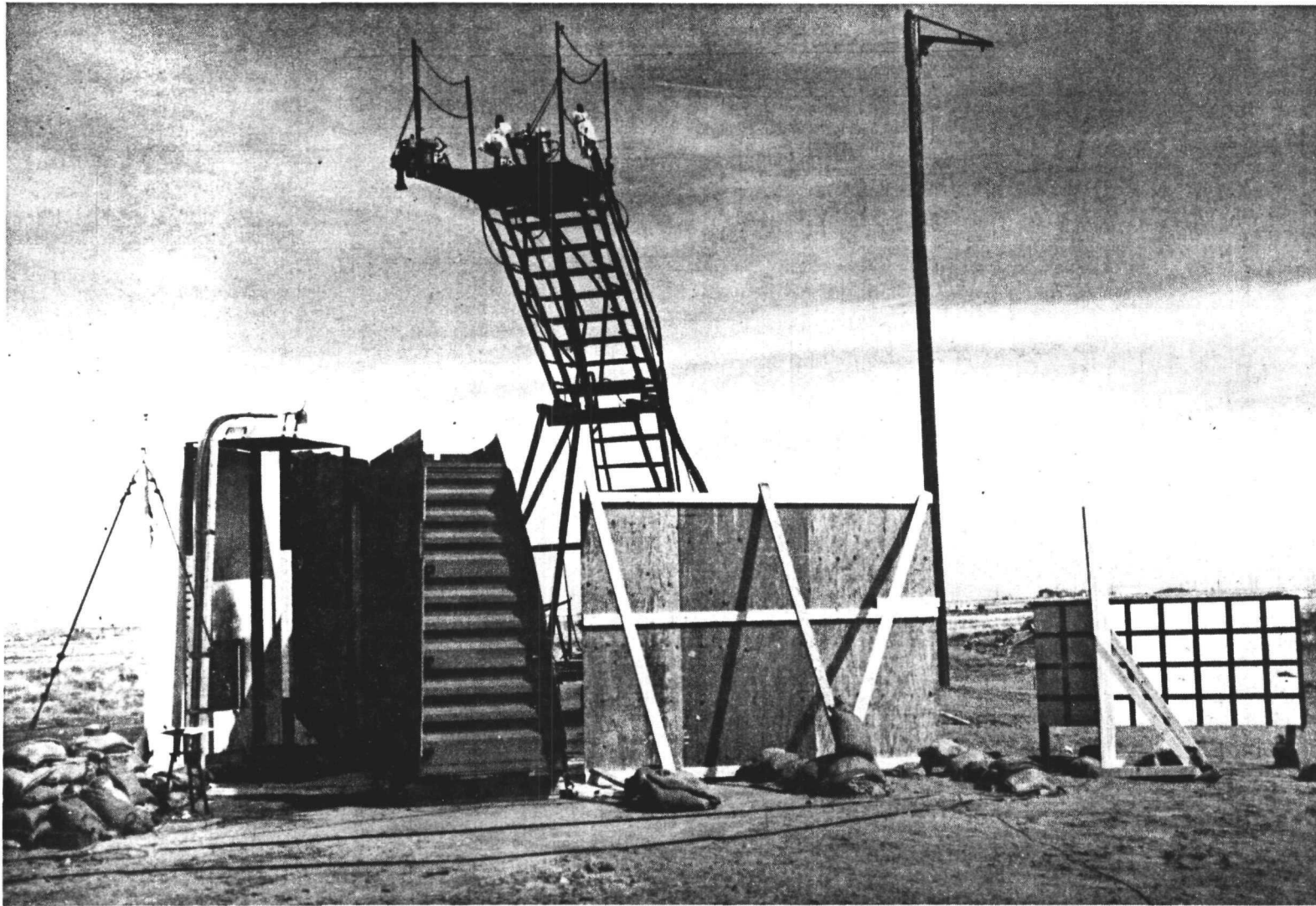


Figure G-29. Photograph Showing Alternate View of Test Arrangement  
For FFT-2

Figure G-30 shows the wing panel and witness board after the test. The hole through the wing under the goal post type structure (i.e., support for photo flash bulbs) is the exit area of the fragment; the witness board appears on the left of the picture. In this test, the velocity reduction was 46% after passage of the fragment through the wing section and the plywood board. The rotation rate was reduced essentially to zero.

The layout for test FFT-3 is shown on Figure G-31, and Figure G-32 shows the actual wing section and sidewall structure as configured for the test. The sidewall structure is to the right of the wing section, which has the two holes from FFT-1 and FFT-2. A rear view of the sidewall structure used in the test is shown on Figure G-33, with the wing structure end shown on the right. (As shown, the sidewall structure is actually positioned incorrectly with respect to the wing, but this was done to ensure that the fragment would intersect both surfaces of the wing section with its internal structure. In reality, and with respect to the wing section as positioned in Figure G-33, the sidewall section would be located at the top of the wing section in the picture and oriented horizontally with the main frame and stub frame pieces skyward.)

Figures G-34 and G-35 show the wing and fuselage sections after the test. Figure G-34 is essentially the same view as Figure G-32 but slightly closer. The exit hole through the wing is the bottom hole on Figure G-34. The fragment rotation, originally about an axis normal to the ground, was reduced significantly (roughly 64%), but a rotation was induced about the orthogonal or horizontal axis such that the fragment sliced through the sidewall section in an edge-on, practically horizontal orientation. The rear view of the sidewall section after the test is shown on Figure G-35 in which the slice through the section is more visible. Although the edge of the fragment sliced through the sidewall panel skin over the main frame, the frame was only nicked and not cut through as was the stub frame. The velocity reduction overall was 40% through both the wing and sidewall; that through only the wing was 25%. The rotation rate reduction about the axis of original spin was 64% as previously mentioned.

G-81

WP2693/1889-736/JD

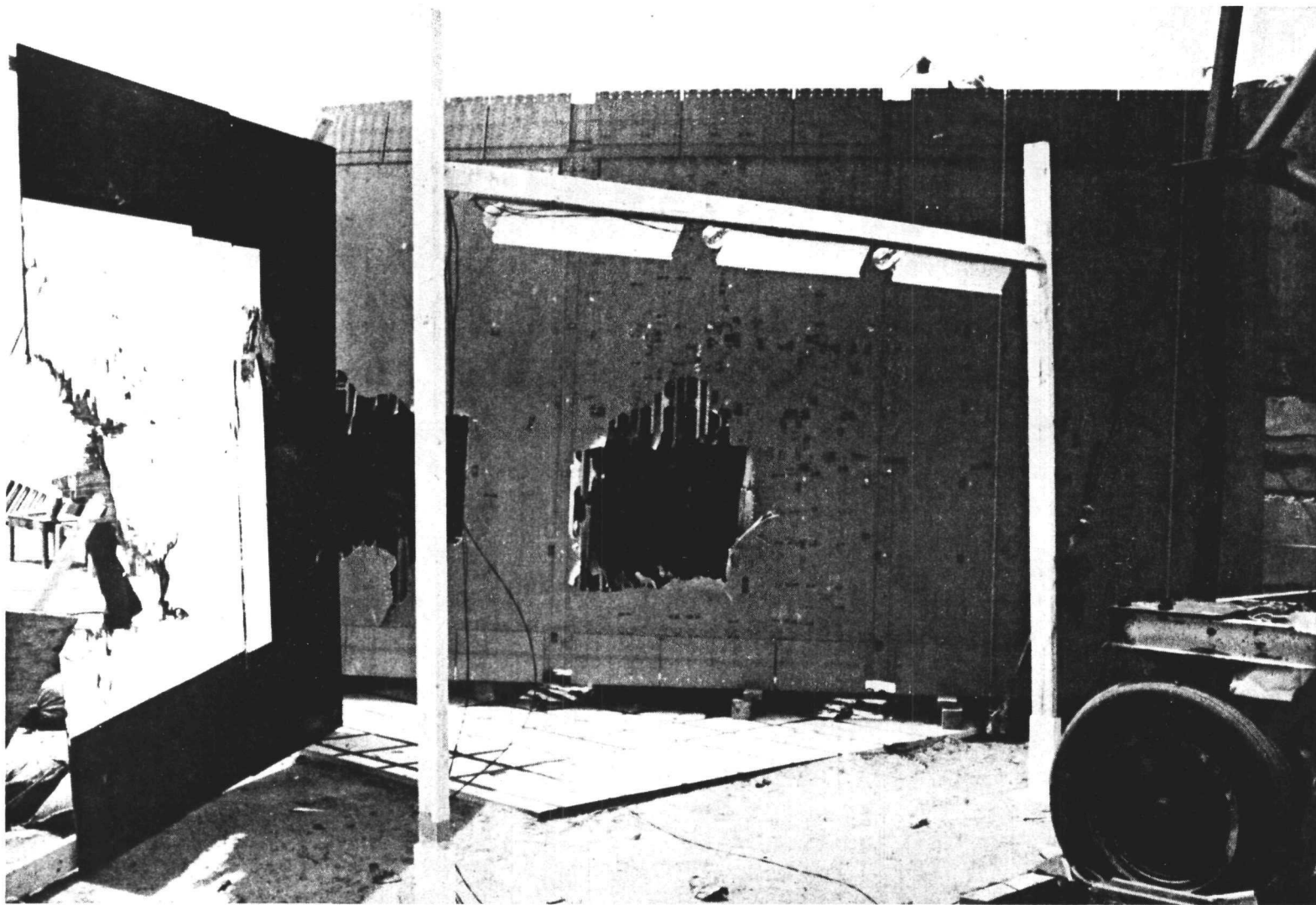


Figure G-30. Post-Test Photograph of FFT-2

FSAR  
APPENDIX G

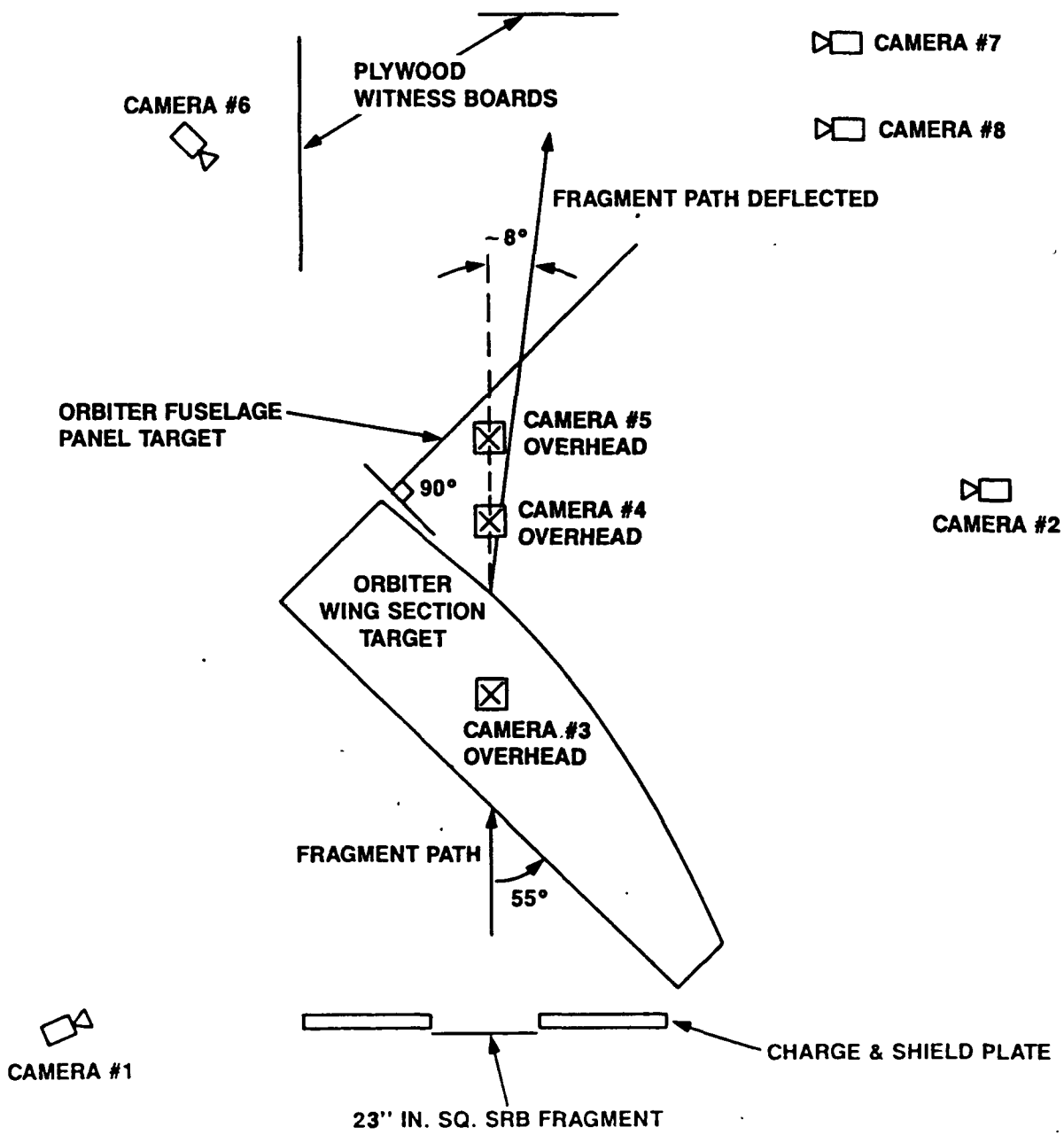


Figure G-31. FFT-3 Layout - Plan View



G-83

WP2693/1889-736/JD

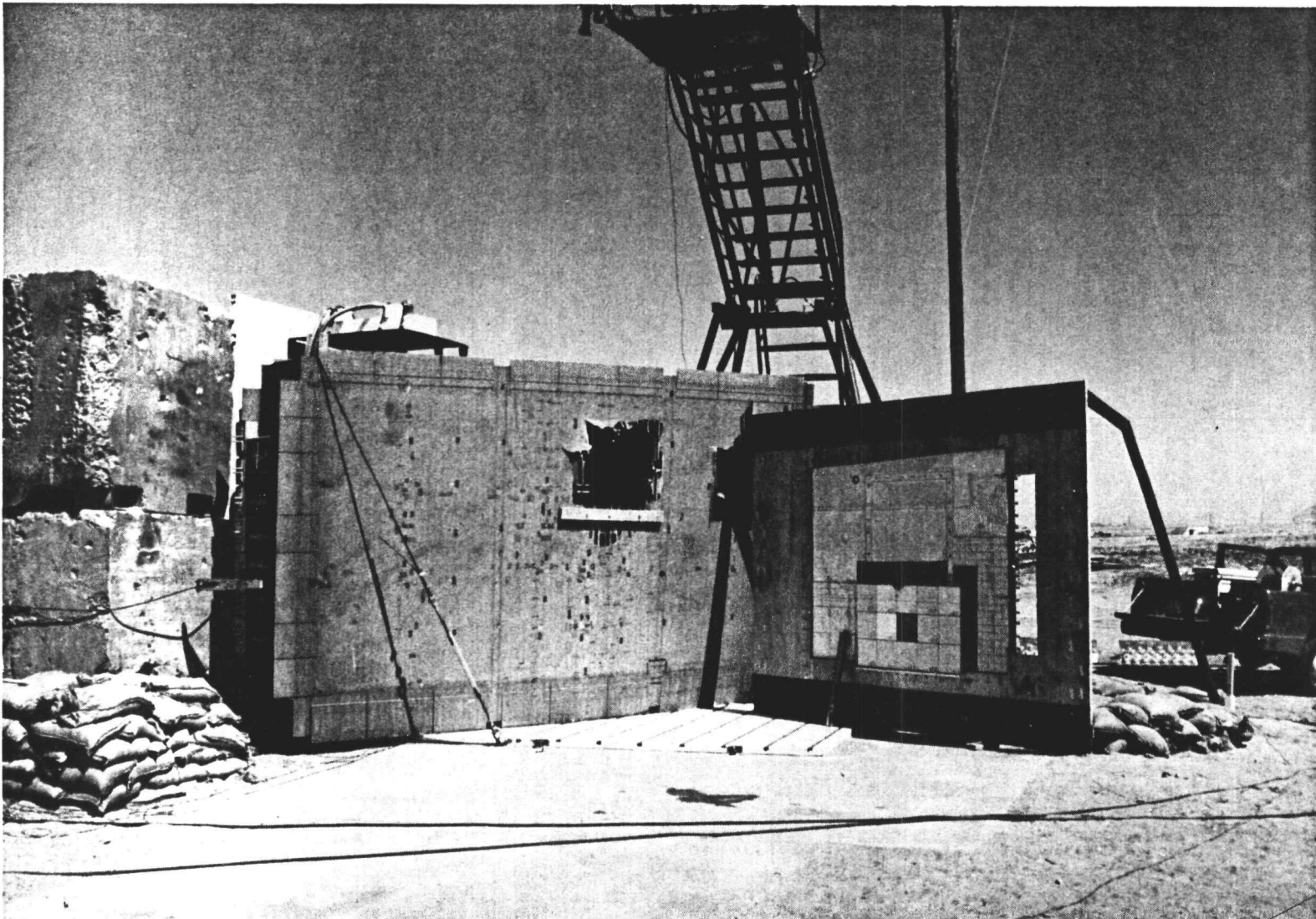


Figure G-32. Photograph of Test Arrangement for FFT-3

FSAR  
APPENDIX G

G-84

MP2693/1889-736/JD

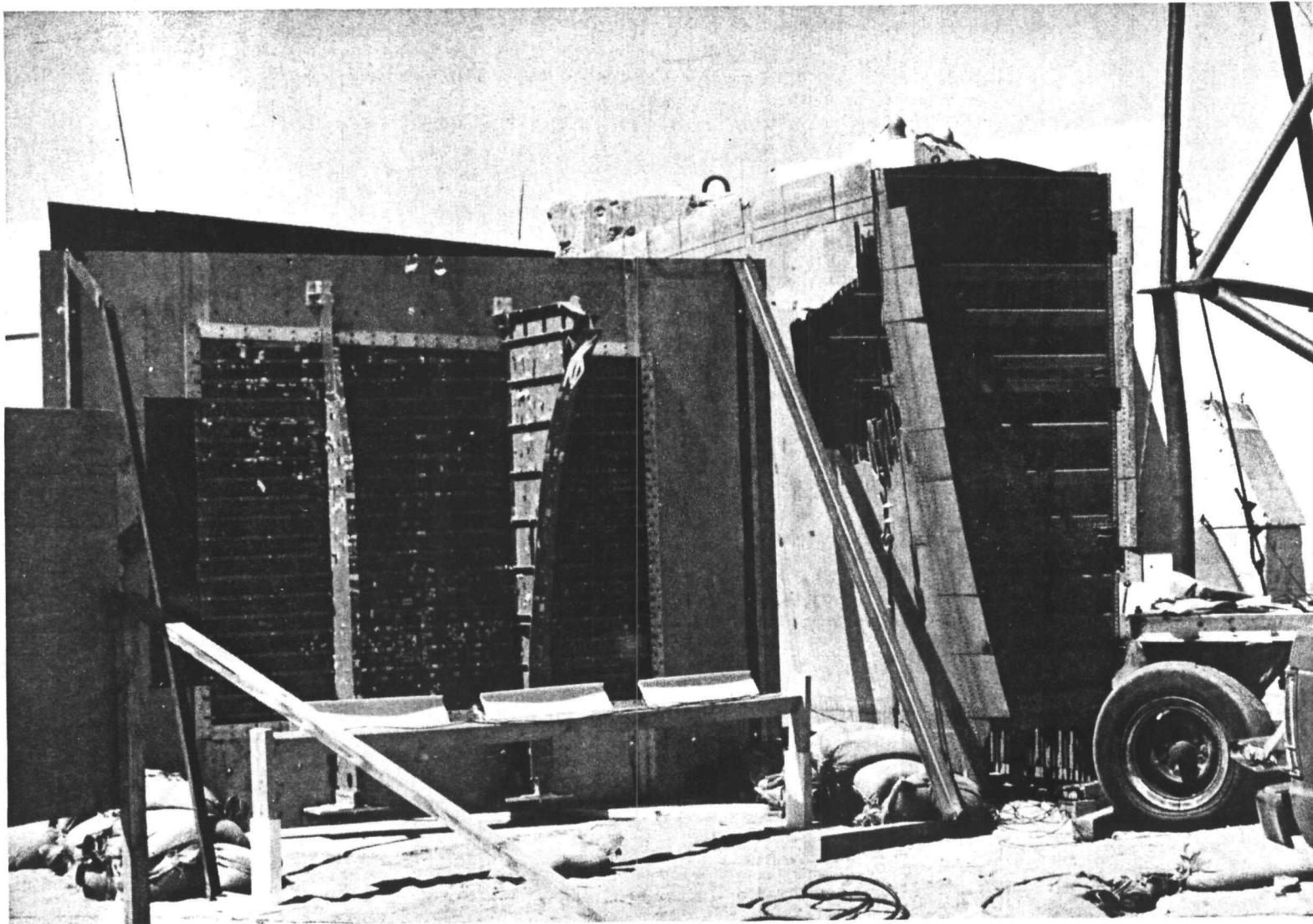


Figure G-33. Alternate View of Sidewall Section (Rear View) - FFT-3

FSAR  
APPENDIX G

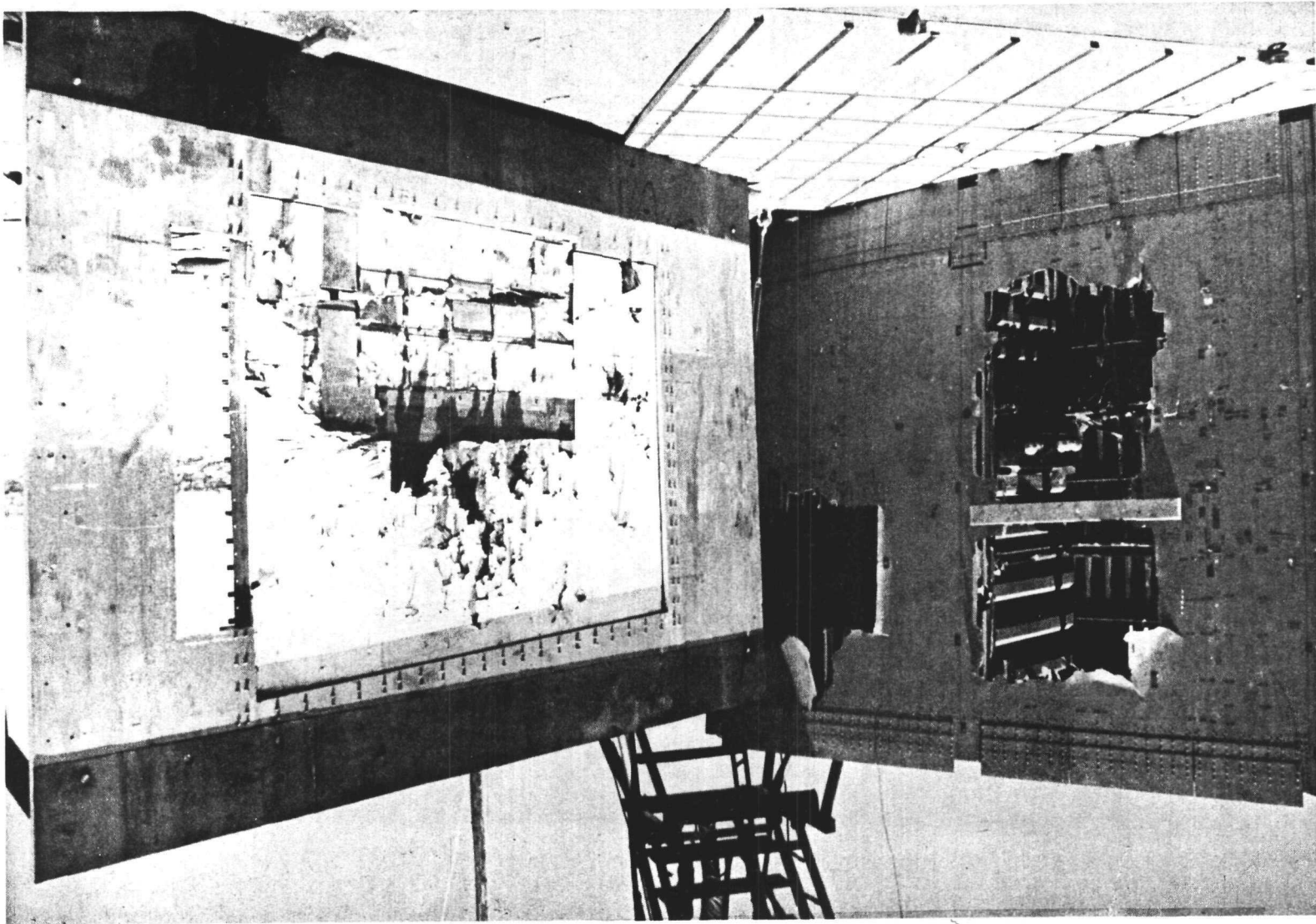


Figure G-34. Photograph of Wind and Sidewall Sections After FFT-3

G-85

MP2693/1889-736/JD

FSAR  
APPENDIX G

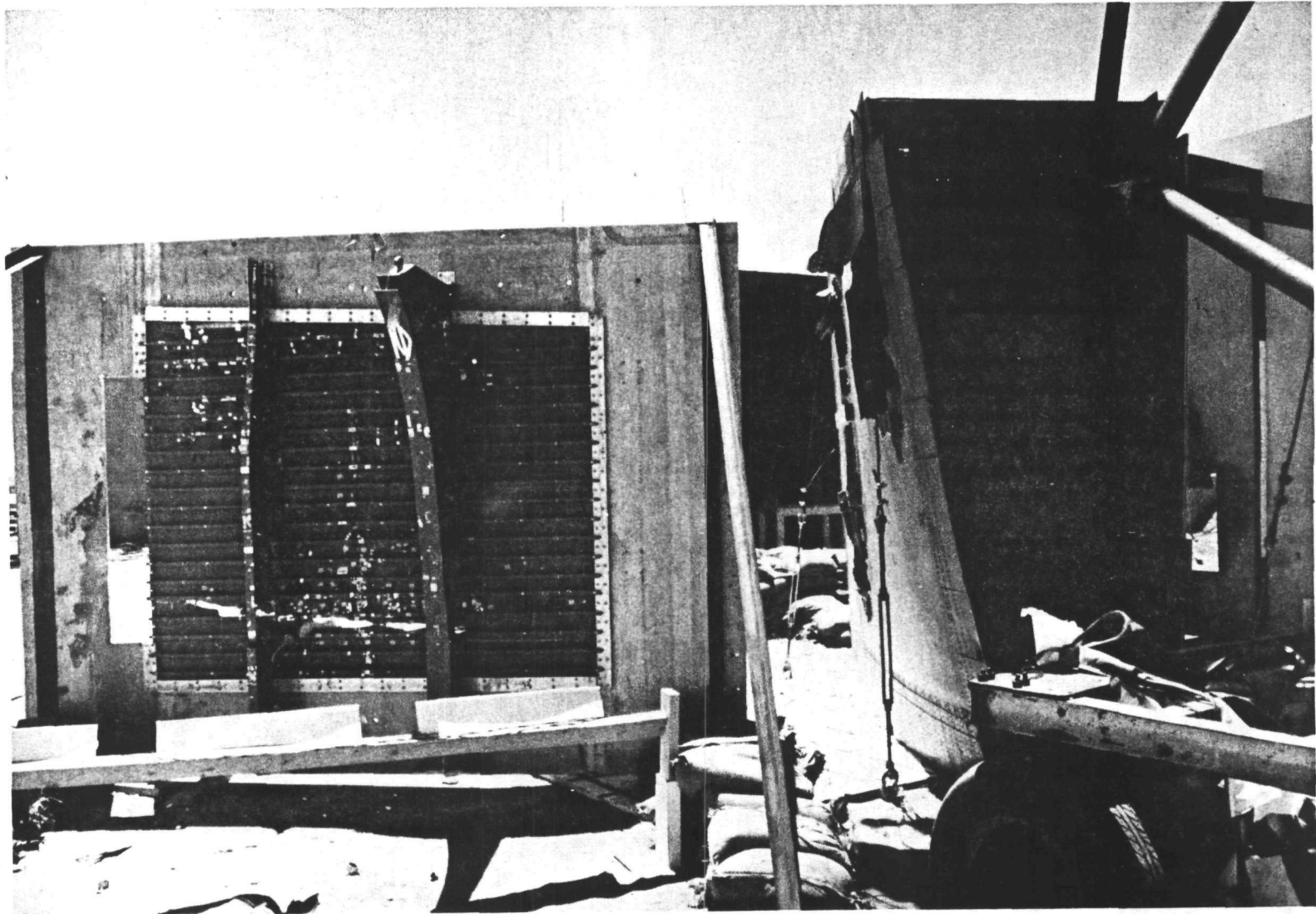


Figure G-35. Rear View of Sidewall Panel After Test FFT-3

Two additional fragment/fuselage tests were completed after the draft FSAR was issued. The fourth test (FFT-4) consisted of a 58.4 cm (23 inch)-square SRB fragment being explosively propelled into a MFA-08 sidewall section of the Orbiter payload bay at a point centered on the largest strut. The flight path of the fragment was at an angle of 42° to the plane of the sidewall section; the initial velocity and rotation rate were 186 m/s (610 fps) and 8 rev/sec, respectively. In test FFT-5, a 58.4 cm-square SRB fragment was propelled at a velocity of 187 m/s (613 fps) and a rotation rate of 8.9 rev/sec into the LI-30 Orbiter wing section; the fragment flight path was normal to the plane of the wing section. The spacing between the initial position of the fragment and the wing section was adjusted so that, at impact with the wing, the SRB fragment would have overrotated (i.e., rotated more than 90° from its original vertically oriented position). The purpose of this test was to determine if there was any difference in the velocity and rotation degradation as compared with the previous tests.

The results of these two tests are included in Table G-25. In test FFT-4 through only the sidewall section, the initial velocity was reduced by 15%. Test FFT-5 resulted in a velocity reduction of 11.8% as compared with 25% for FFT-1. The reduction in rotation rate for tests FFT-4 and FFT-5 was not available before the printing of the FSAR.

#### G.3.5 OTHER TESTS

The other test series was not completed in time to be included in this FSAR. These tests are the GIS Impact Tests (GIT). The results of these tests will be reported when they become available.

REFERENCES

- G-1 LA-9813-PR, "Space Nuclear Safety Program, January 1985," Los Alamos National Laboratory Progress Report, June 1983.
- G-2 LA-9839-PR, "Space Nuclear Safety Program, February 1983," Los Alamos National Laboratory Progress Report, September 1983.
- G-3 LA-9894-PR, "Space Nuclear Safety Program, March 1984," Los Alamos National Laboratory Progress Report, September 1983.
- G-4 GESP-7181, "GPHS-RTG System Explosion Test. DIRECT COURSE EXPERIMENT 5000," Advanced Energy Programs Department, General Electric Company, 1 March 1984.
- G-5 NUS-4543, Revised, "Report of the Space Transportation System (STS) Explosion Working Group (EWG)," NUS Corporation for the Department of Energy, July 8, 1985.
- G-6 "Report of the NASA Management Review Panel on the Safety of Shuttle RTG Missions," Dr. Aaron Cohen, Chairman, Lyndon B. Johnson Space Center transmitted to NASA Headquarters, D/Chief Engineer by cover letter dated February 5, 1985 from Dr. Cohen.
- G-7 Fairchild Presentation, "Analytical Studies. GPHS Response to Explosive Air Shocks," presented by Valley Forge, Pennsylvania, January 24, 1985.
- G-8 George, T.G., Tate, R.E., and Axler, K.M., "General-Purpose Heat Source Development: Safety Verification Test Program Bullet/Fragment Test Series," Los Alamos National Laboratory, LA-10364-MS, May 1985.
- G-9 George, T.G., "General-Purpose Heat Source Development: Safety Verification Test Program. Titanium Bullet/Fragment Test Series," LA-10724-MS, Los Alamos National Laboratory, June 1986.
- G-10 LA-9934-PR, "Space Nuclear Safety Program, June 1983," Los Alamos National Laboratory Progress Report, November 1983.
- G-11 Pavone, D., George, T.G., and Frantz, D.E., "General-Purpose Heat Source Safety Verification Test Series: SVT-1 through SVT-6," LA-10353-MS, Los Alamos National Laboratory, June 1985.
- G-12 George, T.G., and Pavone, D., "General-Purpose Heat Source Safety Verification Test Series: SVT-7 through SVT-10," LA-10408-MS, Los Alamos National Laboratory, September 1985.
- G-13 George, T.G., and Pavone, D., "General-Purpose Heat Source Safety Verification Test Series: SVT-11 through SVT-13," LA-10710-MS, Los Alamos National Laboratory, May 1986.

REFERENCES (Cont'd)

- G-14 Cull, T.A., George, T.G., and Pavone, D., "General-Purpose Heat Source Development: Safety Verification Test Program. Explosion Overpressure Test Series," Los Alamos National Laboratory, LA-10697-MS, September 1986.

APPENDIX H  
VAPORIZATION OF  $\text{PuO}_2$  IN A SPACE SHUTTLE FIREBALL

H.1 INTRODUCTION

This appendix describes analysis performed to determine the extent of vaporization of plutonium dioxide ( $\text{PuO}_2$ ) fuel due to exposure to the fireball resulting from a Shuttle explosion. The degree of vaporization depends upon the heat flux in the fireball, the initial size and size distribution of  $\text{PuO}_2$  particles and the length of time the particles are within the fireball. The analysis described herein is performed parametrically as a function of  $\text{PuO}_2$  particle size and as a function of time duration within the fireball for the two fireball heat flux curves provided by NASA in the Shuttle Data Book (Reference H-1).

H.2 RESULTS

Two models have been developed for the Shuttle fireball; a thermochemical model, and an experimental data model (Reference H-1). Figure H-1 shows the heat fluxes produced by these fireball models as a function of time. From these heat fluxes the fireball temperature can be determined. Figure H-2 gives the fireball temperature as a function of time for both models. The "thermochemical" model is an analytical curve which represents the theoretical upper limit for the fireball heat flux. The "experimental" model represents the upper limit of experimental data. The time scales shown on Figures H-1 and H-2 represent time from explosion of the propellants (zero seconds) to lift-off of the fireball stem (ten seconds). The parametric analysis described in this appendix are conducted for this ten-second time duration.

Figure H-1 shows the fireball heat flux dropping to very low values after stem lift-off. This heat flux discontinuity occurs for a fixed position near the ground but would not be expected for a location which moves with the fireball. Small particles which are swept up with the fireball, therefore, experience a more smooth dropoff of heat flux with time as shown in Figure H-1.



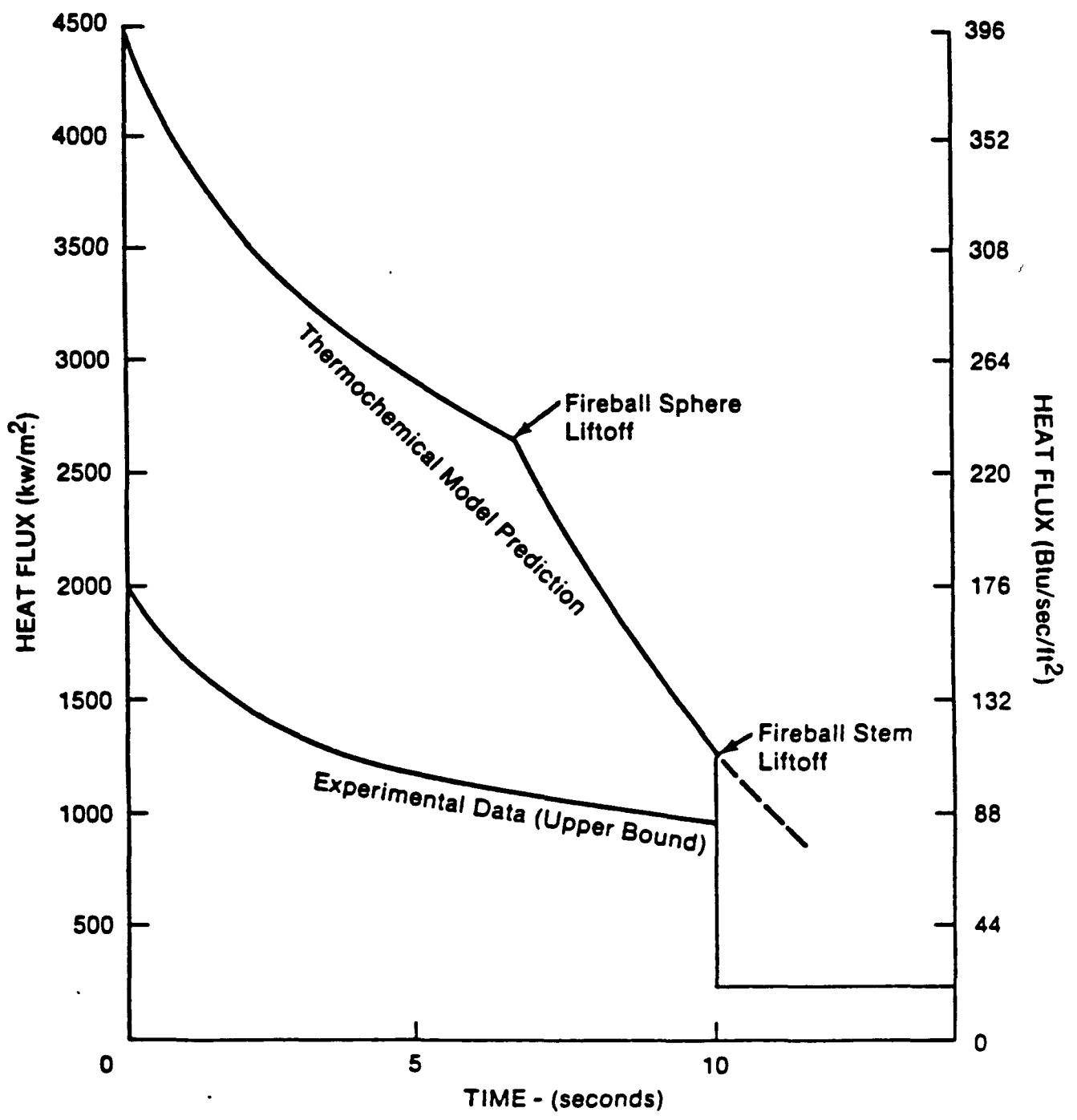


Figure H-1. Heat Flux vs. Time - For Space Shuttle Fireball

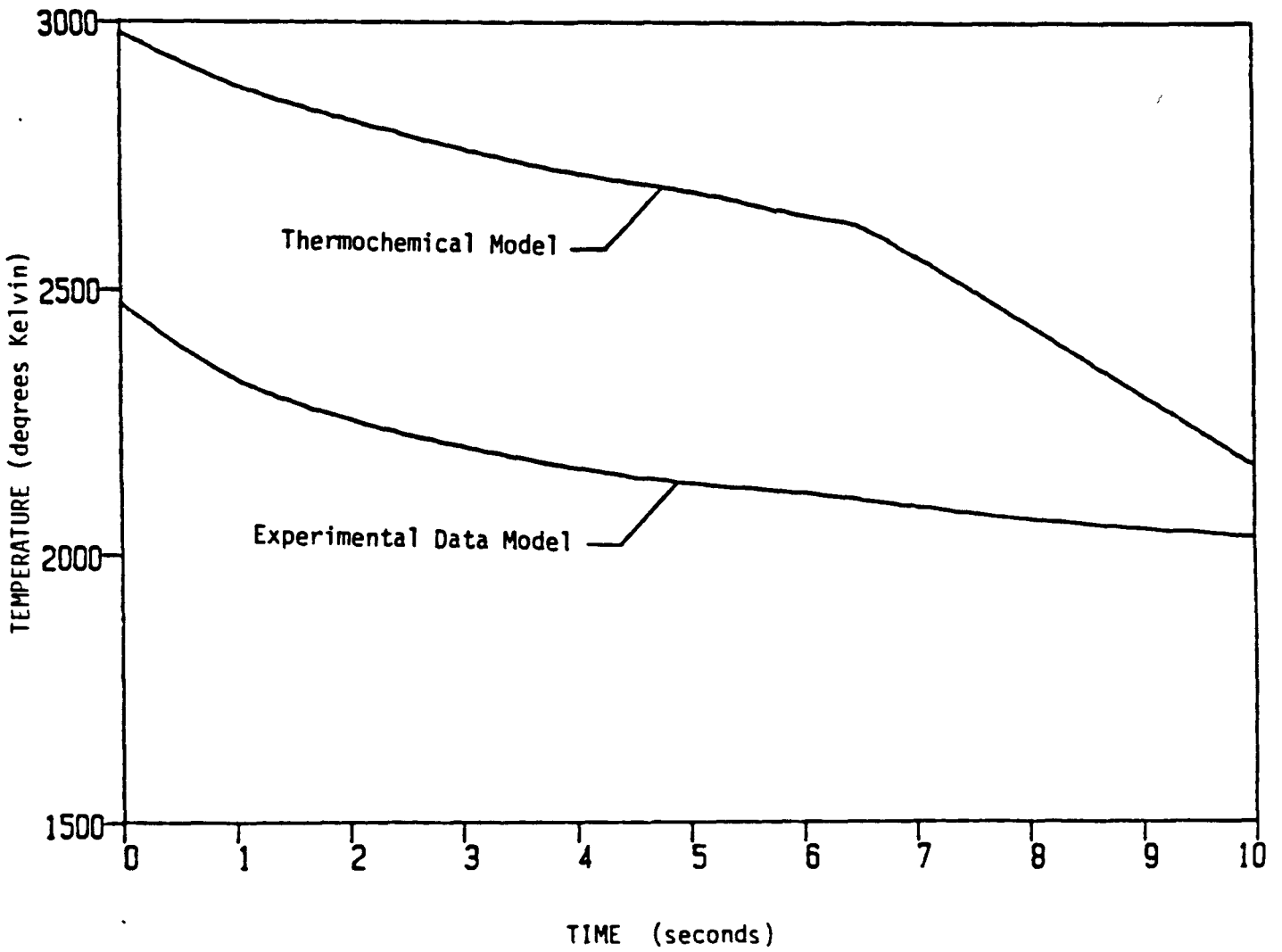


Figure H-2. Space Shuttle Fireball Temperatures as a Function of Time

These small particles can be exposed for longer times than the ten-seconds until stem lift-off. The calculated results presented in this appendix were not extended beyond the range of data provided by NASA. Relatively small additional vaporization would be expected however. First, the fireball heat flux levels and temperature would continue to drop after stem lift-off even within the fireball. The vaporization rate for particles entering the fireball at times near 9-10 seconds or beyond are two to three orders of magnitude less than the rate experienced near fireball initiation. In addition, the calculated results show that many small particles which could be carried up by the fireball are completely vaporized in the time before stem lift-off. Particles less than 5 microns, for the experimental model, and less than 74 microns, for the theoretical model, are completely removed. Finally, many particles exposed to the fireball enter it with appreciable velocities imparted by the original explosion or projectiles from the explosion and will leave the fireball before stem lift-off. No credit is taken for this type of reduced exposure. Overall, therefore, the results presented in this appendix are expected to be conservative, especially considering that even the lower heat flux curve is an upper limit of the test data.

The amount of vaporization which each particle size undergoes is computed for both fireball models. For a fixed fireball duration, the fraction of a particle vaporized is determined as a function of the time at which it is released into the fireball.

The calculated weight fraction of the  $\text{PuO}_2$  fuel particles vaporized as a function of time is given in Figures H-3 through H-6. Figures H-3 and H-4 are the results for the thermochemical fireball model, and the experimental data model results are given in Figures H-5 and H-6. The term, "time released into fireball", refers to the time which expires between fireball initiation and the fuel release into the fireball. If the time released into fireball is zero, fuel is exposed to the fireball for the full ten seconds prior to fireball stem lift-off.

PARTICLE SIZE: 6000 $\mu$  - 10  $\mu$

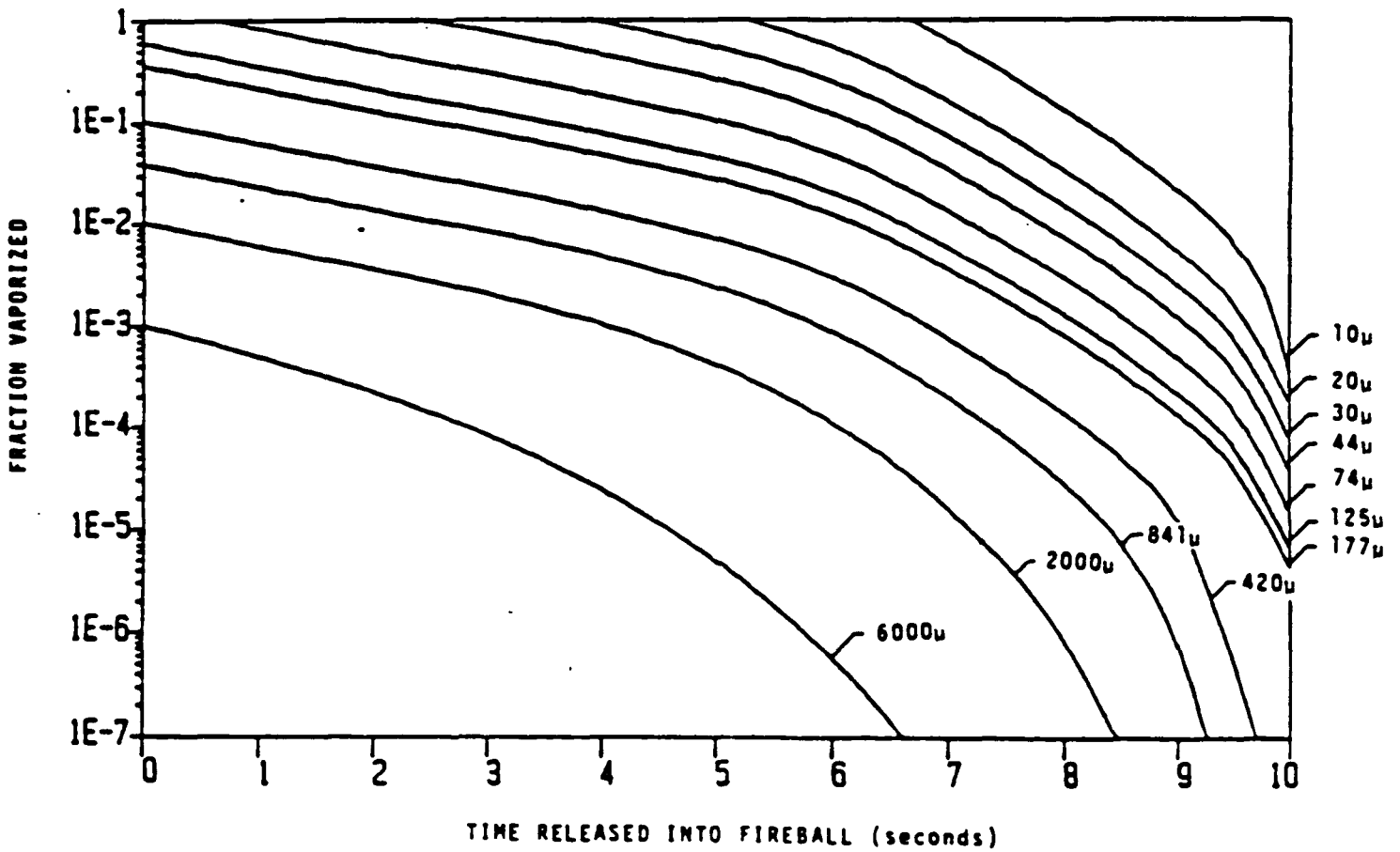


Figure H-3. Thermochemical Fireball Model Particle Vaporization as a Function of Time Released into Fireball

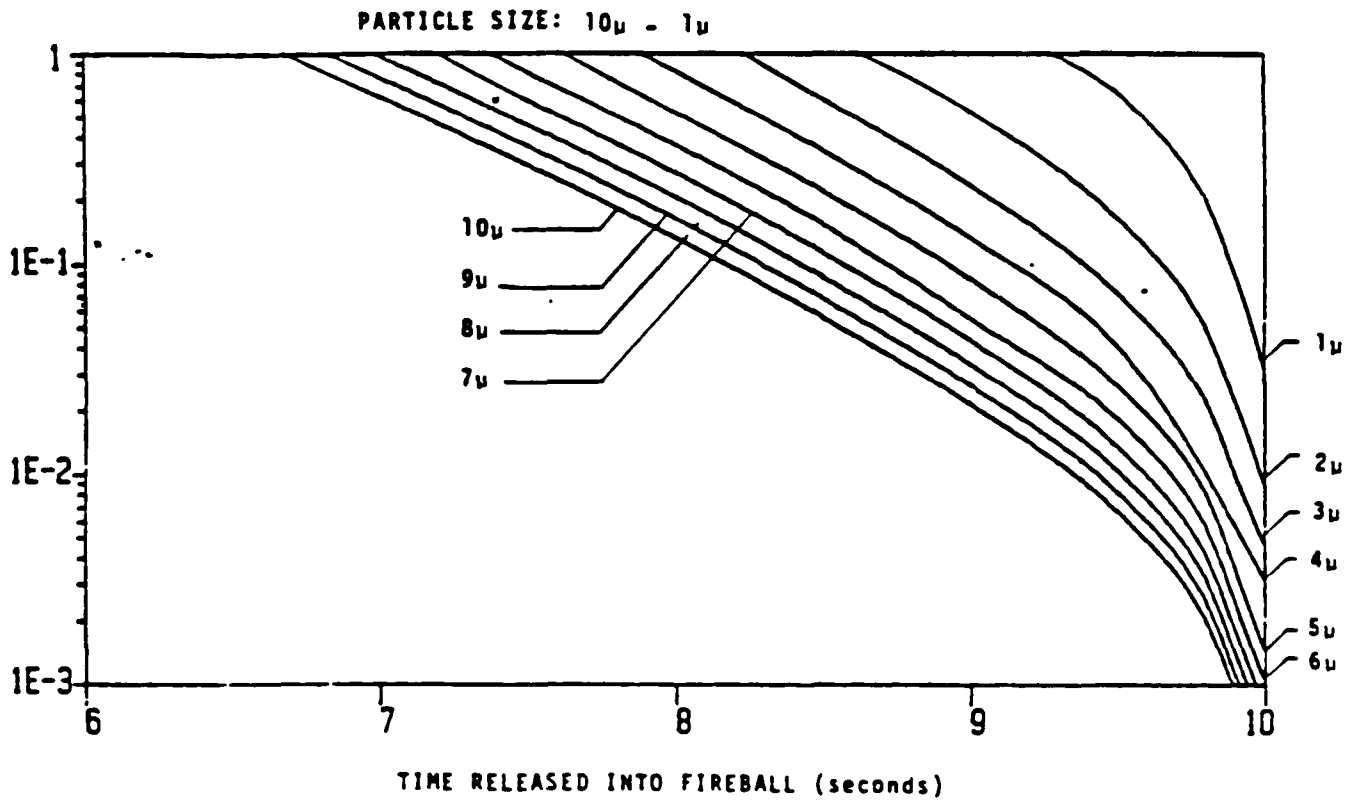


Figure H-4. Thermochemical Fireball Model Particle Vaporization as a Function of Time Released into Fireball

PARTICLE SIZE: 6000 $\mu$  - 10  $\mu$

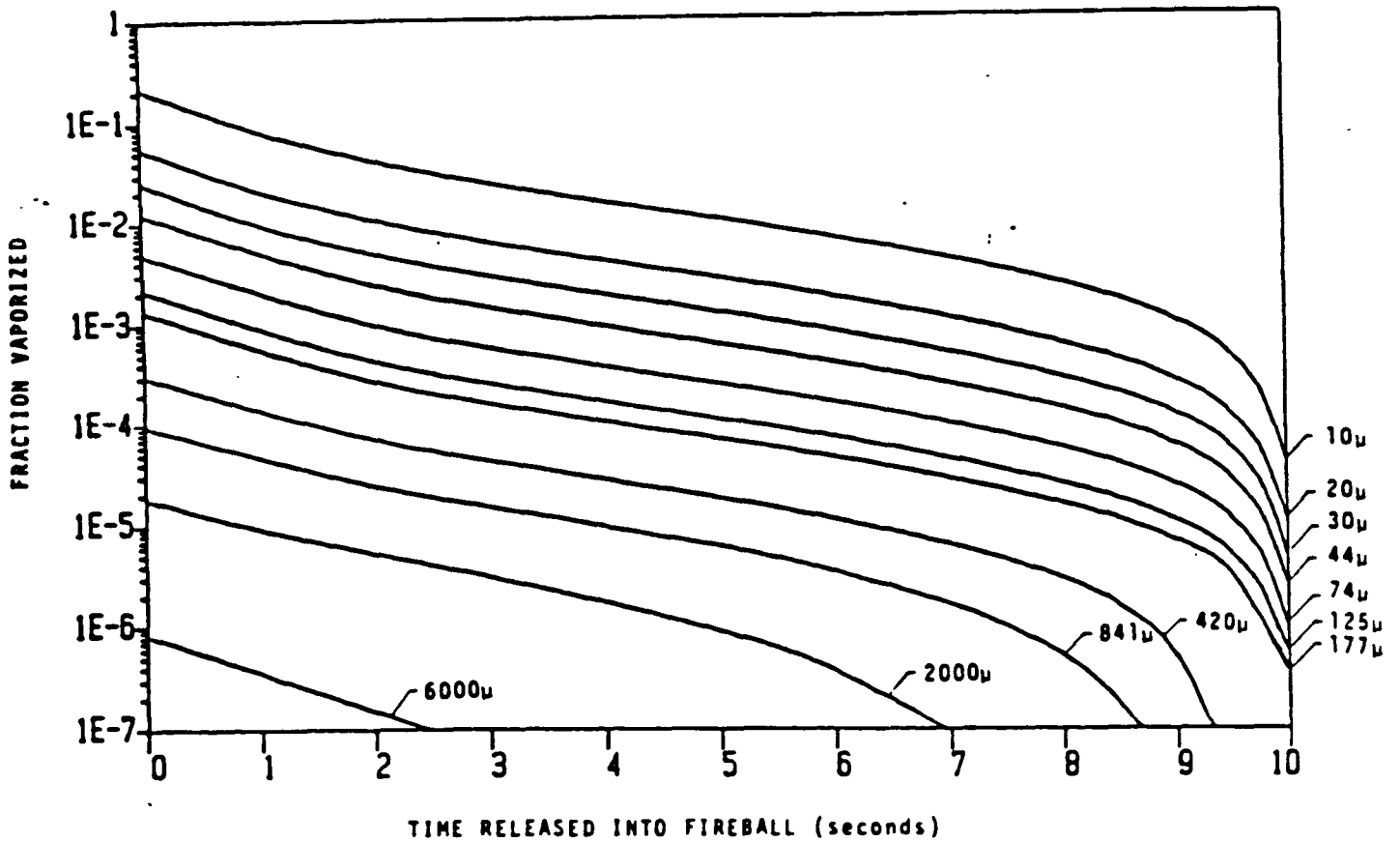


Figure H-5. Experimental Data Fireball Model Particle Vaporization as a Function of Time Released into Fireball

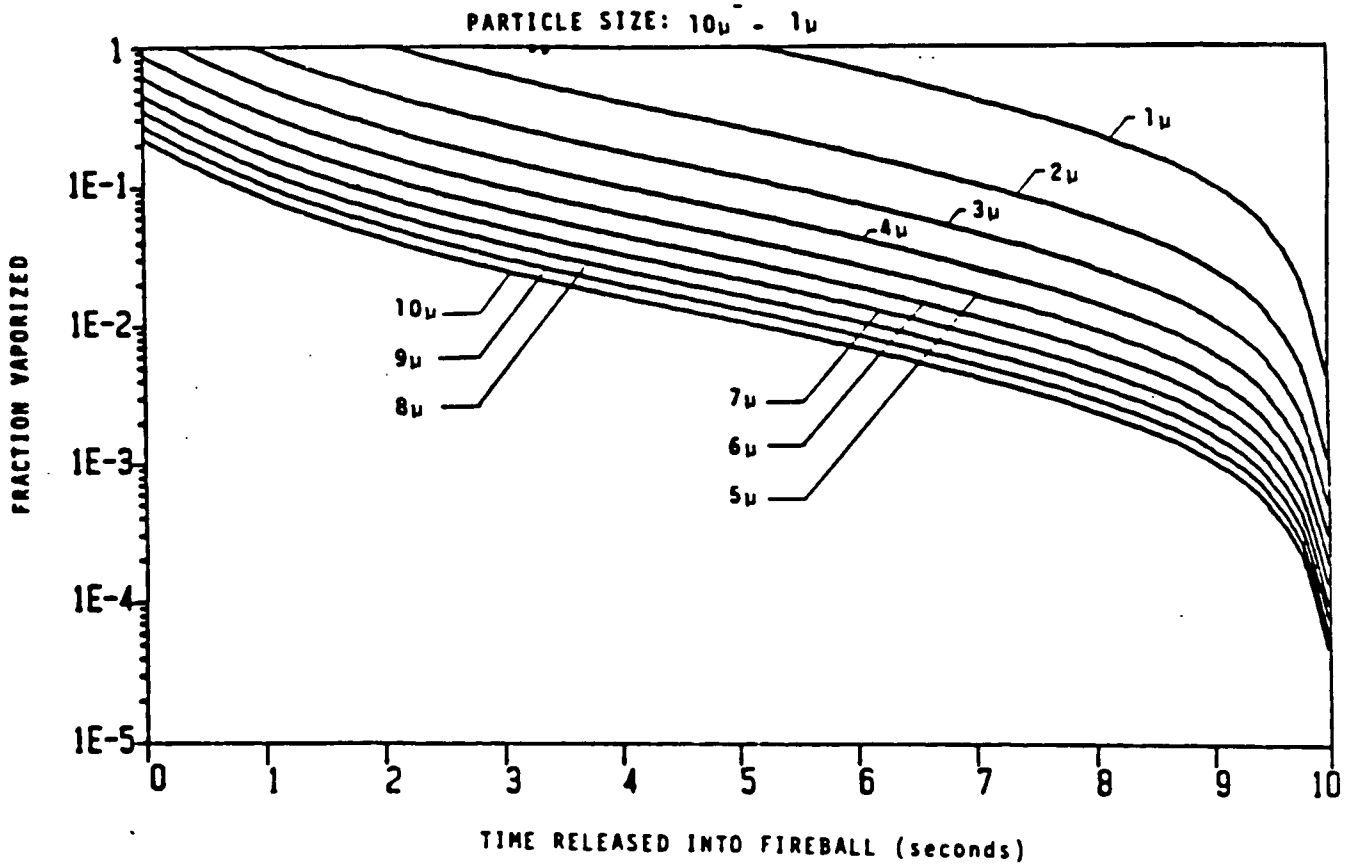


Figure H-6. Experimental Data Fireball Model Particle Vaporization as a Function of Time Released into Fireball

### H.3 ANALYSIS

This section presents the method used to determine the fraction vaporized of each of the PuO<sub>2</sub> particles. A listing and a description of the calculations performed are given, along with a summary of the computation process.

#### H.3.1 FIREBALL TEMPERATURE

As discussed in Reference H-1, the temperature in the fireball can be calculated by assuming that the flux is derived totally by radiation and that the combustion gases radiate as a black body with an emissivity of one. With this characterization, the fireball temperature is given as

$$T_{FB} = \left( \frac{Q_{FB}}{\sigma} \right)^{.25} \quad (1)$$

where

$T_{FB}$  is the absolute temperature of the fireball in K,  
 $Q_{FB}$  is the heat flux of the fireball in W/m<sup>2</sup>,  
 and  $\sigma$  is the Stefan-Boltzmann's constant ( $5.670 \times 10^{-8} \text{W/m}^2\text{K}^4$ )

#### H.3.2 VAPORIZATION MODEL

The analytical model used for the vaporization of the PuO<sub>2</sub> particles, given by Reference H-2, assumes that the particles are spherical, and that the vaporization is controlled by the rate of transfer of vapor away from the saturated boundary layer of the particle. The particle sizes listed in Table H-1 are relatively small, and as a result, the spherical particle assumption is valid.

The expression for the fraction of a spherical particle vaporized per unit time is given by



Table H-1. Fuel Particle Size Distribution (As Report from Test Data)

Particle Size (microns)	
>6000	
6000 - 2000	
2000 - 841	
841 - 420	
420 - 177	
177 - 125	
125 - 74	
44 - 30	
30 - 20	
20 - 10	
10 - 9	9
9 - 8	8
8 - 7	7
7 - 6	6
6 - 5	5
5 - 4	4
4 - 3	3
3 - 2	2
2 - 1	1
1 - 0	0

$$\frac{df}{dt} = 12 \frac{D_v}{\rho_p d_p^2} \left[ 1 + .276 R_e^{1/2} S_c^{1/3} \right] \frac{P_s M_p}{R T_p} \quad (2)$$

where

$D_v$  is the diffusion coefficient in  $\text{cm}^2/\text{sec}$ ,  
 $t$  is the time in seconds,  
 $\rho_p$  is the density of the fuel particle ( $10\text{g}/\text{cm}^3$ ),  
 $d_p$  is the diameter of the particle in cm,  
 $R_e$  is the Reynolds number,  
 $S_c$  is the Schmidt number,  
 $M_p$  is the molecular weight of the particle in g/mol.,  
 $R$  is the gas constant  $82.057 \text{ cm}^3 \text{ ATM}/\text{K mol}$ ,  
 $T_p$  is the absolute temperature of the particle in K,  
and  $P_s$  is the sum of the saturated vapor pressures in atmospheres of all the plutonium species present.

The value of the diffusion coefficient for the plutonium vapors diffusing into the combustion gases is required. An empirical relationship for the diffusion coefficient in gases, as shown by Reference H-3, is

$$D_v = 435.7 \frac{T^{3/2}}{P (V_A^{1/3} + V_B^{1/3})} \sqrt{\frac{1}{M_A} + \frac{1}{M_B}} \quad (3)$$

where

$D_v$  is in  $\text{cm}^2/\text{sec}$ ,  
 $T$  is absolute temperature in K,  
 $P$  is the total system pressure in  $\text{Newtons}/\text{m}^2$ ,  
 $V_A, V_B$  are the molecular volumes of the constituents A and B,  
and  $M_A, M_B$  are the corresponding molecular weights.

A problem encountered with using Equation (3) to compute the diffusion coefficient is that a complete knowledge of the composition of the fireball combustion gases is necessary. Reference H-1 has identified the fireball

propellant to be a combination of LOX and LH<sub>2</sub> (liquid oxygen and liquid hydrogen LOX/LH<sub>2</sub>). The combustion of such a combination results in the production of water vapor. The gaseous composition of the fireball is, then, a complex combination of water vapor, unburned propellants, and air which becomes entrapped by the fireball. As a result the exact composition of the fireball combustion gases is indeterminable. Reference H-2 provides a diffusion coefficient of

$$D_V = 5.402 \text{ cm}^2/\text{sec} \quad (4)$$

for the diffusion of plutonium vapors into the combustion gases of the fireball at 2700K, resulting from the explosion of hydrocarbon propellants. There is no available information on the diffusion coefficient of plutonium vapors into the combustion gases of LOX/LH<sub>2</sub> fireballs. A diffusion coefficient, based on the assumption that the combustion gases of the LOX/LH<sub>2</sub> fireball are the same as air, could be calculated from Equation (3). The value obtained from this calculation would, however, underestimate the actual value of the diffusion coefficient. Instead, the diffusion coefficient given by the hydrocarbon fireball is assumed to be similar to that of the LOX/LH<sub>2</sub> fireball. This is a reasonable estimation for the diffusion coefficient since both fireballs contain entrapped air, and the values of the molecular weights and molecular volumes of the combustion gases of both fireballs have the same order of magnitude. From Equation (3) it is seen that at constant pressure, the value of the diffusion coefficient varies proportionally to the temperature raised to the 3/2 power. Utilizing Equation (4), the value of the diffusion coefficient may then be computed at any temperature from the expression

$$D_V = 5.402 \left( \frac{T_{FB}}{2700} \right)^{3/2} \quad (5)$$

Reference H-2 points out that the diffusion coefficient may be in error by a factor of two. In addition, the plutonium vapor pressure employed in the vaporization calculations (Equation (2)) is a strong function of temperature in the range of interest. The calculated vaporization fraction, therefore, may have significant uncertainty.

The Reynolds number is computed from the relationship

$$R_e = \frac{Vd_p}{\nu} \quad (6)$$

where

$V$  is the velocity of the particle in cm/sec,  
 $d_p$  is the diameter of the particle in cm,  
 and  $\nu$  is the kinematic viscosity of the fireball combustion gases in  $\text{cm}^2/\text{sec}$ .

The kinematic viscosity of the fireball is evaluated as the kinematic viscosity of air. The water vapor and the unburned propellant of the fireball are neglected. This is a conservative approximation of the fireball viscosity since the viscosities of the water vapor and propellant are greater than that of air.

The velocity of the particle is taken to be the terminal fall velocity as shown by Reference H-2. A justification for this assumption is also provided in Reference H-2. The terminal fall velocity is given by the equation

$$V_T = \sqrt{\frac{4 G \rho_p d_p}{3 \rho_{\text{GAS}} C_D}} \quad (7)$$

where

$G$  is the acceleration due to gravity ( $980 \text{ cm}/\text{sec}^2$ ),  
 $\rho_p$  is the density of the particle ( $10\text{g}/\text{cm}^3$ ),  
 $d_p$  is the diameter of the particle cm,  
 $\rho_{\text{GAS}}$  is the density of the fireball combustion gases in  $\text{g}/\text{cm}^3$ ,  
 and  $C_D$  is the drag coefficient for a sphere.

The density of the fireball combustion gases is approximated to be that of air. This is a conservative approximation since the actual fireball density is greater than that of air. The drag coefficient for a sphere was obtained from Reference H-4 and is shown in Figure H-7 as a function of Reynolds number.

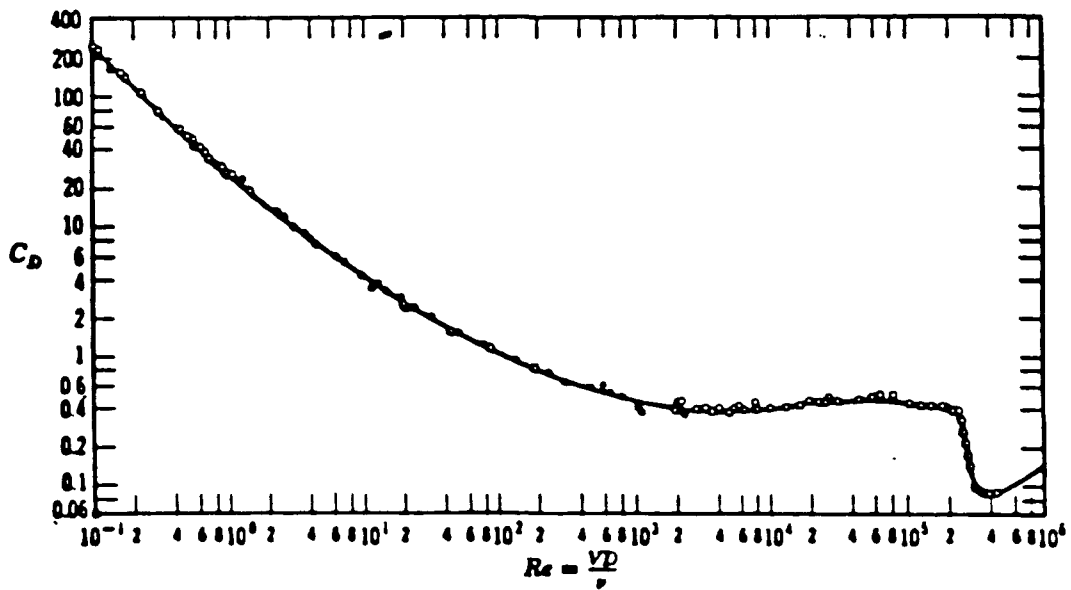


Figure H-7. Drag Coefficient of a Sphere as a Function of Reynolds Number

The Schmidt number is computed from the expression

$$S_c = \frac{\nu}{D_v} \quad (8)$$

where the values of  $\nu$  and  $D_v$  are discussed previously.

The only variable of Equation (2) remaining to be defined is the sum of the saturated vapor pressures of the fuel particle. This value is defined by

$$P_s = 10 \left[ 7.5 - \frac{29260}{T_p} \right] \quad (9)$$

where

$P_s$  is in atmospheres,  
and  $T_p$  is the absolute temperature of the particle in K.

### H.3.3 TEMPERATURE RESPONSE OF THE VAPORIZING PARTICLE

It is shown in Reference H-2 that for particle sizes less than 200 microns, the thermal lag is inconsequential, and the particle temperature is always equal to the fireball temperature. For particle sizes greater than 200 microns, the thermal capacity of the particle becomes significant, and the thermal lag must be considered. The thermal response of larger particles can be determined from the following time derivative expression.

$$\frac{dT_p}{dt} = \frac{6\epsilon_p \sigma}{C_p \rho_p d_p} \left[ T_{FB}^4 - T_p^4 \right] \quad (10)$$

where

$T_p$  is the absolute temperature of the particle in K,  
 $T_{FB}$  is the absolute temperature of the fireball in K,  
 $\epsilon_p$  is the emissivity of the particle, which is given by Reference 4 to be 0.5,

$\sigma$  is the Stefan-Boltzmann constant,  $1.335 \times 10^{-12}$  cal/cm<sup>2</sup>K<sup>4</sup> sec  
 $\rho_p$  is the density of the particle,  
 $C_p$  is the specific heat of the particle, 0.083 cal/gmK  
 and  $d_p$  is the diameter of the particle in cm.

Equation (10) is based upon heating of the particle by radiation only. This assumption is valid for particle sizes greater than 200 microns. The initial temperature of the particle at the time in which it is released into the fireball is taken to be 1516K. This is the average temperature of the fuel when the GPHS (General Purpose Heat Source) is stored in the ACS (Active Cooling System).

#### H.3.4 CALCULATING THE FRACTION VAPORIZED

The fraction vaporized of a particle size is calculated by first determining the fireball temperature as a function of time. Figure H-2 was used to get  $T_{FB}(t)$ , where  $t$  represents time in seconds. If the particle size is larger than 200 microns, then Equation (10) is integrated to determine the particle temperature as a function of time. Equation (10) was integrated numerically to give  $T_p(t)$ . The numerical integration technique used is given in Reference H-5. If the particle size is less than 200 microns, the particle temperature is equal to the fireball temperature, thus  $T_{FB}(t) = T_p(t)$ . The particle temperature as a function of time is then substituted into Equation (9) to get the fuel particle saturation pressure as a function of time. The expression for  $P_s(t)$  is then substituted into Equation (2). Using the same numerical technique as before, Equation (2) is integrated resulting in the fraction vaporized. The bounds of the integrations were between the times of the fuel particle release into the fireball, and the fireball stem lift-off.

#### H.4 DEVELOPMENT OF SOURCE TERMS

The data contained here has been used to compute the source terms for the vaporization of PuO<sub>2</sub> resulting from a space shuttle explosion.

The vaporizations resulting from the Experimental Data Model heat flux (results of Figures H-5 and H-6) were used. As indicated in Reference H-1, this heating provides the expected or average envelope for the heat flux versus time. In computing the source terms, the resulting vaporization fraction for each particle size was determined, and using the distribution appropriate for fragment impacts, the resulting amount of vaporized fuel for each particle size was determined. The total vaporization was determined by summing the amounts calculated for each particle size.

In treating the vaporization at each particle size it was assumed that all the  $\text{PuO}_2$  is released into the fireball at time zero (fireball initiation), and that all the particles reside within the fireball for the duration before lift-off. The kinetics of the situation would indicate that, in fact, most of the fuel would enter the fireball after it had developed for some time and that much of the fuel that entered the fireball would not stay there until all of the heating was completed. At this time, however, detailed computation describing these kinematics are not available and in lieu of such a detailed description the assumption of full duration until lift-off has been made.

## H.5 REFERENCES

- H-1 Space Shuttle Data for Planetary Mission Radioisotope Thermoelectric Generator (RTG) Safety Analysis, NASA, JSC 08118, February 15, 1985.
- H-2 Williams, David C., "Vaporization of Radioisotope Fuels in Launch Vehicle Abort Fires," SC-RR-71 0118, December 1971.
- H-3 Holman, J.P., Heat Transfer, McGraw Hill Co., New York, NY, 1978.
- H-4 Fox, Robert M., McDonald, A.T., Fluid Mechanics, John Wiley and Sons, Inc., New York, NY, 1978.
- H-5 IMSL User's Manual, "Differential Equations", Vol. 1, pgs: Dgear 1-10, IMSL Inc., November 1984.



APPENDIX I  
RTG/GPHS REENTRY RESPONSE

I.1 INTRODUCTION AND BACKGROUND

This appendix presents the analyses that were previously conducted to determine the response of the GPHS-RTG to the various types of reentry conditions that could be imposed due to malfunctions that could occur in the Centaur upper stage as originally planned for the 1986 launches of Galileo and Ulysses. These analyses were largely completed and presented in the Updated Safety Analysis Report (USAR - Reference I-1), and were reported also in the previous Final Safety Analysis Report (FSAR - GESP 7200, 8 October 1985) for Galileo and Ulysses. They are provided in this FSAR for completeness and to provide a continuity of the overall reentry analytical effort.

Some of the general conclusions drawn from the original reentry analysis (i.e., as related to Centaur malfunctions) are as follows:

- The GPHS aeroshell will withstand the forces of reentry.
- Reentry of bare fuel clads will result in melting and loss of the iridium fuel clad and some vaporization of the fuel.
- Reentry of the Graphite Impact Shell, without the aeroshell, will not cause fueled clad melting.

I.1.1 INITIAL REENTRY CONDITIONS

The reentry conditions of interest are those that can occur after the initial Earth orbit (parking orbit) is attained. These conditions can occur as a result of malfunctions taking place in the Centaur such that the Centaur either cannot be propelled beyond the parking orbit or there is a stable and misaligned burn. As defined for purposes of the analyses, a reentry occurs when the Shuttle, Centaur, or spacecraft encounters the sensible atmosphere at a geodetic altitude of 400,000 feet after having first proceeded beyond this altitude.

There are other malfunctions that can occur during the ascent portion of the trajectory that will prevent the launch vehicle and spacecraft from leaving the sensible atmosphere (400,000 feet altitude). In these situations, the Orbiter might return for a controlled landing with the Centaur/spacecraft still aboard, or if other damage or malfunction prevents this, the Orbiter can fall back to Earth on a ballistic trajectory. The payload can still experience aerodynamic heating and loading, but this will be less severe than that from orbit since the energy of the vehicle will be lower. For these reasons, ballistic reentry trajectories prior to orbit have not been analyzed.

The potential envelope of initial reentry conditions (i.e., velocity and flight path angle, also designated  $V$ ,  $\gamma$ ) is obtained from Section 11 of the Shuttle Data Book (JSC-08116). Figures I-A through I-F show the results for Galileo and Ulysses as determined from the NASA Jet Propulsion Laboratory (JPL) study included in JSC-08116. These figures present the reentry conditions arising from potential failure modes in the Centaur guidance system including:

- Altered target vector data in DCU Memory module
- Improper output from the DCU Analog to Digital Converter
- Large drift rate (during coast) in the IMG gyro
- IMG accelerometer failure

All of these failures, except for the accelerometer, are capable of producing random orientations; the accelerometer failure will cause the Centaur to rotate toward the axis containing the failed accelerometer, resulting in preferential pitch down misalignments for failure of a radially-located accelerometer.

Tables I-1 and I-2 present the mission probabilities for the possible reentry types for Galileo and Ulysses, respectively, resulting from the General Dynamics/Convair study included in the Shuttle Data Book. They combine the Centaur guidance failure probabilities with the conditional probabilities of occurrence for the types of reentries related to the results shown in Figures I-A and I-B. The conditional probabilities are shown also in the

Table I-1. Superorbital Reentry Probabilities for Centaur  
 (Galileo Mission)

Centaur Random Misorientation Probability (x10 <sup>-6</sup> )	Resultant Orbit		Probability of Occurrence (x10 <sup>-6</sup> )
	Type	Cond. Prob. (%)	
76	Escape	28	21
	Elliptic Decay	3	2
	Elliptic Delayed	24	18
	Elliptic Prompt	2	1
	Powered Entry	43	33
Centaur Preferential Misorientation (x10 <sup>-6</sup> ) 23	Powered Entry	100	23

Table I-2. Superorbital Reentry Probabilities for Centaur (Ulysses)

Centaur Random Misorientation Probability (x10 <sup>-6</sup> )	Resultant Orbit		Probability of Occurrence (x10 <sup>-6</sup> )
	Type	Cond. Prob. (%)	
76	Escape	35	27
	Elliptic Decay	2	1
	Elliptic Delayed	18	14
	Elliptic Prompt	2	1
	Powered Entry	43	33
Centaur Preferential Misorientation (x10 <sup>-6</sup> ) 23	Powered Entry	100	23

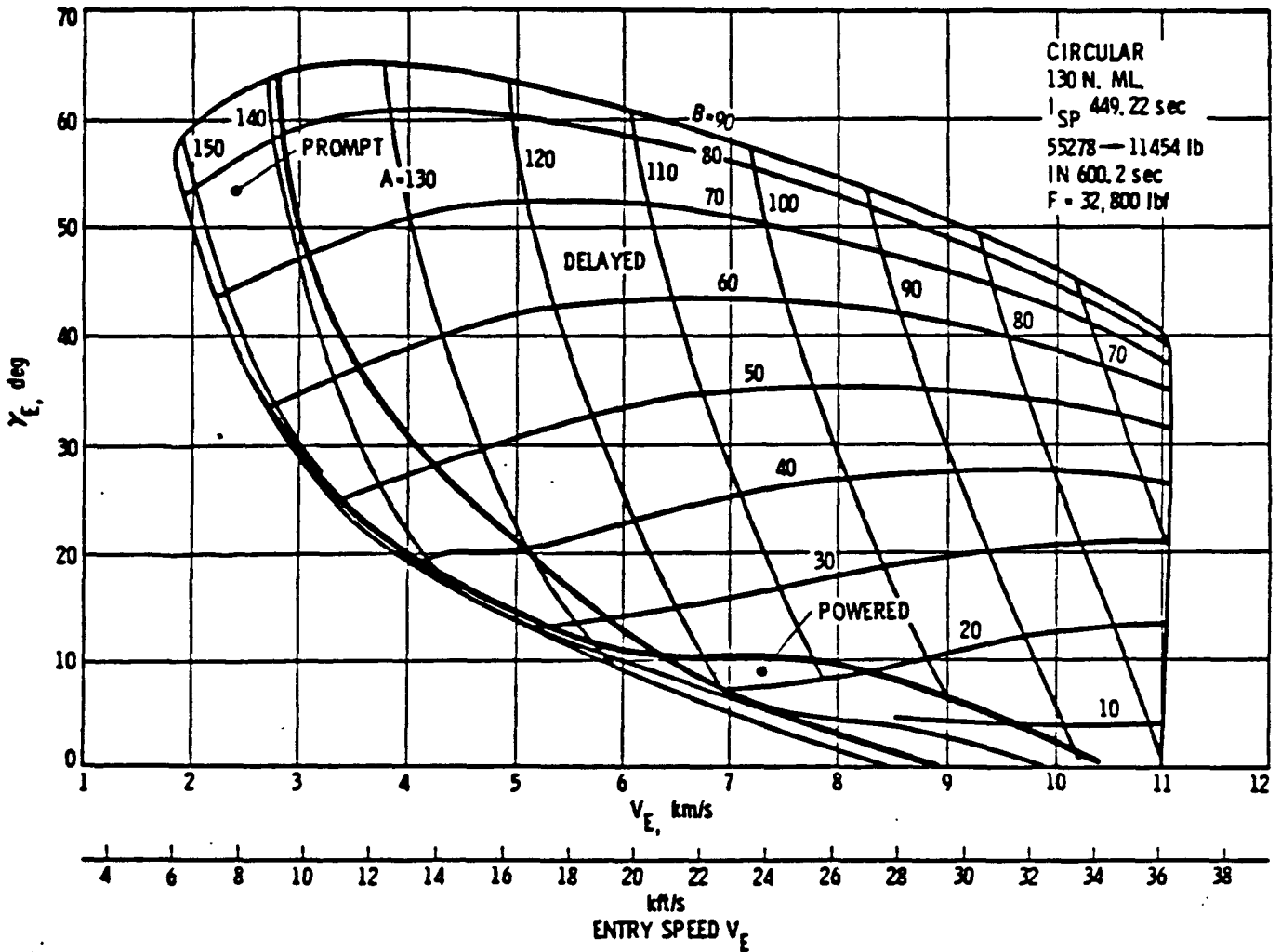


Figure I-A. Galileo/Centaur V- $\gamma$  Map

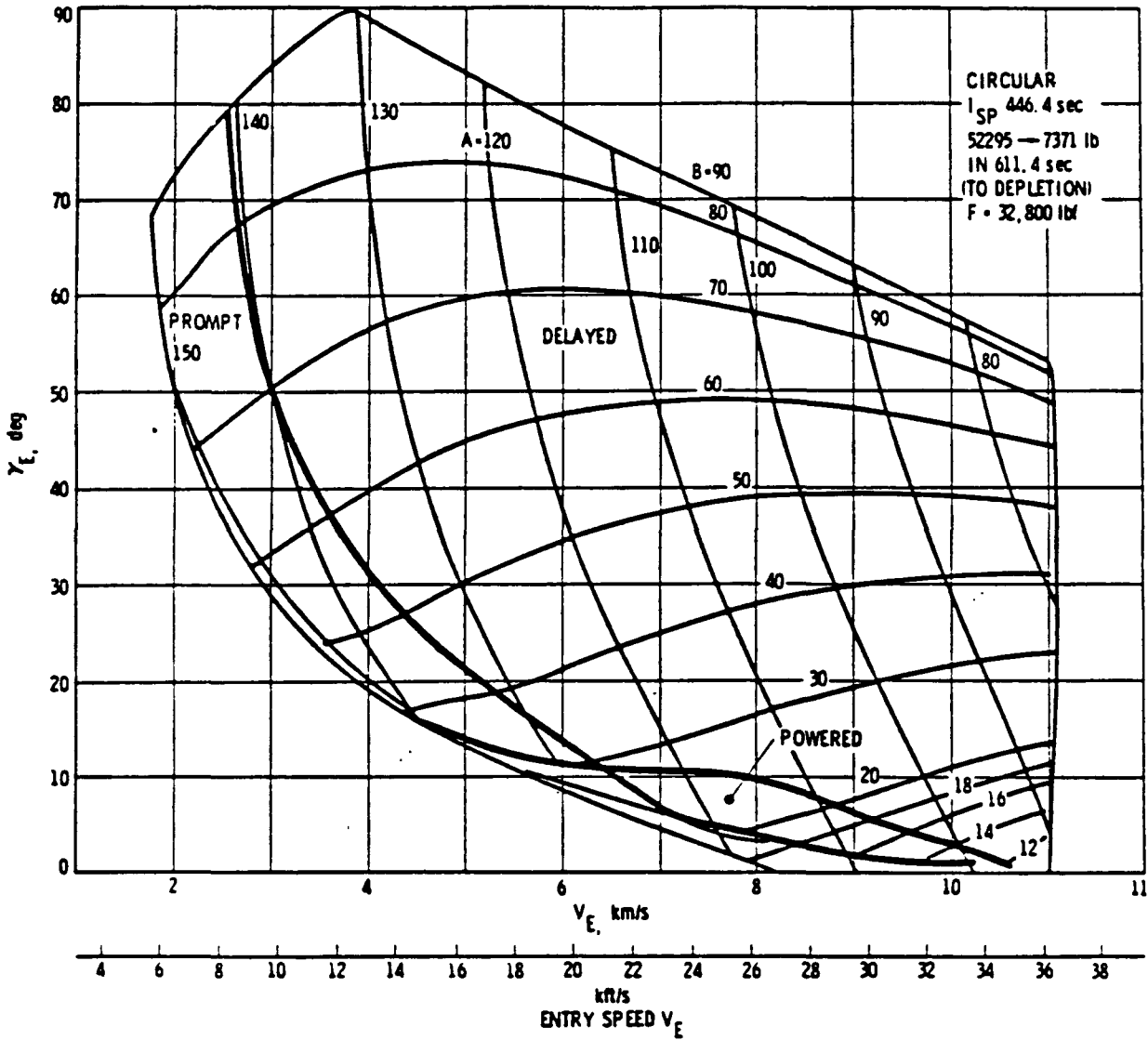


Figure I-B. Ulysses/Centaur V- $\gamma$  Map

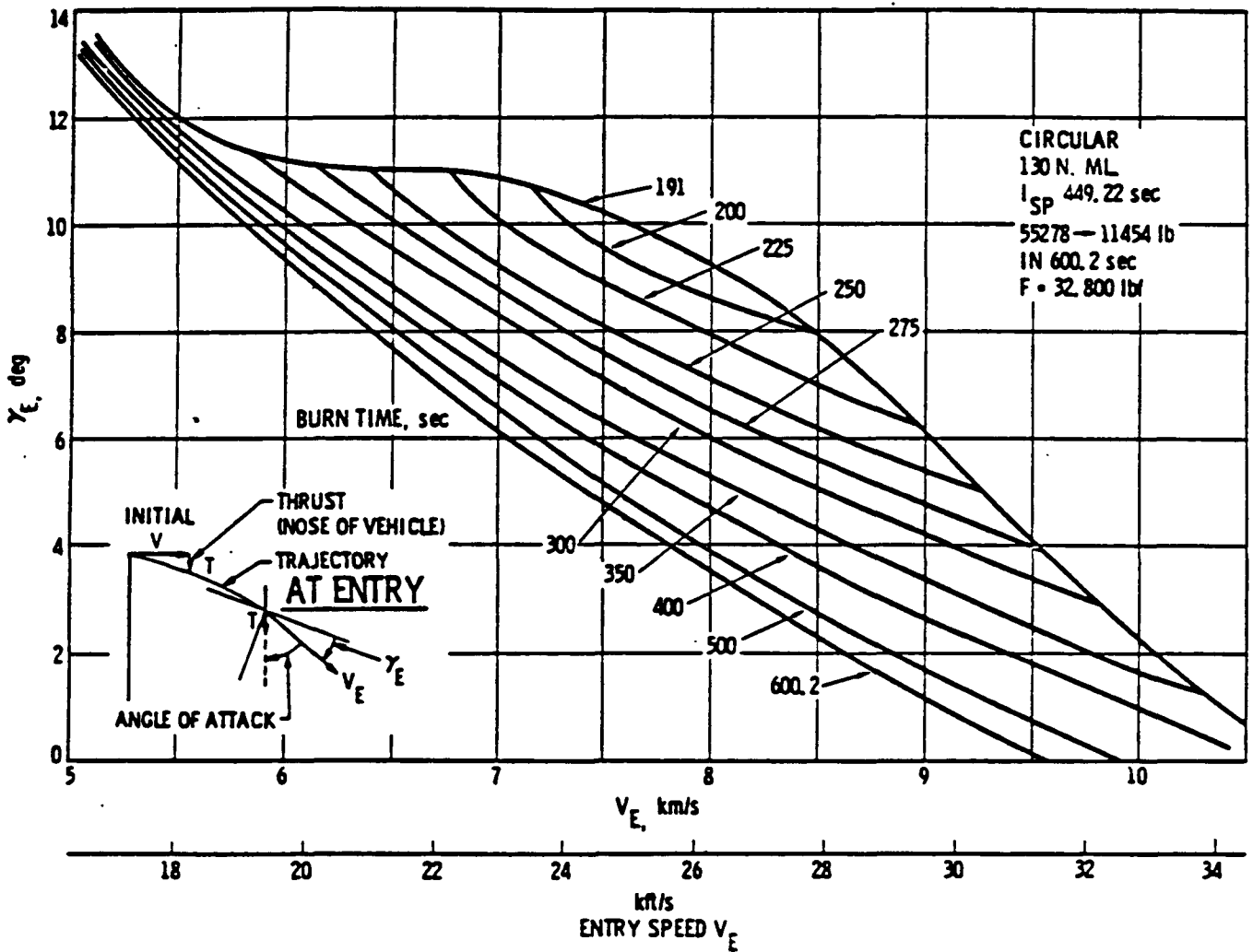


Figure I-C. Galileo/Centaur V- $\gamma$  Map: Powered Entry Cases Burn Times

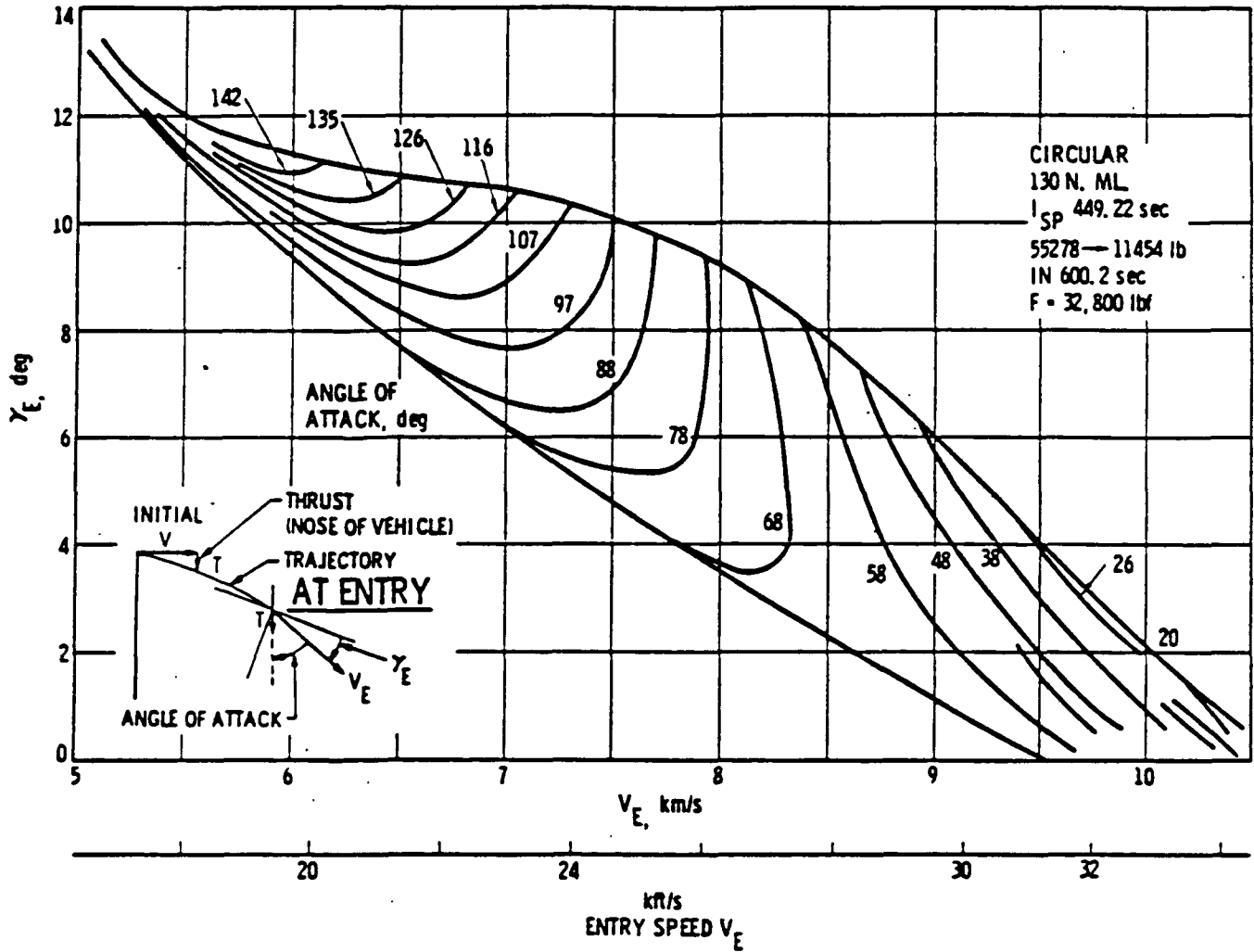


Figure I-D. Galileo/Centaur V- $\gamma$  Map: Powered Entry Cases Angle of Attack

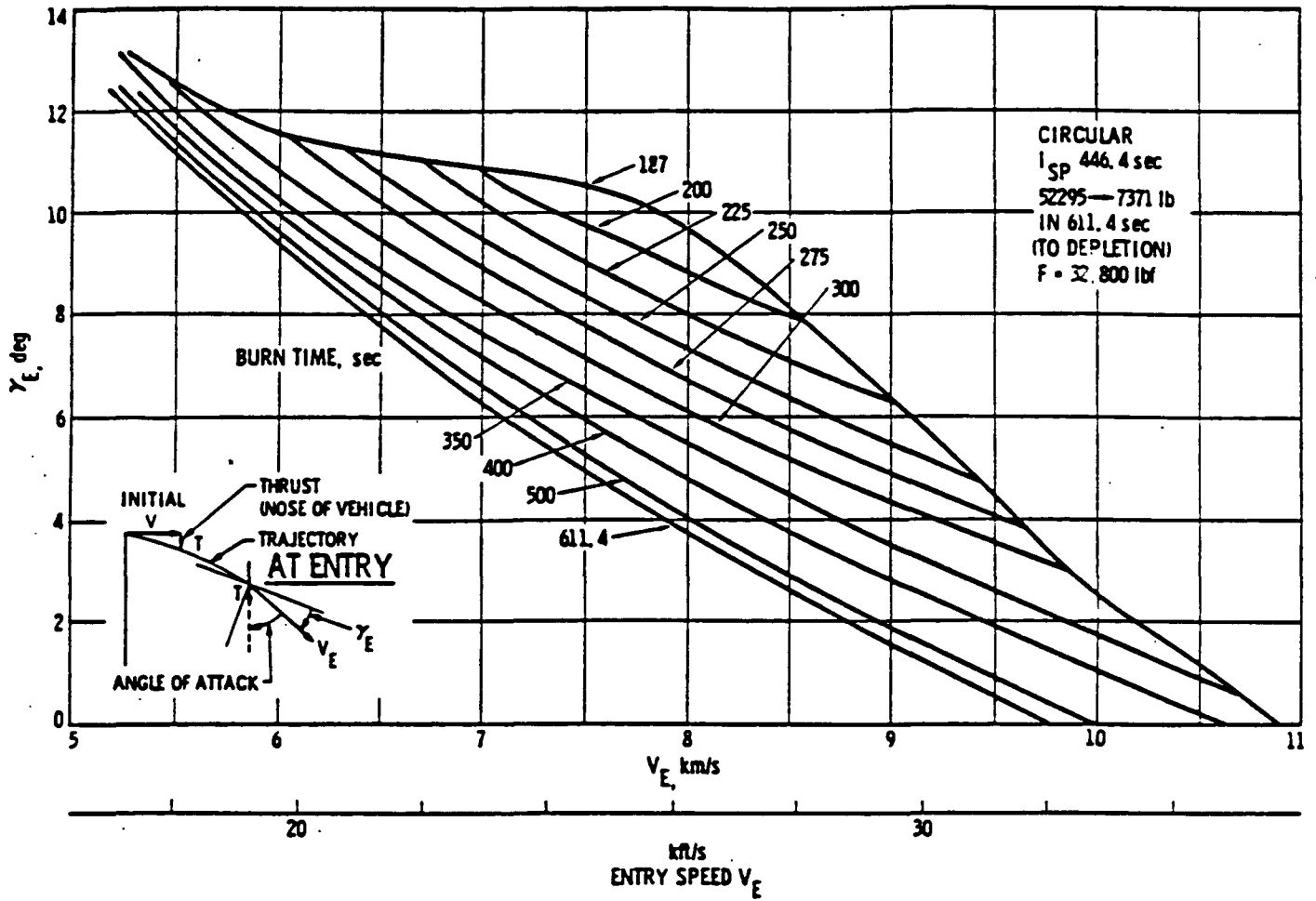


Figure I-E. Ulysses/Centaur V-γ Map: Powered Entry Cases Burn Times



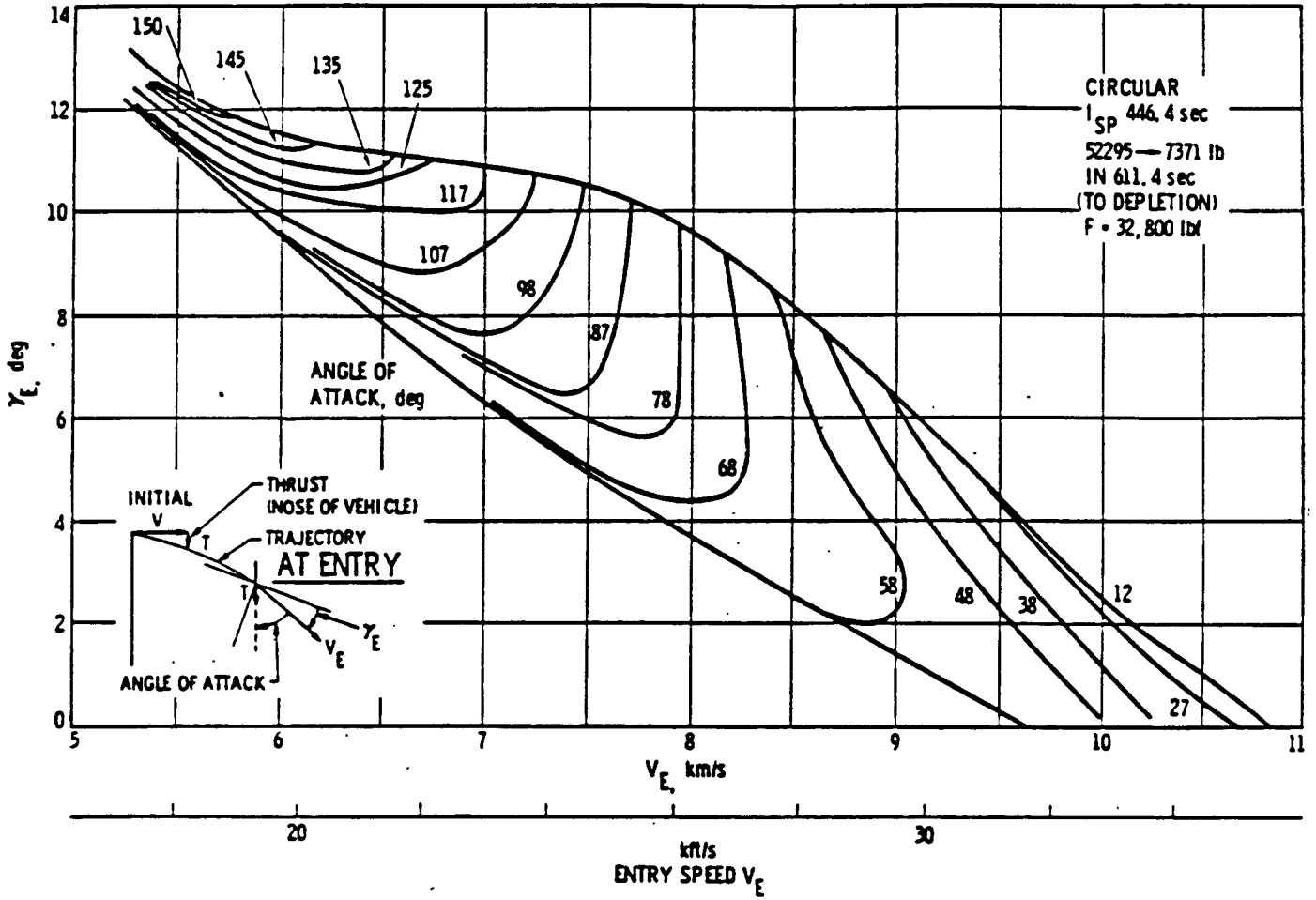


Figure I-F. Ulysses/Centaur V- $\gamma$  Map: Powered Entry Cases Angle of Attack

tables along with the breakdown between the random and preferential misorientation probabilities. The probabilities are based on guidance failures occurring during the coast period prior to Centaur ignition and during the first half of the burn phase since misalignment after this time would not prevent escape of the spacecraft. Deferred Centaur guidance system misalignment failures (i.e., those occurring prior to Centaur deployment) were also factored into the misalignment probabilities.

Another aspect of the General Dynamics study included other Orbiter/Centaur failure modes for the period from OMS-2 burnout to Centaur escape orbit injection that would result in orbit decay cases. The results of this part of the study are shown in Table I-3. Primary Centaur failures are included in the total of the Orbiter failures. Centaur engine start failures are included in the on-orbit failure probabilities.

Table I-3. Orbital Reentry Probabilities ( $\times 10^{-6}$ )

Configuration	Orbit	
	Circular	Elliptical
Orbiter with Centaur/ Spacecraft	228	
Centaur/Spacecraft or Spacecraft only	3296	17224
Totals	3524	17224

The other area of concern involves the superorbital velocity, steep angle type of reentry since the maximum material stress in the components of the GPHS would occur under these conditions. Since velocity is the predominant factor (as compared with reentry angle) in determining the resulting heating rates, which constitute the major factor in the overall stress, the results of the

study (refer to Figures I-A and I-B) show that the most severe reentry conditions occur as follows:

	<u>Velocity (fps)</u>	<u>Angle (°)</u>
Galileo	36,400	40
Ulysses	36,400	52

### I.1.2 SELECTION OF REENTRY CASES FOR ANALYSIS

The determination of the reentry cases to be analyzed was made by the INSRP Reentry Subpanel over an extended period of time from July, 1981, through May, 1983. The first case for Galileo was chosen from the results of preliminary V-γ analyses conducted by the Air Force Weapons Laboratory and General Dynamics/Convair Division (References I-2 and I-3). The second breakup case was selected to be independent of the upper stage used (which later became the Centaur), to as great an extent as possible, due to the uncertainty in the choice of upper stage at that time (around February 1982). Additional cases were selected for both missions during the time span indicated previously. A summary of the initial conditions for the cases selected for analysis for each mission is presented in Table I-4. The case numbers shown at the left of the table apply to both missions and indicate the order in which they were chosen. The nomenclature shown in the table relating to the spacecraft configuration and attitude are the same as those designated by the Reentry Subpanel and do not reflect the variation in attitudes nor attitude changes with time subsequently investigated in the JPL breakup analyses.

### I.1.3 REENTRY RESPONSE OF SPACECRAFT

JPL subsequently analyzed the response of the spacecraft under the various reentry conditions shown in Table I-4. The interim results of the JPL analyses were included in Appendix B of the Galileo/Ulysses USAR (Reference I-1) in order to make them available to the INSRP in a more timely manner. Since that time, the final reports for both missions have been published by JPL (References I-4 and I-5, for Galileo and Ulysses, respectively). The results of the JPL analyses are shown in Table I-5 as

Table I-4. Reentry Cases Selected for Analysis

Case No.	Type Reentry	
	Galileo	Ulysses
1.	Superorbital, Steep Angle <sup>1)</sup>	Superorbital, Steep Angle
2.	Superorbital, Gamma Min <sup>2)</sup>	Orbit Decay
3.	Orbit Decay <sup>3)</sup>	Superorbital, Gamma Min
4.	Powered <sup>4)</sup>	Powered <sup>5)</sup>

Notes: 1)  $V_e = 36,000$  fps,  $\gamma_e = 39^\circ$   
 Cruise Configuration  
 Trimmed Attitude

2)  $V_e = 36,000$  fps  
 $\gamma_e = \text{min. for RTG}$  (i.e., capture on first pass)  
 Cruise Configuration  
 Trimmed Attitude.

3)  $V_e = 25,700$  fps  
 $\gamma_e = 0.02^\circ$   
 Cruise Configuration  
 Trimmed/Spinning Attitude

4)  $V = 21,000$  fps,  $\gamma = 10.5^\circ$   
 27,000 lb. propellants remaining  
 Spacecraft Stowed

5) This case was actually analyzed before Case 3 for Ulysses, thus allowing similarities for both missions to be used more effectively in the powered reentry analytical effort undertaken by JPL.

Table I-5. Conditions at RTG Release—Results of JPL Breakup Analysis

Type Reentry	Case No.	Time (sec)	Altitude (K ft)	Inertial Velocity (fps)	Inertial Angle (deg)
Superorbital, $\gamma$ max.					
Galileo	1.				
Early*		5.6	273	36,104	-38.79
Late*		6.0	253	36,113	-38.76
Ulysses	1.				
Early		6.1-7.0	225-199	36,000	-53.00
Late		6.3-7.3	219-190	36,000	-53.00
Superorbital, $\gamma$ min.					
Galileo	2.				
Early		24	333	36,056	-3.85
Late		36	306	36,073	-3.28
Ulysses	3.				
Early		52	276.7	36,090	-2.54
Late		56	270.5	36,100	-2.39
Orbit Decay					
Galileo	3.				
Early		3710	330	25,704	-0.138
Late		4130	292	25,594	-0.318
Ulysses	2.				
Early		--	291	25,370	-0.51
Late		--	244	24,120	-1.19
Powered					
Galileo	4.				
Early		52	185.8	20,300	-12.0
Late		59	159.0	18,900	-12.2
Ulysses	4.				
Early		50	194.4	20,400	-12.0
Late		67	130.2	11,800	-13.2

\*Early and Late represent the boundaries of the time of release for one-half of the stack of modules and the remaining half stack of modules, respectively, in the Galileo analysis. For Ulysses (formerly Solar-Polar), early and late refers to analytical variations in release of all GPHS modules (i.e., 18) based on a range of initial conditions (a range of subcases)—e.g., spacecraft attitudes causing exposure of the RTG to windward vs. leeward flow conditions.

related to the initial conditions for the cases analyzed in subsequent sections of this appendix. Although these were other subcases investigated by JPL, especially for Ulysses, that are not included in the table, the conditions shown are the ones recommended by JPL for the continuing reentry analysis of the GPHS. Included in the GPHS reentry analysis and which is not shown in Table I-5 is a subcase of the Ulysses  $\gamma$  min, superorbital case (Case No. 3) that results in a skip-out of the GPHS modules with initial release conditions as follows:

Time from entry	80 sec.
Altitude	294,300 feet
Velocity	36,040 ft/sec
Gamma	0.18 deg (down from horizon)

#### I.1.4 SUBSEQUENT ANALYSES

The reentry thermal analysis that had been completed by GE for the Galileo/Ulysses USAR used the conditions that GPHS module would be tumbling randomly during the hypersonic portion of flight and would be stabilized broadside during the subsonic flight. These conditions were based on earlier wind tunnel testing in which limited data was obtained on the aerodynamic coefficients of the GPHS module (Reference I-A). Six degree-of-freedom (6 DOF) motion studies conducted by GE (Reference I-B) indicated that the GPHS would tumble in a random fashion in the hypersonic engine. However, these studies were based on relatively large initial tumble or tip-off rates of the GPHS module (typically in the range of 1200 degrees/second) which was considered to be representative of the event when the module(s) get released from the RTG housing during the reentry breakup of the spacecraft. Later, when JPL was conducting the detailed breakup analyses (see Reference I-4 and I-5), the results of their studies indicated that relatively small initial tumble rates would occur which were based solely on the predicted tumble rates of the spacecraft when the RTG's or GPHS modules were released. Following this disclosure, APL performed additional 6 DOF studies based on the lower rates (in the range of 0-130 degrees/second), Reference I-C, to verify whether or not the module would be tumbling for purposes of the thermal stress

analysis. Two specific cases were investigated by APL with the following initial conditions based on the JPL breakup studies:

<u>Steep Angle Reentry</u>	<u>Orbital Decay Reentry</u>
$h_o$ = 264,000 ft.	$H_o$ = 292,000 ft.
$V_o$ = 36,111 ft/sec	$V_o$ = 24,073 ft/sec
$\gamma_o$ = - 38.78 deg.	$\gamma_o$ = -0.338 deg.
$\alpha$ = 24 degrees	$\alpha$ = 90 deg. and 0 deg.
Pitch Rate = 130 deg/sec	Pitch Rate = zero

Where:

- $h$  = altitude
- $V$  = velocity
- $\gamma$  = path angle
- $\alpha$  = angle of attack

The results indicated that the module would oscillate about the broadface stable altitude (angle of attack nearly zero) for the steep angle reentry conditions. For the orbital decay reentry, the module stabilized at an angle of attack near 60 degrees within around 50 seconds of flight, which was subsequently maintained throughout the hypersonic portion of flight.

General Electric subsequently performed 6 DOF analyses using the same initial conditions and the same aerodynamic data that had been used by APL to corroborate the results. Figures I-1 through I-3 show the GE results for the steep angle reentry, and the orbital decay reentry values are shown on Figures I-4 and I-5. Note that in the steep angle reentry, the angle of attack converges to a value around 8 degrees in the period between 5 - 7 seconds but then diverges slowly upward toward 30 degrees at 12 seconds. The APL simulation did not indicate this divergence. The APL simulation was terminated at 9 seconds corresponding to Mach = 12.2 and an altitude of 95,000 feet; the GE simulation was run to Mach = 4.75 at 12 seconds with the altitude being 81,000 feet.

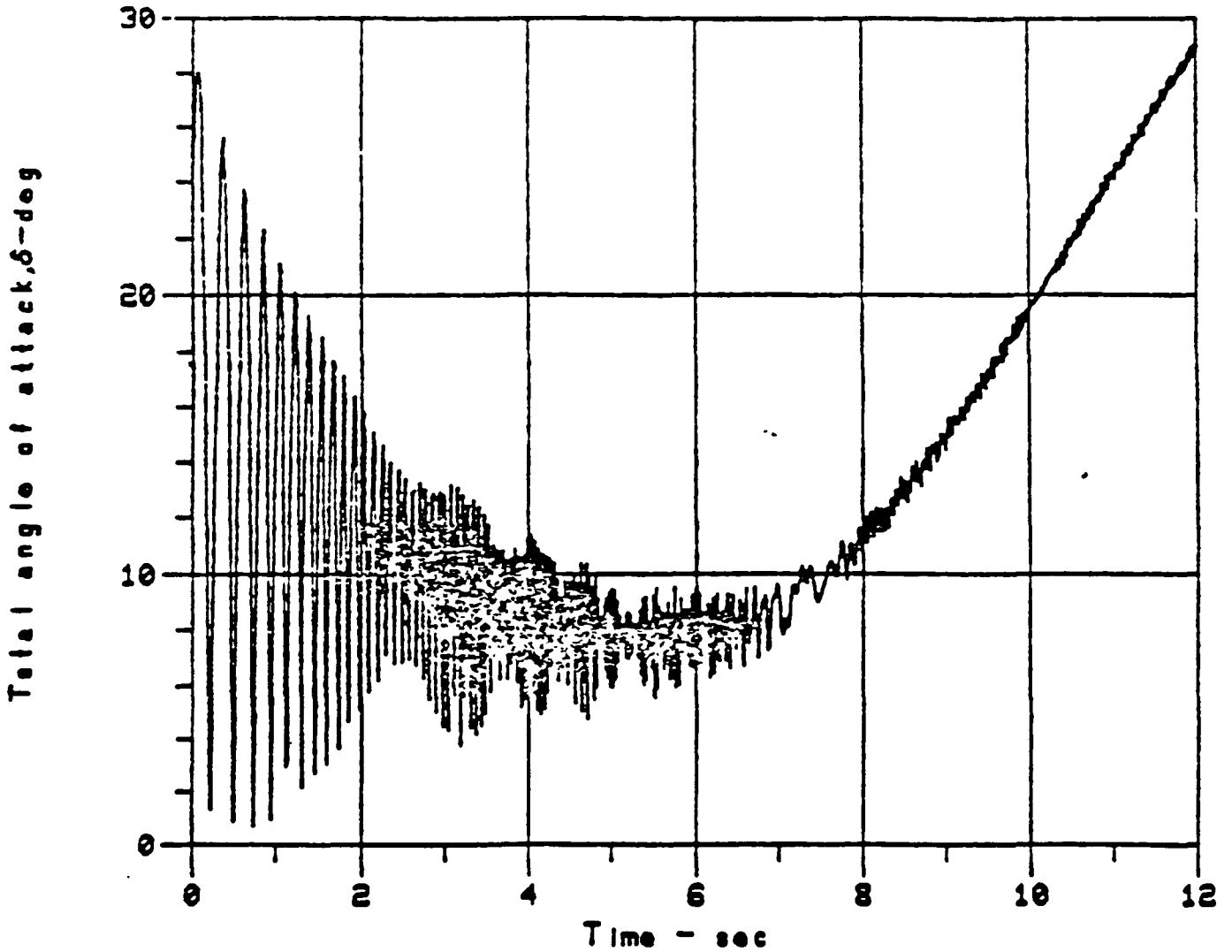


Figure I-1. Steep Entry Angle of Attack History



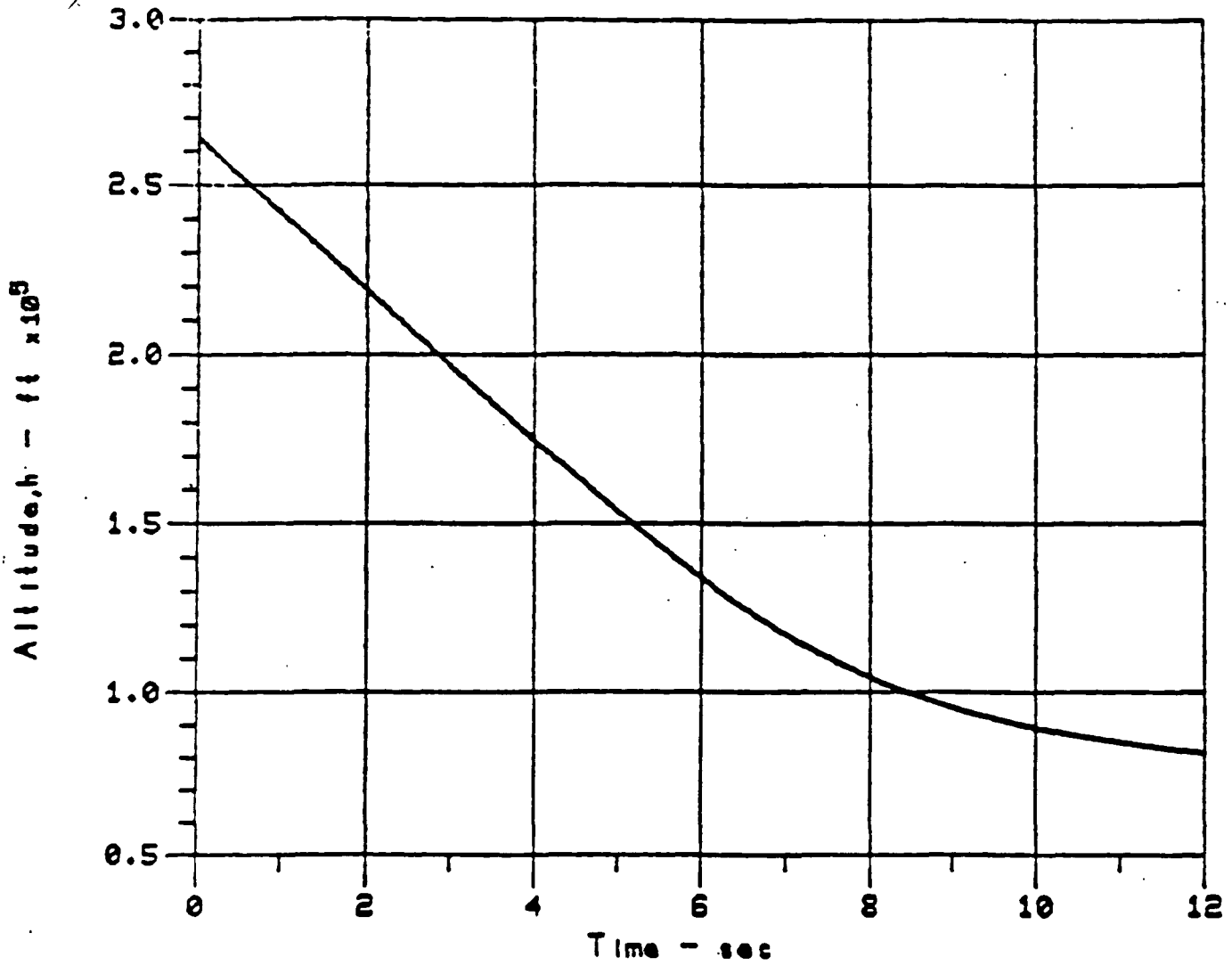


Figure I-2. Steep Entry Altitude History GPHS Module

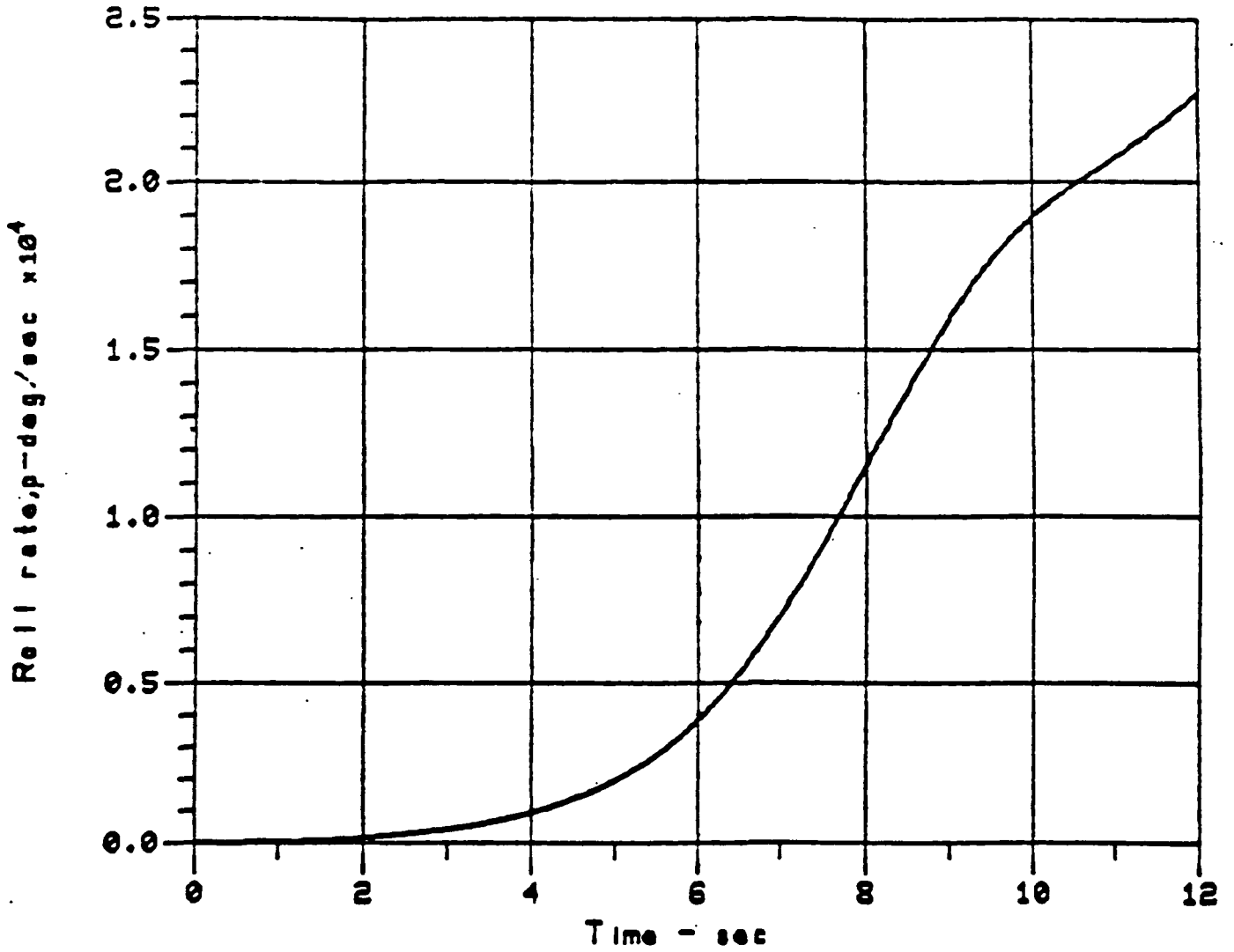


Figure I-3. Steep Entry Roll Rate History GPHS Module

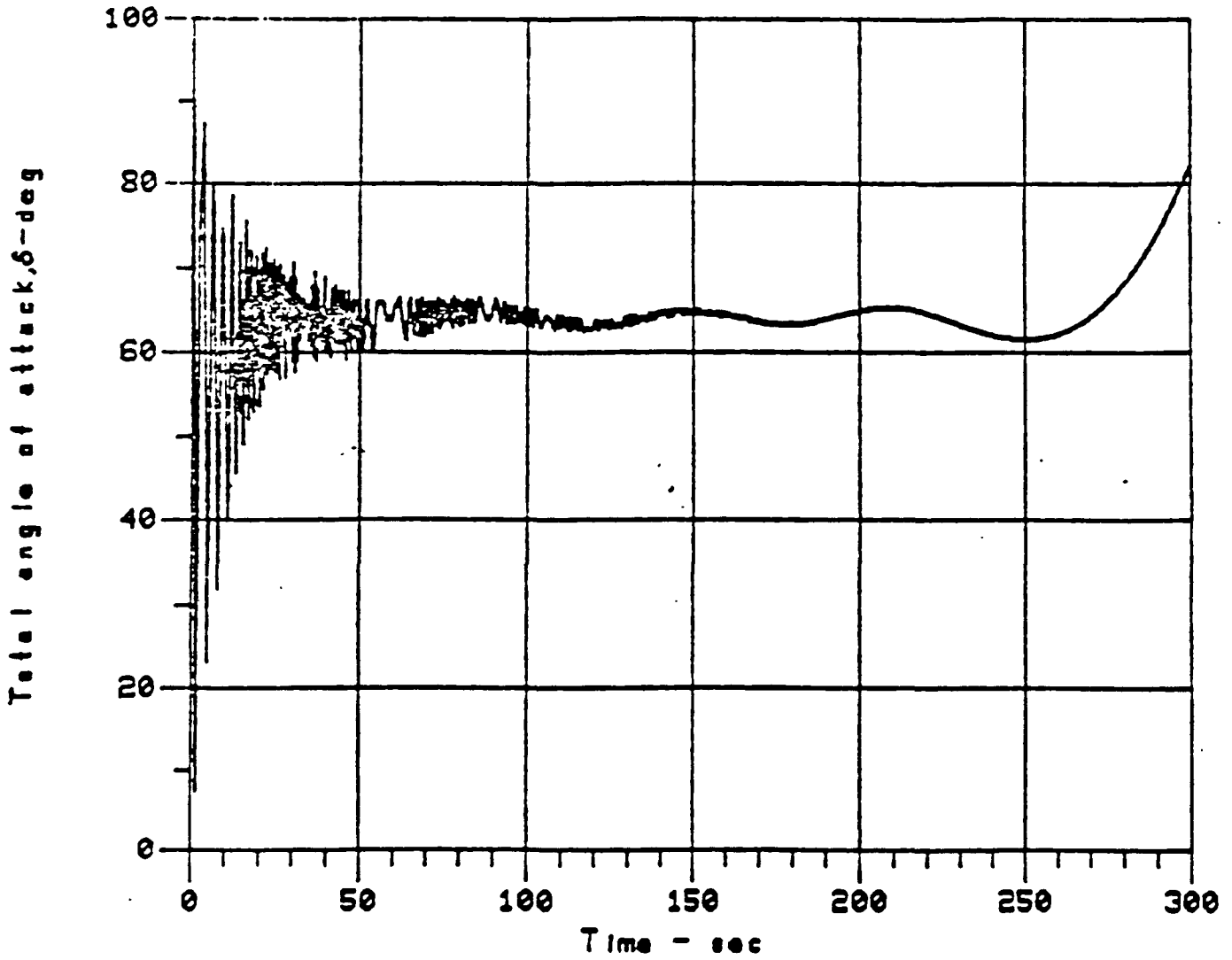


Figure I-4. Orbital Decay Angle of Attack History,  $\alpha = 90^\circ$  GPHS Module

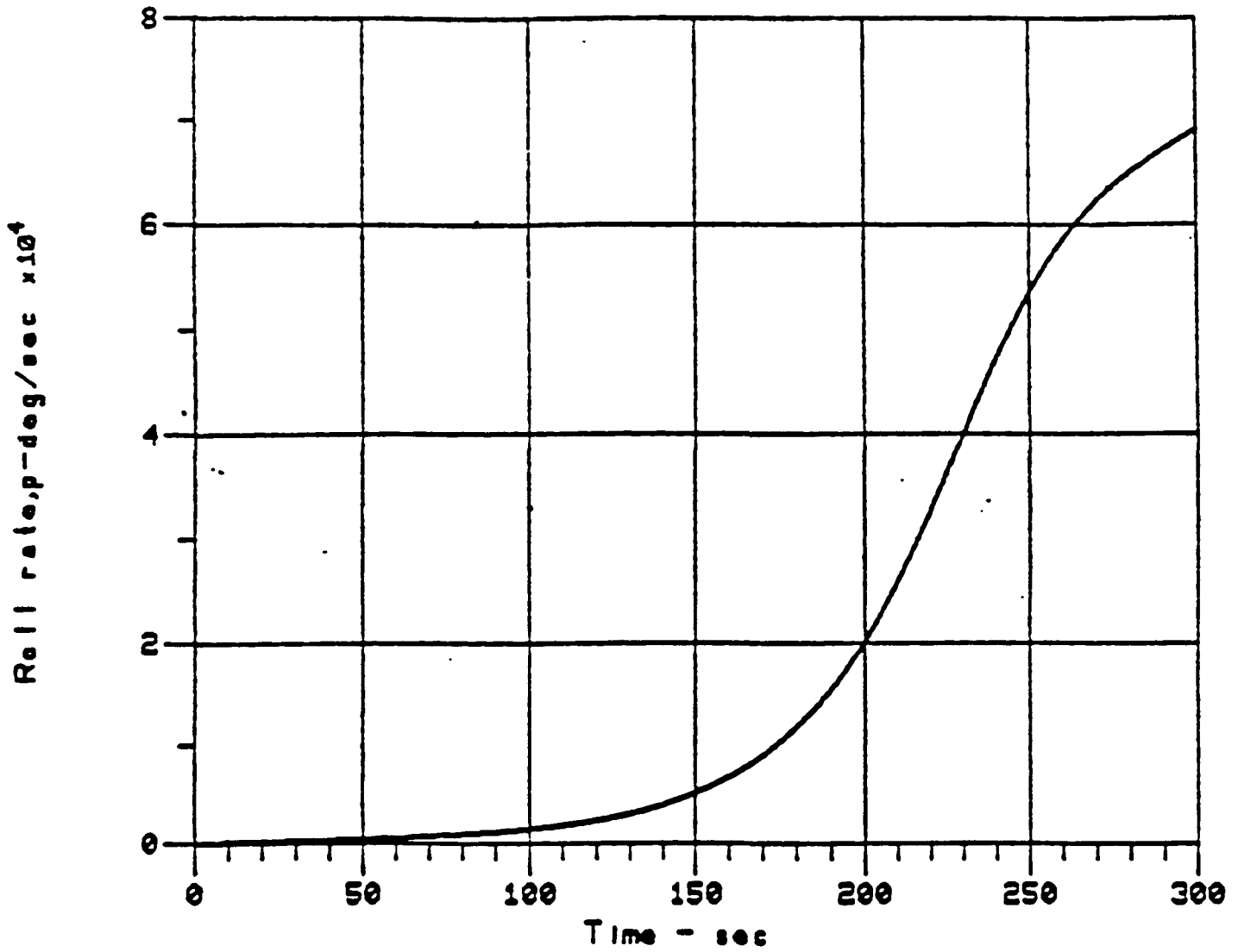


Figure I-5. Orbital Decay Roll Rate History,  $\alpha = 90^\circ$  GPHS Module

The total angle of attack history for the 90 degree initial angle of attack in the orbital decay simulation is shown on Figure I-4. This simulation terminated at Mach = 1 which occurred at 300 seconds. The angle of attack settles into equilibrium around 65 degrees which exists due to a combination of the pitching and rolling motion similarly as in the APL simulation. It is then seen to diverge and to reach a value around 85 degrees at the 300 second time. Although the angle of attack histories agree closely, differences occur in other trajectory parameters. The roll rate increases to 70,000 deg/sec by 300 seconds (Figure I-5) while the APL simulation indicated only about 30,000 deg/sec. This difference is probably accounted for by the difference in altitude versus time history noted in Figure I-6. Mach = 1 is reached in 300 seconds at an altitude of 77,000 feet and the APL simulation reaches altitude region. Therefore the GE simulation flies a higher dynamic pressure history versus time causing a more rapid spin-up. Orbital decay trajectories are very sensitive to differences in the planetary (e.g., planet radius, gravity constants) and climatological models. Thus it is not unexpected to see this difference in motion parameters that are dependent on integrated time histories (roll rate, velocity). Angle of attack is more dependent on the aerodynamic coefficients and thus indicates an insensitivity to the time history.

The second orbital decay trajectory results (i.e., for an initial angle of attack of zero degrees) were not plotted because the angle of attack and roll rate remained near zero down to Mach = 1 which occurred about 280 seconds (due to the large drag) at an altitude of 87,000 feet. The abrupt increase in angle of attack to 60 degrees seen in the APL simulation did not occur because the subsonic region was not simulated.

Because both the GE and APL 6 DOF studies indicated the potential for a stabilized attitude of the GPHS module in the steep angle reentry, the decision was made to perform the thermal stress analyses under these conditions for the Galileo/Ulysses FSAR. In this manner, the differences in the GPHS structural response could be compared between the randomly tumbling versus stabilized attitudes during the reentry. The details and results of this analysis are presented in Section I.6.

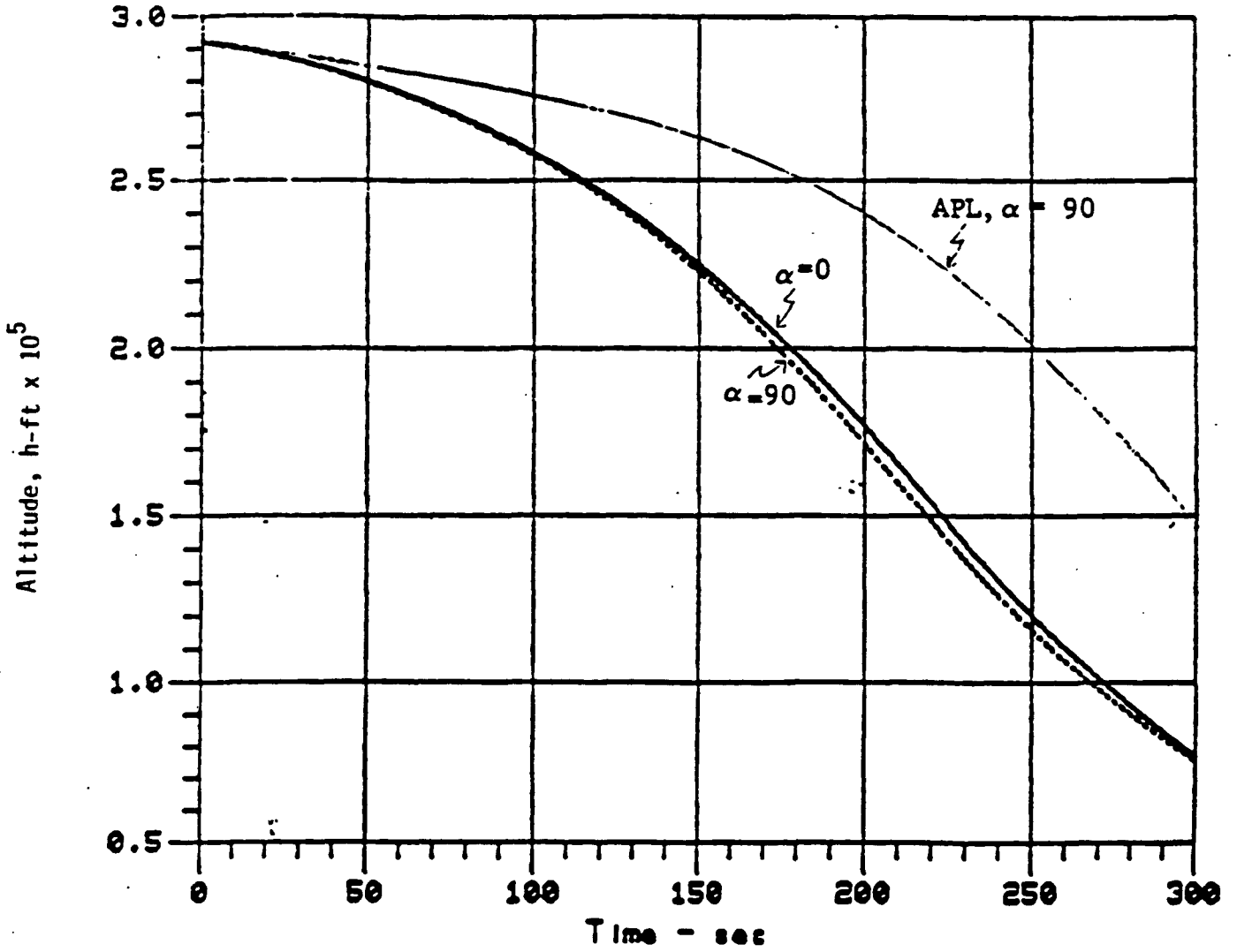


Figure I-6. Comparison of Orbital Decay Altitude Histories GPHS Module

### I.1.5 GPHS AERODYNAMIC CHARACTERISTICS

This section presents the results of testing and analysis performed to determine the aerodynamic characteristics of the General Purpose Heat Source (GPHS). These results are used in other sections of this Appendix to determine trajectories and associated heating rates to be employed for the reentry thermal and structural analysis.

#### I.1.5.1 DRAG COEFFICIENT/TERMINAL VELOCITY

##### I.1.5.1.1 DROP TESTING

Drop tests were conducted at the NASA Wallops Island facility during May 1980. These tests consisted of dropping a number of simulated (configuration, weight, moments of inertia, and center of gravity) GPHS modules from a helicopter and tracking them with radar and high speed movie camera (Reference I-D). Part of the tests investigated the separation of modules assembled with the locking buttons used in the flight RTG assembly. The primary purpose of the tests was to determine the GPHS terminal velocity with a secondary purpose being to determine the motion of the modules during the terminal fall interval.

The results of the nine individual drops yielded an average terminal velocity of 165.1 feet per second with a standard deviation of 8.8 feet per second. Based on the average terminal velocity, the sea level terminal drag coefficient was determined to be  $C_D = 1.01$ . Little useful information was obtained from the motion picture records because of the poor quality of the results (i.e., film was overexposed and poorly focused). The pair of modules used for the separation test did separate successfully after several seconds into the fall.

##### I.1.5.1.2 STATIC STABILITY TESTING

Preliminary testing was conducted in the AEDC (Arnold Engineering and Development Center/U.S. Air Force Facility) Von Karman Tunnel B on the static stability characteristics of the GPHS module at Mach 8 (Reference I-A). (This

testing included heat transfer measurements on the GPHS used to verify or to modify heating correlations then being used in reentry analysis.) As a result of these tests, the hypersonic drag coefficient as a function of the angle of attack ( $\alpha$ ) was obtained as shown on Figure I-G.

#### I.1.5.1.3 DRAG COEFFICIENT DEPENDENCE ON MACH NUMBER

Six degree-of-freedom calculations performed earlier in the GPHS-RTG program showed that the body would tumble (Reference I-F). To provide a basic trajectory to determine heating on the GPHS, an effective average tumbling drag coefficient was estimated. An arbitrary weighting was applied over the angle of attack that emphasized the region of high stability as opposed to that of low stability. The weighting varied linearly from a value of 1.0 at the  $0^\circ$  angle of attack to 0.1 at the  $90^\circ$  angle of attack, and the resulting distribution was integrated to yield the effective average coefficient of  $C_D = 1.427$ .

In order to carry trajectory computations into the lower speed region, the drag coefficient must be extended to the low Mach number region. This has been done using correlations on similar bodies. In Reference I-E, the figure shown as Figure I-H herein represents the variation of the drag coefficient of a tumbling cube with Mach number from subsonic to hypersonic speeds. Because of the similarity of this configuration to the GPHS, this variation with Mach number (as contrasted with the drag coefficient itself) has been applied to the GPHS configuration. The relationship shown by the drag ratio shown on Figure I-H is applied to the effective average drag coefficient for the tumbling GPHS of 1.427 up to the maximum value at Mach= 1.1. From there the curve follows the trend of the remaining drag ratio into and through the subsonic region but is faired into the value of  $C_D = 1.01$  determined from the drop tests. The resulting curve of drag coefficient versus Mach number is shown on Figure I-I.



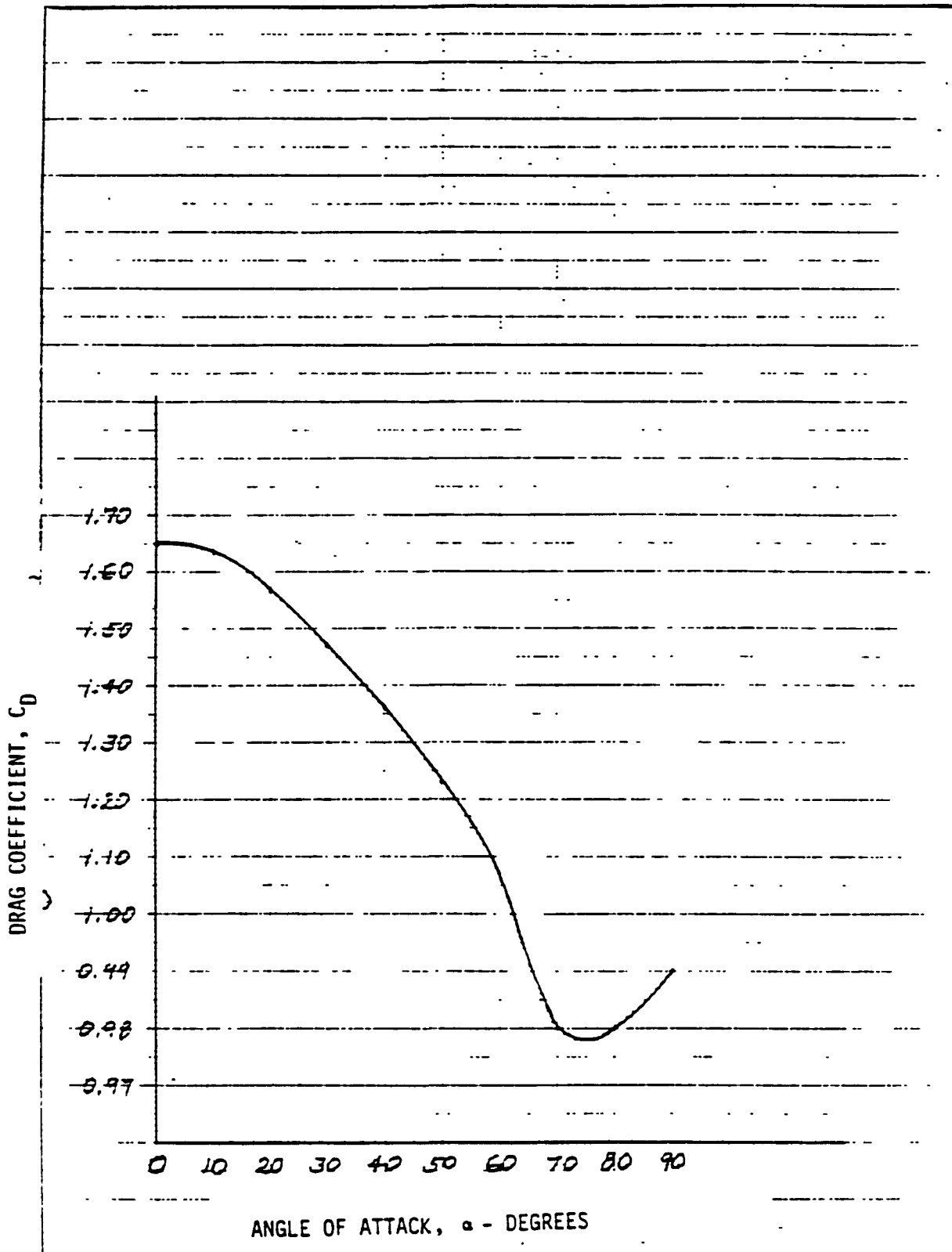


Figure I-G. GPHS Drag Coefficient vs. Angle of Attack (Mach 8)

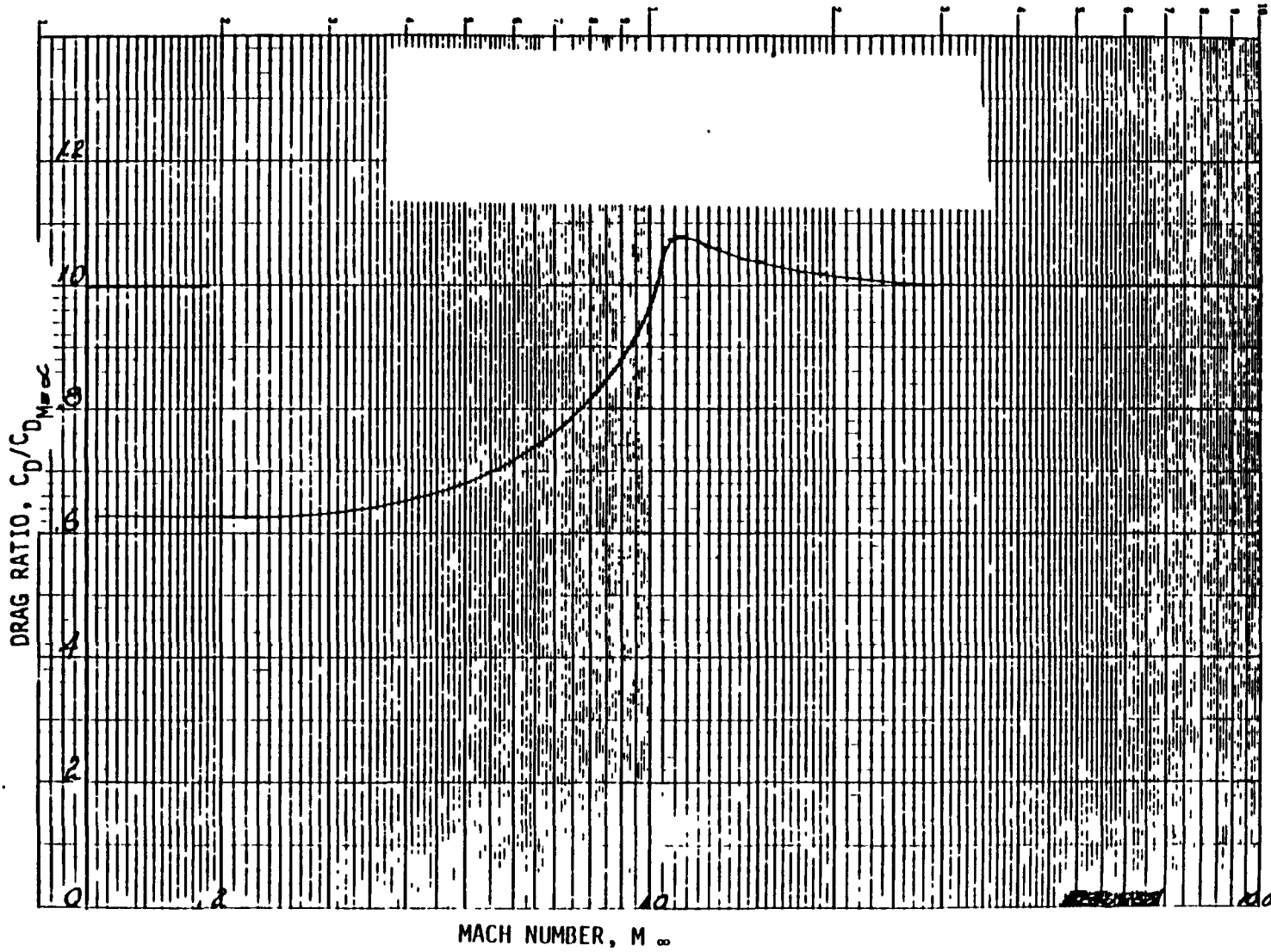


Figure I-H. The Effect of Compressibility on GPHS Drag

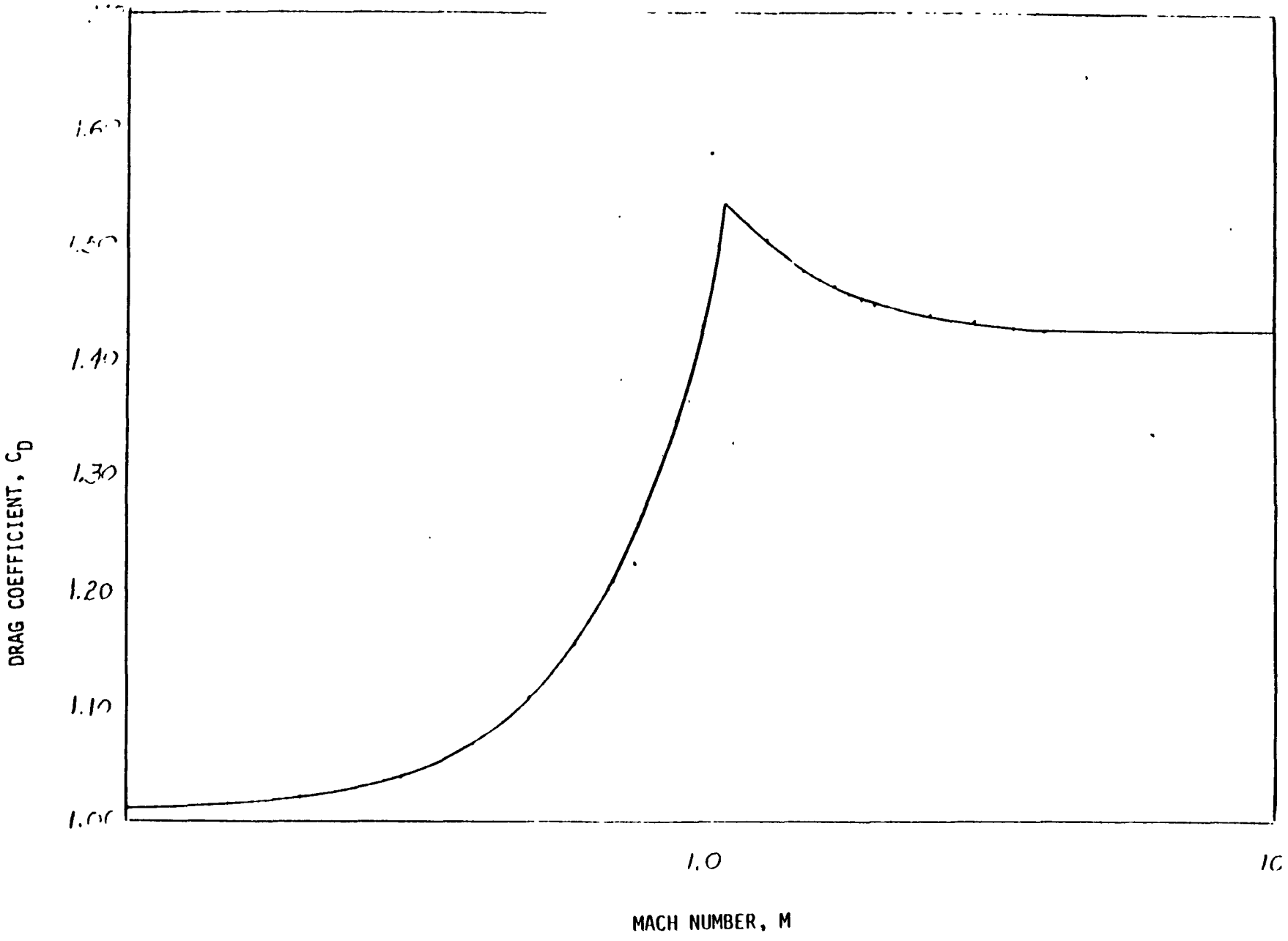


Figure I-I. Averaged Tumbling Drag Coefficient vs. Mach Number

## I.1.5.2 AERODYNAMIC COEFFICIENTS

### I.1.5.2.1 SUBSONIC WIND TUNNEL TESTING

Testing was conducted for the Applied Physics Laboratory of Johns Hopkins University (APL/JHU or APL) at the National Research Council (NRC), Ottawa, Canada, on the subsonic aerodynamic characteristics of the GPHS. Forced oscillation tests were performed to obtain data on aerodynamic pitch and roll damping that can be used to generate input for six degree-of-freedom motion analysis. The tests were conducted at angles of attack between 0 and 90° in the Reynolds number range representative of terminal velocity conditions and also investigated effects of roll angle and edge roundness. These tests were conducted in the period from October 1984 to January 1985.

Tables I-A and I-B present the results of the pitch damping and roll damping tests, respectively. Table I-C is a list of the symbols and nomenclature used in the other tables, and Figure I-J shows the axis systems used in the test explaining also the direction of forces, moments and angles.

The Applied Physics Laboratory (APL/JHU) earlier had conducted tests at the Vought Corporation low speed wind tunnel (Reference I-G). These tests obtained data on the normal, yaw and axial forces and pitching, yawing and rolling moments of the test models at various orientations and at various Reynolds numbers. The results of those tests are shown on Figures I-K through I-P. The model axes and the directions of forces and moments for these tests are the same as those shown on Figure I-J.

### I.1.5.2.2 HYPERSONIC WIND TUNNEL TESTING

Testing has recently been performed in one of the hypersonic wind tunnels at the NASA Langley Research Center at Mach 10.1 to obtain hypersonic aerodynamic data. This testing was performed to obtain more detailed information on the normal force, axial force, and side force coefficients plus rolling moment, pitching moment and yawing moment coefficients. Reduced data from these tests are shown on Figures I-Q through I-U; these figures represent body fixed aerodynamic coefficients that are a function of the total angle of attack,  $\gamma$ .

Table I-A. Pitch Damping Data

FUN	ALPHA	BETA	THETA	PHI	C <sub>mq</sub> + C <sub>mα</sub>	C <sub>mα</sub>	C <sub>m</sub>	FREQ	MACH	Re/ft:				
										RE	V	Q lbs/ft <sup>2</sup>	P lbs/ft <sup>2</sup>	
1	5058	-7.47	0.00	-10.00	0.00	1.124	-.217	.022	.225	.119	.838	132.780	20.690	2086.5
2	5059	.00	0.00	0.00	0.00	-.883	-.185	.001	.221	.121	.852	135.000	21.390	2086.5
3	5060	5.01	0.00	5.03	0.00	-.401	-.191	-.020	.222	.120	.846	134.160	21.110	2086.5
4	5061	9.46	0.00	10.00	0.00	.606	-.206	-.034	.223	.120	.844	133.880	21.030	2086.5
5	5062	17.92	0.00	20.00	0.00	-1.545	-.124	-.063	.222	.120	.844	133.900	21.030	2086.5
6	5063	24.43	0.00	30.00	0.00	-3.461	-.028	-.062	.222	.120	.844	133.880	21.020	2086.5
7	5064	34.95	0.00	40.01	0.00	-3.131	.032	-.051	.222	.120	.844	133.910	21.020	2086.5
8	5065	44.94	0.00	50.00	0.00	-2.437	.073	-.047	.222	.120	.844	133.920	21.020	2086.5
9	5066	57.49	0.00	60.03	0.00	-2.603	.149	-.033	.222	.120	.843	133.860	21.010	2086.5
10	5067	70.00	0.00	70.00	0.00	-3.673	.231	.002	.222	.120	.843	133.910	21.010	2086.5
11	5068	80.03	0.00	74.99	0.00	1.113	.106	.031	.222	.120	.843	133.970	21.030	2086.5
12	5069	85.05	0.00	85.03	0.00	6.889	-.123	.015	.222	.120	.843	133.930	21.010	2086.5
13	5070	84.88	0.00	84.84	0.00	7.304	-.103	-.006	.222	.120	.842	133.920	21.000	2086.5
14	6071	-9.23	3.81	-10.00	-22.50	.604	-.198	.021	.223	.120	.842	133.990	21.020	2086.5
15	6072	.00	0.00	0.00	-22.50	-.674	-.185	.003	.222	.120	.842	133.990	21.020	2086.5
16	6073	4.60	-1.91	4.99	-22.50	-.274	-.203	-.011	.222	.120	.842	134.050	21.030	2086.5
17	6074	9.23	-3.81	10.00	-22.50	.074	-.193	-.021	.223	.120	.842	134.000	21.010	2086.5
18	6075	18.53	-7.52	20.00	-22.50	-1.296	-.111	-.044	.222	.120	.841	134.020	21.010	2086.5
19	6076	28.03	-11.04	30.02	-22.50	-2.006	-.054	-.054	.222	.120	.841	134.040	21.020	2086.5
20	6077	37.72	-14.24	40.00	-22.50	-1.698	-.014	-.050	.222	.120	.841	134.010	21.010	2086.5
21	6078	47.70	-17.05	50.00	-22.50	-1.899	.054	-.041	.222	.120	.841	134.040	21.020	2086.5
22	6079	57.47	-19.35	60.00	-22.50	-1.853	.107	-.026	.222	.120	.841	134.030	21.010	2086.5
23	6080	68.50	-21.08	70.01	-22.50	-1.687	.157	-.007	.222	.120	.841	134.050	21.010	2086.5
24	6081	74.23	-22.14	80.02	-22.50	-2.003	.239	.004	.221	.120	.840	134.060	21.010	2086.5
25	6082	84.63	-22.41	85.01	-22.50	1.406	.120	.021	.222	.120	.840	134.050	21.010	2086.5
26	6083	89.95	-22.50	89.92	-22.50	.940	.161	.030	.222	.120	.840	134.060	21.000	2086.5
27	7084	-7.10	7.06	-10.01	-45.00	-.621	-.208	.011	.222	.120	.840	134.130	21.020	2086.5
28	7085	.00	0.00	0.00	-45.00	-.678	-.171	.002	.222	.120	.840	134.110	21.020	2086.5
29	7086	3.54	-3.54	5.01	-45.00	-.406	-.194	-.010	.222	.120	.840	134.160	21.030	2086.5
30	7087	7.07	-7.05	10.00	-45.00	-.932	-.211	-.014	.222	.120	.840	134.120	21.020	2086.5
31	7088	14.40	-14.01	20.02	-45.00	-.429	-.166	-.036	.222	.120	.839	134.140	21.010	2086.5
32	7089	22.17	-20.72	30.02	-45.00	-1.418	-.049	-.047	.222	.120	.840	134.130	21.020	2086.5
33	7090	30.63	-27.04	40.01	-45.00	-1.556	-.043	-.047	.222	.120	.839	134.130	21.010	2086.5
34	7091	40.08	-32.81	50.02	-45.00	-1.464	-.023	-.049	.222	.120	.839	134.130	21.010	2086.5
35	7092	50.73	-37.77	60.01	-45.00	-1.436	.007	-.039	.222	.120	.839	134.120	21.010	2086.5
36	7093	62.71	-41.65	70.02	-45.00	-1.609	.127	-.063	.222	.120	.839	134.160	21.010	2086.5
37	7094	75.49	-44.14	80.00	-45.00	-2.850	.175	-.009	.221	.120	.839	134.170	21.020	2086.5
38	7095	83.01	-44.78	85.03	-45.00	-1.676	.183	.018	.221	.120	.839	134.150	21.010	2086.5
39	7096	89.89	-45.00	89.89	-45.00	-1.970	.178	.034	.221	.120	.839	134.180	21.010	2086.5
40	8097	-9.22	-3.81	-10.00	22.50	-.604	-.209	.028	.222	.120	.839	134.140	21.010	2086.5
41	8098	.00	0.00	0.00	22.50	-.751	-.192	.003	.222	.120	.839	134.190	21.020	2086.5
42	8099	4.62	1.92	5.01	22.50	-.421	-.197	-.013	.222	.120	.838	134.220	21.020	2086.5
43	8100	9.24	3.82	10.02	22.50	-.672	-.209	-.027	.222	.120	.839	134.190	21.020	2086.5
44	8101	18.54	7.53	20.02	22.50	-1.693	-.120	-.055	.222	.120	.838	134.230	21.020	2086.5
45	8102	28.03	11.04	30.02	22.50	-1.921	-.017	-.058	.222	.120	.838	134.240	21.020	2086.5
46	8103	37.71	14.24	39.99	22.50	-1.392	.001	-.051	.222	.120	.838	134.230	21.020	2086.5
47	8104	47.71	17.05	50.01	22.50	-1.278	.052	-.046	.222	.120	.838	134.230	21.020	2086.5
48	8105	57.47	19.36	60.01	22.50	-1.677	.091	-.033	.221	.120	.838	134.240	21.020	2086.5
49	8106	68.49	21.08	70.00	22.50	-2.753	.144	-.008	.221	.120	.838	134.210	21.010	2086.5
50	8107	79.26	22.14	80.00	22.50	-1.641	.255	.006	.221	.120	.838	134.260	21.010	2086.5

Table I-A. Pitch Damping Data (Cont'd).

51	810P	84.64	22.41	85.03	22.50	1.285	.081	.015	.221	.120	.838	134.260	21.010	2086.5
52	8109	84.89	22.50	89.88	22.50	.391	.115	.020	.221	.120	.837	134.220	21.000	2086.5
53	9110	-7.0P	-7.05	-10.00	45.00	-.772	-.164	.020	.222	.120	.837	134.330	21.020	2086.5
54	9111	-.01	-.01	-.02	45.00	-.831	-.190	.002	.222	.120	.837	134.270	21.010	2086.5
55	9112	3.53	3.54	5.01	45.00	-.646	-.189	-.011	.222	.120	.837	134.290	21.010	2086.5
56	9113	7.10	7.07	10.02	45.00	-.772	-.173	-.021	.222	.120	.837	134.280	21.010	2086.5
57	9114	14.41	14.03	20.05	45.00	-.776	-.163	-.047	.222	.120	.837	134.300	21.010	2086.5
58	9115	27.14	20.70	24.99	45.00	-1.453	-.074	-.051	.222	.120	.836	134.330	21.010	2086.5
59	9116	30.62	27.03	40.00	45.00	-1.578	-.044	-.049	.222	.120	.836	134.320	21.010	2086.5
60	9117	40.06	32.80	50.00	45.00	-1.188	-.033	-.048	.222	.120	.836	134.310	21.000	2086.5
61	9118	50.73	37.77	60.01	45.00	-1.643	-.012	-.044	.222	.120	.836	134.360	21.020	2086.5
62	9119	62.70	41.64	70.01	45.00	-2.009	.119	-.063	.221	.120	.836	134.320	21.000	2086.5
63	9120	75.99	44.14	80.00	45.00	-2.633	.187	-.010	.221	.120	.836	134.350	21.010	2086.5
64	9121	82.98	44.78	85.01	45.00	-2.395	.211	.014	.221	.120	.835	134.340	21.000	2086.5
65	9122	89.94	45.00	89.93	45.00	-1.183	.191	.033	.221	.120	.835	134.360	21.000	2086.5
66	10123	-3.85	-9.23	-10.00	67.50	-.259	-.169	.008	.222	.120	.836	134.360	21.010	2086.5
67	10124	.00	0.00	0.00	67.50	-.605	-.149	.002	.222	.120	.835	134.400	21.020	2086.5
68	10125	1.90	4.61	4.99	67.50	-.615	-.179	-.008	.222	.120	.835	134.390	21.010	2086.5
69	10126	3.84	9.22	9.99	67.50	-.284	-.176	-.010	.222	.120	.835	134.380	21.000	2086.5
70	10127	7.70	18.42	20.00	67.50	.321	-.163	-.023	.222	.120	.835	134.380	21.010	2086.5
71	10128	12.43	27.54	30.03	67.50	-1.275	-.155	-.035	.222	.120	.835	134.430	21.010	2086.5
72	10129	17.75	36.42	39.44	67.50	-1.375	-.089	-.036	.222	.120	.834	134.420	21.010	2086.5
73	10130	24.48	45.06	50.01	67.50	-1.625	-.079	-.036	.222	.120	.835	134.430	21.010	2086.5
74	10131	33.50	53.14	60.00	67.50	-1.170	-.071	-.035	.222	.120	.835	134.430	21.010	2086.5
75	10132	46.43	60.26	70.02	67.50	-1.442	-.044	-.033	.221	.120	.835	134.440	21.010	2086.5
76	10133	65.24	65.48	80.00	67.50	-2.292	.018	-.020	.221	.120	.834	134.460	21.010	2086.5
77	10134	77.12	66.98	85.00	67.50	-1.938	.061	-.004	.221	.120	.834	134.480	21.010	2086.5
78	10135	89.80	67.50	89.92	67.50	-1.644	.035	.010	.221	.120	.834	134.460	21.000	2086.5
79	11136	-3.86	9.23	-10.00	-67.50	-.454	-.186	.004	.222	.120	.834	134.470	21.010	2086.5
80	11137	.00	0.00	0.00	-67.50	-.722	-.156	.001	.222	.120	.834	134.500	21.020	2086.5
81	11138	1.91	-4.63	5.01	-67.50	-.132	-.181	-.006	.222	.120	.834	134.460	21.010	2086.5
82	11139	3.65	-9.23	10.00	-67.50	-.578	-.194	-.008	.222	.120	.833	134.510	21.010	2086.5
83	11140	7.91	-18.42	20.00	-67.50	.195	-.177	-.016	.222	.120	.833	134.510	21.010	2086.5
84	11141	12.43	-27.50	24.99	-67.50	-1.648	-.106	-.021	.222	.120	.833	134.460	21.000	2086.5
85	11142	17.78	-36.43	40.00	-67.50	-1.648	-.080	-.023	.221	.120	.834	134.520	21.020	2086.5
86	11143	24.47	-45.04	49.99	-67.50	-1.114	-.076	-.024	.221	.120	.833	134.510	21.010	2086.5
87	11144	33.49	-53.13	59.99	-67.50	-1.516	-.058	-.033	.221	.120	.833	134.520	21.010	2086.5
88	11145	46.37	-60.23	69.98	-67.50	-1.650	-.033	-.033	.221	.120	.833	134.510	21.010	2086.5
89	11146	65.22	-65.48	79.99	-67.50	-2.460	.040	-.016	.221	.120	.833	134.540	21.020	2086.5
90	11147	77.10	-66.98	84.99	-67.50	-2.056	.073	.005	.221	.120	.832	134.510	21.000	2086.5
91	11148	89.82	-67.50	89.92	-67.50	-2.209	.041	.020	.221	.120	.833	134.560	21.010	2086.5
92	19252	-.01	10.02	-10.02	-90.00	-.424	-.155	-.004	.222	.119	.824	134.190	20.770	2078.1
93	19253	-.01	.01	-.01	-90.00	-.705	-.154	-.004	.222	.119	.826	134.110	20.780	2078.1
94	19254	-.01	-4.99	4.99	-90.00	-.446	-.147	-.004	.222	.119	.825	134.160	20.790	2078.1
95	19255	.00	-10.00	10.00	-90.00	-.510	-.145	.001	.222	.119	.825	134.190	20.790	2078.1
96	19256	.00	-20.00	20.00	-90.00	.266	-.193	.002	.222	.119	.825	134.190	20.780	2078.1
97	19257	-.00	-30.01	30.01	-90.00	-.709	-.178	-.001	.222	.119	.825	134.260	20.800	2078.1
98	19258	-.01	-40.00	40.00	-90.00	-1.413	-.132	-.004	.222	.119	.825	134.260	20.790	2078.1
99	19259	-.00	-50.02	50.02	-90.00	-1.768	-.074	-.001	.222	.119	.825	134.270	20.800	2078.1
100	19260	.00	-60.01	60.01	-90.00	-1.585	-.063	.002	.222	.119	.825	134.260	20.800	2078.1
101	19261	.00	-70.00	70.00	-90.00	-2.112	-.043	.002	.222	.119	.825	134.220	20.790	2078.1
102	19262	-.00	-80.05	80.05	-90.00	-2.878	-.024	-.001	.222	.119	.825	134.220	20.800	2078.1
103	19263	.00	-65.01	65.01	-90.00	-1.641	.027	.003	.222	.119	.825	134.230	20.800	2078.1
104	19264	.03	-84.92	84.92	-90.00	-.720	.022	.003	.222	.119	.826	134.180	20.790	2078.1

Table I-B. Roll Damping Data

RUN	ALPHA	BETA	THETA	PHI	$\delta \dot{\alpha}, \delta \dot{\beta}, \delta \dot{\gamma}, \delta \dot{\phi}$				FREQ	MACH	RE/ft	V	$\bar{Q} = \bar{q}$	
					CLP $\delta$	CM I C $\delta$	CZ I C $\delta$	$\bar{Q}$ (lb/ft <sup>2</sup> )					P (lb/ft <sup>2</sup> )	
1	1036	-20.00	0.00	-20.00	0.00	-.121	.046	.022	.238	.118	.029	133.2	20.8	2107.3
2	1037	-9.99	0.00	-9.99	0.00	-.504	.043	.154	.239	.118	.027	133.0	20.7	2107.3
3	1038	.01	0.00	.01	0.00	.006	-.001	-.000	.238	.119	.022	133.6	20.9	2107.3
4	1039	5.01	0.00	5.01	0.00	-.096	-.016	-.047	.239	.118	.026	132.6	20.6	2107.3
5	1040	10.01	0.00	10.02	0.00	-.226	-.025	-.171	.239	.118	.029	132.8	20.7	2107.3
6	1041	20.01	0.00	20.01	0.00	-.348	-.059	-.024	.238	.118	.031	133.0	20.7	2107.3
7	1042	30.00	0.00	30.00	0.00	-1.003	-.052	.196	.237	.119	.035	133.5	20.9	2107.3
8	1043	40.01	0.00	40.00	0.00	-1.563	-.025	.324	.238	.118	.032	133.0	20.7	2107.3
9	1044	50.02	0.00	50.01	0.00	-2.410	-.019	.449	.239	.118	.031	132.7	20.7	2107.3
10	1045	60.03	0.00	60.01	0.00	-2.448	.001	.520	.238	.118	.031	132.9	20.7	2107.3
11	1046	70.02	0.00	70.00	0.00	-2.363	.040	.563	.239	.118	.029	132.6	20.6	2107.3
12	1047	70.02	0.00	70.00	0.00	-2.228	.040	.562	.239	.118	.029	132.7	20.7	2107.3
13	1048	72.00	0.00	71.98	0.00	-.882	.055	.554	.240	.118	.026	132.2	20.5	2107.3
14	1049	75.01	0.00	74.44	0.00	.856	.075	.532	.240	.118	.027	132.2	20.5	2107.3
15	1050	78.03	0.00	78.01	0.00	2.140	.113	.475	.240	.118	.026	132.1	20.5	2107.3
16	1051	80.04	0.00	80.02	0.00	3.040	.121	.443	.241	.117	.025	131.9	20.4	2107.3
17	1052	85.01	0.00	84.99	0.00	3.880	.116	.400	.240	.118	.027	132.3	20.5	2107.3
18	1053	89.94	0.00	84.97	0.00	4.945	.130	.394	.241	.117	.025	131.9	20.4	2107.3
19	2054	-19.98	0.00	-20.00	0.00	-.094	.070	-.034	.097	.288	2.003	326.7	124.4	2134.5
20	2055	-9.96	0.00	-10.01	0.00	.435	.030	.193	.099	.288	1.985	327.1	124.0	2134.5
21	2056	0.00	0.00	0.00	0.00	.032	0.000	0.000	.099	.288	1.972	326.0	124.1	2134.5
22	2057	4.98	0.00	4.99	0.00	.043	-.019	-.032	.099	.288	1.966	328.8	124.3	2134.5
23	2058	9.95	0.00	9.99	0.00	.728	-.043	-.121	.099	.288	1.963	329.1	124.3	2134.5
24	2059	14.97	0.00	20.00	0.00	1.338	-.073	.005	.099	.288	1.954	329.6	124.3	2134.5
25	2060	30.04	0.00	30.02	0.00	-.760	-.073	.238	.099	.287	1.942	329.1	123.6	2134.5
26	2061	40.06	0.00	40.01	0.00	-1.506	-.063	.405	.098	.287	1.937	329.6	123.6	2134.5
27	2062	50.09	0.00	50.01	0.00	-2.601	-.045	.493	.098	.288	1.939	330.0	123.9	2134.5
28	2063	60.11	0.00	60.01	0.00	-2.936	-.026	.577	.098	.287	1.929	329.1	123.1	2134.5
29	2064	70.14	0.00	70.02	0.00	-2.171	.017	.599	.099	.286	1.922	328.9	122.8	2134.5
30	2065	75.10	0.00	74.97	0.00	1.199	.031	.598	.100	.287	1.896	331.9	123.4	2134.5
31	2066	80.13	0.00	80.01	0.00	4.667	.050	.550	.101	.285	1.909	328.0	121.8	2134.5
32	2067	85.12	0.00	85.01	0.00	9.404	.051	.501	.103	.286	1.911	329.7	122.8	2134.5
33	2068	88.48	0.00	88.87	0.00	7.135	.017	.546	.102	.287	1.903	331.4	123.4	2134.5
34	3069	-20.03	0.00	-20.03	0.00	-.442	.034	.060	.399	.071	.491	80.1	7.5	2132.4
35	3070	-10.02	0.00	-10.02	0.00	-.740	.030	.204	.398	.071	.492	80.8	7.5	2132.4
36	3071	-.01	0.00	-.01	0.00	-.049	0.000	0.000	.396	.071	.494	80.2	7.5	2132.4
37	3072	5.00	0.00	5.00	0.00	-.079	.019	-.042	.396	.071	.494	80.2	7.5	2132.4
38	3073	10.00	0.00	10.00	0.00	-.506	-.013	-.192	.397	.071	.494	80.1	7.5	2132.4
39	3074	20.00	0.00	20.00	0.00	-.748	.020	-.160	.397	.071	.494	80.1	7.5	2132.4
40	3075	30.01	0.00	30.01	0.00	-1.365	-.038	.165	.398	.071	.493	79.9	7.5	2132.4
41	3076	40.01	0.00	40.01	0.00	-1.750	-.053	.376	.400	.070	.492	79.6	7.4	2132.4
42	3077	49.44	0.00	49.44	0.00	-2.026	-.071	.577	.349	.070	.492	79.7	7.4	2132.4
43	3078	50.00	0.00	49.44	0.00	-2.604	-.084	.713	.400	.070	.493	79.5	7.4	2132.4
44	3079	70.02	0.00	70.01	0.00	-1.581	-.003	.671	.400	.070	.493	79.5	7.4	2132.4
45	3080	80.01	0.00	80.00	0.00	.087	.154	.422	.400	.070	.493	79.4	7.4	2132.4
46	3081	85.01	0.00	85.00	0.00	1.234	.140	.379	.400	.070	.493	79.4	7.4	2132.4
47	3082	89.96	0.00	84.97	0.00	2.543	.169	.302	.401	.070	.492	79.3	7.4	2132.4
48	4083	-20.02	0.00	-20.01	0.00	-1.162	.050	.081	.236	.118	.027	133.7	21.0	2132.4
49	4084	-10.02	0.00	-10.02	0.00	-.800	.022	.086	.236	.118	.027	133.7	21.0	2132.4
50	4664	-.02	0.00	-.02	0.00	-.562	0.000	0.000	.235	.119	.029	134.0	21.0	2132.4

I-31

WP2846/1984a-805/JD

Table I-B. Roll Damping Data (Cont'd)

51	4086	5.00	0.00	5.00	0.00	-0.300	-0.011	-0.060	.236	.110	.025	133.5	20.9	2132.4
52	4087	10.00	0.00	10.00	0.00	-0.557	-0.019	-0.100	.237	.110	.025	133.5	20.9	2132.4
53	4088	20.00	0.00	20.01	0.00	-0.935	-0.041	-0.179	.237	.110	.025	133.5	20.9	2132.4
54	4089	30.02	0.00	30.02	0.00	-1.540	-0.082	.222	.230	.110	.022	133.5	20.9	2132.4
55	4090	40.03	0.00	40.02	0.00	-1.061	-0.065	.409	.230	.117	.018	132.8	20.6	2132.4
56	4091	50.02	0.00	50.01	0.00	-2.494	-0.070	.573	.216	.110	.025	133.6	20.9	2132.4
57	4092	60.03	0.00	60.01	0.00	-1.924	-0.036	.642	.237	.110	.023	132.9	20.7	2132.4
58	4093	70.01	0.00	69.99	0.00	.974	.023	.678	.230	.117	.023	132.6	20.6	2132.4
59	4094	75.01	0.00	74.99	0.00	5.533	.054	.675	.230	.117	.023	132.4	20.6	2132.4
60	4095	80.04	0.00	80.02	0.00	10.711	.097	.572	.239	.117	.020	132.0	20.5	2132.4
61	4096	85.04	0.00	85.02	0.00	8.421	.053	.526	.239	.117	.023	132.5	20.6	2132.4
62	4097	89.99	0.00	89.97	0.00	7.463	.030	.515	.239	.117	.022	132.2	20.5	2132.4
63	5098	-20.01	0.00	-20.01	0.00	-1.261	.024	.062	.230	.119	.036	133.9	21.1	2132.4
64	5099	-9.98	0.00	-9.99	0.00	-1.036	.023	.225	.237	.119	.037	134.0	21.2	2132.4
65	5100	0.00	0.00	0.00	0.00	-.244	0.000	0.000	.237	.119	.037	134.2	21.2	2132.4
66	5101	5.00	0.00	5.00	0.00	-.314	-.015	-.046	.230	.119	.034	133.0	21.0	2132.4
67	5102	9.99	0.00	10.00	0.00	-.872	-.030	-.213	.230	.119	.034	133.9	21.1	2132.4
68	5103	20.00	0.00	20.00	0.00	-1.123	-.050	-.019	.240	.110	.031	133.4	20.9	2132.4
69	5104	30.00	0.00	30.00	0.00	-.750	-.067	.190	.239	.110	.031	133.6	21.0	2132.4
70	5105	40.02	0.00	40.01	0.00	-1.257	-.073	.391	.239	.110	.030	133.5	20.9	2132.4
71	5106	50.02	0.00	50.01	0.00	-2.099	-.095	.549	.239	.110	.020	133.4	20.9	2132.4
72	5107	60.02	0.00	60.01	0.00	-2.224	-.073	.599	.239	.110	.029	133.7	21.0	2132.4
73	5108	70.03	0.00	70.01	0.00	-1.543	-.026	.597	.240	.110	.026	133.1	20.8	2132.4
74	5109	80.04	0.00	80.02	0.00	-2.709	.045	.409	.241	.110	.024	132.0	20.7	2132.4
75	5110	82.03	0.00	82.01	0.00	-1.324	.048	.481	.241	.117	.024	132.5	20.6	2132.4
76	5111	84.02	0.00	84.00	0.00	2.029	.069	.439	.241	.117	.025	132.6	20.7	2132.4
77	5112	85.02	0.00	85.00	0.00	3.009	.005	.407	.242	.117	.023	132.6	20.6	2132.4
78	5113	89.99	0.00	89.97	0.00	2.145	.027	.527	.241	.117	.023	132.5	20.6	2132.4
79	6114	-20.01	0.00	-20.02	0.00	-.685	.007	.141	.236	.119	.040	133.6	21.1	2132.4
80	6115	-9.99	0.00	-10.00	0.00	-.949	-.005	.204	.234	.119	.044	134.3	21.3	2132.4
81	6116	.01	0.00	.01	0.00	-.169	0.000	0.000	.234	.119	.044	134.1	21.3	2132.4
82	6117	5.01	0.00	5.01	0.00	-.268	-.026	-.020	.235	.119	.043	133.8	21.2	2132.4
83	6118	10.00	0.00	10.00	0.00	-.436	-.040	-.069	.235	.119	.043	133.9	21.2	2132.4
84	6119	20.00	0.00	20.01	0.00	-.994	-.005	-.023	.235	.119	.044	133.9	21.2	2132.4
85	6120	29.99	0.00	29.99	0.00	-1.036	-.083	.237	.235	.119	.043	133.6	21.2	2132.4
86	6121	40.02	0.00	40.01	0.00	-1.560	-.084	.434	.235	.119	.042	133.5	21.1	2132.4
87	6122	50.01	0.00	50.00	0.00	-2.661	-.097	.597	.234	.119	.045	133.9	21.2	2132.4
88	6123	60.02	0.00	60.00	0.00	-2.663	-.071	.670	.236	.119	.042	133.2	21.0	2132.4
89	6124	70.02	0.00	70.00	0.00	-2.587	-.008	.680	.236	.110	.040	132.9	20.9	2132.4
90	6125	75.01	0.00	74.99	0.00	3.057	.025	.678	.237	.110	.038	133.1	21.0	2132.4
91	6126	80.03	0.00	80.01	0.00	7.695	.065	.597	.237	.110	.040	133.0	21.0	2132.4
92	6127	85.05	0.00	85.03	0.00	6.437	.050	.514	.230	.110	.030	132.0	20.9	2132.4
93	6128	89.99	0.00	89.97	0.00	6.917	.046	.496	.237	.110	.040	133.1	21.0	2132.4
94	6151	-90.00	0.00	-29.98	0.00	4.389	-.041	-.499	.246	.110	.021	133.1	20.6	2133.6
95	6152	-80.03	0.00	-80.01	0.00	1.757	.008	-.680	.245	.110	.024	132.9	20.6	2133.6
96	6153	-70.00	0.00	-69.98	0.00	-2.568	.087	-.811	.243	.119	.029	134.0	21.0	2133.6
97	6154	-60.03	0.00	-60.01	0.00	-2.605	.116	-.754	.242	.119	.031	134.3	21.1	2133.6
98	6155	-50.00	0.00	-49.99	0.00	-2.541	.132	-.672	.242	.119	.032	134.6	21.1	2133.6
99	6156	-40.01	0.00	-40.00	0.00	-1.988	.101	-.489	.241	.120	.036	135.2	21.3	2133.6
100	6157	-30.00	0.00	-30.00	0.00	-1.282	.089	-.296	.242	.120	.035	135.2	21.3	2133.6
101	6158	-19.99	0.00	-19.99	0.00	-.789	.092	-.081	.242	.120	.034	135.0	21.3	2133.6
102	6159	-10.00	0.00	-10.01	0.00	-.513	.062	.124	.242	.120	.036	135.6	21.4	2133.6
103	6160	.01	0.00	-.01	0.00	-2.236	0.000	0.000	.242	.120	.035	135.5	21.4	2133.6
104	6161	9.99	0.00	10.00	0.00	-.233	-.029	-.171	.242	.120	.035	135.6	21.4	2133.6
105	6162	19.99	0.00	20.00	0.00	-.325	-.067	-.020	.243	.120	.034	135.4	21.3	2133.6
106	6163	30.00	0.00	30.00	0.00	-1.017	-.056	.187	.243	.120	.032	135.3	21.3	2133.6
107	6164	40.02	0.00	40.01	0.00	-1.480	-.045	.354	.244	.119	.029	134.0	21.1	2133.6
108	6165	50.02	0.00	50.01	0.00	-2.247	-.028	.447	.244	.119	.030	134.8	21.2	2133.6
109	6166	60.02	0.00	60.00	0.00	-2.233	.000	.505	.245	.119	.026	134.1	20.9	2133.6
110	6167	70.03	0.00	70.01	0.00	-2.165	.057	.512	.245	.119	.027	134.3	21.0	2133.6
111	6168	80.03	0.00	80.01	0.00	-2.060	.131	.410	.245	.119	.025	133.9	20.9	2133.6
112	6169	89.99	0.00	89.97	0.00	-.375	.103	.384	.247	.110	.029	133.9	20.8	2133.6
113	6170	-89.99	-22.50	-89.97	22.50	-3.307	-.038	-.712	.246	.110	.026	133.9	20.8	2133.6



Table I-B. Roll Damping Data (Cont'd)

114	9171	-74.23	-22.14	-80.01	22.50	-3.772	.007	-.644	.246	.110	.026	133.5	20.8	2113.6
115	9172	-68.49	-21.07	-69.97	22.50	-.861	.002	-.790	.244	.119	.030	134.2	21.0	2113.6
116	9173	-73.03	-14.36	-60.01	22.50	-.605	.109	-.781	.244	.119	.032	134.6	21.1	2113.6
117	9174	-47.77	-17.03	-50.00	22.50	-1.263	.151	-.646	.244	.119	.033	134.8	21.2	2113.6
118	9175	-37.77	-14.23	-34.92	22.50	-.847	.114	-.483	.243	.120	.034	135.2	21.3	2113.6
119	9176	-28.07	-11.03	-24.98	22.50	-.776	.072	-.231	.243	.120	.036	135.5	21.4	2113.6
120	9177	-18.58	-7.52	-26.00	22.50	-1.145	.070	-.013	.243	.120	.036	135.5	21.4	2113.6
121	9178	-9.24	-3.81	-9.99	22.50	-.416	.036	.134	.244	.120	.034	135.5	21.4	2113.6
122	9179	0.00	0.00	0.00	22.50	-.045	0.000	0.000	.244	.120	.033	135.3	21.3	2113.6
123	9180	9.25	3.81	10.00	22.50	-.275	-.047	-.094	.246	.119	.020	134.8	21.1	2113.6
124	9181	18.60	7.53	20.02	22.50	-1.106	-.062	-.039	.245	.120	.030	135.1	21.2	2113.6
125	9182	28.00	11.03	30.00	22.50	-1.115	-.047	.160	.245	.120	.032	135.2	21.3	2113.6
126	9183	37.81	14.25	40.02	22.50	-.894	-.027	.303	.245	.120	.031	135.0	21.2	2113.6
127	9184	47.78	17.03	50.01	22.50	-1.104	-.004	.410	.246	.119	.028	134.4	21.0	2113.6
128	9185	58.04	19.36	60.02	22.50	-1.299	.030	.459	.246	.119	.028	134.3	21.0	2113.6
129	9186	68.54	21.00	70.02	22.50	-.879	.063	.510	.246	.119	.027	134.1	20.9	2113.6
130	9187	74.21	22.14	80.00	22.50	-3.247	.047	.515	.246	.119	.025	133.7	20.8	2113.6
131	9188	89.99	22.50	89.97	22.50	-2.953	.095	.493	.246	.119	.026	133.7	20.8	2113.6
132	10189	-89.99	-22.50	-89.97	-22.50	-3.139	-.064	-.570	.247	.110	.024	133.2	20.7	2113.6
133	10190	-79.21	-22.14	-80.00	-22.50	-3.655	.012	-.636	.247	.110	.026	133.1	20.7	2113.6
134	10191	-68.51	-21.07	-69.99	-22.50	-2.373	.044	-.700	.245	.119	.031	134.0	21.0	2113.6
135	10192	-58.02	-14.36	-60.00	-22.50	-1.514	.089	-.741	.245	.119	.034	134.5	21.1	2113.6
136	10193	-47.74	-17.04	-49.97	-22.50	-.936	.110	-.671	.245	.119	.032	134.5	21.1	2113.6
137	10194	-37.79	-14.24	-40.00	-22.50	-.951	.083	-.473	.244	.120	.037	135.2	21.3	2113.6
138	10195	-28.09	-11.03	-30.01	-22.50	-1.053	.069	-.274	.244	.120	.037	135.4	21.4	2113.6
139	10196	-18.57	-7.52	-19.99	-22.50	-.682	.067	-.066	.244	.120	.035	135.3	21.3	2113.6
140	10197	-9.21	-3.80	-9.96	-22.50	-.526	.076	.094	.244	.120	.036	135.5	21.4	2113.6
141	10198	.01	-.00	.01	-22.50	-.102	0.000	0.000	.245	.120	.034	135.3	21.3	2113.6
142	10199	9.26	-3.81	10.01	-22.50	-.245	-.039	-.078	.245	.120	.033	135.2	21.3	2113.6
143	10200	18.60	-7.53	20.02	-22.50	-.693	-.049	.046	.245	.120	.032	135.2	21.3	2113.6
144	10201	28.10	-11.04	30.02	-22.50	-1.002	-.075	.270	.245	.120	.033	135.3	21.3	2113.6
145	10202	37.80	-14.24	40.01	-22.50	-.800	-.054	.382	.246	.119	.028	134.7	21.1	2113.6
146	10203	47.77	-17.03	50.00	-22.50	-.662	-.052	.537	.245	.120	.031	135.0	21.2	2113.6
147	10204	58.03	-19.36	60.01	-22.50	-1.206	.001	.568	.246	.119	.030	134.7	21.1	2113.6
148	10205	68.53	-21.00	70.01	-22.50	-1.702	.031	.538	.246	.119	.027	134.2	21.0	2113.6
149	10206	74.23	-22.14	80.01	-22.50	-3.461	.070	.468	.248	.110	.022	133.3	20.7	2113.6
150	10207	89.99	-22.50	89.97	-22.50	-2.624	.083	.515	.249	.117	.018	132.5	20.5	2113.6
151	11208	-89.98	-45.00	-89.97	45.00	-2.606	-.055	-.249	.249	.117	.018	132.5	20.5	2113.6
152	11209	-76.02	-44.14	-80.00	45.00	-2.892	.015	-.565	.248	.110	.024	132.0	20.6	2113.6
153	11210	-62.76	-41.64	-69.99	45.00	-2.746	.111	-.618	.247	.110	.027	133.4	20.8	2113.6
154	11211	-58.76	-37.76	-60.00	45.00	-3.414	.096	-.550	.247	.119	.028	133.6	20.8	2113.6
155	11212	-48.13	-32.80	-50.00	45.00	-1.246	.089	-.471	.246	.119	.029	133.9	20.9	2113.6
156	11213	-38.70	-27.04	-40.01	45.00	-1.561	.104	-.358	.245	.119	.033	134.7	21.2	2113.6
157	11214	-28.19	-20.69	-29.98	45.00	-1.356	.063	-.135	.246	.119	.030	134.4	21.1	2113.6
158	11215	-14.43	-14.00	-20.00	45.00	-.815	.051	.056	.245	.120	.033	134.0	21.2	2113.6
159	11216	-7.09	-7.04	-9.98	45.00	-.608	.009	.102	.246	.119	.032	134.0	21.2	2113.6
160	11217	.01	.01	.02	45.00	-.075	-.018	.045	.245	.120	.033	135.2	21.3	2113.6
161	11218	7.10	7.05	10.02	45.00	-.460	-.042	-.007	.246	.120	.032	135.1	21.2	2113.6
162	11219	14.44	14.01	20.02	45.00	-1.632	-.056	.033	.246	.120	.032	135.2	21.3	2113.6
163	11220	22.22	20.72	30.02	45.00	-1.139	-.037	.098	.246	.120	.030	135.0	21.2	2113.6
164	11221	30.70	27.04	40.01	45.00	-1.296	-.024	.134	.247	.119	.027	134.4	21.0	2113.6
165	11222	40.13	32.80	50.00	45.00	-1.052	-.006	.314	.247	.119	.027	134.3	21.0	2113.6
166	11223	50.85	37.79	60.01	45.00	-2.994	-.045	.448	.247	.119	.027	134.2	21.0	2113.6
167	11224	62.80	41.65	70.02	45.00	-2.614	-.081	.560	.248	.110	.024	133.5	20.8	2113.6
168	11225	76.04	44.14	80.02	45.00	-2.502	.043	.447	.248	.110	.023	133.5	20.8	2113.6
169	11226	89.98	45.00	89.97	45.00	-2.776	.112	.436	.250	.117	.017	132.3	20.4	2113.6
170	12227	-14.44	14.00	-20.01	-45.00	-.322	.005	.048	.246	.119	.022	134.5	21.0	2117.0
171	12228	-7.11	7.06	-10.01	-45.00	-.240	-.023	.151	.246	.119	.023	134.6	21.0	2117.0
172	12229	.01	.01	.01	-45.00	.019	-.025	.030	.246	.119	.022	134.5	21.0	2117.0
173	12230	3.54	-3.54	5.01	-45.00	.086	-.042	-.007	.246	.119	.022	134.3	20.9	2117.0
174	12231	7.12	-7.07	10.02	-45.00	-.090	-.030	-.068	.246	.119	.024	134.5	21.0	2117.0
175	12232	14.43	-14.00	20.00	-45.00	-.165	-.038	-.059	.246	.119	.024	134.5	21.0	2117.0
176	12233	22.21	-20.70	30.00	-45.00	-.436	-.043	.114	.246	.119	.024	134.4	21.0	2117.0

Table I-B. Roll Damping Data (Cont'd)

177	12234	30.60	-27.03	34.94	-45.00	-.798	-.024	.254	.247	.119	.023	134.0	20.9	2117.0
178	12235	40.16	-32.81	50.03	-45.00	-1.468	-.018	.362	.247	.118	.023	133.9	20.9	2117.0
179	12236	50.74	-37.77	60.01	-45.00	-.811	-.011	.364	.246	.118	.023	133.9	20.9	2117.0
180	12237	62.80	-41.65	70.02	-45.00	-.789	.005	.392	.247	.118	.022	133.7	20.8	2117.0
181	12238	76.07	-44.14	80.04	-45.00	-1.075	.081	.356	.247	.118	.020	133.3	20.7	2117.0
182	12239	82.98	-44.76	85.01	-45.00	-1.183	.116	.361	.247	.116	.022	133.4	20.7	2117.0
183	12240	89.48	-45.06	84.47	-45.00	-2.274	.139	.390	.247	.118	.021	133.3	20.7	2117.0
184	12241	-7.93	-18.43	-20.01	67.50	-1.210	.012	.084	.247	.115	.028	134.0	21.0	2124.0
185	13242	-3.86	-4.23	-10.00	67.50	-.486	-.005	.048	.247	.119	.027	134.0	21.0	2124.0
186	13243	-.01	-.02	-.02	67.50	-.097	-.025	.069	.247	.119	.027	134.1	21.0	2124.0
187	13244	1.91	4.61	4.99	67.50	-.000	-.026	.045	.248	.118	.023	133.5	20.8	2124.0
188	13245	3.87	4.25	10.02	67.50	-.199	-.026	.045	.248	.118	.023	133.7	20.8	2124.0
189	13246	7.93	18.42	20.00	67.50	-1.070	-.052	.060	.248	.118	.025	134.0	20.9	2124.0
190	13247	12.46	27.51	30.00	67.50	-.767	-.056	.079	.248	.118	.024	134.0	20.9	2124.0
191	13248	17.81	36.44	40.01	67.50	-.633	-.025	.159	.249	.118	.020	133.0	20.6	2124.0
192	13249	24.53	45.06	50.01	67.50	-1.260	-.014	.243	.249	.118	.022	133.3	20.7	2124.0
193	13250	33.57	53.16	60.02	67.50	-.982	-.007	.293	.248	.118	.022	133.2	20.7	2124.0
194	13251	46.45	60.25	70.00	67.50	-.537	-.042	.388	.249	.118	.022	132.7	20.6	2124.0
195	13252	65.25	65.48	79.99	67.50	-3.036	.029	.301	.249	.117	.021	132.5	20.6	2124.0
196	13253	77.14	66.48	85.00	67.50	-3.031	.060	.301	.249	.117	.022	132.5	20.6	2124.0
197	13254	84.86	67.50	89.94	67.50	-2.866	.083	.275	.249	.117	.022	132.4	20.5	2124.0
198	14255	-7.43	-18.43	-20.01	67.50	-1.246	.000	.000	.246	.119	.034	134.0	21.1	2124.0
199	14256	-3.86	-9.23	-10.00	67.50	-.340	.000	.000	.247	.119	.033	133.8	21.0	2124.0
200	15257	-7.93	18.43	-20.01	-67.50	-.800	-.013	.130	.248	.118	.026	133.3	20.8	2124.0
201	15258	-3.85	4.22	-9.99	-67.50	-.563	-.023	.119	.249	.118	.023	132.8	20.7	2124.0
202	15259	-.00	0.00	0.00	-67.50	-.072	-.015	.012	.249	.118	.024	132.9	20.7	2124.0
203	15260	1.91	-4.61	4.99	-67.50	.040	-.014	-.022	.249	.118	.023	132.8	20.6	2124.0
204	15261	3.86	-9.24	10.01	-67.50	-.126	-.015	-.027	.249	.118	.024	133.1	20.7	2124.0
205	15262	7.93	-18.42	20.00	-67.50	-.584	-.044	-.031	.249	.118	.023	133.2	20.8	2124.0
206	15263	12.45	-27.50	29.99	-67.50	-.798	-.053	.051	.249	.118	.022	133.2	20.7	2124.0
207	15264	17.80	-36.42	34.94	-67.50	-.394	-.025	.124	.250	.118	.021	133.0	20.7	2124.0
208	15265	24.52	-45.05	50.00	-67.50	-.166	.002	.198	.250	.118	.019	132.8	20.6	2124.0
209	15266	33.54	-53.13	59.94	-67.50	-.845	.017	.241	.251	.117	.017	132.6	20.5	2124.0
210	15267	46.43	-60.24	69.99	-67.50	-1.451	-.009	.327	.251	.117	.015	132.4	20.5	2124.0
211	15268	65.25	-65.46	79.94	-67.50	-3.024	.022	.333	.252	.117	.013	132.1	20.3	2124.0
212	15269	77.11	-66.48	84.94	-67.50	-3.231	.063	.288	.253	.116	.007	131.3	20.1	2124.0
213	15270	84.93	-67.50	89.97	-67.50	-3.151	.079	.234	.253	.116	.009	131.5	20.2	2124.0
214	16271	-19.95	0.00	-14.44	0.00	-.421	0.000	0.000	.143	.117	.015	132.6	20.5	2119.9
215	16272	-10.02	0.00	-10.02	0.00	-.218	0.000	0.000	.143	.118	.018	133.1	20.6	2119.9
216	16273	.01	0.00	.01	0.00	.138	0.000	0.000	.143	.118	.024	132.9	20.7	2119.9
217	16274	5.01	0.00	5.01	0.00	-.012	0.000	0.000	.143	.118	.023	132.7	20.6	2119.9
218	16275	10.02	0.00	10.02	0.00	-.264	0.000	0.000	.143	.118	.023	132.6	20.6	2119.9
219	16276	20.00	0.00	20.00	0.00	-.732	0.000	0.000	.143	.117	.022	132.4	20.5	2119.9
220	16277	29.94	0.00	24.44	0.00	-1.363	0.000	0.000	.144	.117	.022	132.4	20.5	2119.9
221	16278	40.01	0.00	40.01	0.00	1.023	0.000	0.000	.143	.118	.026	132.9	20.7	2119.9
222	16279	50.01	0.00	50.01	0.00	1.023	0.000	0.000	.142	.118	.030	133.5	20.9	2119.9
223	16280	54.94	0.00	54.94	0.00	-1.053	0.000	0.000	.142	.118	.029	133.3	20.8	2119.9
224	16281	70.02	0.00	70.02	0.00	2.311	0.000	0.000	.143	.118	.026	132.7	20.6	2119.9
225	16282	79.94	0.00	74.94	0.00	14.557	0.000	0.000	.144	.118	.025	132.6	20.6	2119.9
226	16283	85.00	0.00	85.00	0.00	7.130	0.000	0.000	.145	.117	.020	131.7	20.3	2119.9
227	16284	84.42	0.00	84.42	0.00	8.942	0.000	0.000	.144	.117	.023	132.1	20.5	2119.9

Table I-C. Symbols and Nomenclature Related to Subsonic Tests

(See Figure C-4 for direction of forces, moments, and angles.)

$C_A$	axial force coefficient, $C_A = \frac{\text{axial force}}{qS}$
$C_l$	rolling moment coefficient, $C_l = \frac{\text{rolling moment}}{qSL}$
$C_{l_p}$	roll damping coefficient, $C_{l_p} = \frac{\partial C_l}{\partial (\frac{\dot{\phi}L}{2V})}$
$C_m$	pitching moment coefficient, $C_m = \frac{\text{pitching moment}}{qSL}$ referenced to the centroid of the rectangular parallelepiped
$C_{m_R}$	$C_{m_R} = C_m \cos \phi - C_y \sin \phi$
$C_n$	yawing moment coefficient, $C_n = \frac{\text{yawing moment}}{qSL}$ referenced to the centroid
$C_N$	normal force coefficient, $C_N = \frac{\text{normal force}}{qS}$
$C_{N_R}$	$C_{N_R} = C_N \cos \phi - C_y \sin \phi$
$C_y$	yaw force coefficient, $C_y = \frac{\text{yaw force}}{qS}$
$x$	length of model along the $x_m$ - axis
$L$	length of model along the $y_m$ - axis; reference length, $L = 0.319$ ft for scale = 1.0
$q$	dynamic pressure, $q = (1/2) \rho V^2$
$R$	corner radius
$Re$	Reynolds number based on length $L$
$S$	reference area: $S = 0.0975$ ft <sup>2</sup>
$V$	velocity
$x, y, z$	axis systems defined in Figure C-4

Table I-C. Symbols and Nomenclature Related to Subsonic Tests (Cont'd)

$X_{c.p}$	longitudinal center of pressure location measured from the leading edge of the model, positive downstream
$\alpha$	body angle of attack
$\alpha_R$	resultant angle of attack; $\alpha_R = \tan^{-1} [\tan \alpha / \cos \phi]$
$\beta$	angle of sideslip; $\beta = -\psi$
$\theta$	pitch orientaton
$\rho$	free stream air density
$\phi$	roll orientation
$\dot{\phi}$	rate of change of $\phi$ ( $d\phi/dt$ )
$\psi$	yaw orientation
$\omega$	oscillation frequency
$\bar{\omega}$	$\bar{\omega} = \omega L / 2V$

Subscripts for Axis Systems

m	model axis system
R	resultant vector derived from y and z components

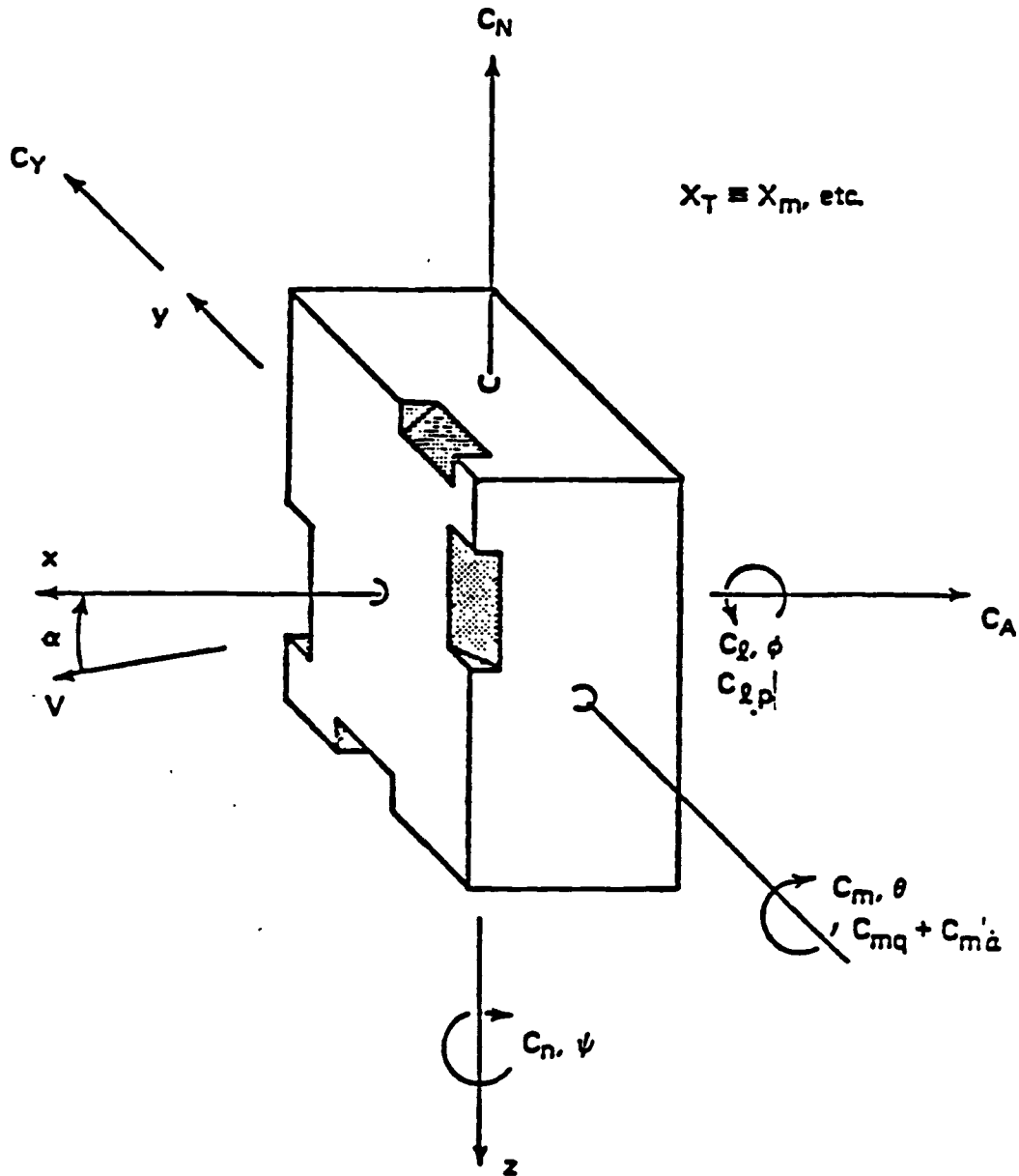


Figure I-J. Model-Fixed and Modified Tunnel Axis System  
 at  $\psi_m = 0^\circ$ ,  $\phi_m = 0^\circ$

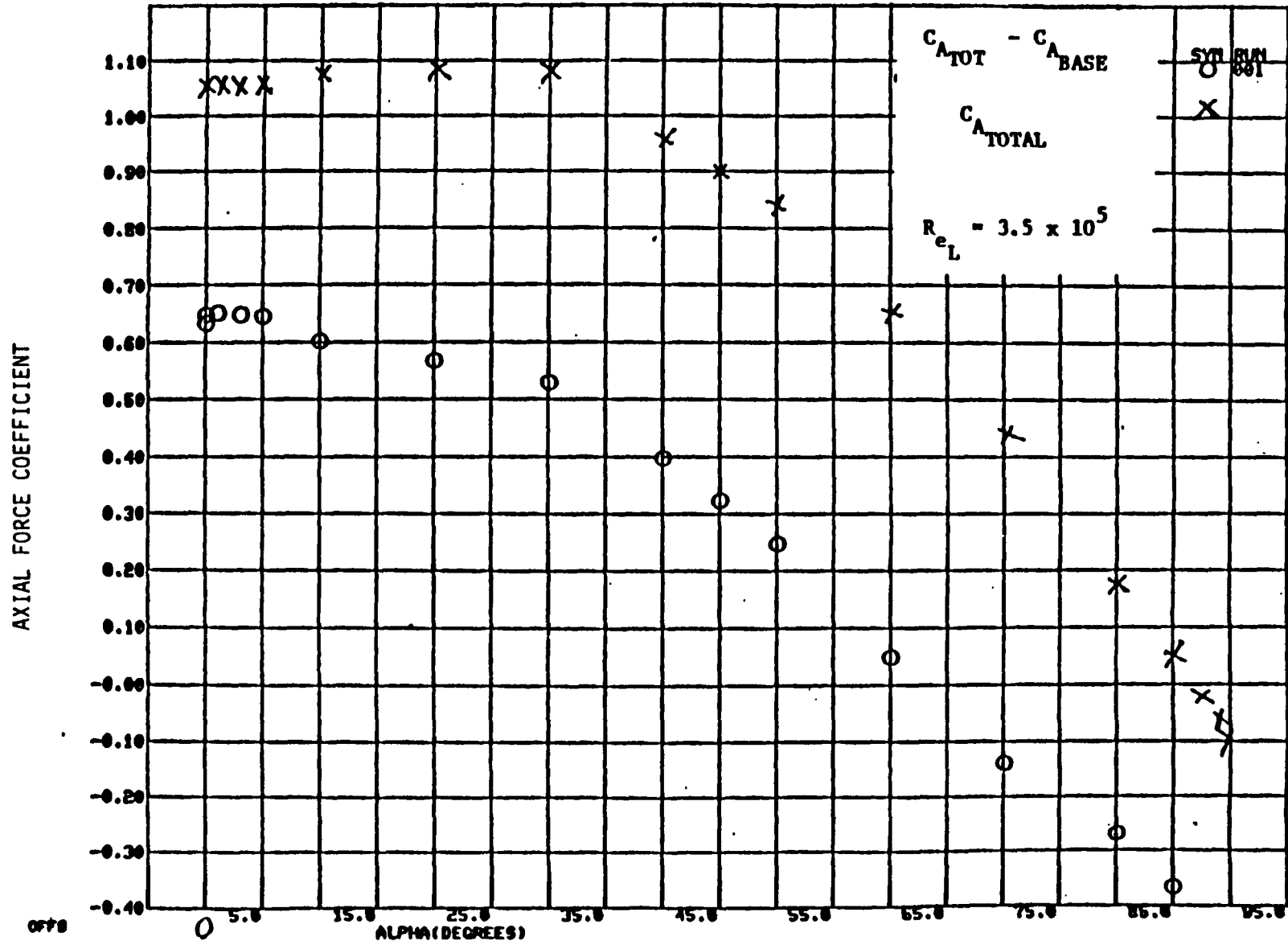


Figure I-K. Axial Force Coefficient Results

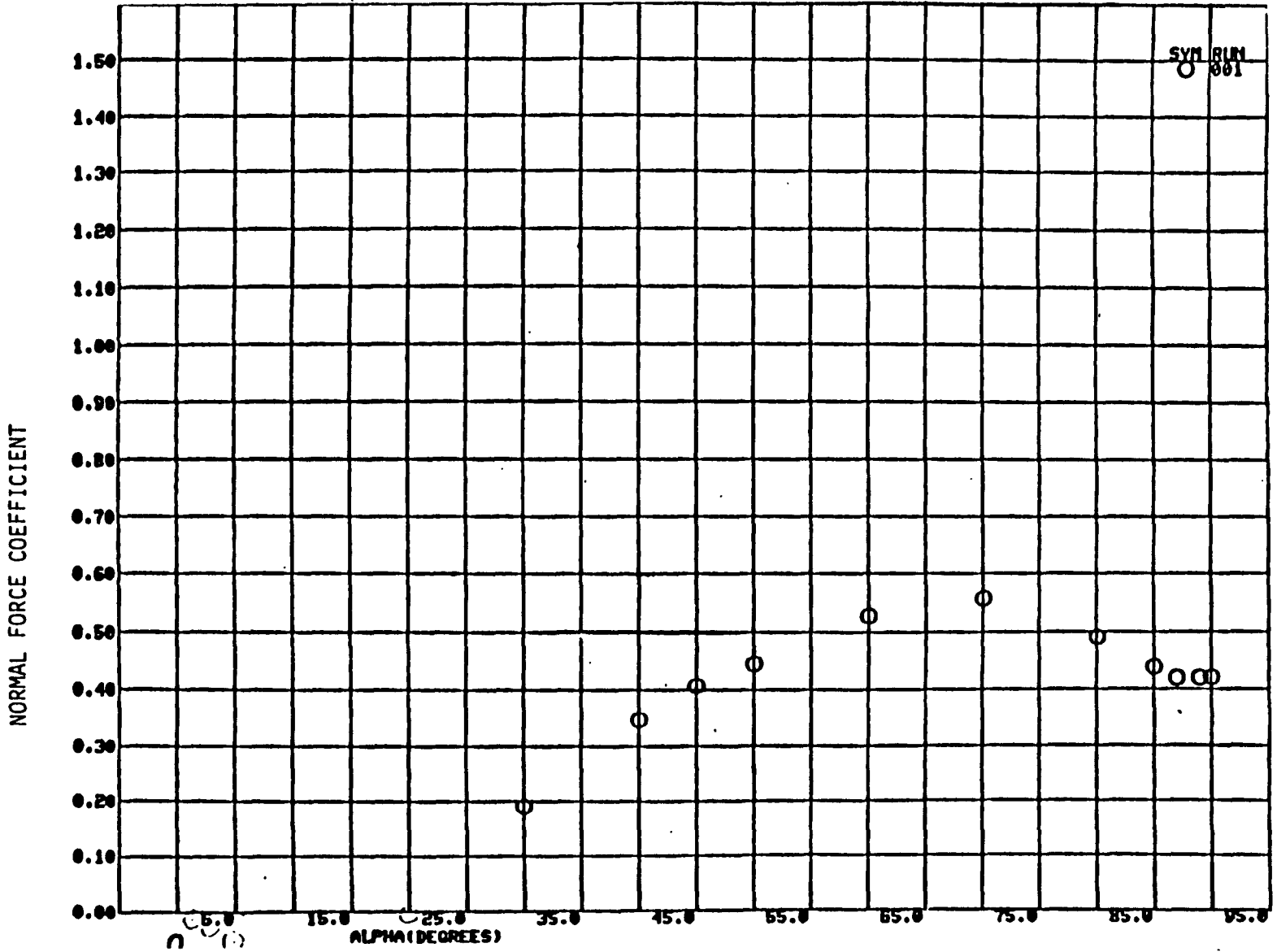


Figure I-L. Normal Force Coefficient Results

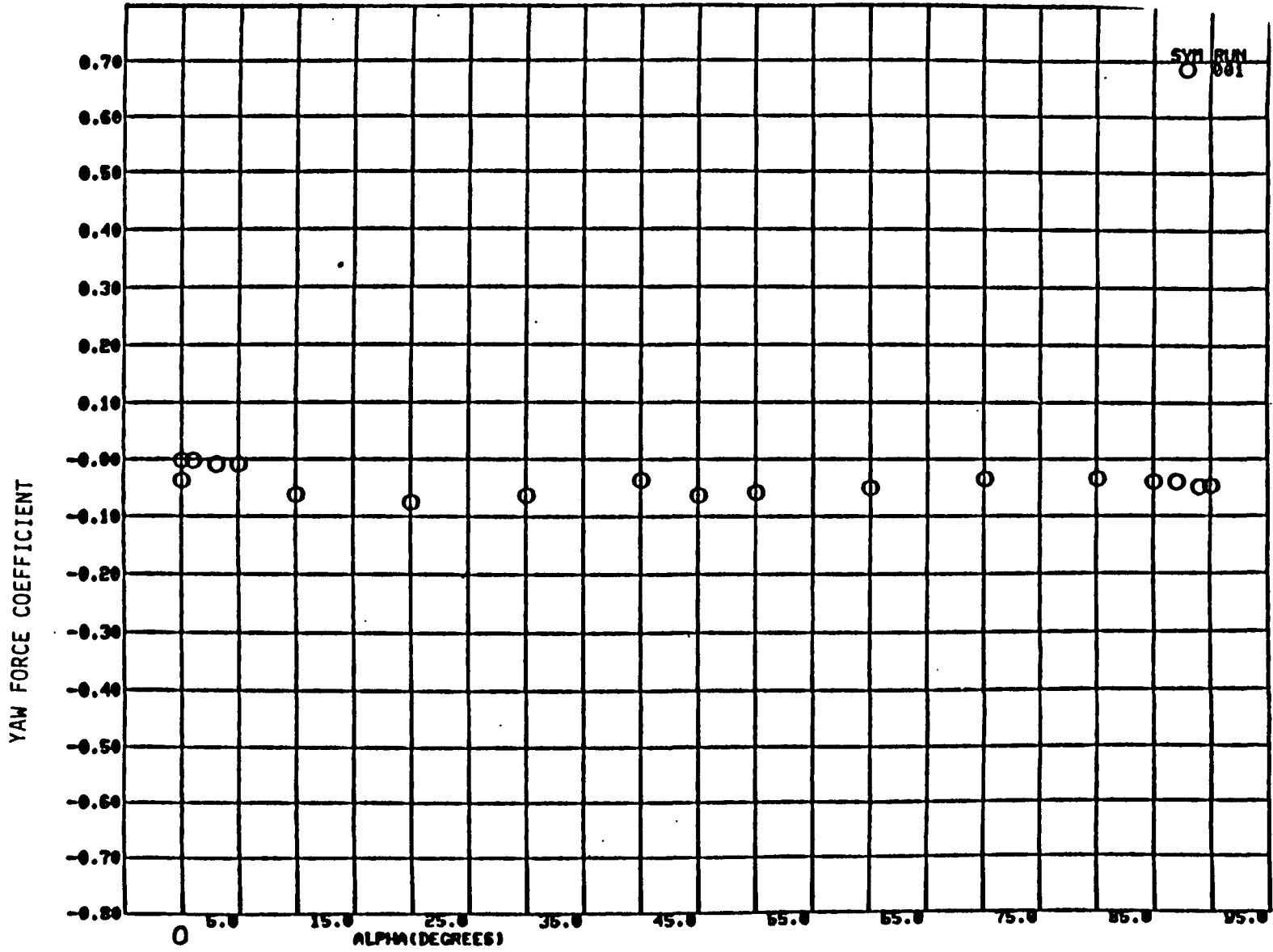


Figure I-M. Yaw Force Coefficient Results



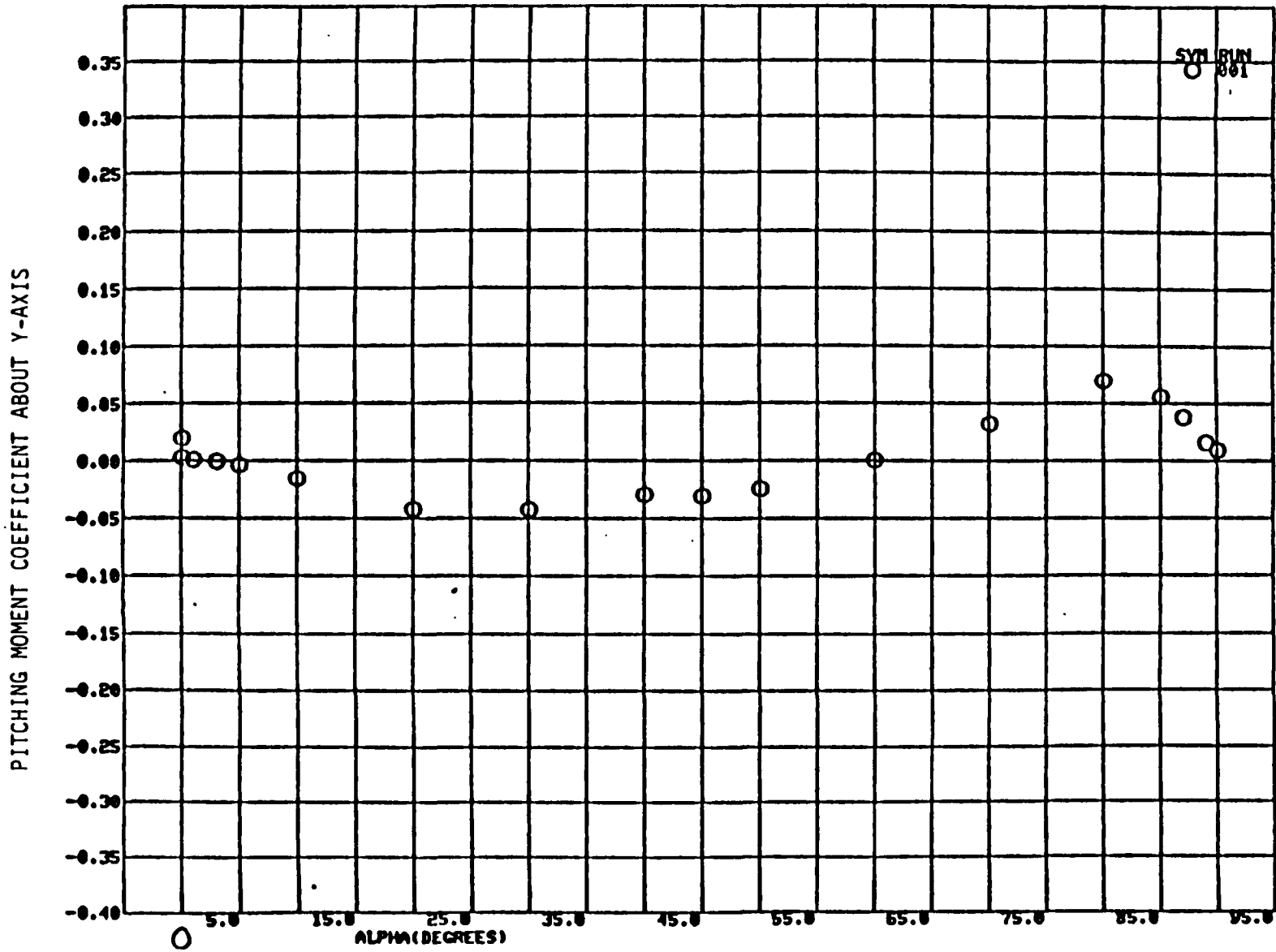


Figure I-N. Pitching Moment Coefficient Results

YAWING MOMENT COEFFICIENT ABOUT Z-AXIS

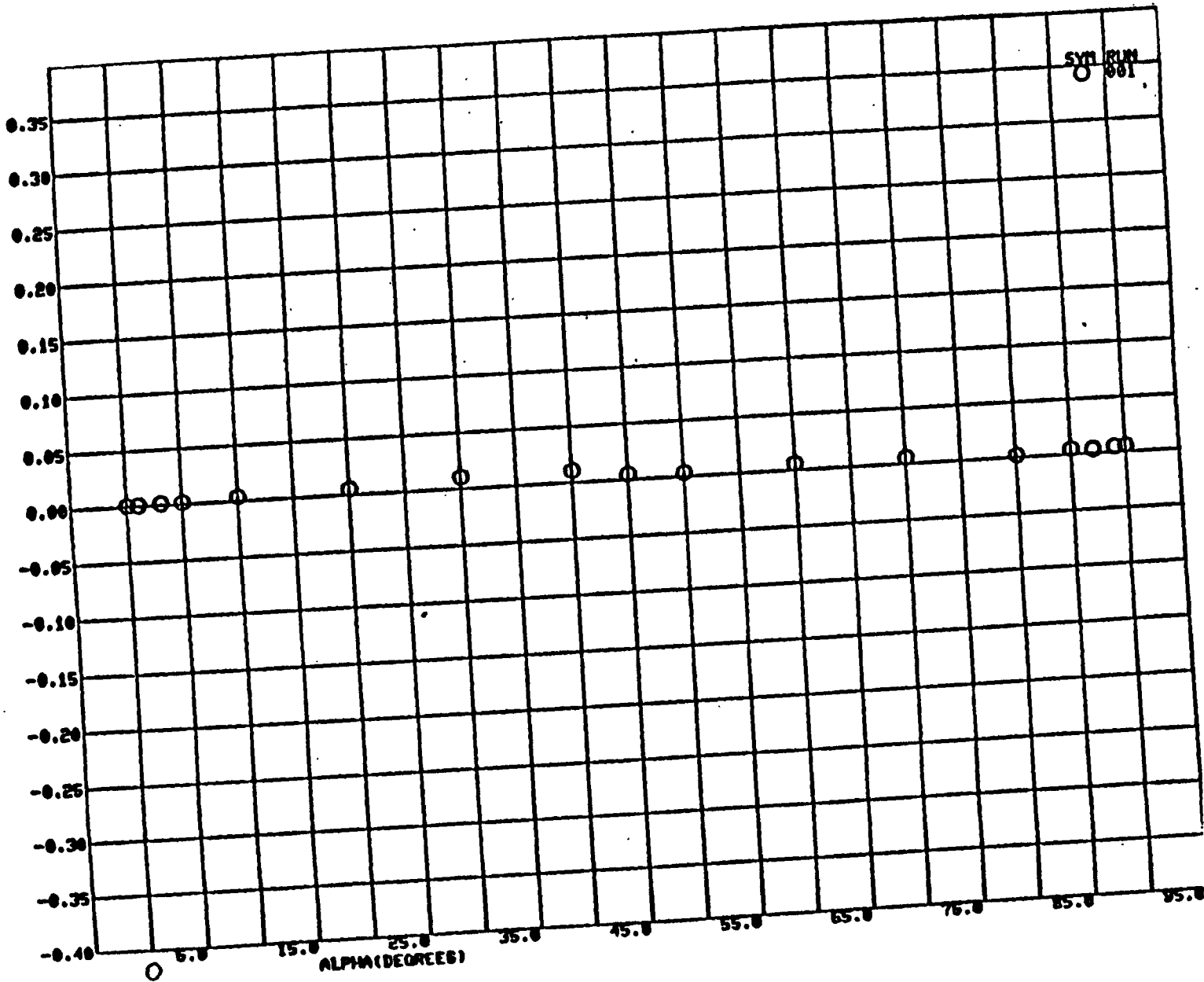


Figure I-Q. Rolling Moment Coefficient Results

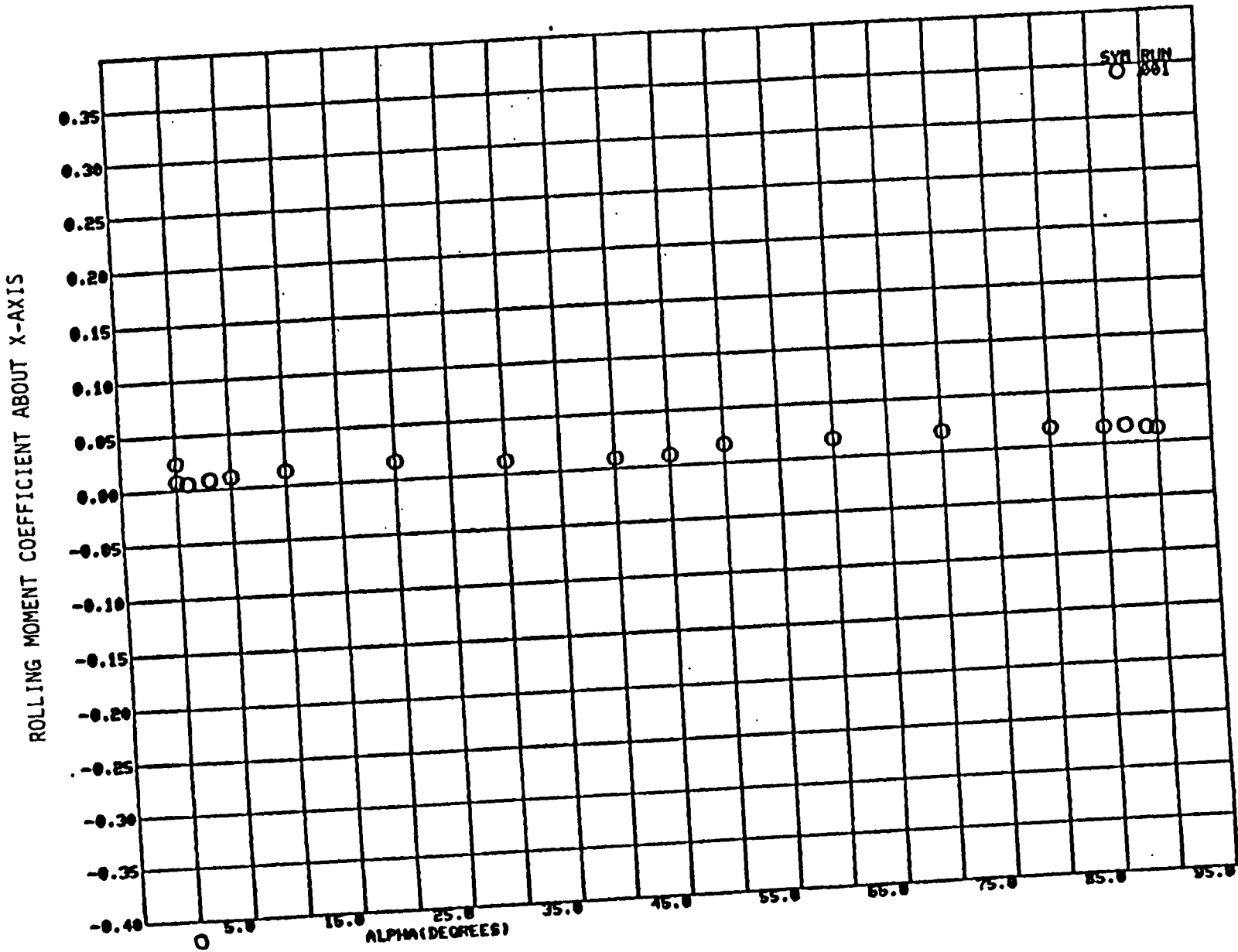


Figure I-P. Yawing Moment Coefficient Results

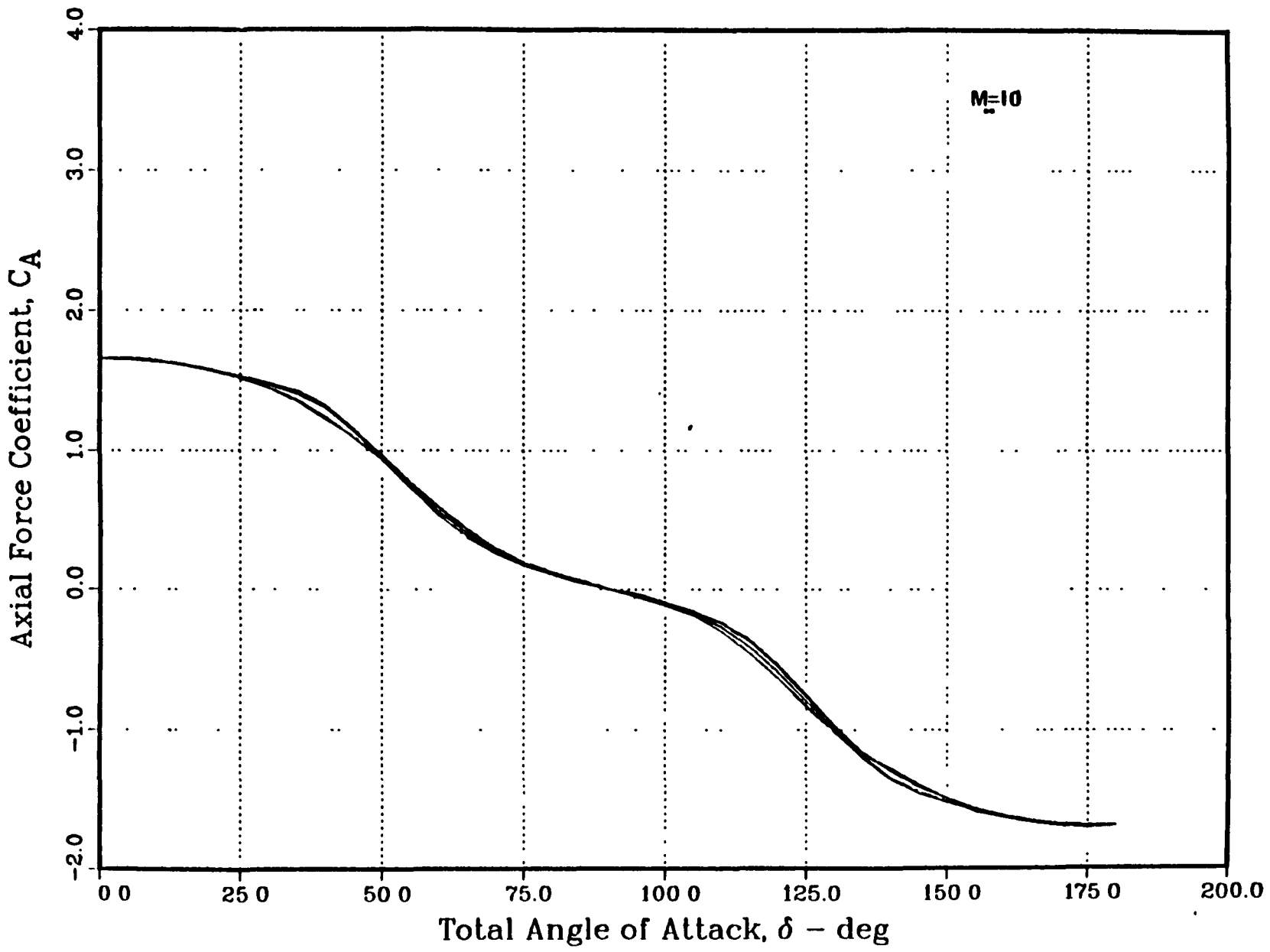


Figure I-Q. Axial Force Coefficient - Hypersonic

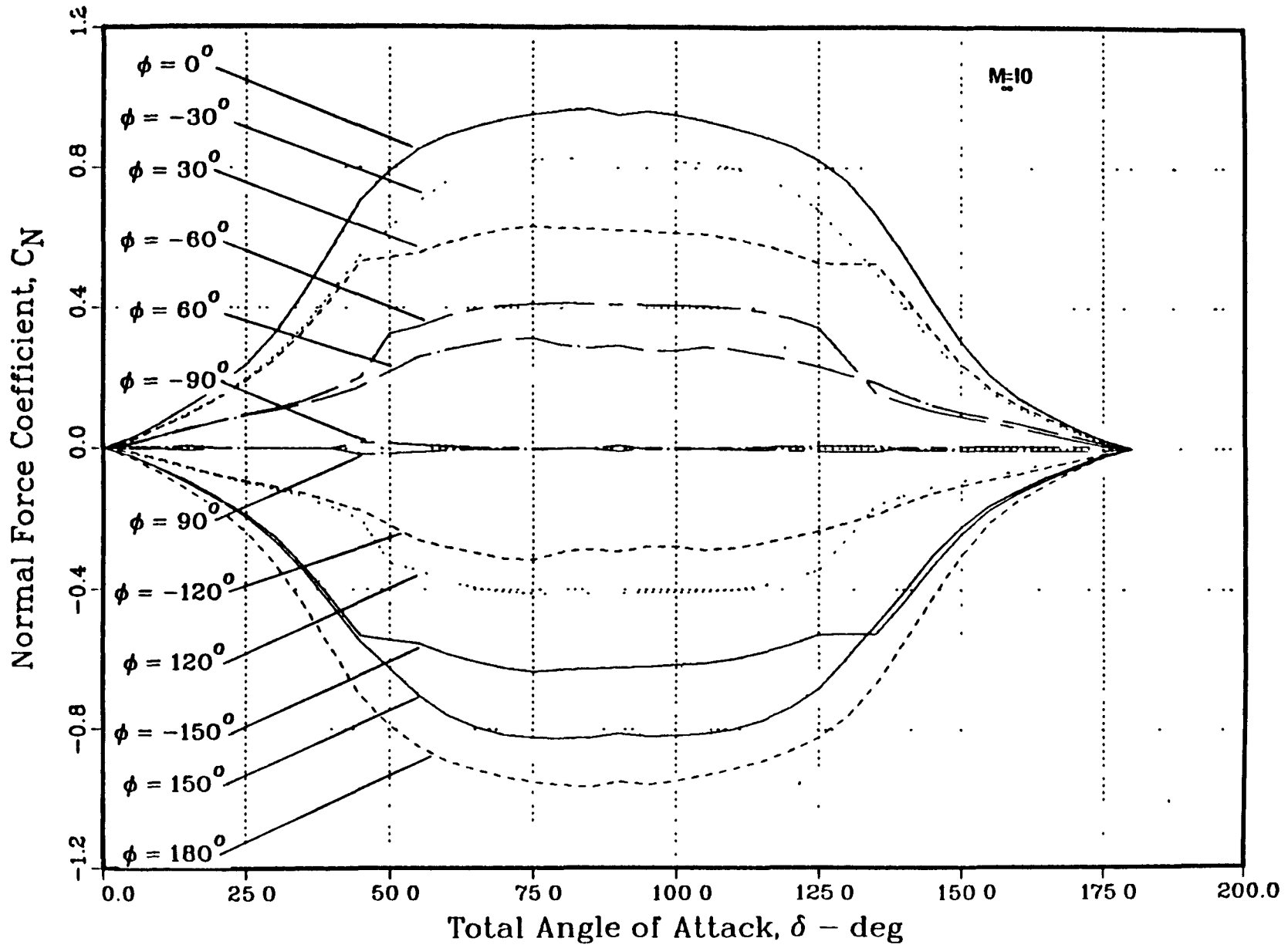


Figure I-R. Normal Force Coefficient - Hypersonic

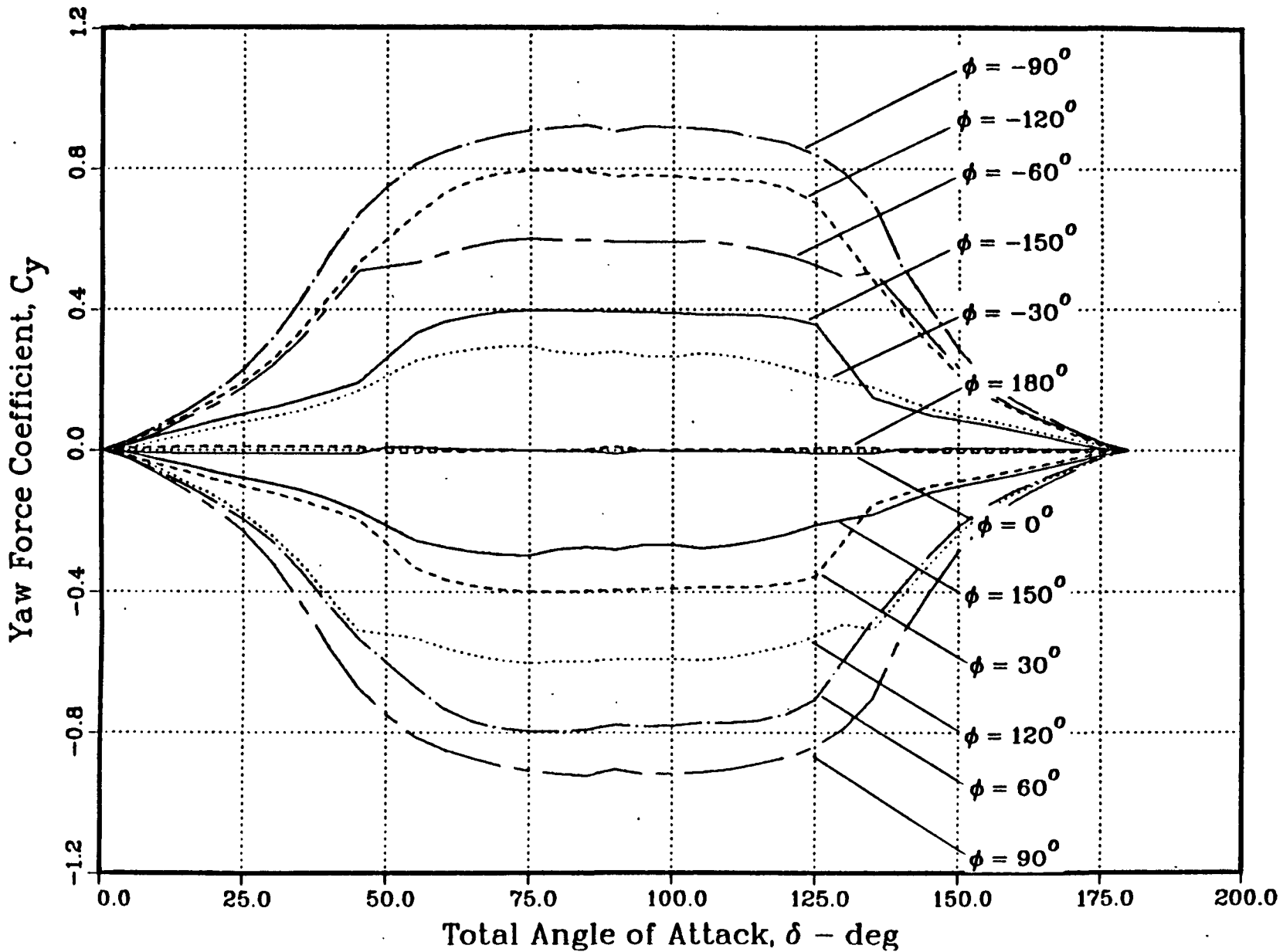


Figure I-S. Yaw Force Coefficient - Hypersonic

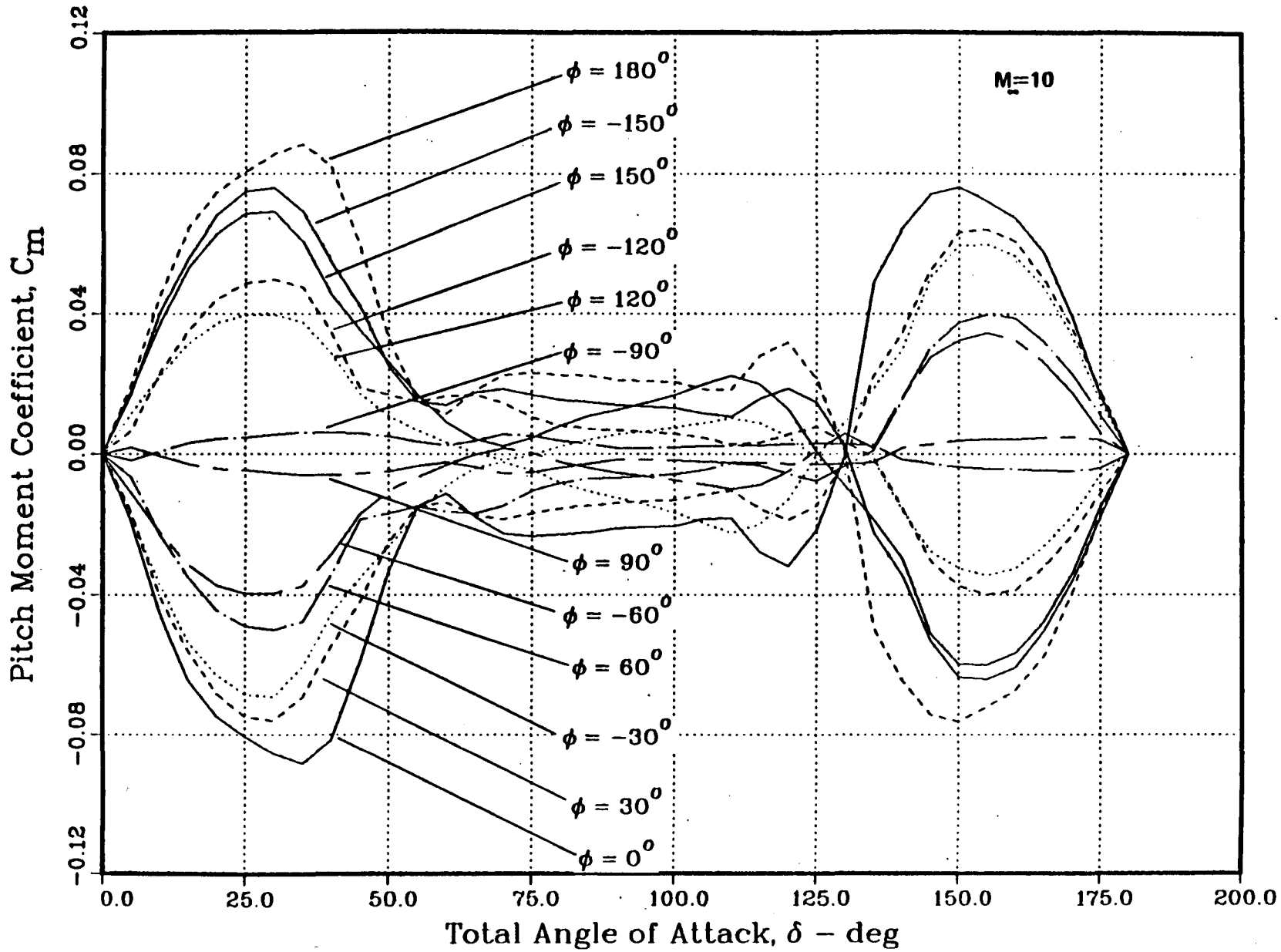


Figure I-T. Pitching Moment Coefficient - Hypersonic

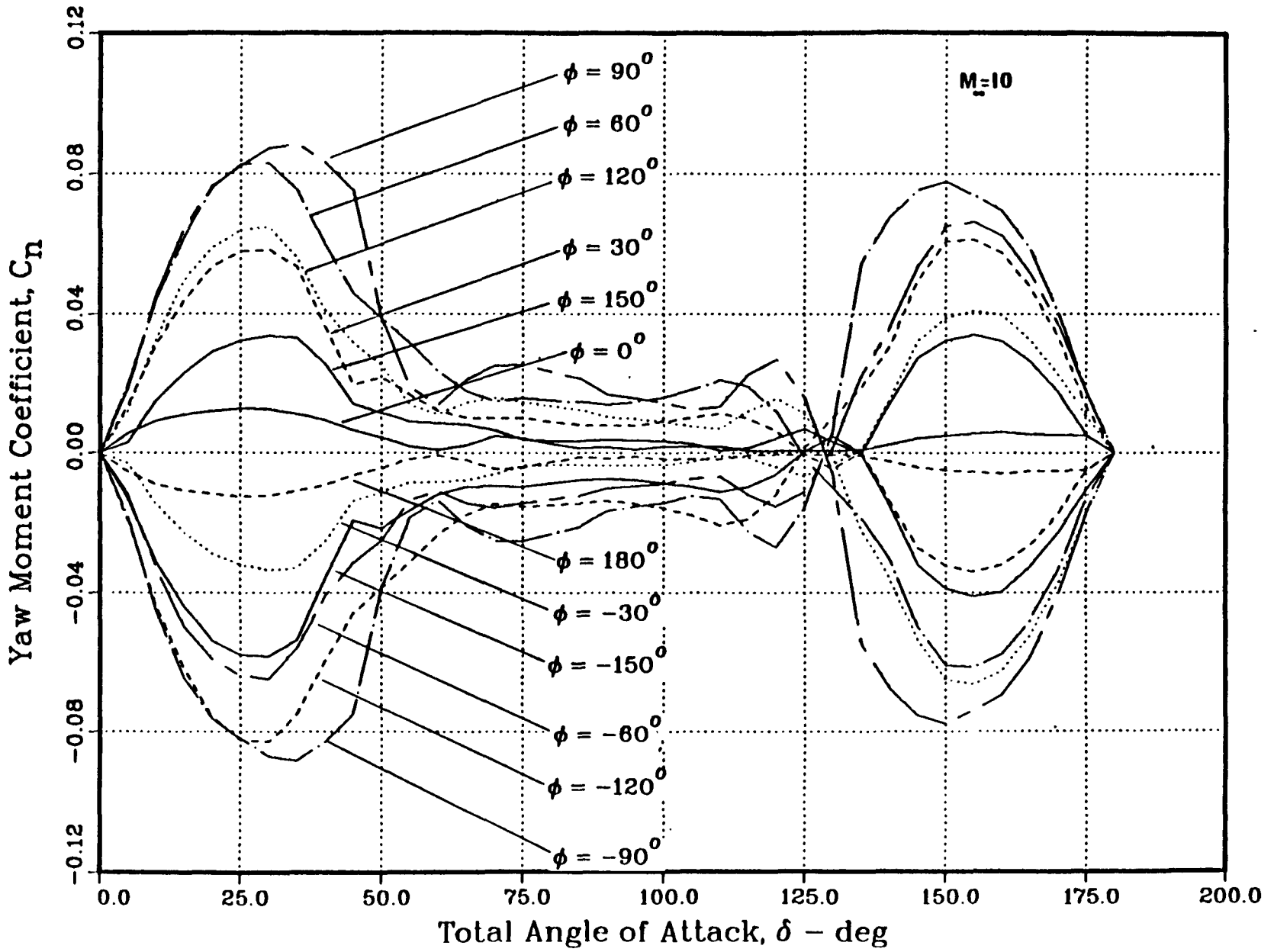


Figure I-U.. Yawing Moment Coefficient - Hypersonic



Note, however, that there is no figure shown for the rolling moment coefficient. When the wind tunnel test data was analyzed, there were still gaps in the data over some ranges of angles. An interpolation scheme first used to fill in the missing areas did not prove to yield realistic values in terms of the symmetry of the curves. There were also some questionable areas in the data. Because of these problems, final resolution of the curves of rolling moment coefficients has not yet been obtained. Therefore, the 6 DOF studies of GPHS reentry motion have not yet been completed. However, initial results based on earlier testing indicate that the GPHS module will stabilize at an angle of approximately 60 degrees (see discussion in Section I.1.4).

## I.2 ANALYSIS SEQUENCE

The reentry analysis of the GPHS-RTG involves the final steps in a sequence of studies to examine a realistic range of environments and system responses. The overall reentry analysis flow chart is shown on Figure I-7. The Reentry Subpanel of the INSRP selected four reentry conditions each for the Galileo and Ulysses missions as described in Section I.1.2. For each of these cases, the Jet Propulsion Laboratory conducted detailed spacecraft breakup analyses, including the RTG case response while still attached to the spacecraft, and determined the conditions at the time of RTG release from the spacecraft or release of the GPHS modules from the RTG, whichever occurred first. The GE analysis begins at the RTG or GPHS release and continues with the evaluation of the GPHS response through the remaining portion of the reentry until impact occurs on the Earth's surface.

## I.3 GPHS THERMAL ANALYSIS

### I.3.1 TRAJECTORY ANALYSIS

The results of the JPL spacecraft breakup analyses indicated in all cases that the GPHS modules would be released from the RTG before the RTG became released from the spacecraft. These results are applicable to both Galileo and Ulysses. The trajectory analysis then consisted of a point mass trajectory computer program being run for the GPHS module trajectories. The state vectors at GPHS separation determined by JPL were used as the initial

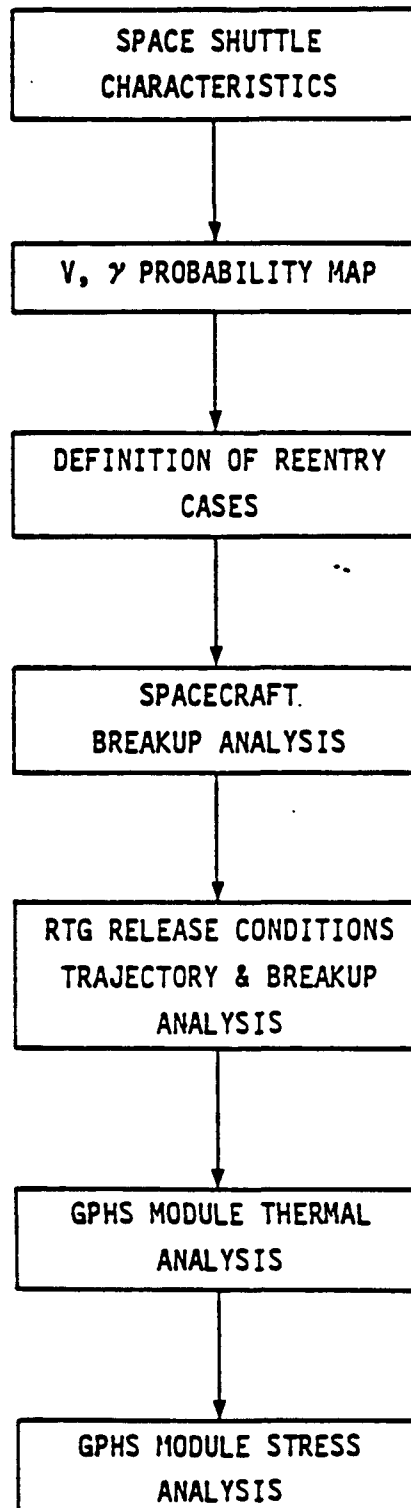


Figure I-7. Reentry Analysis Flow Chart

conditions for the heat source modules. The reentry trajectories analyzed are shown in Table I-6. Trajectory conditions for both the early release and the late release of the GPHS modules are included. For the primary matrix (Cases 1-16 of Table I-6), trajectories were calculated using an averaged drag coefficient based on an assumed tumbling condition. In addition, as indicated in Cases 17-21 of Table I-6, selected entry conditions were run assuming an initial stable orientation at a given angular orientation (i.e., face-on stable for steep angle, superorbital reentry and at a 60° angle for orbital decay reentry). Trajectory data for each reentry case are shown on Figures I-8 through I-70 which show altitude, relative velocity, and relative flight path angle as a function of time. For all of these trajectories, the velocity and time to impact from 10,000 feet to sea level are identical, the values which are given in Table I-7.

It might be noted that in Case 16 (the Ulysses 4° entry with a superorbital velocity) that capture does not initially occur. In this case the GPHS skips out and reenters 19 times before capture occurs. During the vacuum flight the GPHS radiates any heat load that it might have gotten on the previous atmospheric pass. With this condition, the thermal analysis is performed only considering the final entry which is reflected in the trajectory curves for this case.

### I.3.2 INITIAL GPHS TEMPERATURES

In all but the powered reentry cases, the initial GPHS temperatures were those calculated for the situation of normal vacuum RTG operation with a 30 volt load. For the powered reentry cases, a Shuttle launch transient calculation was performed that included the effects of the RTG active cooling system shutdown, xenon release from the converter, nitrogen purge of the RTG, and subsequent transient operation to the point of spacecraft breakup and GPHS release. The transient calculations were performed using the GPHS thermal reentry model described in Section I.3.3. The boundary condition imposed on the model was based on data obtained from the Engineering Unit (RTG) during the launch simulation test conducted at General Electric on March 29, 1982.

Table I-6. Reentry Trajectories Analyzed

Case No.	Mission	Trajectory Type	Module Release*	Altitude
1	Galileo	Steep Angle (SO)	Early	Tumbling
2	Galileo	Steep Angle (SO)	Late	Tumbling
3	Galileo	$\gamma$ min.	Early	Tumbling
4	Galileo	$\gamma$ min.	Late	Tumbling
5	Ulysses	Steep Angle (SO)	Early	Tumbling
6	Galileo	Orbital Decay	Early	Tumbling
7	Galileo	Orbital Decay	Late	Tumbling
8	Ulysses	Orbital Decay	Early	Tumbling
9	Ulysses	Orbital Decay	Late	Tumbling
10	Ulysses	Powered	Early	Tumbling
11	Ulysses	Powered	Late	Tumbling
12	Galileo	Powered	Early	Tumbling
13	Galileo	Powered	Late	Tumbling
14	Ulysses	Shallow Angle (SO)	Early	Tumbling
15	Ulysses	Shallow Angle (SO)	Late	Tumbling
16	Ulysses	Shallow Angle (SO) (-4° Entry Angle)	Early	Tumbling
17	Galileo	Steep Angle (SO)	Early	Stable (Face-on)
18	Galileo	Steep Angle (SO)	Late	Stable (Face-on)
19	Ulysses	Steep Angle (SO)	Early	Stable (Face-on)
20	Galileo	Orbital Decay	Early	Stable (60° above Mach 1 - Face-on below Mach 1)
21	Galileo	Orbital Decay	Late	Stable (60° above Mach 1 - Face-on Below Mach 1)

\*Early and Late represent the boundaries of the time of release for one-half of the stack of modules and the remaining half stack of modules, respectively, in the Galileo and Ulyssis. For Ulysses (formerly, Solar-Polar), early and late refers to analytical variations in release of all PHS modules (i.e., 18) based on a range of initial conditions (a range of subcases) e.g., spacecraft attitudes causing exposure of the RTG to windward vs. leeward flow conditions.

CASE 1  
 $V_1 = 36104. \text{ FT/SEC}$   
 $\gamma_1 = -38.79 \text{ DEG}$   
 $H = 273000. \text{ FT}$

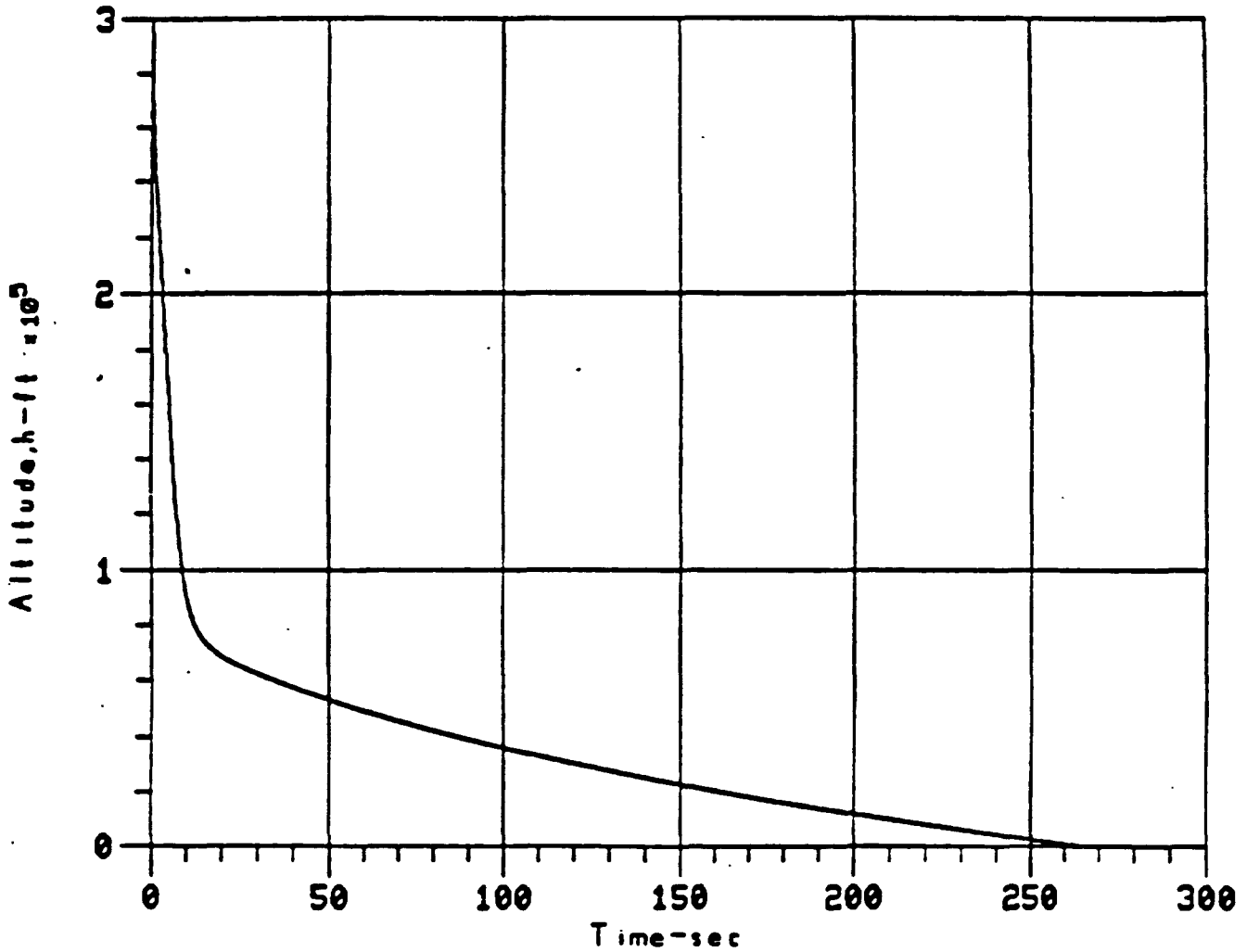


Figure I-8. Case 1 - Altitude

CASE 1

$V_1 = 36104. \text{ FT/SEC}$

$\gamma_1 = -38.79 \text{ DEG}$

$H = 273000. \text{ FT}$

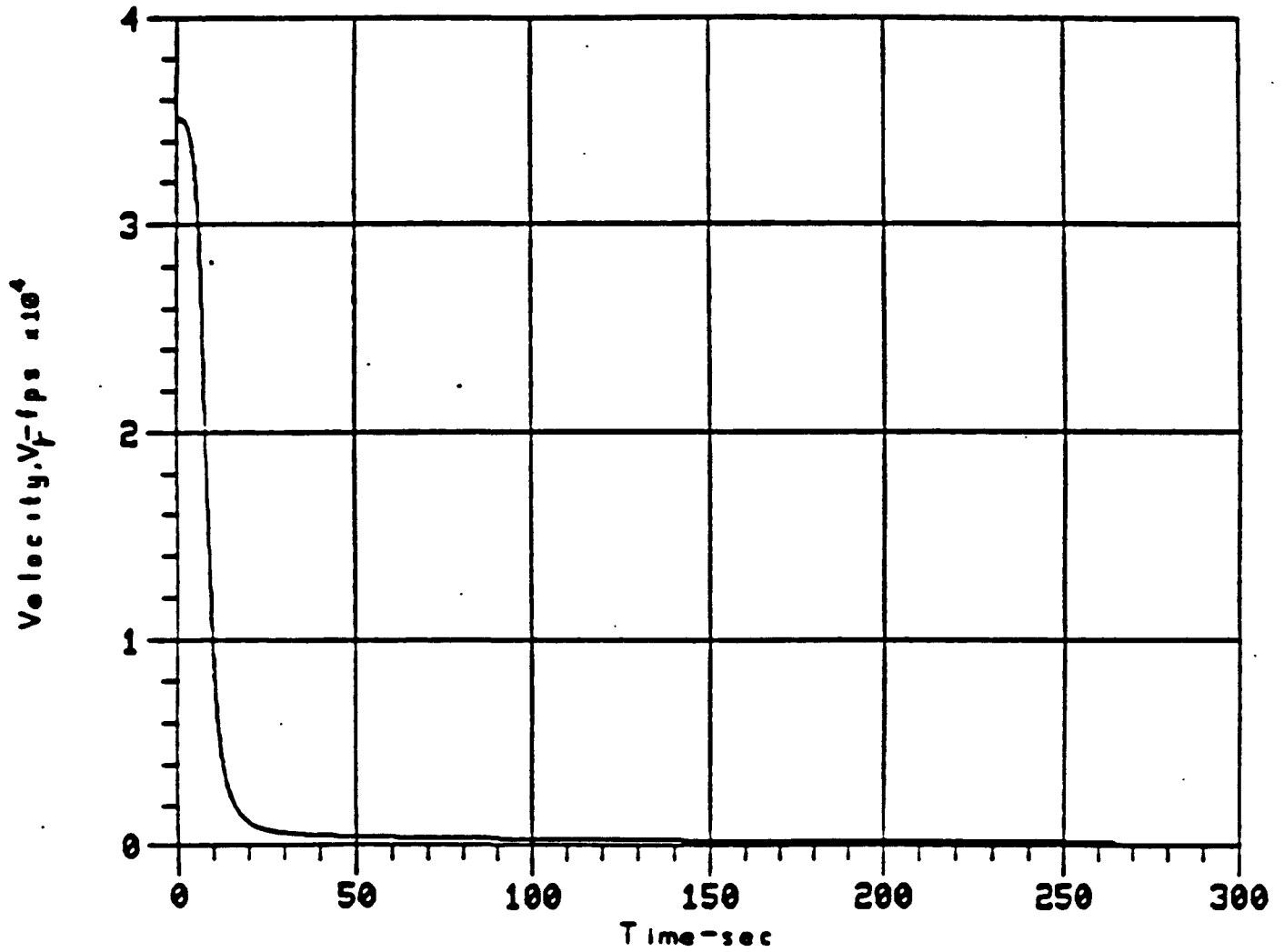


Figure I-9. Case 1 - Velocity

CASE 1

$V_1 = 36104. \text{ FT/SEC}$

$\gamma_1 = -38.79 \text{ DEG}$

$H = 273000. \text{ FT}$

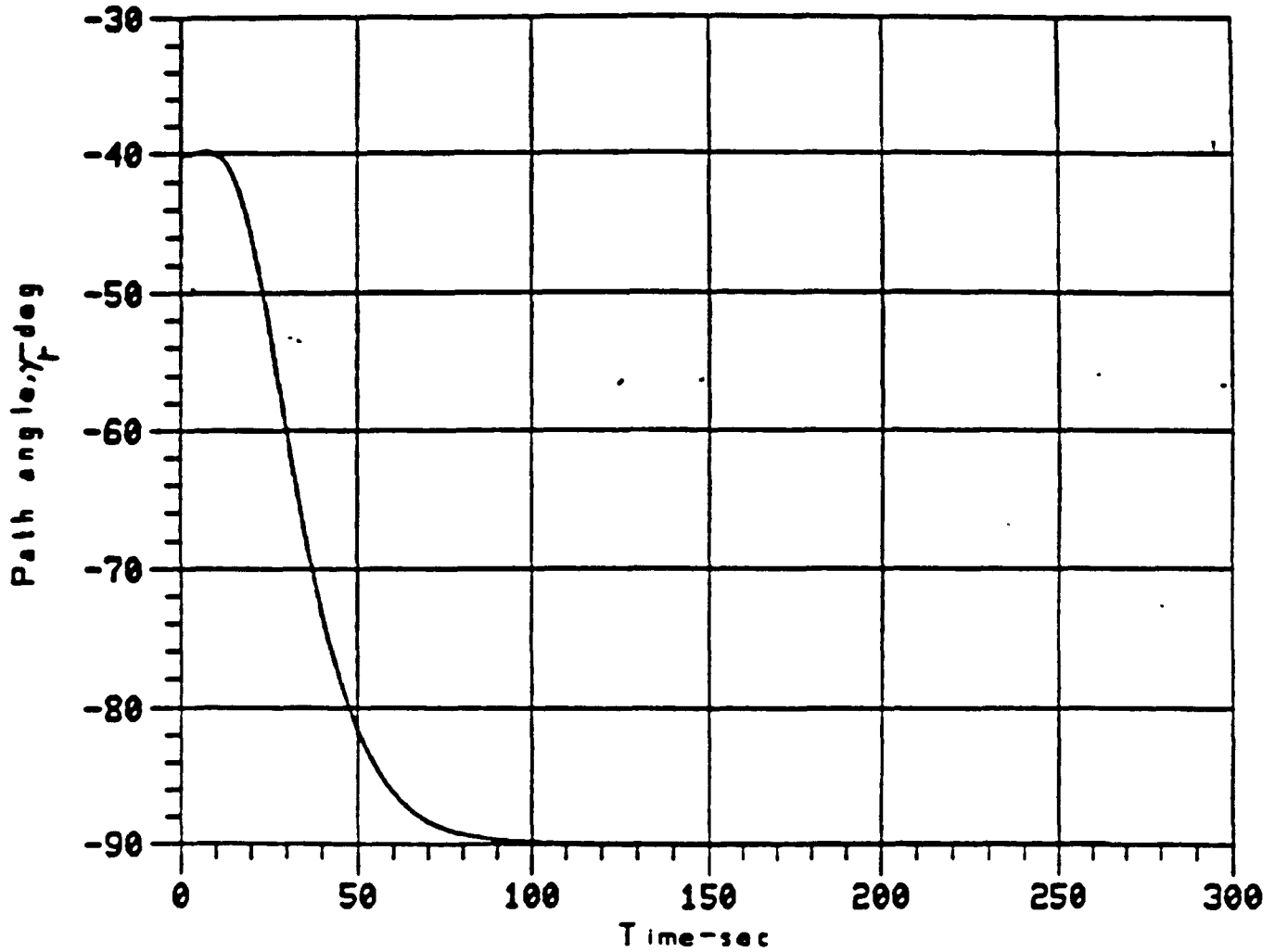


Figure I-10. Case 1 - Path Angle

CASE 2

$V_1 = 36113. \text{ FT/SEC}$

$\gamma_1 = -38.76 \text{ DEG}$

$H = 253000. \text{ FT}$

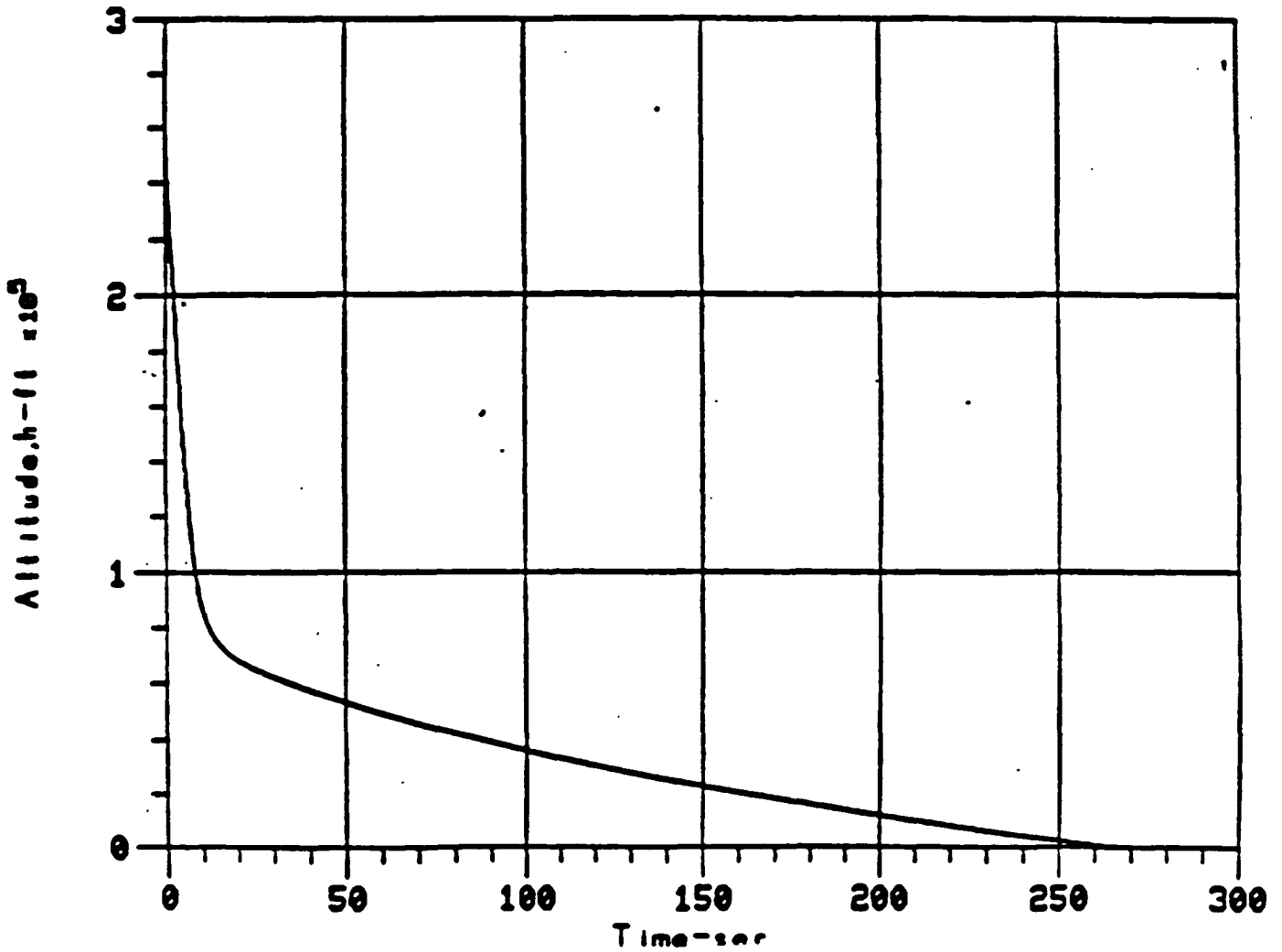


Figure I-11. Case 2 - Altitude



CASE 2  
 $V_1 = 36113. \text{ FT/SEC}$   
 $\gamma_1 = -38.76 \text{ DEG}$   
 $H = 253000. \text{ FT}$

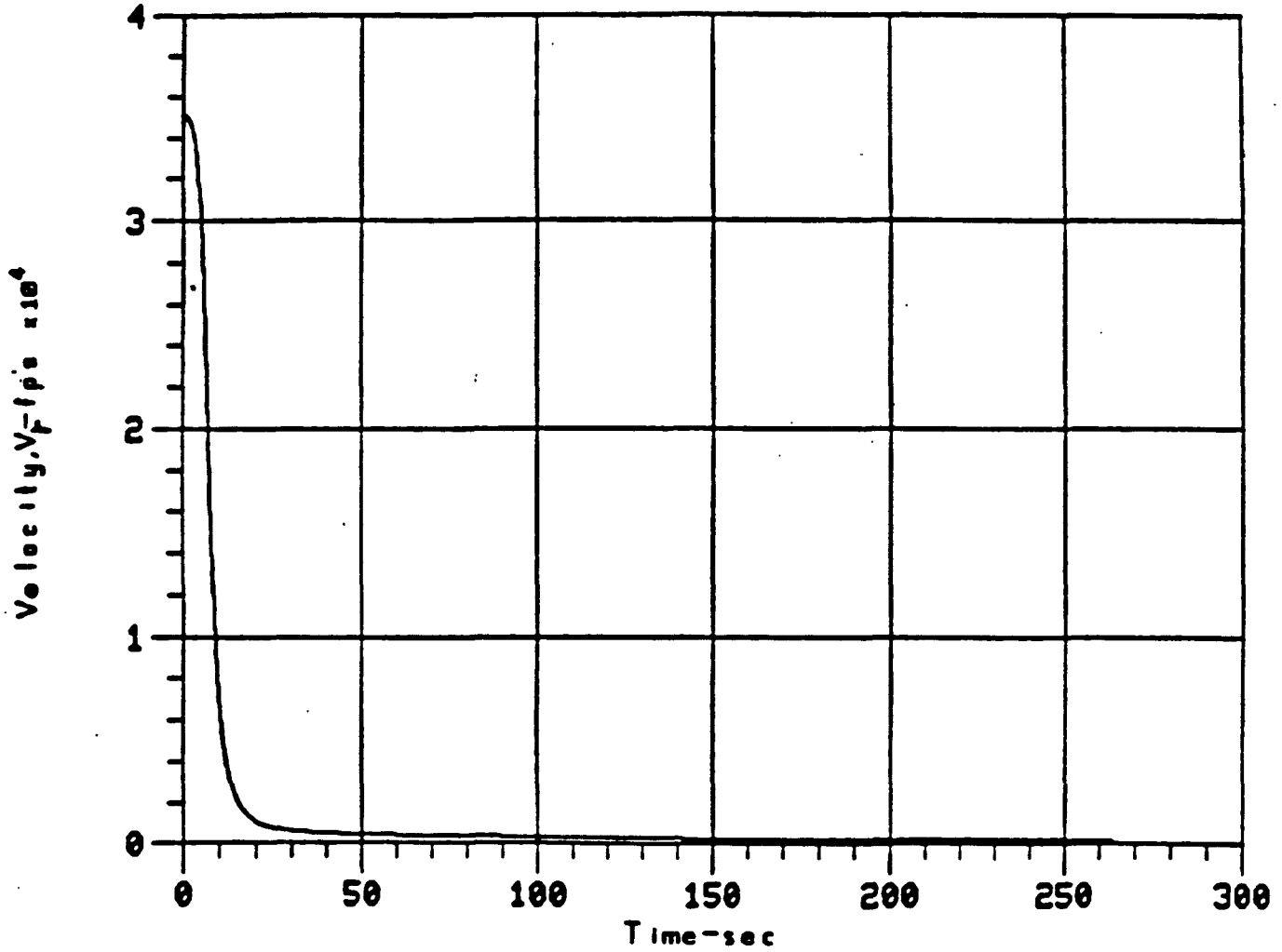


Figure I-12. Case 2 - Velocity

CASE 2

$V_1 = 36113. \text{ FT/SEC}$

$\gamma_1 = -38.76 \text{ DEG}$

$H = 253000. \text{ FT}$

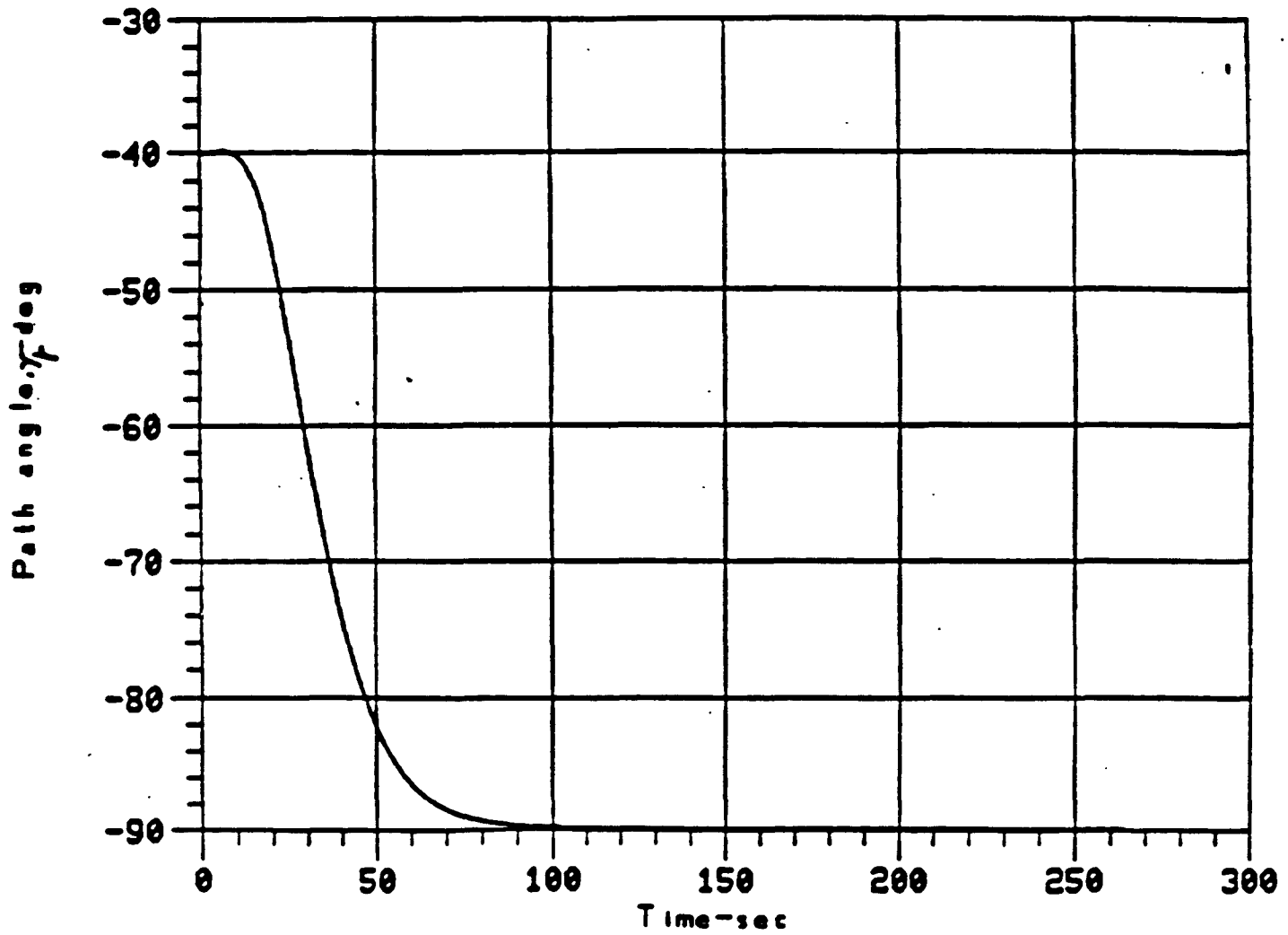


Figure I-13. Case 2 - Path Angle

CASE 3  
 $V_1 = 36056. \text{ FT/SEC}$   
 $\gamma_1 = -3.85 \text{ DEG}$   
 $H = 333000. \text{ FT}$

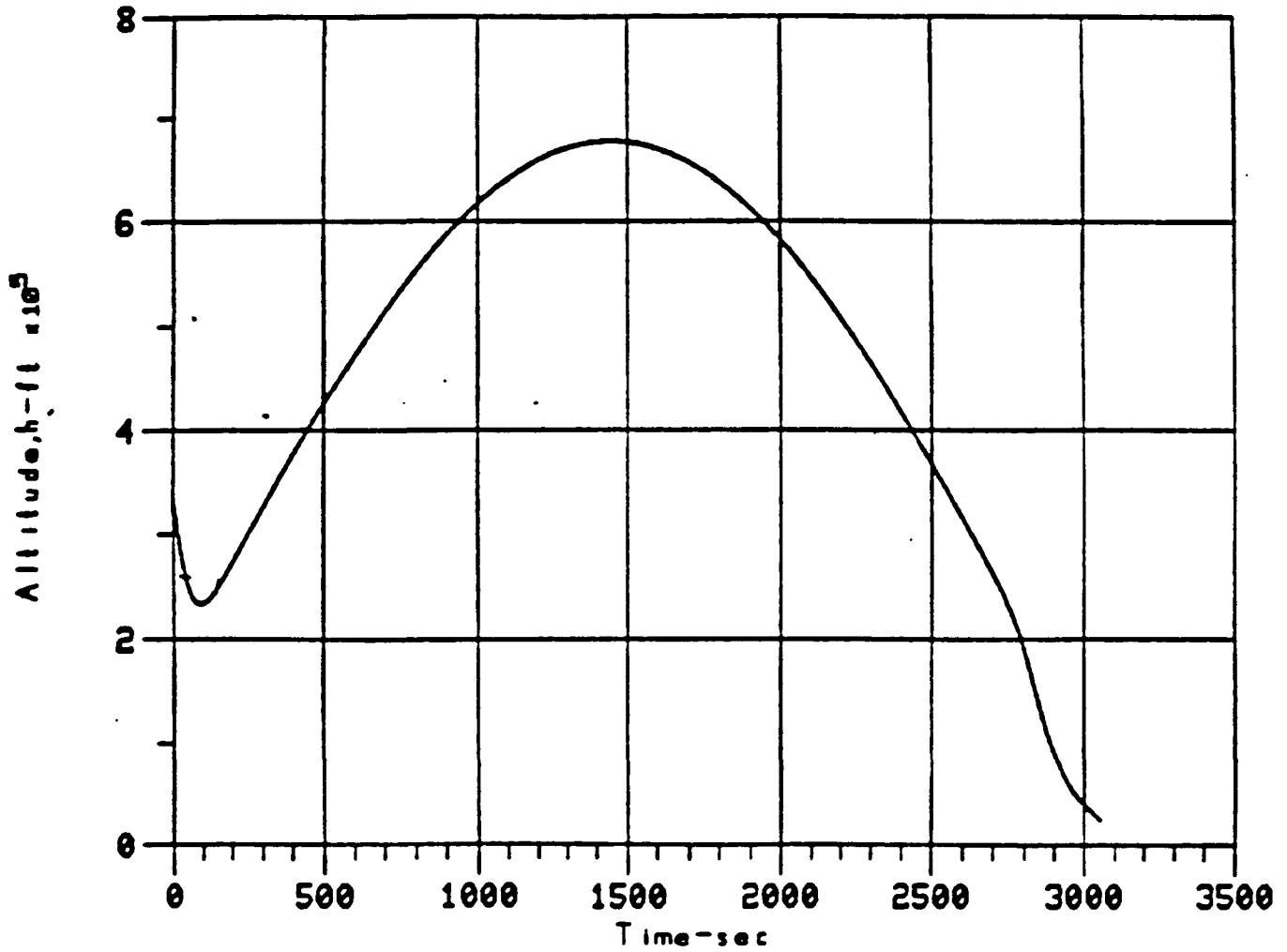


Figure I-14. Case 3 - Altitude

CASE 3

$V_1 = 36056. \text{ FT/SEC}$

$\gamma_1 = -3.85 \text{ DEG}$

$H = 333000. \text{ FT}$

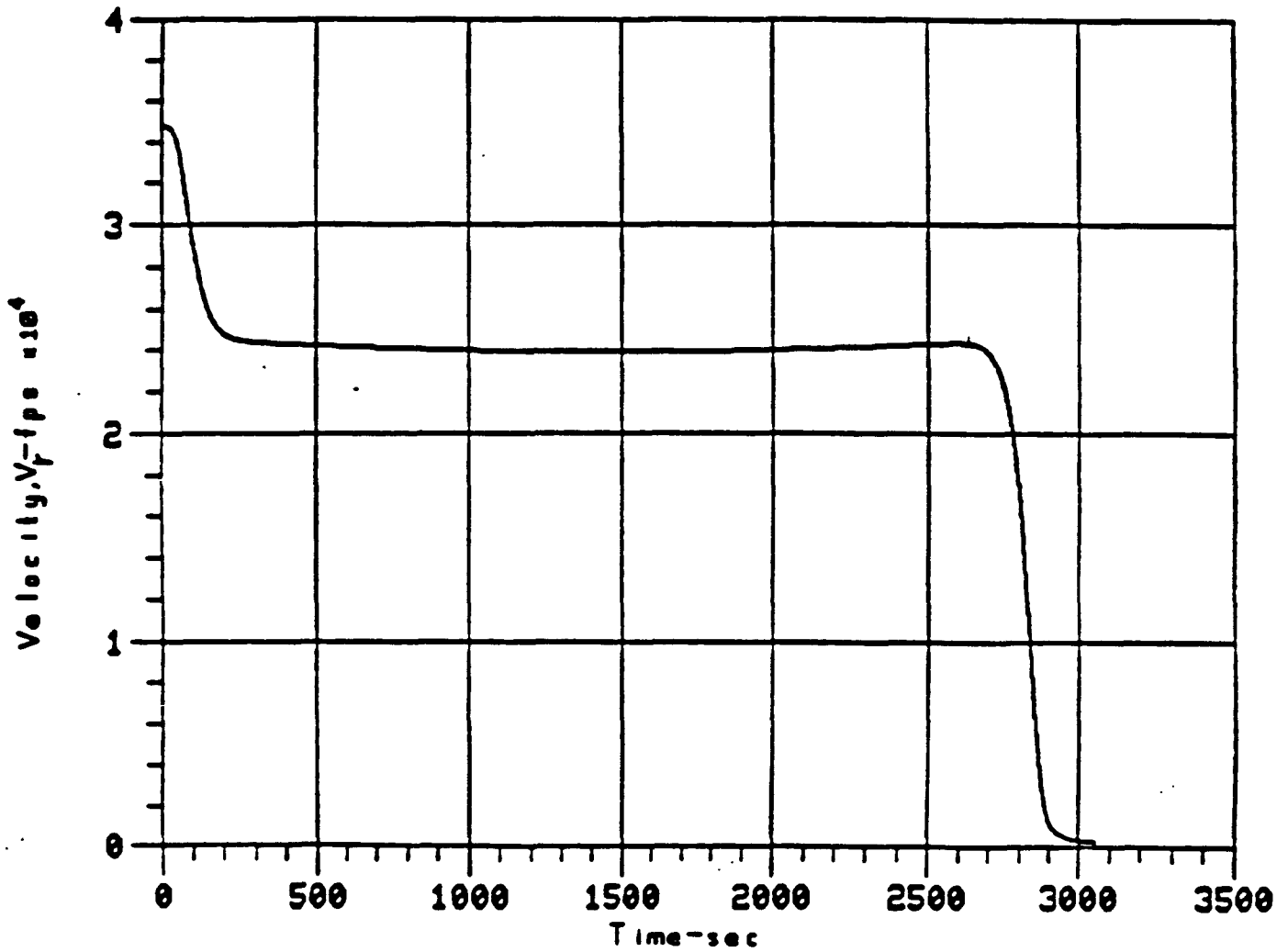


Figure I-15. Case 3 - Velocity

CASE 3

$V_1 = 36056. \text{ FT/SEC}$

$\gamma_1 = -3.85 \text{ DEG}$

$H = 333000. \text{ FT}$

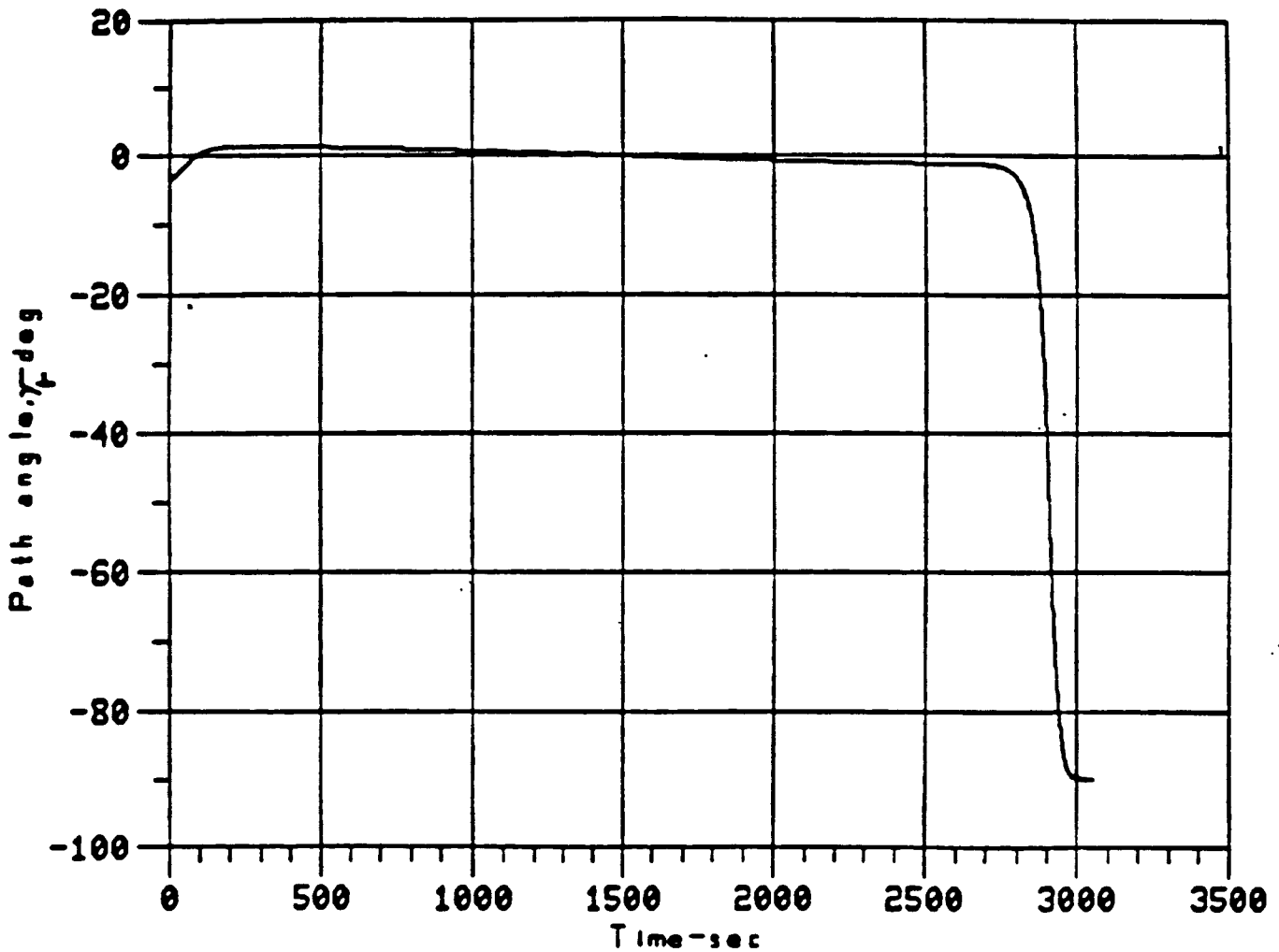


Figure I-16. Case 3 - Path Angle

CASE 4

$V_1 = 36073. \text{ FT/SEC}$

$\gamma_1 = -3.28 \text{ DEG}$

$H = 306000. \text{ FT}$

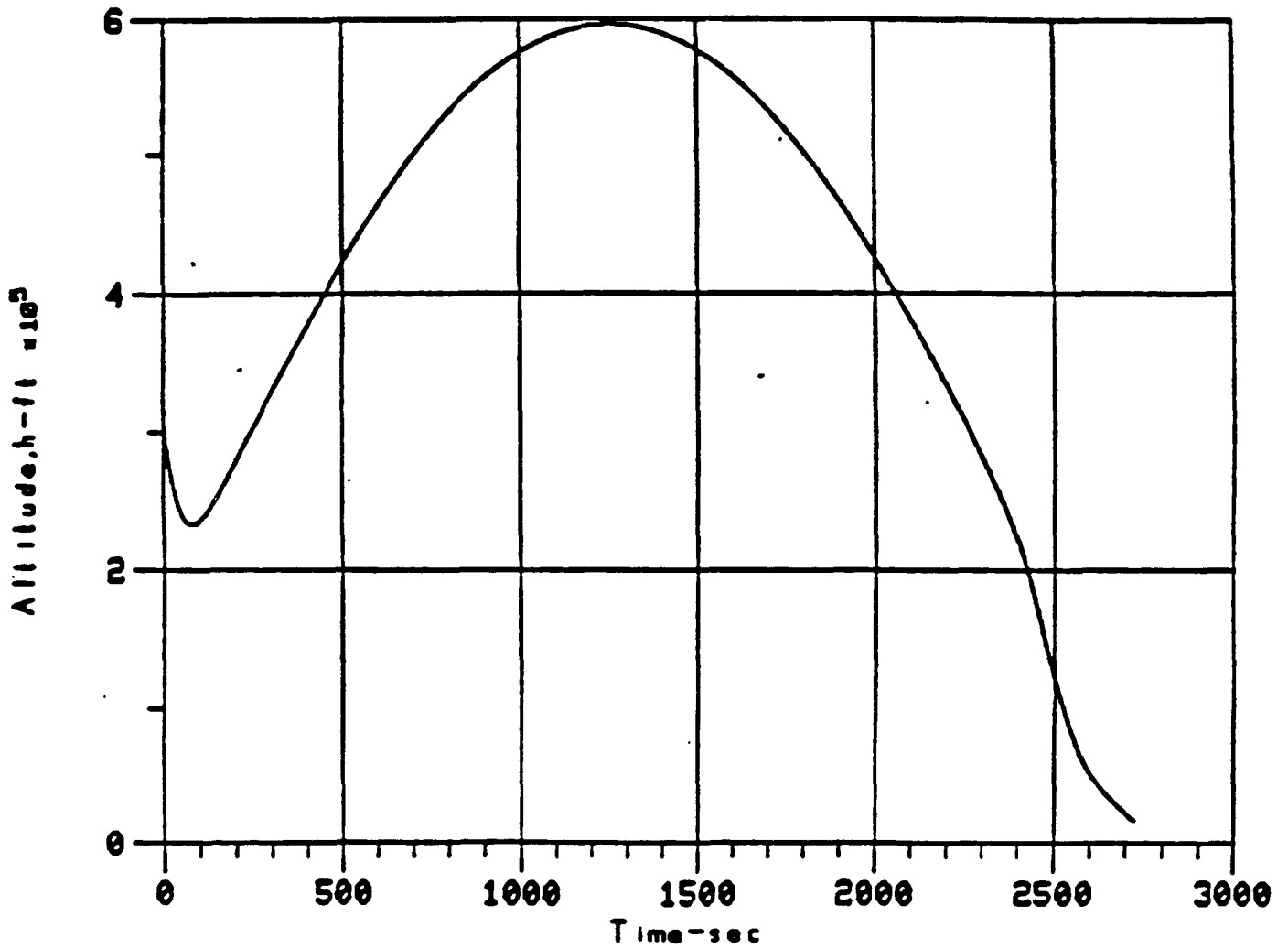


Figure I-17. Case 4 - Altitude

CASE 4  
 $V_1 = 36073. \text{ FT/SEC}$   
 $\gamma_1 = -3.28 \text{ DEG}$   
 $H = 306000. \text{ FT}$

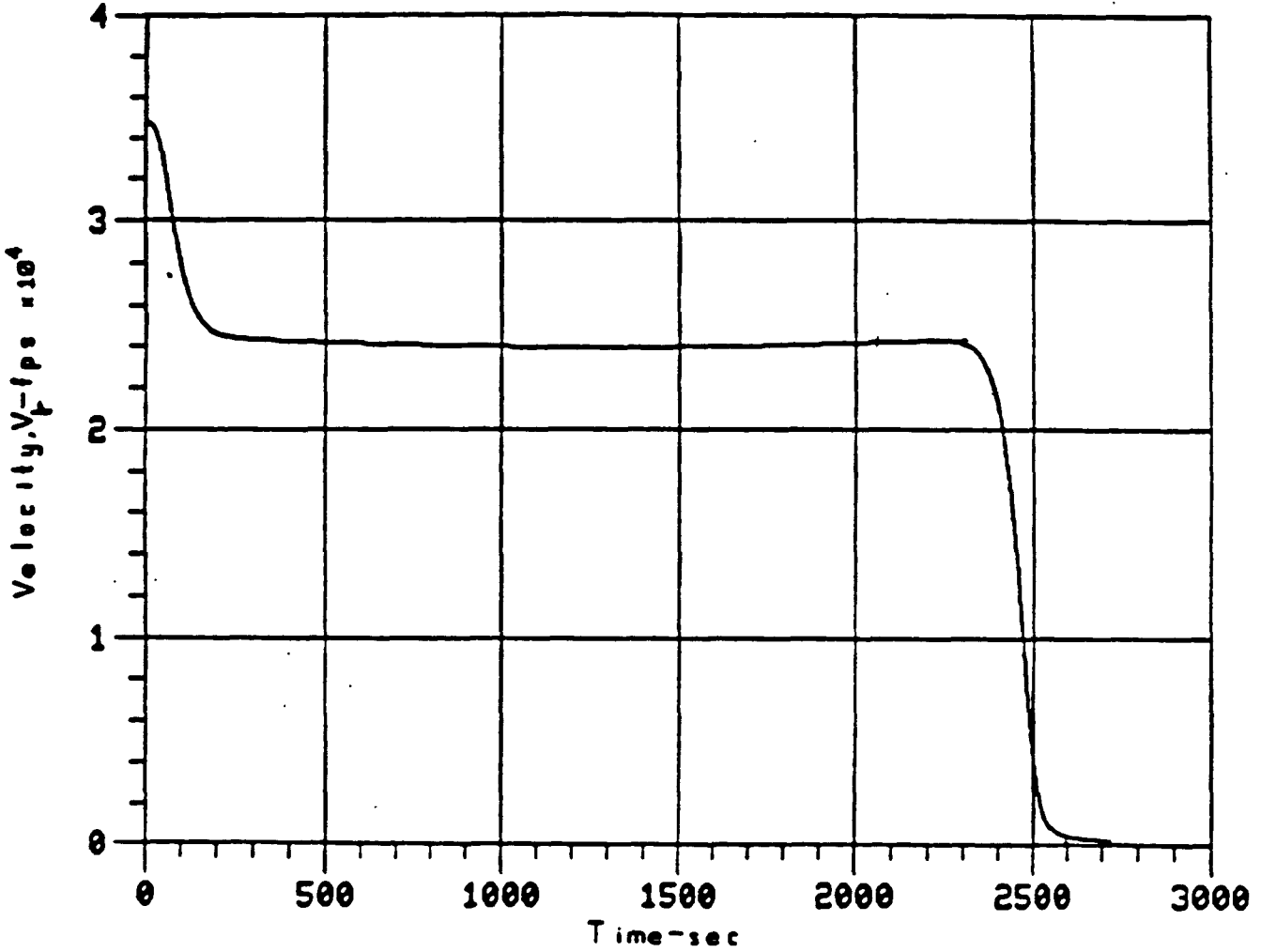


Figure I-18. Case 4 - Velocity

CASE 4  
 $V_1 = 36073. \text{ FT/SEC}$   
 $\gamma_1 = -3.28 \text{ DEG}$   
 $H = 306000. \text{ FT}$

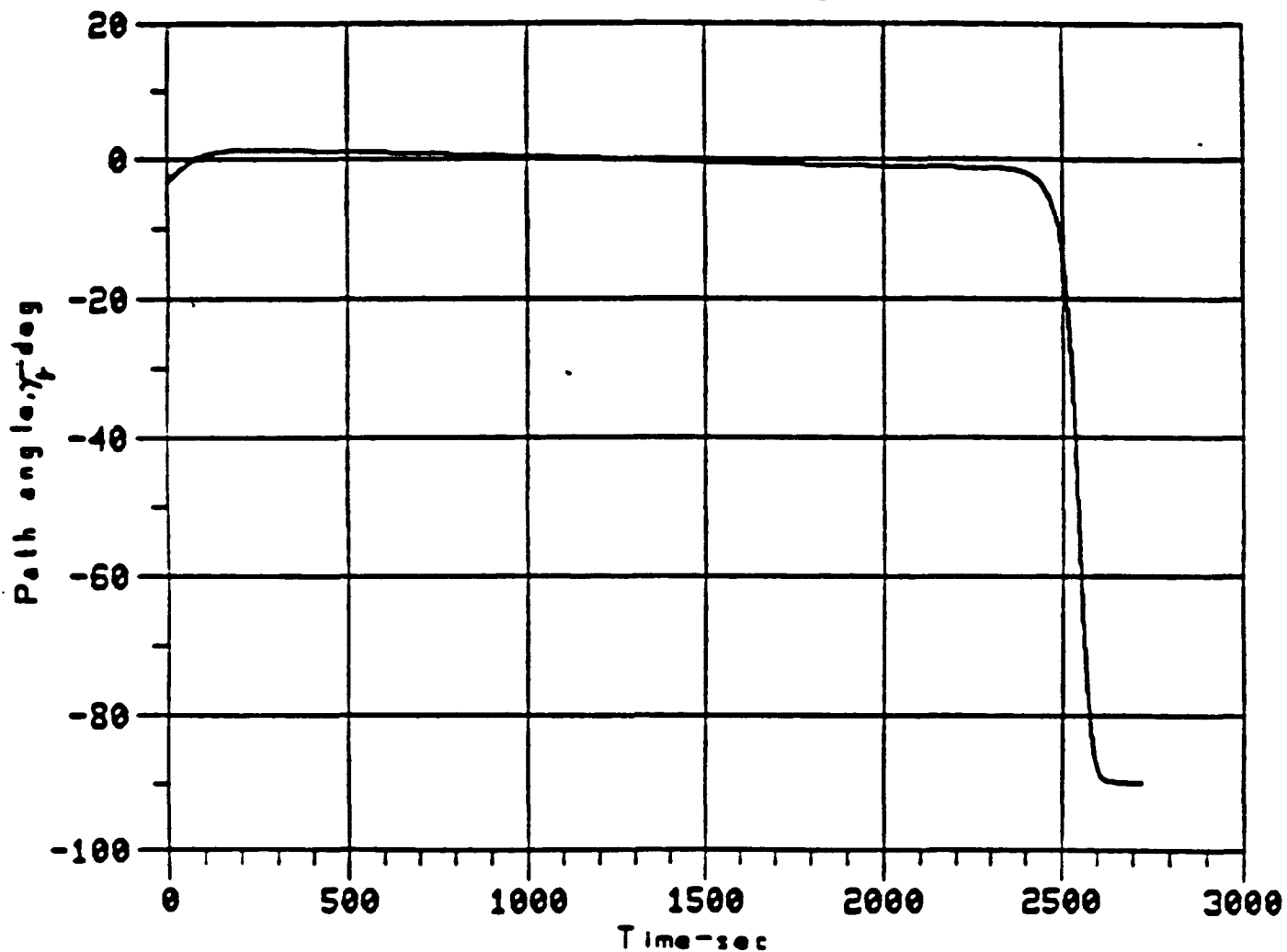


Figure I-19. Case 4 - Path Angle



CASE 5  
 $V_1 = 36000. \text{ FT/SEC}$   
 $\gamma_1 = -53.0 \text{ DEG}$   
 $H = 210000. \text{ FT}$

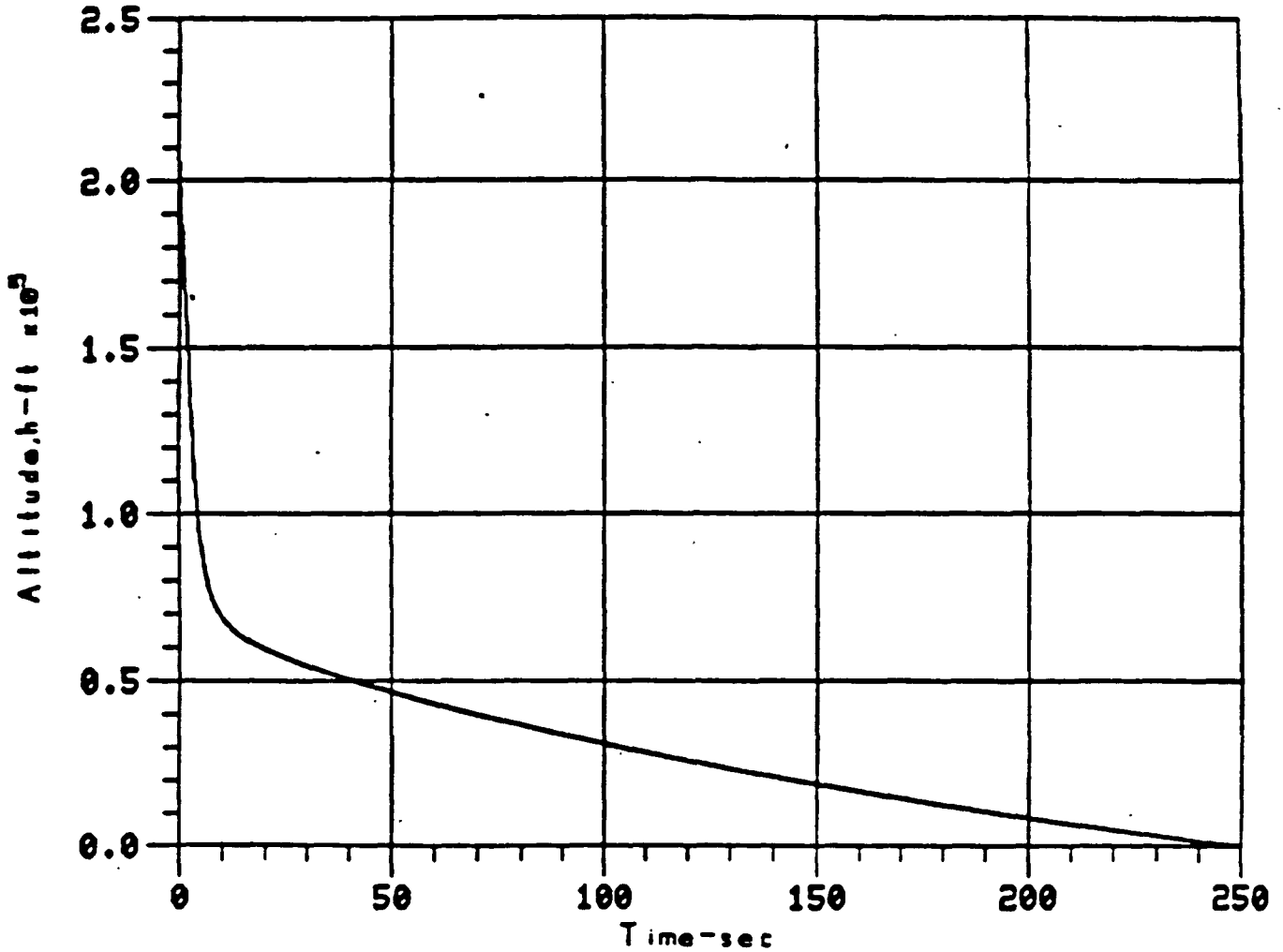


Figure I-20. Case 5 - Altitude

CASE 5

$V_1 = 36000. \text{ FT/SEC}$

$\gamma_1 = -53.0 \text{ DEG}$

$H = 210000. \text{ FT}$

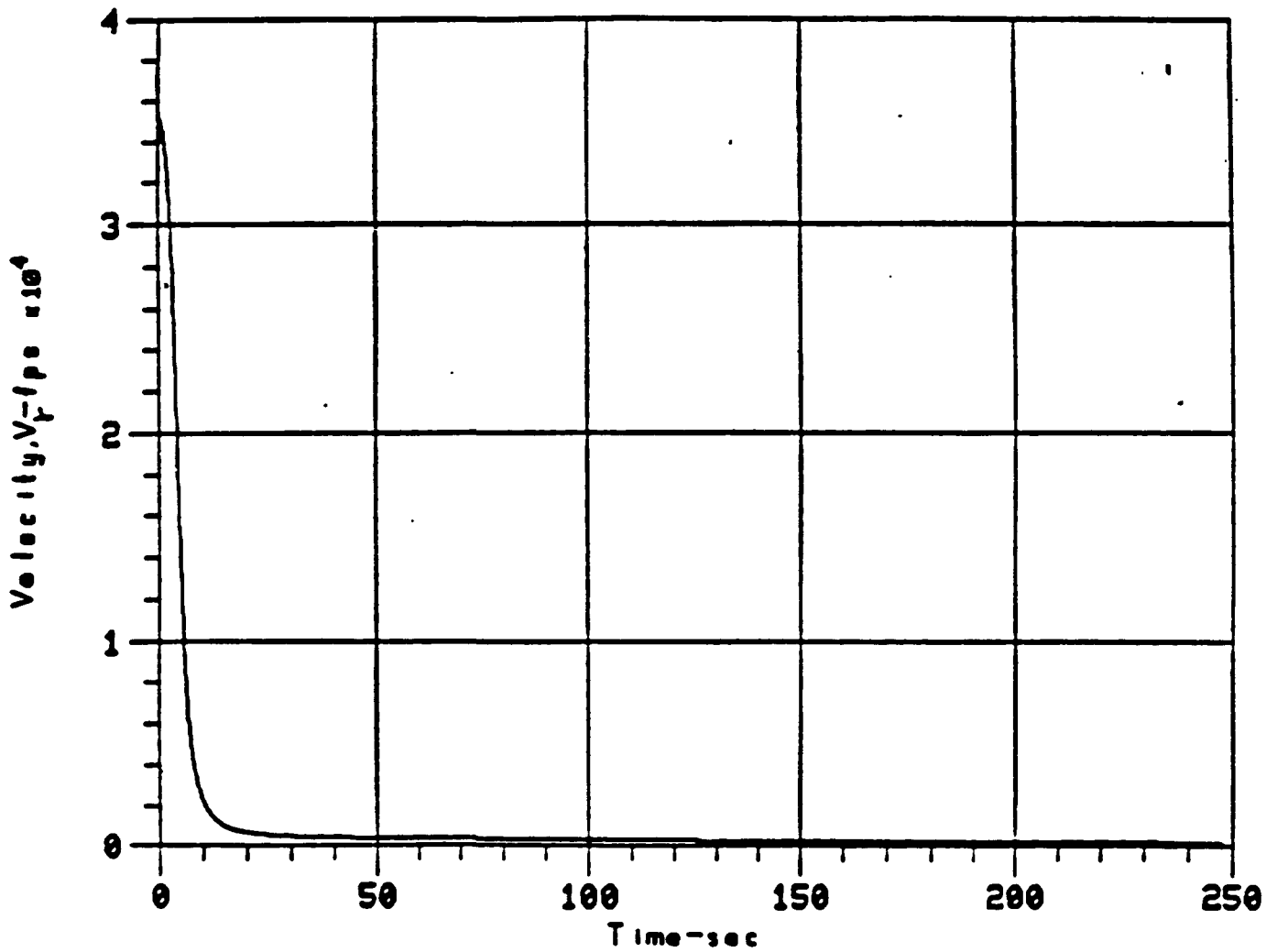


Figure I-21. Case 5 - Velocity

CASE 5  
 $V_1 = 36000. \text{ FT/SEC}$   
 $\gamma_1 = -53.0 \text{ DEG}$   
 $H = 210000. \text{ FT}$

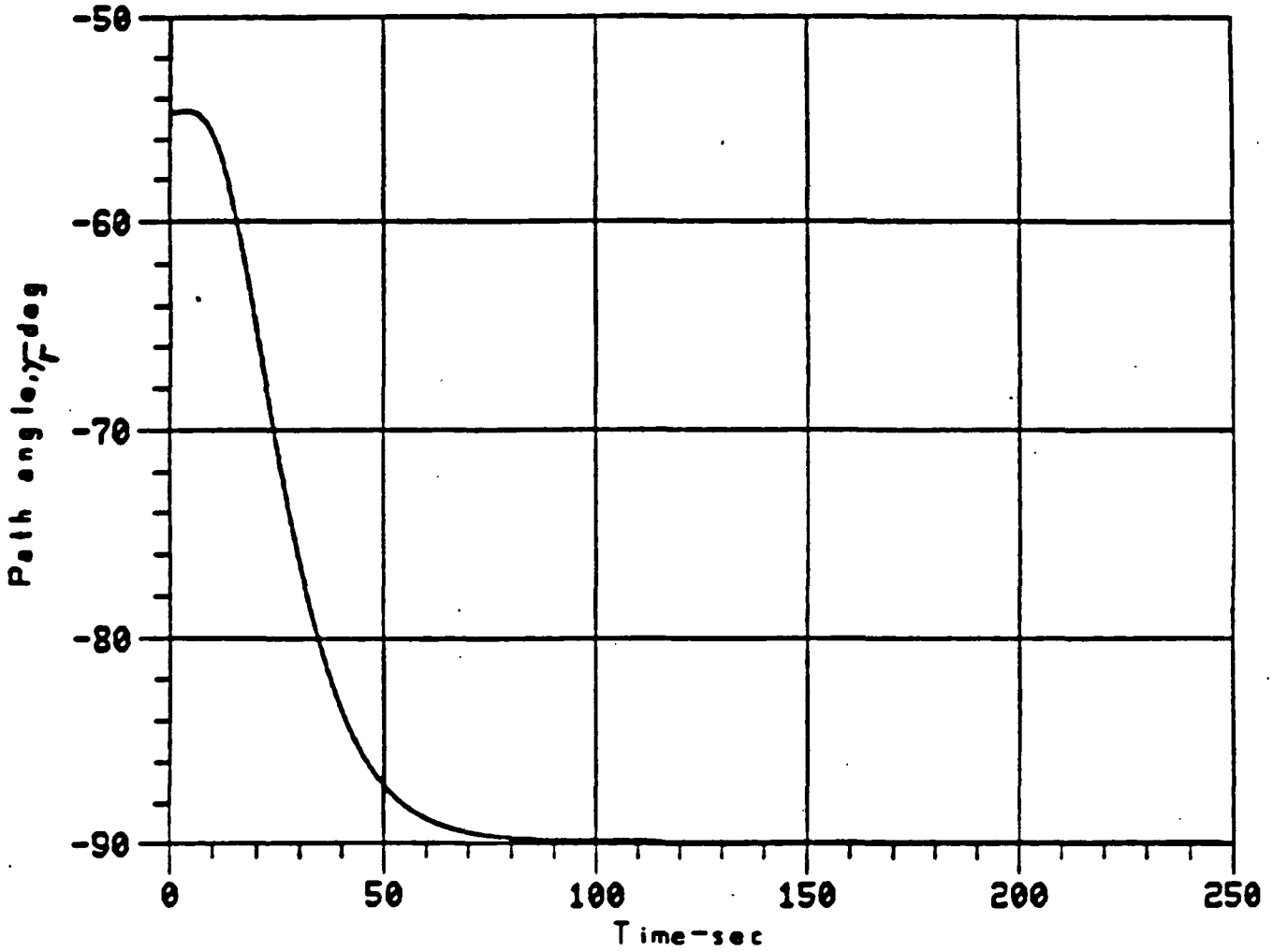


Figure I-22. Case 5 - Path Angle

CASE 6  
VI=25704,GAMI=-.138,H=330000

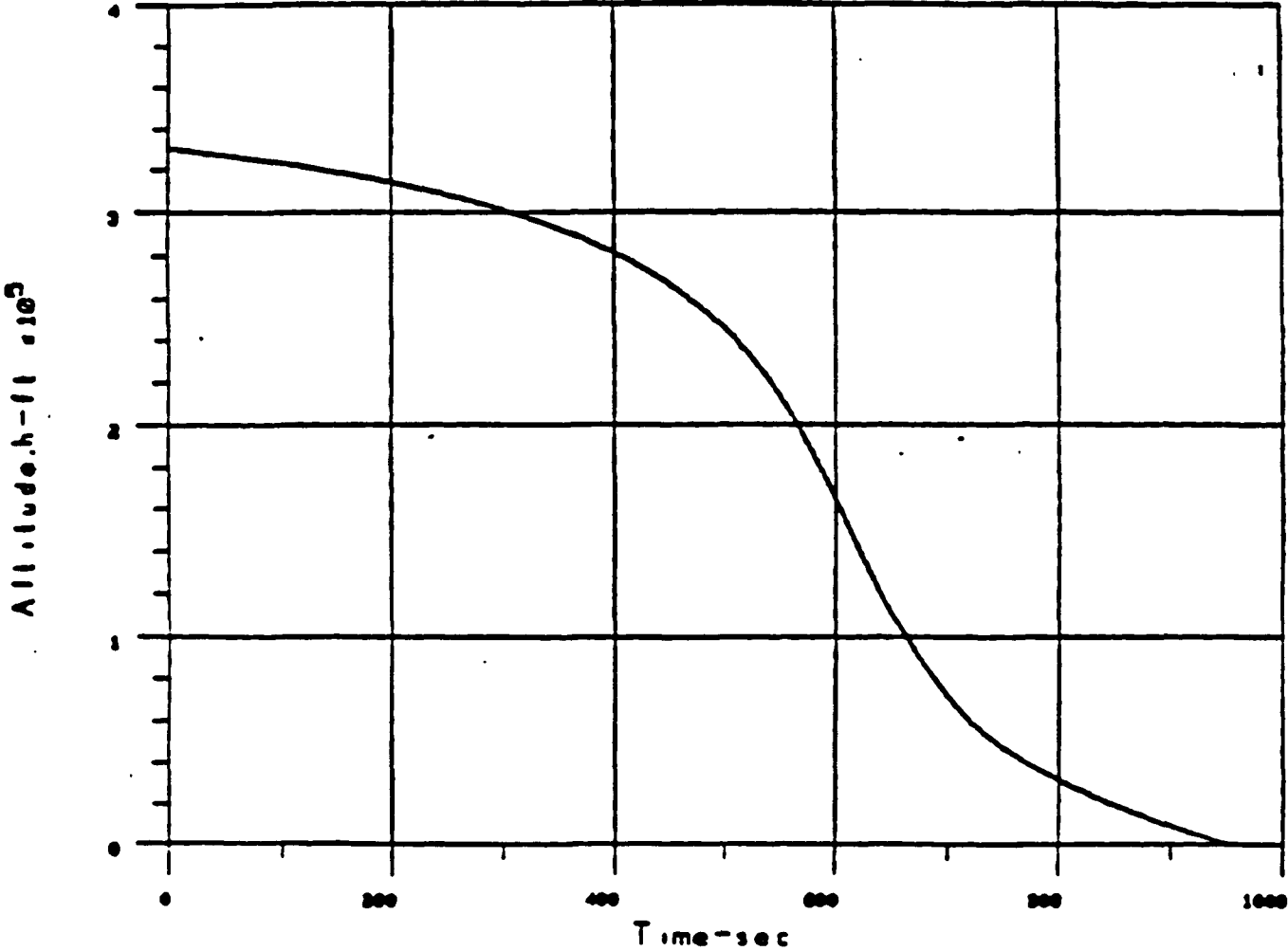


Figure I-23. Case 6 - Altitude

CASE 6  
VI=25704,GAMI=-.138,H=330000

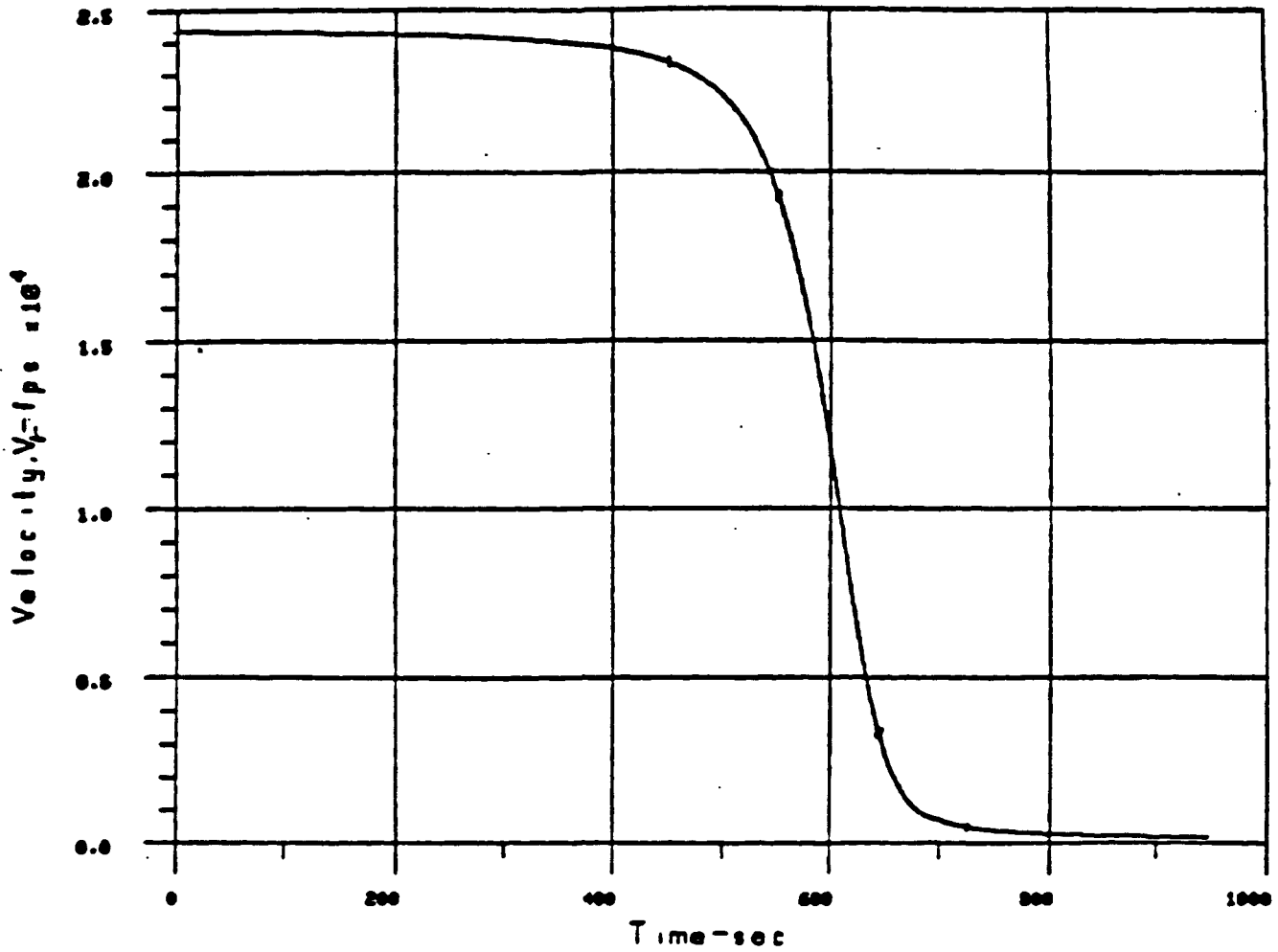


Figure I-24. Case 6 - Velocity

CASE 6  
VI=25704,GAMI=-.138,H=330000

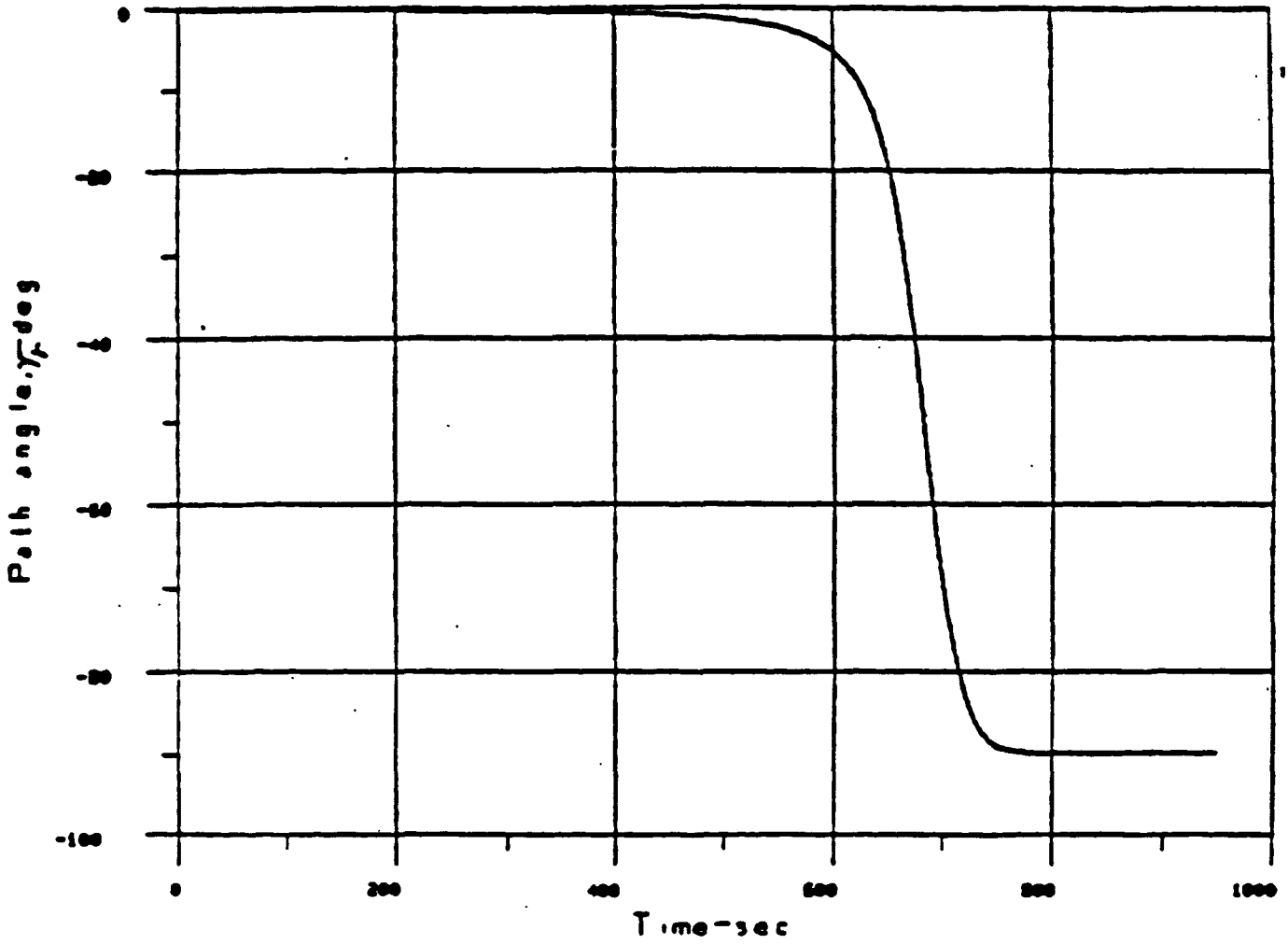


Figure I-25. Case 6 - Path Angle

CASE 7  
VI=25594,GAMI=-0.318,H=292000

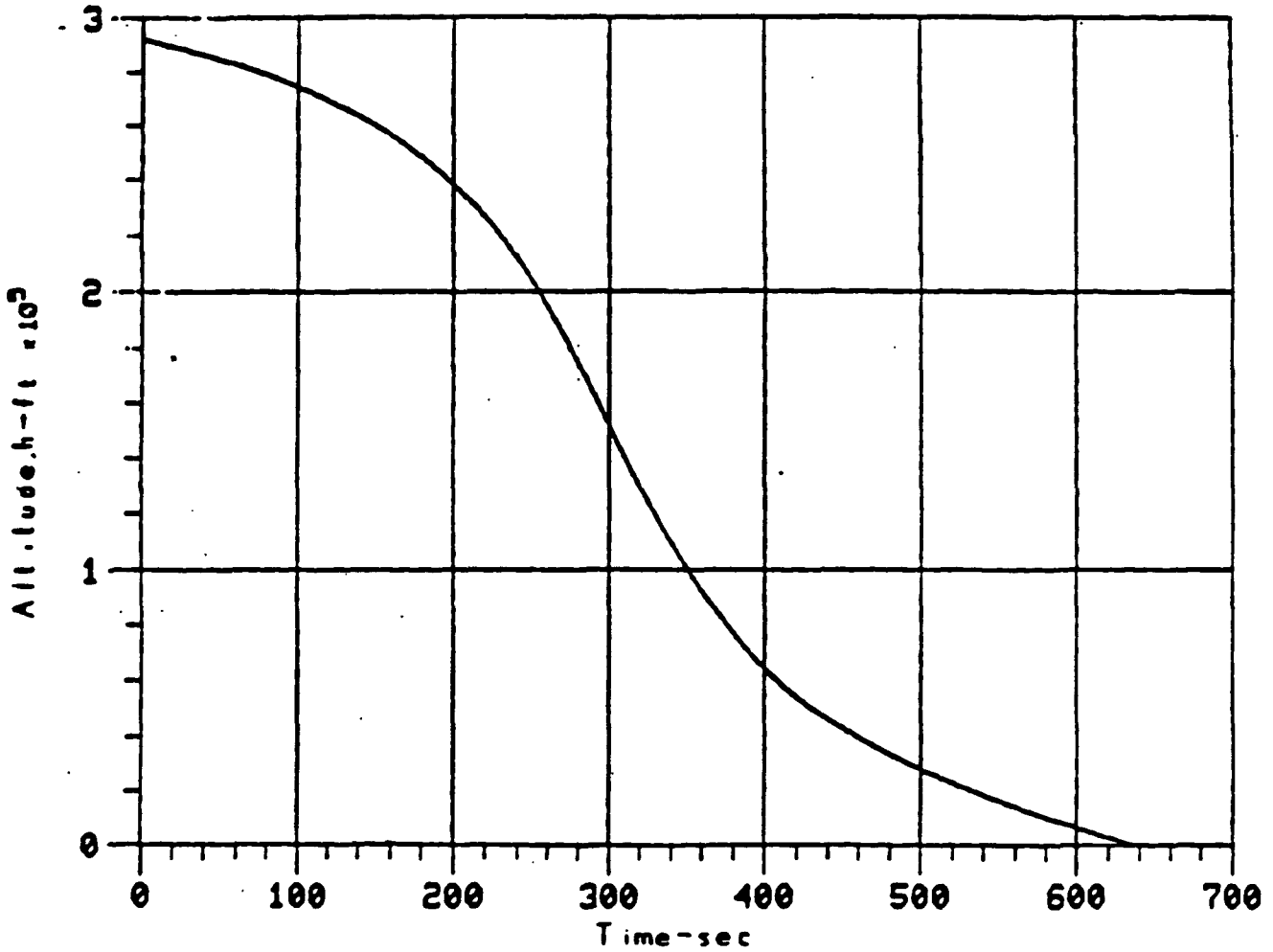


Figure I-26. Case 7 - Altitude

CASE 7  
VI=25594,GAMI=-0.318,H=292000

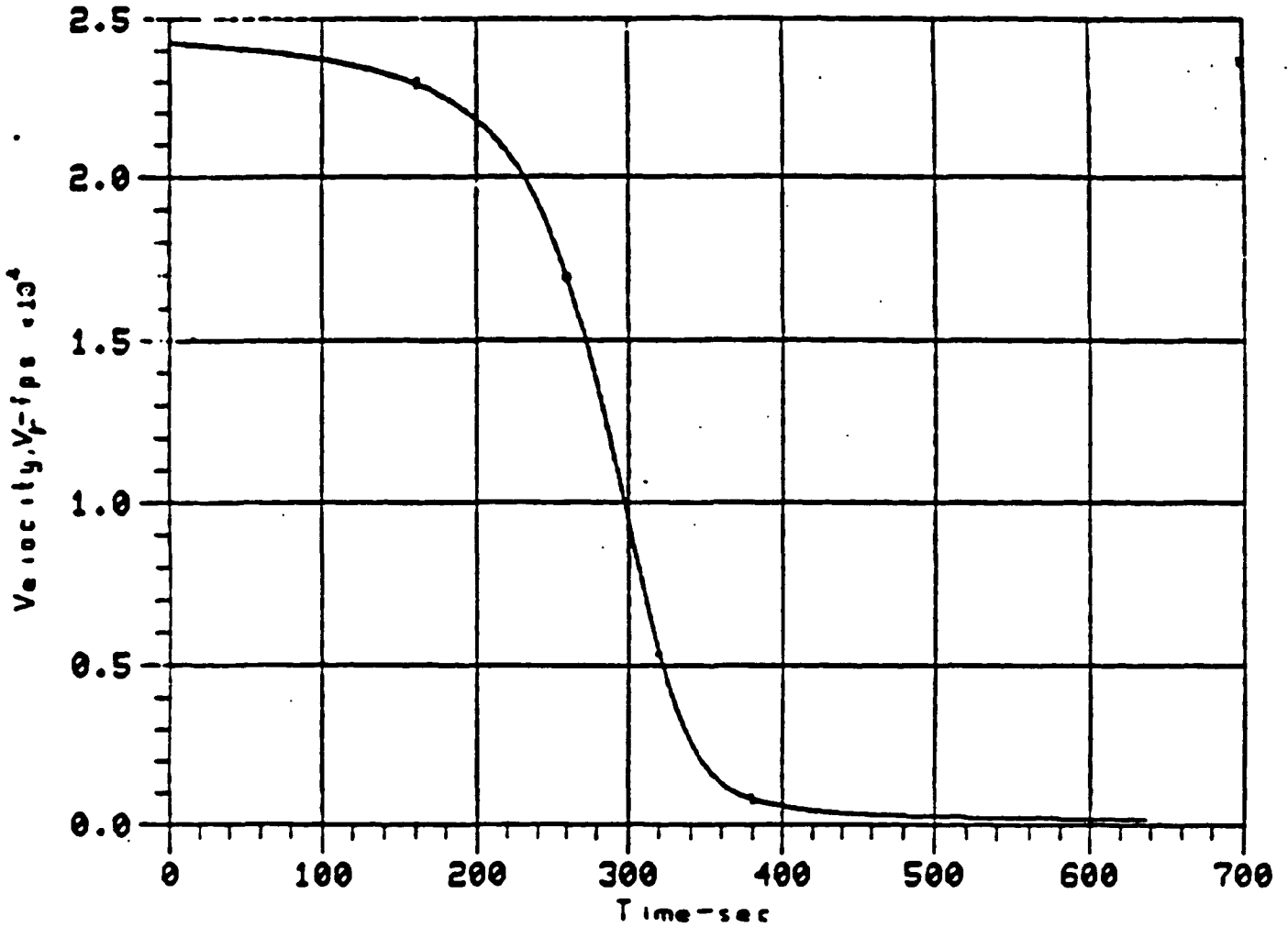


Figure I-27. Case 7 - Velocity



CASE 7  
VI=25594,GAMI=-0.318,H=292000

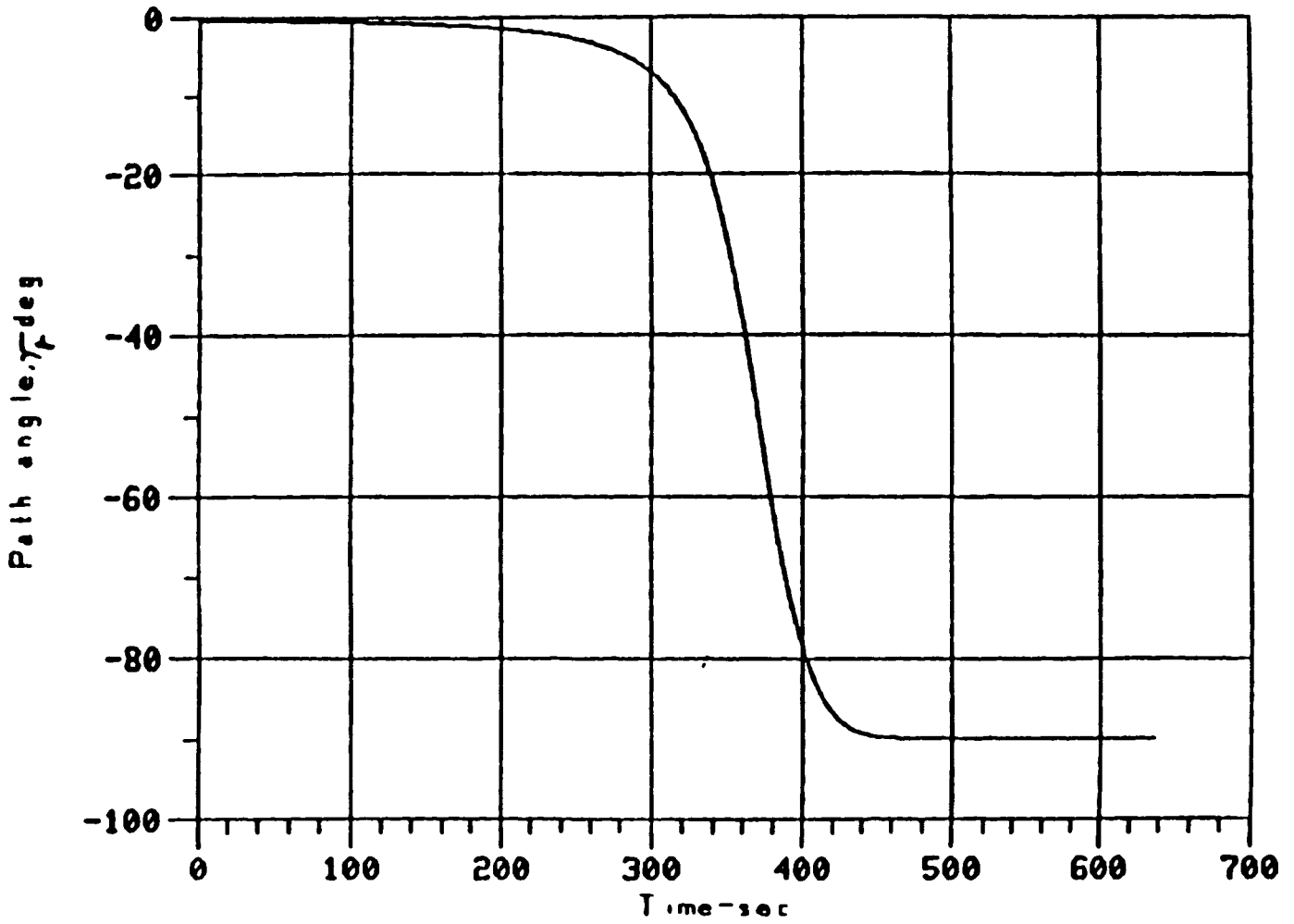


Figure I-28. Case 7 - Path Angle

CASE 8  
VI=25600, GAMI=-0.34, H=305000

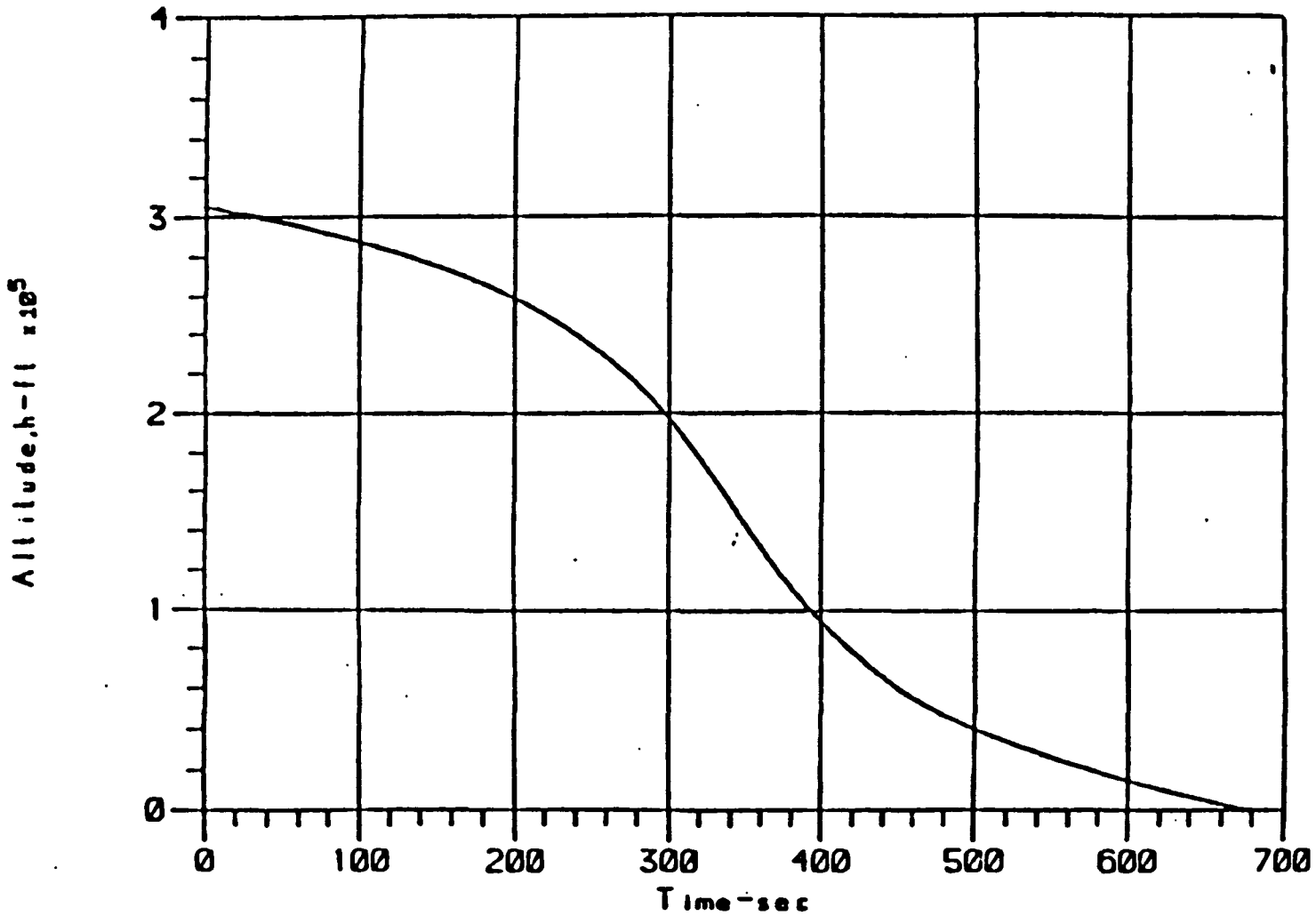


Figure I-29. Case 8 - Altitude

CASE 8  
VI=25600, GAMI=-0.34, H=305000

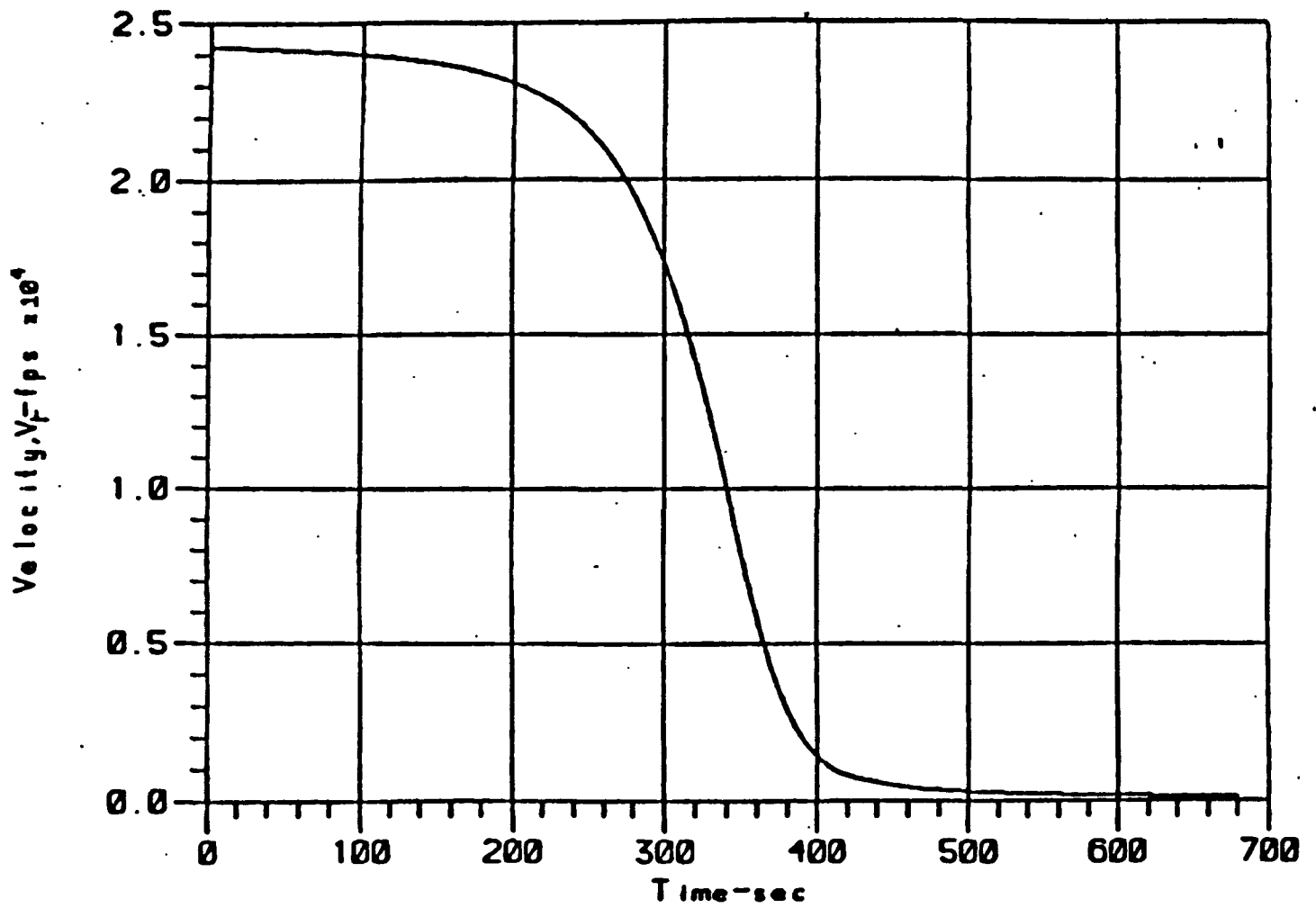


Figure I-30. Case 8 - Velocity

CASE 8  
VI=25600, GAMI=-0.34, H=305000

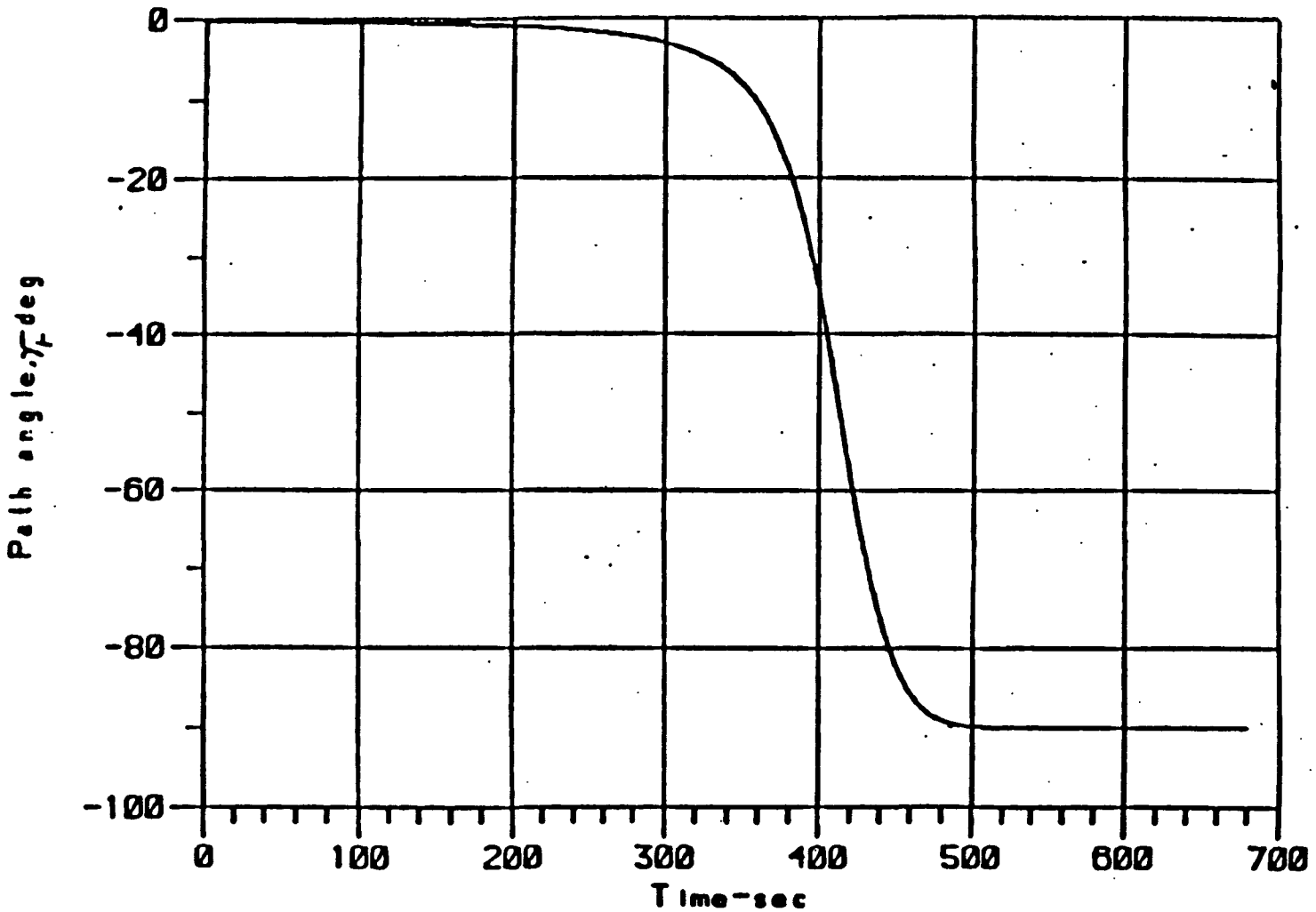


Figure I-31. Case 8 - Path Angle

CASE 9  
VI=23650, GAMI=-1.42, H=247000

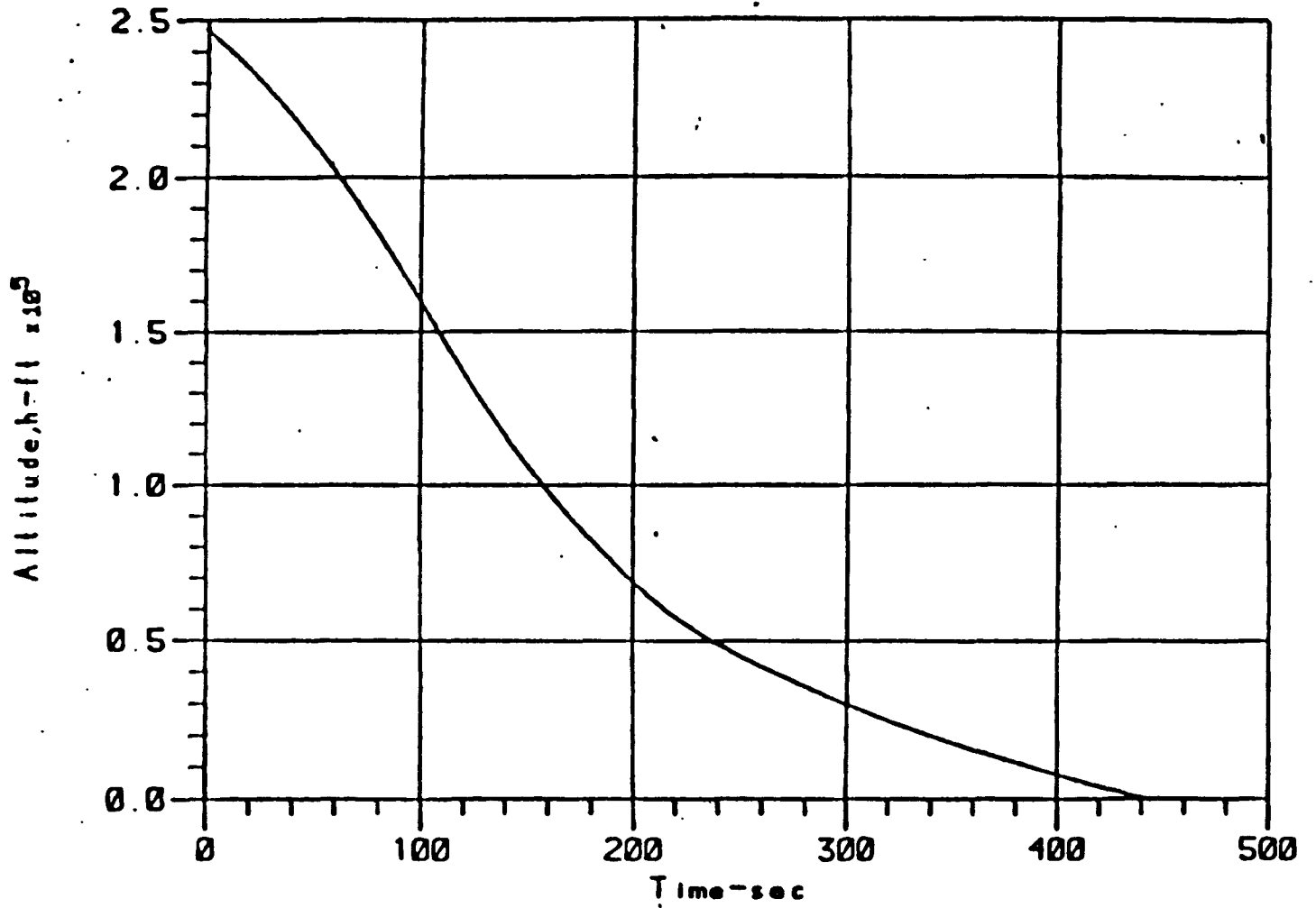


Figure I-32. Case 9 - Altitude

CASE 9  
VI=23650, GAMI=-1.42, H=247000

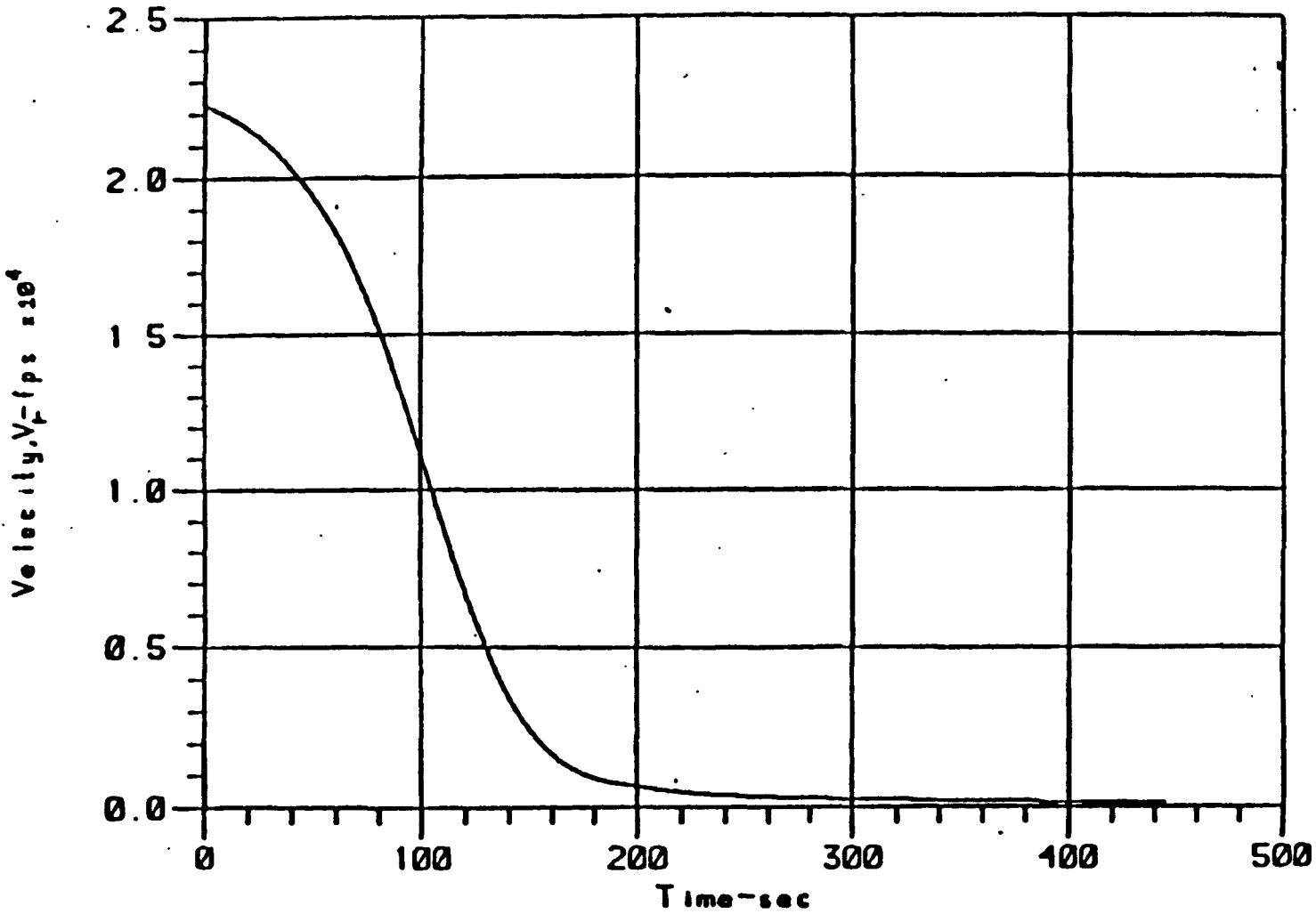


Figure I-33. Case 9 - Velocity

CASE 9  
VI=23650, GAMI=-1.42, H=247000

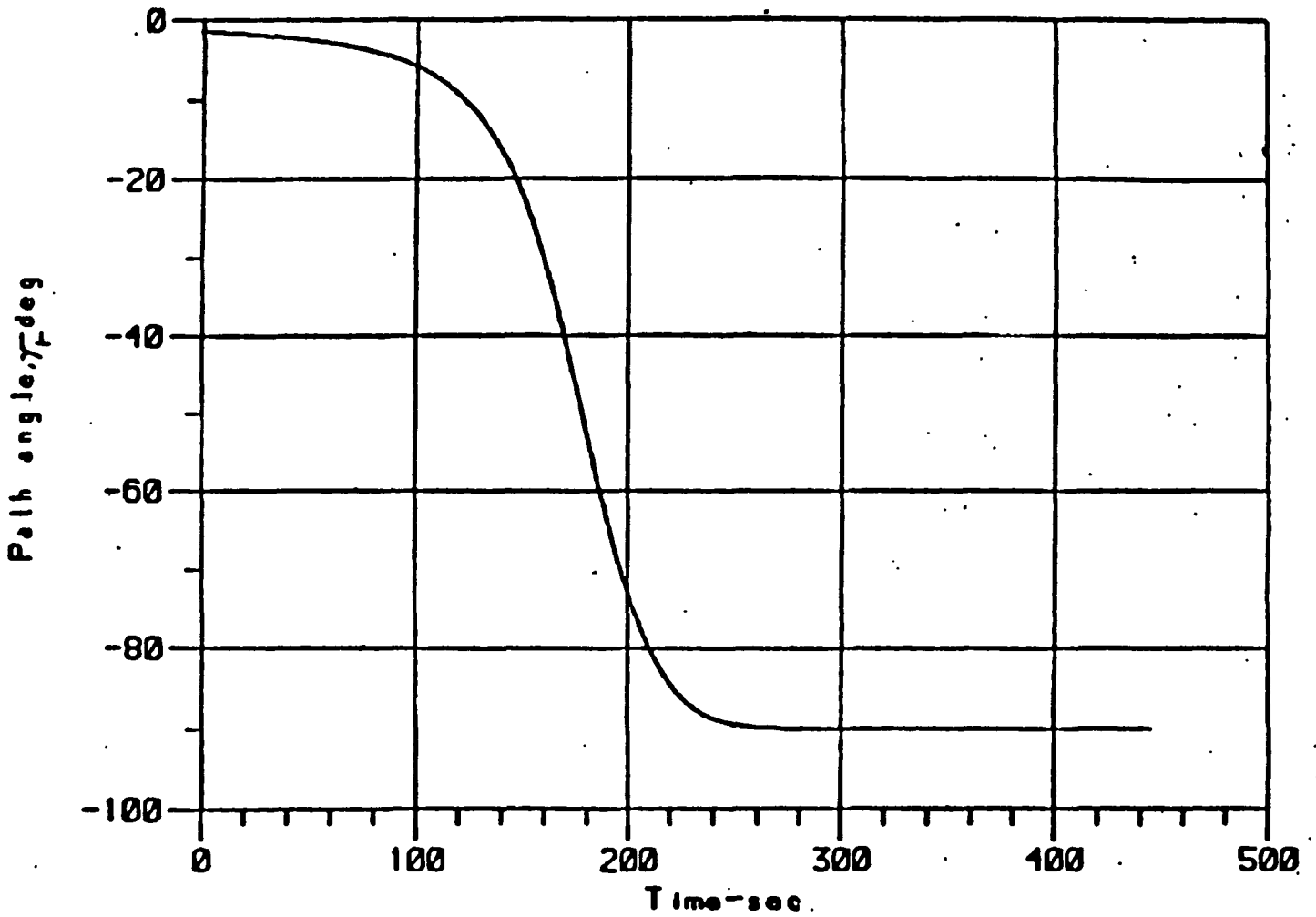


Figure I-34. Case 9 - Path Angle

CASE 10  
VI=20400, GAMI=-12.0, H=194400

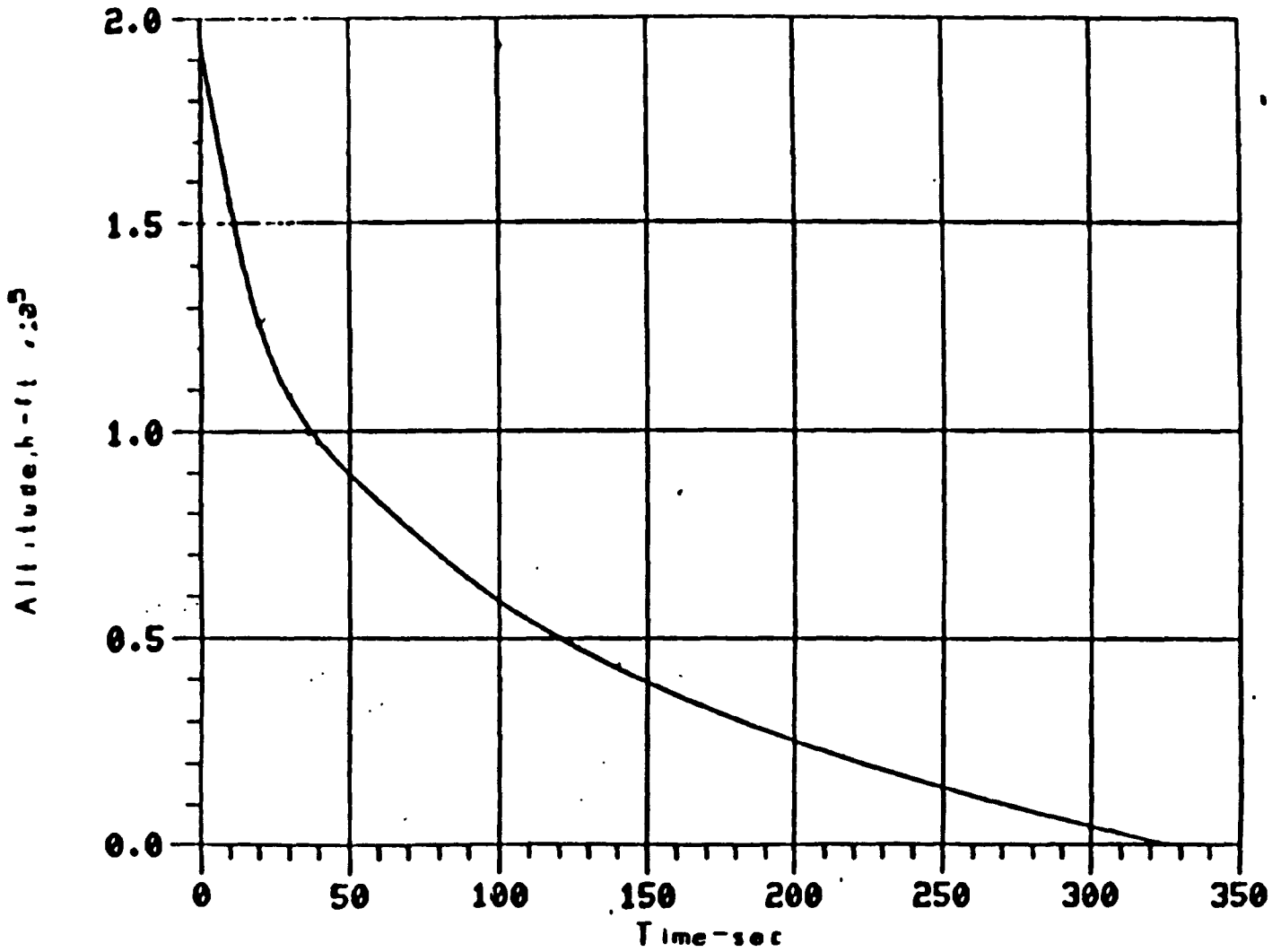


Figure I-35. Case 10 -Altitude



CASE 10  
VI=20400, GAMI=-12.0, H=194400

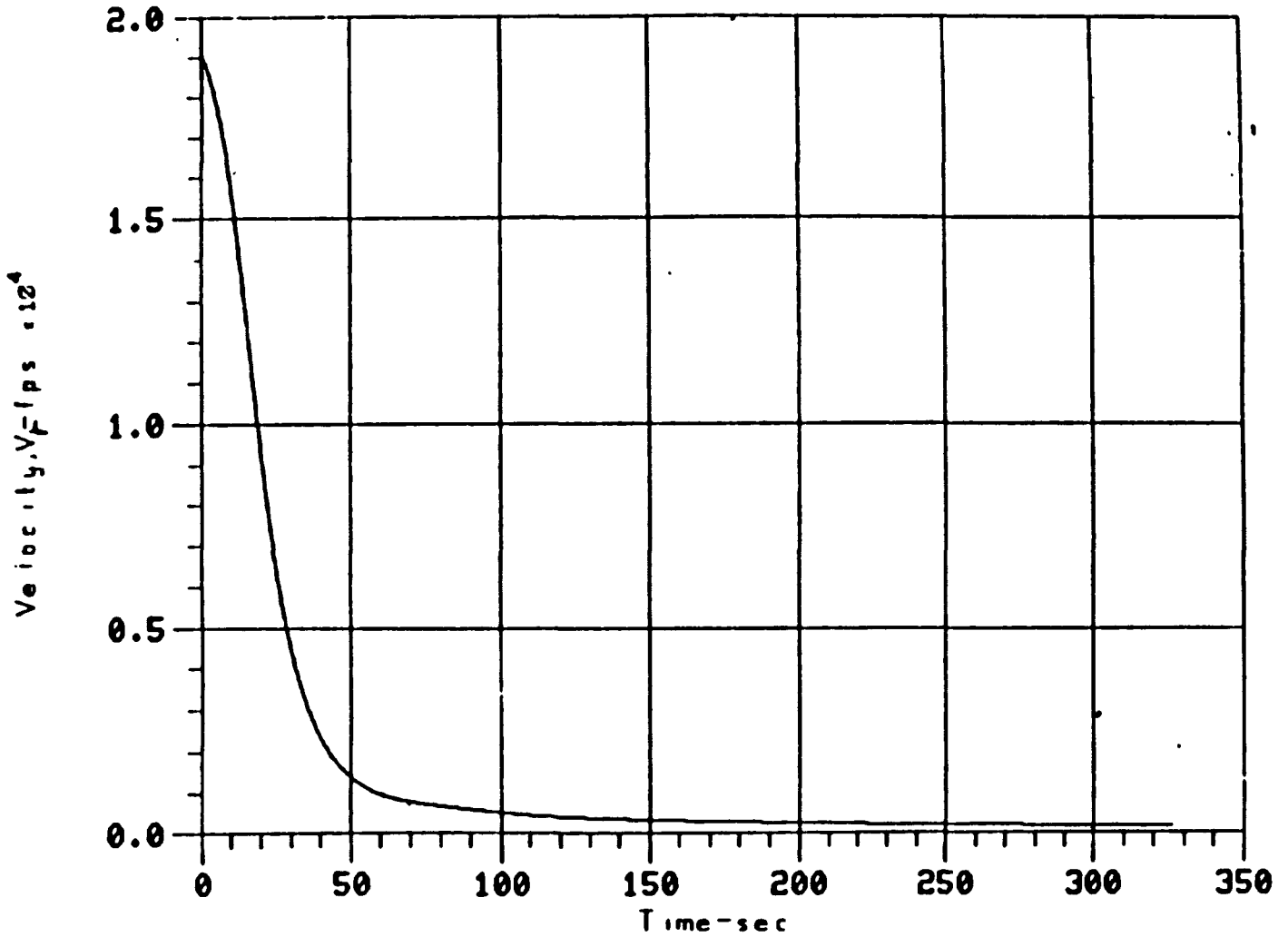


Figure I-36. Case 10 - Velocity

CASE 10  
VI=20400, GAMI=-12.0, H=194400

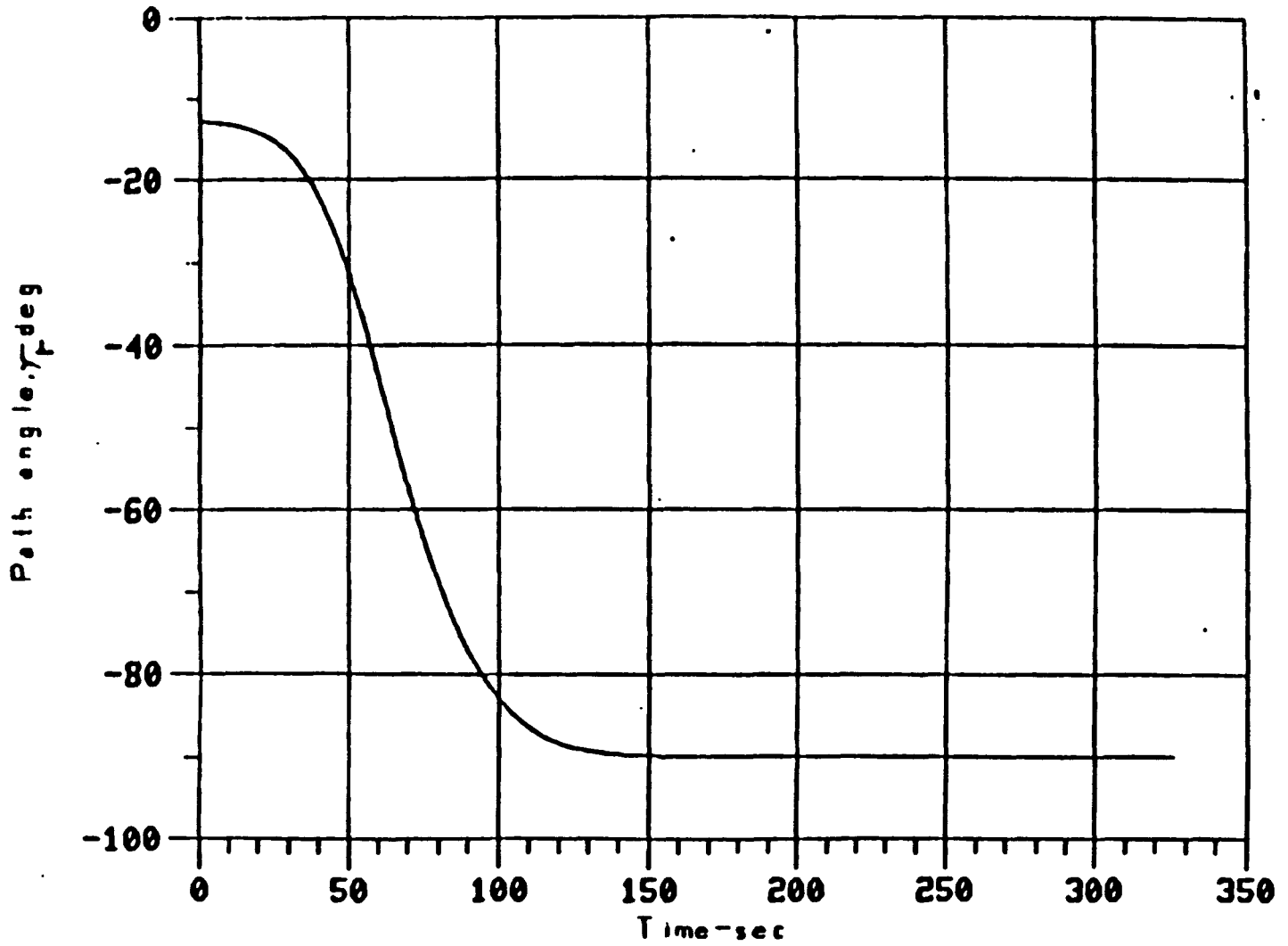


Figure I-37. Case 10 - Path Angle

CASE 11  
VI=11800, GAMI=-13.2, H=130200

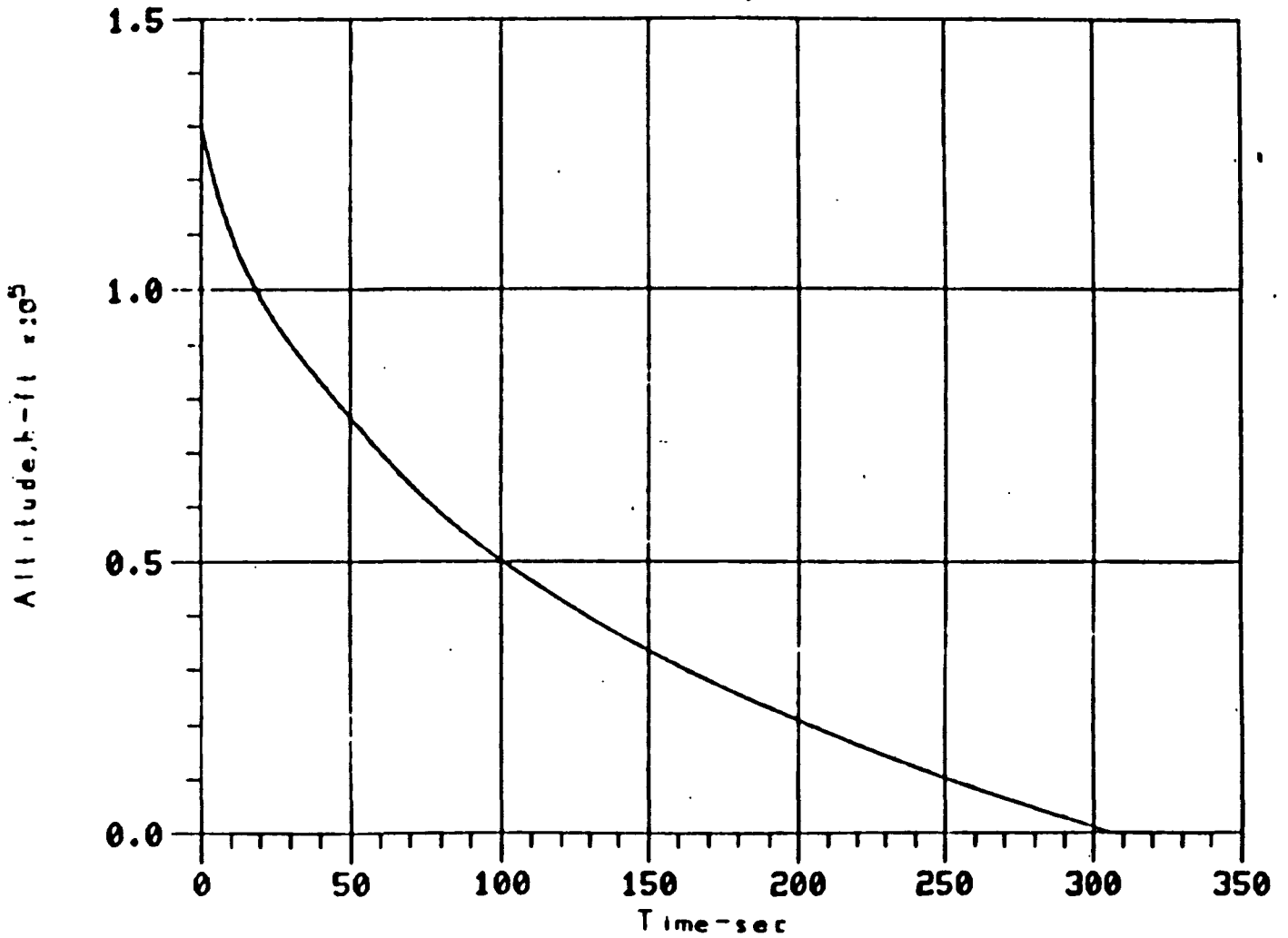


Figure I-38. Case 11 - Altitude

CASE 11  
VI=11800. GAMI=-13.2. H=130200

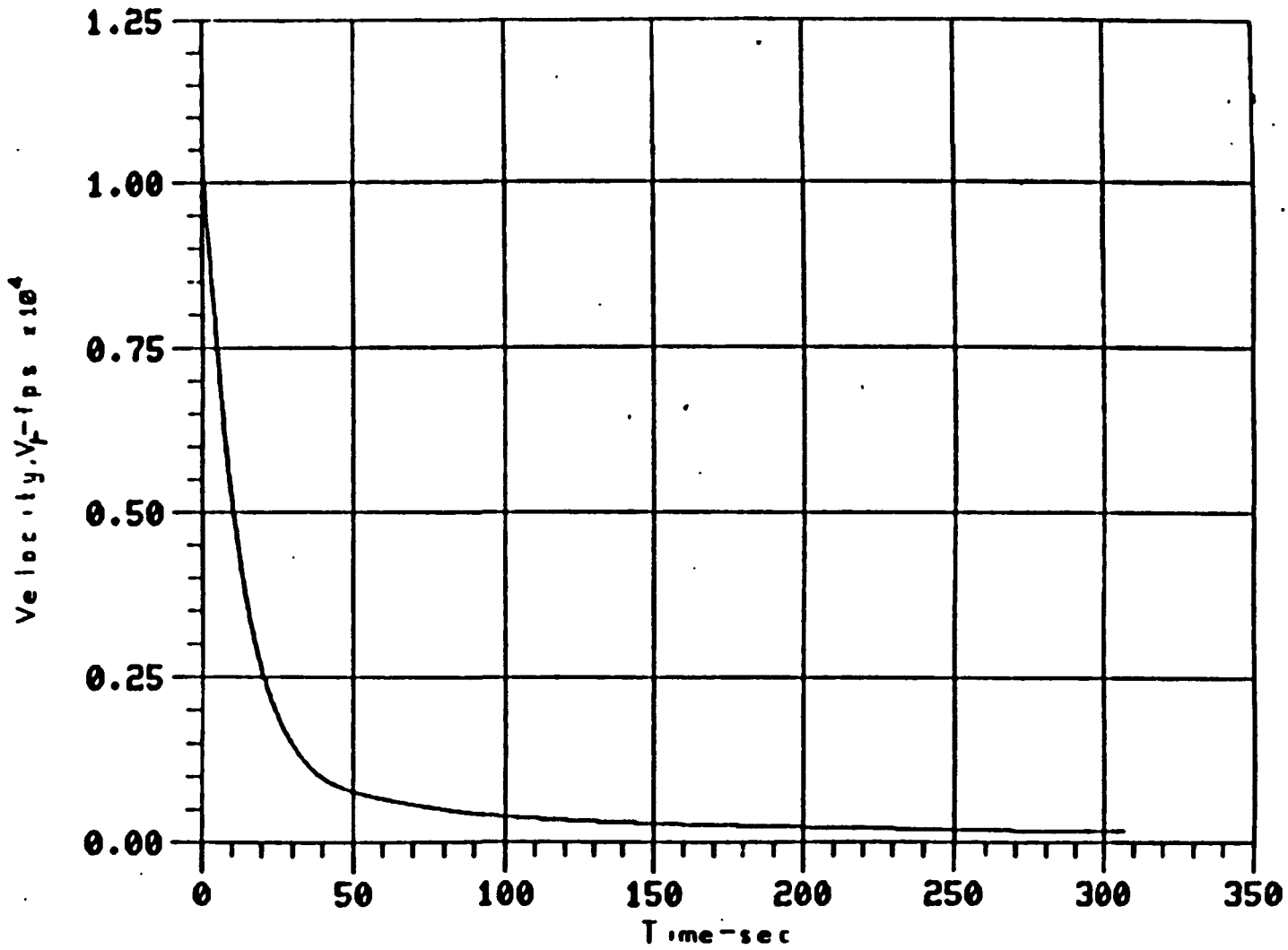


Figure I-39. Case 11 - Velocity

CASE 11  
VI=11800, GAMI=-13.2, H=130200

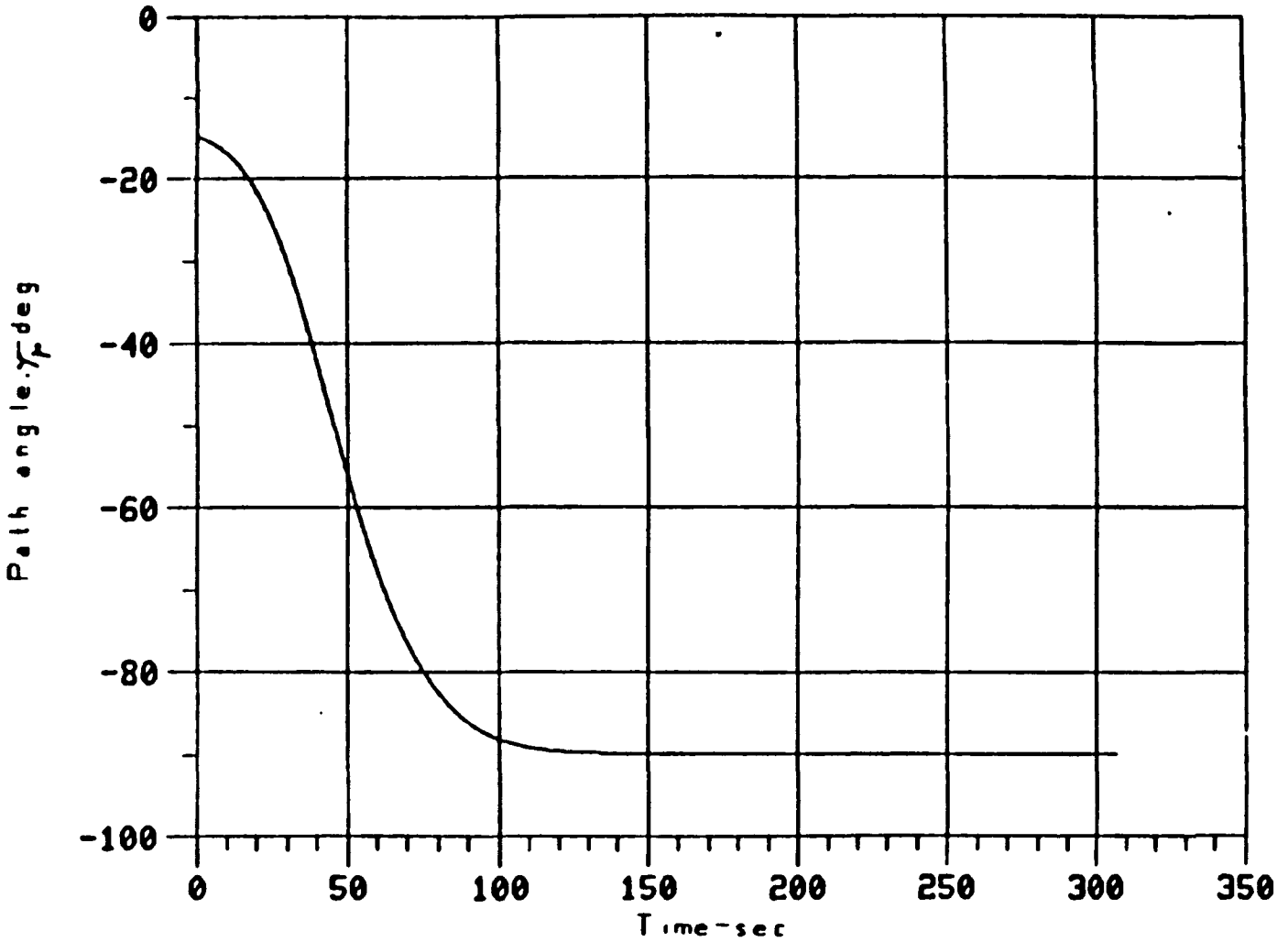


Figure I-40. Case 11 - Path Angle

CASE 12  
VI=20300. GAMI=-12.0. H=185800

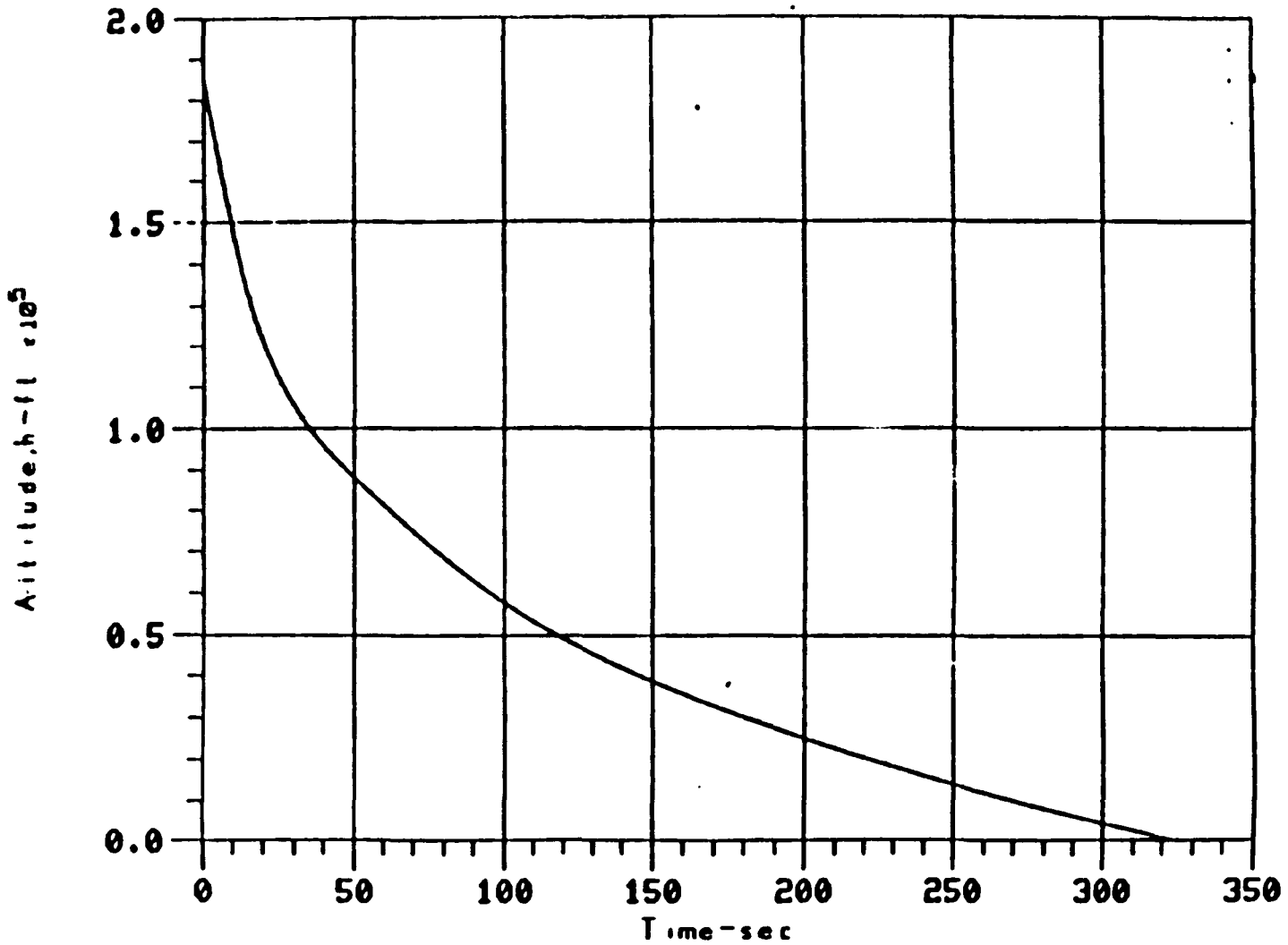


Figure I-41. Case 12 - Altitude

CASE 12  
VI=20300, GAMI=-12.0, H=105800

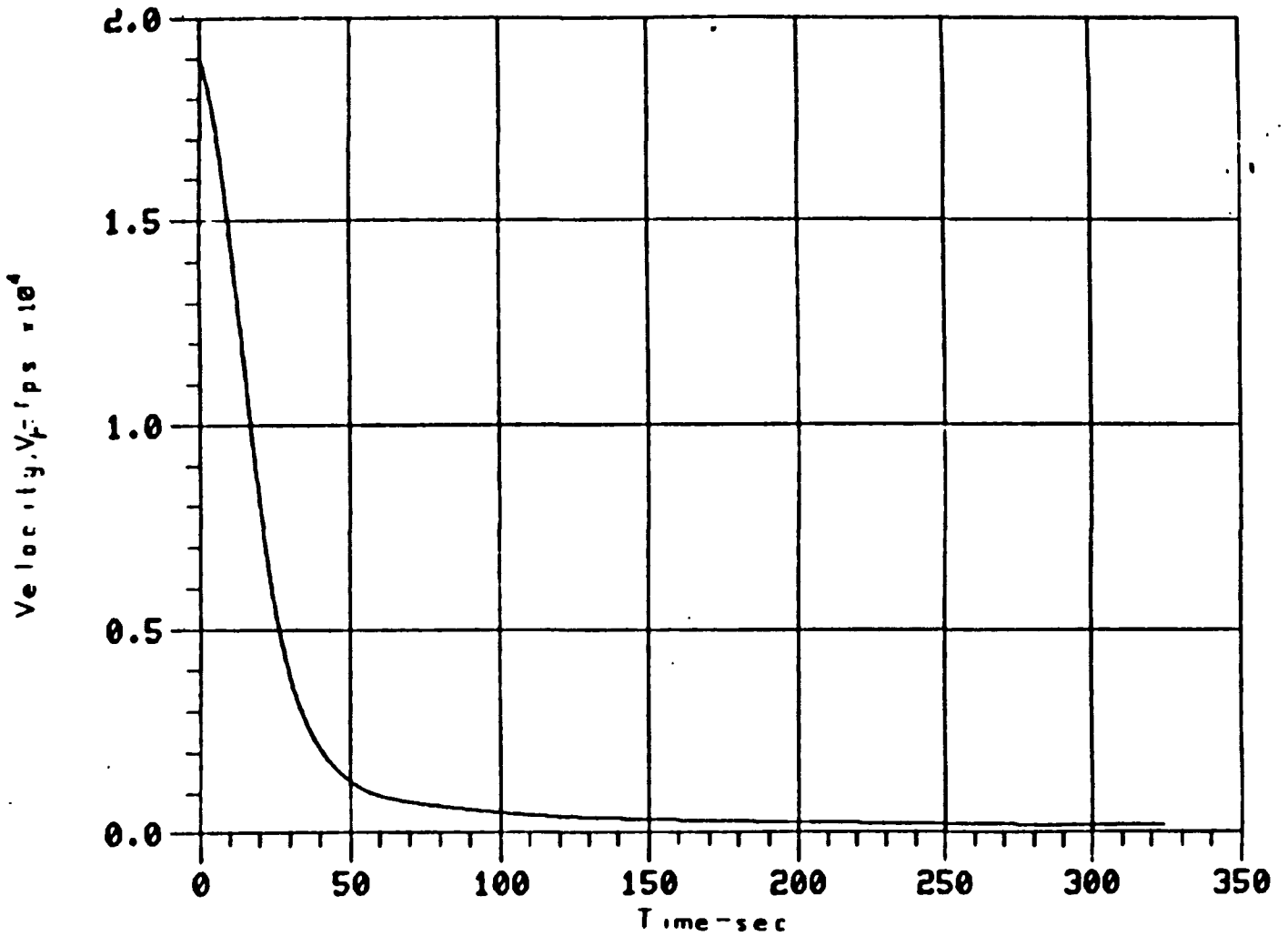


Figure I-42. Case 12 - Velocity

CASE 12  
VI=20300, GAMI=-12.0, H=105800

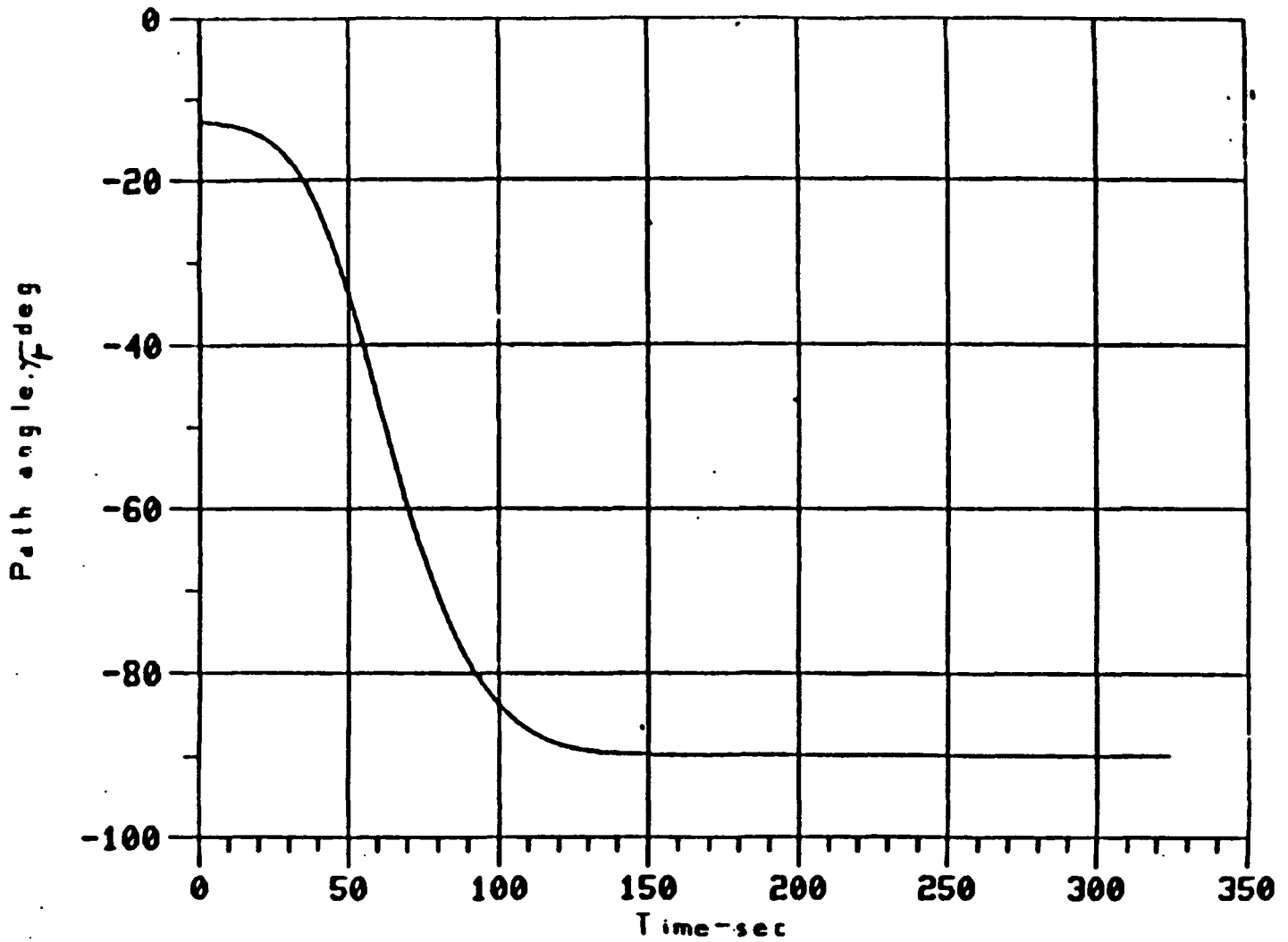


Figure I-43. Case 12 - Path Angle



CASE 13  
VI=18900, GAMI=-12.2, H=159000

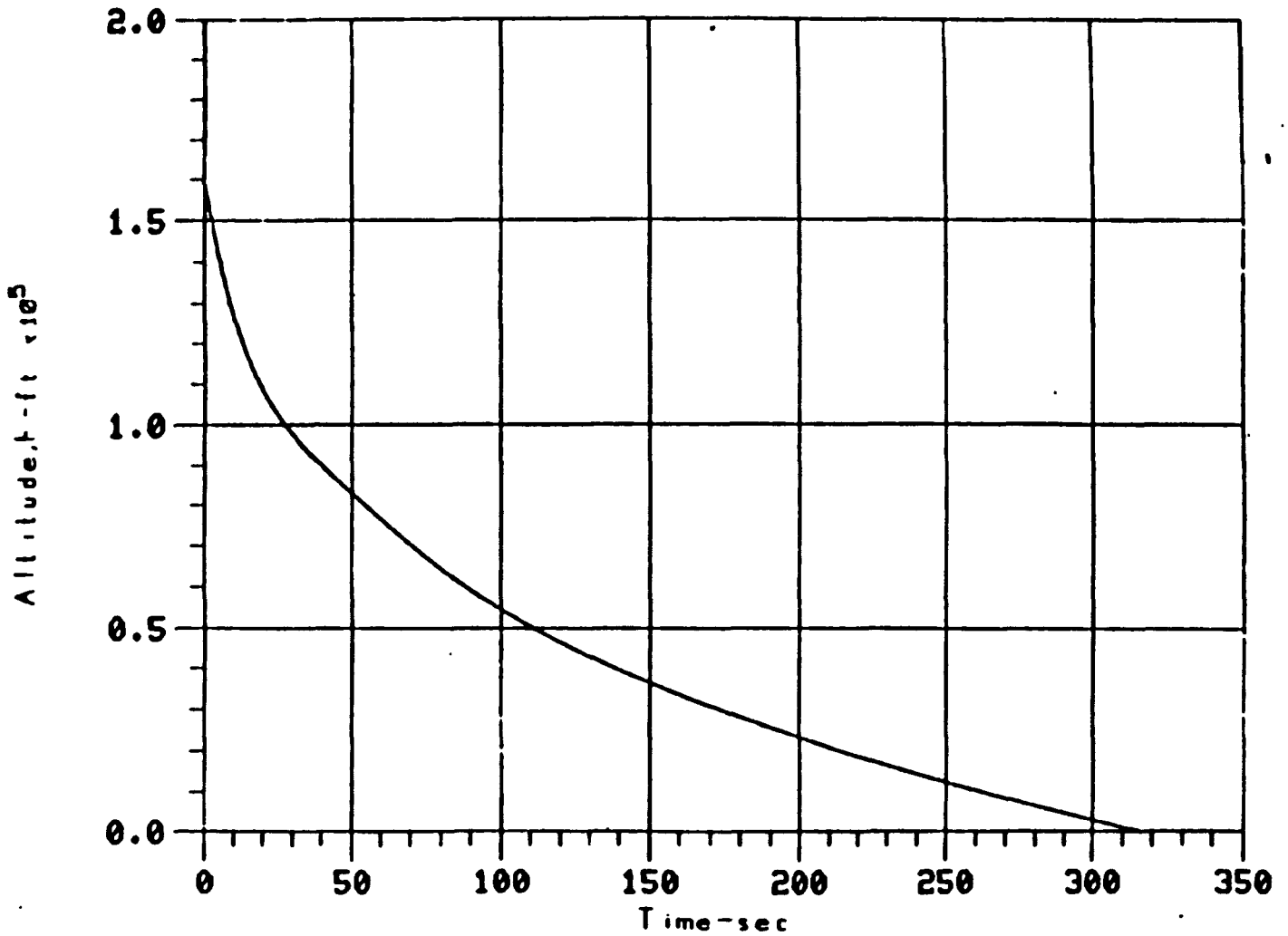


Figure I-44. Case 13 - Altitude

CASE 13  
VI=18900, GAMI=-12.2, H=159000

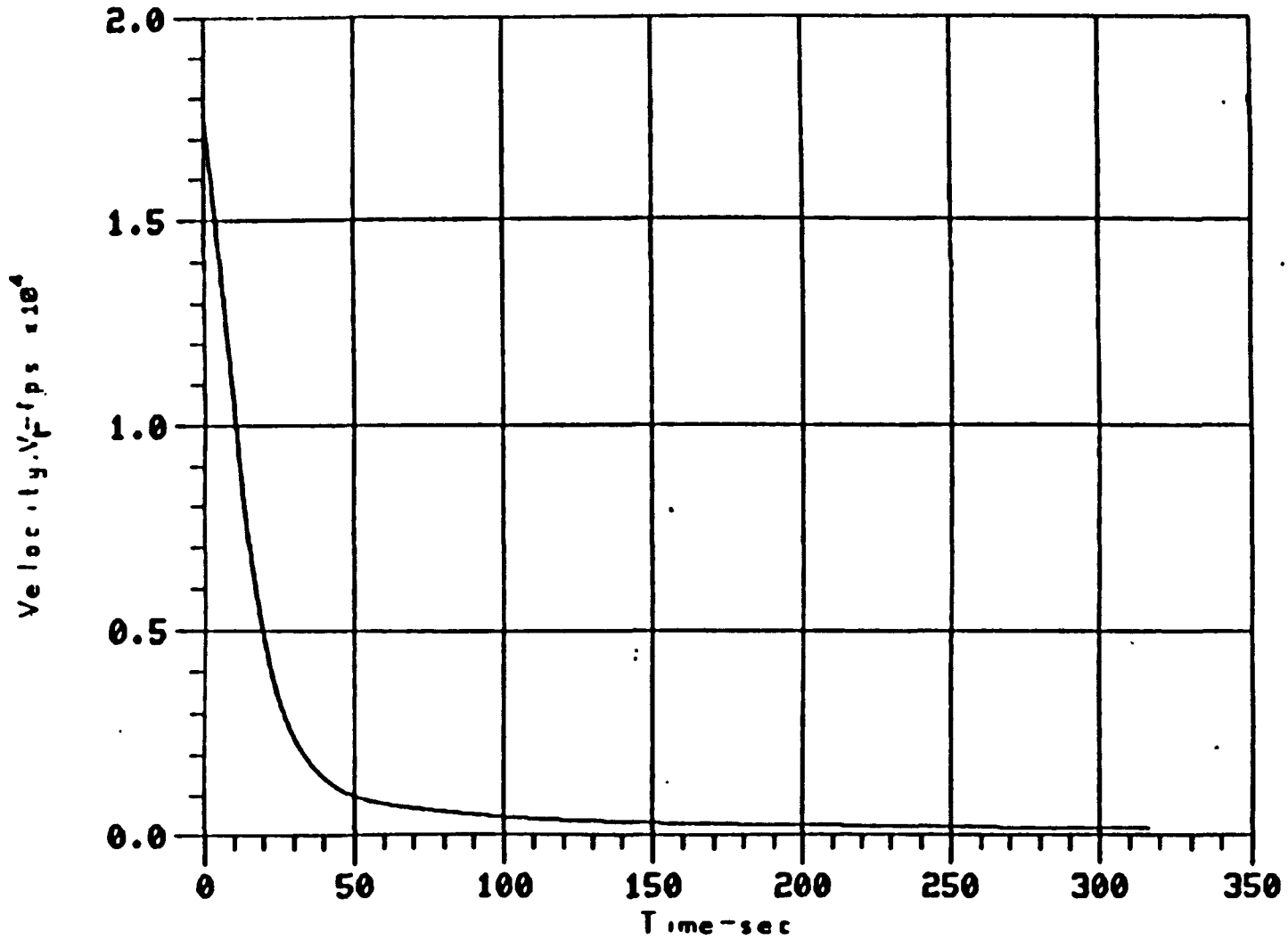


Figure I-45. Case 13 - Velocity

CASE 13  
VI=18900. GAMI=-12.2. H=159000

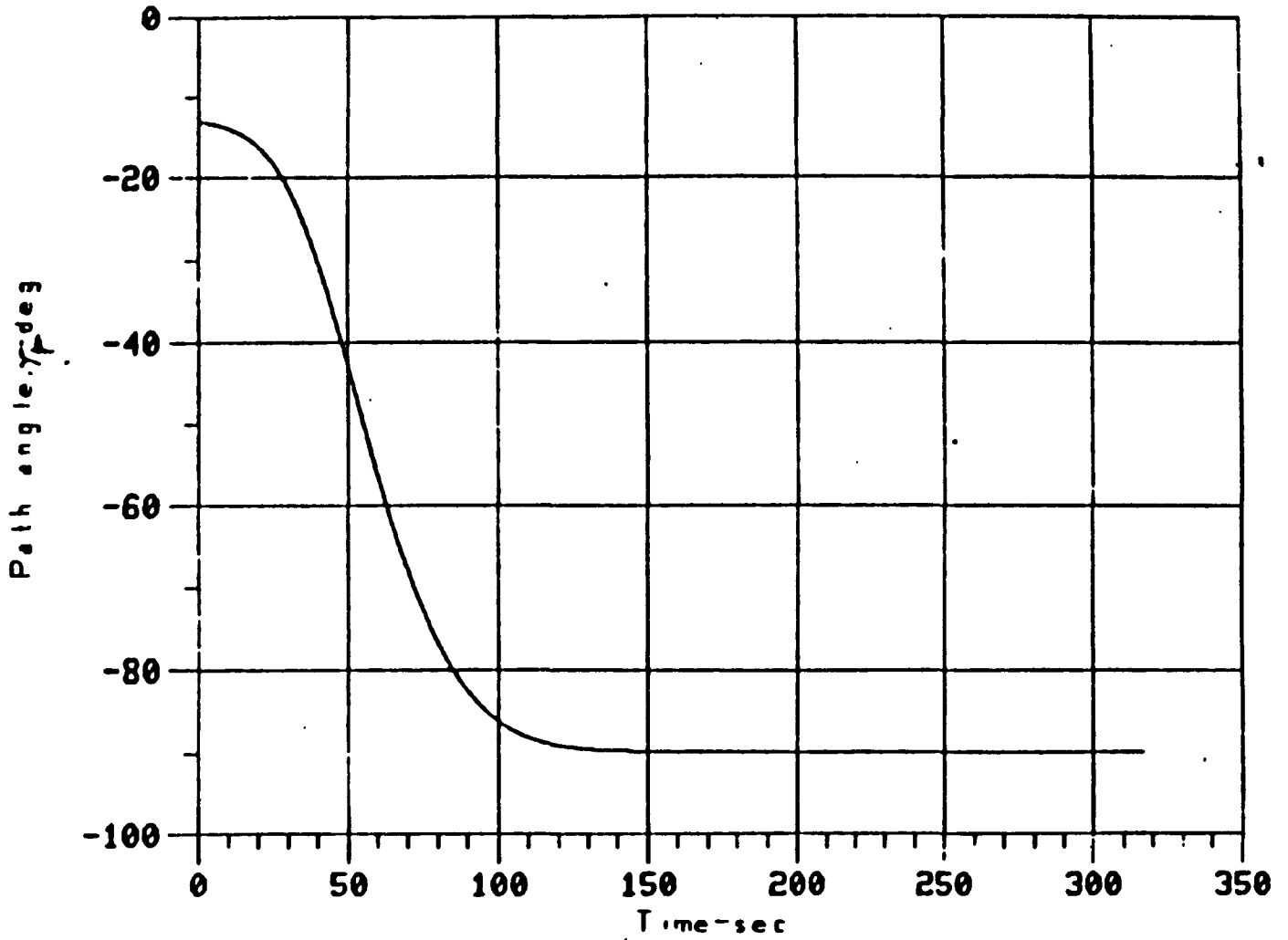


Figure I-46. Case 13 - Path Angle

CASE 14  
VI=36090, GAMI=-2.54, H=276700

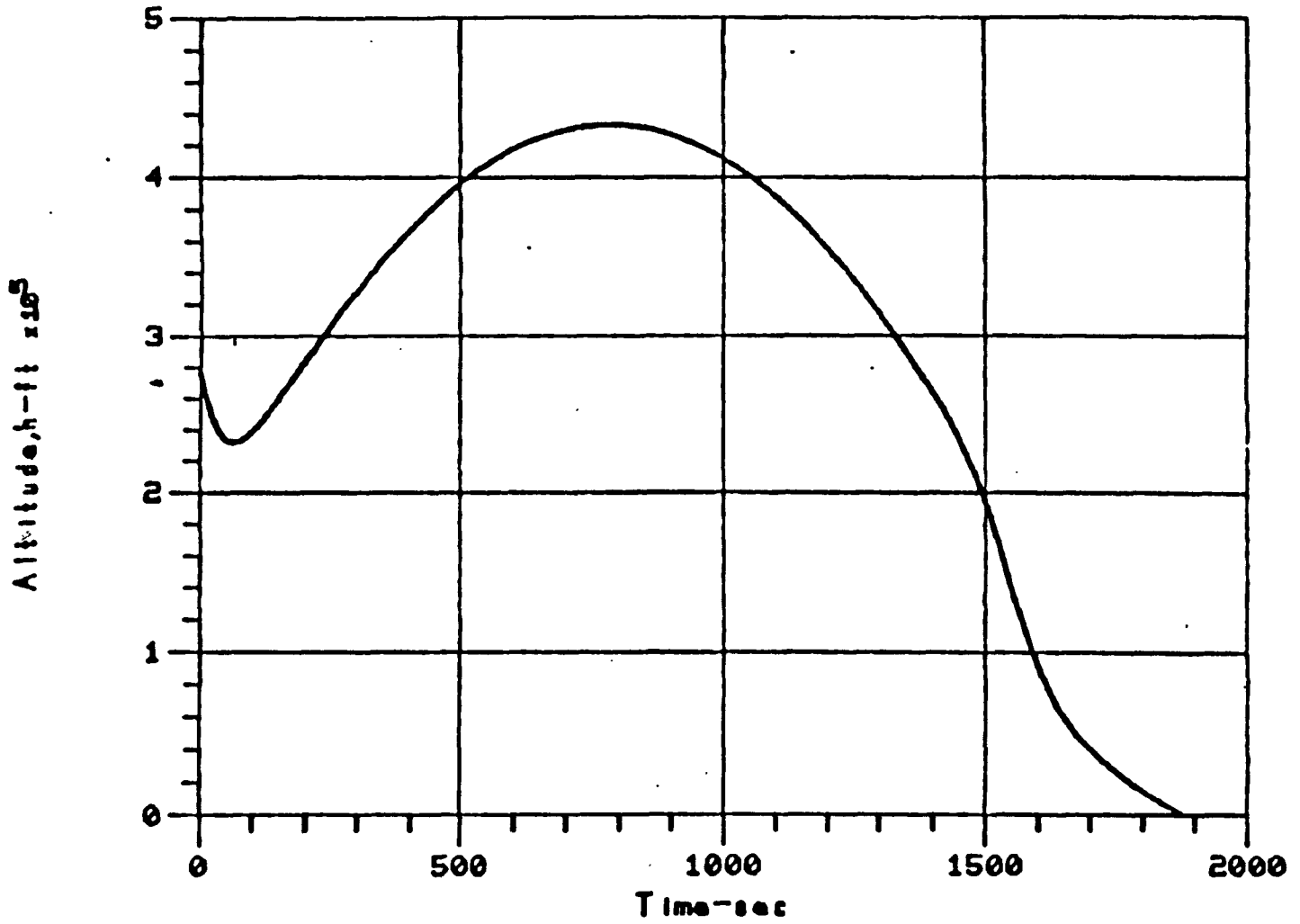


Figure I-47. Case 14 - Altitude

CASE 14  
VI=36090, GAMI=-2.54, H=276700

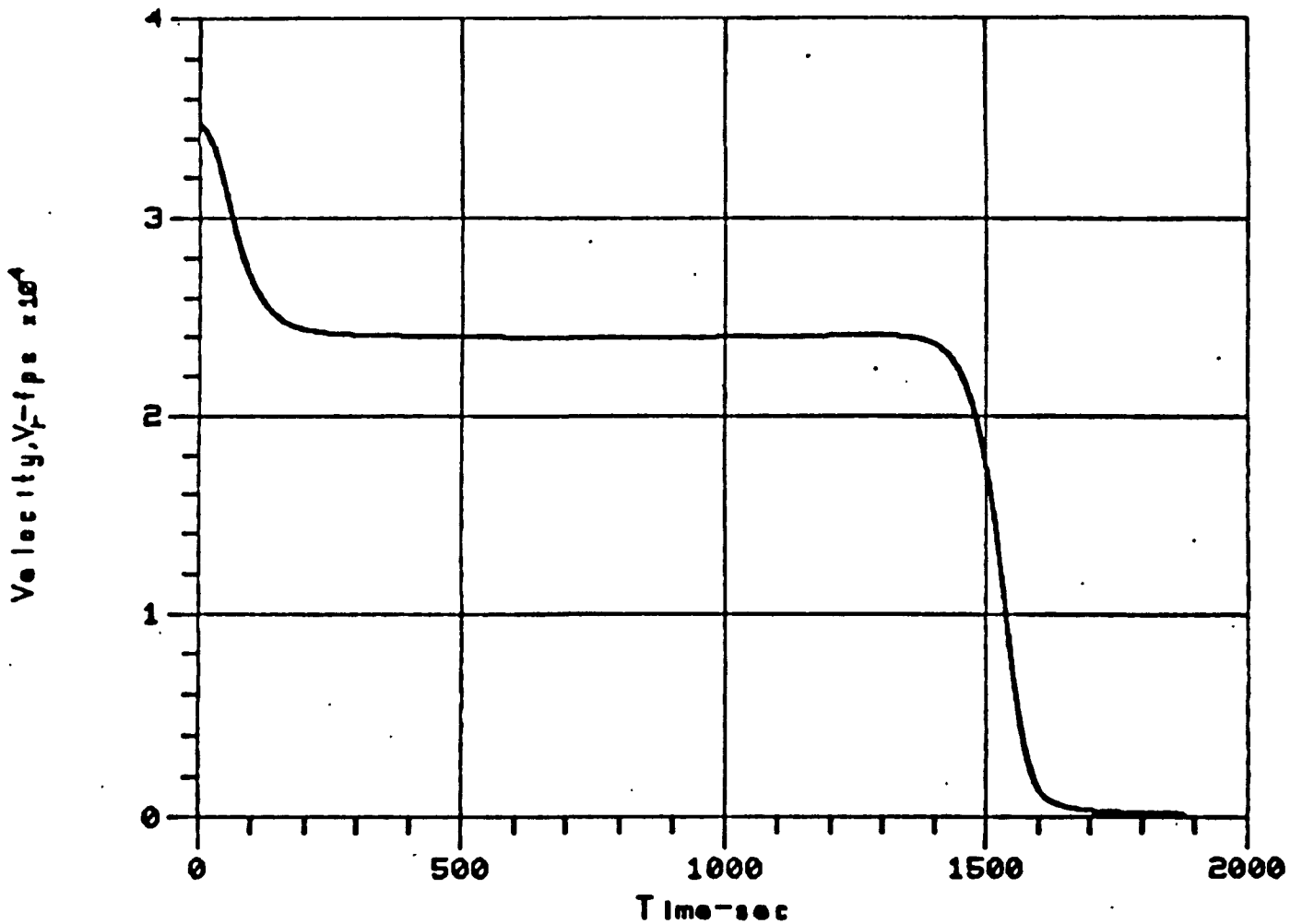


Figure I-48. Case 14 - Velocity

CASE 14  
VI=36090, GAMI=-2.54, H=276700

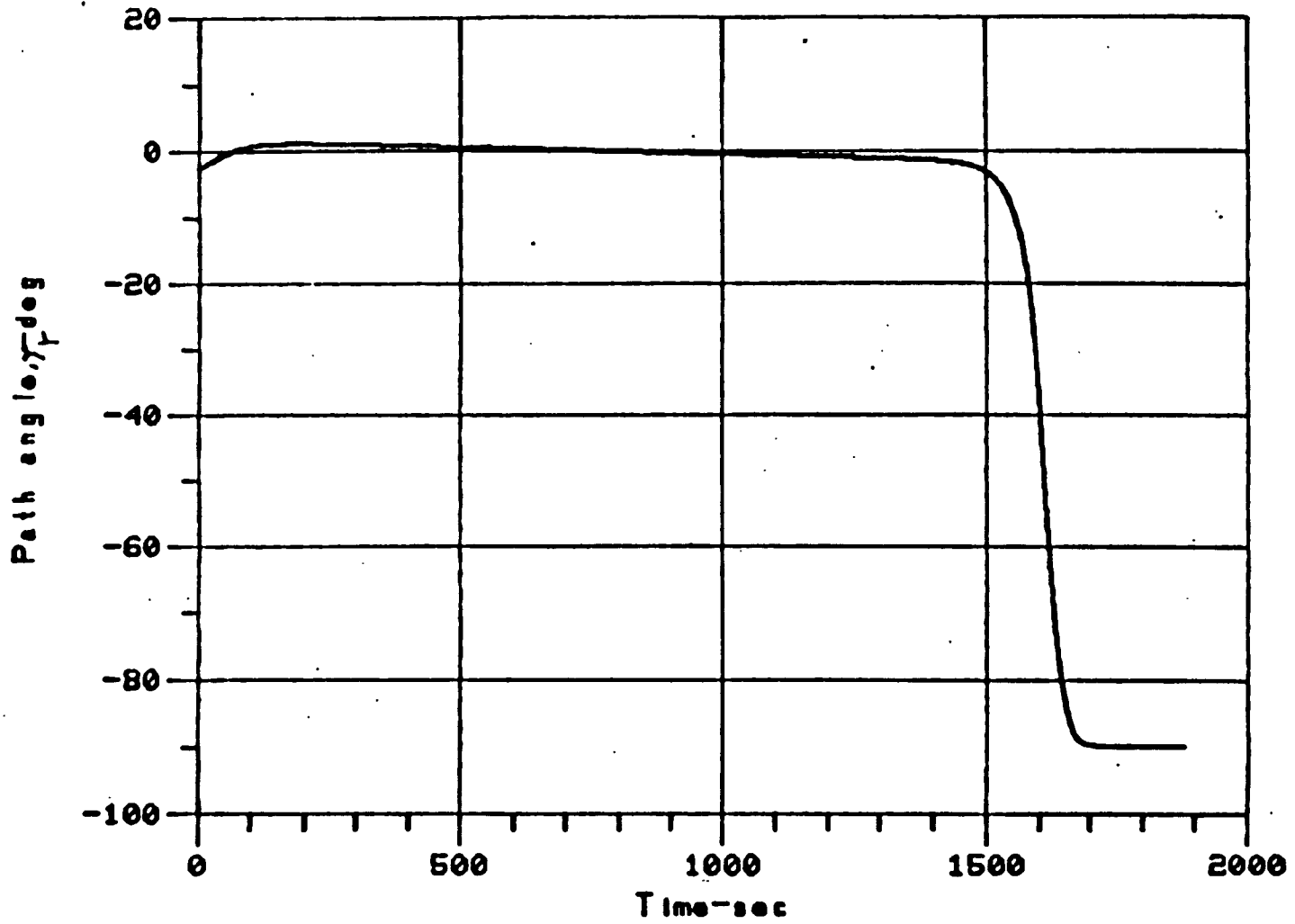


Figure I-49. Case 14 - Path Angle

CASE 15  
VI=36100, GAMI=-2.39, H=270500

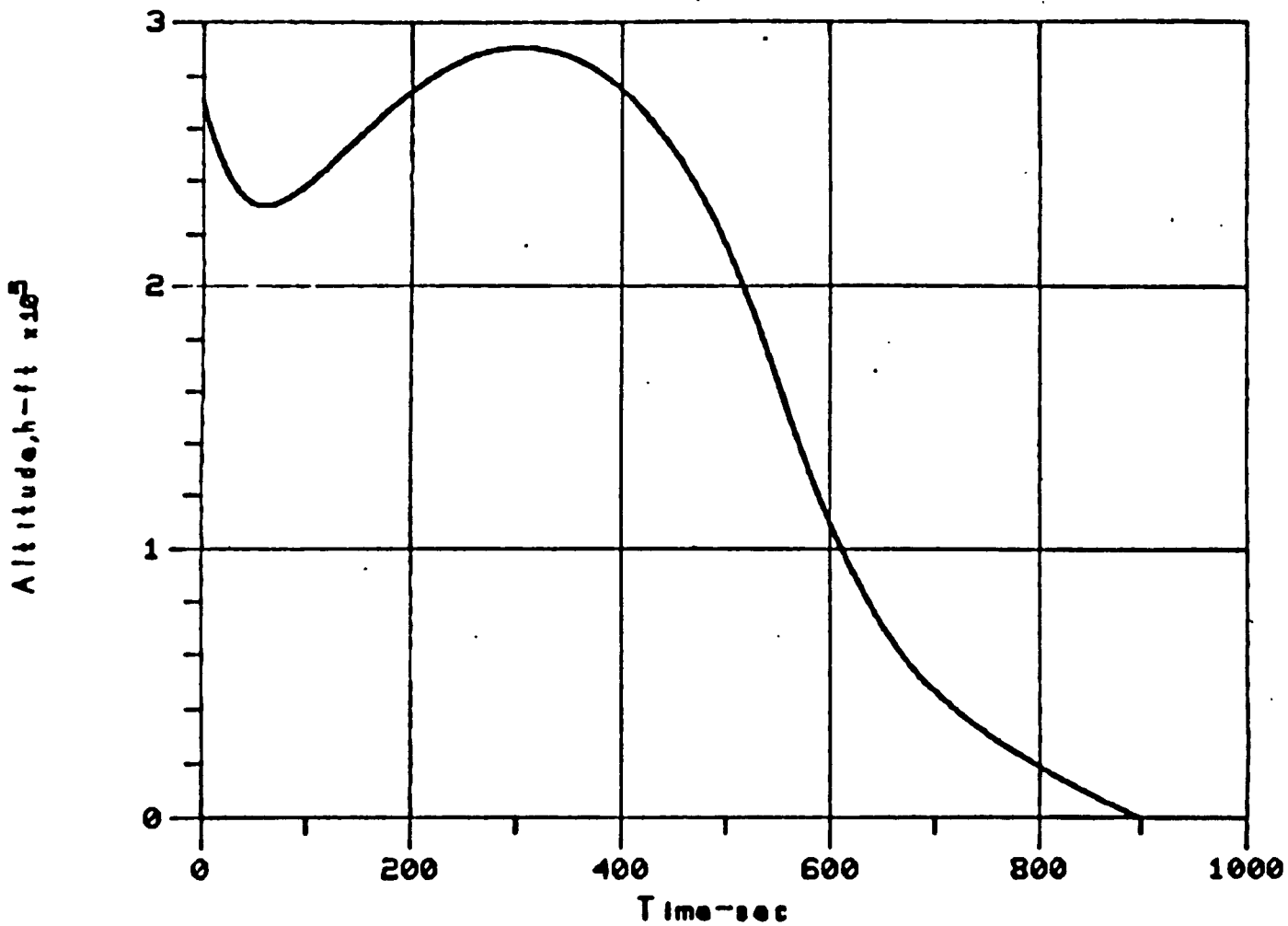


Figure I-50. Case 15 - Altitude

CASE 15  
VI=36100, GAMI=-2.39, H=270500

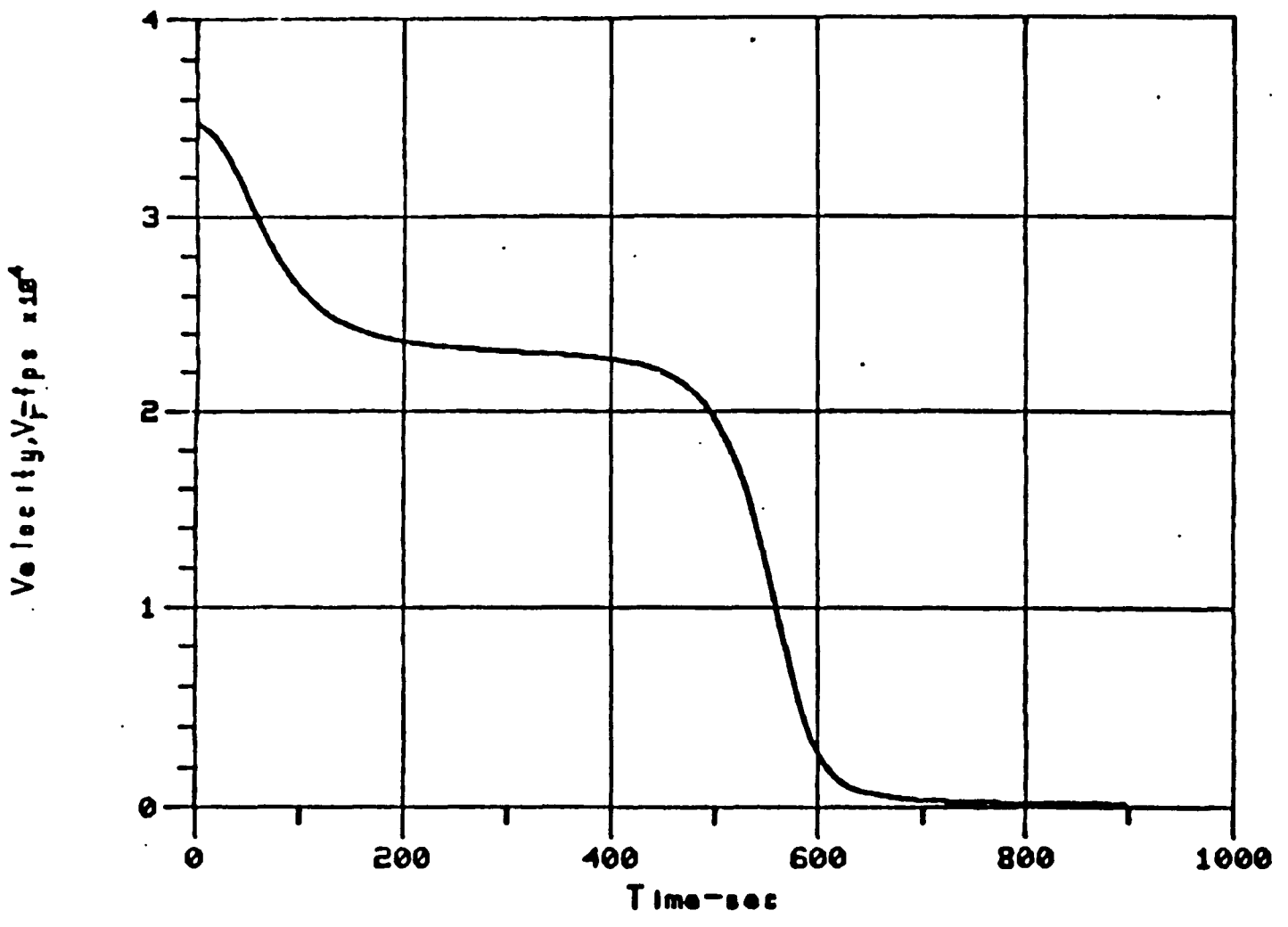


Figure I-51. Case 15 - Velocity



CASE 15  
VI=36100, GAMI=-2.39, H=270500

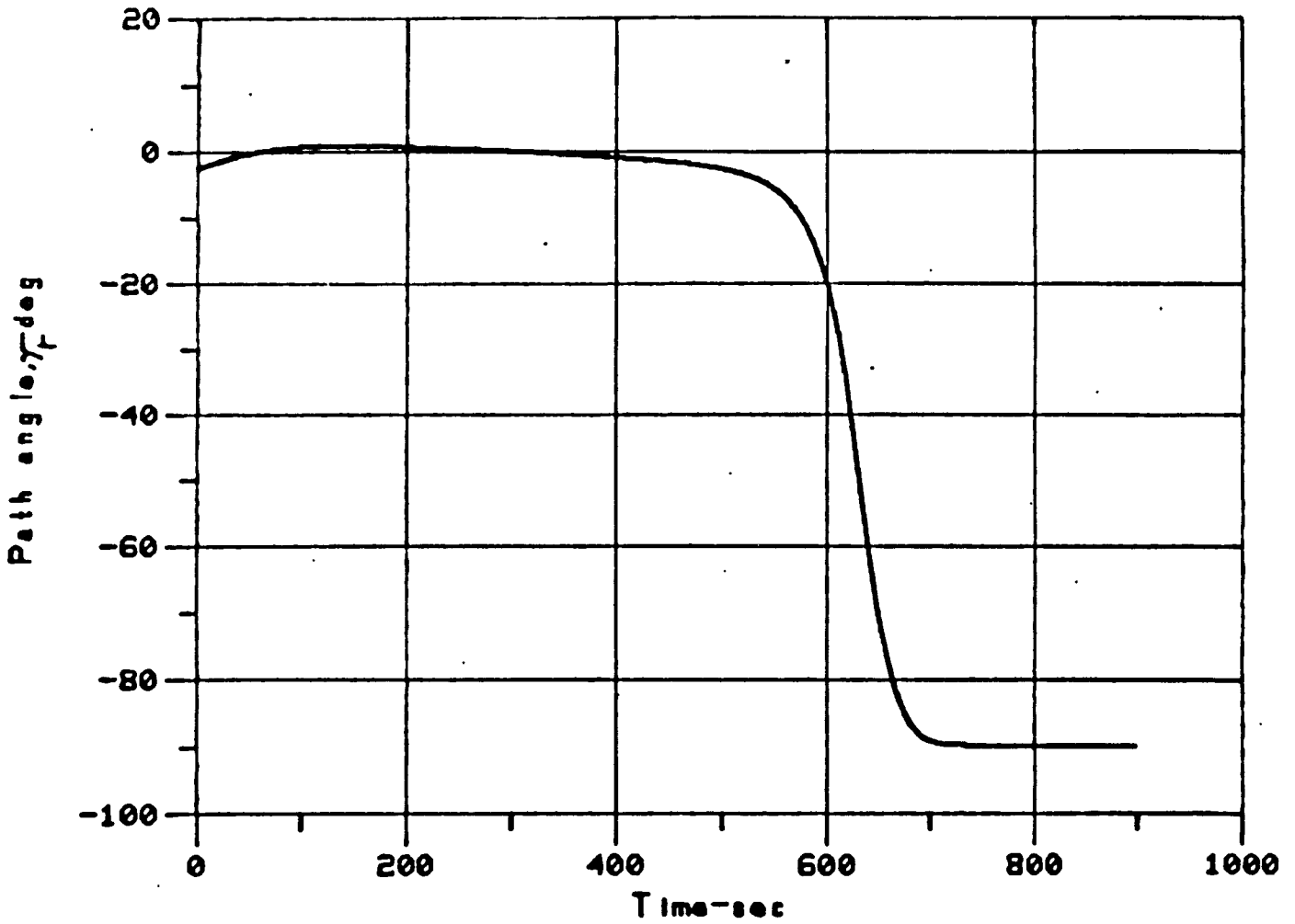


Figure I-52. Case 15 - Path Angle

CASE 16  
VI=36040, GAMI=-0.18, H=294300  
ENTRY ONLY

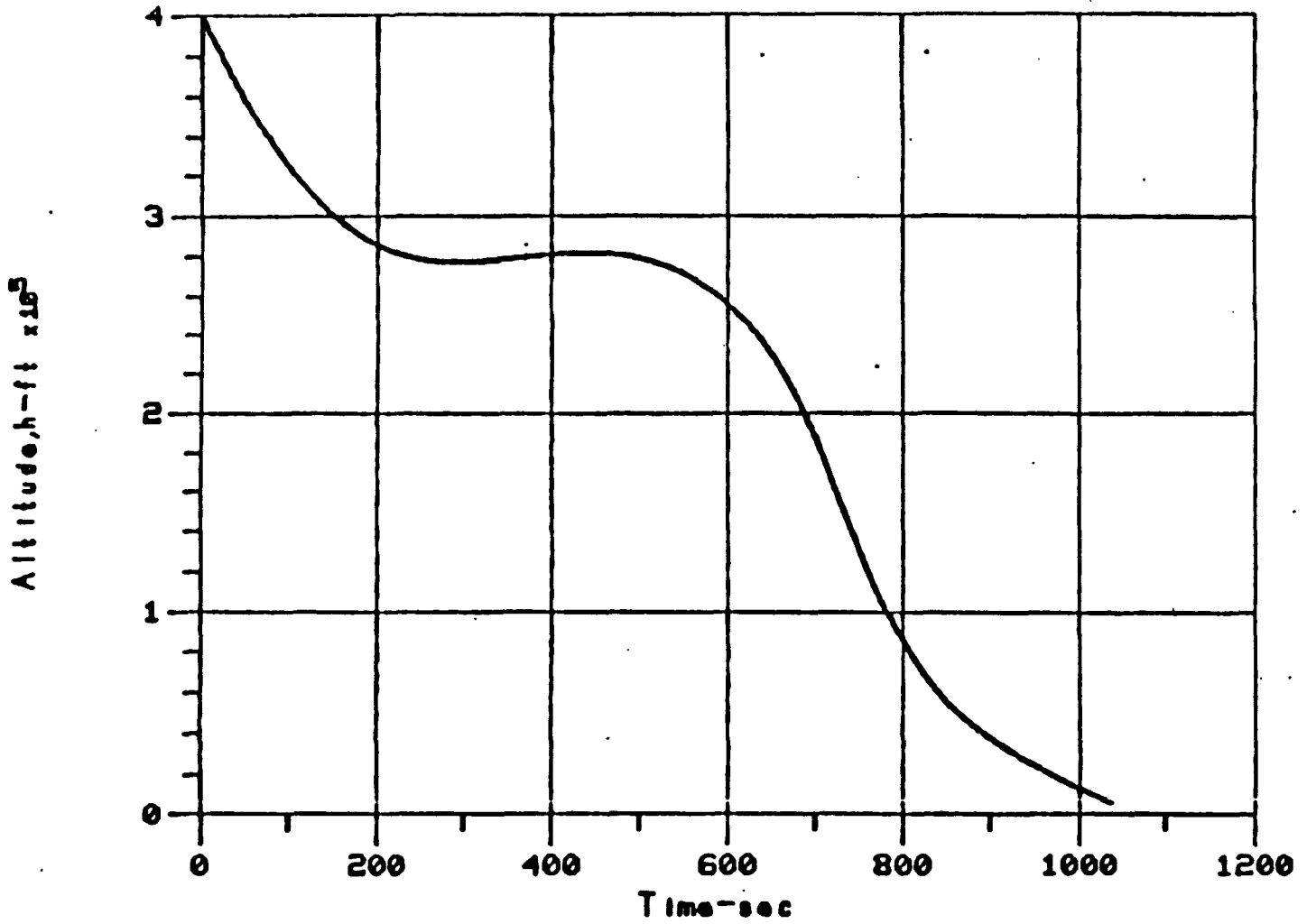


Figure I-53. Case 16 - Altitude

CASE 16  
VI=36040, GAMI=-0.18, H=294300  
ENTRY ONLY

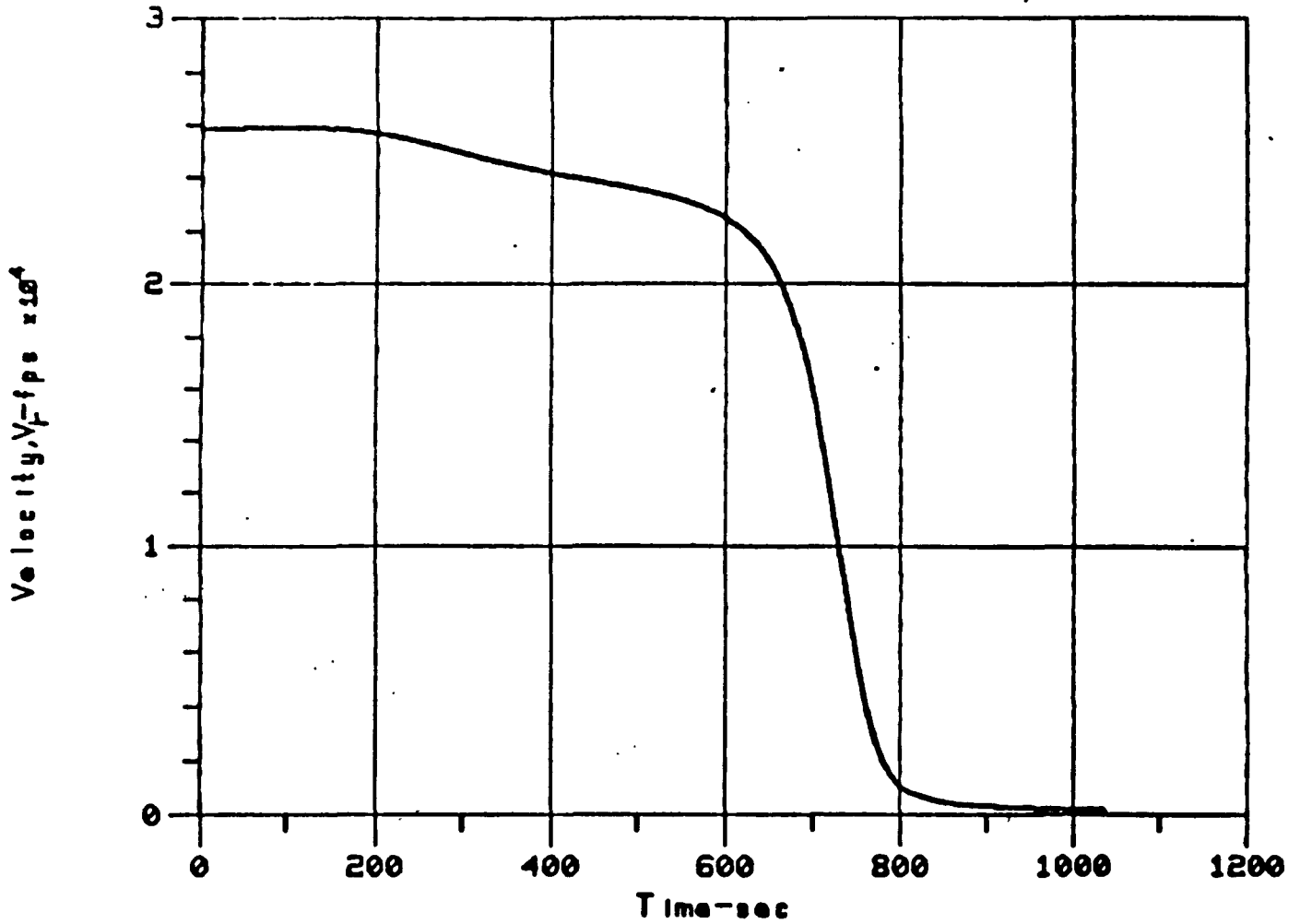


Figure I-54. Case 16 - Velocity

CASE 16  
VI=36040, GAMI=-0.18, H=294300  
ENTRY ONLY

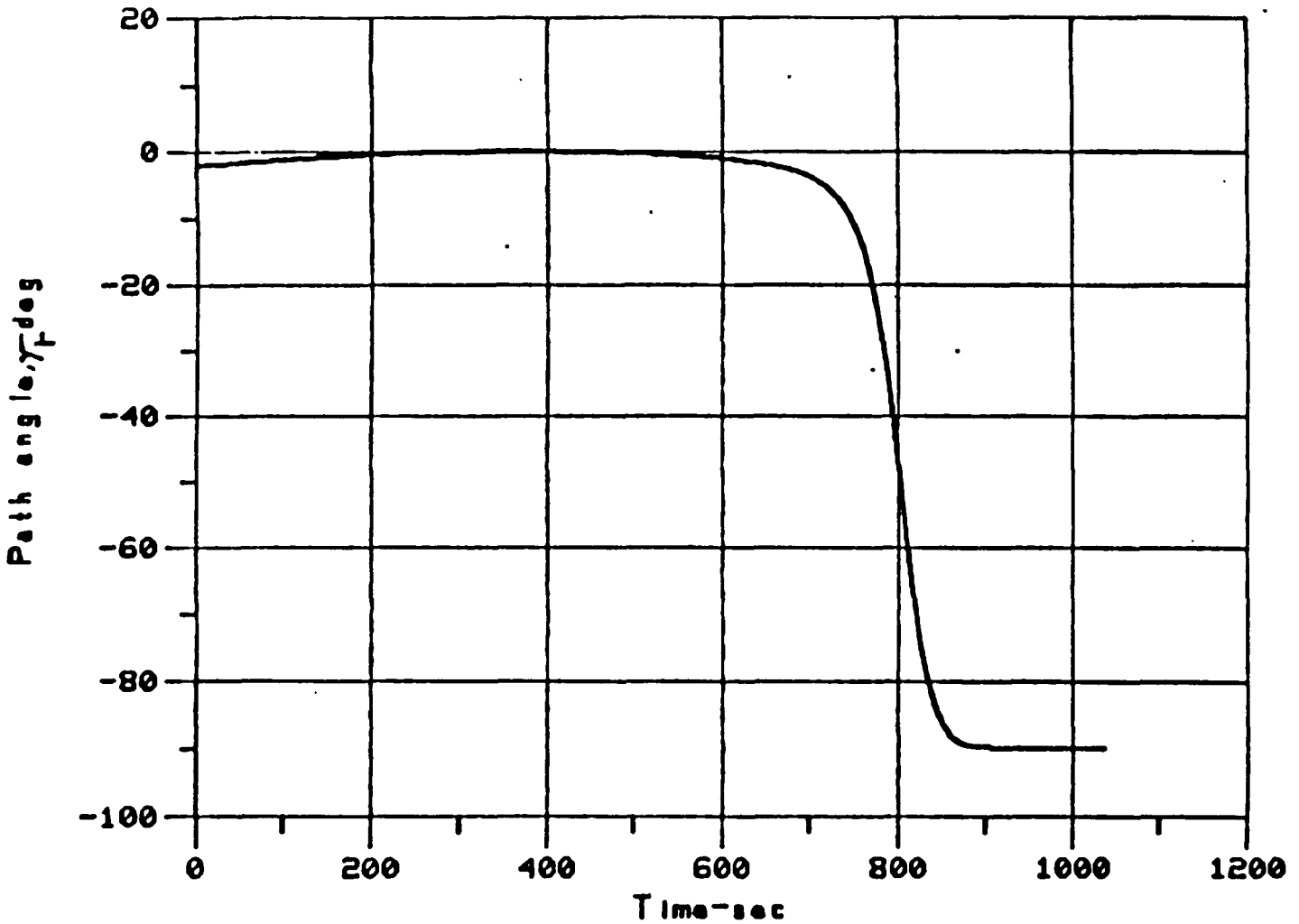


Figure I-55. Case 16 - Path Angle

CASE 17  
VI=36104, GAMI=-38.79, H=273000

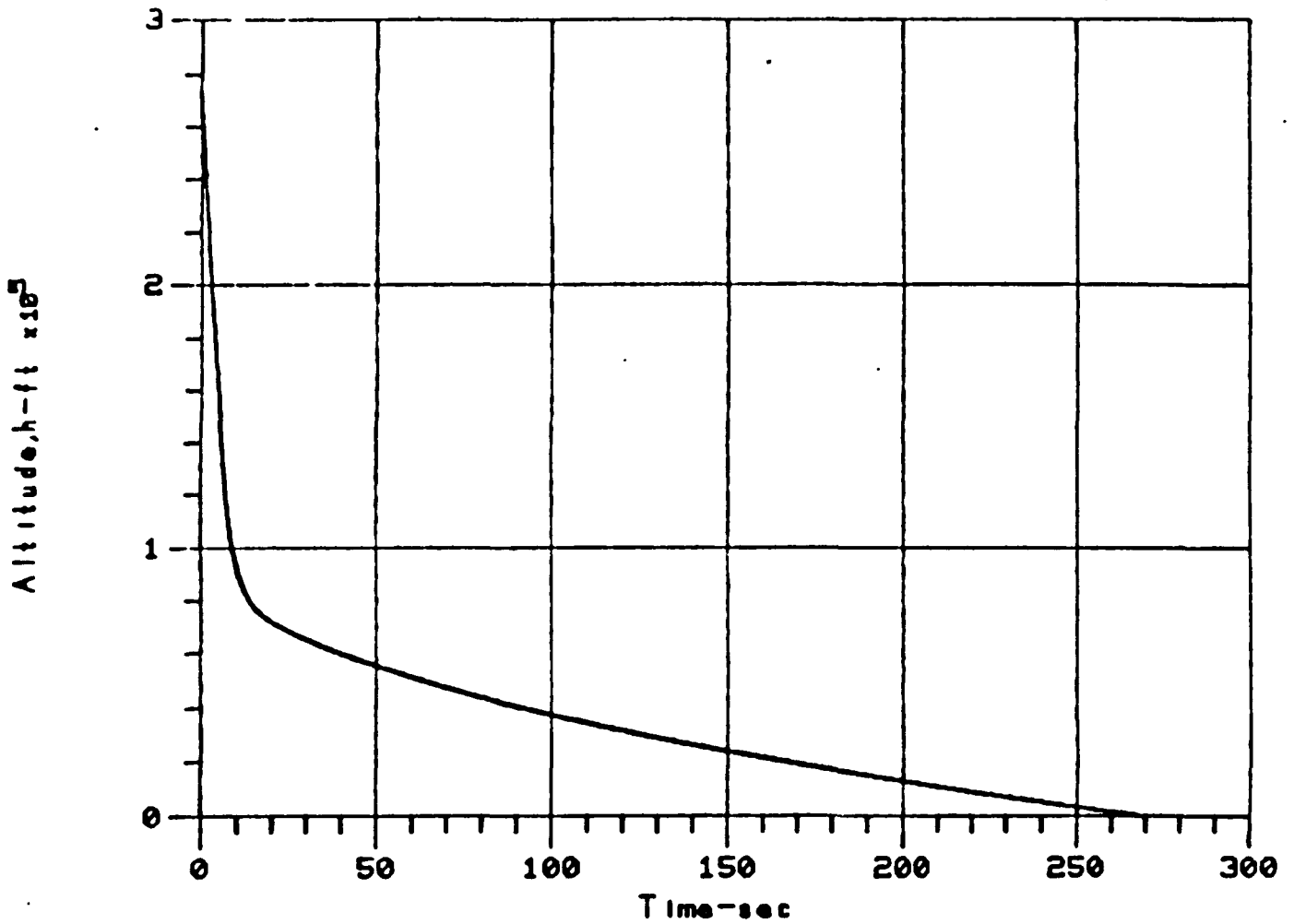


Figure I-56. Case 17 - Altitude

CASE 17  
VI=36104, GAMI=-38.79, H=273000

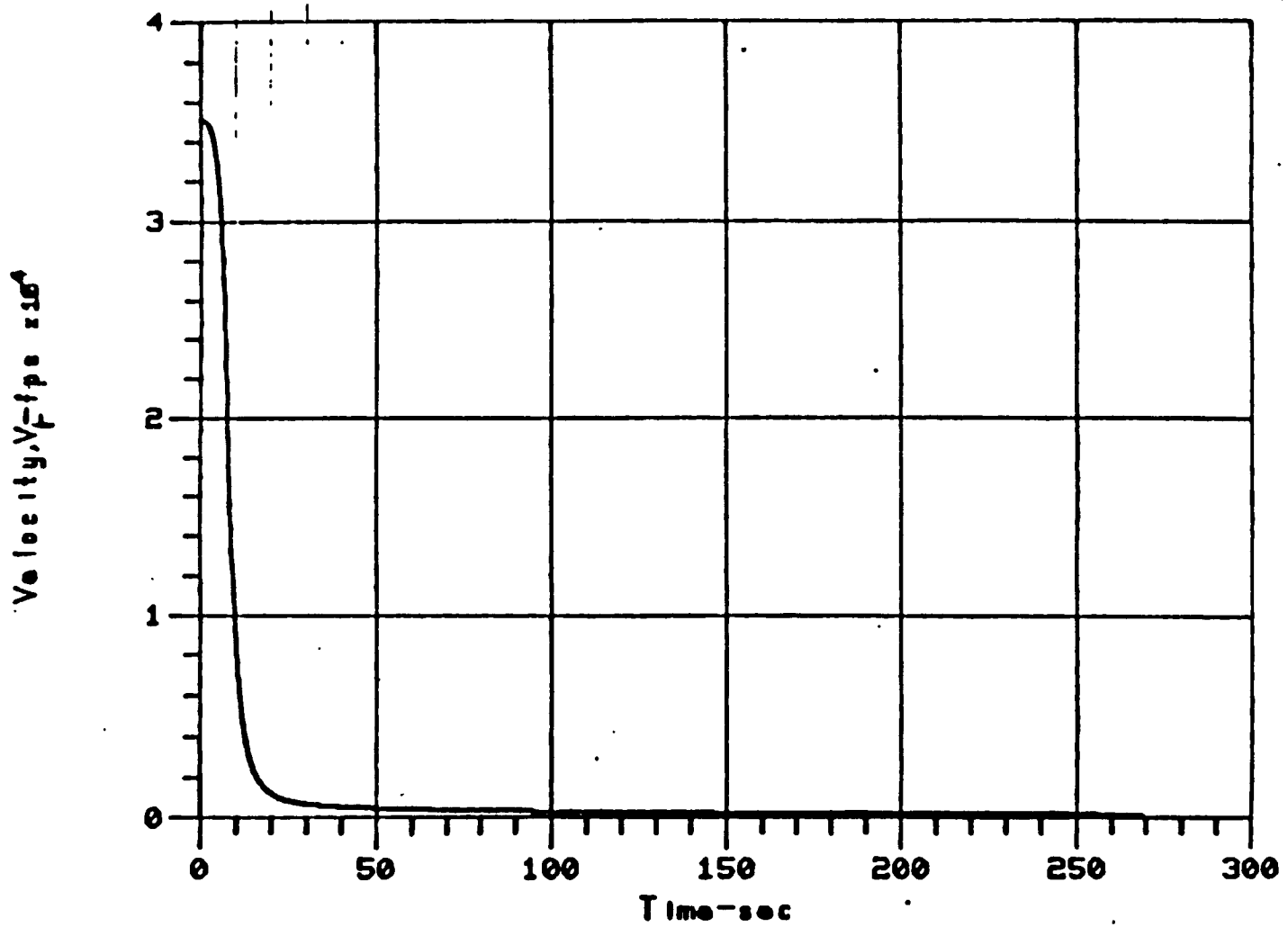


Figure I-57. Case 17 - Velocity

CASE 17  
VI=36104, GAMI=-38.79, H=273000

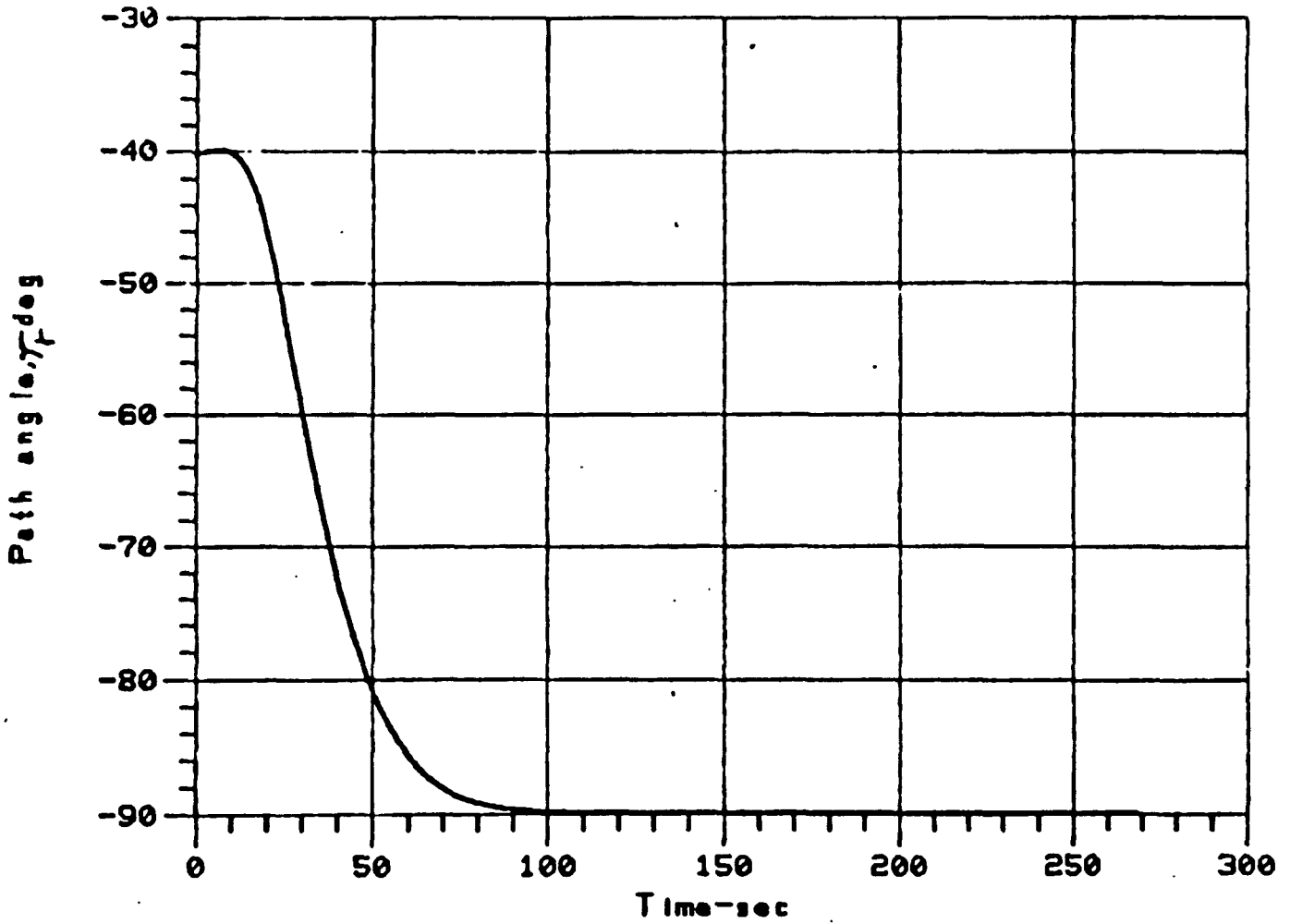


Figure I-58. Case 17 - Path Angle

CASE 18  
VI=36113, GAMI=-38.76, H=253000

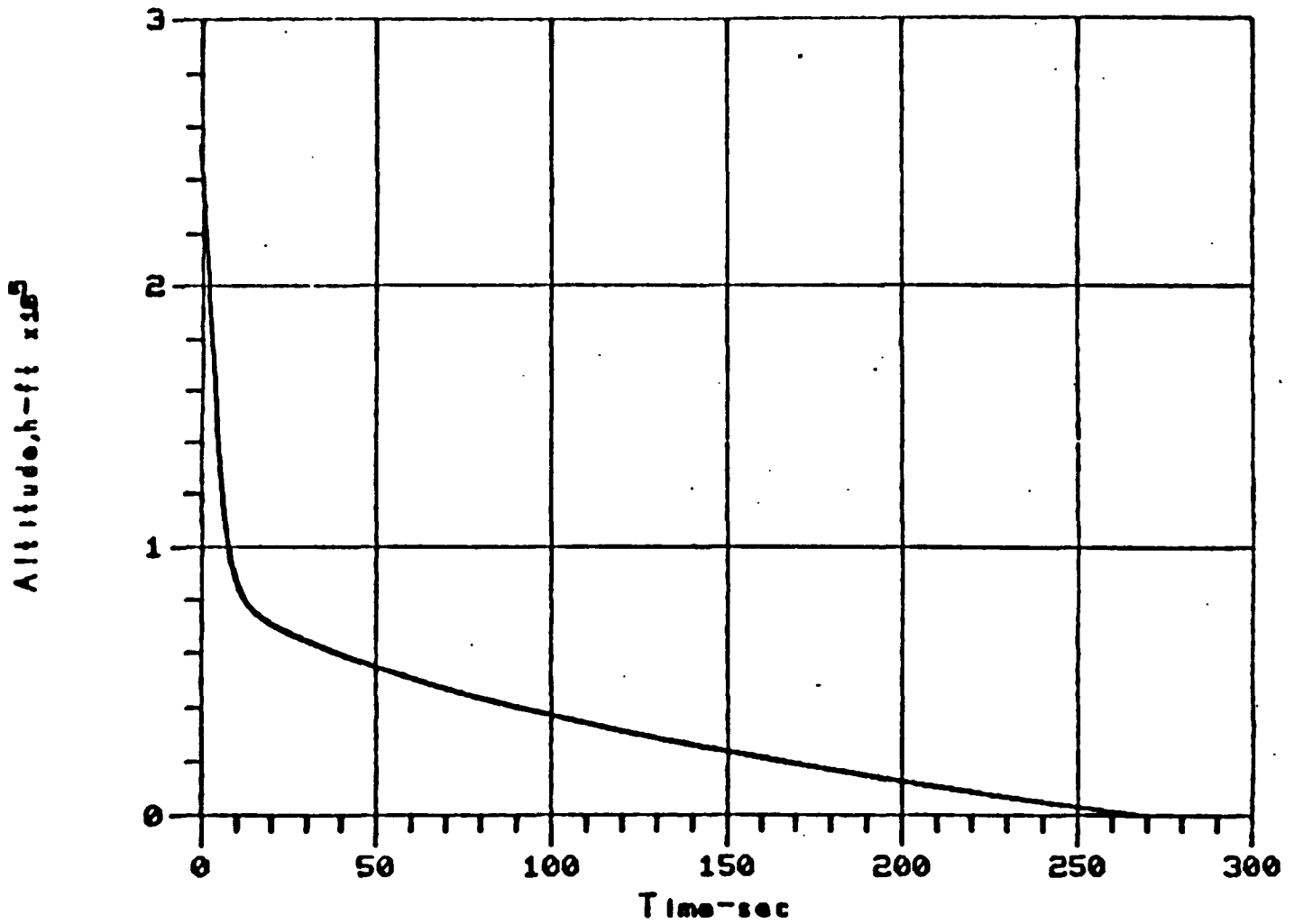


Figure I-59. Case 18 - Altitude



CASE 18  
VI=36113, GAMI=-38.76, H=253000

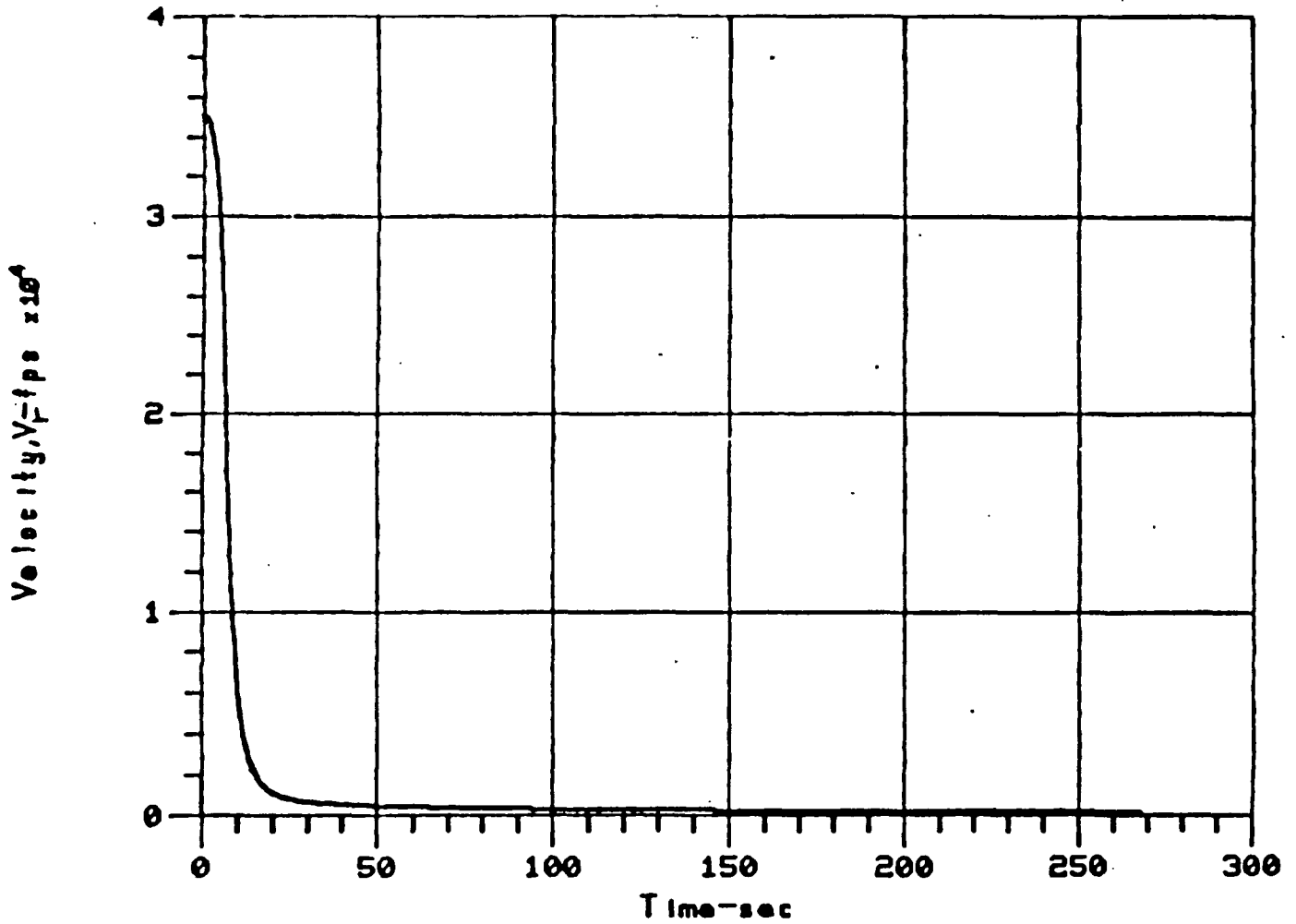


Figure I-60. Case 18 - Velocity

CASE 18  
VI=36113, GAMI=-38.76, H=253000

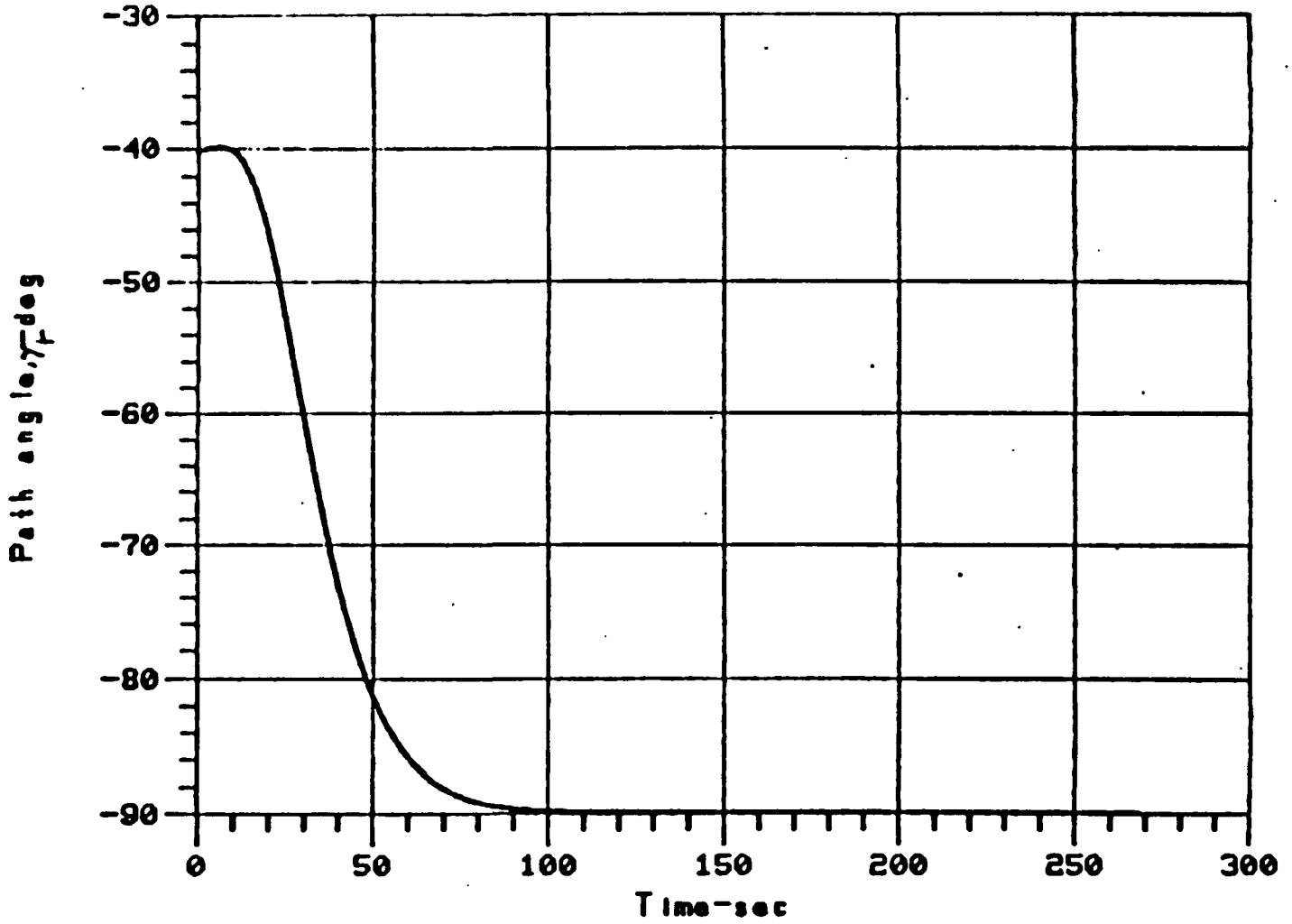


Figure I-61. Case 18 - Path Angle

CASE 19  
VI=36000, GAMI=-53, H=210000

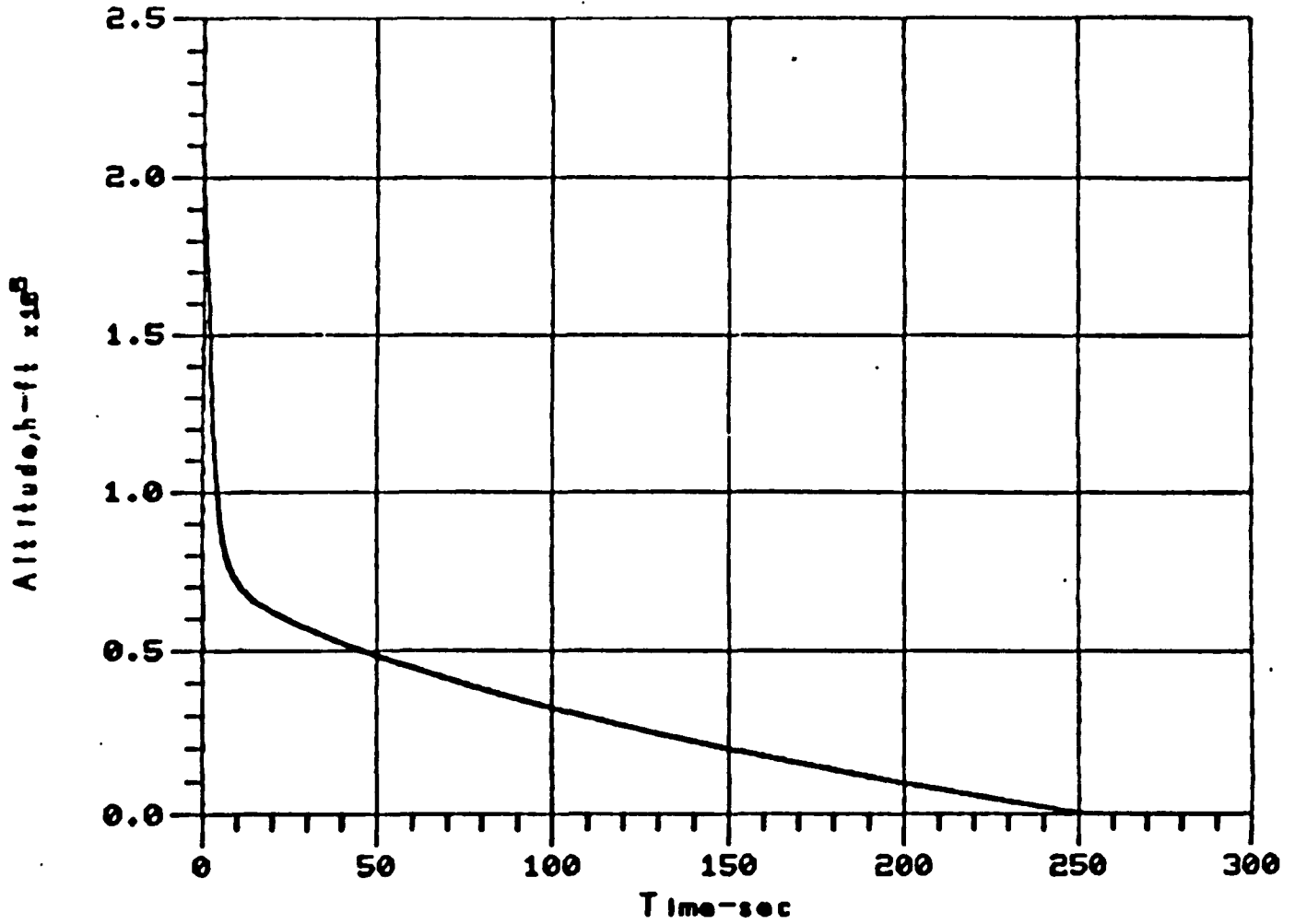


Figure I-62. Case 19 - Altitude

CASE 19  
VI=36000, GAMI=-53, H=210000

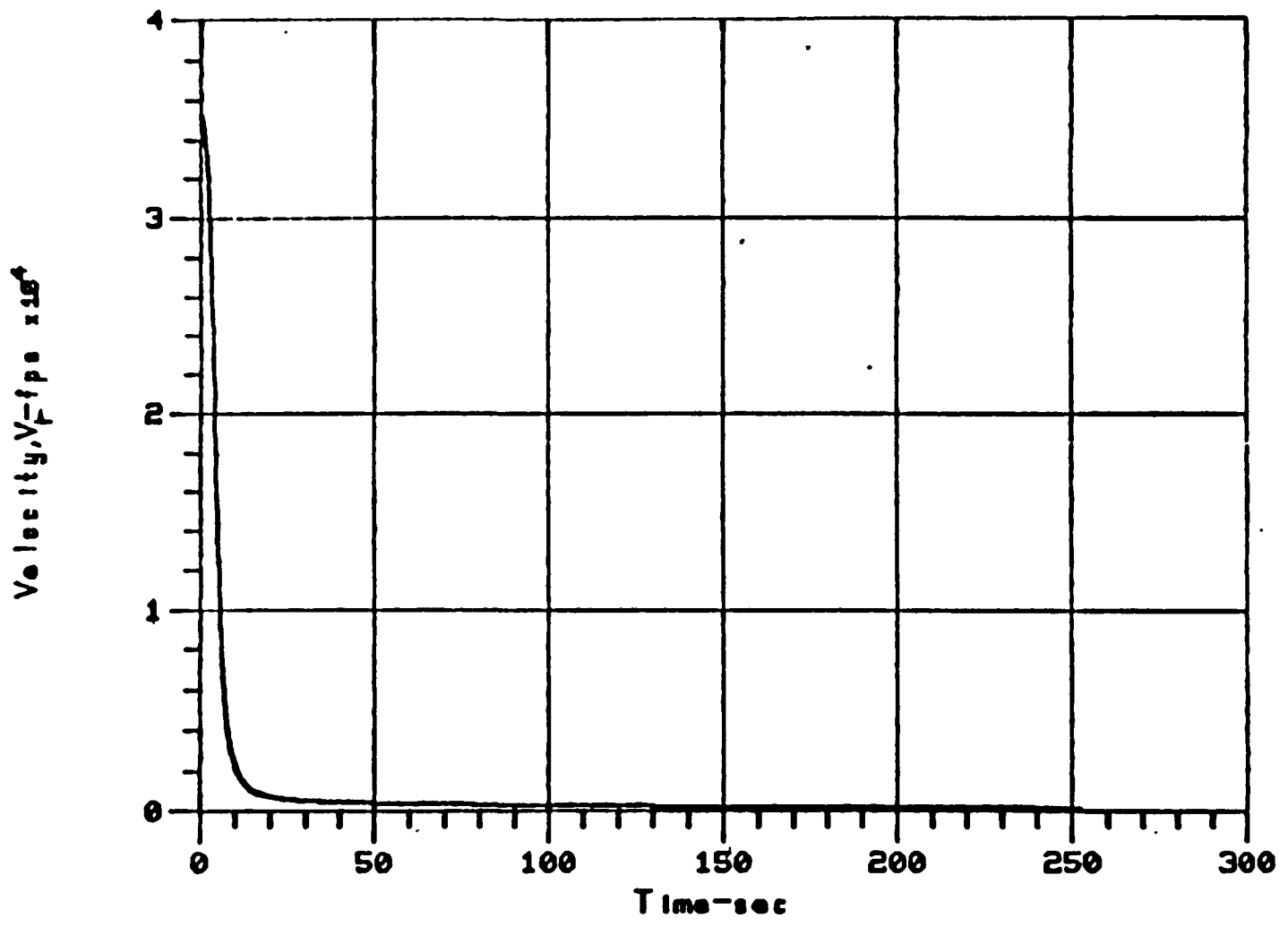


Figure I-63. Case 19 - Velocity

CASE 19  
VI=36000, GAMI=-53, H=210000

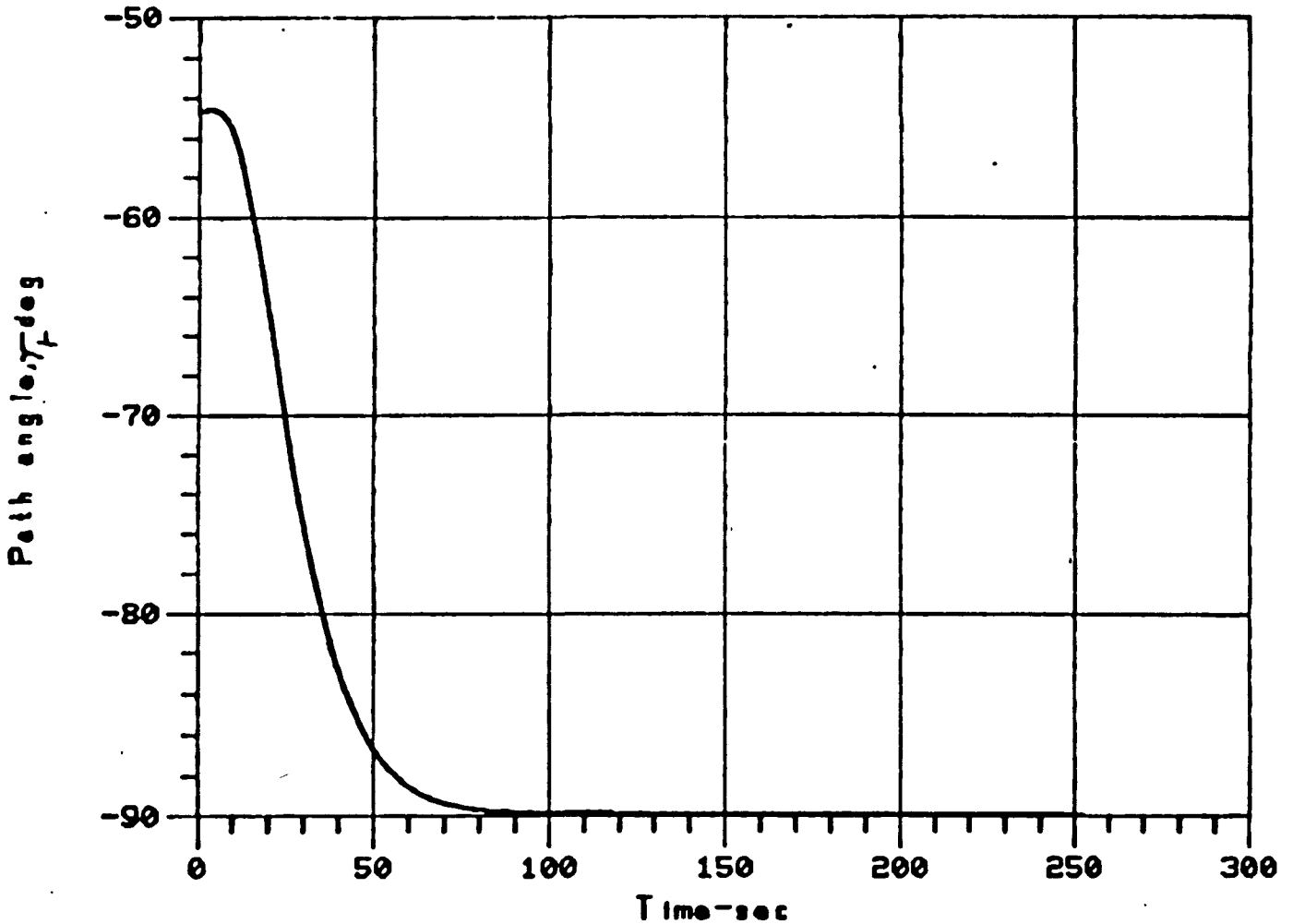


Figure I-64. Case 19 - Path Angle

CASE 20  
VI=25704, GAMI=-.138, H=330000

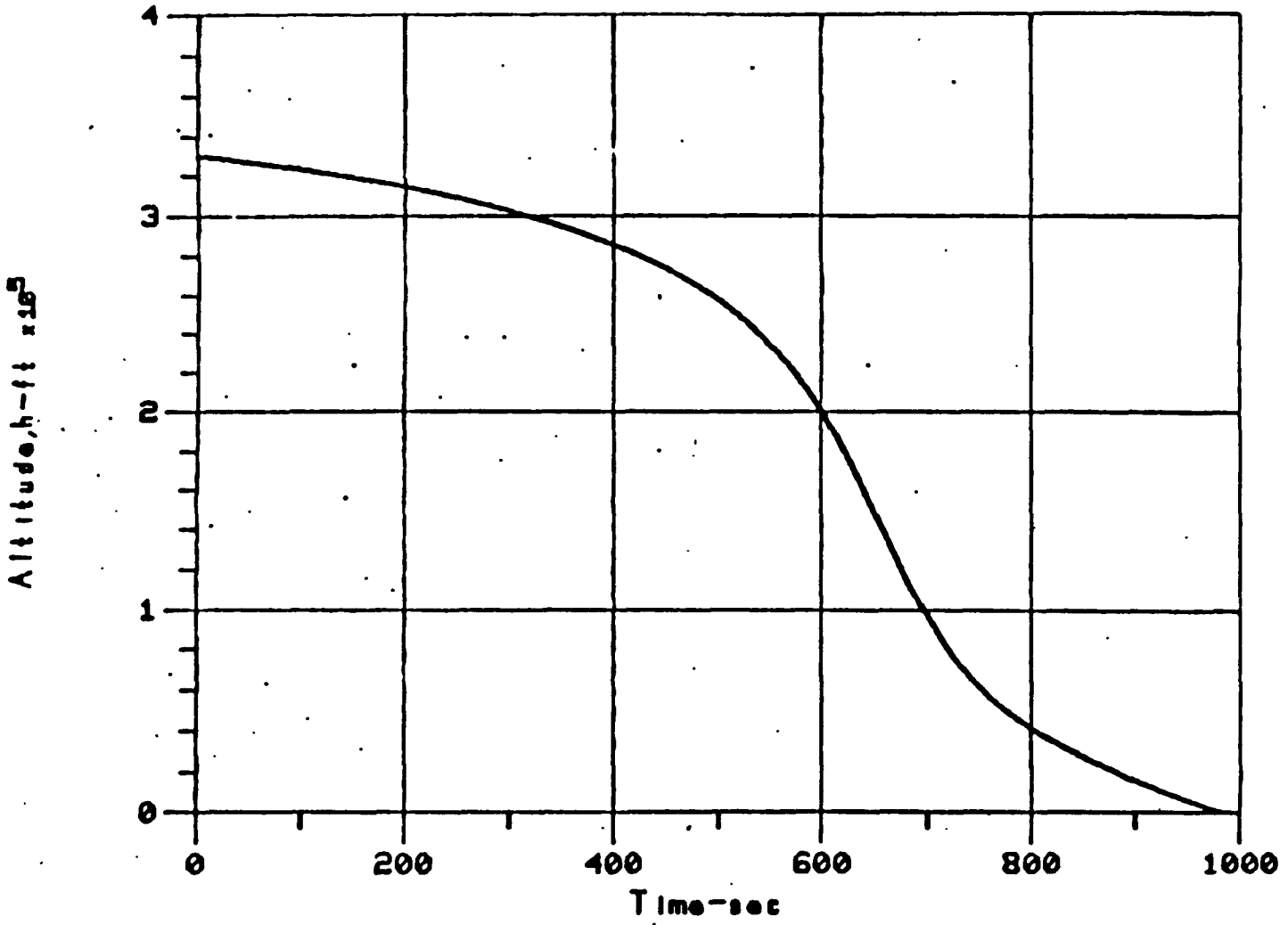


Figure I-65. Case 20 - Altitude

CASE 20  
VI=25704, GAMI=-.138, H=330000

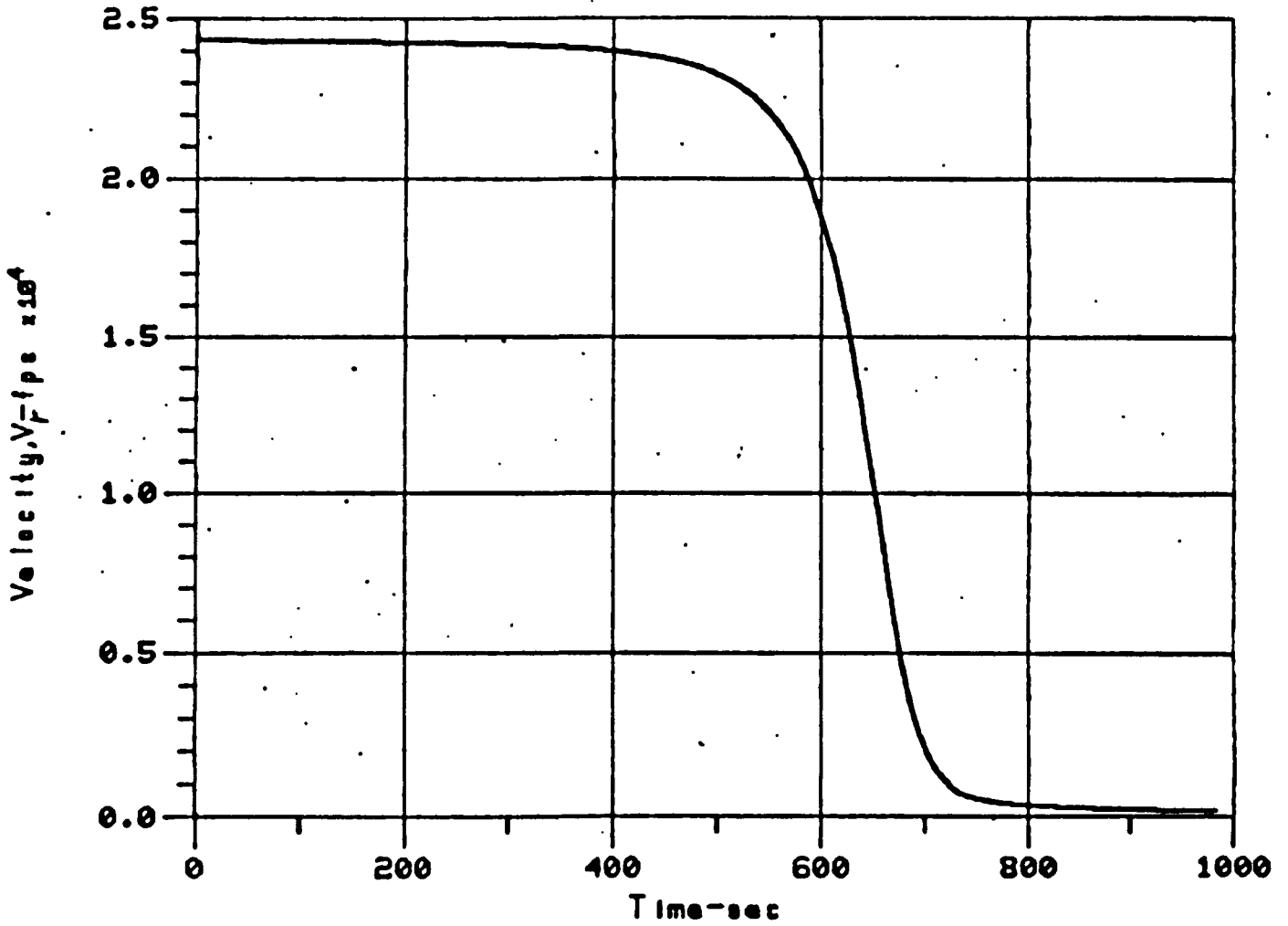


Figure I-66. Case 20 - Velocity

CASE 20  
VI=25704, GAMI=-.138, H=330000

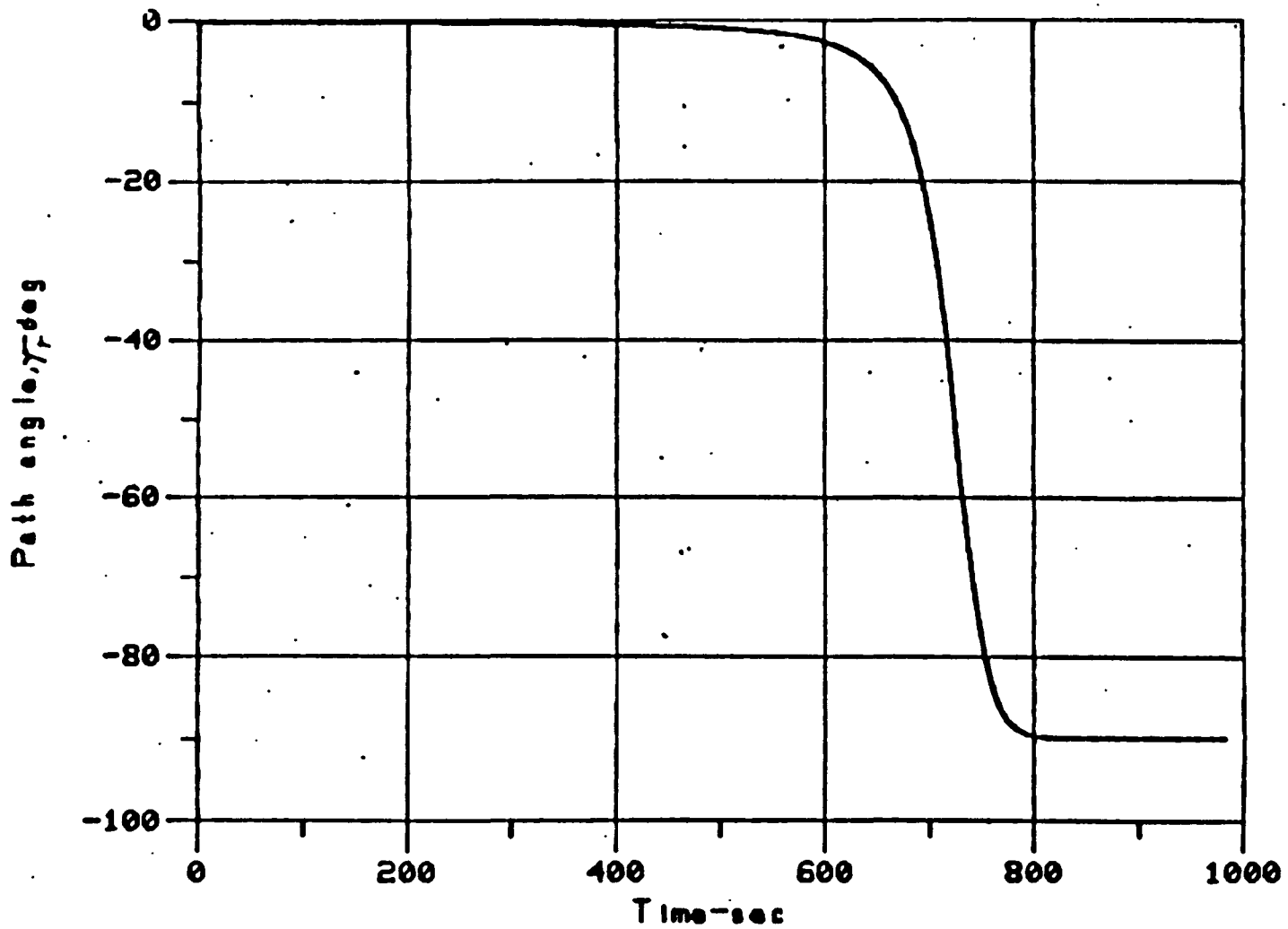


Figure I-67. Case 20 - Path Angle



CASE 21  
VI=25594, GAMI=-.318, H=292000

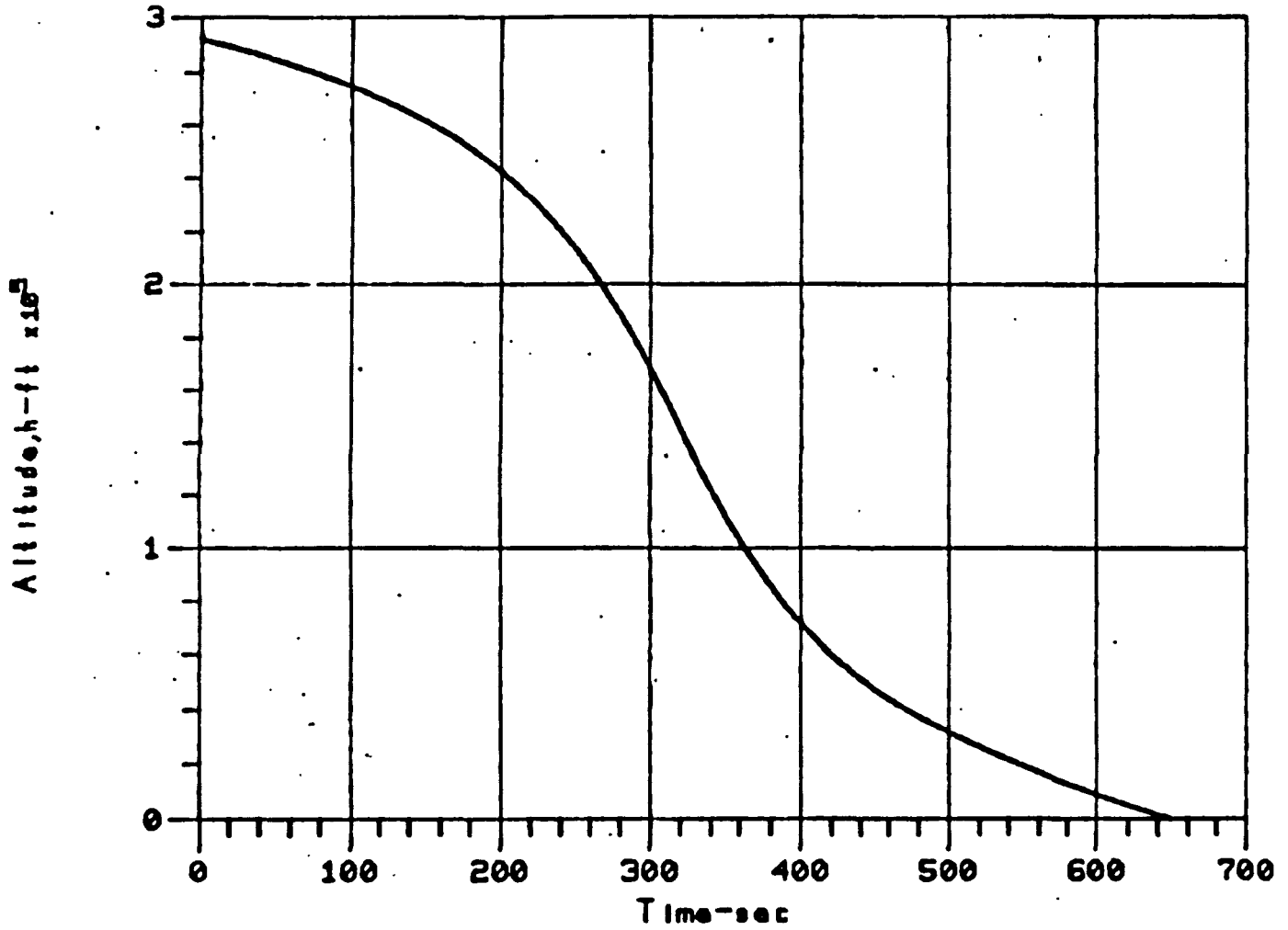


Figure I-68. Case 21 - Altitude

CASE 21  
VI=25594, GAMI=-.318, H=292000

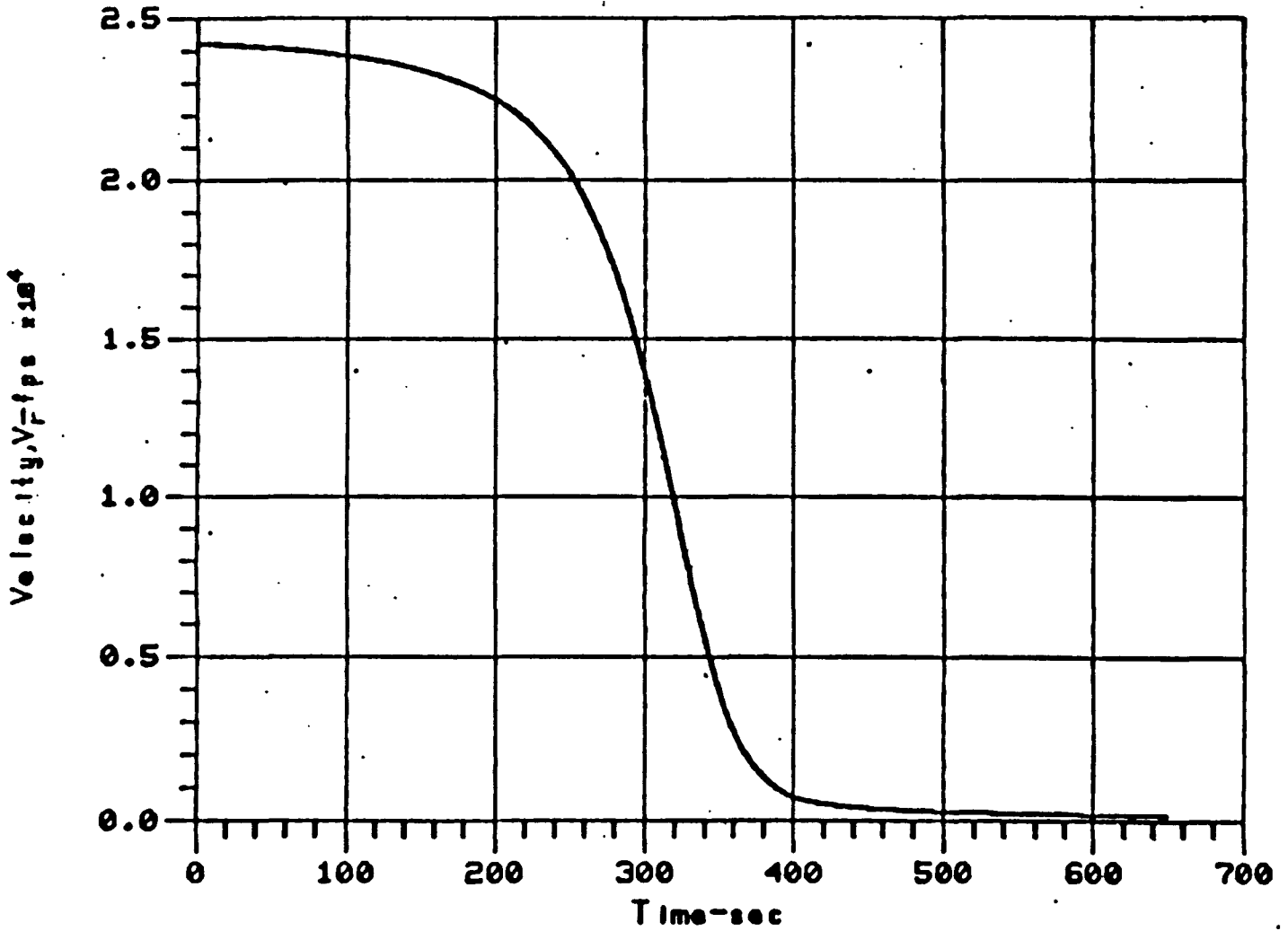


Figure I-69. Case 21 - Velocity

CASE 21  
VI=25594, GAMI=-.318, H=292000

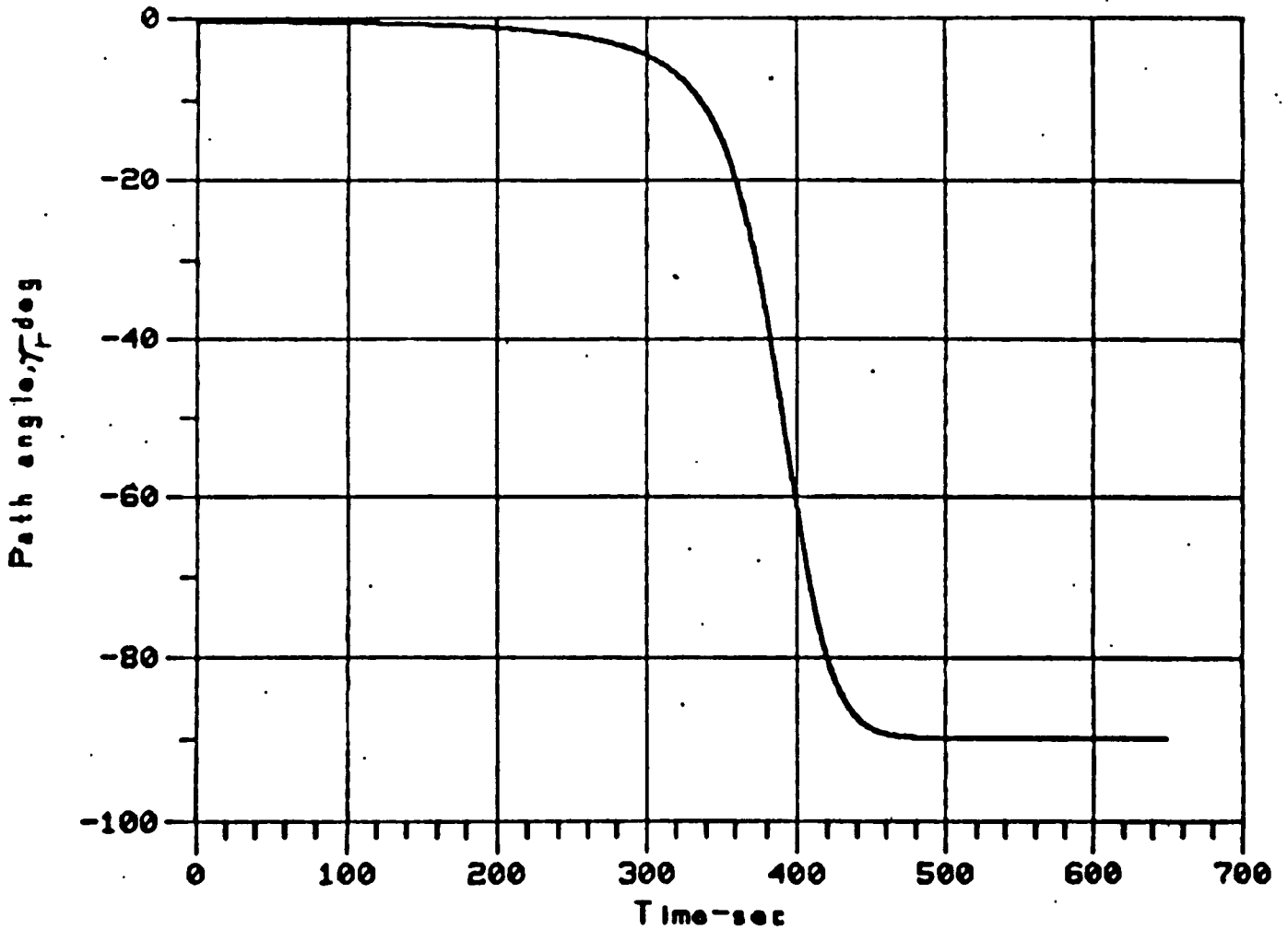


Figure I-70. Case 21 - Path Angle

Table I-7. Velocity Variation with Altitude

Altitude 10 <sup>3</sup> ft	Time to Impact sec.	Velocity ft/sec
10	55.48	194.45
9	50.30	191.48
8	45.04	188.49
7	39.69	185.60
6	34.26	182.81
5	28.75	180.09
4	23.15	177.63
3	17.49	175.24
2	11.74	172.82
1	5.91	170.41
0	0	168.03

### I.3.3 THE GPHS THERMAL REENTRY MODEL

The GPHS module is represented in considerable detail with a 702 node thermal model. Each component is completely described. The model describes one quarter of the module, and an indication of the nodal breakdown is shown in Figures I-71 and I-72. In addition to the geometric detail, effort has been expended in developing several heat transfer mechanisms peculiar to the GPHS module. These are discussed in the following sections.

#### I.3.3.1 CBCF Thermal Conductivity in Vacuum and in Air

During the course of the GPHS module safety analysis, questions have been raised concerning the accuracy of the CBCF thermal conductivity. In addition, at high enough temperatures, the CBCF will undergo graphitization with a consequent increase in its thermal conductivity. These issues were initially reported and evaluated in References I-6, I-7, and I-8.

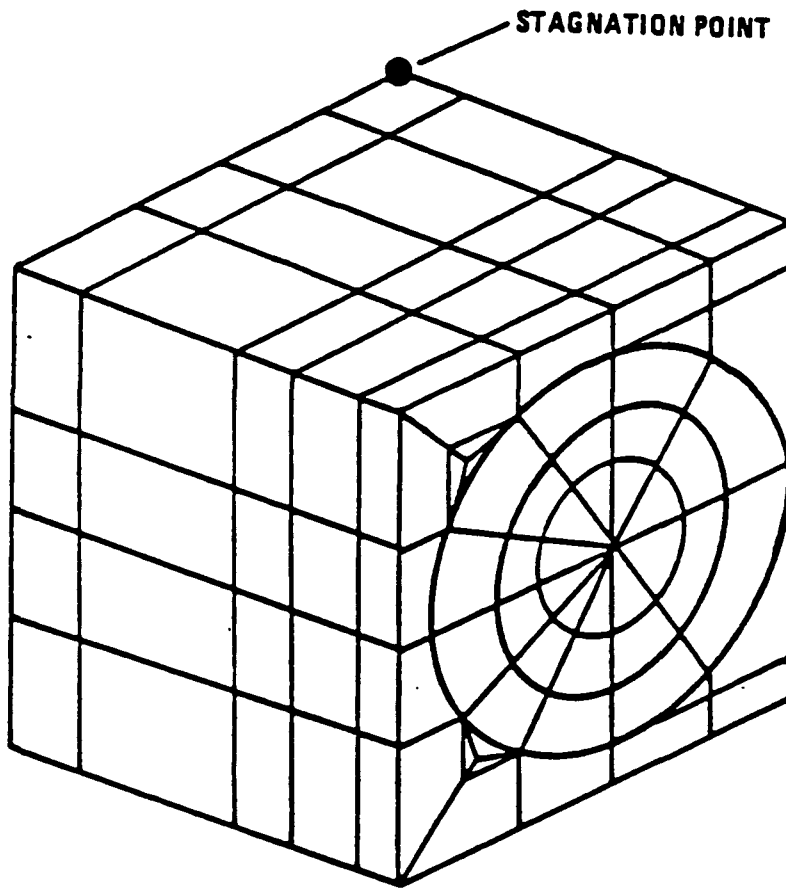


Figure I-71. GE Reentry Thermal Model 1/4 GPHS Module

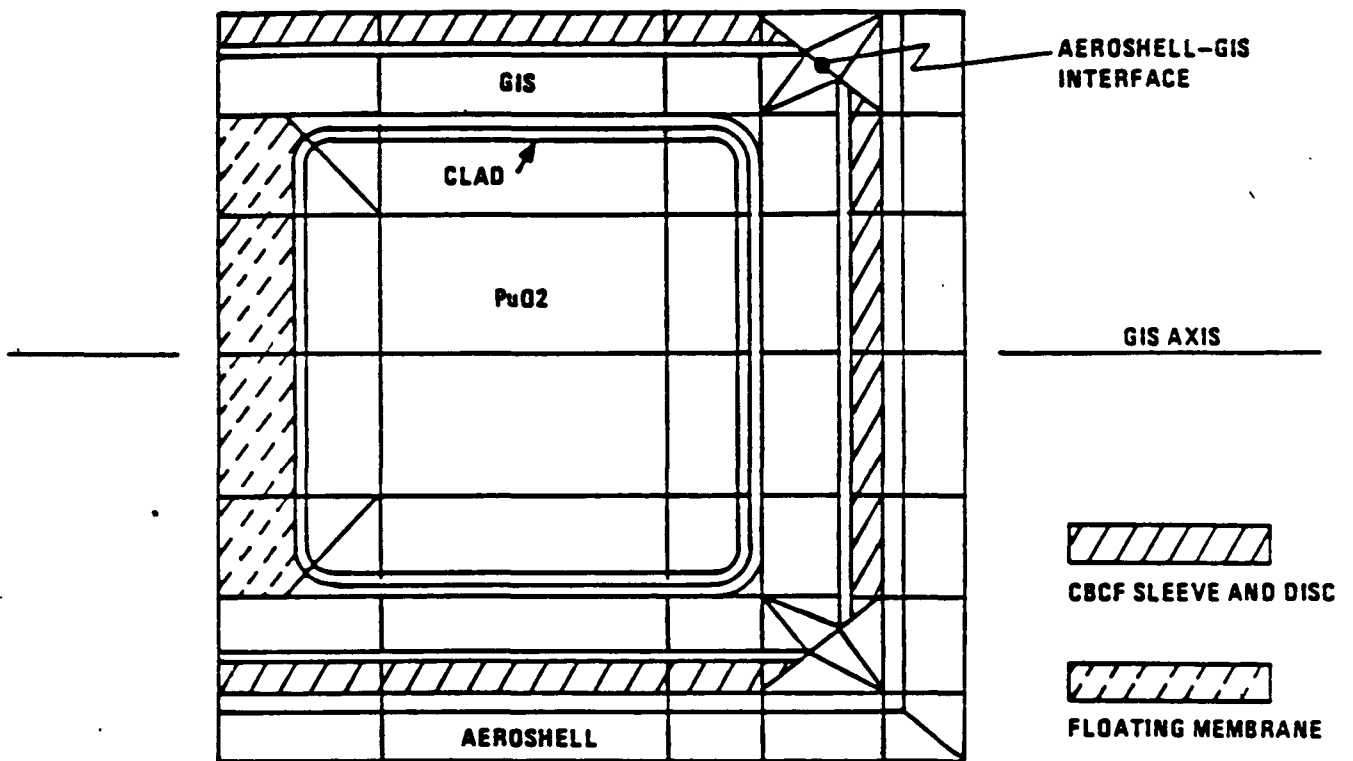


Figure I-72. GE Reentry Thermal Model Section  
Thru GIS Axis Parallel to Broadface

Originally, the CBCF thermal conductivity in vacuum was taken from Reference I-9. The conductivity in air for pressures ranging from near-vacuum to one atmosphere was based upon work reported in Reference I-10.

During the study, as discussed in Reference I-6, questions arose as to the validity of the original data. The current position is one of uncertainty; no firm basis exists upon which to establish CBCF thermal conductivity in vacuum and air.

Nevertheless, estimated upper limits to the vacuum data were reported in Reference I-6. These were subsequently revised upwards by a value of 0.5 mw/cm-°K at all temperatures. (These revised data are commonly referred to as the refined hypothesis No. II data.) The corresponding conductivity in one atmosphere of air was also estimated. The original and the refined hypothesis No. II data are shown in Figure I-73. The original data are lower for the vacuum case, while the reverse is mostly true for the air case.

For intermediate pressures, a simple logarithmic fit was made to the data of Reference I-10. This data consists of thermal conductivity measurements made in a nitrogen atmosphere with the nitrogen pressure ranging between 0.01 and 1.0 atmospheres. All of the measurements were made at a temperature of 1562°F (850°C). The measured data are shown in Figure I-74. The fit to the data of Figure I-74 is given in Equation 1) as a function of the molecular mean free path.

$$K(\lambda)/K_0 = 0.2724 \log (1/\lambda) + 0.2243 \quad (1)$$

where

- $\lambda$  = mean free path (inches)
- $K$  = thermal conductivity
- $K_0$  = thermal conductivity, in vacuum

The mean free path was calculated as

$$\lambda = 6.72 \times 10^{-6} (T/P) \quad (1)$$

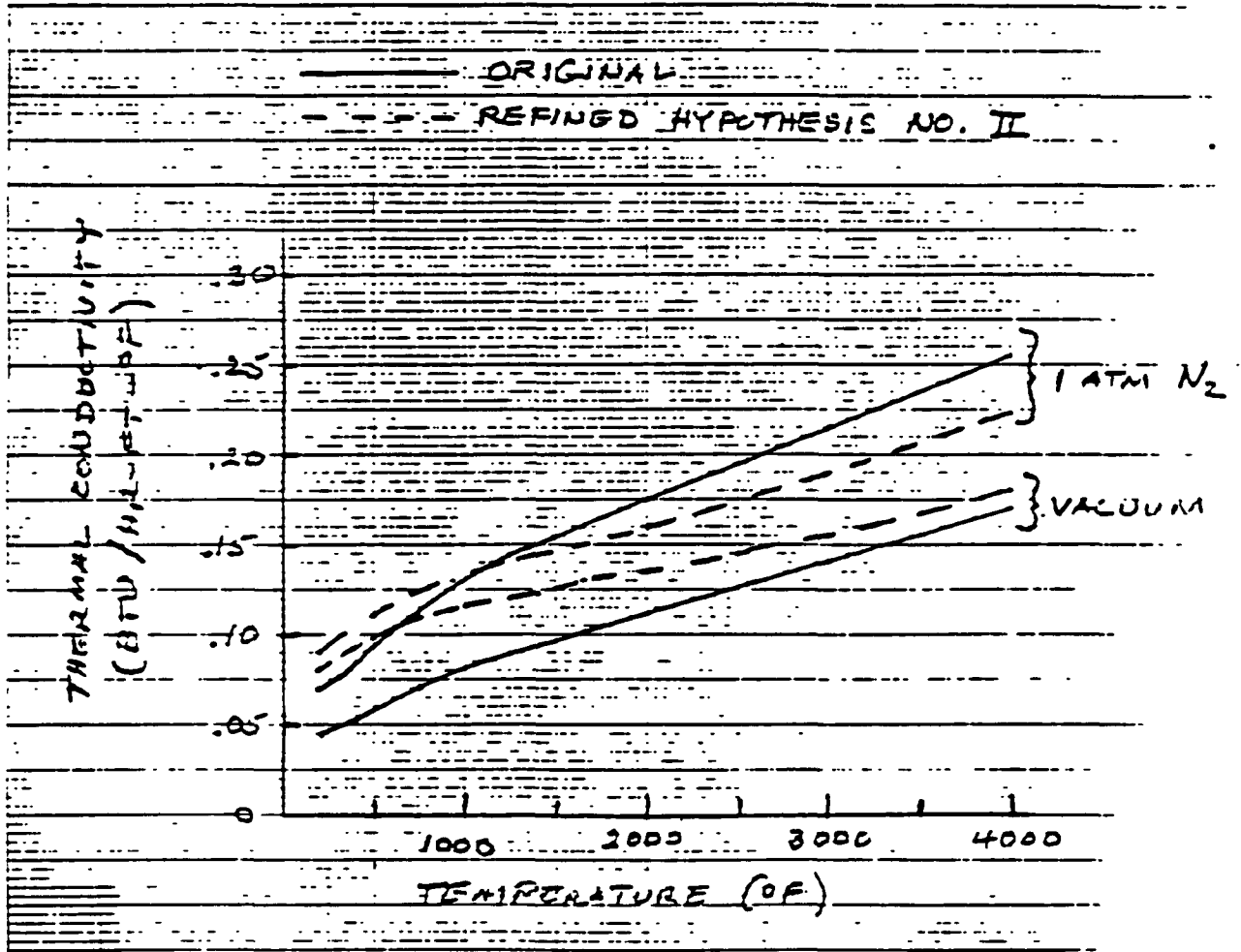


Figure I-73. CBF Thermal Conductivity



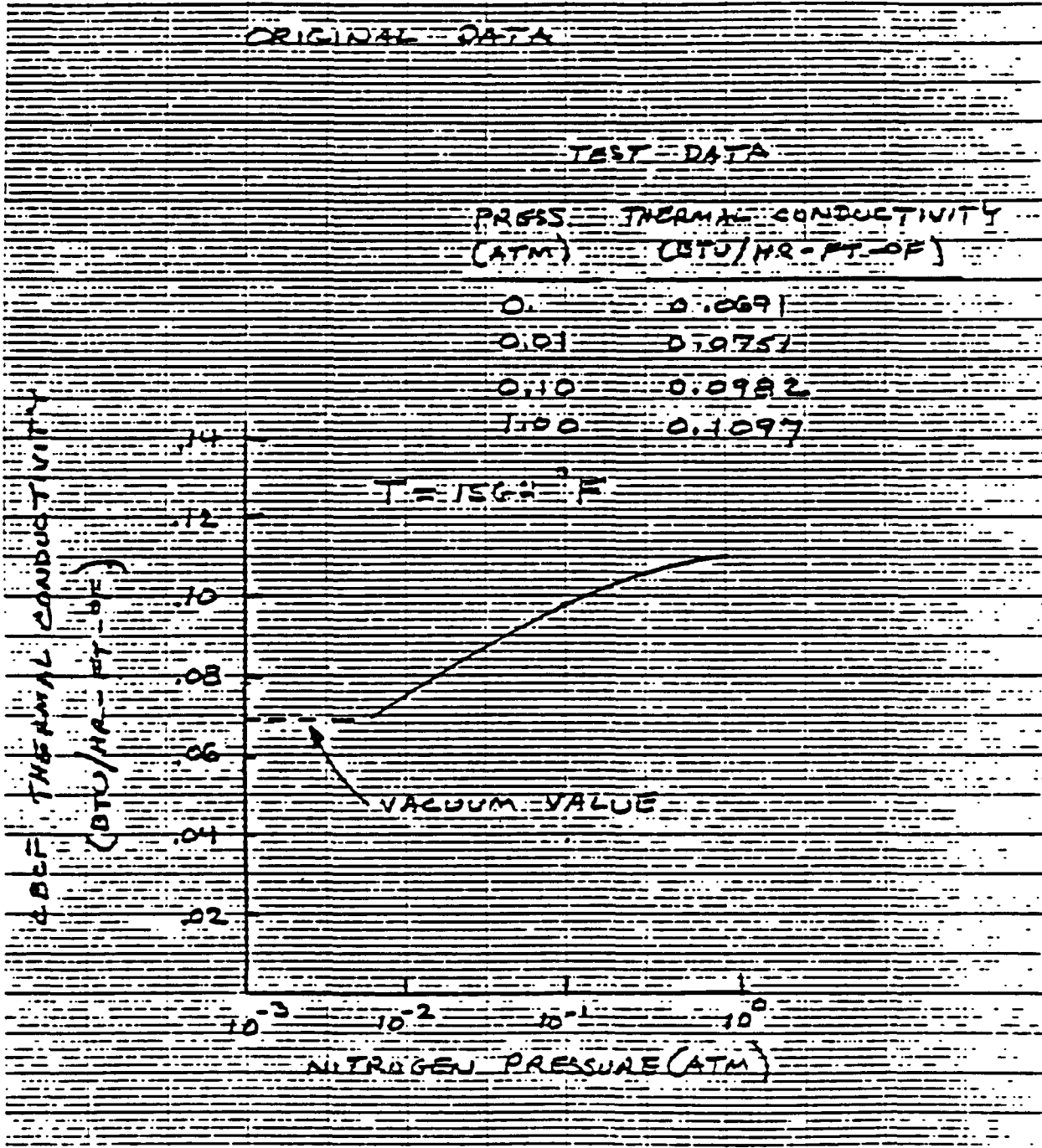


Figure I-74. CBCF Thermal Conductivity in a Nitrogen Atmosphere

where

- T = temperature (K)
- P = pressure (torr)
- $\lambda$  = mean free path (inches)

For values of  $\lambda$  greater than 0.00142 inches, the vacuum value was used. A maximum value of the ratio  $K(\lambda)/K_0$  was set at 1.587, the observed value at 1562°F (850°C). The pressure dependence was measured only at a temperature of 1562°F (850°C). Equation (1) was assumed to apply at all temperatures.

In the case of the refined hypothesis No. II data, a similar pressure dependence was developed at the Applied Physics Laboratory of John Hopkins University and reported in Reference I-11. Their equation is reproduced here as Equation (2).

$$K(\lambda)/K_0 = 0.05 \log (1/\lambda) + 0.904 \quad (2)$$

Again, the vacuum value is used for  $\lambda$  greater than 0.00142 inches, but no upper limit was imposed on the ratio  $K(\lambda)/K_0$ .

Concerning the issue of graphitization of the CBCF, the thermal conductivity data of Table 2, Reference I-8 was used with the additive correction factor of 0.5 MW/cm-°C applied. The pressure dependence corresponding to Equation (1) and (2) was also developed at APL and reported in Reference I-12. The pressure dependence for the graphitized CBCF was given as

$$K(\lambda)/K_0 = 0.08 \log (1/\lambda) + 0.165 \quad (3)$$

In this case, the quantity  $\lambda$  was evaluated as

$$\lambda = 6.72 \times 10^{-6} (1/TP)$$

and the vacuum value of the thermal conductivity was used for values of greater than  $3.652 \times 10^{-11}$ .

When deciding which set of data to use for a given reentry calculation, one must keep in mind the use of the iridium clad temperature at impact as the measure of safety. This margin decreases with decreasing impact temperature.

The orbital decay trajectories are taken to be the most probable and these trajectories also exhibit a relatively long cooling phase. In addition, the air pressure within the module will be relatively high for these trajectories during the cooling phase, thus adding to the cooling rate of the clad.

A look at the thermal conductivity plots of Figure I-73 shows that the original air data provide the maximum conductivity and consequently the minimum thermal resistance between the iridium clad and the convective cooling of the atmosphere during the later stages of the reentry. Based upon this observation, it was decided that all reentry calculations, other than the steep trajectories, would use the original CBCF thermal conductivity. This procedure should result in the lowest expected iridium clad temperatures. In the case of the steep trajectories, the refined hypothesis No. II data were used, since these data contain a consistent set of graphitized and non-graphitized thermal conductivity values and graphitization of the CBCF insulators is expected during these reentry cases. A plot of the graphitization thermal conductivities in vacuum and in air is given in Figure I-75.

#### I.3.3.2 FWPF and CBCF Thermal Conductivity Anisotropy

Both FWPF and CBCF materials exhibit anisotropic thermal conductivities. In each case, the conductivity has two components, one in any direction within a given plane and a second normal to this plane. The ratio of the two components for each material, at least over the temperature range of measurements, is a slowly varying function of temperature. The ratios are plotted in Figure I-76. A simple average value of each ratio is also shown in Figure I-76. These average values have been used in the thermal analyses as opposed to the temperature dependent values.

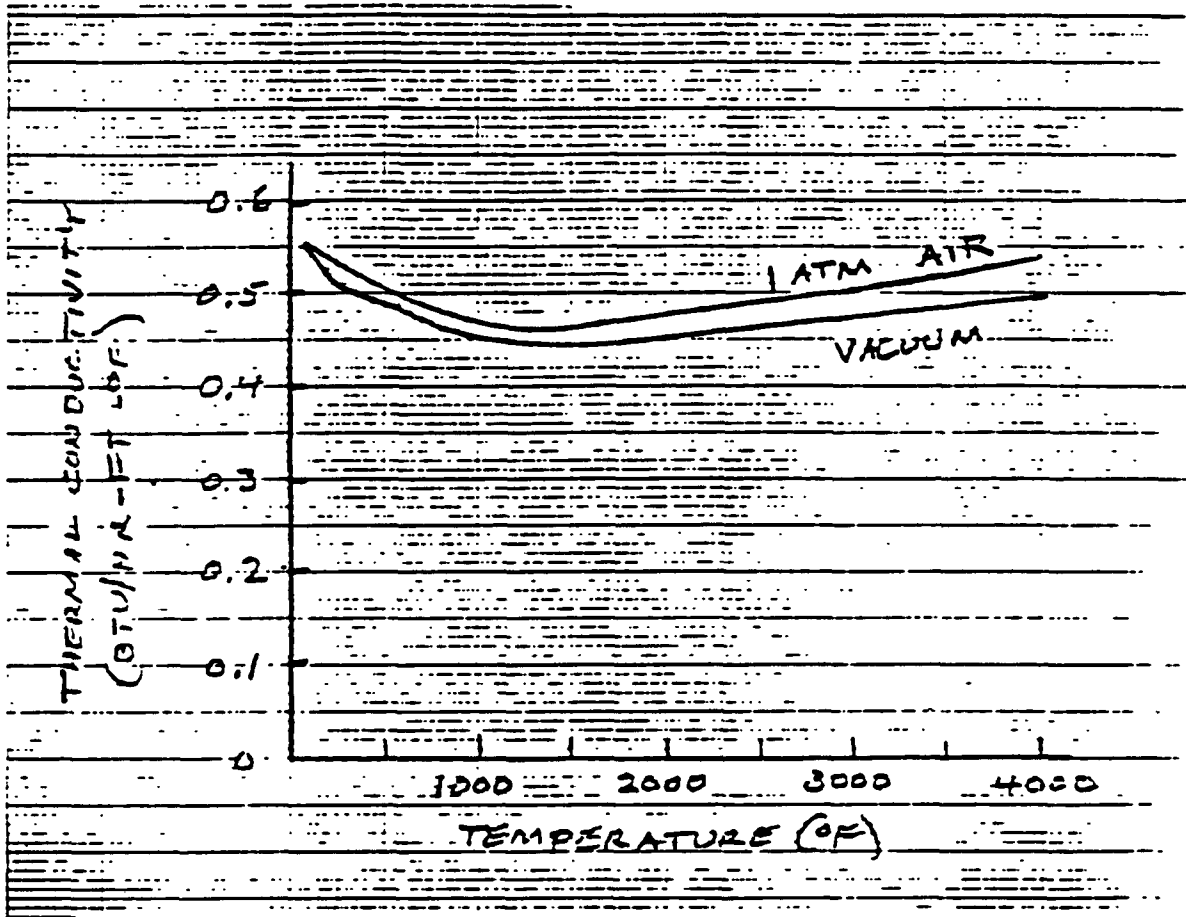


Figure I-75. Graphitized CBCF Thermal Conductivity  
Refined Hypothesis No. II

**RATIO OF THE TWO COMPONENTS  
OF THE THERMAL CONDUCTIVITY**

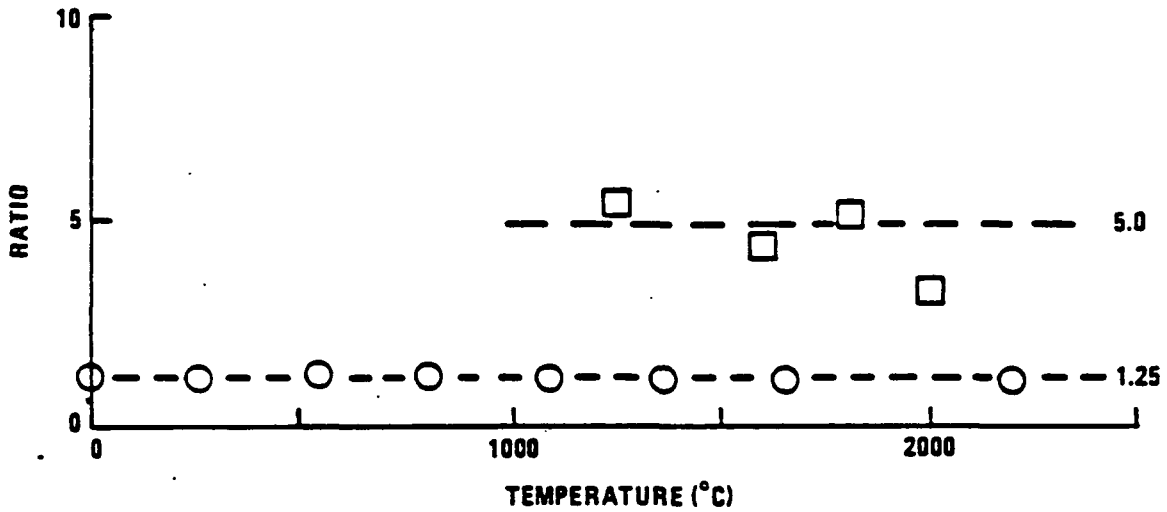


Figure I-76. FWP and CBCF Thermal Conductivity Anisotropy

The CBCF data are rather sparse and, in addition, has been available only for densities greater than that used in the GPHS. The data available indicates an increasing ratio for decreasing density, and consequently a ratio near the upper end of the range of observed values has been chosen for the reentry calculations.

The measured conductivity data have been taken from References I-13 through I-15. The FMPF data in Reference I-13 cover the entire temperature range of interest. The CBCF data of References I-14 and I-15 are restricted to temperatures above 1200°C. In Reference I-14, the CBCF density of 0.25 gm/cm<sup>3</sup>. The data in Reference I-15 includes both conductivity components for densities between 0.27 and 0.64 gm/cm<sup>3</sup>. Only the lower density ratios are plotted in Figure I-76.

### 1.3.3.3 CBCF Disc/Aeroshell Contact Coefficient

The CBCF disc is bonded to the aeroshell. No measurements have been made of the resulting interface thermal resistance. However, a sensitivity analysis has been made by members of Fairchild Space and Electronics Co., and the results of their work are shown below in terms of the iridium clad temperatures at impact for an Orbital Decay reentry trajectory. As shown in the table, the iridium clad impact temperature is insensitive to the choice of contact coefficient for the CBCF disc/aeroshell bonded interface. A value of 0.142 watts/cm<sup>2</sup>-°C has been used in all thermal analyses.

#### EFFECT OF CBCF DISC-TO-AEROSHELL CONTACT CONDUCTANCE Orbital Decay Reentry Trajectory

Disc-to-Aeroshell Contact Conductance (Watts/cm <sup>2</sup> -°C)	Clad Temperature (°C)		
	Initial	Peak	Impact
0.0	1253	1353	873
0.142	1253	1353	873
5.69	1252	1352	868

#### I.3.3.4 Air Thermal Conduction in the GPHS Inter-Component Gaps

During reentry of a GPHS module, air will readily diffuse through the FWPF and CBCF components, introducing a conductive medium in the gaps between the various module components. In general, the conductivity of the air will be both temperature and pressure dependent. In the case of the CBCF effective thermal conductivity, both of these dependencies have been accounted for as discussed in Section I.3.3.1. In the case of the gap at the aeroshell-GIS interface (see Figure I-72), these dependencies are again fully taken into account. In the remainder of the gaps between module components, the air pressure was set equal to the pressure in the boundary layer, averaged over the GPHS surface. When this pressure exceeded 10 torr, continuum air conductance was assumed. Below 10 torr, vacuum conditions were assumed.

At the aeroshell-GIS interface, the effective air thermal conductance is based in part upon measurements made at Battelle Columbus Laboratories. The tests at Battelle were designed to measure the total thermal conductance between the aeroshell and the GIS at the aeroshell-GIS interface. The total conductance is made up of three heat transfer mechanisms, i.e., solid-to-solid contact, air, and radiative conductances.

The major elements of the test set-up for the aeroshell-GIS conductance measurements are shown in Figure I-77. The geometry and material properties of the interface were provided by two FWPF test rings as shown in Figure I-77. The tests were conducted over a temperature range between 600 and 1000°C and a nitrogen atmosphere pressure range between  $10^{-5}$  and 760 torr. In addition, the interface contact pressure was varied between 2.3 and 208 psi.

The test results were reported in terms of a heat transfer rate per unit of temperature difference across the aeroshell-GIS interface. The heat transfer rate was measured on both sides of the FWPF rings. The interface temperature difference was measured with thermocouples placed within each of the rings. As a consequence, the reported conductance included the effects of conduction through a certain thickness of FWPF on either side of the interface.

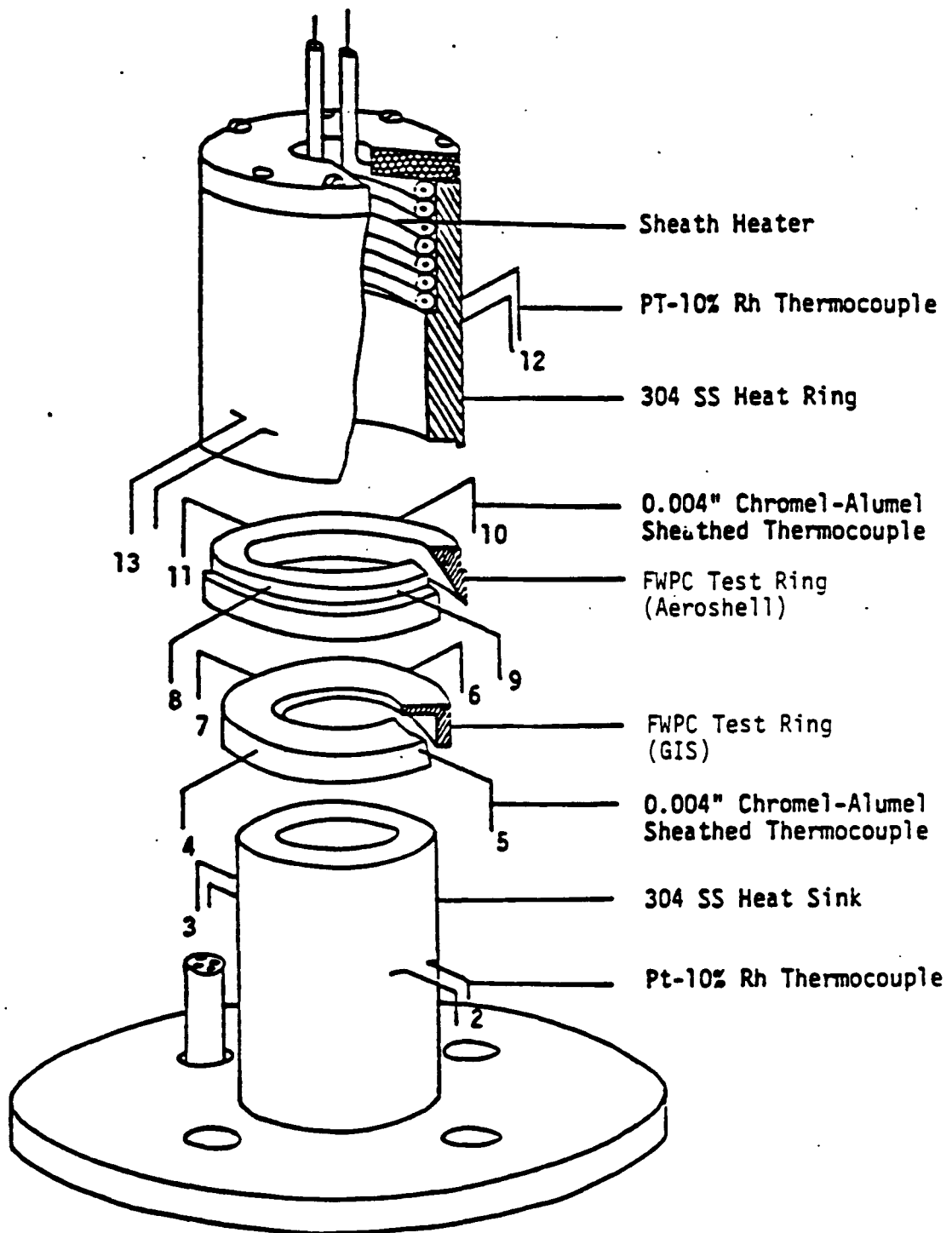


Figure I-77. Aeroshell - GIS Interface Conductance Test



In order to evaluate a solid-to-solid conductance and an air conductance at the interface, modifications were made to the reported data which removed the bulk FWPf and radiative contributions. The evaluation assumed that the contact, air, and radiative conductances at the interface were in parallel. A schematic representation of the various heat transfer paths is shown in Figure I-78. There are two distinct regions which can be thought of as contact and non-contact regions. Actually, depending on the temperatures of the aeroshell and GIS, there may or may not be physical contact at the interface. During the initial phases of reentry, there is thermal growth of the aeroshell relative to the GIS, and then a gap will open up at the contact region in Figure I-78. On the other hand, as the aeroshell cools relative to the GIS, the gap will close and contact will be realized. The interface contact pressure at these times will depend upon the actual temperatures of the two bodies.

The reported data are given in Table I-8. The test force listed in Table I-8 was the applied force during the test. The force refers to a direction parallel to the axis of symmetry of the FWPf rings.

The results of removing the bulk FWPf and radiative contributions to the total measured conductances are given in Table I-9. The partial conductances of Table I-9 are the sum of the contact and nitrogen pressure and setting the contact conductance equal to the vacuum partial conductance, one can establish the nitrogen pressure. This was done for the tests conducted at 600°C and for force values of 1.1 and 7.9 lb. The results are plotted in Figure I-79.

In very broad qualitative terms, the curves of Figure I-79 are consistent with experience and theory. That is, the gas conductance increases with increasing gas pressure. However, analyzing the curves on the basis of a simple one dimensional conductance model reveals some problems.

The model is shown in Figure I-80. Equations have been developed for two regions, i.e., in the region of contact and outside this region. Within the contact region, gas will conduct in those spaces between the aeroshell and GIS which exist as a result of any surface irregularities and misalignment of the components.

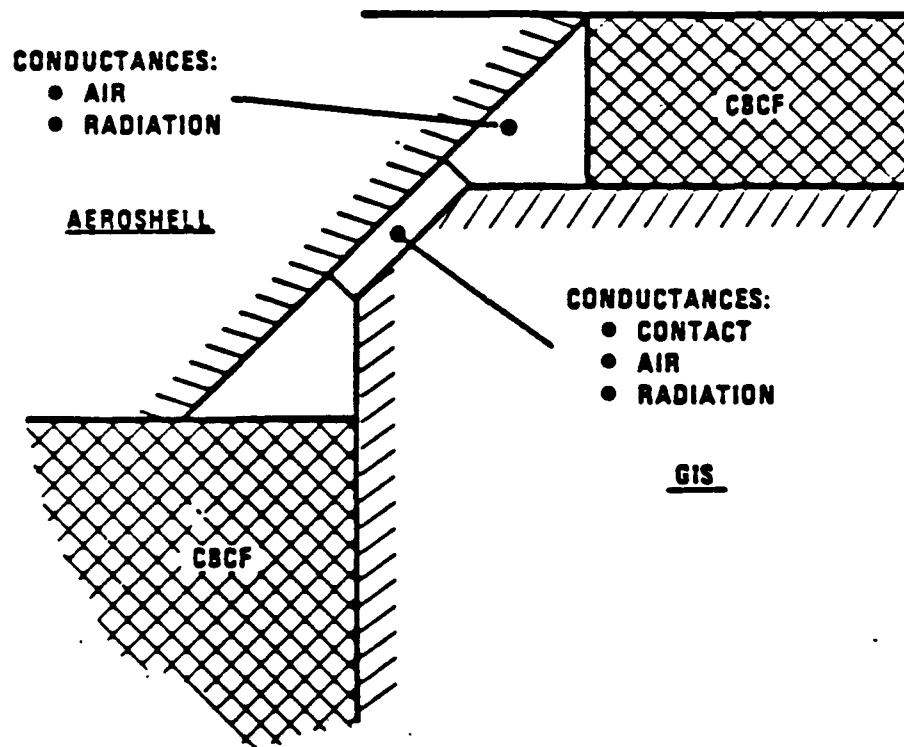


Figure I-78. Heat Transfer at the Aeroshell - GIS Interface

Table I-8. Aeroshell - GIS Interface Conductance

Measured Data			
Force = 1.1 lb Temp. = 600°C		Force = 7.9 lb Temp. = 600°C	
<u>N<sub>2</sub> Press. (Torr)</u>	<u>Conductance (W/°C)</u>	<u>N<sub>2</sub> Press. (Torr)</u>	<u>Conductance (W/°C)</u>
10 <sup>-5</sup>	.25	.0076	1.2
0.1	.36	.076	1.33
1.0	.375	.76	1.5
10.	.44	7.6	1.65
100.	.576	76.	1.65
760	.69	760	1.65
Force = 1.1 lb N <sub>2</sub> Press. = 10 <sup>-5</sup> Torr		Force = 7.9 lb N <sub>2</sub> Press. = 10 <sup>-5</sup> Torr	
<u>Temp. (°C)</u>	<u>Conductance (W/°C)</u>	<u>Temp. (°C)</u>	<u>Conductance (W/°C)</u>
600	.25	615	1.2
844	.4	810	1.3
940	.485	960	1.5
1000	.51	1025	1.6
Force - 50 lb			
<u>N<sub>2</sub> Press. (Torr)</u>	<u>Temp. (°C)</u>		
	<u>600</u>	<u>800</u>	<u>984</u>
10 <sup>-5</sup>	3.6	3.6	3.6
.1	3.5		
1.0	3.9		
10.	3.8		
100.	3.2		
760.	3.6		
			Force = 100. lb Temp. = 1000°C N <sub>2</sub> Press. = 10 <sup>-5</sup> torr Conductance = 3.5 W/°C

Table I-9. Aeroshell - GIS Interface Partial Conductance

Contact and Nitrogen Contribution			
Force = 1.1 lb Temp. = 600°C		Force = 7.9 lb Temp. = 600°C	
<u>N<sub>2</sub> Press. (Torr)</u>	<u>Partial Conductance (W/°C)</u>	<u>N<sub>2</sub> Press. (Torr)</u>	<u>Partial Conductance (W/°C)</u>
10 <sup>-5</sup>	.160	.0076	1.30
0.1	.278	.076	1.48
1.0	.294	.76	1.72
10.	.366	7.6	1.95
100.	.520	76.	1.95
760.	.653	760.	1.95
Force = 1.1 lb N <sub>2</sub> Press. = 10 <sup>-5</sup> Torr		Force = 7.9 lb N <sub>2</sub> Press. = 10 <sup>-5</sup> Torr	
<u>Temp. (°C)</u>	<u>Partial Conductance (W/°C)</u>	<u>Temp. (°C)</u>	<u>Partial Conductance (W/°C)</u>
600	.160	615	1.30
844	.215	810	1.41
940	.255	960	1.69
1000	.236	1025	1.85
Force - 50 lb			
<u>Partial Conductance (W/°C)</u>			
	<u>Temp. (°C)</u>		
<u>N<sub>2</sub> Press. (Torr)</u>	<u>600</u>	<u>800</u>	<u>984</u>
10 <sup>-5</sup>	6.16	7.21	8.45
Force = 100 lb Temp. = 1000°C N <sub>2</sub> Press. = 10 <sup>-5</sup> Torr Partial Conductance = 8.61 W/°C			

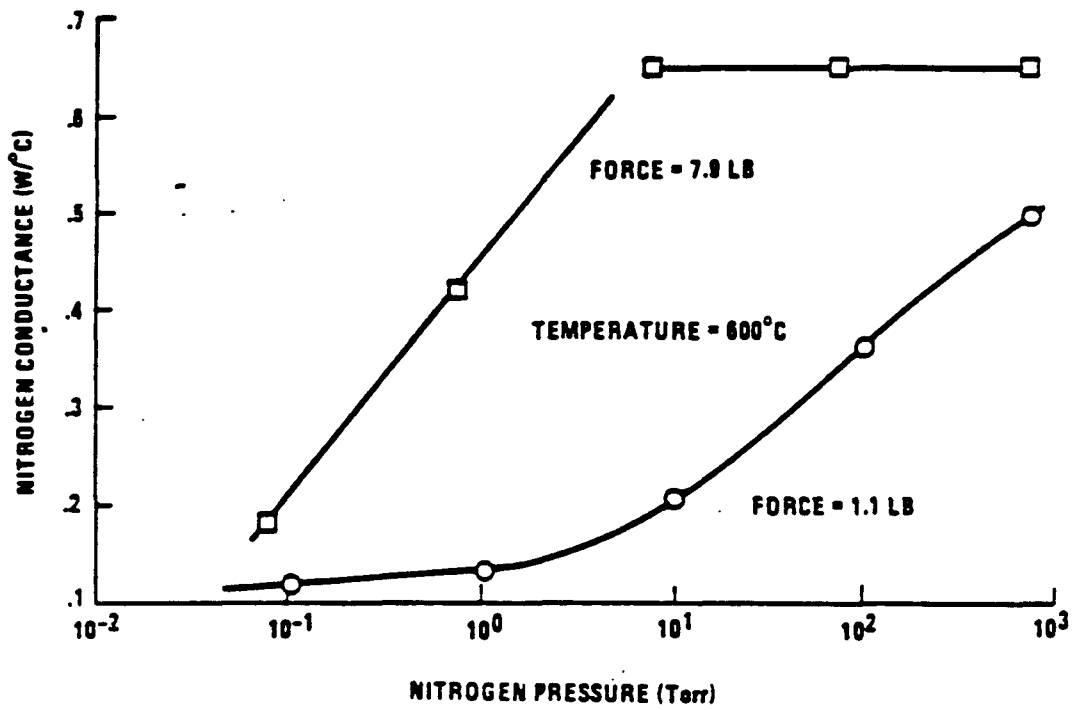


Figure I-79. Nitrogen Conductance vs. Pressure



Since the temperature is the same for both curves, gas properties will also be the same. Hence, the difference between the curves should be a geometry difference, the higher conductance presumably due to a smaller value for the gap size  $g$  in the contact region. However, if  $g$  were smaller during the 7.9 lb. test (the higher conductance curve in Figure I-79, then the knee in that curve becomes difficult to explain. Given the analytical model, the lower curve in Figure I-79 should exhibit a knee at pressures below that of any knee in the upper curve if the gap size  $g$  were actually smaller during the 7.9 lb. test.

The position of the knee in the upper curve suggests that the gap size during that test was on the order of  $10^{-2}$  inches, since the quantity  $C_2$  at the knee is about  $2.4 \times 10^{-3}$  inches. The measured data suggest that for pressures above 7.6 torr, the conductance is independent of pressure. On the basis of the analytical model, this effect will be observed when  $g$  is much larger than  $C_2$ . On the other hand, the lower curve suggests that the gap size  $g$  was no larger than about  $10^{-4}$  inches during the 1.1 lb force test.

A value of  $10^{-4}$  inches for the gap size is consistent with surface irregularities due to manufacturing of the parts. On the other hand, some misalignment of the parts is quite probable.

The data are inconclusive, and consequently, the choice of a value for the gap size is to some extent arbitrary. For the purpose of conducting reentry calculations, a value of  $6.5 \times 10^{-5}$  inches has been used.

#### I.3.3.5 The Contact Conductance at the Aeroshell - GIS Interface

Measured aeroshell - GIS interface conductances have been introduced in Section I.3.3.4. Included in the data are measurements conducted under vacuum conditions. Analysis of the data has resulted in an evaluation of the solid-to-solid-contact conductance as a function of temperature and interface pressure. The results are listed in Table I-9. Equations have been fitted to these data and are included in the GPHS reentry thermal model.

GPMS accelerations and aeroshell/GIS differential thermal growth have been modeled to evaluate the force at the interface. The linear acceleration has been evaluated from the trajectory data. Rotational accelerations have been based upon 6-DOF trajectory calculations performed by General Electric Co. and reported in Reference I-16. The force due to differential thermal growth has been based upon measured aeroshell cap deflections as a function of applied force (see Reference I-17 and Figure I-81) and FWP thermal expansion data shown in Figure I-82 and taken from Reference I-18.

The interference between aeroshell and GIS is calculated as:

$$I = 3.1 [\alpha_{GIS} - \alpha_{AS}] - G_0 \quad (4)$$

where the factor 3.1 is the room temperature length of the GIS in inches and  $G_0$  is the initial gap at the aeroshell - GIS interface measured parallel to the GIS axis and with one end of the GIS in contact with the aeroshell. In other words, if the parts were centered upon each other, the gap at either would be  $G_0/2$ .

When the interference,  $I$ , as calculated by Equation (4) is equated to the deflection of Figure I-81, the interference force is determined from the solid curve in Figure I-81. The dashed curve in Figure I-81 is a result of a hysteresis effect observed when the applied force was reduced. The dashed curve shows that the interference force, and consequently the thermal contact conductance, would be significantly reduced for the case of decreasing force. However, this effect has not been defined well enough experimentally to be used with confidence in the reentry thermal model. Hence, the conservative approach has been taken by assuming that only the solid curve data apply.

#### I.3.3.6 CBCF Graphitization Model

The role of the CBCF insulator sleeve and disc, located between the aeroshell and GIS, is to minimize the temperature drop of the iridium clad during the latter stages of a reentry trajectory. Unfortunately, the CBCF material will graphitize at high enough temperature with a consequent increase in its thermal conductivity and, therefore, a loss in its insulating property.



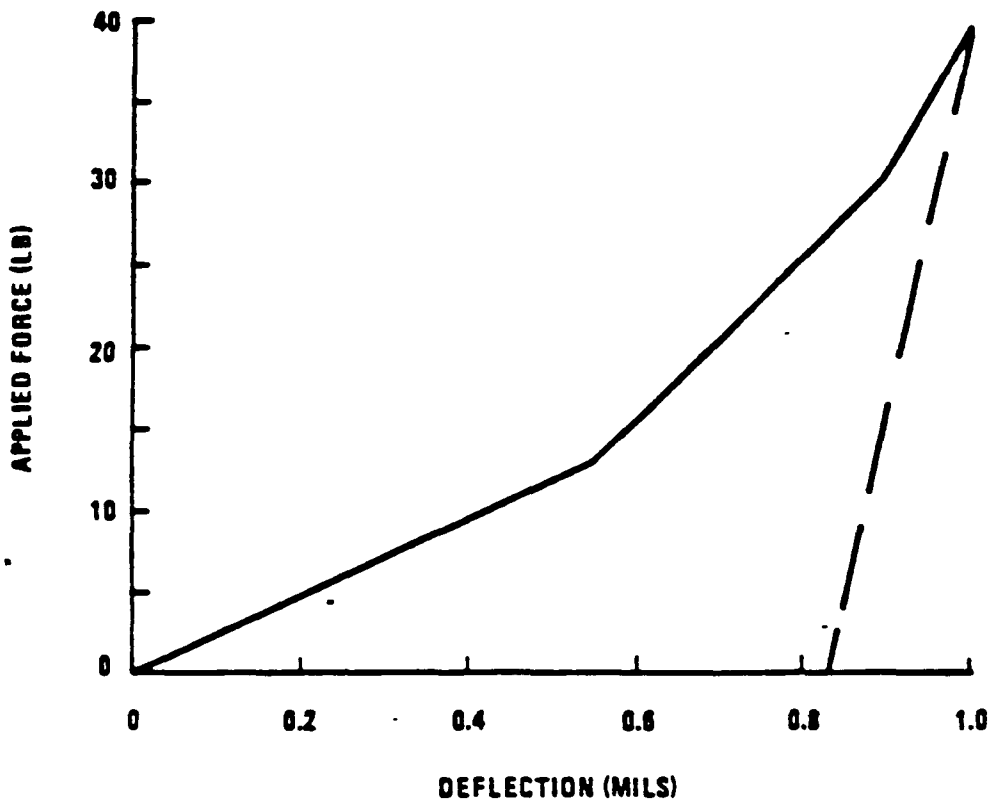


Figure I-81. Relative Deflection of Aeroshell and GIS vs. Applied Force

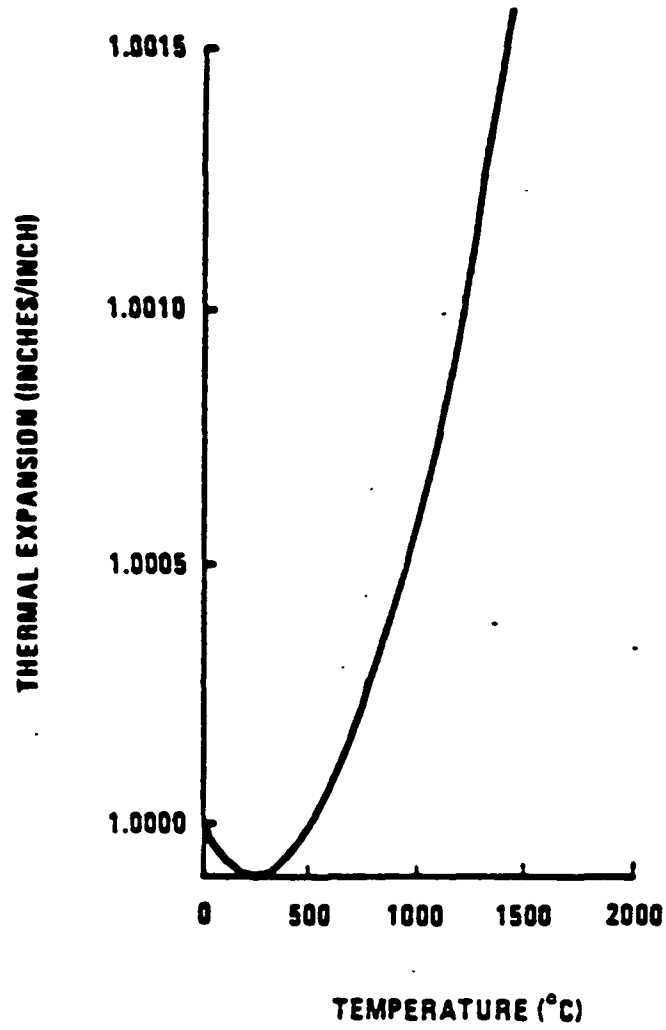


Figure I-82. FWP Thermal Expansion

During a so-called steep reentry, CBCF temperatures have been calculated to reach as high as 5600°F (3093°C). This is well above the temperature at which the graphitization process has been observed, i.e., 4350°F (2400°C) and above. Calculations of the CBCF thermal response to other classes of reentry trajectories do not show CBCF temperatures reaching the graphitization range.

In order to account for the CBCF graphitization, a fairly simple model was added to the THTD computer program. It was assumed that if a given CBCF node temperature exceeded 4712°F (2600°C), its thermal conductivity was switched to graphite values and remained as such regardless of the subsequent temperature history of the node.

The thermal conductivity data for both the CBCF and graphite forms was discussed in Section I.3.3.1. The air pressure within the CBCF pores was set equal to the pressure in the boundary layer averaged over the surface of the heat source module.

The initial CBCF node structure consisted of a single node thru the insulator thickness. To increase the accuracy of the graphitization calculation, the node structure was changed so that there were five nodes across the insulator thickness.

#### I.3.3.7 CBCF Graphitization During Steep Reentry

The steep reentry analysis for Case 17 was performed for three conditions, i.e.,

1. Coarse CBCF node structure and no graphitization.
2. Coarse CBCF node structure with graphitization, and
3. Fine CBCF node structure with graphitization.

The extent of the graphitization and its effect upon the iridium clad impact temperature were rather small.

The region of graphitization, as calculated with the fine node structure, was confined to the insulator sleeve in the vicinity of the windward broad face. In this region, the graphitization extended approximately half way thru the sleeve thickness. The volume fraction graphitized was approximately 15%.

In terms of the iridium impact temperature, the lowest iridium node temperature at impact was 1916°F (1047°C), 1914°F (1046°C) and 1904°F (1040°C) for conditions 1, 2 and 3 above respectively.

#### I.3.4 AERODYNAMIC HEATING MODEL EMPLOYED IN THE GPHS REENTRY ANALYSES

The stagnation point aerodynamic heating rate, without ablation, is based upon the correlations of Detra, Kemp and Riddell (DKR) and Sibulkin-Lees (S-L) for spherical bodies. The S-L expression, used for free stream Mach numbers,  $M$ , less than 6, is:

$$\dot{q}_{SPH}(0) = \frac{0.57}{Pr^{0.6}} \left(2^{1/2}\right) \sqrt{\frac{B_{SPH} U_{\infty}}{2R_N}} \sqrt{\rho_e h_e}_{R=0} (H_T - H_w) \quad (5)$$

The DKR expression, used for  $M_{\infty}$  greater than 6, is:

$$\dot{q}_{SPH}(0) = \frac{17,600}{R_N} \frac{\rho_F}{\rho_{SL}}^{1/2} \frac{U_{\infty}^{3.15}}{26,000} \frac{H_T - H_w}{H_T - H_{CW}} \quad (6)$$

The definitions of the terms are as follows:

- $Pr$  = Air Prandtl number
- $U_{\infty}$  = Speed of reentry body (also referred to as the free stream speed)
- $B_{SPH}$  = Velocity gradient parameter (discussed in Section I.2.4.1)
- $R_N$  = Sphere radius
- $\rho_F$  = Undisturbed air density at the altitude of the reentry body
- $\rho_E$  = Air density at the edge of the boundary layer at the stagnation point

- $\mu_e$  = Air absolute viscosity at the edge of the boundary layer at the stagnation point
- $\rho_{SL}$  = Air density at sea level
- $H_T$  = Total enthalpy at the edge of the boundary layer at the stagnation point
- $H_W$  = Enthalpy at the wall of the reentry body at the stagnation point
- $H_{CW}$  = Air enthalpy at 80°F
- $S$  = Distance from the stagnation point measured along the surface of the reentry body (used as a subscript in Equations (5) and (6) and as well as the argument for  $\dot{q}_{SPH}$  where  $s$  has been set equal to zero)

Stagnation point heating for the GPHS, with one face normal to the velocity vector, is estimated by applying a geometry correction factor to Equations (5) and (6). The correction factor is given as:

$$G = \left( \frac{B_{FFC}}{B_{SPH}} \right)^{1/2} \left( \frac{1}{2^{1/2}} \right) \left( \frac{R_N}{b/2} \right)^{1/2} \left[ 1 + \left( \frac{b}{\ell} \right)^{1/2} \right]^{1/2} \quad (7)$$

The terms in this equation are defined as:

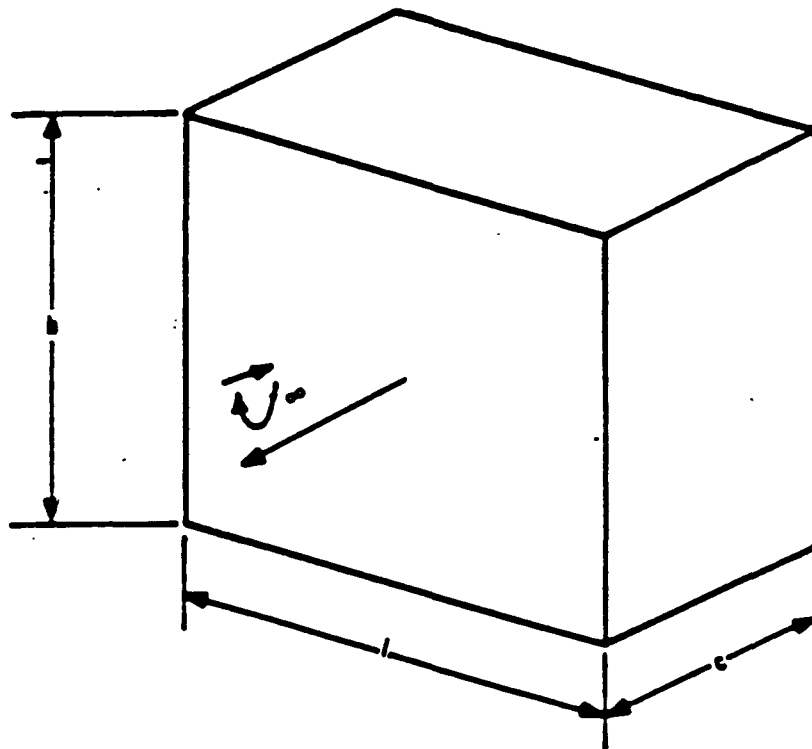
- $B_{FFC}$  = Velocity gradient parameter (see Section I.2.4.1)
- $b, \ell$  = GPHS broadface dimensions (see Figure I-83)

The GPHS stagnation point, non-ablating heating rate, for the so-called broadface-on attitude (see Figure I-83) can now be written as:

$$\dot{q}_{GPHS}(0) = G \times \dot{q}_{SPH}(0) \quad (8)$$

A critique of the use of Equations (5) through (8) for GPHS heating can be found in Reference I-19.

All the terms in Equations (5) through (7), except  $H_w$ , can be evaluated prior to a reentry analysis. Several of the terms are constants, and these include the Prandtl number,  $Pr$ , the reference sphere radius,  $R_N$ , the sea level air density,  $\rho_{SL}$ , and the cold wall air enthalpy,  $H_{CW}$ . The



**b = 3.668 IN.**  
**l = 3.826 IN.**  
**c = 2.09 IN.**

Figure I-83. GPHS in Broadface-On Attitude

remaining terms (except for  $H_w$ , the hot wall enthalpy) are all expressed as functions of the trajectory parameters altitude and speed. The values used for the constants are:

$Pr = 0.72$	(Prandtl No.)
$R_N = .12$ inches	(Sphere radius)
$\rho_{SL} = 0.002377$ slugs/ft <sup>3</sup>	(sea level air density)
$H_{cw} = 129.2$ BTU/lb	(cold wall air enthalpy)

For points on the GPHS surface other than the stagnation point, a heating rate distribution must be applied to Equation (8). Both hypersonic and subsonic heating rate distribution tests have been performed with the GPHS module geometry. (A discussion of the tests, their results and interpretations can be found in References I-20 through I-25.) For Mach numbers greater than 1.0, the distribution as a function of GPHS orientation with respect to the air flow direction is assumed to be independent of Mach number. For the case of a stable face-on orientation (i.e., no rotation, velocity vector normal to one face of the GPHS module) the test results are shown in Figure I-84 (see Reference I-20). The terminology face-on and side-on in Figure I-84 refers to the GPHS geometry, i.e., the faces of the modules are approximately 4 inches by 4 inches and 2 inches by 4 inches.

The term face (or sometimes broadface) refers to the 4 x 4 face while the term side refers to the 2 x 4 face. The terms face-on and side-on indicate that either a face or side is normal to the velocity vector.

Heating distributions for orientations other than face or side-on and for Mach numbers greater than 1.0 can be found in References I-21, I-22, and I-25. These reports also present the results of averaging the heating rates over the GPHS faces for several different tumbling modes. In particular, a random tumbling is assumed for the minimum gamma reentry analyses during the supersonic and hypersonic portions of the trajectory. During this period, the aerodynamic heating is assumed to be uniform over the entire GPHS with a value derived by an averaging process described in the references. The result gives a heating rate at any point equal to 34% of the stagnation value found for the broadface on stable condition. In this case the heating is expressed as:

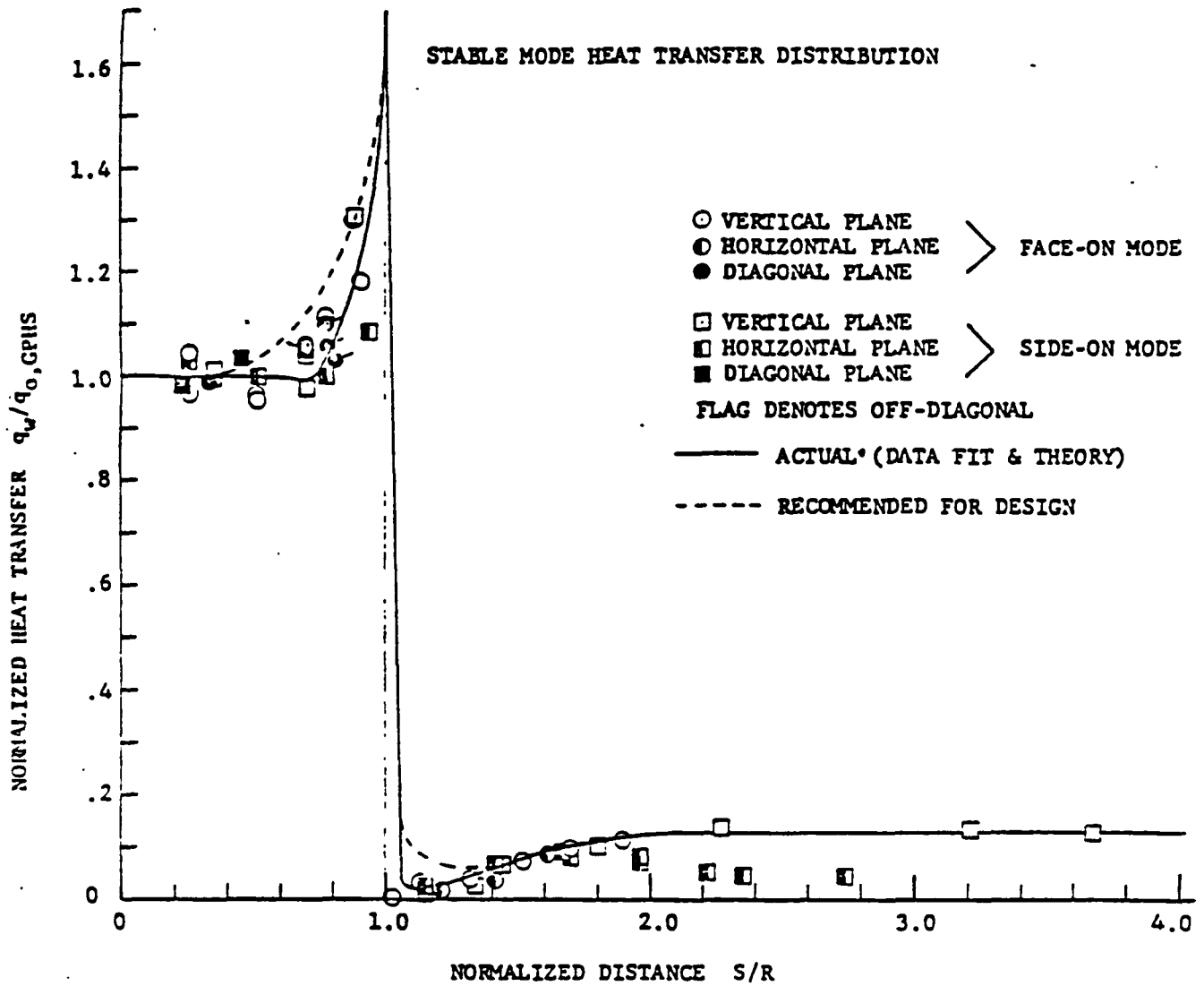


Figure I-84. GPHS Stable Mode Heat Transfer Distribution



$$\dot{q}_{\text{GPHS}}(S) = 0.34 \times G \times q_{\text{SPH}}(0) \quad (9)$$

During the hypersonic and supersonic stages of the orbital decay trajectories, the GPHS module will assume a 60° angle of attack attitude, i.e., the normal to one of the broad faces makes an angle of 60° with the module velocity vector. In addition, the module spins about the normal to its broad faces. In order to establish the aerodynamic heating distribution over the module outer surface for this attitude and spin behavior, a search was made of the test data.

It was determined that two of the test runs applied to the current case, i.e., runs 32 and 42. In both of these runs the angle of attack was 60°. In terms of a spin angle, run 32 was at 0°, by definition, and run 42 was at 35° (see Figure I-85 for a description of the terms).

The heating rate distribution is defined here as the ratio of the heating rate of any given point for the 60° angle of attack case, to the heating rate at the stagnation point for the 0° angle of attack case.

The 0° angle of attack stagnation point heating rate was given the value of 3.24 BTU/FT<sup>2</sup>-SEC. This is the average value of the measured rates as detected by gages 204 and 206 for runs 1, 2, 23 and 24, all of which had a 0° angle of attack, the so-called face-on-stable attitude.

The test data included measurements on three of the four side faces and one of the two broad faces. This was sufficient to estimate the heating rate distributions over the side faces and the windward broad face as a function of spin angle. The leeward broad face was simply given the value of 0.13, the observed value for the 0° angle of attack case (i.e., the face-on attitude).

The spin-angle dependent heating distribution at each point was then averaged over the spin angle to provide the spin averaged heating rate distribution as a function of position on the module outer surface. These values were then introduced into the reentry thermal analysis program.

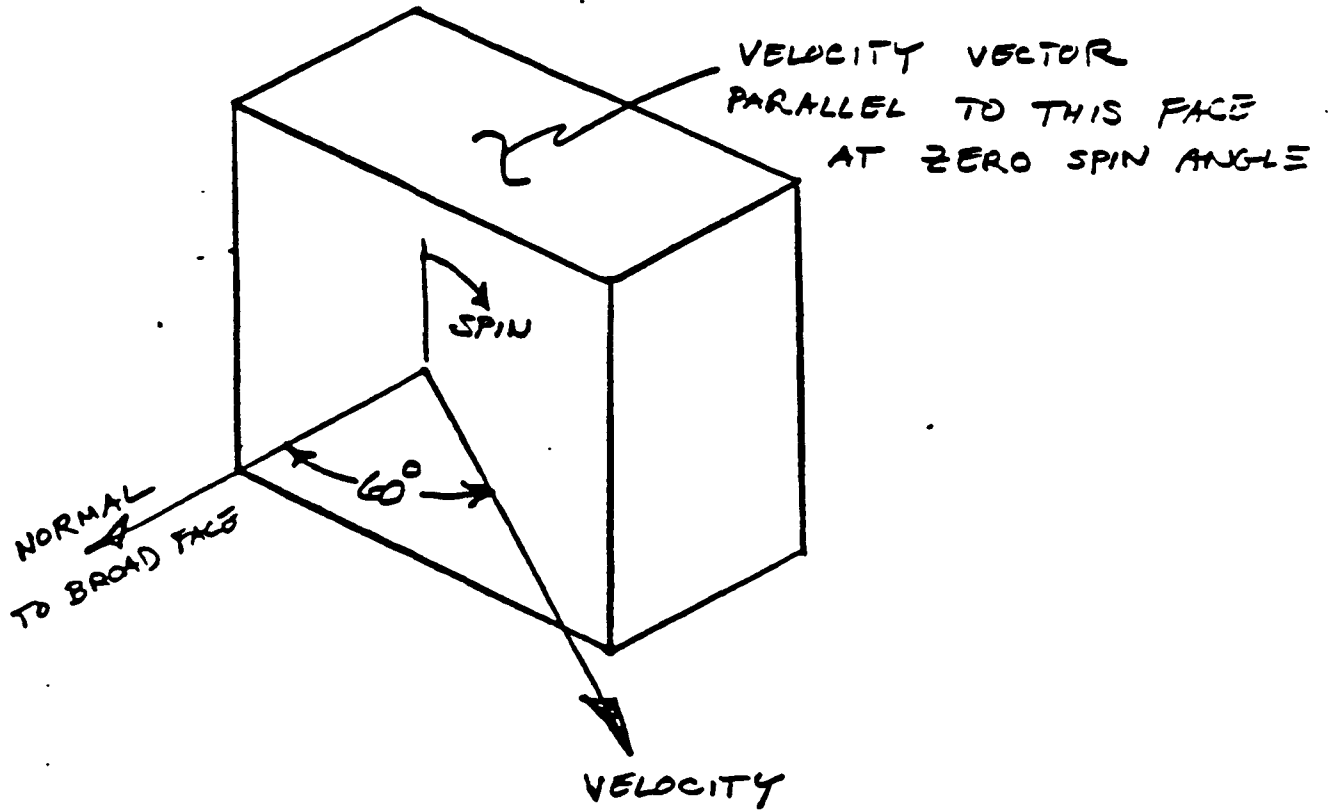


Figure I-85. GPHS Module 60° Angle of Attack

The resulting spin averaged heating rate ratios for the windward broad face and for a side face are shown in Figure I-86.

For Mach numbers less than 1.0, and for the face-on stable orientation, the heating rate is taken to be constant over the front face. For the other module faces, the heating rate is taken to be 88% of the front face rate. This subsonic heating distribution and the test data upon which it is based are discussed in References I-23 and I-24. These references also discuss the tests for other than the face-on orientation.

In general terms, the non-ablating aerodynamic heating on the surface of the GPHS can be written as:

$$\dot{q}_{\text{GPHS}}(s) = f(s) \times G \times \dot{q}_{\text{SPH}}(0) \quad (10)$$

where  $f(s)$  is the heating distribution as a function of  $s$ , the distance from the stagnation point as measured along the surface. By definition,

$$f(s) = \dot{q}_{\text{GPHS}}(s) / \dot{q}_{\text{GPHS}}(0) \quad (11)$$

For tumbling modes of reentry,  $f(s)$  is replaced by an average value,  $\bar{f}$ , whose evaluation is dependent upon the mode of tumbling. In this case:

$$\dot{q}_{\text{GPHS}}(s) = \bar{f} \times G \times \dot{q}_{\text{SPH}}(0) \quad (12)$$

A specific example of equation (12) is given above in equation (9) where  $\bar{f} = 0.34$ , representing the case of random tumbling for Mach numbers greater than 1.0.

In evaluating the methodology described above, members of the Applied Physics Laboratory staff of Johns Hopkins University reached the conclusion that Equation (8) would underestimate the heating rate for Mach numbers greater than 1.0. They recommended the addition of a weighing factor to Equation (8) whose value would be in the range of 1.16 to 1.40. Consequently, the safety study reentry calculations have been conducted using a multiplying factor of

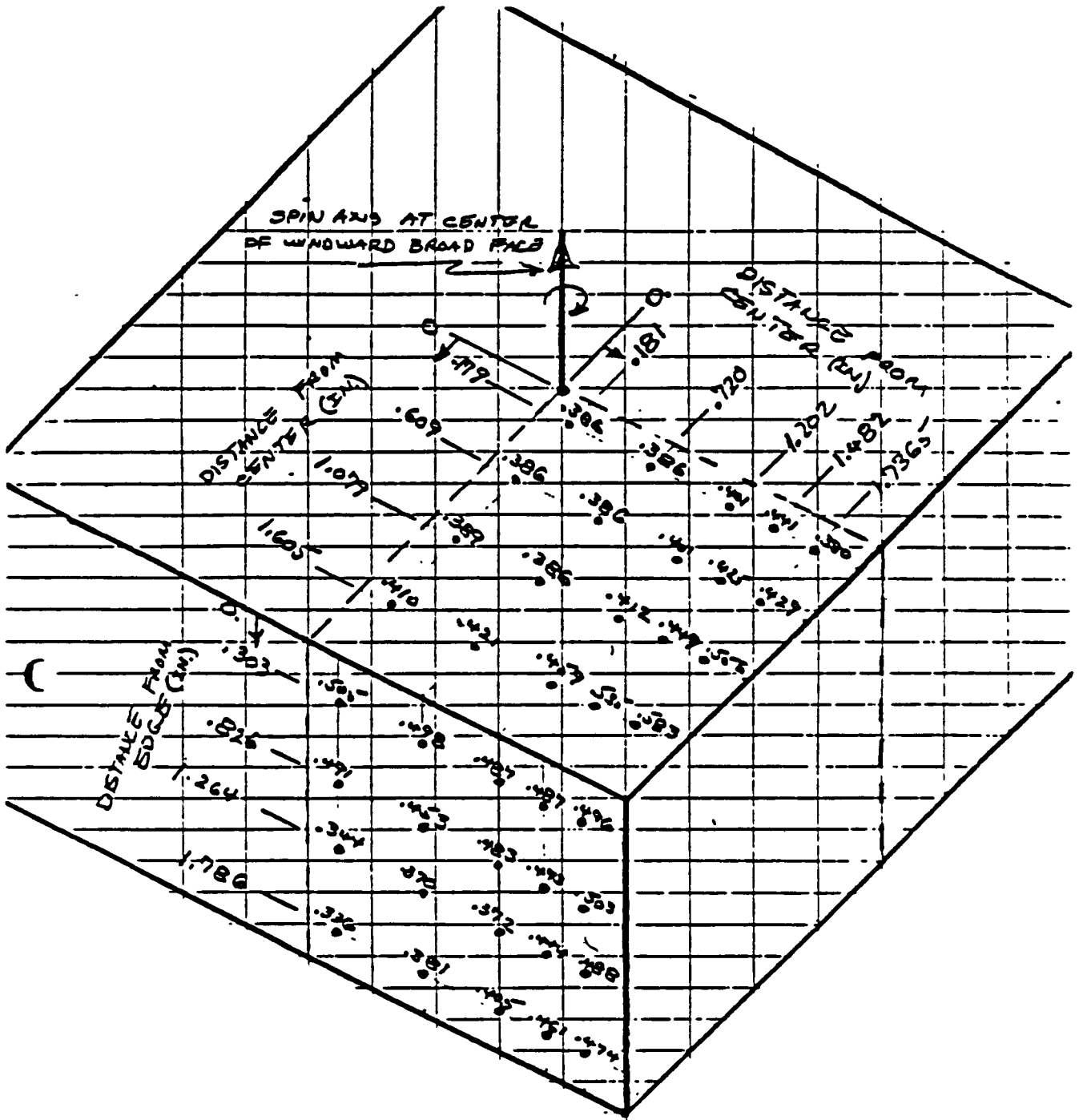


Figure I-86. Heating Rate Distribution for the 60° Angle of Attack Spinning GPHS Module

1.3 on the right hand side of Equations (8), (9), (10) and (12) for Mach numbers greater than unity.

In order to apply equation (10) to any given reentry thermal analysis, a non-ablating heat transfer coefficient is defined as:

$$h \equiv q_{\text{GPHS}}(s)/(H_T - H_w) \quad (13)$$

This coefficient is independent of the reentry body temperature, given the aerodynamic heating correlations used here (see Equations (5) through (7) and the accompanying discussion). Consequently, the coefficient  $h$  can be evaluated independent of the reentry thermal analysis.

Using Equation (13) to evaluate the aerodynamic heating requires the evaluation of the term  $H_w$ , the enthalpy at the wall. Given a set of initial conditions, the wall enthalpy can be evaluated during the course of the reentry analysis.

In general, the wall enthalpy will be a function of the following parameters:

- Wall temperature
- Gas pressure at the wall
- Composition of the gas
- The total enthalpy at the edge of the boundary layer
- Ablation rate

In addition, the heat transfer coefficient,  $h$ , must be modified when the wall is undergoing ablation.

The gas pressure at the wall is assumed to be the same as the pressure at the edge of the boundary layer. For subsonic speeds, the GPHS reentry attitude is taken to be stable and broad face-on. The pressure distribution for these conditions is taken to be a uniform pressure over the leading face, and, on the remaining faces, the pressure is set to 90% of the leading face value. For speeds above Mach 1, the pressure at the wall is taken to be uniform over

all faces since the module is assumed to be randomly tumbling. The pressure in this case is set equal to 19% of the value calculated at the stagnation point for the case of a stable face-on reentry with all other conditions the same.

During periods of ablation, the gas composition at the wall is based upon the CO/CO<sup>2</sup> ratio measurements for graphite made at the General Electric Co. using pyrolytic graphite and measurements made at Battelle Columbus Labs using POCO graphite. The results of those tests are shown in Figure I-87. The lower bound curve has been used in the reentry calculations to date. At the low temperature end of the curve, the dashed line through the GE data has been used rather than the Battelle data.

The ablation rate and the effect of ablation upon the aerodynamic heating are evaluated for two temperature ranges. For wall temperatures between 727°C and 1950°C, the ablation is assumed to be reaction rate controlled. Above 1950°C, it is assumed to be diffusion-sublimation controlled, and the ablation rate is evaluated on the basis of the Perini correlations (see Reference I-26).

#### I.3.4.1 Velocity Gradient Parameters

The stagnation point, non-ablating aerodynamic heating correlations include a velocity gradient term defined as:

$$B = \frac{L}{U_{\infty}} \left( \frac{d U_e}{ds} \right)_{s=0} \quad (14)$$

where

- L = Body characteristic length
- U<sub>∞</sub> = Free stream speed
- U<sub>e</sub> = Air speed at the edge of the boundary layer
- S = Distance from stagnation point measured along the surface of the reentry body

In the case of a sphere, the diameter is used as the characteristic length.

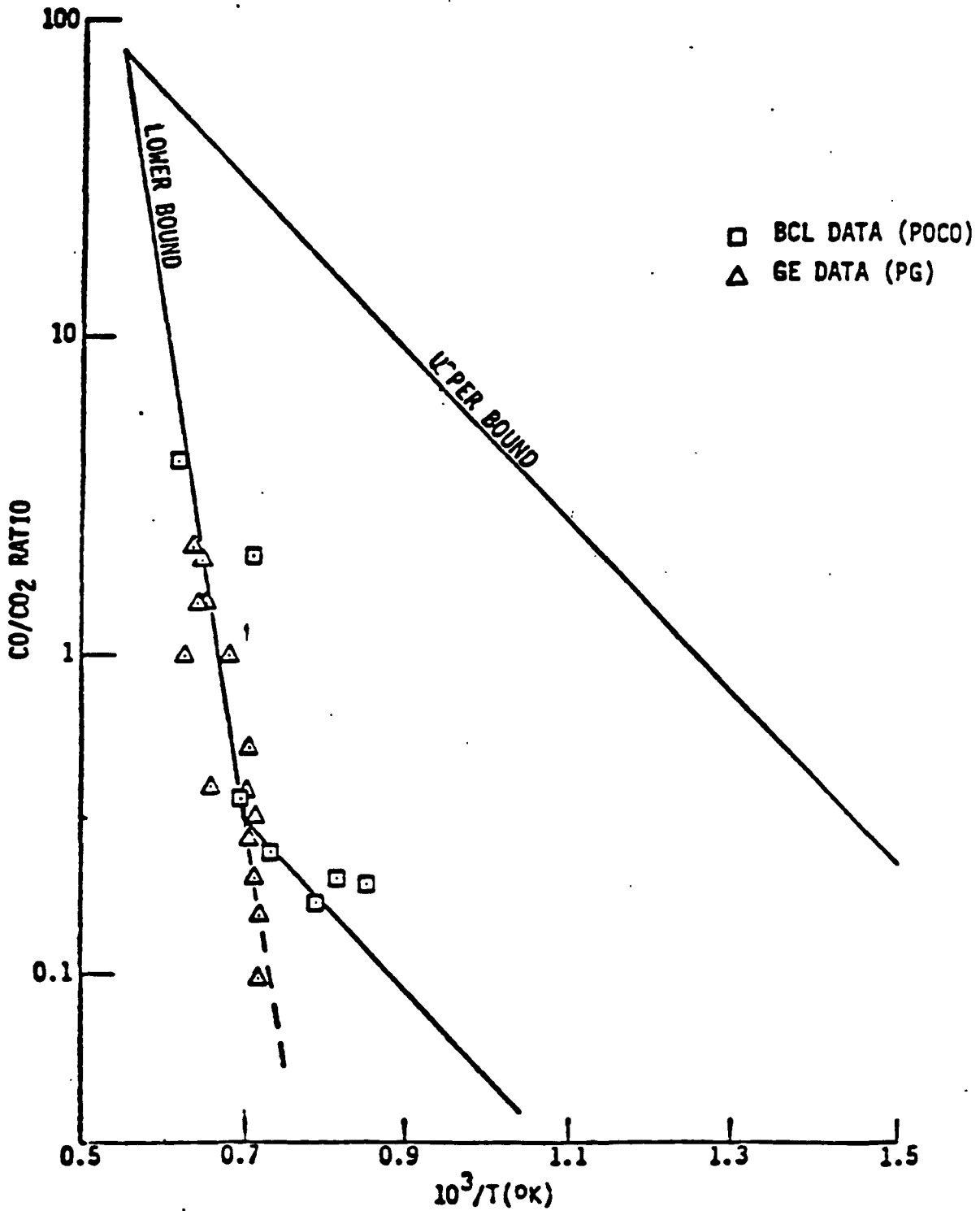


Figure I-87. CO/CO<sub>2</sub> Ratio

Data are lacking in the case of the velocity gradient for the GPHS geometry. However, there are data for the case of a flat faced cylinder, and this is substituted for the GPHS parameter. The spherical (SPH) and flat faced cylinder (FFC) data have been correlated with the free stream Mach number by the staff of the Applied Physics Laboratory of Johns Hopkins University (Reference I-27). The results of their work are given below:

$$B_{SPH} = 1.10 + 1.56/(1 + M_{\infty}^2)^{0.79} \quad (15)$$

$$B_{FCC} = 0.29 + 0.983 (1 + M_{\infty}^2)^{0.312} (1 + M_{\infty}^3) \quad (16)$$

#### I.3.4.2 Air Properties in the Vicinity of a Reentry Body

In the free stream region, i.e., at points unaffected by the presence of the reentry body, the air temperature,  $T_F$ , and air density,  $\rho_F$ , as a function of altitude are taken from an atmospheric properties table. The free stream static pressure is evaluated using the ideal gas law,

$$P_F = R \rho_F T_F \quad (17)$$

The free stream enthalpy is calculated assuming a calorically perfect gas,

$$H_F = C_p T_F \quad (18)$$

where the specific heat has been given the constant value of 0.24 BTU/lb-°F and  $T_F$  is the absolute temperature. The total enthalpy of the free stream,  $H_T$ , is:

$$H_T = H_F + 1/2 U_{\infty}^2 \quad (19)$$

and this value is assumed to apply at the edge of the boundary layer and at all points outside of the boundary layer. In other words, adiabatic flow conditions are assumed in the region outside of the boundary layer. The total pressure at the edge of the boundary layer at the stagnation point,  $P_E$ , is



calculated as a function of free stream static pressure and free stream Mach number. There are four equations, one for each of four Mach number ranges. The equations are as follows:

$$P_E = P_F \times 1.35 \times M_\infty^2 \quad M_\infty \geq 8 \quad (20)$$

$$P_E = P_F \times 1.155 \times M_\infty^{2.075} \quad 5 \leq M_\infty \leq 8 \quad (21)$$

$$P_E = P_F \times 1.89 \times M_\infty^7 \times [6/(7 M_\infty^2 - 1)]^{2.5} \quad 1 \leq M_\infty \leq 5 \quad (22)$$

$$P_E = P_F \times (1.0 + 0.2 M_\infty^2)^{3.5} \quad M_\infty < 1 \quad (23)$$

The density and the temperature at the edge of the boundary layer, again at the stagnation point, have been tabulated (Reference I-28) as a function of  $H_T$  and  $P_E$ , the total enthalpy and the total pressure discussed above.

The absolute viscosity at the edge of the boundary layer is determined using Sutherland's equation, i.e.,

$$\mu_E = 2.27 \times \left( \frac{T_E^{1.5}}{T_E + 198.6} \right) \times 10^{-8} \quad (24)$$

where the temperature is expressed in units of °R and the viscosity in units of lb-sec/ft<sup>2</sup>.

### I.3.5 MATERIAL PROPERTIES

The thermal properties of the GPHS materials as a function of temperature which have been used in the thermal analysis are listed in Table I-10. The FWPF properties were obtained from References I-13 and I-29. The properties of the CBCF in vacuum were obtained from Reference I-9; those in air were obtained from Reference I-10. The value for the CBCF emissivity is undocumented and is an estimated value.

Table I-10. Material Properties Used in Thermal Analysis

<b>FWPF</b> Temperature — °F	100	500	750	1000	1250	1500	1750	2000	2500	3000	4000	4800				
<b>X-Direction</b>																
Conductivity (Btu/Hr-Ft-°F)	94.2	75.8	67.1	59.8	53.3	48.3	44.2	40.0	35.0	30.8	27.9	26.8				
Specific Heat (Btu/Lb-°F)	0.185	0.312	0.355	0.39	0.412	0.43	0.446	0.465	0.485	0.505	0.52	0.525				
Emissivity	0.812	0.814	0.816	0.818	0.821	0.824	0.828	0.832	0.84	0.848	0.865	0.882				
<b>Z-Direction</b>																
Conductivity (Btu/Hr-Ft-°F)	74.0	60.3	53.3	46.9	41.7	37.5	34.2	31.7	28.3	26.7	25.0	24.2				
Specific Heat (Btu/Lb-°F)	0.185	0.312	0.355	0.39	0.412	0.43	0.446	0.465	0.485	0.505	0.52	0.525				
Emissivity	0.642	0.675	0.696	0.718	0.734	0.752	0.77	0.788	0.82	0.853	0.905	0.943				
<b>CBCF (C Direction)</b>																
Temperature — °F	212	392	572	752	932	1112	1292	1472	1652	1832	2012	2192	2372	2552	3000	
Conductivity (Btu/Hr-Ft-°F)	0.0444	0.052	0.061	0.071	0.081	0.086	0.091	0.098	0.101	0.107	0.112	0.117	0.122	0.128	0.141	
Specific Heat (Btu/Lb-°F)	0.214	0.265	0.312	0.351	0.38	0.406	0.424	0.4395	0.45	0.461	0.47	0.478	0.482	0.487	0.5	
Emissivity	0.8	0.8	0.8	0.8	0.8	0.8	0.8	0.8	0.8	0.8	0.8	0.8	0.8	0.8	0.8	
<b>Iridium</b>																
Temperature — °F	0	1000	2000	3000	4000											
Conductivity (Btu/Hr-Ft-°F)	85.0	79.0	76.5	65.5	65.0											
Specific Heat (Btu/Lb-°F)	0.0306	0.0347	0.0388	0.0429	0.047											
Emissivity	0.0838	0.137	0.191	0.245	0.298											
<b>PuO<sub>2</sub></b>																
Temperature — °F	100	572	752	932	1112	1292	1472	1652	1832	2012	2192	2500	3000	3500	4000	
Conductivity (Btu/Hr-Ft-°F)	0.242	0.254	0.266	0.315	0.325	0.335	0.545	0.59	0.635	0.681	0.726	0.747	0.78	0.814	0.848	
Specific Heat (Btu/Lb-°F)	0.062	0.0775	0.0794	0.0805	0.0811	0.0817	0.0821	0.0825	0.0827	0.083	0.0832	0.0835	0.0838	0.084	0.084	
Emissivity	0.6	0.643	0.659	0.676	0.692	0.709	0.725	0.742	0.758	0.775	0.791	0.819	0.865	0.911	0.956	

Values for the iridium conductivity and specific heat were taken from Reference I-30. Reference I-31 was used to obtain the iridium emissivity data as related to the values for the grit blasted and annealed material.

The  $\text{PuO}_2$  fuel specific heat and emissivity data were taken directly from Reference I-30. Conductivity data for the fuel was taken from Reference I-32 and for the measured values from hot pressed and sintered fuel pellets.

### I.3.6 COMPUTER PROGRAMS

#### I.3.6.1 ABTON

The ABTON computer program was used to develop the basic input required for the calculation of the aerodynamic heating. This input consisted of the following:

- Non-ablating enthalpy gradient heat transfer coefficient
- Total enthalpy at the edge of the boundary, and
- Total pressure at the edge of the boundary layer

The details of the calculations for these parameters are given in Section I.3.4

#### I.3.6.2 THT-DA

The THT-DA (Transient Heat Transfer - Version D with Ablation) computer program is a finite difference heat transfer program. It employs the implicit heat balance formulation of the finite difference heat balance equation. The Gauss-Seidel method is used for the iterative solution.

The program accepts temperature dependent properties and treats conductive, convective, and radiative heat transfer mechanisms. Material removal due to ablation is accounted for by changing the appropriate node dimensions. When required, nodes are completely removed from the thermal model.

### I.3.7 THERMAL RESULTS

Figures I-88 through I-105 present the results of the thermal analyses for all cases except for the powered reentries. Table I-11 summarizes these results in terms of the maximum and minimum temperatures experienced by the iridium clads at the peak of reentry and at three altitudes of impact - sea level, 5000 feet, and 10,000 feet. The maximum recession is also presented in that table.

Note should be made that the  $\gamma$  min, superorbital reentry for Galileo and Ulysses result in skip-out of the GPHS modules after breakup of the RTG during the initial pass through the atmosphere. Subsequently, the modules have enough time out of the atmosphere (i.e., above 400,000 feet) to restabilize in temperature as a free body radiating to the space vacuum sink. This results in the fueled clads being around 1010°C at the beginning of the final reentry, and the subsequent impact temperatures are lower than for any other reentry, including the powered reentry.

## I.4 GIS & FUEL PELLETT THERMAL ANALYSIS

### I.4.1 GIS ANALYSIS

A reentry calculation was performed for the case of a single Graphite Impact Shell (GIS) and its contents, which consists of two fuel pellets, their iridium clads and a single floating membrane.

An Orbital Decay Trajectory was investigated. The GIS was assumed to be spinning about its longitudinal axis with two different attitudes: broadside ( $\alpha = 90^\circ$ ) and end-on ( $\alpha = 0^\circ$ ).

The initial trajectory conditions chosen were:

Altitude	400,000 ft.
Relative Speed	25,690 ft/sec
Relative Flight Path Angle	-0.1 deg.
Attitude ( $\alpha$ )	90 deg. and 0 deg.

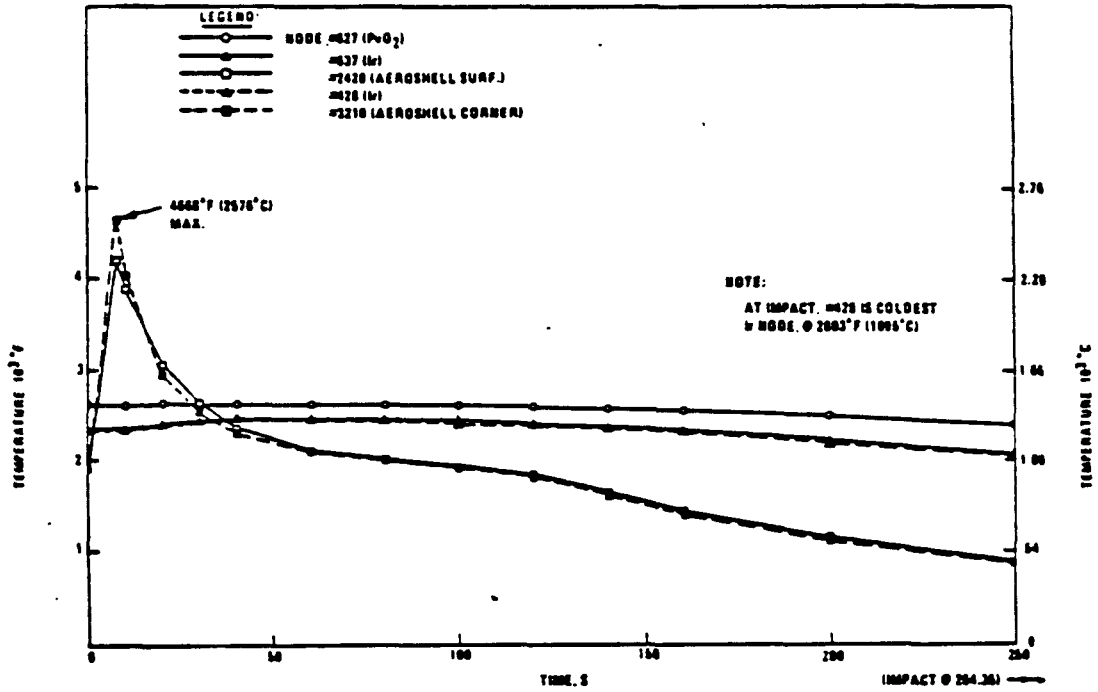


Figure I-88. Case 1 - Steep Reentry - Galileo (Early Release)

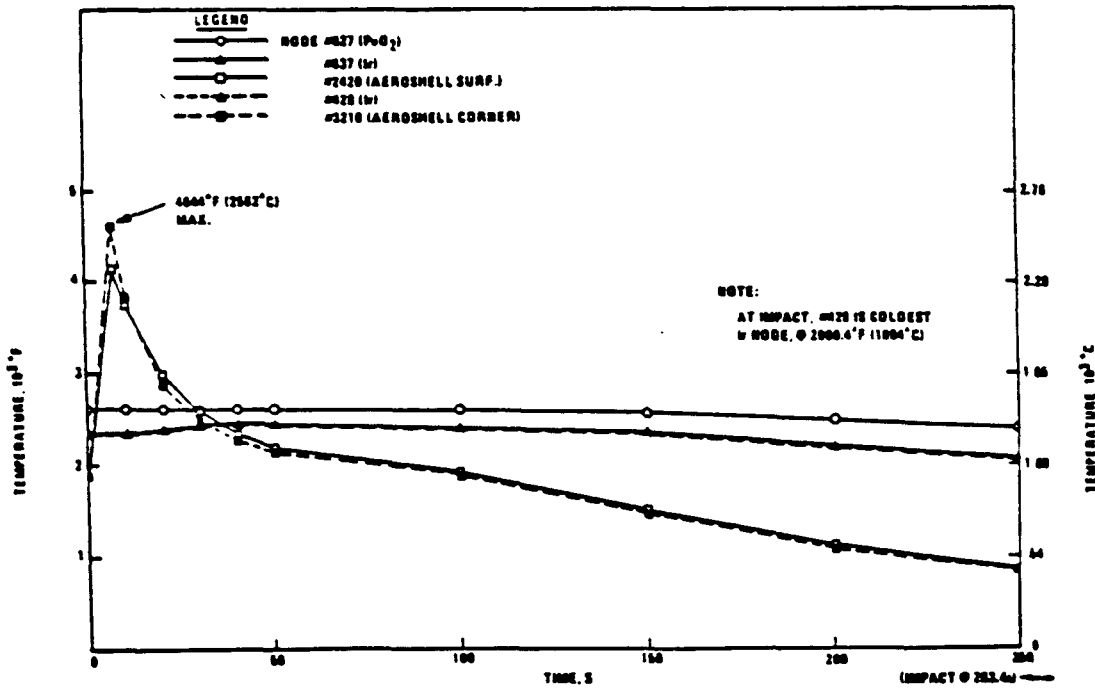


Figure I-89. Case 2 - Steep Reentry - Galileo (Late Release)

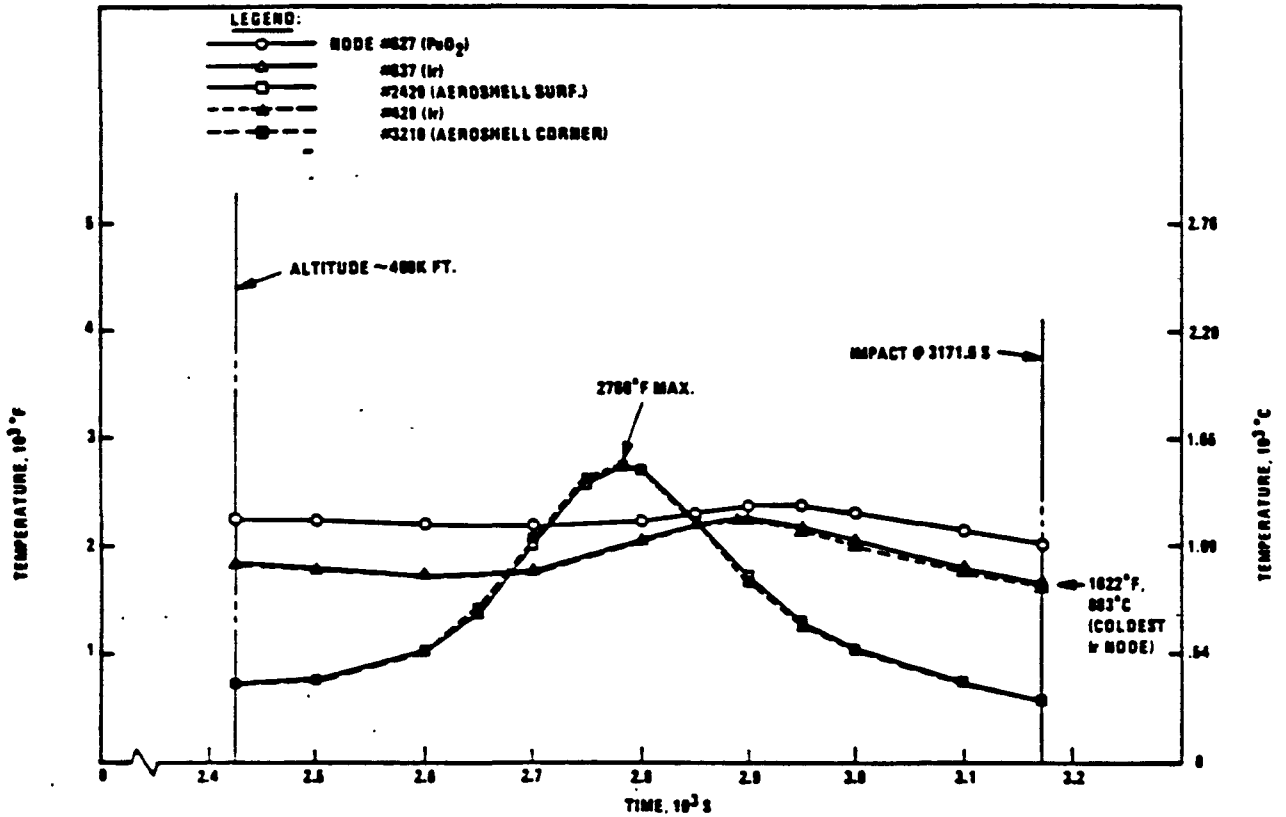


Figure I-90. Case 3 -  $\gamma_{MIN}$  Reentry - Galileo (Early Release)

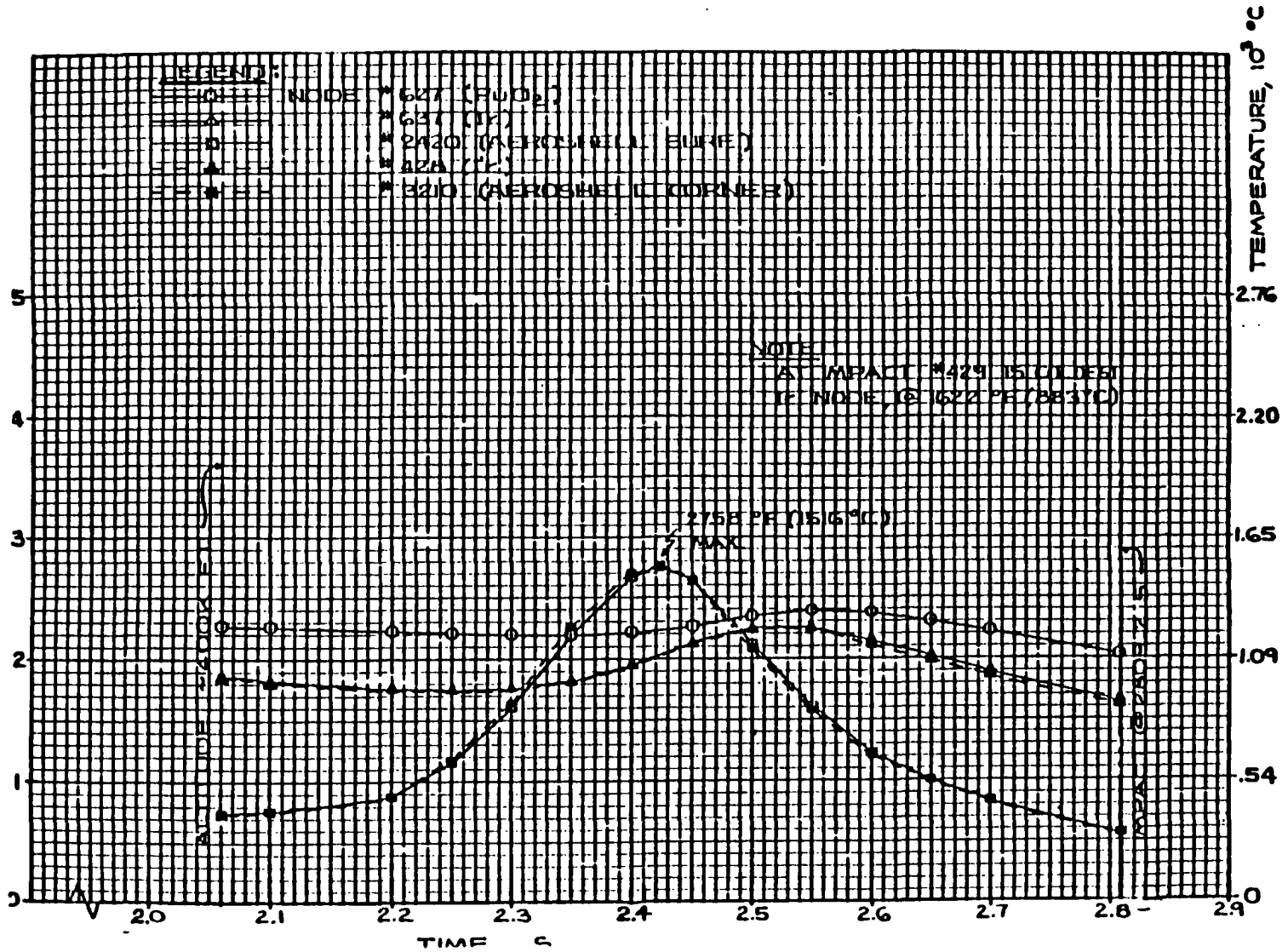


Figure I-91. Case 4 - Shallow Reentry ( $\gamma_{MIN}$ ) - Galileo (Late Release)

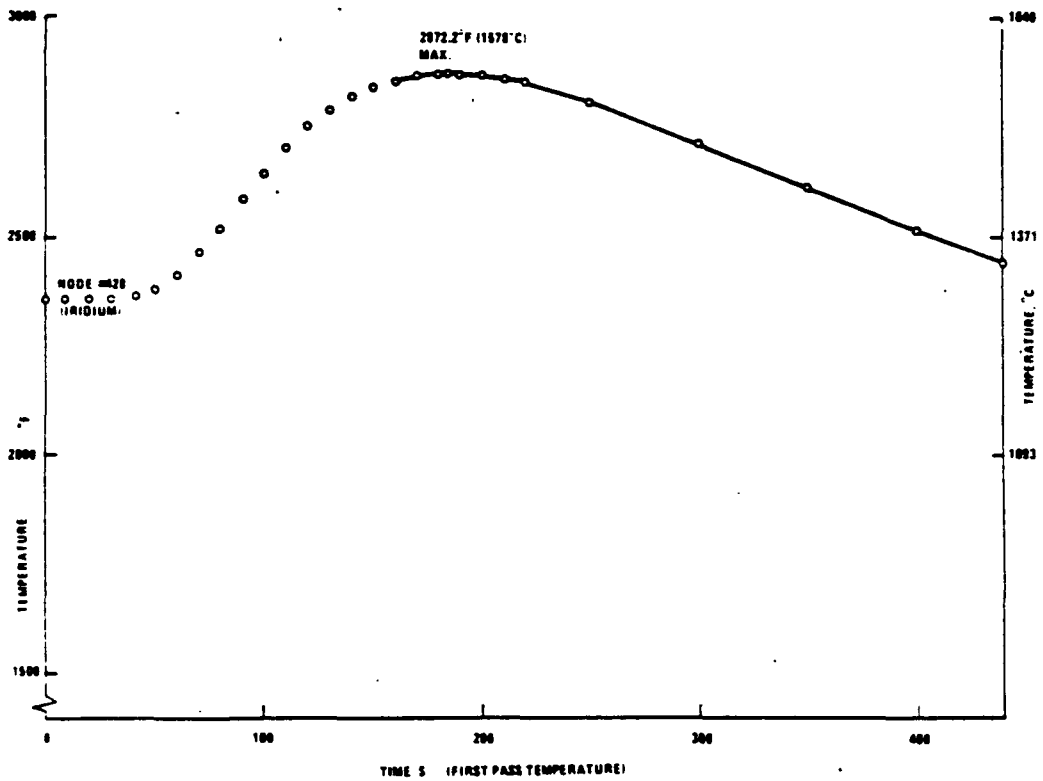


Figure I-92. Case 3 -  $\gamma_{MIN}$  - Galileo (Early Release)

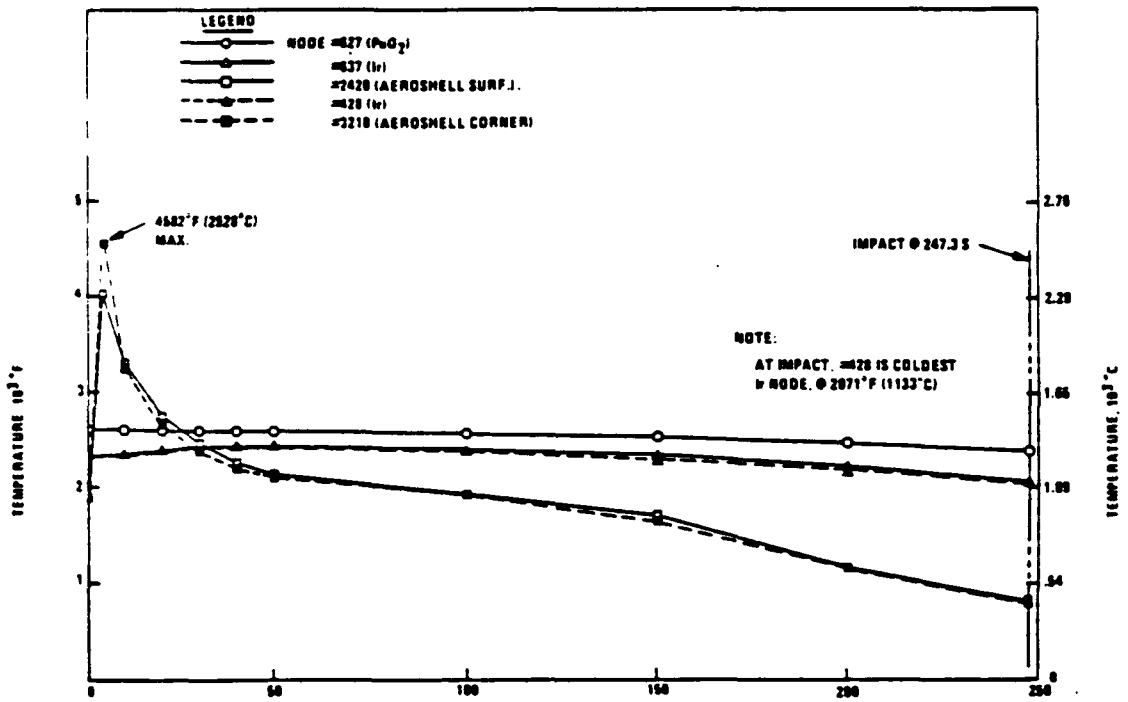


Figure I-93. Case 5 - Steep Angle Reentry - Ulysses (Early Release)



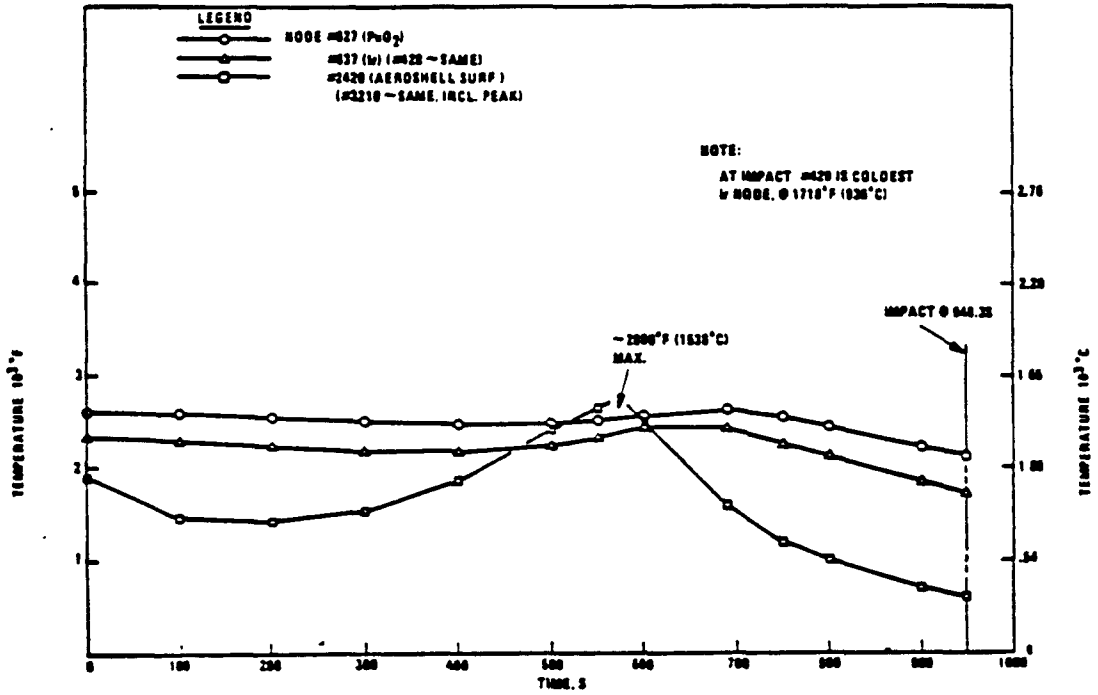


Figure I-94. Case 6 - Orbital Decay - Galileo (Early Release)

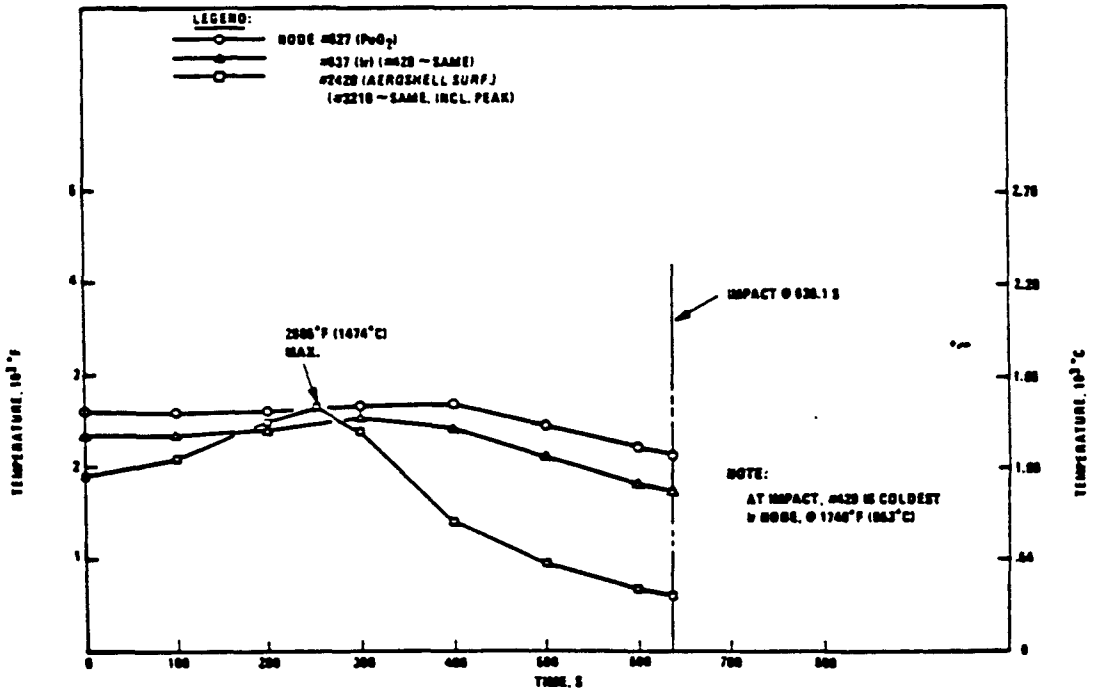


Figure I-95. Case 7 - Orbital Decay - Galileo (Late Release)

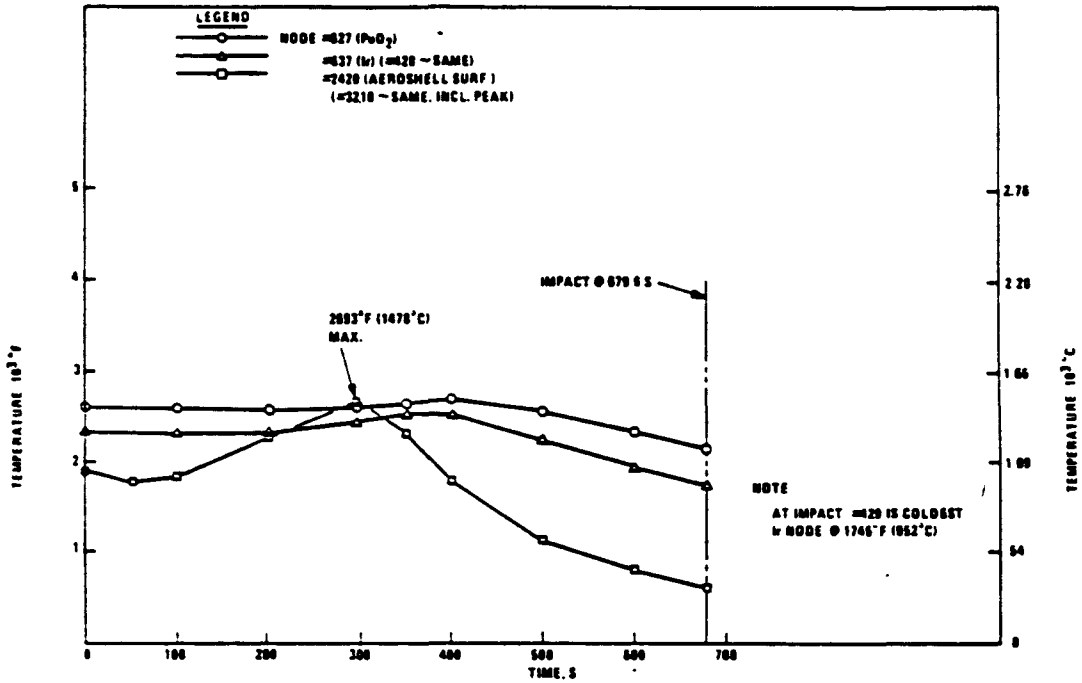


Figure I-96. Case 8 - Orbital Decay - Ulysses (Early Release)

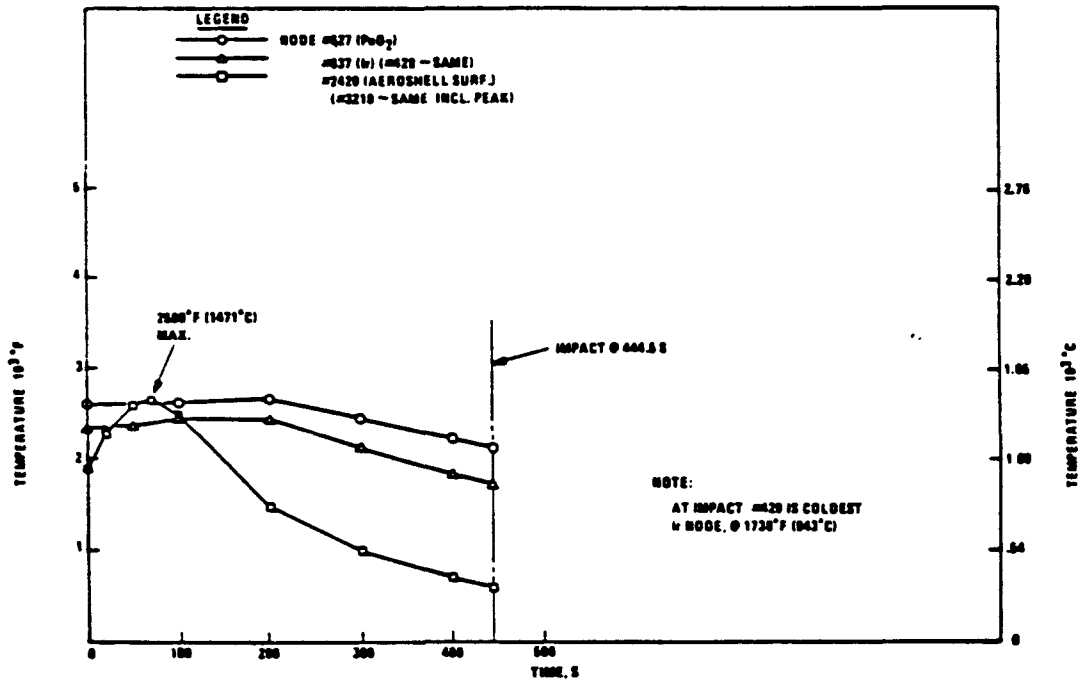


Figure I-97. Case 9 - Orbital Decay - Ulysses (Late Release)

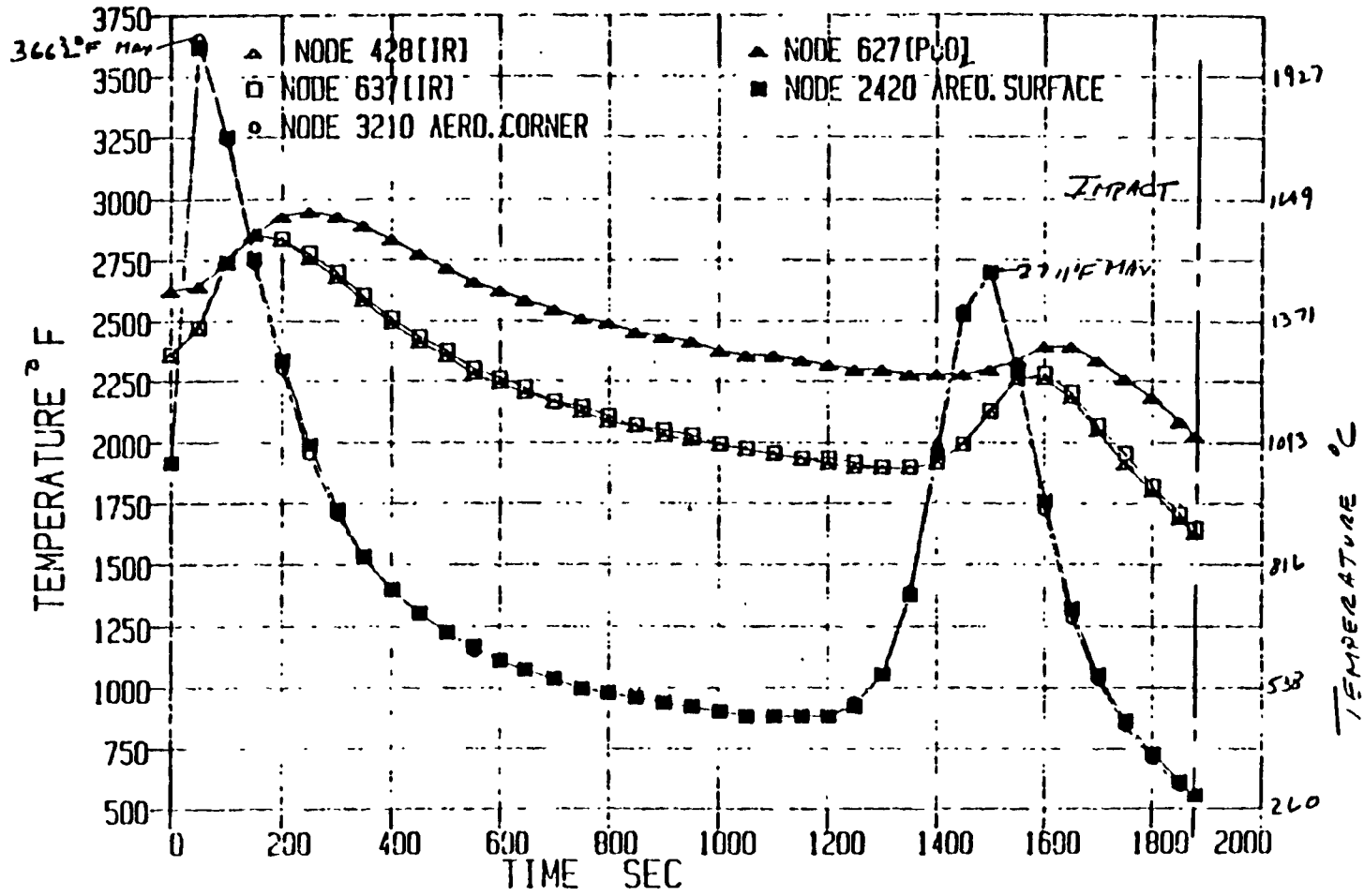


Figure I-98. Case 14 - Ulysses Shallow Angle Reentry (Early)

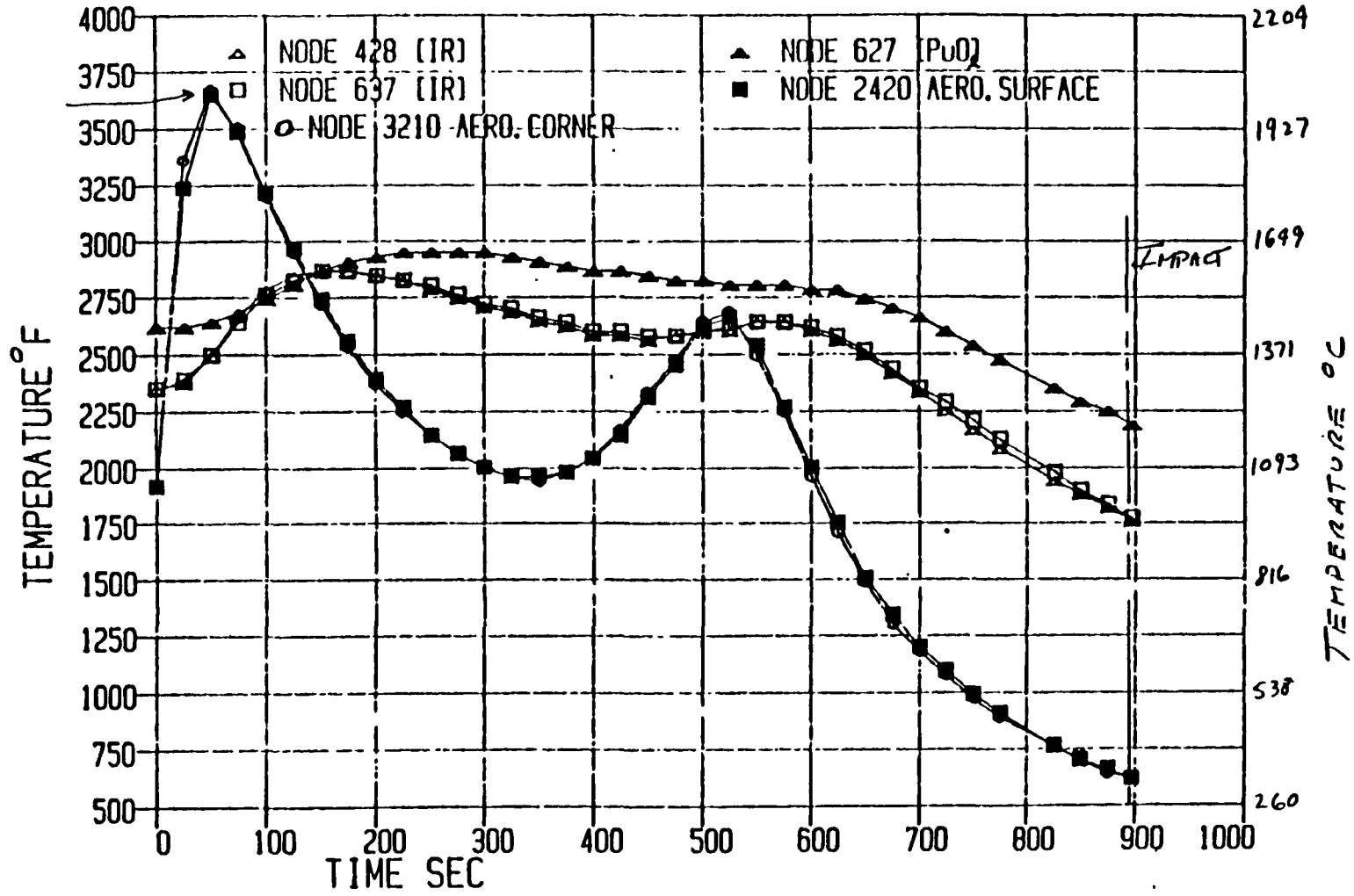


Figure I-99. Case 15 - Ulysses Shallow Reentry (Late)

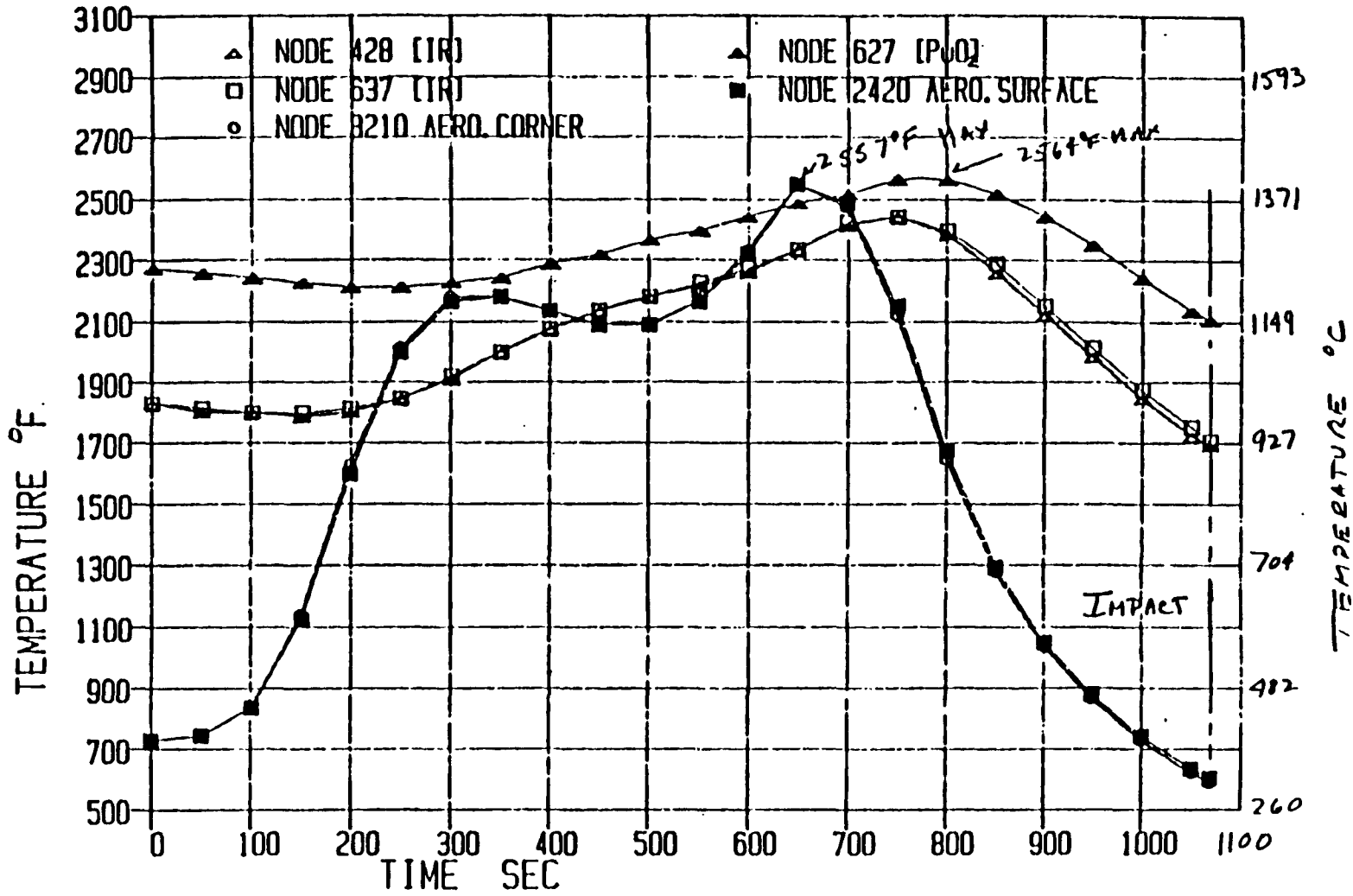


Figure I-100. Case 16 - Ulysses

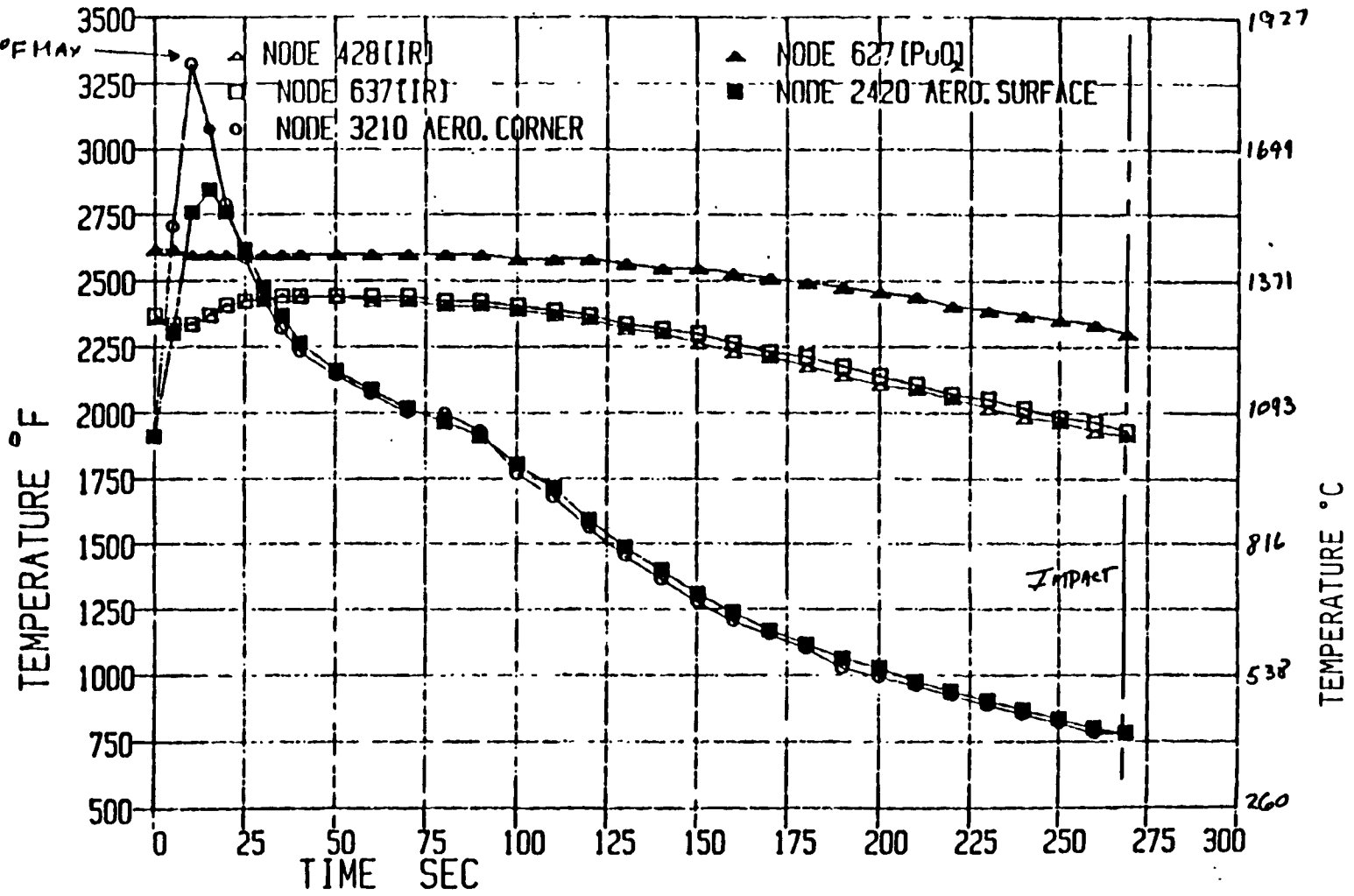


Figure I-101. Case 17 - Galileo - Steep Reentry - Stable (Early)

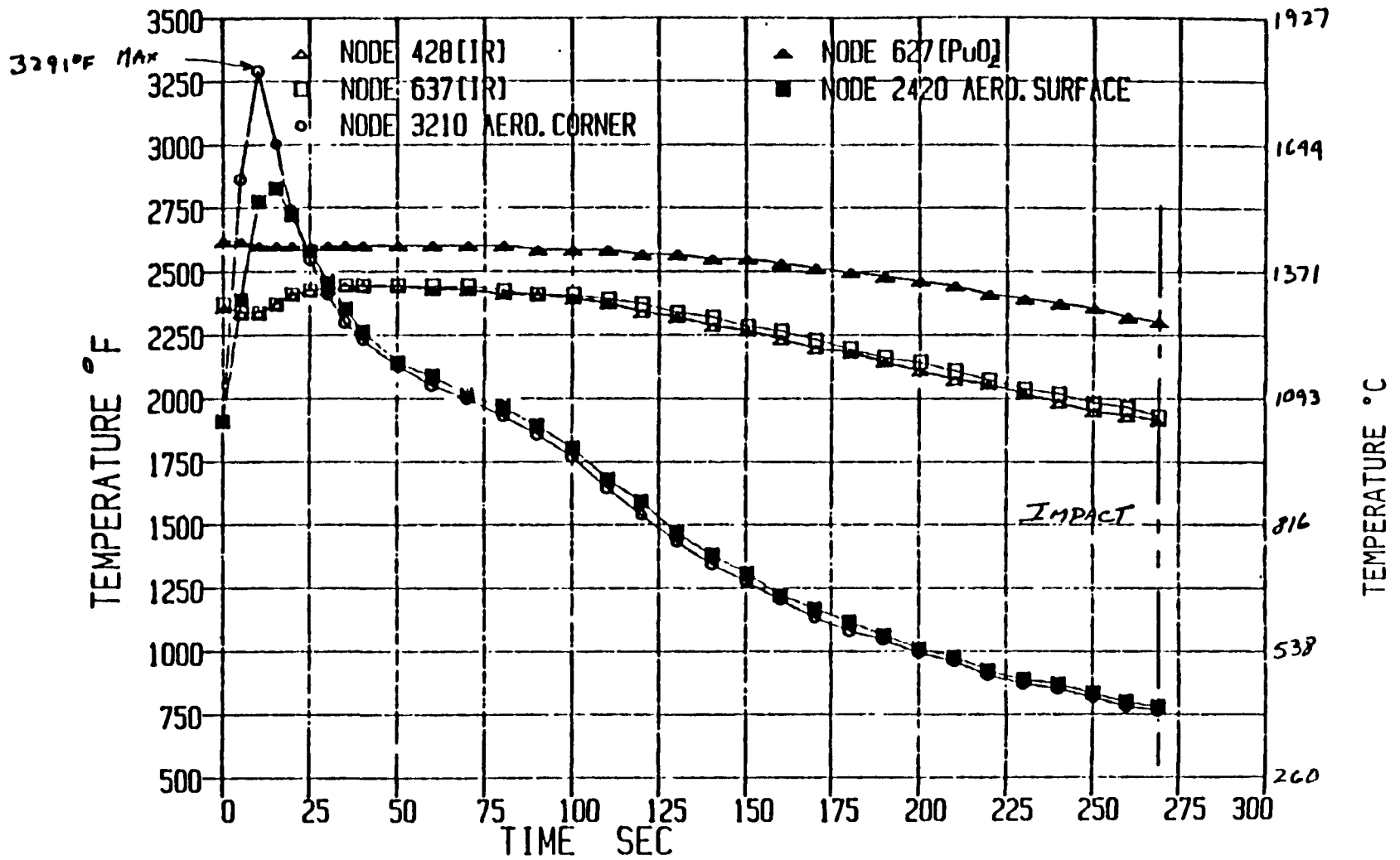


Figure I-102. Case 18 - Galileo - Steep Reentry - Stable (Late)

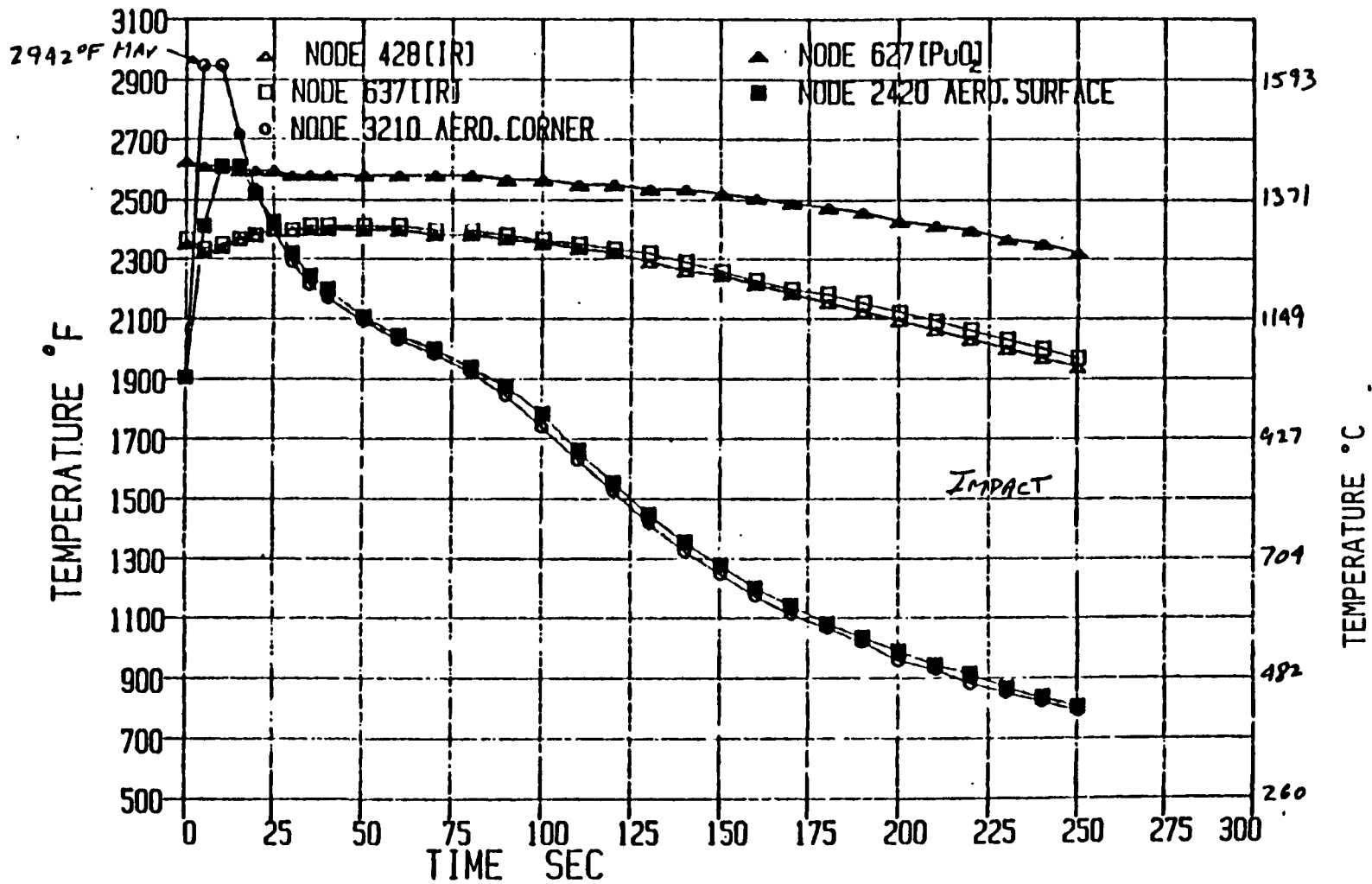


Figure I-103. Case 19 - Ulysses - Steep Reentry - Stable



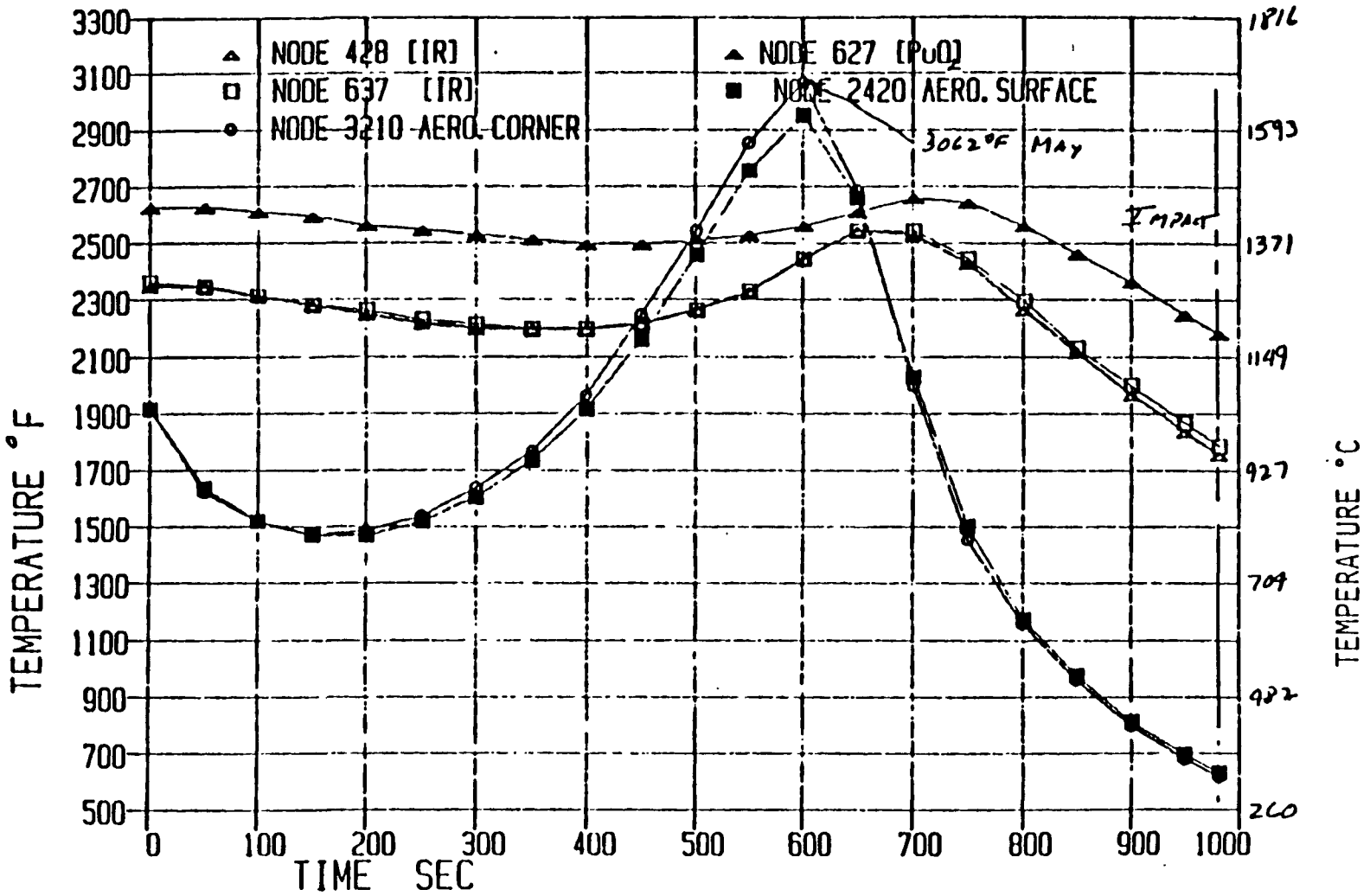


Figure I-104. Case 20 - Galileo - Orbit Decay - Stable (Early)

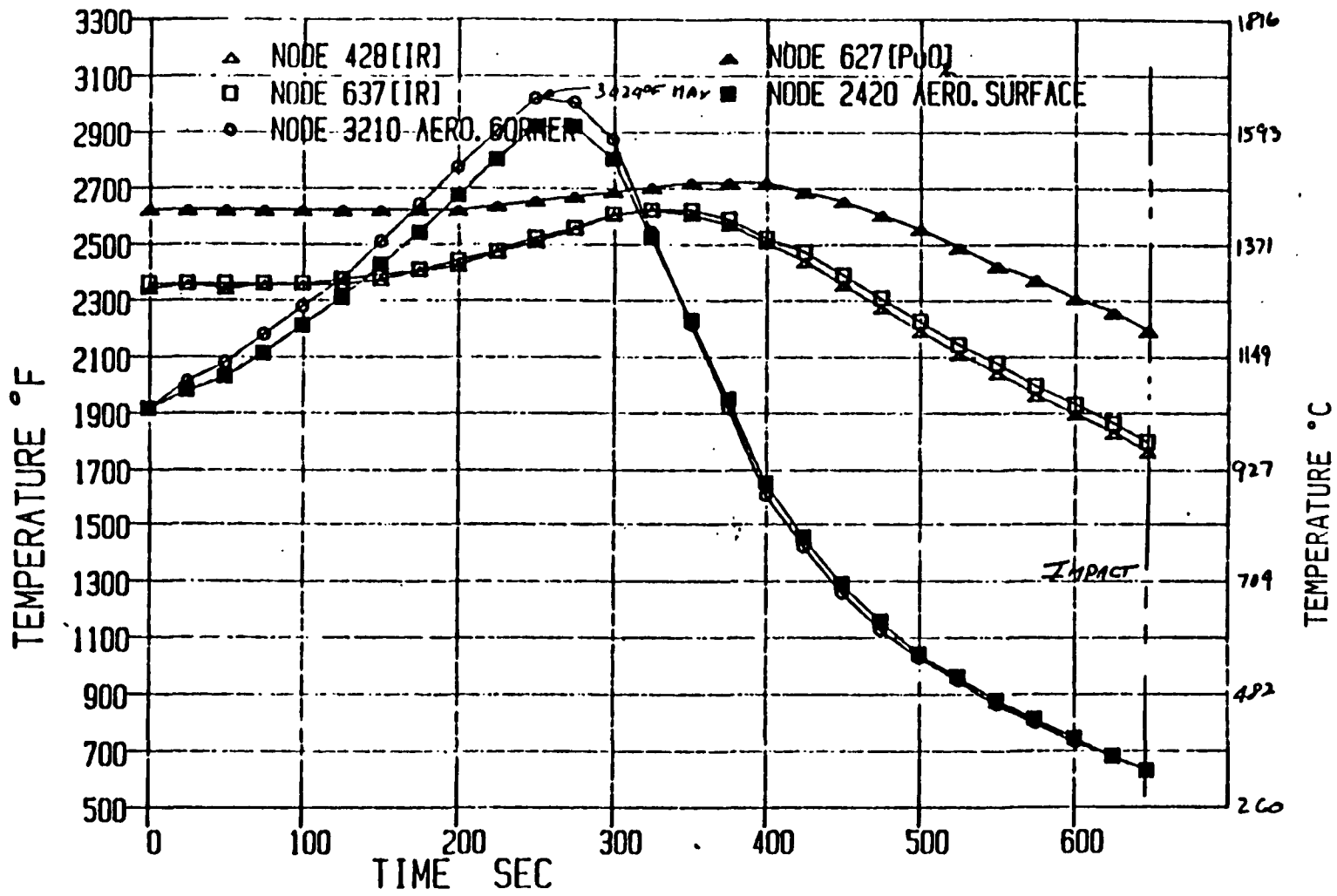


Figure I-105. Case 21 - Galileo - Orbit Decay - Stable (Late)

Table I-11. Reentry Analysis Results

I. RANDOM TUMBLING CASES ANALYZED

RE-ENTRY TYPE	INITIAL TEMP (°C)		PEAK TEMP (°C)		10000 FT IMPACT		5000 FT TEMPERATURE (°C)		SEA LEVEL		MAXIMUM RECESSION (MILS) %	
	MAX	MIN	MAX	MIN	MAX	MIN	MAX	MIN	MAX	MIN		
SUPERORBITAL, $\gamma$ max												
Galileo												
Early	1296	1289	1356	1358	1229	1191	1182	1144	1133	1095	27.2	14.7
Late	1296	1289	1363	1356	1226	1188	1179	1141	1132	1094	27.1	14.6
Ulysses-Early	1296	1289	1349	1341	1260	1229	1219	1183	1171	1133	32.9	17.8
SUPERORBITAL, $\gamma$ min <sup>1</sup>												
Galileo												
Early	1296	1289	1579 <sup>2</sup>	1573	981	950	947	917	914	883	33.2	17.9
Late	1296	1289	1579	1573	981	950	949	918	914	884	33.2	17.9
Ulysses												
Early	1296	1289	1666	1563	980	949	946	914	912	882	33.0	17.8
Late	1296	1289	1576	1571	1072	1035	1031	995	990	955	36.0	19.5
Early (-4°)	1004	998	1344	1338	1023	989	988	955	949	917	23.0	12.4
ORBITAL DECAY												
Galileo												
Early	1296	1289	1370	1364	1047	1013	1009	975	970	936	19.7	10.6
Late	1298	1289	1420	1413	1068	1032	1028	992	988	953	20.0	10.8
Ulysses												
Early	1296	1289	1411	1404	1066	1030	1026	991	986	952	20.6	11.1
Late	1296	1289	1382	1375	1055	1019	1017	982	977	943	16.1	8.7
POWERED												
Galileo												
Early	1212	1204	1241	1233	1011	979	976	946	939	909	8.1	4.4
Late	1212	1204	1230	1222	1001	969	966	935	931	900	5.9	3.2
Ulysses												
Early	1212	1204	1243	1235	1013	980	977	946	941	909	6.6	3.6
Late	1212	1204	1214	1205	959	929	928	897	896	967	0.37	0.2

- NOTES:
1. This re-entry resulted in a single skip-out of the GPHS modules with an orbit duration above 400 kft long enough for the modules to stabilize in temperature with the space vacuum sink. The resulting temperature of the fueled clads at the final entry was around 1010°C.
  2. The peak clad temperature during the final entry was 1233°C max. and 1228°C min.
  3. This value includes 15.3 mils ablation resulting from the initial pass through the atmosphere prior to the skip.

II. STABILIZED ORIENTATION CASES ANALYZED

SUPERORBITAL, $\gamma$ max												
Galileo												
Early	1296	1289	1352	1316	1172	1134	1126	1088	1077	1040	56.0	30.3
Late	1296	1289	1351	1314	1169	1132	1124	1086	1076	1039	57.0	30.8
SUPERORBITAL, $\gamma$ max												
Ulysses												
Early	1296	1289	1327	1300	1183	1147	1142	1104	1094	1057	45.0	24.3
ORBITAL DECAY												
Galileo												
Early	1296	1289	1404	1394	1067	1031	1028	993	986	952	40.0	21.6
Late	1296	1289	1444	1433	1085	1048	1044	1008	1002	967	41.0	22.2

Plots of the resulting altitude and velocity as a function of time are shown in Figures I-106 and I-107.

The nonablating aerodynamic heating was based upon the stagnation point heating for a sphere as described by Equations (5) and (6). These heating values were modified in a rather simple fashion to give an estimate of an average heating value which was assumed to be applied over the entire GIS outer surface.

The sphere-to-cylinder transformation for transverse flow was effected by multiplying the sphere stagnation point heating value by the factor 0.707. Assuming a spinning cylinder, the averaging multiplier factor used was 0.33 for Mach numbers greater than 1.0 and 1.0 for Mach numbers less than 1. When evaluating the stagnation point heating for the sphere, a radius equal to the GIS radius was used.

In other words, for Mach numbers greater than 1.,

$$q(s)_{\text{CYLINDER}} = (0.33) (0.707) q_{\text{SPH}} (0)$$

and for Mach numbers less than 1.,

$$q(s)_{\text{CYLINDER}} = (0.707) q_{\text{SPH}} (0)$$

The effects of ablation on the aerodynamics heating were treated as discussed in Paragraph I.3.4.

Heat transfer in air in the gaps between heat source components was treated as continuum conduction at all times.

A plot of selected node temperatures are shown in Figure I-108. Three nodes were chosen, lying on a common radius passing thru the geometric center of the fuel pellet. The nodes represent PuO<sub>2</sub>, iridium and graphite materials. The PuO<sub>2</sub> node lies adjacent to the iridium node and the graphite node represents the GIS outer surface.

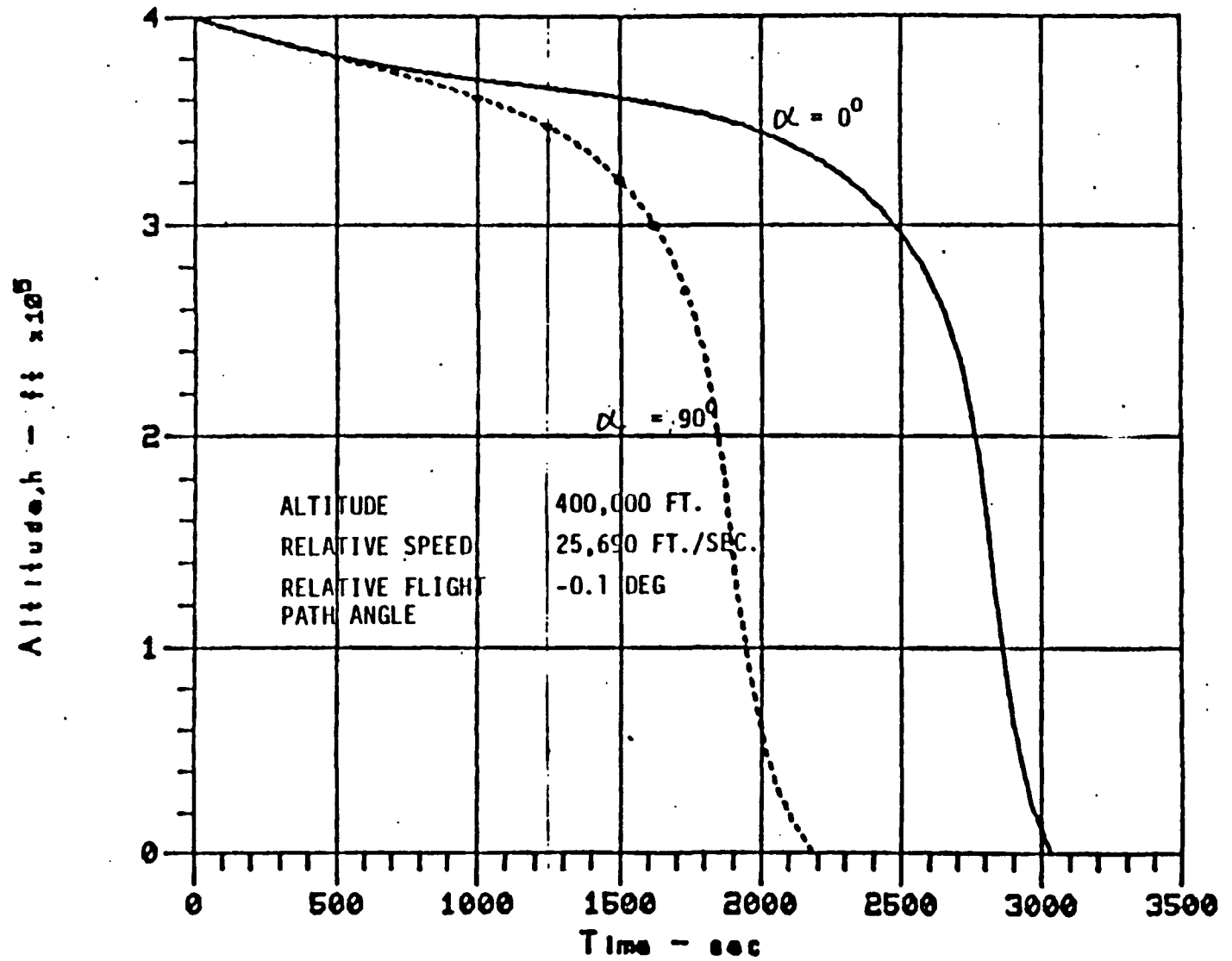


Figure I-106. GIS-Altitude

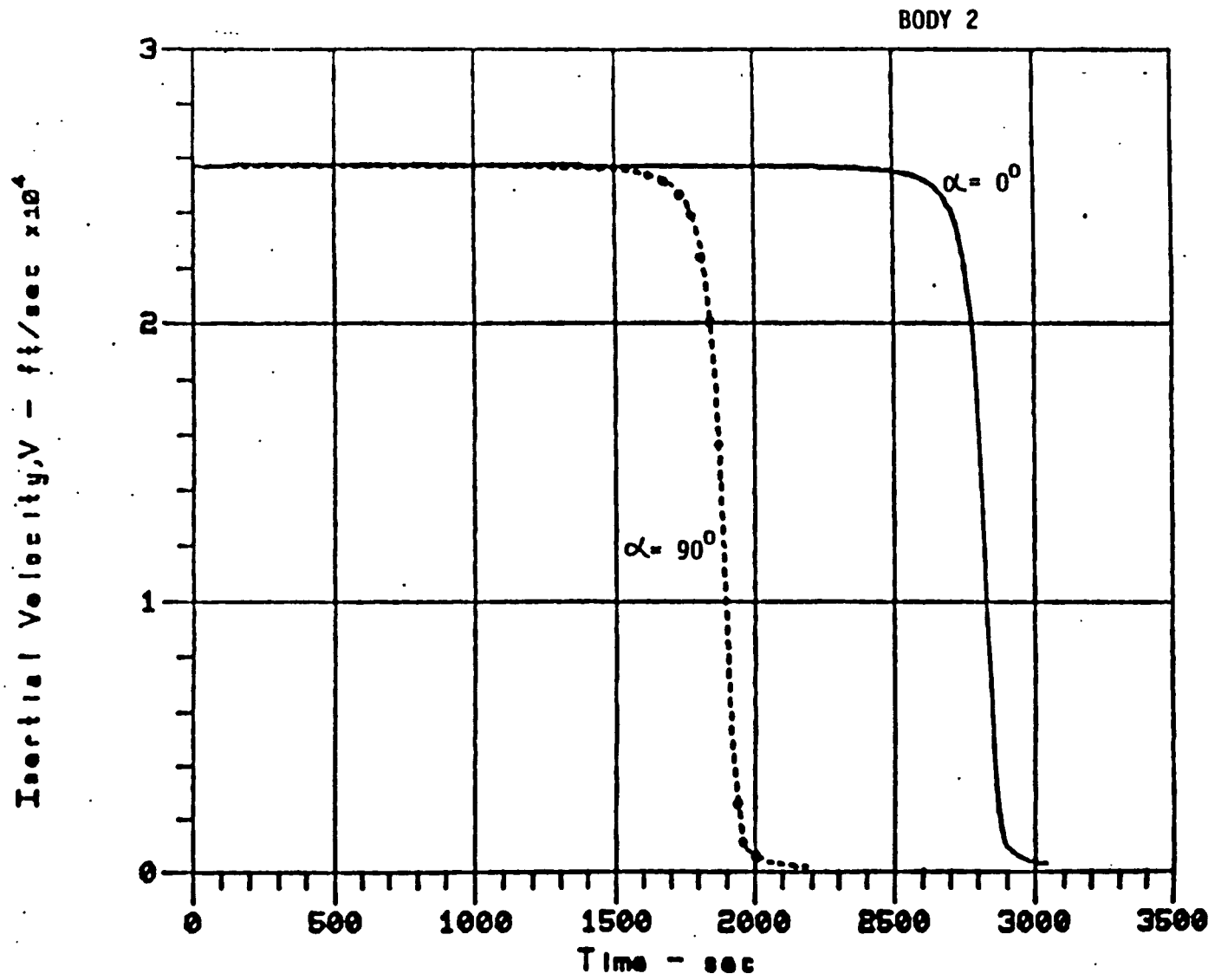


Figure I-107. GIS-Velocity

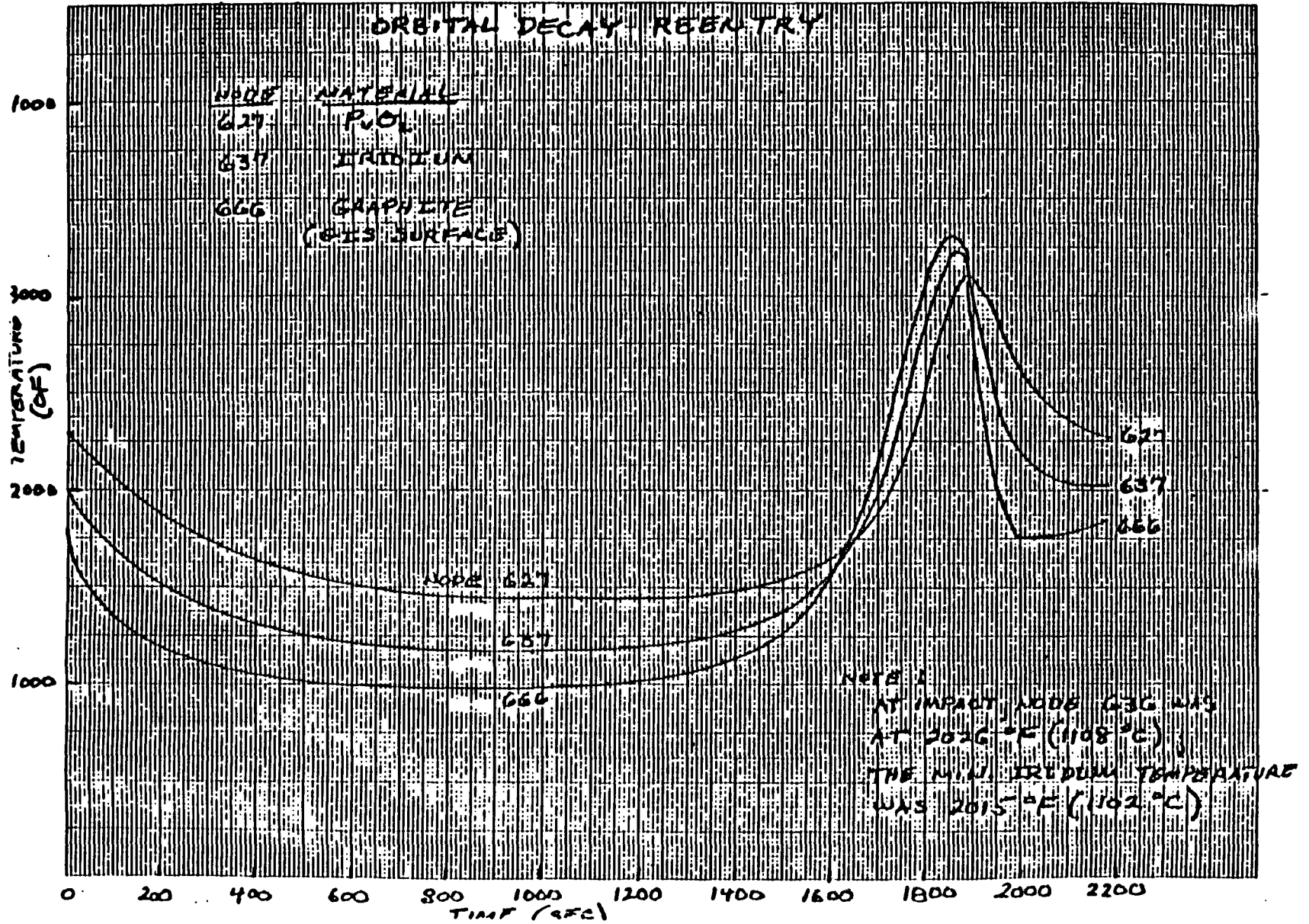


Figure I-108. Graphite Impact Shell (GIS) Orbital Decay Reentry

The recession of the graphite GIS ranged from 45 to 66 mils. The iridium temperatures ranged from 1989°F (1087°C) to 2005°F (1096°C) initially, reached peak temperatures of 3180°F (1749°C) to 3500°F (1926°C), and at impact were between 2014°F (1101°C) and 2032°F (1111°C).

#### I.4.2 FUEL PELLETT ANALYSIS

A reentry thermal analysis was performed for a single unbroken fuel pellet with its iridium clad. An Orbital Decay trajectory was investigated. The pellet was assumed to be spinning about its longitudinal axis with two different attitudes: broadside ( $\alpha = 90^\circ$ ) end-on ( $\alpha = 0^\circ$ ).

The initial trajectory conditions chosen were

Altitude	400,000 ft.
Relative Speed	25690 ft/sec
Relative Flight Path Angle	-0.1 deg.
Attitude ( $\alpha$ )	90. deg. and 0 deg.

Plots of the altitude and velocity as a function of time are shown in Figures I-109A and I-109B.

The same approach as in the case of the GIS was used to estimate an average heating rate to be applied to all points on the outer surface of the fuel pellet. The non-ablating heat transfer ratio was not corrected for any effects such as mass transfer or chemical reactions. Energy requirements for phase changes were accounted for.

The initial iridium clad temperature was set at 1094°C, a temperature which can be expected with the Active Cooling System in operation and the RTG pressurized with Xenon gas. Over the first 600 to 700 seconds of reentry, the clad temperature goes thru a broad minimum dropping to about 950°C. It then increases in temperature until at 2063 seconds into the reentry it reaches its melting point of 2450°C. At 2079 seconds, the clad was completely melted and at this point it was assumed to be removed from the fuel pellet.



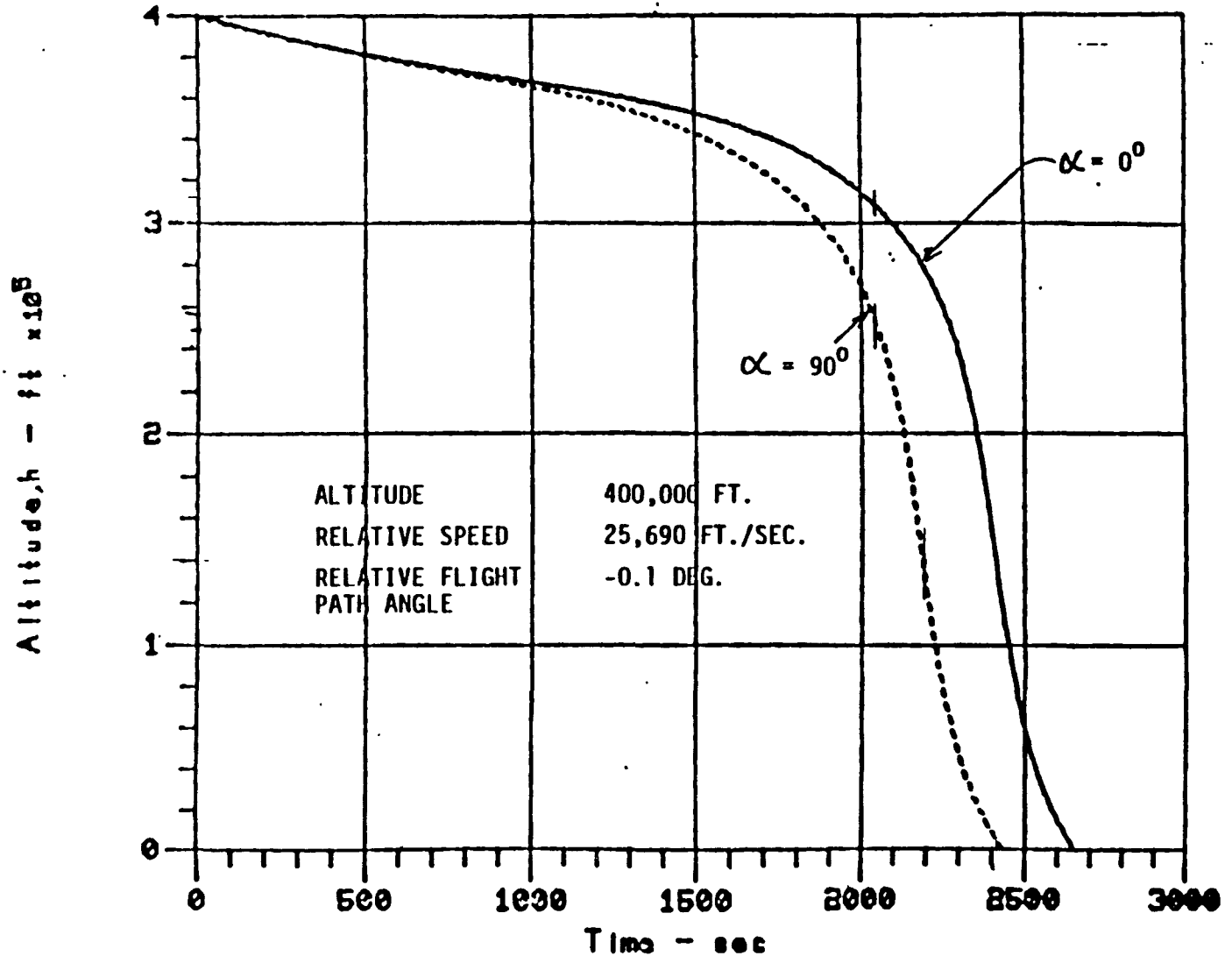


Figure I-109A. Fuel Pellet with Clad - Altitude

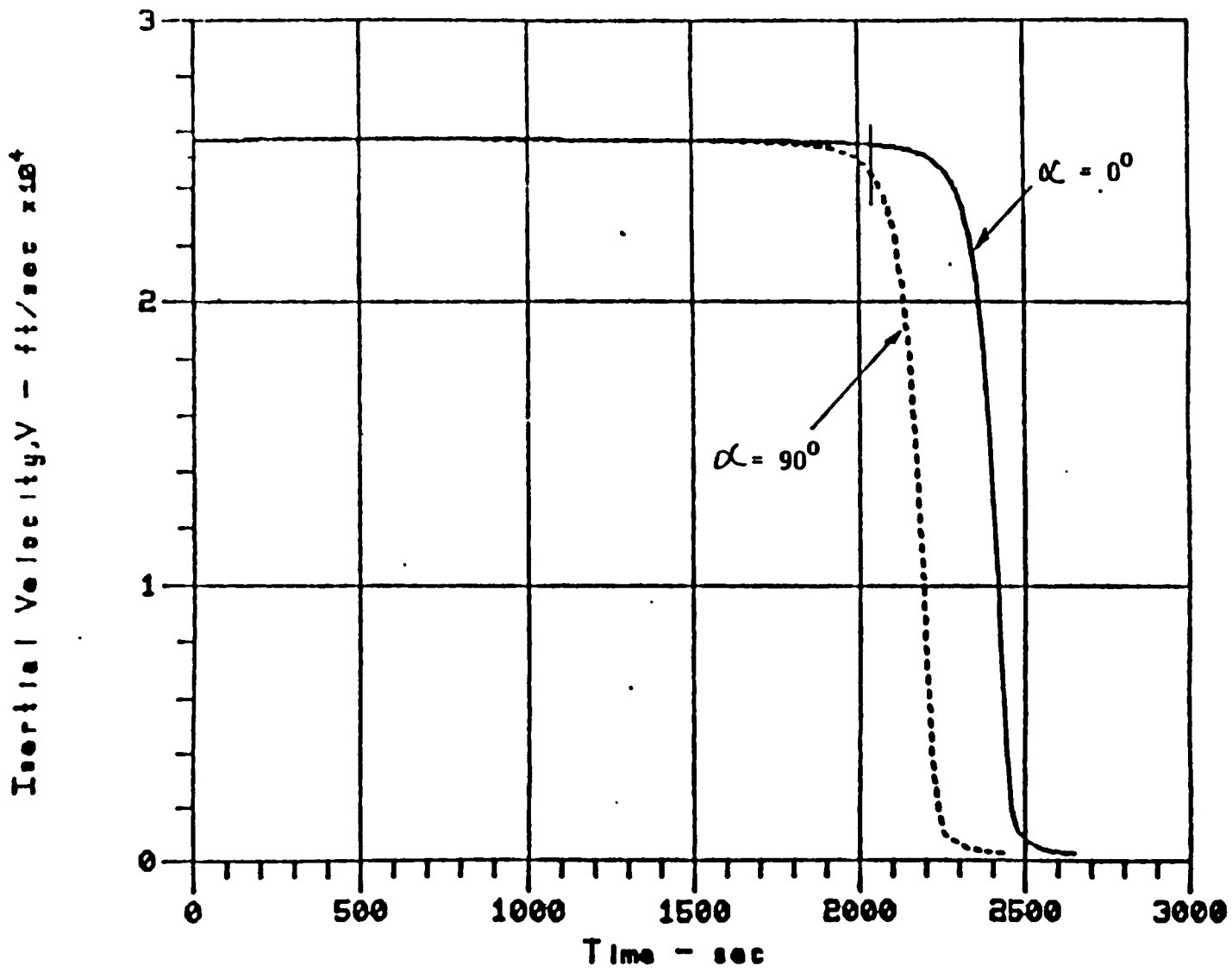


Figure I-109B. Fuel Pellet with Clad - Velocity

Up until this point, the clad temperature was always high enough such that the iridium oxides formed either sublimed at a high rate or only existed as gases. Consequently, it was assumed that the iridium emissivity was not affected by the oxidation process.

At the time the clad had completely melted, an outer layer of fuel about 15 mils thick had also reached its melting point, which was set at 2400°C. Upon removing the clad, the outer fuel surface was free to radiate to space. Given its very high emissivity as compared to the clad emissivity, the temperature of the fuel outer surface rapidly dropped below its melting point and remained well below that temperature for the remainder of the trajectory. At impact, the fuel temperature varied from about 246°C at its outer surface to about 1080°C at its center.

An estimate was made of the  $\text{PuO}_2$  loss to the atmosphere due to vaporization of the fuel after the clad was removed. It was assumed that the vapor was removed from the vicinity of the fuel surface as it was formed. This simplifying assumption will result in an upper limit to the fuel loss for the temperature history as calculated by the reentry analysis. The vaporized fuel was found to be 0.001 lb.

A plot of the calculated iridium clad and  $\text{PuO}_2$  outer surface temperatures are shown in Figure I-110.

### I.5 THERMAL STRESS ANALYSIS - FIXED REENTRY ATTITUDE

This section describes the thermal stress analyses of the GPHS Aeroshell for each of three selected trajectories. These are the same trajectories that were analyzed for the tumbling attitude (hypersonically) of the GPHS and reported previously in the Galileo and Ulysses (nee International Solar-Polar) USAR (GESp-7186, April 1984). Since the peak temperatures and gradients for the late release condition for the Ulysses prompt reentry were not as great as those for Galileo with the GPHS tumbling attitude, the late release condition also was not considered for the Ulysses prompt reentry with the GPHS stable attitude. For each trajectory, an analysis was performed for three separate times during the reentry. The margin of safety for each element are first

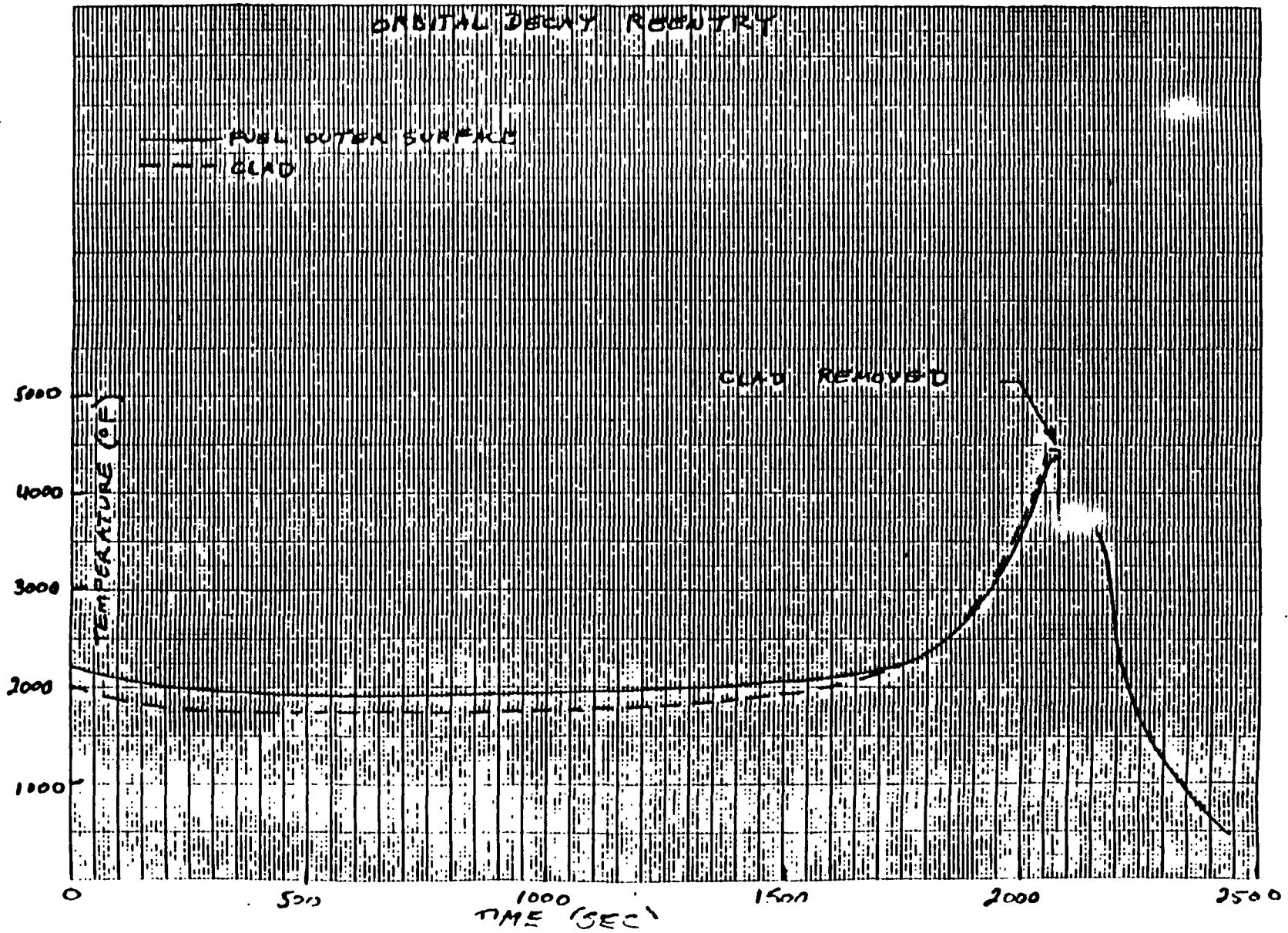


Figure I-110. Fuel Pellet/Clad Orbital Decay Reentry

calculated using conservatively extrapolated temperature dependent properties previously used by APL (Reference 1). The minimum margin of safety versus time was calculated for each of the three times during each trajectory for both tension and compression. The use of these material properties lead to negative margins of safety in tension. Based on tensile test results performed on 3D High Axial Carbon-Carbon Composite at temperatures up to 4500°F, modified temperature dependent properties for FWP were generated. With the modified material properties, the margins of safety based on both stress and strain were positive. The applicability of this procedure was verified during discussions with the principal author of the report which provided the basic (unextrapolated) data that was used in the APL analysis.

#### I.5.1 AEROSHELL MODEL AND ANALYSIS

Taking advantage of symmetry one-half of the aeroshell was modeled. A finite element model was constructed (of the half aeroshell) consisting of 1550 solid elements. Figure I-111 shows the model and identifies the nodal and element layers. Figures I-112 through I-118 show the location of each of the elements. As shown, the aeroshell cap was not modeled. The minimum clearance between the pitch diameters in the body and cap threads is 0.003. In order to transfer shear from one member to the other, the threads must touch firmly. During the steep angle reentry, the thermal analysis has shown that the cap is cooler than the surrounding aeroshell body. Under this condition, the cap will actually loosen relative to the aeroshell body. For this reason, the cap was not included as a structural member.

The temperatures during reentry as a function of time were calculated using the heat transfer program, THTD. Since the nodal points of the structural model did not coincide with the locations at which THTD calculated the temperatures, it was necessary to write a program which would extrapolate and interpolate to assign a temperature to each nodal point. MSC NASTRAN was used to calculate the stresses resulting from the temperature distributions. Another program calculated the allowable stresses associated with the element temperature. This allowable and the calculated stress were used to determine the margin of safety, the minimum margin of safety in each direction and the element in which the minimum margin of safety occurred.

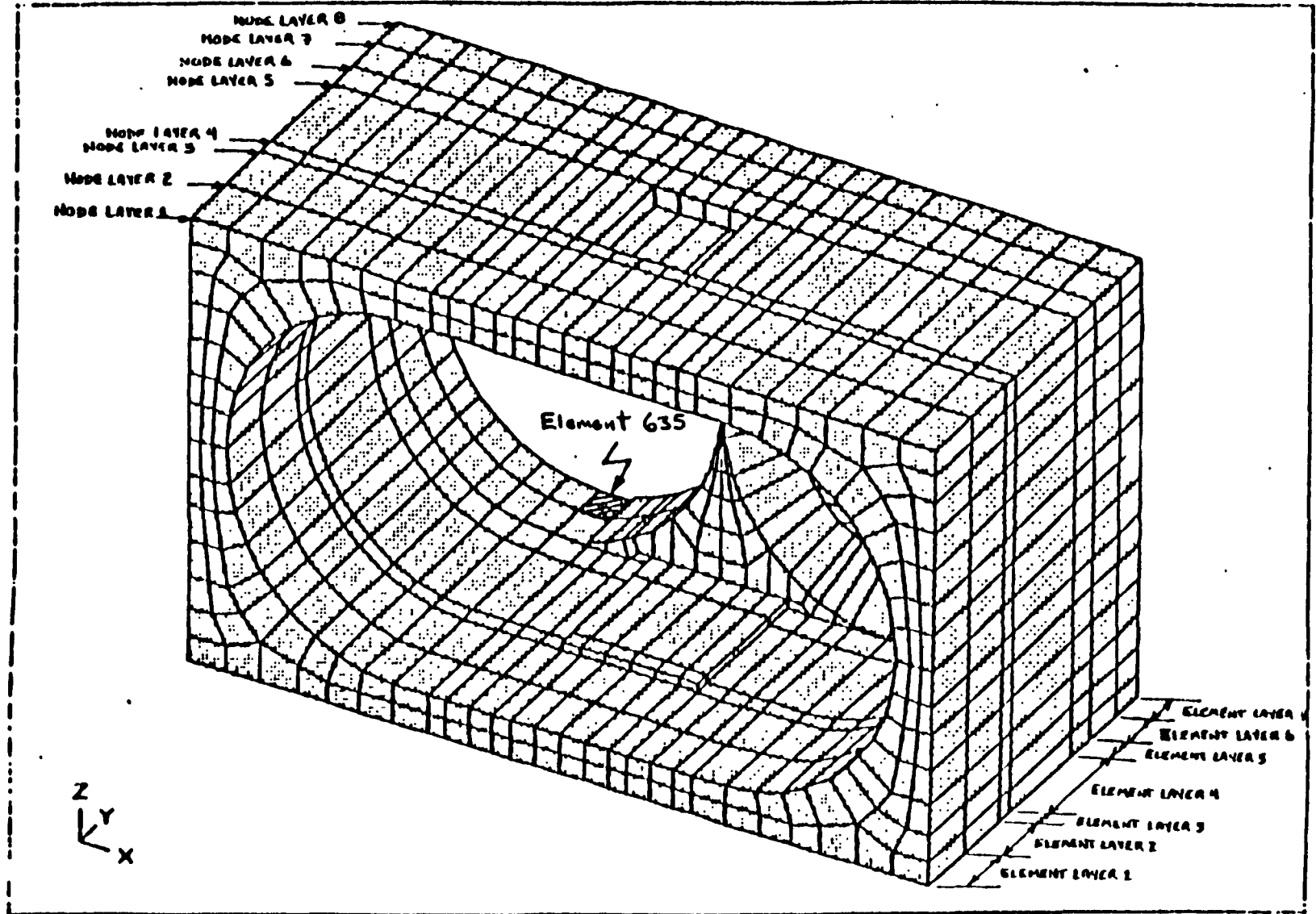


Figure I-111. Output Display

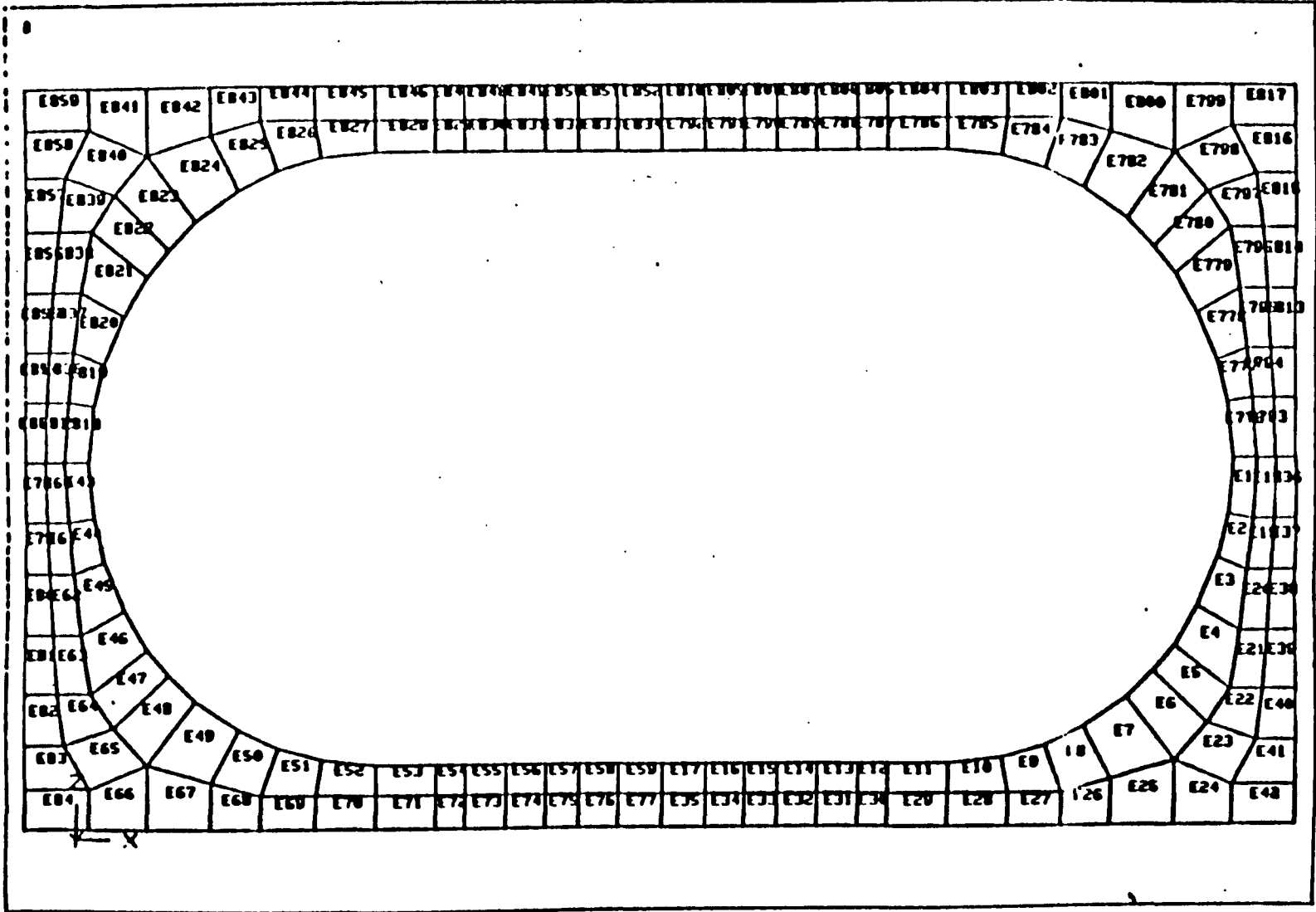


Figure I-112. Model Creation

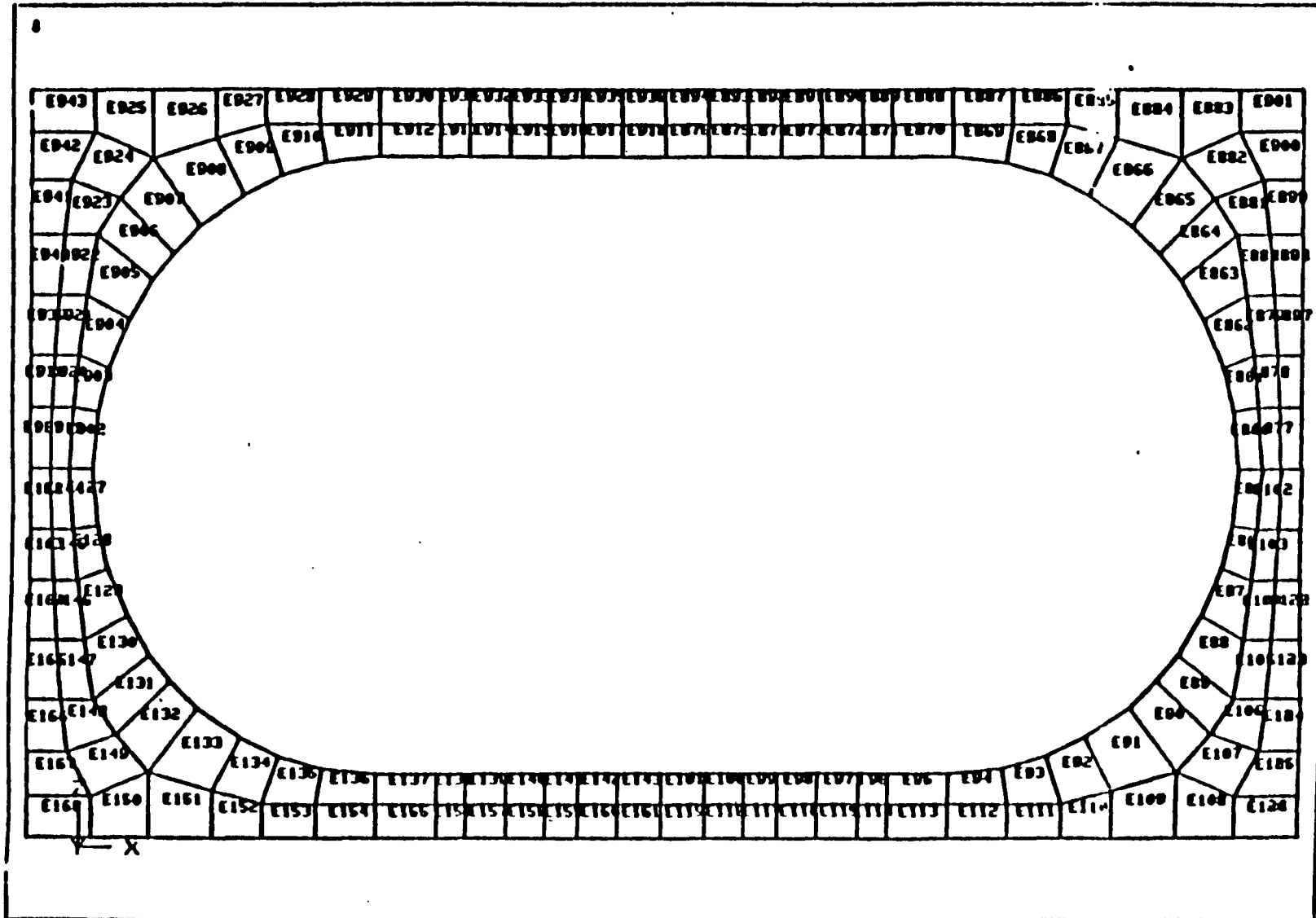
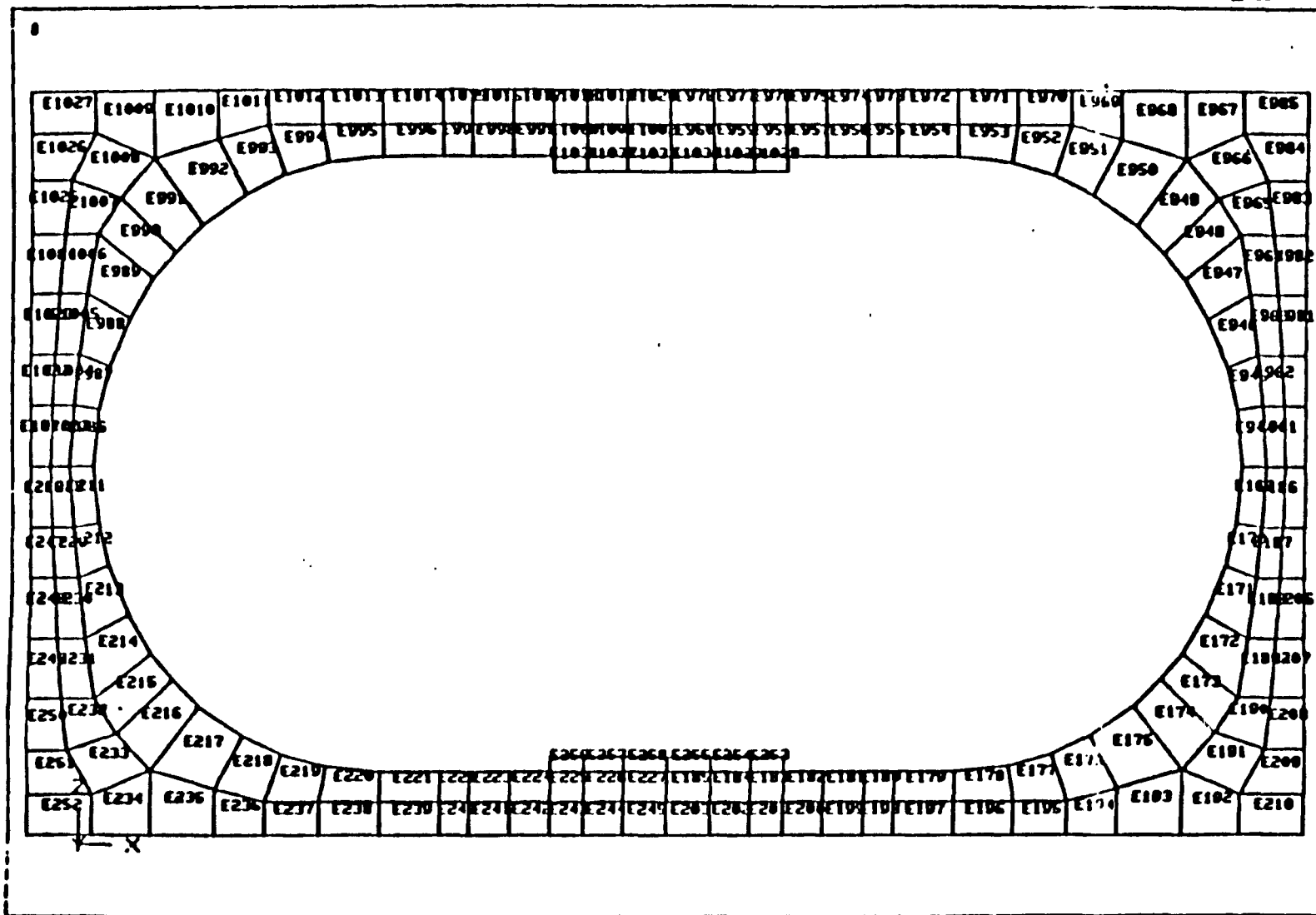


Figure I-113. Model Creation





I-185

MP2849/1984C-805/JD

Figure I-114. Model Creation

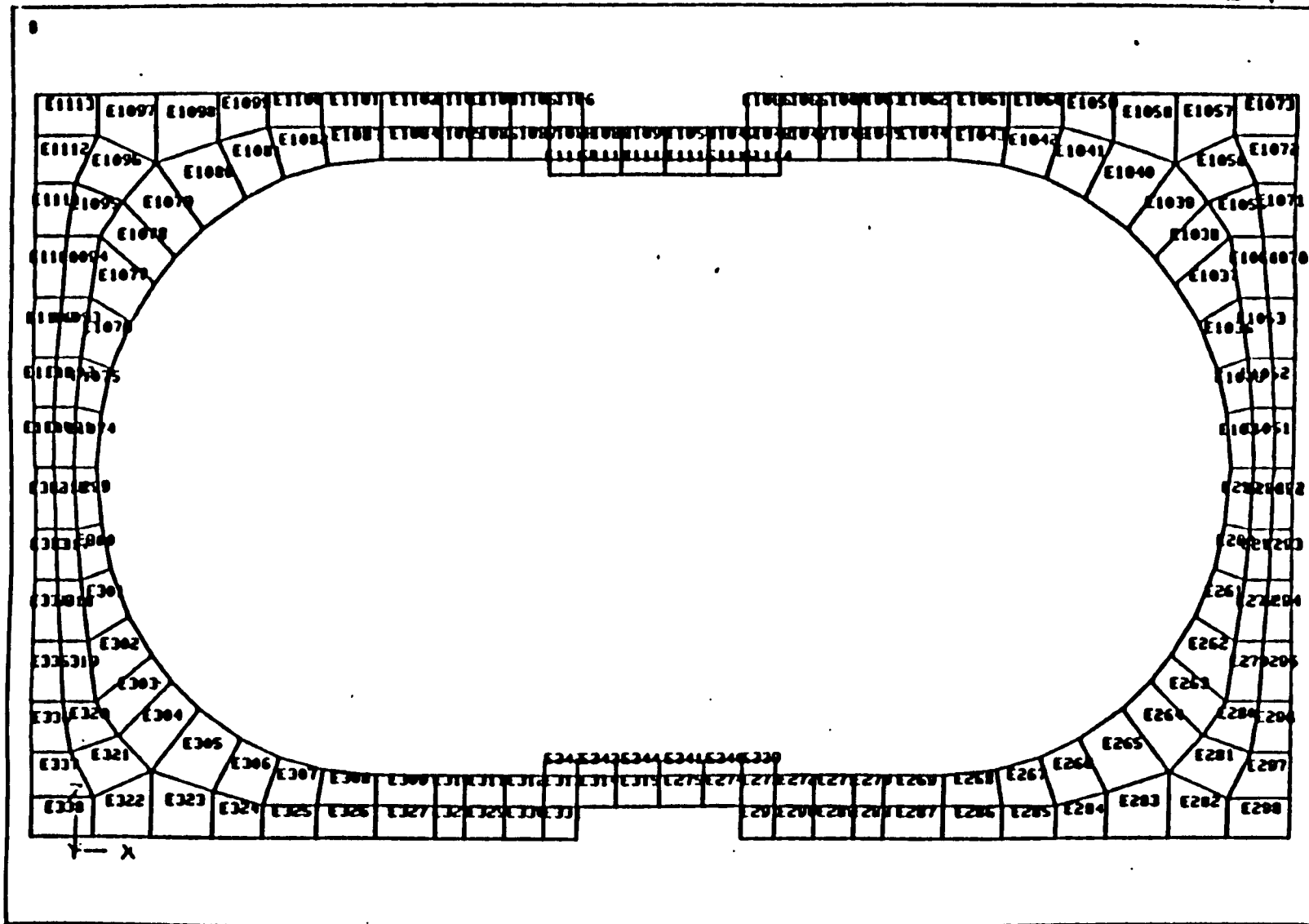
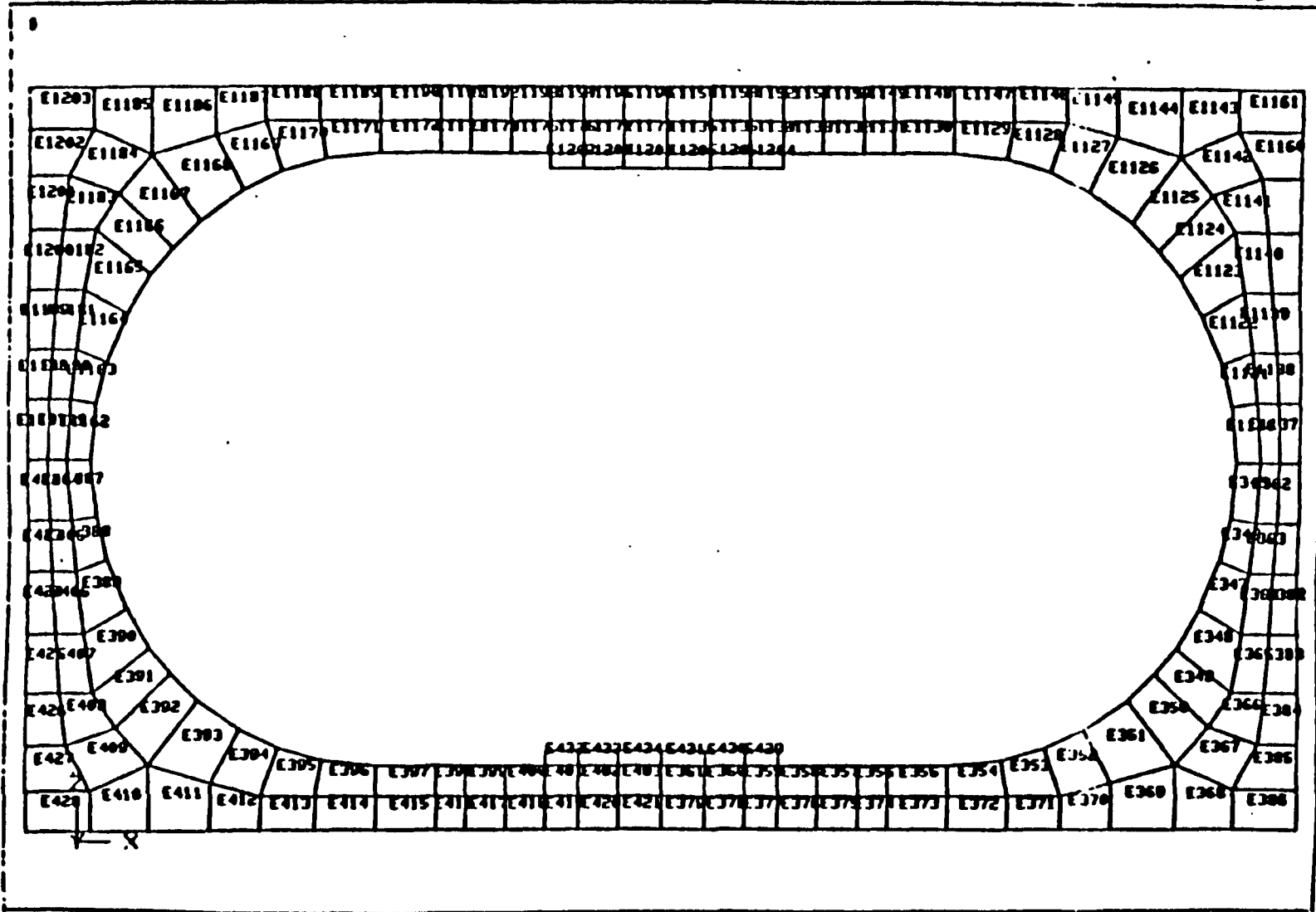


Figure I-115. Model Creation.



I-187

WP2849/1984C-805/JD

Figure I-116. Model Creation

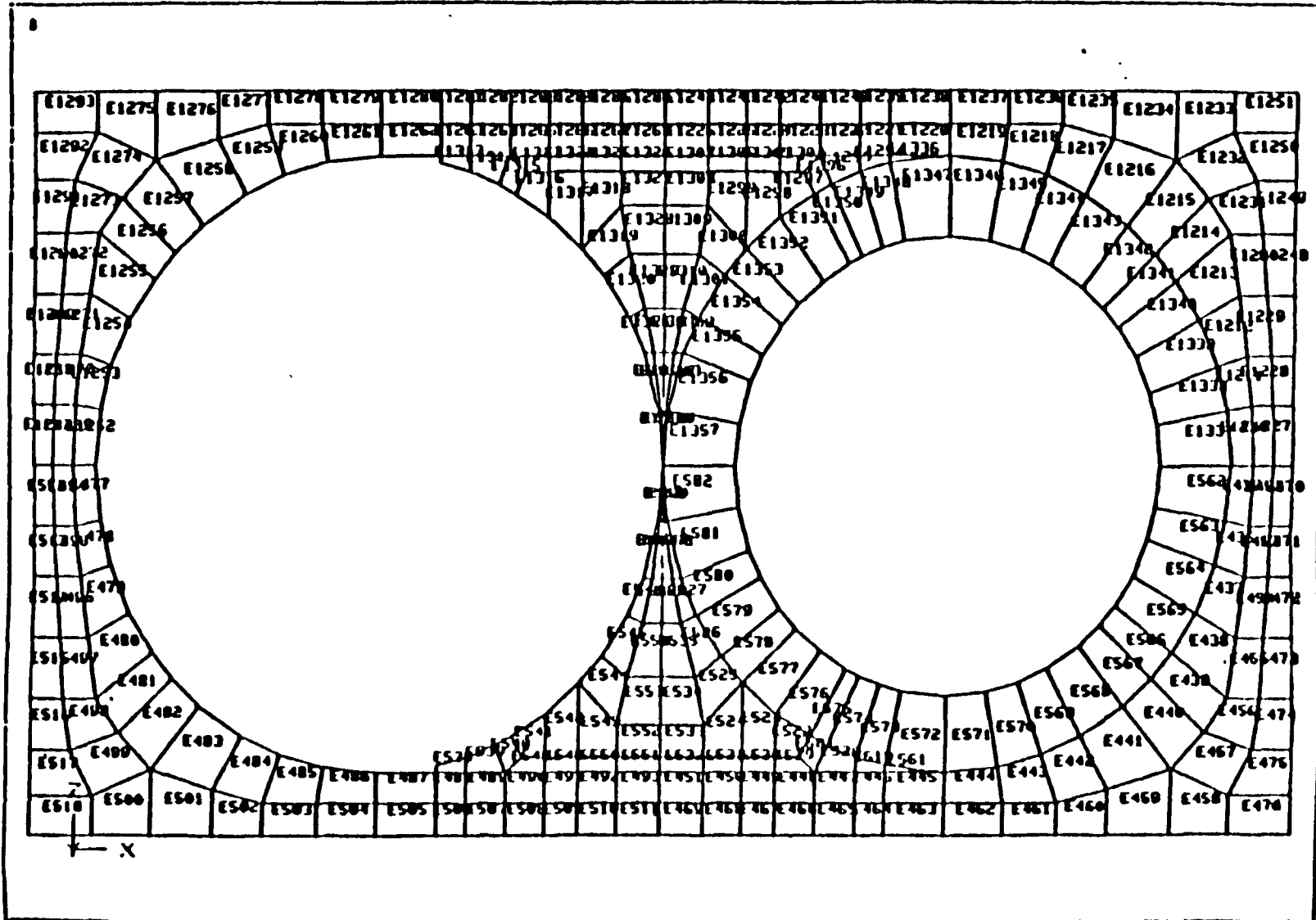
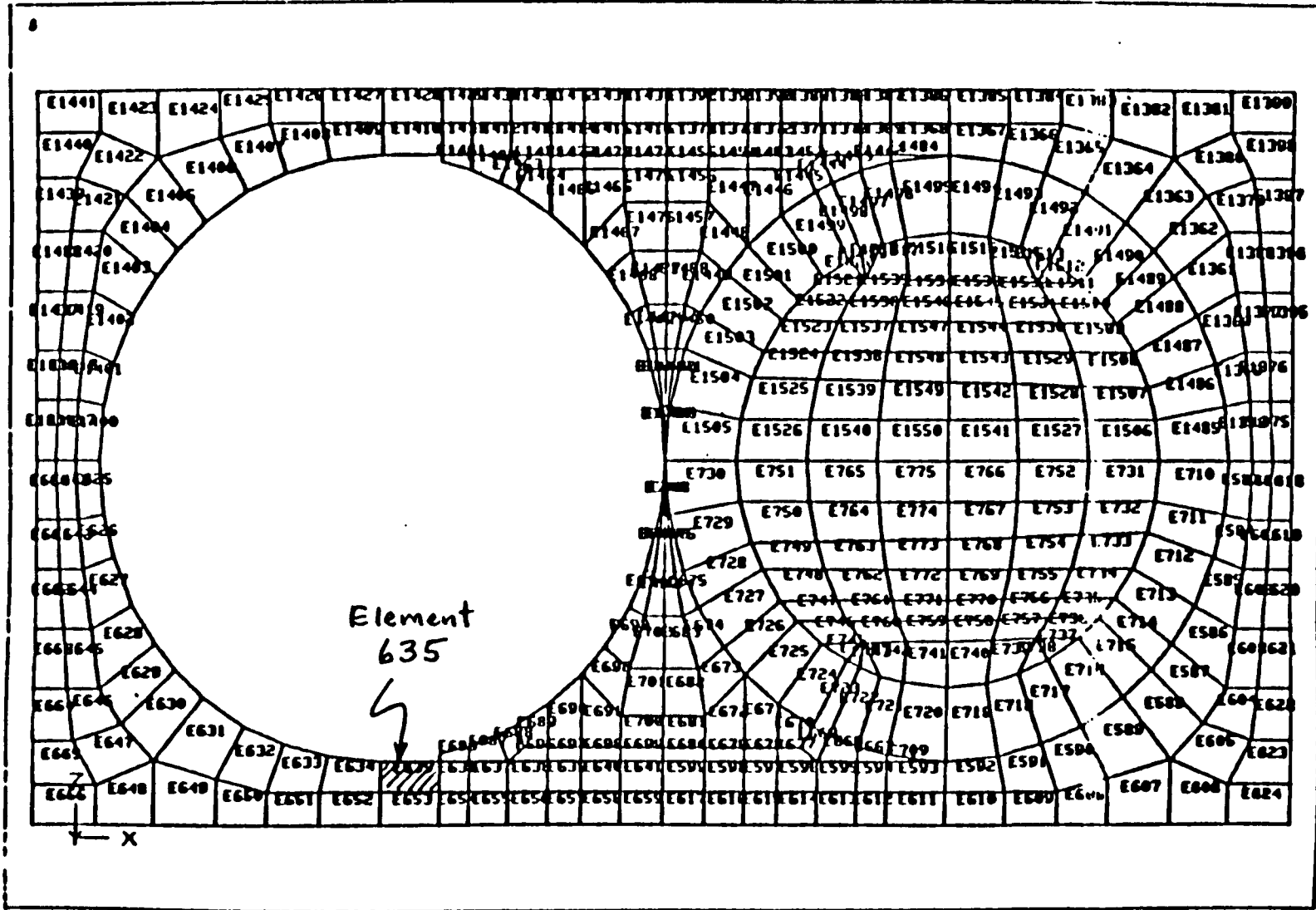


Figure I-117. Model Creation



I-189

WP2849/1984C-805/JD

Figure I-118. Model Creation

Aerodynamic and inertial loads were not included in these analyses. In previous analyses in the Galileo and Ulysses USAR, the stresses due to these effects were found to be small compared to the thermal stresses. Inclusion of these loads would tend to relieve the peak thermal stresses calculated in element 635.

### I.5.2 TRAJECTORY DATA

The three trajectories used for the aeroshell thermal stress analysis are shown in Table I-12. For each of these three trajectories, thermal stresses were calculated for three different times.

Table I-12. Trajectory Data

Case No.	Mission	Type	Altitude (Ft.)	Inertial Speed (Ft/Sec)	Inertial Path Angle (Deg)
17	Galileo	Steep	273,000	36104	-38.79
18	Galileo	Steep	253,000	36113	-38.76
19	Ulysses	Steep	210,000	36000	-53.0

### I.5.3 ANALYTICAL RESULTS

The results of the thermal stress analyses were compared to the temperature dependent material properties used by APL which conservatively extrapolated these properties beyond the temperature range of the available data. The minimum margins of safety using these material properties had negative values due to tensile stresses in the x-direction only and in only about eight (8) elements centered about element No. 635. (see Figures I-111 and I-118) and two (2) elements diametrically opposite this element. In each case, element No. 635 had the smallest (negative) margin of safety. The margins of safety versus time into the reentry are shown on Figure I-119 for this conservative evaluation. The minimum margins of safety calculated using these material

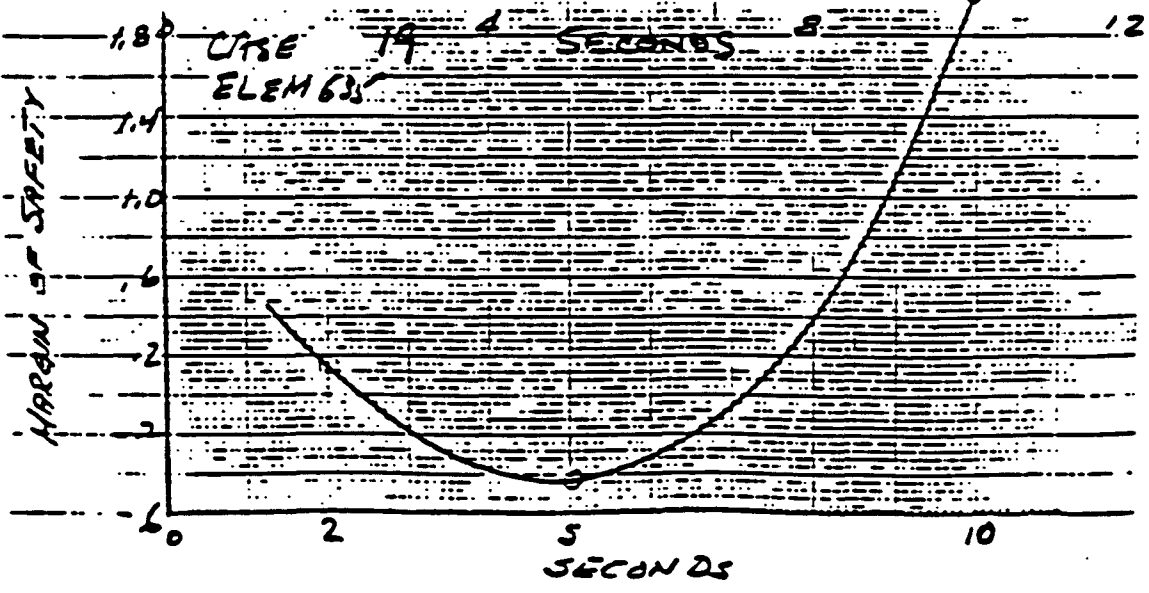
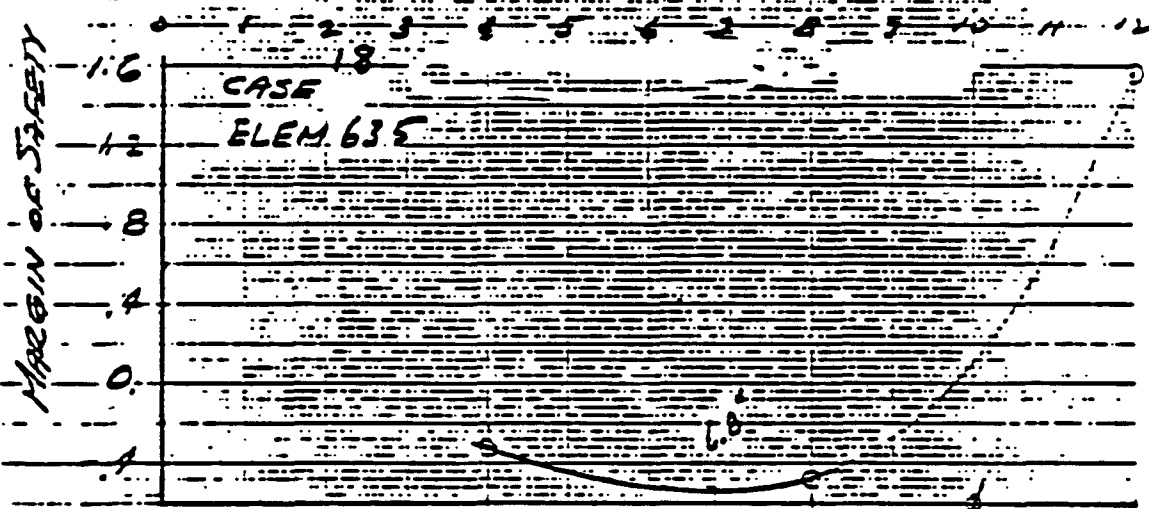
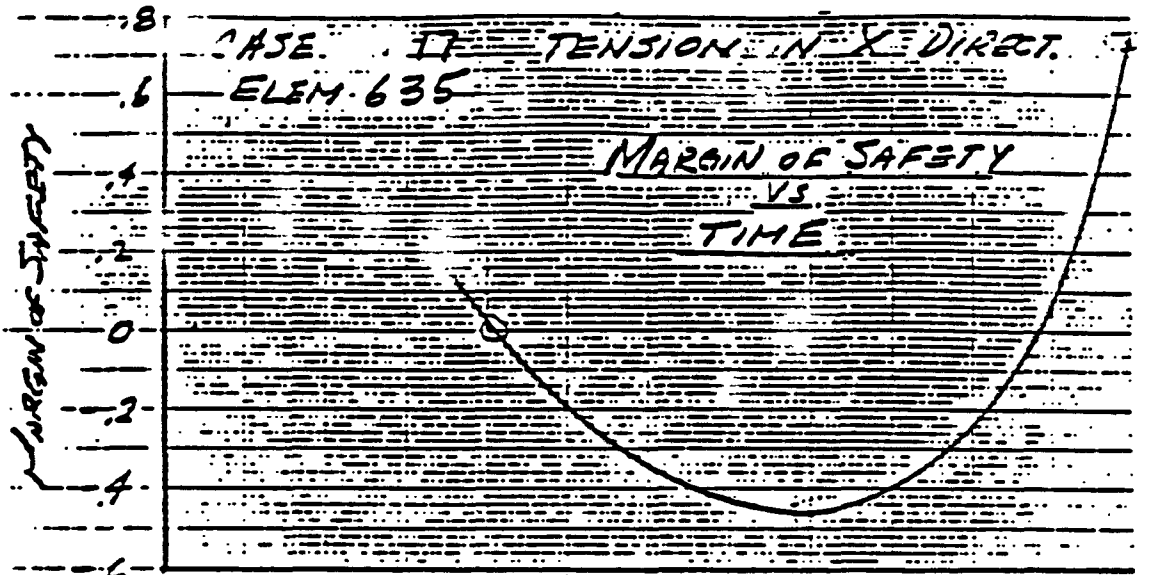


Figure I-119. Margin of Safety vs. Time

properties were negative, indicating that a tensile failure could occur. These minimum margins of safety versus time in the reentry are shown in Figures I-119 through I-122 for tensile stresses and in Figures I-123 through I-125 for compressive stresses.

As shown on these plots, the times selected did not always agree with the minimum margin of safety as shown on the graphs. The original intent of these graphs was to select the time during reentry which resulted in the smallest margin of safety and then to reanalyze the aeroshell for the stresses occurring at that particular time. As seen from Figure I-119, for the element of most interest (element 635), the times did bracket the minimum margin of safety and, in two of the cases selected for analysis, actually appear to be the minimum point. Since these margins of safety in tension were negative, it was decided that it was more productive to determine the degree of conservatism in the allowable stresses originally used.

The material properties (based on SORI tests - Reference I-34) originally used were highly conservative in that the tensile strength was shown to peak at about 2000°F and then start to decrease based on the Air Force P4 data available. Tests of other carbon-carbon composites show increasing strength up to the maximum test temperature of 4500°F in the X, Y directions\*. Figure I-126 compares tensile test data from Reference I-36 of 3D - High Axial carbon-carbon composite at temperatures up to 4500°F in the X, Y directions with the tensile strength versus temperature originally assumed for FWPF. Figure I-127 is a similar comparison for the Z direction.

---

\* Reference 2 (SORI) deliberately did not extrapolate tensile strength data beyond 2000°F. Recent private communications with the principal author of Reference I-34 substantiated non-degradation at strengths up to at least 4500°F. Also the GE Reentry Systems understanding of the excellent resistance of carbon/carbon composites to thermal stress failure of nose tips during reentry was confirmed (See Reference I-35, for example).



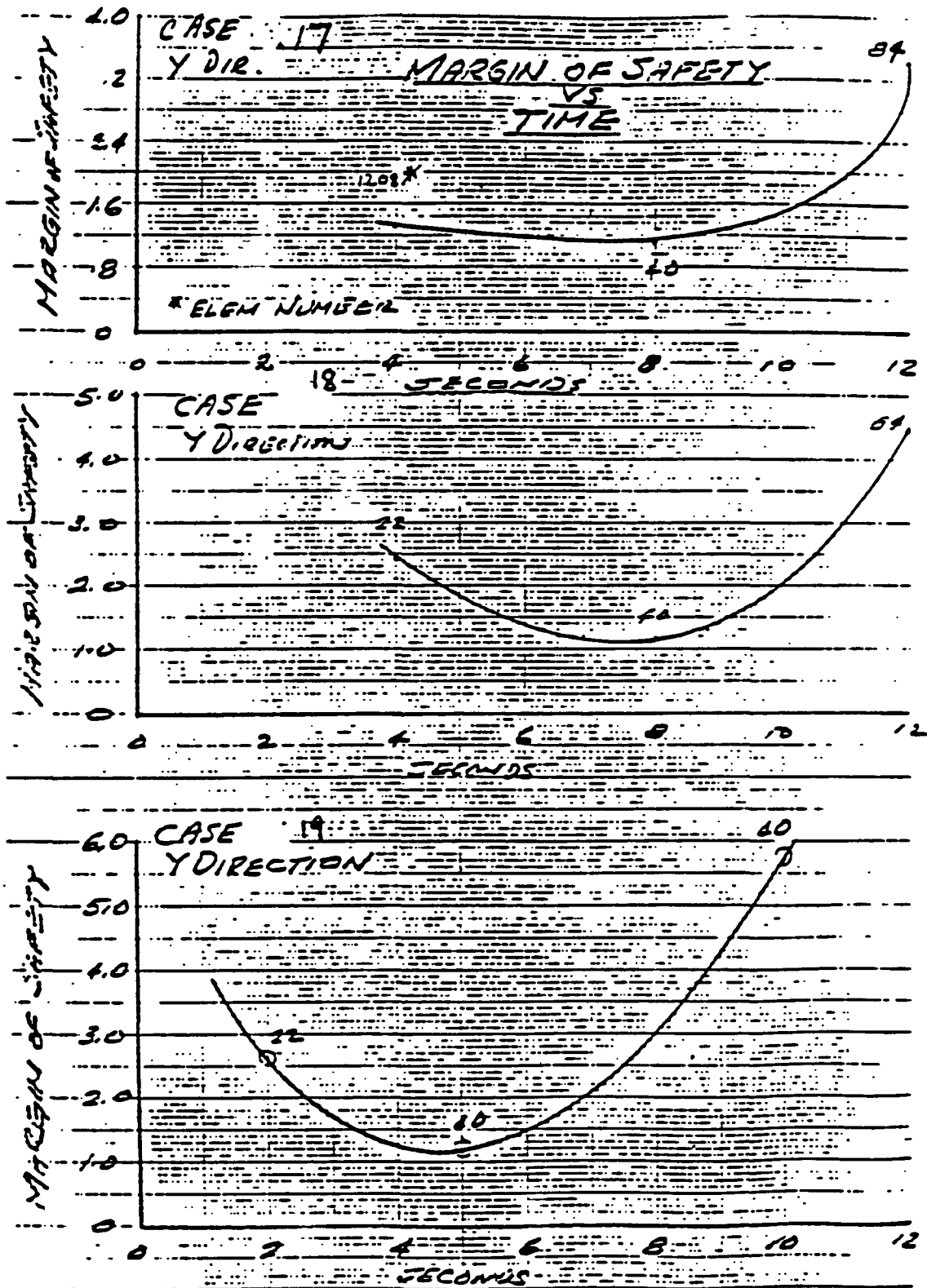


Figure I-120. Margin of Safety vs. Time

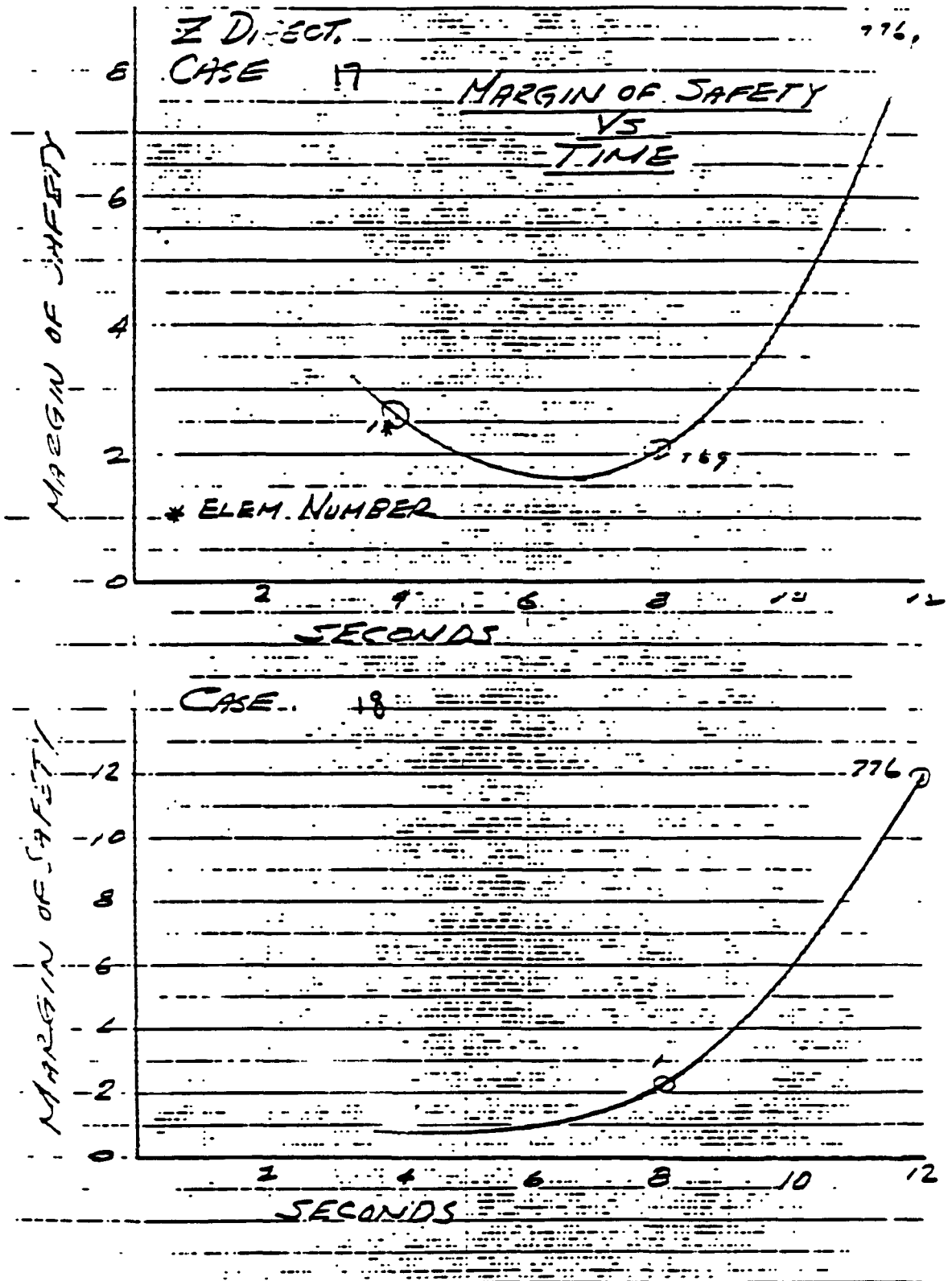


Figure I-121. Margin of Safety vs. Time

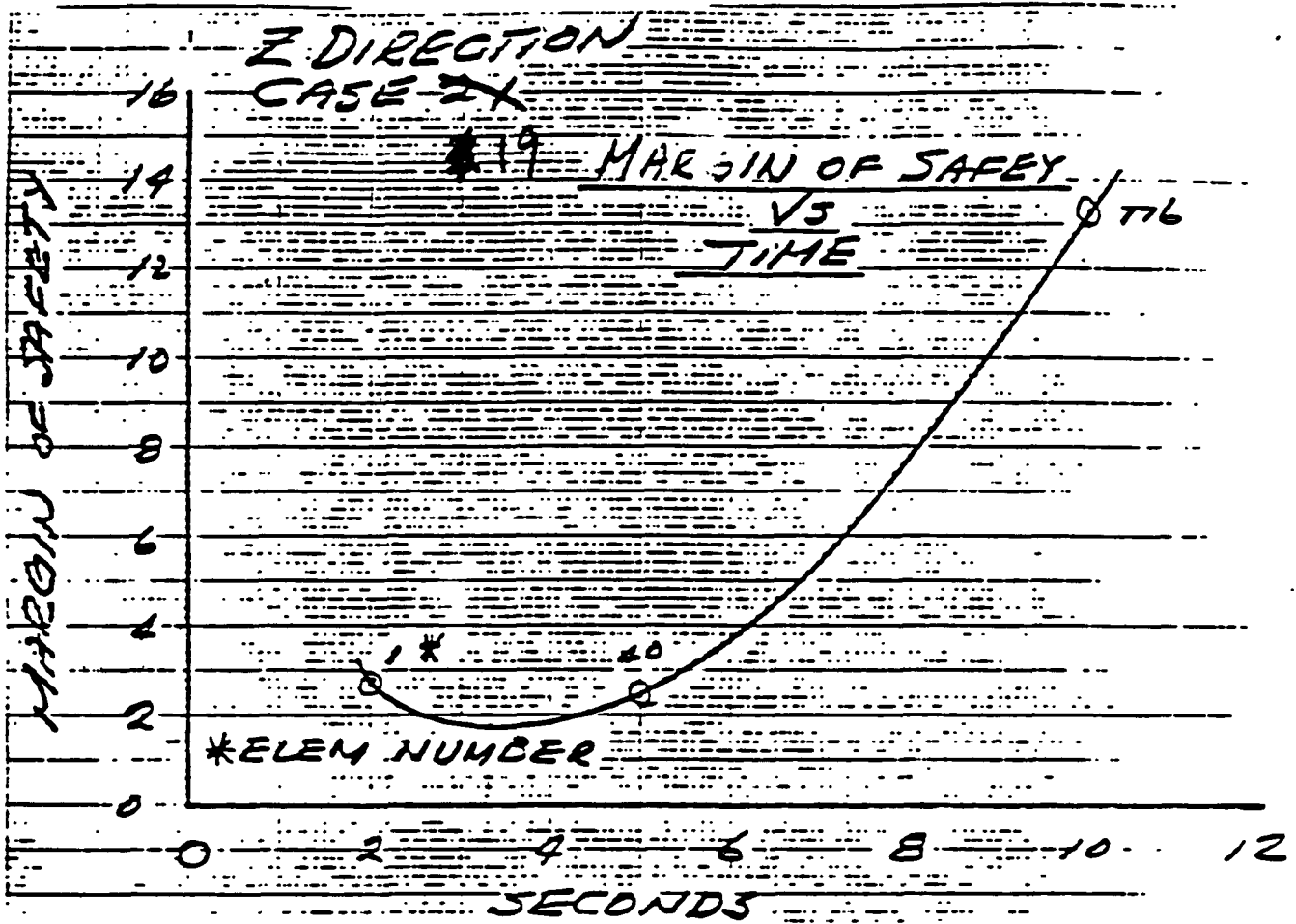


Figure I-122. Margin of Safety vs. Time

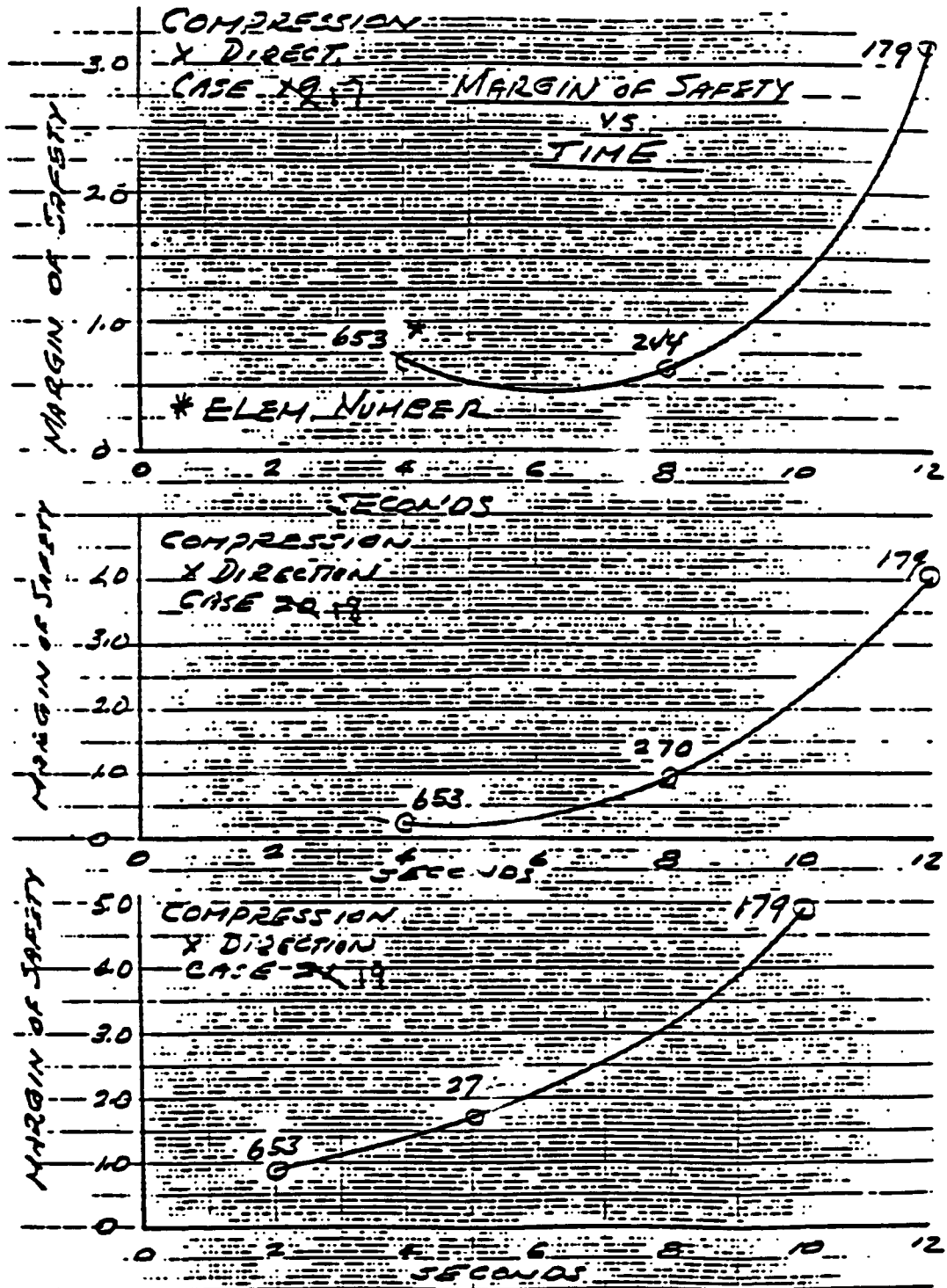


Figure I-123. Margin of Safety vs. Time

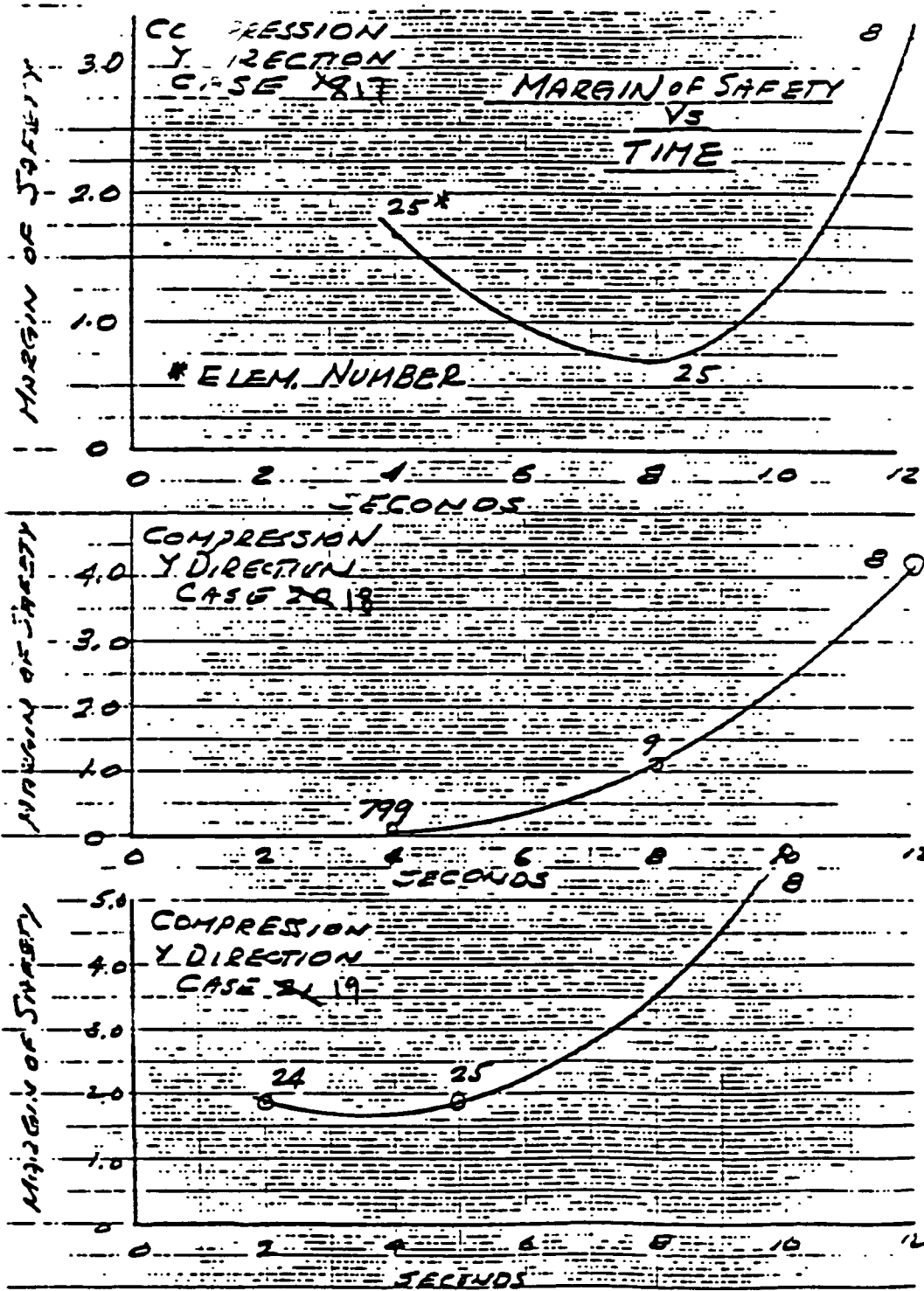


Figure I-124. Margin of Safety vs. Time

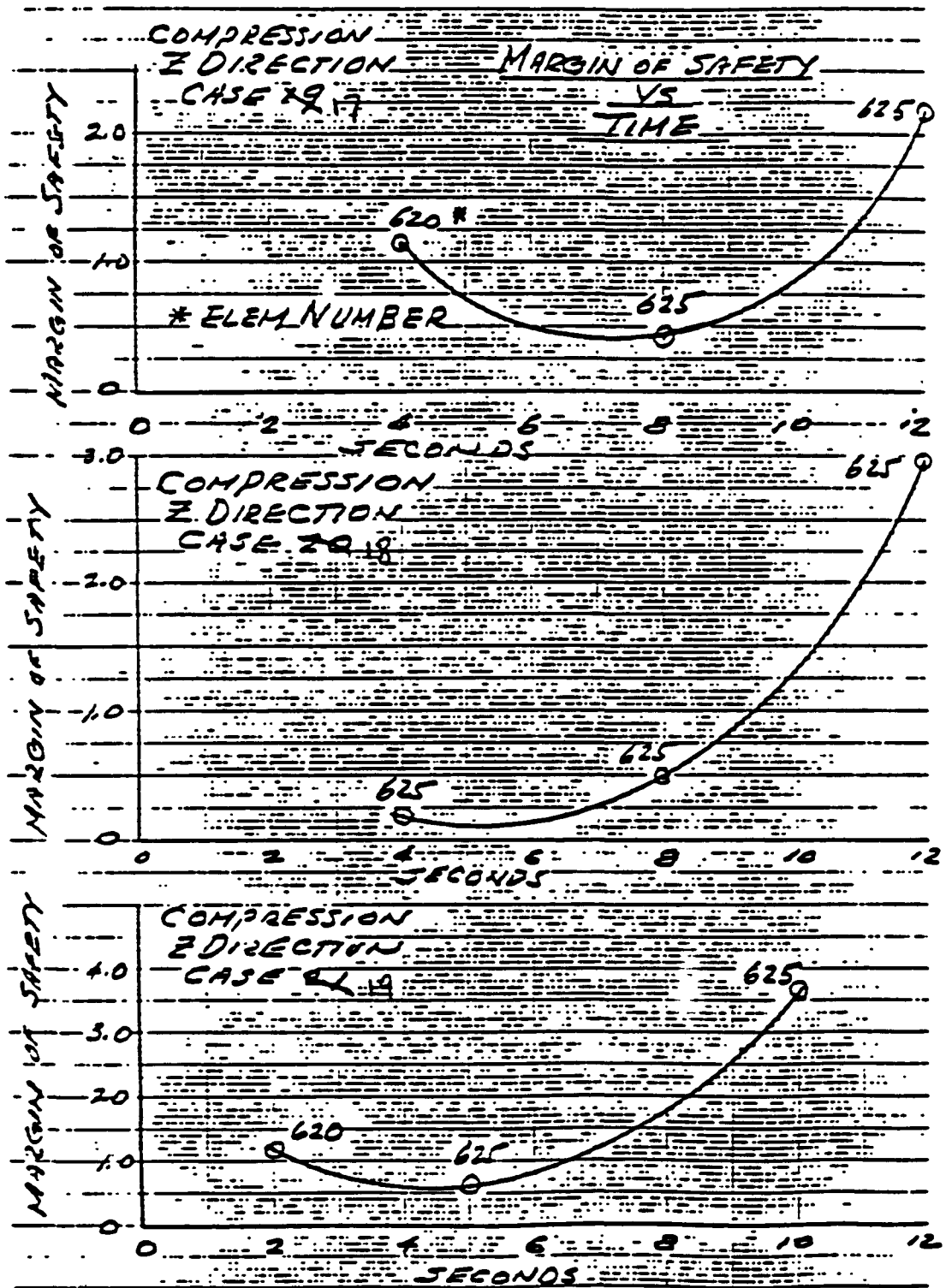


Figure I-125. Margin of Safety vs. Time

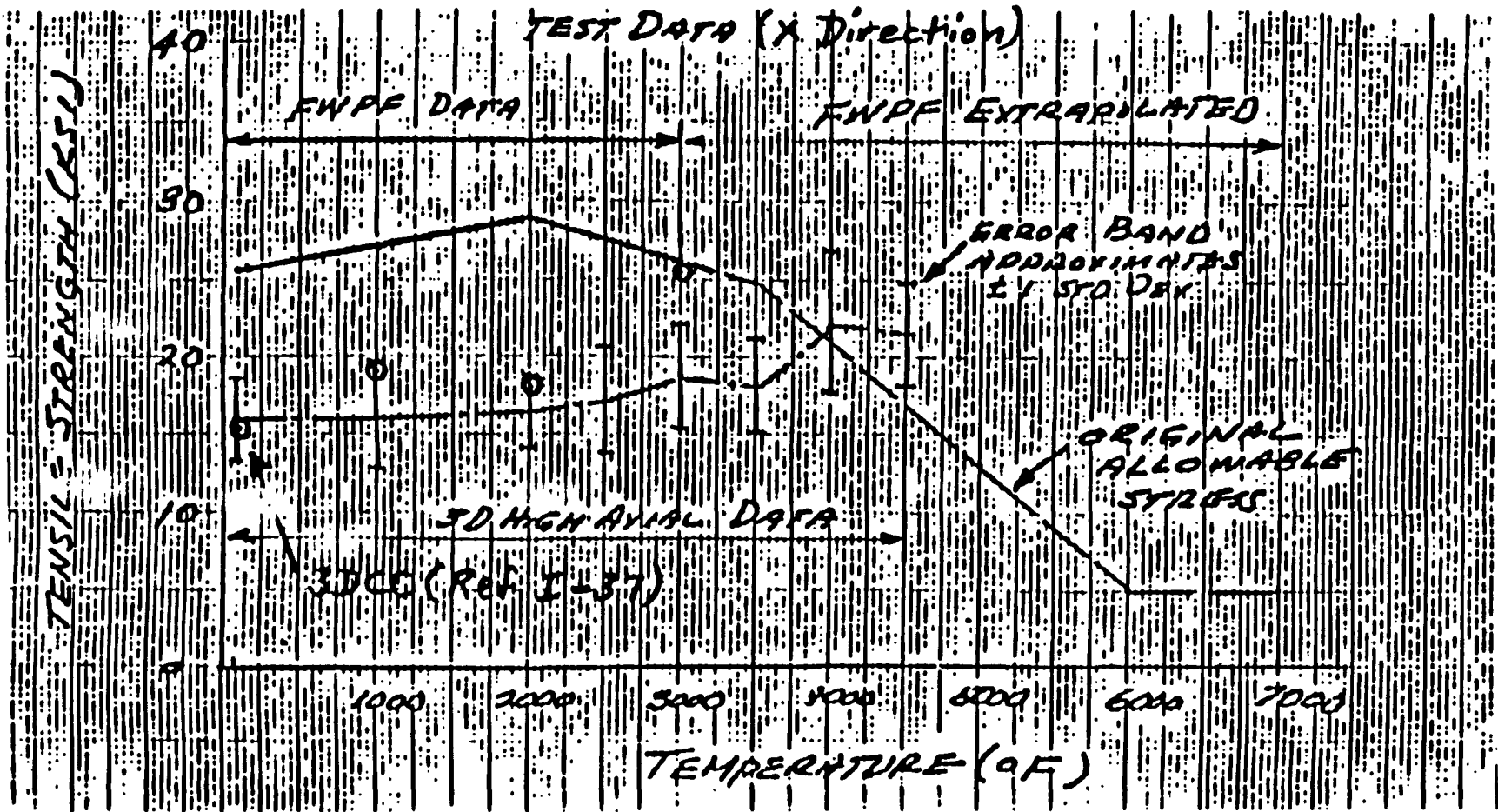


Figure I-126. Comparison of FWP with 3D Carbon/Carbon Composite Data

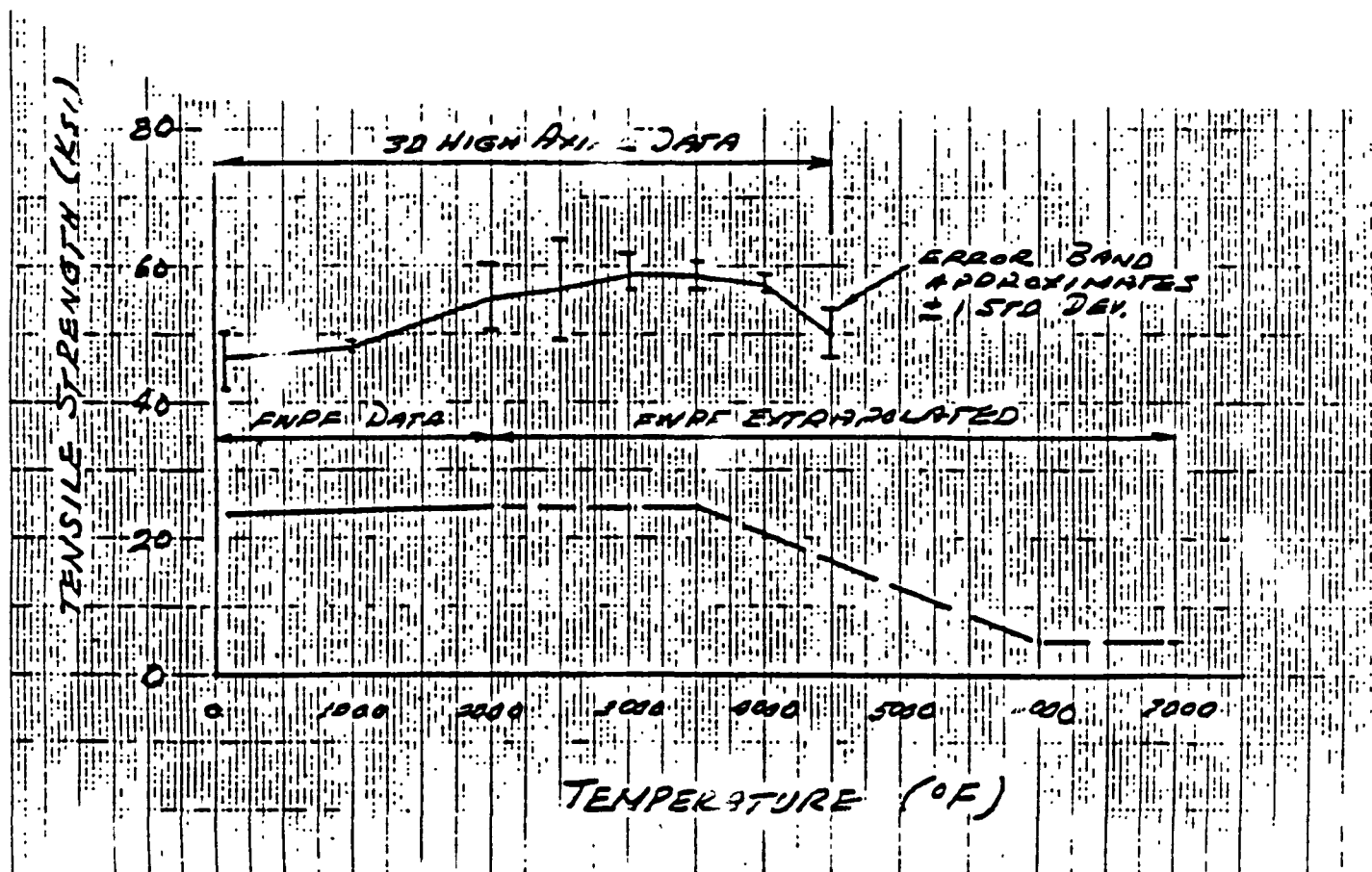


Figure I-127. Comparison of FWP with 3D Carbon/Carbon Composite Data



Three D-High axial carbon-carbon composite is similar in construction to FWPF, but the precursor fiber is different from the PAN fiber used for FWPF. To evaluate the effect of the original fiber on the strength-temperature relationship, tensile strength data were obtained for 3DCC, another carbon-carbon composite which uses the PAN fibers as the precursor. These results (reported in Reference I-37) are for tensile tests in both the hoop and axial direction. The hoop direction tensile values are shown on Figure I-126. Tensile values in the axial direction are plotted on Figure I-127. The object in showing these data from tests of other carbon-carbon composites is to show that the tensile strength increases to at least 4000°F and that the slope of the strength versus temperature curves is similar for carbon-carbon composites.

Figure I-128 shows a curve of allowable tensile stress in the X, Y direction for FWPF extrapolated to 4500°F using the slope of the strength versus temperature curve for the 3D High Axial. Figure I-129 is a curve for the allowable tensile strength of FWPF in the Z direction extrapolated to 4500°F using the slope of the strength versus temperature curve for the 3D-High Axial.

Using these allowables, the minimum margins of safety were recalculated for the X, Y direction. Table I-13 shows these margins of safety and the calculated stresses for the three times in each of the three trajectories. Since all other margins of safety in the Y, Z directions were positive with the original allowables, these margins of safety were not recalculated. The allowable stresses shown in Table I-13 for the two values of temperature that exceed 4500°F were not obtained by extrapolating the curve with the same trend in slope occurring prior to the 4500°F level. Instead, the allowable stress at the 4500°F level was used at these higher levels.

Another method of calculating the margin of safety is based on the calculated strain compared to the strain which causes failure. Table I-14 shows the strain to failure for FWPF taken from Reference I-34 and the strain to failure measured from tests of the 3D - High axial. Failure strain capability is increasing rapidly (with temperature) at 4500°F.

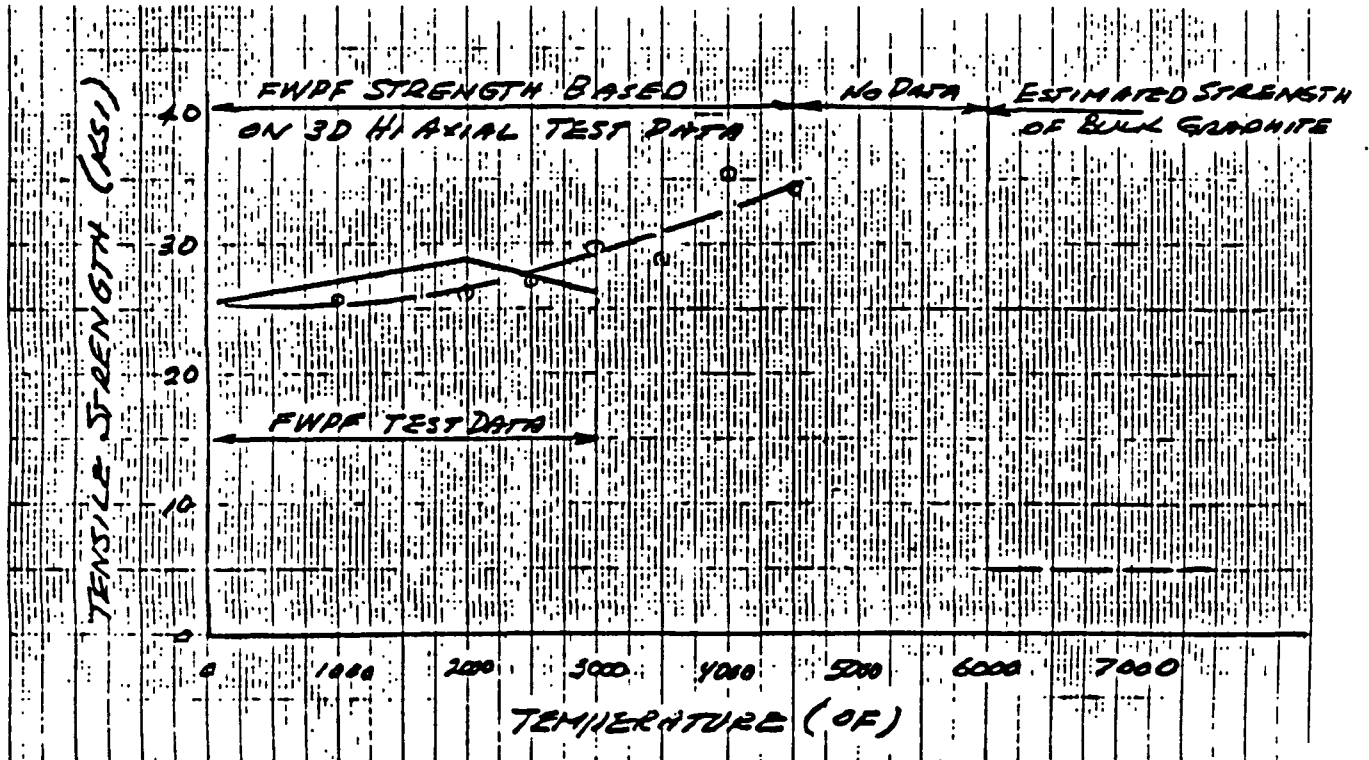


Figure I-128. FWP Allowable Tensile Strength

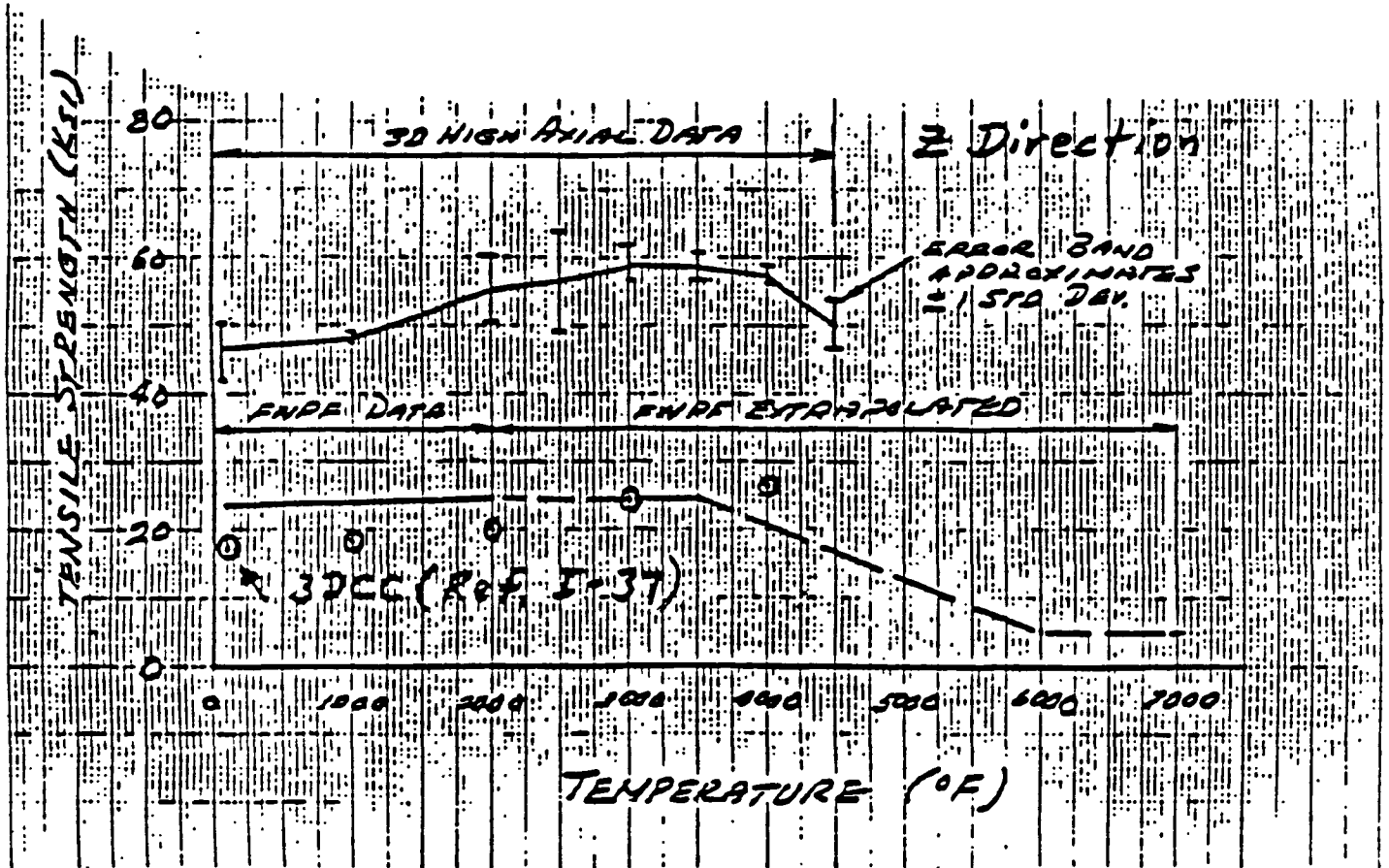


Figure I-129. FWP Allowable Tensile Strength

Table I-13. Steep Angle Reentry Aeroshell Stresses and Margins of Safety\* in X Direction

Case	Time (Sec)	Elem.	Calculate Stresses (PSI)	Temp. (°F)	Allow. Stress (PSI)	M.S.
17	4	635	22,200	3839	29,000	+ .31
17	8	635	23,900	5028	34,000	+ .42
17	12	635	12,200	3970	32,500	+1.66
18	4	635	28,700	4180	33,000	+ .15
18	8	635	27,000	4874	34,000	+ .26
18	12	635	8,920	3781	32,000	+2.57
19	2	635	21,100	3670	31,500	+ .49
19	5	635	30,700	4445	34,000	+ .11
19	10	635	8,360	3461	30,700	+2.67

\* Margin of safety =  $\frac{\text{Allowable Stress}}{\text{Calculated Stress}} - 1 = \text{Factor of Safety} - 1$

Table I-14. Tensile Strain to Failure in the X, Y Direction

Temp. (°F)	FWPF* (%)	3DCC* (%)	3D Hi-Axial (%)
70	.190		.180
1000			.248
2000	.240	.286	.150
2500			.165
3000		.75	.186
3500			.263
4000		1.3	.415
4500			1.000

\* High Modulus (PAN) Fiber used in Manufacture.

Table I-14 compares the tensile strain to failure of the three materials (i.e. FWPF, 3 DCC, 3D Hi-Axial). Note that the two materials using the PAN fiber as the precursor show higher strains to failure than the 3D High Axial. Conservatively, the strains for the 3D High Axial (shown on Figure I-130) were used to calculate the margins of safety based on strain shown in Table I-15. For thermostructural failure, strain criteria are usually preferred to stress criteria since inelastic effects will usually alter stresses much more than strains. Strains computed with an elastic analysis will be smaller than strains computed with plasticity included. When using a strain-based failure criterion against strains computed with an elastic analysis, the margins of safety will not be conservative if the structure would have yielded. However, with the FWPF properties extrapolated on the basis of the trend in the data for the other carbon-carbon composite materials, the yield stress is not exceeded and no yielding occurs.

#### I.5.4 DISCUSSION

Based on GE Reentry Systems Operation (RSO) experience, no thermally induced stress failures have been realized in carbon-carbon composite nose tips either in actual reentry or in testing (e.g. Reference I-35). RSO tests of carbon-carbon composites have shown strengthening up to at least 4500°F in tension. In addition tensile failure strains from tests are significantly higher than the calculated strains.

#### I.5.5 CONCLUSIONS

Based on the analyses performed, the derived allowables and the GE RSO experience with carbon-carbon composites, it is concluded that:

- 1) The minimum margins of safety occur in element 635 (see Figures I-111 and I-120 for location) in the X direction.
- 2) Margins of safety based on FWPF allowables extrapolated from tensile tests to 4500°F of other carbon-carbon composites are positive based both on stress and on strain.
- 3) The GPHS aeroshell should survive reentry for the steep angle reentries defined and in the "face on" stable attitude.

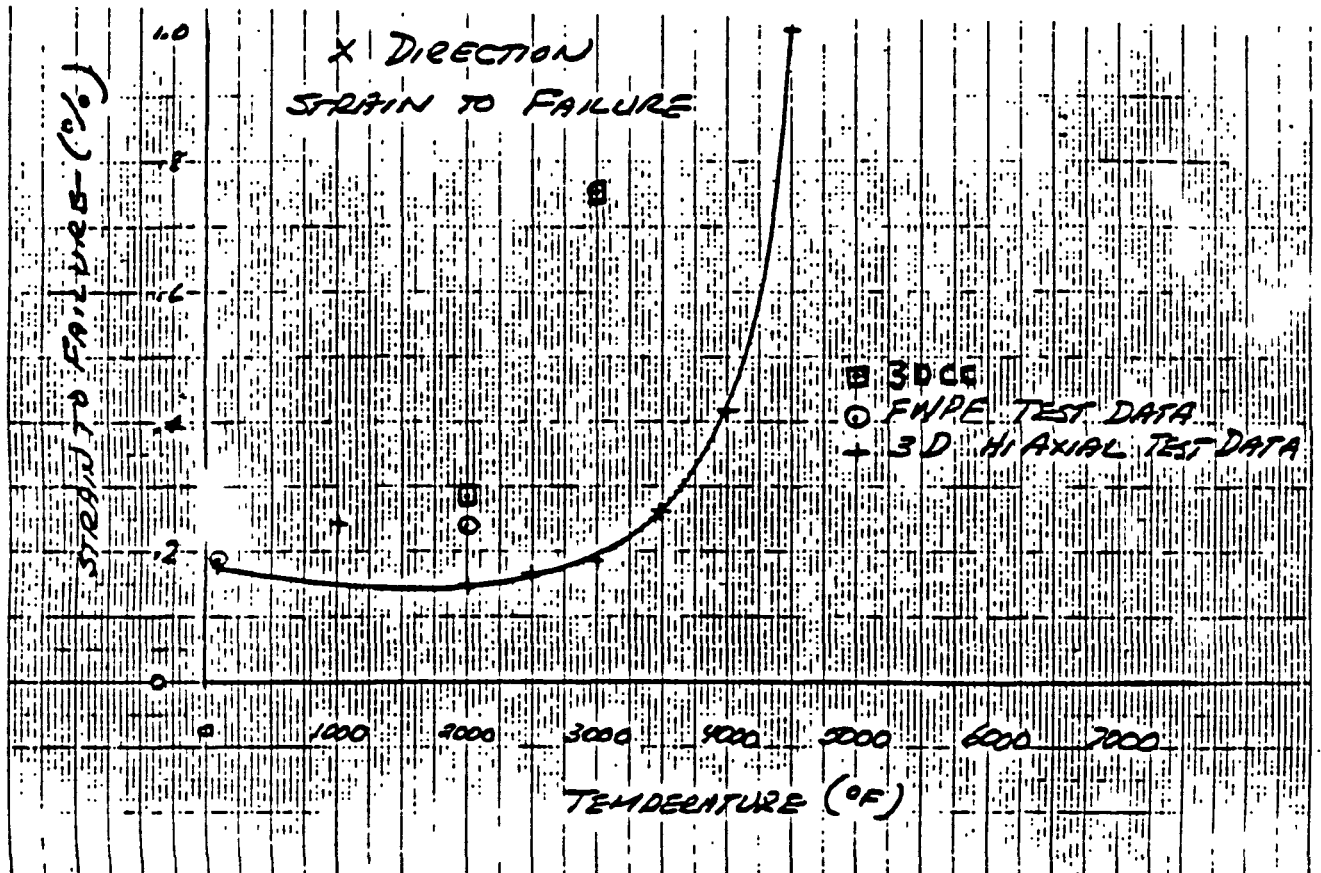


Figure I-130. FWP vs. 3D Hi Axial Carbon/Carbon Strain to Failure

Table I-15. Margin of Safety (X, Y Direction) Based on Strain

Case	Time (Sec)	Stress (PSI)	E (PSI)	Strain $\epsilon$ (%)	Strain to Failure (%)	M.S.
17	4	22,200	$12 \times 10^6$	.185	.36	.946
17	8	23,900	$5.5 \times 10^6$	.435	1.00	1.299
17	12	22,000	$11.5 \times 10^6$	.106	.40	2.774
18	4	28,700	$11 \times 10^6$	.26	.52	1.00
18	8	27,000	$6.6 \times 10^6$	.41	1.0	1.439
18	12	8,920	$12.2 \times 10^6$	.073	.33	3.521
19	2	21,100	$12.7 \times 10^6$	.166	.30	.807
19	5	30,700	$10.0 \times 10^6$	.307	1.0	2.257
19	10	8,360	$13.0 \times 10^6$	.064	.22	2.438

#### I.6 REFERENCES

- I-1 GESP-7186, "Updated Safety Analysis Report for the Galileo Mission and the International Solar-Polar Mission." General Electric Co., April, 1984.
- I-2 Letter to G.D. Walberg, Reentry Subpanel Chairman, from Capt. J.D. Mastens, Air Force Weapons Laboratory, Subject: V-Gamma Results for Galileo, May 11, 1981.
- I-3 Letter to G.J. Schaffer, NASA-Lewis Research Center, from J.E. Sherley, General Dynamics - Convair Division, Subject: Superorbital Reentry Conditions for the Galileo Mission - Steep Reentry Envelope, May 22, 1981.
- I-4 McRonald, A.D. "Galileo RTG Reentry Breakup Analysis," Document No. 1625-228, NASA Jet Propulsion Laboratory, September, 1984.
- I-5 Jaffe, P., et al. "Ulysses Breakup Analysis Final Report." Document No. 1628-54, NASA Jet Propulsion Laboratory, November, 1984.
- I-6 Eatherly, W.P., "Some Considerations on the Thermal Conductivity of CBCF", ORNL internal report of the TSN Projects, October 31, 1983.
- I-7 Taylor, R.E., Groot, H., "Thermal Diffusivity Studies of CBCF", Purdue University, TPRL 357, November, 1983.
- I-8 Letter from W.P. Eatherly, ORNL, to J.C. Hagan, APL, "Graphitization of CBCF", February 9, 1984.
- I-9 Cooper, R.H., Communication to General Electric Co. from Oak Ridge National Laboratory, September 24, 1980.

- I-10 Alexander, C.A., Communication to Fairchild Industries Inc. from Battelle Columbus Laboratories, February 18, 1981.
- I-11 Brenza, P.T., "Sensitivity of the GPHS Thermal Response During Reentry to the Uncertainties for the Thermal Conductivity of the Insulators", JHU/APL, Memo ANSP-255/BFD-4-84-008, May 15, 1984.
- I-12 Conn, D.W., "Computer Programming for the CBCF Air Infiltration and Graphitization", JHU/APL, ANSP-256/BFD-4-84-009, June 7, 1984.
- I-13 Letter from Fornaro, G.F., Southern Research Institute, to Shumann, F., Teledyne Energy Systems, Subject: Thermal Conductivity Data on 3DCC and FWPF, June 14, 1979.
- I-14 Telecommunication, Wei, G.C., Oak Ridge National Laboratory to Hemler, R.J., General Electric Co., Data Package on CBCF3 Insulation.
- I-15 Taylor, R.E., Groot, H., and Shoemaker, R.L., "Thermophysical Properties of Carbon Insulation", Purdue University, December, 1979.
- I-16 Feldman, L., "Trajectory Characteristics of GPHS Configurations A and C", General Electric Co., PIR 6294, April 16, 1981.
- I-17 Beck, G.C., "Results of GPHS Aeroshell/GIS Interface Static Test", General Electric Co., PIR 6271, December 23, 1980.
- I-18 Letter from Fornaro, G.F., Southern Research Institute, to Shumann F., teledyne Energy Systems, "Thermal Expansion Test Data on GE 3DCC and FWPF", May 10, 1979.
- I-19 Perini, L.L., and Conn D.W., "Evaluation of the GPHS 'Face Normal' Stagnation Heating Methodology", APL/JHU Memo ANSP-183/EM-4938, March 28, 1980.
- I-20 Laganelli, A.L., and Fogaroli, R.P., GPHS Stable Reentry Heat Transfer Distribution", GESP-7149 December 21, 1979.
- I-21 Laganelli, A.L., and Fogaroli, R.P., GPHS Pitch and Yaw Heat Transfer Distribution", GESP-7150 Revision A, February 15, 1980.
- I-22 Laganelli, A.L., and Fogaroli, R.P., GPHS Three-Axis Rotation Heat Transfer Distributions", GESP-7154, March 7, 1980.
- I-23 Fogaroli, R.P., "Review of BCL Thermovision Analysis of Subsonic Convective Heat Transfer Coefficient for GPHS Module", 7131-RTG-6290, March 17, 1981.
- I-24 Perini, L.L., "GPHS Subsonic Heat Transfer Test Data Reduction by VPI, BCL and APL", ANSP-217/BFD-4-82-002, March 17, 1982.
- I-25 Laganelli, A.L., and Fogaroli, R.P., "GPHS Single-Axis Rotation (Pitch) Heating Factors", GESP-7151, February 5, 1980.



- I-26 Perini, L.L., "Heat and Mass Transfer Correlation Equations for Subliming Graphite in High Speed Flow", ANSP-M-11, APL/JHU, August, 1974.
- I-27 Perini, L.L., "Compilation of Experimental Stagnation Point Velocity Gradients and Heat Transfer Data in Subsonic and Supersonic Flow", ANSP-068, August 14, 1975.
- I-28 Huber, P.W., "Hypersonic Shock Heated Flow Parameters for Velocities to 46,000 fps and Altitudes to 320,000 Feet", NASA TR R163, 1963 Hilsenroth and Klein, (title unknown), AEDC 59-20, Arnold Engineering, December, 1959.
- I-29 Letter from G.C. Wei, Oak Ridge National Laboratory, to A. Schock, Fairchild Industries, Inc., January 23, 1980.
- I-30 77SDS4206 "Final Safety Analysis Report for the MJS-77 Mission" General Electric Company, January 1977.
- I-31 Letter from R.L. Heestand, Oak Ridge National Laboratory, to R. Hartman, General Electric Company, January 28, 1980.
- I-32 Letter from C.G. Halsted, DOE Savannah River Operations Office to G. Bennett, DOE Advanced Nuclear Systems and Projects Division, Subject: Pu-238 Thermal Properties, March 10, 1980.
- I-33 Enclosure 1, Minutes from INSRP Reentry Subpanel Meeting, April 2-4, 1985, by Ken Waeber (APL).
- I-34 Evaluation of Carbon-Carbon Composites for the PAN Pilot Production Program (P<sup>4</sup>), Volume II: Data Analysis and Interpretation, AFML-TR-78-2 Volume II, Southern Research Institute, May 1979.
- I-35 TR-77-149, "Material Requirements Definition (MRD) Program, Vol. II, Fine-Weave Carbon Carbon Noretip Requirements," Section 5.2, Thermostructural Overtest, Prototype Developments Associates, Inc., For SAMSO, December 1977.
- I-36 Characterization of 3D High Axial Carbon-Carbon Composites: GE, RSO PIR U-74-97-PW-A243, dated October 7, 1974.
- I-37 "Mechanical Properties of a GE 3DCC Cylinder;" Southern Research Institute, SoRI-EAS-81-282-4639-I-F, April, 1981.
- I-A Crosby, W.A., and Knox, E.C. "Heat Transfer and Static Stability Tests of the General Purpose Heat Source (GPHS) Configurations at Mach 8.0" AEDC-TSR-80-V7, Arnold Engineering Development Center, U.S. Air Force, January 1980.
- I-B Feldman, L. "Trajectory Characteristics of GPHS Configurations A and C." General Electric Internal Document No. PIR U-7143-RTG-6294, April 16, 1981.

- I-C Applied Physics Laboratory/John Hopkins University Memo ANSP-247, BFD-4-83-031 by J.C. Hagan to Distribution, Subject: Six Degree-of-Freedom Motion Simulation for the General Purpose Heat Source," October 21, 1983.
- I-D Feldman, L., "Final Report on Wallop's Island Drop Tests". General Electric Co./Space Division Internal Report No. PIR-U-7143-RTG-6235, 14 August 1980.
- I-E Hoerner, S.F., Fluid Dynamic Drag, 1965.
- I-F Presentation made by L. Feldman, General Electric Co., to the INSRP Re-Entry Subpanel on June 5, 1980.
- I-G Letter from J. C. Hagan, APL/JHU, to Dr. G. L. Bennett, ASNP/DOE, Subject: "Transmittal of Report Describing Test Operations for Subsonic Aerodynamic Tests of the GPHS Module", ATD-RL-84-052, ANSP-L-766, July 17, 1984.